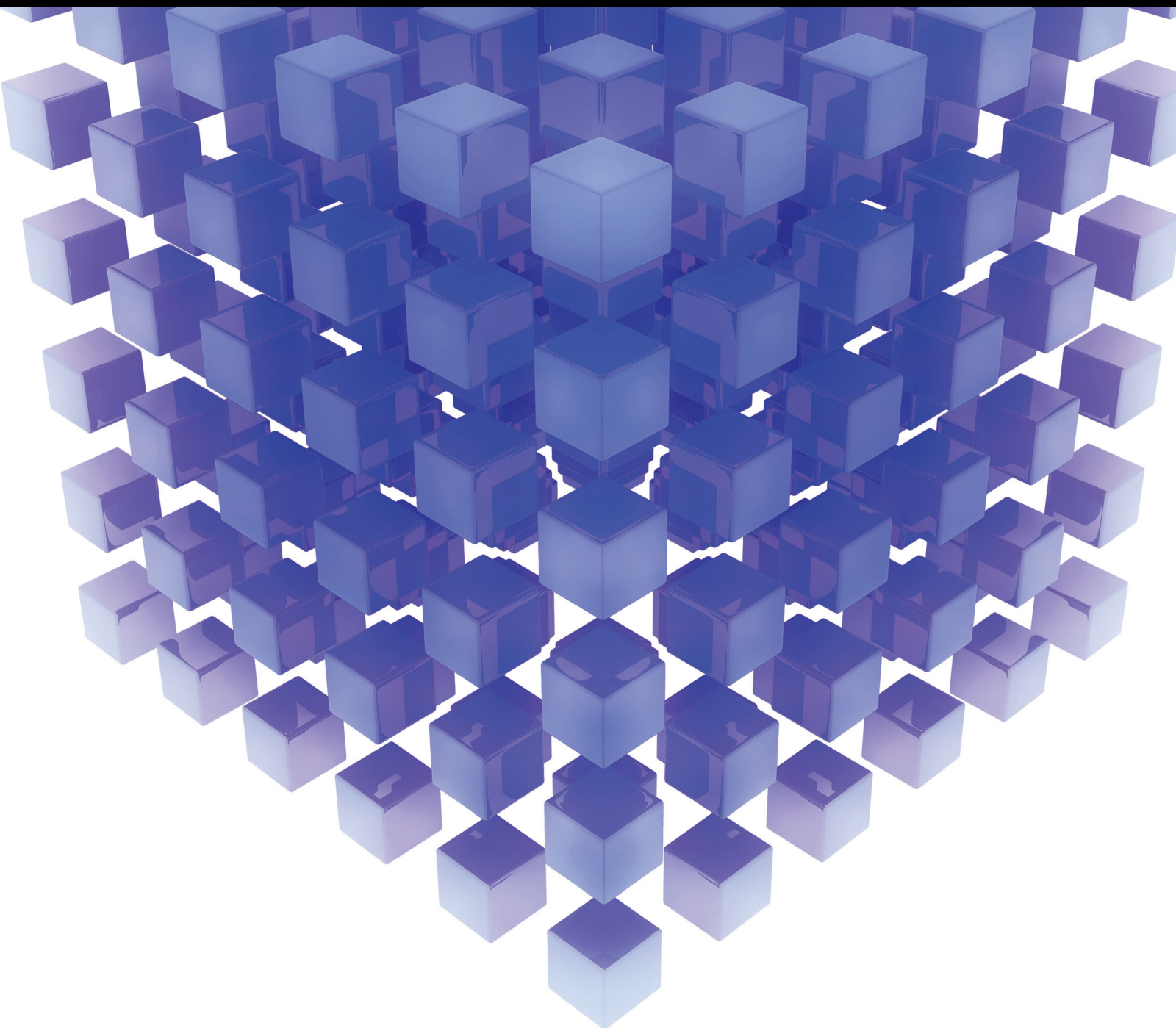


Mathematical Problems in Engineering

Computational Methods for Engineering Science

Guest Editors: K. M. Liew, L. W. Zhang, J. N. Reddy, and Shaofan Li





Computational Methods for Engineering Science

Mathematical Problems in Engineering

Computational Methods for Engineering Science

Guest Editors: K. M. Liew, L. W. Zhang, J. N. Reddy,
and Shaofan Li



Copyright © 2015 Hindawi Publishing Corporation. All rights reserved.

This is a special issue published in “Mathematical Problems in Engineering.” All articles are open access articles distributed under the Creative Commons Attribution License, which permits unrestricted use, distribution, and reproduction in any medium, provided the original work is properly cited.

Editorial Board

Mohamed Abd El Aziz, Egypt
Farid Abed-Meraim, France
Silvia Abrahão, Spain
Paolo Addresso, Italy
Claudia Adduce, Italy
Ramesh Agarwal, USA
Juan C. Agüero, Australia
Ricardo Aguilar-López, Mexico
Tarek Ahmed-Ali, France
Hamid Akbarzadeh, Canada
Muhammad N. Akram, Norway
Mohammad-Reza Alam, USA
Salvatore Alfonzetti, Italy
Francisco Alhama, Spain
Juan A. Almendral, Spain
Lionel Amodeo, France
Igor Andrianov, Germany
Sebastian Anita, Romania
Renata Archetti, Italy
Felice Arena, Italy
Sabri Arik, Turkey
Fumihiro Ashida, Japan
Hassan Askari, Canada
Mohsen Asle Zaeem, USA
Francesco Aymerich, Italy
Seungik Baek, USA
Khaled Bahlali, France
Laurent Bako, France
Stefan Balint, Romania
Alfonso Banos, Spain
Roberto Baratti, Italy
Martino Bardi, Italy
Azeddine Beghdadi, France
Abdel-Hakim Bendada, Canada
Ivano Benedetti, Italy
Elena Benvenuti, Italy
Jamal Berakdar, Germany
Enrique Berjano, Spain
Jean-Charles Beugnot, France
Simone Bianco, Italy
David Bigaud, France
Jonathan N. Blakely, USA
Paul Bogdan, USA
Daniela Boso, Italy
Abdel-Ouahab Boudraa, France

Francesco Braghin, Italy
M. J. Brennan, United Kingdom
Maurizio Brocchini, Italy
Julien Bruchon, France
Javier Buldu, Spain
Tito Busani, USA
P. Cacciola, United Kingdom
Salvatore Caddemi, Italy
Jose E. Capilla, Spain
Ana Carpio, Spain
Miguel E. Cerrolaza, Spain
Mohammed Chadli, France
Gregory Chagnon, France
Ching-Ter Chang, Taiwan
M. J. Chappell, United Kingdom
Kacem Chehdi, France
Chunlin Chen, China
Xinkai Chen, Japan
Francisco Chicano, Spain
Hung-Yuan Chung, Taiwan
Joaquim Ciurana, Spain
John D. Clayton, USA
Carlo Cosentino, Italy
Paolo Crippa, Italy
Erik Cuevas, Mexico
Peter Dabnichki, Australia
Luca D'Acerno, Italy
Weizhong Dai, USA
Purushothaman Damodaran, USA
Farhang Daneshmand, Canada
Fabio De Angelis, Italy
Stefano de Miranda, Italy
Filippo de Monte, Italy
Xavier Delorme, France
Luca Deseri, USA
Yannis Dimakopoulos, Greece
Zhengtao Ding, United Kingdom
Ralph B. Dinwiddie, USA
Mohamed Djemai, France
Alexandre B. Dolgui, France
George S. Dulikravich, USA
Bogdan Dumitrescu, Finland
Horst Ecker, Austria
Ahmed El Hajjaji, France
Fouad Erchiqui, Canada

Anders Eriksson, Sweden
Giovanni Falsone, Italy
Hua Fan, China
Yann Favennec, France
Giuseppe Fedele, Italy
Roberto Fedele, Italy
Jacques Ferland, Canada
Jose R. Fernandez, Spain
Simme Douwe Flapper, Netherlands
Thierry Floquet, France
Eric Florentin, France
Francesco Franco, Italy
Tomonari Furukawa, USA
Mohamed Gadala, Canada
Matteo Gaeta, Italy
Zoran Gajic, USA
Ciprian G. Gal, USA
Ugo Galvanetto, Italy
Akemi Gálvez, Spain
Rita Gamberini, Italy
Maria Gandarias, Spain
Arman Ganji, Canada
Xin-Lin Gao, USA
Zhong-Ke Gao, China
Giovanni Garcea, Italy
Fernando García, Spain
Laura Gardini, Italy
Alessandro Gasparetto, Italy
Vincenzo Gattulli, Italy
Oleg V. Gendelman, Israel
Mergen H. Ghayesh, Australia
Anna M. Gil-Lafuente, Spain
Hector Gómez, Spain
Rama S. R. Gorla, USA
Oded Gottlieb, Israel
Antoine Grall, France
Jason Gu, Canada
Quang Phuc Ha, Australia
Ofer Hadar, Israel
Masoud Hajarian, Iran
Frédéric Hamelin, France
Zhen-Lai Han, China
Thomas Hanne, Switzerland
Takashi Hasuike, Japan
Xiao-Qiao He, China

M.I. Herreros, Spain
 Vincent Hilaire, France
 Eckhard Hitzer, Japan
 Jaromir Horacek, Czech Republic
 Muneo Hori, Japan
 András Horváth, Italy
 Gordon Huang, Canada
 Sajid Hussain, Canada
 Asier Ibeas, Spain
 Giacomo Innocenti, Italy
 Emilio Insfran, Spain
 Nazrul Islam, USA
 Payman Jalali, Finland
 Reza Jazar, Australia
 Khalide Jbilou, France
 Linni Jian, China
 Bin Jiang, China
 Zhongping Jiang, USA
 Ningde Jin, China
 Grand R. Joldes, Australia
 Joaquim Joao Judice, Portugal
 Tadeusz Kaczorek, Poland
 Tamas Kalmar-Nagy, Hungary
 Tomasz Kapitaniak, Poland
 Haranath Kar, India
 Konstantinos Karamanos, Belgium
 C. M. Khalique, South Africa
 Do Wan Kim, Republic of Korea
 Nam-Il Kim, Republic of Korea
 Oleg Kirillov, Germany
 Manfred Krafczyk, Germany
 Frederic Kratz, France
 Jurgen Kurths, Germany
 Kyandoghere Kyamakya, Austria
 Davide La Torre, Italy
 Risto Lahdelma, Finland
 Hak-Keung Lam, United Kingdom
 Antonino Laudani, Italy
 Aime' Lay-Ekuakille, Italy
 Marek Lefik, Poland
 Yaguo Lei, China
 Thibault Lemaire, France
 Stefano Lenci, Italy
 Roman Lewandowski, Poland
 Qing Q. Liang, Australia
 Panos Liatsis, United Kingdom
 Peide Liu, China
 Peter Liu, Taiwan
 Wanquan Liu, Australia
 Yan-Jun Liu, China
 Jean J. Loiseau, France
 Paolo Lonetti, Italy
 Luis M. López-Ochoa, Spain
 Vassilios C. Loukopoulos, Greece
 Valentin Lychagin, Norway
 Fazal M. Mahomed, South Africa
 Yassir T. Makkawi, United Kingdom
 Nouredine Manamanni, France
 Didier Maquin, France
 Paolo Maria Mariano, Italy
 Benoit Marx, France
 Gérard A. Maugin, France
 Driss Mehdi, France
 Roderick Melnik, Canada
 Pasquale Memmolo, Italy
 Xiangyu Meng, Canada
 Jose Merodio, Spain
 Luciano Mescia, Italy
 Laurent Mevel, France
 Y. V. Mikhlin, Ukraine
 Aki Mikkola, Finland
 Hiroyuki Mino, Japan
 Pablo Mira, Spain
 Vito Mocella, Italy
 Roberto Montanini, Italy
 Gisele Mophou, France
 Rafael Morales, Spain
 Aziz Moukrim, France
 Emiliano Mucchi, Italy
 Domenico Mundo, Italy
 Jose J. Muñoz, Spain
 Giuseppe Muscolino, Italy
 Marco Mussetta, Italy
 Hakim Naceur, France
 Hassane Naji, France
 Dong Ngoduy, United Kingdom
 Tatsushi Nishi, Japan
 Ben T. Nohara, Japan
 Mohammed Nouari, France
 Mustapha Nourelfath, Canada
 Sotiris K. Ntouyas, Greece
 Roger Ohayon, France
 Mitsuhiro Okayasu, Japan
 Javier Ortega-Garcia, Spain
 Alejandro Ortega-Moñux, Spain
 Naohisa Otsuka, Japan
 Erika Ottaviano, Italy
 Alkis S. Paipetis, Greece
 Alessandro Palmeri, United Kingdom
 Anna Pandolfi, Italy
 Elena Panteley, France
 Manuel Pastor, Spain
 Pubudu N. Pathirana, Australia
 Francesco Pellicano, Italy
 Haipeng Peng, China
 Mingshu Peng, China
 Zhike Peng, China
 Marzio Pennisi, Italy
 Matjaz Perc, Slovenia
 Francesco Pesavento, Italy
 Maria do Rosário Pinho, Portugal
 Antonina Pirrotta, Italy
 Vicent Pla, Spain
 Javier Plaza, Spain
 Jean-Christophe Ponsart, France
 Mauro Pontani, Italy
 Stanislav Potapenko, Canada
 Sergio Preidikman, USA
 Christopher Pretty, New Zealand
 Carsten Proppe, Germany
 Luca Pugi, Italy
 Yuming Qin, China
 Dane Quinn, USA
 Jose Ragot, France
 Kumbakonam Ramamani Rajagopal, USA
 Gianluca Ranzi, Australia
 Sivaguru Ravindran, USA
 Alessandro Reali, Italy
 Oscar Reinoso, Spain
 Nidhal Rezg, France
 Ricardo Riazza, Spain
 Gerasimos Rigatos, Greece
 José Rodellar, Spain
 Rosana Rodriguez-Lopez, Spain
 Ignacio Rojas, Spain
 Carla Roque, Portugal
 Aline Roumy, France
 Debasish Roy, India
 Rubén Ruiz García, Spain
 Antonio Ruiz-Cortes, Spain
 Ivan D. Rukhlenko, Australia
 Mazen Saad, France
 Kishin Sadarangani, Spain
 Mehrdad Saif, Canada

Miguel A. Salido, Spain
Roque J. Salterén, Spain
Francisco J. Salvador, Spain
Alessandro Salvini, Italy
Maura Sandri, Italy
Miguel A. F. Sanjuan, Spain
Juan F. San-Juan, Spain
Roberta Santoro, Italy
Ilmar Ferreira Santos, Denmark
José A. Sanz-Herrera, Spain
Nickolas S. Sapidis, Greece
Evangelos J. Sapountzakis, Greece
Andrey V. Savkin, Australia
Valery Sbitnev, Russia
Thomas Schuster, Germany
M. Seaid, United Kingdom
Lotfi Senhadji, France
Joan Serra-Sagrasta, Spain
Leonid Shaikhet, Ukraine
Hassan M. Shanechi, USA
Sanjay K. Sharma, India
Bo Shen, Germany
Babak Shotorban, USA
Zhan Shu, United Kingdom
Dan Simon, USA
Luciano Simoni, Italy
Christos H. Skiadas, Greece
Michael Small, Australia
Francesco Soldovieri, Italy
Raffaele Solimene, Italy

Ruben Specogna, Italy
Sri Sridharan, USA
Ivanka Stamova, USA
Yakov Strelniker, Israel
Sergey A. Suslov, Australia
Thomas Svensson, Sweden
Andrzej Swierniak, Poland
Yang Tang, Germany
Sergio Teggi, Italy
Alexander Timokha, Norway
Rafael Toledo, Spain
Gisella Tomasini, Italy
Francesco Tornabene, Italy
Antonio Tornambe, Italy
Fernando Torres, Spain
Fabio Tramontana, Italy
Sébastien Tremblay, Canada
I. N. Trendafilova, United Kingdom
George Tsiatas, Greece
A. Tsourdos, United Kingdom
Vladimir Turetsky, Israel
Mustafa Tutar, Spain
Efstratios Tzirtzilakis, Greece
Filippo Ubertini, Italy
Francesco Ubertini, Italy
Hassan Ugail, United Kingdom
Giuseppe Vairo, Italy
Kuppalapalle Vajravelu, USA
Robertt A. Valente, Portugal
Pandian Vasant, Malaysia

Miguel E. Vázquez-Méndez, Spain
Josep Vehi, Spain
Kalyana C. Veluvolu, Republic of Korea
Fons J. Verbeek, Netherlands
Franck J. Vernerey, USA
Georgios Veronis, USA
Anna Vila, Spain
Rafael J. Villanueva, Spain
Uchechukwu E. Vincent, United Kingdom
Mirko Viroli, Italy
Michael Vynnycky, Sweden
Junwu Wang, China
Shuming Wang, Singapore
Yan-Wu Wang, China
Yongqi Wang, Germany
Desheng D. Wu, Canada
Yuqiang Wu, China
Guangming Xie, China
Xuejun Xie, China
Gen Qi Xu, China
Hang Xu, China
Xinggang Yan, United Kingdom
Luis J. Yebra, Spain
Peng-Yeng Yin, Taiwan
Ibrahim Zeid, USA
Huaguang Zhang, China
Qingling Zhang, China
Jian Guo Zhou, United Kingdom
Quanxin Zhu, China
Mustapha Zidi, France

Contents

Computational Methods for Engineering Science, K. M. Liew, L. W. Zhang, J. N. Reddy, and Shaofan Li
Volume 2015, Article ID 842103, 1 page

Simulating the Range Expansion of *Spartina alterniflora* in Ecological Engineering through Constrained Cellular Automata Model and GIS, Zongsheng Zheng, Bo Tian, L. W. Zhang, and Guoliang Zou
Volume 2015, Article ID 875817, 8 pages

Free Vibration Analysis of Symmetrically Laminated Folded Plate Structures Using an Element-Free Galerkin Method, L. X. Peng
Volume 2015, Article ID 124296, 13 pages

SPH Simulation of Acoustic Waves: Effects of Frequency, Sound Pressure, and Particle Spacing, Y. O. Zhang, T. Zhang, H. Ouyang, and T. Y. Li
Volume 2015, Article ID 348314, 7 pages

Numerical Approximation of Nonlinear Klein-Gordon Equation Using an Element-Free Approach, Dong-mei Huang, Guo-liang Zou, and L. W. Zhang
Volume 2015, Article ID 548905, 11 pages

Elastic Properties of Boron-Nitride Nanotubes through an Atomic Simulation Method, Jixiao Tao, Guangmin Xu, and Yuzhou Sun
Volume 2015, Article ID 240547, 5 pages

Transverse Vibration of Axially Moving Functionally Graded Materials Based on Timoshenko Beam Theory, Suihan Sui, Ling Chen, Cheng Li, and Xinpei Liu
Volume 2015, Article ID 391452, 9 pages

Life Prediction on a T700 Carbon Fiber Reinforced Cylinder with Limited Accelerated Life Testing Data, Ma Xiaobing and Zhang Yongbo
Volume 2015, Article ID 902157, 9 pages

Optimal Harvesting Policies for a Stochastic Food-Chain System with Markovian Switching, Yanming Ge and Yifan Xu
Volume 2015, Article ID 875159, 8 pages

Assembly Line Productivity Assessment by Comparing Optimization-Simulation Algorithms of Trajectory Planning for Industrial Robots, Francisco Rubio, Carlos Llopis-Albert, Francisco Valero, and Josep Lluís Suñer
Volume 2015, Article ID 931048, 10 pages

Numerical Simulation of the Generalized Newtonian Free Surface Flows by a Density Reinitialization SPH Method, Jinlian Ren, Weigang Lu, and Tao Jiang
Volume 2015, Article ID 915973, 17 pages

Drag Reduction in Turbulent Boundary Layers with Half Wave Wall Oscillations, Maneesh Mishra and Martin Skote
Volume 2015, Article ID 253249, 7 pages

Numerical Study of Correlation of Fluid Particle Acceleration and Turbulence Intensity in Swirling Flow, Nan Gui, Xingtuan Yang, Jie Yan, Jiyuan Tu, and Shengyao Jiang
Volume 2015, Article ID 179072, 8 pages

Computational Methods for Coupled Fluid-Structure-Electromagnetic Interaction Models with Applications to Biomechanics, Felix Mihai, Inja Youn, Igor Griva, and Padmanabhan Seshaiyer
Volume 2015, Article ID 253179, 10 pages

Controlling Force in Polarization-Maintaining Fiber Fused Biconical Tapering, Wei Zhang, Weibin Rong, Lefeng Wang, Qing Zheng, and Lining Sun
Volume 2015, Article ID 676457, 9 pages

Predictor-Corrector LU-SGS Discontinuous Galerkin Finite Element Method for Conservation Laws, Xinrong Ma, Sanyang Liu, and Gongnan Xie
Volume 2015, Article ID 940257, 11 pages

A Reconstruction Procedure Associated with Switching Lyapunov Function for Relaxing Stability Assurance of T-S Fuzzy Mode, Yau-Tarng Juang, Chih-Peng Huang, and Chung-Lin Yan
Volume 2015, Article ID 147817, 12 pages

Global Analysis of a Delayed Impulsive Lotka-Volterra Model with Holling III Type Functional Response, Hui Wang, Xiaomin Hu, Zhixing Hu, and Fucheng Liao
Volume 2015, Article ID 473539, 15 pages

Modeling and Analysis in Marine Big Data: Advances and Challenges, Dongmei Huang, Danfeng Zhao, Lifei Wei, Zhenhua Wang, and Yanling Du
Volume 2015, Article ID 384742, 13 pages

Computational Fluid Dynamics Simulation of Oxygen Seepage in Coal Mine Goaf with Gas Drainage, Guo-Qing Shi, Mao-xi Liu, Yan-Ming Wang, Wen-Zheng Wang, and De-Ming Wang
Volume 2015, Article ID 723764, 9 pages

A Practical Method of Nonprobabilistic Reliability and Parameter Sensitivity Analysis Based on Space-Filling Design, Xin-dang He, Wen-xuan Gou, Yong-shou Liu, and Zong-zhan Gao
Volume 2015, Article ID 561202, 12 pages

Numerical Simulation of Interaction between Hall Thruster CEX Ions and SMART-1 Spacecraft, Kang Shan, Yuchuan Chu, Qingyu Li, Liang Zheng, and Yong Cao
Volume 2015, Article ID 418493, 8 pages

Fractional Dynamics in Calcium Oscillation Model, Yoothana Suansook and Kittipaitoonwattanakij
Volume 2015, Article ID 276059, 13 pages

Ship Electric Propulsion Simulation System Reliability Evaluation Based on Improved D-S Expert Weight Calculation Method, Bing Li, Guoliang Gu, Bowen Xing, and Lihong Li
Volume 2015, Article ID 314058, 5 pages

Simulation of Cavitation Water Flows, Piroz Zamankhan
Volume 2015, Article ID 872573, 16 pages

Evolutionary Game Analysis of Competitive Information Dissemination on Social Networks: An Agent-Based Computational Approach, Qing Sun and Zhong Yao

Volume 2015, Article ID 679726, 12 pages

Modeling and Querying Business Data with Artifact Lifecycle, Danfeng Zhao, Wei Zhao, Le Sun, and Dongmei Huang

Volume 2015, Article ID 506272, 9 pages

Seismic Stability Time-Frequency Analysis Method of Reinforced Retaining Wall, Yang Changwei, Zhang Shixian, Zhang Jianjing, and Bi Junwei

Volume 2015, Article ID 178692, 8 pages

Solving the Maximum Weighted Clique Problem Based on Parallel Biological Computing Model,

Zhaocai Wang, Jiangfeng Qin, Zuwen Ji, Dongmei Huang, and Lei Li

Volume 2015, Article ID 275019, 8 pages

Global Quasi-Minimal Residual Method for Image Restoration, Jun Liu, Ting-Zhu Huang,

Xiao-Guang Lv, Hao Xu, and Xi-Le Zhao

Volume 2015, Article ID 943072, 8 pages

An Extended Assessment of Fluid Flow Models for the Prediction of Two-Dimensional Steady-State Airfoil Aerodynamics, José F. Herbert-Acero, Oliver Probst, Carlos I. Rivera-Solorio,

Krystel K. Castillo-Villar, and Santos Méndez-Díaz

Volume 2015, Article ID 854308, 31 pages

Parallel Numerical Simulations of Three-Dimensional Electromagnetic Radiation with MPI-CUDA Paradigms, Bing He, Long Tang, Jiang Xie, XiaoWei Wang, and AnPing Song

Volume 2015, Article ID 823426, 9 pages

Development of Fast-Time Stochastic Airport Ground and Runway Simulation Model and Its Traffic Analysis, Ryota Mori

Volume 2015, Article ID 919736, 11 pages

An Analytical Solution of Partially Penetrating Hydraulic Fractures in a Box-Shaped Reservoir,

He Zhang, Xiaodong Wang, and Lei Wang

Volume 2015, Article ID 726910, 11 pages

Generalized Finite Difference Time Domain Method and Its Application to Acoustics, Jianguo Wei, Song Wang, Qingzhi Hou, and Jianwu Dang

Volume 2015, Article ID 640305, 13 pages

Active Learning Algorithms for the Classification of Hyperspectral Sea Ice Images, Yanling Han, Jing Ren, Zhonghua Hong, Yun Zhang, Long Zhang, Wanting Meng, and Qiming Gu

Volume 2015, Article ID 124601, 10 pages

A Numerical Study on the Improvement of Suction Performance and Hydraulic Efficiency for a Mixed-Flow Pump Impeller, Sung Kim, Kyoung-Yong Lee, Jin-Hyuk Kim, and Young-Seok Choi

Volume 2014, Article ID 269483, 17 pages

A Comparative Assessment of Spalart-Shur Rotation/Curvature Correction in RANS Simulations in a Centrifugal Pump Impeller, Ran Tao, Ruofu Xiao, Wei Yang, and Fujun Wang
Volume 2014, Article ID 342905, 9 pages

Element-Free Approximation of Generalized Regularized Long Wave Equation, Dong-Mei Huang and L. W. Zhang
Volume 2014, Article ID 206017, 10 pages

A Mixed Element Method for the Desorption-Diffusion-Seepage Model of Gas Flow in Deformable Coalbed Methane Reservoirs, Lei Yang
Volume 2014, Article ID 735931, 10 pages

Characteristic Value Method of Well Test Analysis for Horizontal Gas Well, Xiao-Ping Li, Ning-Ping Yan, and Xiao-Hua Tan
Volume 2014, Article ID 472728, 10 pages

A Smoothing Process of Multicolor Relaxation for Solving Partial Differential Equation by Multigrid Method, Xingwen Zhu and Lixiang Zhang
Volume 2014, Article ID 490156, 10 pages

Effect of Rotation on Wave Propagation in Hollow Poroelastic Circular Cylinder, S. M. Abo-Dahab, A. M. Abd-Alla, and S. Alqosami
Volume 2014, Article ID 879262, 16 pages

Unsteady Model for Transverse Fluid Elastic Instability of Heat Exchange Tube Bundle, Jun Liu, Chen Huang, and Naibing Jiang
Volume 2014, Article ID 942508, 7 pages

Fingerprint Classification Combining Curvelet Transform and Gray-Level Cooccurrence Matrix, Jing Luo, Dan Song, Chunbo Xiu, Shuze Geng, and Tingting Dong
Volume 2014, Article ID 592928, 15 pages

Research on Construction Optimization of Three-Connected-Arch Hydraulic Underground Cavities Considering Creep Property, Bao-yun Zhao, Nian-chun Xu, Zi-yun Li, and Tong-qing Wu
Volume 2014, Article ID 967975, 11 pages

Numerical Simulation of Soil Water Movement under Subsurface Irrigation, Xinqiang Qin, Xianbao Duan, Lijun Su, Xiaoqin Shen, and Gang Hu
Volume 2014, Article ID 126398, 9 pages

A Meshfree Quasi-Interpolation Method for Solving Burgers' Equation, Mingzhu Li, Lijuan Chen, and Qiang Ma
Volume 2014, Article ID 492072, 8 pages

Pressure Pulsations of the Blade Region in S-Shaped Shaft-Extension Tubular Pumping System, Fan Yang and Chao Liu
Volume 2014, Article ID 820135, 10 pages

MINRES Seed Projection Methods for Solving Symmetric Linear Systems with Multiple Right-Hand Sides, Xin Li, Hao Liu, and Jingfu Zhu
Volume 2014, Article ID 357874, 6 pages

Numerical Solution of Fractional Integro-Differential Equations by Least Squares Method and Shifted Chebyshev Polynomial, D. Sh. Mohammed
Volume 2014, Article ID 431965, 5 pages

Structure of Small World Innovation Network and Learning Performance, Shuang Song, Xiangdong Chen, and Gupeng Zhang
Volume 2014, Article ID 860216, 12 pages

Editorial

Computational Methods for Engineering Science

K. M. Liew,¹ L. W. Zhang,² J. N. Reddy,³ and Shaofan Li⁴

¹*Department of Architecture and Civil Engineering, City University of Hong Kong, Kowloon, Hong Kong*

²*College of Information Technology, Shanghai Ocean University, Shanghai 201306, China*

³*Department of Mechanical Engineering, Texas A&M University, TX, USA*

⁴*Department of Civil and Environmental Engineering, University of California, Berkeley, CA, USA*

Correspondence should be addressed to K. M. Liew; kmliew@cityu.edu.hk

Received 24 March 2015; Accepted 24 March 2015

Copyright © 2015 K. M. Liew et al. This is an open access article distributed under the Creative Commons Attribution License, which permits unrestricted use, distribution, and reproduction in any medium, provided the original work is properly cited.

This special issue attempts to cover the recent advances on various aspects of theories, analyses, and applications of computational methods in engineering science, reflecting the state of the art in computational methods and their frameworks, applications, networking technologies, and new and advanced engineering applications in emerging technologies such as the bioscience and biotechnology, nanoscience and nanotechnology, numerical modeling, simulation and analysis, and material sciences.

The topics covered by the articles including in this special issue encompass computational mechanics, ocean and offshore engineering, computational fluid dynamics, computational mathematics and statistics, computational physics, computational material sciences, multiscale modeling, disaster simulation and analysis, element-free/meshless/mesh-free methods and dimension-reduction methods, geometric and material nonlinear analyses, damage, fracture and fatigue, contact mechanics and friction, smart structures and health monitoring, structural optimization, nanomechanics, biomechanics, inverse and coupling problems, and reliability theory and application.

We hope that this special issue will be cited for recent advances in these research areas.

*K. M. Liew
L. W. Zhang
J. N. Reddy
Shaofan Li*

Research Article

Simulating the Range Expansion of *Spartina alterniflora* in Ecological Engineering through Constrained Cellular Automata Model and GIS

Zongsheng Zheng,^{1,2} Bo Tian,² L. W. Zhang,¹ and Guoliang Zou¹

¹ Department of Marine Information Technology, Shanghai Ocean University, No. 999 Huchenghuan Road, Shanghai 201306, China

² State Key Laboratory of Estuarine and Coastal Research, East China Normal University, No. 3663 Zhongshan North Road, Shanghai 200062, China

Correspondence should be addressed to Zongsheng Zheng; zszheng@shou.edu.cn

Received 29 August 2014; Accepted 22 September 2014

Academic Editor: Kim M. Liew

Copyright © 2015 Zongsheng Zheng et al. This is an open access article distributed under the Creative Commons Attribution License, which permits unrestricted use, distribution, and reproduction in any medium, provided the original work is properly cited.

Environmental factors play an important role in the range expansion of *Spartina alterniflora* in estuarine salt marshes. CA models focusing on neighbor effect often failed to account for the influence of environmental factors. This paper proposed a CCA model that enhanced CA model by integrating constrain factors of tidal elevation, vegetation density, vegetation classification, and tidal channels in Chongming Dongtan wetland, China. Meanwhile, a positive feedback loop between vegetation and sedimentation was also considered in CCA model through altering the tidal accretion rate in different vegetation communities. After being validated and calibrated, the CCA model is more accurate than the CA model only taking account of neighbor effect. By overlaying remote sensing classification and the simulation results, the average accuracy increases to 80.75% comparing with the previous CA model. Through the scenarios simulation, the future of *Spartina alterniflora* expansion was analyzed. CCA model provides a new technical idea and method for salt marsh species expansion and control strategies research.

1. Introduction

Spartina alterniflora (*S. alterniflora*) which is native to the Atlantic Coast and Gulf Coast of North America is a perennial and deep-rooted salt marsh grass that is found in intertidal wetlands, especially estuarine salt marshes. With its great capacity for reducing tidal wave energy, mitigating erosion, and trapping sediment, *S. alterniflora* has been widely planted on intertidal zones as a species for ecological engineering by many countries at the beginning of the 20th century. *S. alterniflora* was firstly introduced to China in 1979 purposely for beach protection and siltation promotion and has expanded rapidly outside of its original area along the coast of China [1, 2]. In recent years, however, some evidence has been reported that this species may outcompete native plants, alter the mudflat habitat, change and even diminish biodiversity, damage the coastal aquaculture, and cause declines in native species richness in the tidal land [1, 3].

As a result, since 2003, *S. alterniflora* was listed as 1 of the 16 invasive species by the Environmental Protection Bureau of China. *S. alterniflora* is a competent pioneer and serves a series of functions in coastal ecosystem. On the contrary, its rapid spread on tidal lands has made it a dreaded invader.

Chongming Dongtan wetland is an important young tidal wetland in the Yangtze River Estuary that plays an important role in balancing the carbon discharge of the estuary. The wetland was listed in the Chinese Protected Wetlands (1992) and was designated as internationally important under the Ramsar Wetlands Convention (2001) and a national nature reserve (2005). The salt marsh with elevation less than 2 m is characterized by mud flats without any vascular plants. The salt marsh between 2.0 and 2.9 m elevation is dominated by *Scirpus mariqueter* (*S. mariqueter*) community, with some rarer *Scirpus triqueter* community. Above 2.9 m, plant communities are dominated by *Phragmites australis* (*P. australis*) [4]. *S. alterniflora* was introduced to Chongming Dongtan in

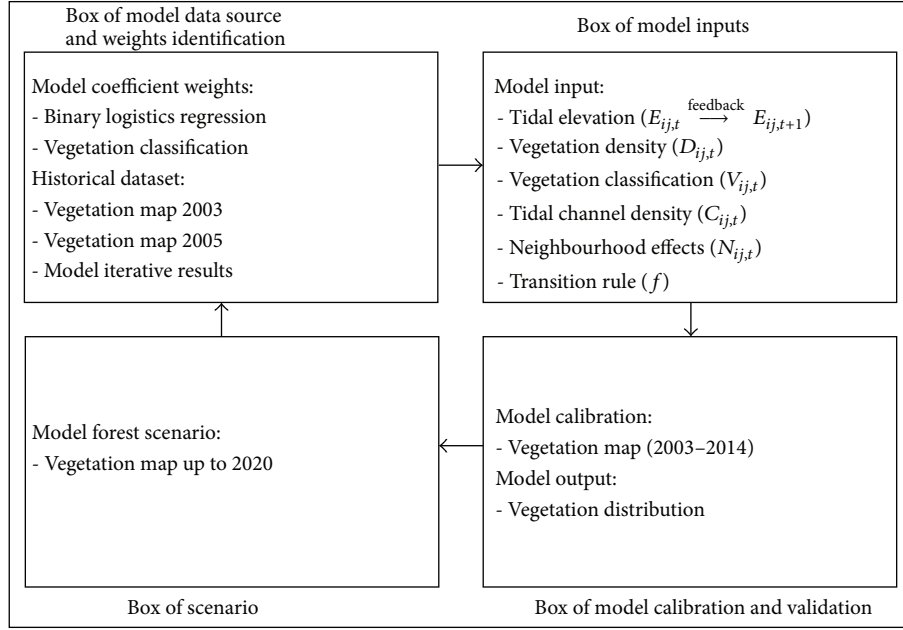


FIGURE 1: Diagram representing the conceptual model framework.

1995. There have been a rapid expansion of this species and hence a significant growth of wetland since then [5]. Over the last 20 years, *S. alterniflora* has gradually invaded large areas formerly covered by *P. australis* and has also started to invade the upper parts of the *S. mariqueter* community [3, 6–8]. In particular, the decrease of *S. mariqueter* on the high tidal flat due to *S. alterniflora* expansion will seriously threaten the habitat suitability for migratory birds at Chongming birds nature reserve [9, 10]. Some physical techniques were already promoted to control the invasion of the exotic species *S. alterniflora* [4, 11–13]. To understand the invasion dynamics and mechanisms of species, simulation model is a key tool to integrate information and test hypotheses and has been of great importance assisting management agencies with the design of effective monitoring and control strategies [14, 15].

Recently some cellular automaton models were constructed to simulate spatial variation as a consequence of competitive interactions [3, 16]. In fact, vegetation patterns are strongly linked to the topographic characteristics of the marsh, which stabilize marsh surface sediments, increase friction to hydrodynamic flow, and reduce water sediment transport, thereby increasing sedimentation from the water column [17, 18]. Such topographic modification could in turn strongly affect the vegetation communities' structure and distribution, providing more niches and thereby facilitating the range expansion [8, 18]. However, the few process-based ecological hypotheses and available parameters obtained from field measurement and experiment limited the accuracy and utility of the models [19]. Huang et al. (2008) only put the elevation parameter on the transition rules and controlled the expansion speed by the selective Moore radius in CA model [20]. In this paper, we employed a constrained CA (CCA) model to simulate the expansion of *S. alterniflora*, which already produced highly acceptable results in urban

environment model. To improve the model accuracy, more environmental factors including elevation, tidal channel density, and vegetation density were incorporated in the CCA model. Meanwhile, a positive feedback loop between vegetation and sedimentation was also considered in CCA model through analyzing the erosion rate in different vegetation communities.

2. Establishment of CCA

A cellular automaton is defined by (S, N, f) . A CA was defined with set language as follows:

$$S^t = f(S^{t-1}, N), \quad (1)$$

where S is a finite set and represents the cell state, t the transition step, f the transition rule or function, and N the cell neighbors. This CA only considers the effect of neighbors, which is called conventional CA. But this kind of CA can be inappropriate when modeling and predicting complex and dynamic vegetation processes realistically, because the vegetation class transitions are driven by the more environmental variables. For purposes of *S. alterniflora* dynamics, a more complex CA model (constrained CA model) is needed, which considers more relative factors. Constrained cellular automata (CCA) are produced with embedding some constraints in the transition rules of cellular automata, which are able to provide much better alternatives to actual development patterns [21].

2.1. Model Description. The CCA model was developed using Matlab software and ArcGIS software, in order to simulate the range expansion of *S. alterniflora* on the coastal mudflats. Figure 1 showed the simulation process with a four-step cycle,

including model inputs, factor weights identification, model calibration and validation, and forecast scenario. E_{ij} , D_{ij} , V_{ij} , C_{ij} , N_{ij} , and the transition potential rule in model inputs box made up the model outputs for the calibration procedure. In model calibration and validation box, CCA was rectified through model results with corresponding vegetation map from remote sensing classification. The final step introduced one vegetation map scenario in scenarios box, which provided spatial information about the vegetation dynamics until 2020. Based on these outputs, the model was validated by comparing the simulated *S. alterniflora* distribution with the observed vegetation map to optimize the model coefficient weights in data source and weights identification box.

2.2. Model Inputs. A number of ecologists have evaluated the environmental factors affecting the plant distribution patterns in salt marsh environments, for example, soil elevation [22, 23], salinity [24, 25], nutrient availability [26, 27], inter- and intraspecific competition [28, 29], and grazing and human management [12, 29]. These researches have provided more information on the controlling factors on vegetation expansion, which can be used to improve simulation models of the overall. In all these factors, tidal elevation is regarded as convenient metric that integrates a number of hydrologic and edaphic factors [24]. In our study area, Ge et al. also reported that the combination of dense *S. alterniflora* meadows with high elevation and weak flow intensity resulted in a higher density of seedling establishment [19]. So tidal elevation (E_{ij}) and vegetation density (D_{ij}) were selected as two important constrain factors in CCA model. Some studies have also shown that location and size of tidal channels are fundamental factors in determining plant distribution patterns, since the tidal channel networks largely control the distribution of tidal flooding within salt marshes [30, 31]. To quantify the effect of tidal channel, the density (C_{ij}) was also regarded as one of the model inputs. Another control factor was vegetation classification (V_{ij}) which indicated the competition between *P. australis*, *S. alterniflora*, and *S. mariqueter*. For example, *P. australis* and *S. alterniflora* were obstacles to each other and can only occupy the cells of *S. mariqueter* [20]. Finally, CCA is an array of cells that interact with one another locally according to some neighborhood rules. Each cell evolves which depends not only on the state of the cell but also on the neighboring cells (N_{ij}).

2.3. Transition Rules. A model transition rule changes each cell state to the state that has the highest potential. Based on this rule, transition potential is calculated for each cell during each time step of the simulation. This potential indicates the vegetation pattern for which the cell is best adapted. The potential for each cell is calculated as follows:

$$S_{ij}^{t+1} = f(S_{ij}^t, E_{ij}^t, D_{ij}^t, V_{ij}^t, C_{ij}^t, N_{ij}^t, v), \quad (2)$$

where S_{ij}^{t+1} , S_{ij}^t represent the cell (i, j) state at time ($t + 1$) and time (t), E_{ij}^t is tidal elevation of the cell (i, j), D_{ij}^t is the vegetation density of cell (i, j), V_{ij}^t is the vegetation type of cell (i, j), C_{ij}^t is tidal channel density of the cell (i, j), N_{ij}^t is

the neighbourhood space effect on the cell (i, j), and v is the random perturbation term at time (t), which is defined as $v = 1 + [-\ln(\text{rand})]^\alpha$, where ($0 < \text{rand} < 1$) is a uniform random variable and α is a stochasticity parameter that adjusts the perturbation size.

The five factors are further divided into suitability, resistant, and neighbor factors. The suitability of vegetation is based on three major factors, namely, elevation, vegetation density, and vegetation type, in which value 0 corresponds to the least suitability and value 1 corresponds to the highest suitability. The vegetation suitability is calculated by the following equation:

$$s_{k,ij}^t = w_1 * E_{k,ij}^t + w_2 * D_{k,ij}^t + w_3 * V_{k,ij}^t. \quad (3)$$

$s_{k,ij}^t$ is the suitability of cell (i, j) for marsh vegetation (k) at time (t). w_1 , w_2 , and w_3 denote the weights associated with elevation, vegetation density, and type. To consider the feedback loop between tidal elevation and vegetation, $E_{k,ij}^t$ is provided as follows:

$$E_{ij}^t = \begin{cases} E_{ij}^0 + n \frac{a}{\sum \text{step}}, & S. \text{alterniflora} \text{ and } P. \text{australis}; \\ E_{ij}^0 + n \frac{b}{\sum \text{step}}, & S. \text{mariqueter}; \\ 0, & \text{bare flat.} \end{cases} \quad (4)$$

E_{ij}^0 is the tidal elevation at the start ($t = 0$). n is the step number of the model. $\sum \text{step}$ is the total simulation steps in one year. a and b are the annual accretion rate of tidal flat. The suitability $s_{k,ij}^t$ for a nonvegetation cell to be converted into a vegetation cell can then be expressed as

$$s_{k,ij}^t = s_{k,ij}^t \times \prod_{r=1}^m C_{r,k,ij} \times v. \quad (5)$$

$\prod_{r=1}^m C_{r,k,ij}$ is the product of a few binary variables used to represent the ecological constraints on the *S. alterniflora* expansion, such as being prevented by tidal channel. $C_{r,k,ij}$ will have a value of 0 if cell (i, j) is preserved due to constraint r where *S. alterniflora* cannot invade into the cell (i, j) occupied by tidal channel.

Salt marsh vegetation parameters in each cell take states of S_{p-a} , S_{s-a} , S_{s-m} , and S_{b-m} , representing *P. australis*, *S. alterniflora*, *S. mariqueter* community, and bare mudflat at the beginning of the simulation S_{ij}^{t-1} . The cell states in the next time step S_{ij}^t are then defined by salt marsh states and species interactions, which can be summarized by the following rule:

$$S_{ij}^t = \begin{cases} S_{p-a}, & S^{t-1} = S_{p-a}; \\ S_{s-a}, & S_{ij}^{t-1} = S_{p-a}, s_{p-a,ij}^{t-1} > \alpha, N_{ij}^{t-1} > \beta; \\ S_{s-a}, & S_{ij}^{t-1} = S_{s-m}, s_{s-m,ij}^{t-1} > \alpha, N_{ij}^{t-1} > \beta; \\ S_{s-a}, & S^{t-1} = S_{s-a}; \\ S_{b-m}, & S^{t-1} = S_{b-m}, \end{cases} \quad (6)$$

where S_{ij}^t and S_{ij}^{t-1} represent the cell states at times t and $t - 1$, respectively. $s_{p-a,ij}^{t-1}$ and $s_{s-m,ij}^{t-1}$ denote the *S. alterniflora*

TABLE 1: Variables retained in the logistic regression model and their coefficients.

	B^1	S.E. ²	Wald ³	Df ⁴	Sig ⁵	Exp(B) ⁶	95% C.I. for Exp(B) ⁷	
							Lower	Upper
W_1	2.817	0.57	2484.209	1	0.000	16.723	14.969	18.682
W_2	-2.449	0.48	2611.628	1	0.000	0.086	0.079	0.095
W_3	1.061	0.28	1396.555	1	0.000	2.889	2.732	3.054

¹ B = logistic coefficient; ²S.E. = standard error of estimate; ³Wald = Wald chi-square values; ⁴Df = degree of freedom; ⁵Sig = significance; ⁶Exp(B) = exponentiated coefficient; ⁷95.0% C.I. for Exp(B): 95% confidence interval for Exp(B).

suitability of cell (i, j) at $P. australis$ and $S. marigueter$ communities at time $(t - 1)$. The thresholds α and β are determined according to the actual cell conversion which is obtained from observation data [32].

2.4. Data Source. The spatial pattern of salt marsh vegetation classification (Figure 1) was based on the multitemporal satellite images of 2000–2005 with the resolution of 30 m on the ground. A supervised classification, using the Maximum Likelihood Classifier in ERDAS Imagine software, was then carried out and the classified imagery was then integrated into a GIS platform [20]. Wetland plants density and tidal channels were mapped from QuickBird image with the resolution of 0.6 m, which was acquired on September 29, 2005. For information not available from high-resolution Lidar elevation data, waterline method combining Landsat TM, tidal gauge, and field elevation transects has been used to generate digital elevation model (DEM) [10, 33–36]. All the data were converted into standard raster data and resampled with a 30 m \times 30 m resolution for a total of 551 \times 582 cells.

2.5. Weights Identification. Methods determining weights are often divided into two categories: subjective and objective weighting. Objective weighting is suitable to tackle the situations where suggestions of experts are not easily attained [37]. Moreover, objective methods are also able to avoid biases from experts or decision makers due to their predilections through some mathematical methods. In order to determine the weights values in the state transition rules, w_1 , w_2 , and w_3 were extracted through binary logistic regression method according to three main categories of $S. alterniflora$ expansion factors. Binary logistic regression establishes a functional relationship between the binary coded $S. alterniflora$ distribution (presence or absence), DEM, classified vegetation, and plants density factors that are recognized as playing a role in $S. alterniflora$ expansion. Regression coefficients $w_0 \sim w_3$ show the contribution of each explanatory variable on suitability $s_{k,ij}^t$. The statistical technique is a multivariate estimation method that examines the relative significance of the factors. By using the statistical analysis software SPSS (19.0), the model coefficients were estimated as shown in Table 1, which were then used to calculate the suitability of $S. alterniflora$ expansion potential for all of the pixels in the study region. A positive value means that the variable helps to increase the probability of change, and a negative value implies the opposite effect. Tidal elevation showed more significant effect on $S. alterniflora$ expansion than the other vegetation from

Table 1. The variables with estimated coefficients having a significance value (Sig) of less than 0.05 were found to be significantly different from zero. These variables can be accepted as influential predictor variables.

The suitability $s_{k,ij}^t$ was a standardized suitability score [0, 1] based on the consideration of factors. The classification threshold α was selected as 0.5 at $t = 0$ in this paper. By overlying multitemporal satellite data, the numbers of neighbor β were obtained through all the new converted $S. alterniflora$ cells around old $S. alterniflora$ cells in the area, where all other factors including tidal elevation, vegetation density, and vegetation type were similar (Figure 2). The average of converted numbers around old $S. alterniflora$ was 5.68 from the statistics of converted pixels and $\beta = 5.68/8 = 0.71$ was selected at $t = 0$ in this research. A series of α and β was tested for $S. alterniflora$ and the tentatively simulated results were compared iteratively with the corresponding salt marsh classification maps until they reached an acceptable range in the calibration procedure.

2.6. Model Calibration and Accuracy Evaluation. Calibration and validation are critical for the performance of CCA models because they largely depend on the appropriateness of the transition rules, which typically involve important parameters [38, 39]. The vegetation maps from 2002 to 2005 were used to calibrate the CCA model by treating the 2002 map as the starting time. The simulated outcome of 2003 and 2005 based on each set of weights was compared with vegetation map of the corresponding year and was used to rectify the model by changing the threshold values α and β . At last the optimized values were used for simulation from 2003 to 2020.

The CCA model accuracy was checked by overlaying the image classification and the simulation output for the whole study area in the ArcGIS platform (Figure 3). By overlaying the predicted $S. alterniflora$ distribution with vegetation map, the percentage match of pixels indicated that 80.75% of $S. alterniflora$ expansion was correctly predicted in the 8 years from 2005 to 2013 (Table 2). The CCA model accuracy ranged from 76% to 85%, which was higher than the CA accuracy ranging from 37% to 75% as discussed by Huang et al. [20].

3. Simulations and Results

3.1. The Past Expansion of $S. alterniflora$. Patches of $S. alterniflora$ were firstly found on the northeast part of the Dongtan wetland in 1995. The seeds possibly came from the coast of

TABLE 2: Comparison between the measured and modeled range expansion of *S. alterniflora*.

Pixels	2003	2005	2007	2009	2013	2020
Measured pixels (number)	—	19550	20718	25978	32097	—
Corresponding area (ha.)	—	1760	1865	2338	2889	—
Modeled pixels (number)	11880	15221	17690	21947	24505	28746
Corresponding area (ha.)	1069	1370	1592	1975	2205	2587
Accuracy (%)	—	78%	85%	84%	76%	—
Average accuracy (%)						80.75%

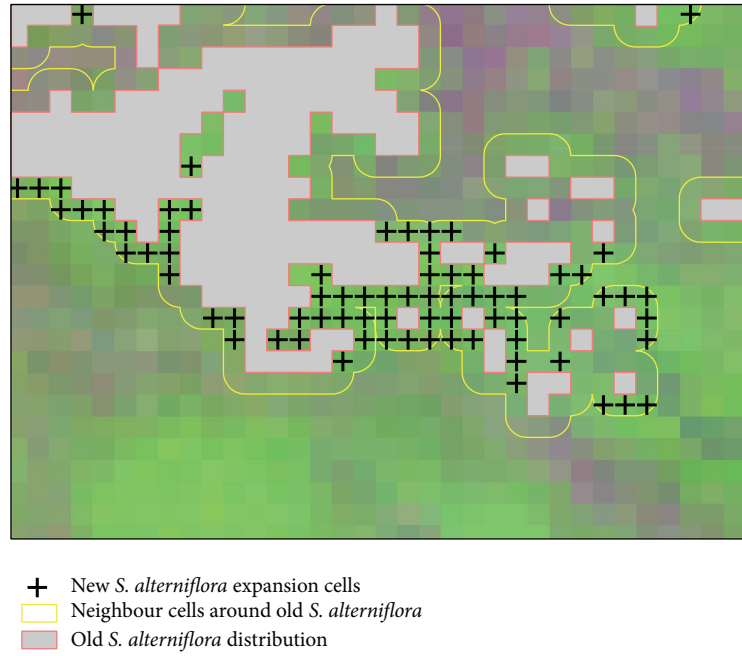


FIGURE 2: Neighbor effects on expansion pattern.

Jiangsu Province despite natural dispersal by tidal currents [40]. Since then, *S. alterniflora* experienced slow expansion and formed many stable communities in colonization. For rapid sediment accretion in salt marsh in the estuary, 337 ha and 370 ha of *S. alterniflora* were planted in a belt on the north and northeast in May 2001 and May 2003, respectively [41]. Since 2003, *S. alterniflora* kept a rapid population growth and range expansion (Figure 3). In the spatial pattern, *S. alterniflora* began to expand towards the east and north and emerged among the original *S. mariqueter* community along with the accretion of elevation. As in the simulation process, *S. alterniflora* increased in the ten years from 1069 ha in 2003 to 2205 ha in 2013, which matched closely the area (2889 ha) based on remote sensing vegetation map in the corresponding year (Table 2). The speed of range expansion of *S. alterniflora* subsequently slowed down after 2013, which distributed dominantly in the northern and eastern marshes in Chongming Dongtan.

3.2. The Future Expansion of *S. alterniflora*. *S. mariqueter* is the pioneer vegetation in the tidal flat, whose emergence and growth create conditions for the colonization of *S. alterniflora* and *P. australis*. *S. alterniflora* has the more rapid

expansion due to its wider ecological niche and stronger competitive capacity than native *P. australis* [2]. *S. alterniflora* will continuously expand northwards and eastwards in the future (Figure 4) and the areas will amount to 2587 ha in 2020 according to the simulation (Table 2). With the accretion of intertidal flats, it could be also anticipated that the rapid range expansion of *S. alterniflora* would last for a considerable time on the Chongming Dongtan. So, more attention should also be paid to the dynamics of *S. alterniflora* in the future. In particular, the decrease of *S. mariqueter* due to *S. alterniflora* expansion will seriously threaten the habitat suitability for migratory birds. Some physical techniques were already promoted to control the invasion of the exotic species *S. alterniflora*. The first stage of control project of *S. alterniflora* on the Chongming Dongtan started in 2011. The third stage also launched in May 2013. The weirs of control project were shown in Figure 4. In the simulation of 2020, these projects were not considered in the CCA model.

4. Conclusions

Present CA models focusing on neighbor effect often failed to account for the influence of environmental factors and

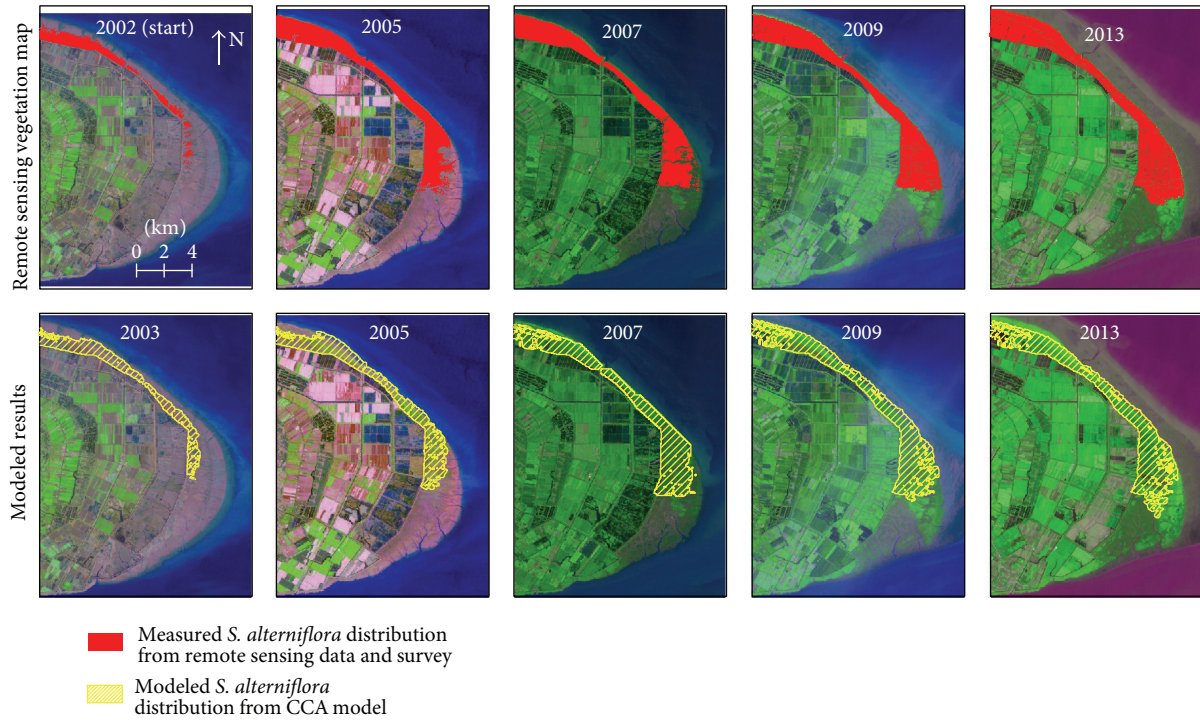


FIGURE 3: Comparison between modeled results and remote sensing classification.

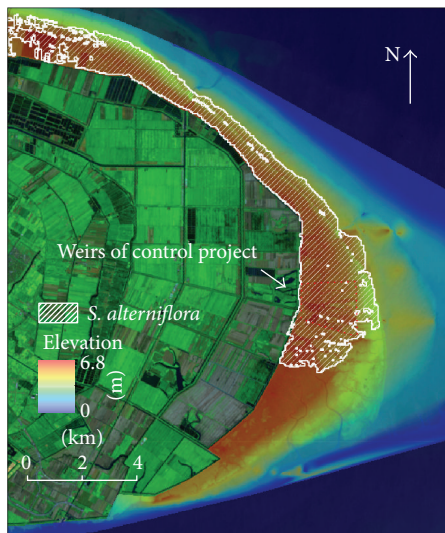


FIGURE 4: The future of *S. alterniflora* distribution in the future of 2020.

were therefore inadequate for accurately simulating salt marsh vegetation evolution. Environmental factors play an important role in *S. alterniflora* dynamics in salt marsh. This paper proposed a CCA model that enhanced CA model by integrating the influence of tidal elevation, vegetation density, vegetation classification, and tidal channels. The average accuracy for the simulated *S. alterniflora* expansion increased to 80.75% comparing with previous CA model accuracy ranging from 37% to 75%. The simulation results

suggest a continuing *S. alterniflora* growth in the study area and show that the future expansion is most likely to take place in the northeast of Chongming Dongtan. Close attention should be paid to these areas to effectively detect, study, and solve the problems associated with such expansions in hope for wetland biodiversity conservation and resource management. Currently, the control project is in progress on the Chongming Dongtan, by integrating physical or mechanical control measures such as cutting, cutting plus waterlogging, and spraying chemicals. Based on the CCA model, the effective assessment of these control strategies should be the key point of the next research.

Conflict of Interests

The authors declare that there is no conflict of interests regarding the publication of this paper.

Acknowledgments

The authors would like to express their sincere appreciation to the anonymous reviewers for their valuable comments, suggestions, and recommendations. This work is funded under the Program Strategic Scientific Alliances between China and the Netherlands (no. 2008DFB90240), Open Research Fund Program for State Key Laboratory of Estuarine and Coastal Research (SKLEC201207), and Open Research Fund Program for Shandong Province Key Laboratory of Marine Ecology Environment and Disaster Prevention (2012011). Landsat TM images were provided by China Remote Sensing Satellite Ground Station.

References

- [1] S. Wan, P. Qin, J. Liu, and H. Zhou, "The positive and negative effects of exotic *Spartina alterniflora* in China," *Ecological Engineering*, vol. 35, no. 4, pp. 444–452, 2009.
- [2] P. Zuo, S. H. Zhao, C. A. Liu, C. H. Wang, and Y. B. Liang, "Distribution of *Spartina* spp. along China's coast," *Ecological Engineering*, vol. 40, pp. 160–166, 2012.
- [3] H.-M. Huang, L.-Q. Zhang, and L. Yuan, "The spatio-temporal dynamics of salt marsh vegetation for Chongming Dongtan National Nature Reserve, Shanghai," *Acta Ecologica Sinica*, vol. 27, no. 10, pp. 4166–4172, 2007 (Chinese).
- [4] H. P. Li and L. Q. Zhang, "An experimental study on physical controls of an exotic plant *Spartina alterniflora* in Shanghai, China," *Ecological Engineering*, vol. 32, no. 1, pp. 11–21, 2008.
- [5] Z. Chen, B. Li, Y. Zhong, and J. Chen, "Local competitive effects of introduced *Spartina alterniflora* on *Scirpus mariqueter* at Dongtan of Chongming Island, the Yangtze River estuary and their potential ecological consequences," *Hydrobiologia*, vol. 528, no. 1–3, pp. 99–106, 2004.
- [6] W. S. He, R. Feagin, J. J. Lu, W. L. Liu, Q. Yan, and Z. F. Xie, "Impacts of introduced *Spartina alterniflora* along an elevation gradient at the Jiuduansha Shoals in the Yangtze Estuary, suburban Shanghai, China," *Ecological Engineering*, vol. 29, no. 3, pp. 245–248, 2007.
- [7] R. Wang, L. Yuan, and L. Zhang, "Impacts of *Spartina alterniflora* invasion on the benthic communities of salt marshes in the Yangtze Estuary, China," *Ecological Engineering*, vol. 36, no. 6, pp. 799–806, 2010.
- [8] D. R. Xiao, L. Q. Zhang, and Z. C. Zhu, "The range expansion patterns of *Spartina alterniflora* on salt marshes in the Yangtze Estuary, China," *Estuarine, Coastal and Shelf Science*, vol. 88, no. 1, pp. 99–104, 2010.
- [9] Z. J. Ma, B. Li, B. Zhao, K. Jing, S. M. Tang, and J. K. Chen, "Are artificial wetlands good alternatives to natural wetlands for waterbirds? A case study on Chongming Island, China," *Biodiversity and Conservation*, vol. 13, no. 2, pp. 333–350, 2004.
- [10] B. Tian, L. Zhang, X. Wang, Y. Zhou, and W. Zhang, "Forecasting the effects of sea-level rise at Chongming Dongtan Nature Reserve in the Yangtze Delta, Shanghai, China," *Ecological Engineering*, vol. 36, no. 10, pp. 1383–1388, 2010.
- [11] L. Tang, Y. Gao, J. Wang et al., "Designing an effective clipping regime for controlling the invasive plant *Spartina alterniflora* in an estuarine salt marsh," *Ecological Engineering*, vol. 35, no. 5, pp. 874–881, 2009.
- [12] L. Yuan, L. Zhang, D. Xiao, and H. Huang, "The application of cutting plus waterlogging to control *Spartina alterniflora* on saltmarshes in the Yangtze Estuary, China," *Estuarine, Coastal and Shelf Science*, vol. 92, no. 1, pp. 103–110, 2011.
- [13] J. H. Chen, L. Wang, Y. L. Li, W. Q. Zhang, X. H. Fu, and Y. Q. Le, "Effect of *Spartina alterniflora* invasion and its controlling technologies on soil microbial respiration of a tidal wetland in Chongming Dongtan, China," *Ecological Engineering*, vol. 41, pp. 52–59, 2012.
- [14] C. M. Taylor and A. Hastings, "Finding optimal control strategies for invasive species: a density-structured model for *Spartina alterniflora*," *Journal of Applied Ecology*, vol. 41, no. 6, pp. 1049–1057, 2004.
- [15] D. L. Strayer, V. T. Eviner, J. M. Jeschke, and M. L. Pace, "Understanding the long-term effects of species invasions," *Trends in Ecology and Evolution*, vol. 21, no. 11, pp. 645–651, 2006.
- [16] J. Silvertown, S. Holtier, J. Johnson, and P. Dale, "Cellular automaton models of interspecific competition for space—the effect of pattern on process," *Journal of Ecology*, vol. 80, no. 3, pp. 527–534, 1992.
- [17] S. L. Yang, "The role of *Scirpus* marsh in attenuation of hydrodynamics and retention of fine sediment in the Yangtze estuary," *Estuarine, Coastal and Shelf Science*, vol. 47, no. 2, pp. 227–233, 1998.
- [18] Z. C. Zhu, L. Q. Zhang, N. Wang, C. Schwarz, and T. Ysebaert, "Interactions between the range expansion of saltmarsh vegetation and hydrodynamic regimes in the Yangtze Estuary, China," *Estuarine, Coastal and Shelf Science*, vol. 96, no. 1, pp. 273–279, 2012.
- [19] Z. Ge, H. Cao, and L. Zhang, "A process-based grid model for the simulation of range expansion of *Spartina alterniflora* on the coastal saltmarshes in the Yangtze Estuary," *Ecological Engineering*, vol. 58, pp. 105–112, 2013.
- [20] H.-M. Huang, L.-Q. Zhang, Y.-J. Guan, and D.-H. Wang, "A cellular automata model for population expansion of *Spartina alterniflora* at Jiuduansha Shoals, Shanghai, China," *Estuarine, Coastal and Shelf Science*, vol. 77, no. 1, pp. 47–55, 2008.
- [21] X. Li and A. Gar-On Yeh, "Modelling sustainable urban development by the integration of constrained cellular automata and GIS," *International Journal of Geographical Information Science*, vol. 14, no. 2, pp. 131–152, 2000.
- [22] V. J. Chapman, *Salt Marshes and Salt Deserts of the World*, Interscience Publishers, London, UK, 1960.
- [23] V. J. Chapman, *Coastal Vegetation*, Pergamon Press, London, UK, 1976.
- [24] S. Sadro, M. Gastil-Buhl, and J. Melack, "Characterizing patterns of plant distribution in a southern California salt marsh using remotely sensed topographic and hyperspectral data and local tidal fluctuations," *Remote Sensing of Environment*, vol. 110, no. 2, pp. 226–239, 2007.
- [25] Y. Xiao, J. B. Tang, H. Qing, C. F. Zhou, and S. Q. An, "Effects of salinity and clonal integration on growth and sexual reproduction of the invasive grass *Spartina alterniflora*," *Flora: Morphology, Distribution, Functional Ecology of Plants*, vol. 206, no. 8, pp. 736–741, 2011.
- [26] H. J. van Wijnen and J. P. Bakker, "Nitrogen and phosphorus limitation in a coastal barrier salt marsh: the implications for vegetation succession," *Journal of Ecology*, vol. 87, no. 2, pp. 265–272, 1999.
- [27] J. Álvarez Rogel, R. Ortiz Silla, and F. Alcaraz Ariza, "Edaphic characterization and soil ionic composition influencing plant zonation in a semiarid Mediterranean salt marsh," *Geoderma*, vol. 99, no. 1–2, pp. 81–98, 2001.
- [28] C. S. B. Costa, J. C. Marangoni, and A. M. G. Azevedo, "Plant zonation in irregularly flooded salt marshes: relative importance of stress tolerance and biological interactions," *Journal of Ecology*, vol. 91, no. 6, pp. 951–965, 2003.
- [29] J. P. M. Lenssen, F. B. J. Menting, and W. H. Van Der Putten, "Do competition and selective herbivory cause replacement of *Phragmites australis* by tall forbs?" *Aquatic Botany*, vol. 78, no. 3, pp. 217–232, 2004.
- [30] E. W. Sanderson, S. L. Ustin, and T. C. Foin, "The influence of tidal channels on salt marsh vegetation," *Plant Ecology*, vol. 146, pp. 29–41, 2000.
- [31] E. W. Sanderson, T. C. Foin, and S. L. Ustin, "A simple empirical model of salt marsh plant spatial distributions with respect to a tidal channel network," *Ecological Modelling*, vol. 139, no. 2–3, pp. 293–307, 2001.

- [32] X. Li and A. G.-O. Yeh, "Neural-network-based cellular automata for simulating multiple land use changes using GIS," *International Journal of Geographical Information Science*, vol. 16, no. 4, pp. 323–343, 2002.
- [33] D. C. Mason, I. J. Davenport, and R. A. Flather, "Interpolation of an intertidal digital elevation model from heightened shorelines: a case study in the western Wash," *Estuarine, Coastal and Shelf Science*, vol. 45, no. 5, pp. 599–612, 1997.
- [34] D. C. Mason, I. J. Davenport, R. A. Flather, and C. Gurney, "A digital elevation model of the inter-tidal areas of the Wash, England, produced by the waterline method," *International Journal of Remote Sensing*, vol. 19, no. 8, pp. 1455–1460, 1998.
- [35] D. C. Mason, M. Amin, I. J. Davenport, R. A. Flather, G. J. Robinson, and J. A. Smith, "Measurement of recent intertidal sediment transport in Morecambe Bay using the waterline method," *Estuarine, Coastal and Shelf Science*, vol. 49, no. 3, pp. 427–456, 1999.
- [36] D. C. Mason, I. J. Davenport, R. A. Flather, C. Gurney, G. J. Robinson, and J. A. Smith, "A sensitivity analysis of the waterline method of constructing a digital elevation model for intertidal areas in ERS SAR scene of Eastern England," *Estuarine, Coastal and Shelf Science*, vol. 53, no. 6, pp. 759–778, 2001.
- [37] H. Deng, C.-H. Yeh, and R. J. Willis, "Inter-company comparison using modified TOPSIS with objective weights," *Computers and Operations Research*, vol. 27, no. 10, pp. 963–973, 2000.
- [38] F. Wu, "Calibration of stochastic cellular automata: the application to rural-urban land conversions," *International Journal of Geographical Information Science*, vol. 16, no. 8, pp. 795–818, 2002.
- [39] B. Straatman, R. White, and G. Engelen, "Towards an automatic calibration procedure for constrained cellular automata," *Computers, Environment and Urban Systems*, vol. 28, no. 1-2, pp. 149–170, 2004.
- [40] Z. Y. Chen, *Ecological impacts of introduced Spartina alterniflora invasions in the coastal ecosystems of Chongming Dongtan, the Yangtze River estuary [Ph.D. thesis]*, Fudan University, Shanghai, China, 2004.
- [41] B. Li, C.-H. Liao, X.-D. Zhang et al., "Spartina alterniflora invasions in the Yangtze River estuary, China: an overview of current status and ecosystem effects," *Ecological Engineering*, vol. 35, no. 4, pp. 511–520, 2009.

Research Article

Free Vibration Analysis of Symmetrically Laminated Folded Plate Structures Using an Element-Free Galerkin Method

L. X. Peng^{1,2}

¹College of Civil Engineering and Architecture, Guangxi University, Nanning 530004, China

²Guangxi Key Laboratory of Disaster Prevention and Engineering Safety, Guangxi University, Nanning 530004, China

Correspondence should be addressed to L. X. Peng; penglx@gxu.edu.cn

Received 21 July 2014; Revised 14 November 2014; Accepted 14 November 2014

Academic Editor: Kim M. Liew

Copyright © 2015 L. X. Peng. This is an open access article distributed under the Creative Commons Attribution License, which permits unrestricted use, distribution, and reproduction in any medium, provided the original work is properly cited.

An element-free Galerkin method for the solution of free vibration of symmetrically laminated folded plate structures is introduced. Employing the mature meshfree folded plate model proposed by the author, a folded laminated plate is simulated as a composite structure of symmetric laminates that lie in different planes. Based on the first-order shear deformation theory (FSDT) and the moving least-squares (MLS) approximation, the stiffness and mass matrices of the laminates are derived and supposed to obtain the stiffness and mass matrices of the entire folded laminated plate. The equation governing the free vibration behaviors of the folded laminated plate is thus established. Because of the meshfree characteristics of the proposed method, no mesh is involved to determine the stiffness and mass matrices of the laminates. Therefore, the troublesome remeshing can be avoided completely from the study of such problems as the large deformation of folded laminated plates. The calculation of several numerical examples shows that the solutions given by the proposed method are very close to those given by ANSYS, using shell elements, which proves the validity of the proposed method.

1. Introduction

Because of high strength/weight ratio, easy forming, and low cost, folded plate structures have been widely used in many engineering branches, such as roofs, corrugated-cores, and cooling towers. They have much higher load carrying capacity compared to flat plates. Before the invention of fiber-reinforced material, folded plates were often made of metal or timber. The application of fiber-reinforced material to folded plate structures was a remarkable advance in engineering, which combined the advantages of fiber-reinforced material and folded plate structure directly and made the structure even lighter and stiffer.

The study of isotropic folded plates had a quite long history, and a variety of methods had emerged. In early days, researchers were short of powerful numerical tools and tried to analyze the structures with various approximations. The beam method and the theory that ignores relative joint displacement were introduced [1]. Although the methods were weak in dealing with generalized folded plate problems,

they were simple and fulfilled the demand of fast and easy computation in engineering. Therefore, they are still used in some design environments, where accurate analysis is not the first concern. Researchers such as Gaafar [2], Yitzhaki [3], Yitzhaki and Reiss [4], and Whitney et al. [5] were the first to consider the relative joint displacement of the structures in their methods, which led to more precise analysis results. Goldberg and Leve [6] used the two-dimensional theory of elasticity and the two-way slab theory to analyze folded plates. In their method, both the simultaneous bending and the membrane action of a folded plate were taken into account, and the degree of freedom (DOF) of each point along the joint of the folded plate was chosen to be four (three components of translation and one rotation). Niyogi et al. [7] considered this method as the first to give an exact static solution for folded plates. Yitzhaki and Reiss [4] took the moments along the joints of folded plates as unknown and applied the slope deflection method to the analysis of the folded plates. Bar-Yoseph and Hersckovitz [8] proposed an approximated

method for folded plates based on Vlasov's theory of thin-wall beams. Their method considered a folded plate as a monolithic structure composed of longitudinal beams, which can give good results for long folded plates. Bandyopadhyay and Laad [9] compared two classical methods for folded plates and studied the suitability of these methods for the preliminary analysis of folded plate structures. Lai et al. [10] gave an equation of the middle surface of a simply supported cross V-shaped folded plate roof by using the inclined coordinate system and generalized functions, sign function and step function, and carried out a nonlinear analysis for the folded plate.

The development of computation techniques and computers has aroused research interest in numerical methods for folded plates. A number of methods, such as the finite strip methods (Cheung [11], Golley and Grice [12], Eterovic and Godoy [13]), the combined boundary element-transfer matrix method (Ohga et al. [14]), and the finite element methods (FEM) (Liu and Huang [15], Perry et al. [16], Niyogi et al. [7], and Duan and Miyamoto [17]), have been introduced to solve folded plate problems. Among these methods, the FEMs are the most successful. They are very versatile as they can deal with the problems with complicated geometry, boundary conditions, or loadings easily. However, FEM also has disadvantages. Their solution of a problem is based on the meshes that discretize the problem domain, and any dramatic change of the problem domain will lead to remeshing of the domain, which results in programming complexity, diminished accuracy, and long computation time. Regarding the disadvantage, some researchers proposed the element-free, meshfree, or meshless methods [18–22]. As alternatives to FEMs, the meshfree methods construct their approximated solution of a problem completely in terms of a set of ordered or scattered points that discretize the problem domain; that is, their solution relies on the points other than meshes. No element is required. Without the limit of meshes, the meshfree methods are more applicable than the FEMs and avoid the aforementioned difficulties caused by remeshing in the FEMs.

Bui et al. [23], Bui and Nguyen [24], and Somireddy and Rajagopal [25] have introduced the meshfree methods for vibration analysis of laminated plates. However, few studies on folded laminated plates have been found. There are only Niyongi et al. [7] and Lee et al.'s [26] work on vibration and the author's work on bending with a meshfree method, which is also the motive for this paper.

The objective of this paper is to introduce an element-free Galerkin method based on the first-order shear deformation theory (FSDT) [27, 28] for the free vibration analysis of folded laminated plates. A symmetrical folded laminated plate is regarded as a composite structure composed of symmetric laminates. The analysis process includes (a) deriving the stiffness and mass matrices of the symmetric laminates that make up a folded plate by the element-free Galerkin method; (b) considering the laminates as super elements and superposing their stiffness and mass matrices to obtain the global stiffness and mass matrices of the folded plate. Some numerical examples are used to demonstrate the convergence and accuracy of the proposed method. The calculated results

are compared with the results from the finite element analytical software ANSYS. The proposed method may be used as a potential meshfree tool for the analysis of laminated shell structures.

2. Moving Least-Squares Approximation

In the moving least-squares approximation (MLS) [18], a function $v(\mathbf{x})$ in a domain Ω can be approximated by $v^d(\mathbf{x})$ in the subdomain $\Omega_{\mathbf{x}}$ and

$$v^d(\mathbf{x}) = \sum_{i=1}^m q_i(\mathbf{x}) b_i(\mathbf{x}) = \mathbf{q}^T(\mathbf{x}) \mathbf{b}(\mathbf{x}), \quad (1)$$

where $q_i(\mathbf{x})$ are the monomial basis functions, $b_i(\mathbf{x})$ are the corresponding coefficients, d is a factor that measures the domain of influence (or the support) of the nodes, and m is the number of basis functions. In this paper, the quadratic basis $\mathbf{q}^T = [1, x, y, x^2, xy, y^2]$ ($m = 6$) are used for the laminates. The unknown coefficients $b_i(\mathbf{x})$ are obtained by the minimization of a weighted discrete L_2 norm

$$\Gamma = \sum_{I=1}^n \omega(\mathbf{x} - \mathbf{x}_I) [\mathbf{q}(\mathbf{x}_I)^T \mathbf{b}(\mathbf{x}) - v_I]^2, \quad (2)$$

where $\omega(\mathbf{x} - \mathbf{x}_I)$ or $\omega_I(\mathbf{x})$ is the weight function that is associated with node I , $\omega_I(\mathbf{x}) = 0$ outside $\Omega_{\mathbf{x}}$, n is the number of nodes in $\Omega_{\mathbf{x}}$ that make the weight function $\omega_I(\mathbf{x}) > 0$, and v_I are the nodal parameters. The minimization of Γ in (2) with respect to $\mathbf{b}(\mathbf{x})$

$$\frac{\partial \Gamma}{\partial \mathbf{b}(\mathbf{x})} = 0 \quad (3)$$

leads to a set of linear equations

$$\mathbf{B}(\mathbf{x}) \mathbf{b}(\mathbf{x}) = \mathbf{A}(\mathbf{x}) \mathbf{v}, \quad (4)$$

where

$$\mathbf{B}(\mathbf{x}) = \sum_{I=1}^n \omega(\mathbf{x} - \mathbf{x}_I) \mathbf{q}(\mathbf{x}_I) \mathbf{q}^T(\mathbf{x}_I), \quad (5)$$

$$\mathbf{A}(\mathbf{x}) = [\omega(\mathbf{x} - \mathbf{x}_1) \mathbf{q}(\mathbf{x}_1), \dots, \omega(\mathbf{x} - \mathbf{x}_n) \mathbf{q}(\mathbf{x}_n)]. \quad (6)$$

The coefficients $\mathbf{b}(\mathbf{x})$ are then derived from (4):

$$\mathbf{b}(\mathbf{x}) = \mathbf{B}^{-1}(\mathbf{x}) \mathbf{A}(\mathbf{x}) \mathbf{v}. \quad (7)$$

By substituting (7) into (1), the approximation $v^d(\mathbf{x})$ is expressed in a standard form as

$$v^d(\mathbf{x}) = \sum_{I=1}^n N_I(\mathbf{x}) v_I, \quad (8)$$

where the shape function $N_I(\mathbf{x})$ is given by

$$N_I(\mathbf{x}) = \mathbf{q}^T(\mathbf{x}) \mathbf{B}^{-1}(\mathbf{x}) \mathbf{A}_I(\mathbf{x}). \quad (9)$$

From (6), we obtain

$$\mathbf{A}_I(\mathbf{x}) = \omega(\mathbf{x} - \mathbf{x}_I) \mathbf{q}(\mathbf{x}_I), \quad (10)$$

and thus (9) can be rewritten as

$$N_I(\mathbf{x}) = \mathbf{q}^T(\mathbf{x}) \mathbf{B}^{-1}(\mathbf{x}) \mathbf{q}(\mathbf{x}_I) \omega(\mathbf{x} - \mathbf{x}_I). \quad (11)$$

3. Meshless Model of a Laminate

The first step in our analysis is to obtain the stiffness and mass matrices of the laminates that make up a folded plate. The meshless model for a laminate in the local coordinate, as shown in Figure 1, is prescribed with a set of nodes. The DOF of every node is $(u_0, v_0, w, \varphi_x, \varphi_y)$, where u_0 , v_0 , and w are the nodal translations of the laminate in the x -direction, y -direction, and z -direction, respectively. φ_x and φ_y are the rotation about the y -axis and the x -axis, respectively. The laminate is assumed to have N layers, and the thickness of each layer is z_i ($i = 1, \dots, N$). Therefore, the thickness of k th layer is $h_k = z_{k+1} - z_k$.

3.1. Displacement Approximation. Based on the FSDT and the MLS approximation, the displacements of the laminate can be approximated by

$$\begin{aligned} u(x, y, z, t) &= u_0(x, y, t) - z\varphi_x(x, y, t) \\ &= \sum_{I=1}^n H_I(x, y) u_{0I}(t) - z \sum_{I=1}^n H_I(x, y) \varphi_{xI}(t), \\ v(x, y, z, t) &= v_0(x, y, t) - z\varphi_y(x, y, t) \\ &= \sum_{I=1}^n H_I(x, y) v_{0I}(t) - z \sum_{I=1}^n H_I(x, y) \varphi_{yI}(t), \\ w(x, y, t) &= \sum_{I=1}^n H_I(x, y) w_I(t), \end{aligned} \quad (12)$$

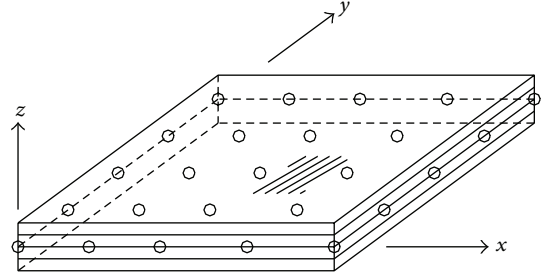


FIGURE 1: Meshfree model of a laminate.

where $\{u_{0I}(t), v_{0I}(t), w_I(t), \varphi_{xI}(t), \varphi_{yI}(t)\}^T = \delta_I$ are the nodal parameters of the I th node of the laminate, n is the number of nodes of the laminate, and φ_x and φ_y are independent of w . The shape functions $H_I(x, y)$ are obtained from (9), and the cubic spline function

$$\omega(s) = \begin{cases} \frac{2}{3} - 4s^2 + 4s^3, & s \leq \frac{1}{2}, \\ \frac{4}{3} - 4s + 4s^2 - \frac{4}{3}s^3, & \frac{1}{2} < s \leq 1, \\ 0, & s > 1 \end{cases} \quad (13)$$

is used as the weight function. Equation (12) can be written in a matrix form as

$$\mathbf{U} = \begin{Bmatrix} u \\ v \\ w \end{Bmatrix} = \sum_{I=1}^n \begin{bmatrix} H_I(x, y) & 0 & 0 & -zH_I(x, y) & 0 \\ 0 & H_I(x, y) & 0 & 0 & -zH_I(x, y) \\ 0 & 0 & H_I(x, y) & 0 & 0 \end{bmatrix} \times \begin{Bmatrix} u_{0I}(t) \\ v_{0I}(t) \\ w_I(t) \\ \varphi_{xI}(t) \\ \varphi_{yI}(t) \end{Bmatrix}. \quad (14)$$

The strains of the laminate are defined as

$$\begin{aligned} \boldsymbol{\kappa} = \begin{Bmatrix} \varepsilon_x \\ \varepsilon_y \\ \gamma_{xy} \end{Bmatrix} &= \begin{bmatrix} u_{0,x} - z\varphi_{x,x} \\ v_{0,y} - z\varphi_{y,y} \\ u_{0,y} + v_{0,x} - z(\varphi_{x,y} + \varphi_{y,x}) \end{bmatrix} = \sum_{I=1}^n \mathbf{B}_I^b \delta_I, \\ \boldsymbol{\gamma} = \begin{Bmatrix} \gamma_{xz} \\ \gamma_{yz} \end{Bmatrix} &= \begin{bmatrix} w_{,x} - \varphi_x \\ w_{,y} - \varphi_y \end{bmatrix} = \sum_{I=1}^n \mathbf{B}_I^s \delta_I, \end{aligned} \quad (15)$$

where

$$\begin{aligned} \mathbf{B}_I^b &= [\mathbf{B}_{0I} \quad -z\mathbf{B}_{1I}] = \begin{bmatrix} H_{I,x} & 0 & 0 & -zH_{I,x} & 0 \\ 0 & H_{I,y} & 0 & 0 & -zH_{I,y} \\ H_{I,y} & H_{I,x} & 0 & -zH_{I,y} & -zH_{I,x} \end{bmatrix}, \\ \mathbf{B}_{0I} &= \begin{bmatrix} H_{I,x} & 0 \\ 0 & H_{I,y} \\ H_{I,y} & H_{I,x} \end{bmatrix}, \quad \mathbf{B}_{1I} = \begin{bmatrix} 0 & H_{I,x} & 0 \\ 0 & 0 & H_{I,y} \\ 0 & H_{I,y} & H_{I,x} \end{bmatrix}, \end{aligned}$$

$$\mathbf{B}_I^s = [\mathbf{0} \quad \mathbf{B}_{2I}] = \begin{bmatrix} 0 & 0 & H_{I,x} & -H_I & 0 \\ 0 & 0 & H_{I,y} & 0 & -H_I \end{bmatrix},$$

$$\mathbf{B}_{2I} = \begin{bmatrix} H_{I,x} & -H_I & 0 \\ H_{I,y} & 0 & -H_I \end{bmatrix}, \quad (16)$$

“ x ” refers to the derivatives of x , and “ y ” refers to the derivatives of y .

3.2. Governing Equation. In free vibration, the strain energy and kinetic energy of the laminate are, respectively,

$$\Pi = \frac{1}{2} \iint \int_{-h/2}^{h/2} \boldsymbol{\kappa}^T \mathbf{D} \boldsymbol{\kappa} \, dz \, dx \, dy + \frac{1}{2} \iint \boldsymbol{\gamma}^T \mathbf{A}_s \boldsymbol{\gamma} \, dx \, dy, \quad (17)$$

$$T_0 = \frac{1}{2} \iint \int_{-h/2}^{h/2} \dot{\mathbf{U}}^T \rho \dot{\mathbf{U}} \, dz \, dx \, dy,$$

where

$$\mathbf{D} = \begin{bmatrix} \bar{Q}_{11}^{(k)} & \bar{Q}_{12}^{(k)} & \bar{Q}_{16}^{(k)} \\ \bar{Q}_{21}^{(k)} & \bar{Q}_{22}^{(k)} & \bar{Q}_{26}^{(k)} \\ \bar{Q}_{61}^{(k)} & \bar{Q}_{62}^{(k)} & \bar{Q}_{66}^{(k)} \end{bmatrix},$$

$$\tilde{\mathbf{A}}_s = \begin{bmatrix} \tilde{A}_{55} & \tilde{A}_{45} \\ \tilde{A}_{45} & \tilde{A}_{44} \end{bmatrix}, \quad (18)$$

$$\tilde{A}_{ij} = k_c \int_{-h/2}^{h/2} \bar{Q}_{ij}^{(k)} \, dz = k_c \sum_{k=1}^N \bar{Q}_{ij}^{(k)} (z_{k+1} - z_k),$$

($i, j = 4, 5$),

\bar{Q}_{ij} ($i, j = 1, 2, 6, 4, 5$) are the material stiffness that are defined in [28], $k_c = 5/6$ is the shear correction factor, and h is the thickness of the laminate. ρ is the density of the material.

According to Hamilton's principle,

$$\delta \int_{t_1}^{t_2} (T_0 - \Pi) \, dt = 0. \quad (19)$$

The substitution of (14) to (17) into (19) gives

$$\mathbf{K} \boldsymbol{\delta} + \mathbf{M} \ddot{\boldsymbol{\delta}} = \mathbf{0}, \quad (20)$$

where

$$\boldsymbol{\delta} = \{\boldsymbol{\delta}_1^T \quad \boldsymbol{\delta}_2^T \quad \dots \quad \boldsymbol{\delta}_n^T\}^T$$

$$= \{u_{01}, v_{01}, w_1, \varphi_{x1}, \varphi_{y1}, \dots, u_{0n}, v_{0n}, w_n, \varphi_{xn}, \varphi_{yn}\}^T,$$

$$[\mathbf{M}]_{IJ} = \iint \begin{bmatrix} h & & & \\ & h & 0 & \\ & & h & \\ 0 & & & \frac{h^3}{12} \\ & & & & \frac{h^3}{12} \end{bmatrix} \rho H_I H_J \, dx \, dy,$$

$$\mathbf{K}_{IJ} = \iint \int_{-h/2}^{h/2} \begin{bmatrix} \mathbf{B}_{0I}^T \\ -z \mathbf{B}_{1I}^T \end{bmatrix} \mathbf{D} [\mathbf{B}_{0J} \quad -z \mathbf{B}_{1J}] \, dz \, dx \, dy$$

$$+ \iint \begin{bmatrix} \mathbf{0} \\ \mathbf{B}_{2I}^T \end{bmatrix} \tilde{\mathbf{A}}_s [\mathbf{0} \quad \mathbf{B}_{2J}] \, dx \, dy$$

$$= \iint \int_{-h/2}^{h/2} \begin{bmatrix} \mathbf{B}_{0I}^T \mathbf{D} \mathbf{B}_{0J} & -z \mathbf{B}_{0I}^T \mathbf{D} \mathbf{B}_{1J} \\ -z \mathbf{B}_{1I}^T \mathbf{D} \mathbf{B}_{0J} & z^2 \mathbf{B}_{1I}^T \mathbf{D} \mathbf{B}_{1J} \end{bmatrix} \, dz \, dx \, dy$$

$$+ \iint \begin{bmatrix} \mathbf{0} & \mathbf{0} \\ \mathbf{0} & \mathbf{B}_{2I}^T \tilde{\mathbf{A}}_s \mathbf{B}_{2J} \end{bmatrix} \, dx \, dy. \quad (21)$$

If $(\tilde{\mathbf{A}}, \tilde{\mathbf{B}}, \tilde{\mathbf{H}}) = \int_{-h/2}^{h/2} \mathbf{D}(1, z, z^2) \, dz$, we obtain

$$\mathbf{K}_{IJ} = \iint \begin{bmatrix} \mathbf{B}_{0I}^T \tilde{\mathbf{A}} \mathbf{B}_{0J} & -\mathbf{B}_{0I}^T \tilde{\mathbf{B}} \mathbf{B}_{1J} \\ -\mathbf{B}_{1I}^T \tilde{\mathbf{B}} \mathbf{B}_{0J} & \mathbf{B}_{1I}^T \tilde{\mathbf{H}} \mathbf{B}_{1J} + \mathbf{B}_{2I}^T \tilde{\mathbf{A}}_s \mathbf{B}_{2J} \end{bmatrix} \, dx \, dy. \quad (22)$$

For the symmetric laminates, $\tilde{\mathbf{B}} = \mathbf{0}$.

4. Formulation for Folded Laminated Plates

In the paper, a folded laminated plate is regarded as a composite structure composed of laminates. We have obtained the stiffness and mass matrices of a single laminate. Therefore, the next step is to take each laminate of the composite structure as a super element, to superpose their stiffness and mass matrices by applying the displacement compatibility conditions along the joints between the laminates, and to give the governing equation of the entire folded laminated plate (Figure 2).

Nevertheless, as pointed out by the author in [20], due to a lack of Kronecker delta properties in the meshfree shape functions given by (9), and that $\boldsymbol{\delta}$ of (20) are nodal parameters other than actual nodal displacements, the stiffness and mass matrices cannot be directly superposed. The full transformation method that was first introduced by Chen et al. [19] to enforce the essential boundary conditions is extended by the author in the paper to modify the stiffness and mass matrices before a superposition. After the modification, the essential boundary conditions can be implemented as those in FEMs.

4.1. Modification of Stiffness and Mass Matrices. From (1), the actual displacement of the nodes, $\bar{\mathbf{v}}(\mathbf{x})$, can be approximated by $\mathbf{v}^d(\mathbf{x})$

$$\bar{\mathbf{v}}(\mathbf{x}) \approx \mathbf{v}^d(\mathbf{x}) = \sum_{I=1}^n N_I(\mathbf{x}) v_I = \boldsymbol{\Phi} \mathbf{v}, \quad (23)$$

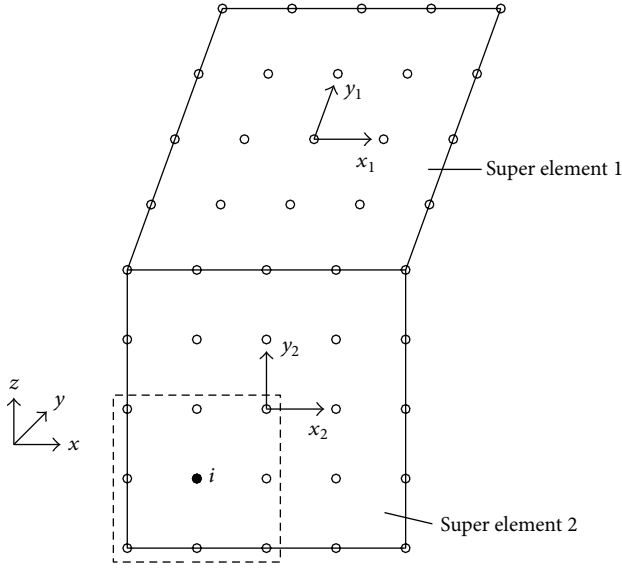


FIGURE 2: A meshfree model of a folded laminated plate that is made up of two super elements (laminates). The domain of influence of node i is indicated by the dashed line.

where

$$\Phi = \begin{bmatrix} N_1(\mathbf{x}_1) & N_2(\mathbf{x}_1) & \dots & N_n(\mathbf{x}_1) \\ N_1(\mathbf{x}_2) & N_2(\mathbf{x}_2) & \dots & N_n(\mathbf{x}_2) \\ \vdots & \vdots & \ddots & \vdots \\ N_1(\mathbf{x}_n) & N_2(\mathbf{x}_n) & \dots & N_n(\mathbf{x}_n) \end{bmatrix} \quad (24)$$

and v_i are the nodal parameters. Therefore, the nodal parameters can be expressed in terms of the actual displacement

$$\mathbf{v} = \Lambda \bar{\mathbf{v}}, \quad (25)$$

where $\Lambda = \Phi^{-1}$.

For the folded laminated plate, we accordingly have

$$\begin{aligned} \mathbf{u}_0 &= \Lambda \bar{\mathbf{u}}_0, & \mathbf{v}_0 &= \Lambda \bar{\mathbf{v}}_0, & \mathbf{w} &= \Lambda \bar{\mathbf{w}}, \\ \boldsymbol{\varphi}_x &= \Lambda \bar{\boldsymbol{\varphi}}_x, & \boldsymbol{\varphi}_y &= \Lambda \bar{\boldsymbol{\varphi}}_y, \end{aligned} \quad (26)$$

where $\bar{\mathbf{u}}_0 = \{\bar{u}_0(\mathbf{x}_1), \bar{u}_0(\mathbf{x}_2), \dots, \bar{u}_0(\mathbf{x}_n)\}^T = \{\bar{u}_{01}, \bar{u}_{02}, \dots, \bar{u}_{0n}\}^T$ are the actual nodal displacement (translation) in the x direction and $\mathbf{u}_0 = \{u_{01}, u_{02}, \dots, u_{0n}\}^T$ are the corresponding nodal parameters. $\mathbf{v}_0, \bar{\mathbf{v}}_0, \mathbf{w}, \bar{\mathbf{w}}, \boldsymbol{\varphi}_x, \bar{\boldsymbol{\varphi}}_x, \boldsymbol{\varphi}_y$, and $\bar{\boldsymbol{\varphi}}_y$ have similar definition. Equation (26) can be written as

$$\boldsymbol{\delta} = \bar{\Lambda} \bar{\boldsymbol{\delta}}, \quad (27)$$

where $\bar{\boldsymbol{\delta}} = \{\bar{\boldsymbol{\delta}}_1^T \bar{\boldsymbol{\delta}}_2^T \dots \bar{\boldsymbol{\delta}}_n^T\}^T = \{\bar{u}_{01}, \bar{v}_{01}, \bar{w}_1, \bar{\varphi}_{x1}, \bar{\varphi}_{y1}, \dots, \bar{u}_{0n}, \bar{v}_{0n}, \bar{w}_n, \bar{\varphi}_{xn}, \bar{\varphi}_{yn}\}^T$ are the actual nodal displacement of all nodes. $\bar{\Lambda}$ is a $5n \times 5n$ modification matrix which combines five Λ . Substituting (27) into (20) and premultiplying both sides of the equation with $\bar{\Lambda}^T$, we obtain

$$\bar{\Lambda}^T \bar{\mathbf{K}} \bar{\Lambda} \bar{\boldsymbol{\delta}} + \bar{\Lambda}^T \bar{\mathbf{M}} \bar{\Lambda} \ddot{\bar{\boldsymbol{\delta}}} = \mathbf{0}. \quad (28)$$

Assuming that $\bar{\mathbf{K}} = \bar{\Lambda}^T \mathbf{K} \bar{\Lambda}$ and $\bar{\mathbf{M}} = \bar{\Lambda}^T \mathbf{M} \bar{\Lambda}$, we have

$$\bar{\mathbf{K}} \bar{\boldsymbol{\delta}} + \bar{\mathbf{M}} \ddot{\bar{\boldsymbol{\delta}}} = \mathbf{0}, \quad (29)$$

the modified governing equation.

4.2. The Governing Equation of the Folded Laminated Plate. Because the stiffness and mass matrices of a laminate in (20) were established in a local coordinate attached to the laminate (Figure 1), the matrices in (29) need to be transformed to the global coordinates before the superposition. The stiffness and mass matrices and the nodal displacement in the global coordinates are

$$\bar{\mathbf{K}} = \mathbf{T} \bar{\mathbf{K}} \mathbf{T}^T, \quad \bar{\mathbf{M}} = \mathbf{T} \bar{\mathbf{M}} \mathbf{T}^T, \quad \bar{\boldsymbol{\delta}} = \mathbf{T} \bar{\boldsymbol{\delta}}, \quad (30)$$

where \mathbf{T} is the $6n \times 6n$ coordinate transformation matrix derived in [20] (note: a drilling degree of freedom φ_z has been added to $\bar{\boldsymbol{\delta}}$, and $\bar{\mathbf{K}}$ and $\bar{\mathbf{M}}$ must be expanded accordingly by inserting some zero elements). If there are J (no. 1 to J) coincident nodes along the joint between super elements 1 and 2 (Figure 2), we have

$$\bar{\boldsymbol{\delta}}_b^1 = \bar{\boldsymbol{\delta}}_b^2, \quad \ddot{\bar{\boldsymbol{\delta}}}_b^1 = \ddot{\bar{\boldsymbol{\delta}}}_b^2, \quad (31)$$

where $\bar{\boldsymbol{\delta}}_b^1 = \{\bar{u}_{01}^1, \bar{v}_{01}^1, \bar{w}_1^1, \bar{\varphi}_{x1}^1, \bar{\varphi}_{y1}^1, \bar{\varphi}_{z1}^1, \dots, \bar{u}_{0J}^1, \bar{v}_{0J}^1, \bar{w}_J^1, \bar{\varphi}_{xJ}^1, \bar{\varphi}_{yJ}^1, \bar{\varphi}_{zJ}^1\}^T$ are the actual displacement of the nodes of super element 1 along the joint between super element 1 and super element 2 and $\bar{\boldsymbol{\delta}}_b^2 = \{\bar{u}_{01}^2, \bar{v}_{01}^2, \bar{w}_1^2, \bar{\varphi}_{x1}^2, \bar{\varphi}_{y1}^2, \bar{\varphi}_{z1}^2, \dots, \bar{u}_{0J}^2, \bar{v}_{0J}^2, \bar{w}_J^2, \bar{\varphi}_{xJ}^2, \bar{\varphi}_{yJ}^2, \bar{\varphi}_{zJ}^2\}^T$ are the actual displacement of the nodes of super element 2 along the joint between super element 1 and super element 2. After necessary elementary transformation, the governing equation of super elements 1 and 2 can be written in block forms

$$\begin{bmatrix} \bar{\mathbf{k}}_{ii}^1 & \bar{\mathbf{k}}_{ib}^1 \\ \bar{\mathbf{k}}_{bi}^1 & \bar{\mathbf{k}}_{bb}^1 \end{bmatrix} \begin{Bmatrix} \bar{\boldsymbol{\delta}}_i^1 \\ \bar{\boldsymbol{\delta}}_b^1 \end{Bmatrix} + \begin{bmatrix} \bar{\mathbf{m}}_{ii}^1 & \bar{\mathbf{m}}_{ib}^1 \\ \bar{\mathbf{m}}_{bi}^1 & \bar{\mathbf{m}}_{bb}^1 \end{bmatrix} \begin{Bmatrix} \ddot{\bar{\boldsymbol{\delta}}}_i^1 \\ \ddot{\bar{\boldsymbol{\delta}}}_b^1 \end{Bmatrix} = \mathbf{0}, \quad (32)$$

$$\begin{bmatrix} \bar{\mathbf{k}}_{bb}^2 & \bar{\mathbf{k}}_{bi}^2 \\ \bar{\mathbf{k}}_{ib}^2 & \bar{\mathbf{k}}_{ii}^2 \end{bmatrix} \begin{Bmatrix} \bar{\boldsymbol{\delta}}_b^2 \\ \bar{\boldsymbol{\delta}}_i^2 \end{Bmatrix} + \begin{bmatrix} \bar{\mathbf{m}}_{bb}^2 & \bar{\mathbf{m}}_{bi}^2 \\ \bar{\mathbf{m}}_{ib}^2 & \bar{\mathbf{m}}_{ii}^2 \end{bmatrix} \begin{Bmatrix} \ddot{\bar{\boldsymbol{\delta}}}_b^2 \\ \ddot{\bar{\boldsymbol{\delta}}}_i^2 \end{Bmatrix} = \mathbf{0},$$

where $\bar{\boldsymbol{\delta}}_i^1$ and $\bar{\boldsymbol{\delta}}_i^2$ are the actual displacement of the nodes of super elements 1 and 2 that are not along the joint, respectively. Equation (32) are supposed to give the equation governing the dynamic behaviors of the entire structure

$$\begin{bmatrix} \bar{\mathbf{k}}_{ii}^1 & \bar{\mathbf{k}}_{ib}^1 & \mathbf{0} \\ \bar{\mathbf{k}}_{bi}^1 & \bar{\mathbf{k}}_{bb}^1 + \bar{\mathbf{k}}_{bb}^2 & \bar{\mathbf{k}}_{bi}^2 \\ \mathbf{0} & \bar{\mathbf{k}}_{ib}^2 & \bar{\mathbf{k}}_{ii}^2 \end{bmatrix} \begin{Bmatrix} \bar{\boldsymbol{\delta}}_i^1 \\ \bar{\boldsymbol{\delta}}_b^1 \\ \bar{\boldsymbol{\delta}}_i^2 \end{Bmatrix} + \begin{bmatrix} \bar{\mathbf{m}}_{ii}^1 & \bar{\mathbf{m}}_{ib}^1 & \mathbf{0} \\ \bar{\mathbf{m}}_{bi}^1 & \bar{\mathbf{m}}_{bb}^1 + \bar{\mathbf{m}}_{bb}^2 & \bar{\mathbf{m}}_{bi}^2 \\ \mathbf{0} & \bar{\mathbf{m}}_{ib}^2 & \bar{\mathbf{m}}_{ii}^2 \end{bmatrix} \begin{Bmatrix} \ddot{\bar{\boldsymbol{\delta}}}_i^1 \\ \ddot{\bar{\boldsymbol{\delta}}}_b^1 \\ \ddot{\bar{\boldsymbol{\delta}}}_i^2 \end{Bmatrix} = \mathbf{0}. \quad (33)$$

Taking

$$\mathbf{K}_G = \begin{bmatrix} \tilde{\mathbf{k}}_{ii}^1 & \tilde{\mathbf{k}}_{ib}^1 & \mathbf{0} \\ \tilde{\mathbf{k}}_{bi}^1 & \tilde{\mathbf{k}}_{bb}^1 + \tilde{\mathbf{k}}_{bb}^2 & \tilde{\mathbf{k}}_{bi}^2 \\ \mathbf{0} & \tilde{\mathbf{k}}_{ib}^2 & \tilde{\mathbf{k}}_{ii}^2 \end{bmatrix},$$

$$\mathbf{M}_G = \begin{bmatrix} \tilde{\mathbf{m}}_{ii}^1 & \tilde{\mathbf{m}}_{ib}^1 & \mathbf{0} \\ \tilde{\mathbf{m}}_{bi}^1 & \tilde{\mathbf{m}}_{bb}^1 + \tilde{\mathbf{m}}_{bb}^2 & \tilde{\mathbf{m}}_{bi}^2 \\ \mathbf{0} & \tilde{\mathbf{m}}_{ib}^2 & \tilde{\mathbf{m}}_{ii}^2 \end{bmatrix}, \quad (34)$$

$$\delta_G = \begin{Bmatrix} \tilde{\delta}_i^1 \\ \tilde{\delta}_b^1 \\ \tilde{\delta}_i^2 \end{Bmatrix},$$

we have

$$\mathbf{K}_G \delta_G + \mathbf{M}_G \ddot{\delta}_G = \mathbf{0}. \quad (35)$$

The solution of the corresponding eigenvalue problem

$$(\mathbf{K}_G - \omega^2 \mathbf{M}_G) \delta_0 = \mathbf{0} \quad (36)$$

gives us the free vibration frequencies of the folded laminated plate.

5. Results and Discussion

In order to show the convergence and accuracy of the proposed method, several numerical examples are calculated with the method and the finite element software ANSYS. For all the laminates in the examples, the plies are assumed to have the same thickness and material properties: $E_1 = 2.5 \times 10^7$ Pa, $E_2 = 1 \times 10^6$ Pa, $G_{12} = G_{13} = 5 \times 10^5$ Pa, $G_{23} = 2 \times 10^5$ Pa, $\mu_{12} = 0.25$, and $\rho = 2823$ kg/m³. Unless otherwise specified, for each example a total of two cases of symmetric laminates, cross-ply or angle-ply, which make up the folded plates, are studied: $(0^\circ/90^\circ/90^\circ/0^\circ)$ and $(-45^\circ/45^\circ/-45^\circ/45^\circ/-45^\circ \dots)_{10}$. In ANSYS, the folded laminated plates in the examples are all modeled as shells, and the linear layered structural shell element SHELL99 [29] is used to discretise the folded plates.

5.1. Validation Studies. To carry out the validation studies, a cantilever square laminate with a lamination scheme of $(-45^\circ/45^\circ/45^\circ/-45^\circ)$ is considered (Figure 3). The width of the plate is 1.8 m, and the thickness is 0.018 m. The solution from ANSYS (5000 elements to discretise the laminate) is taken to be the exact solution. The validation studies consist of a convergence study and a study on the effect of the size of support and the completeness order of the basis functions on the convergence of solutions.

Firstly, we choose a certain meshless scheme (11×11 nodes for the laminate) and let the scaling factor β and the completeness order N_c of the basis function vary. β defines

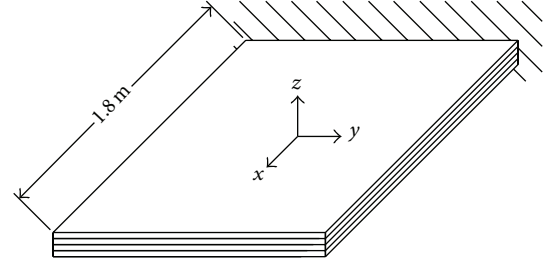


FIGURE 3: A cantilevered laminate.

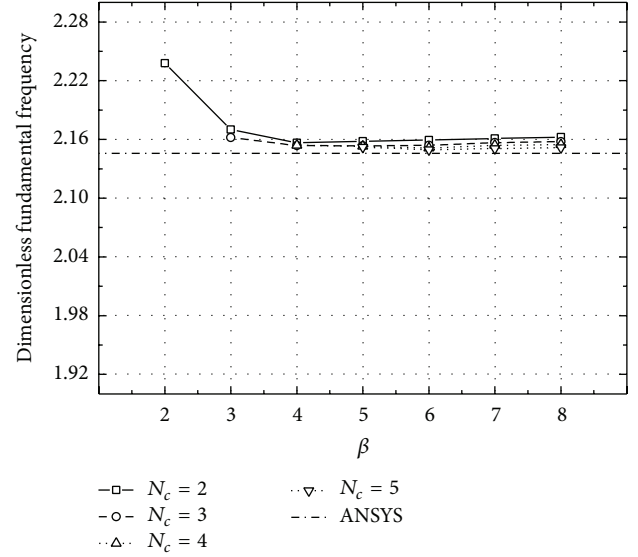


FIGURE 4: Variation of dimensionless fundamental frequency of the laminate under different β and N_c .

the size of the support of nodes. In this paper, a rectangular support is used and

$$\begin{aligned} h_x &= \beta \cdot I_x, \\ h_y &= \beta \cdot I_y, \end{aligned} \quad (37)$$

where h_x , h_y are the lengths of the support in the x and y directions, respectively, and I_x , I_y are the distances between two neighbouring nodes in the x - and y -directions, respectively. The dimensionless fundamental frequency of the laminate as calculated by the proposed method under different values of β and N_c is shown in Figure 4 and is compared with the solution that is given by ANSYS. The dimensionless frequency is defined as

$$\bar{\omega} = \omega \left(\frac{L^2}{h} \right) \sqrt{\left(\frac{\rho}{E_2} \right)}, \quad (38)$$

where L is the width of the laminate and ω is the vibration frequency. From Figure 4, it can be observed that for a certain meshless scheme (in this case 11×11 nodes), all of the solutions for different completeness orders (N_c) of the basis functions converge when the support size (β) is larger than 5. Higher completeness orders (N_c) need a larger support size

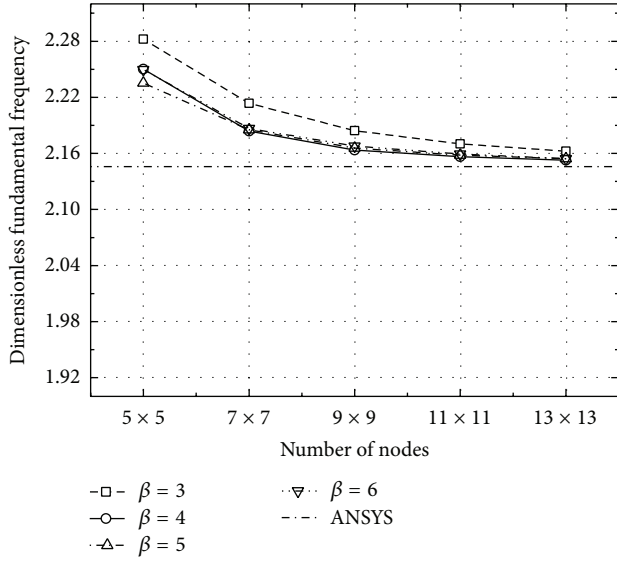


FIGURE 5: Variation of dimensionless fundamental frequency of the laminate, $N_c = 2$.

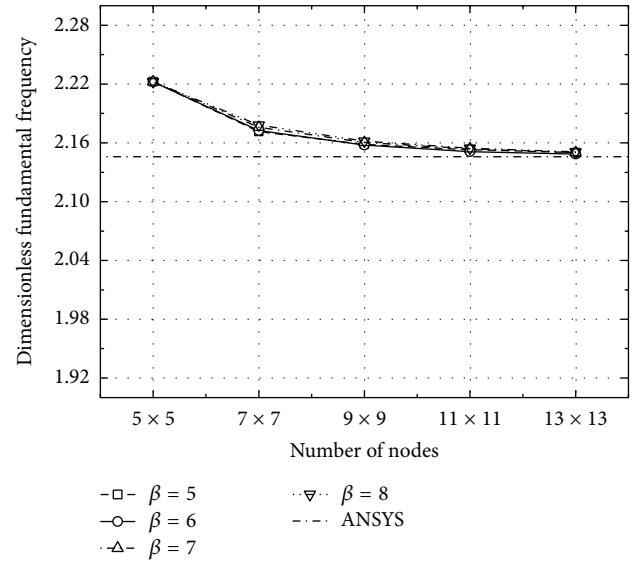


FIGURE 7: Variation of dimensionless fundamental frequency of the laminate, $N_c = 4$.

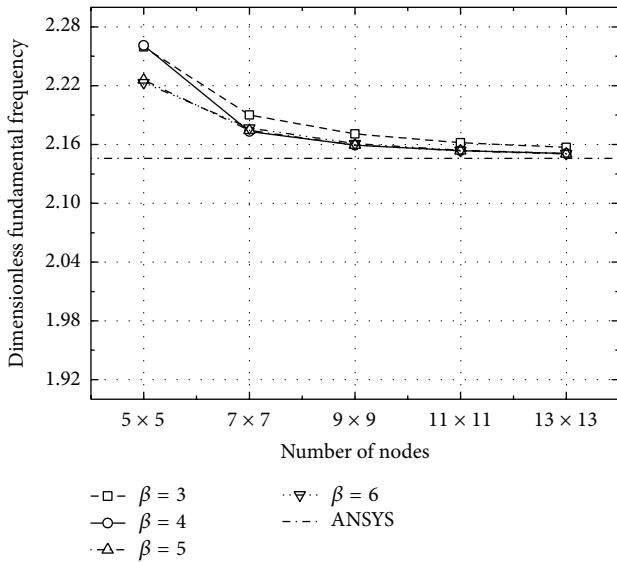


FIGURE 6: Variation of dimensionless fundamental frequency of the laminate, $N_c = 3$.

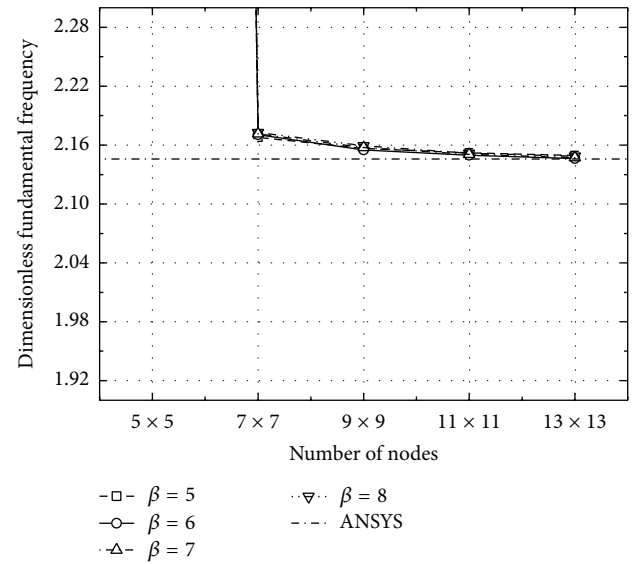


FIGURE 8: Variation of dimensionless fundamental frequency of the laminate, $N_c = 5$.

to make the solution converge (the solution under $N_c = 2$ converges at $\beta = 4$ while the solution under $N_c = 5$ converges at $\beta = 5$).

Secondly, we vary the meshless scheme and obtain the variations of the dimensionless fundamental frequency under certain completeness order of the basis functions (N_c), which are shown in Figures 5, 6, 7, and 8, respectively. The solution that is given by ANSYS is also in the figures for comparison. Figures 5 to 8 indicate that for certain β , the solution converges when the number of nodes increases. For an N_c , the solutions for larger support sizes (β) converge before those for smaller support sizes do.

From the studies, we find that when the order of basis functions $N_c = 2$ and the support size $\beta = 4$ for the laminate, the solutions are precise enough with a relatively lower computational cost. Therefore, all of the following examples are calculated with $N_c = 2$, $\beta = 4$.

5.2. A Folded Plate That Is Made Up of Two Laminates.

A clamped laminated folded plate that is made up of two identical square laminates is studied (Figure 9). The width of each laminate is $L = 1$ m, and the thickness $h = 0.012$ m. The dimensionless frequencies of the first five vibration modes of the folded plate that are obtained by the proposed method (11×11 nodes for each laminate) are listed in Tables 1 and 2

TABLE 1: Dimensionless free vibration frequencies of the onefold laminated plate with the lamination scheme $(0^\circ/90^\circ/90^\circ/0^\circ)$.

Crank angle	Modes	Present results	ANSYS results	Relative errors
$\alpha = 90^\circ$	1	8.9128	8.89037	0.25%
	2	10.0977	10.06576	0.32%
	3	12.9276	12.87695	0.39%
	4	13.8224	13.77692	0.33%
	5	28.836	28.70447	0.46%
$\alpha = 150^\circ$	1	8.91325	8.89121	0.25%
	2	10.1036	10.06659	0.37%
	3	12.9008	12.8508	0.39%
	4	13.7894	13.74465	0.33%
	5	28.841	28.71003	0.46%

TABLE 2: Dimensionless free vibration frequencies of the onefold laminated plate with the lamination scheme $(-45^\circ/45^\circ/-45^\circ/45^\circ/-45^\circ \dots)_{10}$.

Crank angle	Modes	Present results	ANSYS results	Relative errors
$\alpha = 90^\circ$	1	10.5522	10.48862	0.61%
	2	15.7311	15.63222	0.63%
	3	19.2923	19.11888	0.91%
	4	22.6269	22.45392	0.77%
	5	35.233	34.9528	0.80%
$\alpha = 150^\circ$	1	10.5784	10.49001	0.84%
	2	15.4292	15.32843	0.66%
	3	19.5467	19.09968	2.34%
	4	21.6468	21.4844	0.76%
	5	35.3159	34.97227	0.98%

alongside the results that are given by ANSYS (3200 elements to discretise the folded plate) for comparison, and the first five mode shapes of vibration of the folded plate are also plotted graphically in Figures 10 and 11. Different crank angles of the folded plate, $\alpha = 90^\circ$ and $\alpha = 150^\circ$, are considered. The results of the two methods are very close.

When the folded plate is clamped at one side, which makes it a cantilevered folded plate (Figure 12), the dimensionless frequencies of the first five vibration modes of the structure are listed in Tables 3 and 4, and the five vibration mode shapes are shown in Figures 13 and 14.

5.3. A Folded Plate That Is Made Up of Three Laminates. A folded plate that is made up of three identical square laminates and clamped at one side is studied (Figure 15, $\alpha = 90^\circ$). The width of each laminate is $L = 1$ m, and the thickness $h = 0.01$ m. The dimensionless frequencies of the first five vibration modes of the folded plate, which are calculated with the proposed method and ANSYS, are listed in Tables 5 and 6, and the first five mode shapes of vibration of the folded plate are also plotted graphically in Figures 16 and 17. In

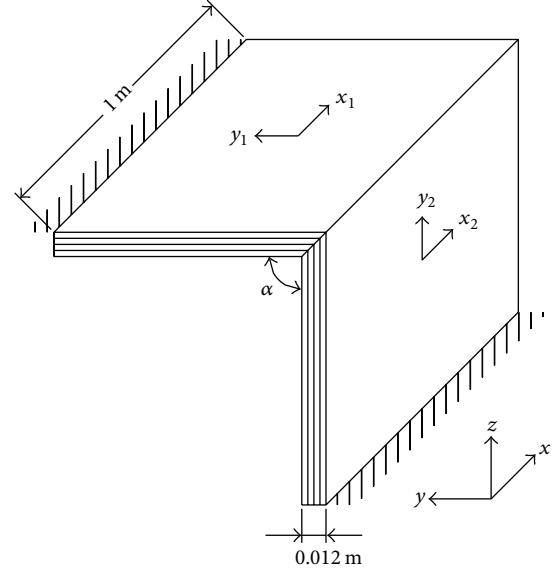


FIGURE 9: The onefold laminated plate with two sides fixed.

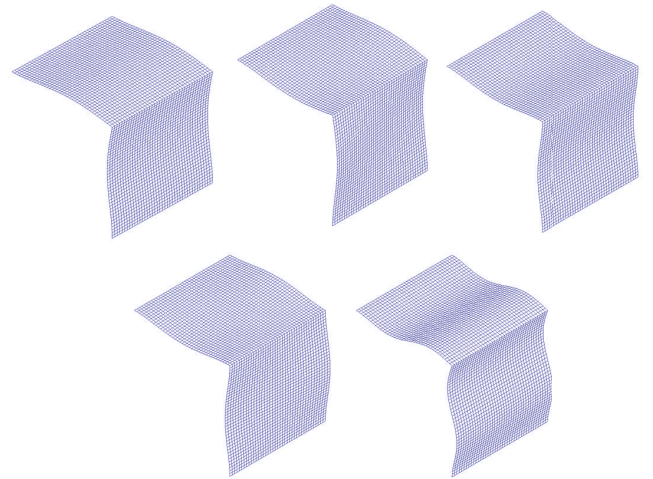


FIGURE 10: First five vibration mode shapes of the clamped folded plate ($\alpha = 90^\circ$).

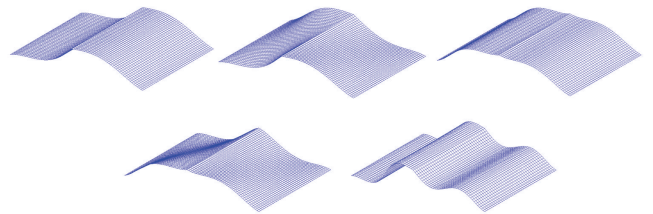


FIGURE 11: First five vibration mode shapes of the clamped folded plate ($\alpha = 150^\circ$).

ANSYS, 4800 elements are used to discretise the structure. The agreement between the two sets of results is good.

When the crank angle $\alpha = 60^\circ$ and the laminates are assumed to be connected with one another, we obtain a tub structure with three folds (Figure 18). The dimensionless frequencies of the first five vibration modes of the structure

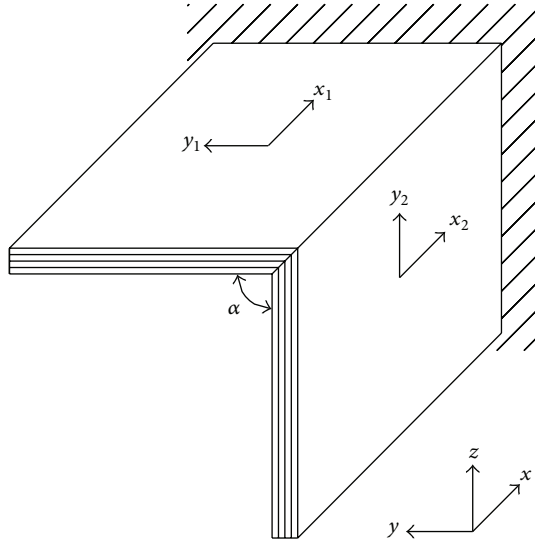


FIGURE 12: The cantilevered onefold laminated plate.

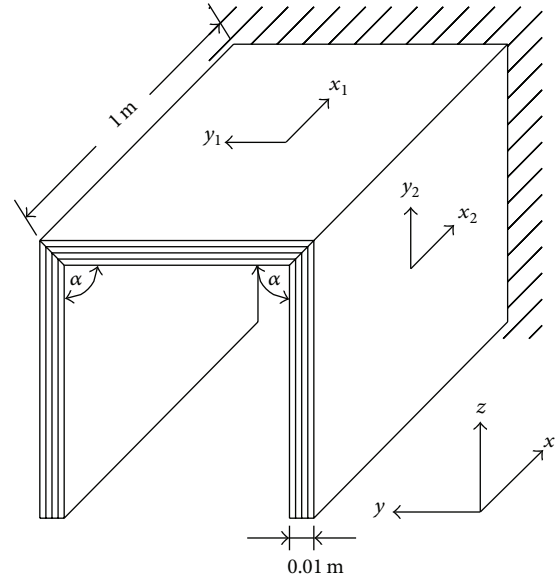
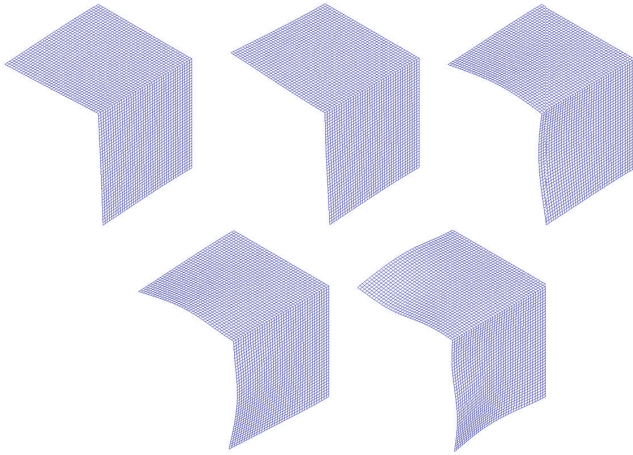
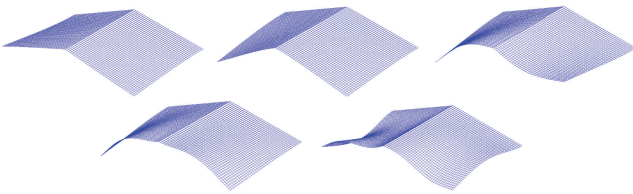
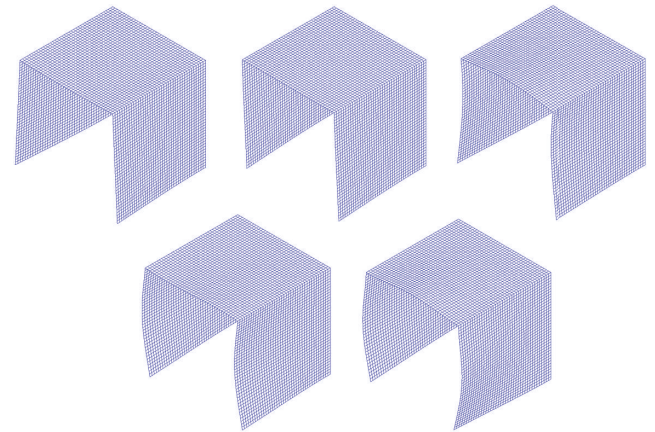
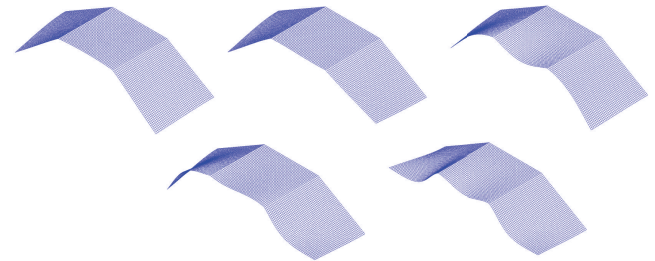


FIGURE 15: A cantilevered folded plate that is made up of three identical square laminates.

FIGURE 13: First five vibration mode shapes of the cantilevered folded plate ($\alpha = 90^\circ$).FIGURE 14: First five vibration mode shapes of the cantilevered folded plate ($\alpha = 150^\circ$).

are listed in Tables 7 and 8, and the first five mode shapes are shown in Figure 19.

5.4. A Laminated Shell. If the three laminates in Section 5.3 are joined with each other vertically, we obtain a laminated shell (or half of a box structure) (Figure 20). The structure is pinned at points A, B, and C. All of the DOFs, except the rotations of these points, are set to zero.

FIGURE 16: First five vibration mode shapes of the cantilevered folded plate ($\alpha = 90^\circ$) that is made up of three identical square laminates.FIGURE 17: First five vibration mode shapes of the cantilevered folded plate ($\alpha = 150^\circ$) that is made up of three identical square laminates.

Three lamination schemes are considered. Case 1: laminate 1 is taken to be $(45^\circ/-45^\circ/-45^\circ/45^\circ)$ and laminates 2 and 3 to be $(-45^\circ/45^\circ/45^\circ/-45^\circ)$, as is demonstrated in Figure 21(a); Case 2: laminate 1 is taken to be $(-45^\circ/45^\circ/45^\circ/-45^\circ)$ and

TABLE 3: Dimensionless free vibration frequencies of the cantilevered onefold laminated plate with the lamination scheme $(0^\circ/90^\circ/90^\circ/0^\circ)$.

Crank angle	Modes	Present results	ANSYS results	Relative errors
$\alpha = 90^\circ$	1	4.97836	4.97752	0.02%
	2	5.47994	5.47883	0.02%
	3	10.9922	10.97741	0.13%
	4	14.3614	14.32497	0.25%
	5	29.6419	29.62531	0.06%
$\alpha = 150^\circ$	1	4.97887	4.97752	0.03%
	2	5.47507	5.47410	0.02%
	3	11.0002	10.98326	0.15%
	4	14.0093	13.97611	0.24%
	5	29.6493	29.63643	0.04%

TABLE 4: Dimensionless free vibration frequencies of the cantilevered onefold laminated plate with the lamination scheme $(-45^\circ/45^\circ/-45^\circ/45^\circ \dots)_{10}$.

Crank angle	Modes	Present results	ANSYS results	Relative errors
$\alpha = 90^\circ$	1	5.19091	5.16586	0.48%
	2	6.37998	6.35766	0.35%
	3	15.5232	15.42413	0.64%
	4	18.0588	17.93153	0.71%
	5	20.3733	20.27757	0.47%
$\alpha = 150^\circ$	1	5.23049	5.16336	1.30%
	2	6.30941	6.27921	0.48%
	3	15.6594	15.4258	1.51%
	4	17.6398	17.50867	0.75%
	5	20.2856	20.15211	0.66%

TABLE 5: Dimensionless free vibration frequencies of the cantilevered twofold laminated plate with the lamination scheme $(0^\circ/90^\circ/0^\circ)$.

Crank angle	Modes	Present results	ANSYS results	Relative errors
$\alpha = 90^\circ$	1	5.15051	5.14912	0.03%
	2	5.27945	5.27765	0.03%
	3	9.42541	9.40889	0.18%
	4	12.4088	12.37671	0.26%
	5	14.3156	14.25922	0.40%
$\alpha = 150^\circ$	1	5.15063	5.14912	0.03%
	2	5.27544	5.27331	0.04%
	3	9.41916	9.40088	0.19%
	4	12.3053	12.27255	0.27%
	5	14.162	14.10833	0.38%

TABLE 6: Dimensionless free vibration frequencies of the cantilevered twofold laminated plate with the lamination scheme $(-45^\circ/45^\circ/-45^\circ/45^\circ/-45^\circ \dots)_{10}$.

Crank angle	Modes	Present results	ANSYS results	Relative errors
$\alpha = 90^\circ$	1	5.55864	5.53036	0.51%
	2	6.01129	5.98305	0.47%
	3	13.3613	13.2764	0.64%
	4	16.8974	16.755	0.85%
	5	18.1847	18.02859	0.87%
$\alpha = 150^\circ$	1	5.55885	5.51233	0.84%
	2	5.9971	5.94399	0.89%
	3	13.4186	13.21197	1.56%
	4	16.8014	16.59041	1.27%
	5	17.9625	17.78489	1.00%

TABLE 7: Dimensionless free vibration frequencies of the cantilevered tub structure with the lamination scheme $(0^\circ/90^\circ/90^\circ/0^\circ)$.

Modes	Present results	ANSYS results	Relative errors
1	9.14727	9.126463	0.23%
2	9.14957	9.126797	0.25%
3	14.1263	14.06026	0.47%
4	23.6554	23.53825	0.50%
5	31.4647	31.43285	0.10%

TABLE 8: Dimensionless free vibration frequencies of the cantilevered tub structure with the lamination scheme $(-45^\circ/45^\circ/-45^\circ/45^\circ/-45^\circ \dots)_{10}$.

Modes	Present results	ANSYS results	Relative errors
1	12.6681	12.56399	0.83%
2	12.7663	12.56399	1.61%
3	18.6702	18.49329	0.96%
4	31.407	31.05495	1.13%
5	33.1907	32.96984	0.67%

laminates 2 and 3 to be $(45^\circ/-45^\circ/-45^\circ/45^\circ)$, as is demonstrated in Figure 21(b); and Case 3: laminate 1 is taken to be $(90^\circ/0^\circ/0^\circ/90^\circ)$ and laminates 2 and 3 to be $(0^\circ/90^\circ/90^\circ/0^\circ)$, as is shown in Figure 21(c).

The dimensionless frequencies of the first five vibration modes of the structures are computed by both the proposed method and ANSYS and listed in Tables 9, 10, and 11, and the first five mode shapes are shown in Figures 22, 23, and 24. In ANSYS, 4800 elements are used to discretise the structure. The agreement of the two sets of results is good.

TABLE 9: Dimensionless free vibration frequencies of the laminated shell (Figure 21(a)).

Modes	Present results	ANSYS results	Relative errors
1	8.10352	8.01745	1.1%
2	8.10352	8.01745	1.1%
3	10.01294	9.86091	1.5%
4	13.70969	13.49473	1.6%
5	15.17441	14.93191	1.6%

TABLE 10: Dimensionless free vibration frequencies of the laminated shell (Figure 21(b)).

Modes	Present results	ANSYS results	Relative errors
1	9.18846	9.08674	1.1%
2	9.18846	9.08674	1.1%
3	9.65333	9.58148	0.7%
4	13.41558	13.23601	1.4%
5	14.99186	14.81606	1.2%

TABLE 11: Dimensionless free vibration frequencies of the laminated shell (Figure 21(c)).

Modes	Present results	ANSYS results	Relative errors
1	7.09973	7.07069	0.4%
2	7.09973	7.07069	0.4%
3	9.75645	9.71035	0.5%
4	15.16616	15.11418	0.3%
5	18.02388	17.94379	0.4%

6. Conclusions

An element-free Galerkin method that is based on the FSDT is proposed for the free vibration analysis of folded symmetrically laminated plate structures. A folded laminated plate is considered to be a composite structure of flat symmetrical laminates. The global stiffness and mass matrices of the folded plate are formed by superposing the stiffness and mass matrices of the laminates that are derived with the meshfree method. In order to ensure the success of the superposition, a treatment initially developed for the enforcement of essential boundary conditions is extended to modify the stiffness and mass matrices before the superposition, which has overcome the difficulties that the EFG handles displacement compatibility and improved the applicability of EFG to composite structures. The proposed method does not rely on meshes; therefore, mesh disorder due to the large deformation of problem domain is avoided. The convergence and accuracy of the proposed method are demonstrated by a comparison of the solutions of several examples with those that are given by ANSYS. Good agreement between the two sets of results is observed. The proposed method used a relatively small number of nodes to obtain the calculated results close to the

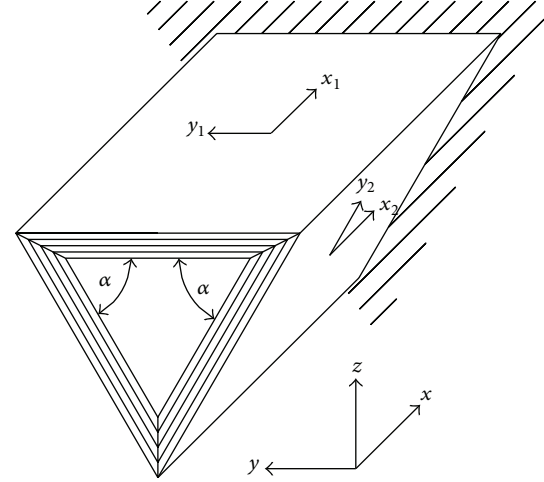


FIGURE 18: A tub structure with three folds.

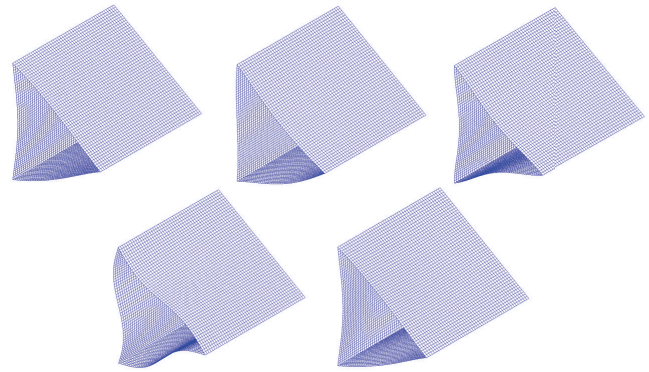


FIGURE 19: First five vibration mode shapes of the tub structure.

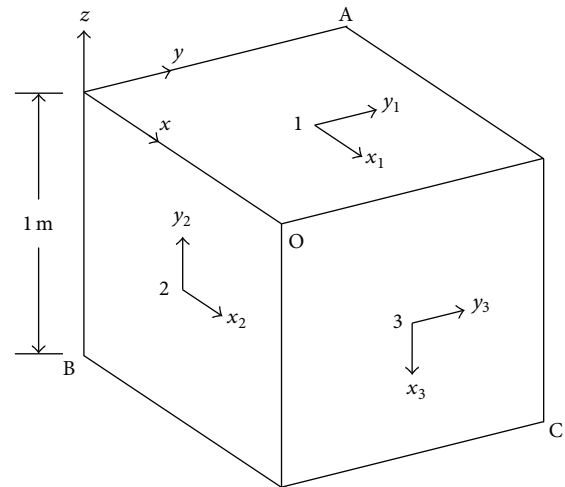


FIGURE 20: A laminated shell structure.

solutions given by ANSYS with a large number of nodes, and the linear analysis by the proposed meshless method in the paper can be the basis for future nonlinear analysis. The treatment introduced with the proposed method has provided a clue for EFG to be applied to composite structures.

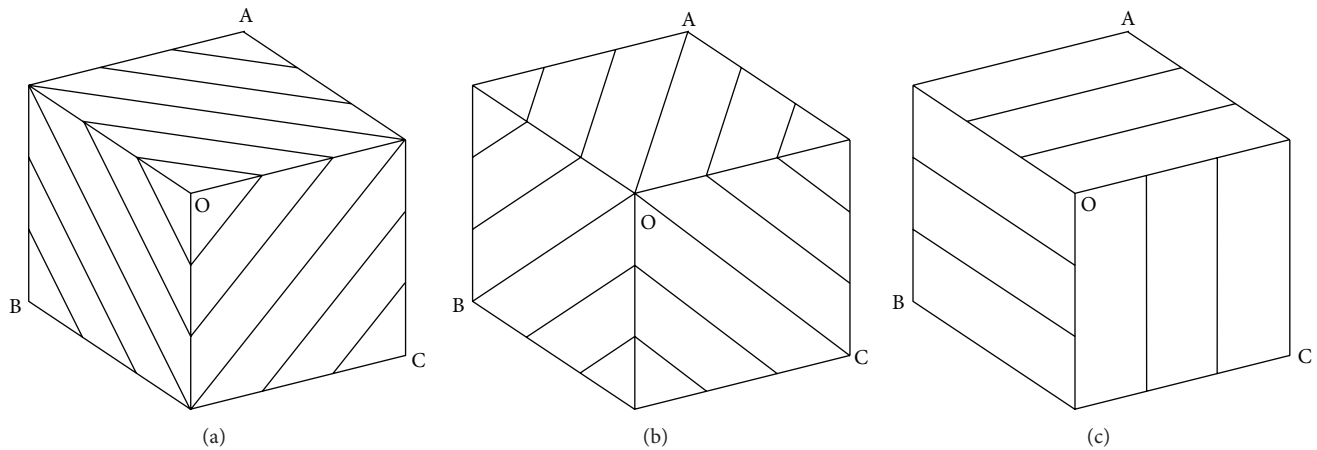


FIGURE 21: Lamination schemes of the laminated shell.

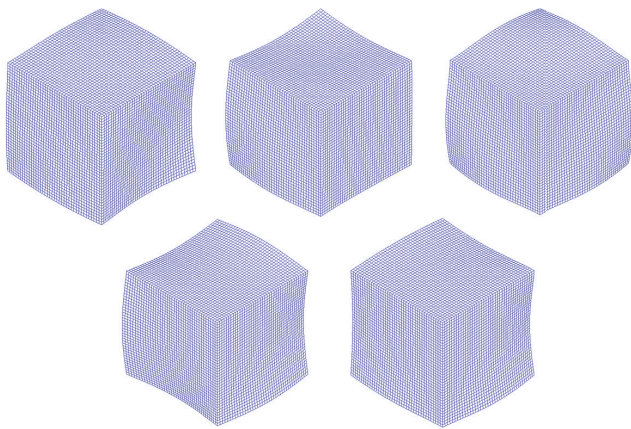


FIGURE 22: First five vibration mode shapes of the laminated shell (Case 1).

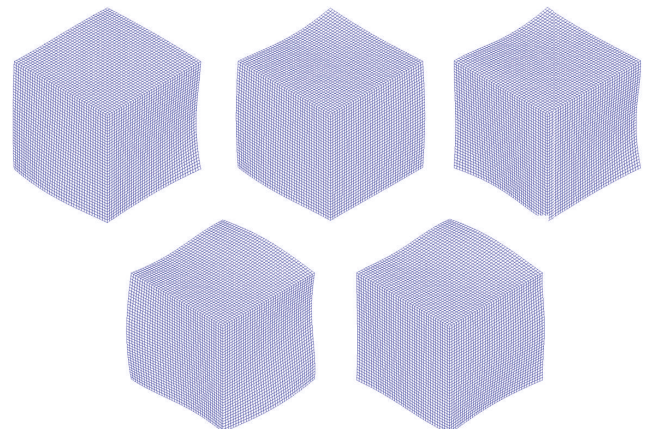


FIGURE 24: First five vibration mode shapes of the laminated shell (Case 3).

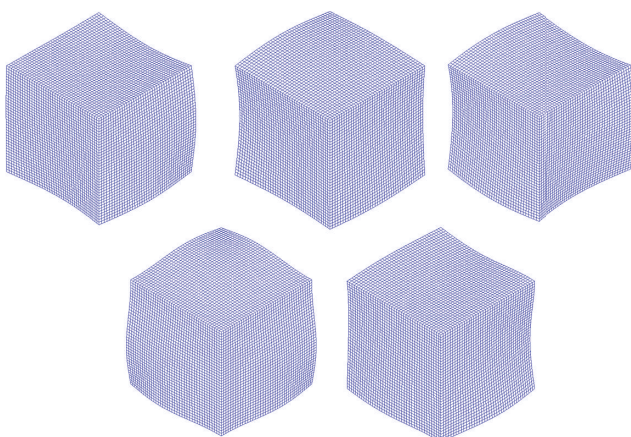


FIGURE 23: First five vibration mode shapes of the laminated shell (Case 2).

Conflict of Interests

The author declares that there is no conflict of interests regarding the publication of this paper.

Acknowledgments

The work that is described in this paper has been supported by the grants awarded by the National Natural Science Foundation of China (Projects nos. 11102044, 51168003, and 11562001), the Systematic Project of Guangxi Key Laboratory of Disaster Prevention and Structural Safety (Project no. 2012ZDX07), and Key Project of Guangxi Science and Technology Lab Center (Fund no. LGZX201101).

References

- [1] Task Committee, "Phase I report on folded plate construction. Report of the Task Committee on folded plate construction. Committee on Masonry and Reinforced Concrete of the Structural Division," *Journal of Structural Division*, vol. 89, pp. 365–406, 1963.
- [2] I. Gaafar, "Hipped plate analysis considering joint displacement," *Transaction of ASCE*, vol. 119, pp. 743–784, 1954.
- [3] D. Yitzhaki, *The Design of Prismatic and Cylindrical Shell Roofs*, Haifa Science, Haifa, Israel, 1958.
- [4] D. Yitzhaki and M. Reiss, "Analysis of folded plates," *ASCE Journal of the Structural Division*, vol. 88, pp. 107–142, 1962.

- [5] C. S. Whitney, B. G. Anderson, and H. Birnbaum, "Reinforced concrete folded plate construction," *ASCE Journal of the Structural Division*, vol. 85, pp. 15–43, 1959.
- [6] J. E. Goldberg and H. L. Leve, "Theory of prismatic folded plate structures," *International Association for Bridge and Structural Engineering*, vol. 17, pp. 59–86, 1957.
- [7] A. G. Niyogi, M. K. Laha, and P. K. Sinha, "Finite element vibration analysis of laminated composite folded plate structures," *Shock and Vibration*, vol. 6, no. 5, pp. 273–283, 1999.
- [8] P. Bar-Yoseph and I. Hersckovitz, "Analysis of folded plate structures," *Thin-Walled Structures*, vol. 7, no. 2, pp. 139–158, 1989.
- [9] J. N. Bandyopadhyay and P. K. Laad, "Comparative analysis of folded plate structures," *Computers & Structures*, vol. 36, no. 2, pp. 291–296, 1990.
- [10] Y. Lai, Z. Wu, Y. Zhu, and A. Sun, "Geometrical non-linear analysis of a simply-supported cross V-shaped folded plate roof," *Thin-Walled Structures*, vol. 37, no. 3, pp. 259–275, 2000.
- [11] Y. K. Cheung, "Folded plate structures by finite strip method," *Journal of the Structural Division, ASCE*, vol. 95, pp. 2963–2979, 1969.
- [12] B. W. Golley and W. A. Grice, "Prismatic folded plate analysis using finite strip-elements," *Computer Methods in Applied Mechanics and Engineering*, vol. 76, no. 2, pp. 101–118, 1989.
- [13] A. L. Eterovic and L. A. Godoy, "An exact strip method for folded plate structures," *Computers and Structures*, vol. 32, no. 2, pp. 263–276, 1989.
- [14] M. Ohga, T. Shigematsu, and S. Kohigashi, "Analysis of folded plate structures by a combined boundary element-transfer matrix method," *Computers and Structures*, vol. 41, no. 4, pp. 739–744, 1991.
- [15] W. H. Liu and C. C. Huang, "Vibration analysis of folded plates," *Journal of Sound and Vibration*, vol. 157, no. 1, pp. 123–137, 1992.
- [16] B. Perry, P. Bar-Yoseph, and G. Rosenhouse, "Rectangular hybrid shell element for analysing folded plate structures," *Computers and Structures*, vol. 44, no. 1-2, pp. 177–185, 1992.
- [17] M. Duan and Y. Miyamoto, "Effective hybrid/mixed finite elements for folded-plate structures," *Journal of Engineering Mechanics*, vol. 128, no. 2, pp. 202–208, 2002.
- [18] T. Belytschko, Y. Y. Lu, and L. Gu, "Element-free Galerkin methods," *International Journal for Numerical Methods in Engineering*, vol. 37, no. 2, pp. 229–256, 1994.
- [19] J.-S. Chen, C. Pan, C.-T. Wu, and W. K. Liu, "Reproducing kernel particle methods for large deformation analysis of non-linear structures," *Computer Methods in Applied Mechanics and Engineering*, vol. 139, no. 1-4, pp. 195–227, 1996.
- [20] L. X. Peng, S. Kitipornchai, and K. M. Liew, "Bending analysis of folded plates by the FSDT meshless method," *Thin-Walled Structures*, vol. 44, no. 11, pp. 1138–1160, 2006.
- [21] L. X. Peng, S. Kitipornchai, and K. M. Liew, "Analysis of rectangular stiffened plates under uniform lateral load based on FSDT and element-free Galerkin method," *International Journal of Mechanical Sciences*, vol. 47, no. 2, pp. 251–276, 2005.
- [22] L. X. Peng, S. Kitipornchai, and K. M. Liew, "Free vibration analysis of folded plate structures by the FSDT mesh-free method," *Computational Mechanics*, vol. 39, no. 6, pp. 799–814, 2007.
- [23] T. Q. Bui, M. N. Nguyen, and C. Zhang, "An efficient meshfree method for vibration analysis of laminated composite plates," *Computational Mechanics*, vol. 48, no. 2, pp. 175–193, 2011.
- [24] T. Q. Bui and M. N. Nguyen, "Meshfree Galerkin Kriging model for bending and buckling analysis of simply supported laminated composite plates," *International Journal of Computational Methods*, vol. 10, no. 3, Article ID 1350011, 2013.
- [25] M. Somireddy and A. Rajagopal, "Meshless natural neighbor Galerkin method for the bending and vibration analysis of composite plates," *Composite Structures*, vol. 111, no. 1, pp. 138–146, 2014.
- [26] S.-Y. Lee, S.-C. Wooh, and S.-S. Yhim, "Dynamic behavior of folded composite plates analyzed by the third order plate theory," *International Journal of Solids and Structures*, vol. 41, no. 7, pp. 1879–1892, 2004.
- [27] J. N. Reddy, *Theory and Analysis of Elastic Plates*, Taylor & Francis, London, UK, 1999.
- [28] J. N. Reddy and A. Miravete, *Practical Analysis of Composite Laminates*, CRC Press, Boca Raton, Fla, USA, 1995.
- [29] SHELL99, Element Reference, ANSYS Documentation.

Research Article

SPH Simulation of Acoustic Waves: Effects of Frequency, Sound Pressure, and Particle Spacing

Y. O. Zhang,^{1,2} T. Zhang,^{1,3} H. Ouyang,⁴ and T. Y. Li^{1,3}

¹*School of Naval Architecture and Ocean Engineering, Huazhong University of Science and Technology, Wuhan 430074, China*

²*Department of Mechanical and Aerospace Engineering, University of California, San Diego, La Jolla, CA 92093, USA*

³*Hubei Key Laboratory of Naval Architecture and Ocean Engineering Hydrodynamics, Huazhong University of Science and Technology, Wuhan 430074, China*

⁴*School of Engineering, University of Liverpool, The Quadrangle, L69 3GH Liverpool, UK*

Correspondence should be addressed to T. Zhang; zhangt7666@mail.hust.edu.cn

Received 30 August 2014; Revised 15 November 2014; Accepted 15 November 2014

Academic Editor: Kim M. Liew

Copyright © 2015 Y. O. Zhang et al. This is an open access article distributed under the Creative Commons Attribution License, which permits unrestricted use, distribution, and reproduction in any medium, provided the original work is properly cited.

Acoustic problems consisting of multiphase systems or with deformable boundaries are difficult to describe using mesh-based methods, while the meshfree, Lagrangian smoothed particle hydrodynamics (SPH) method can handle such complicated problems. In this paper, after solving linearized acoustic equations with the standard SPH theory, the feasibility of the SPH method in simulating sound propagation in the time domain is validated. The effects of sound frequency, maximum sound pressure amplitude, and particle spacing on numerical error and time cost are then subsequently discussed based on the sound propagation simulation. The discussion based on a limited range of frequency and sound pressure demonstrates that the rising of sound frequency increases simulation error, and the increase is nonlinear, whereas the rising sound pressure has limited effects on the error. In addition, decreasing the particle spacing reduces the numerical error, while simultaneously increasing the CPU time. The trend of both changes is close to linear on a logarithmic scale.

1. Introduction

Some classic numerical methods such as the finite element method (FEM) [1, 2], the boundary element method (BEM) [3], and other modified or coupled methods [4–6] are widely used for acoustic simulations. However, these mesh-based methods are not ideal for solving acoustic problems consisting of a variety of media or with deformable boundaries.

Meshfree methods can handle such complicated problems. The method of fundamental solutions (MFS) [7], the multiple-scale reproducing kernel particle method (RKPM) [8], the element-free Galerkin method (EFGM) [9], and other meshfree methods [10, 11] have been applied to these acoustic problems.

The smoothed particle hydrodynamics (SPH) method, as a meshfree, Lagrangian method, was first independently pioneered by Lucy [12] and Gingold and Monaghan [13] to solve astrophysical problems in 1977. In addition, the SPH

method has been used in many different fields [14–16]. It not only has most advantages of a meshfree method, but also is suitable for solving problems with material separation or large ranges of density as illustrated in recent reviews by Li and Liu [17], Springel [18], M. B. Liu and G. R. Liu [19], and Monaghan [20] due to its Lagrangian property. Introducing the SPH method to acoustic computation also brings its advantages to some fields like bubble acoustic, combustion noise, sound propagation in multiphase flows, and so on.

With the advance of the SPH method in acoustic simulation, some research literatures [21, 22] discussed solving fluid dynamic equations to simulate sound waves. In addition, we published a conference paper [23] that used the SPH method to solve linearized acoustic equations for modeling sound propagation and interference. Numerical results showed that the SPH method was capable of accurately modeling sound propagation, but the effects of frequency and sound pressure on the SPH simulation need further discussion. Therefore, the

present paper focuses on discussing the effect of frequency and sound pressure of the acoustic waves on the numerical error caused by the SPH simulation.

The present paper is organized as follows. In Section 2, the standard SPH theory is used to solve the linearized acoustic equations. In Section 3, a one-dimensional sound propagation model is built. In Section 4, a numerical experiment is given based on standard SPH algorithms, and the effect of frequency, sound pressure, and particle spacing on the simulation is analyzed with considering the changes of particle spacing and Courant number. Section 5 summarizes the results of this work.

2. SPH Formulations of Sound Waves

2.1. Basic Formulations of SPH. As a meshfree, Lagrangian particle method, the SPH method is an important method widely used in recent years. Formulations in the SPH theory are represented in a particle approximation form. The properties of each particle are computed using an interpolation process over its neighboring particles [24]. In this way, the integral of a field function $f(\mathbf{r})$ can be represented as

$$\langle f(\mathbf{r}) \rangle = \int_{\Omega} f(\mathbf{r}') W(\mathbf{r} - \mathbf{r}', h) d\mathbf{r}', \quad (1)$$

where $\langle \cdot \rangle$ is the kernel approximation operator, f is a function of the vector \mathbf{r} , Ω is the volume of the integral, W is the smoothing kernel, and h is the smoothing length.

The particle approximation for the function $f(\mathbf{r})$ at particle i within the support domain can be written as

$$\langle f(\mathbf{r}_i) \rangle = \sum_{j=1}^N \frac{m_j}{\rho_j} f(\mathbf{r}_j) \cdot W_{ij}, \quad (2)$$

where \mathbf{r}_i and \mathbf{r}_j are the position of particles i and j , N is the number of particles in the computational domain, m_j is the mass of particle j , $W_{ij} = W(r_{ij}, h)$, and r_{ij} is the distance between particle i and particle j .

Similarly, the gradient of function $f(\mathbf{r})$ at particle i is obtained as

$$\langle \nabla \cdot f(\mathbf{r}_i) \rangle = \sum_{j=1}^N \frac{m_j}{\rho_j} f(\mathbf{r}_j) \cdot \nabla_i W_{ij}, \quad (3)$$

where $\nabla_i W_{ij} = ((\mathbf{r}_i - \mathbf{r}_j)/r_{ij})(\partial W_{ij}/\partial r_{ij})$.

2.2. SPH Formulations of Sound Waves. In acoustic simulation, the governing equations for constructing SPH formulations are the laws of continuity, momentum, and state. The simplest and most common acoustical problem occurs under some assumptions. On one hand, the medium is lossless and at rest, so an energy equation is unnecessary; on the other hand, a small departure from quiet conditions occurs as follows:

$$\rho = \rho_0 + \delta\rho, \quad |\delta\rho| \ll \rho_0 \quad (4)$$

$$P = p_0 + p, \quad |p| \ll \rho_0 c_0^2 \quad (5)$$

$$\mathbf{u} = \mathbf{0} + \mathbf{u}, \quad |\mathbf{u}| \ll c_0, \quad (6)$$

where ρ is the fluid density, ρ_0 is the quiescent density which does not vary in time and space, $\delta\rho$ is the change of density, P is the instantaneous pressure at time t of the fluid, p_0 is the quiescent pressure, p is the sound pressure, c_0 is the speed of sound, and \mathbf{u} is the flow velocity. $\delta\rho$, p , and \mathbf{u} are taken to be small quantities of first order.

By discarding second-order terms in the acoustic equations, the linearized continuity, momentum, and state equations (for ideal air) governing sound waves are obtained as

$$\frac{\partial(\delta\rho)}{\partial t} = -\rho \nabla \cdot \mathbf{u} \quad (7)$$

$$\frac{\partial \mathbf{u}}{\partial t} = -\frac{1}{\rho} \nabla p \quad (8)$$

$$p = c_0^2 \delta\rho. \quad (9)$$

Applying the SPH particle approximation (see (3)) to (7), the particle approximation equation of the continuity of acoustic waves is written as

$$\frac{\partial(\delta\rho_i)}{\partial t} = (\rho_0 + \delta\rho_i) \sum_{j=1}^N \frac{m_j}{(\rho_0 + \delta\rho_j)} \mathbf{u}_{ij} \cdot \nabla_i W_{ij}, \quad (10)$$

where ρ_0 is the quiescent density which does not vary in time and space, p_0 is the quiescent pressure, and $\mathbf{u}_{ij} = \mathbf{u}_i - \mathbf{u}_j$.

The momentum equation in SPH method is obtained as

$$\frac{\partial \mathbf{u}_i}{\partial t} = \sum_{j=1}^N m_j \left[\frac{p_i}{(\rho_0 + \delta\rho_i)^2} + \frac{p_j}{(\rho_0 + \delta\rho_j)^2} \right] \nabla_i W_{ij}. \quad (11)$$

Particle approximation of the equation of state is

$$p_i = c_0^2 \delta\rho_i. \quad (12)$$

The cubic spline function given by Monaghan and Lattanzio [25] is used as the smoothing kernel in this paper, which is written as

$$W(r, h) = \alpha_D \begin{cases} 1 - \frac{3}{2}q^2 + \frac{3}{4}q^3 & 0 \leq q \leq 1 \\ \frac{1}{4}(2-q)^3 & 1 \leq q \leq 2 \\ 0 & q \geq 2, \end{cases} \quad (13)$$

where α_D is $1/h$ in one-dimensional space, $q = r/h$, r is the distance between two particles, and h is the smoothing length which defines the influence area of smoothing function W .

The second-order leap-frog integration [26] is used in the present paper. All-pair search approach [24], as a direct and simple algorithm, is used to realize the neighbor particles searching in the acoustic wave simulation.

3. Sound Propagation Model

In order to evaluate the effect of sound pressure and frequency, a one-dimensional sound wave which propagates in a pipe with uniform cross section is used. The acoustic model is shown in Figure 1. The sound pressure at $t = 0$ is plotted with

TABLE 1: Model parameters and computational parameters for the numerical experiment.

Model parameters	p_{Amp} 50 Pa	ω 50 rad/s	c_0 340 m/s	t 0.1 s
Computational parameters	Particle spacing 0.04 m	Smoothing length 0.13 m	Courant number 0.05	Particle mass 0.04 kg

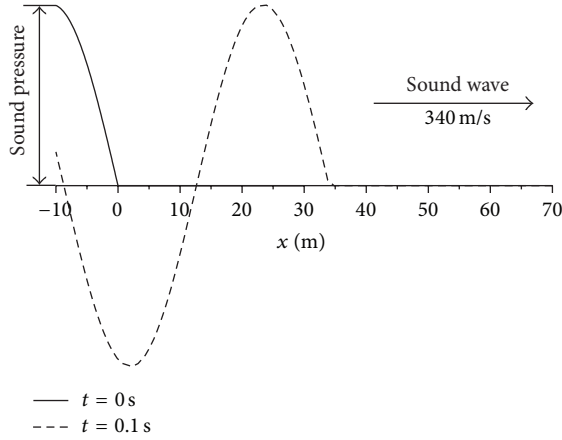


FIGURE 1: One-dimensional sound propagation model.

a solid line, while the sound pressure at $t = 0.1$ s is plotted with a dashed line.

Sound pressure of the source of sound wave in Figure 1 is

$$p(t, x < 0) = p_{\text{Amp}} \sin(\omega t - kx), \quad (14)$$

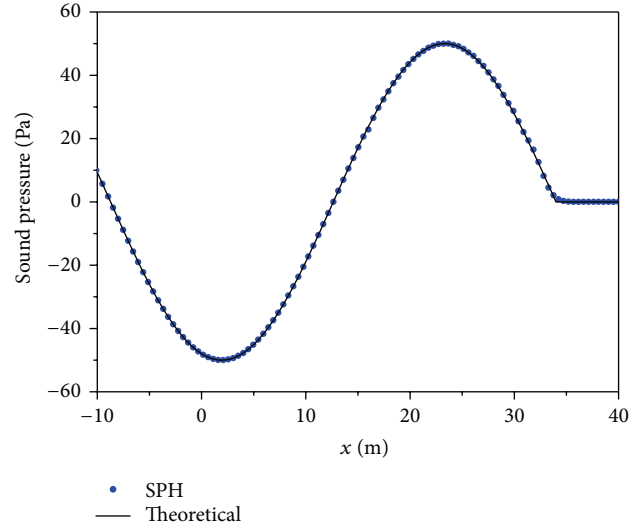
where t represents time (propagation starts when $t = 0$), x is the geometric position, p_{Amp} is the maximum sound pressure of the acoustic wave, ω is the circular frequency of the acoustic wave, $k = \omega/c_0$ is the wave number, and the sound speed c_0 is 340 m/s.

The sound propagates from $x < 0$ to $x \geq 0$, with the SPH computational region going from -10 m to 70 m. In the computation, the region of the sound source is from -10 m to 0 m, which is determined by the theoretical solutions, while the region of sound propagation is from 0 m to 70 m, which is obtained by the SPH method. At the end of the sound propagation domain, the particles are set free in the computation. Since the SPH computational region is far longer than the sound propagation distance, any effects caused by ignoring this boundary will not propagate to the sound propagation domain and therefore can be neglected. The simulation results at the time $t = 0.1$ s are used to compare with the theoretical solutions. A similar numerical model is used in our recent conference paper [23].

In the evaluation of numerical results, the nondimensional simulation error of the sound pressure is defined by

$$\varepsilon_{\text{pre}} = \frac{1}{N \cdot p_{\text{Amp}}} \sqrt{\sum_{j=1}^N (p_j^* - p(x_j))^2}, \quad (15)$$

where p_j^* is the simulation pressure of the particle j and $p(x_j)$ is the theoretical pressure at the position of particle j .

FIGURE 2: Sound pressure comparison between SPH results and theoretical solutions. ($p_{\text{Amp}} = 50$ Pa, $\omega = 50$ rad/s, and $t = 0.1$ s).

4. Results and Discussion

4.1. Numerical Experiment. A sound propagation model is built to confirm agreement between SPH simulation results and the theoretical solution. The parameters used in the numerical experiment of the sound waves are listed in Table 1. The physical time required for the modeling was 141.6 seconds.

A comparison between the SPH results and theoretical solutions of sound pressure at $t = 0.1$ s is shown in Figure 2. The theoretical solution is plotted with a solid line while the SPH results are plotted with red points. In order to clearly identify the numerical results, the points are plotted at intervals of 12.

As shown in Figure 2, the sound pressure of the sound wave changes along with the position, and a peak and a valley appear in the final wave at $t = 0.1$ s. Comparing with the analytical data, it can be seen that the SPH method can accurately simulate the sound pressure of an acoustic wave as the values of sound pressure can be obtained precisely, and the simulation error is 1.6×10^{-4} . The trend of both the SPH results and the theoretical solutions also has a similar tendency.

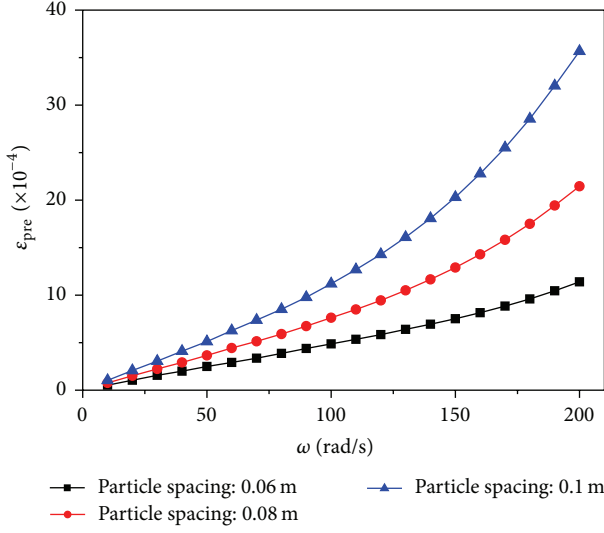


FIGURE 3: Sound pressure error versus circular frequency for different particle spacings.

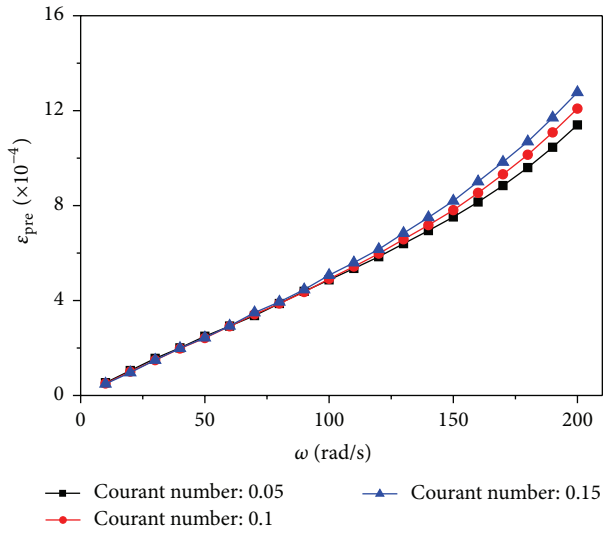


FIGURE 4: Sound pressure error versus circular frequency for different Courant numbers.

4.2. Effect of Frequency. Different sound propagation models with the circular frequency of sound changing from 10 rad/s to 200 rad/s are simulated, and the effect of circular frequency is discussed. In the discussion, different computational parameters, namely, the particle spacing and the Courant number, are also considered.

Figure 3 gives the numerical error for different computational cases with different ω and particle spacing. Figure 4 shows the sound pressure error for different cases with different values of circular frequency and Courant number. Each point in both figures stands for a computational case. The Courant number used in the computational cases in Figure 3 is 0.05, and the particle spacing used in all cases in Figure 4 is 0.06 m.

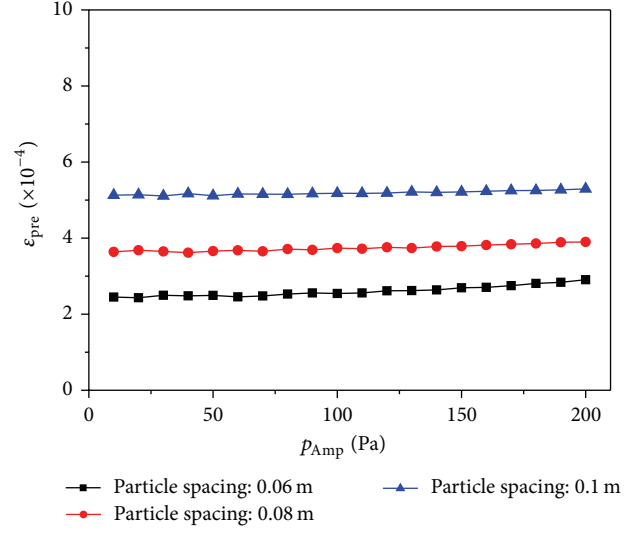


FIGURE 5: Sound pressure error versus maximum sound pressure amplitude for different particle spacings.

As can be seen from Figure 3, ϵ_{pre} increases along with the increase of ω , and the increase of ϵ_{pre} is nonlinear. Along with the increase of ω , the increase of ϵ_{pre} is larger. On the other hand, we can see from the line graph that ϵ_{pre} is much larger than other positions when ω is 200 rad/s. The numerical error grows faster when the particle spacing is larger.

As shown in Figure 4, ϵ_{pre} increases along with the increase of ω . What is more, three lines represent three different Courant numbers, namely, three different choices of time step when the particle spacing is the same. ϵ_{pre} obtained from three different Courant numbers has almost the same value when ω is under 100 rad/s. After that, some difference is shown among three lines when ω becomes larger, but the Courant number affects the effect of ω less in general.

4.3. Effect of Sound Pressure. In the present section, different sound propagation models with the maximum sound pressure amplitude changing from 10 Pa to 200 Pa are simulated, and the effects of sound pressure are discussed. At the same time, different computational parameters, namely, the particle spacing and the Courant number, are also used in the simulation. The ω of the sound in all computational cases in this section is 50 rad/s.

Figure 5 illustrates the changes of sound pressure error when the numerical model uses different p_{Amp} and particle spacing. Figure 6 describes the changes of error with different p_{Amp} and different Courant numbers. Each point in both figures stands for a computational case. The Courant number used in all computational cases in Figure 5 is 0.05, and the particle spacing used in all cases in Figure 6 is 0.06 m.

It can be seen from the line graph that ϵ_{pre} has limited change, which is a little increase, along with the increase of p_{Amp} . The trend of the line is approximately linear when p_{Amp} changes from 10 Pa to 200 Pa. The value of three lines in the figure is around 2.7×10^{-4} , 3.7×10^{-4} , and 5.2×10^{-4} corresponding to the particle spacing changes from 0.06 m

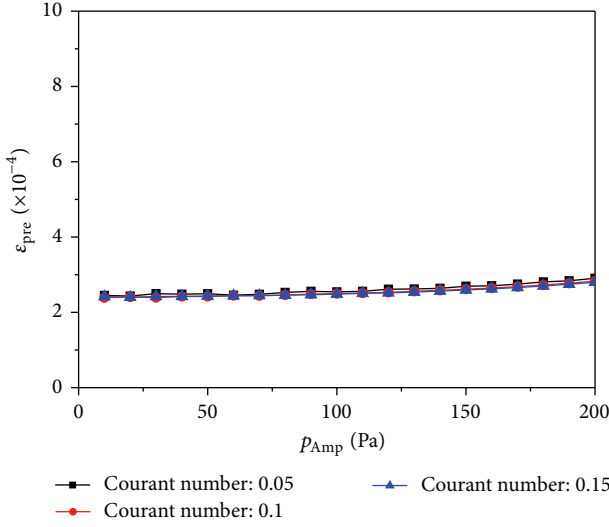


FIGURE 6: Sound pressure error versus maximum sound pressure amplitude for different Courant numbers.

to 0.1 m. In other words, when the particle spacing increases, the error shows an upward trend.

Similarly, ϵ_{pre} rises a little along with the increase of the amplitude of sound wave as shown in Figure 6. Specifically, ϵ_{pre} stays at about 2.6×10^{-4} when the amplitude of sound changes from 10 Pa to 200 Pa. Although with different Courant number, the error of numerical results has similar values. The largest difference of ϵ_{pre} among three lines is 2.0×10^{-5} , which happens when p_{Amp} reaches 200 Pa.

4.4. Effect of Particle Spacing. In addition to the accuracy, the convergence and the computational efficiency are also worth concern. Particle spacing, as an important parameter in the SPH simulation, affects these indexes a lot. In this section, the effects of the particle spacing are analyzed based on the model in Section 4.1 with the particle spacing (Δx) changes from 0.03 m to 0.3 m.

Different sound pressure errors corresponding to the SPH simulation results with different Δx are shown in Figure 7. Three different types of points are used in the figure to represent Courant numbers of 0.05, 0.10, and 0.15 in the computation. In order to clearly show the trend, logarithmic scales are used for both axes in the figure.

As can be seen from Figure 7, there is an approximately linear relation between ϵ_{pre} and Δx with double logarithmic coordinates. As Δx increases, ϵ_{pre} also increases. This result indicates a convergence of the simulation, as a smaller Δx leads to a more accurate result. Note that the errors generated with the three different Courant numbers all have similar values. A linear fitted curve obtained by using all ϵ_{pre} results produces a slope of approximately 1.4 for the fitted line.

The required CPU cost in terms of time to perform the SPH simulation corresponding to different Δx values is given in Figure 8. Three different point types were also used to represent different Courant numbers in the computation. The

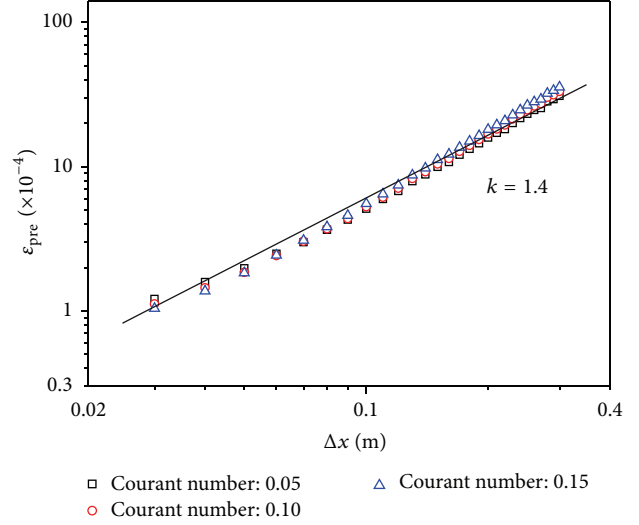


FIGURE 7: Sound pressure error versus particle spacing for different Courant numbers.

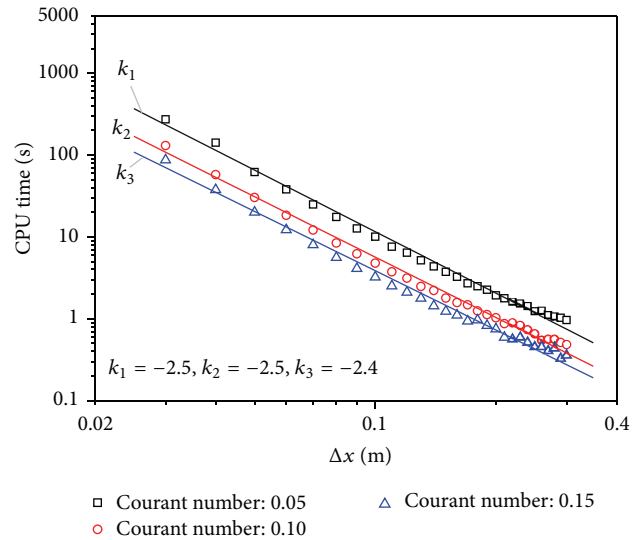


FIGURE 8: CPU time versus particle spacing for different Courant numbers.

figure also shows the linear fit lines for each Courant number, as well as the calculated slopes.

The graph shows that the CPU time logarithmically decreases from hundreds of seconds to about one second as Δx increases from 0.03 m to 0.3 m. This decreasing trend is roughly linear, with an absolute slope value of approximately 2.5. Although the CPU time is different for each Courant number, the trends are similar. Thus, an appropriate particle spacing value can be decided within a certain range by comparing the results in Figures 7 and 8 for a given application.

5. Conclusions

In this work, the meshfree, Lagrangian SPH method is used to solve linearized acoustic equations. The feasibility of

the SPH method in simulating acoustic waves is evaluated using a numerical experiment of one-dimensional sound propagation model. The effect of frequency, sound pressure, and particle spacing is then subsequently discussed based on the numerical error with considering the Courant number.

- (1) The results of computational cases, with the acoustic wave frequency changes from 10 rad/s to 200 rad/s, show that the rising of sound frequency increases simulation error, and the increase is nonlinear.
- (2) As the maximum sound pressure amplitude changes from 10 Pa to 200 Pa, the rising sound pressure increases the simulation error. However, the resulting change in error is limited and marginal.
- (3) Decreasing the particle spacing in the computation reduces the numerical error, while simultaneously increasing the CPU time. The trend of both changes is close to linear on a logarithmic scale. The Courant number has little effect on the error generated with different sound frequency or sound pressure, whereas the particle spacing has a more significant influence on both properties.

Conflict of Interests

The authors declare that there is no conflict of interests regarding the publication of this paper.

Acknowledgments

This study was supported by the Independent Innovation Foundation for National Defence of Huazhong University of Science and Technology (no. 01-18-140019). Y. O. Zhang is supported by the China Scholarship Council (201406160032).

References

- [1] F. Ihlenburg, *Finite Element Analysis of Acoustic Scattering*, Springer, 1998.
- [2] I. Harari, "A survey of finite element methods for time-harmonic acoustics," *Computer Methods in Applied Mechanics and Engineering*, vol. 195, no. 13–16, pp. 1594–1607, 2006.
- [3] P. K. Kythe, *An Introduction to Boundary Element Methods*, CRC Press, 1995.
- [4] A. Warszawski, D. Soares Jr., and W. J. Mansur, "A FEM-BEM coupling procedure to model the propagation of interacting acoustic-acoustic/acoustic-elastic waves through axisymmetric media," *Computer Methods in Applied Mechanics and Engineering*, vol. 197, no. 45–48, pp. 3828–3835, 2008.
- [5] D. Soares Jr., "Coupled numerical methods to analyze interacting acoustic-dynamic models by multidomain decomposition techniques," *Mathematical Problems in Engineering*, vol. 2011, Article ID 245170, 28 pages, 2011.
- [6] J. Feng, X. Zheng, H. Wang, Y. Zou, Y. Liu, and Z. Yao, "Low-frequency acoustic-structure analysis using coupled FEM-BEM method," *Mathematical Problems in Engineering*, vol. 2013, Article ID 583079, 8 pages, 2013.
- [7] A. Tadeu and I. Castro, "Coupling the BEM/TBEM and the MFS for the numerical simulation of wave propagation in heterogeneous fluid-solid media," *Mathematical Problems in Engineering*, vol. 2011, Article ID 159389, 26 pages, 2011.
- [8] R. A. Uras, C. T. Chang, Y. Chen, and W. K. Liu, "Multiresolution reproducing kernel particle methods in acoustics," *Journal of Computational Acoustics*, vol. 5, no. 1, pp. 71–94, 1997.
- [9] P. Bouillard and S. Suleau, "Element-free Galerkin solutions for Helmholtz problems: formulation and numerical assessment of the pollution effect," *Computer Methods in Applied Mechanics and Engineering*, vol. 162, no. 1–4, pp. 317–335, 1998.
- [10] S. Wang, S. Li, Q. Huang, and K. Li, "An improved collocation meshless method based on the variable shaped radial basis function for the solution of the interior acoustic problems," *Mathematical Problems in Engineering*, vol. 2012, Article ID 632072, 20 pages, 2012.
- [11] F. Z. Wang and K. H. Zheng, "Analysis of the boundary knot method for 3D Helmholtz-type equation," *Mathematical Problems in Engineering*, vol. 2014, Article ID 853252, 9 pages, 2014.
- [12] L. B. Lucy, "A numerical approach to the testing of the fission hypothesis," *The Astronomical Journal*, vol. 82, pp. 1013–1024, 1977.
- [13] R. A. Gingold and J. J. Monaghan, "Smoothed Particle Hydrodynamics-theory and application to non-spherical stars," *Monthly Notices of the Royal Astronomical Society*, vol. 181, pp. 375–389, 1977.
- [14] F. Caleyron, A. Combescure, V. Faucher, and S. Potapov, "SPH modeling of fluid-solid interaction for dynamic failure analysis of fluid-filled thin shells," *Journal of Fluids and Structures*, vol. 39, pp. 126–153, 2013.
- [15] P. F. Hopkins, "A general class of Lagrangian smoothed particle hydrodynamics methods and implications for fluid mixing problems," *Monthly Notices of the Royal Astronomical Society*, vol. 428, no. 4, pp. 2840–2856, 2013.
- [16] G. W. Ma, Q. S. Wang, X. W. Yi, and X. J. Wang, "A modified SPH method for dynamic failure simulation of heterogeneous material," *Mathematical Problems in Engineering*, vol. 2014, Article ID 808359, 14 pages, 2014.
- [17] S. Li and W. K. Liu, "Meshfree and particle methods and their applications," *Applied Mechanics Reviews*, vol. 55, no. 1, pp. 1–34, 2002.
- [18] V. Springel, "Smoothed particle hydrodynamics in astrophysics," *Annual Review of Astronomy and Astrophysics*, vol. 48, pp. 391–430, 2010.
- [19] M. B. Liu and G. R. Liu, "Smoothed particle hydrodynamics (SPH): an overview and recent developments," *Archives of Computational Methods in Engineering. State of the Art Reviews*, vol. 17, no. 1, pp. 25–76, 2010.
- [20] J. J. Monaghan, "Smoothed particle hydrodynamics and its diverse applications," in *Annual Review of Fluid Mechanics*, vol. 44 of *Annual Review of Fluid Mechanics*, pp. 323–346, Annual Reviews, Palo Alto, Calif, USA, 2012.
- [21] C. T. Wolfe and S. K. Semwal, *Acoustic Modeling of Reverberation Using Smoothed Particle Hydrodynamics*, University of Colorado, Springs, Colo, USA, 2007.
- [22] P. Hahn and D. Negrut, "On the use of meshless methods in acoustic simulations," in *Proceedings of the International Mechanical Engineering Congress and Exposition (IMECE '09)*, pp. 185–199, November 2009.
- [23] Y. O. Zhang, T. Zhang, H. Ouyang, and T. Y. Li, "SPH simulation of sound propagation and interference," in *Proceedings of the 5th International Conference on Computational Method (ICCM '14)*, Cambridge, UK, July 2014.

- [24] G. R. Liu and M. B. Liu, *Smoothed Particle Hydrodynamics: a Meshfree Particle Method*, World Scientific, 2003.
- [25] J. J. Monaghan and J. C. Lattanzio, "A refined particle method for astrophysical problems," *Astronomy and Astrophysics*, vol. 149, pp. 135–143, 1985.
- [26] M. Kelager, *Lagrangian Fluid Dynamics Using Smoothed Particle Hydrodynamics*, University of Copenhagen, Copenhagen, Denmark, 2006.

Research Article

Numerical Approximation of Nonlinear Klein-Gordon Equation Using an Element-Free Approach

Dong-mei Huang, Guo-liang Zou, and L. W. Zhang

College of Information Technology, Shanghai Ocean University, Shanghai 201306, China

Correspondence should be addressed to L. W. Zhang; lwzhang@shou.edu.cn

Received 1 July 2014; Accepted 22 August 2014

Academic Editor: Kim M. Liew

Copyright © 2015 Dong-mei Huang et al. This is an open access article distributed under the Creative Commons Attribution License, which permits unrestricted use, distribution, and reproduction in any medium, provided the original work is properly cited.

Numerical approximation of nonlinear Klein-Gordon (KG) equation with quadratic and cubic nonlinearity is performed using the element-free improved moving least squares Ritz (IMLS-Ritz) method. A regular arrangement of nodes is employed in this study for the numerical integration to compute the system equation. A functional formulation for the KG equation is established and discretized by the Ritz minimization procedure. Newmark's integration scheme combined with an iterative technique is applied to the resulting nonlinear system equations. The effectiveness and efficiency of the IMLS-Ritz method for the KG equation have been testified through convergence analyses and comparison study between the present results and the exact solutions.

1. Introduction

The Klein-Gordon (KG) equation is essentially a relativistic version of the Schrödinger equation. It has wide applications in many scientific fields, such as quantum mechanics, solid state physics, and nonlinear optics [1]. Similar to the Schrödinger equation, the KG equation is considered as one of the important equations in mathematical physics, as well as kinds of solitons studies, especially in the investigation of solitons interactions for a collisionless plasma and the recurrence of initial states [2, 3].

As a kind of essential nonlinear PDEs, the KG type equations have received considerable attention in deriving both analytical and numerical solutions by using different types of methods, such as the Adomian decomposition method [3, 4], the sine-cosine ansatz and the tanh methods [2, 5, 6], the auxiliary equation method, the Weierstrass elliptic function method, the elliptic equation rational expansion method, and the extended F -function method [7–9]. In the process, various numerical schemes have also been developed based on different theories, such as the homotopy method [10], the cubic B-spline collocation method on a uniform mesh [11], and the approximation with thin plate splines (TPS) radial basis functions (RBF) based collocation approach [12].

To seek for an effective and efficient numerical technique, the meshless method has been successfully developed to

solve partial differential equations that used to describe many physical and engineering problems. The advantages of these meshless methods are as follows: (i) solutions can be obtained with only a minimum of meshing or no meshing at all [13–18]; (ii) a set of scattered nodes is used instead of meshing the entire domain of the problem. Several meshless methods have been proposed and can be chosen as an alternative to search for approximate solutions of the KG equations [19, 20]. Based on different approximation functions, various meshless methods were proposed, such as the element-free Galerkin (EFG) method [21], the moving least squares differential quadrature method [22], the radial point interpolation method [23], the smooth particle hydrodynamics methods [24], the radial basis function [25], the element-free kp-Ritz method [26–30], the meshless local Petrov-Galerkin method [31], the reproducing kernel particle method [32], and the local Kriging method [33].

In this study, by combining the IMLS approximation and the Ritz procedure, the element-free IMLS-Ritz method for numerical solution of the nonlinear KG equation is presented. The cubic spline weight function and linear basis are employed in this study. A regular arrangement of nodes is employed for numerical integration to compute the system equation. A functional formulation for the KG equation is established and discretized by the Ritz procedure. The essential boundary conditions are imposed by the penalty

method. Newmark's integration scheme is employed to solve the nonlinear system equations. The applicability of the IMLS-Ritz method is examined on a few selected example problems. The accuracy of the presented method is also investigated by comparing the obtained numerical results with the existing analytical solutions.

2. Theoretical Formulation

2.1. Equivalent Functional of the One-Dimensional Nonlinear KG Equation. We consider the following KG equation including the nonlinear term as

$$\frac{\partial^2 u(x, t)}{\partial t^2} + \alpha \frac{\partial^2 u(u, t)}{\partial x^2} + \beta u(u, t) + \gamma u^k = f(x, t), \quad (1)$$

$$x \in \Omega, \quad 0 < t \leq T,$$

subject to the initial condition

$$u(x, 0) = u_0, \quad a \leq x \leq b \quad (2)$$

and the boundary conditions

$$u(a, t) = g_1(t), \quad u(b, t) = g_2(t), \quad 0 < t \leq T, \quad (3)$$

where $\Omega = [a, b] \subset \mathbf{R}$, $u(x, t)$ denotes the wave displacement at position x and time t , u_0 , $g_1(t)$, and $g_2(t)$ are known functions, and α , β , and γ are real numbers ($\gamma \neq 0$). The function u is to be determined when functions f , g_1 , and g_2 are given; $k = 2$ for the case of quadratic nonlinearity and $k = 3$ for a cubic nonlinearity.

An equivalent functional is defined in the weighted integral form based on (1) with the initial condition in the following form:

$$\Pi(u) = \int_{\Omega} w \left[\frac{\partial^2 u(x, t)}{\partial t^2} + \alpha \frac{\partial^2 u(u, t)}{\partial x^2} + \beta u(u, t) + \gamma u^k - f(x, t) \right] d\Omega. \quad (4)$$

Using integration by parts and the divergence theorem, (4) yields the following expression:

$$\Pi(u) = \int_{\Omega} \left[-\frac{\alpha}{2} \left(\frac{\partial u}{\partial x} \right)^2 - \frac{1}{2} \left(\frac{\partial u}{\partial t} \right)^2 + \frac{1}{2} \beta u^2 + \frac{\gamma}{k+1} u^{k+1} - u f(x, t) \right] d\Omega, \quad (5)$$

where the weight w is set to be u in this numerical study.

2.2. Improved Moving Least Squares Shape Functions. The IMLS approximation was proposed for construction of the shape functions in the element-free method. In one-dimensional IMLS approximation, for all $f(x)$, $g(x) \in \text{span}(\mathbf{p})$, we define

$$(f, g) = \sum_{l=1}^n w(x - x_l) f(x_l) g(x_l), \quad (6)$$

where (f, g) is an inner product and $\text{span}(\mathbf{p})$ is the Hilbert space.

In $\text{span}(\mathbf{p})$, for the set of points $\{x_i\}$ and weight functions $\{w_i\}$, if functions $p_1(x), p_2(x), \dots, p_m(x)$ satisfy the conditions

$$(p_k, p_j) = \sum_{i=1}^n w_i p_k(x_i) p_j(x_i) = \begin{cases} 0, & k \neq j \\ A_k, & k = j \end{cases} \quad (7)$$

$$(k, j = 1, 2, \dots, m),$$

we furnish the function set $p_1(x), p_2(x), \dots, p_m(x)$ as a weighted orthogonal function set with a weight function $\{w_i\}$ about points $\{x_i\}$. If $p_1(x), p_2(x), \dots, p_m(x)$ are polynomials, the function set $p_1(x), p_2(x), \dots, p_m(x)$ is called a weighted orthogonal polynomials set with a weight function $\{w_i\}$ about points $\{x_i\}$.

Consider an equation system from MLS approximation:

$$\mathbf{A}(x) \mathbf{a}(x) = \mathbf{B}(x) \mathbf{u}, \quad (8)$$

where \mathbf{A} is the moment matrix. Then, (8) can be expressed as

$$\begin{bmatrix} (p_1, p_1) & (p_1, p_2) & \cdots & (p_1, p_m) \\ (p_2, p_1) & (p_2, p_2) & \cdots & (p_2, p_m) \\ \vdots & \vdots & \ddots & \vdots \\ (p_m, p_1) & (p_m, p_2) & \cdots & (p_m, p_m) \end{bmatrix} \begin{bmatrix} a_1(\mathbf{x}) \\ a_2(\mathbf{x}) \\ \vdots \\ a_m(\mathbf{x}) \end{bmatrix} = \begin{bmatrix} (p_1, u_I) \\ (p_2, u_I) \\ \vdots \\ (p_m, u_I) \end{bmatrix}. \quad (9)$$

If the basis function set $p_i(x) \in \text{span}(\mathbf{p})$, $i = 1, 2, \dots, m$, is a weighted orthogonal function set about points $\{x_i\}$, that is, if

$$(p_i, p_j) = 0, \quad (i \neq j), \quad (10)$$

then (8) becomes

$$\begin{bmatrix} (p_1, p_1) & 0 & \cdots & 0 \\ 0 & (p_2, p_2) & \cdots & 0 \\ \vdots & \vdots & \ddots & \vdots \\ 0 & 0 & \cdots & (p_m, p_m) \end{bmatrix} \begin{bmatrix} a_1(\mathbf{x}) \\ a_2(\mathbf{x}) \\ \vdots \\ a_m(\mathbf{x}) \end{bmatrix} = \begin{bmatrix} (p_1, u_I) \\ (p_2, u_I) \\ \vdots \\ (p_m, u_I) \end{bmatrix}. \quad (11)$$

Subsequently, coefficients $a_i(x)$ can be determined accordingly:

$$a_i(x) = \frac{(p_i, u_I)}{(p_i, p_i)}, \quad i = 1, 2, \dots, m; \quad (12)$$

that is,

$$\mathbf{a}(x) = \tilde{\mathbf{A}}(x) \mathbf{B}(x) \mathbf{u}, \quad (13)$$

where

$$\bar{\mathbf{A}}(x) = \begin{bmatrix} \frac{1}{(p_1, p_1)} & 0 & \cdots & 0 \\ 0 & \frac{1}{(p_2, p_2)} & \cdots & 0 \\ \vdots & \vdots & \ddots & \vdots \\ 0 & 0 & \cdots & \frac{1}{(p_m, p_m)} \end{bmatrix}. \quad (14)$$

From (8) and (12), the expression of approximation function $u^h(x)$ is

$$u^h(x) = \bar{\Phi}(x) \mathbf{u} = \sum_{I=1}^n \bar{\Phi}_I(x) u_I, \quad (15)$$

where $\bar{\Phi}(x)$ is the shape function and

$$\bar{\Phi}(x) = (\bar{\Phi}_1(x), \bar{\Phi}_2(x), \dots, \bar{\Phi}_n(x)) = \mathbf{p}^T(x) \bar{\mathbf{A}}(x) \mathbf{B}(x). \quad (16)$$

The abovementioned formulation details an IMLS approximation in which coefficients $a_i(x)$ are obtained directly. It is, therefore, avoiding forming an ill-conditioned or singular equation system.

From (16), we have

$$\bar{\Phi}_I(x) = \sum_{j=1}^m p_j(x) [\bar{\mathbf{A}}(x) \mathbf{B}(x)]_{jI}, \quad (17)$$

which represents the shape function of the IMLS approximation corresponding to node I . From (17), the partial derivatives of $\bar{\Phi}_I(x)$ lead to

$$\bar{\Phi}_{I,i}(x) = \sum_{j=1}^m [p_{j,i}(\bar{\mathbf{A}}\mathbf{B})_{jI} + p_j(\bar{\mathbf{A}}_{,i}\mathbf{B} + \bar{\mathbf{A}}\mathbf{B}_{,i})_{jI}]. \quad (18)$$

The weighted orthogonal basis function set $\mathbf{p} = (p_i)$ is formed by using the Schmidt method as

$$\begin{aligned} p_1 &= 1, \\ &\vdots \\ p_i &= r^{i-1} - \sum_{k=1}^{i-1} \frac{(r^{i-1}, p_k)}{(p_k, p_k)} p_k, \quad i = 2, 3, \dots \end{aligned} \quad (19)$$

Moreover, using the Schmidt method, the weighted orthogonal basis function set $\mathbf{p} = (p_i)$ can be formed from the monomial basis function. For example, for the monomial basis function

$$\bar{\mathbf{p}} = (\bar{p}_i) = (1, x_1, x_2, x_3, x_1x_2, x_1x_3, x_2x_3, x_1^2, x_2^2, x_3^2, \dots), \quad (20)$$

the weighted orthogonal basis function set can be generated by

$$p_i = \bar{p}_i - \sum_{k=1}^{i-1} \frac{(\bar{p}_i, p_k)}{(p_k, p_k)} p_k, \quad i = 1, 2, 3, \dots \quad (21)$$

When the weighted orthogonal basis functions in (20) and (21) are used, there exist fewer coefficients in the trial function.

3. The Ritz Minimization Procedure and Discretion Implementation

In the present work, the penalty method is used to modify the constructed functional in implementing the specified Dirichlet boundary conditions for a domain Ω bounded by Γ . We use a penalty parameter λ to penalize the difference between the displacement of the IMLS approximation and the prescribed displacement on the essential boundary. The penalty function can be expressed as

$$T = \frac{\lambda}{2} \int_{\Gamma_1} (u - \bar{u})^2 d\Gamma, \quad (22)$$

where λ is the penalty parameter and \bar{u} is the specified function on the Dirichlet boundary Γ_1 . Normally, λ is chosen as $10^3 \sim 10^7$ which is case dependent.

The resulting functional enforcing the Dirichlet boundary conditions for the KG equation is

$$\Pi^*(u) = \Pi(u) + T. \quad (23)$$

Substituting (5) and (22) into the functional of (23), we have the modified functional

$$\begin{aligned} \Pi^*(u) &= \int_{\Omega} \left[-\frac{\alpha}{2} \left(\frac{\partial u}{\partial x} \right)^2 - \frac{1}{2} \left(\frac{\partial u}{\partial t} \right)^2 + \frac{1}{2} \beta u^2 \right. \\ &\quad \left. + \frac{\gamma}{k+1} u^{k+1} - u f(x, t) \right] d\Omega \\ &\quad + \frac{\lambda}{2} \int_{\Gamma_u} (u - \bar{u})^2 d\Gamma. \end{aligned} \quad (24)$$

The approximation of the field function can be obtained from (15) as follows:

$$\begin{aligned} u^h(x, t) &= \sum_{I=1}^n \bar{\Phi}_I(x) u_I(t) = \Phi(x) \mathbf{U}(t), \\ \frac{\partial u^h(x, t)}{\partial x} &= \sum_{I=1}^n \bar{\Phi}_{I,x}(x) u_I(t) = \Phi_x(x) \mathbf{U}(t), \\ \frac{\partial^2 u^h(x, t)}{\partial t^2} &= \sum_{I=1}^n \bar{\Phi}_{I,x}(x) \frac{\partial^2 u_I(t)}{\partial t^2} = \Phi_x(x) \ddot{\mathbf{U}}(t), \end{aligned} \quad (25)$$

where

$$\begin{aligned} \Phi(x) &= (\Phi_1(x), \Phi_2(x), \dots, \Phi_n(x)), \\ \Phi_x(x) &= (\Phi_{1,x}(x), \Phi_{2,x}(x), \dots, \Phi_{n,x}(x)), \\ \ddot{\mathbf{U}}(t) &= \left(\frac{\partial^2 u_1(t)}{\partial t^2}, \frac{\partial^2 u_2(t)}{\partial t^2}, \dots, \frac{\partial^2 u_n(t)}{\partial t^2} \right)^T. \end{aligned} \quad (26)$$

Substituting (25) into (24) and applying the Ritz minimization procedure to the maximum energy function Π^*

$$\frac{\partial \Pi^*}{\partial u_I(t)} = 0, \quad I = 1, 2, \dots, n, \quad (27)$$

that yields the following matrix form:

$$\mathbf{M}\ddot{\mathbf{u}} + \bar{\mathbf{K}}\mathbf{u} = \bar{\mathbf{F}}, \quad (28)$$

where

$$\bar{\mathbf{K}} = \beta \mathbf{M} - \alpha \mathbf{K} + \mathbf{K}^a,$$

$$\bar{\mathbf{F}} = \mathbf{F} + \mathbf{F}^a,$$

$$\mathbf{M} = \int_{\Omega} \Phi^T \Phi d\Omega,$$

$$\mathbf{K} = \int_{\Omega} \Phi_x^T \Phi_x d\Omega,$$

$$\mathbf{F} = \int_{\Omega} \Phi f(x, t) d\Omega,$$

$$K_{IJ}^a = \alpha \left(\Phi_I(x)^T \Phi_J(x) \Big|_{x=a} + \Phi_I(x)^T \Phi_J(x) \Big|_{x=b} \right),$$

$$F_I^a = -\gamma \int_{\Omega} \Phi_I u^k d\Omega + \lambda \left(\Phi_I(x) \bar{u} \Big|_{x=a} + \Phi_I(x) \bar{u} \Big|_{x=b} \right). \quad (29)$$

To solve the above nonlinear system, time discretization of (28) is forming with Newmark's integration scheme. According to the fundamental assumptions of Newmark's integration

$$\dot{\mathbf{u}}_{t+\Delta t} = \dot{\mathbf{u}}_t + [(1-\delta)\ddot{\mathbf{u}}_t + \delta\ddot{\mathbf{u}}_{t+\Delta t}] \Delta t, \quad (30)$$

$$\mathbf{u}_{t+\Delta t} = \mathbf{u}_{tt} + \dot{\mathbf{u}}_t \Delta t + \left[\left(-\frac{1}{2} - \alpha \right) \ddot{\mathbf{u}}_t + \alpha \ddot{\mathbf{u}}_{t+\Delta t} \right] \Delta t^2,$$

we have

$$\ddot{\mathbf{u}}_{t+\Delta t} = \frac{1}{\alpha \Delta t^2} (\mathbf{u}_{t+\Delta t} - \mathbf{u}_t) - \frac{1}{\alpha \Delta t} \dot{\mathbf{u}}_t - \left(\frac{1}{2\alpha} - 1 \right) \ddot{\mathbf{u}}_t,$$

$$\dot{\mathbf{u}}_{t+\Delta t} = \frac{\delta}{\alpha \Delta t} (\mathbf{u}_{t+\Delta t} - \mathbf{u}_t) + \left(1 - \frac{\delta}{\alpha} \right) \dot{\mathbf{u}}_t + \left(1 - \frac{\delta}{2\alpha} \right) \Delta t \ddot{\mathbf{u}}_t, \quad (31)$$

where $\delta \geq 0.5$ and $\alpha \geq 0.25(0.5 + \delta)^2$ are redefined as parameters here to influence the accuracy and stability of the integration.

The dynamic form of (28) at $t + \Delta t$ can be written as

$$\mathbf{M}\ddot{\mathbf{u}}_{t+\Delta t} + \bar{\mathbf{K}}\mathbf{u}_{t+\Delta t} = \mathbf{F}_{t+\Delta t}. \quad (32)$$

Substituting (31) into (32), we have the full discretized equation

$$\left(\bar{\mathbf{K}} + \frac{1}{\alpha \Delta t^2} \mathbf{M} \right) \mathbf{u}_{t+\Delta t} = \bar{\mathbf{F}}_{t+\Delta t} + \mathbf{M} \left(\frac{1}{\alpha \Delta t^2} \mathbf{u}_t + \frac{1}{\alpha \Delta t} \dot{\mathbf{u}}_t + \left(\frac{1}{2\alpha} - 1 \right) \ddot{\mathbf{u}}_t \right). \quad (33)$$

By solving the above iteration equations, we can obtain numerical solutions to the one-dimensional nonlinear Klein-Gordon equation.

TABLE 1: Values of L_2 -norm errors and L_{∞} -norm errors and CPU time as functions of the number of nodes (N) for the solutions of Example 1 ($t = 10$, $\Delta t = 0.1$, and $d_{\max} = 3$).

N	L_2 -norm error	L_{∞} error	CPU time (s)
11	4.7172×10^{-4}	2.0891×10^{-4}	1.5224
21	6.6446×10^{-4}	2.1335×10^{-4}	1.7486
51	1.0503×10^{-3}	2.1488×10^{-4}	5.2065
101	1.5343×10^{-3}	2.1500×10^{-4}	10.3477
201	2.1912×10^{-3}	2.1504×10^{-4}	19.8889
251	2.3485×10^{-3}	2.1505×10^{-4}	25.6620

4. Numerical Results and Discussion

Three selected examples are included with their numerical solutions obtained by the presented method for the nonlinear KG equation. The problems are solved using regular node arrangements. The convergence study is carried out for the results of the KG equation. The accuracy and efficiency of the IMLS-Ritz method are compared with available analytical solutions by evaluating the L_2 -norm and L_{∞} errors defined as

$$L_2 = \|u_{\text{exact}} - u_{\text{numerical}}\|_2 = \sqrt{\sum_{i=0}^N |u_{\text{exact}}^i - u_{\text{numerical}}^i|^2}, \quad (34)$$

$$L_{\infty} = \|u_{\text{exact}} - u_{\text{numerical}}\|_{\infty} = \max_i |u_{\text{exact}}^i - u_{\text{numerical}}^i|,$$

where u_{exact} and $u_{\text{numerical}}$ present the exact solution and numerical approximation, respectively.

4.1. Example 1. Consider the KG equation (1) with quadratic nonlinearity ($k = 2$), by taking the parameters $\alpha = -1$, $\beta = 0$, $\gamma = 1$, and $f(x, t) = -x \cos t + x^2 \cos^2 t$.

The exact solution of the equation is given as [1]

$$u(x, t) = x \cos t, \quad -1 \leq x \leq 1. \quad (35)$$

The corresponding initial conditions and Dirichlet boundary function can be extracted from the analytical solution directly as

$$\begin{aligned} u(x, 0) &= x, \quad -1 \leq x \leq 1, \\ u_t(x, 0) &= 0, \quad -1 \leq x \leq 1, \end{aligned} \quad (36)$$

$$u(x, t) = \begin{cases} -\cos t & x = -1 \\ \cos t & x = 1. \end{cases}$$

In the present example, the numerical solutions are obtained as the penalty factor $\alpha = 10^3$ and $d_{\max} = 3$. We examine the convergence of the element-free IMLS-Ritz method by varying the number of nodes (N) from 11 to 201. The L_2 -norm and L_{∞} errors of $u(x, t)$ with CPU times are computed at $t = 10$ with $\Delta t = 0.1$ and tabulated in Table 1. We found that both L_2 -norm and L_{∞} errors arise as N increases.

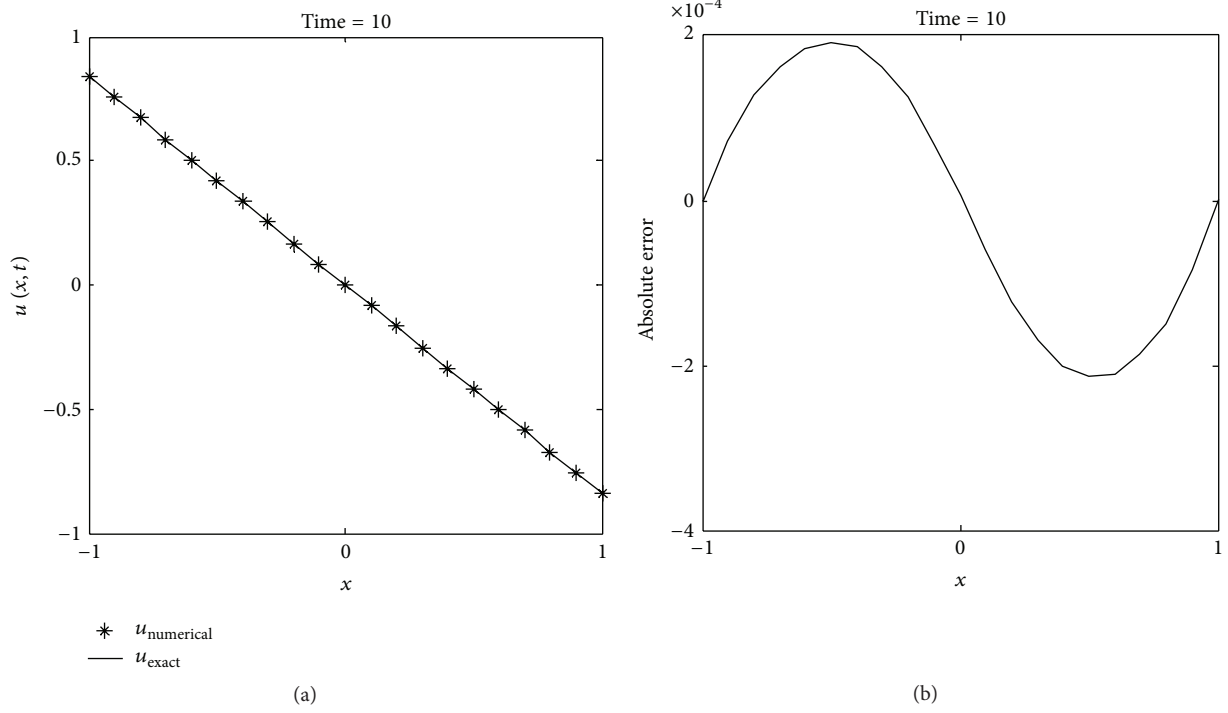


FIGURE 1: IMLS-Ritz and exact solutions of $u(x, t)$ at $N = 21$, $\Delta t = 0.1$ (Example 1). (a) Solutions of $u(x, t)$; (b) absolute error.

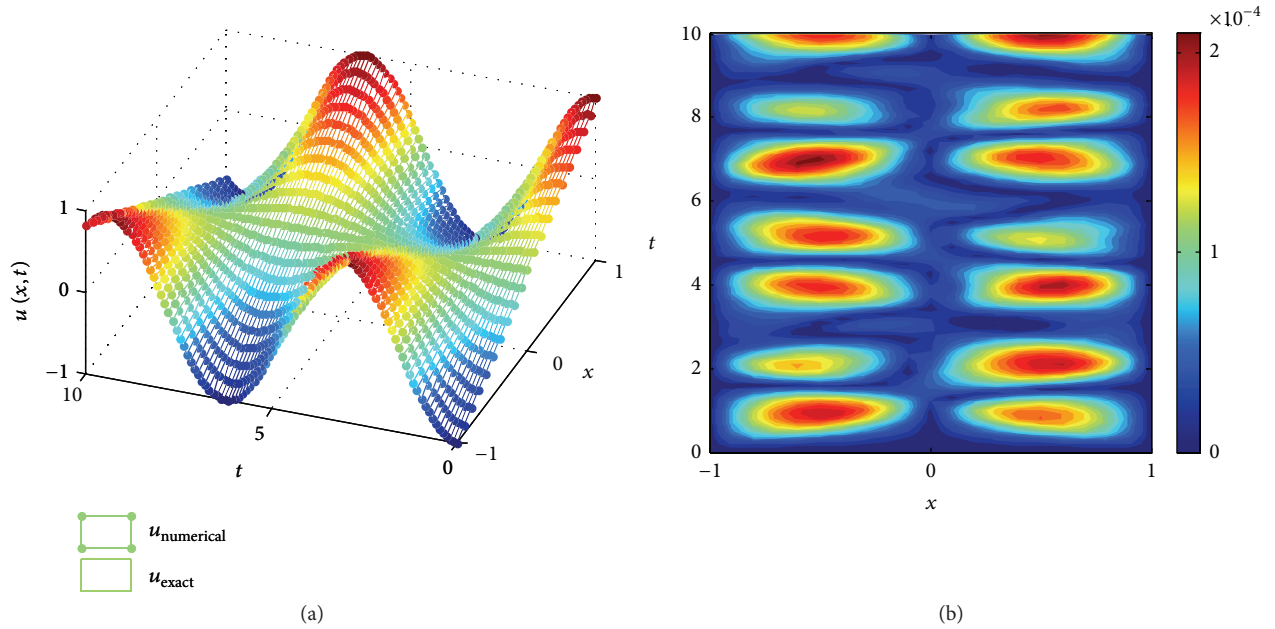


FIGURE 2: IMLS-Ritz solutions and absolute errors of $u(x, t)$ at different times (Example 1). (a) Solution surface of $u(x, t)$; (b) absolute error contour.

This may be due to that once convergent result has been obtained, in this case on $N = 11$, the additional arranged nodes will cause errors being accumulated. Based on this observation, the following analysis will be performed using $N = 11$ for accuracy consideration. We also investigated the influence of d_{\max} on the accuracy of the IMLS-Ritz method. As illustrated in Table 2, by varying d_{\max} from 2 to 3, accurate

results can be furnished when $d_{\max} = 2$. Furthermore, the predicted results are compared with the available exact solutions at $t = 10$ and illustrated in Figure 1. It is apparent that a close agreement is obtained from the illustrated results. The computed results of $u(x, t)$ for a time history are also predicted between $t = 0$ s and $t = 10$ s ($\Delta t = 0.1$) (see Figure 2(a)). The corresponding absolute error contour is

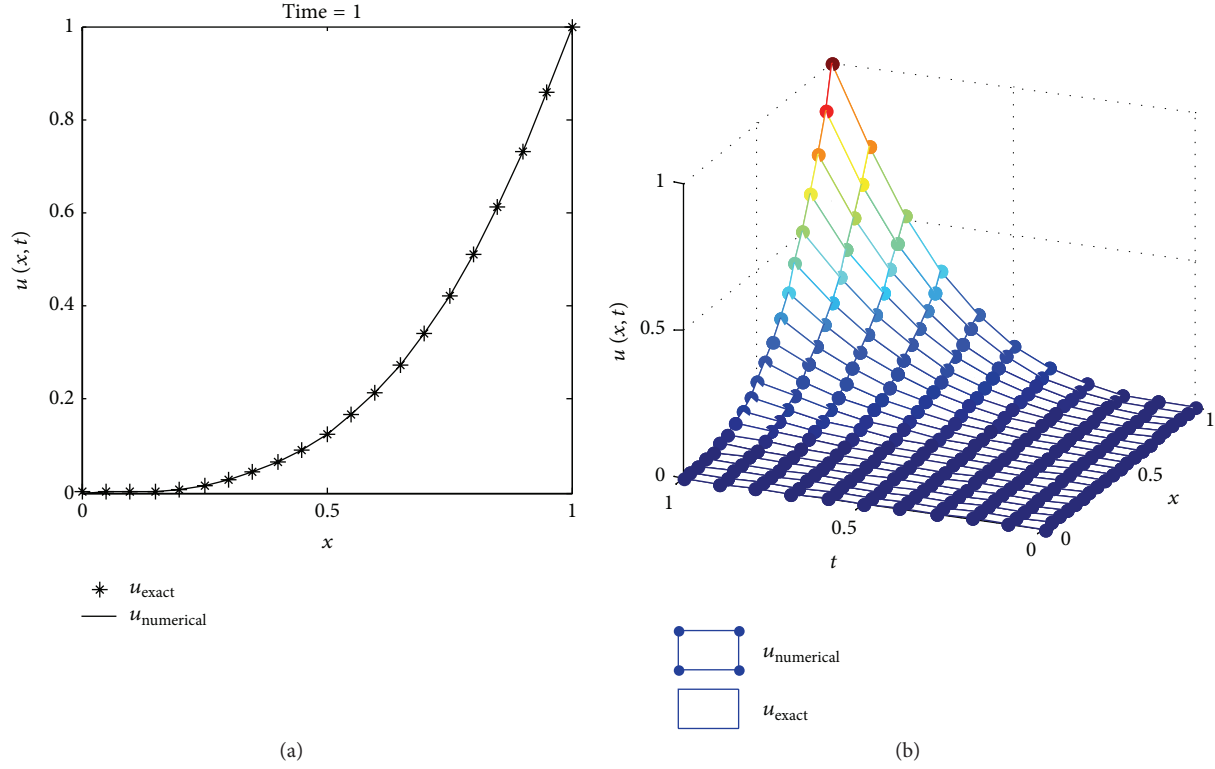


FIGURE 3: IMLS-Ritz and exact solutions of $u(x, t)$ (Example 2). (a) Solutions of $u(x, t)$ at $N = 21$, $\Delta t = 0.1$; (b) solution surface of $u(x, t)$.

TABLE 2: Values of L_2 -norm errors and L_∞ -norm errors and CPU time as functions of the d_{\max} for the solution of Example 1 ($N = 11$, $t = 10$, and $\Delta t = 0.1$).

d_{\max}	L_2 -norm error	L_∞ error	CPU time (s)
2	6.7304×10^{-4}	2.1170×10^{-4}	1.7510
2.2	6.9125×10^{-4}	2.1913×10^{-4}	1.7888
2.4	7.1843×10^{-4}	2.2411×10^{-4}	1.8604
2.6	6.5686×10^{-4}	2.2234×10^{-4}	1.7744
2.8	6.4655×10^{-4}	2.1186×10^{-4}	1.7812
3	6.6445×10^{-4}	2.1335×10^{-4}	1.7949

plotted in Figure 2(b). From the presented results, we can conclude that the approximate solutions generated by the IMLS-Ritz method agree well with the analytical results.

4.2. Example 2. In the present numerical example, we consider KG in (1) with a quadratic nonlinearity ($k = 2$), by taking the parameters $\alpha = -1$, $\beta = 0$, $\gamma = 1$, and $f(x, t) = 6xt(x^2 - t^2) + x^6t^6$. The initial conditions are described by

$$\begin{aligned} u(x, 0) &= 0, \quad 0 \leq x \leq 1, \\ u_t(x, 0) &= 0, \quad 0 \leq x \leq 1. \end{aligned} \quad (37)$$

The exact solution of the equation is given as [1]

$$u(x, t) = x^3 t^3, \quad 0 \leq x \leq 1. \quad (38)$$

TABLE 3: Values of L_2 -norm errors and L_∞ -norm errors and CPU time as functions of the number of nodes (N) for the solutions of Example 2 ($t = 1$, $\Delta t = 0.1$, and $d_{\max} = 2.2$).

N	L_2 -norm error	L_∞ error	CPU time (s)
6	2.1937×10^{-2}	1.7231×10^{-2}	0.1081
21	3.3745×10^{-4}	2.0891×10^{-4}	0.2683
26	3.7023×10^{-4}	1.6600×10^{-4}	0.3275
51	5.1750×10^{-4}	1.6589×10^{-4}	0.6268
101	7.2991×10^{-4}	1.6588×10^{-4}	1.1983

The corresponding Dirichlet boundary function can be extracted from the analytical solution directly as

$$u(x, t) = \begin{cases} 0 & x = 0 \\ t^3 & x = 1. \end{cases} \quad (39)$$

In this analysis, numerical solutions are predicted and compared with the analytical solutions at $t = 1$, $\Delta t = 0.01$, $d_{\max} = 2.2$, and the penalty factor $\lambda = 10^3$. Table 3 presents the convergence patterns of the IMLS-Ritz results by varying N from 6 to 101. A similar convergence trend is observed in Example 1; that is, convergent results can be obtained from $N = 6$ to 21; then, the errors are accumulated as N increases. Table 4 illustrates the values of L_2 -norm and L_∞ errors as d_{\max} varying from 2 to 3.5. A growing trend of L_2 -norm and L_∞ errors is observed from Table 4, and the CPU time rises oscillatory as d_{\max} increases. As presented in Figure 3,

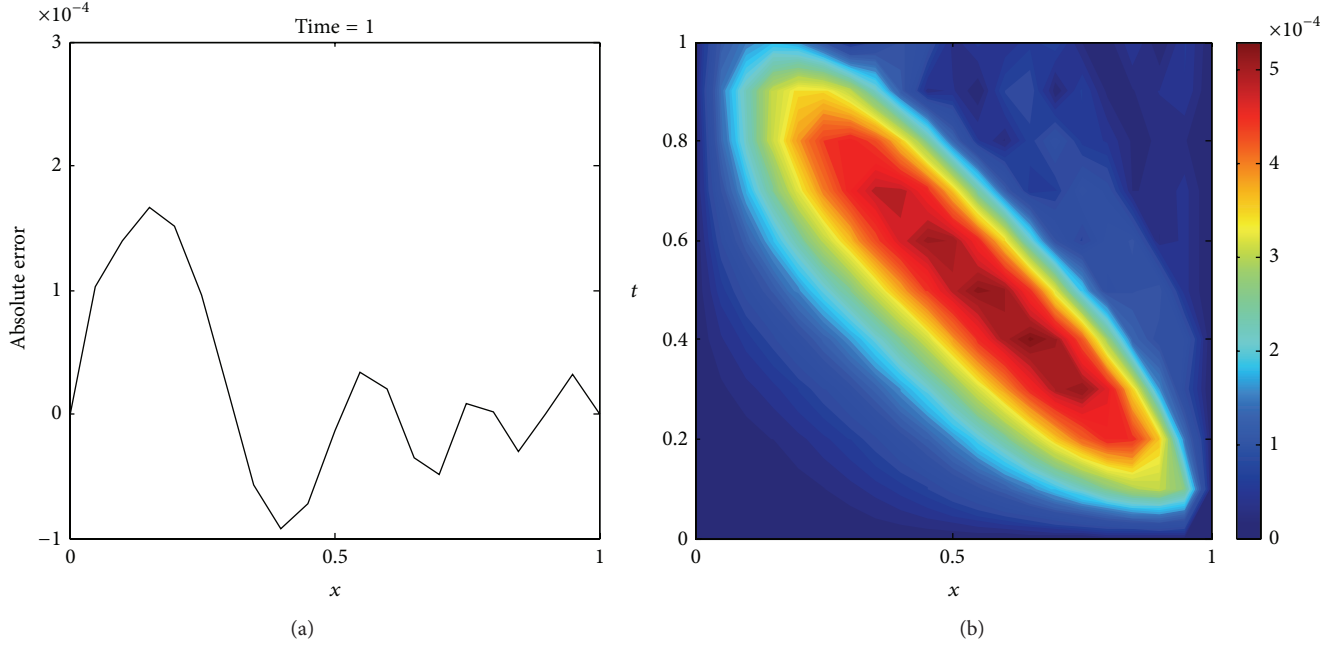


FIGURE 4: Absolute errors of $u(x, t)$ at $N = 21$ (Example 2). (a) Absolute errors of $u(x, t)$ at $\Delta t = 0.1$; (b) absolute errors contour.

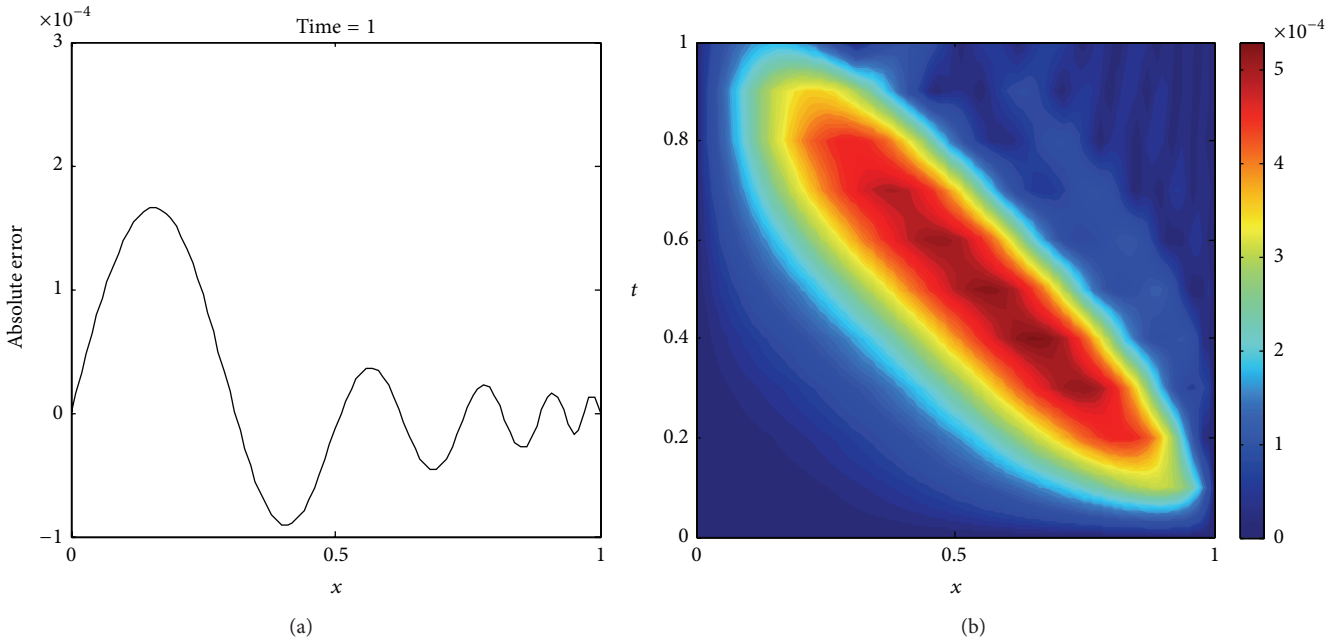


FIGURE 5: Absolute errors of $u(x, t)$ at $N = 101$ (Example 2). (a) Absolute errors of $u(x, t)$ at $\Delta t = 0.1$; (b) absolute errors contour.

the comparison study shows that the IMLS-Ritz method provides very similar solutions to the exact results. In Figure 4, the absolute errors of $u(x, t)$ at a selected time point ($t = 1$) and the absolute error contour on a time period ($0 \leq t \leq 1$) are exhibited at $N = 21$. Figure 5 is plotted at $N = 101$ for comparison with Figure 4. Although the increase in number of nodes has been identified to be unaided in enhancing the accuracy of the approximation, it influences the smoothness of the solutions indeed.

4.3. Example 3. Consider the nonlinear Klein-Gordon equation (1) with a cubic nonlinearity ($k = 3$), by taking parameters as $\alpha = -2.5$, $\beta = 1$, $\gamma = 1.5$, and $f(x, t) = 0$. The initial conditions are given by

$$\begin{aligned} u(x, 0) &= B \tan(Kx), \quad 0 \leq x \leq 1, \\ u_t(x, 0) &= BcK \sec^2(Kx), \quad 0 \leq x \leq 1, \end{aligned} \quad (40)$$

where $B = \sqrt{\beta/\gamma}$ and $K = \sqrt{-\beta/2(\alpha + c^2)}$ and $c = 0.05$.

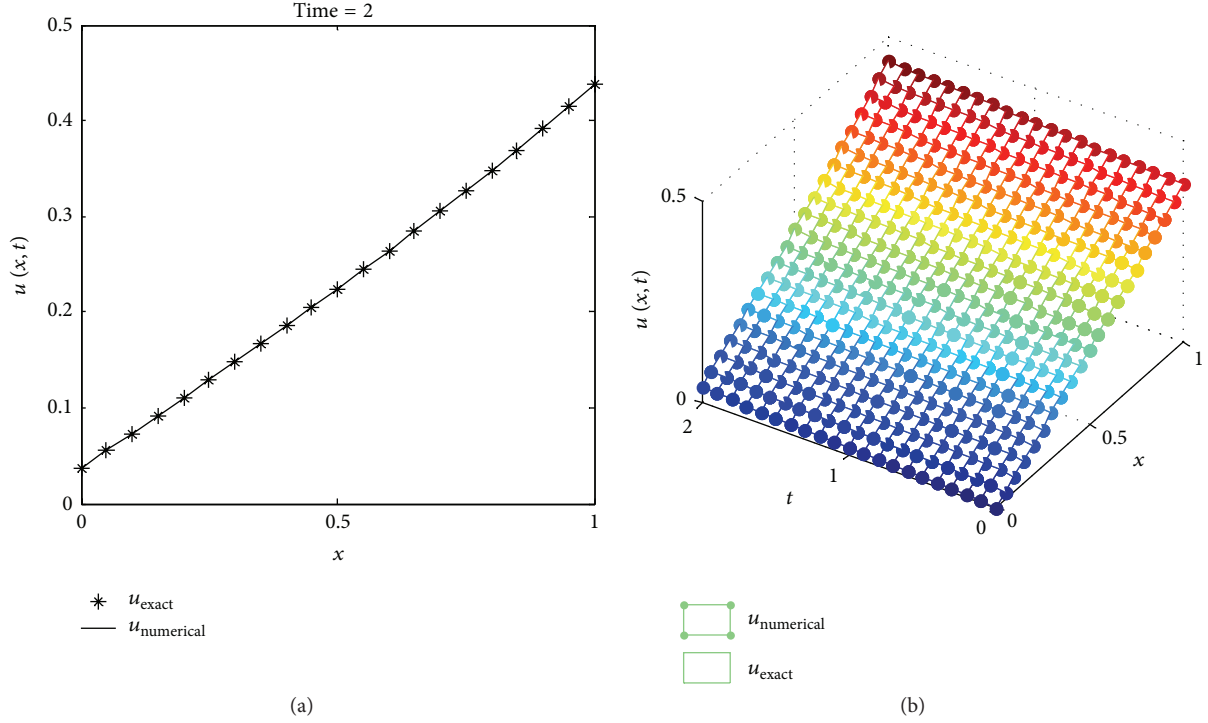


FIGURE 6: IMLS-Ritz and exact solutions of $u(x, t)$ (Example 3). (a) Solutions of $u(x, t)$ at $N = 21$, $\Delta t = 0.1$; (b) solution surface of $u(x, t)$.

TABLE 4: Values of L_2 -norm errors and L_∞ -norm errors and CPU time as functions of the d_{\max} for the solution of Example 2 ($N = 11$, $t = 1$, and $\Delta t = 0.1$).

d_{\max}	L_2 -norm error	L_∞ error	CPU time (s)
2	3.3081×10^{-4}	2.1170×10^{-4}	0.2637
2.2	3.3746×10^{-4}	1.6616×10^{-4}	0.2644
2.4	3.4597×10^{-4}	1.6866×10^{-4}	0.2754
2.6	3.7193×10^{-4}	1.7459×10^{-4}	0.2690
2.8	3.8596×10^{-4}	1.8276×10^{-4}	0.2686
3	3.8960×10^{-4}	1.9179×10^{-4}	0.2650
3.2	4.2300×10^{-4}	1.999×10^{-4}	0.2644
3.5	4.9035×10^{-4}	2.3717×10^{-4}	0.2819

The exact solution of the equation is given as [4]

$$u(x, t) = B \tan [K(x + ct)], \quad 0 \leq x \leq 1. \quad (41)$$

The IMLS-Ritz computation is carried out by setting $\Delta t = 0.1$, the penalty factor $\lambda = 10^3$, and $d_{\max} = 2.5$. The L_2 -norm and L_∞ errors of u are computed with the number of nodes varied from 13 to 201. The results are tabulated in Table 5. It is apparent that both L_2 -norm and L_∞ errors decrease as N increases, indicating that convergent results are obtained by the IMLS-Ritz method. From Table 6, the results of numerical analysis suggested that satisfied accuracy can be achieved when $d_{\max} = 2$. In Figure 6, the numerical and analytical solutions are plotted on a time point ($t = 2$) and a time period ($0 \leq t \leq 2$). From the comparison results, we can conclude that the IMLS-Ritz method provides very similar solutions to the exact results. In Figures 7 and 8, the absolute errors of

TABLE 5: Values of L_2 -norm errors and L_∞ -norm errors and CPU time as functions of the number of nodes (N) for the solutions of Example 3 ($t = 2$, $\Delta t = 0.1$, and $d_{\max} = 2.5$).

N	L_2 -norm error	L_∞ error	CPU time (s)
13	1.9791×10^{-5}	1.3049×10^{-5}	447.3713
21	9.5355×10^{-6}	5.7505×10^{-6}	559.7717
51	2.8692×10^{-6}	1.7171×10^{-6}	600.6953
101	1.8512×10^{-6}	1.3635×10^{-6}	650.4551
126	1.4819×10^{-6}	1.0907×10^{-6}	687.4458
201	7.8596×10^{-7}	5.3053×10^{-7}	721.8184

TABLE 6: Values of L_2 -norm errors and L_∞ -norm errors and CPU time as functions of the d_{\max} for the solution of Example 3 ($N = 11$, $t = 10$, and $\Delta t = 0.1$).

d_{\max}	L_2 -norm error	L_∞ error	CPU time (s)
2	5.5466×10^{-6}	3.4260×10^{-6}	793.1491
2.2	1.8244×10^{-5}	1.0416×10^{-5}	826.7344
2.4	3.2447×10^{-5}	1.8490×10^{-5}	891.1543
2.6	4.5397×10^{-5}	2.5715×10^{-5}	945.6493
2.8	4.4504×10^{-5}	2.6234×10^{-5}	975.9027
3	2.7963×10^{-5}	1.6959×10^{-5}	1027.5762
3.2	3.2756×10^{-5}	1.6014×10^{-5}	1070.3232

$u(x, t)$ at a selected time point ($t = 2$) and the absolute error contour on a time period ($0 \leq t \leq 1$) are depicted at $N = 21$ and $N = 201$, respectively. As expected, more accurate results can be obtained as N increases in this example. From the results presented in both tables and figures, it is evident

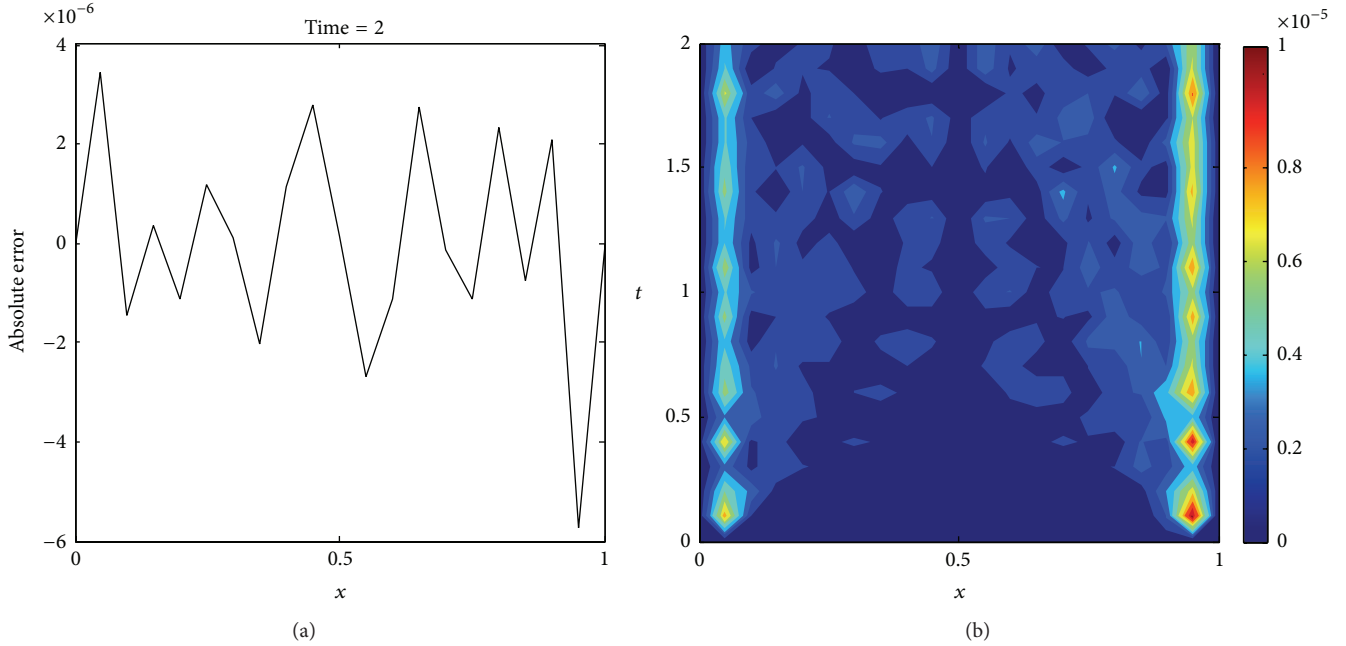


FIGURE 7: Absolute errors of $u(x, t)$ at $N = 21$ (Example 3). (a) Absolute errors of $u(x, t)$ at $\Delta t = 0.1$; (b) absolute errors contour.

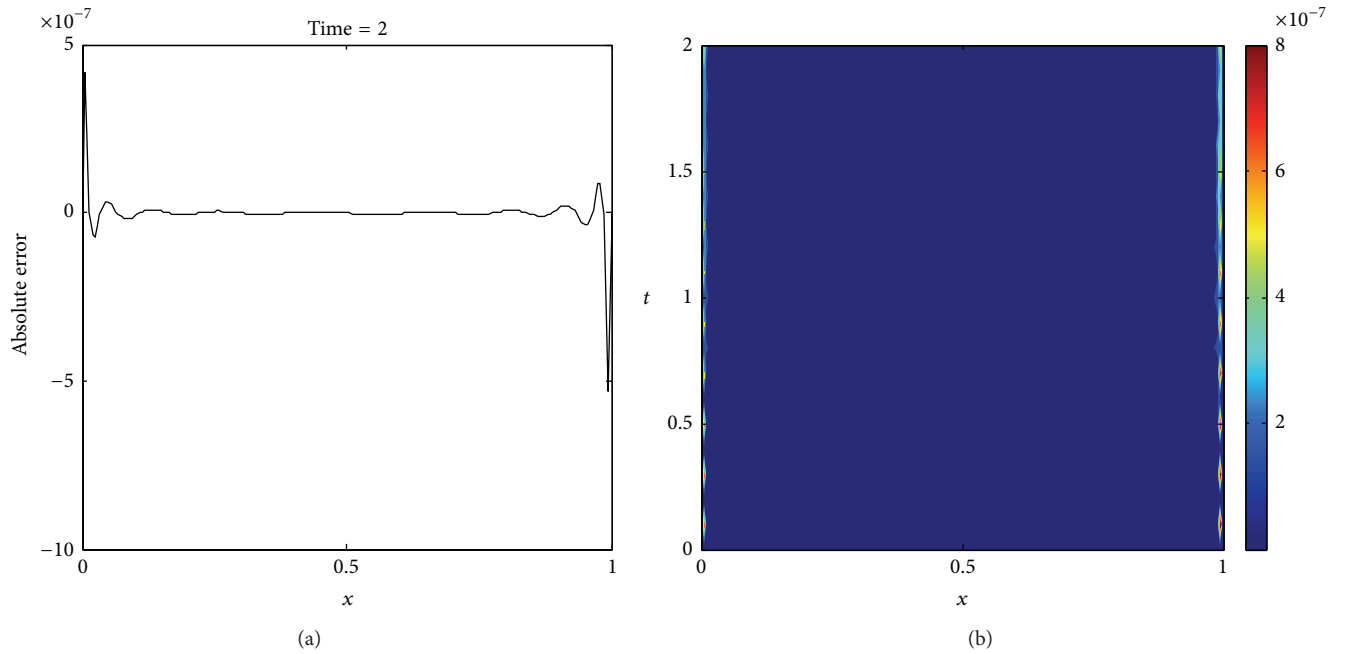


FIGURE 8: Absolute errors of $u(x, t)$ at $N = 201$ (Example 3). (a) Absolute errors of $u(x, t)$ at $\Delta t = 0.1$; (b) absolute errors contour.

that the IMLS-Ritz values almost coincide with the exact solutions.

5. Conclusion

In this paper, an element-free IMLS-Ritz method and its numerical implementation on three examples of nonlinear KG equation have been presented. The effectiveness and

efficiency of the IMLS-Ritz method for KG equation have been testified through convergence and comparison studies. From the numerical results, it is concluded that the agreement of the IMLS-Ritz solutions with the exact results is excellent. Due to difficulties of constructing analytical solutions for many nonlinear PDEs, the element-free IMLS-Ritz method will have great advantages for solving them through simple implementation with high accuracy.

Conflict of Interests

The authors declare that there is no conflict of interests regarding the publication of this paper.

Acknowledgments

The work described in this paper was partly supported by the National Natural Science Foundation of China (Grant no. 61272098 and Grant no. 11402142), Open Research Fund Program for State Key Laboratory of Estuarine and Coastal Research (SKLEC201207), and Open Research Fund Program for Shandong Province Key Laboratory of Marine Ecology Environment and Disaster Prevention (2012011).

References

- [1] A.-M. Wazwaz, "The modified decomposition method for analytic treatment of differential equations," *Applied Mathematics and Computation*, vol. 173, no. 1, pp. 165–176, 2006.
- [2] A.-M. Wazwaz, "Compactons, solitons and periodic solutions for some forms of nonlinear Klein-Gordon equations," *Chaos, Solitons & Fractals*, vol. 28, no. 4, pp. 1005–1013, 2006.
- [3] S. M. El-Sayed, "The decomposition method for studying the Klein-Gordon equation," *Chaos, Solitons and Fractals*, vol. 18, no. 5, pp. 1025–1030, 2003.
- [4] D. Kaya and S. M. El-Sayed, "A numerical solution of the Klein-Gordon equation and convergence of the decomposition method," *Applied Mathematics and Computation*, vol. 156, no. 2, pp. 341–353, 2004.
- [5] A.-M. Wazwaz, "New travelling wave solutions to the Boussinesq and the Klein-Gordon equations," *Communications in Nonlinear Science and Numerical Simulation*, vol. 13, no. 5, pp. 889–901, 2008.
- [6] A.-M. Wazwaz, "The tanh and the sine-cosine methods for compact and noncompact solutions of the nonlinear Klein-Gordon equation," *Applied Mathematics and Computation*, vol. 167, no. 2, pp. 1179–1195, 2005.
- [7] Sirendaoreji, "A new auxiliary equation and exact travelling wave solutions of nonlinear equations," *Physics Letters A: General, Atomic and Solid State Physics*, vol. 356, no. 2, pp. 124–130, 2006.
- [8] A. Sirendaoreji, "Auxiliary equation method and new solutions of Klein-Gordon equations," *Chaos, Solitons & Fractals*, vol. 31, no. 4, pp. 943–950, 2007.
- [9] Sirendaoreji, "Exact travelling wave solutions for four forms of nonlinear Klein-Gordon equations," *Physics Letters: A*, vol. 363, no. 5–6, pp. 440–447, 2007.
- [10] D. Kumar, J. Singh, and S. Kumar, "Numerical computation of Klein-Gordon equations arising in quantum field theory by using homotopy analysis transform method," *Alexandria Engineering Journal*, vol. 53, no. 2, pp. 469–474, 2014.
- [11] J. Rashidinia, M. Ghasemi, and R. Jalilian, "Numerical solution of the nonlinear Klein-Gordon equation," *Journal of Computational and Applied Mathematics*, vol. 233, no. 8, pp. 1866–1878, 2010.
- [12] M. Dehghan and A. Shokri, "Numerical solution of the nonlinear Klein-Gordon equation using radial basis functions," *Journal of Computational and Applied Mathematics*, vol. 230, no. 2, pp. 400–410, 2009.
- [13] K. M. Liew, T. Y. Ng, X. Zhao, and J. N. Reddy, "Harmonic reproducing kernel particle method for free vibration analysis of rotating cylindrical shells," *Computer Methods in Applied Mechanics and Engineering*, vol. 191, no. 37–38, pp. 4141–4157, 2002.
- [14] K. M. Liew, X. L. Chen, and J. N. Reddy, "Mesh-free radial basis function method for buckling analysis of non-uniformly loaded arbitrarily shaped shear deformable plates," *Computer Methods in Applied Mechanics and Engineering*, vol. 193, no. 3–5, pp. 205–224, 2004.
- [15] K. M. Liew, Y. Cheng, and S. Kitipornchai, "Boundary element-free method (BEFM) and its application to two-dimensional elasticity problems," *International Journal for Numerical Methods in Engineering*, vol. 65, no. 8, pp. 1310–1332, 2006.
- [16] F. X. Sun, C. Liu, and Y. M. Cheng, "An improved interpolating element-free Galerkin method based on nonsingular weight functions," *Mathematical Problems in Engineering*, vol. 2014, Article ID 323945, 13 pages, 2014.
- [17] N. Zhao and H. Ren, "The interpolating element-free Galerkin method for 2D transient heat conduction problems," *Mathematical Problems in Engineering*, vol. 2014, Article ID 712834, 9 pages, 2014.
- [18] Q. Wei and R. Cheng, "The improved moving least-square Ritz method for the one-dimensional sine-Gordon equation," *Mathematical Problems in Engineering*, vol. 2014, Article ID 383219, 10 pages, 2014.
- [19] W. Shao and X. Wu, "The numerical solution of the nonlinear Klein-Gordon and sine-Gordon equations using the Chebyshev tau meshless method," *Computer Physics Communications*, vol. 185, no. 5, pp. 1399–1409, 2014.
- [20] A. Hussain, S. Haq, and M. Uddin, "Numerical solution of Klein-Gordon and sine-Gordon equations by meshless method of lines," *Engineering Analysis with Boundary Elements*, vol. 37, no. 11, pp. 1351–1366, 2013.
- [21] T. Belytschko, Y. Y. Lu, and L. Gu, "Element-free Galerkin methods," *International Journal for Numerical Methods in Engineering*, vol. 37, no. 2, pp. 229–256, 1994.
- [22] K. M. Liew, Y. Q. Huang, and J. N. Reddy, "Moving least squares differential quadrature method and its application to the analysis of shear deformable plates," *International Journal for Numerical Methods in Engineering*, vol. 56, no. 15, pp. 2331–2351, 2003.
- [23] K. M. Liew and X. L. Chen, "Buckling of rectangular Mindlin plates subjected to partial in-plane edge loads using the radial point interpolation method," *International Journal of Solids and Structures*, vol. 41, no. 5–6, pp. 1677–1695, 2004.
- [24] J. J. Monaghan, "An introduction to SPH," *Computer Physics Communications*, vol. 48, no. 1, pp. 89–96, 1988.
- [25] W. Chen, "New RBF collocation methods and kernel RBF with applications," in *Meshfree Methods for Partial Differential Equations*, vol. 1, pp. 75–86, Springer, 2000.
- [26] K. M. Liew, X. Zhao, and T. Y. Ng, "The element-free kp-Ritz method for vibration of laminated rotating cylindrical panels," *International Journal of Structural Stability and Dynamics*, vol. 2, pp. 523–558, 2002.
- [27] X. Zhao and K. M. Liew, "Geometrically nonlinear analysis of functionally graded plates using the element-free kp-Ritz method," *Computer Methods in Applied Mechanics and Engineering*, vol. 198, no. 33–36, pp. 2796–2811, 2009.
- [28] L. W. Zhang, Z. X. Lei, K. M. Liew, and J. L. Yu, "Static and dynamic of carbon nanotube reinforced functionally graded

- cylindrical panels,” *Composite Structures*, vol. 111, no. 1, pp. 205–212, 2014.
- [29] L. W. Zhang, Y. J. Deng, and K. M. Liew, “An improved element-free Galerkin method for numerical modeling of the biological population problems,” *Engineering Analysis with Boundary Elements*, vol. 40, pp. 181–188, 2014.
- [30] L. W. Zhang, Z. X. Lei, K. M. Liew, and J. L. Yu, “Large deflection geometrically nonlinear analysis of carbon nanotube-reinforced functionally graded cylindrical panels,” *Computer Methods in Applied Mechanics and Engineering*, vol. 273, pp. 1–18, 2014.
- [31] S. N. Atluri and T. Zhu, “A new meshless local Petrov-Galerkin (MLPG) approach in computational mechanics,” *Computational Mechanics*, vol. 22, no. 2, pp. 117–127, 1998.
- [32] W. K. Liu, S. Jun, and Y. F. Zhang, “Reproducing kernel particle methods,” *International Journal for Numerical Methods in Fluids*, vol. 20, no. 8-9, pp. 1081–1106, 1995.
- [33] L. W. Zhang, P. Zhu, and K. M. Liew, “Thermal buckling of functionally graded plates using a local Kriging meshless method,” *Composite Structures*, vol. 108, no. 1, pp. 472–492, 2014.

Research Article

Elastic Properties of Boron-Nitride Nanotubes through an Atomic Simulation Method

Jixiao Tao,¹ Guangmin Xu,² and Yuzhou Sun¹

¹*School of Civil Engineering and Architecture, Zhongyuan University of Technology, Zhengzhou 450007, China*

²*Department of Architectural Engineering, Zhengzhou Railway Vocational and Technical College, Zhengzhou 451460, China*

Correspondence should be addressed to Yuzhou Sun; yuzhousun@126.com

Received 29 August 2014; Revised 29 October 2014; Accepted 29 October 2014

Academic Editor: Kim M. Liew

Copyright © 2015 Jixiao Tao et al. This is an open access article distributed under the Creative Commons Attribution License, which permits unrestricted use, distribution, and reproduction in any medium, provided the original work is properly cited.

The elastic properties of the boron-nitride nanotubes are studied based on an atomic simulation method that is called atomic-scale finite element method. The Tersoff-Brenner potential is used to describe the interaction between boron and nitrogen atoms, and the computational method is established in an atomic-scale scheme similar to the classical finite element method. Young's modulus is evaluated for the boron-nitride nanotubes, and their buckling behavior is analyzed. It is shown that the diameter has an obvious influence on Young's modulus of BNNTs, and the buckling is little related to the length of the nanotubes.

1. Introduction

Boron-nitride nanotubes (BNNTs) are a very promising one-dimensional material and have a structural analogy to carbon nanotubes [1–3]. Some research reports have shown that BNNTs possess unique structural, mechanical, thermal, electrical, and chemical properties. For example, Young's modulus of BNNTs is on the order of 1 TPa [4, 5]. The thermal conductivity along the nanotube is also very high. BNNTs have always large band gaps regardless of the chirality and diameter and are therefore semiconductors which are contrary to carbon nanotubes. The atomic simulation methods are important to the development of nanotechnology and to the study of nanomaterials and nanosystems. Molecular dynamics [6, 7] is a commonly used atomic-scale method, in which the conjugate gradient method is used for the energy minimization that consumes a large amount of computational resources, and is only available for the very small size. The atomic-scale finite element method (AFEM) is proposed by Liu et al. [8, 9], and it can achieve a high computational efficiency with the same accuracy as molecular dynamics. In the present study, AFEM is used to obtain the stiffness matrix and nonequilibrium force vector of the system, and the equilibrium state is determined with the nonlinear iteration.

In the field of theoretical research, only a few researches have been reported about the tensile and compressive properties of BNNTs. Oh used the continuum lattice approach to estimate elastic properties of BNNTs, in which the Tersoff-Brenner potential was used to describe the interaction between boron and nitrogen atoms, but some potential parameters have been modified to fit the cohesive energy and the bond length of boron nitride [10]. Song et al. employed an atomic-based continuum theory to study Young's modulus, stress-strain curve, and nonlinear bifurcation in BNNTs [11]. They pointed out that the mechanical behavior of BNNTs is virtually independent of the diameter and length of BNNTs but has a strong dependence on chirality. Wei et al. used classical molecular dynamics simulations to investigate compressive and tensile behaviors of the carbon nanotubes and boron-nitride nanotubes [12]. From the computational analyses, they found that the chirality is the main factor affecting the behavior of the nanotubes, and the nanotubes in different materials but with the same chirality have similar deformation patterns. Liao et al. investigated the deformation behaviors of an (8, 8) boron-nitride nanotube under axial tensile strains, in which Tersoff potential was employed with the appropriate potential parameters [13]. According to their results, the BNNT starts to fail at the failure strain of 26.7%

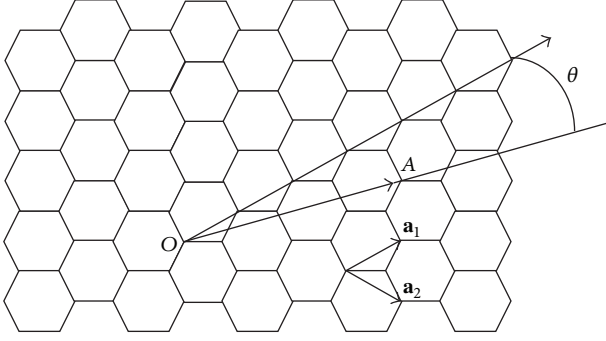


FIGURE 1: The definitions for the basis unit vectors, chiral vector, and chiral angle.

and the local elongation dominates the tensile failure of the BNNT. In this paper, the widely used Tersoff-Brenner potential is employed in the atomistic simulation, and a set of potential parameters modified by Oh are used to investigate the elastic properties of boron-nitride nanotubes [10]. AFEM is used to obtain the equilibrium states.

2. Atomic-Scale Modeling Method

2.1. Boron-Nitride Nanotubes. An undeformed BNNT can be visualized as a hollow cylinder that is formed by rolling up a BN sheet into a cylindrical shape. It can be uniquely characterized by a chiral vector Γ in terms of a set of two integers (n, m) corresponding to BN sheet unit vectors \mathbf{a}_1 and \mathbf{a}_2 (Figure 1):

$$\Gamma = n\mathbf{a}_1 + m\mathbf{a}_2. \quad (1)$$

This tube is denoted as an (n, m) tube with its diameter given by

$$D = \frac{\sqrt{3}}{\pi} a_{\text{B-N}} \sqrt{n^2 + mn + m^2}, \quad (2)$$

where $a_{\text{B-N}}$ is the bond length in the BN sheet. The tubes with $n = m$ are commonly referred to as armchair tubes and those with $m = 0$ as zigzag tubes. Other tubes are called chiral tubes in general with the chiral angle θ which is defined as that between the vector Γ and the zigzag direction \mathbf{a}_1 :

$$\theta = \tan^{-1} \left[\frac{3m}{2n + m} \right], \quad (3)$$

where θ ranges from 0° for zigzag ($m = 0$) to 30° for armchair ($m = n$) tubes ($n \geq m$ is used for convention). Shown in Figure 2 are Zigzag and armchair BNNTs.

2.2. The Atomic-Scale Finite Element. The present research adopts AFEM that was proposed by Liu et al. [8, 9]. The basic idea is to divide nanotubes into finite number of elements, and each element is characterized by a set of discrete atoms. The positions of all atoms are determined by minimizing the energy in the system.

For a system of N atoms, the energy stored in the atomic bond can be denoted by the function of each atom coordinate:

$$U_t = U_t(x_1, x_2, \dots, x_n) = \sum_{i < j}^N V_B(x_j - x_i). \quad (4)$$

Tersoff-Brenner potential [14, 15] is a manybody potential and can better describe the interaction between C, B, H, and N atoms. In the present study, Tersoff-Brenner potential $V_B(r_{ij})$ is used to describe the interaction between the boron and nitrogen atoms:

$$V_B(r_{ij}) = V_R(r_{ij}) - B_{ij}V_A(r_{ij}), \quad (5)$$

where V_R and V_A are the repulsive pair potential and attractive pair potential; r_{ij} is the distance from atom i to atom j ; B_{ij} is the bond order function. The sets of potential parameters modified by Oh [10] are used which are listed in Table 1.

The total energy is thus evaluated as

$$E_t(x) = U_t(x) - \sum_{i=1}^N F_i \cdot x_i, \quad (6)$$

where $x = (x_1, x_2, \dots, x_n)^T$, F_i is the external force exerted on atom i . The state of minimal energy corresponds to

$$\frac{\partial E_t}{\partial x} = 0. \quad (7)$$

Giving Taylor expansion of $E_t(x)$ and substituting it into (7) yield the following equation:

$$K\Delta u = P, \quad (8)$$

where Δu is displacement increment and K and P are, respectively, the stiffness matrix and nonequilibrium force vector given by

$$K = \frac{\partial^2 E_t}{\partial x \partial x} = \frac{\partial^2 U_t}{\partial x \partial x}, \quad P = -\frac{\partial E_t}{\partial x} = F - \frac{\partial U_t}{\partial x}. \quad (9)$$

Newton iteration method can be used to solve the present problem. It is much faster than the widely used conjugate gradient method because the first and second order derivatives were used. Materials may display softening behavior when they were under axial compression. For problems involving material softening, K is nonpositive definite and K may be replaced by $K^* = K + I\alpha$ to ensure the convergence, where I is the identity matrix and α is a positive number slightly larger than the absolute value of the minimum negative eigenvalue of the stiffness matrix [16, 17].

2.3. The Simulation Process. The above method has been written as a Fortran code for BNNTs, in which the following steps are used to compute the elastic properties of BNNTs and determine their buckling deformation.

Step 1. First, construct the initial configuration of BNNTs with uniform bond length using a separate program; store the coordinates and each piece of bond information in an array.

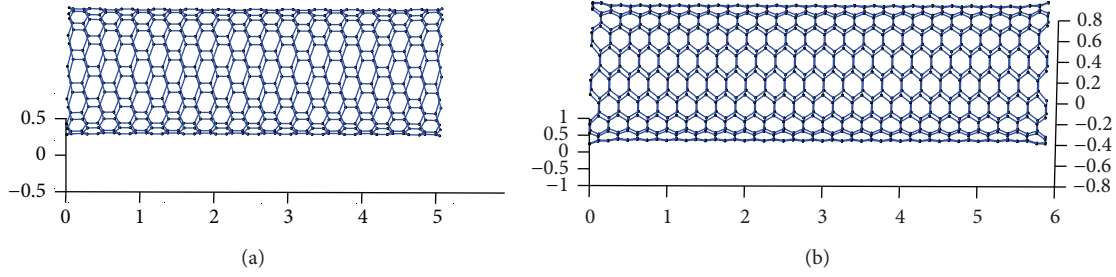


FIGURE 2: The atomic structure of the zigzag and armchair BNNTs.

TABLE 1: Potential parameters.

Parameter	$D^{(e)}$ (eV)	S	β	$R^{(e)}$	$R^{(1)}$ (Å)	$R^{(2)}$ (Å)	δ	a_0	c_0	d_0
	6.36	1.0769	22.0	0.133	1.9	2.1	0.382	2.0813	330	3.5

Step 2. Using the coordinate and bond number of arrays, find the first and second neighbor atoms information and store them in an array.

Step 3. Call a separate program to make the system back to the equilibrium coordinates for given initial coordinates and boundary conditions of BNNTs.

Step 4. Apply displacement field to equilibrium coordinates. This process adopts the constant displacement values at each load step.

Step 5. Store the potential of BNNTs against applied displacement filed. Using the polynomial curve fitting, fit data for equation of potential in terms of displacement filed (strain).

Step 6. Calculate Young's modulus using equations in Section 3.1.

Boundary conditions in Step 3 are to restrain one side of BNNTs and make the other side free until the system returns to the equilibrium configuration. During the process of axial tensile or compression, one end of the BNNT is completely fixed, and the tensile or compression is achieved by incrementally imposing an axial movement at another end. The length of the tube is changed by 0.01 nm per loading step until material appears buckling.

3. Results and Discussions

3.1. Young's Modulus. In continuum mechanics, the constitutive response between the load and deformation is established prior to solving a specific problem. If the material is homogeneous and isotropic, the material can be represented by two independent constants, namely, Young's modulus Y and Poisson's ratio ν . For a material undergoing a uniaxial deformation, Y is defined as

$$Y = \frac{2(V_\delta - V_0)L^2}{V_{ol}\delta^2} = \frac{kL^2}{V_{ol}}, \quad k = \frac{2(V_\delta - V_0)}{\delta^2}, \quad (10)$$

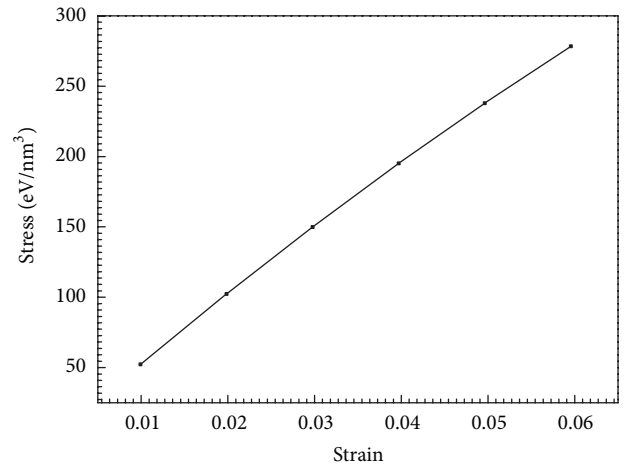


FIGURE 3: Stress-strain curve of an (8, 0) BNNT.

where V_{ol} is the volume, L is the initial nanotube length, and V_0 and V_δ are the equilibrium (minimised) potentials corresponding to the initial and deformed equilibrium configurations, respectively. δ is the length change in BNNTs, and k is the stiffness of the BNNT, as $\delta \rightarrow 0$ $k \rightarrow k_0$.

The thickness is often taken as 0.34 nm [11–13, 18] in the evaluation of V_{ol} . V_δ can be expressed as

$$V_\delta = a_1 + a_2\delta + a_3\delta^2 + a_4\delta^3. \quad (11)$$

The stiffness constant k_0 is then obtained as

$$k_0 = \lim_{\delta \rightarrow 0} \frac{\partial^2 V_\delta}{\partial \delta^2} = 2a_3. \quad (12)$$

Deformation behavior of an (8, 0) BNNT under axial tensile strains is first investigated in this paper. It has 23 hexagonal cells along the axis, and its initial length and radius are 5.037 nm and 0.326 nm, respectively. Figure 3 shows the stress-strain curve. Plot of equilibrium potential energy versus the length change is displayed in Figure 4.

The potential equation (11) is obtained from Figure 4 using polynomial curve fitting. Replace k_0 with $2a_3 = 745.8$. Substituting (12) into (10), the obtained Y is 863.85 GPa.

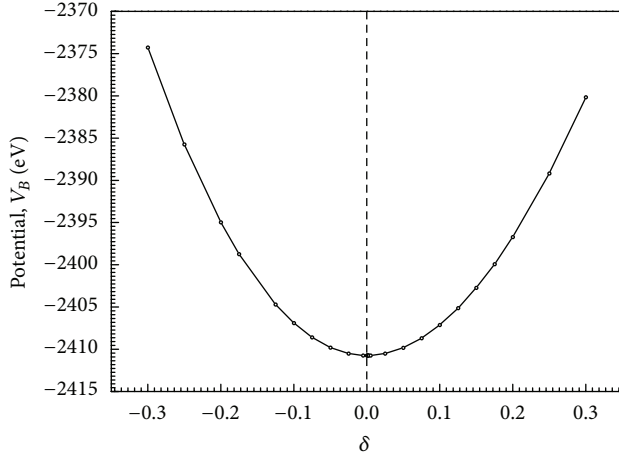


FIGURE 4: Potential versus the length change of an $(8, 0)$ BNNT for axial tensile/compressive deformation.

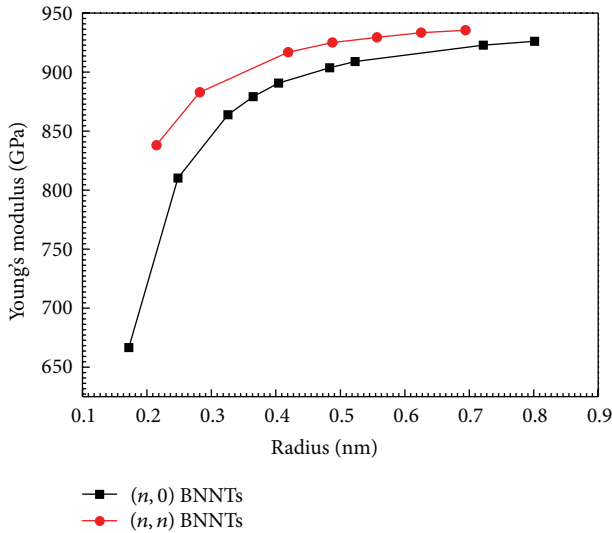


FIGURE 5: Young's moduli versus tube radius for $(n, 0)$ and (n, n) BNNTs.

Using the above steps, armchair (n, n) and zigzag $(n, 0)$ BNNTs are also simulated. Figure 5 shows the variation of the axial Young's moduli with the tube radius. It can be seen that Young's moduli of both armchair and zigzag BNNTs increase with increasing tube diameter, and this trend becomes much obvious for small radii zigzag tubes. With an increasing tube radius, the axial Young's moduli tend to the same constant. Employing an atomistic-based continuum theory, Song et al. [11] obtained the normalized Young's modulus of BNNT for the armchair (n, n) and zigzag $(n, 0)$ BNNTs with the varying tube diameter, and they compared their results with tight binding [4] and ab initio calculation [5]. The present results agree well with those from [4, 5, 10, 11].

3.2. Axial Buckling of BNNTs. AFEM is also applied to present a complete numerical simulation of buckling behavior. At each loading step, the stable state is solved with Newton's

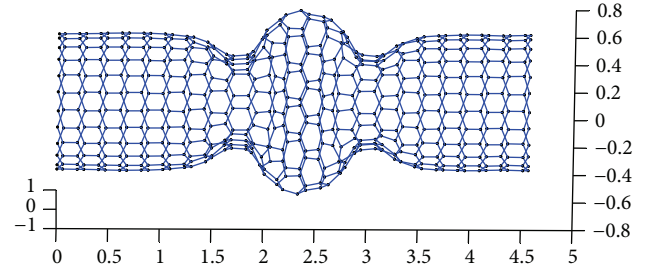


FIGURE 6: Buckling deformation.

method, and then the further compressive displacement is used. The penalty function method [19–21] is used to enforce the essential boundary condition. When BNNTs appear buckling, K is nonpositive definite. The iterative convergence is achieved to replace K with $K^* = K + I\alpha$, where I is the identity matrix and α is a positive number larger than the minimum negative eigenvalue of the stiffness matrix.

The buckling deformation of an $(8, 0)$ BNNT is shown in Figure 6 and it is very similar to the single-wall carbon nanotube studied by some researchers. The molecular dynamic method is the most popular atomic simulation method, in which the conjugate gradient method is used to achieve the energy minimization. The present method has the same accuracy with the molecular dynamic method because they both are atomic-scale methods. The conjugate gradient method is an order- N^2 method, and its computational cost is very huge. In the present AFEM, Newton iteration method is applied to obtain the equilibrium state, in which the first and second order derivatives are used and 3–5 iterative steps can achieve a good convergence. The computation is far faster than molecular dynamic method. Liew et al. showed that MD simulation of the buckling behavior of a $(10, 10)$ SWCNT containing 2,000 atoms required 36 hours in a single CPU of SGI origin 2000, whereas the computation for a four-walled MWCNT containing 15,097 atoms took four months [2, 6]. The computational time in AFEM scales linearly with number of atoms and the numbers of iteration steps is approximately independent of the atom number, which implies that AFEM is an order- N method and is very effective for the nanostructure with a larger number of atoms.

Our results are in good agreement with Wei et al. who have used classical molecular dynamics simulations to investigate compressive behaviors of the boron-nitride nanotubes [12]. In order to investigate the relationship between the bulking and length of single-walled boron-nitride nanotubes, some $(n, 0)$ BNNTs were simulated. Figure 7 shows the buckling strain versus length for several zigzag BNNTs. It is observed that the curve is nearly flat so that the nanotube length has little influence on buckling.

4. Conclusions

This paper has used AFEM to study the elastic properties of boron-nitride nanotubes based on interatomic potentials for boron and nitrogen atoms. It is shown that Young's moduli of both armchair and zigzag BNNTs closely related to tube

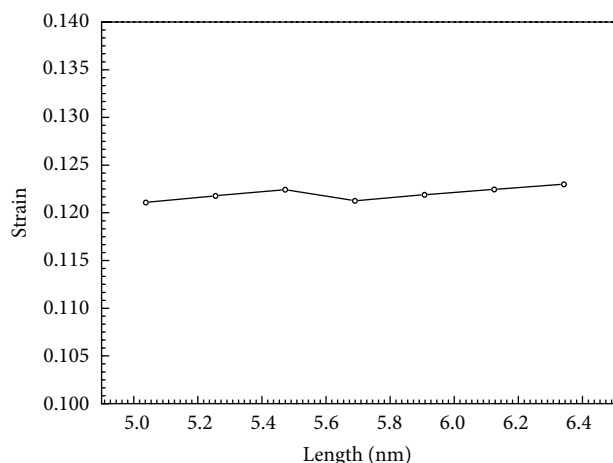


FIGURE 7: The buckling strain versus the length for several zigzag boron-nitride nanotubes.

diameter, especially for small radii zigzag tubes. When radius exceeds 1 nm, Young's moduli tend to the same constant. For zigzag BNNTs, the buckling strain is virtually independent of the nanotube length, and its average strain is 12%. This is consistent with the conclusions that the mechanical behavior of BNNTs is independent of the diameter and length of BNNTs by some researchers. AFEM is an efficient and accurate computation method and it is also readily applicable for solving many physics related optimization problems.

Conflict of Interests

The authors declare that there is no conflict of interests regarding the publication of this paper.

Acknowledgments

The work in this research was supported by the Natural Science Foundation of China (Grant no. 11472316), the Program for New Century Excellent Talents in University, China (Project no. NCET-12-0700), and Program for Science and Technology Innovation Talents in Universities of Henan Province (Project no. 2012HASTIT021).

References

- [1] S. Iijima, "Helical microtubules of graphitic carbon," *Nature*, vol. 354, no. 6348, pp. 56–58, 1991.
- [2] K. M. Liew, C. H. Wong, X. Q. He, M. J. Tan, and S. A. Meguid, "Nanomechanics of single and multiwalled carbon nanotubes," *Physical Review B*, vol. 69, no. 11, Article ID 115429, 2004.
- [3] K. M. Liew, C. H. Wong, and M. J. Tan, "Buckling properties of carbon nanotube bundles," *Applied Physics Letters*, vol. 87, no. 4, Article ID 041901, 2005.
- [4] E. Hernández, C. Goze, P. Bernier, and A. Rubio, "Elastic properties of C and $B_xC_yN_z$ composite nanotubes," *Physical Review Letters*, vol. 80, no. 20, pp. 4502–4505, 1998.
- [5] K. N. Kudin, G. E. Scuseria, and B. I. Yakobson, " C_2F_4 , BN, and C nanoshell elasticity from *ab initio* computations," *Physical Review B*, vol. 64, no. 23, Article ID 235406, 2001.
- [6] K. M. Liew, X. Q. He, and C. H. Wong, "On the study of elastic and plastic properties of multi-walled carbon nanotubes under axial tension using molecular dynamics simulation," *Acta Materialia*, vol. 52, no. 9, pp. 2521–2527, 2004.
- [7] K. M. Liew, C. H. Wong, X. Q. He, and M. J. Tan, "Thermal stability of single and multi-walled carbon nanotubes," *Physical Review B: Condensed Matter and Materials Physics*, vol. 71, no. 7, Article ID 075424, 2005.
- [8] B. Liu, Y. Huang, H. Jiang, S. Qu, and K. C. Hwang, "The atomic-scale finite element method," *Computer Methods in Applied Mechanics and Engineering*, vol. 193, no. 17–20, pp. 1849–1864, 2004.
- [9] B. Liu, H. Jiang, Y. Huang, S. Qu, M.-F. Yu, and K. C. Hwang, "Atomic-scale finite element method in multiscale computation with applications to carbon nanotubes," *Physical Review B—Condensed Matter and Materials Physics*, vol. 72, no. 3, Article ID 035435, 2005.
- [10] E. S. Oh, "Elastic properties of boron-nitride nanotubes through the continuum lattice approach," *Materials Letters*, vol. 64, no. 7, pp. 859–862, 2010.
- [11] J. Song, Y. Huang, H. Jiang, K. C. Hwang, and M. F. Yu, "Deformation and bifurcation analysis of boron-nitride nanotubes," *International Journal of Mechanical Sciences*, vol. 48, no. 11, pp. 1197–1207, 2006.
- [12] R. B. Wei, Y. L. Tian, V. Eichhorn, and S. Fatikow, "Compressive and tensile behaviors of carbon and boron nitride nanotubes," in *Proceedings of the International Conference on Manipulation, Manufacturing and Measurement on the Nanoscale (3M-NANO '12)*, pp. 301–304, Shaanxi, China, September 2012.
- [13] M.-L. Liao, Y.-C. Wang, S.-P. Ju, T.-W. Lien, and L.-F. Huang, "Deformation behaviors of an armchair boron-nitride nanotube under axial tensile strains," *Journal of Applied Physics*, vol. 110, no. 5, Article ID 054310, 2011.
- [14] D. W. Brenner, "Empirical potential for hydrocarbons for use in simulating the chemical vapor deposition of diamond films," *Physical Review B*, vol. 42, no. 15, pp. 9458–9471, 1990.
- [15] J. Tersoff, "New empirical approach for the structure and energy of covalent systems," *Physical Review B*, vol. 37, no. 12, pp. 6991–7000, 1988.
- [16] Y. Sun and K. M. Liew, "The buckling of single-walled carbon nanotubes upon bending: the higher order gradient continuum and mesh-free method," *Computer Methods in Applied Mechanics and Engineering*, vol. 197, no. 33–40, pp. 3001–3013, 2008.
- [17] K. M. Liew and Y. Sun, "Elastic properties and pressure-induced structural transitions of single-walled carbon nanotubes," *Physical Review B—Condensed Matter and Materials Physics*, vol. 77, no. 20, Article ID 205437, 2008.
- [18] Y. Z. Sun and K. M. Liew, "Effect of higher-order deformation gradients on buckling of single-walled carbon nanotubes," *Composite Structures*, vol. 109, no. 1, pp. 279–285, 2014.
- [19] T. Zhu and S. N. Atluri, "A modified collocation method and a penalty formulation for enforcing the essential boundary conditions in the element free Galerkin method," *Computational Mechanics*, vol. 21, no. 3, pp. 211–222, 1998.
- [20] Y. Sun and K. M. Liew, "Mesh-free simulation of single-walled carbon nanotubes using higher order Cauchy-Born rule," *Computational Materials Science*, vol. 42, no. 3, pp. 444–452, 2008.
- [21] Y. Sun and K. M. Liew, "Application of the higher-order Cauchy-Born rule in mesh-free continuum and multiscale simulation of carbon nanotubes," *International Journal for Numerical Methods in Engineering*, vol. 75, no. 10, pp. 1238–1258, 2008.

Research Article

Transverse Vibration of Axially Moving Functionally Graded Materials Based on Timoshenko Beam Theory

Suihan Sui, Ling Chen, Cheng Li, and Xinpei Liu

School of Urban Rail Transportation, Soochow University, Suzhou 215006, China

Correspondence should be addressed to Cheng Li; licheng@suda.edu.cn

Received 16 August 2014; Accepted 18 October 2014

Academic Editor: Kim M. Liew

Copyright © 2015 Suihan Sui et al. This is an open access article distributed under the Creative Commons Attribution License, which permits unrestricted use, distribution, and reproduction in any medium, provided the original work is properly cited.

The transverse free vibration of an axially moving beam made of functionally graded materials (FGM) is investigated using a Timoshenko beam theory. Natural frequencies, vibration modes, and critical speeds of such axially moving systems are determined and discussed in detail. The material properties are assumed to vary continuously through the thickness of the beam according to a power law distribution. Hamilton's principle is employed to derive the governing equation and a complex mode approach is utilized to obtain the transverse dynamical behaviors including the vibration modes and natural frequencies. Effects of the axially moving speed and the power-law exponent on the dynamic responses are examined. Some numerical examples are presented to reveal the differences of natural frequencies for Timoshenko beam model and Euler beam model. Moreover, the critical speed is determined numerically to indicate its variation with respect to the power-law exponent, axial initial stress, and length to thickness ratio.

1. Introduction

The axially moving systems are extensively applied in machinery, electronics, and some other related fields. Many engineering devices such as band-saw blade, power transmission belts, and crane hoist cables can be modeled as axially moving systems. Transverse vibration of axially moving systems may induce some disadvantageous effects. For example, the transverse vibration of power transmission belts causes noise and accelerated wear of the belt; the vibration of the blade in band saws leads to poor cutting quality. Therefore, research of the transverse vibration of axially moving beams is indispensable, which has important engineering significance in controlling and optimizing the transverse dynamics. At present, the axially moving beam structures have been widely studied, of which most literatures are based on Euler-Bernoulli beam model. Öz [1] computed natural frequencies of an axially moving beam in contact with a small stationary mass under pinned-pinned or clamped-clamped boundary conditions. Chen et al. [2] studied the dynamic stability of an axially accelerating viscoelastic beam and analyzed the effects of the dynamic viscosity, the mean axial speed, and the tension on the stability conditions. Chen and Yang [3]

developed two nonlinear models for transverse vibration of an axially accelerating viscoelastic beam and applied the method of multiple scales to compare the corresponding steady-state responses and their stability. Chen and Yang [4] presented the first two mode frequencies of axially moving elastic and viscoelastic beams under simple supports with torsion springs. Lee and Jang [5] studied the effects of the continuously incoming and outgoing semi-infinite beam parts on the dynamic characteristics and stability of an axially moving beam by using the spectral element method. Lin and Qiao [6] determined some numerical results for natural frequency of an axially moving beam in fluid based on a differential quadrature method. Ghayesh et al. [7] developed an approximate analytical solution for nonlinear dynamic responses of a simply supported Kelvin-Voigt viscoelastic beam with an attached heavy intraspan mass. Lv et al. [8] investigated natural frequency, bifurcation, and stability of transverse vibration of axially accelerating moving viscoelastic sandwich beams with time-dependent axial tension.

All the cases aforementioned are in the framework of Euler-Bernoulli beam model. However, it does not contain the information about shear stress and moment of inertia in Euler-Bernoulli beam model. Consequently, the Timoshenko

beam model has received more attention in modeling the axially moving structures in recent years. Lee et al. [9] formulated the spectral element model for the transverse vibration of an axially moving Timoshenko beam subjected to a constant axial tension and verify its high accuracy by comparing with the solutions by other methods. Tang et al. [10] analyzed the parametric resonance of axially moving Timoshenko beams with time-dependent speed. Ghayesh and Balar [11] presented nonlinear vibration and stability analysis of an axially moving Timoshenko beam for two dynamic models and employed the multiple scales method to obtain the mode shape equations, natural frequencies, and steady-state responses of the system. Li et al. [12] studied the nonlinear free transverse vibrations of the axially moving Timoshenko beam with constant speed. Ghayesh and Amabili [13] investigated the nonlinear forced vibrations and stability of an axially moving Timoshenko beam with an intraspan spring-support. All the literatures using axially moving Timoshenko beam model receive more accurate results and it is applicable to the stubby axially moving structures.

In engineering practices, the axially moving beam may be made by FGM. The present study is concerned with the axially moving FGM Timoshenko beam. In the related literatures, most are focused on the mechanical properties of FGM without axial motion but the studies of axially moving FGM Timoshenko beam are very few. Ding et al. [14] derived a series of analytical solutions for anisotropic FGM beams with various end conditions using an Airy stress function in the generalized polynomial form. Kang and Li [15] investigated the mechanical behaviors of a nonlinear FGM cantilever beam subjected to an end force by using large and small deformation theories. Zhou et al. [16] studied the mechanical responses of a functionally graded cantilever beam by use of two kinds of particle with different properties based on discrete element method. Şimşek [17] investigated the forced vibration of a functionally graded beam under a moving mass by using Euler-Bernoulli, Timoshenko, and the third-order shear deformation beam theories. Alshorbagy et al. [18] studied the free vibration of a functionally graded beam by finite element method with material graduation axially or transversally through the thickness. Ke et al. [19] investigated nonlinear free vibration of size-dependent functionally graded microbeams based on the modified couple stress theory and von Kármán geometric nonlinearity. Şimşek et al. [20] analytically examined static bending of functionally graded microbeams based on the modified couple stress theory and Euler-Bernoulli and Timoshenko beam theories, respectively.

Considering the wide application of axially moving structures and the excellent characteristics of FGM, the investigation of transverse vibration of axially moving beams made of FGM is of great significance both in theoretical study and engineering application. In this paper, the transverse vibration of an axially moving, initially tensioned beam made of FGM is investigated. The Timoshenko beam model is utilized and the complex mode approach is performed to obtain the natural frequencies and the modal functions. With the numerical example for boundary condition of simply

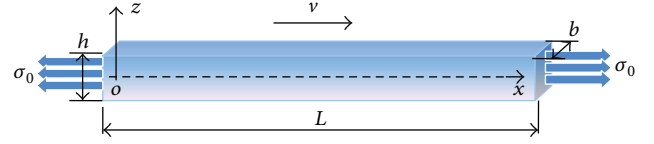


FIGURE 1: Schematics of an axially moving FGM beam.

supported on both ends, the effects of power-law exponent, axial speed, and initial stress to the natural frequencies are analyzed and discussed in detail. Finally, the critical speed is determined to show its variation with different power-law exponent, axial initial stress, and length to thickness ratio.

2. Physical Model

For an axially moving FGM beam as shown in Figure 1, the beam travels at a speed v between two boundaries separated by distance L under an applied axial initial stress σ_0 . The cross section is a rectangle of thickness h and width b . The coordinate system (Oxz) is defined on the middle plane of the beam. Note that the x -axis is taken along the middle plane and the z -axis in the thickness direction.

The elastic modulus E (N/m²) and density ρ (kg/m³) of the beam are assumed to vary through the thickness following a simple power-law distribution. They can be described by

$$\begin{aligned} E(z) &= (E_c - E_m) \left(\frac{z}{h} + \frac{1}{2} \right)^k + E_m, \\ \rho(z) &= (\rho_c - \rho_m) \left(\frac{z}{h} + \frac{1}{2} \right)^k + \rho_m, \end{aligned} \quad (1)$$

$$-\frac{h}{2} \leq z \leq \frac{h}{2},$$

where k stands for the power-law exponent. As the FGM beam is assumed to be made of pure Alumina ceramics and pure steel metal, subscripts c and m refer to the ceramic ($E_c = 390$ GPa, $\rho_c = 3960$ kg/m³) and metal ($E_m = 210$ GPa, $\rho_m = 7800$ kg/m³), respectively.

3. Governing Equation and Theoretical Formulation

Based on the Timoshenko beam theory, the total transverse deflection and the angle of rotation due to bending are denoted by $w(x, t)$ and $\psi(x, t)$, respectively. The kinetic energy T and potential energies V are given by

$$\begin{aligned} T &= \frac{1}{2} \int_0^L \left\{ \rho_{T0} \left[v^2 + \left(\frac{\partial w}{\partial t} + v \frac{\partial w}{\partial x} \right)^2 \right] \right. \\ &\quad \left. + \rho_{T2} \left(\frac{\partial \psi}{\partial t} + v \frac{\partial \psi}{\partial x} \right)^2 \right\} dx, \\ V &= \frac{1}{2} \int_0^L \left\{ (EI)_{eq} \left(\frac{\partial \psi}{\partial x} \right)^2 + \kappa G_T \left(\frac{\partial w}{\partial x} - \psi \right)^2 \right. \\ &\quad \left. + \sigma_0 A \left(\frac{\partial w}{\partial x} \right)^2 \right\} dx, \end{aligned} \quad (2)$$

where

$$\begin{aligned}\rho_{T0} &= \int_A \rho(z) dA, & \rho_{T2} &= \int_A \rho(z) z^2 dA, \\ G_T &= \int_A G(z) dA, & (EI)_{eq} &= \int_A E(z) z^2 dA, \\ G(z) &= \frac{E(z)}{2(1+\mu)},\end{aligned}\quad (3)$$

in which μ is the Poisson's ratio and κ is the shear correction factor.

Substitute (2) into the extended Hamilton's principle

$$\int_{t_1}^{t_2} (\delta T - \delta V) dt = 0. \quad (4)$$

The detail is shown in Appendix A from which the equations of motion for the axially moving FGM Timoshenko beam can be derived as

$$\begin{aligned}\kappa G_T \left(\frac{\partial^2 w}{\partial x^2} - \frac{\partial \psi}{\partial x} \right) - \rho_{T0} \left(\frac{\partial^2 w}{\partial t^2} + 2v \frac{\partial^2 w}{\partial t \partial x} + v^2 \frac{\partial^2 w}{\partial x^2} \right) \\ + \sigma_0 A \frac{\partial^2 w}{\partial x^2} = 0,\end{aligned}\quad (5)$$

$$\begin{aligned}(EI)_{eq} \frac{\partial^2 \psi}{\partial x^2} - \rho_{T2} \left(\frac{\partial^2 \psi}{\partial t^2} + 2v \frac{\partial^2 \psi}{\partial t \partial x} + v^2 \frac{\partial^2 \psi}{\partial x^2} \right) \\ + \kappa G_T \left(\frac{\partial w}{\partial x} - \psi \right) = 0.\end{aligned}\quad (6)$$

Decoupling (5) and (6) yields the governing equation for the transverse vibration of such axially moving FGM Timoshenko beams

$$\begin{aligned}(1 - a_2 v^2) (1 + a_4 - a_1 v^2) \frac{\partial^4 w}{\partial x^4} \\ - 2v (a_1 + a_2 + a_2 a_4 - 2a_1 a_2 v^2) \frac{\partial^4 w}{\partial t \partial x^3} \\ + a_3 (a_1 v^2 - a_4) \frac{\partial^2 w}{\partial x^2} - (a_1 + a_2 + a_2 a_4 - 6a_1 a_2 v^2) \\ \times \frac{\partial^4 w}{\partial t^2 \partial x^2} + 4a_1 a_2 v \frac{\partial^4 w}{\partial t^3 \partial x} + 2a_1 a_3 v \frac{\partial^2 w}{\partial t \partial x} \\ + a_1 a_3 \frac{\partial^2 w}{\partial t^2} + a_1 a_2 \frac{\partial^2 w}{\partial t^4} = 0,\end{aligned}\quad (7)$$

where

$$\begin{aligned}a_1 &= \frac{\rho_{T0}}{\kappa G_T}, & a_2 &= \frac{\rho_{T2}}{(EI)_{eq}}, \\ a_3 &= \frac{\kappa G_T}{(EI)_{eq}}, & a_4 &= \frac{\sigma_0 A}{\kappa G_T}.\end{aligned}\quad (8)$$

4. Case Studies

4.1. Natural Frequencies and Mode Function. The boundary conditions for the simple supports at both ends are given by

$$\begin{aligned}w(0, t) &= 0; & w(L, t) &= 0; \\ \frac{\partial^2 w(0, t)}{\partial x^2} &= 0; & \frac{\partial^2 w(L, t)}{\partial x^2} &= 0.\end{aligned}\quad (9)$$

The solution to (7) can be assumed as

$$w(x, t) = \varphi_n(x) e^{i\omega_n t} + \bar{\varphi}_n(x) e^{-i\omega_n t}, \quad (10)$$

where φ_n and ω_n denote the n th mode function and natural frequency, respectively. $\bar{\varphi}_n$ represents the complex conjugate of φ_n . Substitution of (10) into (7) and (9) leads to

$$\begin{aligned}(1 - a_2 v^2) (1 + a_4 - a_1 v^2) \varphi_n^{(4)} \\ - 2i\omega_n v (a_1 + a_2 + a_2 a_4 - 2a_1 a_2 v^2) \varphi_n^{(3)} \\ + [a_3 (a_1 v^2 - a_4) + \omega_n^2 (a_1 + a_2 + a_2 a_4 - 6a_1 a_2 v^2)] \varphi_n'' \\ - 2ia_1 v \omega_n (2a_2 \omega_n^2 - a_3) \varphi_n' - a_1 \omega_n^2 (a_3 - a_2 \omega_n^2) \varphi_n = 0,\end{aligned}\quad (11)$$

$$\begin{aligned}\varphi_n(0) &= 0; & \varphi_n(L) &= 0; \\ \varphi_n''(0) &= 0; & \varphi_n''(L) &= 0,\end{aligned}\quad (12)$$

where $\varphi_n^{(4)}$, $\varphi_n^{(3)}$, φ_n'' , and φ_n' denote the derivative with respect to coordinate x . The solution to ordinary differential equation (11) can be expressed by

$$\varphi_n(x) = C_{1n} e^{\beta_{1n} x} + C_{2n} e^{\beta_{2n} x} + C_{3n} e^{\beta_{3n} x} + C_{4n} e^{\beta_{4n} x}, \quad (13)$$

where $C_{1n} \sim C_{4n}$ are four unknown constants and $\beta_{1n} \sim \beta_{4n}$ are four complex eigenvalues of (11). Substituting (13) into (12) yields

$$C_{1n} + C_{2n} + C_{3n} + C_{4n} = 0, \quad (14a)$$

$$C_{1n} e^{\beta_{1n}} + C_{2n} e^{\beta_{2n}} + C_{3n} e^{\beta_{3n}} + C_{4n} e^{\beta_{4n}} = 0, \quad (14b)$$

$$C_{1n} \beta_{1n}^2 + C_{2n} \beta_{2n}^2 + C_{3n} \beta_{3n}^2 + C_{4n} \beta_{4n}^2 = 0, \quad (14c)$$

$$C_{1n} \beta_{1n}^2 e^{\beta_{1n}} + C_{2n} \beta_{2n}^2 e^{\beta_{2n}} + C_{3n} \beta_{3n}^2 e^{\beta_{3n}} + C_{4n} \beta_{4n}^2 e^{\beta_{4n}} = 0. \quad (14d)$$

Rewrite (14a), (14b), (14c), and (14d) in the form of a matrix as

$$\begin{pmatrix} 1 & 1 & 1 & 1 \\ e^{\beta_{1n}} & e^{\beta_{2n}} & e^{\beta_{3n}} & e^{\beta_{4n}} \\ \beta_{1n}^2 & \beta_{2n}^2 & \beta_{3n}^2 & \beta_{4n}^2 \\ \beta_{1n}^2 e^{\beta_{1n}} & \beta_{2n}^2 e^{\beta_{2n}} & \beta_{3n}^2 e^{\beta_{3n}} & \beta_{4n}^2 e^{\beta_{4n}} \end{pmatrix} \begin{pmatrix} C_{1n} \\ C_{2n} \\ C_{3n} \\ C_{4n} \end{pmatrix} = 0. \quad (15)$$

For the nontrivial solution of (15), the determinant of the coefficient matrix must be zero.

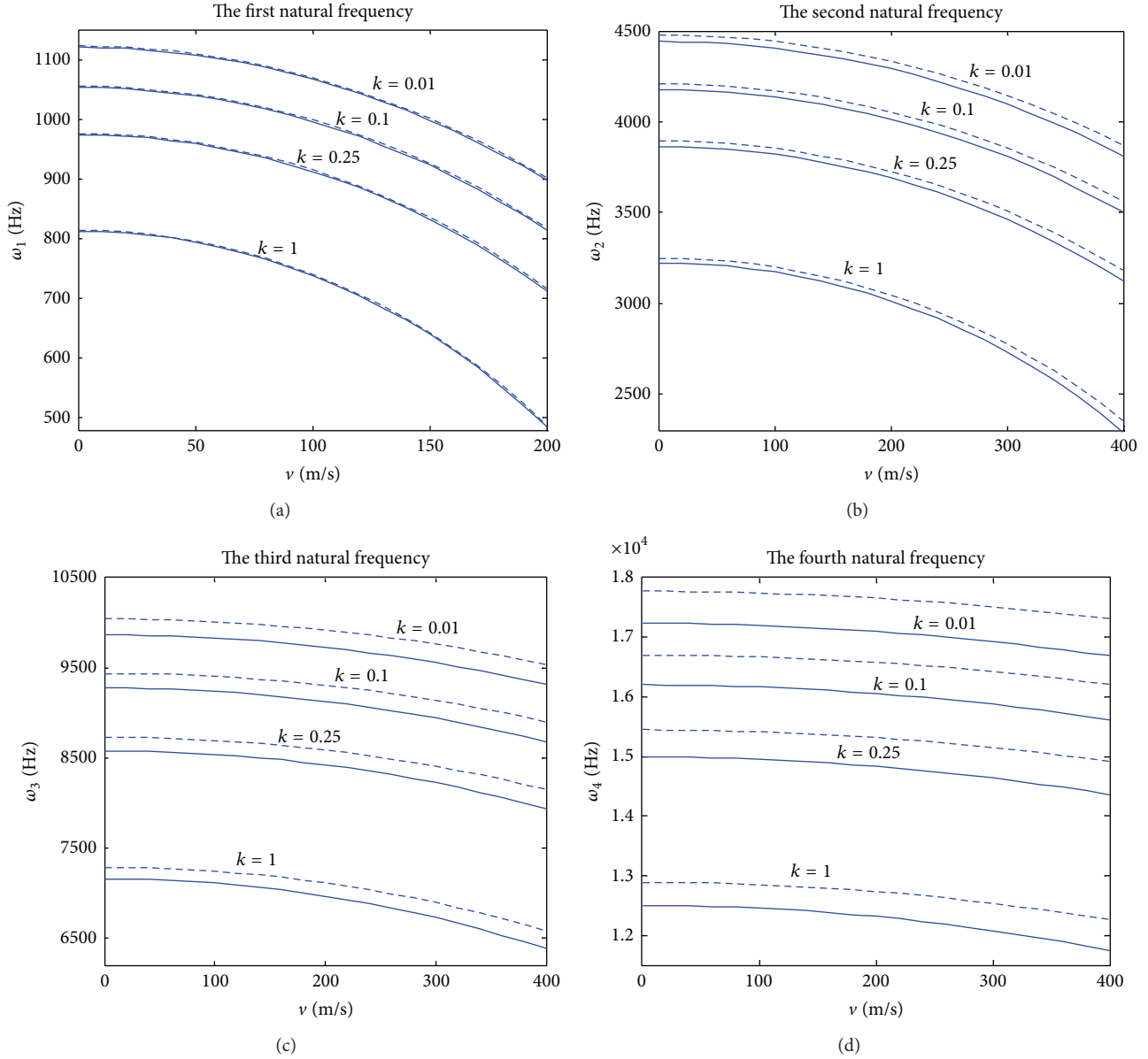


FIGURE 2: The natural frequencies versus axially moving speeds for different power-law exponents ($\sigma_0 = 1$ MPa).

Consider

$$\begin{aligned}
 & \left[e^{(\beta_{1n} + \beta_{2n})} + e^{(\beta_{3n} + \beta_{4n})} \right] (\beta_{1n}^2 - \beta_{2n}^2) (\beta_{3n}^2 - \beta_{4n}^2) \\
 & - \left[e^{(\beta_{1n} + \beta_{3n})} + e^{(\beta_{2n} + \beta_{4n})} \right] (\beta_{1n}^2 - \beta_{3n}^2) (\beta_{2n}^2 - \beta_{4n}^2) \\
 & + \left[e^{(\beta_{2n} + \beta_{3n})} + e^{(\beta_{1n} + \beta_{4n})} \right] (\beta_{2n}^2 - \beta_{3n}^2) (\beta_{1n}^2 - \beta_{4n}^2) = 0.
 \end{aligned} \quad (16)$$

Using (15) and (16), one can obtain the coefficients of (13); the expressions of $C_{2n} \sim C_{4n}$ are listed in Appendix B.

The n th modal function of the axially moving FGM beam is determined as

$$\begin{aligned}
 \varphi_n(x) &= \left\{ e^{\beta_{1n}x} - \frac{(\beta_{4n}^2 - \beta_{1n}^2)(e^{\beta_{3n}} - e^{\beta_{1n}})}{(\beta_{4n}^2 - \beta_{2n}^2)(e^{\beta_{3n}} - e^{\beta_{2n}})} e^{\beta_{2n}x} \right. \\
 & - \frac{(\beta_{4n}^2 - \beta_{1n}^2)(e^{\beta_{2n}} - e^{\beta_{1n}})}{(\beta_{4n}^2 - \beta_{3n}^2)(e^{\beta_{2n}} - e^{\beta_{3n}})} e^{\beta_{3n}x} \\
 & + \left(-1 + \frac{(\beta_{4n}^2 - \beta_{1n}^2)(e^{\beta_{3n}} - e^{\beta_{1n}})}{(\beta_{4n}^2 - \beta_{2n}^2)(e^{\beta_{3n}} - e^{\beta_{2n}})} \right. \\
 & \left. \left. + \frac{(\beta_{4n}^2 - \beta_{1n}^2)(e^{\beta_{2n}} - e^{\beta_{1n}})}{(\beta_{4n}^2 - \beta_{3n}^2)(e^{\beta_{2n}} - e^{\beta_{3n}})} \right) e^{\beta_{4n}x} \right\} C_{1n}.
 \end{aligned} \quad (17)$$

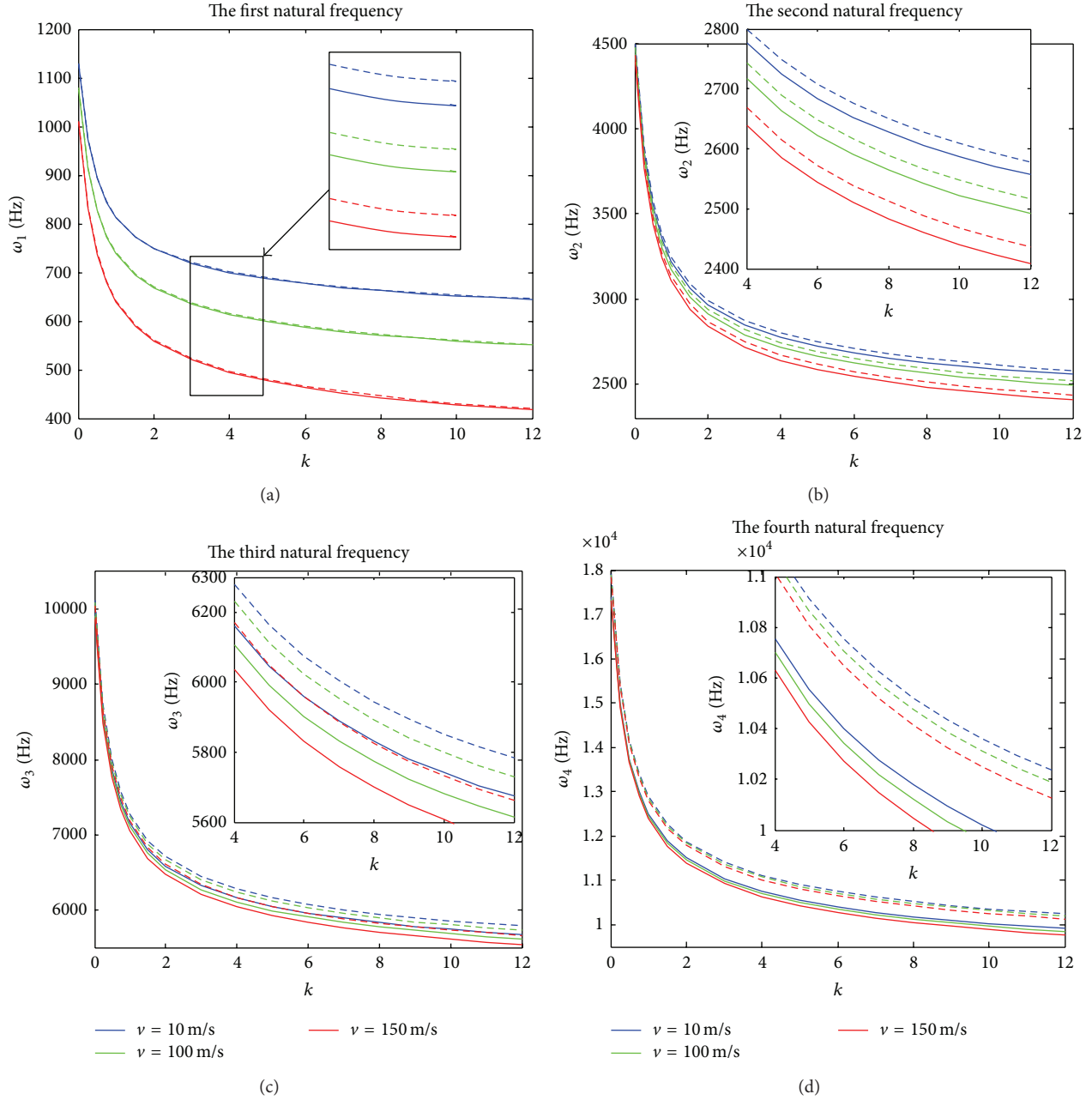


FIGURE 3: The natural frequencies versus power-law exponent for different axially moving speeds ($\sigma_0 = 1$ MPa).

4.2. Critical Speeds. The time-independent equilibrium form of the linear equation (7) can be written as

$$(1 - a_2 v^2)(1 + a_4 - a_1 v^2) \frac{\partial^4 w}{\partial x^4} + a_3(a_1 v^2 - a_4) \frac{\partial^2 w}{\partial x^2} = 0. \quad (18)$$

The characteristic equation of (18) is

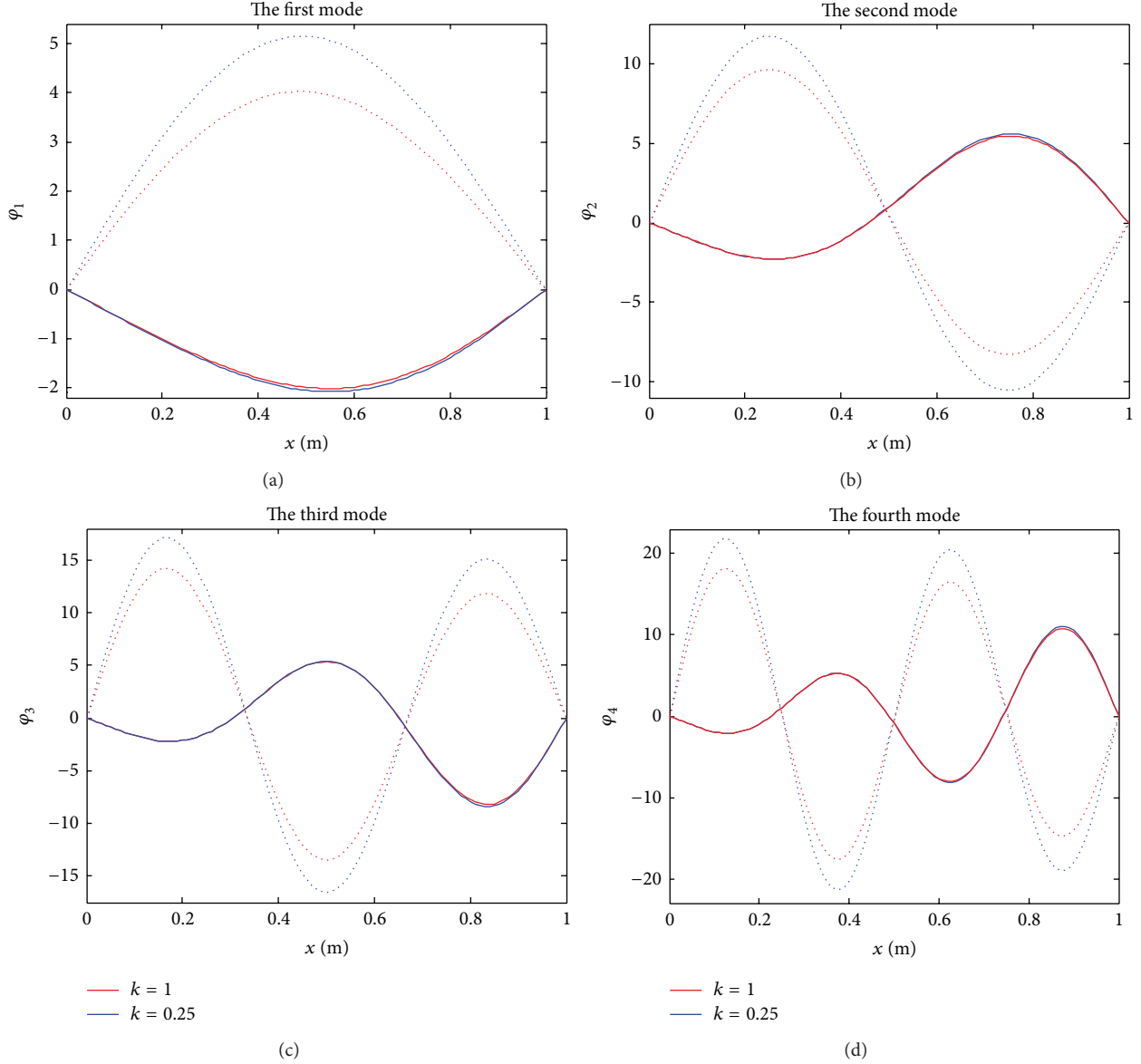
$$(1 - a_2 v^2)(1 + a_4 - a_1 v^2) r^4 + a_3(a_1 v^2 - a_4) r^2 = 0. \quad (19)$$

When v is higher than 100 m/s, numerical results demonstrate that $(1 - a_2 v^2)(1 + a_4 - a_1 v^2)$ and $a_3(a_1 v^2 - a_4)$ are positive numbers. Consequently, the solution to (19) is determined as

$$r_1 = r_2 = 0, \quad r_3 = r_4 = \pm i \sqrt{\frac{a_3(a_1 v^2 - a_4)}{(1 - a_2 v^2)(1 + a_4 - a_1 v^2)}}. \quad (20)$$

On the other hand, the solution to (18) can be expressed by

$$w(x) = C_1 + C_2 x + C_3 \cos(\beta x) + C_4 \sin(\beta x), \quad (21)$$

FIGURE 4: The first four modal functions ($v = 100$ m/s, $\sigma_0 = 1$ MPa).

where

$$\beta = \sqrt{\frac{a_3(a_1 v^2 - a_4)}{(1 - a_2 v^2)(1 + a_4 - a_1 v^2)}}. \quad (22)$$

Substituting (21) into the boundary condition of (9) yields

$$\begin{pmatrix} 1 & 0 & 1 & 0 \\ 1 & L & \cos(\beta L) & \sin(\beta L) \\ 0 & 0 & -\beta^2 & 0 \\ 0 & 0 & -\beta^2 \cos(\beta L) & -\beta^2 \sin(\beta L) \end{pmatrix} \begin{pmatrix} C_1 \\ C_2 \\ C_3 \\ C_4 \end{pmatrix} = 0. \quad (23)$$

For the nontrivial solution of (23), the determinant of the coefficient matrix must be zero, which results in

$$L\beta^4 \sin(L\beta) = 0. \quad (24)$$

Using (22) and (24), as well as the conditions $\beta L = n\pi$ and $n = 1$, one can get the critical speeds of axially moving FGM beam as follows:

$$v_c = \sqrt{\frac{M - N}{2\pi^2 a_1 a_2}} \quad (25)$$

or

$$v_c = \sqrt{\frac{M + N}{2\pi^2 a_1 a_2}}, \quad (26)$$

where

$$\begin{aligned} M &= \pi^2 (a_1 + a_2 + a_2 a_4) + L^2 a_1 a_3, \\ N &= \left((a_1 (\pi^2 + L^2 a_3) + \pi^2 a_2 (1 + a_4))^2 \right. \\ &\quad \left. - 4\pi^2 a_1 a_2 (\pi^2 + \pi^2 a_4 + L^2 a_3 a_4) \right)^{1/2}. \end{aligned} \quad (27)$$

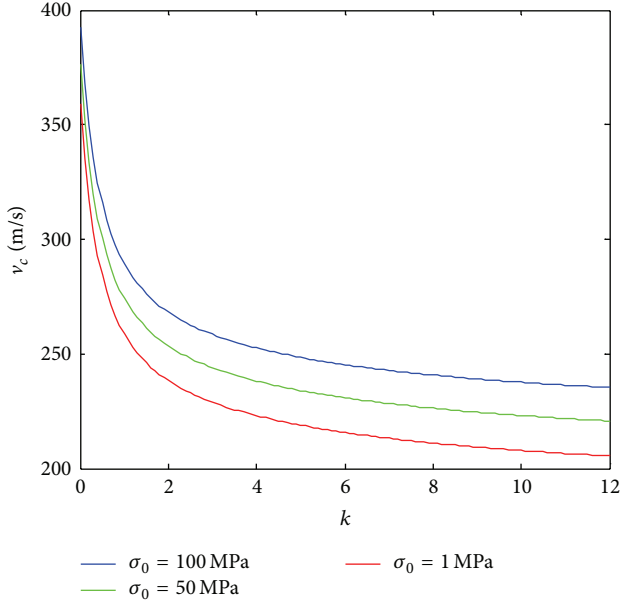


FIGURE 5: The critical speeds versus power-law exponent for different initial stress.

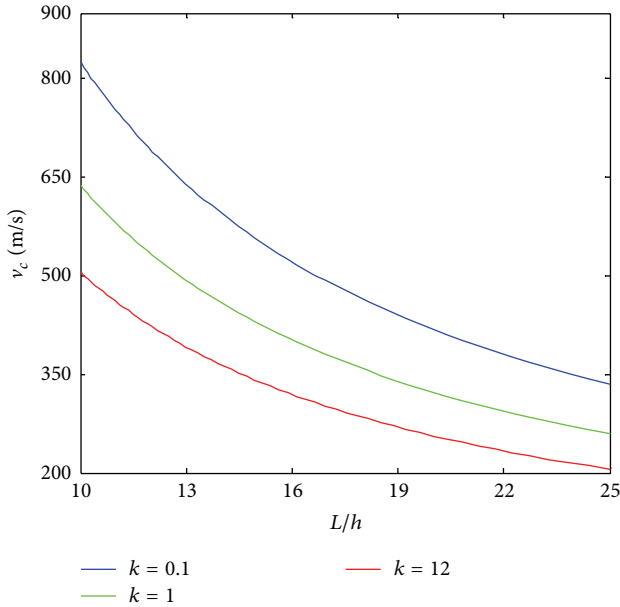


FIGURE 6: The critical speeds versus L/h ratio for different power-law exponents ($\sigma_0 = 1$ MPa).

Combined with numerical results in Section 4.3, it can be verified that the critical speed can be determined by equation (25) only.

4.3. Numerical Results and Discussions. In the following numerical computation, the beam is made of steel metal and Alumina ceramics; several parameters are chosen to be

$$L = 1 \text{ m}, \quad h = 0.04 \text{ m}, \quad b = 0.04 \text{ m}, \quad \mu = 0.3, \quad \kappa = \frac{5}{6}. \quad (28)$$

TABLE 1: Effect of initial stress on first four frequencies for FGM beam ($v = 100$ m/s).

k	σ_0 (MPa)	ω_1 (Hz)	ω_2 (Hz)	ω_3 (Hz)	ω_4 (Hz)
0.001	1	1075	4436	9900	17322
	50	1129	4490	9955	17377
	100	1182	4545	10010	17433
	Increase rate	9.95%	2.46%	1.11%	0.64%
1	1	738	3170	7109	12455
	50	790	3221	7160	12506
	100	841	3272	7211	12559
	Increase rate	13.96%	3.22%	1.43%	0.84%
100	1	496	2304	5209	9147
	50	553	2357	5262	9200
	100	605	2409	5315	9254
	Increase rate	21.98%	4.56%	2.03%	1.17%

Natural frequencies are found by numerically solving (11) and (16), simultaneously, with different speeds, different power-law exponents, and different initial stresses. Figure 2 illustrates the effect of axial speed on the first four natural frequencies for different power-law exponents. As observed, with the increase of axially moving speed, natural frequencies decrease. Increasing the power-law exponent on the other hand causes a decrease in natural frequencies. Figure 3 illustrates the effect of power-law exponents on the first four natural frequencies under different axially moving speeds. As observed, with the increase of power-law exponent, natural frequencies decrease, and the decrease becomes more and more gentle.

In Figures 2 and 3 the solid lines and dashed lines denote the Timoshenko model and the Euler beam model, respectively. The frequencies are lower with Timoshenko model comparing with the Euler model, as other parameters are fixed. Besides, the numerical results demonstrate that the difference of the natural frequencies with the two models becomes more significant as the order increases.

The frequencies of a FGM beam always remain between the frequencies of its constituent material of the beam; that is, when k is small, the content of ceramic in the beam is high; then the natural frequencies of FGM beams are close to the natural frequencies of the pure ceramic beam. When k is large, the content of metal in the beam is high, and the natural frequencies of FGM beams approach the natural frequencies of the pure metal beam.

Table 1 shows the first four natural frequencies with different σ_0 and different k . It is seen that natural frequencies are increasing with increasing σ_0 and decreasing with an increase in k . Moreover, with the increase of k , the increase rate of each order raises to some extent and the first frequencies raise the most.

After obtaining the natural frequencies of the system, the solution $\beta_{1n} \sim \beta_{4n}$ of (11) can be obtained. Subsequently, using (17), one can get the modal function of the axially moving FGM beam. Figure 4 presents the first four modal functions, in which the solid lines and dashed lines denote the real and

imaginary parts of the modal functions, respectively, where $\nu = 100$ m/s and $\sigma_0 = 1$ MPa are adopted.

With an increase of axially moving speed, each order of the frequency tends to vanish. The exact values at which the first natural frequency vanishes are called the critical speeds. If axially moving speed is higher than the critical speed, the system is unstable. Figure 5 illustrates the effect of k on the critical speeds for different initial stress. The numerical results indicate that the critical speeds of the beam decrease with the increasing k and the decreasing σ_0 . For a specific initial stress, for example, $\sigma_0 = 1$ MPa, with an increase of k , the critical speeds begin to decrease rapidly and then gently. The effects of the L/h ratio on the critical speeds for different k are shown in Figure 6. The larger L/h ratio leads to lower critical speeds for given k and the higher the critical speeds the smaller the k for given L/h ratio.

5. Conclusions

This work is devoted to the transverse dynamic responses of axially moving, initially tensioned Timoshenko beams made of FGM. The complex mode approach is performed to obtain the natural frequencies and modal functions, respectively. The effects of some parameters including axially moving speed and the power-law exponent on the natural frequencies are investigated. Some numerical examples are presented to demonstrate the comparisons of natural frequencies for Timoshenko beam model and Euler beam model. The critical speeds are determined and numerically investigated. The results show that an increase of the power-law exponent or the axial speed results in a lower natural frequency, while the axial initial stress tends to increase the natural frequencies. With the increase of the power-law exponent or the L/h ratio, the critical speeds decrease, while the axial initial stress tends to increase the critical speeds. The results reported in this work could be useful for designing and optimizing the axially moving FGM Timoshenko beam-like structures.

Appendices

A. Result of Substituting (2) into (4) Leads to

Consider

$$\begin{aligned} & \int_{t_1}^{t_2} \int_0^L \left[\kappa G_T \left(\frac{\partial^2 w}{\partial x^2} - \frac{\partial \psi}{\partial x} \right) \right. \\ & \quad \left. - \rho_{T0} \left(\frac{\partial^2 w}{\partial t^2} + 2\nu \frac{\partial^2 w}{\partial t \partial x} + \nu^2 \frac{\partial^2 w}{\partial x^2} \right) \right. \\ & \quad \left. + \sigma_0 A \frac{\partial^2 w}{\partial x^2} \right] \delta w \, dx \, dt \\ & + \int_{t_1}^{t_2} \int_0^L \left[(EI)_{eq} \frac{\partial^2 \psi}{\partial x^2} - \rho_{T2} \left(\frac{\partial^2 \psi}{\partial t^2} + 2\nu \frac{\partial^2 \psi}{\partial t \partial x} + \nu^2 \frac{\partial^2 \psi}{\partial x^2} \right) \right. \\ & \quad \left. + \kappa G_T \left(\frac{\partial w}{\partial x} - \psi \right) \right] \delta \psi \, dx \, dt \end{aligned}$$

$$\begin{aligned} & + \rho_{T0} \int_{t_1}^{t_2} \int \left(\nu \frac{\partial w}{\partial t} \delta w + \nu^2 \frac{\partial w}{\partial x} \delta w \right) \Big|_0^L dt \\ & + \rho_{T0} \int_0^L \left(\frac{\partial w}{\partial t} \delta w + \nu \frac{\partial w}{\partial x} \delta w \right) \Big|_{t_1}^{t_2} dx \\ & + \rho_{T2} \int_{t_1}^{t_2} \left(\nu \frac{\partial \psi}{\partial t} \delta \psi + \nu^2 \frac{\partial \psi}{\partial x} \delta \psi \right) \Big|_0^L dt \\ & + \rho_{T2} \int_0^L \left(\frac{\partial \psi}{\partial t} \delta \psi + \nu \frac{\partial \psi}{\partial x} \delta \psi \right) \Big|_{t_1}^{t_2} dx \\ & - \kappa G_T \int_{t_1}^{t_2} \left(\frac{\partial w}{\partial x} \delta w + \psi \delta w \right) \Big|_0^L dt - \sigma_0 A \int_{t_1}^{t_2} \frac{\partial w}{\partial x} \delta w \Big|_0^L dt \\ & - (EI)_{eq} \int_{t_1}^{t_2} \frac{\partial \psi}{\partial x} \delta \psi \Big|_0^L dt = 0. \end{aligned} \tag{A.1}$$

B. The Coefficient of (13)

Consider

$$\begin{aligned} C_{2n} &= - \frac{(\beta_{4n}^2 - \beta_{1n}^2)(e^{\beta_{3n}} - e^{\beta_{1n}})}{(\beta_{4n}^2 - \beta_{2n}^2)(e^{\beta_{3n}} - e^{\beta_{2n}})} C_{1n}, \\ C_{3n} &= - \frac{(\beta_{4n}^2 - \beta_{1n}^2)(e^{\beta_{2n}} - e^{\beta_{1n}})}{(\beta_{4n}^2 - \beta_{3n}^2)(e^{\beta_{2n}} - e^{\beta_{3n}})} C_{1n}, \\ C_{4n} &= \left[-1 + \frac{(\beta_{4n}^2 - \beta_{1n}^2)(e^{\beta_{3n}} - e^{\beta_{1n}})}{(\beta_{4n}^2 - \beta_{2n}^2)(e^{\beta_{3n}} - e^{\beta_{2n}})} \right. \\ & \quad \left. + \frac{(\beta_{4n}^2 - \beta_{1n}^2)(e^{\beta_{2n}} - e^{\beta_{1n}})}{(\beta_{4n}^2 - \beta_{3n}^2)(e^{\beta_{2n}} - e^{\beta_{3n}})} \right] C_{1n}. \end{aligned} \tag{B.1}$$

Conflict of Interests

The authors declare that there is no conflict of interests regarding the publication of this paper.

Acknowledgments

This work was supported by National Natural Science Foundation of China (nos. 11202145, 51405321), the Jiangsu Provincial Natural Science Foundation of China (no. BK2012175), and the Natural Science Foundation of the Jiangsu Higher Education Institutions of China (no. 14KJB460026).

References

- [1] H. R. Öz, "Natural frequencies of axially travelling tensioned beams in contact with a stationary mass," *Journal of Sound and Vibration*, vol. 259, no. 2, pp. 445–456, 2003.
- [2] L.-Q. Chen, X.-D. Yang, and C.-J. Cheng, "Dynamic stability of an axially accelerating viscoelastic beam," *European Journal of Mechanics—A/Solids*, vol. 23, no. 4, pp. 659–666, 2004.

- [3] L. Q. Chen and X. D. Yang, "Steady-state response of axially moving viscoelastic beams with pulsating speed: comparison of two nonlinear models," *International Journal of Solids and Structures*, vol. 42, no. 1, pp. 37–50, 2005.
- [4] L.-Q. Chen and X.-D. Yang, "Vibration and stability of an axially moving viscoelastic beam with hybrid supports," *European Journal of Mechanics A: Solids*, vol. 25, no. 6, pp. 996–1008, 2006.
- [5] U. Lee and I. Jang, "On the boundary conditions for axially moving beams," *Journal of Sound and Vibration*, vol. 306, no. 3-5, pp. 675–690, 2007.
- [6] W. Lin and N. Qiao, "Vibration and stability of an axially moving beam immersed in fluid," *International Journal of Solids and Structures*, vol. 45, no. 5, pp. 1445–1457, 2008.
- [7] M. H. Ghayesh, F. Alijani, and M. A. Darabi, "An analytical solution for nonlinear dynamics of a viscoelastic beam-heavy mass system," *Journal of Mechanical Science and Technology*, vol. 25, no. 8, pp. 1915–1923, 2011.
- [8] H. Lv, Y. Li, L. Li, and Q. Liu, "Transverse vibration of viscoelastic sandwich beam with time-dependent axial tension and axially varying moving velocity," *Applied Mathematical Modelling*, vol. 38, no. 9-10, pp. 2558–2585, 2014.
- [9] U. Lee, J. Kim, and H. Oh, "Spectral analysis for the transverse vibration of an axially moving Timoshenko beam," *Journal of Sound and Vibration*, vol. 271, no. 3-4, pp. 685–703, 2004.
- [10] Y.-Q. Tang, L.-Q. Chen, and X.-D. Yang, "Parametric resonance of axially moving Timoshenko beams with time-dependent speed," *Nonlinear Dynamics*, vol. 58, no. 4, pp. 715–724, 2009.
- [11] M. H. Ghayesh and S. Balar, "Non-linear parametric vibration and stability analysis for two dynamic models of axially moving Timoshenko beams," *Applied Mathematical Modelling*, vol. 34, no. 10, pp. 2850–2859, 2010.
- [12] B. Li, Y. Tang, and L. Chen, "Nonlinear free transverse vibrations of axially moving Timoshenko beams with two free ends," *Science China Technological Sciences*, vol. 54, no. 8, pp. 1966–1976, 2011.
- [13] M. H. Ghayesh and M. Amabili, "Nonlinear vibrations and stability of an axially moving Timoshenko beam with an intermediate spring support," *Mechanism and Machine Theory*, vol. 67, pp. 1–16, 2013.
- [14] H. J. Ding, D. J. Huang, and W. Q. Chen, "Elasticity solutions for plane anisotropic functionally graded beams," *International Journal of Solids and Structures*, vol. 44, no. 1, pp. 176–196, 2007.
- [15] Y.-A. Kang and X.-F. Li, "Bending of functionally graded cantilever beam with power-law non-linearity subjected to an end force," *International Journal of Non-Linear Mechanics*, vol. 44, no. 6, pp. 696–703, 2009.
- [16] F.-X. Zhou, S.-R. Li, Y.-M. Lai, and Y. Yang, "Analyzing of functionally graded materials by discrete element method," *Applied Mechanics and Materials*, vol. 29–32, pp. 1948–1953, 2010.
- [17] M. Şimşek, "Vibration analysis of a functionally graded beam under a moving mass by using different beam theories," *Composite Structures*, vol. 92, no. 4, pp. 904–917, 2010.
- [18] A. E. Alshorbagy, M. A. Eltaher, and F. F. Mahmoud, "Free vibration characteristics of a functionally graded beam by finite element method," *Applied Mathematical Modelling*, vol. 35, no. 1, pp. 412–425, 2011.
- [19] L. L. Ke, Y. S. Wang, J. Yang, and S. Kitipornchai, "Nonlinear free vibration of size-dependent functionally graded microbeams," *International Journal of Engineering Science*, vol. 50, no. 1, pp. 256–267, 2012.
- [20] M. Şimşek, T. Kocatürk, and Ş. D. Akbaş, "Static bending of a functionally graded microscale Timoshenko beam based on the modified couple stress theory," *Composite Structures*, vol. 95, pp. 740–747, 2013.

Research Article

Life Prediction on a T700 Carbon Fiber Reinforced Cylinder with Limited Accelerated Life Testing Data

Ma Xiaobing¹ and Zhang Yongbo²

¹*School of Reliability and Systems Engineering, Beihang University, Beijing 100191, China*

²*Research Center of Small Sample Technology, Beihang University, Beijing 100191, China*

Correspondence should be addressed to Zhang Yongbo; zhang19840504@163.com

Received 14 July 2014; Revised 10 September 2014; Accepted 10 September 2014

Academic Editor: Shaofan Li

Copyright © 2015 M. Xiaobing and Z. Yongbo. This is an open access article distributed under the Creative Commons Attribution License, which permits unrestricted use, distribution, and reproduction in any medium, provided the original work is properly cited.

An accelerated life testing investigation was conducted on a composite cylinder that consists of aluminum alloy and T700 carbon fiber. The ultimate failure stress predictions of cylinders were obtained by the mixing rule and verified by the blasting static pressure method. Based on the stress prediction of cylinder under working conditions, the constant stress accelerated life test of the cylinder was designed. However, the failure data cannot be sufficiently obtained by the accelerated life test due to the time limitation. Therefore, most of the data presented to be high censored in high stress level and zero-failure data in low stress level. When using the traditional method for rupture life prediction, the results showed to be of lower confidence. In this study, the consistency of failure mechanism for carbon fiber and cylinder was analyzed firstly. According to the analysis result, the statistical test information of carbon fiber could be utilized for the accelerated model constitution. Then, rupture life prediction method for cylinder was proposed based on the accelerated life test data and carbon fiber test data. In this way, the life prediction accuracy of cylinder could be improved obviously, and the results showed that the accuracy of this method increased by 35%.

1. Introduction

In recent years, T700 carbon fiber replacing T300 becomes the new general carbon fiber since densification gives the T700 higher tensile strength [1–6]. The cylinder of new special equipment consists of T700 carbon fiber composite materials, glass fiber composites, and aluminum alloy. The main role of aluminum alloy is to improve the axial modulus and corrosion resistance of cylinder, the glass fiber composite material is to guarantee the aluminum alloy being adapted to higher working because of large prestress, and the carbon fiber composite material is to improve the strength and modulus of the cylinder and it is also the main load-bearing material between the three-layer materials.

The introduction of carbon fiber into the new generation cylinder improves the failure stress of the cylinder, but it also brings new problem to the reliability evaluation of the cylinder. The cylinder wound by T700 carbon fiber exhibits long life and high reliability in high-speed rotation mode, and the sufficient data cannot be obtained by the traditional

life tests. Therefore, the accelerated test must be introduced, and the reliability index in the normal stress could be extrapolated by the statistical analysis using the high stress level data [7]. The maximum likelihood estimation method [8, 9] is very suitable for the censored data analysis, but this method only has good properties for the large sample. And it needs to iterate for the transcendental equations; sometimes the computation is difficulties and not convergence. The integral best linear unbiased estimation method [10, 11] solves problems by regression analysis based on linear transformation acceleration model. The information between different stresses is used comprehensively, and the estimation accuracy can be improved. But the evaluation accuracy is still unable to meet the actual engineering requirement of the cylinder structure with great life dispersion.

This study found that the failure mode of the cylinder wound by T700 carbon fiber was carbon fiber breakage in the working mode with high-speed rotation. Therefore, there would be some relationship between the rupture life of fiber carbon and the cylinder. In this study, we analyzed the

mechanical properties of the cylinder composite material and obtained the ultimate failure stress by mixing rules, which were verified by the static pressure burst test method. Then we designed accelerated life tests on the carbon fiber and the cylinder. According to the test results, we proposed the integral best unbiased estimate method for the cylinder life prediction. The evaluation accuracy was greatly improved by comprehensive evaluation using the information of T700 carbon fiber based on the test results of the accelerated equivalence and failure mechanisms.

2. Mechanical Analysis

2.1. Mechanical Analysis of the Composite Material. The new generation cylinder consists of aluminium alloy, glass fiber, and T700 carbon fiber, and its structure is illustrated in Figure 1.

The main role of the aluminium alloy is to improve the axial modulus and anticorrosion of the cylinder. The glass fiber is to impose prestress to the aluminium alloy according to winding, and so it could improve the maximum capacity. The carbon fiber is the main bearing materials and for their high strength and modulus the ultimate failure stress of cylinder is greatly improved. The mechanical properties of the glass fiber and the carbon fiber can be obtained by mixing rules according to tensile strength, modulus, and the volume content of each fiber. Thus, the overall mechanical properties of the cylinder could also be estimated by the mixing rule basing on the material properties and structures.

According to the property test of T700 carbon fiber, the tensile strength is 4900 Mpa, the modulus is 230 GPa, and the strain is approximately 2%. Also, the matrix strength of the composite material is 85 MPa, the modulus is 2.8 Gpa, and the strain is 4%. The mix rule is

$$X_t = \sigma_f V_f + \sigma_m (1 - V_f), \quad (1)$$

where the X_t is tensile strength of composite, σ_f is the tensile strength of fiber, σ_m is the tensile strength of matrix, and V_f is the fiber volume. Therefore, for the fiber volume of composite material used in this study is 72%, the tensile strength of this composite would be calculated as 3551.8 MPa.

For the glass fiber, the tensile strength is 3400 MPa, the modulus is 91 GPa, and the strain is approximately 3.7%. And the matrix is the same with the T700 carbon fiber reinforced composite. While the percentage of fiber volume is 76%, according to the mix rule, the tensile strength of this glass fiber reinforced composite would be calculated as 2604.4.

The lining of the cylinder is aluminium alloy, its elastic modulus is 70 GPa, yield strength is 610 Mpa, tensile strength is 640 Mpa, and strain is greater than 4% [12].

2.2. Failure Stress Analysis of the Cylinder. The tensile modulus of the glass fiber and the aluminium alloy is significantly lower than the outer carbon fiber composite material by the previous analysis. And according to the thickness of each laminate listed in Table 1, it is obvious that the carbon fiber is the main load-bearing material in the entire cylinder. When the outer T700 carbon fiber reinforced composite

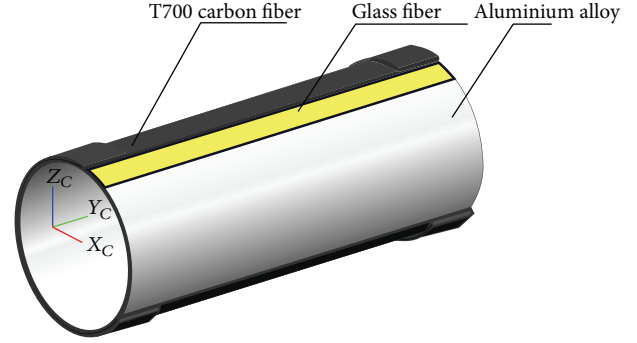


FIGURE 1: Structure of the cylinder.

is destructed, the glass fiber and aluminum alloy would be instantaneously destroyed due to the large load. The stress-strain curves of glass fiber and carbon fiber reinforced composite materials presented to be linear like the tensile stress-strain curves of glass fiber and carbon fiber that are shown in Figures 2 and 3.

The bearing stress of glass fiber is 380 MPa that is the reverse stress to impose on the aluminum alloy; therefore, its bearing stress is 1777 MPa when the conditions are the same with the outer carbon fiber. The tensile strength of aluminum alloy is 640 MPa, we consider that it imposed the reverse prestress of 380 MPa, its bearing stress is 260 MPa when the breaking elongation is 2%, and its thickness is 1.2 mm. The thickness of glass fiber and the carbon fiber is 0.85 mm and 1.5 mm, respectively. Therefore, according to the mixing rule, the ultimate failure stress of the cylinder is theoretical as

$$\sigma = \frac{\sigma_l \times t_l + \sigma_g \times t_g + \sigma_f \times t_f}{t_l + t_g + t_f} = 2004 \text{ MPa}. \quad (2)$$

The strip tensile test method [13] for ultimate failure stress of the cylinder cannot meet the requirements of test accuracy with a few samples. The NOL [13] ring stretching method is sensitive to the boundary effects and sample processing is very difficult. Therefore, we chose the blasting static pressure method [14] for the ultimate failure stress testing which dealt with the data as a whole and thus could reflect the mechanical properties better.

The test samples were produced according to the national standard GB/T15560, and the processing technical, raw materials were the same with the cylinder. Figure 4 shows the size of this test sample. As shown, two ends of the cylinder were strengthened by carbon fiber layers of 30 mm width. Table 2 shows the parameters of this static pressure burst test. Table 3 shows the test result.

It can be seen from Table 3 that the mean of the ultimate test failure stress is 2067.6 MPa, which is slightly higher than the theoretical prediction of 2004 MPa. It may be the reason that the overall performance of the cylinder material would be slightly higher than fiber samples. The parameters used for theoretical prediction were the mean value of the tensile test results of fiber sample, and thus its volatility is relatively large. Another main reason may be that the length of the test sample in the static pressure burst test was required to be

TABLE 1: Geometry parameters and properties of each laminate.

	Aluminium alloy	Glass fiber	Carbon fiber
Thickness (mm)	1.20	0.85	1.50
Modulus (GPa)	71	70, 20 (90°)	163, 8 (90°)
Density (g/cm ³)	2.8	2.15	1.58

TABLE 2: Parameters of the static pressure burst test.

Aluminium alloy (mm)	Process conditions		Resin formula	Curing system
	Glass fiber	Carbon fiber		
Thickness: 1.2 Length: 350	5 layers	10 layers	Proprietary formula	75°C/4 h + 80°C/12 h

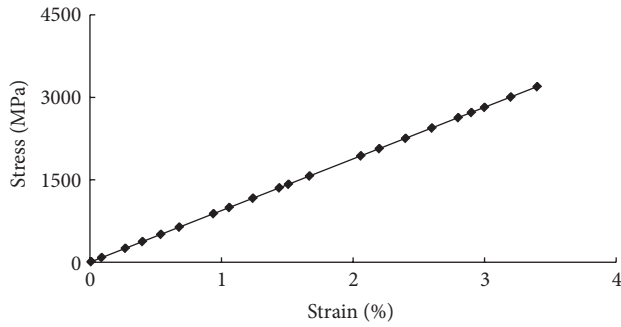


FIGURE 2: Tensile stress-strain curves of the glass fiber.

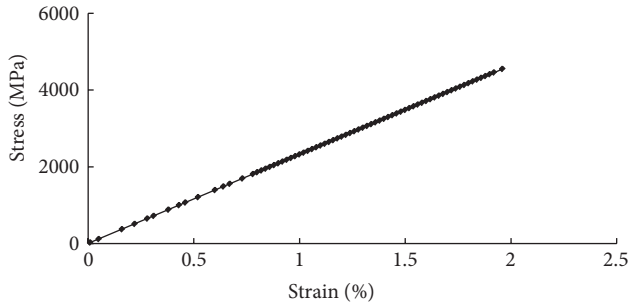


FIGURE 3: Tensile stress-strain curves of the carbon fiber.

TABLE 3: Test result of the static pressure burst test.

Number	σ_b (MPa)	ϵ_b (%)	E (GPa)
1	2032.4	1.88	112.5
2	2087.6	1.87	113.3
3	2060.9	1.94	109.9
4	2180.9	2.02	112.3
5	2049.0	1.85	112.2
6	2110.5	1.93	112.3
7	1932.4	1.84	108.2
8	2086.7	1.91	112.6
Mean	2067.6	1.91	111.7
Dispersion	3.44%	3.08%	1.43%

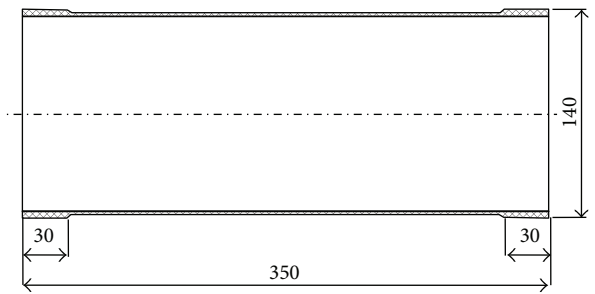


FIGURE 4: Size of the static pressure burst test.

at least 5 times greater than the diameter in test standard of GB/T15560. But this long diameter ratio of our test sample is only 2.7. As the shorter sample is sensitive to the effects of the end portion in the testing process, this may be the main reason that the test results are slightly higher than the prediction result. In all, the test results of the static pressure burst test made a good agreement with the prediction result, and it is feasible to verify the overall performance of the cylinder. This test result would be taken as the important reference for the constant stress accelerated life test in the following research.

3. Accelerated Life Test

3.1. Experiment Preparation. In the working conditions, the bearing stress of cylinder is about 913.8 Mpa, which is equivalent to 45.5% of the ultimate failure stress. We calculated

the stress level of the cylinder by the finite element method, and the result shows that the bearing stress of the lining aluminum alloy is 240 MPa, the bearing stress of the glass fiber is 1060 Mpa, and the bearing of carbon fiber is 1350 MPa. The related parameters are shown in Table 1.

The cylinder used in the accelerated life test is the same as that used in the static pressure burst test, as shown in Figure 5. Then, the cylinder is filled with hydraulic oil up to certain pressure and maintains this pressure for a long time so that the cylinder bears a uniform inner pressure in every direction. The test device is placed in one oven where working temperature could be maintained. The pressure can be tested by the pressure sensor. If the pressure of the cylinder drops significantly, the cylinder was considered to be failure and the failure time is automatically recorded.

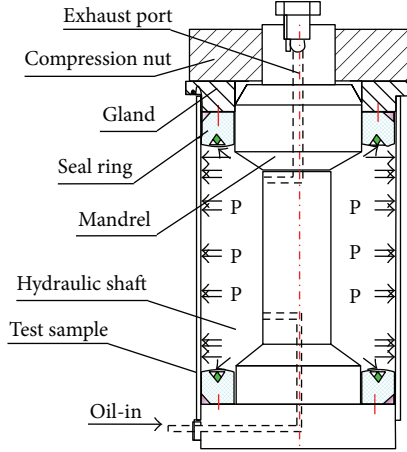


FIGURE 5: Diagram of the reliability test unit of the cylinder.

3.2. The Accelerated Test Plan of the Cylinder. We know the ultimate failure stress is 2067.6 Mpa given by the static pressure burst test and the working stress is 913.8 Mpa, which is equivalent to 45.5% of the ultimate failure stress of the cylinder. The stress-strain curve is close to linear in the scope of the ultimate failure stress of the cylinder.

According to GB 2689.1-81, we divided the cylinders into five groups for constant stress accelerated life test. And we set the minimum stress level to be 1315 MPa (almost 63.6% of the ultimate failure stress) and the maximum stress level to be 1861 MPa (almost 90% of the ultimate failure stress). Also, other stress levels were set to be 72.7%, 80%, and 85% of the ultimate failure stress, respectively. According to the test standard of GB 2689.1-81, this test level setting could ensure that the failure mechanism of cylinders was the same. The working temperature of the cylinder will not exceed 40°C, so the test temperature is controlled at $40 \pm 2^\circ\text{C}$.

4. Results and Discussion

4.1. The Method on Rupture Life Evaluation of the Cylinder. We assume that there are n_j samples prepared for type-I censored test in the v_j ($j = 1, 2, \dots, s$) stress level and the censored time is ξ_j^* . There are q_j ($1 \leq q_j \leq n_j$) failures and the censored data is $\xi_{j1} \leq \dots \leq \xi_{jq_j}$.

Hypothesis 1. The product life follows Weibull distribution $W(m_j, \eta_j)$ in the v_j stress level.

Hypothesis 2. The failure mechanisms of the carbon fiber and the cylinder are the same in each stress level.

Hypothesis 3. The relationship between characteristic life η_j and stress level v_j follows the inverse power law model: $\eta_j = Av_j^{-c}$, $j = 1, 2, \dots, s$. And A, c are parameters that should be estimated.

The linear expression can be obtained by logarithmic transformation on the accelerated model in Hypothesis 3:

$$\ln \eta_j = a + bx_j. \quad (3)$$

Then the logarithmic life follows the extreme value distribution and the relationship between the logarithmic life and the logarithmic stress can be written as

$$y_j = a + bx_j + \varepsilon_{jk}, \quad \varepsilon_{jk} \sim EV(0, \sigma), \quad (4)$$

$$(j = 1, 2, \dots, s; k = 1, 2, \dots, q_j + 1),$$

where $y_j = \ln \eta_j$, $x_j = \ln v_j$, $a = \ln A$, and $b = -c$. Parameter a reflects the characteristic of test product; parameter b reflects the acceleration characteristic of the test; σ is the scale parameter of the extreme value distribution and the measure parameter for the consistency of the failure mechanism.

In the condition of Hypothesis 1, type-I censored data $y_{j1} \leq \dots \leq y_{jq_j}$ can be taken as the value of the former q_j order statistics $Y_{j1} \leq \dots \leq Y_{jq_j}$ for the extreme value distribution with size n_j . $y_{j(q_j+1)} = y_j^*$ can be taken as the value of the q_j th interval statistics $Y_{j(q_j+1)}$ with the same sample.

From literature [9, 10], we can obtain the estimations of a , b , and σ by partial derivative for Q

$$Q = \sum_{j=1}^s \sum_{k,l=1}^{q_j+1} (y_{jk} - a - bx_j - \sigma u_{jk}) \times g_{jkl} (y_{jl} - a - bx_j - \sigma u_{jl}). \quad (5)$$

The estimations of a , b , and σ are

$$\begin{aligned} \hat{a} &= \bar{y} - \hat{b}\bar{x} - \hat{\sigma}\bar{u}, \\ \hat{b} &= \frac{L_{22}L_{1y} - L_{12}L_{2y}}{L_{11}L_{22} - L_{12}^2}, \\ \hat{\sigma} &= \frac{L_{11}L_{2y} - L_{12}L_{1y}}{L_{11}L_{22} - L_{12}^2}, \end{aligned} \quad (6)$$

where

$$\bar{y} = \frac{1}{n^*} \sum_{j=1}^s \sum_{k,l=1}^{q_j+1} g_{jkl} y_{jk}, \quad \bar{u} = \frac{1}{n^*} \sum_{j=1}^s \sum_{k,l=1}^{q_j+1} g_{jkl} u_{jk},$$

$$\bar{x} = \frac{1}{n^*} \sum_{j=1}^s \sum_{k,l=1}^{q_j+1} g_{jkl} x_j, \quad n^* = \sum_{j=1}^s \sum_{k,l=1}^{q_j+1} g_{jkl},$$

$$L_{1y} = \sum_{j=1}^s \sum_{k,l=1}^{q_j+1} g_{jkl} (x_j - \bar{x}) (y_{jk} - \bar{y}),$$

$$L_{2y} = \sum_{j=1}^s \sum_{k,l=1}^{q_j+1} g_{jkl} (u_{jk} - \bar{u}) (y_{jl} - \bar{y}),$$

$$L_{11} = \sum_{j=1}^s \sum_{k,l=1}^{q_j+1} g_{jkl} (x_j - \bar{x})^2,$$

$$\begin{aligned}
L_{12} &= \sum_{j=1}^s \sum_{k,l=1}^{q_j+1} g_{jkl} (x_j - \bar{x}) (u_{jk} - \bar{u}), \\
L_{22} &= \sum_{j=1}^s \sum_{k,l=1}^{q_j+1} g_{jkl} (u_{jk} - \bar{u}) (u_{jl} - \bar{u}).
\end{aligned} \quad (7)$$

And the covariance matrix of a, b , and σ is

$$\text{cov}(\hat{a}, \hat{b}, \hat{\sigma}) = \sigma^2 C,$$

$$C = \begin{bmatrix} \sum_{j,k,l} g_{jkl} & \sum_{j,k,l} g_{jkl} x_j & \sum_{j,k,l} g_{jkl} u_{jk} \\ \sum_{j,k,l} g_{jkl} x_j & \sum_{j,k,l} g_{jkl} x_j^2 & \sum_{j,k,l} g_{jkl} x_j u_{jk} \\ \sum_{j,k,l} g_{jkl} u_{jk} & \sum_{j,k,l} g_{jkl} x_j u_{jk} & \sum_{j,k,l} g_{jkl} u_{jk} u_{jl} \end{bmatrix}^{-1}, \quad (8)$$

where $G = (g_{jkl})_{(q_j+1) \times (q_j+1)} = V^{-1} = (v_{jkl})_{(q_j+1) \times (q_j+1)}$, u_{jk} ($k=1, 2, \dots, q_j$) is the mean of the k th order statistic for the standard extreme value distribution with size n_j , v_{jkl} ($k, l=1, 2, \dots, q_j$) is the covariance of the k th and l th order statistic for the standard extreme value distribution with size n_j , $u_{j(q_j+1)}$ is the mean of the $(q_j + 1)$ th order statistic for the standard extreme value distribution with size $n_j + 1$, and $v_{jk(q_j+1)} = v_{j(q_j+1)k}$ ($k=1, 2, \dots, q_j + 1$) is the covariance of the k th and $(q_j + 1)$ th order statistic for the standard extreme value distribution with size $n_j + 1$. These values could be all obtained by formula or table lookup [15].

The reliability rupture life with reliability of R and its upper and lower limits with confidence level γ could be calculated as follows:

$$\begin{aligned}
y_R &= \hat{a} + \hat{b}x + \hat{\sigma} \ln \ln \frac{1}{R}, \\
y_{RU} &= \hat{a} + \hat{b}x \\
&\quad + \frac{\hat{\sigma}}{1 - u_{\gamma}^2 c_{33}} \left[\ln \ln \frac{1}{R} + u_{\gamma}^2 (c_{13} + c_{23}x) + u_{\gamma} \sqrt{\omega_R} \right], \quad (9) \\
y_{RL} &= \hat{a} + \hat{b}x \\
&\quad + \frac{\hat{\sigma}}{1 - u_{\gamma}^2 c_{33}} \left[\ln \ln \frac{1}{R} + u_{\gamma}^2 (c_{13} + c_{23}x) - u_{\gamma} \sqrt{\omega_R} \right],
\end{aligned}$$

where c_{ij} are elements of the matrix C , $\omega_R = \omega + c_{33}(\ln \ln(1/R))^2 + 2(c_{13} + c_{23}x) \ln \ln(1/R)$, and $\omega = u_{\gamma}^2 (c_{13} + c_{23}x)^2 + (1 - c_{33}u_{\gamma}^2)(c_{11} + 2c_{12}x + c_{22}x^2)$.

The Failure Mechanism Consistency Analysis. This analysis focused on the consistency of failure mechanism and accelerated model parameter between the carbon fiber and cylinder in the accelerated life test. Denote the model parameters of the carbon fiber and the cylinder as a_1, b_1 , and σ_1 and a_2, b_2 , and σ_2 , respectively. We assume the following.

- (1) The distribution parameters σ_1, σ_2 are two independent normal populations. If the failure mechanism of the carbon fiber is the same with the cylinder, the mean and variance of the two normal populations are the same [16, 17].
- (2) Parameters of a_1 and a_2 reflect the life characteristic of carbon fiber and cylinder, and then a_1 and a_2 have no relation.
- (3) The model parameters b_1, b_2 are two independent normal populations. If the acceleration of the carbon fiber is the same with the cylinder, the mean and variance of the two normal populations are the same.

Based on the above assumptions, $(\hat{b}_1, \hat{\sigma}_1)$ and $(\hat{b}_2, \hat{\sigma}_2)$ can be taken as two bivariate normal populations. We can judge the consistency of the mean vector and covariance matrix of the two bivariate normal populations by hypothesis test.

(1) The Consistency Judgment of the Mean Vector. The two independent normal populations are denoted by $(\hat{b}_1, \hat{\sigma}_1) \sim N_2(\mu_1, \Sigma_1)$ and $(\hat{b}_2, \hat{\sigma}_2) \sim N_2(\mu_2, \Sigma_2)$. We sample $n, m > 2$ specimens from them, respectively, and denote the mean vectors by \bar{X}, \bar{Y} , respectively, and the variance matrix by S_i ($i=1, 2$). The hypothesis is

$$H_0: \mu_1 = \mu_2 \quad H_1: \mu_1 \neq \mu_2. \quad (10)$$

When $\Sigma_1 = \Sigma_2$ and they were unknown, the test statistic

$$T^2 = \frac{nm}{n+m} (\bar{X} - \bar{Y})^T S^{-1} (\bar{X} - \bar{Y}), \quad (11)$$

where

$$S = \frac{(n-1)S_1 + (m-1)S_2}{n+m-2}. \quad (12)$$

And $F = (((n+m-2)-1)/2(n+m-2))T^2 \sim F(2, n+m-3)$.

Then the rejection region with the significance level α is

$$\{F > F_{1-\alpha}(2, n+m-3)\}. \quad (13)$$

(2) The Consistency Judgment of the Variance Matrix. The hypothesis is

$$H_0: \Sigma_1 = \Sigma_2 \quad H_1: \Sigma_1 \neq \Sigma_2. \quad (14)$$

The amendatory likelihood ratio statistic is

$$\lambda^* = \frac{(n+m-2)^{(n+m-2)} |S_1|^{(n-1)/2} |S_2|^{(m-1)/2}}{(n-1)^{(n-1)/2} (m-1)^{(m-1)/2} |S_1 + S_2|^{(n+m-2)/2}}. \quad (15)$$

Then,

$$-2 \ln \lambda^* \sim \chi^2 \left(\frac{f}{1-d} \right), \quad (16)$$

where

$$f = \frac{1}{2}p(p+1)(k-1),$$

$$d = \frac{2p^2 + 3p - 1}{6(p+1)(k-1)} \left(\frac{1}{n-1} + \frac{1}{m-1} - \frac{1}{n+m-k} \right) \quad (17)$$

and $k = p = 2$.

Then the rejection region with the significance level α is

$$\left\{ \chi^2 < \chi_\alpha^2 \left(\frac{f}{1-d} \right) \right\}. \quad (18)$$

The information fusion method

Based on the result of the integral best linear unbiased estimation and the consistency analysis of failure mechanism, we proposed an information fusion method for the covariance matrixes of the T700 carbon fiber and the cylinder. The fusion process can be accomplished by the two steps: firstly, fusing the information only related to parameters b and σ in the covariance matrix and then, secondly, to further improve the evaluation accuracy of the covariance matrix for model parameter of the cylinder, fusing the other information related to b and σ .

Denote the point estimations of T700 carbon fiber and the cylinder by \hat{a}_1, \hat{b}_1 , and $\hat{\sigma}_1$ and \hat{a}_2, \hat{b}_2 , and $\hat{\sigma}_2$, respectively, and their covariance matrix is

$$\text{cov}(\hat{a}_i, \hat{b}_i, \hat{\sigma}_i) = \begin{bmatrix} \text{var}(\hat{a}_i) & \text{cov}(\hat{a}_i, \hat{b}_i) & \text{cov}(\hat{a}_i, \hat{\sigma}_i) \\ \text{cov}(\hat{a}_i, \hat{b}_i) & \text{var}(\hat{b}_i) & \text{cov}(\hat{b}_i, \hat{\sigma}_i) \\ \text{cov}(\hat{a}_i, \hat{\sigma}_i) & \text{cov}(\hat{b}_i, \hat{\sigma}_i) & \text{var}(\hat{\sigma}_i) \end{bmatrix}, \quad (19)$$

$(i = 1, 2).$

Denote the covariance matrix of the bivariate normal distribution of b_1, σ_1 and b_2, σ_2 , respectively, by

$$\hat{V}_i = \begin{bmatrix} \text{var}(\hat{b}_i) & \text{cov}(\hat{b}_i, \hat{\sigma}_i) \\ \text{cov}(\hat{b}_i, \hat{\sigma}_i) & \text{var}(\hat{\sigma}_i) \end{bmatrix}, \quad (i = 1, 2). \quad (20)$$

The elements of the above matrixes are one part of (19).

The first step is fusing the information only related to parameters b and σ in the covariance matrix.

If the covariance matrixes V_1 and V_2 are certified to be the same by the consistency analysis of the bivariate normal distribution (b_1, σ_1) and (b_2, σ_2) , the unbiased estimation of the covariance matrix of the bivariate normal distribution can be obtained by the following equation:

$$\hat{V} = \frac{(n_1 - 1)\hat{V}_1 + (n_2 - 1)\hat{V}_2}{n_1 + n_2 - 2}. \quad (21)$$

Compared to the small ratio of failure and high censored time of the cylinder life test, the data and failures of the carbon fiber are much greater and thus the evaluation result is more accurate. Therefore, when the matrix \hat{V}_2 is replaced by \hat{V} with fusing the information of parameters b and σ according to the above method, the prediction result of the cylinder is more

accurate. The covariance matrix of b and σ based on fusion could be written as

$$\hat{V} = \begin{bmatrix} \text{var}(\hat{b}_{12}) & \text{cov}(\hat{b}_{12}, \hat{\sigma}_{12}) \\ \text{cov}(\hat{b}_{12}, \hat{\sigma}_{12}) & \text{var}(\hat{\sigma}_{12}) \end{bmatrix}. \quad (22)$$

The covariance matrix $\text{cov}(\hat{a}_2, \hat{b}_2, \hat{\sigma}_2)$ for the cylinder with bottom right four elements replaced by \hat{V} could be written as

$$\text{cov}(\hat{a}_2, \hat{b}_2, \hat{\sigma}_2)' = \begin{bmatrix} \text{var}(\hat{a}_2) & \text{cov}(\hat{a}_2, \hat{b}_2) & \text{cov}(\hat{a}_2, \hat{\sigma}_2) \\ \text{cov}(\hat{a}_2, \hat{b}_2) & \text{var}(\hat{b}_{12}) & \text{cov}(\hat{b}_{12}, \hat{\sigma}_{12}) \\ \text{cov}(\hat{a}_2, \hat{\sigma}_2) & \text{cov}(\hat{b}_{12}, \hat{\sigma}_{12}) & \text{var}(\hat{\sigma}_{12}) \end{bmatrix}. \quad (23)$$

The second step is fusing the other elements related to b, σ of the covariance matrix.

Based on the same correlation coefficient between the parameters, the value of $\text{cov}(\hat{a}_2, \hat{b}_{12})$, $\text{cov}(\hat{a}_2, \hat{\sigma}_{12})$ with fusing the information of the T700 carbon fiber can be calculated as

$$\text{cov}(\hat{a}_2, \hat{b}_{12}) = \sqrt{\frac{\text{var}(\hat{b}_{12})}{\text{var}(\hat{b}_2)}} \cdot \text{cov}(\hat{a}_2, \hat{b}_2), \quad (24)$$

$$\text{cov}(\hat{a}_2, \hat{\sigma}_{12}) = \sqrt{\frac{\text{var}(\hat{\sigma}_{12})}{\text{var}(\hat{\sigma}_2)}} \cdot \text{cov}(\hat{a}_2, \hat{\sigma}_2).$$

According to the above two steps, the covariance matrix $\text{cov}(\hat{a}_2, \hat{b}_{12}, \hat{\sigma}_{12})$ can be written as

$$\text{cov}(\hat{a}_2, \hat{b}_{12}, \hat{\sigma}_{12}) = \begin{bmatrix} \text{var}(\hat{a}_2) & \text{cov}(\hat{a}_2, \hat{b}_{12}) & \text{cov}(\hat{a}_2, \hat{\sigma}_{12}) \\ \text{cov}(\hat{a}_2, \hat{b}_{12}) & \text{var}(\hat{b}_{12}) & \text{cov}(\hat{b}_{12}, \hat{\sigma}_{12}) \\ \text{cov}(\hat{a}_2, \hat{\sigma}_{12}) & \text{cov}(\hat{b}_{12}, \hat{\sigma}_{12}) & \text{var}(\hat{\sigma}_{12}) \end{bmatrix}. \quad (25)$$

Comparing with (25) and (19) ($i = 2$), it can be found that the elements of parameter covariance matrix of the cylinder have changed in addition to the variance $\text{var}(\hat{a}_2)$ by fusing the carbon fiber test information, thus making the evaluation result more reasonable. It should be noted that the parameter covariance matrix can be obtained by the integrated best linear unbiased estimation as follows:

$$\text{cov}(\hat{a}, \hat{b}, \hat{\sigma}) = \sigma^2 C. \quad (26)$$

In the calculation of the upper and lower limits for the reliability rupture life, the matrix C would be used. Therefore, in fusion process of the covariance matrix with T700 carbon fiber information and cylinder information, we can introduce the matrix C directly in the above method to make the calculation easier.

4.2. Examples. To verify the design level of the rupture life of a certain type of cylinder, a unit made accelerated life tests for T700 carbon fiber composite material and the cylinder

TABLE 4: Accelerated life test information for T700 carbon fiber and the cylinder.

Subjects	Stress level				
	1700	1800	1900	—	—
T700 carbon fiber (N)	1700	1800	1900	—	—
Cylinder (the percentage of limit load %)	63.6	72.7	80	85	90

structure, respectively. The test temperature is 40°C, and the test load conditions are shown in Table 4.

The diagram of rupture life data for T700 carbon fiber and the cylinder structure from the test is as in Figures 6 and 7.

(1) *The Result of the Integral Best Unbiased Estimation.* The results of model parameters and the matrix C obtained by the integrated best linear unbiased estimation are shown in Table 5.

(2) *The Test of Mean Vector and Covariance Matrix Equal to $(\hat{b}, \hat{\sigma})$ of the Carbon Fiber and the Cylinder.* We consider parameters $(\hat{b}, \hat{\sigma})$ as a bivariate normal population and test whether the mean vectors and covariance matrixes of $(\hat{b}, \hat{\sigma})$ for the carbon fiber and the cylinder are equal or not, and the results are shown in Table 6.

From Table 6, the observed values of the test statistic are

$$F = 8.09725 < F_{0.975}(2, 5) = 8.43, \quad (27)$$

$$\chi^2 = 1.9468 > \chi_{0.025}^2(5).$$

Then, we can receive the null hypothesis. The mean vectors and the covariance matrixes of $(\hat{b}, \hat{\sigma})$ for the carbon fiber and the cylinder are equal.

(3) *The Information Fusion of the T700 Carbon Fiber and the Cylinder.* By using the method in this paper, the matrix information of carbon fiber in Table 5 can be fused into the cylinder and the upper and lower limits of the reliability rupture life at confidence level $\gamma = 0.95$ can be calculated. The comparison results are shown in Table 7.

From Table 7, when the reliability is 0.9, the evaluation accuracy of the reliability life of the cylinder is increased by 35%.

The curves of upper and lower limits of the logarithmic reliability rupture life y_R changed with the reliability R are shown in Figure 7.

Figure 8 shows that the upper and lower limits of the reliability rupture life will be more accurate with the reliability changed after fusion of the information of T700 carbon fiber and the interval length is much shorter.

5. Conclusion

- (1) Since the carbon fiber bears the main load at work, the acceleration and failure mechanism of T700 carbon fiber and the cylinder are the same. And it can be proved by the structure analysis and the statistic test of the test data.

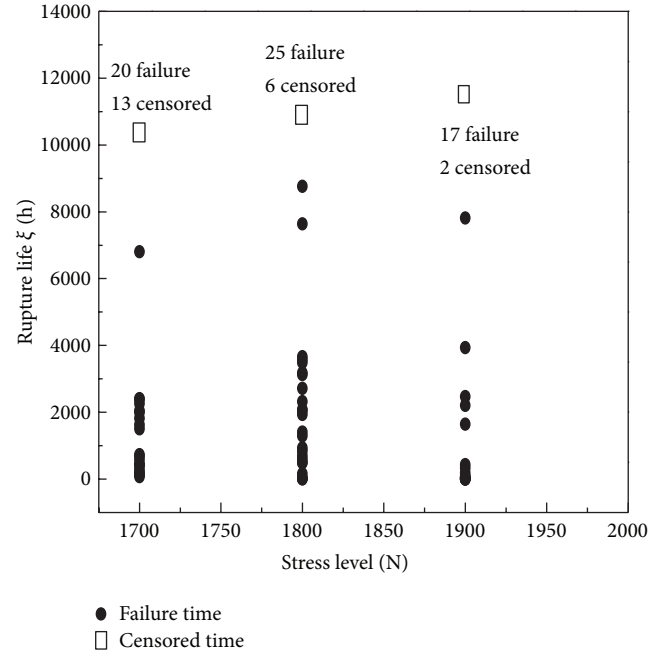


FIGURE 6: Rupture life of T700 carbon fiber.

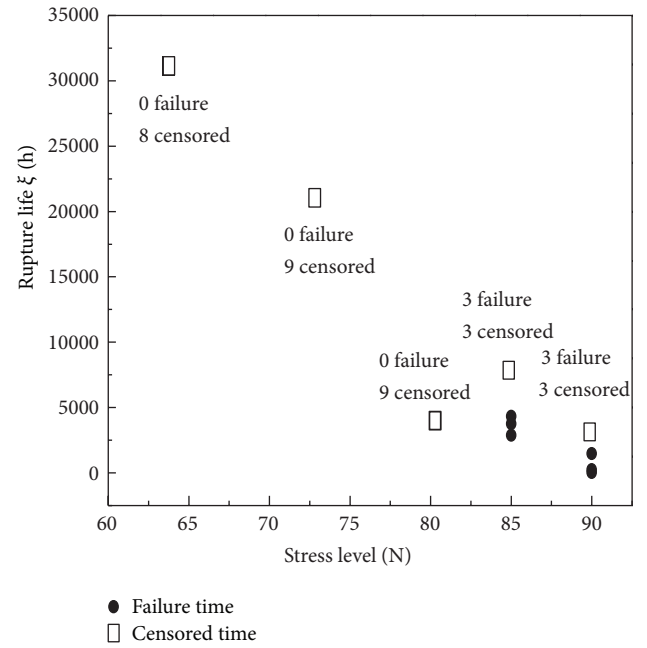


FIGURE 7: Ruptures life of the cylinder.

- (2) When the acceleration and failure mechanism are the same, the evaluation accuracy of the reliability life for the cylinder can be improved by fusion of the information of the carbon fiber.
- (3) The method in this paper is based on Weibull distribution and the inverse power law model for structured products. It can be applied to other location-scale family distribution and acceleration models.

TABLE 5: Contrast result between T700 carbon fiber and the cylinder with the integrated best linear unbiased estimation.

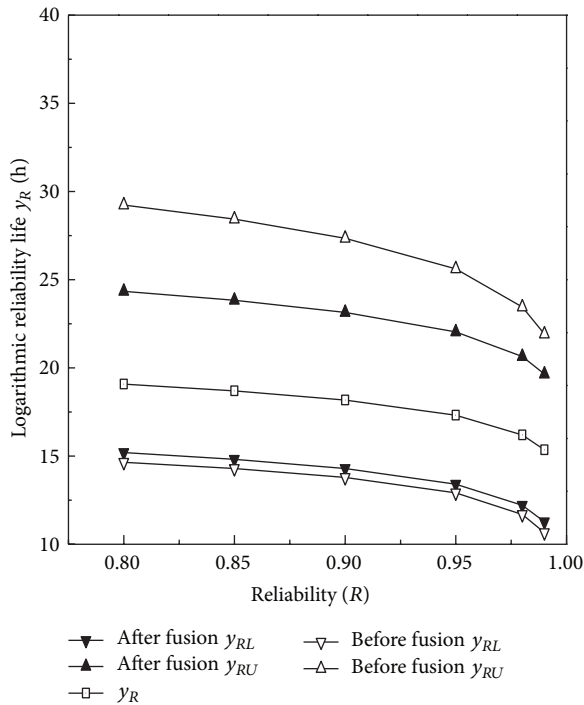
Result	T700 carbon fiber	Cylinder
$(\hat{a}, \hat{b}, \hat{\sigma})$	(157.177, -19.872, 2.32)	(6.39, -18.41, 1.20)
C	$\begin{bmatrix} 495.06 & -66.08 & 0.46 \\ -66.08 & 8.82 & -0.06 \\ 0.46 & -0.06 & 0.012 \end{bmatrix}$	$\begin{bmatrix} 0.53 & 2.70 & -0.06 \\ 2.70 & 21.49 & -1.05 \\ -0.06 & -1.05 & 0.13 \end{bmatrix}$

TABLE 6: The test results of mean vector and covariance matrix for a bivariate normal population $(\hat{b}, \hat{\sigma})$ of carbon fiber and cylinder.

Null hypothesis	Rejection region	Observation value	Critical value $\alpha = 0.025$
$\mu_1 = \mu_2$	$\{F > F_{1-\alpha}(2, n + m - 3)\}$	8.09725	8.43
$\Sigma_1 = \Sigma_2$	$\{\chi^2 < \chi_{\alpha}^2(f/(1-d))\}$	1.9468	0.831

TABLE 7: Contrast result of cylinder after fusion information of T700 carbon fiber.

Result	The original data	Fusion of the information of T700
C	$\begin{bmatrix} 0.53 & 2.70 & -0.06 \\ 2.70 & 21.49 & -1.05 \\ -0.06 & -1.05 & 0.13 \end{bmatrix}$	$\begin{bmatrix} 0.53 & 2.08 & -0.037 \\ 2.08 & 12.76 & -0.37 \\ -0.037 & -0.37 & 0.049 \end{bmatrix}$
The interval estimation of y_R	[13.79, 27.35]	[14.29, 23.15]
Interval length	13.56	8.86

FIGURE 8: Change curves for y_R and upper and lower limits.

Conflict of Interests

The authors declare that there is no conflict of interests regarding the publication of this paper.

Acknowledgments

The work described in this paper was supported by the National Natural Science Foundation of China (Grants nos. 61104133 and 61473014). The authors fully appreciate the financial support. The authors would like to thank the reviewers and the editor for many suggestions that helped improve this paper.

References

- [1] D. F. Li, H. J. Wang, and F. He, "Structure and properties of T300 and T700 carbon fiber," *New Carbon Materials*, vol. 22, no. 1, pp. 59–64, 2007.
- [2] G. T. Zhang, W. G. Chen, and B. Yang, "Testing research on mechanical properties of T700 carbon fiber/epoxy composites," *Fiber Composites*, vol. 2, pp. 49–52, 2009.
- [3] Y. X. Zhou, M. A. Baseer, H. Mahfuz, and S. Jeelani, "Statistical analysis on the fatigue strength distribution of T700 carbon fiber," *Composites Science and Technology*, vol. 66, no. 13, pp. 2100–2106, 2006.
- [4] Z. G. Yu, S. C. Yang, and B. F. Song, "Comparison of wet and hot aging resistance of T700 and T300 carbon fiber strengthened epoxy resin composites," *Materials for Mechanical Engineering*, vol. 33, no. 6, pp. 48–51, 2009.
- [5] X. Gu and X. Xu, "Numerical simulation of damage in fiber reinforced composite laminates under high velocity impact," *Acta Materiae Compositae Sinica*, vol. 29, no. 1, pp. 150–161, 2012.
- [6] J. Liu, Y. X. Bai, Y. L. Tian, X. Y. Huang, C. H. Wang, and J. Y. Liang, "Effect of the process of electrochemical modification on the surface structure and properties of PAN-based carbon fibers," *Acta Materiae Compositae Sinica*, vol. 29, no. 2, pp. 16–25, 2012.

- [7] W. Yurkosky, R. E. Schafer, and J. M. Finkelstein, "Accelerated testing technology," Tech. Rep. NO.RADC-TR-67-420, 1-2, 1967.
- [8] J. S. Zhao, G. M. Zhuang, and Z. G. Wang, "The introduction of the maximum likelihood estimation method," *Journal of Changchun University of Science and Technology*, vol. 5, no. 6, pp. 53–54, 2010.
- [9] H.-M. Fu and X.-R. Yue, "Regression analysis method for type-I censored data," *Journal of Aerospace Power*, vol. 25, no. 1, pp. 142–147, 2010.
- [10] X. Ma, T. Wang, J. Wang, and Z. Liu, "Method on accelerated rupture life evaluation for composite material based on type-II censored data," *Advanced Materials Research*, vol. 284–286, pp. 439–443, 2011.
- [11] A. J. Watkins, "Review: Likelihood method for fitting Weibull log-linear models to accelerated life-test data," *IEEE Transactions on Reliability*, vol. 43, no. 3, pp. 361–365, 1994.
- [12] G. Q. Jiao and P. R. Jia, *Mechanics of Composites*, Northwestern Polytechnical University Press, Xian, China, 2008.
- [13] L. F. Gui and Y. T. Cao, *Handbook of Mechanical Engineering Materials Testing*, Liaoning Science and Technology Press, Liaoning, China, 2001.
- [14] J. H. Sun and Y. H. Wang, "Standard test method for short-time hydraulic failure and resistance to constant internal pressure of the plastics pipes for the transport of fluids," GB/T15560, China, 1995.
- [15] P. S. B. Chan, "Order statistics from extreme value distribution: I-table of mean, variances and covariances," *Communications in Statistics-Simulation and Computation*, vol. 21, no. 4, pp. 1199–1217, 1992.
- [16] Y. Q. Zhou, Z. X. Weng, and X. T. Ye, "Study on accelerated factor and condition for constant failure mechanism (I)—the case for lifetime is a random variable," *Journal of Systems Engineering and Electronics*, vol. 1, pp. 55–67, 1996.
- [17] Z. L. Sun, "A condition for constant failure mechanism," *Electronic Product Reliability and Environmental Testing*, vol. 26, no. 4, pp. 6–8, 2008.

Research Article

Optimal Harvesting Policies for a Stochastic Food-Chain System with Markovian Switching

Yanming Ge^{1,2} and Yifan Xu¹

¹ School of Management, Fudan University, Shanghai 200433, China

² College of Information Technology, Shanghai Ocean University, Shanghai 201306, China

Correspondence should be addressed to Yanming Ge; ymge@shou.edu.cn

Received 12 August 2014; Accepted 13 November 2014

Academic Editor: L. W. Zhang

Copyright © 2015 Y. Ge and Y. Xu. This is an open access article distributed under the Creative Commons Attribution License, which permits unrestricted use, distribution, and reproduction in any medium, provided the original work is properly cited.

An optimal harvesting problem for a stochastic food-chain system with Markovian switching is investigated in this paper. Firstly, the existence, uniqueness, and positivity of the food-chain system's solution are proved. Secondly, persistent in mean of the system is obtained. Then the optimal harvesting policy is discussed. Finally, the main results are illustrated by several examples.

1. Introduction

Optimal harvesting problem is an important and interesting topic from both biological and mathematical point of view. Since Clark's works [1, 2], one of the most important area-optimal harvesting problems have received a lot of attention and been studied widely. Among these studies, a large number of literatures were focused on deterministic models [3–9], with some on the stochastic versions [10–17], but only a few on the food-chain systems. Furthermore, it is well known that the theory of food chains illustrated the balance of nature and that no animal or plant can exist independently. Motivated by these arguments presented above, we are interested in the optimal harvesting problems on the following stochastic food-chain system:

$$\begin{aligned} dx &= \left[r_1(\xi(t)) - e - a_1 x - \frac{a_2 y}{m_1(\xi(t)) + x} \right] x dt \\ &\quad + \sigma_1(\xi(t)) x dB_1(t), \\ dy &= \left[r_2(\xi(t)) - \frac{b_1 y}{m_1(\xi(t)) + x} - \frac{b_2 z}{m_2(\xi(t)) + y} \right] y dt \\ &\quad + \sigma_2(\xi(t)) y dB_2(t), \end{aligned}$$

$$\begin{aligned} dz &= \left[r_3(\xi(t)) - \frac{cz}{m_2(\xi(t)) + y} \right] z dt \\ &\quad + \sigma_3(\xi(t)) z dB_3(t) \end{aligned} \quad (1)$$

with the initial value (x_0, y_0, z_0) . Where $B_i(t)$, $i = 1, 2, 3$, is a standard Brownian motion and e is the harvesting effort (control parameter), and $x(t)$, $y(t)$, $z(t)$ represent the population densities of three species (resource, consumer, and predator) at time t , respectively. All parameters are positive constants and parametric functions are continuous and positive. $r_i(\cdot)$, $i = 1, 2, 3$, represent the intrinsic growth rate of species x , y , z , respectively; a_1 measures the strength of competition among individuals of species x ; a_2 is the maximum value of the per capita reduction rate of x due to y ; b_1 , b_2 , and c have similar meaning to a_2 ; $m_1(\cdot)$ measures the extent to which the environment provides protection to species x and y ; $m_2(\cdot)$ measures the extent to which the environment provides protection to species y and z ; $\xi(t)$ be a right continuous Markov chain; $\sigma_i(\cdot)$, $i = 1, 2, 3$, represents the intensity of the white noise. This system is the extension of a predator-prey model with modified Leslie-Gower and Holling-type II schemes with stochastic perturbation which was discussed by Ji et al. [18], Song et al. [19], and

Guo et al. [20], and there the factor of Markovian switching is not considered.

In the most literatures [1, 2] the sustainable yield function is used as the harvesting function. Here the harvesting function associated with (1) is

$$F(e) = e \lim_{t \rightarrow \infty} \frac{\int_0^t x(s) ds}{t}. \quad (2)$$

This type of harvesting function is also used by some other papers, such as Wang [21, chapter 4] and Zou and Wang [22] and defined as the time averaging yield function. The optimal harvesting problem considered in this paper is then stated as follows. Find a harvesting effort e^* such that

$$F(e^*) = \sup_{e \geq 0} \{F(e)\}. \quad (3)$$

Based on the aforementioned discussion, obviously, the first and most important duty is to discuss the existence of $\lim_{t \rightarrow \infty} (\int_0^t x(s) ds / t)$ and then the optimal harvesting problem. Therefore, the rest of the paper is organized as follows. In Section 2, we show that system has a global positive solution. In Section 3, we obtain some long time behavior of the solution, especially the property of persistent in mean, which ensures the existence of the time averaging yield function and its explicit expression is given. In Section 4, the optimal harvesting policies are investigated. In Section 5, we illustrate our main results through several numerical examples. Last but not least, conclusions are drawn in Section 6.

On the other hand, for convenience, we give some notations and assumptions in the rest of this section.

Throughout this paper, unless otherwise specified, let $(\Omega, \mathcal{F}, \{\mathcal{F}_t\}_{t \geq 0}, P)$ be a complete probability space with a filtration $\{\mathcal{F}_t\}_{t \geq 0}$ satisfying the usual conditions (i.e., it is increasing and right continuous while \mathcal{F}_0 contains all P-null sets). The standard Brownian motion $B_i(t)$, $i = 1, 2, 3$, is defined on this probability space.

The right continuous Markov chain $\xi(t)$ on this probability space taking values in a finite-state space $S = \{1, 2, \dots, N\}$ with the generator $\gamma = (\gamma_{kl})_{N \times N}$ is given by

$$\begin{aligned} P(\xi(t + \delta) = l \mid \xi(t) = k) \\ = \begin{cases} \gamma_{kl}\delta + o(\delta) & \text{if } l \neq k, \\ 1 + \gamma_{kk}\delta + o(\delta) & \text{if } l = k, \end{cases} \end{aligned} \quad (4)$$

where $\delta > 0$. Here γ_{kl} is the transition rate from k to l and $\gamma_{kl} \geq 0$ if $l \neq k$, while

$$\gamma_{kk} = 1 - \sum_{l \neq k} \gamma_{kl}. \quad (5)$$

We assume that the Markov chain $\xi(\cdot)$ and the Brownian motion $B_i(\cdot)$ are independent of each other, $i = 1, 2, 3$. As a standing hypothesis we also assume in this paper that the Markov chain $\xi(t)$ is irreducible. This is very reasonable as it means that the system will switch from any regime to any other regime. This is equivalent to the condition that, for any

$k, l \in S$, one can find finite numbers $i_1, \dots, i_n \in S$ such that $\gamma_{ki_1} \gamma_{i_1 i_2} \cdots \gamma_{i_n l} > 0$. Under this condition, the Markov chain has a unique stationary distribution $\pi = (\pi_1, \pi_2, \dots, \pi_N) \in R^N$ and $\pi_k > 0$ for any $k \in S$.

In order to obtain some properties of the system, some assumptions are given in the following. These assumptions are conventional; they guarantee that the ecosystem is not collapsed as time lapses.

Assumption 1. Consider $0 < D_1 := \min_{\xi \in S} \{r_1(\xi) - e - 0.5\sigma_1^2(\xi)\}$, $0 < D_i := \min_{\xi \in S} \{r_i(\xi) - 0.5\sigma_i^2(\xi)\} \leq \max_{\xi \in S} \{r_i(\xi) - 0.5\sigma_i^2(\xi)\} := A_i$, $i = 2, 3$.

Assumption 2. $D_2 - b_2(P_3 + \epsilon) > 0$, $D_1 - a_2(P_2 + \epsilon) > 0$, $P_1 > 0$, where $P_3 := (1/c) \sum_{i=1}^N \pi_i(r_3(i) - 0.5\sigma_3^2(i))$, $P_2 := (1/b_1) [\sum_{i=1}^N \pi_i(r_2(i) - 0.5\sigma_2^2(i)) - b_2 P_3]$, $P_1 := (1/a_1) [\sum_{i=1}^N \pi_i(r_1(i) - e - 0.5\sigma_1^2(i)) - a_2 P_2]$, and ϵ is positive and sufficiently small.

Let $\check{m}_i = \max_{\xi \in S} \{m(\xi)\}$, $\widehat{m}_i = \min_{\xi \in S} \{m(\xi)\}$, $i = 1, 2$, and K denotes a float constant in the rest of this paper, which expresses different constants in different positions.

The key method used in this paper is the comparison theorem for stochastic equations. This theorem for stochastic differential equations was developed by Ikeda and Watanabe [23] and has been used by many authors [24–26].

2. Positive and Global Solutions

As the state of the system $(x(t), y(t), z(t))$ is the population density of species in the system at time t , it should be nonnegative. Moreover, in order for a stochastic differential equation to have a unique global (i.e., no explosion in a finite time) solution for any given initial data, the coefficients of the equation are generally required to satisfy the linear growth condition and local Lipschitz condition [25]. However, the coefficients of each equation in system obey neither the linear growth condition nor local Lipschitz continuous. In this section, we show existence and uniqueness of the positive solution.

Lemma 3. For any initial value $x_0 > 0$, $y_0 > 0$, $z_0 > 0$, system has a unique positive local solution $(x(t), y(t), z(t))$ for $t \in [0, \tau_e)$ almost surely (a.s.), where τ_e is the explosion time.

Proof. To begin with, consider the following equations:

$$\begin{aligned} du(t) \\ = \left[b_1(\xi(t)) - a_1 e^{u(t)} - \frac{a_2 e^{v(t)}}{m_1(\xi(t)) + e^{u(t)}} \right] dt \\ + \sigma_1(\xi(t)) dB_1(t), \\ dv(t) \\ = \left[b_2(\xi(t)) - \frac{b_1 e^{v(t)}}{m_1(\xi(t)) + e^{u(t)}} - \frac{b_2 e^{w(t)}}{m_2(\xi(t)) + e^{v(t)}} \right] dt \\ + \sigma_2(\xi(t)) dB_2(t), \end{aligned}$$

$$dw(t) = \left[b_3(\xi(t)) - \frac{ce^{w(t)}}{m_2(\xi(t)) + e^{v(t)}} \right] dt + \sigma_3(\xi(t)) dB_3(t) \quad (6)$$

on $t \geq 0$ with initial value $u(0) = \ln x_0$, $v(0) = \ln y_0$, $w(0) = \ln z_0$, where $b_1(t) = r_1(\xi(t)) - e - 0.5\sigma_1^2(\xi(t))$, $b_i(t) = r_i(\xi(t)) - 0.5\sigma_i^2(\xi(t))$, $i = 2, 3$. Notice that the last equations' coefficients satisfy the local Lipschitz condition; thus there is a unique solution $(u(t), v(t), w(t))$ on $t \in [0, \tau_e)$. Therefor, it follows from Itô's formula that $x(t) = e^{u(t)}$, $y(t) = e^{v(t)}$, $z(t) = e^{w(t)}$ is the unique positive local solution of system with initial value $x_0 > 0$, $y_0 > 0$, $z_0 > 0$. \square

Lemma 3 only tells us that there is a unique positive local solution to (1). Next, we show this solution is global, that is, $\tau_e = +\infty$. For convenience, we define six equations:

$$\begin{aligned} d\tilde{x}(t) &= [r_1(\xi(t)) - e - a_1\tilde{x}] \tilde{x} dt \\ &\quad + \sigma_1(\xi(t)) \tilde{x} dB_1(t), \\ \tilde{x}(0) &= x_0, \\ d\tilde{y}(t) &= \left[r_2(\xi(t)) - \frac{b_1\tilde{y}}{m_1(\xi(t)) + \tilde{x}} \right] \tilde{y} dt \\ &\quad + \sigma_2(\xi(t)) \tilde{y} dB_2(t), \\ \tilde{y}(0) &= y_0, \\ d\tilde{z}(t) &= \left[r_3(\xi(t)) - \frac{c\tilde{z}}{m_2(\xi(t))} \right] \tilde{z} dt \\ &\quad + \sigma_3(\xi(t)) \tilde{z} dB_3(t), \\ \tilde{z}(0) &= z_0, \\ d\check{z}(t) &= \left[r_3(\xi(t)) - \frac{c\check{z}}{m_2(\xi(t)) + \tilde{y}} \right] \check{z} dt \\ &\quad + \sigma_3(\xi(t)) \check{z} dB_3(t), \\ \check{z}(0) &= z_0, \\ d\hat{y}(t) &= \left[r_2(\xi(t)) - \frac{b_1\hat{y}}{\hat{m}_1} - \frac{b_2\check{z}}{\hat{m}_2} \right] \hat{y} dt \\ &\quad + \sigma_2(\xi(t)) \hat{y} dB_2(t), \\ \hat{y}(0) &= y_0, \\ d\hat{x}(t) &= \left[r_1(\xi(t)) - e - a_1\hat{x} - \frac{a_2\check{y}}{\hat{m}_1} \right] \hat{x} dt \\ &\quad + \sigma_1(\xi(t)) \hat{x} dB_1(t), \\ \hat{x}(0) &= x_0. \end{aligned} \quad (7)$$

Obviously, when $t \in [0, \tau_e)$, by the comparison theorem for stochastic equations [27, Theorem 3.1], it yields

$$\hat{x} \leq x \leq \tilde{x}, \quad \hat{y} \leq y \leq \tilde{y}, \quad \hat{z} \leq z \leq \check{z}. \quad (8)$$

Furthermore, \hat{x} , \tilde{x} , \hat{y} , \tilde{y} , \hat{z} , \check{z} are all existing on $t \geq 0$, and hence we have the following.

Theorem 4. *There is a unique positive solution $x(t)$, $y(t)$, $z(t)$ on $t \geq 0$ to (1) a.s. for any initial value $x_0 > 0$, $y_0 > 0$, $z_0 > 0$, and relations*

$$\hat{x} \leq x \leq \tilde{x}, \quad \hat{y} \leq y \leq \tilde{y}, \quad \hat{z} \leq z \leq \check{z} \quad (9)$$

are all satisfied on $t \geq 0$.

3. The Long Time Behavior

Theorem 4 shows that the solution of the system (1) will remain in the positive cone R_+^3 . This nice property provides us with a great opportunity to discuss how the solution varies in R_+^3 in detail. In this section we will give some long time behavior of the solution, especially the property of persistent in mean, which ensures the existence of $\lim_{t \rightarrow \infty} (\int_0^t x(s) ds / t)$.

Lemma 5 (see [28]). *If Assumption 1 is satisfied, then one has*

$$\lim_{t \rightarrow \infty} \frac{\ln \tilde{x}(t)}{t} = 0, \quad \lim_{t \rightarrow \infty} \frac{\ln \tilde{z}(t)}{t} = 0 \text{ a.s.} \quad (10)$$

Lemma 6. *If Assumption 1 is satisfied, then one has*

$$\lim_{t \rightarrow \infty} \frac{\ln \tilde{y}(t)}{t} = 0, \quad \lim_{t \rightarrow \infty} \frac{\ln \check{z}(t)}{t} = 0 \text{ a.s.} \quad (11)$$

Proof. Firstly, we give an auxiliary equation

$$\begin{aligned} d\bar{y}(t) &= \left[r_2(\xi(t)) - \frac{b_1\bar{y}}{\bar{m}} \right] \bar{y} dt + \sigma_2(\xi(t)) \bar{y} dB_2(t), \\ \bar{y}(0) &= y_0. \end{aligned} \quad (12)$$

Obviously, $\bar{y}(t) \leq \tilde{y}(t)$, and using the similar method of Lemma 5, we have

$$\lim_{t \rightarrow \infty} \frac{\ln \bar{y}(t)}{t} = 0 \text{ a.s.} \quad (13)$$

Therefore,

$$0 = \liminf_{t \rightarrow \infty} \frac{\ln \bar{y}(t)}{t} \leq \liminf_{t \rightarrow \infty} \frac{\ln \tilde{y}(t)}{t} \text{ a.s.} \quad (14)$$

Next, we need only to prove $\limsup_{t \rightarrow \infty} (\ln \tilde{y}(t)/t) \leq 0$ a.s.

The quadratic variation of $\int_0^t \sigma_2(\xi(s)) dB_2(s)$ is $\int_0^t \sigma_2^2(\xi(s)) ds \leq Kt$, and by the strong law of large numbers for local martingales, we have

$$\frac{\int_0^t \sigma_2(\xi(s)) dB_2(s)}{t} \rightarrow 0 \text{ a.s., } t \rightarrow \infty. \quad (15)$$

Therefore, for all $\epsilon > 0$, $\exists 0 < T < \infty$, we have

$$\left| \int_0^t \sigma_2(\xi(s)) dB_2(s) \right| < \epsilon t \text{ a.s., } t \geq T. \quad (16)$$

From this, we have

$$\left| \int_s^t \sigma_2(\xi(s)) dB_2(s) \right| < \epsilon(s+t) \text{ a.s., } t > s \geq T. \quad (17)$$

On the other hand, from Lemma 5, we have

$$-\epsilon t \leq \ln \tilde{x}(t) \leq \epsilon t \text{ a.s., } t \geq T. \quad (18)$$

By the arguments as above, when $t > s \geq T$, we can get

$$\begin{aligned} & \frac{1}{\tilde{y}(t)} \\ &= e^{-[\int_T^t (r_2(\xi(s)) - 0.5\sigma_2^2(\xi(s))) ds + \int_T^t \sigma_2(\xi(s)) dB_2(s)]} \\ & \times \left[\frac{1}{\tilde{y}(T)} + \int_T^t \frac{b_1}{m_1(\xi(s)) + \tilde{x}} \right. \\ & \quad \left. \times e^{\int_T^s (r_2(\xi(\tau)) - 0.5\sigma_2^2(\xi(\tau))) d\tau + \int_T^s \sigma_2(\xi(\tau)) dB_2(\tau)} ds \right] \\ & \geq \int_T^t \frac{b_1}{m_1(\xi(s)) + \tilde{x}} e^{\int_T^s (r_2(\xi(\tau)) - 0.5\sigma_2^2(\xi(\tau))) d\tau + \int_T^s \sigma_2(\xi(\tau)) dB_2(\tau)} ds \\ & \geq \int_T^t \frac{b_1}{m_1(\xi(s)) + e^{\epsilon s}} e^{\int_T^s (r_2(\xi(\tau)) - 0.5\sigma_2^2(\xi(\tau))) d\tau + \int_T^s \sigma_2(\xi(\tau)) dB_2(\tau)} ds \\ & \geq \int_T^t \frac{b_1}{m_1(\xi(s)) + 1} e^{-\epsilon s} e^{A_2(s-T)} e^{-\epsilon(t+s)} ds \\ & \geq \frac{b_1}{\tilde{m}_1 + 1} e^{-(A_2+\epsilon)t} \int_T^t e^{(A_2-2\epsilon)s} ds \\ & = \frac{b_1}{(\tilde{m}_1 + 1)(A_2 - 2\epsilon)} e^{-(A_2+\epsilon)t} (e^{(A_2-2\epsilon)t} - e^{(A_2-2\epsilon)T}). \end{aligned} \quad (19)$$

Therefore, we obtain

$$A_2 + \epsilon \geq \limsup_{t \rightarrow \infty} \frac{\ln \tilde{y}(t)}{t} + A_2 - 2\epsilon; \quad (20)$$

that is

$$\limsup_{t \rightarrow \infty} \frac{\ln \tilde{y}(t)}{t} \leq 3\epsilon. \quad (21)$$

For the arbitrary of $\epsilon > 0$, we must have

$$\limsup_{t \rightarrow \infty} \frac{\ln \tilde{y}(t)}{t} \leq 0. \quad (22)$$

Hence, $\lim_{t \rightarrow \infty} (\ln \tilde{y}(t)/t) = 0$ a.s., and the second conclusion can be proved similarly. \square

Theorem 7. *If Assumption 1 is satisfied, then we have*

$$\lim_{t \rightarrow \infty} \frac{\ln z(t)}{t} = 0 \text{ a.s.,} \quad (23)$$

$$\begin{aligned} & \lim_{t \rightarrow \infty} \frac{\int_0^t (z(s) / (m_2(\xi(s)) + y(s))) ds}{t} \\ &= \frac{1}{c} \sum_{i=1}^N \pi_i (r_3(i) - 0.5\sigma_3^2(i)). \end{aligned} \quad (24)$$

Proof. Following from $\lim_{t \rightarrow \infty} (\ln \tilde{z}(t)/t) = 0$ a.s., $\lim_{t \rightarrow \infty} (\ln \tilde{z}(t)/t) = 0$ a.s., and $\tilde{z} \leq z \leq \tilde{z}$. Obviously, we have

$$\lim_{t \rightarrow \infty} \frac{\ln z(t)}{t} = 0 \text{ a.s.} \quad (25)$$

In the following, we prove the second conclusion.

Let $V(z, \xi) = \ln z$; applying Itô's formula gives

$$\begin{aligned} d \ln z(t) &= \left(r_3(\xi(t)) - 0.5\sigma_3^2(\xi(t)) - \frac{cz(t)}{m_2(\xi(t)) + y(t)} \right) dt \\ &+ \sigma_3(\xi(t)) dB_3(t). \end{aligned} \quad (26)$$

Hence

$$\begin{aligned} & \ln z(t) - \ln z_0 \\ &= \int_0^t (r_3(\xi(s)) - 0.5\sigma_3^2(\xi(s))) ds \\ &- \int_0^t \frac{cz(s)}{m_2(\xi(s)) + y(s)} ds + \int_0^t \sigma_3(\xi(s)) dB_3(s). \end{aligned} \quad (27)$$

Based on the first conclusion in this theorem, the strong law of large numbers for local martingales, and the ergodic property of Markov chain, the second conclusion is proved. \square

Theorem 8. *If Assumptions 1 and 2 are satisfied, then one has*

$$\begin{aligned} & \lim_{t \rightarrow \infty} \frac{\ln y(t)}{t} = 0, \quad \lim_{t \rightarrow \infty} \frac{\ln x(t)}{t} = 0, \text{ a.s.} \\ & \lim_{t \rightarrow \infty} \frac{\int_0^t (y(s) / m_1(\xi(s)) + x(s)) ds}{t} \\ &= \frac{1}{b_1} \left[\sum_{i=1}^N \pi_i (r_2(i) - 0.5\sigma_2^2(i)) - b_2 P_3 \right], \quad (28) \\ & \lim_{t \rightarrow \infty} \frac{\int_0^t x(s) ds}{t} \\ &= \frac{1}{a_1} \left[\sum_{i=1}^N \pi_i (r_1(i) - e - 0.5\sigma_1^2(i)) - a_2 P_2 \right]. \end{aligned}$$

Proof. Based on $\lim_{t \rightarrow \infty} (\ln \tilde{y}(t)/t) = 0$ and $y \leq \tilde{y}$, we have

$$\limsup_{t \rightarrow \infty} \frac{\ln y(t)}{t} \leq \limsup_{t \rightarrow \infty} \frac{\ln \tilde{y}(t)}{t} = 0 \text{ a.s.} \quad (29)$$

Next, we need only to prove $\liminf_{t \rightarrow \infty} (\ln y(t)/t) \geq 0$ a.s.

The quadratic variation of $\int_0^t \sigma_2(\xi(s)) dB_2(s)$ is $\int_0^t \sigma_2^2(\xi(s)) ds \leq Kt$, and by the strong law of large numbers for local martingales, we have

$$\frac{\int_0^t \sigma_2(\xi(s)) dB_2(s)}{t} \rightarrow 0 \text{ a.s., } t \rightarrow \infty. \quad (30)$$

Therefore, for all $\epsilon > 0$, $\exists 0 < T < \infty$, we have

$$\left| \int_0^t \sigma_2(\xi(s)) dB_2(s) \right| < \epsilon t \text{ a.s., } t \geq T. \quad (31)$$

From this, we have

$$\left| \int_s^t \sigma_2(\xi(s)) dB_2(s) \right| < \epsilon(s+t) \text{ a.s., } t > s \geq T. \quad (32)$$

On the other hand, from Lemma 5, we have

$$-\epsilon t \leq \ln \tilde{x}(t) \leq \epsilon t \text{ a.s., } t \geq T. \quad (33)$$

By the arguments as above, when $t > s \geq T$, we can get

$$\begin{aligned} \frac{1}{y(t)} &= \frac{1}{y(T)} e^{-[\int_T^t (r_2(\xi(s)) - 0.5\sigma_2^2(\xi(s)))ds - \int_T^t (b_2 z(s)/(m_2(\xi(s)) + y(s)))ds + \int_T^t \sigma_2(\xi(s))dB_2(s)]} \\ &\quad + \int_T^t \frac{b_1}{m_1(\xi(s)) + x(s)} e^{\int_t^s (r_2(\xi(\tau)) - 0.5\sigma_2^2(\xi(\tau)))d\tau - \int_t^s (b_2 z(\tau)/(m_2(\xi(\tau)) + y(\tau)))d\tau + \int_t^s \sigma_2(\xi(\tau))dB_2(\tau)} ds \\ &\leq \frac{1}{y(T)} e^{-[\int_T^t (r_2(\xi(s)) - 0.5\sigma_2^2(\xi(s)))ds - \int_T^t (b_2 z(s)/(m_2(\xi(s)) + y(s)))ds + \int_T^t \sigma_2(\xi(s))dB_2(s)]} \\ &\quad + \int_T^t \frac{b_1}{\widehat{m}_1} e^{\int_t^s (r_2(\xi(\tau)) - 0.5\sigma_2^2(\xi(\tau)))d\tau - \int_t^s (b_2 z(\tau)/(m_2(\xi(\tau)) + y(\tau)))d\tau + \int_t^s \sigma_2(\xi(\tau))dB_2(\tau)} ds \\ &=: I_1 + I_2. \end{aligned} \quad (34)$$

Based on the second conclusion of Theorem 7, for all $\epsilon > 0$, $\exists 0 < T < \infty$, when $t > s > T$, we have

$$\begin{aligned} \int_T^t \frac{z(s)}{m_2(\xi(s)) + y(s)} ds &< (P_3 + \epsilon)t - (P_3 - \epsilon)T \text{ a.s.,} \\ \int_s^t \frac{z(\tau)}{m_2(\xi(\tau)) + y(\tau)} d\tau &< (P_3 + \epsilon)t - (P_3 - \epsilon)s \text{ a.s.} \end{aligned} \quad (35)$$

Thus,

$$\begin{aligned} I_1 &\leq \frac{1}{y(T)} e^{-[D_2 - b_2(P_3 + \epsilon)](t-T) + [t + (2b_2 + 1)T]\epsilon} \\ &\leq Ke^{[t + (2b_2 + 1)T]\epsilon} \text{ a.s.,} \end{aligned} \quad (36)$$

$$I_2 \leq \int_T^t Ke^{[t + (2b_2 + 1)s]\epsilon} ds \leq Ke^{(2b_2 + 2)t\epsilon} \text{ a.s.}$$

Hence, we obtain $1/y(t) \leq 2Ke^{(2b_2 + 2)t\epsilon}$ a.s., and furthermore

$$\limsup_{t \rightarrow \infty} \left(\frac{-\ln y(t)}{t} \right) \leq (2b_2 + 2)\epsilon. \quad (37)$$

In other words,

$$\liminf_{t \rightarrow \infty} \frac{\ln y(t)}{t} \geq -(2b_2 + 2)\epsilon. \quad (38)$$

For the arbitrary of $\epsilon > 0$, we must have

$$\liminf_{t \rightarrow \infty} \frac{\ln y(t)}{t} \geq 0. \quad (39)$$

The first assertion is proved. The assertion $\lim_{t \rightarrow \infty} (\ln x(t)/t) = 0$, a.s. can be proved similarly.

Similarly to the proof of the second assertion of Theorem 7, the last two assertions can be proved. \square

Definition 9 (see [5]). The system is said to be persistent in mean, if

$$\begin{aligned} \liminf_{t \rightarrow \infty} \frac{\int_0^t x(s) ds}{t} &> 0, \\ \liminf_{t \rightarrow \infty} \frac{\int_0^t y(s) ds}{t} &> 0, \\ \liminf_{t \rightarrow \infty} \frac{\int_0^t z(s) ds}{t} &> 0 \text{ a.s.} \end{aligned} \quad (40)$$

Theorem 10. If Assumptions 1 and 2 are satisfied, then the system is persistent in mean.

Proof. $\liminf_{t \rightarrow \infty} (\int_0^t x(s)ds/t) > 0$ is already proved in Theorem 8.

From the third assertion of Theorem 8, we have

$$\liminf_{t \rightarrow \infty} \frac{\int_0^t y(s) ds}{\widehat{m}_1 t} \geq \lim_{t \rightarrow \infty} \frac{\int_0^t (y(s) / (m_1(\xi(s)) + x(s))) ds}{t} = P_2 > 0; \quad (41)$$

that is, $\liminf_{t \rightarrow \infty} (\int_0^t y(s)ds/t) > 0$.

From the second assertion of Theorem 7, we have

$$\begin{aligned} \liminf_{t \rightarrow \infty} \frac{\int_0^t z(s) ds}{\widehat{m}_2 t} \\ \geq \lim_{t \rightarrow \infty} \frac{\int_0^t (z(s) / (m_2(\xi(s)) + y(s))) ds}{t} = P_3 > 0; \end{aligned} \quad (42)$$

that is, $\liminf_{t \rightarrow \infty} (\int_0^t z(s) ds / t) > 0$.

This theorem is proved. \square

4. The Optimal Harvesting Policies

Based on the explicit expression of the time averaging yield function obtained in the last section, here we discuss the optimal harvesting problem mentioned in Section 1.

Theorem 11. *If Assumptions 1 and 2 is satisfied, then the optimal harvesting effort is*

$$e^* = \min \{ \overline{D}_1 - a_2(P_2 + \epsilon), \bar{e} \}, \quad (43)$$

where $\overline{D}_1 = \min_{\xi \in S} \{r_1(\xi) - 0.5\sigma_1^2(\xi)\}$, $\bar{e} = 0.5\Sigma - 0.5a_2P_2$, $\Sigma = \sum_{i=1}^N \pi_i(r_1(i) - 0.5\sigma_1^2(i))$, and the optimal harvesting output is

$$F(e^*) = \frac{1}{a_1} [(\Sigma - a_2P_2)e^* - (e^*)^2]. \quad (44)$$

Proof. Based on Theorem 8, the optimization problem can be expressed as follows:

$$\begin{aligned} \max \quad & F(e) = \frac{1}{a_1} [(\Sigma - a_2P_2)e - e^2] \\ \text{s.t.} \quad & e \leq \overline{D}_1 \quad (\text{Assumption 1}) \\ & e \leq \overline{D}_1 - a_2(P_2 + \epsilon) \quad (\text{Assumption 2}) \\ & e \leq \Sigma - a_2P_2 \quad (\text{Assumption 2}) \\ & e \geq 0. \end{aligned} \quad (45)$$

From the definitions of \overline{D}_1 and Σ , we get $\overline{D}_1 \leq \Sigma$. Therefore, the above optimization problem can be simplified as follows:

$$\begin{aligned} \max \quad & F(e) = \frac{1}{a_1} [(\Sigma - a_2P_2)e - e^2] \\ \text{s.t.} \quad & 0 \leq e \leq \overline{D}_1 - a_2(P_2 + \epsilon). \end{aligned} \quad (46)$$

Because the objective function is concave, and we can obtain the unique maximum point easily as

$$e^* = \min \{ \overline{D}_1 - a_2(P_2 + \epsilon), \bar{e} \}, \quad (47)$$

here the \bar{e} is obtained by letting $dF(e)/d(e) = 0$.

Substituting it into the harvesting function, we obtain the optimal harvesting output

$$F(e^*) = \frac{1}{a_1} [(\Sigma - a_2P_2)e^* - (e^*)^2]. \quad (48)$$

This theorem is proved. \square

Remark 12. (i) That the feasible zone of optimization problem (46) is nonempty is guaranteed by Assumptions 1 and 2.

(ii) From the explicit expression of the optimal harvesting effort, we can easily investigate how the parameters influence on it, such that e^* is decreasing in a_2 , and this claim coincides with the fact that if the consumer's ($y(t)$) consuming capacity is enhanced (a_2 augments), the harvesting effort must reduce (e^* go down), or the resource ($x(t)$) will be extinct and the whole ecosystem is crashed.

5. Numerical Results

We present numerical experiments in this section to show how the proposed model works in the constructive examples. The results enhance the readers to understand the theoretical conclusions from the practical applications.

Here, we use the Milstein method [29] to construct the discretization equation of (1); that is,

$$\begin{aligned} x_{k+1} &= x_k + x_k \left[r_1(\xi(k\Delta t)) - e - a_1x_k - \frac{a_2y_k}{m_1(\xi(k\Delta t)) + x_k} \right] \Delta t \\ &\quad + \sigma_1(\xi(k\Delta t)) x_k \sqrt{\Delta t} \zeta_k \\ &\quad + 0.5\sigma_1^2(\xi(k\Delta t)) x_k^2 (\zeta_k^2 - 1) \Delta t, \\ y_{k+1} &= y_k + y_k \left[r_2(\xi(k\Delta t)) - \frac{b_1y_k}{m_1(\xi(k\Delta t)) + x_k} \right. \\ &\quad \left. - \frac{b_2z_k}{m_2(\xi(k\Delta t)) + y_k} \right] \Delta t \\ &\quad + \sigma_2(\xi(k\Delta t)) y_k \sqrt{\Delta t} \eta_k \\ &\quad + 0.5\sigma_2^2(\xi(k\Delta t)) y_k^2 (\eta_k^2 - 1) \Delta t, \\ z_{k+1} &= z_k + z_k \left[r_3(\xi(k\Delta t)) - \frac{cz_k}{m_2(\xi(k\Delta t)) + y_k} \right] \Delta t \\ &\quad + \sigma_3(\xi(k\Delta t)) z_k \sqrt{\Delta t} \varsigma_k \\ &\quad + 0.5\sigma_3^2(\xi(k\Delta t)) z_k^2 (\varsigma_k^2 - 1) \Delta t, \end{aligned} \quad (49)$$

where ζ_k , η_k , and ς_k , $k = 1, \dots, n$, are the Gaussian random variables.

For simplicity, assume that the random environments are modeled by a two-state Markov chain with state set $S = \{1, 2\}$ and generator

$$Q = \begin{pmatrix} -7 & 7 \\ 5 & 5 \end{pmatrix}. \quad (50)$$

The other parameters are defined as follows: $r_1(1) = 8$, $r_1(2) = 9$, $r_2(1) = 6$, $r_2(2) = 6$, $r_3(1) = 4$, $r_3(2) = 3$, $\sigma_1(1) = 0.8$, $\sigma_1(2) = 0.9$, $\sigma_2(1) = 0.6$, $\sigma_2(2) = 0.6$, $\sigma_3(1) = 0.4$, $\sigma_3(2) =$

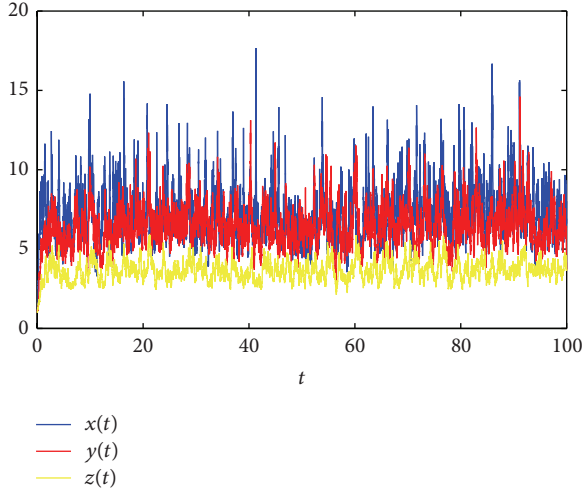


FIGURE 1: Sample path of (1) with initial condition $(x_0, y_0, z_0) = (1, 1, 1)$ and $\xi(t) \equiv 1$.

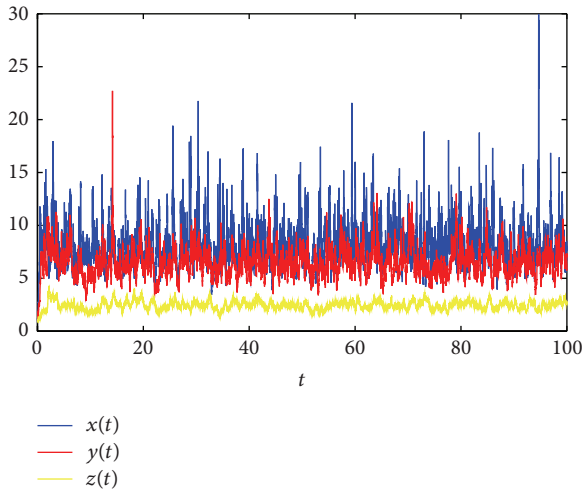


FIGURE 2: Sample path of (1) with initial condition $(x_0, y_0, z_0) = (1, 1, 1)$ and $\xi(t) \equiv 2$.

$0.3, m_1(1) = 5, m_1(2) = 4, m_2(1) = 3, m_2(2) = 2, a_1 = a_2 = b_2 = 1, b_1 = c = 10, e = 0$. In this scenario, $B_1 = 7.68, B_2 = 5.82, B_3 = 2.955, P_1 = 7.66, P_2 = 0.55, P_3 = 0.34, B_1 - a_2(P_2 + \varepsilon) = 7.13 - \varepsilon$, and $B_2 - b_2(P_3 + \varepsilon) = 5.48 - \varepsilon$. Obviously, Assumptions 1 and 2 are satisfied.

Based on the aforementioned discussion, we obtain the following results.

Figures 1 and 2 show that the solutions of (1) are positive in the deterministic environment (without regime switching); that is, $\xi(t) \equiv 1$ or 2. Figure 4 shows that the solutions of (1) are positive in the random environment (with regime switching); the random environment is described by Figure 3. They are all identical to Theorem 4. Figure 5 shows $\lim_{t \rightarrow \infty} (\ln x(t)/t) = 0, \lim_{t \rightarrow \infty} (\ln y(t)/t) = 0$, and $\lim_{t \rightarrow \infty} (\ln z(t)/t) = 0$ in the random environment described by Figure 3, and this is consistent with Theorems 7 and 8.

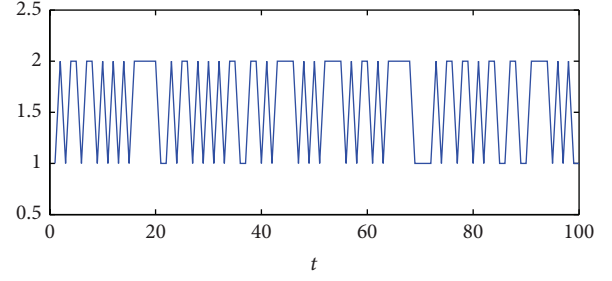


FIGURE 3: Sample path of $\xi(t)$ with initial condition $\xi(0) \equiv 1$.

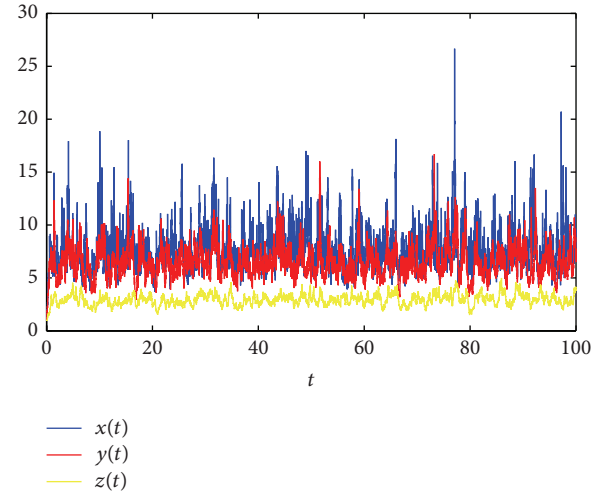


FIGURE 4: Sample path of (1) with initial condition $(x_0, y_0, z_0) = (1, 1, 1)$ and sample path of $\xi(t)$ is Figure 3.

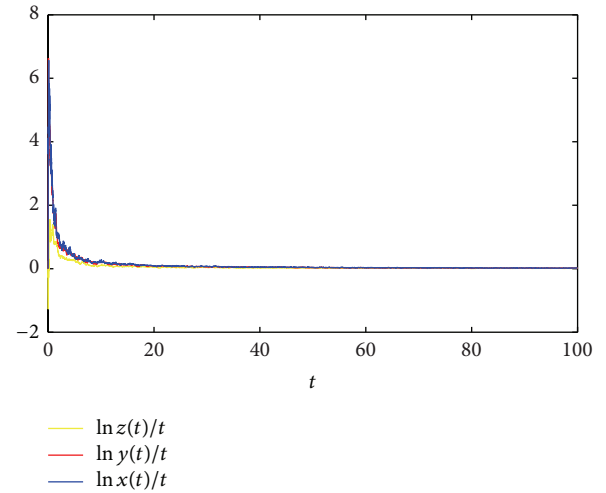


FIGURE 5: The curves of $\ln x/t, \ln y/t$, and $\ln z/t$.

6. Conclusions

This paper studies an optimal harvesting problem for a food-chain system with markovian switching. Based on the properties, the food-chain system's solution is existing, unique, and positive; the system is persistent in mean, and the

rationality of the optimal harvesting problem is proved. Then the optimal harvesting policy is obtained.

Nevertheless, there are rooms to continue work on this issue, such that more than one of control variables in the system are considered. The permanence and extinction of the system and the stability in distribution need to be investigated too.

Conflict of Interests

The authors declare that there is no conflict of interests regarding the publication of this paper.

Acknowledgments

The authors thank the editor and referees for their helpful comments that improved the presentation of the paper.

References

- [1] C. W. Clark, *Mathematical Bioeconomics: The Optimal Management of Renewable Resources*, Wiley, New York, NY, USA, 1976.
- [2] C. W. Clark, *Mathematical Bioeconomics: The Optimal Management of Renewable Resources*, John Wiley & Sons, New York, NY, USA, 2nd edition, 1990.
- [3] Y. L. Feng, K. Wang, and J. Y. Sun, "Persistence and extinction of logistic single-species population with pollution and harvesting," *Journal of Biomathematics*, vol. 21, no. 3, pp. 365–369, 2006.
- [4] M. Fan and K. Wang, "Study on harvested population with diffusional migration," *Journal of Systems Science and Complexity*, vol. 14, no. 2, pp. 139–148, 2001.
- [5] X. Zhang, Z. Shuai, and K. Wang, "Optimal impulsive harvesting policy for single population," *Nonlinear Analysis: Real World Applications*, vol. 4, no. 4, pp. 639–651, 2003.
- [6] W. Jing and W. Ke, "The optimal harvesting problems of a stage-structured population," *Applied Mathematics and Computation*, vol. 148, no. 1, pp. 235–247, 2004.
- [7] L. Bai and K. Wang, "Gilpin-Ayala model with spatial diffusion and its optimal harvesting policy," *Applied Mathematics and Computation*, vol. 171, no. 1, pp. 531–546, 2005.
- [8] L. Bai and K. Wang, "A diffusive single-species model with periodic coefficients and its optimal harvesting policy," *Applied Mathematics and Computation*, vol. 187, no. 2, pp. 873–882, 2007.
- [9] Z. Shuai, L. Bai, and K. Wang, "Optimization problems for general simple population with n -impulsive harvest," *Journal of Mathematical Analysis and Applications*, vol. 329, no. 1, pp. 634–646, 2007.
- [10] J. R. Beddington and R. M. May, "Harvesting natural populations in a randomly fluctuating environment," *Science*, vol. 197, no. 4302, pp. 463–465, 1977.
- [11] R. Lande, S. Engen, and B. E. Saether, "Optimal harvesting of fluctuating populations with a risk of extinction," *The American Naturalist*, vol. 145, no. 5, pp. 728–745, 1995.
- [12] E. M. Lungu and B. Øksendal, "Optimal harvesting from a population in a stochastic crowded environment," *Mathematical Biosciences*, vol. 145, no. 1, pp. 47–75, 1997.
- [13] L. H. Alvarez, "Optimal harvesting under stochastic fluctuations and critical depensation," *Mathematical Biosciences*, vol. 152, no. 1, pp. 63–85, 1998.
- [14] M. A. Shah and U. Sharma, "Optimal harvesting policies for a generalized Gordon-Schaefer model in randomly varying environment," *Applied Stochastic Models in Business and Industry*, vol. 19, no. 1, pp. 43–49, 2003.
- [15] W. Li, K. Wang, and H. Su, "Optimal harvesting policy for stochastic Logistic population model," *Applied Mathematics and Computation*, vol. 218, no. 1, pp. 157–162, 2011.
- [16] X. Zou, W. Li, and K. Wang, "Ergodic method on optimal harvesting for a stochastic Gompertz-type diffusion process," *Applied Mathematics Letters*, vol. 26, no. 1, pp. 170–174, 2013.
- [17] H. Qiu, J. Lv, and K. Wang, "The optimal harvesting policy for non-autonomous populations with discount," *Applied Mathematics Letters*, vol. 26, no. 2, pp. 244–248, 2013.
- [18] C. Ji, D. Jiang, and N. Shi, "Analysis of a predator-prey model with modified Leslie-Gower and Holling-type II schemes with stochastic perturbation," *Journal of Mathematical Analysis and Applications*, vol. 359, no. 2, pp. 482–498, 2009.
- [19] Z. Song, B. Zhen, and J. Xu, "Species coexistence and chaotic behavior induced by multiple delays in a food chain system," *Ecological Complexity*, vol. 19, pp. 9–17, 2014.
- [20] L. Guo, Z.-G. Song, and J. Xu, "Complex dynamics in the Leslie-Gower type of the food chain system with multiple delays," *Communications in Nonlinear Science and Numerical Simulation*, vol. 19, no. 8, pp. 2850–2865, 2014.
- [21] K. Wang, *Stochastic Biomathematics Models*, Science Press, Beijing, China, 2010.
- [22] X. Zou and K. Wang, "Optimal harvesting for a stochastic regime-switching logistic diffusion system with jumps," *Nonlinear Analysis: Hybrid Systems*, vol. 13, pp. 32–44, 2014.
- [23] N. Ikeda and S. Watanabe, "A comparison theorem for solutions of stochastic differential equations and its applications," *Osaka Journal of Mathematics*, vol. 14, no. 3, pp. 619–633, 1977.
- [24] B. E. Saether, S. Engen, R. Lande, P. Arcese, and J. N. Smith, "Estimating the time to extinction in an island population of song sparrows," *Proceedings of the Royal Society of London B: Biological Sciences*, vol. 267, pp. 621–626, 2013.
- [25] X. Mao and C. Yuan, *Stochastic Differential Equations with Markovian Switching*, Imperial College Press, London, UK, 2006.
- [26] X. Mao, *Stochastic Differential Equations and Applications*, Horwood Publishing, Chichester, UK, 2nd edition, 2007.
- [27] S. Peng and X. Zhu, "Necessary and sufficient condition for comparison theorem of 1-dimensional stochastic differential equations," *Stochastic Processes and their Applications*, vol. 116, no. 3, pp. 370–380, 2006.
- [28] C. Zhu and G. Yin, "On competitive Lotka-Volterra model in random environments," *Journal of Mathematical Analysis and Applications*, vol. 357, no. 1, pp. 154–170, 2009.
- [29] D. J. Higham, "An algorithmic introduction to numerical simulation of stochastic differential equations," *SIAM Review*, vol. 43, no. 3, pp. 525–546, 2001.

Research Article

Assembly Line Productivity Assessment by Comparing Optimization-Simulation Algorithms of Trajectory Planning for Industrial Robots

Francisco Rubio, Carlos Llopis-Albert, Francisco Valero, and Josep Lluís Suñer

Centro de Investigación en Ingeniería Mecánica (CIIM), Universitat Politècnica de València-Camino de Vera s/n, 46022 Valencia, Spain

Correspondence should be addressed to Carlos Llopis-Albert; cllopisa@gmail.com

Received 25 July 2014; Revised 20 September 2014; Accepted 22 September 2014

Academic Editor: Shaofan Li

Copyright © 2015 Francisco Rubio et al. This is an open access article distributed under the Creative Commons Attribution License, which permits unrestricted use, distribution, and reproduction in any medium, provided the original work is properly cited.

In this paper an analysis of productivity will be carried out from the resolution of the problem of trajectory planning of industrial robots. The analysis entails economic considerations, thus overcoming some limitations of the existing literature. Two methodologies based on optimization-simulation procedures are compared to calculate the time needed to perform an industrial robot task. The simulation methodology relies on the use of robotics and automation software called GRASP. The optimization methodology developed in this work is based on the kinematics and the dynamics of industrial robots. It allows us to pose a multiobjective optimization problem to assess the trade-offs between the economic variables by means of the Pareto fronts. The comparison is carried out for different examples and from a multidisciplinary point of view, thus, to determine the impact of using each method. Results have shown the opportunity costs of non using the methodology with optimized time trajectories. Furthermore, it allows companies to stay competitive because of the quick adaptation to rapidly changing markets.

1. Introduction

Time needed to perform a trajectory for industrial robots is a very important issue in order to improve productivity in many economic activities. Specifically, most algorithms seek to find the minimum time trajectory in order to increase the working time and subsequently to reduce the unproductive time. The existing literature shows a lack of studies that consider both the economic issues and the motion of industrial robots.

In this paper, the working times of industrial robots are compared between two different approaches while taking into account the corresponding economic impacts. The comparison is applied to several examples, which covers a wide range of parameters that govern the kinematics and dynamics of the industrial robots. The first methodology is based on a robotic simulation program called GRASP (BYG System Ltd) and the second on optimization techniques.

When the working times have been calculated, the assembly line productivity is estimated by means of the time

difference, so that we can quantify the impact of each method. Productivity is quantified by conducting an economic study based on the working times of robotic tasks and, more specifically, the time needed to manufacture and assemble a certain product.

A multiobjective optimization problem is posed to assess the trade-offs between the economic variables by means of the Pareto fronts (see Section 6). These fronts will serve to determine those variables that mostly influence the increase of productivity of the assembly line. We will prove that working times (not working cycles) are critical from an economic point of view and so are the methods to obtain them.

Those times will enable us to set conclusions about which method is more useful in order to increase the productivity of the robotic system.

The paper is organized as follows. Initially, we will explain in detail the main characteristics of the trajectory planning methodology and how the time is obtained. Consequently, the economic analysis will provide insight on the productivity

of assembly lines. Finally, the conclusions will be discussed in the last section.

2. Background of the Trajectory Planning Problem

Currently there are a great number of methodologies to solve the trajectory planning problem for industrial robots which give the time needed to perform a task. But few papers tackle the analysis of productivity related to the working times obtained.

Over the years, the algorithms have been polished and the working assumptions of the robotic systems have been increasingly adjusted to real conditions. This fact has been achieved by analysing the complete behaviour of the robotic system, particularly the characteristics of the actuators and the mechanical structure of the robot. To tackle this problem other important working parameters and variables have been taken into account, such as the input torques, the energy consumed, and the power transmitted. Furthermore, the kinematic properties of the robot's links, such as the velocities, accelerations, and jerks, must be also considered. The aforementioned algorithms provide a smooth robot motion for the robotic system.

To obtain the best trajectories in terms of minimum times, some of the working parameters have been included in the appropriate objective function of the optimization procedure (input torques, the energy consumed, and the power transmitted). The optimization criteria most widely used can be sorted as follows.

- (1) Minimum time required, which is directly bounded to productivity.
- (2) Minimum jerk, which is bounded to the quality of work, accuracy, and equipment maintenance.
- (3) Minimum energy consumed or minimum actuator effort, both linked to savings.
- (4) Hybrid criteria, for example, minimum time and energy.

In the past, the early algorithms that solved the trajectory planning problem tried to minimize the time needed for performing the task (see [1–3]). One disadvantage of those minimum-time algorithms was that the trajectories had discontinuous values of acceleration and torques which led to dynamic problems during the trajectory performance. Those problems were avoided by imposing smooth trajectories to be followed, such as spline functions which have been used in both path and trajectory planning.

The early algorithms in trajectory planning sought to minimize the time needed for performing the task. The dynamics properties of actuators were neglected. A recent example of this type of algorithm can be found in [4], which determines smooth and near time-optimal path-constrained trajectories. It considers not only velocity and acceleration but also jerk.

Later, the trajectory planning problem was tackled by searching for jerk-optimal trajectories. Jerks are highly

important for working with precision and without vibration. They also have an effect on the control system and the wearing of mobile parts such as joints and bars. These methods allow a reduction in errors during trajectory tracking, the stresses in the actuators and also in the mechanical structure of the robot, and the excitement of resonance frequencies. Jerk restriction is introduced by other authors [5, 6].

In [7] a method is introduced for determining smooth and time-optimal path-constrained trajectories for robotic manipulators by imposing limits on the actuator jerks.

In [8] a global minimum-jerk trajectory planning algorithm of a space manipulator is presented.

Another different approach to solving the trajectory planning problem is based on minimizing the torque and the energy consumed instead of the trajectory time or the jerk. This approach leads to smoother trajectories. An early example is seen in [9].

Similarly, in [10], the authors searched for the minimum energy consumed. They proposed a method for solving the trajectory generation problem in redundant degree of freedom manipulators. They used a variational approach and the B-Spline curve was introduced to minimize the electrical energy consumed in a robot manipulator system.

The work in [11] also takes into account energy minimization for the trajectory planning problem.

In [12] the authors proposed a technique of iterative dynamic programming to plan minimum energy consumption trajectories for robotic manipulators. The dynamic programming method was modified to perform a series of dynamic programming passes over a small reconfigurable grid covering only a portion of the solution space at any one pass. Although strictly no longer a global optimization process, this iterative approach retained the ability to avoid certain poor local minima while avoiding the dimensional issue associated with a pure dynamic programming approach. The modified dynamic programming approach was verified experimentally by planning and executing a minimum energy consumed path for a Reis V15 industrial manipulator.

Afterwards, new perspectives appear for solving the trajectory planning problem. The main point was to use a weighted objective function to optimize the working parameters [13]. There, the cost function is a weighted balance of transfer time, the mean average of the torques, and power.

In this paper we will introduce two methods to solve the trajectory planning problem for industrial robots working in complex environments. The time will be used in the economical study.

In the first method, the procedure calculates the optimal trajectory by neglecting initially the potential presence of obstacles in the workspace. By removing the obstacles (real or potential) from the optimization problem, the algorithm will calculate a minimum time trajectory as a starting point. Then the procedure must take into account the real obstacles presented in the workspace. When obstacles are considered, the initial trajectory will not be feasible and will have to evolve so that it can become a solution. The way this initial trajectory evolves until a new feasible collision-free trajectory is obtained is presented in this paper. It is a direct algorithm that works in a discrete space of trajectories, approaching the

first solution to the global solution as the discretization is refined. The solutions obtained are efficient trajectories (i.e., the minimum time trajectories). All the trajectories obtained meet the physical limitations of the robot. The solution also avoids collisions and takes into account the constraint of energy consumed.

The second method calculates the times using the kinematic properties of the robotic system by means of a simulation program called GRASP.

3. Time Obtained Using the Proposed Optimization Trajectory Planner

Our objective is to calculate the minimum time trajectory (t) between the initial and final configurations. Any robot configuration $C^j = C^j(\alpha_i^j, p_k^j)$ can be expressed unequivocally by means of the Cartesian coordinates of significant points of the robot $\alpha_i^j = (\alpha_{xi}^j, \alpha_{yi}^j, \alpha_{zi}^j)$.

We calculate the time needed to go from C^i to C^f . This process is based on an optimization problem to obtain the minimum time between these two configurations. The problem is transformed into obtaining the minimum time over an interpolated trajectory between both configurations, subjected to physical constraints in the actuators.

This optimization problem can be stated as in [7] as follows:

$$\text{Find } q(t), \tau(t), t_f \quad (1)$$

between each of the two configurations (see Section 3.3),

$$\text{Minimizing } \min_{\tau \in \Omega} J = \int_0^{t_f} dt, \quad (2)$$

where $\tau(t) \in R^n$ is the vector of the actuator torques and Ω is the space state in which the vector of the actuator torques is feasible.

The optimization problem is subject to:

(1) the robot dynamics

$$M(q(t))\ddot{q}(t) + C(q(t), \dot{q}(t))\dot{q}(t) + g(q(t)) = \tau(t); \quad (3)$$

(2) unknown boundary conditions (position, velocity, and acceleration) for intermediate configurations a priori

$$\begin{aligned} q(t_{\text{int}-1}) &= q_{\text{int}-1}; & q(t_{\text{int}}) &= q_{\text{int}}, \\ \dot{q}(t_{\text{int}-1}) &= \dot{q}_{\text{int}-1}; & \dot{q}(t_{\text{int}}) &= \dot{q}_{\text{int}-1}, \\ \ddot{q}(t_{\text{int}-1}) &= \ddot{q}_{\text{int}-1}; & \ddot{q}(t_{\text{int}}) &= \ddot{q}_{\text{int}-1}; \end{aligned} \quad (4)$$

(3) boundary conditions for initial and final configurations

$$\begin{aligned} q(0) &= q_0; & q(t_f) &= q_f, \\ \dot{q}(0) &= 0; & \dot{q}(t_f) &= 0; \end{aligned} \quad (5)$$

(4) collision avoidance within the robot workspace

$$d_{ij} \geq r_j + w_i; \quad (6)$$

d_{ij} being the distance from any obstacle j (sphere, cylinder, or prism) to robot arm i ; r_j is the characteristic radius of the obstacle and w_i is the radius of the smallest cylinder that contains the arm i ;

(5) actuator torque rate limits

$$\tau_i^{\min} \leq \tau_i(t) \leq \tau_i^{\max} \quad \forall t \in [0, t_{\min}], \quad i = 1, \dots, \text{dof}; \quad (7)$$

(6) maximum power in the actuators

$$P_i^{\min} \leq \tau_i(t) \dot{q}_i(t) \leq P_i^{\max} \quad \forall t \in [0, t_{\min}], \quad i = 1, \dots, \text{dof}; \quad (8)$$

(7) maximum jerk on the actuators

$$\ddot{\ddot{q}}_i^{\min} \leq \ddot{\ddot{q}}_i(t) \leq \ddot{\ddot{q}}_i^{\max} \quad \forall t \in [0, t_{\min}], \quad i = 1, \dots, \text{dof}, \quad (9)$$

($\ddot{\ddot{q}}_i$ is the jerk of actuator i);

(8) energy consumed

$$\sum_{j=1}^{m-1} \left(\sum_{i=1}^{\text{dof}} \varepsilon_{ij} \right) \leq E, \quad (10)$$

where ε_{ij} is the energy consumed by the actuator i between the configurations c^j and c^{j+1} .

Here, the main definitions and processes used to obtain the free-collision trajectories of the robot (and subsequently the time needed to perform the trajectory) are detailed.

3.1. Robot Configuration. It is expressed in joint coordinates $c^k(q_i)$ with a view to define kinematics and dynamics of the robot. When dealing with collisions, Cartesian coordinates $c^k(\lambda_j)$ will be used, being $i = 1, \dots, \text{dof}$; $j = 1, \dots, \text{npc}$; dof : robot degrees of freedom; npc : number of Cartesian points used for the wired model of the robot in collision detection; and k is the configuration itself; see [14–16].

3.2. Adjacent Configuration. Given a feasible configuration of the robot c^k , it is said that c^l is adjacent to it if it is feasible and meets the following two conditions.

(i) The robot end-effector occupies a position corresponding to a node of the discretized workspace in Cartesian coordinates and its distance to the end-effector position in the configuration c^k is less than a given value.

(ii) c^l is such that it minimizes the function

$$\sum_{i=1}^{\text{dof}} (q_i^l - q_i^k)^2. \quad (11)$$

3.3. Trajectory. Given a sequence of m robot configurations $= \{c^1(q_i^1), c^2(q_i^2), \dots, c^m(q_i^m)\}$, the trajectory s is defined by means of cubic interpolation functions between adjacent configurations so that the resulting time t_{\min} to perform the trajectory is minimum. We have that

$$\forall t \in [t_{j-1}, t_j] \longrightarrow q_{ij} = a_{ij} + b_{ij}t + d_{ij}t^2 + e_{ij}t^3, \quad (12)$$

where $i = 1, \dots, \text{dof}$, $j = 1, \dots, m-1$.

To ensure continuity, the following conditions associated with the given configurations are considered.

(a) Position: for each interval j the initial and final positions must match c^j and c^{j+1} ; this gives a total of $(2 \text{ dof}(m-1))$ equations:

$$\begin{aligned} q_{ij}(t_{j-1}) &= q_i^j, \\ q_{ij}(t_j) &= q_i^{j+1}. \end{aligned} \quad (13)$$

(b) Velocity: the initial and final velocities of the trajectory must be zero, obtaining (2 dof) equations

$$\begin{aligned} \dot{q}_{i1}(t_0) &= 0, \\ \dot{q}_{im-1}(t_{m-1}) &= 0. \end{aligned} \quad (14)$$

When passing through each intermediate configuration, the final velocity of previous interval must be equal to the initial velocity of the next interval; that gives $(\text{dof}(m-2))$ equations

$$\dot{q}_{ij}(t_j) = \dot{q}_{ij+1}(t_j). \quad (15)$$

(c) Acceleration: for each intermediate configuration, the final actuator acceleration of the previous interval must be equal to the initial acceleration of the next, resulting in $(\text{dof}(m-2))$ equations

$$\ddot{q}_{ij}(t_j) = \ddot{q}_{ij+1}(t_j). \quad (16)$$

Knowing the time required to perform the trajectory between the different configurations, using the above equations, the coefficients of the cubic polynomials can be obtained efficiently by means of the calculation of the normal time [15].

In addition, the minimum time trajectory s must meet the following four types of constraints:

(d) maximum torque in the actuators,

(e)

$$\tau_i^{\min} \leq \tau_i(t) \leq \tau_i^{\max} \quad \forall t \in [0, t_{\min}], \quad i = 1, \dots, \text{dof}, \quad (17)$$

(f) maximum power in the actuators,

(g)

$$P_i^{\min} \leq \tau_i(t) \dot{q}_i(t) \leq P_i^{\max} \quad \forall t \in [0, t_{\min}], \quad i = 1, \dots, \text{dof}, \quad (18)$$

(h) maximum jerk on the actuators,

(i)

$$\ddot{q}_i^{\min} \leq \ddot{q}_i(t) \leq \ddot{q}_i^{\max} \quad \forall t \in [0, t_{\min}], \quad i = 1, \dots, \text{dof}, \quad (19)$$

(j) energy consumed

$$\sum_{j=1}^{m-1} \left(\sum_{i=1}^{\text{dof}} \varepsilon_{ij} \right) \leq E, \quad (20)$$

where ε_{ij} is the energy consumed by the actuator i between the configurations c^j and c^{j+1} .

To obtain the minimum time, an optimization problem is solved using variables defined in time increment at each interval (see [17]) so that in the interval between c^j and c^{j+1} , the variable is $\Delta t_j = t_j - t_{j-1}$ and the objective function is

$$\sum_{j=1}^{m-1} \Delta t_j = t_{\min}. \quad (21)$$

3.4. Offspring Trajectory. Let s^j be a minimum time trajectory associated to the sequence of m configurations C^j under the conditions described in Section 3.5. It is said that the trajectory s^k is an offspring of s^j when the following conditions are met:

(a) $C^k = C^j \cup c^n$;

(b) $n \neq 1$;

(c) $n \neq m+1$.

So the trajectories of a certain generation will have one passing configuration more than the previous generation, but they will keep the same initial and final configurations.

3.5. Obtaining of the Collision-Free Trajectory. The problem of obtaining a feasible and efficient trajectory for a robot in an environment with static obstacles allowing the motion between two given configurations (c^i and c^f) is posed. An efficient trajectory is that performed in a minimum time, with a reasonable computational cost, and subject to the limitations of the robot dynamics, the jerk constraints, and power consumption. Clearly the feasibility of the trajectory means that there are no collisions.

The proposed process for solving the problem involves the following steps which are implemented in the algorithm.

(a) Obtaining the minimum time trajectory: using the procedure described in Section 3.3, the trajectory s_{\min} is obtained corresponding to the sequence of configurations $C = \{c^i, c^f\}$.

(b) Search for collisions: the first configuration from s_{\min} which has collision c^c is determined, and a previous configuration c^a is searched for whose distance is less than d_{seg} (so that the smallest patterned obstacle used to represent the work environment can never be between c^c y c^a).

TABLE 1: Kinematic characteristics of PUMA 560 robot.

Joint	1	2	3	4	5	6
Minimum angle (°)	-160.0	-215.0	-45.0	-140.0	-100.0	-266.0
Maximum angle (°)	160.0	35.0	225.0	140.0	100.0	266.0
Maximum velocity (°/s)	82.0	54.0	122.0	228.0	241.0	228.0

- (c) Obtaining adjacent configurations: up to six new adjacent configurations to c^a can be achieved as defined in Section 3.2 (c_j^a $j = 1, \dots, 6$).
- (d) Obtaining offspring trajectories: for each one of the l adjacent configurations obtained in the previous section that have no collision with obstacles, the offspring trajectory s_k is obtained from s_{\min} , such that $C^k = C \cup c_k^a$ ($k = 1, \dots, l$).
- (e) Trajectory selection: the generated trajectories are introduced in previous section (d) on the set of trajectories ordered by time $T_t = \{s_1 \dots s_p\}$, taking the minimum time trajectory s_1 and checking for no collisions as it was done in previous section (b). If s_1 has no collision, the algorithm goes to the next section; otherwise it returns to section (c) and the process is repeated.
- (f) Refining the trajectory: in case that the collision-free trajectory s_1 does not belong to the first generation (direct offspring of s_{\min} , with a sequence of three configurations), we have s_1 such that $C^1 = \{c^i, c^2, c^3, \dots, c^{m-1}, c^f\}$ (m being the number of configurations that define the trajectory).

$m - 2$ sets of configurations C_p^1 are taken such that $C^1 = C_p^1 \cup c^p$ for $p = 2, \dots, m-1$, obtaining the corresponding set of collision-free trajectories T_r . If it is empty then it is said that s_1 cannot be reduced; otherwise the process is repeated for the new trajectories and the results are included in T_r . The process finishes when the algorithm cannot obtain new trajectories.

Finally the trajectory s_1 is included in T_r and the reduced trajectory s_r is defined as the trajectory belonging to T_r with minimum time.

The proposed solution to the problem is s_r , which will be a minimum time offspring trajectory s_{\min} and with a small number of passing configurations.

4. Time Obtained Using a Robotic Environment Simulation Program Called GRASP

The simulation program GRASP10 for robotic environments is used to obtain the time needed to perform the motion between two given configurations. Among other tasks, GRASP10 can model and simulate the robot kinematic behavior. In this paper we have used the original model of PUMA 560 robot that comes with the program as a comparator. It is assumed that the point to point trajectory calculation procedures of GRASP10 correspond to the

real robot. The robot kinematic characteristics are shown in Table 1.

It should be noted that GRASP10 does not perform dynamic calculations but only kinematic ones. It is therefore very important to indicate the maximum working velocities, which have been obtained from actual robot by considering the properties of each actuator, primarily its maximum power, and the working torque.

When the trajectory is generated by GRASP10, the working actuators act simultaneously and at least one of them is moved to its maximum speed, calculated as follows for each actuator: (see Table 1)

$$\omega_{\max} = \frac{P}{t_{\min}}, \quad (22)$$

where P stands for the power and t_{\min} for the torque in the corresponding actuator.

This methodology (use of GRASP10 for calculating the time required to perform a trajectory) has been applied to the same examples that have been resolved by the optimization algorithm explained in Section 3 in order to compare their efficiency.

For each example, the initial data are the initial and final configurations and the kinematics of the robot. The obstacle has been incorporated after the generation of the path, so that it burdens the previously calculated one.

5. Productivity and Economic Study

In this section the productivity will be quantified by conducting an economic study based on the working times of robotic tasks.

The aim is to increase the profitability of production lines by designing flexible manufacturing systems. This allows companies to stay competitive because of the quick adaptation to rapidly changing markets. For instance, by adjusting the working hours in assembly lines or by deciding which products are more suitable to be manufactured according to the current demand.

This is performed by posing a multiobjective optimization problem, which makes use of the optimization algorithm, above presented, to solve the kinematics and dynamics of robot arms. The optimization method finds the minimum time trajectory to perform industrial tasks in production lines while taking into consideration the physical constraints of the real posed problem and then economic issues are also considered in the process.

Furthermore, Pareto fronts will be introduced, which will serve to determine those variables which mainly affect the improved productivity. To be more precise, the multiobjective optimization problem allows obtaining the Pareto frontiers,

which provides information about the trade-offs between the competing variables (i.e., execution times and benefits for the different products that can be manufactured at the production line).

Therefore, the economic study starts by defining the economic objective function to be used. It is formulated as follows:

$$\text{Max } B = \frac{1}{(1+r)^T} \left[\sum_{p=1}^n (P_p - C_p) \cdot N_p(t) \right], \quad (23)$$

where B is the objective function to be maximized and represents the current value of the net benefit from a generic product (in €) defined as the revenue of the items manufactured at a production line minus total costs; r is the annual discount rate; T represents number of years; P_p is the market unitary price of the product p (in €); C_p stands for the unitary cost to perform the product p (in €), ranging from costs of raw materials, energy, amortization, labor force, maintenance, and taxes to direct and indirect costs; $N_p(t)$ is a function accounting for the number of products carried out per hour. It is calculated like

$$N_p(t) = \frac{K}{t(S_k)^\mu}, \quad (24)$$

where S_k is the set of tasks needed to manufacture and assemble a certain product (p) and it constitutes the work load, where k represents the number of tasks. $t(S_k) = \sum_{j \in S_k} t_j$ is the cumulated task time and it is called the product time. A cubic function of t_{\min} has been considered. μ is a parameter that refers to the economic environment and the market seasonality. K is a constant related to the current number of working hours per year.

Each one of these tasks is performed by the robot arm, which uses a certain time to describe the optimal trajectory. As above mentioned, the developed algorithm (Section 3) returns the minimum time $t_{\min p}$ to perform the task of the robot arm in order to obtain the product p , while considering the time of the other tasks as constant. The lower the time used by the robot to perform its task, the greater the number of products manufactured per hour. Then, the cumulative time of all tasks can be defined as follows:

$$t(S_k) = t_{\min p} + \sum_{j \in S_{\text{robot}}} t_j. \quad (25)$$

Besides, the amount that an additional item adds to a company's total revenue during a period is called the marginal revenue of the product (MRP).

This factor is defined as the additional products manufactured per hour because of reducing the time used by the robot arm ($t_{\min p}$). The additional products manufactured increase the company's output and, therefore, the company's total revenue.

The marginal revenue product can be obtained by multiplying the marginal product (MP) of the factor by the marginal revenue (MR). In a perfectly competitive market, the marginal revenue a company receives equals the market-determined price of the product P_p .

Therefore, for companies in perfect competition, the marginal revenue product MRP can be expressed as follows:

$$\text{MRP} = \text{MP} \times P_p. \quad (26)$$

The law of diminishing marginal returns tells us that if the quantity of a factor is increased while other inputs are held constant, its marginal product will eventually decline. If marginal product is falling (MP ↓), MRP must be falling as well (MRP ↓).

The marginal revenue of a product (calculated in Section 7) will be used to obtain the total annual benefits in an assembly line, as well as to determine the trade-offs between the benefits and the times obtained in the multiobjective optimization problem.

6. Pareto Optimality

Many real-world problems face two different types of mathematical difficulties. Those difficulties are the existence of multiple and conflicting objectives and a highly complex search space. Contrary to a single optimal solution, competing goals entail a set of compromise solutions generally denoted by the Pareto-optimal, for example, [18]. When there is lack of preference information, none of the corresponding trade-offs between decision variables could be said to be better than that of others. The optimal set of solutions in multiobjective optimization problems is named the Pareto-optimal set.

A solution is defined as Pareto optimal if no improvement in one objective can be accomplished without adversely affecting at least one other objective. In the objective space, the hypersurface that represents all possible Pareto-optimal solutions is termed as the Pareto front or frontier. A design that is located along the Pareto front is neither better nor worse than any other solution along the Pareto front. Hence, the solutions that compose the Pareto-optimal set are equivalently optimal. The objective of multiobjective optimization using this technique is to generate as many Pareto-optimal solutions as possible to adequately represent the Pareto front. This allows obtaining sufficient information for a trade-off decision between competing variables. The Pareto front can be discontinuous, concave, or convex and, in general, is not known a priori.

The concept of domination enables the comparison of a set of designs with multiple objectives. Such a concept is not required for single objective optimization on account of the fact that the value of the objective function is the only measure of the quality of the design.

Then, in a direct comparison of two designs, if one design dominates another, the dominating design is superior and nearer to the Pareto front. Instead, if neither design dominates the other, the designs are nondominant to each other. Therefore, the best designs (with equally good objective vectors) in an arbitrary set of solutions can be distinguished because they are not dominated by any other design in the set; they compose the nondominated subset. Similarly, the designs that compose the Pareto-optimal set are the nondominated set associated with the entire feasible space and are located along the Pareto front.

TABLE 2: Working times needed to perform the trajectory for each example.

Example		1	2	3	4	5	6	7	8	9	10
Optimization algorithm	Working time (s)	0.7488	0.5909	0.7511	1.5557	0.7488	0.5115	1.3920	0.7118	0.4529	1.0000
	Example	11	12	13	14	15	16	17	18	19	20
	Working time (s)	0.7488	0.5909	0.7511	1.5557	0.7488	0.5115	1.3920	0.7118	0.4529	1.0000
Example		1	2	3	4	5	6	7	8	9	10
Simulation software GRASP	Working time (s)	0.7500	0.6200	0.7700	1.6000	0.7600	0.5300	1.4000	0.7200	0.4600	1.2000
	Example	11	12	13	14	15	16	17	18	19	20
	Working time (s)	0.7500	0.6000	0.7600	1.5600	0.7500	0.5200	1.4300	0.7400	0.4600	1.3000

Consequently, the trajectory planning optimization problem in robotics can be defined as finding a motion law along a given geometric path, taking into account some predefined requirements, while generating minimum trajectory time of the robot arm. The inputs of the trajectory planning problem are the geometric path and the kinematic and dynamic constraints, while the output is the trajectory of the joints (or of the end-effector). The trajectory is expressed as a time sequence of position, velocity, and acceleration values. The optimized trajectory should also meet the physical limitations of the robot, the constraint of energy consumption and collisions avoidance.

The times obtained from the simulation-optimization procedures lead to different benefits. Therefore the Pareto fronts can be determined, thus showing the trade-offs between the benefits and the obtained times. They show the opportunity cost of time higher than the minimum (see Section 7).

7. Results of the Application of the Methodology to Different Examples

The proposed multiobjective optimization methodology and the Pareto optimality have been applied to different examples in order to set the above mentioned trade-offs between the benefits and the obtained times. Therefore, now the objective is conducting an economic study to quantify the productivity of the assembly line by comparing the minimum time trajectory to perform certain industrial tasks. It is obtained using two methods: an optimization algorithm and the simulation software GRASP.

These times are obtained while taking into consideration the physical constraints of the real working problem and the economic issues involved in the process. Twenty examples have been solved. The examples differ in the initial and final configurations of the robot, that is, the location of the end-effector (see Table 2). The optimization algorithm simulates the PUMA 560 robot.

This industrial robot arm is probably the most common robot in university laboratories. It is a 6-R (revolution) type robot, with 6 degrees of freedom, and uses direct current (DC) servo motors as its actuators. This robot is a compact computer-controlled robot not only to perform service tasks, but also to carry out medium-to-lightweight assembly, welding, materials handling, packaging, inspection

applications, personal care, and so forth. The Series 500 is the most widely used model in the PUMA line of electrically driven robots.

With a 36-inch reach and 5-pound payload capacity, this robot is designed with a high degree of flexibility and reliability. The range of these angles from θ_1 to θ_6 is the following (320°, 250°, 270°, 280°, 200°, and 532°). The corresponding link lengths from L1 to L6 are (432, 432, 433, 56, 56, and 37.5) mm.

Table 2 presents the results obtained for the developed algorithm and GRASP, that is, the working time required for the robot to perform the industrial tasks.

With regard to the economic issues associated with the robot industrial tasks we suppose for all examples the following quantities and considerations:

unitary cost to produce a certain item: 0.8 € (without considering the cost of the energy consumed);

item price: 1 €. For the sake of simplicity, we assume that only one product is produced at this point.

When the cost of the energy consumed is considered, the different examples have different costs because of the different working times. Therefore cost of the consumed energy: 0.0676 €/kWh (it is an average cost). This cost has been added to the cost of 0.8 €.

For reasons of clarity, the manufactured products are obtained in only one shift of 8 hours (365 working days in a year). The benefits B are presented for a period of one year.

The time of the other industrial tasks needed to produce the item has been defined as 90 s, that is, the summation of times shown in (25), $\sum_{j \in S_{\text{robot}}}^k t_j$.

The optimization algorithm presents different working times for the different examples, thus leading also to different benefits.

For instance, the case number 19, which has no constraints in both the jerk and the energy consumed, presents the maximum annual revenue (Figure 1). Contrary, case 4, with severe physical constraints, shows the minimum benefits.

The benefits for all examples obtained by means of the optimization algorithm are depicted in Figure 1. With the current demand, the mean value of the benefit for the 20 examples analyzed is 23,142.40 €/year, while the standard deviation is 90.32.

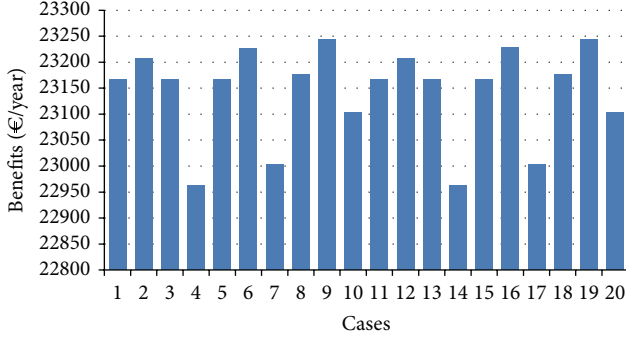


FIGURE 1: Annual revenue for each example based on the current demand.

The industrial tasks are carried out in only a few seconds, so that the time scale is based on seconds. Note that the GRASP working times are similar to those obtained with the developed optimization algorithm, although slightly higher.

Then total benefits are also similar to those reported in Figure 1, although the higher working times lead to lower benefits.

Consequently, a lower mean value of the benefits is obtained, that is, 23,132.84 €/year with a standard deviation of 96.02.

Note that different prices, costs, and number of items produced by year may lead to higher differences in benefits between the optimization algorithm and GRASP. However, the selected values are only intended to illustrate the importance of using efficient algorithms of robot trajectory optimization for saving time and reducing costs in production lines.

In addition, a new analysis is carried out using Pareto optimality to illustrate the loss of benefits on account of not using optimization algorithms.

For that, we consider that three different products can be manufactured and assembled in the same production line. The loss of benefits is represented by the Pareto fronts for three different products. They differ in their cumulative time to be manufactured and assembled but share the same working time ($t_{\min p}$) of the robot arm.

Then the minimum trajectory time for case 4 is used for the three products, in this example, 1.55 s. These products also differ in the total costs (without considering the energy costs), prices, and values of the parameter μ , which is intended to simulate different economic environments and market seasonality. The total cost of Product 1 is 0.8 €, Product 2 is 0.82 €, and Product 3 is 0.84 €, while the prices are 1.0 € for Product 1, 1.05 € for Product 2, and 1.03 € for Product 3. In this analysis, $t(S_k)$ has been defined as a cubic function of $t_{\min p}$. The parameter μ takes the values for each product of 0.6, 0.5, and 0.55, respectively.

Consequently, if the market conditions do not change and the optimization algorithm is not used, the minimum trajectory time is not obtained.

In this scenario, there is a benefit loss due to the fact that robot arm may present higher working times.

Moreover, the multiobjective optimization problem allows obtaining the Pareto frontiers, which provides

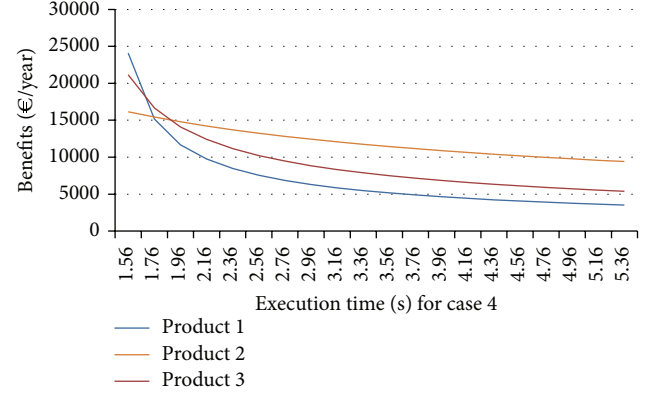


FIGURE 2: Pareto frontiers obtained with the optimization algorithm for “example 4” and the three different products manufactured.

information about the trade-off of the decision variables. One main trade-off is between the benefits and the working time (i.e., the Pareto frontier). Results for example 4 are shown in Figure 2, considering the manufacturing of three different products. That is, the algorithm allows quantifying the benefit loss because of not using the optimization algorithm. Each solution in the front will have optimal objective function value, optimal value of variables, and the constraints value. All constraints will be satisfied by any solution in the Pareto optimal front.

It is worth pointing out that for the analyzed examples, the differences between their annual energy costs are almost negligible compared with the other costs.

Furthermore, the concept of nondomination sorting can be used to categorize each design within a set into a hierarchy of nondominated levels or fronts. Each different level of nondomination represents a relative distance from the Pareto front. The best nondominated front is closest to the Pareto front and each subsequent front lags further behind and is, hence, increasingly inferior.

Through this sorting, each design is associated with a front that defines the quality of the design relative to the rest of the group. To isolate the various fronts, the designs that belong to the nondominated subset of the entire group are first identified. These designs are the best in the group, the closest to (or members of) the Pareto front. For instance, in our multiobjective trajectory optimization, the nondominated subset (i.e., the best solution in terms of greater benefits) is represented by the Pareto frontier of Product 2 for times higher than 1.96 s (see Figure 2).

Any design belonging to this front is then temporarily set aside and another comparison process determines the next level of nondominated designs from the remaining population.

This nondominated subset is the front of Product 3 and the procedure is repeated until the entire population has been sorted into the appropriate level, that is, the Pareto frontier of Product 1.

Note, however, that for working times lower than 1.76 s the Pareto frontier of Product 1 dominates the frontier of Product 2. That is, higher benefits are expected to be achieved in the assembly line for Product 1.

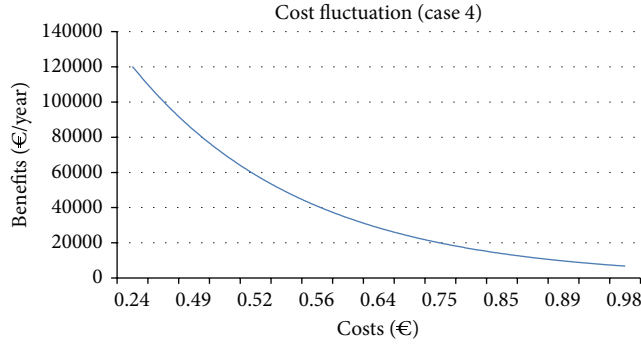


FIGURE 3: Benefits obtained for Product 1 and “example 4” versus costs.

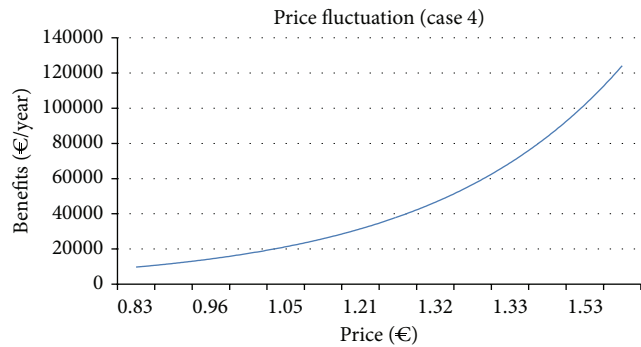


FIGURE 4: Benefits obtained for Product 1 and “example 4” versus price.

Additionally, for the twenty examples analyzed in this work, a normal distribution function of the cost (C) and the price (P) has been defined for a certain product based on the current market economic fluctuations. The benefits resulting from these market fluctuations are provided in Figures 3 and 4.

Figure 3 has been obtained when a normal distribution of the cost fluctuation is considered on account of hypothetical market changes. The statistics that define the normal distribution (mean and variance) are based on the current total costs above mentioned.

Figure 4 has been obtained when a normal distribution of the price fluctuation is considered on account of hypothetical market changes. The statistics that define the normal distribution (mean and variance) are based on the current prices.

For the sake of conciseness, the cost and price fluctuations have been considered only for Product 1. Its current market values are $m_c = 0.8\text{€}$ for costs and $m_p = 1\text{€}$ for prices, while the standard deviation (σ) is defined as $m/3$. With these functions, the market changes, regarding costs and prices, are intended to be modeled. $C(C = C_p * N_p)$ gives the cost to manufacture p products (N_p). P_p gives the revenue as defined by (2), that is, multiplying the price of the products manufactured.

These functions are sampled, with these values being used in the multiobjective optimization problem to obtain the results presented in Figures 3 and 4.

These figures show a hypothetical fluctuation in the market conditions with regard to costs and prices for case 4.

The fluctuations can be directly translated into benefits using the algorithm, thus allowing managers in the decision making process regarding which products should be manufactured, and also to define an efficient scheduling. Therefore, the design and planning of the robot tasks are considerably improved.

Finally, the algorithm has also been run for example 4 to simulate an increase in the future demand of a 20% compared with the current demand (i.e., a total of 137,778 products manufactured per year). The aim is to answer the question about how many extra working hours are needed to respond to that increase in the demand. The best solution is given by the optimization algorithm, since it reports the minimum trajectory time. The solution is that we need an additional 3,504 hours per year to meet such demand. This information can be used during the decision making process to design an efficient scheduling.

8. Conclusions

This work deals with trajectory planning of industrial robots for assembly lines in a cost-efficient way, thus overcoming limitations of the economic analysis methods which are currently available. It has been demonstrated that the multiobjective optimization algorithm finds the minimum time trajectory of industrial robots and the maximum annual revenue. This means greater annual revenue and better adaptation to market fluctuations in terms of costs, prices, and product demands. This is carried out by taking under consideration the physical constraints of the real working problem and the economic issues involved in the process. The proposed procedure has been successfully validated in different examples of robotic industrial tasks, where a better planning and design of production lines have been found.

The results from different examples have been compared using two methodologies, an optimization procedure and a simulation technique.

We have checked that the results obtained with the optimization procedure lead to lower working times and therefore greater annual revenues in comparison with those obtained with the simulation technique. Consequently the number of products manufactured and profits are increased while the number of the shifts required is reduced. The core of this paper is the procedure to obtain the best working times in real complex industrial robots with many degrees of freedom and mechanical constraints.

This has shown the worth of the methodology, with the overall objective of improving the profitability of production lines by designing flexible manufacturing systems. Furthermore, an entire set of equally optimal solutions for each process, the Pareto-optimal sets, are generated.

This provides information about the trade-offs between the different competing variables of the multiobjective optimization problem (i.e., working times and profits for the different products that can be manufactured at the production line).

Once the optimal time to perform each process is obtained in a cost-effective manner the results can be used for improving a wide variety of robotic industrial tasks. This can help managers in the decision making process regarding which products should be manufactured and to define an efficient scheduling to produce them. This is because it allows adjusting the number of shifts needed according to the existing demand of the products manufactured. Then companies may stay competitive because the algorithm allows a quick adaptation to rapidly changing markets.

As a further research this methodology will be extended to deal with new decision variables in the multiobjective optimization problem such as the energy consumed and time simultaneously since they are conflicting variables.

Conflict of Interests

The authors declare that there is no conflict of interests regarding the publication of this paper.

Acknowledgment

This paper has been possible due to the funding from the Science and Innovation Ministry of the Spanish Government by means of the Researching and Technologic Development Project DPI2010-20814-C02-01 (IDEMOV).

References

- [1] J. E. Bobrow, S. Dubowsky, and J. S. Gibson, "Time-optimal control of robotic manipulators along specified paths," *International Journal of Robotics Research*, vol. 4, no. 3, pp. 3–17, 1985.
- [2] K. G. Shin and N. D. McKay, "Minimum -time control of robotic manipulators with geometric path constraints," *IEEE Transactions on Automatic Control*, vol. AC-30, no. 6, pp. 531–541, 1985.
- [3] Y. Chen and A. A. Desrochers, "Structure of minimum-time control law for robotic manipulators with constrained paths," in *Proceedings of the IEEE International Conference on Robotics and Automation*, pp. 971–976, Scottsdale, Ariz, USA, May 1989.
- [4] J. Mattmüller and D. Gislser, "Calculating a near time-optimal jerk-constrained trajectory along a specified smooth path," *International Journal of Advanced Manufacturing Technology*, vol. 45, no. 9-10, pp. 1007–1016, 2009.
- [5] K. J. Kyriakopoulos and G. N. Saridis, "Minimum jerk path generation," in *Proceedings of the IEEE International Conference on Robotics and Automation*, vol. 1, pp. 364–369, Philadelphia, Pa, USA, 1988.
- [6] D. Simon and C. Işık, "A trigonometric trajectory generator for robotic arms," *International Journal of Control*, vol. 57, no. 3, pp. 505–517, 1993.
- [7] D. Constantinescu and E. A. Croft, "Smooth and time-optimal trajectory planning for industrial manipulators along specified paths," *Journal of Robotic Systems*, vol. 17, no. 5, pp. 233–249, 2000.
- [8] P. Huang, Y. Xu, and B. Liang, "Global minimum-jerk trajectory planning of space manipulator," *International Journal of Control, Automation and Systems*, vol. 4, no. 4, pp. 405–413, 2006.
- [9] D. Garg and C. Ruengcharungpong, "Force balance and energy optimization in cooperating manipulators," in *Proceedings of the 23rd Annual Pittsburgh Modeling and Simulation Conference*, pp. 2017–2024, Pittsburgh, Pa, USA, 1992.
- [10] A. R. Hirakawa and A. Kawamura, "Proposal of trajectory generation for redundant manipulators using variational approach applied to minimization of consumed electrical energy," in *Proceedings of the 4th International Workshop on Advanced Motion Control (AMC '96)*, pp. 687–692, Mie, Japan, March 1996.
- [11] B. H. Cho, B. S. Choi, and J. M. Lee, "Time-optimal trajectory planning for a robot system under torque and impulse constraints," *International Journal of Control, Automation and Systems*, vol. 4, no. 1, pp. 10–16, 2006.
- [12] G. Field and Y. Stepanenko, "Iterative dynamic programming: an approach to minimum energy trajectory planning for robotic manipulators," in *Proceedings of the 13th IEEE International Conference on Robotics and Automation*, pp. 2755–2760, Minneapolis, Minn, USA, April 1996.
- [13] X. F. Zha, "Optimal pose trajectory planning for robot manipulators," *Mechanism and Machine Theory*, vol. 37, no. 10, pp. 1063–1086, 2002.
- [14] F. Valero, V. Mata, and A. Besa, "Trajectory planning in workspaces with obstacles taking into account the dynamic robot behaviour," *Mechanism and Machine Theory*, vol. 41, no. 5, pp. 525–536, 2006.
- [15] F. J. Valero, J. L. Suñer, V. Mata, and F. J. Rubio, "Optimal time trajectory for robots with torque jerk and energy constraints," in *Proceedings of the ECCOMAS Thematic Conference on Multi-body Dynamics*, 2009.
- [16] F. Rubio, F. Valero, J. Sunyer, and V. Mata, "Direct step-by-step method for industrial robot path planning," *Industrial Robot*, vol. 36, no. 6, pp. 594–607, 2009.
- [17] J. L. Suñer, F. J. Valero, J. J. Ródenas, and A. Besa, "Comparación entre procedimientos de solución de la interpolación por funciones splines para la planificación de trayectorias de robots industriales," in *Proceedings of the 8th Congreso Iberoamericano de Ingeniería Mecánica*, Cusco, Peru, October 2007.
- [18] R. Sanders, "The pareto principle: its use and abuse," *Journal of Product & Brand Management*, vol. 1, no. 2, pp. 37–40, 1992.

Research Article

Numerical Simulation of the Generalized Newtonian Free Surface Flows by a Density Reinitialization SPH Method

Jinlian Ren,¹ Weigang Lu,¹ and Tao Jiang^{1,2}

¹ Department of Mathematics, School of Hydraulic, Energy and Power Engineering, Yangzhou University, Yangzhou 225002, China

² Department of Applied Mathematics, Northwestern Polytechnical University, Xi'an 710129, China

Correspondence should be addressed to Tao Jiang; jtrjl_2007@126.com

Received 15 June 2014; Revised 22 October 2014; Accepted 23 October 2014

Academic Editor: Kim M. Liew

Copyright © 2015 Jinlian Ren et al. This is an open access article distributed under the Creative Commons Attribution License, which permits unrestricted use, distribution, and reproduction in any medium, provided the original work is properly cited.

A periodic density reinitialization smoothed particle hydrodynamics (PDRI-SPH) method is proposed to treat the generalized Newtonian free surface flows, which is based on the concept of Taylor series expansion. Meanwhile, an artificial stress term is also presented and tested, for the purpose of eliminating the unphysical phenomenon of particle clustering in fluid stretching. The free surface phenomena of a Cross model droplet impacting and spreading on an inclined rigid plate at low impacting angles are investigated numerically using the proposed PDRI-SPH method. In particular, the effect of the surface inclination and the different regimes of droplet impact, spreading and depositing on an inclined surface, are illustrated; the influence of surface inclination on the tensile instability is also concerned. The numerical results show that the accuracy and the stability of the conventional SPH are all improved by the periodic density reinitialization scheme. All numerical results agree well with the available reference data.

1. Introduction

The problems of free surface flows for polymers are important in today's industry, such as the structured reactors, surface coating, container filling in the food, and pharmaceutical industries of polymers. All the flows involved almost exhibit nonlinear behavior, for example, the viscoelastic or shear-thinning behavior. In these processes, the impacting, spreading, and depositing of liquid droplets on solid surface play a crucial role.

In the early stage of research, many methods based on the Eulerian description of motion are mainly presented to capture the complex free surface of polymers, including particle in cell (PIC) [1], marker and cell (MAC) [2], volume of fluid (VOF) [3], level set [4], and phase-field [5] methods. These methods are based upon grid-based numerical methods such as finite difference methods (FDM) and finite element methods (FEM) that are commonly used to solve the Navier-Stokes equations. However, it is difficult for the simulation of large deformation.

In order to overcome the shortcomings of grid-based methods and effectively handle the problem of large

deformation, the various mesh-free methods [6–8] or particle methods have been proposed in a Lagrangian framework. Among the various particle methods [9–12], the smoothed particle hydrodynamics (SPH) method [9, 13] is the earliest one and it is also most widely used. The SPH has the following main advantages over grid-based methods. (1) It handles convection dominated flows and large deformation problems without any numerical diffusion. (2) Complex free surfaces are modeled easily and naturally without the need of explicit surface tracking technique. (3) It is easy to program for complex problems compared with grid-based methods. In 1994, it was firstly used to deal with fluid mechanic problems [14]. Since then, it has been extensively studied in many areas such as viscous flows [15, 16], incompressible fluids [17, 18], multiphase flows [19, 20], geophysical flows [21, 22], viscoelastic flows [23, 24], and viscoelastic free surface flows [25].

Unfortunately, the consistency between mass, density, and occupied area cannot be enforced exactly (see [15, 26]) when the evolved particle density is obtained by the continuity equation in standard SPH method [23–25]. In this work, a periodic density reinitialization method based on

the corrective kernel estimate [27] of a Taylor series expansion is proposed to overcome the problem of the consistency between mass, density, and the occupied area. Moreover, we can know that the tensile instability is related to the sign of both the stress and the second derivative of the kernel function as noticed by [28]. And then, a changing artificial stress term is presented and tested to remove the unphysical phenomenon of particle clustering in the simulations of a generalized Newtonian droplet impact and spreading on an inclined rigid plate, which is different from the one in [25].

This paper has been directly motivated by the polymer industry where materials tend to be shear-thinning but not necessarily viscoelastic. Due to the fact that the Cross model [29] or some similar model can describe the shear-thinning behavior better, then here we choose the Cross model. In general, the phenomena of free surface can be complex. Therefore, the two-dimensional shear-thinning free surface flows of a Cross droplet impact and spreading on an inclined rigid plate are discussed. During these processes, the effect and ability of the mentioned above periodic density reinitialization method and artificial stress term for capturing the complex polymer free surfaces are also analyzed.

The structure of this paper is organized as follows. The governing equations for the Cross model are introduced in Section 2. Section 3 describes the PDRI-SPH discretization of the Navier-Stokes equations, including artificial viscosity, boundary conditions, and temporal discretization of the governing equations. In particular, the density reinitialization method and tensile instability are also discussed in Section 3. In Section 4, the validity of the proposed PDRI-SPH combined with the mentioned artificial stress term is first tested. Subsequently, a numerical example of a Cross model droplet impacting on an inclined dry surface is solved to demonstrate the capability of the PDRI-SPH method in handling generalized Newtonian free surface flows. Some concluding remarks are reported in Section 5.

2. Governing Equations for the Cross Model

2.1. Governing Equations. In a Lagrangian frame, the generalized Newtonian fluid is governed by the conservation of mass and momentum equations, together with a nonlinear constitutive equation. The isothermal, incompressible fluid is usually described by the following equations:

$$\frac{D\rho}{Dt} = -\rho \frac{\partial v^\beta}{\partial x^\beta}, \quad (1)$$

$$\frac{Dv^\alpha}{Dt} = \frac{1}{\rho} \frac{\partial \sigma^{\alpha\beta}}{\partial x^\beta} + g^\alpha, \quad (2)$$

where ρ denotes the fluid density, v^β the β th component of the fluid velocity, $\sigma^{\alpha\beta}$ the (α, β) th component of the total stress tensor, g^α is the α th component of the gravitational acceleration, and the $D/Dt = \partial/\partial t + v^\beta \cdot (\partial/\partial x^\beta)$ is the material derivative. The spatial coordinates x^β and time t are the independent variables.

The total stress tensor in (2) is commonly made up of the isotropic pressure p and the components of extra stress tensor $\tau^{\alpha\beta}$:

$$\sigma^{\alpha\beta} = -p\delta^{\alpha\beta} + \tau^{\alpha\beta}, \quad (3)$$

where $\delta^{\alpha\beta} = 1$ if $\alpha = \beta$ and $\delta^{\alpha\beta} = 0$ if $\alpha \neq \beta$. In order to study a shear-thinning polymer material, the relating constitutive equation must be provided.

2.2. Cross Model. In this paper, the surface problem based on the generalized Newtonian fluid is mainly considered. The generalized Newtonian fluid displays more complex fluid characters than the Newtonian fluid, and the constitutive model for describing the generalized Newtonian fluid can be derived from the Newtonian model; that is, the viscosity is variable for the generalized Newtonian fluid. Several constitutive models for describing generalized Newtonian fluid have been proposed, in which the Cross fluid model with four parameters (see (6)) [29, 30] is usually used to represent the polymer material and describe the shear-thinning behavior during polymer processing. Then the typical constitutive model of Cross fluid with four parameters is employed to study the influences of shear-thinning behavior on the free surface in polymers impact process. It is worth noting that the surface tension is not considered in the following simulations. The measure of fluid droplet is centimeter level in the following simulations, so that the effect of surface tension can be omitted according to the physical knowledge. In addition, the detailed description of Cross model with four parameters can also be found in [29, 30].

The extra stress tensor τ for the generalized Newtonian fluid based on the Cross model [29, 30] is expressed as

$$\tau = 2\mu(\dot{\gamma}) \mathbf{d}, \quad (4)$$

where $\mu(\dot{\gamma}) = \rho\nu(\dot{\gamma})$ is the dynamic viscosity and the $\nu(\dot{\gamma})$ is the kinematic viscosity. The symmetric strain rate tensor \mathbf{d} is defined as

$$\mathbf{d} = [d^{\alpha\beta}] = \frac{1}{2} \left[\frac{\partial v^\alpha}{\partial x^\beta} + \frac{\partial v^\beta}{\partial x^\alpha} \right]. \quad (5)$$

The kinematic viscosity $\nu(\dot{\gamma})$ represents the shear-thinning nature of the fluid; it is defined as

$$\nu(\dot{\gamma}) = \nu_\infty + \frac{\nu_0 - \nu_\infty}{(1 + (K\dot{\gamma})^m)}, \quad (6)$$

where m , ν_0 , ν_∞ , and K are given positive constants. The $\dot{\gamma}$ is the local shear rate defined by

$$\dot{\gamma} = [2 \operatorname{tr}(\mathbf{d}^2)]^{1/2}, \quad (7)$$

and the symbol “tr” denotes the trace of matrix. Here, the positive constants K and m are all chosen equal to 1.0.

2.3. Equation of State. The incompressible flows were sometimes treated as slightly compressible flows by adopting a suitable equation of state in many previous works (see

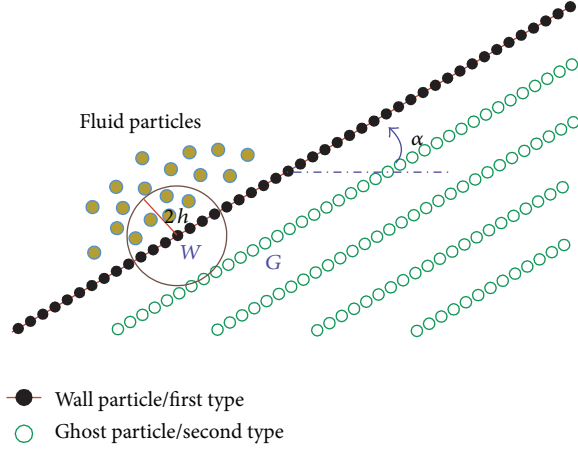


FIGURE 1: The sketch of wall particle and ghost particle at impact angle of α .

Monaghan [14] and Morris et al. [15]). Here, the incompressible flows are also treated as weakly compressible flows using the following equation of state [24]:

$$p(\rho) = \frac{c^2 \rho^2}{2\rho_0}, \quad (8)$$

where c is the speed of sound and ρ_0 is reference density. An artificial, lower sound speed is usually used to avoid the instability and extremely small time steps. To keep the density variation of fluid less than 1% of the reference density, the Mach number M ($M \equiv V/c$, where V is a typical reference velocity) [9] must be smaller than 0.1. In other words, the sound speed must be ten times higher than maximum fluid velocity.

3. PDRI-SPH Formulation

3.1. Discretization Schemes of Standard SPH. The SPH method [9, 13] is based on the interpolation theory, which is the theory of integral interpolates using a kernel function. Namely, the fluid domain Ω is discretized into a finite number of particles, where all the relevant physical quantities are approximated in terms of the integral representation over neighboring particles. Each particle carries a mass m , velocity \mathbf{v} , and other physical quantities depending on the problem. Any function $f(\mathbf{r})$ defined at the position $\mathbf{r} = (x, y)$ can be expressed by the following integral:

$$\langle f(\mathbf{r}) \rangle = \int_{\Omega} f(\mathbf{r}') W(\mathbf{r} - \mathbf{r}', h) d\mathbf{r}', \quad (9)$$

where W represents the kernel function (or smoothing function) and h denotes the smoothing length defining the influence area of W . The kernel function W is usually required to meet three properties, namely, the regular condition, Dirac delta function property, and compactly supported condition [9, 13]. In addition, the smoothing function is also usually chosen as an even function over Ω .

According to (9), the integrating principle by parts and the divergence theorem, the particle discretization scheme of

standard SPH for a function $f(\mathbf{r})$, and its first derivative at the position $\mathbf{r} = (x, y)$ of the particle i can be written in the following condensed forms:

$$f_i = \sum_j \frac{m_j}{\rho_j} f_j W_{ij}, \quad (10)$$

$$\left(\frac{\partial f}{\partial \mathbf{r}_i} \right) = \sum_j \frac{m_j}{\rho_j} (f_j - f_i) \frac{\partial W_{ij}}{\partial \mathbf{r}_i}, \quad (11)$$

where m_j and ρ_j are the mass and density of the j th particle, and $f_j = f(\mathbf{r}_j)$. The m_j/ρ_j represents the occupied volume by the j th particle. The $W_{ij} = W(|\mathbf{r}_i - \mathbf{r}_j|, h)$, $\partial W_{ij}/\partial \mathbf{r}_i = -\partial W_{ji}/\partial \mathbf{r}_j$.

In this paper, the cubic spline function is chosen as the smoothing function which is the function about $r_{ij} = |\mathbf{r}_i - \mathbf{r}_j|$ and $q = r_{ij}/h$. Then it reads for 2-D as follows:

$$W_{ij} = W(r, h) = \frac{15}{7\pi h^2} \begin{cases} \frac{2}{3} - q^2 + \left(\frac{1}{2}\right)q^3, & 0 \leq q < 1, \\ \left(\frac{1}{6}\right)(2 - q)^3, & 1 \leq q < 2, \\ 0, & q \geq 2. \end{cases} \quad (12)$$

In order to have an accurate interpolation, the smoothing length h should be chosen bigger than the mean interparticle distance. Here, the smoothing length h is given by $1.5d_0$ with d_0 as the initial distance between neighboring particles. The compact support domain size is $2h$.

Considering the discrete gradient equation (11) and the following identity: $(1/\rho)(\partial \sigma^{\alpha\beta}/\partial x^\beta) = \partial(\sigma^{\alpha\beta}/\rho)/\partial x^\beta + (\sigma^{\alpha\beta}/\rho^2)(\partial \rho/\partial x^\beta)$, the particle discretization schemes of the governing equations can be obtained at the particle i :

$$\left(\frac{D\rho}{Dt} \right)_i = \rho_i \sum_j \frac{m_j}{\rho_j} (v_i^\beta - v_j^\beta) \frac{\partial W_{ij}}{\partial x_i^\beta}, \quad (13)$$

$$\left(\frac{Dv^\alpha}{Dt} \right)_i = \sum_j m_j \left(\frac{\sigma_i^{\alpha\beta}}{\rho_i^2} + \frac{\sigma_j^{\alpha\beta}}{\rho_j^2} \right) \frac{\partial W_{ij}}{\partial x_i^\beta} + g^\alpha. \quad (14)$$

Introducing the velocity gradient

$$\kappa_i^{\alpha\beta} = \left(\frac{\partial v^\alpha}{\partial x^\beta} \right)_i = \sum_j \frac{m_j}{\rho_j} (v_j^\alpha - v_i^\alpha) \frac{\partial W_{ij}}{\partial x_i^\beta}, \quad (15)$$

then the particle approximation schemes of constitutive equation for the Cross model can be obtained as

$$\begin{aligned} \sigma_i^{\alpha\beta} &= -p_i \delta^{\alpha\beta} + \mu (\dot{\gamma}_i) (\kappa_i^{\alpha\beta} + \kappa_i^{\beta\alpha}), \\ \dot{\gamma}_i &= [2 \operatorname{tr}(\mathbf{d}_i^2)]^{1/2}. \end{aligned} \quad (16)$$

3.2. Density Reinitialization Method. In the standard SPH method, each particle has a fixed mass. If the number of particles is constant, mass conservation is intrinsically

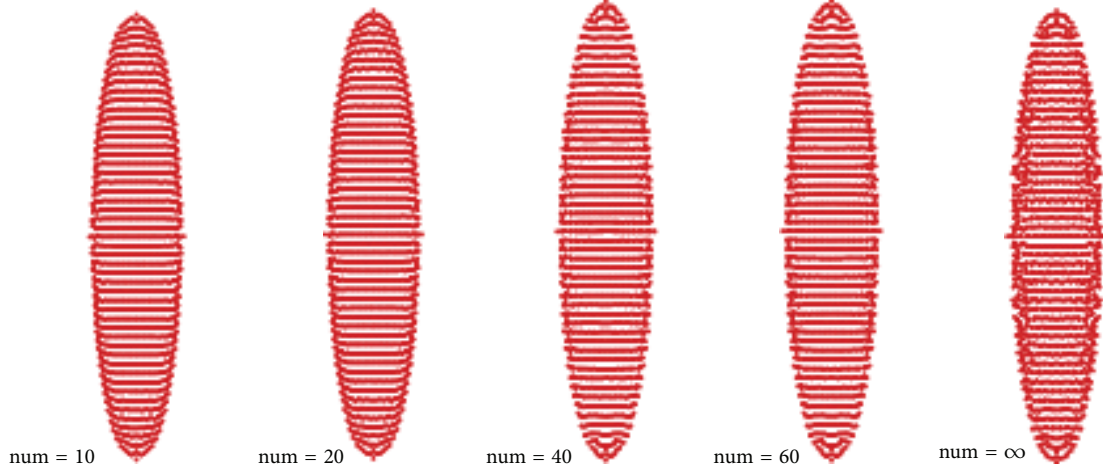


FIGURE 2: The position of particles calculated by PDRI-SPH method at the time 0.01 s.

satisfied. However, the consistency between mass, density, and the occupied area could not be enforced exactly (see [15, 26]) if the evolved particle density is determined by the evolution equation (1) for simulating the weakly compressible flows. Although the density field is periodically reinitialized by applying the following equation for removing this problem in [15]:

$$\rho_i = \sum_j m_j W_{ij}, \quad (17)$$

the particle approximations (17) do not have first order accuracy and C^0 , C^1 consistency for boundary regions or irregularly distributed particles (see [31]). Therefore, the above periodic density reinitialization method (see (17)) cannot well alleviate the above problem.

In order to well overcome this problem, we use a second-order accurate particle approximation scheme based on Taylor series expansion (see [27, 31]) to periodically reinitialize the density field:

$$\rho_i = \sum_j m_j W_{ij}^{\text{Tay}}, \quad (18a)$$

where the corrected kernel function W_{ij}^{Tay} is given by

$$W_{ij}^{\text{Tay}} = B \left[\sum_j A(\mathbf{r}_i) V_j \right]^{-1} W, \quad (18b)$$

$$A(\mathbf{r}_i) = \begin{pmatrix} W_{ij} & x_{ji} \cdot W_{ij} & y_{ji} \cdot W_{ij} \\ \frac{\partial W_{ij}}{\partial x_i} & x_{ji} \cdot \frac{\partial W_{ij}}{\partial x_i} & y_{ji} \cdot \frac{\partial W_{ij}}{\partial x_i} \\ \frac{\partial W_{ij}}{\partial y_i} & x_{ji} \cdot \frac{\partial W_{ij}}{\partial y_i} & y_{ji} \cdot \frac{\partial W_{ij}}{\partial y_i} \end{pmatrix},$$

$$B = (1, 0, 0), \quad W = \begin{pmatrix} W_{ij} \\ \frac{\partial W_{ij}}{\partial x_i} \\ \frac{\partial W_{ij}}{\partial y_i} \end{pmatrix}. \quad (18c)$$

Here $x_{ji} = x_j - x_i$, $y_{ji} = y_j - y_i$, and V_j is replaced by m_j/ρ_j . The particle approximations scheme (18a)–(18c) possesses C^0 , C^1 consistency for boundary regions or irregularly distributed particles (see [31]).

When the density reinitialization method is applied in above standard SPH method, an inversion matrix of 3×3 should be solved for each fluid particle; thus, the computing time is increased slightly. Considering the computational cost and the efficiency of using periodic density reinitialization, we can apply this procedure every fixed (about 10~40, see Section 4.1) time step in our numerical simulations. In particular, for the purpose of preserving that the corrected particle approximations (18a) at least have C^0 consistency on the whole domain, the matrix $\sum_j A(\mathbf{r}_i) V_j$ may be replaced by $\sum_j W_{ij} V_j$ if the matrix of (18b) is singular (it occurs occasionally). Now, the above discretization schemes of standard SPH combined with the periodic density reinitialization method may be called the “PDRI-SPH” method.

3.3. Artificial Viscosity Model. According to previous works [15, 32], the artificial viscosity is first introduced to enhance the numerical stability and accuracy in the simulations of strong shock problems [32]. On the other hand, the artificial viscosity term guarantees the conservation of the angular momentum without external force when it is added into the momentum equation of TSPH schemes. For that reason, the artificial viscosity term is usually also considered and employed in the SPH simulations of viscous or viscoelastic fluid flows problems with large deformation, which can be seen in recent works [18, 25, 33]. Through the simulations

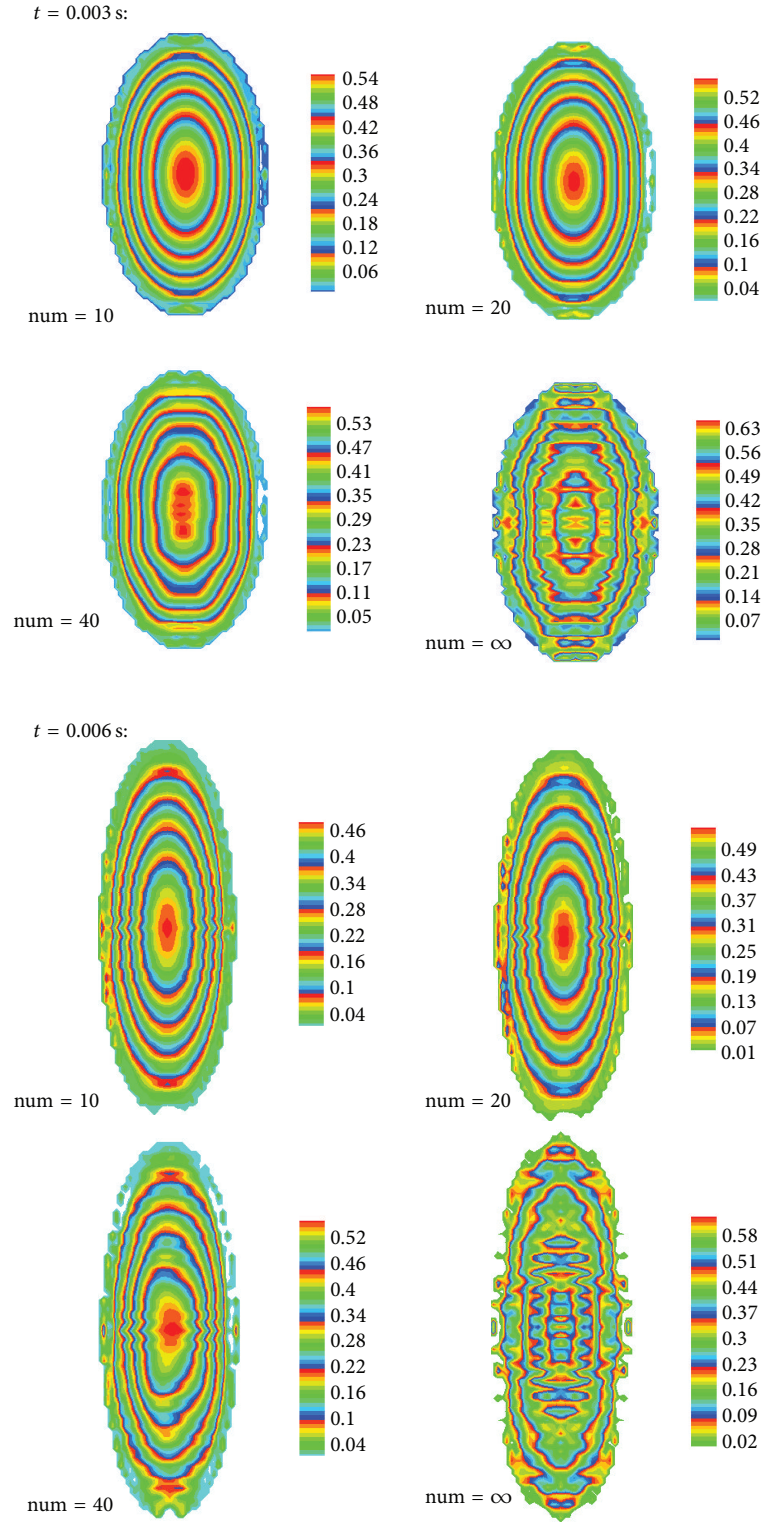


FIGURE 3: The pressure field distribution ($p/10^7$) obtained using the PDRI-SPH method with different “num” at time 0.003 s and 0.006 s, respectively.

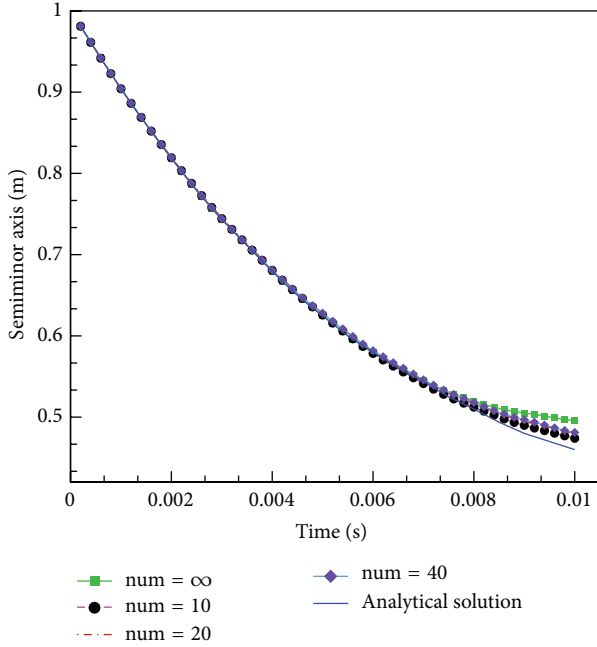


FIGURE 4: The comparisons of numerical results obtained using PDRI-SPH method about the semiminor axis varying with time.

of viscoelastic droplet impact problem in [25] and our numerical simulation experience of using SPH or improved SPH method, we find that it is necessary to employ an artificial viscosity term in the discrete momentum equation (14) for improving the numerical stability (see Section 4.2). Here, the artificial viscosity term is also added to the discrete momentum equation (14) of PDRI-SPH method, which is usually chosen as [32, 34]

$$\Pi_{ij} = \begin{cases} \frac{-\alpha_{\Pi} \bar{c}_{ij} \phi_{ij} + \beta_{\Pi} \phi_{ij}^2}{\bar{\rho}_{ij}}, & \mathbf{v}_{ij} \cdot \mathbf{r}_{ij} < 0, \\ 0, & \mathbf{v}_{ij} \cdot \mathbf{r}_{ij} \geq 0, \end{cases} \quad (19a)$$

where

$$\phi_{ij} = \frac{h \mathbf{u}_{ij} \cdot \mathbf{r}_{ij}}{|\mathbf{r}_{ij}|^2 + 0.01h^2}, \quad \bar{c}_{ij} = \frac{c_i + c_j}{2}, \quad \bar{\rho}_{ij} = \frac{\rho_i + \rho_j}{2}, \quad (19b)$$

$$\mathbf{v}_{ij} = \mathbf{v}_i - \mathbf{v}_j, \quad \mathbf{r}_{ij} = \mathbf{r}_i - \mathbf{r}_j.$$

The $0.01h^2$ term is included to prevent numerical divergence when two particles get too close to each other. The α_{Π} and β_{Π} are usually chosen approximately equal to 1. In the artificial viscosity, the first term associated with α_{Π} involves shear and bulk viscosity, while the second term associated with β_{Π} is similar to the von-Neumann-Richtmeyer viscosity for resolving shocks and is very important in preventing unrealistic particle penetration.

3.4. Artificial Stress Model. In 1995, the “tensile instability” was first investigated in detail by Swegle et al. [28], which pointed out that the phenomenon of unphysical clustering of particles arises when the standard SPH method is applied to Euler problem. At present, a number of methods have been proposed to remove the tensile instability in elastic dynamics of solid materials. The artificial stress method [35, 36] is one of the most successful approaches, which has been successfully extended and applied to non-Newtonian fluid free surface flows [25]. In [35, 36], the authors think the “tensile instability” is mainly caused by tension (positive stress in tension), so that the adopted artificial stress term [25, 35, 36] is only related to the positive stress. As noticed by [28], the “tensile instability” is related to the sign of both the stress and the second derivative of the kernel function, which implies that the instability is caused by not only the tension but also the compression (negative stress in compression). Therefore, we use the following artificial stress term by extending the conclusions in [28, 36] to eliminate the “tensile instability”:

$$f_{ij}^n (S_i^{\alpha\beta} + S_j^{\alpha\beta}), \quad (20a)$$

where $n = W(0, h)/W(d_0, h)$, $f_{ij} = W_{ij}(|\mathbf{r}_i - \mathbf{r}_j|, h)/W_{ij}(d_0, h)$.

The components of the artificial stress tensor $S_i^{\alpha\beta}$ are given as

$$S_i^{\alpha\beta} = \begin{cases} -\frac{b\sigma_i^{\alpha\beta}}{\rho^2}, & \text{if } \left(\sum_j W_{ij}''^{\alpha\beta} \right) \cdot \sigma_i^{\alpha\beta} > 0, \\ 0, & \text{other,} \end{cases} \quad (20b)$$

where b is a positive parameter ($0 < b < 1$), and the $W_{ij}''^{\alpha\beta} = \partial^2 W_{ij} / (\partial x^\alpha \cdot \partial x^\beta)$.

Introducing the $K_{ij} = f_{ij}^n (S_i^{\alpha\beta} + S_j^{\alpha\beta})$, the artificial viscosity term (19a) and the artificial stress term (20a) are added to the discrete momentum equation (14) of PDRI-SPH and we can obtain

$$\left(\frac{Dv^\alpha}{Dt} \right)_i = \sum_j m_j \left(\frac{\sigma_i^{\alpha\beta}}{\rho_i^2} + \frac{\sigma_j^{\alpha\beta}}{\rho_j^2} - \Pi_{ij} \delta^{\alpha\beta} + K_{ij} \right) \frac{\partial W_{ij}}{\partial x_i^\beta} + g^\alpha. \quad (21)$$

Usually, the particle positions are updated by the following equation:

$$\frac{Dx_i^\alpha}{Dt} = v_i^\alpha. \quad (22)$$

3.5. Boundary Condition Treatment. In most engineering problems, the physical boundary might be the surface of rigid bodies enclosing fluid or enclosed by fluid, fully or partially. The boundary can be stationary or in motion. We know that the treatment of boundary conditions is very important in the numerical simulation process using SPH method.

Several methods for treating rigid wall boundary conditions have been presented in previous work. There are mainly two methods; that is, (1) the solid walls may be simulated

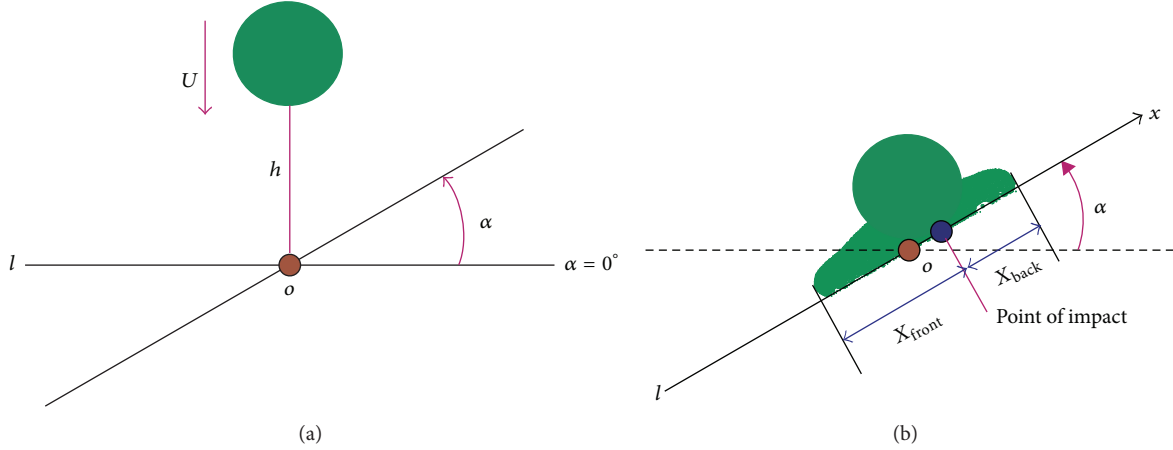


FIGURE 5: The initial state of a droplet impact (a) and side view of a droplet on an inclined rigid plate (b).

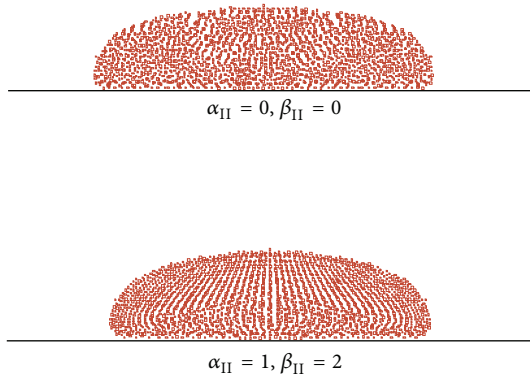


FIGURE 6: The particles distribution predicted by standard SPH method for a Newtonian droplet impact on horizontal rigid plate at dimensionless time $t = 5.2$. Without artificial viscosity (first row), artificial viscosity (second row).

by particles, which exert repulsive force by employing an artificial repulsive force (see [14]) on inner fluid particles to prevent them from penetrating the wall. (2) The wall boundary conditions can also be modeled either by fixed particles [37] or by virtual particles that mirror the physical properties of inner fluid particles. The above methods of boundary treatment have been discussed in 2009 [38], and the literature shows that the virtual particles approach has better stability and affectivity than the artificial repulsive force method. So, the boundary particles in this work do not employ an artificial repulsive force instead of adopting the virtual particles on approaching real particles to prevent fluid particles from penetrating rigid walls.

As shown in Figure 1, two types of virtual particles are used to implement the boundary conditions on a rigid wall. The first type virtual particles are located right on the rigid wall, namely “wall particles.” The density of wall particles is not evolved unlike Morris et al. [15]. Meanwhile, the nonslip condition is enforced on the solid wall and the positions of wall particles remain fixed in time. If the no-slip condition was not considered in the simulations, the fluid particles

may penetrate the wall and the numerical simulations will be terminated. The pressure on the wall particles is calculated according to the following approximation formulation:

$$p_i = \frac{\sum_j p_j (2h - r_{ij})}{\sum_j (2h - r_{ij})}, \quad (23a)$$

where i represents the index of a wall particles and j denotes the index of its neighboring fluid particles only.

The second type virtual particles are placed just outside the solid wall and fill a domain with at least a range of depth comparable with the compact support of the kernel used in the computations, which are called “ghost particles” and have fixed density and positions. The velocity and the pressure on the ghost particles are computed in the following way.

- (1) For each ghost particle G , we assign a corresponding point W just on the rigid wall and point F inside domain, respectively. Meanwhile, these three kinds of points lie in a line which is perpendicular to the wall.
- (2) In order to calculate conveniently we can define the normal distances d_G and d_F of the points G and F to the rigid wall, respectively.
- (3) The pressure p_G and velocity v_G^α for the ghost particles can be obtained through the following linear extrapolation:

$$\mathbf{L}_G = \mathbf{L}_F + \left(1 + \frac{d_G}{d_F}\right)(\mathbf{L}_W - \mathbf{L}_F), \quad (23b)$$

where \mathbf{L} represents the vector of variables (p, v^α) . To specify the values for \mathbf{L}_F , the interpolation formulation (23a) is applied again. Here, we let the $d_F = d_0$.

Moreover, the following total stress-free condition must be satisfied in the computational domain for surface particles:

$$\boldsymbol{\sigma} \cdot \mathbf{n} = 0, \quad (24)$$

where \mathbf{n} denotes a unit normal vector to the surface. In this paper, the surface tensor is neglected and a Dirichlet

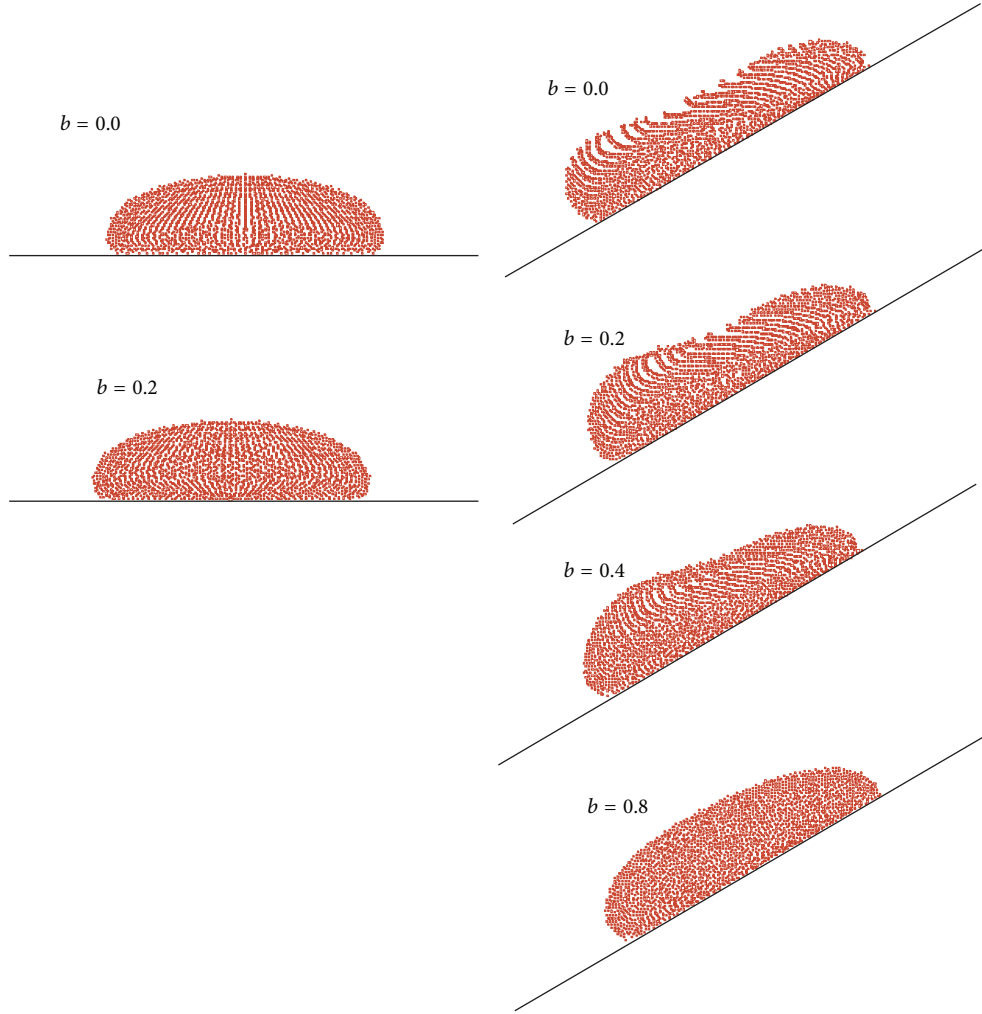


FIGURE 7: The shape of a Newtonian droplet impact on horizontal (left) or inclined ($\alpha = 30^\circ$, right) rigid plate obtained by PDRI-SPH method with $\alpha_{II} = 1$, $\beta_{II} = 2$ and different artificial stress parameter b , at dimensionless time $t = 6.2$.

boundary condition of zero pressure is given to the surface particles. This condition, that is, (24), is satisfied naturally by the PDRI-SPH method.

3.6. Time Integration Scheme. In order to better illustrate the effect of the density reinitialization method, a suitable time integration schemes is chosen necessarily in practice. Considering that the predictor-corrector scheme possesses second-order accuracy and better stability, we chose the predictor-corrector scheme for solving the system of ordinary differential equations (13), (21), and (22). The predictor step consists of an Eulerian explicit evaluation of all quantities for each particle

$$\tilde{\mathbf{X}}_i^{n+1} = \mathbf{X}_i^n + \frac{\Delta t}{2} \Gamma_i^n, \quad (25a)$$

where \mathbf{X}_i represents the vector of the unknown variables (ρ_i, v_i^α) and Γ_i denotes the vector of right-hand sides of (13),

(21), and (22). In the corrected step, the updated value of \mathbf{X}_i at the end of each time step is given by

$$\mathbf{X}_i^{n+1} = \mathbf{X}_i^n + \frac{\Delta t}{2} (\Gamma_i^n + \tilde{\Gamma}_i^n). \quad (25b)$$

To ensure the numerical stability, the time step and space step must satisfy the well-known Courant-Friedrichs-Lewy (CFL) condition. According to [15], we may choose the following stability condition:

$$\Delta t \leq \min \left[0.25 \frac{h}{c}, 0.25 \left(\frac{h}{F_a} \right)^{1/2}, 0.125 \frac{h^2}{v_0} \right], \quad (25c)$$

where F_a is the hydrodynamical force acting on the particle, and $v_0 = \eta/\rho_0$ is the kinematic viscosity.

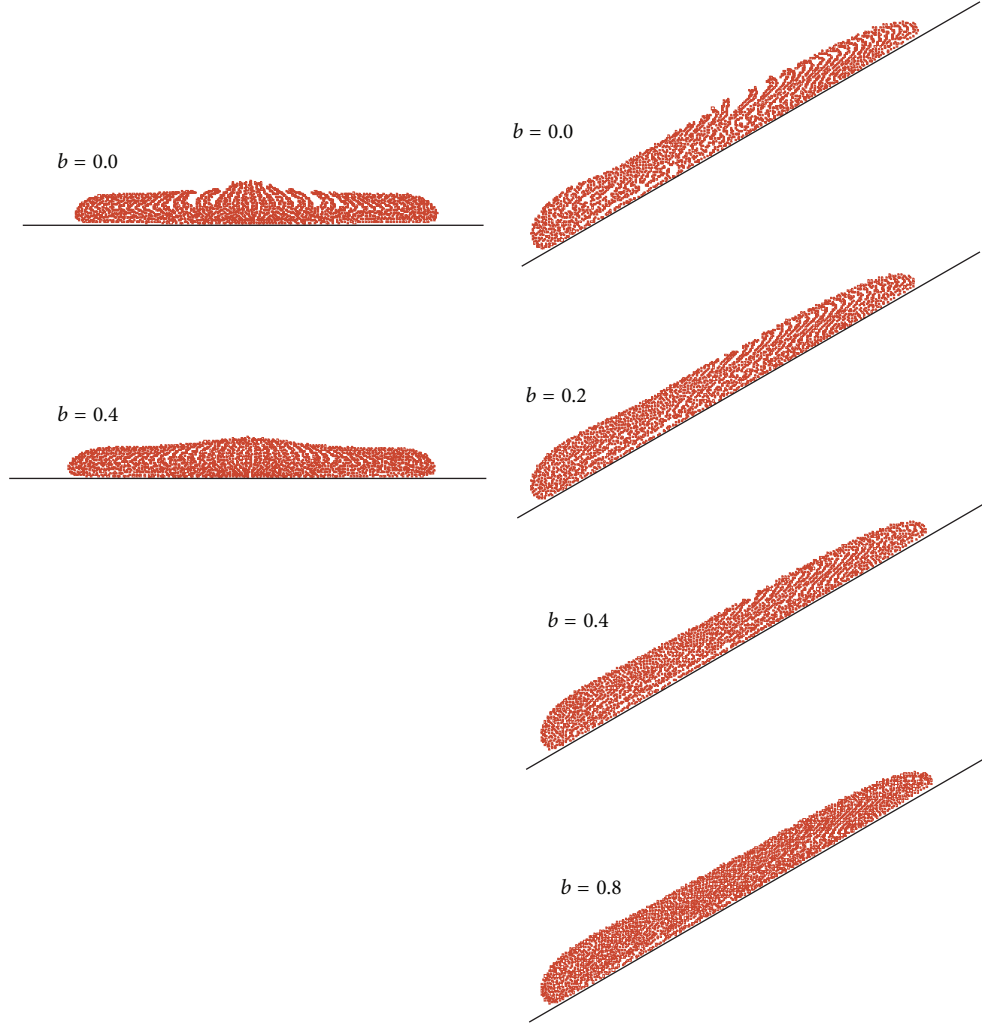


FIGURE 8: The shape of a Cross droplet impact on horizontal (left) or inclined ($\alpha = 30^\circ$, right) rigid plate obtained by PDRI-SPH method with $\alpha_{II} = 1$, $\beta_{II} = 2$ and different artificial stress parameter b , at dimensionless time $t = 4.3$.

4. Test Examples and Numerical Simulations for the Cross Model

Firstly, the effect and the validity of modified models for simulating generalized Newtonian free surface flows using the PDRI-SPH method are obviously demonstrated through applying the periodic density reinitialization method, artificial viscosity model, and artificial stress model. Subsequently, the capacity of PDRI-SPH method for solving a Cross model droplet impact, spreading and depositing on an inclined rigid plate, is shown in Section 4.3.

4.1. Effect of the Periodic Density Reinitialization Scheme. In order to show the effect of PDRI-SPH method and compare with the conventional SPH method, the two-dimensional benchmark problem of the stretching of an initially circular water drop is simulated using PDRI-SPH and SPH, respectively, without enforcing the artificial viscosity, artificial stress, and rigid boundary condition. This example has been

used in the literature [14, 33] of using SPH method, and its corresponding analytical solution can be obtained from [14, 33].

All the physical quantities are the same as those in [33, Figure 1], the reference density $\rho_0 = 1000 \text{ kgm}^{-3}$, the viscosity $\eta = 0.001 \text{ kgm}^{-1} \text{ s}^{-1}$, and the speed of sound $c = 1400 \text{ ms}^{-1}$. The initial geometry of the water drop is a circle of radius $R = 1 \text{ m}$ with its center located at the origin ($x = 0$, $y = 0$). There is no external forces but initial velocity field $v_0^x = -A_0 x$, $v_0^y = A_0 y$ with $A_0 = 100 \text{ s}^{-1}$ and the initial pressure field $p_0 = (1/2)\rho_0 A_0^2 [R^2 - (x^2 + y^2)]$. The number of fluid particles is 1961 and corresponding to the initial distance $d_0 = 0.02 \text{ m}$, and the time step $dt = 10^{-5} \text{ s}$. During the stretching process of water drop, the water drop remains elliptical shape and the value of $\tilde{a} \cdot \tilde{b}$ (\tilde{a} is the semiminor axis and \tilde{b} is the semimajor axis) remains constant. We let “num” denote the interval time step of the periodic density reinitialization of PDRI-SPH, and the PDRI-SPH method becomes the SPH method if $\text{num} = \infty$.

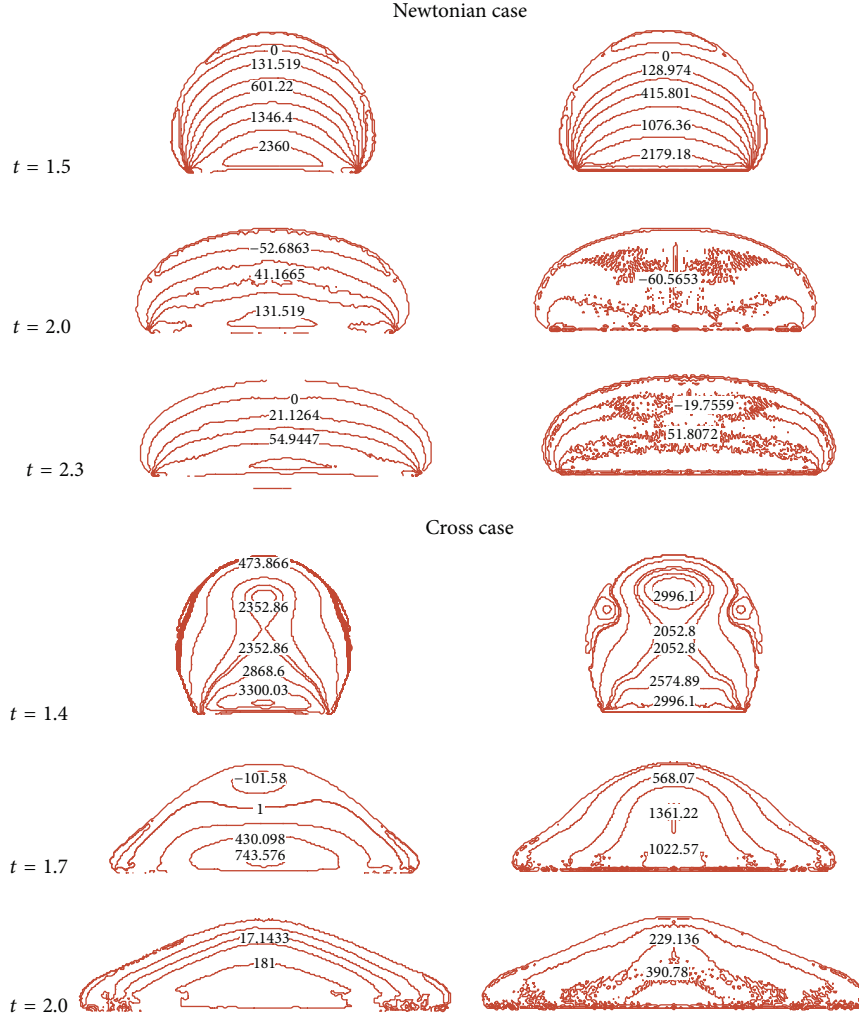


FIGURE 9: The distribution of pressure contour for a Newtonian/Cross drop impact on horizontal rigid plate obtained using PDRI-SPH (left column) or SPH (right column) at different dimensionless time.

Figure 2 shows the positions of 1961 particles calculated by PDRI-SPH method with different interval time steps $\text{num} = 10, 20, 40, 60, \infty$ at the time 0.01 s. The distributed particles of using PDRI-SPH ($\text{num} \neq \infty$) are all more uniform and the outer surfaces are all far smoother than the ones of SPH method ($\text{num} = \infty$). From Figure 2, we can observe that the better results belong to $\text{num} = 10$ and 20. In fact, the more uniformly distributed the particles are, the better the numerical accuracy is (see [31]). In other words, the accuracy of numerical results using SPH can be improved by periodic density reinitialization with appropriate “num.” For further exhibiting the merit of the PDRI-SPH method, the pressure field distribution ($p/10^7$) and numerical accuracy obtained using PDRI-SPH are shown in Figures 3 and 4, respectively. We can know that the problem of pressure oscillations of using SPH can be effectively reduced by PDRI-SPH (see Figure 3). The pressure distribution has certain defect around the boundary region in Figure 3, due to the reduced particles on the boundary. Figure 4 demonstrates that the PDRI-SPH has better accuracy than the standard SPH.

In a word, the effect of the density reinitialization method used in the standard SPH method is obvious. Through the results of Figures 2–4, and considering the computational cost and the effect of PDRI-SPH with different “num,” we choose the interval time step $\text{num} = 20$ in all the following numerical simulations.

4.2. Validity of the Artificial Viscosity and Artificial Stress Models. In this subsection, the example of a droplet impact and spreading on a horizontal or an inclined plate is considered. The initial state of a droplet impact on an inclined surface is shown in Figure 5(a). When a droplet impacts on the inclined rigid plate, the shape of the droplet distorts and spreads symmetrically ($\alpha = 0^\circ$) or asymmetrically ($\alpha \neq 0^\circ$) relative to the point of impact, which is shown in Figure 5(b). We define the positive value of the elongation X_{back} and the negative value of the elongation X_{front} (see Figure 5(b)), in which asymmetry increases with time. The front edge of the droplet spreads forward, while the back edge spreads backward or slips forward.

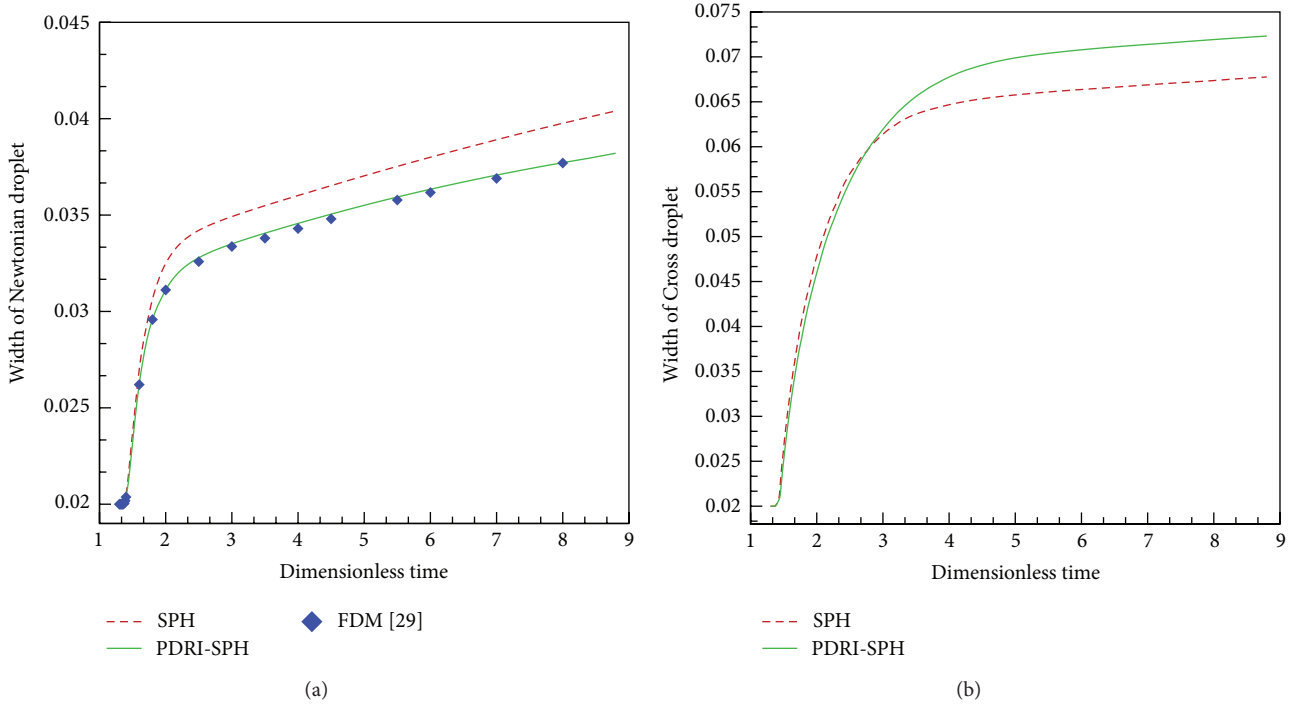


FIGURE 10: Comparison of the numerical results obtained using SPH or PDRI-SPH method for the width of a Newtonian (a) and Cross (b) droplet impact on horizontal rigid plate varying with dimensionless time.

All the physical parameter values for a Newtonian droplet are chosen as follows. Its initial diameter and velocity are $D = 0.02$ m and $U_0 = -1$ ms⁻¹, respectively. The total viscosity is $\eta = 4$ Pa · s, the reference density is $\rho_0 = 10^3$ kgm⁻³, the speed of sound is $c = 12$ ms⁻¹, and the gravitational force acts downwards with $g_y = -9.81$ ms⁻²: in this subsection, 1961 fluid particles, 251 wall particles, and 753 ghost particles. The initial spacing $d_0 = 0.0004$ m and the time-step $dt = 1 \times 10^{-5}$. The height of dropping is $H = 0.04$ m from the center of drop to the center (o) of inclined rigid wall (see Figure 5(a)). For the Cross model droplet, $v_0 = 4 \times 10^{-3}$ m² s⁻¹, $v_\infty = 4 \times 10^{-4}$ m² s⁻¹, and the other parameter values are the same as the case of Newtonian droplet.

Although the artificial viscosity term (19a) is adopted for simulating the Newtonian drop case with considering a horizontal plate in [25], the role of the artificial viscosity has not been obviously demonstrated in [25]. Here, the effect of artificial viscosity is illustrated in Figure 6. And then, we can obtain three advantages of using the artificial viscosity in the example of droplet impact. (1) The particles are more uniformly distributed than those without using it. (2) The numerical accuracy and stability are improved. (3) The phenomenon of unphysical clustering becomes weakened. Note that the artificial stress term and the density reinitialization method are all not considered in Figure 6. In all subsequent simulations, the artificial viscosity ($\alpha_{II} = 1$, $\beta_{II} = 2$) is adopted.

Figures 7 and 8 show the effect of the artificial stress for simulating a Newtonian/Cross model droplet impact

on horizontal/inclined ($\alpha = 30^\circ$) rigid plate using PDRI-SPH method with different artificial stress parameters. It can be seen that the droplet fractures unrealistically for the problem of droplet impact without the artificial stress term ($b = 0$), and the simulations may be eventually diverged. The phenomenon of fracture is observable for the Newtonian droplet impact on horizontal rigid plate with artificial stress $b = 0.2$, but it is much severer when the Newtonian droplet impacts on inclined plate. For the Cross model droplet, the unphysical fracture is obvious no matter how the droplet impacts on horizontal or inclined rigid plate even if the artificial viscosity is adopted. Observing Figures 7 and 8, we can get the following. (1) The problem of tensile instability occurs more evidently for the Cross droplet than the Newtonian case when the droplet impacts on horizontal rigid plate. (2) A droplet impacts on rigid plate fracture more likely at low impact angles $\alpha \neq 0^\circ$ than $\alpha = 0^\circ$. In fact, the tensile instability is also related to the ratio of the kinematic viscosity v_0, v_∞ for a Cross droplet impact on plate. Here, we can find that the fracture is avoided completely by increasing the value of b up to 0.8 for the Newtonian/Cross model droplet impact on inclined plate. In other words, it is necessary that the artificial stress parameter b is chosen appropriately for simulating a droplet impact on inclined rigid plate at low impact angles using PDRI-SPH method.

4.3. Numerical Simulations Based on Cross Model Using PDRI-SPH. In this subsection, we mainly focus on the PDRI-SPH/SPH method combined with the artificial viscosity

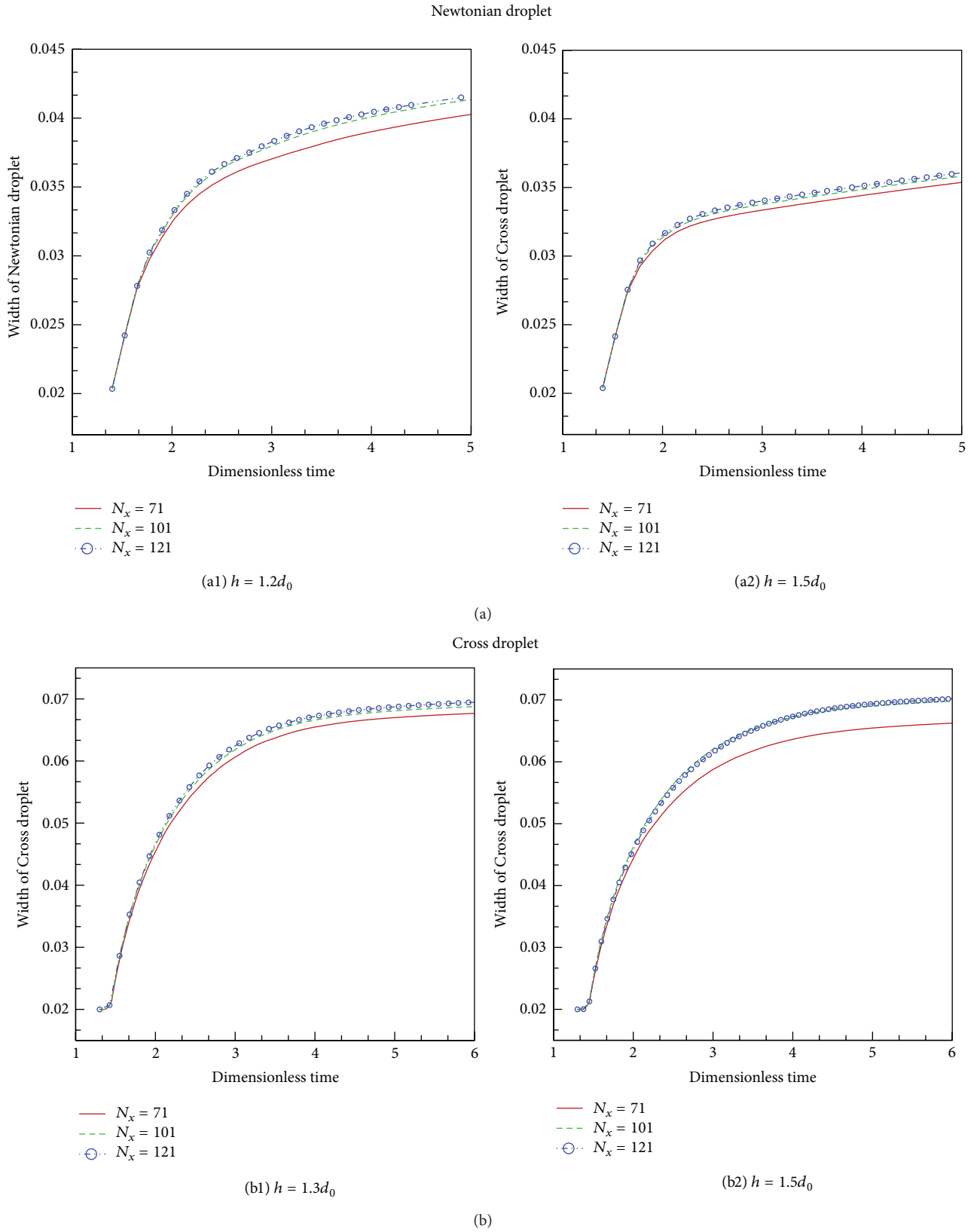


FIGURE 11: Numerical convergence of the PDRI-SPH results with different smoothing length h and particles number N_x (along the x -axis direction): (a1)-(a2) Newtonian droplet; (b1)-(b2) Cross droplet (which corresponds to Figure 10).

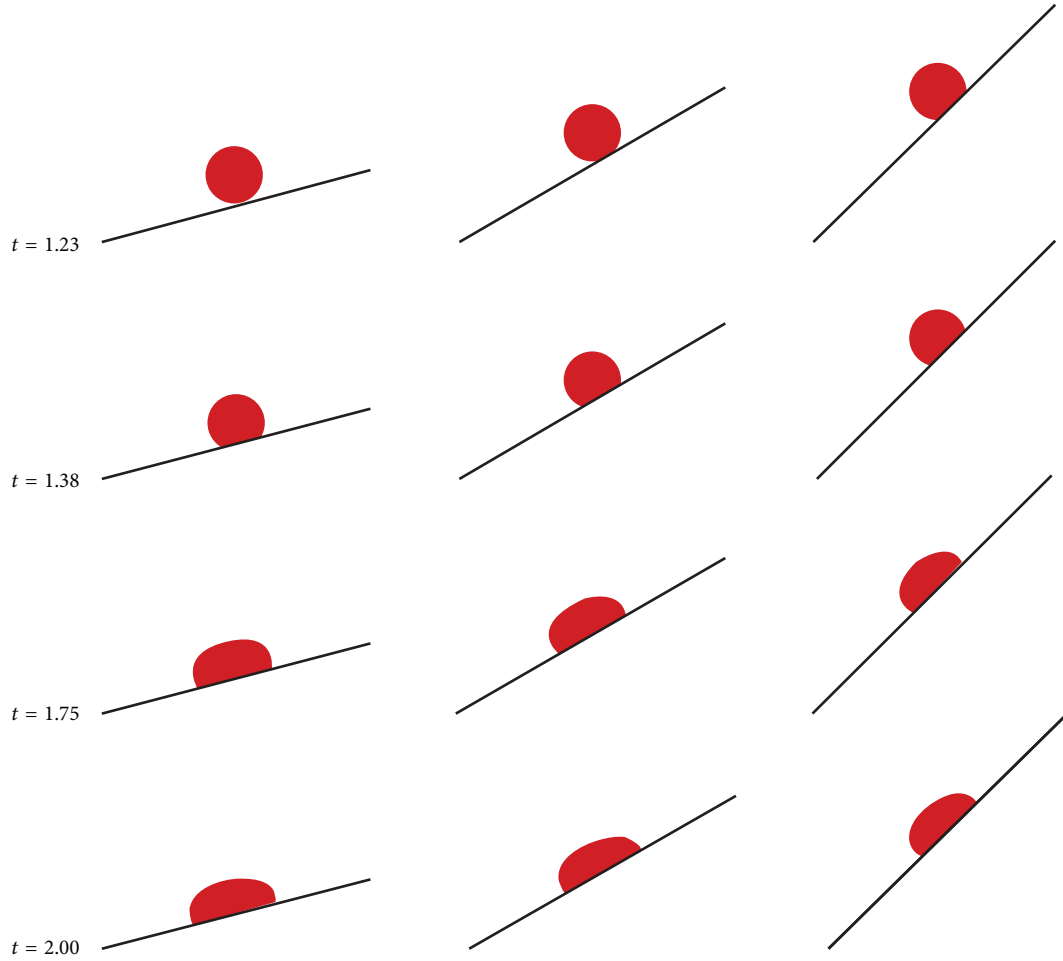


FIGURE 12: The shape of a Newtonian droplet at impact angles of 15° (first column), 30° (second column), and 45° (third column) obtained using PDRI-SPH, varying with short dimensionless time.

($\alpha_{II} = 1$, $\beta_{II} = 2$), artificial stress ($b = 0.8$), and boundary condition for simulating a Cross droplet impact on inclined rigid plate at different low impact angles $\alpha = 15^\circ, 30^\circ, 45^\circ$, respectively. For the purpose of comparison, the Newtonian droplet case is also considered. The number of fluid particles is set to 7845, corresponding to the initial spacing $d_0 = 0.0002$ m, 501 wall particles, and 1503 ghost particles. The time-step is 5×10^{-6} . The other physical parameters values are the same as those in Section 4.2.

The effect of the proposed periodic density reinitialization method is obviously shown by predicting the pressure distribution for the problem of droplet impact in Figure 9. At the short time of droplet impact, the phenomenon of pressure oscillations occurs for the SPH method combined with the above improved models. The pressure oscillations grow near the rigid plate varying with time and later progressively destroy the whole pressure field, resulting in making its physical interpretation and possible practical use difficult. However, the pressure field maintains a much smoother character obtained using the proposed PDRI-SPH method than the SPH, especially on the boundary regions. We can also know that the wall particles and ghost particles contribute to

the evolution of the density of the fluid particles; pressures on both fluid and virtual particles increase when fluid particles are near the rigid wall. The presented boundary treatment is strong enough to prevent fluid particles from penetrating the rigid wall without employing an additional artificial repulsive force.

Figure 10 shows the comparison of the numerical results obtained using SPH or PDRI-SPH method for the width of a Newtonian and Cross droplet varying with dimensionless time. The Newtonian/Cross droplet spreads symmetrically along the wall after impact with time. The PDRI-SPH results much closer to the results in [39] than the SPH results in the numerical simulations of Newtonian droplet impact. There are also certain differences between the numerical results of using PDRI-SPH and those of using SPH for solving the width of a Cross droplet impact on horizontal rigid plate with time in Figure 10(b). Considering the analysis of Section 4.1 and the results in Figure 9, it is not difficult to believe that the results obtained using the PDRI-SPH method are more reliable than those using SPH method. From Figure 10, we also can observe that the width of a Cross droplet becomes much larger than the corresponding Newtonian droplet case

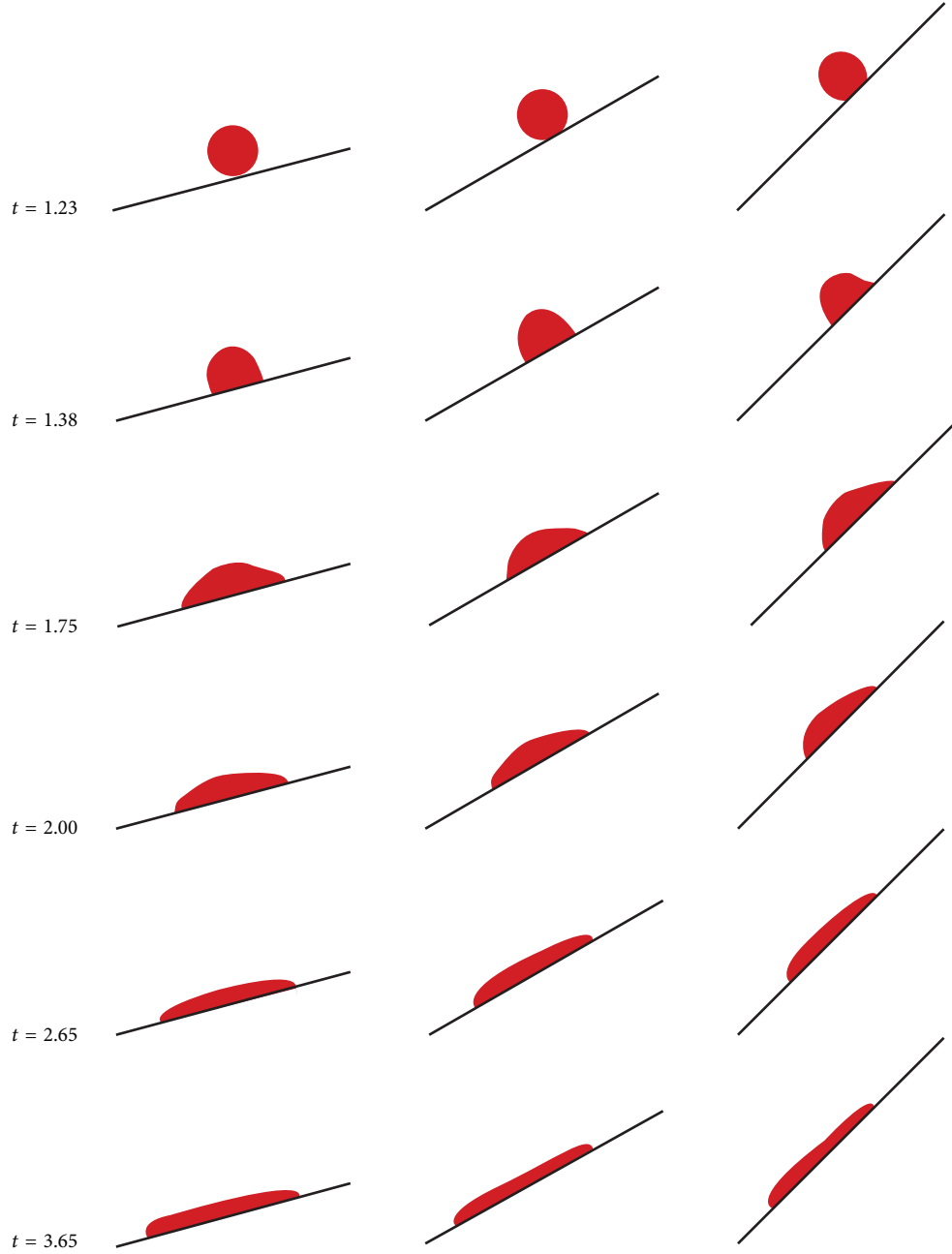


FIGURE 13: The shape of a Cross droplet at impact angles of 15° (first column), 30° (second column), and 45° (third column) obtained using PDRI-SPH, varying with short dimensionless time.

at the short time (about dimensionless time $t \leq 3$) of droplet impact, due to the shear-thinning behavior of the Cross model droplet (see [29, 30]).

In order to further demonstrate the feasibility and the credibility of the proposed method to simulate the impact problem, the numerical convergence of the PDRI-SPH results with different smoothing length h and particles number N_x (along the x -axis direction) is shown in Figure 11. From Figures 10 and 11, we can get that (a) the proposed method is convergent to simulate the Newtonian or Cross droplet impact on horizontal rigid plate under different smoothing length; (b) the results of Newtonian droplet for $h = 1.5d_0$

are more accurate than those for $h = 1.2d_0$ by observing Figures 10(a) and 11(a), which implies that it is credible to adopt the $h = 1.5d_0$ in the simulations of Section 4.3; (c) the credibility of the PDRI-SPH for simulating the impact problem based on the Cross fluid is further verified by Figure 11(b).

We can observe the shapes of a Newtonian drop spreading over inclined rigid surfaces ($\alpha = 15^\circ, 30^\circ, 45^\circ$) at different dimensionless times from Figure 12. It can be seen that the first phase of impact involving the initial deformation of the droplet for all the cases of $\alpha = 15^\circ, 30^\circ, 45^\circ$ is similar to that of impact angle $\alpha = 0^\circ$; namely, the front edge spreads

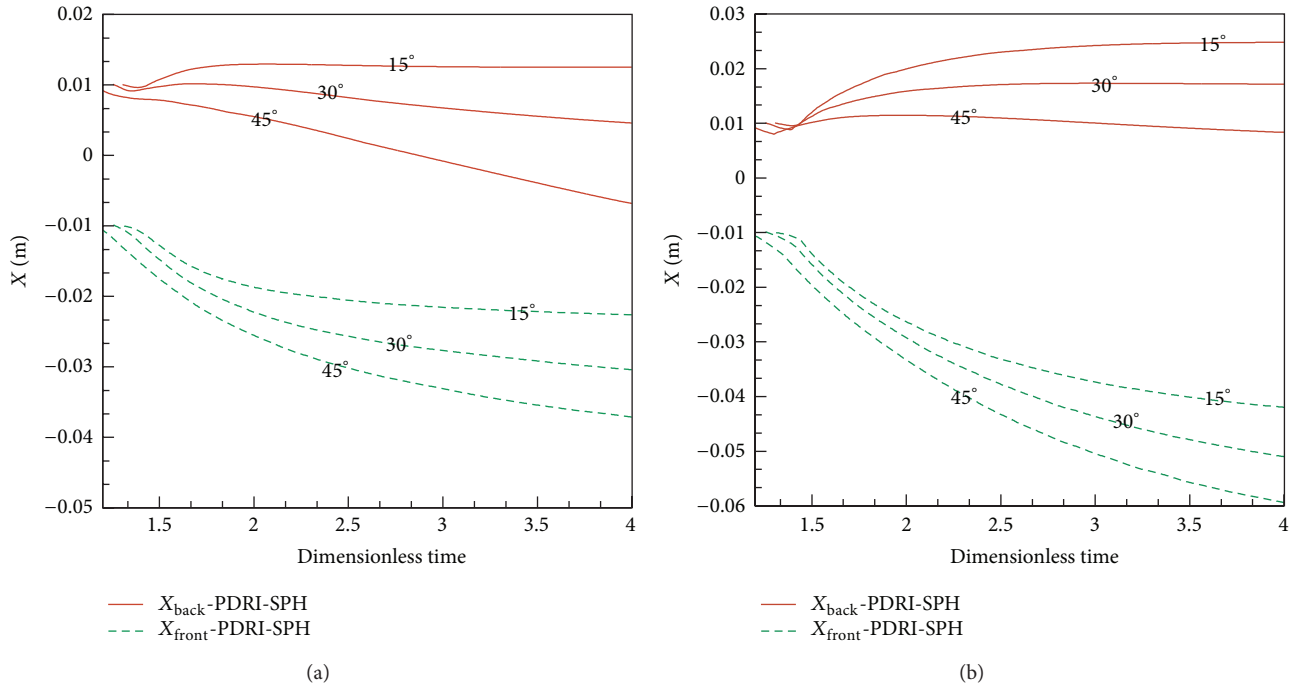


FIGURE 14: Evolution of the elongation of a Newtonian (a) and a Cross (b) spreading droplet at different impact angles, obtained using PDRI-SPH.

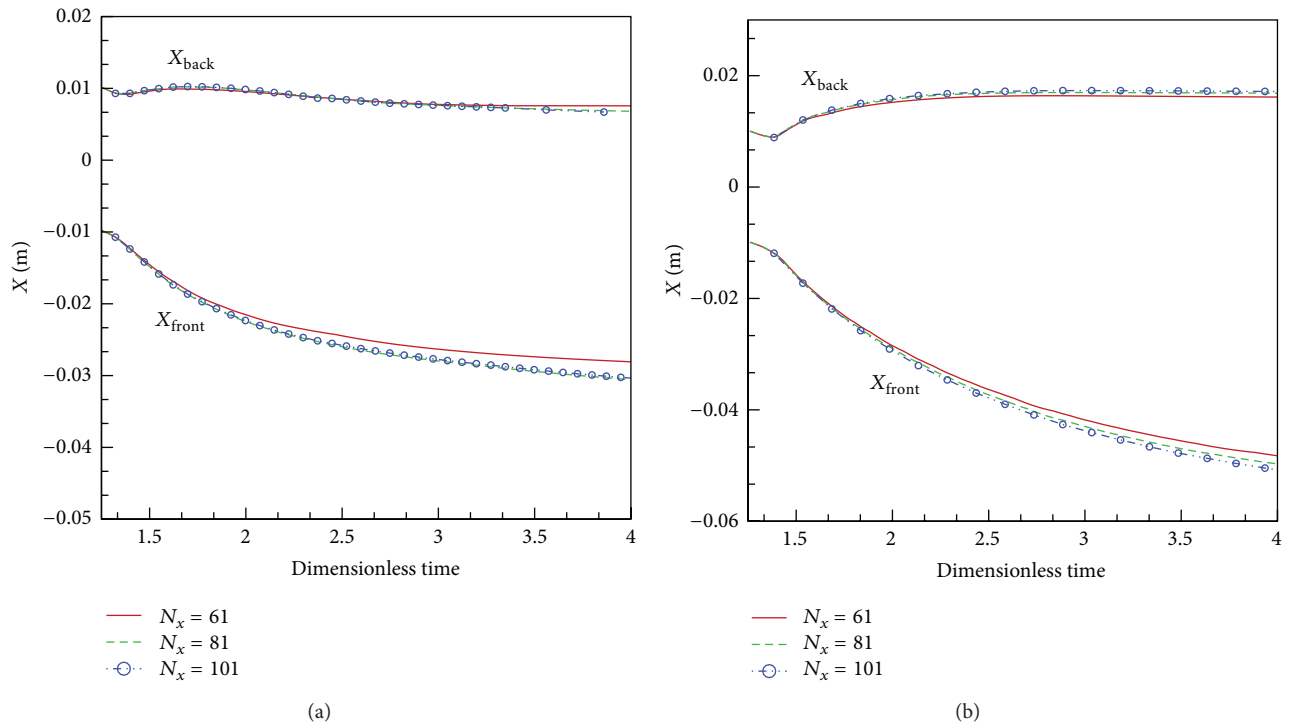


FIGURE 15: Numerical convergence of evolution of a Newtonian droplet (a) and a Cross droplet (b) spreading on an inclined plate with impact angle 30° and smoothing length $h = 1.5d_0$ obtained using PDRI-SPH method.

forward and the back edge spreads backward. Subsequently, the front edge spreads forward and the back edge slips forward, which can be clearly observed in Figure 14(a). The phenomenon of precipitation appears versus time, which becomes more evident with an increase of impact angle. The PDRI-SPH results are similar to the results of a water droplet impact on inclined surface obtained using VOF in [40, 41].

From Figure 13, we can get that the shapes of the Cross drop spreading over inclined rigid surfaces ($\alpha = 15^\circ, 30^\circ, 45^\circ$) at different dimensionless time are different from the case of Newtonian (see Figure 12) under the same total viscosity. There are some obvious differences between the Newtonian drop and the Cross model droplet case, which are shown in Figures 12–14. The speed of a Cross droplet spreading over inclined rigid plate is faster than its Newtonian counterpart. Moreover, an indentation is formed only for the Cross droplet with time at lower impact angle ($\alpha = 15^\circ$) because of the shear-thinning of the Cross fluid.

To further exemplify the reliability of the proposed method for simulating the droplet spreading over inclined rigid surface, Figure 15 shows the numerical convergence of evolution of a Newtonian droplet and a Cross droplet spreading on an inclined plate with impact angle 30° and smoothing length $h = 1.5d_0$. Observing Figure 15, the numerical results for $N_x = 81$ are very close to those for $N_x = 101$, which demonstrates that the proposed method possesses preferable numerical convergence for simulating the impact problem. In short, it is feasible and reliable to simulate the impact problem of a Newtonian or Cross droplet spreading on an inclined plate using the proposed PDRI-SPH method.

5. Conclusions

Aiming at the deficiency of standard SPH method, a periodic density reinitialization method which is called the PDRI-SPH method is proposed to preserve the consistency between mass, density, and the occupied area. In order to verify the validity and ability of the proposed PDRI-SPH, the benchmark problem of drop stretching is simulated by PDRI-SPH. Due to the density reinitialization, the PDRI-SPH has better accuracy than the SPH, and the distributed pressure field is much smoother likewise. Meanwhile, an artificial stress is successfully presented and tested to simulate a Cross droplet impact onto an inclined rigid plate of using PDRI-SPH. The effect of the proposed PDRI-SPH combined with an artificial viscosity, an artificial stress, and boundary condition treatment is further shown in the physical problem of impact of droplet onto inclined rigid plate and compared with the standard SPH. All the numerical results declare that the proposed PDRI-SPH has some merits comparing with the SPH, and it is a powerful tool to simulate the complex free surface for generalized Newtonian fluid. It is expected to be widely used and further improved to solve complex free surface flows in future.

Conflict of Interests

The authors declare that there is no conflict of interests regarding the publication of this paper.

Acknowledgments

Project is supported by the Postdoctoral Science Foundation of China (Grant no. 2014M550310), the Natural Science Foundation of Jiangsu Province, China (Grant no. BK20130436), and the Innovation Cultivation Funds of Yangzhou University, China (Grant no. 2013CXJ003).

References

- [1] F. H. Harlow, "The particle-in-cell method for numerical solution of problems in fluid dynamics," in *Proceedings of the Symposium in Applied Mathematics*, vol. 15, pp. 269–288, 1963.
- [2] F. H. Harlow and J. E. Welch, "Numerical calculation of time-dependent viscous incompressible flow of fluid with free surface," *Physics of Fluids*, vol. 8, no. 12, pp. 2182–2189, 1965.
- [3] C. W. Hirt and B. D. Nichols, "Volume of fluid (VOF) method for the dynamics of free boundaries," *Journal of Computational Physics*, vol. 39, no. 1, pp. 201–225, 1981.
- [4] S. Osher and J. A. Sethian, "Fronts propagating with curvature-dependent speed: algorithms based on Hamilton-Jacobi formulations," *Journal of Computational Physics*, vol. 79, no. 1, pp. 12–49, 1988.
- [5] M. Do-Quang and G. Amberg, "Numerical simulation of the coupling problems of a solid sphere impacting on a liquid free surface," *Mathematics and Computers in Simulation*, vol. 80, no. 8, pp. 1664–1673, 2010.
- [6] L. W. Zhang, Y. J. Deng, and K. M. Liew, "An improved element-free Galerkin method for numerical modeling of the biological population problems," *Engineering Analysis with Boundary Elements*, vol. 40, pp. 181–188, 2014.
- [7] L. W. Zhang and K. M. Liew, "An improved moving least-squares Ritz method for two-dimensional elasticity problems," *Applied Mathematics and Computation*, vol. 246, pp. 268–282, 2014.
- [8] L. W. Zhang, P. Zhu, and K. M. Liew, "Thermal buckling of functionally graded plates using a local Kriging meshless method," *Composite Structures*, vol. 108, no. 1, pp. 472–492, 2013.
- [9] R. A. Gingold and J. J. Monaghan, "Smoothed particle hydrodynamics theory and application to non-spherical stars," *Monthly Notices of the Royal Astronomical Society*, vol. 181, pp. 375–389, 1977.
- [10] S. Li, D. Qian, W. K. Liu, and T. Belytschko, "A meshfree contact-detection algorithm," *Computer Methods in Applied Mechanics and Engineering*, vol. 190, no. 24–25, pp. 3271–3292, 2001.
- [11] S. Li and W. K. Liu, "Mesh-free particle methods and their applications," *Applied Mechanics Review*, vol. 54, pp. 1–34, 2002.
- [12] V. P. Nguyen, T. Rabczuk, S. Bordas, and M. Duflot, "Meshless methods: a review and computer implementation aspects," *Mathematics and Computers in Simulation*, vol. 79, no. 3, pp. 763–813, 2008.
- [13] L. B. Lucy, "A numerical approach to the testing of the fission hypothesis," *The Astronomical Journal*, vol. 83, pp. 1013–1024, 1977.
- [14] J. J. Monaghan, "Simulating Free Surface Flows with SPH," *Journal of Computational Physics*, vol. 110, no. 2, pp. 399–406, 1994.
- [15] J. P. Morris, P. J. Fox, and Y. Zhu, "Modeling low Reynolds number incompressible flows using SPH," *Journal of Computational Physics*, vol. 136, no. 1, pp. 214–226, 1997.

- [16] S. J. Watkins, A. S. Bhattal, N. Francis, J. A. Turner, and A. P. Whitworth, "A new prescription for viscosity in smoothed particle Hydro dynamics," *Astronomy and Astrophysics Supplement Series*, vol. 119, no. 1, pp. 177–187, 1996.
- [17] S. J. Cummins and M. Rudman, "An SPH projection method," *Journal of Computational Physics*, vol. 152, no. 2, pp. 584–607, 1999.
- [18] S. Shao and E. Y. M. Lo, "Incompressible SPH method for simulating Newtonian and non-Newtonian flows with a free surface," *Advances in Water Resources*, vol. 26, no. 7, pp. 787–800, 2003.
- [19] J. J. Monaghan and A. Kocharyan, "SPH simulation of multi-phase flow," *Computer Physics Communications*, vol. 87, no. 1-2, pp. 225–235, 1995.
- [20] J. P. Morris, "Simulating surface tension with smoothed particle hydrodynamics," *International Journal for Numerical Methods in Fluids*, vol. 33, no. 3, pp. 333–353, 2000.
- [21] R. Ata and A. Soulaïmani, "A stabilized SPH method for inviscid shallow water flows," *International Journal for Numerical Methods in Fluids*, vol. 47, no. 2, pp. 139–159, 2005.
- [22] L. Oger and S. B. Savage, "Smoothed particle hydrodynamics for cohesive grains," *Computer Methods in Applied Mechanics and Engineering*, vol. 180, no. 1-2, pp. 169–183, 1999.
- [23] M. Ellero, M. Kröger, and S. Hess, "Viscoelastic flows studied by smoothed particle dynamics," *Journal of Non-Newtonian Fluid Mechanics*, vol. 105, no. 1, pp. 35–51, 2002.
- [24] M. Ellero and R. I. Tanner, "SPH simulations of transient viscoelastic flows at low Reynolds number," *Journal of Non-Newtonian Fluid Mechanics*, vol. 132, no. 1-3, pp. 61–72, 2005.
- [25] J. Fang, R. G. Owens, L. Tacher, and A. Parriaux, "A numerical study of the SPH method for simulating transient viscoelastic free surface flows," *Journal of Non-Newtonian Fluid Mechanics*, vol. 139, no. 1-2, pp. 68–84, 2006.
- [26] W. Benz, "Smooth particle hydrodynamics: a review," in *The Numerical Modelling of Nonlinear Stellar Pulsations: Problems and Prospects*, J. R. Buchler, Ed., vol. 302 of NATO ASI Series, pp. 269–288, Kluwer Academic Publishers, Boston, Mass, USA, 1990.
- [27] J. K. Chen and J. E. Beraun, "A generalized smoothed particle hydrodynamics method for nonlinear dynamic problems," *Computer Methods in Applied Mechanics and Engineering*, vol. 190, no. 1-2, pp. 225–239, 2000.
- [28] J. W. Swegle, D. L. Hicks, and S. W. Attaway, "Smoothed particle hydrodynamics stability analysis," *Journal of Computational Physics*, vol. 116, no. 1, pp. 123–134, 1995.
- [29] M. F. Tomé, B. Duffy, and S. McKee, "A numerical technique for solving unsteady non-Newtonian free surface flows," *Journal of Non-Newtonian Fluid Mechanics*, vol. 62, no. 1, pp. 9–34, 1996.
- [30] M. F. Tome, L. Grossia, A. Castelo et al., "A numerical method for solving three-dimensional generalized Newtonian free surface flows," *Journal of Non-Newtonian Fluid Mechanics*, vol. 123, pp. 85–103, 2004.
- [31] M. B. Liu and G. R. Liu, "Restoring particle consistency in smoothed particle hydrodynamics," *Applied Numerical Mathematics*, vol. 56, no. 1, pp. 19–36, 2006.
- [32] J. J. Monaghan, "Smoothed particle hydrodynamics," *Reports on Progress in Physics*, vol. 68, no. 8, pp. 1703–1759, 2005.
- [33] J. Fang, A. Parriaux, M. Rentschler, and C. Ancey, "Improved SPH methods for simulating free surface flows of viscous fluids," *Applied Numerical Mathematics*, vol. 59, no. 2, pp. 251–271, 2009.
- [34] J. J. Monaghan, "Smoothed particle hydrodynamics," *Annual Review of Astronomy and Astrophysics*, vol. 30, no. 1, pp. 543–574, 1992.
- [35] J. P. Gray, J. J. Monaghan, and R. P. Swift, "SPH elastic dynamics," *Computer Methods in Applied Mechanics and Engineering*, vol. 190, no. 49-50, pp. 6641–6662, 2001.
- [36] J. J. Monaghan, "SPH without a tensile instability," *Journal of Computational Physics*, vol. 159, no. 2, pp. 290–311, 2000.
- [37] J. J. Monaghan and A. Kos, "Solitary waves on a cretan beach," *Journal of Waterway, Port, Coastal and Ocean Engineering*, vol. 125, no. 3, pp. 145–154, 1999.
- [38] M. Yildiz, R. A. Rook, and A. Suleman, "SPH with the multiple boundary tangent method," *International Journal for Numerical Methods in Engineering*, vol. 77, no. 10, pp. 1416–1438, 2009.
- [39] M. F. Tomé, N. Mangiavacchi, J. A. Cuminato, A. Castelo, and S. McKee, "A finite difference technique for simulating unsteady viscoelastic free surface flows," *Journal of Non-Newtonian Fluid Mechanics*, vol. 106, no. 2-3, pp. 61–106, 2002.
- [40] S. F. Lunkad, V. V. Buwa, and K. D. P. Nigam, "Numerical simulations of drop impact and spreading on horizontal and inclined surfaces," *Chemical Engineering Science*, vol. 62, no. 24, pp. 7214–7224, 2007.
- [41] Š. Šikalo, C. Tropea, and E. N. Ganić, "Impact of droplets onto inclined surfaces," *Journal of Colloid and Interface Science*, vol. 286, no. 2, pp. 661–669, 2005.

Research Article

Drag Reduction in Turbulent Boundary Layers with Half Wave Wall Oscillations

Maneesh Mishra and Martin Skote

School of Mechanical & Aerospace Engineering, Nanyang Technological University, 50 Nanyang Avenue, Singapore 639798

Correspondence should be addressed to Martin Skote; mskote@ntu.edu.sg

Received 29 August 2014; Revised 17 October 2014; Accepted 17 October 2014

Academic Editor: Kim M. Liew

Copyright © 2015 M. Mishra and M. Skote. This is an open access article distributed under the Creative Commons Attribution License, which permits unrestricted use, distribution, and reproduction in any medium, provided the original work is properly cited.

Spatial square waves with positive cycle are used as steady forcing technique to study drag reduction effects on a turbulent boundary layer flow. Pseudospectral method is used for performing direct numerical simulations on very high resolution grids. A smooth step function is employed to prevent Gibbs phenomenon at the sharp discontinuities of a square wave. The idea behind keeping only the positive cycle of the spatial forcing is to reduce the power consumption to boost net power savings. For some spatial frequency of the oscillations with half waves, it is possible to prevent recovery of skin friction back to the reference case values. A set of wall oscillation parameters is numerically simulated to study its effect on the power budget.

1. Introduction

Turbulent drag reduction is one of the active areas of research in fluid mechanics especially due to its global impact on sustainability challenges we are facing today. One of the active techniques for reducing drag is through spanwise oscillation of the wall which reduces the skin friction and promises to have large potential for energy savings.

This curious phenomenon was first observed by Jung et al. [1] through direct numerical simulations (DNS) in a channel flow. Since then, a lot of research efforts have been made in this direction for different flow configurations like channel flow [2–9], pipe flow [10, 11], and boundary layer flows [12–14]. These investigations have been made either through experiments or using DNS.

Most of these studies have dealt with temporal form of wall oscillations which are specified as

$$w(t)_{y=0} = W_m \sin(\omega t), \quad (1)$$

where W_m is the amplitude and ω is the frequency of the imposed oscillations.

A few studies have been devoted to explore the spatial oscillations and its impact on reducing skin friction has been found to be greater than for temporal oscillations [15–19].

Spatial oscillations can be realized by enforcing the following boundary condition:

$$w(x)_{y=0} = W_m \sin(kx), \quad (2)$$

where k is the spatial frequency of oscillation and is related to the wavelength (λ) as $k = 2\pi/\lambda$.

Spatial wall oscillation technique has its advantages and disadvantages. It can have greater drag reduction as compared to temporal oscillations and, hence, there are higher net energy savings. It is an open-loop method so we do not require an array of distributed sensors on the surface. However, the implementation remains a challenge as it requires numerous moving parts which makes it impractical. Although there have been advances in the field of material science research to realize such waveforms in practical situations, the physical realization still remains elusive with the current technology.

Almost all of the previous works have implemented oscillation waveforms using sinusoidal functions. A recent study by Cimarelli et al. [20] explored different temporal waveforms. In this work, we would like to explore the possibility of using spatial square waves for drag reduction. In order to reduce the power required to incorporate these oscillations, we consider only the positive cycles of these oscillations. One of the ways to realize spatial oscillations can be via pulsed jets

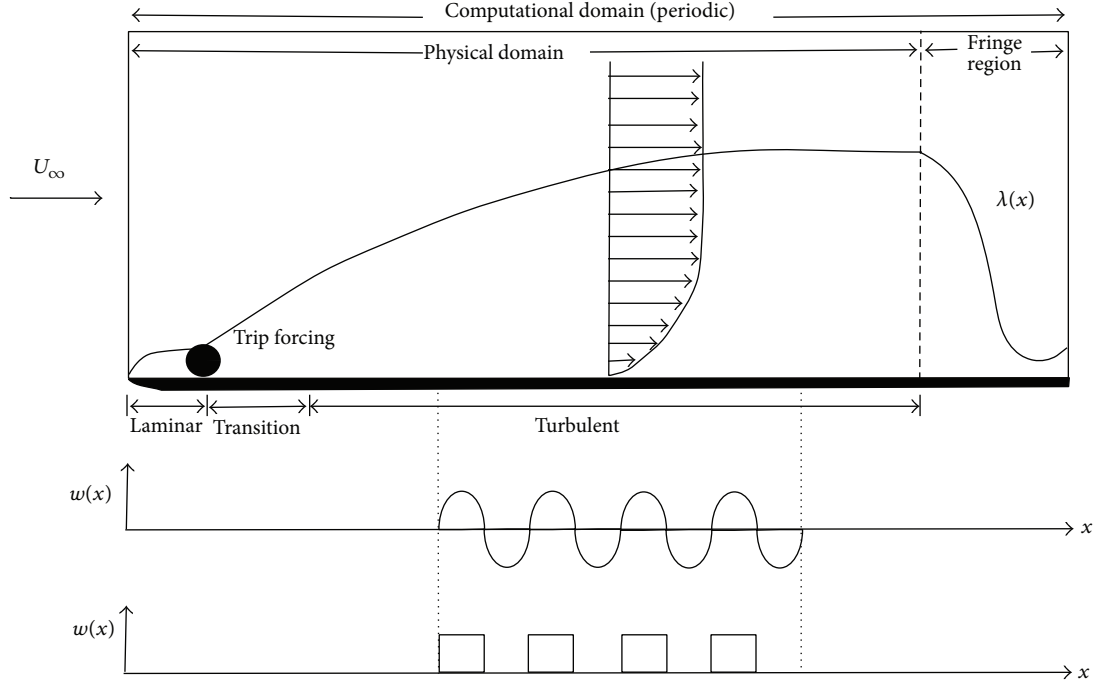


FIGURE 1: Computational box as seen from the negative z -direction with the growth of boundary layer illustrated. Fringe region forces the solution back to the prescribed laminar inflow thus enforcing periodic boundary condition. The lower part illustrates the spanwise velocity forcing which is applied in a part of the wall under the turbulent boundary layer. Half square waves are used in the present study as shown in the bottom figure.

in the spanwise direction for the near wall region. Another possibility is to actively manipulate wall roughness optimally distributed along the surface. The main contribution of the present work is to illustrate the use of smooth step functions to approximate the square waves which otherwise may give rise to Gibbs phenomenon when using spectral methods.

2. Methodology

2.1. Governing Equations. The governing equations which are used for the simulations here are the Navier-Stokes equations which are formulated in terms of velocity-vorticity and written in tensor notation as

$$\frac{\partial u_i}{\partial t} = -\frac{\partial p}{\partial x_i} + \epsilon_{ijk} u_j \omega_k - \frac{\partial}{\partial x_i} \left(\frac{1}{2} u_j u_j \right) + \frac{1}{\text{Re}} \nabla^2 u_i + F_i, \quad (3)$$

$$\frac{\partial u_i}{\partial x_i} = 0, \quad (4)$$

where u_i are the velocity components, ω_i are the vorticity components, p denotes pressure, and F_i is the body force. The nondimensional constant $\text{Re} = U_\infty \delta^* / \nu$ is the Reynolds number with U_∞ being the streamwise freestream velocity, δ^* is the displacement thickness at $x = 0$, and ν is the kinematic viscosity. x_i represents the coordinate system with (x, y, z) as streamwise, wall-normal, and spanwise coordinates and t denotes time.

These equations are solved using a pseudospectral method with appropriate boundary conditions. The basic

idea with spectral methods is to express the solution as a sum of *basis functions* and then compute their coefficients such that they satisfy the governing partial differential equations and the boundary conditions.

A third-order Runge-Kutta-scheme is used to perform time integration for the nonlinear terms. A second-order Crank-Nicolson method is used for the linear terms. For removing aliasing errors, a 3/2-rule is applied to the evaluation of the nonlinear terms when calculating Fourier transforms in the wall parallel $(x-z)$ plane. The numerical code (SIMSON [21]) used for the simulations in this work has been developed at KTH, Stockholm. Earlier simulations of both temporal [12, 13] and spatial [15, 16] wall forcing have been performed with the code.

2.2. Numerical Setup. Since we are trying to simulate a turbulent boundary layer with a spatially growing boundary layer, we need to choose our basis functions accordingly. A basic sketch for the computational setup is shown in Figure 1. For the discretization in the streamwise-spanwise plane, Fourier basis is chosen assuming the solutions are periodic in these directions. However, for the wall normal direction, periodicity does not apply and Chebyshev polynomials are instead used as basis functions for the y (wall-normal) direction. The technique is similar to other spectral codes used for channel flows [5–8, 17, 18], and the spectral accuracy is a considerable advantage as compared to other discretizations, such as the finite volume methods used in, for example, [9, 14].

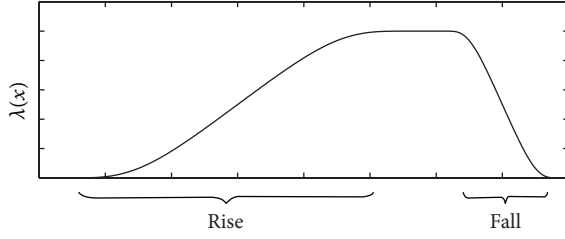


FIGURE 2: Schematic picture of the fringe region.

For initializing the simulations, a laminar base flow is required and is given as the Blasius similarity solution [22]. A trip forcing using a random volume force is then incorporated at $x = 5$ for the flow to undergo transition and thereafter we have turbulent flow regime. Figure 1 depicts this scheme.

Particular attention must be given to the streamwise direction since the boundary layer is growing downstream and hence no natural periodicity exists in that direction. Therefore, for the purpose of artificially creating a periodic computational domain, a fringe region is introduced at the end to achieve this. The purpose of this fringe region is to dampen the velocity fluctuations to zero and bring the velocity field back to the laminar Blasius solution such that there are minimum upstream effects [23]. This is achieved by introducing the volume forcing F_i in (3):

$$F_i = \lambda(x) (\tilde{u}_i - u_i), \quad (5)$$

where $\lambda(x)$ is the strength of the forcing and \tilde{u}_i is the laminar inflow velocity profile. The function λ is defined as

$$\lambda(x) = \lambda_{\max} f(x) \quad (6)$$

with

$$f(x) = S\left(\frac{x - x_{\text{start}}}{\Delta x_{\text{rise}}}\right) - S\left(\frac{x - x_{\text{end}}}{\Delta x_{\text{fall}}} + 1\right). \quad (7)$$

Here λ_{\max} is the maximum strength of the fringe, x_{start} and x_{end} denote the spatial extent of the region where the fringe is nonzero, and Δx_{rise} and Δx_{fall} are the rise and fall distance of the fringe function, respectively. Figure 2 shows a schematic of how the fringe function varies. $S(\eta)$ is a continuous step function that varies from zero for $\eta \leq 0$ to unity for $\eta \geq 1$ and is given by

$$S(\eta) = \begin{cases} 0, & \eta \leq 0, \\ \frac{1}{(1 + e^{(1/(\eta-1)+1/\eta)})}, & 0 < \eta < 1, \\ 1, & \eta \geq 1. \end{cases} \quad (8)$$

2.3. Wall Oscillation Implementation. The form of wall oscillation implemented here is a spatial square wave with only positive forcing to reduce power consumption. However, there are numerical challenges in implementing this using pseudospectral method. A square wave when represented using Fourier basis gives rise to Gibbs phenomenon which

TABLE 1: Oscillation parameters for the simulations presented.

Parameter set (PS)	W_m	k
PS1	(0.1, 0.25, 0.4, 0.5, 0.6, 0.75, 1)	0.0628
PS2	(0.1, 0.25, 0.4, 0.5, 0.6, 0.75, 1)	0.1256
PS3	(0.1, 0.25, 0.4, 0.5, 0.6, 0.75, 1)	0.2512

is shown in Figure 3(a). When we try to approximate the strong discontinuity in the square wave, it results in strong oscillations at the edges. These result in spurious values causing numerical instability and large computational errors. Increasing the number of terms in the Fourier series approximation does reduce the oscillation but it does not eliminate it completely.

In order to avoid Gibbs phenomenon, we utilize the same step function as we used for fringe region (8). Using the step function is advantageous as it has continuous derivatives at all points and does not exhibit the spurious ringing phenomenon. Figure 3(b) shows the use of $f(x)$ in implementing the wall boundary condition for the present simulations. By including only a few Fourier coefficients, we can approximate the function quite accurately and eliminate Gibbs rings.

Spatial wall oscillation can be incorporated with the following boundary condition:

$$w(x)_{y=0} = W_m f(x), \quad (9)$$

where $f(x)$ is the same profile function as used for fringe region (see equation (7)) and W_m is the amplitude of the spatial oscillations.

2.4. Numerical Parameters. All quantities are nondimensionalized by the free-stream velocity (U_∞) and the displacement thickness (δ^*) at the starting position of the simulation ($x = 0$), where the flow is laminar. The Reynolds number is set by specifying $Re_{\delta^*} = U_\infty \delta^* / \nu$ at the laminar inlet ($x = 0$). Note that, unless otherwise stated, the + superscript indicates that the quantity is made nondimensional with the friction velocity of the unmanipulated boundary layer (the reference case), denoted by u_τ^0 , and the kinematic viscosity (ν).

A computational domain with $L_x = 600$, $L_y = 30$, and $L_z = 34$ is chosen with a mesh resolution of $800 \times 201 \times 144$, respectively. The resolution of these simulations in wall units is $\Delta x^+ = 16$, $\Delta y_{\min}^+ = 0.04$, and $\Delta z^+ = 5.1$. All scalings are done based on u_τ^0 from reference case at the starting position of wall forcing ($x = 200$). Wall oscillation boundary conditions are employed between $x_{\text{start}} = 200$ and $x_{\text{end}} = 450$ once it is ascertained that the flow has become fully turbulent. The Reynolds number based on momentum thickness varies between $450 < Re_\theta < 715$ in the control region.

Table 1 summarizes the parameters chosen for the steady spatial oscillation in the present work. Only the positive forcing has been employed for these simulation setups as shown in Figure 3(b). The spatial frequencies have been doubled and halved with respect to PS2 to see its impact on drag reduction performance. Also, the amplitude of oscillations is varied to understand its impact on drag reduction. The aim is to observe the effect of removing the negative forcing of the

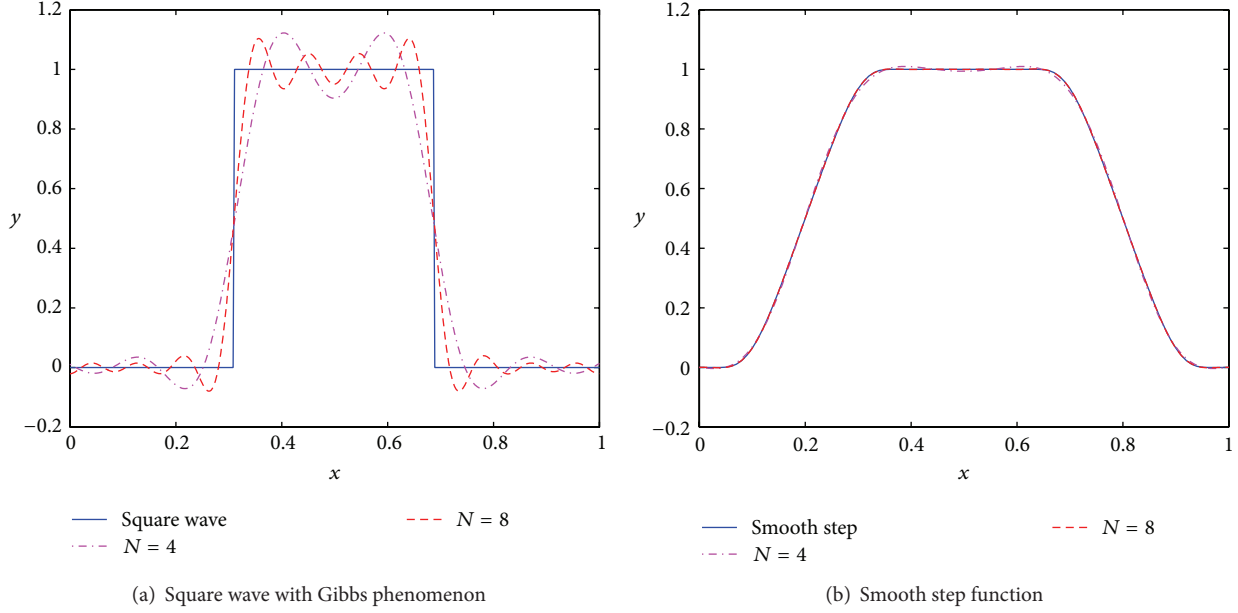
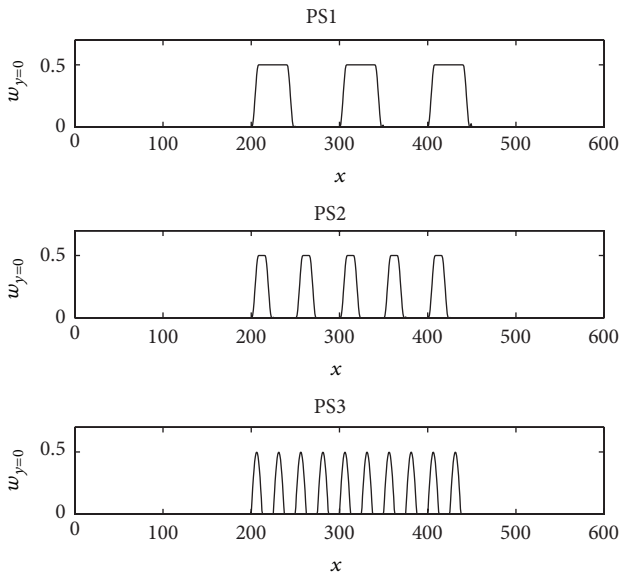


FIGURE 3: Function approximations using finite Fourier series terms.

FIGURE 4: Wall boundary condition set for spanwise velocity component for PS1, PS2, and PS3 at $W_m = 0.5$.

wall boundary and its effects on power budget and net energy savings. Figure 4 shows the wall boundary condition for the three parameter sets at $W_m = 0.5$.

3. Results and Discussion

In this section, we look into two aspects of the results obtained from our numerical simulations. First, we look into attenuation of c_f values with respect to the reference case.

Subsequently, we present the power budget based on the different forcings.

3.1. Skin Friction Attenuation. We compare skin friction from the unoscillated or the reference case with the oscillated cases. Skin friction coefficient for turbulent flows is defined as

$$c_f = 2 \left(\frac{u_\tau}{U_\infty} \right)^2, \quad (10)$$

where u_τ is the friction velocity and is computed based on mean streamwise velocity gradient at the wall:

$$u_\tau = \sqrt{\nu \left. \frac{\partial u}{\partial y} \right|_{y=0}}. \quad (11)$$

The resulting drag reduction (DR) is then calculated from

$$\text{DR} (\%) = 100 \frac{c_f^0 - c_f}{c_f^0}, \quad (12)$$

where c_f^0 is the skin friction of the reference case. In contrast to internal flows [1–11], the DR is varying in the downstream direction for the present case of boundary layer flow. Figure 5 shows the results for the skin friction variation along streamwise direction. All three cases show skin friction attenuation. As soon as wall oscillation is applied at $x_{\text{start}} = 200$, we see a strong gradient which marks the spatial transient for c_f . For PS1, we have a longer wavelength and, due to discontinuous half waves, we observe recovery of c_f back towards the reference case. However, for PS2 and PS3, due to smaller wavelength, this recovery process is weaker. This is a crucial observation as it indicates that, with positive forcing itself, we can get drag reduction of a similar order of magnitude as with

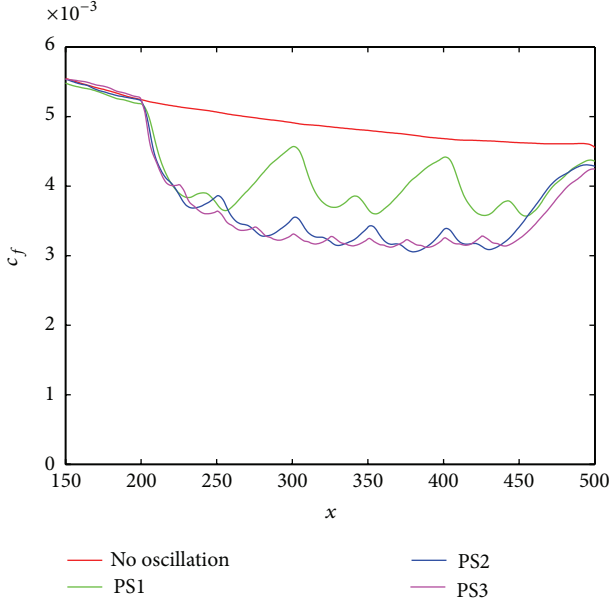


FIGURE 5: Spatial development of skin friction along streamwise direction at $W_m = 1$.

a full cycle of wall oscillation. This would reduce the power required for forcing the wall oscillation and this increases our net power saving as will be presented in the next section. At $x_{\text{end}} = 450$, the oscillations are stopped and skin friction attains the reference case values.

3.2. Power Budget. To compute the net energy savings, we need to take into account the energy required for wall oscillation as compared to the savings due to drag reduction. The derivation of these terms was given for channel flow by Quadrio and Ricco [6] which was extended to the boundary layer case by Skote [13].

In order to compute the saved power $P_{\text{sav}}(\%)$, DR (as percentage of ratio of skin-friction coefficients from reference and oscillated cases; see (12)) is integrated for the region with wall oscillation. The total saved power can be written as

$$P_{\text{sav}}(\%) = \frac{1}{L} \int_{x_{\text{start}}}^{x_{\text{end}}} \text{DR}(\%) \, dx, \quad (13)$$

where x_{start} denotes the position at which the wall oscillation is started, x_{end} denotes the endpoint for oscillation, and $L = x_{\text{start}} - x_{\text{end}}$.

Similarly, the wall oscillation requires power input which can also be defined in terms of the friction power of the reference flow [13] and can be written as

$$P_{\text{req}}(\%) = \frac{\int_{x_{\text{start}}}^{x_{\text{end}}} \nu \left(\frac{\partial w}{\partial y} \right) \Big|_{y=0} W \, dx}{\int_{x_{\text{start}}}^{x_{\text{end}}} (u_{\tau}^0)^2 U_{\infty} \, dx}. \quad (14)$$

The net saved power is then defined as $P_{\text{net}} = P_{\text{sav}} - P_{\text{req}}$. If P_{net} is negative it indicates that the input power required to oscillate the wall is greater than the saved power due to

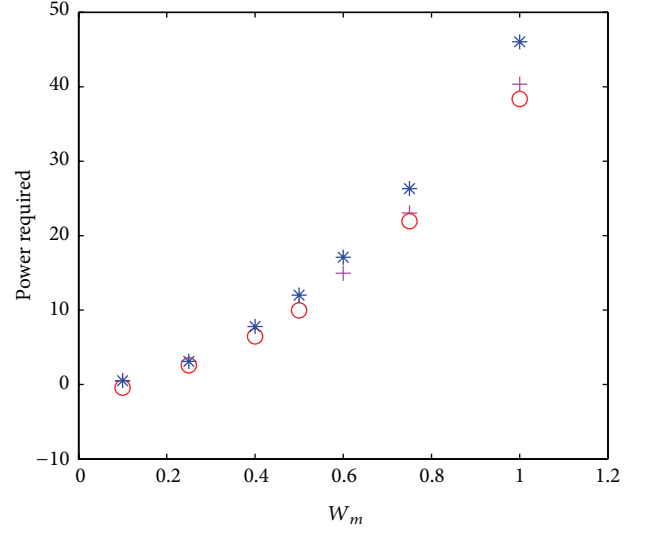


FIGURE 6: Power required for wall oscillation.

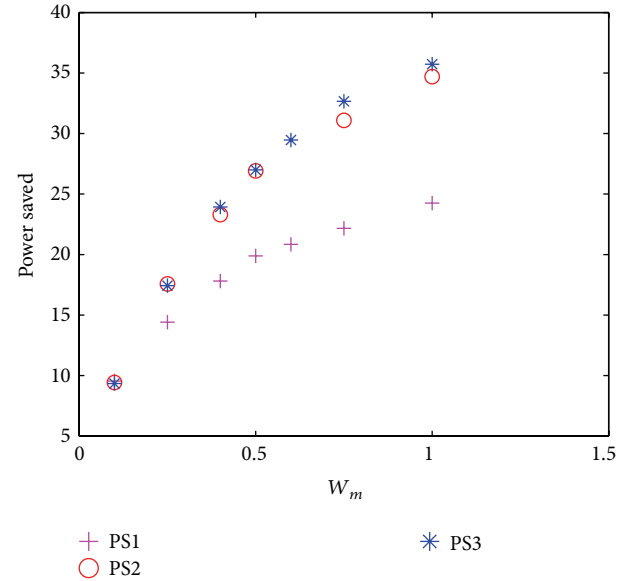


FIGURE 7: Power saved for the three chosen parameter sets.

streamwise drag reduction. However, it is possible that, for an optimized set of oscillation parameters, one may achieve positive energy budget. As reported by other researchers [15, 18, 19], a positive net energy is more attainable for spatial forcing than for temporal forcing.

Power required for the three oscillation cases is shown in Figure 6. For lower amplitudes of forcing, we require lesser power and it grows exponentially for larger amplitudes. For different spatial frequencies, there is not much difference in input power required. Figure 7 shows the power saved based on (13). Here, we see that with increasing amplitude, the power saving saturates after a limit. The effect of spatial

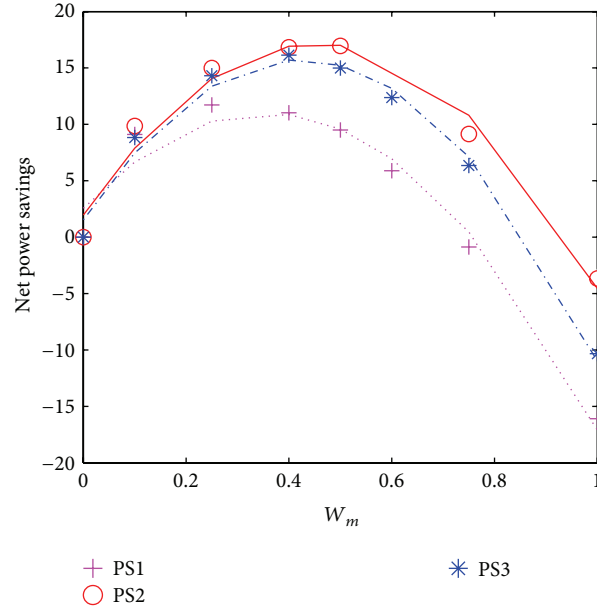


FIGURE 8: Net power savings for the three chosen parameter sets together with a quadratic curve fit.

frequency is rather interesting as we see that the power saved for PS2 and PS3 is almost the same. PS1 has a lower power saving and that can be attributed to the recovery to unoscillated skin friction values discussed previously in Section 3.1.

Figure 8 shows the net power savings for the different parameter sets. PS2 with $W_m = 0.5$ gives us the maximum net power saving ($\sim 18\%$) amidst our chosen parameter space. Performance quickly deteriorates for larger amplitudes which show negative net power savings indicating that we spend more power in oscillating the wall as compared to the power savings. No complete description of the drag reduction mechanism exists to date. Thus, the influence of the parameters on the drag reduction remains largely unexplained. The parameter space explored in the current work is definitely not exhaustive. Viotti et al. [17] show power budget statistics for a wide parameter space using sinusoidal wall oscillation. The maximum net power savings achieved is reported as 23% which was found at $W_m^+ = 6$. On the other hand, they showed maximum net power savings of 6% at $W_m^+ = 12$, which is the amplitude comparable to the present case. They concluded that lower amplitudes give higher net power savings, even though the drag reduction values are lower. The simulation cases in the present study are not as exhaustive due to the computational demands for spatially developing boundary layers. Nevertheless, for the current study we obtain the maximum savings of 18% at $W_m^+ = 10$. The current suboptimal results may very well be further improved by increasing the parametric space.

Although the results look promising in terms of the net power savings, one of the drawbacks of the proposed methodology is that it induces crossflow which might be undesirable in certain situations. In order to illustrate the phenomena,

a horizontal plane at $y^+ = 10$ is shown in Figure 9. The figure has been compressed by a factor 4 in the streamwise direction for better visualization. From the figure it is observed that, after the first oscillation stops, the streaks reorient themselves to the streamwise direction. However, a spanwise crossflow manifests itself as can be seen by the oblique streaks in the regions after the second and third periods of forcing.

Note that this phenomena would not occur if a periodic function with equal amount of positive and negative spanwise wall velocity is used, as in the study of temporal nonsinusoidal wall forcing by Cimarelli et al. [20].

4. Conclusion

A new form of steady spatial wall oscillation technique in the form of square waves with positive forcing has been presented with promising results for developing an active drag reduction technique. Spectral methods were used to solve the governing equations and the use of a smooth step has been demonstrated to approximate a square wave to overcome Gibbs phenomenon and avoid sharp discontinuities. Downstream development of skin friction and power budget for different oscillation parameters have been presented. An optimal set of wall oscillation parameters for the current parameter space was found to have $\sim 18\%$ net energy savings.

Conflict of Interests

The authors declare that there is no conflict of interests regarding the publication of this paper.

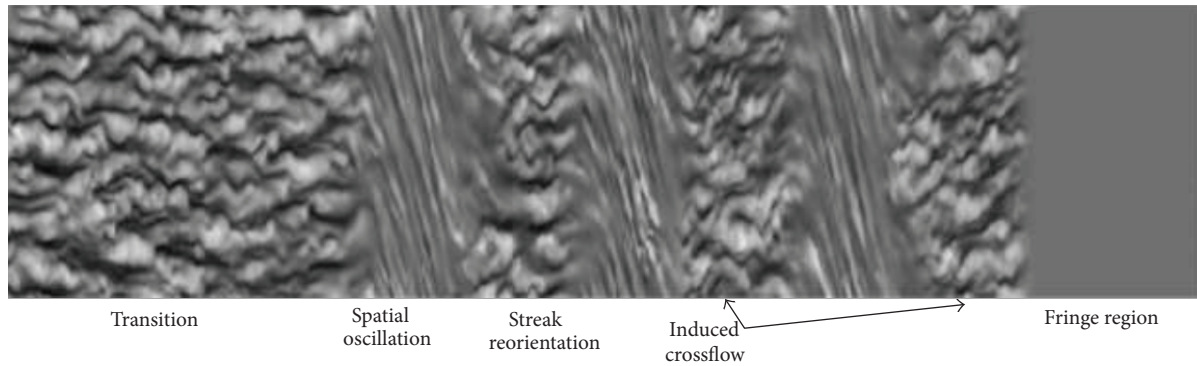


FIGURE 9: Half wave oscillations inducing crossflow in the spanwise direction. A horizontal plane ($y^+ = 10$) in the computational box is shown. The dark grey indicates low-speed regions and lighter shades indicate high-speed patches. The plane is stretched by a factor of four in the spanwise direction for clarity.

Acknowledgment

This research work is supported in part by Singapore MOE Tier-2 Grant no. MOE2012-T2-1-030.

References

- [1] W. J. Jung, N. Mangiavacchi, and R. Akhavan, "Suppression of turbulence in wall-bounded flows by high-frequency spanwise oscillations," *Physics of Fluids A*, vol. 4, no. 8, pp. 1605–1607, 1992.
- [2] A. Baron and M. Quadrio, "Turbulent drag reduction by spanwise wall oscillations," *Applied Scientific Research*, vol. 55, no. 4, pp. 311–326, 1995.
- [3] J.-I. Choi, C.-X. Xu, and H. J. Sung, "Drag reduction by spanwise wall oscillation in wall-bounded turbulent flows," *AIAA Journal*, vol. 40, no. 5, pp. 842–850, 2002.
- [4] C.-X. Xu and W.-X. Huang, "Transient response of Reynolds stress transport to spanwise wall oscillation in a turbulent channel flow," *Physics of Fluids*, vol. 17, no. 1, Article ID 018101, 2005.
- [5] M. Quadrio and P. Ricco, "Initial response of a turbulent channel flow to spanwise oscillation of the walls," *Journal of Turbulence*, vol. 4, article 7, 2003.
- [6] M. Quadrio and P. Ricco, "Critical assessment of turbulent drag reduction through spanwise wall oscillations," *Journal of Fluid Mechanics*, vol. 521, pp. 251–271, 2004.
- [7] P. Ricco and M. Quadrio, "Wall-oscillation conditions for drag reduction in turbulent channel flow," *International Journal of Heat and Fluid Flow*, vol. 29, no. 4, pp. 891–902, 2008.
- [8] P. Ricco, C. Ottonelli, Y. Hasegawa, and M. Quadrio, "Changes in turbulent dissipation in a channel flow with oscillating walls," *Journal of Fluid Mechanics*, vol. 700, pp. 77–104, 2012.
- [9] E. Toubert and M. A. Leschziner, "Near-wall streak modification by spanwise oscillatory wall motion and drag-reduction mechanisms," *Journal of Fluid Mechanics*, vol. 693, pp. 150–200, 2012.
- [10] A. Duggeby, K. S. Ball, and M. R. Paul, "The effect of spanwise wall oscillation on turbulent pipe flow structures resulting in drag reduction," *Physics of Fluids*, vol. 19, no. 12, Article ID 125107, 2007.
- [11] F. Auteri, A. Baron, M. Belan, G. Campanardi, and M. Quadrio, "Experimental assessment of drag reduction by traveling waves in a turbulent pipe flow," *Physics of Fluids*, vol. 22, no. 11, Article ID 115103, 2010.
- [12] I. Yudhistira and M. Skote, "Direct numerical simulation of a turbulent boundary layer over an oscillating wall," *Journal of Turbulence*, vol. 12, article N9, 2011.
- [13] M. Skote, "Temporal and spatial transients in turbulent boundary layer flow over an oscillating wall," *International Journal of Heat and Fluid Flow*, vol. 38, pp. 1–12, 2012.
- [14] S. Lardeau and M. A. Leschziner, "The streamwise drag-reduction response of a boundary layer subjected to a sudden imposition of transverse oscillatory wall motion," *Physics of Fluids*, vol. 25, no. 7, Article ID 075109, 2013.
- [15] M. Skote, "Comparison between spatial and temporal wall oscillations in turbulent boundary layer flows," *Journal of Fluid Mechanics*, vol. 730, pp. 273–294, 2013.
- [16] M. Skote, "Turbulent boundary layer flow subject to streamwise oscillation of spanwise wall-velocity," *Physics of Fluids*, vol. 23, no. 8, Article ID 081703, 2011.
- [17] C. Viotti, M. Quadrio, and P. Luchini, "Streamwise oscillation of spanwise velocity at the wall of a channel for turbulent drag reduction," *Physics of Fluids*, vol. 21, no. 11, Article ID 115109, 2009.
- [18] M. Quadrio, P. Ricco, and C. Viotti, "Streamwise-travelling waves of spanwise wall velocity for turbulent drag reduction," *Journal of Fluid Mechanics*, vol. 627, pp. 161–178, 2009.
- [19] M. Skote, "Scaling of the velocity profile in strongly drag reduced turbulent flows over an oscillating wall," *International Journal of Heat and Fluid Flow*, vol. 50, pp. 352–358, 2014.
- [20] A. Cimarelli, B. Frohnäpfel, Y. Hasegawa, E. De Angelis, and M. Quadrio, "Prediction of turbulence control for arbitrary periodic spanwise wall movement," *Physics of Fluids*, vol. 25, no. 7, Article ID 075102, 2013.
- [21] M. Chevalier, P. Schlatter, A. Lundbladh, and D. S. Henningson, "Simson—a pseudo-spectral solver for incompressible boundary layer flows," Tech. Rep. TRITA-MEK 2007:07, KTH Mechanics, Stockholm, Sweden, 2007.
- [22] H. Schlichting, *Boundary Layer Theory*, McGraw-Hill, New York, NY, USA, 7th edition, 1979.
- [23] F. P. Bertolotti, T. Herbert, and P. R. Spalart, "Linear and non-linear stability of the Blasius boundary layer," *Journal of Fluid Mechanics*, vol. 242, pp. 441–474, 1992.

Research Article

Numerical Study of Correlation of Fluid Particle Acceleration and Turbulence Intensity in Swirling Flow

Nan Gui,^{1,2} Xingtuan Yang,¹ Jie Yan,³ Jiyuan Tu,^{1,4} and Shengyao Jiang¹

¹*Institute of Nuclear and New Energy Technology of Tsinghua University and the Key Laboratory of Advanced Reactor Engineering and Safety, Ministry of Education, Beijing 100084, China*

²*Department of Thermal Energy Engineering, College of Mechanical and Transportation Engineering, China University of Petroleum, Beijing 102249, China*

³*China Academy of Space Technology, Beijing 10094, China*

⁴*School of Aerospace, Mechanical & Manufacturing Engineering, RMIT University, Melbourne, VIC 3083, Australia*

Correspondence should be addressed to Shengyao Jiang; shengyaojiang@sina.com

Received 30 June 2014; Accepted 26 August 2014

Academic Editor: Junuthula N. Reddy

Copyright © 2015 Nan Gui et al. This is an open access article distributed under the Creative Commons Attribution License, which permits unrestricted use, distribution, and reproduction in any medium, provided the original work is properly cited.

Numerical investigation of correlation between the fluid particle acceleration and the intensity of turbulence in swirling flows at a large Reynolds number is carried out via direct numerical simulation. A weak power-law form correlation $u_{r.m.s}^E \sim C(a^L)^{\varphi}$ between the Lagrangian acceleration and the Eulerian turbulence intensity is derived. It is found that the increase of the swirl level leads to the increase of the exponent φ and the trajectory-conditioned correlation coefficient $\rho(a^L, u^E)$ and results in a weak power-law augmentation of the acceleration intermittency. The trajectory-conditioned convection of turbulence fluctuation in the Eulerian viewpoint is generally linearly proportional to the fluctuation of Lagrangian accelerations, indicating a weak but clear relation between the Lagrangian intermittency and Eulerian intermittency effects. Moreover, except the case with vortex breakdown, the weak linear dependency is maintained when the swirl levels change, only with the coefficient of slope varied.

1. Introduction

As well known, the swirling flow, especially for the strongly swirling jets at large Reynolds numbers to which few studies were devoted, is one type of anisotropic turbulence, which is less understood than the homogenous and isotropic turbulence [1, 2]. In the past decades, the swirling flows have been studied extensively under the Eulerian framework, including a variety of scientific research topics and industrial applications, for example, swirling recirculating flow field [3, 4], open Von Kármán swirling flow [5], gas-liquid cylindrical cyclone [6], gas-liquid two-phase jet flow [7], gas turbine combustor [8], and so on. However, the swirling flows based on the Lagrangian framework have not been well investigated. Referring to the recent investigations of Lagrangian acceleration in highly turbulent flows [9, 10], the turbulent anisotropic flows with either a swirling or a rotating flow pattern are of specific interest. Unfortunately,

the characteristics of Lagrangian acceleration for highly swirling flows are still not well known.

Moreover, due to the fundamental importance of the Lagrangian characteristics of fluid particle motion to transporting and mixing in turbulence and reacting systems [11], the Lagrangian measurement/modeling method has been well used recently as it is a powerful approach for improving the understanding of turbulent flows [12, 13]. Therefore, a large number of excellent studies have been carried out contributing to the Lagrangian characteristics of fluid particle motion, especially on the acceleration structure or Lagrangian velocity spectrum [14–18].

On the other hand, as the investigations of turbulence under the Eulerian frame are better developed than those under the Lagrangian frame, establishing the relationship between the Lagrangian statistics and Eulerian statistics should be helpful in determining the common intrinsic statistical features of turbulence. However, the joint Lagrangian

and Eulerian statistics of fluid particles are not well understood yet. For example, the relationship between acceleration intermittency (from the Lagrangian viewpoint) and turbulence intensity (from the Eulerian viewpoint) is unknown.

Additionally, to carry out direct numerical simulation of strongly swirling jets at a larger Reynolds number is a state-of-the-art challenging work. Thus, direct numerical simulation of the strongly swirling jet is very essential and important to the scientific research of anisotropic turbulence.

In conclusion, a numerical study of direct numerical simulation of the Lagrangian motion of fluid particles at large Reynolds numbers is performed in present study, where the Lagrangian statistics and Eulerian statistics are combined together. The main aim of this study is to show the dependence of correlation between fluid particle acceleration and the intensity of turbulence on various levels of swirls and show the correlation between the Lagrangian acceleration and Eulerian convection of turbulence fluctuation in strongly swirling jets at a large Reynolds number.

2. Numerical Description

2.1. Governing Equations. The Navier-Stokes equations for incompressible fluids, based on the conservation laws of mass and momentum, are formulated in dimensionless forms as follows:

$$(1) \text{ continuum equation: } \partial u_i / \partial x_i = 0,$$

$$(2) \text{ momentum equation: } (\partial u_i / \partial t) + u_j (\partial u_i / \partial x_j) = -(\partial p / \partial x_i) + (1/\text{Re})(\partial / \partial x_j)(\partial / \partial x_j)u_i.$$

To solve the governing equations, the finite difference method is applied. The upwind compact schemes [19] are used to discretize the convection term. The fourth-order compact difference schemes [20] are applied for space derivatives and the pressure-gradient terms. The third-order explicit schemes are used to deal with the boundary points, keeping the global fourth-order spatial accuracy. The fourth-order Runge-Kutta schemes [21] are used for time integration. The pressure-Poisson equation is solved to obtain the pressure via using the fourth-order finite difference method [22]. The methods have already been successfully applied in my recently published literature [23].

2.2. Simulation Setup. The parameters used in the present simulation are listed in Table 1. In the momentum equation, the Reynolds number is defined as $\text{Re}_\lambda = U_0 \cdot \lambda / \nu = 387.3$, where U_0 is the axial inlet velocity; λ is the Taylor microscale; and the kinematic viscosity $\nu = 10^{-6} \text{ (m}^2/\text{s)}$ (water at 20.3°C).

The configurations of swirling flow are illustrated in Figure 1(a), which are similar to those from an earlier study [24]. A round jet of diameter d is imparted with a rotational azimuthal velocity at the inlet and issued into a rectangular

TABLE 1: Parameters used in simulation.

Characteristic diameter d^* (mm)	1.0
Characteristic inflow velocity U_0^* (m/s)	5, 8 and 10
Scales of the flow domain	$13.3d \times 10d \times 10d$
Grid numbers, $N_x \times N_y \times N_z$ (-)	$640 \times 480 \times 480$
Spatial resolution δ (μm)	20.8
Reynolds number, Re_d	10000
Swirl number, S	0.49, 1.08 and 1.42
Density of fluid, ρ_f (kg/m^3)	1.0×10^3
Kinematic viscosity of fluid, ν (m^2/s)	1.0×10^{-6}
Time step, Δt (μs)	0.2
Total simulation time, T_s (ms)	40

*The characteristic variable.

flow domain of $13.3d \times 10d \times 10d$. The swirl level is the ratio of the maximum azimuthal velocity $U_{a,\max}$ to the streamwise velocity U_0 ; that is, $S = 2U_{a,\max}/U_0$ [25]. The axial and azimuthal inlet velocity profiles are the same as those mentioned in earlier studies [24, 26, 27] (Figures 1(b) and 1(c)). No inflow disturbance is introduced to keep the intrinsic feature of the strongly swirling flow. Three swirl numbers, that is, $S = 0.49, 1.08$, and 1.42 , are simulated in the present study by varying the azimuthal velocity. The nonreflecting boundary condition is utilized for the outlet condition [28], and the side walls are set to be nonslipping wall boundaries.

The flow domain is discretized by $640 \times 480 \times 480 = 147\,456\,000$ Cartesian mesh grids. With this spatial discretization ($\delta = 20.8 \mu\text{m}$), the jet inlet area ($\pi d^2/4$) is covered by 1791 mesh grids. It is estimated that the Kolmogorov length scale is about $\eta \approx 0.85\delta$, which is in the same order of the finest mesh scale. According to [29], it is fine enough to capture the smallest scale of turbulence. For time integration, the time step is $0.2 \mu\text{s}$ and the total simulated time is 40 ms, about three convective periods.

The particles issued from the 1791 grid points inside the jet inlet area are traced, and, for each grid point, one particle is issued into the flow domain every 200 time steps. In this way, a total number of 179,100 fluid particles are traced in this study. The fluid particles originated from these 1791 points are designated as $\mathbf{x}(j, t)$, $j = \text{mod}(n, 1791)$, where n is the particle number and j designates the group number. Then, all the particles can be divided into 1791 groups. Each group has the same initial location and velocity. However, the trajectories of fluid particles within each group are not the same because the system of fluid flow dynamics is strongly nonlinear. An ensemble average over each group of particles is utilized to carry out the Lagrangian statistics. For each group, the instantaneous acceleration for 100 particles is traced and recorded at any time for analysis. Thus, each data group includes $\sim O(10^6)$ points. The ensemble average process should be statistically reliable over such a large number of data points.

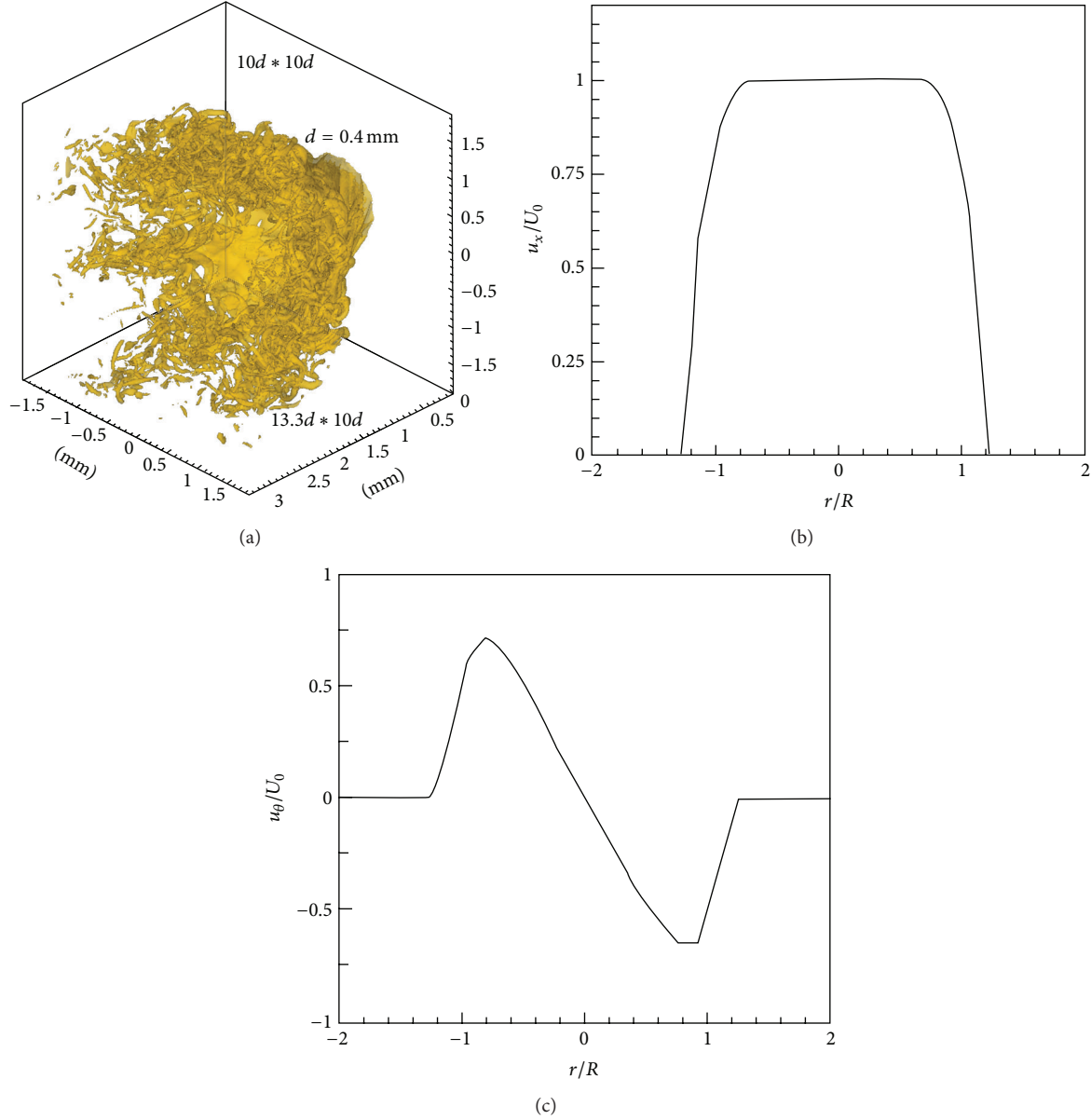


FIGURE 1: (a) Sketch of flow configuration and typical vorticity and the axial (b) and azimuthal (c) inlet velocity profiles.

3. Results and Discussions

3.1. Fluid Vortex Structures and Particle Trajectory. The typical vortex structure of $S = 1.42$ is visualized in Figure 1(a). It is clearly seen that a bubble region is enclosed by the nearly axisymmetric vortices, forming an open angle toward downstream. It is so called the central recirculation zone (CRZ) or vortex breakdown (VB). Moreover, strong small vortices are observed due to the highly turbulent and swirling fluid flow.

Corresponding to this type of vortex structure, the fluid particles are transported from the initial locations to the downstream. The trajectories of one typical group of fluid particles originated from the same initial location at the inlet of the flow are shown in Figure 2. It is found that the fluid

trajectories enclose a bubble region statistically too, which are initiated from the location where the axial motion of fluid particle is decreased to zero, that is, the stagnation point. After that, an immediate expansion in the lateral and spanwise directions is established. This feature of fluid trajectory reflects the structural characteristics of swirling flow under the Lagrangian viewpoint.

3.2. Joint Distribution of Acceleration and Turbulence Intensity. In general, the velocity field depends on the location and time, that is, $\mathbf{u}^E(\mathbf{x}, t)$, where “E” denotes the “Eulerian” viewpoint. To average $\mathbf{u}^E(\mathbf{x}, t)$ in time, the velocity field can be divided into a time averaged part $\bar{\mathbf{U}}^E(\mathbf{x})$ and a fluctuation part $\mathbf{u}'^E(\mathbf{x}, t)$, corresponding to the mean flow field

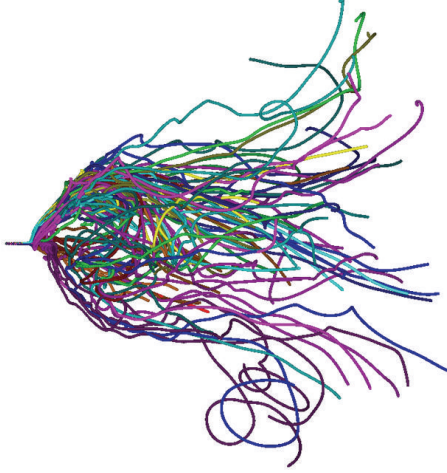


FIGURE 2: The trajectories of one group of particles for $S = 1.42$.

and the turbulent fluctuation field, respectively. Hence, the root mean square (RMS) values of velocity $u_{r.m.s}^E(\mathbf{x}) = ((1/\Delta T) \int_t^{t+\Delta T} |\mathbf{u}^E(\mathbf{x}, \tau) - \bar{\mathbf{u}}^E(\mathbf{x})|^2 d\tau)^{1/2}$ can be used to evaluate the local intensity of turbulence at location \mathbf{x} . On the other hand, the motion of fluid particles can be traced under the Lagrangian framework. The velocity and acceleration of the traced particles are defined as $\mathbf{a}^L(j, t)$ and $\mathbf{u}^L(j, t)$, respectively, where j denotes the fluid particle and “ L ” denotes the “Lagrangian” viewpoint. In this way, the statistical characteristics of Lagrangian motion of fluid particles with regard to the acceleration $\mathbf{a}^L(j, t)$, velocity $\mathbf{u}^L(j, t)$, and trajectories are obtained for analysis.

Assuming a “steady” turbulence field is reached, the turbulence intensity field can be quantified using the time-averaging method. The fluid particle moves through the “steady” turbulence field with temporally and spatially varied Lagrangian acceleration of $a^L = a^L(j; \mathbf{r}, t)$. Focusing on $u_{r.m.s}^E$ and $a^L = a^L(j; \mathbf{r}, t)$ on the particle trajectories, a joint distribution of $(a^L(j; t), u_{r.m.s}^E)$ can be obtained for analysis via the Eulerian-Lagrangian joint statistics of turbulence. It is termed as the trajectory conditioned joint distribution here.

As shown in Figure 3, the trajectory conditioned distribution of $(a^L(j; t), u_{r.m.s}^E)$ for different levels of swirl is indicated. Every point in Figure 3 illustrates the pair of $(a^L(j; t), u_{r.m.s}^E)$ on the trajectories which the j th group particles go through. Zonal distributions are observed for $S = 0.49, 1.08$, and 1.42 , with the widths being increased under larger swirling levels. Thus, it is indicated that the $u_{r.m.s}^E$ and $a^L(j)$ are correlated in some manner. Generally, this correlation may follow the form of power-law $y = a + x^b$. Note that the linear relationship is also included in the power-law, provided $b = 1$. Based on this assumption, the data are fitted by the near power-law expression.

The \log - \log distribution of $a^L(j)$ and $u_{r.m.s}^E$ for $S = 1.42$ is illustrated in Figure 4. The trend of the \log - \log plot is approximately linear, although the data points are scattered widely. As the data points are corresponding to all fluid particles

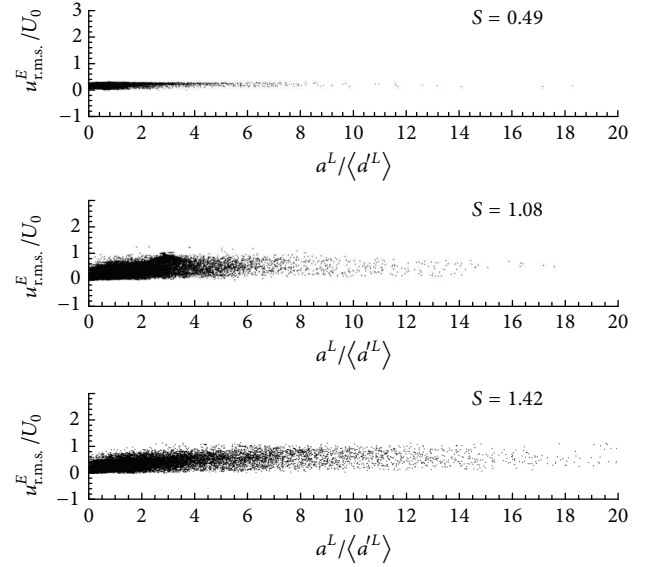


FIGURE 3: The distributions of Lagrangian acceleration a^L and the Eulerian turbulence intensity $u_{r.m.s}^E$ for $S = 0.49, 1.08$, and 1.42 .

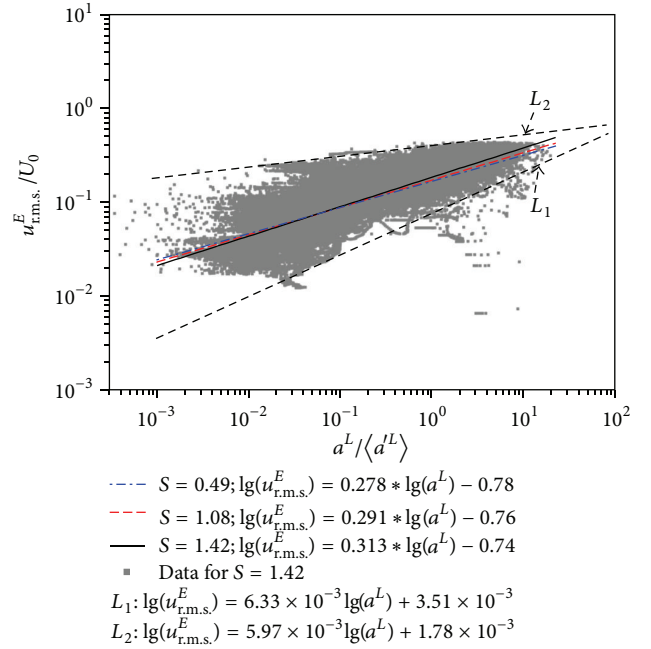


FIGURE 4: The fitting lines obtained by the linear regression of one group of fluid particles.

within the flow, the distribution should be scattered due to the stochastic and turbulent fluctuations of particles. Moreover, it could indicate the intrinsic Lagrangian characteristics of turbulent swirling flows, especially for the general trends of distribution and the statistical relationships between $a^L(j)$ and $u_{r.m.s}^E$.

In addition, it is seen from Figure 4 that the slope of the fitting line increases when the swirl level increases. The fitting equations are listed in Table 2. By these fitted expressions,

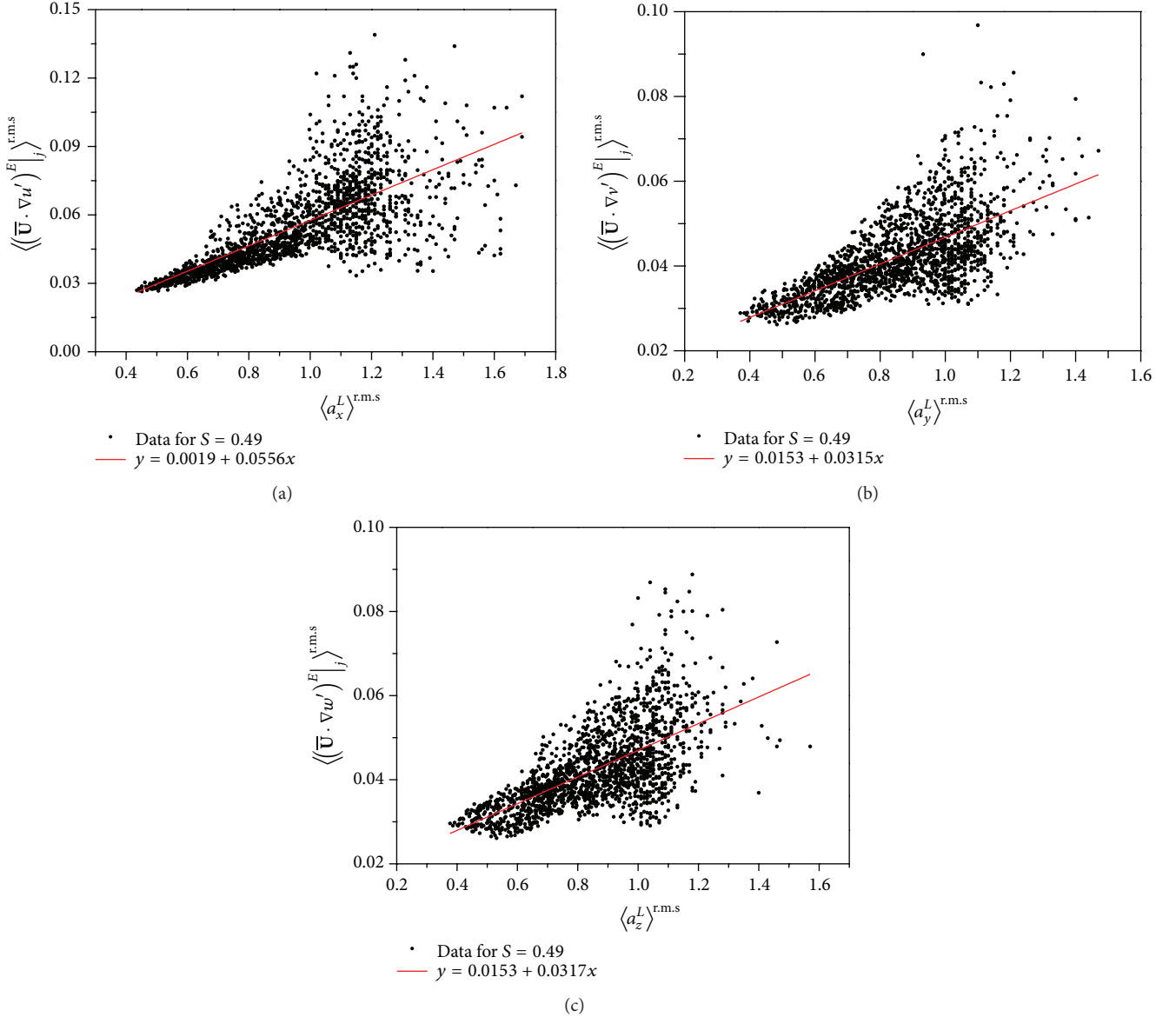


FIGURE 5: The correlation between the Eulerian convection term of turbulence fluctuations u' (a), v' (b), and w' (c) and the Lagrangian acceleration fluctuations in the x , y , and z directions, respectively, for $S = 0.49$.

the relationship between the Lagrangian acceleration and the local Eulerian turbulence intensity is indicated to follow a weak power-law form

$$u_{r.m.s}^E \sim C(a^L)^\varphi. \quad (1)$$

Statistically, the turbulence intensity should be large where the fluid particles always pass through with large acceleration and vice versa. If the averaged turbulence intensity level is in the same order as that with the same Reynolds number and no extra disturbance, the effect of the swirl upon the Lagrangian characteristics could be achieved through a change in the exponent φ and coefficient C . Hence, the characteristics of intermittency are closely related to swirl level and exponent φ . With the increase of swirl levels, the exponent φ becomes

larger. Consequently, the Lagrangian acceleration is nearly power-exponentially increased, leading to the augmented characteristics of intermittency.

In addition, Figure 4 shows that the scope of distribution of $(a^L(j; t), u_{r.m.s}^E)$ can be generally sketched by an inferior line (L_1) and a superior line (L_2) (Table 3). The majority of the data points are restricted inside the sketched scopes. The superior and inferior limiting lines show the proper limiting cases of the near power-law joint distribution; that is,

$$1.0 \left(\frac{a^L}{\langle a_{r.m.s}^L \rangle} \right)^\alpha < \left(\frac{u_{r.m.s}^E}{U_0} \right) < 1.5 \left(\frac{a^L}{\langle a_{r.m.s}^L \rangle} \right)^\alpha, \quad (2)$$

where the limiting exponent is about $\alpha = 6.16^{\pm 0.17} \times 10^{-3}$.

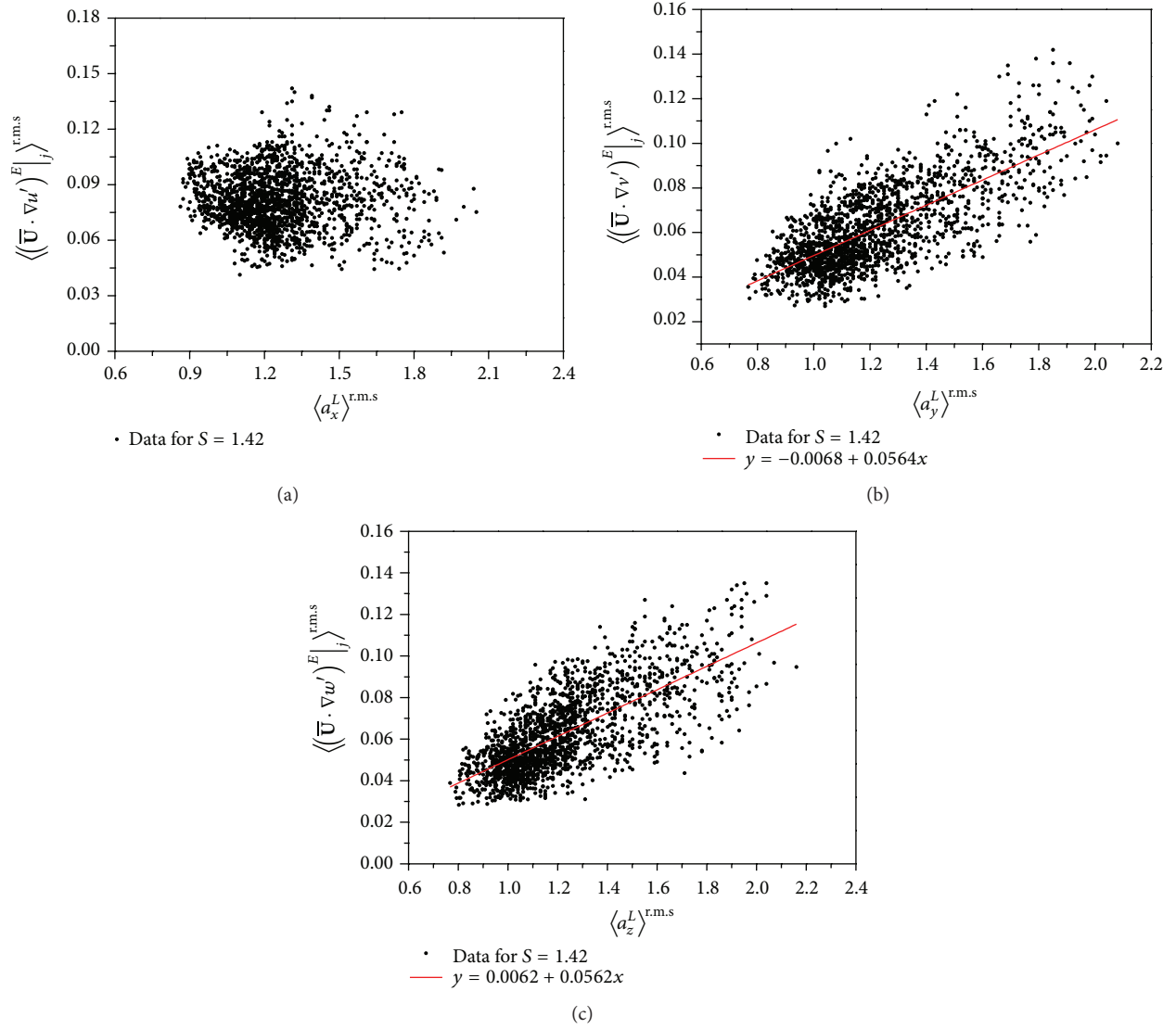


FIGURE 6: The correlation between the Eulerian convection term of turbulence fluctuations u' (a), v' (b), and w' (c) and the Lagrangian acceleration fluctuations in the x , y , and z directions, respectively, for $S = 1.42$.

TABLE 2: Fitting expressions.

	Expressions	Inverse expressions
$S = 0.49$	$\frac{u_{\text{r.m.s}}^E}{U_0} \sim 0.166 \left(\frac{a^L}{\langle a_{\text{r.m.s}}^L \rangle} \right)^{0.278}$	$\frac{a^L}{\langle a_{\text{r.m.s}}^L \rangle} \sim 639 \left(\frac{u_{\text{r.m.s}}^E}{U_0} \right)^{3.6}$
$S = 1.08$	$\frac{u_{\text{r.m.s}}^E}{U_0} \sim 0.171 \left(\frac{a^L}{\langle a_{\text{r.m.s}}^L \rangle} \right)^{0.291}$	$\frac{a^L}{\langle a_{\text{r.m.s}}^L \rangle} \sim 429 \left(\frac{u_{\text{r.m.s}}^E}{U_0} \right)^{3.4}$
$S = 1.42$	$\frac{u_{\text{r.m.s}}^E}{U_0} \sim 0.183 \left(\frac{a^L}{\langle a_{\text{r.m.s}}^L \rangle} \right)^{0.312}$	$\frac{a^L}{\langle a_{\text{r.m.s}}^L \rangle} \sim 228 \left(\frac{u_{\text{r.m.s}}^E}{U_0} \right)^{3.2}$

TABLE 3: Inferior and superior curves of the data points.

Inferior	$\lg \left(\frac{u_{\text{r.m.s}}^E}{U_0} \right) = 6.332 \times 10^{-3} \lg \left(\frac{a^L}{\langle a_{\text{r.m.s}}^L \rangle} \right) + 3.514 \times 10^{-3}$	$\left(\frac{u_{\text{r.m.s}}^E}{U_0} \right) = 1.0 \left(\frac{a^L}{\langle a_{\text{r.m.s}}^L \rangle} \right)^{6.33 \times 10^{-3}}$
Superior	$\lg \left(\frac{u_{\text{r.m.s}}^E}{U_0} \right) = 5.974 \times 10^{-3} \lg \left(\frac{a^L}{\langle a_{\text{r.m.s}}^L \rangle} \right) + 1.777 \times 10^{-3}$	$\left(\frac{u_{\text{r.m.s}}^E}{U_0} \right) = 1.5 \left(\frac{a^L}{\langle a_{\text{r.m.s}}^L \rangle} \right)^{6.0 \times 10^{-3}}$

3.3. Turbulent Convective Effect versus Lagrangian Acceleration. On the other hand, the Lagrangian acceleration is formulated as $D_t^E = \partial_t + (\mathbf{u}^E \cdot \nabla)$. With $\mathbf{u}^E = 0$, the Lagrangian acceleration is equivalent to the Eulerian acceleration. Thus, the nonlinear convective term $\mathbf{u}^E \cdot \nabla$ plays a dominant role in correlation as well as the difference between the Eulerian statistics and the Lagrangian statistics of turbulence. Moreover, from the Eulerian viewpoint, $\mathbf{u}^E \cdot \nabla = \bar{\mathbf{U}}^E \cdot \nabla + \mathbf{u}'^E \cdot \nabla$, where $\bar{\mathbf{U}}^E$ is the time-averaged velocity and \mathbf{u}'^E is the fluctuation velocity. Based on the order analysis, it is assumed that the $\bar{\mathbf{U}}^E \cdot \nabla$ term plays a leading role in turbulence convection. Under this assumption, it is appropriate to consider that the term $\bar{\mathbf{U}}^E \cdot \nabla \mathbf{u}'^E$ represents the effect of convection of turbulence fluctuations. Remember that it is based on the Eulerian viewpoint. Then, moving with a Lagrangian fluid particle, it is natural to calculate the $\bar{\mathbf{U}}^E \cdot \nabla \mathbf{u}'^E$ along the particle trajectory. We call it the trajectory-conditioned $\bar{\mathbf{U}}^E \cdot \nabla \mathbf{u}'^E|_j$, namely, $\bar{\mathbf{U}}^E \cdot \nabla \mathbf{u}'^E|_j$. In this way, the joint Eulerian and Lagrangian statistics on correlation between the convection of turbulence fluctuation and the Lagrangian fluctuation of particle acceleration can be performed.

Figure 5 shows the RMS values of $\bar{\mathbf{U}}^E \cdot \nabla \mathbf{u}'^E|_j$ and acceleration \mathbf{a}^L for $S = 0.49$ in the x , y , and z directions, respectively. One point within Figure 5(a) represents the results for one group of particles. It is seen that, for low swirl levels ($S = 0.49$), the RMS values are distributed nearly linearly. After linear regression, the fitted expression is $\langle \bar{\mathbf{U}}^E \cdot \nabla \mathbf{u}'^E|_j \rangle^{\text{r.m.s}} \approx 0.0556 \langle a_x^L \rangle^{\text{r.m.s}}$. Moreover, it is observed from Figure 5(b) and Figure 5(c) that this nearly linear correlation also exists in the other directions; that is, $\langle \bar{\mathbf{U}}^E \cdot \nabla \mathbf{v}'^E|_j \rangle^{\text{r.m.s}} \approx 0.0315 \langle a_y^L \rangle^{\text{r.m.s}}$ and $\langle \bar{\mathbf{U}}^E \cdot \nabla \mathbf{w}'^E|_j \rangle^{\text{r.m.s}} \approx 0.0317 \langle a_z^L \rangle^{\text{r.m.s}}$. It indicates the correlation between the convection of turbulence fluctuations and the Lagrangian acceleration fluctuations along the particle trajectory; namely, the large fluctuation of Lagrangian acceleration indicates the large fluctuation of Eulerian convection of turbulence and vice versa. As a result, although scattered widely, the trends of the scattering distributions show the statistical correlation between the Lagrangian intermittency effects, which corresponds to the extreme events of the largely fluctuated Lagrangian acceleration, and the Eulerian intermittency effects of turbulence fluctuations, that is, the extreme events of convection of turbulence fluctuations.

However, for large swirl levels (Figure 6, $S = 1.42$), this linear correlation in the axial direction seems to be disturbed, since the data points are widely scattered within a local domain. In contrast, the nearly linear correlation also occurs in the other directions. Remembering the occurrence of recirculation phenomena in the axial direction within the bubble-breakdown region, it is appropriate to explain that the disturbance of linear correlation is due to the formation of bubble vortex breakdown—a dramatic change of the large scale flow structure. In this way, the correlation of Lagrangian intermittency effects as well as the Eulerian intermittency

effects becomes complex. It is correlated in the lateral and spanwise directions and attenuated in the axial direction.

4. Conclusion

The present study focuses on the effect of swirl levels on the correlation between the Lagrangian and Eulerian evaluations of turbulence. The statistical correlations between the Lagrangian and Eulerian evaluations of turbulence are demonstrated. It is found that the Lagrangian acceleration follows a weak power-exponential form of augmentation by the increase of swirl levels, leading to the augmented characteristics of intermittency. Moreover, the fluctuations of $a^L(\mathfrak{F}, t)$ and $u^E(\mathbf{r}, t)$ become increasingly correlated to each other with the increase of the swirl levels. Additionally, the Eulerian convection of turbulence fluctuations is weakly proportional to the Lagrangian acceleration fluctuations, indicating the proportionally close correlation between the Eulerian and Lagrangian intermittency effects.

Conflict of Interests

The authors declare that there is no conflict of interests regarding the publication of this paper.

Acknowledgment

The authors are grateful for the support of this research by the National Natural Science Foundation of China (Grant no. 51106180).

References

- [1] J. Baldyga and J. R. Bourne, "Mixing and fast chemical reaction-VIII: initial deformation of material elements in isotropic, homogeneous turbulence," *Chemical Engineering Science*, vol. 39, no. 2, pp. 329–334, 1984.
- [2] J. S. Marshall and Y. Huang, "Simulation of light-limited algae growth in homogeneous turbulence," *Chemical Engineering Science*, vol. 65, no. 12, pp. 3865–3875, 2010.
- [3] M. Freitag, M. Klein, M. Gregor et al., "Mixing analysis of a swirling recirculating flow using DNS and experimental data," *International Journal of Heat and Fluid Flow*, vol. 27, no. 4, pp. 636–643, 2006.
- [4] A. Giannadakis, K. Perrakis, and T. Panidis, "A swirling jet under the influence of a coaxial flow," *Experimental Thermal and Fluid Science*, vol. 32, no. 8, pp. 1548–1563, 2008.
- [5] T. Xing, "Direct numerical simulation of Open von Kármán Swirling Flow," *Journal of Hydrodynamics*, vol. 26, no. 2, pp. 165–177, 2014.
- [6] R. Hreiz, C. Gentric, and N. Midoux, "Numerical investigation of swirling flow in cylindrical cyclones," *Chemical Engineering Research and Design*, vol. 89, no. 12, pp. 2521–2539, 2011.
- [7] G. A. Siamas, X. Jiang, and L. C. Wrobel, "Numerical investigation of a perturbed swirling annular two-phase jet," *International Journal of Heat and Fluid Flow*, vol. 30, no. 3, pp. 481–493, 2009.
- [8] S. Tanaka, M. Shimura, N. Fukushima, M. Tanahashi, and T. Miyauchi, "DNS of turbulent swirling premixed flame in a

- micro gas turbine combustor,” *Proceedings of the Combustion Institute*, vol. 33, no. 2, pp. 3293–3300, 2011.
- [9] A. La Porta, G. A. Voth, A. M. Crawford, J. Alexander, and E. Bodenschatz, “Fluid particle accelerations in fully developed turbulence,” *Nature*, vol. 409, no. 6823, pp. 1017–1019, 2001.
 - [10] H. G. Sun and W. Chen, “Fractal derivative multi-scale model of fluid particle transverse accelerations in fully developed turbulence,” *Science in China, Series E: Technological Sciences*, vol. 52, no. 3, pp. 680–683, 2009.
 - [11] S. B. Pope, “Lagrangian PDF methods for turbulent flows,” *Annual Review of Fluid Mechanics*, vol. 26, pp. 23–63, 1994.
 - [12] A. R. Rammohan, A. Kemoun, M. H. Al-Dahhan, and M. P. Dudukovic, “A lagrangian description of flows in stirred tanks via computer-automated radioactive particle tracking (CARPT),” *Chemical Engineering Science*, vol. 56, no. 8, pp. 2629–2639, 2001.
 - [13] G. Falkovich, K. Gawędzki, and M. Vergassola, “Particles and fields in fluid turbulence,” *Reviews of Modern Physics*, vol. 73, no. 4, pp. 913–975, 2001.
 - [14] G. A. Voth, K. Satyanarayan, and E. Bodenschatz, “Lagrangian acceleration measurements at large Reynolds numbers,” *Physics of Fluids*, vol. 10, no. 9, pp. 2268–2280, 1998.
 - [15] N. Mordant, A. M. Crawford, and E. Bodenschatz, “Three-dimensional structure of the lagrangian acceleration in turbulent flows,” *Physical Review Letters*, vol. 93, Article ID 214501, 2004.
 - [16] A. M. Crawford, N. Mordant, and E. Bodenschatz, “Joint statistics of the lagrangian acceleration and velocity in fully developed turbulence,” *Physical Review Letters*, vol. 94, no. 2, Article ID 024501, 2005.
 - [17] N. Mordant, P. Metz, O. Michel, and J.-F. Pinton, “Measurement of lagrangian velocity in fully developed turbulence,” *Physical Review Letters*, vol. 87, no. 21, Article ID 214501, 2001.
 - [18] L. Chevillard, S. G. Roux, E. Levêque, N. Mordant, J.-F. Pinton, and A. Arneodo, “Lagrangian velocity statistics in turbulent flows: effects of dissipation,” *Physical Review Letters*, vol. 91, no. 21, Article ID 214502, 2003.
 - [19] D. X. Fu and Y. W. Ma, “A high order accurate difference scheme for complex flow fields,” *Journal of Computational Physics*, vol. 134, no. 1, pp. 1–15, 1997.
 - [20] S. K. Lele, “Compact finite difference schemes with spectral-like resolution,” *Journal of Computational Physics*, vol. 103, no. 1, pp. 16–42, 1992.
 - [21] A. Jameson and W. Schmidt, “Some recent developments in numerical methods for transonic flows,” *Computer Methods in Applied Mechanics and Engineering*, vol. 51, no. 1–3, pp. 467–493, 1985.
 - [22] U. Anantha Krishnaiah, R. Manohar, and J. W. Stephenson, “Fourth-order finite difference methods for three-dimensional general linear elliptic problems with variable coefficients,” *Numerical Methods for Partial Differential Equations*, vol. 3, no. 3, pp. 229–240, 1987.
 - [23] N. Gui, J. Yan, Z. Li, and J. Fan, “Direct numerical simulation of confined swirling jets,” *International Journal of Computational Fluid Dynamics*, vol. 28, no. 1–2, pp. 76–88, 2014.
 - [24] N. Gui, J. Fan, and S. Chen, “Numerical study of particle-vortex interaction and turbulence modulation in swirling jets,” *Physical Review E: Statistical, Nonlinear, and Soft Matter Physics*, vol. 82, no. 5, Article ID 056323, 2010.
 - [25] P. Billant, J.-M. Chomaz, and P. Huerre, “Experimental study of vortex breakdown in swirling jets,” *Journal of Fluid Mechanics*, vol. 376, pp. 183–219, 1998.
 - [26] N. Gui, J. R. Fan, K. F. Cen, and S. A. Chen, “A direct numerical simulation study of coherent oscillation effects of swirling flows,” *Fuel*, vol. 89, no. 12, pp. 3926–3933, 2010.
 - [27] N. Gui, J. R. Fan, and S. Chen, “Numerical study of particle-particle collision in swirling jets: a DEM-DNS coupling simulation,” *Chemical Engineering Science*, vol. 65, no. 10, pp. 3268–3278, 2010.
 - [28] I. Orlanski, “A simple boundary condition for unbounded hyperbolic flows,” *Journal of Computational Physics*, vol. 21, no. 3, pp. 251–269, 1976.
 - [29] P. Moin and K. Mahesh, “Direct numerical simulation: a tool in turbulence research,” *Annual Review of Fluid Mechanics*, vol. 30, pp. 539–578, 1998.

Research Article

Computational Methods for Coupled Fluid-Structure-Electromagnetic Interaction Models with Applications to Biomechanics

Felix Mihai, Inja Youn, Igor Griva, and Padmanabhan Seshaiyer

Department of Mathematical Sciences, College of Science, George Mason University, 4400 University Drive, MS 3F2, Fairfax, VA 22030, USA

Correspondence should be addressed to Padmanabhan Seshaiyer; pseshaiy@gmu.edu

Received 29 August 2014; Accepted 15 November 2014

Academic Editor: Kim M. Liew

Copyright © 2015 Felix Mihai et al. This is an open access article distributed under the Creative Commons Attribution License, which permits unrestricted use, distribution, and reproduction in any medium, provided the original work is properly cited.

Multiphysics problems arise naturally in several engineering and medical applications which often require the solution to coupled processes, which is still a challenging problem in computational sciences and engineering. Some examples include blood flow through an arterial wall and magnetic targeted drug delivery systems. For these, geometric changes may lead to a transient phase in which the structure, flow field, and electromagnetic field interact in a highly nonlinear fashion. In this paper, we consider the computational modeling and simulation of a biomedical application, which concerns the fluid-structure-electromagnetic interaction in the magnetic targeted drug delivery process. Our study indicates that the strong magnetic fields, which aid in targeted drug delivery, can impact not only fluid (blood) circulation but also the displacement of arterial walls. A major contribution of this paper is modeling the interactions between these three components, which previously received little to no attention in the scientific and engineering community.

1. Introduction

In the last decade, the rapid development of computational science has provided new methodologies to solve complex multiphysics applications involving fluid-structure interaction to a variety of fields. These include solving applications involving blood flow interactions with the arterial wall to computational aeroelasticity of flexible wing micro-air vehicles to magnetohydrodynamic of liquid-metal cooled nuclear reactor to ferromagnetics with biological applications. In these applications, the challenge is to understand and develop algorithms that allow the structural deformation, the flow field, and temperature variations to interact in a highly nonlinear fashion.

Coupling these multiphysics with electromagnetic effects makes the associated computational model too complex. Not only is the nonlinearity in the geometry challenging but in many of these applications the material is nonlinear as well, which makes the problem even more complex. Direct

numerical solution of the highly nonlinear equations governing even the most simplified two-dimensional models of such multiphysics interaction requires that all the unknown fields, such as fluid velocity, pressure, the magnetic and the electric field, the temperature field, and the domain shape, be determined as part of the solution, since neither is known a priori.

The past few decades, however, have seen significant advances in the development of finite element and domain decomposition methods. These have provided new algorithms for solving such large scale multiphysics simulations. There have been several methods that have been introduced in this regard and their performance has been analyzed for a variety of problems. One such technique is the mortar finite element method which has been shown to be stable mathematically and has been successfully applied to a variety of applications and references therein. The basic idea is to replace the strong continuity condition at the interfaces between the different subdomains modeling different

multiphysics by a weaker one to solve the problem in a coupled fashion. Such novel techniques provide hope for us to develop new faster and efficient algorithms to solve complex multiphysics applications. A variety of methods have been introduced including the level set methods [1], fictitious domain methods [2, 3], nonconforming hp finite element methods [4, 5], multilevel multigrid methods [6], and the immersed boundary methods [7]. While these methods help enhance our ability to understand complex processes, there is still a great need for efficient computational methods that cannot only help simulate physiologically realistic situations qualitatively but also analyze and study modeling of such processes quantitatively. Such multiphysics applications involve the interaction of various components, such as fluid with the structure, electromagnetics with the fluid, or fluid-structure interacting completely with electromagnetics.

1.1. Electromagnetic-Fluid Interaction. An important application involving interaction of electromagnetics with fluid which describes the behavior of electrically conducting fluid is very complex under a magnetic field, since the additional Lorentz force is caused by the interaction between velocity field and electromagnetic field. Understanding such coupled behavior not only helps us to create efficient algorithms but also applies to a variety of magnetohydrodynamic (MHD) applications. Due to its multidisciplinary applications, a solid understanding of the MHD is required. In this regard, the Hartmann flow has been studied extensively. The Hartmann flow is the steady flow of an electrically conducting fluid between two parallel walls, under the effect of a normal magnetic and electric field. A thorough understanding of such models for electromagnetic fluid interaction can help us in developing new techniques for complex problems such as magnetic drug targeting in cancer therapy. Such a model would involve ferrohydrodynamics of blood that helps to study external magnetic field and its interaction with blood flow containing a magnetic carrier substance. The analytic models would involve solving Maxwell's equations in conjunction with Navier-Stokes equations. While new models in this area are just starting to evolve, these often consider the structure to be fixed. There is a need to extend these models to include fluid-structure interaction with electromagnetics, which would be another focus of this work.

1.2. Proposed New Models. In this paper, we will develop a computational infrastructure for solving coupled fluid-structure interaction with electromagnetic and temperature effects. The rest of the work is organized as follows. Section 2 presents the models, methods, and background required to develop and solve the coupled multiphysics systems. In Section 3, we consider the model of a blood vessel, a permanent magnet, and surrounding tissue and air in two dimensions. We will consider both a nonmoving structure and a moving structure. The deformed structure provides a new geometry, where the Navier-Stokes equations are solved for the velocity and pressure fields in the bloodstream. A magnetic vector potential generated by the permanent magnet is calculated, which in turn creates a magnetic volume force that

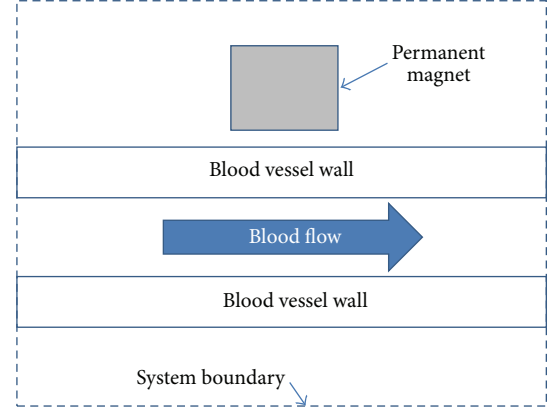


FIGURE 1: Electromagnetic fluid-structure interaction model.

impacts the flow in the blood vessel. The flow field changes the displacement of the structure, and the problem is solved once again for the new geometry. The proposed models are validated against benchmark applications numerically. Section 4 presents conclusion and a discussion of the results. Future work on the proposed problems is also presented.

A magnetically targeted drug delivery system [8] is based on magnetic particles under the action of an external magnetic field. This is becoming an increasingly effective approach in drug therapy. As this field has evolved in the last decade, lots of scientific interest led to this inquiry into efficient computational models that simulate this experimental process [9]. Our study indicates that the strong magnetic fields which aid in targeted drug delivery can impact not only fluid (blood) circulation but also the displacement of arterial walls. Thus, it is important to have a model, which includes the interactions between fluid, structure, and magnetic field in order to study and optimize drug delivery.

In this section, we will present a model that describes the interaction between these three components, which previously received little to no attention in the scientific community. To develop an electromagnetic fluid-structure interaction, we incorporate the effects of the electromagnetic field into a fluid-structure model. Gaining a thorough understanding of such a coupled model can help us to understand the efficacy of magnetic nanoparticle-based drug delivery for diseases such as cancer as has been proposed by various researchers [10, 11]. There is significant evidence that indicates a need for more promising models which overcome current limitations and improve magnetic targeting technique.

2. Mathematical Model and Governing Equations

The model we consider is a blood vessel with a permanent magnet near its surface, as illustrated in Figure 1. For simplicity of presentation, we consider a computational model that comprises three components. Let the computational domain $\Omega \subset \mathbb{R}^2$ be an open set with global system boundary Γ . Let Ω be decomposed into the four disjoint open sets, a fluid subdomain Ω_f denoted by blood flow, two solid

subdomains Ω_s^i , $i = 1, 2$ (blood vessel walls) with respective boundaries Γ_f and Γ_s , and one electromagnetic domain Ω_m (permanent magnet). Let Γ_I^j , $j = 1, 2, 3, 4$ be the interface between the solid, fluid, and electromagnetic domains. The structural domain consists of two symmetric arterial vessel walls denoted by Ω_s^1 and Ω_s^2 . The electromagnetic domain consists of a permanent magnet of dimensions $10 \mu\text{m} \times 40 \mu\text{m}$ placed in free space. The arterial wall describes a structural mechanism that interacts with the flow dynamics of blood which in turn is impacted by a permanent magnet, which is described next.

For this, we use Maxwell's equation for the magnetostatic case (the field quantities do not vary with time) that relates the magnetic field intensity \mathbf{H} and the electric current density \mathbf{J} [12]:

$$\begin{aligned}\nabla \times \mathbf{H} &= \mathbf{J}, \\ \nabla \cdot \mathbf{J} &= 0.\end{aligned}\quad (1)$$

The constitutive relations between \mathbf{B} and \mathbf{H} depend on the domain [12, 13]:

$$\mathbf{B} = \begin{cases} \mu_0 \mu_{r,\text{mag}} \mathbf{H} + \mathbf{B}_{\text{rem}} & \text{for the permanent magnet} \\ \mu_0 (\mathbf{H} + \mathbf{M}_{ff}(\mathbf{H})) & \text{for the blood stream} \\ \mu_0 \mathbf{H} & \text{for the tissue and air,} \end{cases} \quad (2)$$

where μ_0 is the magnetic permeability of vacuum ($\text{V}\cdot\text{s}/(\text{A}\cdot\text{m})$), $\mu_{r,\text{mag}}$ is the relative magnetic permeability of the permanent magnet (dimensionless), \mathbf{B}_{rem} is the remanent magnetic flux (A/m), and \mathbf{M}_{ff} is the magnetization vector in the blood stream (A/m), which is a function of the magnetic field, \mathbf{H} . By defining a magnetic vector potential \mathbf{A} such that

$$\mathbf{B} = \nabla \times \mathbf{A}, \quad \text{with } \nabla \cdot \mathbf{A} = 0, \quad (3)$$

we get

$$\nabla \times \left(\frac{1}{\mu} \nabla \times \mathbf{A} - \mathbf{M} \right) = \mathbf{J}. \quad (4)$$

Assuming no perpendicular currents, we can simplify to a 2D problem and reduce this equation to

$$\nabla \times \left(\frac{1}{\mu_0} \nabla \times \mathbf{A} - \mathbf{M} \right) = \mathbf{0}. \quad (5)$$

This assumes that the magnetic vector potential has a nonzero component only perpendicularly to the plane, which is $\mathbf{A} = (0, 0, A_z)$. The induced magnetization $\mathbf{M}_{ff}(x, y) = (M_{ffx}, M_{ffy})$ is characterized by [14–17]

$$\begin{aligned}M_x &= \alpha \arctan \left(\frac{\beta}{\mu_0} \frac{\partial A_z}{\partial y} \right), \\ M_y &= \alpha \arctan \left(\frac{\beta}{\mu_0} \frac{\partial A_z}{\partial x} \right).\end{aligned}\quad (6)$$

To capture the magnetic fields of interest we can linearize these expressions to obtain

$$M_x = \frac{\chi}{\mu_0} \frac{\partial A_z}{\partial y}, \quad M_y = \frac{\chi}{\mu_0} \frac{\partial A_z}{\partial x}, \quad (7)$$

where $\chi = \alpha\beta$ is the magnetic susceptibility. This magnetic field induces a body force on the fluid. With the assumption that the magnetic nanoparticles in the fluid do not interact, the magnetic force $\mathbf{F} = (F_x, F_y)$ on the ferrofluid for relatively weak fields is given by [16]

$$\mathbf{F} = |\mathbf{M}| \nabla |\mathbf{H}|. \quad (8)$$

Substituting (2) and (3) in (8) leads to the expression

$$\begin{aligned}F_x &= k_{ff} \frac{\chi}{\mu_0 \mu_r^2} \left(\frac{\partial A_z}{\partial x} \frac{\partial^2 A_z}{\partial x^2} + \frac{\partial A_z}{\partial y} \frac{\partial^2 A_z}{\partial x \partial y} \right), \\ F_y &= k_{ff} \frac{\chi}{\mu_0 \mu_r^2} \left(\frac{\partial A_z}{\partial x} \frac{\partial^2 A_z}{\partial x \partial y} + \frac{\partial A_z}{\partial y} \frac{\partial^2 A_z}{\partial y^2} \right),\end{aligned}\quad (9)$$

where k_{ff} is the fraction of the fluid which is ferrofluid. The vector $\mathbf{F}_f = (F_x, F_y)$ is the volume force, which is input for the Navier-Stokes equations in the next subsection.

2.1. Modeling the Unsteady Blood Flow. We model the fluid domain for the blood flow via the unsteady Navier-Stokes equations for an incompressible, isothermal fluid flow written in nonconservative form as

$$\begin{aligned}\rho_f \frac{\partial \mathbf{u}_f}{\partial t} + \rho_f (\mathbf{u}_f \cdot \nabla) \mathbf{u}_f + \nabla p &= \nabla \cdot \boldsymbol{\tau}_f + \mathbf{F}_f, \\ \rho_f \nabla \cdot \mathbf{u}_f &= 0,\end{aligned}\quad (10)$$

where \mathbf{u}_f is the velocity, ρ_f is the density, p is the pressure, and \mathbf{F}_f is the body forces. The viscous stress tensor is $\boldsymbol{\tau}(\mathbf{u}_f) = 2\eta D(\mathbf{u}_f)$, where η is the dynamic viscosity and the deformation tensor is

$$D(\mathbf{u}_f) = \mu_s \left(\frac{\nabla \mathbf{u}_f + (\nabla \mathbf{u}_f)^T}{2} \right). \quad (11)$$

The fluid equations are subject to the boundary conditions:

$$\begin{aligned}u_f &= u_{\text{wall}}, \quad x \in \Gamma_I^j, \quad j = 2, 3 \\ \boldsymbol{\tau}_f \cdot \mathbf{n} &= \mathbf{t} \cdot \mathbf{n}, \quad x \in \Gamma_N, \\ u_f &= \frac{\partial d_s}{\partial t}, \quad x \in \Gamma_I^j, \quad j = 2, 3,\end{aligned}\quad (12)$$

where $\mathbf{t} = -p\mathbf{I} + 2D(\mathbf{u}_f)$ is the prescribed tractions on the Neumann part of the boundary with \mathbf{n} being the outward unit normal vector to the boundary surface of the fluid. Conditions of displacement compatibility and force equilibrium along the structure-fluid interface are enforced. In order to solve a fluid-structure interaction problem in a coupled fashion we employ an arbitrary Lagrangian-Eulerian (ALE) formulation where the characterizing velocity is no longer the material velocity \mathbf{u}_f , but a grid velocity $\hat{\mathbf{u}}_f$. This allows us to replace the material velocity \mathbf{u}_f in (10) with the convective

velocity $c = u_f - \hat{u}_f$ [5]. The weak variational formulation of the fluid problem then becomes

$$\begin{aligned} & \int_{\Omega_f} \tau_f \cdot \nabla \phi \, d\Omega_f \\ &= \int_{\Omega_f} F \cdot \phi \, d\Omega_f + \int_{\Gamma_f} t \cdot \phi \, d\Gamma \\ &+ \int_{\Omega_f} \rho_f \frac{\partial u}{\partial t} \cdot \phi \, d\Omega_f + \int_{\Omega_f} \rho_f (c \cdot \nabla) u_f \cdot \phi \, d\Omega_f, \\ & \int_{\Omega_f} q \nabla \cdot u \, d\Omega_f = 0. \end{aligned} \quad (13)$$

2.2. Modeling the Structure Equations. The structural domains for the blood vessel walls consist of the arterial vessel walls denoted by Ω_s^1, Ω_s^2 . They are modeled via the following equation:

$$\rho_s \frac{\partial^2 d_s}{\partial t^2} = \nabla \cdot \tau_s + F_s, \quad (14)$$

where d_s is the structure displacement, ρ_s is the structure density, τ_s is the solid stress tensor, and $\partial^2 d_s / \partial t^2$ is the local acceleration of the structure. This is solved with the boundary conditions:

$$\begin{aligned} d_s &= d_s^D \quad x \in \Gamma_S^D, \\ \tau_s \cdot n_s &= t_s \quad x \in \Gamma_S^N, \\ \tau_s \cdot n_s &= -\tau \cdot n + t_s^I \quad x \in \Gamma_I^j \quad j = 2, 3. \end{aligned} \quad (15)$$

Here Γ_S^D and Γ_S^N are the respective parts of the structural boundary where the Dirichlet and Neumann boundary conditions are prescribed. Also, t_s are the applied tractions on Γ_S^N and t_s^I are the externally applied tractions to the interface boundaries Γ_I^j , $j = 1, 2, 3, 4$. The unit outward normal vector to the boundary surface of the structure is n_s . The stresses are computed using the constitutive relation described next. Equations (15) enforce the equilibrium of the traction between the fluid and the structure on the respective fluid-structure interfaces. The total strain tensor for a typical geometrically nonlinear model is written in terms of displacement gradients:

$$\varepsilon = \frac{1}{2} (\nabla d_s + \nabla d_s^T + \nabla d_s \nabla d_s^T). \quad (16)$$

For small deformations, the last term on the right hand side is omitted to obtain a geometrically linear model. Since the objective of this section is to investigate the influence of electromagnetic effects on fluid-structure interaction models, we will consider a geometrically linear model combined with a linear constitutive law. The solid stress tensor τ_s is given in terms of the second Piola-Kirchoff stress S :

$$\tau_s = (S \cdot (I + \nabla d_s)). \quad (17)$$

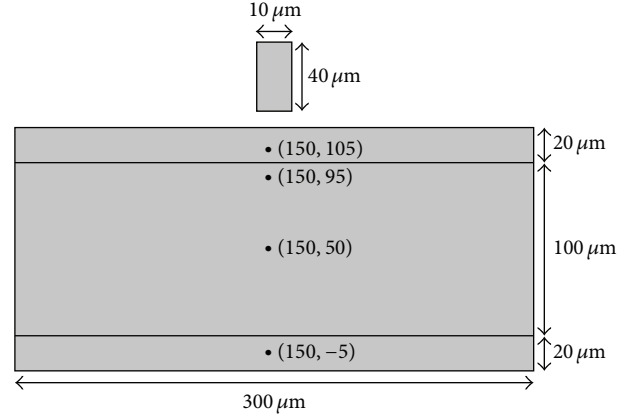


FIGURE 2: Domain and points of interest.

For the linear material model, we employ the following constitute law relating the stress tensor to the strain tensor:

$$S = S_0 + C : \varepsilon, \quad (18)$$

where C is the 4th order elasticity tensor and “:” stands for the double-dot tensor product. S_0 and ε_0 are initial stresses and strains, respectively. The weak variational form of the structural equations then becomes the following: find the structure displacement u_s such that

$$\begin{aligned} & \int_{\Omega_s} \tau_s \cdot \varepsilon_s \, d\Omega_s \\ &= \int_{\Omega_f} F_s \cdot \phi_s \, d\Omega_s + \int_{\Gamma_S^N} t_s \cdot \phi_s \, d\Gamma \\ &- \int_{\Omega_f} \rho_s \frac{\partial^2 d_s}{\partial t^2} \cdot \phi_s \, d\Omega_s - \int_{\Gamma_I} (t_s^I - \tau_f \cdot n) \cdot \phi_s \, d\Gamma. \end{aligned} \quad (19)$$

3. Numerical Results

In this section, we present the numerical results for the electromagnetic-fluid-structure interaction model problem presented in this section. To understand the effects of the coupling between electromagnetic field and fluid-structure interaction models better, we first consider the interaction with a rigid structure, which is often employed in the most research problems that are only interested in studying the electromagnetic-fluid interaction. The computational domain (see Figure 2) represents a blood vessel that is 300 micrometers long and 100 micrometers in diameter, with walls 20 micrometers in thickness. All the results presented are for three magnetic fields: 0 T (no magnetic field), 0.5 T, and 1 T. The structure model we consider is linear (MLGL), which was introduced in Section 2.

3.1. Coupled Interaction with Rigid Structure. Figures 3(a), 4(a), and 5(a) illustrate the influence of the magnetic field on the interaction. These figures show the surface von Mises

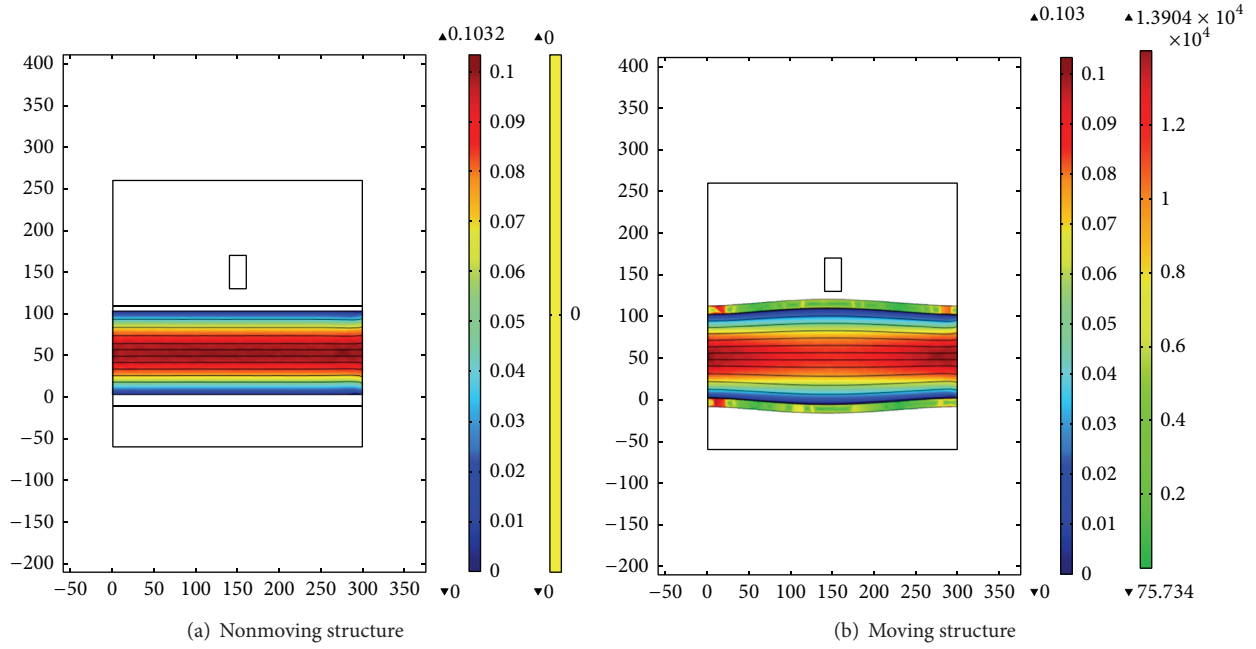


FIGURE 3: Surface von Mises stress with streamlines of spatial velocity field and magnetic field for $\mathbf{B}_{\text{rem}} = 0 \text{ T}$ at $t = 0.215$. Time = 0.215, surface: von Mises stress (N/m^2), surface: velocity magnitude (m/s), and streamline: velocity field (spatial).

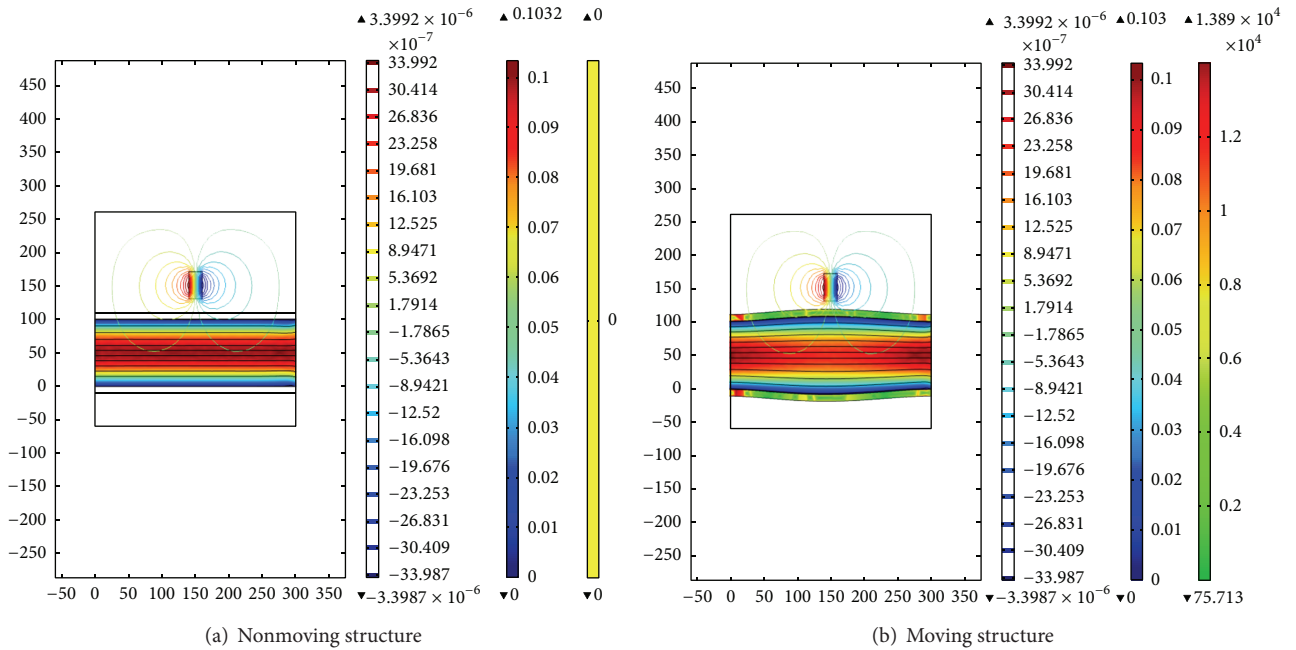


FIGURE 4: Surface von Mises stress with streamlines of spatial velocity field and magnetic field for $\mathbf{B}_{\text{rem}} = 0.5 \text{ T}$ at $t = 0.215$. Time = 0.215, surface: von Mises stress (N/m^2), surface: velocity magnitude (m/s), contour: magnetic vector potential, z component (Wb/m), and streamline: velocity field (spatial).

stress along with streamlines of spatial velocity field and the z -component of the magnetic vector potential. While there is no significant impact of increasing the magnetic field on the velocity profile in each of the graphs in Figures 3(a), 4(a), and 5(a), the impact on the magnetic vector potential is as

expected. As it can be seen, the z -component of the magnetic potential doubles when magnetic field doubles.

Figures 6(a), 7(a), and 8(a) compare the effect of varying the magnetic field on the surface pressure. Unlike the impact on the velocity profile, these figures suggest that the surface

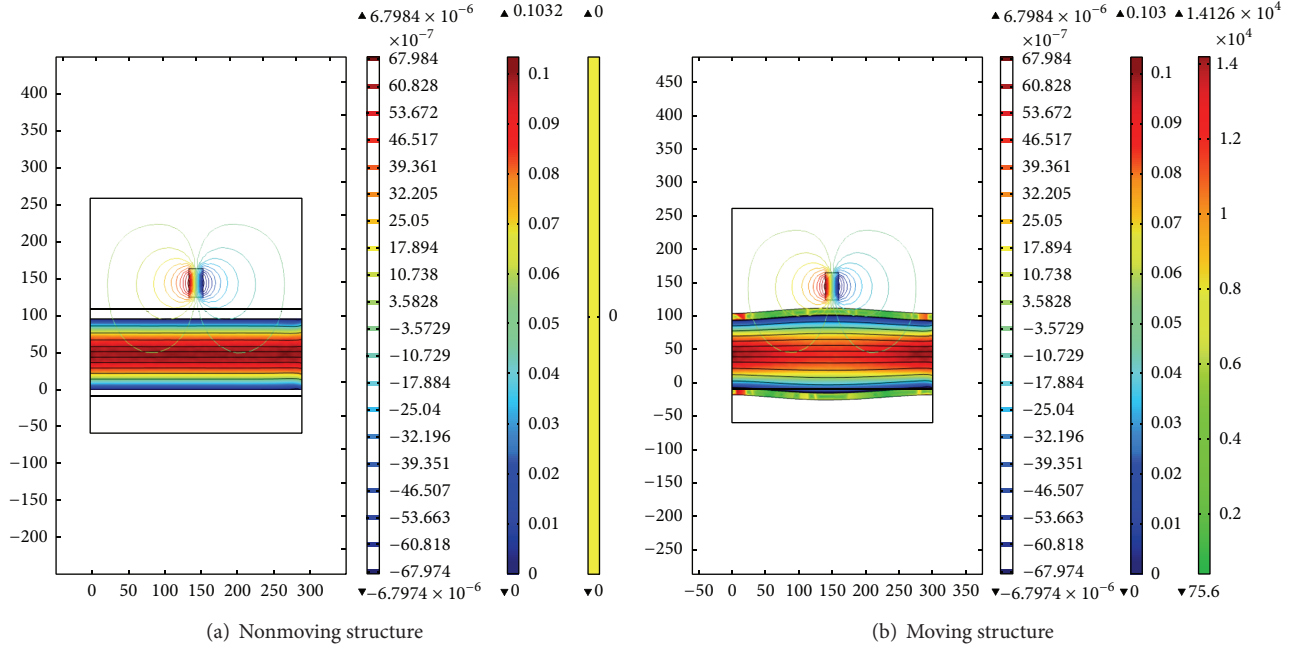


FIGURE 5: Surface von Mises stress with streamlines of spatial velocity field and magnetic field for $B_{\text{rem}} = 1$ T at $t = 0.215$. Time = 0.215, surface: von Mises stress (N/m^2), surface: velocity magnitude (m/s), contour: magnetic vector potential, z component (Wb/m), and streamline: velocity field (spatial).

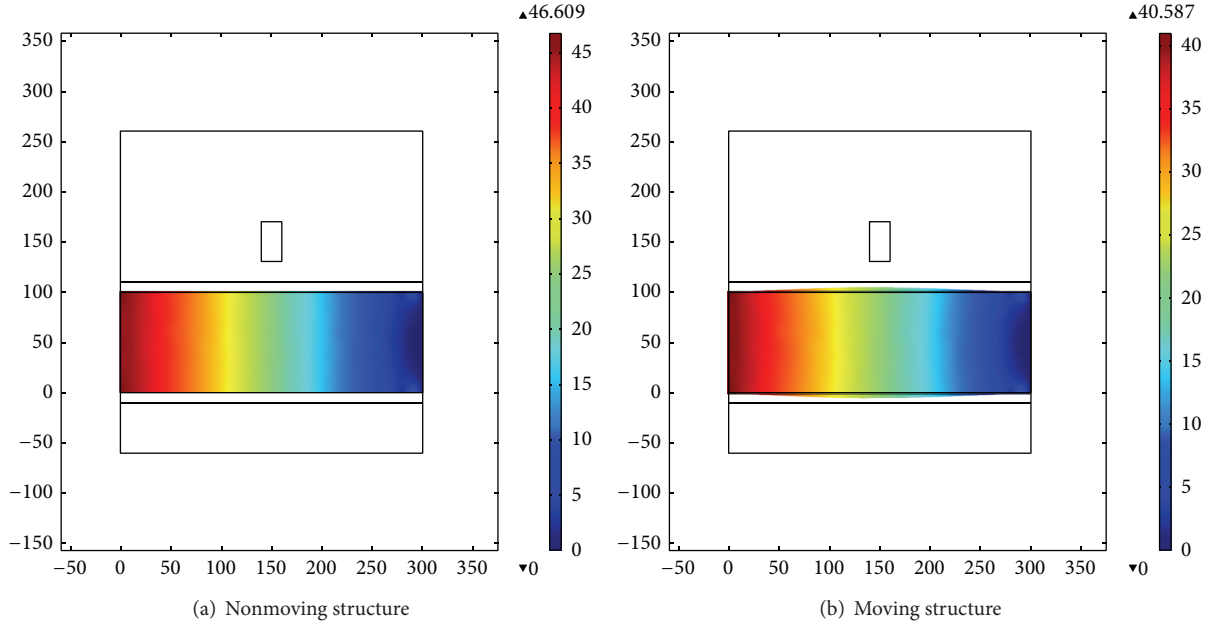


FIGURE 6: Pressure for $B_{\text{rem}} = 0$ T shown at $t = 4$. Time = 4; surface: pressure (Pa).

pressure is impacted by increasing the magnetic field and the doubling effect is also seen as expected.

3.2. Coupled Interaction with Moving Structure. Next, we consider the benchmark problem presented with the structure moving. For this, we employ the ALE formulation for the fluid-structure interaction as described in Section 2. We notice from Figures 3(b), 4(b), and 5(b) that, at $t = 0.215$

(when the fluid velocity has maximum value), the structure and the flow pattern are not very much impacted by the magnet. For the maximum studied magnetic field of 1 T, the arterial wall is slightly bent towards the magnet. For even larger magnetic fields not shown in the picture (the order of magnetic field of 5 T), the magnet intersects with the arterial wall.

Even though we have not seen a big difference in structural deformation and fluid flow for our study case, the

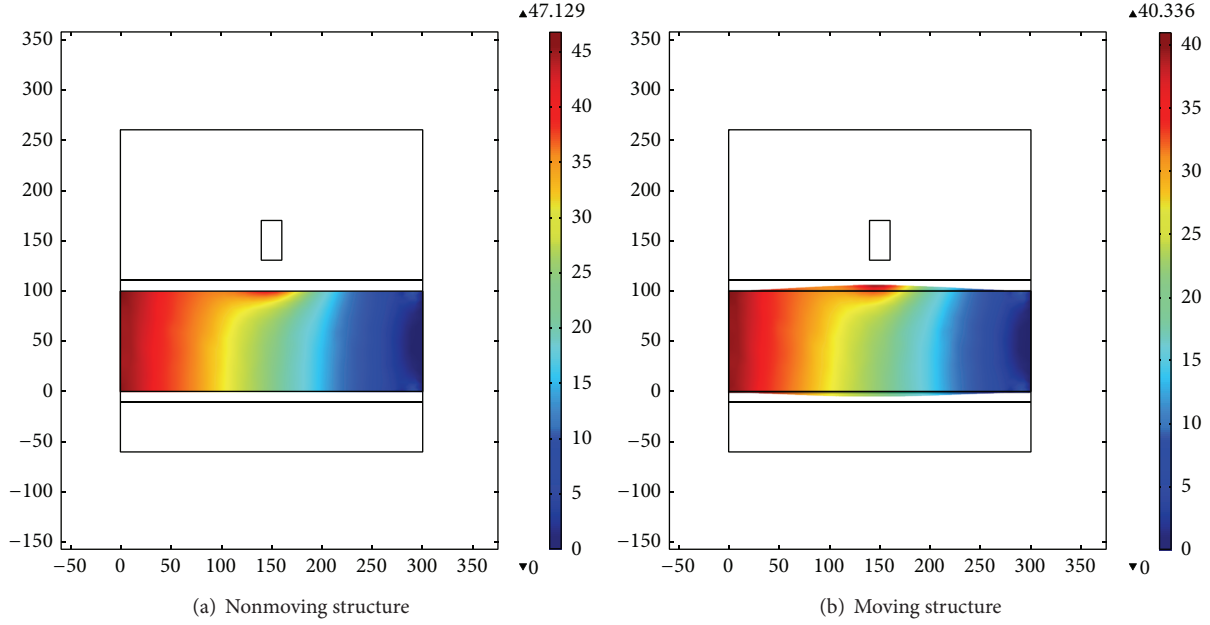


FIGURE 7: Pressure for $B_{rem} = 0.5$ T shown at $t = 4$. Time = 4; surface: pressure (Pa).

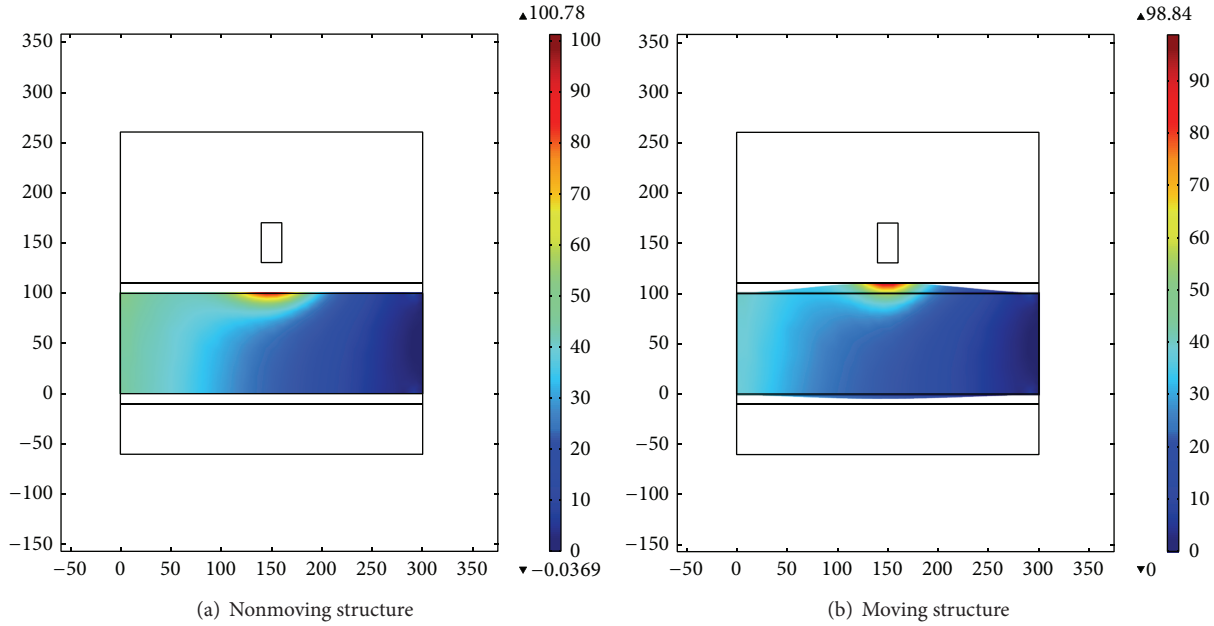


FIGURE 8: Pressure for $B_{rem} = 1$ T shown at $t = 4$. Time = 4; surface: pressure (Pa).

fluid pressure is entirely different between two considered magnetic fields (see Figures 6(b), 7(b), and 8(b)). If for $B_{rem} = 0$ T the pressure is completely symmetric with respect to the x -axis, the pressure around the magnet increases when magnetization is 0.5 T and becomes more than double the maximum pressure in the rest of the fluid when $B_{rem} = 1$ T.

Another experiment we perform is to measure the velocity profile and displacement of two specific points. From Figures 9 and 10, we notice that, as expected, the velocity and pressure decrease at the center and increase around the

boundaries when the structure is moving, mainly because of the dilatation of the structure. While the pressure in the center is not affected much by the presence or absence of magnetic field, near the magnet the pressure is steadily increasing with the time.

For the measured displacement, we notice in Figure 11 that the wall towards the magnet is getting closer to the magnet because of the increasing pressure, while the other wall is virtually unaffected by the presence of the magnetic field.

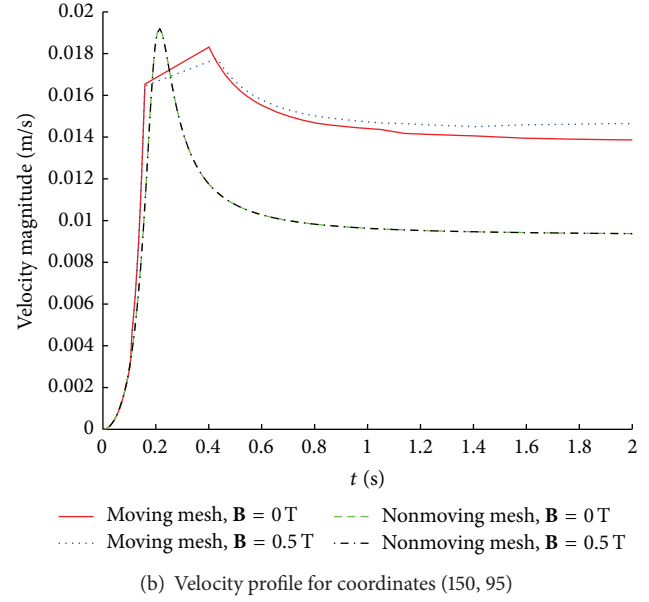
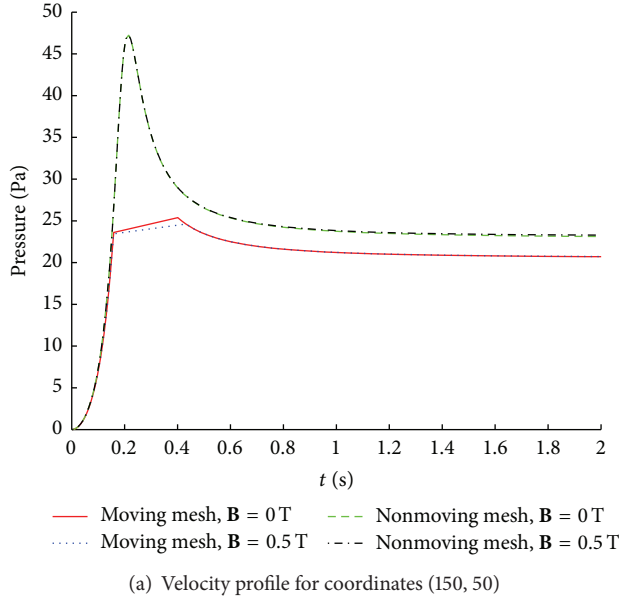


FIGURE 9: Velocity for a center and edge point inside the fluid.

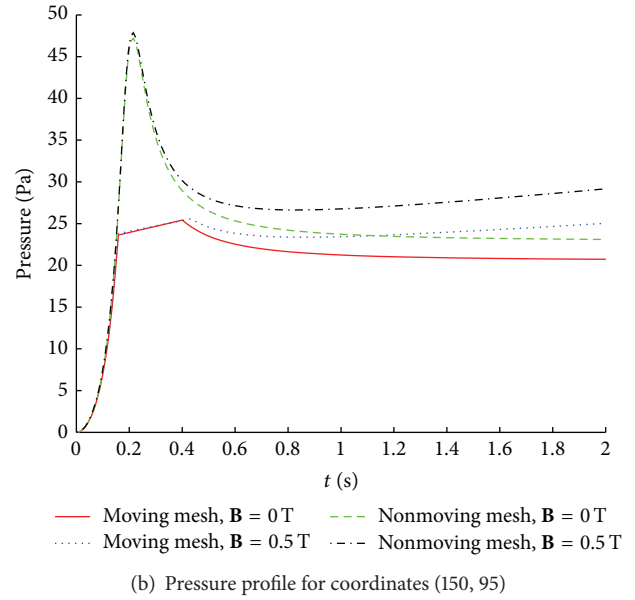
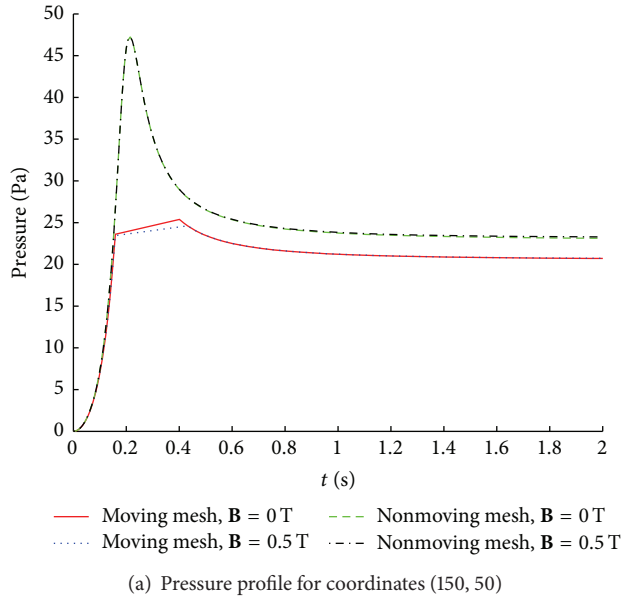


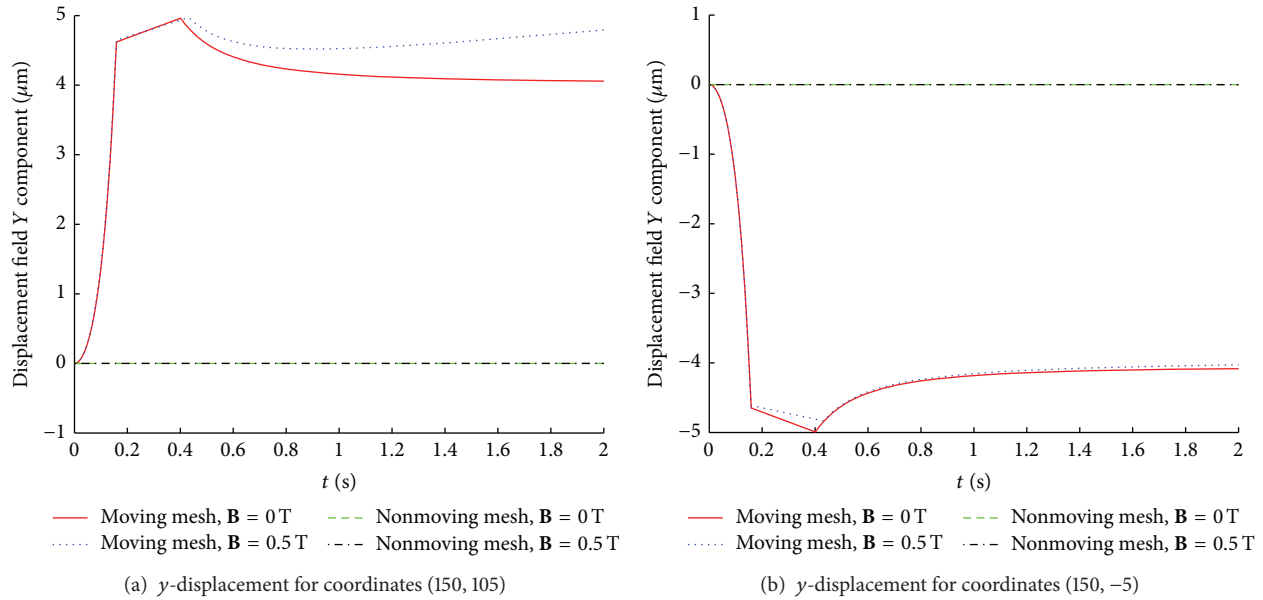
FIGURE 10: Pressure for a center and edge point inside the fluid.

4. Conclusion

In this work, we presented the computational modeling and simulation of coupled multiphysics applications. These included a variety of processes such as fluid dynamics, structural mechanics, and electromagnetic interaction that impacted the behavior of the physical system in a coupled way. Specifically, this work considered the research question of “how does incorporating electromagnetic field into fluid-structure interaction models influence the fluid flow and structural deformation?” In answering this question, this

work led to the development of a two-dimensional multi-physics problem involving electromagnetics coupled with fluid-structure interaction.

In order to answer this research question, we first presented the mathematical background and simulation of the interaction between fluid, structure, and magnetic field. The motivation of this came from researching models for targeted drug delivery for delivering drugs in human body, to increase the concentration of the drug in the target area. For example, the chemotherapy drug dosage is limited by the negative impact on the drugs on the healthy cells. By delivering the

FIGURE 11: y -displacement of two points.

drugs with high accuracy and maximum concentration to specific areas of the body, it is possible to increase local dosage of the drug on the tumor, with lower concentration in the rest of the body. The drug effectiveness is increased while the side effects are reduced. Other examples of the applications of magnetic drug targeting are treatment of cardiovascular conditions, such as stenosis and thrombosis. Thus, it is important to model not only the blood circulation but also the deformation of the blood vessel, in order to improve the accuracy which is the focus of the second problem in this thesis. In particular, it is important to have an accurate model of the interaction between the three components for optimizing the shape, size, and magnetic power, in order to deliver the drugs efficiently in the desired place and minimize the side effects. Our results from this work clearly indicate the importance of the magnetic field to be coupled with a fluid-structure interaction model. More importantly, the results suggest the importance of using moving walls versus nonmoving walls in this coupled electromagnetic fluid-structure interaction.

While this work provided a lot of insight into the importance of electromagnetic effects in fluid-structure interaction, there is scope to enhance this work by considering effects of non-Newtonian rheological properties incorporated along with the extension to materially and geometrically nonlinear models. In the last two decades, collagenous soft tissues have been found to exhibit viscoelastic behavior, which includes time-dependent creep and stress relaxation, rate-dependence, and hysteresis in a loading cycle. As suggested in [18], this hysteresis is less sensitive than the stiffness to the loading rate, and this phenomenon is generally found in soft tissues and elastomers [18]. One of the future directions would be to extend the structural mechanics module to incorporate viscoelasticity and then study the influence of this on our models. The computational models in this

work included two-dimensional models for simplicity, but our models can be naturally extended to three dimensions. With increasing the size of the problem comes the need for more computational resources. There is intensive work that is evolving in the area of domain decomposition that helps to address how to solve coupled multiphysics problems efficiently. So as the problem dimension becomes bigger, one must also resort to domain decomposition type approaches which can then open up more venues on parallelization of the algorithms that have been developed.

Conflict of Interests

The authors declare that there is no conflict of interests regarding the publication of this paper.

Acknowledgment

The authors wish to thank the STEM Accelerator Program in the College of Science at George Mason University for supporting this project in part to help promote scientific development for high school students and undergraduate and graduate students to learn about multidisciplinary research in STEM.

References

- [1] Y. C. Chang, T. Y. Hou, B. Merriman, and S. Osher, "A level set formulation of Eulerian interface capturing methods for incompressible fluid flows," *Journal of Computational Physics*, vol. 124, no. 2, pp. 449–464, 1996.
- [2] F. P. Baaijens, "A fictitious domain/mortar element method for fluid-structure interaction," *International Journal for Numerical Methods in Fluids*, vol. 35, no. 7, pp. 743–761, 2001.

- [3] R. Glowinski, T. W. Pan, T. I. Hesla, D. D. Joseph, and J. P eriaux, "A fictitious domain approach to the direct numerical simulation of incompressible viscous flow past moving rigid bodies: application to particulate flow," *Journal of Computational Physics*, vol. 169, no. 2, pp. 363–426, 2001.
- [4] P. Seshaiyer, "Stability and convergence of nonconforming *hp* finite-element methods," *Computers & Mathematics with Applications*, vol. 46, no. 1, pp. 165–182, 2003.
- [5] E. W. Swim and P. Seshaiyer, "A nonconforming finite element method for fluid-structure interaction problems," *Computer Methods in Applied Mechanics and Engineering*, vol. 195, no. 17, pp. 2088–2099, 2006.
- [6] E. Aulisa, A. Cervone, S. Manservigi, and P. Seshaiyer, "A multilevel domain decomposition approach for studying coupled flow applications," *Communications in Computational Physics*, vol. 6, no. 2, pp. 319–341, 2009.
- [7] C. S. Peskin, "Numerical analysis of blood flow in the heart," *Journal of Computational Physics*, vol. 25, no. 3, pp. 220–252, 1977.
- [8] A. O. Mulyar, *Magnetically Targeted Drug Delivery System*, GRIN Verlag, 2010.
- [9] A. D. Grief and G. Richardson, "Mathematical modelling of magnetically targeted drug delivery," *Journal of Magnetism and Magnetic Materials*, vol. 293, no. 1, pp. 455–463, 2005.
- [10] J. Dobson, "Magnetic nanoparticles for drug delivery," *Drug Development Research*, vol. 67, no. 1, pp. 55–60, 2006.
- [11] S.-I. Takeda, F. Mishima, S. Fujimoto, Y. Izumi, and S. Nishijima, "Development of magnetically targeted drug delivery system using superconducting magnet," *Journal of Magnetism and Magnetic Materials*, vol. 311, no. 1, pp. 367–371, 2007.
- [12] J. M. Jin, *The Finite Element Method in Electromagnetics*, John Wiley & Sons, 2002.
- [13] J. D. Jackson, *Classical Electrodynamics*, John Wiley & Sons, 1998.
- [14] D. Strauss, *Magnetic Drug Targeting in Cancer Therapy*, 2005, <http://www.comsol.com/showroom>.
- [15] R. E. Rosensweig, "An introduction to ferrohydrodynamics," *Chemical Engineering Communications*, vol. 67, no. 1, pp. 1–18, 1988.
- [16] R. E. Rosensweig, *Ferrohydrodynamics*, Dover, 1997.
- [17] P. A. Voltairas, D. I. Fotiadis, and L. K. Michalis, "Hydrodynamics of magnetic drug targeting," *Journal of Biomechanics*, vol. 35, no. 6, pp. 813–821, 2002.
- [18] Y. C. Fung, *Biomechanics: Mechanical Properties of Living Tissues*, Springer, 1993.

Research Article

Controlling Force in Polarization-Maintaining Fiber Fused Biconical Tapering

Wei Zhang,¹ Weibin Rong,¹ Lefeng Wang,¹ Qing Zheng,² and Lining Sun¹

¹ State Key Laboratory of Robotics and System, Harbin Institute of Technology, Harbin 150080, China

² AVIC Xi'an Flight Automatic Control Research Institute, Xi'an 710065, China

Correspondence should be addressed to Weibin Rong; rwb@hit.edu.cn

Received 10 August 2014; Accepted 4 November 2014

Academic Editor: Junuthula N. Reddy

Copyright © 2015 Wei Zhang et al. This is an open access article distributed under the Creative Commons Attribution License, which permits unrestricted use, distribution, and reproduction in any medium, provided the original work is properly cited.

Fused biconical tapering (FBT) is an important method of manufacturing polarization-maintaining fiber (PMF) couplers. However, the tension on the ends of the fibers can affect the performance of the coupler. In this paper, a computer-based method of controlling the drawing force was presented. The system includes a drawing mechanism, rotary position encoders, and a control circuit. A three-dimensional model of a permanent magnet and a coil is constructed, and the relationship among the coil current, rotation angle of the clamp, and electromagnetic force is determined using finite element simulations. Electromagnetic force control based on these simulations can be realized. The method is verified experimentally, and it is shown that a drawing force of 0–1.8 gf can be achieved with an error of within 3.04%. This result can be used in the FBT-based manufacture of fiber components such as fiber couplers and gratings.

1. Introduction

Polarization-maintaining fiber (PMF) couplers are important passive components for achieving polarization light coupling, splitting, and multiplexing. They are widely used in fiber optic sensing and coherent communications [1, 2]. PMF couplers are typically fabricated using fiber biconical tapering (FBT) method, which involves fixing two optical fibers at a certain tension, heating the fibers to molten status, and drawing the fibers to form a biconical or dumbbell shape [3, 4]. Although the FBT method yields less extinction ratio of couplers than the polishing method, it has better thermal stability and smaller excess and insertion losses. FBT is controlled by three process parameters, the drawing speed, heating temperature, and drawing force, and the tension force on the fibers directly affects the performance of the PMF coupler. The translation stage in conventional FBT machines [5–8] consists of translation stage parts as well as heating and fiber clamping parts, and the translation stage parts are controlled with a computer to realize a precise drawing speed, but there is little control over the drawing force. Identically spring-loaded fiber pulling stages were introduced to impart a uniform tension

to a pair of fibers, and this alleviated problems associated with sudden changes in the tension force [9]. However, the elongation of the spring changes the tension force on the fibers, which does not allow the tension force control during the drawing process. Our experiments have shown that crystallization of the fiber surface may occur when the drawing force is large, which will increase the excess loss. FBT is also an important method of manufacturing long-period fiber gratings, and the periodic decrease in the fiber cross section depends on the drawing force on the fiber. The drawing tension was usually controlled by clamping one end of the fiber to a translation stage and attaching a mass to the other end of the fiber to keep it under a constant axial tension [10, 11]. When the fiber is being drawn, however, the translation stage does not move at a constant velocity, so the tension in the optical fiber varies. It is difficult to adjust the tension in the fiber during the drawing process.

We propose here a computer-based method of controlling the drawing mechanism and drawing force during FBT. In the method, the drawing force is generated through the control of the coil current by detecting the rotation of the fiber clamp, which thus achieves semiclosed loop control. The drawing

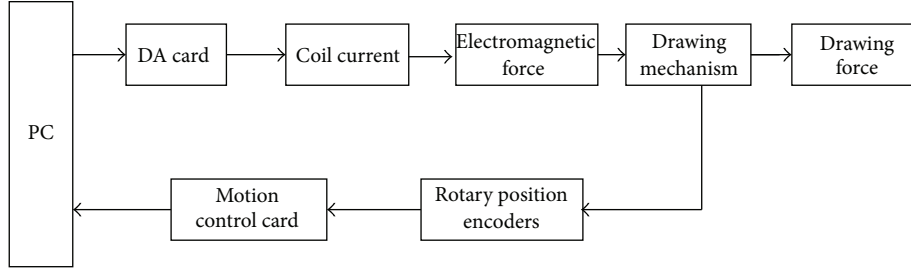


FIGURE 1: Block diagram of the force control system for the PMF FBT.

mechanism and control principle are introduced in Section 2. The force exerted on the permanent magnet by an electromagnetic coil is simulated using a three-dimensional (3D) finite element method in Section 3. Based on the analysis, a mathematical equation for the coil current, rotation angle of the fiber clamp, and electromagnetic force is established, and this equation is used to control the electromagnetic force. The drawing mechanism is analyzed and a simplified force model is presented in Section 4. In Section 5, we present the device used to detect the tension and an experimentally derived expression of the relationship among the coil current, rotation clamp angle, and drawing force. Control of the drawing force is also demonstrated in Section 5.

2. Setup and Control Method

The PMF fused taper drawing control system, shown in Figure 1, links the drawing mechanism, electromagnetic coil, rotary position encoders, digital-to-analog (DA) card, and motion control card to a personal computer (PC). The drawing mechanism (Figure 2) consists of a connect piece, drum wheel, fiber clamp, mass, permanent magnet, coil, and rotary position encoders.

The PC controls the current through the coil via the DA card to produce a certain magnetic field that interacts with the permanent magnet and generates the desired electromagnetic force. This causes the drawing force on the fiber clamp. As the two drum wheels are connected by two pieces, they rotate with the same rotation angle. The glass-disk rotary position encoders are linked to the drum wheel so that the rotary position encoders can detect the rotation angle. The drawing length of the clamped fibers is thus determined from the rotation angle. During the drawing, the distance between the permanent magnet and the coil changes so that the drawing force on the fiber clamp varies. The force can also be varied by changing the coil current in regard to the wheel rotation angle.

3. Analysis and Calculation of Electromagnetic Force

3.1. Theoretical Analysis. A cylindrical permanent magnet is used in the drawing mechanism. For a cylindrical permanent magnet that is magnetized along the z -direction with height

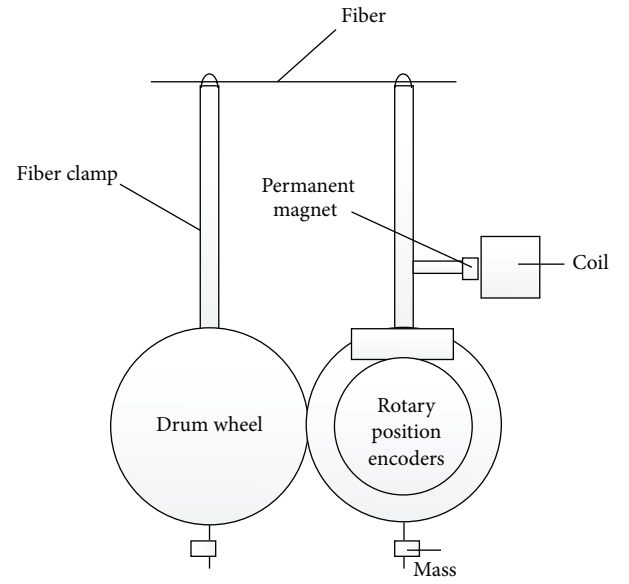


FIGURE 2: Structure of drawing mechanism.

Z_0 and radius a , the magnetic field distribution B at a point (r, ϕ, z) [12, 13] is

$$\begin{aligned}
 B_z &= \frac{\mu_0 J}{2\pi} \int_{-z_0/2}^{z_0/2} \frac{1}{[(a+r)^2 + (z-z')^2]^{1/2}} \\
 &\quad \times \left[\frac{a^2 + r^2 - (z-z')^2}{(a-r)^2 + (z-z')^2} E(k) + K(k) \right] dz', \\
 B_r &= \frac{\mu_0 J}{2\pi} \int_{-z_0/2}^{z_0/2} \frac{z-z'}{r [(a+r)^2 + (z-z')^2]^{1/2}} \\
 &\quad \times \left[\frac{a^2 + r^2 + (z-z')^2}{(a-r)^2 + (z-z')^2} E(k) - K(k) \right] dz',
 \end{aligned} \tag{1}$$

where $K(k)$ and $E(k)$ are complete elliptic integrals of the first and second kind, respectively;

$$k = \sqrt{\frac{4ar}{(a+r)^2 + (z-z')^2}},$$

$$K[k] = \int_0^{\pi/2} \frac{1}{\sqrt{1 - k \sin^2(\phi)}} d\phi,$$

$$E[k] = \int_0^{\pi/2} \sqrt{1 - k \sin^2(\phi)} d\phi. \quad (2)$$

The electromagnetic force can be calculated using the Lorentz force method, Maxwell stress tensor method, or the virtual work method [14]. As the Lorentz force method is suitable for calculating the force of a carrier fluid in a magnetic field, it was chosen in this study. The electromagnetic force F_m applied to the permanent magnet and the electromagnetic force F_c applied to the current coil are action and reaction forces; that is,

$$F_m = -F_c = - \int_V f dv = - \int_V J \times B dv, \quad (3)$$

$$J = I \cdot \frac{N}{S},$$

where f is the electromagnetic force per unit volume of the coil, J is the current density in the coil, B is the magnetic induction of the coil, I is the current in the coil of N turns, and S is the cross-sectional area of the coil wires.

3.2. Finite Element Analysis. The movement of the clamp is moving so that an accurate two-dimensional (2D) simulation cannot be performed when the cylindrical permanent magnet enters the coil. Thus, a 3D simulation model was created. The center of the drum wheel rotation defines the origin, with the x - and y -axes lying parallel to the length of the coil and fiber clamp, respectively. An insulating nylon frame was used for the coil, which is 24 mm long with inner and outer diameters of 20 and 40 mm, respectively, and consists of 1676 turns. $\text{Nd}_2\text{Fe}_{14}\text{B}$ was chosen as the material for the permanent magnet as it has a high energy product, coercive force, and energy density [15]. The surface magnetic induction of the permanent magnet was 389 mT, as measured by a Gauss meter (GV-300).

During the movement of the fiber clamp, the center of the permanent magnet and the angle vary with respect to the horizontal plane. Figure 3 shows a 2D view of the model structure in the $z = 0$ plane. Assuming that the center of the permanent magnet is at point B with coordinates of (p_x, p_y) , then the coordinates of point B when the fiber clamp is rotated by an angle θ are

$$p_x = L_1 \sin \theta + L_2 \cos \theta, \quad (4)$$

$$p_y = L_1 \cos \theta + L_2 \sin \theta,$$

where L_1 and L_2 are the length of the A - O and A - B lines, respectively.

We created a cube of air with a side length of 130 mm to simulate the magnetic field distribution. This cube has insulating boundary conditions; that is, $\mathbf{n} \times \mathbf{A} = 0$, where \mathbf{n} is the vector normal to the surface and \mathbf{A} is the magnetic vector potential [16, 17]. Free tetrahedral elements are adopted in

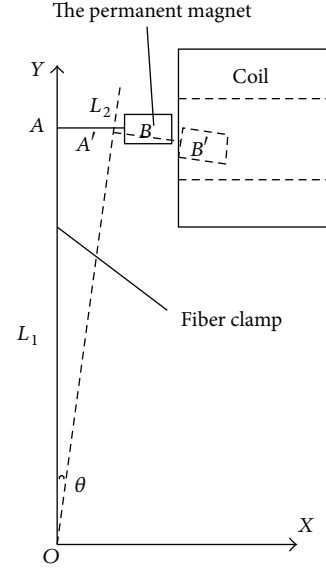


FIGURE 3: 2D schematic model of the drawing mechanism.

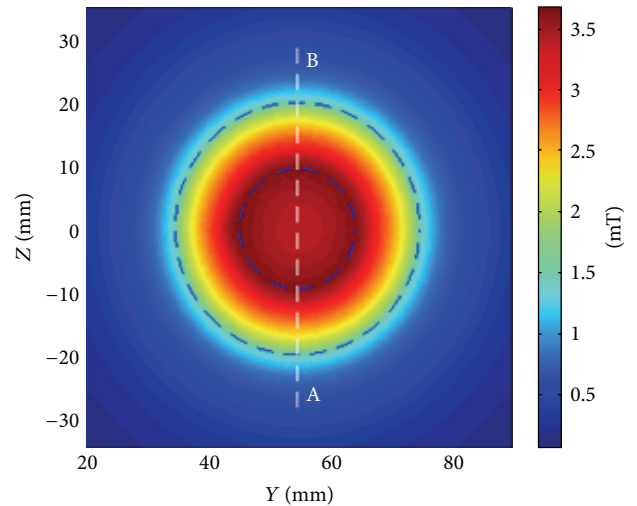


FIGURE 4: Simulated magnetic flux norm distribution at $x = 35$ mm.

the finite element simulation. Finer meshes are used for the coil and permanent magnet to improve the accuracy and calculation speed, and fine meshes are used for the cube of air. A total of 44743 finite division elements were used. The electromagnetic force is obtained from the calculation of the Lorentz force.

3.3. Simulation Results. The magnetic flux norm distribution in the $x = 35$ mm plane, which is between the permanent magnet and the coil and 1 mm away from the coil, for a current of 0.1 A passing through the coil is shown in Figure 4. Figure 5 shows the distribution along the line A - B through the center of the coil. These results show that the magnetic flux norm is related to the distance from the coil center. Inside the inner coil radius, the magnetic flux norm decreases toward the center to a minimum of 3.41 mT. This value agrees

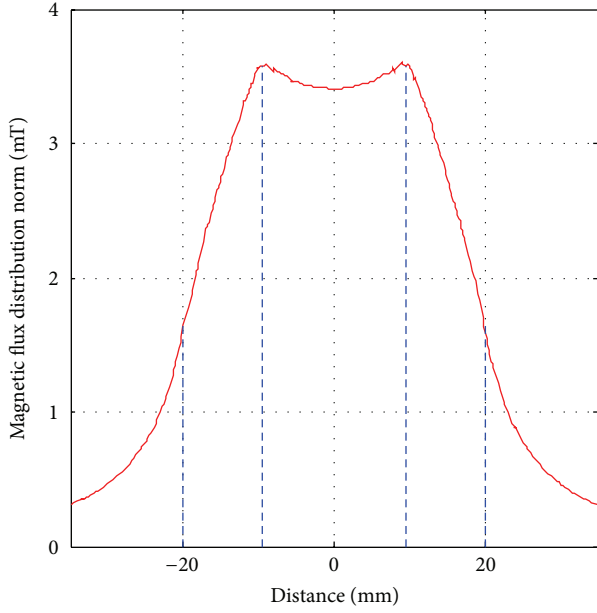


FIGURE 5: Magnetic flux norm along the line A-B in Figure 4.

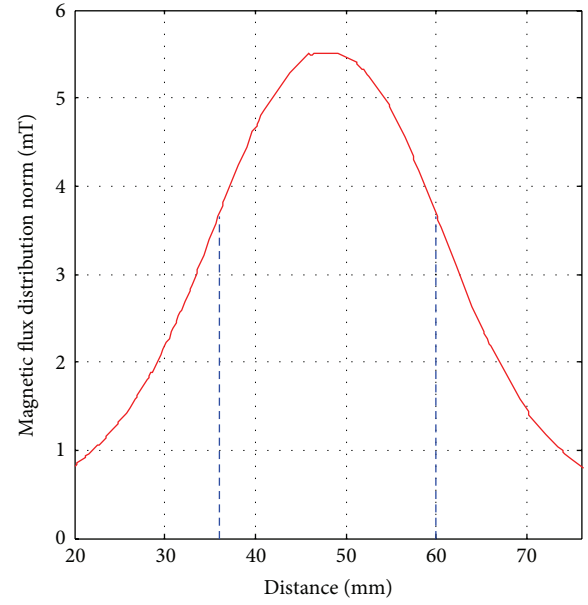
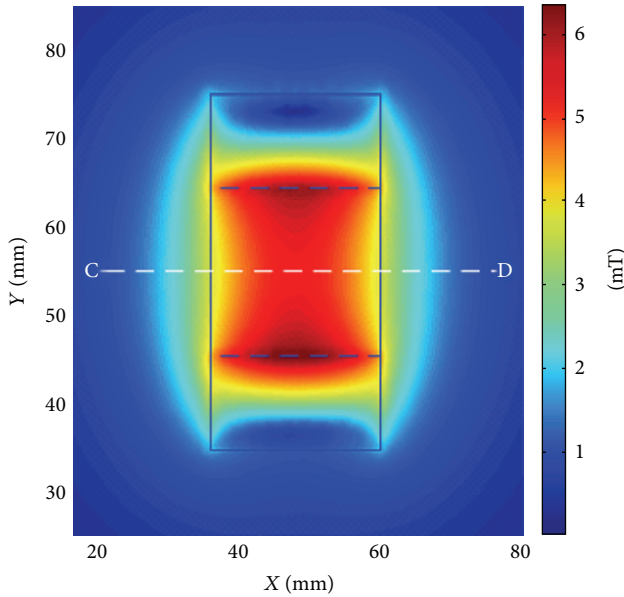


FIGURE 7: Simulated magnetic flux density norm along the line C-D in Figure 6.

FIGURE 6: Simulated magnetic flux norm distribution at $z = 0$.

well with the analytical value of 3.46 mT given in the literature [18]. The difference between the maximum and minimum magnetic flux norm value is 0.2 mT, which indicates that the rate of change is low. Outside the inner coil radius, the magnetic flux norm decreases rapidly with increasing distance from the maximum at the inner diameter of the coil. The magnetic flux distribution in the $z = 0$ plane which is shown in Figures 6 and 7 shows the distribution along the longitudinal axis of the coil (line C-D). The magnetic flux norm is symmetric about the longitudinal axis of the coil and achieves a maximum value at the center of the coil. Near the coil, the change in the magnetic flux norm is approximately linear.

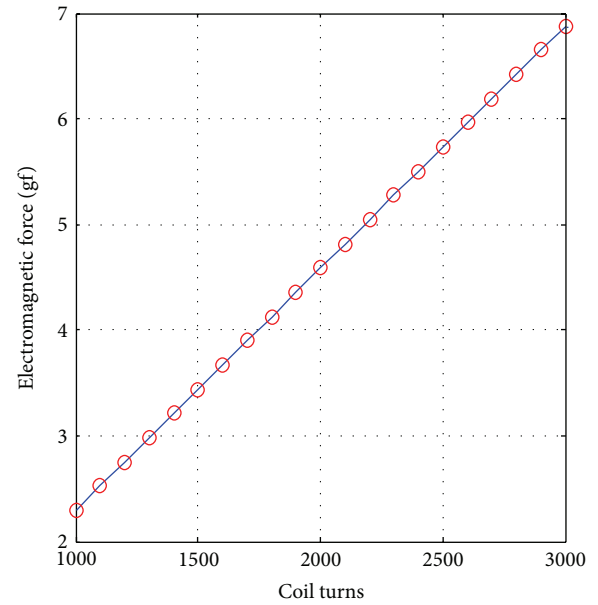
FIGURE 8: Simulated electromagnetic force as a function of the number of coil turns for $\theta = 0^\circ$ and $I = 0.1$ A.

Figure 8 shows the relationship between the electromagnetic force and the number of coil turns for $\theta = 0^\circ$ and $I = 0.1$ A. A least-squares fit of the data gives the linear relationship:

$$F_m = 0.0023N - 0.0026. \quad (5)$$

The number of coil turns, however, is fixed to $N = 1676$ for the simulations. Figure 9 shows the relationship between

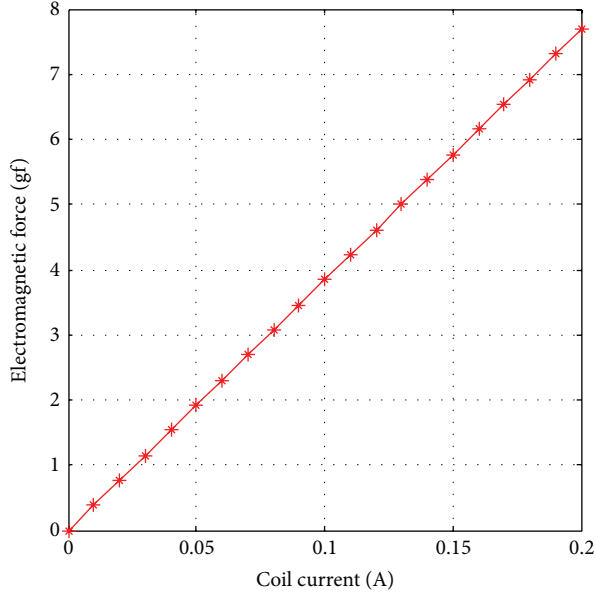


FIGURE 9: Simulated electromagnetic force as a function of the coil current for $\theta = 0^\circ$ and $N = 1676$.

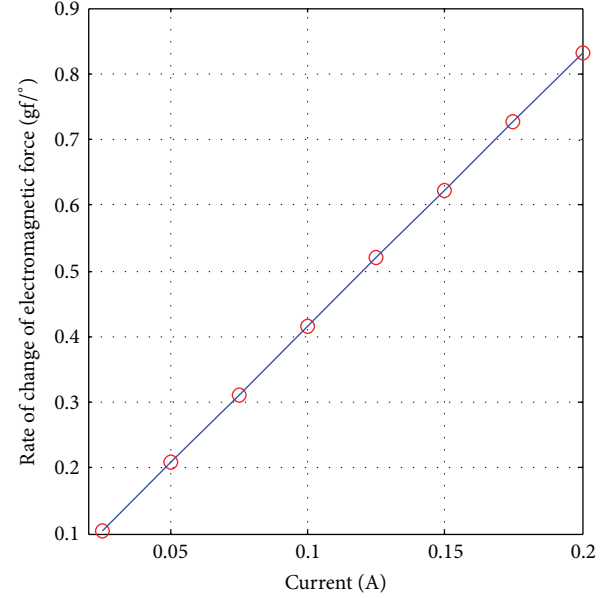


FIGURE 11: Simulated rate of change of the electromagnetic force as a function of the current.

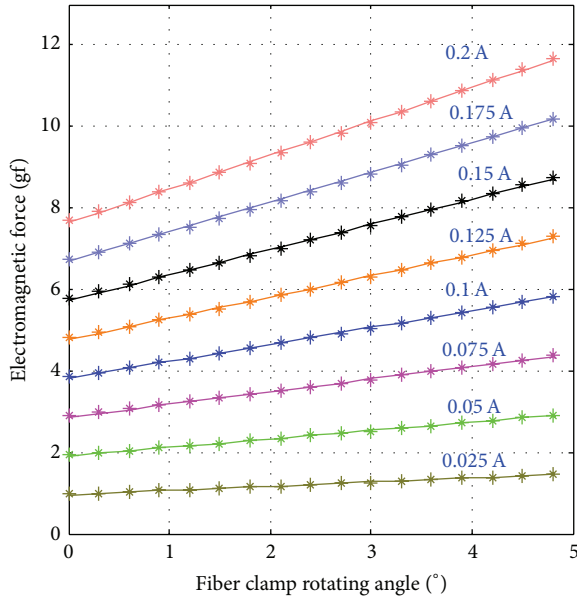


FIGURE 10: Simulated electromagnetic force as a function of the rotating angle for various coil currents.

the electromagnetic force and coil current for $\theta = 0^\circ$ and $N = 1676$, which also reveals linear behavior of

$$F_m = 38.4558I. \quad (6)$$

Changing the rotation angle θ of the clamp will change the position of the permanent magnet and hence the electromagnetic force. Figure 10 shows the relationship between the rotation angle θ and the electromagnetic force for a constant coil current. Again, we see a linear relationship, but the gradient, which is defined as the rate of change of

the electromagnetic force, depends on the current. The gradient $K_{F\theta}$ can be expressed as

$$K_{F\theta} = \frac{\Delta F_m}{\Delta \theta}, \quad (7)$$

where ΔF_m is the change of the electromagnetic force of the permanent magnet (in units of gram-force) and $\Delta \theta$ is the change of the rotation angle of the clamp (in units of degrees). The rate of change of the electromagnetic force is shown as a function of the current in Figure 11. A linear fit gives

$$K_{F\theta} = 4.1517 \cdot I. \quad (8)$$

Changing θ will also change the relationship between the electromagnetic force and the current. For a constant angle, the electromagnetic force coefficient, K_{FI} , can be defined as

$$K_{FI} = \frac{\Delta F_m}{\Delta I}, \quad (9)$$

where ΔI is the change of the coil current (in units of amperes). Figure 12 shows K_{FI} as a function of the rotating angle (0° to 4.8°), and a linear fit yields

$$K_{FI} = 4.1517\theta + 38.1982. \quad (10)$$

We thus obtain a mathematical expression for the relationship among F_m , I , and θ :

$$I = 0.026F_m - \frac{0.108F_m\theta}{(4.1517\theta + 38.1982)}. \quad (11)$$

The electromagnetic force can be controlled by adjusting the coil current on the basis of (11). Figure 13 shows that a relatively constant electromagnetic force can be achieved for fiber clamp rotating angles from 0° to 4.8° once the coil current control is implemented. Table 1 lists the simulation error of the electromagnetic force, and it indicates that the force can be controlled accurately with an error of about 1%.

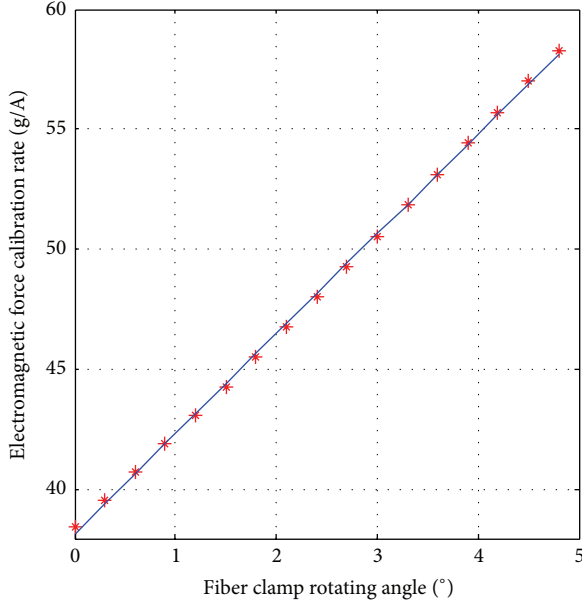


FIGURE 12: Simulated electromagnetic force calibration rate as a function of the rotating angle.

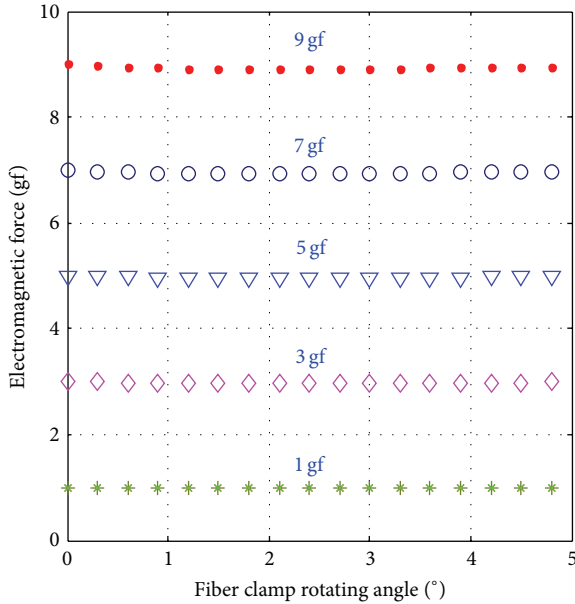


FIGURE 13: Simulated electromagnetic force as a function of the rotating angles after implementing current control.

TABLE 1: Simulated control error.

Electromagnetic force (gf)	1	3	5	7	9
Error (%)	0.98	1.03	1.03	1.02	1.01

4. Drawing Force Analysis

The drawing mechanism contains two spring pieces that are used to connect the two drum wheels and maintain equal clamp rotation angles. The bending elastic force of the two

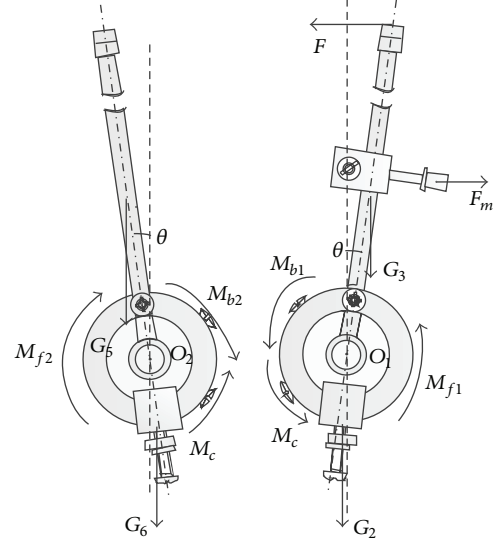


FIGURE 14: Force and moment analysis model of two separate clamps.

pieces can be neglected as it is considerably smaller than the drawing force. As the drawing force and the rotation angles of the clamps are equal, the following analysis can be performed for a single clamp (in this case, the clamp on the right). Figures 14 and 15 outline the force and torque components for the analysis of the two clamps. For a rotation angle of 0° – 5° , the torque-balanced expression for the fiber holders is

$$M_{G6} + M_{b2} + M_{f2} = M_{G5} + M_c, \quad (12)$$

$$\begin{aligned} M_{G2} + M_{b1} + M_{f1} + F \cdot L_F \cdot \cos \theta + M_c \\ = M_{G3} + F_m \cdot L_m \cdot \cos \theta, \end{aligned} \quad (13)$$

where M_{b2} (M_{b1}) is the torque generated by the spring piece and fastening bolts on the left (right) fiber clamp; M_{f2} (M_{f1}) is the torque generated by friction during the rotation of the left (right) fiber clamp; M_{G6} (M_{G2}) is the torque generated by the mass on the bottom of the left (right) fiber clamp; M_{G5} is the torque generated by the left fiber clamp; M_{G3} is the torque generated by the right fiber holder, permanent magnet, and fixed base; F is the drawing force generated by the right fiber clamp; L_F is the distance between the rotation center O_1 and the application point of F_1 for $\theta = 0^\circ$; L_m is the distance between the application point of F_m and O_1 for $\theta = 0^\circ$; and M_c is the torque generated by the connect piece. From (12), we see that M_{G6} can be varied by adjusting the position of the mass on the left fiber holder such that M_c will be zero. The position of the mass on the bottom of the right fiber clamp is then adjusted so that M_{G2} satisfies

$$M_{G2} + M_{b1} + M_{f1} = M_{G3}. \quad (14)$$

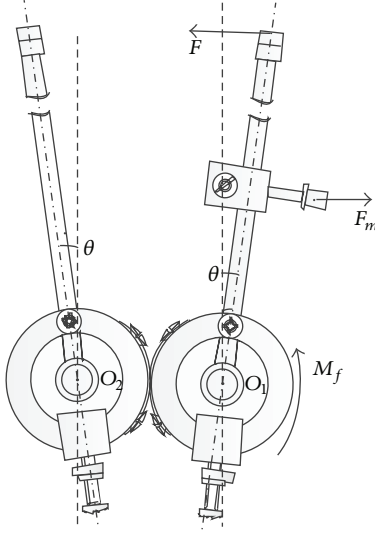


FIGURE 15: Overall force and moment analysis model of the clamps.

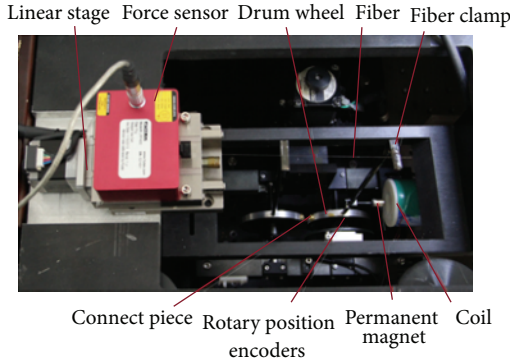


FIGURE 16: Drawing force detection device.

The mechanical force of the drawing mechanism is thus described in Figure 15, and the drawing mechanism then satisfies the torque balance equation

$$M_{f1} + F \cdot L_F \cdot \cos \theta = F_m \cdot L_m \cdot \cos \theta. \quad (15)$$

The drawing mechanism used in this study has precision deep groove ball bearings that have a friction coefficient of 0.001–0.0015. The friction during the fiber clamp rotation is also small by comparison with the drawing force and can also be neglected. Thus, (15) can be simplified as

$$F = F_m \cdot \frac{L_m}{L_F}. \quad (16)$$

When the right clamp is at 0° and the coil current is 0.1 A, the theoretical value of the electromagnetic force is 3.8437 gf, which yields a drawing force of 1.127 gf according to (16).

5. Force Detection Experiment

The experimental force detection device, shown in Figure 16, includes a precision electric linear stage, force sensor, and the

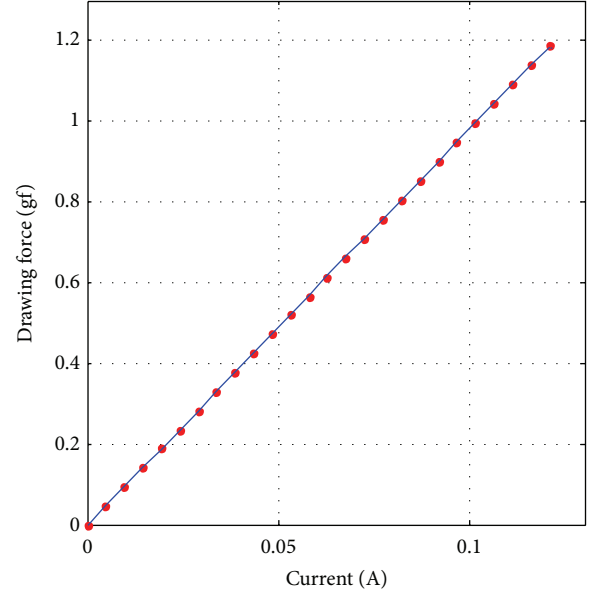


FIGURE 17: Experimental drawing force as a function of the coil current.

control system shown in Figure 1. The linear stage has a repeat accuracy of $1 \mu\text{m}$. The force sensor has a resolution of 0.1 mgf and is fixed on the linear stage connected to the right fiber clamp by the fiber. The rotation of the fiber clamp is controlled by the motion control card in the PC through the linear stage. Setting the rotation angle of the right fiber clamp to zero and the coil current to 0.100 A yields a drawing force on the right fiber clamp end of 0.9952 gf, which is in reasonable agreement with the simulation result of 1.127 gf.

For a rotating angle of zero, the relationship between the drawing force and current is linear, as was shown in Section 3, and to confirm this experimentally the drawing force F was measured for currents of 0 to 0.2 A (Figure 17). A fit to the experimental data gave

$$F = 9.8512I - 0.0027, \quad (17)$$

which includes a nonzero constant owing to friction and assembly errors.

The drawing force is shown as a function of the rotating angle (0° to 4.8°) in Figure 18 for various coil currents. As predicted by the simulations, there is a linear relationship between the drawing force and the rotating angle, and the rate of change of the drawing force (Figure 19) is given by

$$K_{F\theta} = 0.7119I_c - 0.0078. \quad (18)$$

Figure 20 shows the drawing force calibration rate as a function of the rotating angle, which can be expressed as

$$K_{FI} = 0.7133\theta + 9.9860. \quad (19)$$

The relationship among F , I , and θ can then be summarized as

$$I_c = 101.5F + 0.2741 - \frac{1000(723F - 76)\theta}{(7133\theta + 99860)}. \quad (20)$$

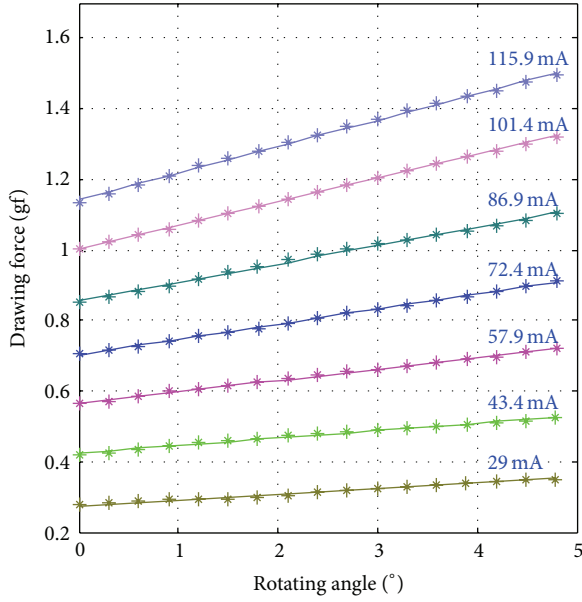


FIGURE 18: Experimental drawing force as a function of the rotating angle for various coil currents.

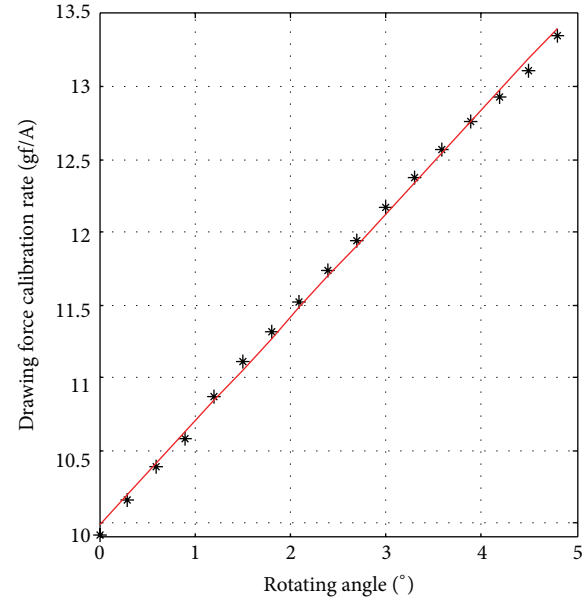


FIGURE 20: Experimental drawing force calibration rate as a function of the rotating angle.

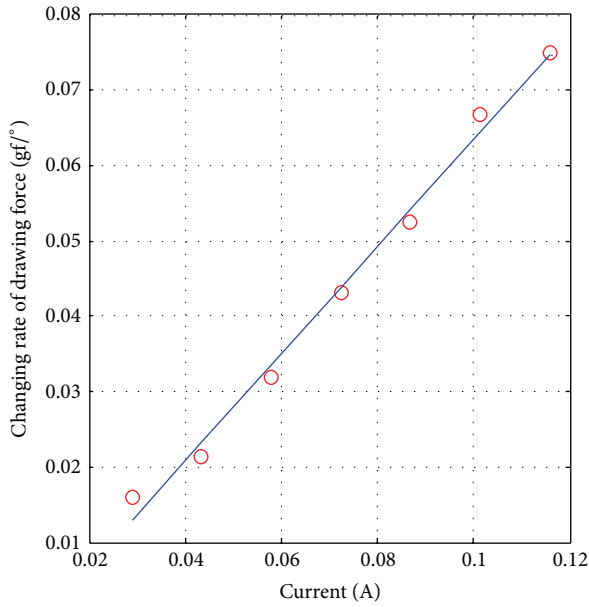


FIGURE 19: Experimental rate of change of the drawing force as a function of the current.

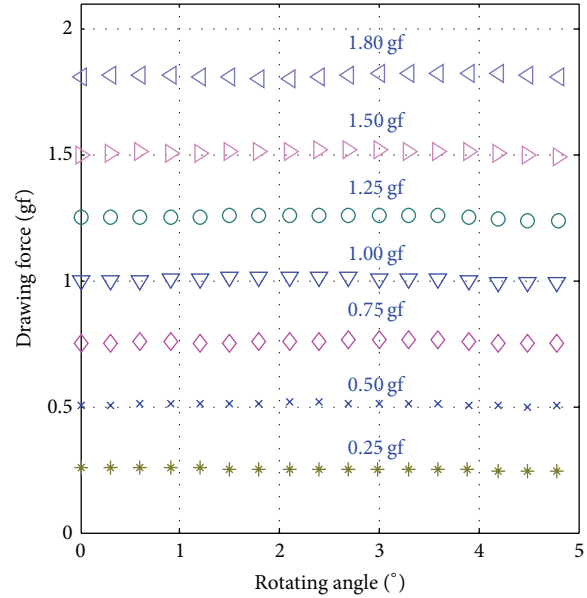


FIGURE 21: Experimental drawing force as a function of the rotating angle after implementing current control.

The rotation angle of the clamp, detected by the rotary position encoders, can thus be used in determining the current to apply to the coil, which is controlled by the DA output voltage, for a known drawing force. In this way, the drawing force can be controlled. Figure 21 shows the drawing force as a function of the rotating angle after implementing the current control, and the errors in the experimental control are listed in Table 2. The maximum error generated by a constant force is 3.04%. A maximum force of 1.8 gf was obtained, but (5) and (17) indicate that a higher force can

TABLE 2: Experimental control error.

Drawing force (gf)	0.25	0.5	0.75	1	1.25	1.5	1.8
Error (%)	2.48	3.04	2.23	1.28	1.00	1.18	1.36

be applied by increasing the number of turns and the coil current.

6. Conclusion

The drawing force applied to the fibers can affect the coupling performance in PMF FBT, and we have proposed a method for controlling the force during FBT. We constructed a 3D model of the permanent magnet in the drawing mechanism and established an equation of motion for the magnet. We developed an expression for the relationship among the coil current, rotation angle of the fiber clamp, and the electromagnetic force by simulation and used this expression to control the electromagnetic force; the calculation error was within 1.03%. The mechanical model of the stretching mechanism was simplified by adjusting the mass, and the relationship between the drawing force on the fiber clamp and the electromagnetic force was established. The relationship among the coil current, rotation angle of the clamp, and drawing force was confirmed experimentally, and experimental control of the driving force (0–1.8 gf) was accurate enough with an error less than 3.04%. The results presented here have verified the feasibility of the proposed control method for FBT. Using this method, the drawing force on the fibers can be controlled effectively.

Conflict of Interests

The authors declare that there is no conflict of interests regarding the publication of this paper.

Acknowledgments

This research was supported by Self-Planned Task of State Key Laboratory of Robotics and System (SKLRS201301A01) and the Program for Changjiang Scholars and Innovative Research Team in University (IRT0915).

References

- [1] D. P. Davé, T. Akkin, and T. E. Milner, "Polarization-maintaining fiber-based optical low-coherence reflectometer for characterization and ranging of birefringence," *Optics Letters*, vol. 28, no. 19, pp. 1775–1777, 2003.
- [2] M. Bin and X. Jian, "Experimental research of coupling fiber-optic sensor for vibration measurement," in *Proceedings of the International Symposium on Photonics and Optoelectronics (SOPO '10)*, pp. 1–4, IEEE, Chengdu, China, June 2010.
- [3] B. S. Kawasaki, K. O. Hill, and R. G. Lamont, "Biconical-taper single-mode fiber coupler," *Optics Letters*, vol. 6, no. 7, pp. 327–328, 1981.
- [4] R. G. Lamont, D. C. Johnson, and K. O. Hill, "Power transfer in fused biconical-taper single-mode fiber couplers: dependence on external refractive index," *Applied Optics*, vol. 24, no. 3, pp. 327–332, 1985.
- [5] S. W. Harun, K. S. Lim, C. K. Tio, K. Dimiyati, and H. Ahmad, "Theoretical analysis and fabrication of tapered fiber," *Optik*, vol. 124, no. 6, pp. 538–543, 2013.
- [6] C. S. Hsieh, T. L. Wu, and W. H. Cheng, "Optimum approach for fabrication of low loss fused fiber couplers," *Materials Chemistry and Physics*, vol. 69, no. 1–3, pp. 199–203, 2001.
- [7] Y. Wang and H. Liu, "The comparison of two methods to manufacture fused biconical tapered optical fiber coupler," in *Photonics and Optoelectronics Meetings (POEM) 2009: Fiber Optic Communication and Sensors*, vol. 7514 of *Proceedings of SPIE*, October 2009.
- [8] C. Shuai, C. Gao, Y. Nie, H. Hu, and S. Peng, "Microstructure analysis in the coupling region of fiber coupler with a novel electrical micro-heater," *Optical Fiber Technology*, vol. 17, no. 6, pp. 541–545, 2011.
- [9] B. P. Pal, P. R. Chaudhuri, and M. R. Shenoy, "Fabrication and modeling of fused biconical tapered fiber couplers," *Fiber and Integrated Optics*, vol. 22, no. 2, pp. 97–117, 2003.
- [10] F. Dürr, G. Rego, P. V. S. Marques et al., "Tomographic stress profiling of arc-induced long-period fiber gratings," *Journal of Lightwave Technology*, vol. 23, no. 11, pp. 3947–3953, 2005.
- [11] G. Rego, O. Okhotnikov, E. Dianov, and V. Sulimov, "High-temperature stability of long-period fiber gratings produced using an electric arc," *Journal of Lightwave Technology*, vol. 19, no. 10, pp. 1574–1579, 2001.
- [12] B. Ebrahimi, M. B. Khamesee, and M. F. Golnaraghi, "Design and modeling of a magnetic shock absorber based on eddy current damping effect," *Journal of Sound and Vibration*, vol. 315, no. 4–5, pp. 875–889, 2008.
- [13] J. S. Agashe and D. P. Arnold, "A study of scaling and geometry effects on the forces between cuboidal and cylindrical magnets using analytical force solutions," *Journal of Physics D: Applied Physics*, vol. 41, no. 10, Article ID 105001, 2008.
- [14] Y.-D. Chun and J. Lee, "Comparison of magnetic levitation force between a permanent magnet and a high temperature superconductor using different force calculation methods," *Physica C: Superconductivity*, vol. 372–376, part 3, pp. 1491–1494, 2002.
- [15] N. Leventis and X. Gao, "Nd-Fe-B permanent magnet electrodes. Theoretical evaluation and experimental demonstration of the paramagnetic body forces," *Journal of the American Chemical Society*, vol. 124, no. 6, pp. 1079–1088, 2002.
- [16] A. Alferenok, M. Werner, M. Gramss, U. Luedtke, and B. Halbedel, "Numerical optimization of the magnet system for the Lorentz Force Velocimetry of electrolytes," *International Journal of Applied Electromagnetics and Mechanics*, vol. 38, no. 2–3, pp. 79–92, 2012.
- [17] M. Ziolkowski and H. Brauer, "Fast computation technique of forces acting on moving permanent magnet," *IEEE Transactions on Magnetics*, vol. 46, no. 8, pp. 2927–2930, 2010.
- [18] C. Pawashe, S. Floyd, and M. Sitti, "Modeling and experimental characterization of an untethered magnetic micro-robot," *International Journal of Robotics Research*, vol. 28, no. 8, pp. 1077–1094, 2009.

Research Article

Predictor-Corrector LU-SGS Discontinuous Galerkin Finite Element Method for Conservation Laws

Xinrong Ma,^{1,2} Sanyang Liu,¹ and Gongnan Xie³

¹Department of Applied Mathematics, Xidian University, Xi'an 710071, China

²Department of Applied Mathematics, Xianyang Normal University, Xianyang 712000, China

³School of Mechanical Engineering, Northwestern Polytechnical University, Xi'an 710072, China

Correspondence should be addressed to Xinrong Ma; mxryx1021@163.com

Received 23 June 2014; Revised 31 August 2014; Accepted 31 August 2014

Academic Editor: Shaofan Li

Copyright © 2015 Xinrong Ma et al. This is an open access article distributed under the Creative Commons Attribution License, which permits unrestricted use, distribution, and reproduction in any medium, provided the original work is properly cited.

Efficient implicit predictor-corrector LU-SGS discontinuous Galerkin (DG) approach for compressible Euler equations on unstructured grids is investigated by adding the error compensation of high-order term. The original LU-SGS and GMRES schemes for DG method are discussed. Van Albada limiter is employed to make the scheme monotone. The numerical experiments performed for the transonic inviscid flows around NACA0012 airfoil, RAE2822 airfoil, and ONERA M6 wing indicate that the present algorithm has the advantages of low storage requirements and high convergence acceleration. The computational efficiency is close to that of GMRES scheme, nearly 2.1 times greater than that of LU-SGS scheme on unstructured grids for 2D cases, and almost 5.5 times greater than that of RK4 on unstructured grids for 3D cases.

1. Introduction

High-order discontinuous Galerkin (DG) finite element methods were developed based on weighted residual theory; they maintain advantages of both the traditional high resolution finite difference method and the finite volume method while overcoming their shortcomings. Indeed, the DG method can be considered as a mixture of classic finite element method (FEM) and finite volume method (FVM), which is a better solution strategy for solving problems in the presence of strong shocks and discontinuities because the solution across each element can be discontinuous. DG methods can easily deal with complex boundary-value problem and flexibly handle discontinuity, which have a low requirement of the regularity of grids. And high accuracy can be achieved by selecting appropriate basis functions by improving the order of the piecewise interpolation polynomials functions. In addition, the methods are highly parallelizable as each element is independent and the interelement communications are minimal. And they have several useful mathematical properties.

While DG method was introduced by Reed and Hill [1] for solving the neutron transport equation back in 1973, nowadays, DG methods have been widely used in the computational fluid dynamics, computational aeroacoustics, and computational electromagnetics. See [2–25].

In recent years, significant progress has been made in developing numerical algorithms for solving the compressible flow problems. Many numerical methods are based on the semidiscrete approach: DG methods are used for the spatial discretization, rendering the original partial differential equations (PDE) into a system of ordinary differential equations (ODE) in time. Usually, for time-dependent problems, DG methods have been used in conjunction with explicit high-order accurate time-integration methods, such as nonlinear stable Runge-Kutta DG methods in the literatures [7–13]. In general, explicit schemes are easy to implement and parallelize and require only limited memory storage. Such methods are well suited for problems with similar spatial and temporal scales, while being notoriously time-consuming and inefficient for problems with disparate temporal and spatial scales, such as low reduced frequency phenomena and

steady-state problems. As a consequence, implicit time-integration strategies should be developed exclusively in order to avoid the stability restrictions of explicit methods, which are unconditionally stable; for details, refer to [5, 6, 26]. Implicit solvers, which do allow large time steps, are widely used in the computational fluid dynamics community for the steady solution of nonlinear conservation laws in [27]. The Newton-Krylov-Schwarz method has recently emerged as a promising technique for the parallel implicit solution of large-scale aerodynamics problems in [28], which is specially well suited for the discontinuous spectral Galerkin method, since each subdomain can be treated separately.

The lower-upper symmetric Gauss-Seidel (LU-SGS) time-marching scheme, which was originally given for structured grids, has been established in [29] and has been applied to tetrahedral/prism unstructured grids. Another attractive implicit scheme is the generalized minimum residual scheme (GMRES), which was introduced by Saad and Schultz [2] firstly. Then, Bassi and Rebay showed the efficiency of GMRES method in [14] and used a simple block Jacobi preconditioner for the implicit solution of the compressible Navier-Stokes equations. Xia and Luo [3] presented a matrix-free GMRES algorithm with an LU-SGS preconditioner reconstructed discontinuous Galerkin method on tetrahedron grids for compressible flow problems. Then, they proposed implicit reconstructed discontinuous Galerkin (IRDG) method based on the automatic differentiation technique [4].

In this work, we focus exclusively on a predictor-corrector LU-SGS (PCLU-SGS) strategy for discontinuous Galerkin method in conjunction with Van Albada limiter [30] to solve the Euler equations on unstructured grids. The governing equations are listed in Section 2. DG method is presented and the limiter and numerical flux are described in detail in Section 3. The implicit time-marching procedures are given including TVD Runge-Kutta, LU-SGS, and GMRES schemes, and the PCLU-SGS scheme is established in Section 4. The numerical experiments are discussed in Section 5. Conclusion is given in Section 6.

2. Governing Equations

The unsteady, compressible inviscid 2D Euler equations can be expressed in the following conservative form:

$$\frac{\partial \mathbf{U}(x, t)}{\partial t} + \frac{\partial \mathbf{F}(\mathbf{U}(x, t))}{\partial x} + \frac{\partial \mathbf{G}(\mathbf{U}(x, t))}{\partial y} = 0 \quad (1)$$

in $\Omega \times (0, T)$,

where $T > 0$ is the length of time interval and Ω is a two-dimensional bounded domain. The conservative state vector \mathbf{U} and the inviscid flux component vectors $\mathbf{F}(\mathbf{U})$ and $\mathbf{G}(\mathbf{U})$ are defined by

$$\mathbf{U} = \begin{pmatrix} \rho \\ \rho u \\ \rho v \\ \rho e \end{pmatrix}, \quad \mathbf{F}(\mathbf{U}) = \begin{pmatrix} \rho u \\ \rho u^2 + p \\ \rho uv \\ (\rho e + p)u \end{pmatrix},$$

$$\mathbf{G}(\mathbf{U}) = \begin{pmatrix} \rho v \\ \rho uv \\ \rho v^2 \\ (\rho e + p)v \end{pmatrix}, \quad (2)$$

where the notations ρ , p , and e denote the density, pressure, and specific total energy per unit mass of the fluid, respectively. u and v are the velocity components of the flow in the x and y coordinate directions. This set of equations is completed by the perfect gas equation of state given as follows:

$$p = (\gamma - 1) \rho \left[e - \frac{1}{2} (u^2 + v^2) \right], \quad (3)$$

where γ is defined as the ratio of specific heat of the fluid ($\gamma = 1.4$ for air). Then the equations are applied with the initial and boundary conditions denoted by (4), where $\partial\Omega$ represents the boundary of domain Ω . Consider the following:

$$\begin{aligned} \mathbf{U}(x, 0) &= \mathbf{U}_0(x), \\ B(\mathbf{U}) &= 0 \quad \text{on } \partial\Omega \times (0, T). \end{aligned} \quad (4)$$

3. Discontinuous Galerkin Finite Element Method

3.1. DG Spatial Discretization. The computational domain Ω is partitioned into an ensemble of nonoverlapping elements, triangles in 2D; that is, $\Omega = e_1 \cup e_2 \cup \dots \cup e_n$, where n denotes the number of elements in the domain. We consider possible choices of the piecewise basis functions and then obtain the following weak formulation of (5) by multiplying a test function Φ and integrating by parts over the e_m :

$$\begin{aligned} \frac{d}{dt} \int_{e_m} \Phi_h \mathbf{U}_h dV - \int_{e_m} \left[\frac{\partial \Phi_h}{\partial x} \mathbf{F}(\mathbf{U}_h) + \frac{\partial \Phi_h}{\partial y} \mathbf{G}(\mathbf{U}_h) \right] dV \\ + \int_{\partial e_m} \Phi_h [\mathbf{F}(\mathbf{U}_h) n_x + \mathbf{G}(\mathbf{U}_h) n_y] dS = 0 \quad \forall \Phi, \end{aligned} \quad (5)$$

where \mathbf{U}_h and Φ_h represent the finite element approximations of the analytical solution \mathbf{U} and the test function Φ , respectively. $\mathbf{n} = (n_x, n_y)$ is the unit normal vector of outward to the boundary. Let the approximate solution and test function \mathbf{U}_h and Φ_h be expressed as

$$\mathbf{U}_h = \sum_{j=1}^N U_j(t) \varphi_j^p(x), \quad \Phi_h = \sum_{j=1}^N \Phi_j \varphi_j^p(x), \quad (6)$$

where $\varphi_j^p(x)$ is the shape function of the polynomials of degree p . Equation (5) must be satisfied for any test function

Φ_h , so by substituting (6) to (5), we obtain the following system of N equations:

$$\begin{aligned} & \frac{dU_j(t)}{dt} \int_{e_m} \varphi_i^p \varphi_j^p dV \\ & - \int_{e_m} \left[\frac{\partial \varphi_i^p}{\partial x} \mathbf{F} \left(\sum_{j=1}^N U_j \varphi_j^p \right) + \frac{\partial \varphi_i^p}{\partial y} \mathbf{G} \left(\sum_{j=1}^N U_j \varphi_j^p \right) \right] dV \\ & + \int_{\partial e_m} \varphi_i^p \left[\mathbf{F} \left(\sum_{j=1}^N U_j \varphi_j^p \right) n_x + \mathbf{G} \left(\sum_{j=1}^N U_j \varphi_j^p \right) n_y \right] dS = 0 \end{aligned} \quad (7)$$

$i = 1, 2, \dots, N.$

The interface flux function $\mathbf{F}(\mathbf{U}_h) \mathbf{n}_x + \mathbf{G}(\mathbf{U}_h) \mathbf{n}_y$ can be treated as a numerical Riemann flux function $\mathbf{H}(\mathbf{U}_h^L, \mathbf{U}_h^R, \mathbf{n})$, where \mathbf{U}_h^L and \mathbf{U}_h^R represent the internal element interface solution and neighboring element interface solution, respectively. In the present work, the Roe, LLF, and HLLC approximate Riemann solvers are employed. The domain and boundary integrals in (7) are calculated by use of $2p$ and $2p + 1$ order accurate Gauss quadrature formulas [31, 32] with a number of quadrature points corresponding to the degree of interpolating polynomials.

By grouping together all the elemental time-dependent and spatial contributions, (7) can be written as a system of ordinary differential equations:

$$\mathbf{M} \frac{d\mathbf{U}}{dt} = \mathbf{R}(\mathbf{U}), \quad (8)$$

where the mass matrix \mathbf{M} has identical diagonal blocks \mathbf{M}_{ij} , \mathbf{U} is the global vector of the degrees of freedom, and $\mathbf{R}(\mathbf{U})$ represents the steady state residual vector. As a result, the inverse of the mass matrix \mathbf{M} can be easily computed, especially, using the orthogonal basis functions, and stored in advance due to the fact that it remains unchanged during the process.

In the present paper, we explore the orthogonal basis functions through Gram-Schmidt orthogonalization method, and high accuracy can be achieved by improving the order of the piecewise interpolation polynomials functions. For 2D problems, $\varphi_0 = 1$, $\varphi_1 = \xi$, $\varphi_2 = \eta$, $\varphi_3 = \xi^2, \dots$, and, for 3D problems, $\varphi_0 = 1$, $\varphi_1 = \xi$, $\varphi_2 = \eta$, $\varphi_3 = \zeta, \dots$

3.2. Flux Functions. The numerical flux function can be evaluated using any upwind flux functions. This is exactly similar to FVM because discontinuities can be allowed across the interface. Therefore, approximate Riemann solvers can be used to compute the flux function. In the present work, three flux functions have been employed including HLLC Riemann numerical solver by Toro [33] which has easier and lower computational cost in comparison with many other available Riemann solvers, such as local Lax-Friedrich (LLF) scheme. HLLC flux function not only maintains the advantages of the HLL solver but also resolves isolated contact discontinuities

exactly, which has been extended in conjunction with time-derivative preconditioning to compute flow problems at all speeds. HLL flux can be expressed as

$$\mathbf{F}^{\text{HLL}} = \begin{cases} \mathbf{F}_L & \text{if } S_L > 0 \\ \mathbf{F}_{LR}^* & \text{if } S_L \leq 0 \leq S_R \\ \mathbf{F}_R & \text{if } S_R < 0, \end{cases} \quad (9)$$

where S_L and S_R represent the fastest wave speed for the left and right states, respectively. \mathbf{F}_{LR}^* is written as

$$\mathbf{F}_{LR}^* = \frac{S_R \mathbf{F}_L - S_L \mathbf{F}_R + S_L S_R (\mathbf{U}_R - \mathbf{U}_L)}{S_R - S_L}. \quad (10)$$

The HLLC flux is a modification of HLL flux, which can be written as

$$\mathbf{F}^{\text{HLLC}} = \begin{cases} \mathbf{F}_L & 0 < S_L \\ \mathbf{F}_L^* = \mathbf{F}_L + S_L (\mathbf{U}_L^* - \mathbf{U}_L) & S_L \leq 0, S_M > 0 \\ \mathbf{F}_R^* = \mathbf{F}_R + S_R (\mathbf{U}_R^* - \mathbf{U}_R) & S_M \leq 0, S_R \geq 0 \\ \mathbf{F}_R & 0 > S_R, \end{cases} \quad (11)$$

where S_M is constant between the two acoustic waves:

$$S_M = \frac{p_R - p_L + \rho_L q_L (S_L - q_L) - \rho_R q_R (S_R - q_R)}{\rho_L (S_L - q_L) - \rho_R (S_R - q_R)}. \quad (12)$$

For details, refer to [33, 34].

The second flux function implemented in this paper is LLF solver [35]. It is more dissipate than both the HLLC flux function and the Roe flux function, but it is more robust. The LLF flux can be written as

$$\mathbf{F}^{\text{LLF}} = \frac{1}{2} [\mathbf{F}_L + \mathbf{F}_R - (|\lambda'| + c') (\mathbf{U}_R - \mathbf{U}_L)], \quad (13)$$

where λ' is the velocity normal to the interface and c' is the speed of sound at the interface. $|\lambda'| + c'$ is the largest wave speed in the direction normal to the interface.

The third flux function is Roe numerical flux by Roe [36]. Roe format is a typical flux differential splitting scheme, which contains more feature information, and therefore has a strong ability to capture shock. The Roe flux can be expressed as

$$\mathbf{F}^{\text{Roe}} = \frac{1}{2} [\mathbf{F}_L + \mathbf{F}_R - |\tilde{\mathbf{A}}| (\mathbf{U}_R - \mathbf{U}_L)], \quad (14)$$

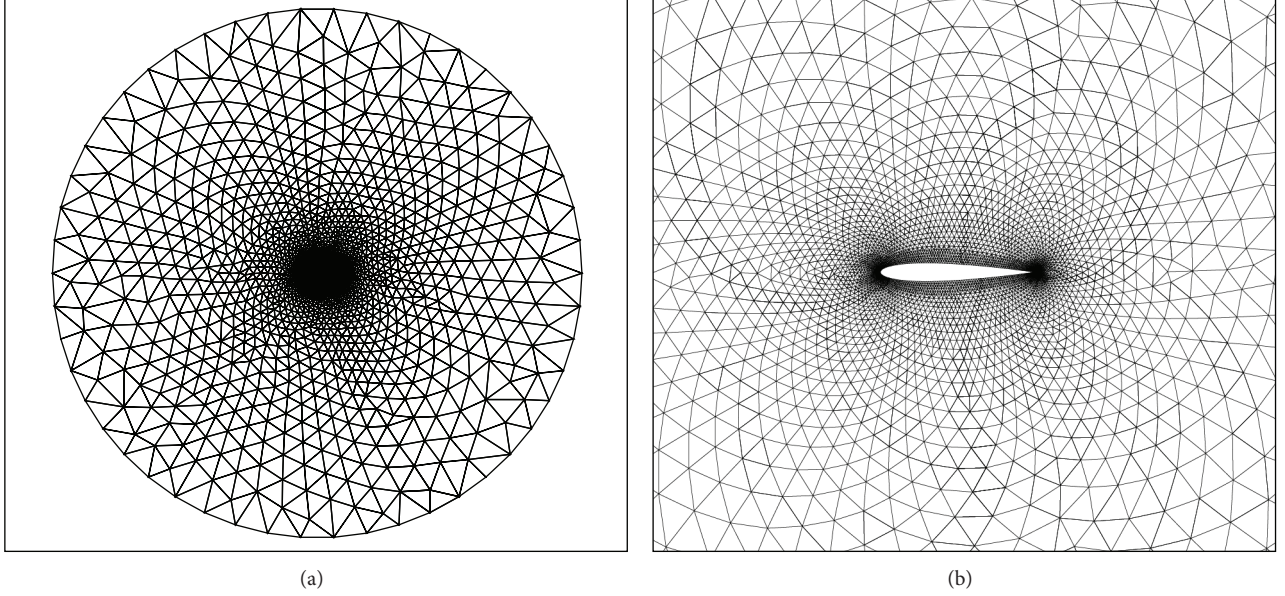


FIGURE 1: Mesh around NACA0012 airfoil: (a) whole and (b) close-up mesh near the airfoil.

where

$$\begin{aligned}
 |\tilde{\mathbf{A}}| (\mathbf{U}_R - \mathbf{U}_L) &= \begin{pmatrix} \alpha_4 \\ u\alpha_4 + n_x\alpha_5 + \alpha_6 \\ v\alpha_4 + n_y\alpha_5 + \alpha_7 \\ h\alpha_4 + \lambda'\alpha_5 + u\alpha_6 + v\alpha_7 - \frac{(c')^2}{\gamma-1}\alpha_1 \end{pmatrix}, \\
 \alpha_1 &= |\lambda'| \left(\Delta p - \frac{\Delta p}{(c')^2} \right), \quad \alpha_2 = \frac{|\lambda' + c'| (\Delta p + \rho c' \Delta \lambda')}{2(c')^2}, \\
 \alpha_3 &= \frac{|\lambda' - c'| (\Delta p - \rho c' \Delta \lambda')}{2(c')^2}, \quad \alpha_4 = \alpha_1 + \alpha_2 + \alpha_3, \\
 \alpha_5 &= c' (\alpha_2 - \alpha_3), \quad \alpha_6 = \rho |\lambda'| (\Delta u - n_x \Delta \lambda'), \\
 \alpha_7 &= \rho |\lambda'| (\Delta v - n_y \Delta \lambda'),
 \end{aligned} \quad (15)$$

λ' is the velocity normal to the interface, and c' is the speed of sound at the interface.

In this paper, Van Albada limiter [30] is employed to make the scheme monotone for 2D problems and Barth-Jespersen limiter [37] is used for 3D problems.

4. Time-Marching Schemes

In order to resolve the time-dependent problem, the semidiscrete system can be integrated in time in this paper. The implicit time-integration schemes have been widespread for

DG discretization. Iterative algorithms such as GMRES and CGS are often used to approximately solve the sparse linear equations due to the enormous computational cost and the large memory requirement of direct methods. Another implicit scheme, the LU-SGS scheme originally developed for structured grids, has been extended to unstructured and hybrid grids, which does not require any extra storage compared to explicit methods. The LU-SGS procedures are described as follows.

4.1. PCLU-SGS Scheme. In the original LU-SGS approach [29], (8) can be translated into the following system:

$$\mathbf{A} \Delta \mathbf{Q} = \mathbf{Res}^n, \quad (16)$$

where \mathbf{Res}^n represents residual term.

Then the coefficient matrix using the decomposition method can be written as $\mathbf{A} = \mathbf{D} + \mathbf{L} + \mathbf{U}$; we obtain

$$(\mathbf{D} + \mathbf{L}) \mathbf{D}^{-1} (\mathbf{D} + \mathbf{U}) \Delta \mathbf{Q}^n = \mathbf{Res}^n + (\mathbf{L} \mathbf{D}^{-1} \mathbf{U}) \Delta \mathbf{Q}^n, \quad (17)$$

where \mathbf{D} represents the diagonal matrix and \mathbf{L} and \mathbf{U} represent the lower and upper matrices. Ignoring the infinitesimal quantity $(\mathbf{L} \mathbf{D}^{-1} \mathbf{U}) \Delta \mathbf{Q}^n$, (17) is then solved using one sweep of symmetric Gauss-Seidel iteration as shown in the following:

forward sweep:

$$(\mathbf{D} + \mathbf{L}) \Delta \tilde{\mathbf{Q}} = \mathbf{Res}^n, \quad (18)$$

backward sweep:

$$\mathbf{D}^{-1} (\mathbf{D} + \mathbf{U}) \Delta \bar{\mathbf{Q}} = \Delta \tilde{\mathbf{Q}}. \quad (19)$$

While ignoring the higher-order infinitesimal quantity does not affect the accuracy of the method, increasing the truncation error will affect the rate of convergence. Therefore, we

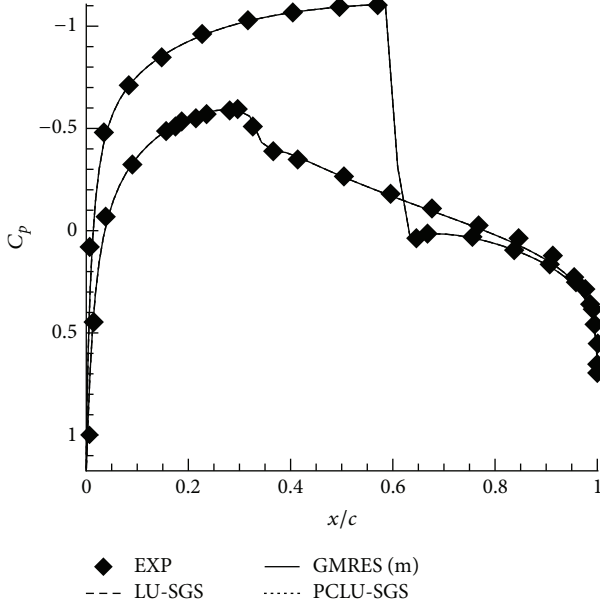


FIGURE 2: Pressure coefficient distribution with different time-marching format for transonic flow around NACA0012 airfoil ($p = 2$).

obtain the PCLU-SGS algorithm through the compensation of high-order term for the original LU-SGS scheme. The computational procedure is shown in detail as follows.

- (1) Use the original LU-SGS scheme to solve $\Delta \bar{\mathbf{Q}}$,

forward sweep and backward sweep:

$$(\mathbf{D} + \mathbf{L}) \Delta \bar{\mathbf{Q}} = \mathbf{Res}^n, \quad \mathbf{D}^{-1} (\mathbf{D} + \mathbf{U}) \Delta \bar{\mathbf{Q}} = \Delta \bar{\mathbf{Q}}. \quad (20)$$

- (2) Compute the high-order infinitesimal quantity $(\mathbf{LD}^{-1}\mathbf{U})\Delta \bar{\mathbf{Q}}^n$ using the value of $\Delta \bar{\mathbf{Q}}$ to correct the residual \mathbf{Res}^n .

- (3) Use the original LU-SGS scheme to compute $\Delta \mathbf{Q}$:

$$(\mathbf{D} + \mathbf{L}) \mathbf{D}^{-1} (\mathbf{D} + \mathbf{U}) \Delta \mathbf{Q}^n = \overline{\mathbf{Res}^n} = \mathbf{Res}^n + (\mathbf{LD}^{-1}\mathbf{U}) \Delta \bar{\mathbf{Q}}. \quad (21)$$

4.2. TVD Runge-Kutta Scheme. The explicit time-integration schemes have been widespread for DG discretization. The TVD Runge-Kutta scheme of Cockburn [10] for Euler equations can be expressed as follows.

- (1) Denote $\mathbf{u}_h^0 = P_{v_h}(\mathbf{u}_0)$, where P_{v_h} is the projection operator on L_2 .
- (2) For $n = 0, 1, \dots, N-1$, compute \mathbf{u}_h^{n+1} and denote $\mathbf{u}_h^0 = \mathbf{u}_h^n$, and,



FIGURE 3: Flood contours.

for $j = 1, \dots, p + 1$, compute the intermediate function, $\mathbf{u}_h^{(j)}$:

$$\mathbf{u}_h^{(j)} = \sum_{m=0}^{j-1} \alpha_{jm} \mathbf{u}_h^{(m)} + \beta_{jm} \Delta t^n \mathbf{M}^{-1} L_h(\mathbf{u}_h^{(m)}, \gamma_h(t^n + d_m \Delta t^n)). \quad (22)$$

- (3) Denote $\mathbf{u}_h^{n+1} = \mathbf{u}_h^{p+1}$.

The scheme is linearly stable for a Courant number less than or equal to $1/(2p + 1)$. In this paper, the RK4 scheme is employed to compute the Euler equations.

5. Numerical Experiments

5.1. Transonic Flow around NACA0012 Airfoil. Consider the calculation state $Ma_\infty = 0.8$ and 1.25° angle of attack. The pressure coefficient distribution using different time-marching schemes compared with the experiment results for transonic flow around NACA0012 airfoil is given in Figure 2. Good agreement can be seen in terms of the location and strength of shocks (see Figure 1). The flood contours are shown in Figure 3. From Figure 4 it can be seen that it takes only 1500 iterations to obtain the result by using the present algorithm, which are far fewer than the 4500 iterations required to obtain the same results by using the original LU-SGS method. The computational efficiency is close to that of GMRES algorithm and nearly 2.1 times greater than that of the LU-SGS one. Figure 5 shows that LLF solver similar to the HLL solver is more dissipate than both the HLLC flux function and the Roe flux function. Figure 6 shows the effects of convergence performance with different CFL number; it can be clearly seen that the results are almost the same when CFL number is greater than 100. The results of the test cases verify the effectiveness and the ability to capture discontinuous of PCLU-SGS DG method.

Furthermore, the Sod shock tube problem with the initial conditions is given as follows:

$$\mathbf{U} = \begin{cases} (\rho_L, u_L, p_L)^T = (1, 0, 1)^T, & \text{if } -5 \leq x \leq 0 \\ (\rho_R, u_R, p_R)^T = (0.125, 0, 0.1)^T, & \text{if } 0 \leq x \leq 5, \end{cases} \quad (23)$$

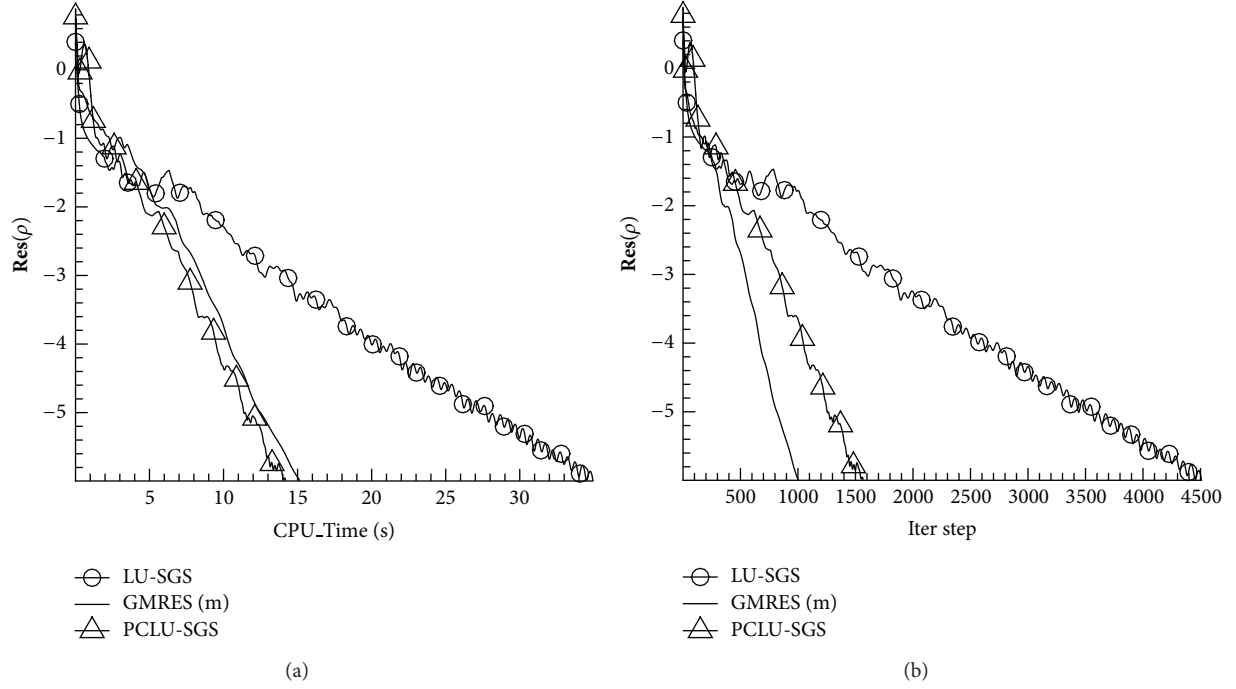


FIGURE 4: Convergence history for transonic flow around NACA0012 airfoil: (a) CPU-Time and (b) iteration number.

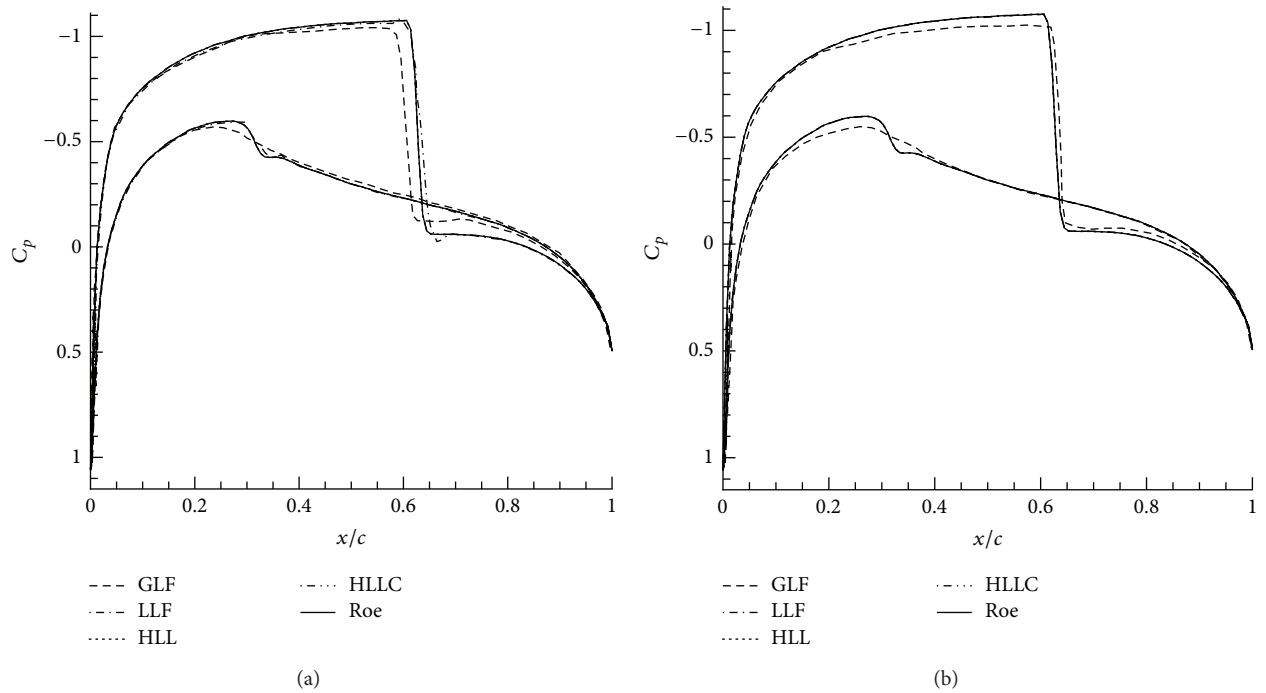


FIGURE 5: Pressure coefficient distribution with different numerical flux for transonic flow around NACA0012 airfoil: (a) $p = 2$ and (b) $p = 3$.

where $t = 2.0$, and the mesh consists of 100 elements in Figure 7.

Obviously, with the improvement of the accuracy, the method with HLLC flux resolves better contact discontinuity.

In the present paper, though the LLF flux function is more dissipate than both the HLLC flux function and the Roe flux function, it is more robust and more economical. Then we use it in the following examples.

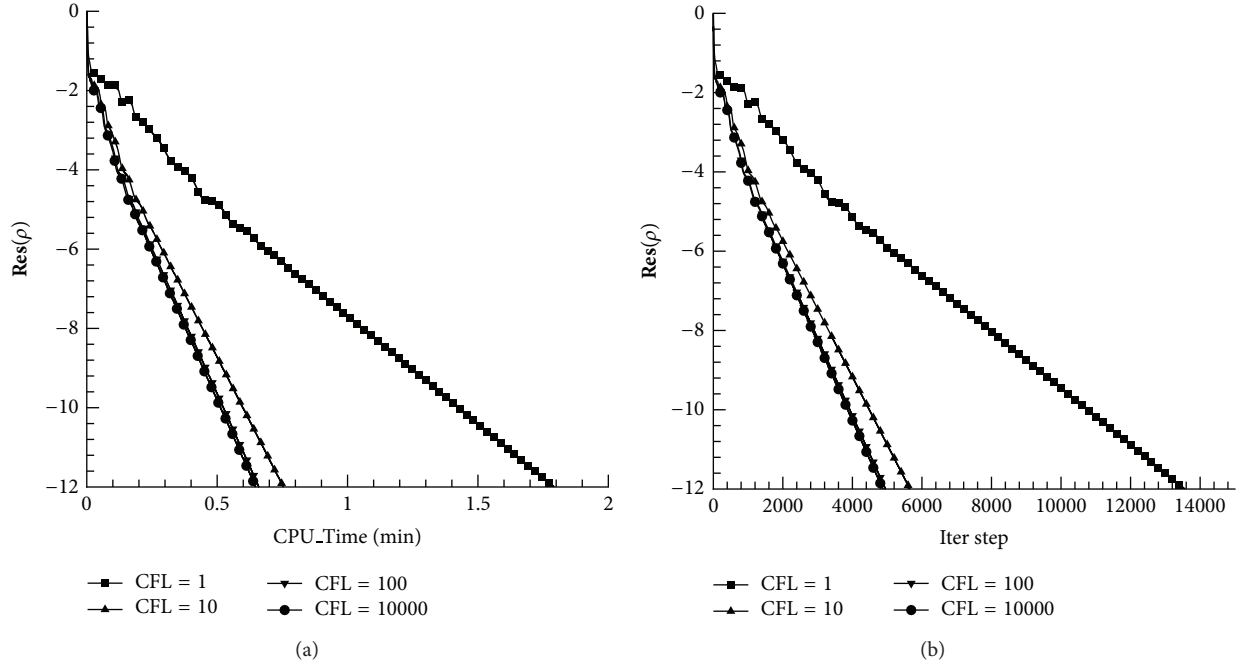


FIGURE 6: Convergence history with different CFL number for transonic flow around NACA0012 airfoil: (a) CPU-Time and (b) iteration number.

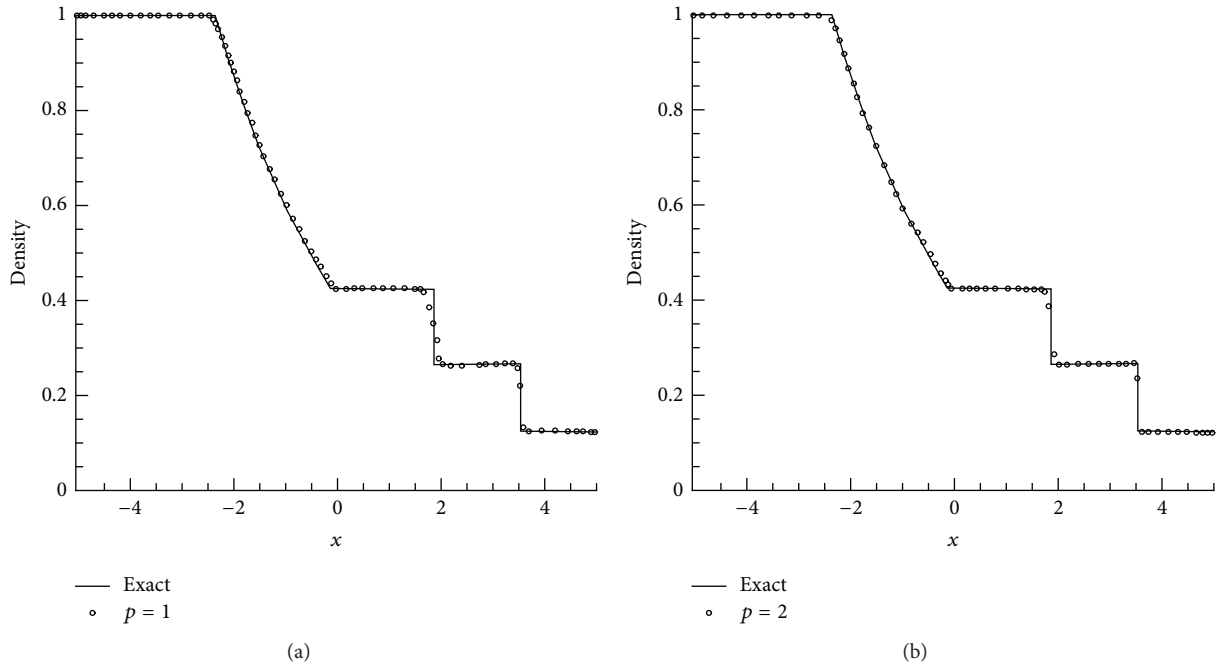


FIGURE 7: Density with HLLC flux for Sod shock tube problem: (a) $p = 1$ and (b) $p = 2$.

5.2. Transonic Flow around RAE2822 Airfoil. Consider the calculation state $Ma = 0.725$ and angle of attack $\alpha = 2.54^\circ$. The pressure coefficient distribution using different time-marching schemes for transonic flow around RAE2822 airfoil

is given in Figure 8. The numerical solutions demonstrate that it takes only 1200 iterations to obtain the result by using the present algorithm, which are far fewer than 4000 iterations required to obtain the same results by using the original

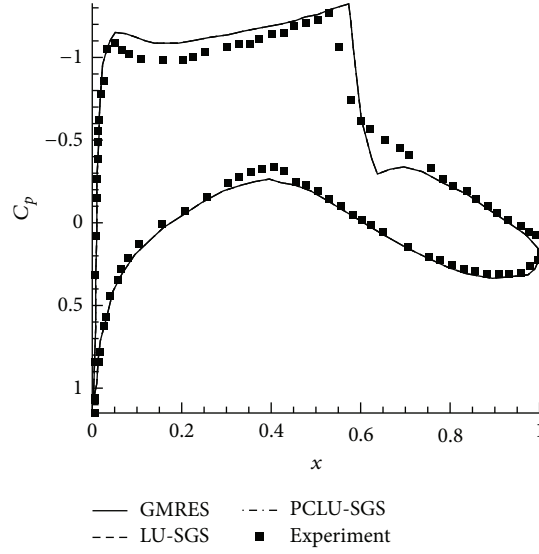


FIGURE 8: Pressure coefficient distribution with different time-marching format flow around RAE2822 airfoil ($p = 2$).

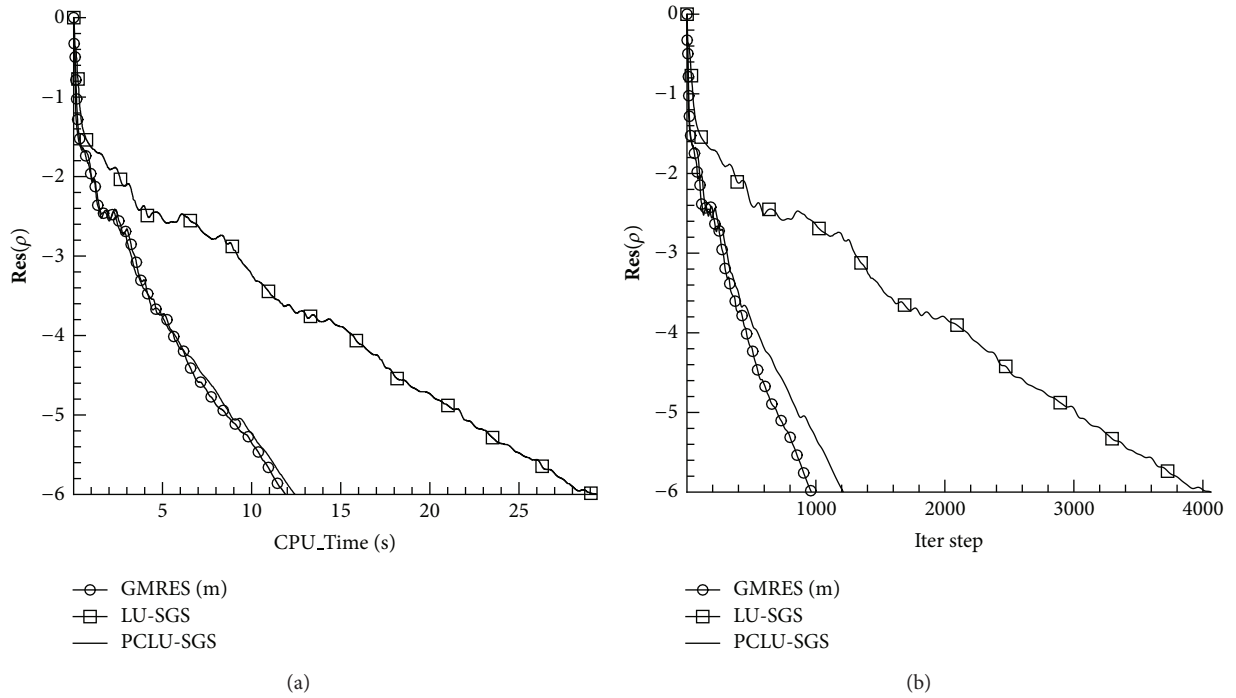


FIGURE 9: Convergence history with different time-marching format for transonic flow around RAE2822 airfoil: (a) CPU-Time and (b) iteration number.

LU-SGS method. And the results show that the convergence acceleration is nearly 2.3 times that of the original LU-SGS one from Figure 9.

5.3. Transonic Flow over ONERA M6 Wing. This case is about a transonic flow at Mach number $Ma = 0.84$ around the ONERA M6 wing with $\alpha = 3.06^\circ$ angle of attack. The unstructured mesh consists of 582752 triangles in Figure 10.

The surface pressure coefficient distribution with different spanwise location is given in Figure 12. From Figure 11 it can be seen that it takes only 5050 iterations to obtain the result by using the present algorithm, which are far fewer than 44021 iterations required to obtain the same results by using the RK4 method. The convergence acceleration is nearly 5.5 times that of the RK4 one and nearly half that of GMRES one. The convergence performance is similar to that in [38].

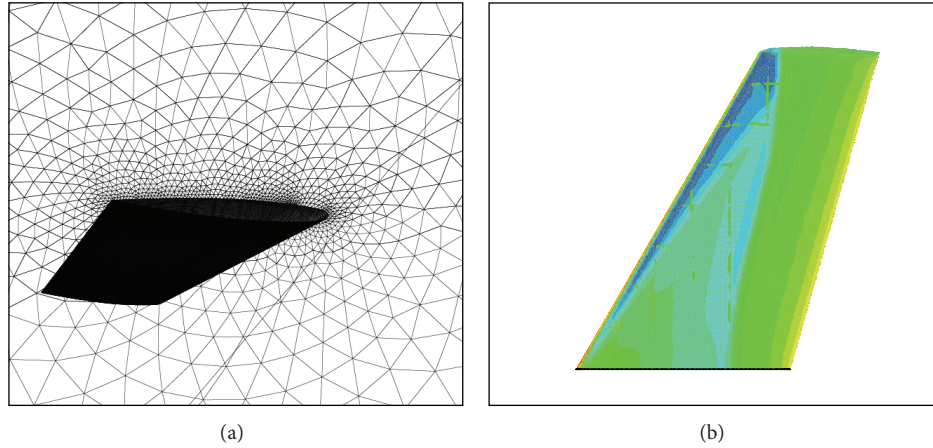


FIGURE 10: Surface mesh around ONERA M6 wing and flood contours: (a) surface mesh and (b) flood contours.

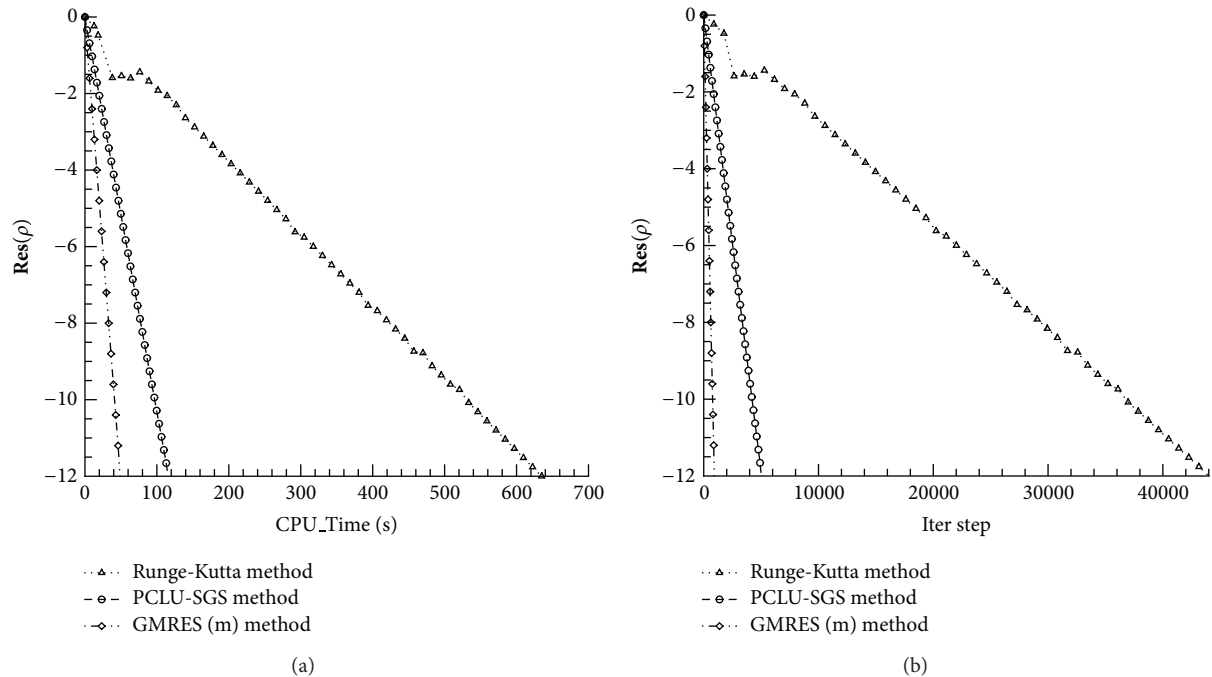


FIGURE 11: Convergence history with different time-marching format for transonic flow around ONERA M6 wing: (a) CPU-Time and (b) iteration number.

The results are not as good as those in the literature [39], because the shock detector is used, which directly affect the accuracy of solutions on smooth region. How to accurately judge problem units will be our future efforts.

6. Conclusion

An improved implicit time-marching scheme based on the original LU-SGS scheme is developed and applied for the discontinuous Galerkin method on unstructured grids. The developed new algorithm has been used to compute

the transonic flows around NACA0012 airfoil, RAE2822 airfoil, and ONERA M6 wing. The implicit PCLU-SGS scheme for the DG method on unstructured grids is significantly more efficient and robust than the original LU-SGS scheme. The convergence performance of the present scheme can compete with the GMRES scheme.

Conflict of Interests

The authors declare that there is no conflict of interests regarding the publication of this paper.

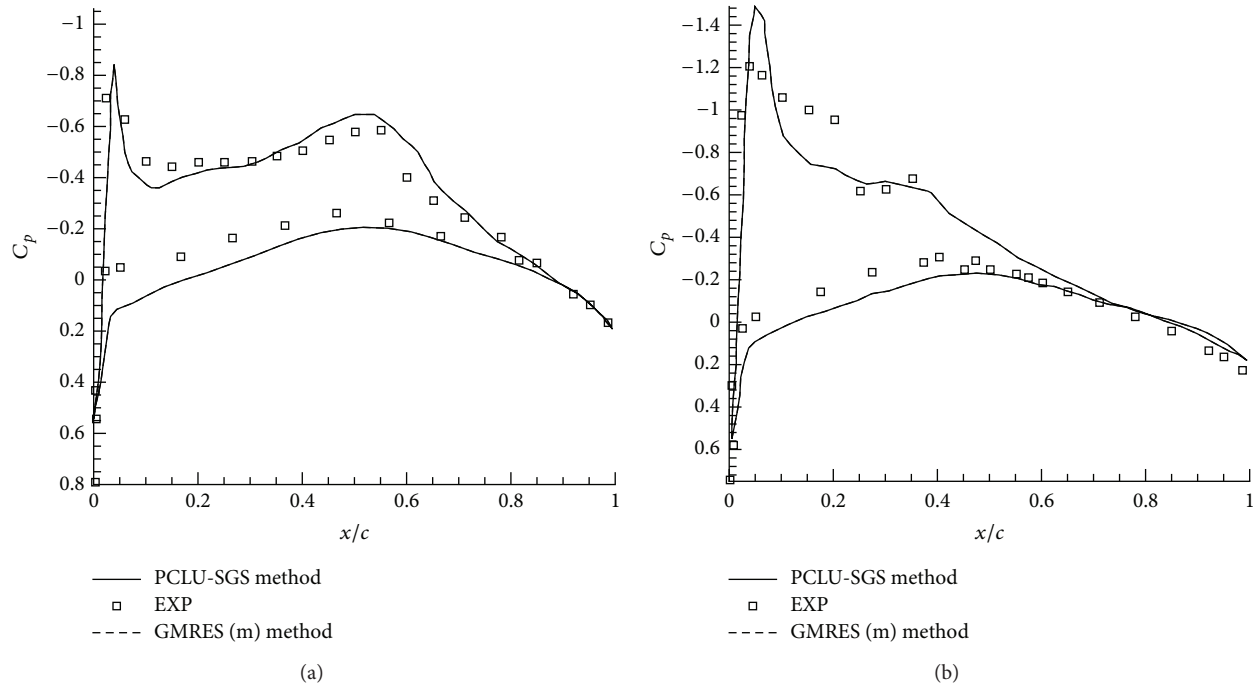


FIGURE 12: Surface pressure coefficient distribution with different spanwise location for transonic flow over ONERA M6 wing: (a) 20% and (b) 80% ($p = 1$).

Acknowledgments

This research was supported by the National Natural Science Funds of China under Grants nos. 11002117 and 61373174 and the Xianyang Normal University Research Funds under Grants nos. 09XSYK209 and 09XSYK204.

References

- [1] W. H. Reed and T. R. Hill, "Triangular mesh methods for the neutron transport equation," Tech. Rep. LA-UR-73-479, Los Alamos Scientific Laboratory, 1973.
- [2] Y. Saad and M. H. Schultz, "GMRES: a generalized minimal residual algorithm for solving nonsymmetric linear systems," *Society for Industrial and Applied Mathematics: Journal on Scientific and Statistical Computing*, vol. 7, no. 3, pp. 856–869, 1986.
- [3] Y. Xia and H. Luo, "An implicit method for a reconstructed discontinuous Galerkin method on tetrahedron grids," in *Proceedings of the 42nd AIAA Fluid Dynamics Conference and Exhibit*, pp. 2012–2834, AIAA, New Orleans, La, USA, June 2012.
- [4] Y. Xia and H. Luo, "An implicit reconstructed discontinuous Galerkin method based on automatic differentiation for the compressible flows on tetrahedral grids," in *Proceedings of the 51st AIAA Aerospace Sciences Meeting including the New Horizons Forum and Aerospace Exposition*, Grapevine, Tex, USA, January 2013.
- [5] V. Dolejsi and M. Feistauer, "A semi-implicit discontinuous Galerkin finite element method for the numerical solution of inviscid compressible flow," *Journal of Computational Physics*, vol. 198, no. 2, pp. 727–746, 2004.
- [6] P. Rasetarinera and M. Y. Hussaini, "An efficient implicit discontinuous spectral Galerkin method," *Journal of Computational Physics*, vol. 172, no. 2, pp. 718–738, 2001.
- [7] B. Cockburn and C.-W. Shu, "TVB Runge-Kutta local projection discontinuous Galerkin finite element method for conservation laws. II. GENERAL framework," *Mathematics of Computation*, vol. 52, no. 186, pp. 411–435, 1989.
- [8] B. Cockburn, S. Y. Lin, and C.-W. Shu, "TVB Runge-Kutta local projection discontinuous Galerkin finite element method for conservation laws III: one-dimensional systems," *Journal of Computational Physics*, vol. 84, no. 1, pp. 90–113, 1989.
- [9] B. Cockburn, S. Hou, and C.-W. Shu, "The Runge-Kutta local projection discontinuous Galerkin finite element method for conservation laws. IV. The multidimensional case," *Mathematics of Computation*, vol. 54, no. 190, pp. 545–581, 1990.
- [10] B. Cockburn and C.-W. Shu, "The Runge-Kutta discontinuous Galerkin method for conservation laws V: multidimensional systems," *Journal of Computational Physics*, vol. 141, no. 2, pp. 199–224, 1998.
- [11] B. Cockburn, "Devising discontinuous Galerkin methods for non-linear hyperbolic conservation laws," *Journal of Computational and Applied Mathematics*, vol. 128, no. 1-2, pp. 187–204, 2001.
- [12] B. Cockburn and C.-W. Shu, "Runge-Kutta discontinuous Galerkin methods for convection-dominated problems," *Journal of Scientific Computing*, vol. 16, no. 3, pp. 173–261, 2001.
- [13] H. Luo, J. D. Baum, and R. Löhner, "A p -multigrid discontinuous Galerkin method for the Euler equations on unstructured grids," *Journal of Computational Physics*, vol. 211, no. 2, pp. 767–783, 2006.
- [14] F. Bassi and S. Rebay, "GMRES discontinuous Galerkin solution of the compressible Navier-Stokes equations," in *Discontinuous*

- Galerkin Methods*, vol. 11, pp. 197–208, Springer, Berlin, Germany, 2000.
- [15] J. S. Hesthaven and T. Warburton, *Nodal Discontinuous Galerkin Methods: Algorithms, Analysis, and Applications*, Springer, New York, NY, USA, 2007.
 - [16] B. T. Helenbrook, D. Mavriplis, and H. L. Atkins, “Analysis of p -multigrid for continuous and discontinuous finite element discretizations,” *AIAA Paper* 3989, 2003.
 - [17] K. J. Fidkowski, T. A. Oliver, J. Lu, and D. L. Darmofal, “ p -Multigrid solution of high-order discontinuous Galerkin discretizations of the compressible Navier-Stokes equations,” *Journal of Computational Physics*, vol. 207, no. 1, pp. 92–113, 2005.
 - [18] H. Luo, J. D. Baum, and R. Löhner, “Fast p -multigrid discontinuous Galerkin method for compressible flows at all speeds,” *AIAA Journal*, vol. 46, no. 3, pp. 635–652, 2008.
 - [19] F. Bassi, A. Crivellini, S. Rebay, and M. Savini, “Discontinuous Galerkin solution of the Reynolds-averaged Navier-Stokes and k - ω turbulence model equations,” *Computers & Fluids*, vol. 34, no. 4-5, pp. 507–540, 2005.
 - [20] F. Li and C.-W. Shu, “Locally divergence-free discontinuous Galerkin methods for MHD equations,” *Journal of Scientific Computing*, vol. 22-23, pp. 413–442, 2005.
 - [21] S. Vukovic and L. Sopta, “ENO and WENO schemes with the exact conservation property for one-dimensional shallow water equations,” *Journal of Computational Physics*, vol. 179, no. 2, pp. 593–621, 2002.
 - [22] A. Taube, M. Dumbser, D. S. Balsara, and C.-D. Munz, “Arbitrary high-order discontinuous Galerkin schemes for the magnetohydrodynamic equations,” *Journal of Scientific Computing*, vol. 30, no. 3, pp. 441–464, 2007.
 - [23] J. Loverich and U. Shumlak, “A discontinuous Galerkin method for the full two-fluid plasma model,” *Computer Physics Communications*, vol. 169, no. 1-3, pp. 251–255, 2005.
 - [24] I. Touloupoulos and J. A. Ekaterinaris, “High-order discontinuous Galerkin discretizations for computational aeroacoustics in complex domains,” *AIAA Journal*, vol. 44, no. 3, pp. 502–511, 2006.
 - [25] V. Aizinger and C. Dawson, “The local discontinuous Galerkin method for three-dimensional shallow water flow,” *Computer Methods in Applied Mechanics and Engineering*, vol. 196, no. 4-6, pp. 734–746, 2007.
 - [26] H. Bijl, M. H. Carpenter, V. N. Vatsa, and C. A. Kennedy, “Implicit time integration schemes for the unsteady compressible Navier-Stokes equations: laminar flow,” *Journal of Computational Physics*, vol. 179, no. 1, pp. 313–329, 2002.
 - [27] L. Fezoui and B. Stoufflet, “A class of implicit upwind schemes for Euler simulations with unstructured meshes,” *Journal of Computational Physics*, vol. 84, no. 1, pp. 174–206, 1989.
 - [28] D. E. Keyes, “Aerodynamic applications of Newton-Krylov-Schwarz solvers,” in *Proceedings of the 14th International Conference on Numerical Methods in Fluid Dynamics*, pp. 1–20, Springer, Berlin, Germany, 1995.
 - [29] A. Jameson and S. Yoon, “Lower-upper implicit schemes with multiple grids for the Euler equations,” *AIAA Journal*, vol. 25, no. 7, pp. 929–935, 1987.
 - [30] P. Jawahar and H. Kamath, “A high-resolution procedure for Euler and Navier-Stokes computations on unstructured grids,” *Journal of Computational Physics*, vol. 164, no. 1, pp. 165–203, 2000.
 - [31] D. A. Dunavant, “Economical symmetrical quadrature rules for complete polynomials over a square domain,” *International Journal for Numerical Methods in Engineering*, vol. 21, no. 10, pp. 1777–1784, 1985.
 - [32] D. A. Dunavant, “High degree efficient symmetrical Gaussian quadrature rules for the triangle,” *International Journal for Numerical Methods in Engineering*, vol. 21, no. 6, pp. 1129–1148, 1985.
 - [33] E. F. Toro, *Riemann Solvers and Numerical Methods for Fluid Dynamics*, Springer, New York, NY, USA, 1999.
 - [34] P. Batten, N. Clarke, C. Lambert, and D. M. Causon, “On the choice of wavespeeds for the HLLC Riemann solver,” *SIAM Journal on Scientific Computing*, vol. 18, no. 6, pp. 1553–1570, 1997.
 - [35] G. Toth and D. Odstrcil, “Comparison of some flux corrected transport and total variation diminishing numerical schemes for hydrodynamic and magnetohydrodynamic problems,” *Journal of Computational Physics*, vol. 128, no. 1, pp. 82–100, 1996.
 - [36] P. L. Roe, “Approximate Riemann solvers, parameter vectors, and difference schemes,” *Journal of Computational Physics*, vol. 43, no. 2, pp. 357–372, 1981.
 - [37] L. Krivodonova, J. Xin, J.-F. Remacle, N. Chevaugeon, and J. E. Flaherty, “Shock detection and limiting with discontinuous Galerkin methods for hyperbolic conservation laws,” *Applied Numerical Mathematics*, vol. 48, no. 3-4, pp. 323–338, 2004.
 - [38] H. Luo, J. D. Baum, and R. Löhner, “A fast, matrix-free implicit method for compressible flows on unstructured grids,” *Journal of Computational Physics*, vol. 146, no. 2, pp. 664–690, 1998.
 - [39] H. Luo, Y. Xia, S. Spiegel, R. Nourgaliev, and Z. Jiang, “A reconstructed discontinuous Galerkin method based on a hierarchical WENO reconstruction for compressible flows on tetrahedral grids,” *Journal of Computational Physics*, vol. 236, pp. 477–492, 2013.

Research Article

A Reconstruction Procedure Associated with Switching Lyapunov Function for Relaxing Stability Assurance of T-S Fuzzy Mode

Yau-Tarng Juang,¹ Chih-Peng Huang,² and Chung-Lin Yan¹

¹ Department of Electrical Engineering, National Central University, Jhongli City, Taoyuan County 320, Taiwan

² Department of Computer Science, University of Taipei, Taipei 100, Taiwan

Correspondence should be addressed to Chih-Peng Huang; ponytony@seed.net.tw

Received 1 August 2014; Accepted 27 September 2014

Academic Editor: Junuthula N. Reddy

Copyright © 2015 Yau-Tarng Juang et al. This is an open access article distributed under the Creative Commons Attribution License, which permits unrestricted use, distribution, and reproduction in any medium, provided the original work is properly cited.

This paper proposes a novel reconstruction procedure to lessen the conservatism of stability assurance of T-S Fuzzy Mode. By dividing the state variables into some bounded regions, the considered T-S fuzzy model can be first transferred to an alternative form via a reconstructing procedure. Thus, we can attain some relaxing stability criteria based on the switching quadratic Lyapunov function (SQLF) method. Notably, these proposed conditions are explicitly formulated by linear matrix inequality (LMI) form and can handily be evaluated by current software tools. Finally some illustrative examples are given to experimentally demonstrate the validity and merit of the proposed method.

1. Introduction

A class of empirical control architecture, fuzzy logic control (FLC), is originally proposed in the past two decades [1]. And, it then has become one of the most active and fruitful areas in this research community. Many researchers have dedicated a lot of time and great effort to both theoretical research and implementation techniques for FLC. The basic idea behind FLC is to incorporate the “expert experience” of a human operator into a system. Notably, a complicated dynamic model is not necessary any more. However, model-free type of fuzzy control is useful and practical, but this control technique is insufficient of mathematical support. In order to systematically analyze the stability of the fuzzy system, Takagi-Sugeno (T-S) fuzzy model [2, 3] was presented to open a different viewpoint from the traditional fuzzy system. Based on the T-S fuzzy model, a complicated system can be represented as a set of fuzzy IF-THEN rules, each of which represents the local linear subsystem in a different state-space region. By the fuzzy blending operating, they thus can approximately represent some uncertain or/and nonlinear systems [4–8].

The stability issues of T-S fuzzy model were first analyzed by Tanaka and Sugeno [3]. Based on Lyapunov direct method, they presented some sufficient conditions that could systematically achieve the stability analysis and stabilization of fuzzy systems [9, 10]. Moreover, the stability conditions could be cast into linear matrix inequality (LMI) forms [1, 10–13]. For earlier research, most works are devoted to common quadratic Lyapunov function (CQLF) methods. Thus, the proposed criteria require finding a common positive definite matrix \mathbf{P} of a CQLF to satisfy all the subsystems [3, 14–19]. But, if the number of fuzzy rules is large, a common matrix \mathbf{P} may hardly be obtained or does not exist in all the subsystems. Instead of CQLF, a switching quadratic Lyapunov function (SQLF) was involved [20–24]. This SQLF method beforehand divides the state space into several regions, and, in each region we can try to find the individual positive-definite matrix \mathbf{P}_i for the SQLF. Furthermore, we need to guarantee the SQLF $V_i(\mathbf{x}(t))$ be the same in the region boundary but did not expect that all \mathbf{P}_i are equal. In previous works, the stability criteria need to involve bilinear matrix inequality (BMI) conditions, which cannot be directly evaluated by traditional LMI solver [25].

In this work, based on SQLF method, we devote the stability criteria of T-S fuzzy model to the relaxing. Firstly, we use a distinct region-division approach for the state space. When assuming that the state variables of the considered T-S fuzzy model can be correspondingly formulated by single membership function at the region boundary, we thus propose a reconstructing procedure for substituting. Thus, based on the SQLF method, more relaxed stability criteria can be derived and expressed by LMI manner. Finally, an illustrative example is given to verify the efficiency and superiority of the proposed method.

2. Problem Description and Preliminaries

T-S fuzzy model can approximately represent some intractable systems with parametric uncertainty or nonlinearity via the fuzzy IF-THEN rules interpretation. This mode mainly characterizes the local dynamics behaviors of a system by the fuzzy rules where their consequent parts are represented by some locally linear models. Thus, an overall system can be achieved via the fuzzy “blending” for these linear models. The r rules of a T-S fuzzy model are expressed as follows:

Model Rule i —(MR _{i}):

IF $x_1(t)$ is M_{i1} and $x_2(t)$ is $M_{i2} \cdots$ and $x_n(t)$ is M_{in} ,

$$\text{THEN } \dot{\mathbf{x}}(t) = \mathbf{A}_i \mathbf{x}(t) \quad i = 1, 2, \dots, r, \quad (1)$$

where MR _{i} denotes the model rule i ; M_{ij} denotes the fuzzy set corresponding to the state variable $x_j(t)$ of MR _{i} ; r is the number of IF-THEN fuzzy model rules; $\mathbf{x}(t) = [x_1(t) \ x_2(t) \ \cdots \ x_n(t)]^T \in \mathcal{R}^n$ is the state vector; $\mathbf{A}_i \in \mathcal{R}^{n \times n}$ denotes the system matrix of the subsystem.

The T-S fuzzy model in (1) is assumed to be inferred by center average defuzzification (CAD) and can be described by

$$\dot{\mathbf{x}}(t) = \frac{\sum_{i=1}^r w_i(\mathbf{x}(t)) \mathbf{A}_i \mathbf{x}(t)}{\sum_{i=1}^r w_i(\mathbf{x}(t))} = \sum_{i=1}^r h_i(\mathbf{x}(t)) \mathbf{A}_i \mathbf{x}(t), \quad (2)$$

where

$$w_i(\mathbf{x}(t)) = \prod_{j=1}^n M_{ij}(x_j(t)), \quad (3)$$

$$\sum_{i=1}^r w_i(\mathbf{x}(t)) > 0, \quad w_i(\mathbf{x}(t)) \geq 0, \quad i = 1, 2, \dots, r.$$

$M_{ij}(x_j(t))$ is the grade of membership of $x_j(t)$ in membership function M_{ij} . And, the inferred grade function is normalized as

$$h_i(\mathbf{x}(t)) = \frac{w_i(\mathbf{x}(t))}{\sum_{i=1}^r w_i(\mathbf{x}(t))}, \quad (4)$$

$$\sum_{i=1}^r h_i(\mathbf{x}(t)) = 1, \quad h_i(\mathbf{x}(t)) \geq 0, \quad i = 1, 2, \dots, r.$$

Based on Lyapunov stability theory, a candidate Lyapunov function with a constant matrix P is given by

$$V(\mathbf{x}(t)) = \mathbf{x}^T(t) \mathbf{P} \mathbf{x}(t) \quad (5)$$

with $P > 0$. Thus, for stability assurance, the chosen Lyapunov function needs to satisfy the following four conditions:

- (1) V is C^1 ,
- (2) $\mathbf{x}(t) = \mathbf{0} \Leftrightarrow V(\mathbf{x}(t)) = 0$,
- (3) $\mathbf{x}(t) \neq \mathbf{0} \Leftrightarrow V(\mathbf{x}(t)) > 0$,
- (4) $\|\mathbf{x}(t)\| \rightarrow \infty \Rightarrow V(\mathbf{x}(t)) \rightarrow \infty$,

where C^1 is the set of all real-valued functions that have a continuous first derivative on $(-\infty, \infty)$ and $\|\cdot\|$ denotes the Euclidean norm for the considered vectors.

Based on (5), Tanaka and Sugeno [3] originally proposed a stability criterion as follows.

Lemma 1 (see [3]). *The equilibrium of the autonomous T-S fuzzy system in (2) is asymptotically stable in the large, if there exists a common positive-definite symmetric matrix P such that*

$$\mathbf{A}_i^T \mathbf{P} + \mathbf{P} \mathbf{A}_i < \mathbf{0}, \quad i = 1, 2, \dots, r. \quad (6)$$

Remark 2. Lemma 1 shows that we need to find a common matrix P to satisfy all the conditions in (6) for global stability assurance. Based on Lemma 1, some less conservative results [12, 16] with a common positive-definite symmetric matrix P were achieved by involving some extra slack matrices in criteria.

3. Switching T-S Fuzzy Model and Stability Issues

3.1. Switching T-S Fuzzy Model. Consider

Region Model Rule q —(RMR _{q}):

IF $\mathbf{x}(t) \in \text{Region } q$

THEN

Local Model Rule i —(LMR _{i}):

IF $x_1(t)$ is M_{qi1} and $x_2(t)$ is $M_{qi2} \cdots$ and $x_n(t)$ is M_{qin} ,

THEN $\dot{\mathbf{x}}(t) = \mathbf{A}_{qi} \mathbf{x}(t) + \mathbf{B}_{qi} \mathbf{u}(t)$

$$i = 1, 2, \dots, r_q, \quad q = 1, 2, \dots, 2^n, \quad (7)$$

where RMR _{q} denotes the region model rule q . LMR _{i} denotes the local model rule i . M_{qij} denotes the fuzzy set corresponding to the state variable $x_j(t)$ of LMR _{i} in Region q . r_q is the number of IF-THEN fuzzy local model rules in Region q . 2^n is the number of region. n is the number of state variables. $r = \sum_{q=1}^{2^n} r_q$ is the total number of IF-THEN fuzzy model rules. $\mathbf{A}_{qi} \in \mathcal{R}^{n \times n}$ denotes the system matrix of the subsystem. $\mathbf{B}_{qi} \in \mathcal{R}^{n \times m}$ denotes the input matrix of the subsystem.

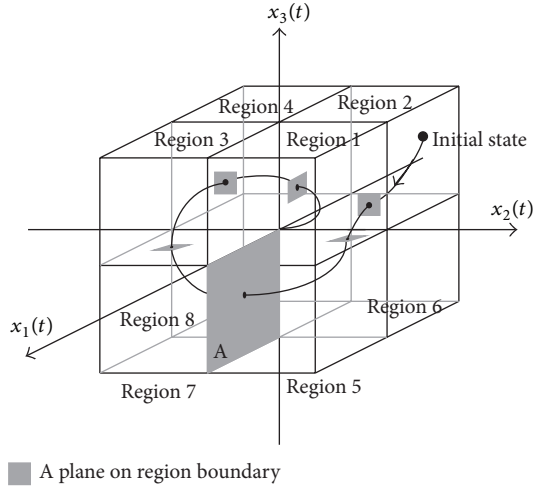


FIGURE 1: Divided state space and change of state.

Each linear consequent equation, $\mathbf{A}_{qi}\mathbf{x}(t) + \mathbf{B}_{qi}\mathbf{u}(t)$, is called a subsystem.

Given a pair of $(\mathbf{x}(t), \mathbf{u}(t))$, the final output of the T-S fuzzy model (7) is inferred by CAD and can be represented as follows [23]:

$$\dot{\mathbf{x}}(t) = \sum_{q=1}^{2^n} \sum_{i=1}^{r_q} \eta_q(\mathbf{x}(t)) h_{qi}(\mathbf{x}(t)) \{ \mathbf{A}_{qi}\mathbf{x}(t) + \mathbf{B}_{qi}\mathbf{u}(t) \}, \quad (8)$$

where

$$\eta_q(\mathbf{x}(t)) = \begin{cases} 1, & \mathbf{x}(t) \in R_q \\ 0, & \mathbf{x}(t) \notin R_q. \end{cases} \quad (9)$$

$h_{qi}(\mathbf{x}(t))$ is the normalized membership function of the LMR_i in Region q and satisfies

$$\begin{aligned} \sum_{q=1}^{2^n} \sum_{i=1}^{r_q} \eta_q(\mathbf{x}(t)) h_{qi}(\mathbf{x}(t)) &= 1, \\ \sum_{q=1}^{2^n} \sum_{i=1}^{r_q} \eta_q(\mathbf{x}(t)) h_{qi}(\mathbf{x}(t)) &\geq 0, \end{aligned} \quad (10)$$

$$i = 1, 2, \dots, r_q.$$

In the q th region, we define

$$\begin{aligned} R_q(s_{1q}, s_{2q}, \dots, s_{nq}) \\ s_{kq} = \begin{cases} 1, & x_k(t) \geq 0 \\ 0, & x_k(t) < 0 \end{cases} \quad k = 1, 2, \dots, n, \end{aligned} \quad (11)$$

where the number of the state variables is equal to n and its corresponding state space can be divided into 2^n region. For clarification, assume that the considered state space has three dimensions and each separated region corresponds to a quadrant. Figure 1 depicts that the trajectory of a given initial state passes over the different quadrants in a three-dimensional

space. The state in Figure 1 passes through Region 2, Region 1, Region 5, Region 7, Region 3, Region 4, and Region 2 in turn. To guarantee the stability of T-S fuzzy system, we suppose that the trajectory of a system cannot be motionless on the region boundaries.

3.2. Switching Quadratic Lyapunov Function. Consider

$$V(\mathbf{x}(t)) = \begin{cases} \mathbf{x}^T(t) \mathbf{P}_1 \mathbf{x}(t), & \mathbf{x}(t) \in \text{Region 1} \\ \mathbf{x}^T(t) \mathbf{P}_2 \mathbf{x}(t), & \mathbf{x}(t) \in \text{Region 2} \\ \vdots & \vdots \\ \mathbf{x}^T(t) \mathbf{P}_{2^n} \mathbf{x}(t), & \mathbf{x}(t) \in \text{Region } 2^n, \end{cases} \quad (12)$$

where $\mathbf{P}_q \in \mathfrak{R}^{n \times n} \forall q$ are a set of positive-definite symmetric matrices. This function is continuous on region boundaries if \mathbf{P}_q satisfies the following constraint [23]:

$$\mathbf{P}_q = \begin{bmatrix} p_{11\zeta(1,q)} & p_{12\psi(1,2,q)} & \cdots & p_{1m\psi(1,n,q)} \\ p_{12\psi(1,2,q)} & p_{22\zeta(2,q)} & \cdots & p_{2m\psi(2,n,q)} \\ \vdots & \vdots & \ddots & \vdots \\ p_{1m\psi(1,n,q)} & p_{2m\psi(2,n,q)} & \cdots & p_{mm\zeta(n,q)} \end{bmatrix}, \quad (13)$$

$$\zeta(k, q) = 2 - s_{kq}, \quad \psi(k, l, q) = -s_{kq} - 2s_{lq} + 4.$$

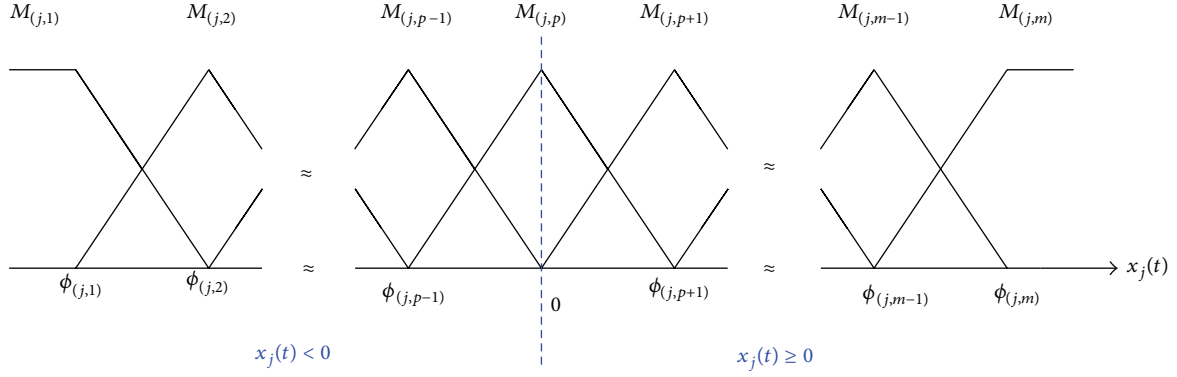
Since the involved property is crucial for discussing the SQLF, an example is illustrated as follows.

Example 3 (see [23]). As in Figure 1, consider a system with three state variables $x_1(t)$, $x_2(t)$, and $x_3(t)$. The state space can be divided into the following eight regions, eight quadrants:

$$\begin{aligned} R_1(1, 1, 1), \quad R_2(0, 1, 1), \quad R_3(1, 0, 1), \\ R_4(0, 0, 1); \quad R_5(1, 1, 0), \quad R_6(0, 1, 0), \\ R_7(1, 0, 0), \quad R_8(0, 0, 0). \end{aligned} \quad (14)$$

Based on the notation of a region, that is, $R_q(s_{1q}, s_{2q}, \dots, s_{nq})$, each \mathbf{P}_q is represented as follows:

$$\begin{aligned} P_1 &= \begin{bmatrix} p_{111} & p_{121} & p_{131} \\ p_{121} & p_{221} & p_{231} \\ p_{131} & p_{231} & p_{331} \end{bmatrix}, & P_2 &= \begin{bmatrix} p_{112} & p_{122} & p_{132} \\ p_{122} & p_{221} & p_{231} \\ p_{132} & p_{231} & p_{331} \end{bmatrix}, \\ P_3 &= \begin{bmatrix} p_{111} & p_{123} & p_{131} \\ p_{123} & p_{222} & p_{232} \\ p_{131} & p_{232} & p_{331} \end{bmatrix}, & P_4 &= \begin{bmatrix} p_{112} & p_{124} & p_{132} \\ p_{124} & p_{222} & p_{232} \\ p_{132} & p_{232} & p_{331} \end{bmatrix}, \\ P_5 &= \begin{bmatrix} p_{111} & p_{121} & p_{133} \\ p_{121} & p_{221} & p_{233} \\ p_{133} & p_{233} & p_{332} \end{bmatrix}, & P_6 &= \begin{bmatrix} p_{112} & p_{122} & p_{134} \\ p_{122} & p_{221} & p_{233} \\ p_{134} & p_{233} & p_{332} \end{bmatrix}, \\ P_7 &= \begin{bmatrix} p_{111} & p_{123} & p_{133} \\ p_{123} & p_{222} & p_{234} \\ p_{133} & p_{234} & p_{332} \end{bmatrix}, & P_8 &= \begin{bmatrix} p_{112} & p_{124} & p_{134} \\ p_{124} & p_{222} & p_{234} \\ p_{134} & p_{234} & p_{332} \end{bmatrix}. \end{aligned} \quad (15)$$

FIGURE 2: State variable $x_j(t)$ triggers one fuzzy set at $x_j(t) = 0$.

On the region boundary between Regions 5 and Regions 7, a plane A in Figure 1 for $\mathbf{x}(t) = [x_1(t) \ 0 \ x_3(t)]^T$, the SQLF is calculated as

$$\begin{aligned}
 V(\mathbf{x}(t)) &= \mathbf{x}^T(t) P_5 \mathbf{x}(t) \\
 &= [x_1(t) \ 0 \ x_3(t)] \begin{bmatrix} p_{111} & p_{121} & p_{133} \\ p_{121} & p_{221} & p_{233} \\ p_{133} & p_{233} & p_{332} \end{bmatrix} \begin{bmatrix} x_1(t) \\ 0 \\ x_3(t) \end{bmatrix} \\
 &= p_{111}x_1^2(t) + 2p_{133}x_1(t)x_3(t) + p_{332}x_3^2(t) \\
 &= [x_1(t) \ 0 \ x_3(t)] \begin{bmatrix} p_{111} & p_{123} & p_{133} \\ p_{123} & p_{222} & p_{234} \\ p_{133} & p_{234} & p_{332} \end{bmatrix} \begin{bmatrix} x_1(t) \\ 0 \\ x_3(t) \end{bmatrix} \\
 &= \mathbf{x}^T(t) P_7 \mathbf{x}(t).
 \end{aligned} \tag{16}$$

Furthermore, the illustrative results can be similarly extended to the other region boundaries of $\mathbf{x}(t)$.

Remark 4. Based on the SQLF, (13), we have shown that the state trajectory crossed a plane; that is, $\mathbf{x}(t) = [x_1(t) \ 0 \ x_3(t)]^T$ is continuous. In addition, it is also continuous when the trajectory crosses a line, such as $\mathbf{x}(t) = [0 \ x_2(t) \ 0]^T$ [23].

4. Main Result

Considering in general fuzzy inference rules, a single state variable triggers no more than two fuzzy sets. Thus, fuzzy sets for a premise variable $x_j(t)$ can be assumed to have two different patterns, defined in Figures 2 and 3, respectively, where their differences are at $x_j(t) = 0$ including single membership function or two membership functions.

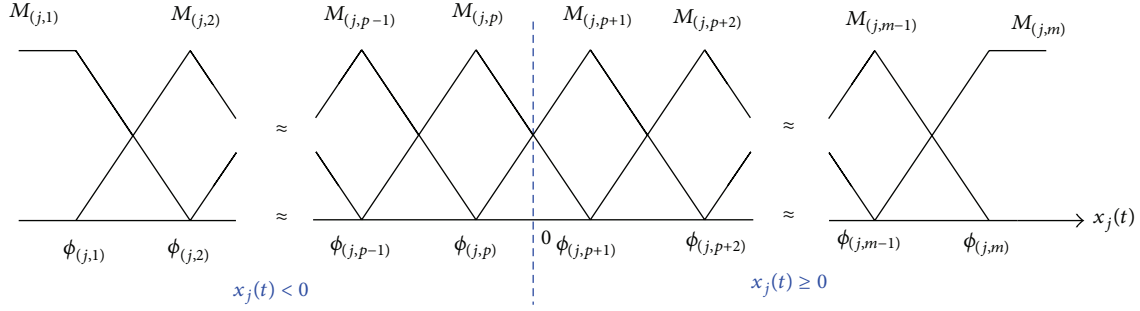
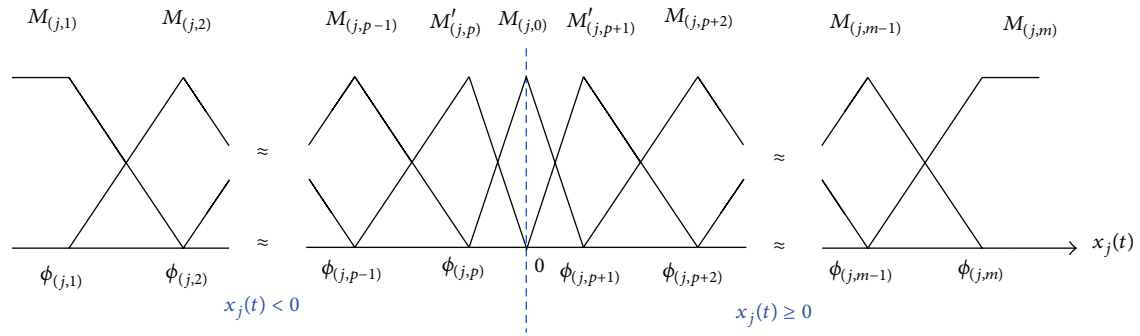
For generalization and unification, our proposed approach merely focuses on addressing the pattern with $x_j(t) = 0$ with single fuzzy set, that is, as in Figure 2. Thus, if the pattern is like Figure 3, we need to beforehand perform a reconstruction procedure described in the following.

By illustrating from the pattern in Figure 3, the reconstruction procedure has two stages. Stage 1 is to delete the two $M_{(j,p)}$, $M_{(j,p+1)}$ regarding $x_j(t) = 0$ and retain the other fuzzy sets. Stage 2 is to establish three new fuzzy sets $M'_{(j,p)}$, $M_{(j,0)}$, and $M'_{(j,p+1)}$ for $x_j(t) = 0$ include single membership function. The achieved pattern can thus be depicted by Figure 4. The membership function $M'_{(j,p)}(x_j(t))$, $M_{(j,0)}(x_j(t))$, and $M'_{(j,p+1)}(x_j(t))$ can be, respectively, constructed by

$$\begin{aligned}
 &M'_{(j,p)}(x_j(t)) \\
 &= \begin{cases} M_{(j,p)}(x_j(t)), & \text{for } \phi_{(j,p-1)} \leq x_j(t) \leq \phi_{(j,p)} \\ M_{(j,p)}(x_j(t)) - \frac{M_{(j,p)}(0)M_{(j,p+1)}(x_j(t))}{M_{(j,p+1)}(0)}, & \text{for } \phi_{(j,p)} \leq x_j(t) \leq 0 \end{cases} \tag{17}
 \end{aligned}$$

$$\begin{aligned}
 &M_{(j,0)}(x_j(t)) \\
 &= \begin{cases} \frac{M_{(j,p+1)}(x_j(t))}{M_{(j,p+1)}(0)}, & \text{for } \phi_{(j,p)} \leq x_j(t) \leq 0 \\ \frac{M_{(j,p)}(x_j(t))}{M_{(j,p)}(0)}, & \text{for } 0 \leq x_j(t) \leq \phi_{(j,p+1)} \end{cases} \tag{18}
 \end{aligned}$$

$$\begin{aligned}
 &M'_{(j,p+1)}(x_j(t)) \\
 &= \begin{cases} M_{(j,p+1)}(x_j(t)) - \frac{M_{(j,p+1)}(0)M_{(j,p)}(x_j(t))}{M_{(j,p)}(0)}, & \text{for } 0 \leq x_j(t) \leq \phi_{(j,p+1)} \\ M_{(j,p+1)}(x_j(t)), & \text{for } \phi_{(j,p+1)} \leq x_j(t) \leq \phi_{(j,p+2)}. \end{cases} \tag{19}
 \end{aligned}$$

FIGURE 3: State variable $x_j(t)$ triggers two fuzzy set at $x_j(t) = 0$.FIGURE 4: Reconstruction of fuzzy sets with state variable $x_j(t)$.

4.1. Reconstruction of Switching Takagi-Sugeno Fuzzy Model via Vertex Expression. Consider

Region Model Rule $(q_1, q_2, \dots, q_n) - (\text{RMR}_{(q_1, q_2, \dots, q_n)})$:

IF $x_1(t)$ is $N_{(1, q_1)}$ and $x_2(t)$ is $N_{(2, q_2)} \dots$
and $x_n(t)$ is $N_{(n, q_n)}$,

THEN

Local Model Rule $(i_1, i_2, \dots, i_n) - (\text{LMR}_{(i_1, i_2, \dots, i_n)})$:

IF $x_1(t)$ is $M_{q_1, (1, i_1)}$ and $x_2(t)$ is $M_{q_2, (2, i_2)} \dots$
and $x_n(t)$ is $M_{q_n, (n, i_n)}$,

THEN $\dot{\mathbf{x}}(t) = \mathbf{A}_{(q_1, q_2, \dots, q_n)(i_1, i_2, \dots, i_n)} \mathbf{x}(t)$

$+ \mathbf{B}_{(q_1, q_2, \dots, q_n)(i_1, i_2, \dots, i_n)} \mathbf{u}(t)$

$$q_j = 0, 1, \quad i_j = 1, 2, \dots, r_{jq_j}, \quad j = 1, 2, \dots, n, \quad (20)$$

where $\text{RMR}_{(q_1, q_2, \dots, q_n)}$ denotes the region model rule (q_1, q_2, \dots, q_n) , $\text{LMR}_{(i_1, i_2, \dots, i_n)}$ denotes the local model rule (i_1, i_2, \dots, i_n) , and $N_{(j, q_j)}$ denotes the crisp set corresponding to the state variable $x_j(t)$ in divisional region q_j .

The membership function $N_{(j, q_j)}(x_j(t))$ of crisp set $N_{(j, q_j)}$ is defined as below:

$$N_{(j, 0)}(x_j(t)) = \begin{cases} 1 & \text{for } x_j(t) < 0 \\ 0 & \text{for } x_j(t) \geq 0 \end{cases} \quad (21)$$

$$N_{(j, 1)}(x_j(t)) = \begin{cases} 1 & \text{for } x_j(t) \geq 0 \\ 0 & \text{for } x_j(t) < 0. \end{cases}$$

$M_{q_j, (j, i_j)}$ denotes the fuzzy set corresponding to the state variable $x_j(t)$ of $\text{LMR}_{(i_1, i_2, \dots, i_n)}$ in divisional region q_j . r_{jq_j} is the number of $x_j(t)$'s fuzzy sets in divisional region q_j . $r_{(q_1, q_2, \dots, q_n)} = \prod_{j=1}^n r_{jq_j}$ is the number of IF-THEN region model rule (q_1, q_2, \dots, q_n) . $r = \sum_{q_1=0}^1 \sum_{q_2=0}^1 \dots \sum_{q_n=0}^1 r_{(q_1, q_2, \dots, q_n)}$ is the total number of IF-THEN fuzzy model rules. $\mathbf{A}_{(q_1, q_2, \dots, q_n)(i_1, i_2, \dots, i_n)} \in \mathfrak{R}^{n \times n}$ denotes the system matrix of the subsystem. And, $\mathbf{B}_{(q_1, q_2, \dots, q_n)(i_1, i_2, \dots, i_n)} \in \mathfrak{R}^{n \times m}$ denotes the input matrix of the subsystem.

Each linear consequent equation $\mathbf{A}_{(q_1, q_2, \dots, q_n)(i_1, i_2, \dots, i_n)} \mathbf{x}(t) + \mathbf{B}_{(q_1, q_2, \dots, q_n)(i_1, i_2, \dots, i_n)} \mathbf{u}(t)$ is called a subsystem. Given a pair of $(\mathbf{x}(t), \mathbf{u}(t))$, the final output of the T-S fuzzy model (20) inferred by CAD can be represented as follows:

$$\dot{\mathbf{x}}(t) = \sum_{q_1=0}^1 \sum_{q_2=0}^1 \dots \sum_{q_n=0}^1 \sum_{i_1=1}^{r_{1q_1}} \sum_{i_2=1}^{r_{2q_2}} \dots \sum_{i_n=1}^{r_{nq_n}} \eta_{(q_1, q_2, \dots, q_n)}(\mathbf{x}(t))$$

$$\begin{aligned} & \times h_{(q_1, q_2, \dots, q_n)(i_1, i_2, \dots, i_n)}(\mathbf{x}(t)) \\ & \times \left\{ \mathbf{A}_{(q_1, q_2, \dots, q_n)(i_1, i_2, \dots, i_n)} \mathbf{x}(t) + \mathbf{B}_{(q_1, q_2, \dots, q_n)(i_1, i_2, \dots, i_n)} \mathbf{u}(t) \right\}, \end{aligned} \quad (22)$$

where the normalized membership function of the $\text{RMR}_{(q_1, q_2, \dots, q_n)}$ is

$$\eta_{(q_1, q_2, \dots, q_n)}(\mathbf{x}(t)) = \prod_{j=1}^n N_{(j, q_j)}(x_j(t)), \quad (23)$$

and the fire strength of the $\text{LMR}_{(i_1, i_2, \dots, i_n)}$ in $R_{(q_1, q_2, \dots, q_n)}$ is

$$w_{(q_1, q_2, \dots, q_n)(i_1, i_2, \dots, i_n)}(\mathbf{x}(t)) = \prod_{j=1}^n M_{q_j, (j, i_j)}(x_j(t)) \quad (24)$$

for all t . And the term $M_{q_j, (j, i_j)}(x_j(t))$ is the grade of membership of $x_j(t)$ in $M_{q_j, (j, i_j)}$.

The normalized membership function of the $\text{LMR}_{(i_1, i_2, \dots, i_n)}$ in $R_{(q_1, q_2, \dots, q_n)}$ can be described by

$$\begin{aligned} & h_{(q_1, q_2, \dots, q_n)(i_1, i_2, \dots, i_n)}(\mathbf{x}(t)) \\ & = \frac{w_{(q_1, q_2, \dots, q_n)(i_1, i_2, \dots, i_n)}(\mathbf{x}(t))}{\sum_{i_1=1}^{r_{1q_1}} \sum_{i_2=1}^{r_{2q_2}} \dots \sum_{i_n=1}^{r_{nq_n}} w_{(q_1, q_2, \dots, q_n)(i_1, i_2, \dots, i_n)}(\mathbf{x}(t))} \end{aligned} \quad (25)$$

with

$$\begin{aligned} & \sum_{i_1=1}^{r_{1q_1}} \sum_{i_2=1}^{r_{2q_2}} \dots \sum_{i_n=1}^{r_{nq_n}} h_{(q_1, q_2, \dots, q_n)(i_1, i_2, \dots, i_n)}(\mathbf{x}(t)) = 1, \\ & h_{(q_1, q_2, \dots, q_n)(i_1, i_2, \dots, i_n)}(\mathbf{x}(t)) \geq 0, \\ & i_j = 1, 2, \dots, r_{jq_j}, \quad j = 1, 2, \dots, n. \end{aligned} \quad (26)$$

Example 5. Consider a system with two state variables $x_1(t)$ and $x_2(t)$. The T-S fuzzy model is assumed to have 16 subsystems and four fuzzy sets for each state variable. A state space with two dimension can be divided into the following four regions: $R(0, 0)$, $R(0, 1)$, $R(1, 0)$, and $R(1, 1)$ as shown in Figure 5. The T-S fuzzy model that uses the process of reconstruction can obtain the following new T-S fuzzy model as shown in Figure 6. The new T-S fuzzy model has 25 subsystems and five fuzzy sets for each state variable

$$\begin{aligned} A_{(0,1)} &= M_{(1,2)}(x_1(t)) A_{(2,1)} + M_{(1,3)}(x_1(t)) A_{(3,1)}, \\ A_{(0,2)} &= M_{(1,2)}(x_1(t)) A_{(2,2)} + M_{(1,3)}(x_1(t)) A_{(3,2)}, \\ A_{(0,3)} &= M_{(1,2)}(x_1(t)) A_{(2,3)} + M_{(1,3)}(x_1(t)) A_{(3,3)}, \\ A_{(0,4)} &= M_{(1,2)}(x_1(t)) A_{(2,4)} + M_{(1,3)}(x_1(t)) A_{(3,4)}, \\ A_{(1,0)} &= M_{(2,2)}(x_2(t)) A_{(1,2)} + M_{(2,3)}(x_2(t)) A_{(1,3)}, \\ A_{(2,0)} &= M_{(2,2)}(x_2(t)) A_{(2,2)} + M_{(2,3)}(x_2(t)) A_{(2,3)}, \end{aligned}$$

$$\begin{aligned} A_{(3,0)} &= M_{(2,2)}(x_2(t)) A_{(3,2)} + M_{(2,3)}(x_2(t)) A_{(3,3)}, \\ A_{(4,0)} &= M_{(2,2)}(x_2(t)) A_{(4,2)} + M_{(2,3)}(x_2(t)) A_{(4,3)}, \\ A_{(0,0)} &= M_{(1,2)}(x_1(t)) M_{(2,2)}(x_2(t)) A_{(2,2)} \\ &+ M_{(1,3)}(x_1(t)) M_{(2,2)}(x_2(t)) A_{(3,2)} \\ &+ M_{(1,2)}(x_1(t)) M_{(2,3)}(x_2(t)) A_{(2,3)} \\ &+ M_{(1,3)}(x_1(t)) M_{(2,3)}(x_2(t)) A_{(3,3)}. \end{aligned} \quad (27)$$

For the new T-S fuzzy model in Figure 6, it can be separated at region boundaries and depicted as Figure 7.

4.2. Relaxed Stability Conditions Based on Switching Quadratic Lyapunov Function. Consider

Region Function Rule $(q_1, q_2, \dots, q_n) - (\text{RFR}_{(q_1, q_2, \dots, q_n)})$:

IF $x_1(t)$ is $N_{(1, q_1)}$ and $x_2(t)$ is $N_{(2, q_2)} \dots$

and $x_n(t)$ is $N_{(n, q_n)}$,

THEN $V(\mathbf{x}(t)) = \mathbf{x}^T(t) \mathbf{P}_{(q_1, q_2, \dots, q_n)} \mathbf{x}(t)$,

$$q_j = 0, 1, \quad j = 1, 2, \dots, n, \quad (28)$$

where $\text{RFR}_{(q_1, q_2, \dots, q_n)}$ denotes the region function rule (q_1, q_2, \dots, q_n) . $\mathbf{P}_{(q_1, q_2, \dots, q_n)} \in \mathfrak{R}^{n \times n}$ is a set of positive-definite symmetric matrices.

Based on the CAD for the $\text{RFR}_{(q_1, q_2, \dots, q_n)}$. The overall SFQLF is given as

$$\begin{aligned} & V(\mathbf{x}(t)) \\ & = \sum_{q_1=0}^1 \sum_{q_2=0}^1 \dots \sum_{q_n=0}^1 \eta_{(q_1, q_2, \dots, q_n)}(\mathbf{x}(t)) \mathbf{x}^T(t) \mathbf{P}_{(q_1, q_2, \dots, q_n)} \mathbf{x}(t). \end{aligned} \quad (29)$$

This function is continuous on region boundaries if $\mathbf{P}_{(q_1, q_2, \dots, q_n)}$ satisfies the following constraint:

$$\mathbf{P}_{(q_1, q_2, \dots, q_n)} = \begin{bmatrix} P_{11q_1} & P_{12(2q_1+q_2)} & \dots & P_{1n(2q_1+q_n)} \\ P_{12(2q_1+q_2)} & P_{22q_2} & \dots & P_{2n(2q_2+q_n)} \\ \vdots & \vdots & \ddots & \vdots \\ P_{1n(2q_1+q_n)} & P_{2n(2q_2+q_n)} & \dots & P_{nnq_n} \end{bmatrix}. \quad (30)$$

The autonomous switching T-S fuzzy system via vertex expression with (22) can be represented as

$$\begin{aligned} \dot{\mathbf{x}}(t) &= \sum_{q_1=0}^1 \sum_{q_2=0}^1 \dots \sum_{q_n=0}^1 \sum_{i_1=1}^{r_{1q_1}} \sum_{i_2=1}^{r_{2q_2}} \dots \sum_{i_n=1}^{r_{nq_n}} \eta_{(q_1, q_2, \dots, q_n)}(\mathbf{x}(t)) \\ &\quad \times h_{(q_1, q_2, \dots, q_n)(i_1, i_2, \dots, i_n)}(\mathbf{x}(t)) \mathbf{A}_{(q_1, q_2, \dots, q_n)(i_1, i_2, \dots, i_n)} \mathbf{x}(t). \end{aligned} \quad (31)$$

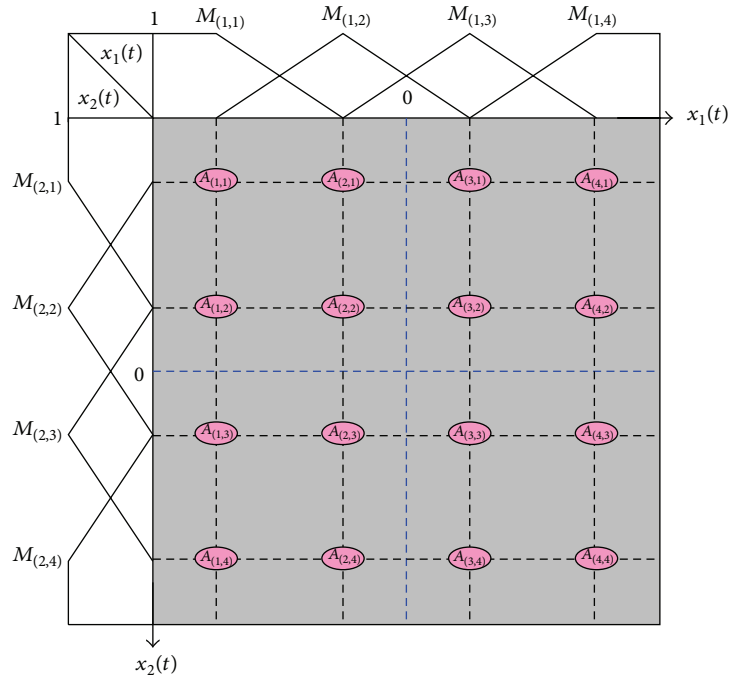


FIGURE 5: Rules illustration of Example 5.

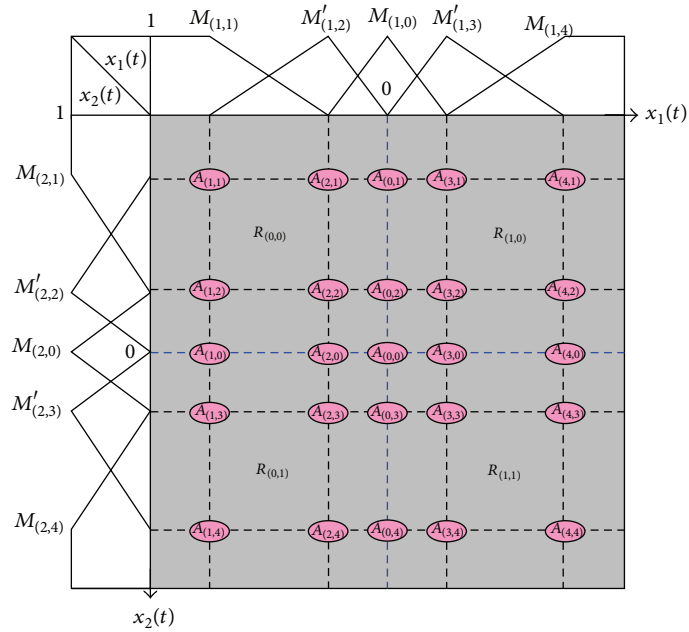


FIGURE 6: Rules illustration of Example 5 by the first process of reconstruction.

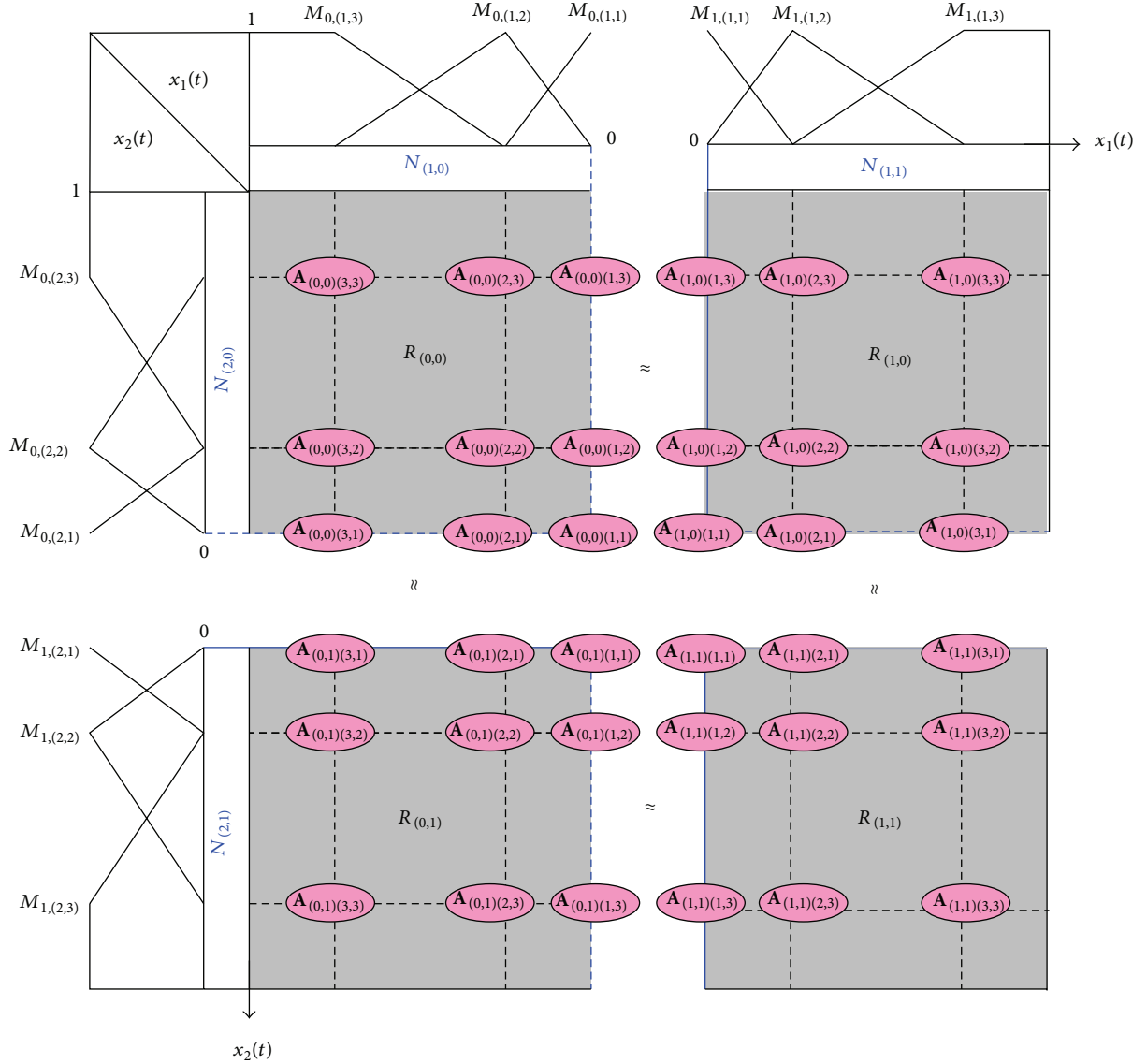


FIGURE 7: Rules illustration of Example 5 by the second process of reconstruction.

By reconstruction of the switching T-S fuzzy model, we can obtain relaxed stability conditions for autonomous switching T-S fuzzy systems via vertex expression (31) based on SFQLF.

Theorem 6. *The equilibrium of the reconstructive autonomous switching T-S fuzzy system (31) is globally asymptotically stable if there exist a set of matrices $\mathbf{P}_{(q_1, q_2, \dots, q_n)}$ such that (30) and (32):*

$$\mathbf{P}_{(q_1, q_2, \dots, q_n)} > \mathbf{0}, \quad q_j = 0, 1, \quad j = 1, 2, \dots, n,$$

$$\begin{aligned} & \mathbf{A}_{(q_1, q_2, \dots, q_n)(i_1, i_2, \dots, i_n)}^T \mathbf{P}_{(q_1, q_2, \dots, q_n)} \\ & + \mathbf{P}_{(q_1, q_2, \dots, q_n)} \mathbf{A}_{(q_1, q_2, \dots, q_n)(i_1, i_2, \dots, i_n)} < \mathbf{0}, \end{aligned}$$

$$q_j = 0, 1, \quad i_j = 1, 2, \dots, r_{j q_j}, \quad j = 1, 2, \dots, n. \quad (32)$$

Proof. Consider a candidate of Lyapunov function (29):

$$\begin{aligned} \dot{V}(\mathbf{x}(t)) &= \sum_{q_1=0}^1 \sum_{q_2=0}^1 \cdots \sum_{q_n=0}^1 \eta_{(q_1, q_2, \dots, q_n)}(\mathbf{x}(t)) \\ &\quad \times \left\{ \dot{\mathbf{x}}^T(t) \mathbf{P}_{(q_1, q_2, \dots, q_n)} \mathbf{x}(t) + \mathbf{x}^T(t) \mathbf{P}_{(q_1, q_2, \dots, q_n)} \dot{\mathbf{x}}(t) \right\}. \end{aligned} \quad (33)$$

By (22), we manipulate the above equation and it then yields (34) (see below). Thus, from (30) and (32), the considered T-S fuzzy system (31) is asserted to be globally asymptotically stable.

$$\begin{aligned}
\dot{V}(\mathbf{x}(t)) &= \sum_{q_1=0}^1 \sum_{q_2=0}^1 \dots \sum_{q_n=0}^1 \eta_{(q_1, q_2, \dots, q_n)}(\mathbf{x}(t)) \\
&\times \left\{ \left(\sum_{i_1=1}^{r_{1q_1}} \sum_{i_2=1}^{r_{2q_2}} \dots \sum_{i_n=1}^{r_{nq_n}} h_{(q_1, q_2, \dots, q_n)(i_1, i_2, \dots, i_n)}(\mathbf{x}(t)) \mathbf{x}^T(t) \mathbf{A}_{(q_1, q_2, \dots, q_n)(i_1, i_2, \dots, i_n)}^T \right) \times \mathbf{P}_{(q_1, q_2, \dots, q_n)} \mathbf{x}(t) \right. \\
&\quad \left. + \mathbf{x}^T(t) \mathbf{P}_{(q_1, q_2, \dots, q_n)} \times \left(\sum_{i_1=1}^{r_{1q_1}} \sum_{i_2=1}^{r_{2q_2}} \dots \sum_{i_n=1}^{r_{nq_n}} h_{(q_1, q_2, \dots, q_n)(i_1, i_2, \dots, i_n)}(\mathbf{x}(t)) \mathbf{A}_{(q_1, q_2, \dots, q_n)(i_1, i_2, \dots, i_n)} \mathbf{x}(t) \right) \right\} \quad (34) \\
&= \sum_{q_1=0}^1 \sum_{q_2=0}^1 \dots \sum_{q_n=0}^1 \sum_{i_1=1}^{r_{1q_1}} \sum_{i_2=1}^{r_{2q_2}} \dots \sum_{i_n=1}^{r_{nq_n}} \eta_{(q_1, q_2, \dots, q_n)}(\mathbf{x}(t)) h_{(q_1, q_2, \dots, q_n)(i_1, i_2, \dots, i_n)}(\mathbf{x}(t)) \\
&\quad \times \mathbf{x}^T(t) \left\{ \mathbf{A}_{(q_1, q_2, \dots, q_n)(i_1, i_2, \dots, i_n)}^T \mathbf{P}_{(q_1, q_2, \dots, q_n)} \mathbf{x}(t) + \mathbf{P}_{(q_1, q_2, \dots, q_n)} \mathbf{A}_{(q_1, q_2, \dots, q_n)(i_1, i_2, \dots, i_n)} \right\} \mathbf{x}(t).
\end{aligned}$$

□

5. Illustrative Example

Revisit Example 1 in the previous work [26]. By our proposed approach, we can beforehand use the reconstruction procedure for this T-S fuzzy model and thus can suitably perform the stability verification by Theorem 6 with SFQLF described in the sequel.

Example 7. Consider the following reconstructed switching T-S fuzzy model:

RMR_(0,0) : IF $x_1(t)$ is $N_{(1,0)}$ and $x_2(t)$ is $N_{(2,0)}$

THEN LMR_(1,1) : IF $x_1(t)$ is $M_{0,(1,1)}$ and $x_2(t)$ is $M_{0,(2,1)}$

THEN $\dot{\mathbf{x}}(t) = \mathbf{A}_{(0,0)(1,1)} \mathbf{x}(t)$

LMR_(2,1) : IF $x_1(t)$ is $M_{0,(1,2)}$ and $x_2(t)$ is $M_{0,(2,1)}$

THEN $\dot{\mathbf{x}}(t) = \mathbf{A}_{(0,0)(2,1)} \mathbf{x}(t)$

LMR_(1,2) : IF $x_1(t)$ is $M_{0,(1,1)}$ and $x_2(t)$ is $M_{0,(2,2)}$

THEN $\dot{\mathbf{x}}(t) = \mathbf{A}_{(0,0)(1,2)} \mathbf{x}(t)$

LMR_(2,2) : IF $x_1(t)$ is $M_{0,(1,2)}$ and $x_2(t)$ is $M_{0,(2,2)}$

THEN $\dot{\mathbf{x}}(t) = \mathbf{A}_{(0,0)(2,2)} \mathbf{x}(t)$

RMR_(1,0) : IF $x_1(t)$ is $N_{(1,1)}$ and $x_2(t)$ is $N_{(2,0)}$

THEN LMR_(1,1) : IF $x_1(t)$ is $M_{1,(1,1)}$ and $x_2(t)$ is $M_{0,(2,1)}$

THEN $\dot{\mathbf{x}}(t) = \mathbf{A}_{(1,0)(1,1)} \mathbf{x}(t)$

LMR_(2,1) : IF $x_1(t)$ is $M_{1,(1,2)}$ and $x_2(t)$ is $M_{0,(2,1)}$

THEN $\dot{\mathbf{x}}(t) = \mathbf{A}_{(1,0)(2,1)} \mathbf{x}(t)$

LMR_(1,2) : IF $x_1(t)$ is $M_{1,(1,1)}$ and $x_2(t)$ is $M_{0,(2,2)}$

THEN $\dot{\mathbf{x}}(t) = \mathbf{A}_{(1,0)(1,2)} \mathbf{x}(t)$

LMR_(2,2) : IF $x_1(t)$ is $M_{1,(1,2)}$ and $x_2(t)$ is $M_{0,(2,2)}$

THEN $\dot{\mathbf{x}}(t) = \mathbf{A}_{(1,0)(2,2)} \mathbf{x}(t)$

RMR_(0,1) : IF $x_1(t)$ is $N_{(1,0)}$ and $x_2(t)$ is $N_{(2,1)}$

THEN LMR_(1,1) : IF $x_1(t)$ is $M_{0,(1,1)}$ and $x_2(t)$ is $M_{1,(2,1)}$

THEN $\dot{\mathbf{x}}(t) = \mathbf{A}_{(0,1)(1,1)} \mathbf{x}(t)$

LMR_(2,1) : IF $x_1(t)$ is $M_{0,(1,2)}$ and $x_2(t)$ is $M_{1,(2,1)}$

THEN $\dot{\mathbf{x}}(t) = \mathbf{A}_{(0,1)(2,1)} \mathbf{x}(t)$

LMR_(1,2) : IF $x_1(t)$ is $M_{0,(1,1)}$ and $x_2(t)$ is $M_{1,(2,2)}$

THEN $\dot{\mathbf{x}}(t) = \mathbf{A}_{(0,1)(1,2)} \mathbf{x}(t)$

LMR_(2,2) : IF $x_1(t)$ is $M_{0,(1,2)}$ and $x_2(t)$ is $M_{1,(2,2)}$

THEN $\dot{\mathbf{x}}(t) = \mathbf{A}_{(0,1)(2,2)} \mathbf{x}(t)$

RMR_(1,1) : IF $x_1(t)$ is $N_{(1,1)}$ and $x_2(t)$ is $N_{(2,1)}$

THEN LMR_(1,1) : IF $x_1(t)$ is $M_{1,(1,1)}$ and $x_2(t)$ is $M_{1,(2,1)}$

THEN $\dot{\mathbf{x}}(t) = \mathbf{A}_{(1,1)(1,1)} \mathbf{x}(t)$

LMR_(2,1) : IF $x_1(t)$ is $M_{1,(1,2)}$ and $x_2(t)$ is $M_{1,(2,1)}$

THEN $\dot{\mathbf{x}}(t) = \mathbf{A}_{(1,1)(2,1)} \mathbf{x}(t)$

LMR_(1,2) : IF $x_1(t)$ is $M_{1,(1,1)}$ and $x_2(t)$ is $M_{1,(2,2)}$

THEN $\dot{\mathbf{x}}(t) = \mathbf{A}_{(1,1)(1,2)} \mathbf{x}(t)$

LMR_(2,2) : IF $x_1(t)$ is $M_{1,(1,2)}$ and $x_2(t)$ is $M_{1,(2,2)}$

THEN $\dot{\mathbf{x}}(t) = \mathbf{A}_{(1,1)(2,2)} \mathbf{x}(t),$

(35)

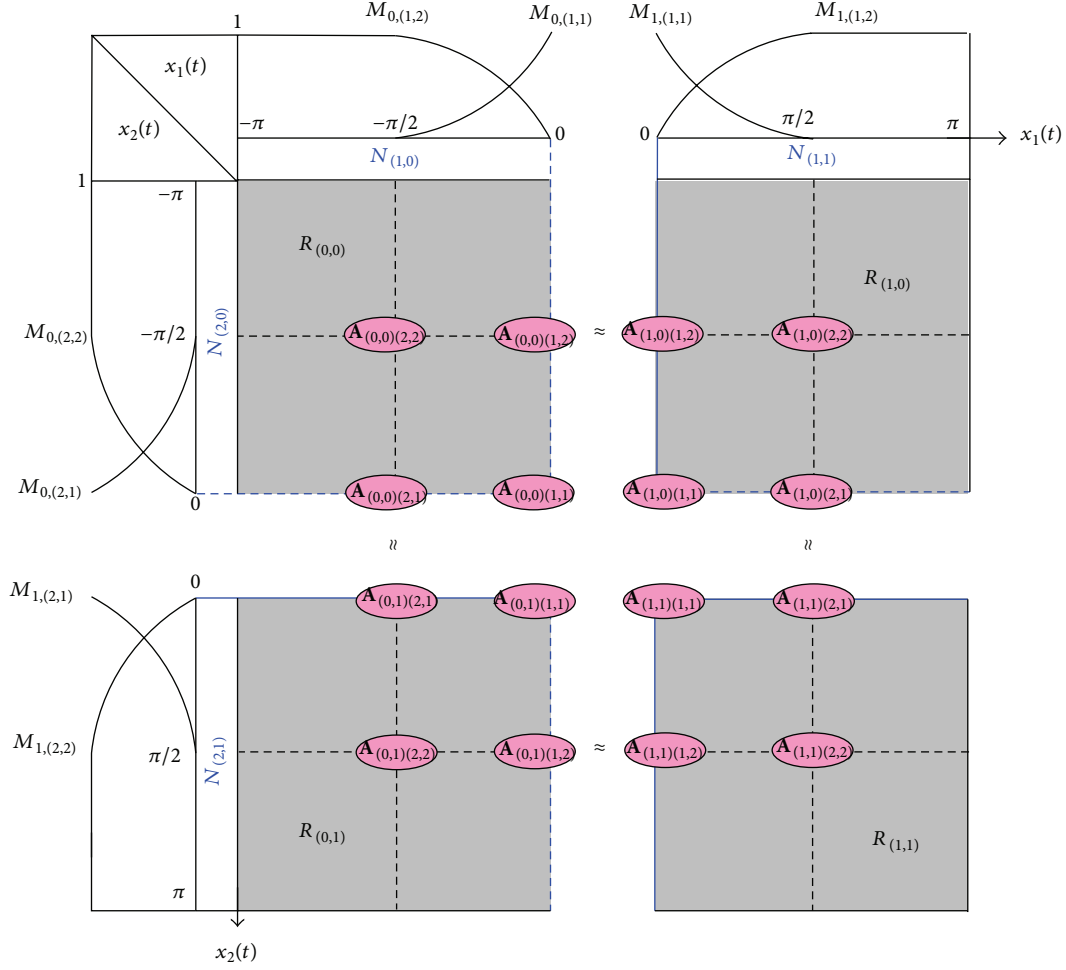


FIGURE 8: Rules illustration of switching T-S fuzzy model via vertex expression for Example 7.

where the original system matrices of the subsystem are

$$\begin{aligned} \mathbf{A}_1 &= \begin{bmatrix} -5 & -4 \\ -1 & a \end{bmatrix}, & \mathbf{A}_2 &= \begin{bmatrix} -4 & -4 \\ \frac{1}{5}(3b-2) & \frac{1}{5}(3a-4) \end{bmatrix}, \\ \mathbf{A}_3 &= \begin{bmatrix} -3 & -4 \\ \frac{1}{5}(2b-3) & \frac{1}{5}(2a-6) \end{bmatrix}, & \mathbf{A}_4 &= \begin{bmatrix} -2 & -4 \\ b & -2 \end{bmatrix}. \end{aligned} \quad (36)$$

By the reconstructing procedure, the considered system associated with rules illustration via vertex expression is depicted in Figure 8. Thus, the systems' matrices can be, respectively, calculated as

$$\begin{aligned} \mathbf{A}_{(0,0)(2,2)} &= \mathbf{A}_2, & \mathbf{A}_{(0,0)(1,2)} &= \frac{\mathbf{A}_2 + \mathbf{A}_4}{2}, \\ \mathbf{A}_{(1,0)(1,2)} &= \frac{\mathbf{A}_2 + \mathbf{A}_4}{2}, & \mathbf{A}_{(1,0)(2,2)} &= \mathbf{A}_4, \\ \mathbf{A}_{(0,0)(2,1)} &= \frac{\mathbf{A}_1 + \mathbf{A}_2}{2}, & \mathbf{A}_{(0,0)(1,1)} &= \frac{\mathbf{A}_1 + \mathbf{A}_2 + \mathbf{A}_3 + \mathbf{A}_4}{4}, \end{aligned}$$

$$\begin{aligned} \mathbf{A}_{(1,0)(1,1)} &= \frac{\mathbf{A}_1 + \mathbf{A}_2 + \mathbf{A}_3 + \mathbf{A}_4}{4}, & \mathbf{A}_{(1,0)(2,1)} &= \frac{\mathbf{A}_3 + \mathbf{A}_4}{2}, \\ \mathbf{A}_{(0,1)(2,1)} &= \frac{\mathbf{A}_1 + \mathbf{A}_2}{2}, & \mathbf{A}_{(0,1)(1,1)} &= \frac{\mathbf{A}_1 + \mathbf{A}_2 + \mathbf{A}_3 + \mathbf{A}_4}{4}, \\ \mathbf{A}_{(1,1)(1,1)} &= \frac{\mathbf{A}_1 + \mathbf{A}_2 + \mathbf{A}_3 + \mathbf{A}_4}{4}, & \mathbf{A}_{(1,1)(2,1)} &= \frac{\mathbf{A}_3 + \mathbf{A}_4}{2}, \\ \mathbf{A}_{(0,0)(2,2)} &= \mathbf{A}_1, & \mathbf{A}_{(0,1)(1,2)} &= \frac{\mathbf{A}_1 + \mathbf{A}_3}{2}, \\ \mathbf{A}_{(1,1)(1,2)} &= \frac{\mathbf{A}_1 + \mathbf{A}_3}{2}, & \mathbf{A}_{(1,1)(2,2)} &= \mathbf{A}_3, \end{aligned} \quad (37)$$

with

$$\begin{aligned} N_{(1,0)}(x_1(t)) &= \begin{cases} 1, & \text{for } x_1(t) < 0 \\ 0, & \text{for } x_1(t) \geq 0, \end{cases} \\ N_{(1,1)}(x_1(t)) &= \begin{cases} 1, & \text{for } x_1(t) \geq 0 \\ 0, & \text{for } x_1(t) < 0, \end{cases} \end{aligned}$$

$$\begin{aligned}
N_{(2,0)}(x_2(t)) &= \begin{cases} 1, & \text{for } x_2(t) < 0 \\ 0, & \text{for } x_2(t) \geq 0, \end{cases} \\
N_{(2,1)}(x_2(t)) &= \begin{cases} 1, & \text{for } x_2(t) \geq 0 \\ 0, & \text{for } x_2(t) < 0. \end{cases} \\
M_{0,(1,2)}(x_1(t)) &= \begin{cases} 1, & \text{for } x_1(t) \leq -\frac{\pi}{2} \\ -\sin(x_1(t)), & \text{for } -\frac{\pi}{2} \leq x_1(t) \leq 0, \end{cases} \\
M_{0,(1,1)}(x_1(t)) &= \begin{cases} 0, & \text{for } x_1(t) \leq -\frac{\pi}{2} \\ 1 + \sin(x_1(t)), & \text{for } -\frac{\pi}{2} \leq x_1(t) \leq 0 \end{cases} \\
M_{1,(1,1)}(x_1(t)) &= \begin{cases} 1 - \sin(x_1(t)), & \text{for } x_1(t) \leq \frac{\pi}{2} \\ 0, & \text{for } \frac{\pi}{2} \leq x_1(t) \end{cases} \\
M_{1,(1,2)}(x_1(t)) &= \begin{cases} \sin(x_1(t)) & \text{for } 0 \leq x_1(t) \leq \frac{\pi}{2} \\ 1 & \text{for } \frac{\pi}{2} \leq x_1(t) \end{cases} \\
M_{0,(2,2)}(x_2(t)) &= \begin{cases} 1, & \text{for } x_2(t) \leq -\frac{\pi}{2} \\ -\sin(x_2(t)), & \text{for } -\frac{\pi}{2} \leq x_2(t) \leq 0 \end{cases} \\
M_{0,(2,1)}(x_2(t)) &= \begin{cases} 0, & \text{for } x_2(t) \leq -\frac{\pi}{2} \\ 1 + \sin(x_2(t)), & \text{for } -\frac{\pi}{2} \leq x_2(t) \leq 0 \end{cases} \\
M_{1,(2,1)}(x_2(t)) &= \begin{cases} 1 - \sin(x_2(t)), & \text{for } x_2(t) \leq \frac{\pi}{2} \\ 0, & \text{for } \frac{\pi}{2} \leq x_2(t) \end{cases} \\
M_{1,(2,2)}(x_2(t)) &= \begin{cases} \sin(x_2(t)) & \text{for } 0 \leq x_2(t) \leq \frac{\pi}{2} \\ 1 & \text{for } \frac{\pi}{2} \leq x_2(t). \end{cases}
\end{aligned} \tag{38}$$

In this example, by applying a current tool, Matlab software, we experimentally attain a widely feasible region for the parameters' pair (a, b) via SQLF method compared to that of the CQLF method. The feasible parameter pairs (a, b) of the CQLF and the SQLF methods are shown in Figures 9 and 10, respectively. By observation, the proposed approach can dramatically lessen the conservatism of the stability assurance.

Conflict of Interests

The authors declare that there is no conflict of interests regarding the publication of this paper.

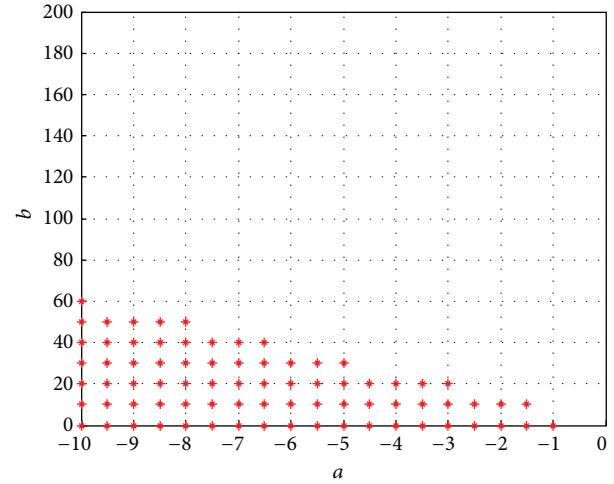


FIGURE 9: Feasible area for Example 7 that uses the CQLF method.

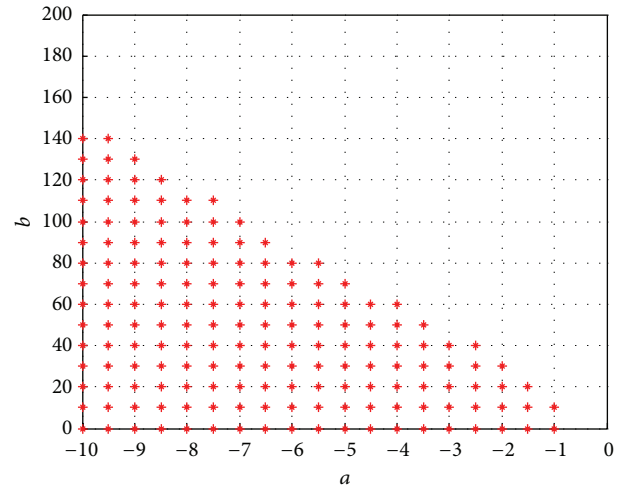


FIGURE 10: Feasible area for Example 7 that uses the SQLF method.

References

- [1] L. A. Zadeh, "Outline of new approach to the analysis of complex systems and decision processes," *IEEE Transactions on Systems, Man, and Cybernetics*, vol. 3, pp. 28–44, 1973.
- [2] T. Takagi and M. Sugeno, "Fuzzy identification of systems and its applications to modeling and control," *IEEE Transactions on Systems, Man, and Cybernetics Part B*, vol. SMC-15, no. 2, pp. 116–132, 1985.
- [3] K. Tanaka and M. Sugeno, "Stability analysis and design of fuzzy control systems," *Fuzzy Sets and Systems*, vol. 45, no. 2, pp. 135–156, 1992.
- [4] K. Tanaka and M. Sano, "A robust stabilization problem of fuzzy control systems and its application to backing up control of a truck-trailer," *IEEE Transactions on Fuzzy Systems*, vol. 2, no. 2, pp. 119–134, 1994.
- [5] P. P. Angelov and D. P. Filev, "An approach to online identification of Takagi-Sugeno fuzzy models," *IEEE Transactions on Systems, Man, and Cybernetics, Part B: Cybernetics*, vol. 34, no. 1, pp. 484–498, 2004.

- [6] I. Kar, P. K. Patchaikani, and L. Behera, "On balancing a cart-pole system using T-S fuzzy model," *Fuzzy Sets and Systems*, vol. 207, pp. 94–110, 2012.
- [7] J. X. Xu, Z. Q. Guo, and T. H. Lee, "Design and implementation of a Takagi-Sugeno-type fuzzy logic controller on a two-wheeled mobile robot," *IEEE Transactions on Industrial Electronics*, vol. 60, no. 12, pp. 5717–5727, 2013.
- [8] L. Zhang, X. Chang, and H. R. Karimi, "Fuzzy modeling and control for a class of inverted pendulum system," *Abstract and Applied Analysis*, vol. 2014, Article ID 936868, 6 pages, 2014.
- [9] H. O. Wang, K. Tanaka, and M. F. Griffin, "Parallel distributed compensation of nonlinear systems by Takagi-Sugeno fuzzy model," in *Proceedings of 4th IEEE International Conference on Fuzzy Systems and the 2nd International Fuzzy Engineering Symposium*, vol. 2, pp. 531–538, Yokohama, Japan, March 1995.
- [10] H. O. Wang, K. Tanaka, and M. F. Griffin, "An approach to fuzzy control of nonlinear systems: stability and design issues," *IEEE Transactions on Fuzzy Systems*, vol. 4, no. 1, pp. 14–23, 1996.
- [11] K. Tanaka, T. Ikeda, and H. O. Wang, "Robust stabilization of a class of uncertain nonlinear system via fuzzy control," *IEEE Transactions on Fuzzy Systems*, vol. 4, pp. 1–13, 1996.
- [12] K. Tanaka, T. Ikeda, and H. O. Wang, "Fuzzy regulators and fuzzy observers: relaxed stability conditions and LMI-based designs," *IEEE Transactions on Fuzzy Systems*, vol. 6, no. 2, pp. 250–265, 1998.
- [13] M. Narimani, H. K. Lam, R. Dilmaghani, and C. Wolfe, "LMI-based stability analysis of fuzzy-model-based control systems using approximated polynomial membership functions," *IEEE Transactions on Systems, Man, and Cybernetics, Part B: Cybernetics*, vol. 41, no. 3, pp. 713–724, 2011.
- [14] L. K. Wong, F. H. F. Leung, and P. K. S. Tam, "Lyapunov function-based design of fuzzy logic controllers and its application on combining controllers," *IEEE Transactions on Industrial Electronics*, vol. 45, no. 3, pp. 502–509, 1998.
- [15] M. Sugeno, "On stability of fuzzy systems expressed by fuzzy rules with singleton consequents," *IEEE Transactions on Fuzzy Systems*, vol. 7, pp. 201–224, 1999.
- [16] E. Kim and H. Lee, "New approaches to relaxed quadratic stability condition of fuzzy control systems," *IEEE Transactions on Fuzzy Systems*, vol. 8, pp. 523–533, 2000.
- [17] K. Tanaka and H. O. Wang, *Fuzzy Control Systems Design and Analysis: A Linear Matrix Inequality Approach*, John Wiley & Sons, New York, NY, USA, 2001.
- [18] H. D. Tuan, P. Apkarian, T. Narikiyo, and Y. Yamamoto, "Parameterized linear matrix inequality techniques in fuzzy control system design," *IEEE Transactions on Fuzzy Systems*, vol. 9, no. 2, pp. 324–332, 2001.
- [19] J.-M. Zhang, R.-H. Li, and P.-A. Zhang, "Stability analysis and systematic design of fuzzy control systems," *Fuzzy Sets and Systems*, vol. 120, no. 1, pp. 65–72, 2001.
- [20] M. Johansson, A. Rantzer, and K. E. Årzén, "Piecewise quadratic stability of fuzzy systems," *IEEE Transactions on Fuzzy Systems*, vol. 7, no. 6, pp. 713–722, 1999.
- [21] M. Feng and C. J. Harris, "Piecewise Lyapunov stability conditions of fuzzy systems," *IEEE Transactions on Systems, Man, and Cybernetics, Part B*, vol. 31, no. 2, pp. 259–262, 2001.
- [22] Z. H. Xiu and G. Ren, "Stability analysis and systematic design of Takagi-Sugeno fuzzy control systems," *Fuzzy Sets and Systems*, vol. 151, no. 1, pp. 119–138, 2005.
- [23] H. Ohtake, K. Tanaka, and H. O. Wang, "Switching fuzzy controller design based on switching Lyapunov function for a class of nonlinear systems," *IEEE Transactions on Systems, Man, and Cybernetics B*, vol. 36, no. 1, pp. 13–23, 2006.
- [24] W. J. Wang, Y. J. Chen, and C. H. Sun, "Relaxed stabilization criteria for discrete-time T-S fuzzy control systems based on a switching fuzzy model and piecewise Lyapunov function," *IEEE Transactions on Fuzzy Systems*, vol. 37, no. 3, pp. 551–559, 2007.
- [25] P. Gahinet, A. Nemirovski, A. Laub, and M. Chilali, *LMI Control Toolbox*, The MathWorks Inc., 1995.
- [26] B.-J. Rhee and S. Won, "A new fuzzy Lyapunov function approach for a Takagi-Sugeno fuzzy control system design," *Fuzzy Sets and Systems*, vol. 157, no. 9, pp. 1211–1228, 2006.

Research Article

Global Analysis of a Delayed Impulsive Lotka-Volterra Model with Holling III Type Functional Response

Hui Wang, Xiaomin Hu, Zhixing Hu, and Fucheng Liao

School of Mathematics and Physics, University of Science and Technology Beijing, Beijing 100083, China

Correspondence should be addressed to Hui Wang; bkdwh@163.com

Received 9 July 2014; Revised 6 October 2014; Accepted 6 October 2014

Academic Editor: Shaofan Li

Copyright © 2015 Hui Wang et al. This is an open access article distributed under the Creative Commons Attribution License, which permits unrestricted use, distribution, and reproduction in any medium, provided the original work is properly cited.

A delayed impulsive Lotka-Volterra model with Holling III type functional response was established. With the help of Mawhin's Continuation Theorem in coincidence degree theory, a sufficient condition is found for the existence of positive periodic solutions of the system under consideration. By applying the comparison theorem and constructing a suitable Lyapunov functional, the permanence and global attractivity of the model are proved. Two numerical simulations are also given to illustrate our main results.

1. Introduction

Recently, many complicated but realistic predator-prey systems based on classical Holling type functional responses have been analyzed by ecologists and mathematicians; see papers [1–6] and so forth. For example, a positive periodic solution to a Lotka-Volterra model with mutual interference and Holling III type functional response was proposed by Lv and Du in [2]; Zhang and his coworkers studied positive periodic solutions in a predator-prey model with Hassell-Varley type functional response, nonselective harvesting, and multiple delays in paper [6]. The theoretical values of these studies not only have great significance in biological economics but also provide strong support for the management and development of renewable energy.

Hassell [7] introduced the following predator-prey system with mutual interference m ($0 < m \leq 1$):

$$\begin{aligned}\dot{x} &= xg(x) - \varphi(x)y^m, \\ \dot{y} &= y(-d - k\varphi(x)y^{m-1} - q(y)).\end{aligned}\quad (1)$$

After that more scholars have further conducted research. For example, Du and Lv investigated a Lotka-Volterra model with mutual interference and time delays in [8]:

$$\dot{x} = x(t)(r_1(t) - b_1(t)x(t - \tau(t))) - \frac{c_1(t)x^2(t)}{x^2(t) + k^2}y^m(t),$$

$$\begin{aligned}\dot{y} &= y(t)(-r_2(t) - b_2(t)y(t)) + \frac{c_2(t)x^2(t)}{x^2(t) + k^2}y^m(t), \\ (0 < m < 1, k > 0).\end{aligned}\quad (2)$$

Some criteria on the permanence and global attractivity of the above system are found. As far as we know, delay models have been studied and applied extensively in biology, physics, population dynamics, and other fields. However, the assumption of these models with constant environment is rarely the case in real life. A system must be nonautonomous if the environmental fluctuation is taken into account, such as seasonal effects of weather, food supplies, and harvesting. Therefore, it is rational to consider the ecosystem with periodic or almost periodic coefficients. On the other hand, there exist a few discontinuous and impulsive phenomena; for instance, many species are given birth seasonally. If we introduce these impulsive factors into the systems, it is more realistic to analyze the ecology models. For example, Wang and Zhu [4] considered a delayed impulsive prey-predator system with mutual interference:

$$\begin{aligned}\dot{x} &= x(t)(r_1(t) - b_1(t)x(t - \tau)) - c_1(t)x(t)y^m(t), \\ \dot{y} &= y(t)(-r_2(t) - b_2(t)y(t - \sigma)) + c_2(t)x(t)y^m(t), \\ t &\neq t_k, \quad k \in \mathbb{Z}^+, \end{aligned}$$

$$\begin{aligned}
\Delta x(t) &= d_k x(t), \\
\Delta y(t) &= f_k y(t), \\
t &= t_k, \quad k \in Z^+.
\end{aligned} \tag{3}$$

But as far as we all know, there are few results on the existence and global attractivity of positive periodic solutions of model (1) with delays and impulses. Motivated by these facts, we formulate a delayed impulsive Lotka-Volterra model with Holing III type functional response

$$\begin{aligned}
\dot{x} &= x(t) (r_1(t) - b_1(t) x(t - \tau_1(t))) - \frac{c_1(t) x^2(t)}{x^2(t) + K^2} y^m(t), \\
\dot{y} &= y(t) (-r_2(t) - b_2(t) y(t - \tau_2(t))) + \frac{c_2(t) x^2(t)}{x^2(t) + K^2} y^m(t), \\
t &\neq t_k, \quad k \in Z^+, \tag{4}
\end{aligned}$$

$$\Delta x(t) = d_k x(t),$$

$$\Delta y(t) = h_k y(t),$$

$$t = t_k, \quad k \in Z^+,$$

with initial conditions

$$\begin{aligned}
x(t) &= \varphi(t), \quad \varphi \in C([- \tau, 0], R_+), \quad \varphi(0) > 0, \\
y(t) &= \phi(t), \quad \phi \in C([- \tau, 0], R_+), \quad \phi(0) > 0,
\end{aligned} \tag{5}$$

where d_k and h_k represent the regular harvest or death from spraying pesticide of the predator and prey at time t_k , $\tau = \max_{t \in [0, \omega]} \{\tau_1(t), \tau_2(t)\}$. In this paper, Z , Z^+ , and R denote integers, positive integers, and real numbers, respectively, and $R_+ = [0, \infty)$; $r_i(t)$, $b_i(t)$, and $c_i(t)$ ($i = 1, 2$) are continuously nonnegative periodic functions with period $\omega > 0$; $\tau_i(t)$ ($i = 1, 2$) are nonnegative and continuously differentiable periodic functions with period ω on R , and $\min\{1 - \dot{\tau}_i(t)\} > 0$; m and K are positive constants and $m < 1$; x and y satisfy $\Delta x(t) = x(t^+) - x(t) = \lim_{s \rightarrow t^+} x(s) - \lim_{s \rightarrow t^-} x(s)$.

Furthermore, suppose that the following conditions hold.

(H1) There exists an integer $l \geq 1$, such that $[0, \omega] \cap \{t_k\} = \{t_1, t_2, \dots, t_l\}$, $t_{k+l} = t_k + \omega$, and $0 < t_1 < t_2 < \dots < t_k < \dots$ are fixed points with $\lim_{k \rightarrow \infty} t_k = +\infty$.

(H2) $-1 < d_k \leq 0$, $-1 < h_k \leq 0$ are constants, and $d_k = d_{k+l}$, $h_k = h_{k+l}$.

This paper is organized as follows. In Section 2, we introduce some useful lemmas. In Section 3, we not only prove the existence of periodic solutions but also study the permanence and the global attractivity of system (4). In Section 4, two examples are given to illustrate the feasibility of our results by using simulation. The last section is a brief conclusion.

2. Preliminaries

Under the assumptions (H1) and (H2), we consider a new system as follows:

$$\begin{aligned}
\dot{p}(t) &= p(t) [r_1(t) - B_1(t) p(t - \tau_1(t))] \\
&\quad - \frac{C_1(t) p^2(t)}{A p^2(t) + K^2} q^m(t), \\
\dot{q}(t) &= q(t) [-r_2(t) - B_2(t) q(t - \tau_2(t))] \\
&\quad + \frac{C_2(t) p^2(t)}{A p^2(t) + K^2} q^m(t),
\end{aligned} \tag{6}$$

with initial conditions

$$\begin{aligned}
p(t) &= \varphi(t), \quad \varphi \in C([- \tau, 0], R_+), \quad \varphi(0) > 0, \\
q(t) &= \phi(t), \quad \phi \in C([- \tau, 0], R_+), \quad \phi(0) > 0,
\end{aligned} \tag{7}$$

where

$$\begin{aligned}
B_1(t) &= b_1(t) \prod_{0 < t_k < t - \tau_1(t)} (1 + d_k), \\
C_1(t) &= c_1(t) \prod_{0 < t_k < t} (1 + d_k) (1 + h_k)^m, \\
B_2(t) &= b_2(t) \prod_{0 < t_k < t - \tau_2(t)} (1 + h_k), \\
C_2(t) &= c_2(t) \prod_{0 < t_k < t} (1 + d_k)^2 (1 + h_k)^{m-1}, \\
A &= \prod_{0 < t_k < t} (1 + d_k)^2, \quad 0 < A < 1.
\end{aligned} \tag{8}$$

Lemma 1. Suppose that (H1) and (H2) hold; then we have the following.

(i) If $(p(t), q(t))^T$ is a solution of systems (6) and (7), then $(x(t), y(t))^T$ is a solution of systems (4) and (5), where

$$x(t) = \prod_{0 < t_k < t} (1 + d_k) p(t), \quad y(t) = \prod_{0 < t_k < t} (1 + h_k) q(t). \tag{9}$$

(ii) If $(x(t), y(t))^T$ is a solution of systems (4) and (5), then $(p(t), q(t))^T$ is a solution of systems (6) and (7), where

$$\begin{aligned}
p(t) &= \prod_{0 < t_k < t} (1 + d_k)^{-1} x(t), \\
q(t) &= \prod_{0 < t_k < t} (1 + h_k)^{-1} y(t).
\end{aligned} \tag{10}$$

Proof. (i) For any $t \neq t_k, k \in \mathbb{Z}_+$, we have

$$\begin{aligned} & \dot{x}(t) - x(t)(r_1(t) - b_1(t)x(t - \tau_1(t))) + \frac{c_1(t)x^2(t)}{x^2(t) + K^2}y^m(t) \\ &= \prod_{0 < t_k < t} (1 + d_k) \\ & \times \left\{ \dot{p}(t) - p(t) \right. \\ & \times \left(r_1(t) - b_1(t) \prod_{0 < t_k < t - \tau_1(t)} (1 + d_k) p(t - \tau_1(t)) \right) \\ & \left. - \frac{c_1(t) \prod_{0 < t_k < t} (1 + d_k) p^2(t)}{\prod_{0 < t_k < t} (1 + d_k)^2 p^2(t) + K^2} \prod_{0 < t_k < t} (1 + h_k)^m q^m(t) \right\} \\ &= 0. \end{aligned} \quad (11)$$

Similarly, we have

$$\begin{aligned} & \dot{y}(t) - y(t)(-r_2(t) - b_2(t)y(t - \tau_2(t))) \\ & - \frac{c_2(t)x^2(t)}{x^2(t) + K^2}y^m(t) \\ &= \prod_{0 < t_k < t} (1 + h_k) \\ & \times \left\{ \dot{q}(t) - q(t) \right. \\ & \times \left(-r_2(t) - b_2(t) \prod_{0 < t_k < t - \tau_2(t)} (1 + h_k) q(t - \tau_2(t)) \right) \\ & \left. - \frac{c_2(t) \prod_{0 < t_k < t} (1 + d_k)^2 p^2(t)}{\prod_{0 < t_k < t} (1 + d_k)^2 p^2(t) + K^2} \prod_{0 < t_k < t} (1 + h_k)^{m-1} q^m(t) \right\} \\ &= 0. \end{aligned} \quad (12)$$

On the other hand, for any $t = t_k$, by definition, we obtain that

$$\begin{aligned} x(t_k^+) &= \lim_{t \rightarrow t_k^+} \prod_{0 < t_i < t} (1 + d_i) p(t) = \prod_{0 < t_i \leq t_k} (1 + d_i) p(t_k), \\ x(t_k^+) &= \lim_{t \rightarrow t_k^+} \prod_{0 < t_i < t} (1 + h_i) q(t) = \prod_{0 < t_i \leq t_k} (1 + h_i) q(t_k), \end{aligned} \quad (13)$$

and $x(t_k) = \prod_{0 < t_i < t_k} (1 + d_i) p(t_k)$, $y(t_k) = \prod_{0 < t_i < t_k} (1 + h_i) q(t_k)$. Then we get $x(t_k^+) = (1 + d_k)x(t_k)$, $y(t_k^+) = (1 + h_k)y(t_k)$. Hence, $(x(t), y(t))^T$ is a solution of systems (4) and (5).

(ii) $x(t) = \prod_{0 < t_k < t} (1 + d_k) p(t)$ and $y(t) = \prod_{0 < t_k < t} (1 + h_k) q(t)$ are continuous on each interval $(t_k, t_{k+1}]$.

Since $x(t_k^+) = (1 + d_k)x(t_k)$ and $y(t_k^+) = (1 + h_k)y(t_k)$, we have

$$\begin{aligned} p(t_k^+) &= \prod_{0 < t_i \leq t_k} (1 + d_i)^{-1} x(t_k^+) \\ &= \prod_{0 < t_i < t_k} (1 + d_i)^{-1} x(t_k) = p(t_k), \\ p(t_k^+) &= \prod_{0 < t_i \leq t_k} (1 + h_i)^{-1} y(t_k^+) \\ &= \prod_{0 < t_i < t_k} (1 + h_i)^{-1} y(t_k) = q(t_k). \end{aligned} \quad (14)$$

And combining

$$\begin{aligned} p(t_k^-) &= \prod_{0 < t_i \leq t_{k-1}} (1 + d_i)^{-1} x(t_k^-) \\ &= \prod_{0 < t_i < t_k} (1 + d_i)^{-1} x(t_k) = p(t_k), \\ q(t_k^-) &= \prod_{0 < t_i \leq t_{k-1}} (1 + h_i)^{-1} y(t_k^-) \\ &= \prod_{0 < t_i < t_k} (1 + h_i)^{-1} y(t_k) = q(t_k), \end{aligned} \quad (15)$$

we know that $p(t)$ and $q(t)$ are continuous on interval $[-\tau, +\infty)$.

Similarly,

$$\begin{aligned} & \dot{p}(t) - p(t)(r_1(t) - B_1(t)p(t - \tau_1(t))) \\ & + \frac{C_1(t)p^2(t)}{Ap^2(t) + K^2}q^m(t) = 0, \\ & \dot{q}(t) - q(t)(-r_2(t) - B_2(t)q(t - \tau_2(t))) \\ & - \frac{C_2(t)p^2(t)}{Ap^2(t) + K^2}q^m(t) = 0. \end{aligned} \quad (16)$$

Therefore, $(p(t), q(t))^T$ is a solution of systems (6) and (7). \square

From Lemma 1, we notice that if we want to discuss the existence of an ω -periodic solution of systems (4) and (5), we only need to discuss the existence of an ω -periodic solution of systems (6) and (7).

Let X and Y be two normed linear spaces, let $L : \text{Dom } L \subset X \rightarrow Y$ be a linear map, and let $N : X \rightarrow Y$ be a continuous map. If $\dim \text{Ker } L = \text{codim Im } L < +\infty$ and $\text{Im } L$ is closed in Y , then L is called Fredholm operator. If L is a Fredholm operator with index zero, there exist continuous projections $P : X \rightarrow X$ and $Q : Y \rightarrow Y$ such that $\text{Ker } L = \text{Im } P$ and $\text{Ker } Q = \text{Im } L = \text{Im}(I - Q)$. Hence, $L|_{\text{Dom } L \cap \text{Ker } P} : (I - P)X \rightarrow \text{Im } L$ has an inverse mapping K_p . The mapping N is called L -compact on $\overline{\Omega}$, if $\Omega \subset X$ is an open bounded subset, and $QN(\overline{\Omega})$ is bounded, $K_p(I - Q)N : \overline{\Omega} \rightarrow X$ is compact. Since $\text{Ker } L$ is isomorphic to $\text{Im } Q$, there exists an isomorphism $J : \text{Im } Q \rightarrow \text{Ker } L$.

Lemma 2 (see [9], (Continuation Theorem)). *Let both X and Y be Banach spaces; $L : \text{Dom } L \subset X \rightarrow Y$ is a Fredholm operator with index zero; continuous projection $N : \overline{\Omega} \rightarrow Y$ is called L -compact on $\overline{\Omega}$, where Ω is an open bounded subset on X . If all the following conditions hold,*

- (1) *for any $\lambda \in (0, 1)$, each solution of $Lx = \lambda Nx$ satisfies $x \notin \partial\Omega$,*
- (2) *any $x \in \text{Ker } L \cap \partial\Omega$, $QNx \neq 0$,*
- (3) *$\deg\{JQN, \Omega \cap \text{Ker } L, 0\} \neq 0$, where $J : \text{Im } Q \rightarrow \text{Ker } L$ is an isomorphism, then the equation $Lx = Nx$ has at least one solution in $\text{Dom } L \cap \overline{\Omega}$.*

Lemma 3 (see [10]). *If $a > 0$, $b > 0$, and $\dot{x} \leq (\leq)x(a - bx^\gamma)$, where γ is a positive constant, then*

$$\liminf_{t \rightarrow \infty} x(t) \geq \left(\frac{a}{b}\right)^{1/\gamma}, \quad \left(\limsup_{t \rightarrow \infty} x(t) \leq \left(\frac{a}{b}\right)^{1/\gamma}\right). \quad (17)$$

Lemma 4 (see [11]). *If $\tau \in C^1(R, R)$ with $\tau(t + \omega) = \tau(t)$ and $1 - \dot{\tau}(t) > 0$ for any $t \in [0, \omega]$, then function $\mu(t) = t - \tau(t)$ has a unique inverse $\mu^{-1}(t)$ satisfying $\mu \in C(R, R)$ with $\mu^{-1}(s + \omega) = \mu^{-1}(s) + \omega$, for $s \in [0, \omega]$.*

3. Main Results

In order to express the formulas conveniently, we introduce a few concepts

$$\begin{aligned} \bar{f} &= \frac{1}{\omega} \int_0^\omega f(t) dt, & f^L &= \min\{f(t)\}, \\ f^U &= \max\{f(t)\}, & t &\in [0, \omega], \end{aligned} \quad (18)$$

where f is a periodic function with period ω .

Let $(p(t), q(t))^T \in R^2$ be an arbitrary positive solution of systems (6) and (7), for all $t \in R$. Set $u(t) = \ln p(t)$ and $v(t) = \ln q(t)$. Consider the following model:

$$\begin{aligned} \dot{u}(t) &= r_1(t) - B_1(t) e^{u(t-\tau_1(t))} - \frac{C_1(t) e^{u(t)+mv(t)}}{Ae^{2u(t)} + K^2}, \\ \dot{v}(t) &= -r_2(t) - B_2(t) e^{v(t-\tau_2(t))} + \frac{C_2(t) e^{2u(t)+(m-1)v(t)}}{Ae^{2u(t)} + K^2}. \end{aligned} \quad (19)$$

Apparently, if system (19) has an ω -periodic solution $(u(t), v(t))^T$, then $(p(t), q(t))^T = (e^{u(t)}, e^{v(t)})^T$ is an ω -periodic solution of systems (6) and (7). Hence, we only need to show that system (19) has an ω -periodic solution.

Set

$$\begin{aligned} X &= Y \\ &= \{z(t) = (u(t), v(t))^T \in C(R, R^2) \mid z(t + \omega) = z(t)\}, \end{aligned} \quad (20)$$

where $C(R, R^2) = \{z : R \rightarrow R^2 \mid z \text{ is continuous at } t \neq t_k, z(t_k^+), z(t_k^-) = z(t_k) \text{ exist}\}$ and the norm $\|z\| = \|(u(t), v(t))^T\| = \max\{|u(t)| + |v(t)|\}$, $t \in [0, \omega]$. Then both X and Y are Banach spaces.

Define operators L , P , and Q as follows, respectively:

$$\begin{aligned} L : \text{Dom } L \subset X &\longrightarrow Y, & Lz &= \dot{z}; \\ P(z) &= \frac{1}{\omega} \int_0^\omega z(t) dt; & Q(z) &= \frac{1}{\omega} \int_0^\omega z(t) dt. \end{aligned} \quad (21)$$

Define $N : X \rightarrow Y$, satisfying

$$Nz = \begin{pmatrix} r_1(t) - B_1(t) e^{u(t-\tau_1(t))} - \frac{C_1(t) e^{u(t)+mv(t)}}{Ae^{2u(t)} + K^2} \\ -r_2(t) - B_2(t) e^{v(t-\tau_2(t))} + \frac{C_2(t) e^{2u(t)+(m-1)v(t)}}{Ae^{2u(t)} + K^2} \end{pmatrix}. \quad (22)$$

Note that $\text{Ker } L = R^2$, $\dim \text{Ker } L = \text{codim Im } L = 2$, and $\text{Im } L = \{z \in Y \mid \int_0^\omega z(t) dt = 0\}$ is closed in Y and P and Q are continuous maps satisfying $\text{Ker } L = \text{Im } P$ and $\text{Ker } Q = \text{Im } L = \text{Im}(I - Q)$. Hence, L is a Fredholm operator with index zero. It implies that L has a unique inverse $K_P : \text{Im } P \rightarrow \text{Dom } L \cap \text{Ker } P$. So we have

$$K_P(z) = \int_0^t z(s) ds - \frac{1}{\omega} \int_0^\omega \int_0^t z(s) ds dt. \quad (23)$$

By a straightforward calculation, we get

$$QNz = \begin{pmatrix} \frac{1}{\omega} \int_0^\omega \left[r_1(t) - B_1(t) e^{u(t-\tau_1(t))} - \frac{C_1(t) e^{u(t)+mv(t)}}{Ae^{2u(t)} + K^2} \right] dt \\ \frac{1}{\omega} \int_0^\omega \left[-r_2(t) - B_2(t) e^{v(t-\tau_2(t))} + \frac{C_2(t) e^{2u(t)+(m-1)v(t)}}{Ae^{2u(t)} + K^2} \right] dt \end{pmatrix},$$

$$K_P(I - Q)Nz = \begin{pmatrix} \int_0^t \left[r_1(s) - B_1(s) e^{u(s-\tau_1(s))} - \frac{C_1(s) e^{u(s)+mv(s)}}{Ae^{2u(s)} + K^2} \right] ds \\ \int_0^t \left[-r_2(s) - B_2(s) e^{v(s-\tau_2(s))} + \frac{C_2(s) e^{2u(s)+(m-1)v(s)}}{Ae^{2u(s)} + K^2} \right] ds \end{pmatrix} - E + F(t), \quad (24)$$

where

$$E = \begin{pmatrix} \frac{1}{\omega} \int_0^\omega \int_0^t \left[r_1(s) - B_1(s) e^{u(s-\tau_1(s))} - \frac{C_1(s) e^{u(s)+mv(s)}}{Ae^{2u(s)} + K^2} \right] ds dt \\ \frac{1}{\omega} \int_0^\omega \int_0^t \left[-r_2(s) - B_2(s) e^{v(s-\tau_2(s))} + \frac{C_2(s) e^{2u(s)+(m-1)v(s)}}{Ae^{2u(s)} + K^2} \right] ds dt \end{pmatrix}, \quad (25)$$

$$F(t) = \begin{pmatrix} \left(\frac{1}{2} - \frac{t}{\omega} \right) \int_0^\omega \left[r_1(s) - B_1(s) e^{u(s-\tau_1(s))} - \frac{C_1(s) e^{u(s)+mv(s)}}{Ae^{2u(s)} + K^2} \right] ds \\ \left(\frac{1}{2} - \frac{t}{\omega} \right) \int_0^\omega \left[-r_2(s) - B_2(s) e^{v(s-\tau_2(s))} + \frac{C_2(s) e^{2u(s)+(m-1)v(s)}}{Ae^{2u(s)} + K^2} \right] ds \end{pmatrix}.$$

By the Lebesgue Convergence Theorem, it is not difficult to notice that QN and $K_P(I - Q)N$ are continuous. By applying the Arzela-Ascoli Theorem, we know that the operator $QN(\bar{\Omega})$ is bounded and $K_P(I - Q)N(\bar{\Omega})$ is compact, for any open set $\Omega \in X$. Therefore, $N \in \Omega$ is L -compact on $\bar{\Omega}$.

In order to use Lemma 2, we need to find an appropriate open and bounded set Ω .

Theorem 5. Assume the following.

(i) $\bar{C}_2 > A(\bar{r}_2 + \Delta_2^U)$, where $\Delta_2 = B_2(\mu_2^{-1}(t))/(1 - \dot{\tau}_2(\mu_2^{-1}(t)))$, $\min\{1 - \dot{\tau}_2(t)\} > 0$.

(ii) The following algebraic equation set

$$\begin{aligned} \bar{r}_1 - \bar{B}_1 e^{u(t)} - \frac{\bar{C}_1 e^{u(t)+mv(t)}}{Ae^{2u(t)} + K^2} &= 0, \\ -\bar{r}_2 - \bar{B}_2 e^{v(t)} + \frac{\bar{C}_2 e^{2u(t)+(m-1)v(t)}}{Ae^{2u(t)} + K^2} &= 0, \end{aligned} \quad (26)$$

has finite solutions $(u_i^*(t), v_i^*(t))$, $i = 1, 2, \dots, n$, and then systems (6) and (7) have at least one ω -periodic solution.

Proof. Considering the operator equation $Lz = \lambda Nz$, $\lambda \in (0, 1)$, we have

$$\begin{aligned} \dot{u}(t) &= \lambda \left[r_1(t) - B_1(t) e^{u(t-\tau_1(t))} - \frac{C_1(t) e^{u(t)+mv(t)}}{Ae^{2u(t)} + K^2} \right], \\ \dot{v}(t) &= \lambda \left[-r_2(t) - B_2(t) e^{v(t-\tau_2(t))} + \frac{C_2(t) e^{2u(t)+(m-1)v(t)}}{Ae^{2u(t)} + K^2} \right]. \end{aligned} \quad (27)$$

Integrating (27) on the interval $[0, \omega]$, we have

$$\bar{r}_1 \omega = \int_0^\omega \left[B_1(t) e^{u(t-\tau_1(t))} + \frac{C_1(t) e^{u(t)+mv(t)}}{Ae^{2u(t)} + K^2} \right] dt, \quad (28)$$

$$\bar{r}_2 \omega + \int_0^\omega B_2(t) e^{v(t-\tau_2(t))} dt = \int_0^\omega \frac{C_2(t) e^{2u(t)+(m-1)v(t)}}{Ae^{2u(t)} + K^2} dt,$$

yielding

$$\int_0^\omega |\dot{u}(t)| dt \leq 2\bar{r}_1 \omega, \quad (29)$$

$$\int_0^\omega |\dot{v}(t)| dt \leq 2 \left(\bar{r}_2 \omega + \int_0^\omega B_2(t) e^{v(t-\tau_2(t))} dt \right).$$

In view of Lemma 4, we obtain that

$$\begin{aligned} \int_0^\omega B_1(t) e^{u(t-\tau_1(t))} dt &= \int_0^\omega \frac{B_1(\mu_1^{-1}(t)) e^{u(t)}}{1 - \dot{\tau}_1(\mu_1^{-1}(t))} dt, \\ \int_0^\omega B_2(t) e^{v(t-\tau_2(t))} dt &= \int_0^\omega \frac{B_2(\mu_2^{-1}(t)) e^{v(t)}}{1 - \dot{\tau}_2(\mu_2^{-1}(t))} dt, \end{aligned} \quad (30)$$

which together with (28) give

$$\bar{r}_1 \omega = \int_0^\omega \left[\frac{B_1(\mu_1^{-1}(t)) e^{u(t)}}{1 - \dot{\tau}_1(\mu_1^{-1}(t))} + \frac{C_1(t) e^{u(t)+mv(t)}}{Ae^{2u(t)} + K^2} \right] dt, \quad (31)$$

$$\bar{r}_2 \omega + \int_0^\omega \frac{B_2(\mu_2^{-1}(t)) e^{v(t)}}{1 - \dot{\tau}_2(\mu_2^{-1}(t))} dt = \int_0^\omega \frac{C_2(t) e^{2u(t)+(m-1)v(t)}}{Ae^{2u(t)} + K^2} dt. \quad (32)$$

From (31), we have

$$\int_0^\omega e^{u(t)} dt \leq \frac{\bar{r}_1 \omega}{\Delta_1^L} \equiv \omega N_1, \quad (33)$$

where $\Delta_1 = B_1(\mu_1^{-1}(t))e^{u(t)}/(1 - \dot{\tau}_1(\mu_1^{-1}(t)))$.

Multiplying the first equation of system (27) by $e^{u(t)}$ and the second one by $e^{v(t)}$ and integrating them on $[0, \omega]$, we get

$$\begin{aligned} \int_0^\omega r_1(t) e^{u(t)} dt \\ = \int_0^\omega \frac{B_1(\mu_1^{-1}(t)) e^{2u(t)}}{1 - \dot{\tau}_1(\mu_1^{-1}(t))} dt + \int_0^\omega \frac{C_1(t) e^{2u(t)+mv(t)}}{Ae^{2u(t)} + K^2} dt, \end{aligned} \quad (34)$$

$$\begin{aligned} \int_0^\omega r_2(t) e^{v(t)} dt + \int_0^\omega \frac{B_2(\mu_2^{-1}(t)) e^{2v(t)}}{1 - \dot{\tau}_2(\mu_2^{-1}(t))} dt \\ = \int_0^\omega \frac{C_2(t) e^{2u(t)+mv(t)}}{Ae^{2u(t)} + K^2} dt, \end{aligned} \quad (35)$$

which imply that

$$\int_0^\omega \frac{e^{2u(t)+mv(t)}}{Ae^{2u(t)} + K^2} dt \leq \frac{r_1^U}{C_1^L} \int_0^\omega e^{u(t)} dt, \quad (36)$$

$$\int_0^\omega e^{v(t)} dt \leq \frac{C_2^U}{r_2^L} \int_0^\omega \frac{e^{2u(t)+mv(t)}}{Ae^{2u(t)} + K^2} dt \leq \frac{r_1^U C_2^U \omega N_1}{r_2^L C_1^L} \equiv \omega N_2. \quad (37)$$

If $v(t) \geq 0$, then $e^{v(t)} \geq 1$ and $N_2 \geq (1/\omega) \int_0^\omega e^{v(t)} dt \geq 1$, which implies that there must be a constant $\eta_1 \in [0, \omega]$ such that $v(\eta_1) \leq \ln N_2$. From (33) and (37),

$$N_1 \geq \frac{1}{\omega} \int_0^\omega e^{u(t)} dt \geq \frac{r_2^L C_1^L}{r_1^U C_2^U \omega} \int_0^\omega e^{v(t)} dt \geq \frac{r_2^L C_1^L}{r_1^U C_2^U}; \quad (38)$$

then there exists a constant $\xi_1 \in [0, \omega]$ such that $u(\xi_1) \leq \max\{|\ln N_1|, |\ln(r_2^L C_1^L / r_1^U C_2^U)|\}$.

On the other hand, it follows from (35) and the Hölder inequality that

$$r_2^L \omega \leq \frac{C_2^U}{A} \int_0^\omega e^{mv(t)} dt \leq \frac{C_2^U}{A} \omega^{1-m} \left(\int_0^\omega e^{v(t)} dt \right)^m; \quad (39)$$

that is

$$\int_0^\omega e^{v(t)} dt \geq \left(\frac{r_2^L \omega A}{C_2^U \omega^{1-m}} \right)^{1/m} \equiv \omega N_3. \quad (40)$$

Since $v(t) \geq 0$ and $m < 1$, then $0 < e^{(m-1)v(t)} < 1$ and $e^{v(t)} \geq 1$.

From (32), $\bar{r}_2 \omega + \Delta_2^L \omega \leq (C_2^U / K^2) \int_0^\omega e^{2u(t)} dt$, that is,

$$\int_0^\omega e^{2u(t)} dt \geq \frac{(\bar{r}_2 + \Delta_2^L) \omega K^2}{C_2^U} \equiv \omega N_4. \quad (41)$$

If $v(t) < 0$, then $0 < e^{mv(t)} < 1$, $0 < e^{v(t)} < 1$, and $e^{(m-1)v(t)} > 1$.

From (31), we obtain that

$$\begin{aligned} \bar{r}_1 \omega &\leq \Delta_1^U \int_0^\omega e^{u(t)} dt + \frac{C_1^U}{K^2} \int_0^\omega e^{u(t)+mv(t)} dt \\ &\leq \Delta_1^U \int_0^\omega e^{u(t)} dt + \frac{C_1^U}{K^2} \int_0^\omega e^{u(t)} dt, \end{aligned} \quad (42)$$

that is,

$$\int_0^\omega e^{u(t)} dt \geq \frac{\bar{r}_1 \omega K^2}{\Delta_1^U K^2 + C_1^U} \equiv \omega N_5. \quad (43)$$

Together with (33) and (41), we notice that there exists a constant $\xi_2 \in [0, \omega]$ such that

$$u(\xi_2) \leq \max \left\{ |\ln N_1|, \left| \ln \frac{r_2^L C_1^L}{r_1^U C_2^U} \right|, \frac{1}{2} |\ln N_4|, |\ln N_5| \right\} \equiv A_1. \quad (44)$$

Furthermore, according to the condition $\bar{C}_2 > A(\bar{r}_2 + \Delta_2^U)$ and (32), we have

$$\begin{aligned} \int_0^\omega C_2(t) e^{(m-1)v(t)} dt - A \left(\bar{r}_2 \omega + \int_0^\omega \frac{B_2(\mu_2^{-1}(t)) e^{v(t)}}{1 - \dot{\tau}_2(\mu_2^{-1}(t))} dt \right) \\ = \int_0^\omega \frac{K^2 C_2(t) e^{(m-1)v(t)}}{Ae^{2u(t)} + K^2} dt; \end{aligned} \quad (45)$$

then

$$\begin{aligned} 0 < \omega (\bar{C}_2 - A\bar{r}_2 - A\Delta_2^U) &\leq \frac{K^2 C_2^U}{A} \int_0^\omega \frac{e^{(m-1)v(t)}}{e^{2u(t)}} dt \\ &\leq \frac{K^2 C_2^U \omega^{3/2}}{A} \frac{\left[\int_0^\omega e^{2(m-1)v(t)} dt \right]^{1/2}}{\left[\int_0^\omega e^{u(t)} dt \right]^2} \\ &\leq \frac{K^2 C_2^U \omega^{3/2}}{A \omega^2 N_5^2} \left[\int_0^\omega e^{2(m-1)v(t)} dt \right]^{1/2}, \end{aligned} \quad (46)$$

that is

$$\int_0^\omega e^{2(m-1)v(t)} dt \geq \left(\frac{\omega^{3/2} N_5^2 A (\bar{C}_2 - A\bar{r}_2 - A\Delta_2^U)}{K^2 C_2^U} \right)^2 \equiv \omega N_6. \quad (47)$$

We can find a constant $\eta_2 \in [0, \omega]$ such that

$$v(\eta_2) \leq \max \left\{ |\ln N_2|, |\ln N_3|, \left| \frac{\ln N_6}{2(m-1)} \right| \right\} \equiv A_2. \quad (48)$$

Hence, (19), (44), and (48) combine together to make us know that

$$\begin{aligned} |u(t)| &\leq |u(\xi_2)| + \frac{1}{2} \int_0^\omega |\dot{u}(t)| dt \leq A_1 + \bar{r}_1 \omega \equiv D_1, \\ |v(t)| &\leq |v(\eta_2)| + \frac{1}{2} \int_0^\omega |\dot{v}(t)| dt \\ &\leq A_2 + \bar{r}_2 \omega + \Delta_2^U \omega e^{A_2} \equiv D_2. \end{aligned} \quad (49)$$

Consider the algebraic equation set

$$\begin{aligned} \bar{r}_1 - \bar{B}_1 e^{u(t)} - \frac{\bar{C}_1 e^{u(t)+mv(t)}}{Ae^{2u(t)} + K^2} &= 0, \\ -\bar{r}_2 - \bar{B}_2 e^{v(t)} + \frac{\bar{C}_2 e^{2u(t)+(m-1)v(t)}}{Ae^{2u(t)} + K^2} &= 0. \end{aligned} \quad (50)$$

From the assumption, there exist finite solutions $(u_i^*(t), v_i^*(t))$, $i = 1, 2, \dots, n$, of the above system. By simple computing, we can get its Jacobian matrix

$$G(u, v) = \begin{pmatrix} -\bar{B}_1 e^u - \frac{\bar{C}_1 e^{u+mv}}{Ae^{2u} + K^2} + \frac{2Ae^{3u+mv}}{(Ae^{2u} + K^2)^2} & -\frac{m\bar{C}_1 e^{u+mv}}{Ae^{2u} + K^2} \\ \frac{2\bar{C}_2 e^{2u+(m-1)v}}{Ae^{2u} + K^2} - \frac{2A\bar{C}_2 e^{4u+(m-1)v}}{(Ae^{2u} + K^2)^2} & -\bar{B}_2 e^v + \frac{(m-1)\bar{C}_2 e^{2u+(m-1)v}}{Ae^{2u} + K^2} \end{pmatrix}, \quad (51)$$

obviously $\det(G(u, v)) > 0$.

Set $W = A_1 + A_2 + \delta$ and $\Omega = \{z \in X \mid \|z\| < W\}$, $z(t_k^+) \in \Omega$, where δ is a large enough number satisfying $|u_i^*| + |v_i^*| < \delta$. If $z \in \partial\Omega \cap \text{Ker } L = \partial\Omega \cap R^2$, then z satisfies

$$QNz = \begin{pmatrix} \bar{r}_1 - \bar{B}_1 e^{u(t)} - \frac{\bar{C}_1 e^{u(t)+mv(t)}}{Ae^{2u(t)} + K^2} \\ -\bar{r}_2 - \bar{B}_2 e^{v(t)} + \frac{\bar{C}_2 e^{2u(t)+(m-1)v(t)}}{Ae^{2u(t)} + K^2} \end{pmatrix} \neq 0, \quad (52)$$

and $\deg(JQNz, \Omega \cap \text{Ker } L, 0) = \sum_{i=1}^n \text{sign}(\det G(u_i^*, v_i^*)) = n \neq 0$, where $J : \text{Im } Q \rightarrow \text{Ker } L$ is an isomorphism. Hence, Ω is a bounded open set. System (19) has at least one ω -periodic solution $(u^*(t), v^*(t))^T$ in $\text{Dom } L \cap \bar{\Omega}$; that is, system (6) has at least one ω -periodic solution $(e^{u^*(t)}, e^{v^*(t)})^T$. \square

Corollary 6. Suppose that Theorem 5 holds; system (4) also has at least one ω -periodic solution $(x^*(t), y^*(t)) = (\prod_{0 < t_k < t} (1 + d_k) e^{u^*(t)}, \prod_{0 < t_k < t} (1 + h_k) e^{v^*(t)})$.

Now, we discuss the permanence of models (6) and (7). Before the main results, we give the definition of permanence.

Definition 7. System (6) is permanent, if there exist positive constants m_i, M_i ($0 < m_i < M_i$, $i = 1, 2$) and time $t_0 > 0$ such that any solution of system (6) with initial condition (7) satisfies $m_i \leq x_i(t) \leq M_i$ for all $t \geq t_0$.

Denote

$$\begin{aligned} M_1 &= \frac{r_1^U e^{r_1^U \tau}}{B_1^L}, \\ m_1 &= \left(\frac{r_1^L}{B_1^U} - \frac{C_1^U M_2^m M_1}{B_1^U K^2} \right) \\ &\quad \times \exp \left\{ \left(r_1^L - B_1^U M_1 - \frac{C_1^U M_2^m M_1}{K^2} \right) \tau \right\}, \end{aligned}$$

$$\begin{aligned} M_2 &= \left[\frac{C_2^U}{A r_2^L} + c \right]^{1/(1-m)}, \\ m_2 &= \left[\frac{C_2^L m_1^2 (r_2^U + B_2^U M_2)^{-1}}{(A M_1^2 + K^2)} - c \right]^{1/(1-m)}. \end{aligned} \quad (53)$$

Theorem 8. If $r_1^L - C_1^U M_1 M_2^m / K^2 > 0$, then system (6) is permanent.

Proof. From the first equation of model (6), we have $\dot{p}(t) \leq r_1(t)p(t)$, integrating it on interval $[t - \tau_1(t), t]$,

$$\begin{aligned} p(t) &\leq p(t - \tau_1(t)) e^{\int_{t-\tau_1(t)}^t r_1(s) ds} \leq p(t - \tau_1(t)) e^{r_1^U \tau_1(t)} \\ &\leq p(t - \tau_1(t)) e^{r_1^U \tau}, \quad t > \tau; \end{aligned} \quad (54)$$

then we get

$$\dot{p}(t) \leq p(t) \left[r_1^U - B_1^L e^{-r_1^U \tau} p(t) \right], \quad t > \tau. \quad (55)$$

According to Lemma 3, we have $\lim_{t \rightarrow \infty} \sup p(t) \leq r_1^U e^{r_1^U \tau} / B_1^L \equiv M_1$, $t > \tau$, and then there exists a sufficiently large time $t_1 > \tau$ such that $p(t) \leq M_1$ for all $t > t_1$.

At the same time, we can find time $t_2 = t_1 + \tau$ such that $p(t - \tau_1(t)) \leq M_1$ for $t > t_2$.

From the second equation of model (6), we have

$$\dot{q}(t) \leq -r_2^L q(t) + \frac{C_2^U}{A} q^m(t) = q^m(t) \left(\frac{C_2^U}{A} - r_2^L q^{1-m}(t) \right); \quad (56)$$

that is,

$$\frac{d(q^{1-m}(t))}{dt} \leq (1-m) \left(\frac{C_2^U}{A} - r_2^L q^{1-m}(t) \right). \quad (57)$$

By solving equation, we obtain that

$$q^{1-m}(t) \leq \left[\frac{C_2^U}{Ar_2^L} + \left(q^{1-m}(0) - \frac{C_2^U}{Ar_2^L} \right) e^{-r_2^L(1-m)t} \right]; \quad (58)$$

then there must be $t_3 > t_2$ such that $q(t) \leq [C_2^U/Ar_2^L + c]^{1/(1-m)} \equiv M_2$ for all $t > t_3$, where c is a constant.

Further, there exists time $t_4 = t_3 + \tau$ such that $q(t - \tau_2(t)) \leq M_2$ for all $t > t_4$. In view of the first equation of model (6), we have

$$\dot{p}(t) \geq p(t) \left(r_1^L - B_1^U p(t - \tau_1(t)) - \frac{C_1^U M_2^m M_1}{K^2} \right), \quad t > t_4. \quad (59)$$

Assume that $p(\hat{t})$ is local minimal value of system (59); then $\dot{p}(\hat{t}) = 0$. Thus, we have that

$$r_1^L - B_1^U p(\hat{t} - \tau_1(\hat{t})) - \frac{C_1^U M_2^m M_1}{K^2} \leq 0, \quad t > t_4, \quad (60)$$

that is,

$$p(\hat{t} - \tau_1(\hat{t})) \geq \frac{r_1^L}{B_1^U} - \frac{C_1^U M_2^m M_1}{B_1^U K^2}. \quad (61)$$

Integrating (59) on $[\hat{t} - \tau_1(\hat{t}), \hat{t}]$ and noticing that

$$\begin{aligned} & \ln \frac{p(\hat{t})}{p(\hat{t} - \tau_1(\hat{t}))} \\ & \geq \int_{\hat{t} - \tau_1(\hat{t})}^{\hat{t}} \left(r_1^L - B_1^U p(t - \tau_1(t)) - \frac{C_1^U M_2^m M_1}{K^2} \right) dt \quad (62) \\ & \geq \left(r_1^L - B_1^U M_1 - \frac{C_1^U M_2^m M_1}{K^2} \right) \tau, \end{aligned}$$

we can easily get that

$$\begin{aligned} p(\hat{t}) & \geq \left(\frac{r_1^L}{B_1^U} - \frac{C_1^U M_2^m M_1}{B_1^U K^2} \right) \\ & \times \exp \left\{ \left(r_1^L - B_1^U M_1 - \frac{C_1^U M_2^m M_1}{K^2} \right) \tau \right\} \equiv m_1. \end{aligned} \quad (63)$$

Thus, there must be a large enough time $t_5 > t_4$ such that $p(t) \geq p(\hat{t}) \geq m_1$ for $t > t_5$.

In view of the second equation of system (6), we have

$$\dot{q}(t) \geq q^m(t) \left[\frac{C_2^L m_1^2}{AM_1^2 + K^2} - (r_2^U + B_2^U M_2) q^{1-m}(t) \right], \quad (64)$$

$$t > t_5.$$

Similarly, by solving the equation, we obtain that

$$\begin{aligned} & q^{1-m}(t) \\ & \geq \frac{C_2^L m_1^2 (r_2^U + B_2^U M_2)^{-1}}{(AM_1^2 + K^2)} \\ & + \left(q^{1-m}(0) - \frac{C_2^L m_1^2 (r_2^U + B_2^U M_2)^{-1}}{(AM_1^2 + K^2)} \right) e^{(m-1)(r_2^U + B_2^U M_2)t}. \end{aligned} \quad (65)$$

For the above constant c , we can seek time $t_6 > t_5$ such that, for $t > t_6$,

$$q(t) \geq \left[\frac{C_2^L m_1^2 (r_2^U + B_2^U M_2)^{-1}}{(AM_1^2 + K^2)} - c \right]^{1/(1-m)} \equiv m_2. \quad (66)$$

In summary, $m_1 \leq p(t) \leq M_1$ and $m_2 \leq q(t) \leq M_2$ for $t > t_6$. Therefore, system (6) is permanent. \square

Theorem 9. If $r_1^L - C_1^U M_1 M_2^m / K^2 > 0$, then system (4) is permanent and enters eventually into the region D , where

$$\begin{aligned} D = \left\{ (x(t), y(t)) \mid x(t) \in \left(\prod_{0 < t_k < t} (1 + d_k) m_1, \right. \right. \\ \left. \prod_{0 < t_k < t} (1 + d_k) M_1 \right), \\ y(t) \in \left(\prod_{0 < t_k < t} (1 + h_k) m_2, \right. \\ \left. \prod_{0 < t_k < t} (1 + h_k) M_2 \right) \Big\}. \end{aligned} \quad (67)$$

Corollary 10. If $r_1^L - C_1^U M_1 M_2^m / K^2 > 0$, then systems (6) and (7) have a positive ω -periodic solution.

Definition 11. System (6) is globally attractive, if

$$\lim_{t \rightarrow +\infty} (|p(t) - p_*(t)| + |q(t) - q_*(t)|) = 0, \quad (68)$$

for any two positive solutions $(p(t), q(t))$ and $(p_*(t), q_*(t))$ of systems (6) and (7).

Theorem 12. If system (6) satisfies $r_1^L - C_1^U M_1 M_2^m / K^2 > 0$, $\liminf_{t \rightarrow +\infty} \Phi(t) > 0$, and $\liminf_{t \rightarrow +\infty} \Psi(t) > 0$, then system (6) is globally attractive, where

$$\begin{aligned} \Phi(t) & = \alpha B_1(t) - \frac{\alpha A C_1(t) M_1^2 M_2^m}{(A m_1^2 + K^2)^2} - \frac{2 K^2 C_2(t) M_1 M_2^{m-1}}{(A m_1^2 + K^2)^2} \\ & - \int_t^{\mu_1^{-1}(t)} B_1(\xi) d\xi \end{aligned}$$

$$\begin{aligned}
& \cdot \left[\alpha \left(r_1(t) + B_1(t) M_1 + \frac{C_1(t) M_1 M_2^m}{A m_1^2 + K^2} \right) \right. \\
& \quad + \frac{\alpha C_1(t) M_1 M_2^m (A M_1^2 + K^2)}{(A m_1^2 + K^2)^2} \\
& \quad \left. + \frac{2 K^2 C_2(t) M_1 M_2^m}{(A m_1^2 + K^2)^2} + \frac{\alpha M_1 B_1(\mu_1^{-1}(t))}{1 - \dot{\tau}_1(\mu_1^{-1}(t))} \right], \\
\Psi(t) &= B_2(t) - \frac{\alpha C_1(t) M_1 m m_2^{m-1}}{A m_1^2 + K^2} - \int_t^{\mu_1^{-1}(t)} B_1(\xi) d\xi \\
& \cdot \left[\frac{\alpha C_1(t) M_1^2 m m_2^{m-1}}{A m_1^2 + K^2} + r_2(t) + B_2(t) M_2 \right. \\
& \quad + \frac{C_2(t) M_1^2 M_2^{m-1}}{A m_1^2 + K^2} + \frac{C_2(t) M_1^2 M_2 (1-m) m_2^{m-2}}{A m_1^2 + K^2} \Big] \\
& - \frac{M_2 B_2(\mu_2^{-1}(t))}{1 - \dot{\tau}_2(\mu_2^{-1}(t))} \int_{\mu_2^{-1}(t)}^{\mu_2^{-1}(\mu_2^{-1}(t))} B_2(\xi) d\xi.
\end{aligned} \tag{69}$$

Proof. Assume $(p(t), q(t))$ and $(p_*(t), q_*(t))$ are two positive solutions of systems (6) and (7). According to Theorem 8, there exist two positive constants m_i, M_i ($0 < m_i < M_i$, $i = 1, 2$) and t_6 such that, for $t > t_6$,

$$\begin{aligned}
m_1 &\leq p(t), & p_*(t) &\leq M_1, \\
m_2 &\leq q(t), & q_*(t) &\leq M_2.
\end{aligned} \tag{70}$$

Define a function

$$V_1(t) = \alpha |\ln p(t) - \ln p_*(t)| + |\ln q(t) - \ln q_*(t)|, \quad t > t_6. \tag{71}$$

By calculating its upper right derivative along the solution of system (6), we get that

$$\begin{aligned}
D^+ V_1(t) &= \alpha \operatorname{sign}(p(t) - p_*(t)) \left[\frac{\dot{p}(t)}{p(t)} - \frac{\dot{p}_*(t)}{p_*(t)} \right] \\
& \quad + \operatorname{sign}(q(t) - q_*(t)) \left[\frac{\dot{q}(t)}{q(t)} - \frac{\dot{q}_*(t)}{q_*(t)} \right] \\
&= \alpha \operatorname{sign}(p(t) - p_*(t)) \\
& \quad \times \left\{ B_1(t) [p_*(t - \tau_1(t)) - p(t - \tau_1(t))] \right. \\
& \quad \left. + C_1(t) \left(\frac{p_*(t) q_*(t)}{A p_*^2(t) + K^2} - \frac{p(t) q(t)}{A p^2(t) + K^2} \right) \right\} \\
& \quad + \operatorname{sign}(q(t) - q_*(t))
\end{aligned}$$

$$\begin{aligned}
& \times \left\{ B_2(t) [q_*(t - \tau_2(t)) - q(t - \tau_2(t))] \right. \\
& \quad \left. + C_2(t) \left(\frac{p^2(t) q^{m-1}(t)}{A p^2(t) + K^2} - \frac{p_*^2(t) q_*^{m-1}(t)}{A p_*^2(t) + K^2} \right) \right\} \\
&\leq -\alpha B_1(t) |p(t) - p_*(t)| \\
& \quad + \alpha B_1(t) \int_{t-\tau_1(t)}^t |\dot{p}(s) - \dot{p}_*(s)| ds \\
& \quad + \frac{\alpha C_1(t) p_*(t)}{A p_*^2(t) + K^2} |q^m(t) - q_*^m(t)| \\
& \quad + \frac{\alpha A C_1(t) p(t) p_*(t) q^m(t)}{(A p_*^2(t) + K^2)(A p^2(t) + K^2)} |p(t) - p_*(t)| \\
& \quad - B_2(t) |q(t) - q_*(t)| \\
& \quad + B_2(t) \int_{t-\tau_2(t)}^t |\dot{q}(s) - \dot{q}_*(s)| ds \\
& \quad + \frac{K^2 C_2(t) q_*^{m-1}(t) (p(t) + p_*(t))}{(A p_*^2(t) + K^2)(A p^2(t) + K^2)} |p(t) - p_*(t)|,
\end{aligned} \tag{72}$$

where

$$\begin{aligned}
& \int_{t-\tau_1(t)}^t |\dot{p}(s) - \dot{p}_*(s)| ds \\
&= \int_{t-\tau_1(t)}^t \left| \left[r_1(s) - B_1(s) p(s - \tau_1(s)) - \frac{C_1(s) p(s)}{A p^2(s) + K^2} q^m(s) \right] \right. \\
& \quad \times (p(s) - p_*(s)) \\
& \quad + p_*(s) B_1(s) [p_*(s - \tau_1(s)) - p(s - \tau_1(s))] \\
& \quad \left. + p_*(s) C_1(s) \left[\frac{p_*(s) q_*^m(s)}{A p_*^2(s) + K^2} - \frac{p(s) q^m(s)}{A p^2(s) + K^2} \right] \right| ds \\
&\leq \int_{t-\tau_1(t)}^t \left\{ \left[r_1(s) + B_1(s) p(s - \tau_1(s)) + \frac{C_1(s) p(s) q^m(s)}{A p^2(s) + K^2} \right] \right. \\
& \quad \times |p(s) - p_*(s)| \\
& \quad + B_1(s) p_*(s) |p_*(s - \tau_1(s)) - p(s - \tau_1(s))| \\
& \quad + \frac{C_1(s) p_*^2(s)}{A p_*^2(s) + K^2} |q^m(s) - q_*^m(s)| \\
& \quad + \frac{C_1(s) p_*(s) q^m(s) (A p_*(s) p(s) + K^2)}{(A p_*^2(s) + K^2)(A p^2(s) + K^2)} \\
& \quad \left. \times |p(s) - p_*(s)| \right\} ds, \\
& \int_{t-\tau_2(t)}^t |\dot{q}(s) - \dot{q}_*(s)| ds
\end{aligned}$$

$$\begin{aligned}
&= \int_{t-\tau_2(t)}^t \left\| \left[-r_2(s) - B_2(s) q(s - \tau_2(s)) \right. \right. \\
&\quad \left. \left. + \frac{C_2(s) p^2(s)}{Ap^2(s) + K^2} q^{m-1}(s) \right] \right. \\
&\quad \times (q(s) - q_*(s)) \\
&\quad + q_*(s) B_2(s) [q_*(s - \tau_2(s)) - q(s - \tau_2(s))] \\
&\quad + q_*(s) C_2(s) \\
&\quad \times \left[\frac{p^2(s) q^{m-1}(s)}{Ap^2(s) + K^2} - \frac{p_*^2(s) q_*^{m-1}(s)}{Ap_*^2(s) + K^2} \right] \Big\| ds \\
&\leq \int_{t-\tau_2(t)}^t \left\{ \left[r_2(s) + B_2(s) q(s - \tau_2(s)) \right. \right. \\
&\quad \left. \left. + \frac{C_2(s) p^2(s) q^{m-1}(s)}{Ap^2(s) + K^2} \right] \right. \\
&\quad \times |q(s) - q_*(s)| \\
&\quad + q_*(s) B_2(s) |q_*(s - \tau_2(s)) - q(s - \tau_2(s))| \\
&\quad + \frac{C_2(s) p^2(s) q_*(s)}{Ap^2(s) + K^2} |q^{m-1}(s) - q_*^{m-1}(s)| \\
&\quad + \frac{K^2 C_2(s) q_*^m(s) (p_*(s) + p(s))}{(Ap_*^2(s) + K^2)(Ap^2(s) + K^2)} \\
&\quad \times |p(s) - p_*(s)| \Big\} ds.
\end{aligned} \tag{73}$$

Thus, for $t > t_6$,

$$\begin{aligned}
&D^+ V_1(t) \\
&\leq -\alpha B_1(t) |p(t) - p_*(t)| \\
&\quad + \alpha B_1(t) \\
&\quad \times \int_{t-\tau_1(t)}^t \left\{ \left[r_1(s) + B_1(s) M_1 + \frac{C_1(s) M_1 M_2^m}{Am_1^2 + K^2} \right] \right. \\
&\quad \times |p(s) - p_*(s)| \\
&\quad + M_1 B_1(s) |p_*(s - \tau_1(s)) - p(s - \tau_1(s))| \\
&\quad + \frac{C_1(s) M_1^2}{Am_1^2 + K^2} |q^m(s) - q_*^m(s)| \\
&\quad + \frac{C_1(s) M_1 M_2^m (AM_1^2 + K^2)}{(Am_1^2 + K^2)^2} \\
&\quad \times |p(s) - p_*(s)| \Big\} ds
\end{aligned}$$

$$\begin{aligned}
&+ \frac{\alpha C_1(t) M_1}{Am_1^2 + K^2} |q^m(t) - q_*^m(t)| \\
&+ \frac{\alpha AC_1(t) M_1^2 M_2^m}{(Am_1^2 + K^2)^2} |p(t) - p_*(t)| - B_2(t) |q(t) - q_*(t)| \\
&+ B_2(t) \\
&\times \int_{t-\tau_2(t)}^t \left\{ \left[r_2(s) + B_2(s) M_2 + \frac{C_2(s) M_1^2 M_2^{m-1}}{Am_1^2 + K^2} \right] \right. \\
&\quad \times |q(s) - q_*(s)| \\
&\quad + M_2 B_2(s) |q_*(s - \tau_2(s)) - q(s - \tau_2(s))| \\
&\quad + \frac{C_2(s) M_1^2 M_2}{Am_1^2 + K^2} |q^{m-1}(s) - q_*^{m-1}(s)| \\
&\quad + \frac{2K^2 C_2(s) M_1 M_2^m}{(Am_1^2 + K^2)^2} |p(s) - p_*(s)| \Big\} ds \\
&+ \frac{2K^2 C_2(t) M_1 M_2^{m-1}}{(Am_1^2 + K^2)^2} |p(t) - p_*(t)| \\
&= -\alpha B_1(t) |p(t) - p_*(t)| \\
&\quad + \alpha B_1(t) \int_{t-\tau_1(t)}^t W_1(s) ds + \frac{\alpha C_1(t) M_1}{Am_1^2 + K^2} |q^m(t) - q_*^m(t)| \\
&\quad + \frac{\alpha AC_1(t) M_1^2 M_2^m}{(Am_1^2 + K^2)^2} |p(t) - p_*(t)| - B_2(t) |q(t) - q_*(t)| \\
&\quad + B_2(t) \int_{t-\tau_2(t)}^t W_2(s) ds \\
&\quad + \frac{2K^2 C_2(t) M_1 M_2^{m-1}}{(Am_1^2 + K^2)^2} |p(t) - p_*(t)|,
\end{aligned} \tag{74}$$

where

$$\begin{aligned}
&W_1(s) \\
&= \left[r_1(s) + B_1(s) M_1 + \frac{C_1(s) M_1 M_2^m}{Am_1^2 + K^2} \right] |p(s) - p_*(s)| \\
&\quad + M_1 B_1(s) |p_*(s - \tau_1(s)) - p(s - \tau_1(s))| \\
&\quad + \frac{C_1(s) M_1^2}{Am_1^2 + K^2} |q^m(s) - q_*^m(s)| \\
&\quad + \frac{C_1(s) M_1 M_2^m (AM_1^2 + K^2)}{(Am_1^2 + K^2)^2} |p(s) - p_*(s)|, \\
&W_2(s) \\
&= \left[r_2(s) + B_2(s) M_2 + \frac{C_2(s) M_1^2 M_2^{m-1}}{Am_1^2 + K^2} \right]
\end{aligned}$$

$$\begin{aligned}
& \times |q(s) - q_*(s)| \\
& + M_2 B_2(s) |q_*(s - \tau_2(s)) - q(s - \tau_2(s))| \\
& + \frac{C_2(s) M_1^2 M_2}{Am_1^2 + K^2} |q^{m-1}(s) - q_*^{m-1}(s)| \\
& + \frac{2K^2 C_2(s) M_1 M_2^m}{(Am_1^2 + K^2)^2} |p(s) - p_*(s)|.
\end{aligned} \tag{75}$$

Define further

$$\begin{aligned}
V_2(t) &= \alpha \int_t^{\mu_1^{-1}(t)} \int_{\tau_1(\xi)}^t B_1(\xi) W_1(s) ds d\xi, \\
V_3(t) &= \int_t^{\mu_2^{-1}(t)} \int_{\tau_2(\xi)}^t B_2(\xi) W_2(s) ds d\xi.
\end{aligned} \tag{76}$$

For $t > t_6$, yielding that

$$\begin{aligned}
D^+ V_1(t) &+ \dot{V}_2(t) + \dot{V}_3(t) \\
&\leq -\alpha B_1(t) |p(t) - p_*(t)| + \frac{\alpha C_1(t) M_1}{Am_1^2 + K^2} |q^m(t) - q_*^m(t)| \\
&+ \frac{\alpha AC_1(t) M_1^2 M_2^m}{(Am_1^2 + K^2)^2} |p(t) - p_*(t)| \\
&+ \frac{2K^2 C_2(t) M_1 M_2^{m-1}}{(Am_1^2 + K^2)^2} |p(t) - p_*(t)| \\
&- B_2(t) |q(t) - q_*(t)| + \alpha W_1(t) \int_t^{\mu_1^{-1}(t)} B_1(\xi) d\xi \\
&+ W_2(t) \int_t^{\mu_2^{-1}(t)} B_2(\xi) d\xi.
\end{aligned} \tag{77}$$

Further define

$$\begin{aligned}
V_4(t) &= \alpha M_1 \int_{t-\tau_1(t)}^t \int_{\mu_1^{-1}(\eta)}^{\mu_1^{-1}(\mu_1^{-1}(\eta))} \frac{B_1(\xi) B_1(\mu_1^{-1}(\eta))}{1 - \dot{\tau}_1(\mu_1^{-1}(\eta))} \\
&\quad \times |p(\eta) - p_*(\eta)| d\xi d\eta, \\
V_5(t) &= M_2 \int_{t-\tau_2(t)}^t \int_{\mu_2^{-1}(\eta)}^{\mu_2^{-1}(\mu_2^{-1}(\eta))} \frac{B_2(\xi) B_2(\mu_2^{-1}(\eta))}{1 - \dot{\tau}_2(\mu_2^{-1}(\eta))} \\
&\quad \times |q(\eta) - q_*(\eta)| d\xi d\eta.
\end{aligned} \tag{78}$$

Then we choose the Lyapunov functional as follows:

$$V(t) = V_1(t) + V_2(t) + V_3(t) + V_4(t) + V_5(t); \tag{79}$$

then

$$\begin{aligned}
D^+ V(t) &\leq -\alpha B_1(t) |p(t) - p_*(t)| + \frac{\alpha C_1(t) M_1}{Am_1^2 + K^2} |q^m(t) - q_*^m(t)| \\
&- B_2(t) |q(t) - q_*(t)| \\
&+ \frac{\alpha AC_1(t) M_1^2 M_2^m}{(Am_1^2 + K^2)^2} |p(t) - p_*(t)| \\
&+ \frac{2K^2 C_2(t) M_1 M_2^{m-1}}{(Am_1^2 + K^2)^2} |p(t) - p_*(t)| \\
&+ \int_t^{\mu_1^{-1}(t)} B_1(\xi) d\xi \cdot \alpha \left[r_1(t) + B_1(t) M_1 + \frac{C_1(t) M_1 M_2^m}{Am_1^2 + K^2} \right] \\
&\times |p(t) - p_*(t)| \\
&+ \int_t^{\mu_1^{-1}(t)} B_1(\xi) d\xi \cdot \frac{\alpha C_1(t) M_1 M_2^m (Am_1^2 + K^2)}{(Am_1^2 + K^2)^2} \\
&\times |p(t) - p_*(t)| \\
&+ \int_t^{\mu_1^{-1}(t)} B_1(\xi) d\xi \cdot \frac{\alpha C_1(t) M_1^2}{Am_1^2 + K^2} |q^m(t) - q_*^m(t)| \\
&+ \int_t^{\mu_2^{-1}(t)} B_2(\xi) d\xi \cdot \left[r_2(t) + B_2(t) M_2 + \frac{C_2(t) M_1^2 M_2^{m-1}}{Am_1^2 + K^2} \right] \\
&\times |q(t) - q_*(t)| \\
&+ \int_t^{\mu_2^{-1}(t)} B_2(\xi) d\xi \cdot \frac{C_2(t) M_1^2 M_2}{Am_1^2 + K^2} |q^{m-1}(t) - q_*^{m-1}(t)| \\
&+ \int_t^{\mu_2^{-1}(t)} B_2(\xi) d\xi \cdot \frac{2K^2 C_2(t) M_1 M_2^m}{(Am_1^2 + K^2)^2} |p(t) - p_*(t)| \\
&+ \int_{\mu_1^{-1}(t)}^{\mu_1^{-1}(\mu_1^{-1}(t))} B_1(\xi) d\xi \cdot \frac{\alpha M_1 B_1(\mu_1^{-1}(t))}{1 - \dot{\tau}_1(\mu_1^{-1}(t))} |p(t) - p_*(t)| \\
&+ \int_{\mu_2^{-1}(t)}^{\mu_2^{-1}(\mu_2^{-1}(t))} B_2(\xi) d\xi \cdot \frac{M_2 B_2(\mu_2^{-1}(t))}{1 - \dot{\tau}_2(\mu_2^{-1}(t))} |q(t) - q_*(t)|.
\end{aligned} \tag{80}$$

Since $0 < m < 1$, then

$$\begin{aligned}
|q^m(t) - q_*^m(t)| &\leq mm_2^{m-1} |q(t) - q_*(t)|, \\
|q^{m-1}(t) - q_*^{m-1}(t)| &\leq (1-m)m_2^{m-2} |q(t) - q_*(t)|;
\end{aligned} \tag{81}$$

hence, we have

$$D^+ V(t) \leq -\Phi(t) |p(t) - p_*(t)| - \Psi(t) |q(t) - q_*(t)|. \tag{82}$$

It follows from $\Phi^L > 0$ and $\Psi^L > 0$ that

$$D^+ V(t) \leq -\Phi^L |p(t) - p_*(t)| - \Psi^L |q(t) - q_*(t)|, \tag{83}$$

for $t > t_6$. Integrating both sides of the above inequality on $[t_6, t]$, we have

$$\begin{aligned}
V(t) + \Phi^L |p(t) - p_*(t)| + \Psi^L |q(t) - q_*(t)| \\
\leq V(t_6) < +\infty.
\end{aligned} \tag{84}$$

Since $|p(t) - p_*(t)|$ and $|q(t) - q_*(t)|$ are uniformly continuous on $[t_6, +\infty)$, by Barbalat's Lemma [12], we obtain that

$$\lim_{t \rightarrow +\infty} |p(t) - p_*(t)| = 0, \quad \lim_{t \rightarrow +\infty} |q(t) - q_*(t)| = 0, \quad (85)$$

that is, $\lim_{t \rightarrow +\infty} (|p(t) - p_*(t)| + |q(t) - q_*(t)|) = 0$. Therefore, system (6) is globally attractive. Together with

$$\begin{aligned} & \lim_{t \rightarrow +\infty} |x(t) - x_*(t)| \\ &= \lim_{t \rightarrow +\infty} \prod_{0 < t_k < t} (1 + d_k) |p(t) - p_*(t)| = 0, \\ & \lim_{t \rightarrow +\infty} |y(t) - y_*(t)| \\ &= \lim_{t \rightarrow +\infty} \prod_{0 < t_k < t} (1 + h_k) |q(t) - q_*(t)| = 0, \end{aligned} \quad (86)$$

that is, $\lim_{t \rightarrow +\infty} |x(t) - x_*(t)| + |y(t) - y_*(t)| = 0$, system (4) is globally attractive. \square

Corollary 13. Let $\tau(t) \equiv \tau$, where τ is a nonnegative constant. If system (6) satisfies $r_1^L - C_1^U M_1 M_2^m / K^2 > 0$, $\liminf_{t \rightarrow +\infty} \Phi(t) > 0$, and $\liminf_{t \rightarrow +\infty} \Psi(t) > 0$, then system (6) has a unique positive almost ω -periodic solution which is globally attractive.

4. Numerical Simulation

Example 14. Assume $\tau(t) \equiv \tau$. Considering the following model as application:

$$\begin{aligned} \dot{p}(t) &= p(t) [8 + 0.1 \sin t - 8p(t - 0.05)] \\ &\quad - \frac{(4 + 0.3 \sin t) p^2(t)}{0.5p^2(t) + 1} q^{0.5}(t), \\ \dot{q}(t) &= q(t) [-(2.5 - 0.5 \sin t) - 2q(t - 0.1)] \\ &\quad + \frac{(2.5 + 0.5 \sin t) p^2(t)}{0.5p^2(t) + 1} q^{0.5}(t), \end{aligned} \quad (87)$$

corresponding to model (87), we take

$$\begin{aligned} r_1(t) &= 8 + 0.1 \sin t, & B_1(t) &= 8, \\ C_1(t) &= 4 + 0.3 \sin t, \\ r_2(t) &= 2.5 - 0.5 \sin t, & B_2(t) &= 2, \\ C_2(t) &= 2.5 + 0.5 \sin t, \\ A &= 0.5, & m &= 0.5, & K &= 1, \\ \tau_1(t) &= 0.05, & \tau_2(t) &= 0.1. \end{aligned} \quad (88)$$

By direct computation, we have $\bar{C}_2 - A(\bar{r}_2 + \Delta_2^U) = 0.25 > 0$, which satisfies the conditions of Theorem 5 and Corollary 6. We can see that system (87) has a positive periodic solution (see Figures 1 and 2).

Example 15. Assume $\tau(t) \equiv \tau$. Considering the following model as application

$$\begin{aligned} \dot{p}(t) &= p(t) [8 + 0.1 \sin t - 8p(t - 0.04)] \\ &\quad - \frac{(3 + 0.3 \sin t) p^2(t)}{0.5p^2(t) + 1} q^{0.5}(t), \\ \dot{q}(t) &= q(t) [-(5 - 0.5 \sin t) - 3.5q(t - 0.2)] \\ &\quad + \frac{(1.5 + 0.5 \sin t) p^2(t)}{0.5p^2(t) + 1} q^{0.5}(t), \end{aligned} \quad (89)$$

corresponding to model (89), we take

$$\begin{aligned} r_1(t) &= 8 + 0.1 \sin t, & B_1(t) &= 8, \\ C_1(t) &= 3 + 0.3 \sin t, \\ r_2(t) &= 5 - 0.5 \sin t, & B_2(t) &= 3.5, \\ C_2(t) &= 1.5 + 0.5 \sin t, \\ A &= 0.5, & m &= 0.5, & K &= 1, \\ \tau_1(t) &= 0.04, & \tau_2(t) &= 0.2. \end{aligned} \quad (90)$$

By direct computation, we have $r_1^L - C_1^U M_1 M_2^m / K^2 \approx 1.2237 > 0$, $\liminf_{t \rightarrow +\infty} \Phi(t) > 0$, and $\liminf_{t \rightarrow +\infty} \Psi(t) > 0$. We can see that system (89) is permanent and has a unique positive 2π -periodic solution, which is globally attractive (see Figures 3 and 4). It is easy to verify the accuracy of Theorems 8, 9, and 12 and Corollaries 10 and 13.

5. Conclusion

In the study of population dynamics, we focus on two aspects: (1) the time-varying evolution of the population and (2) how to implement manual intervention to protect, develop, and utilize the population. Precisely, these two issues are reflected in our model. Regarding the first aspect, we take into account the impact of limited resources on population size; that is, its density has a restriction on the growth of the population size. Hence, we not only use the interspecific growth terms $b_1(t)x(t - \tau_1(t))$ and $b_2(t)x(t - \tau_2(t))$ to reflect the model, where $\tau_1(t)$ and $\tau_2(t)$ are delays, but also consider the interference constant m and Holling III type functional response. Taking into account the second aspect, we propose a regular pulse harvest in the model. The corresponding ecological system of the model we considered is more complex and has practical significance.

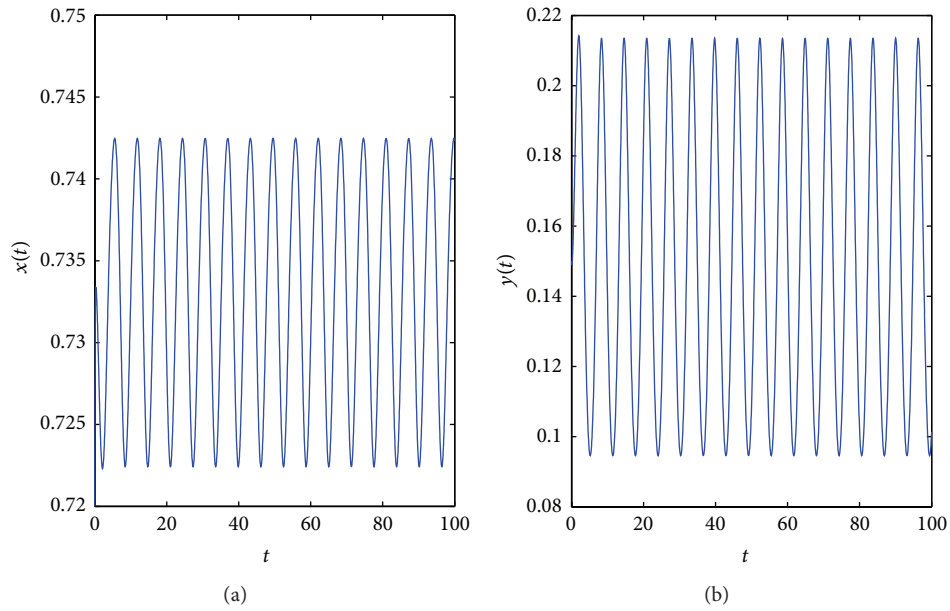


FIGURE 1: The integral curves of prey-time and predator-time.

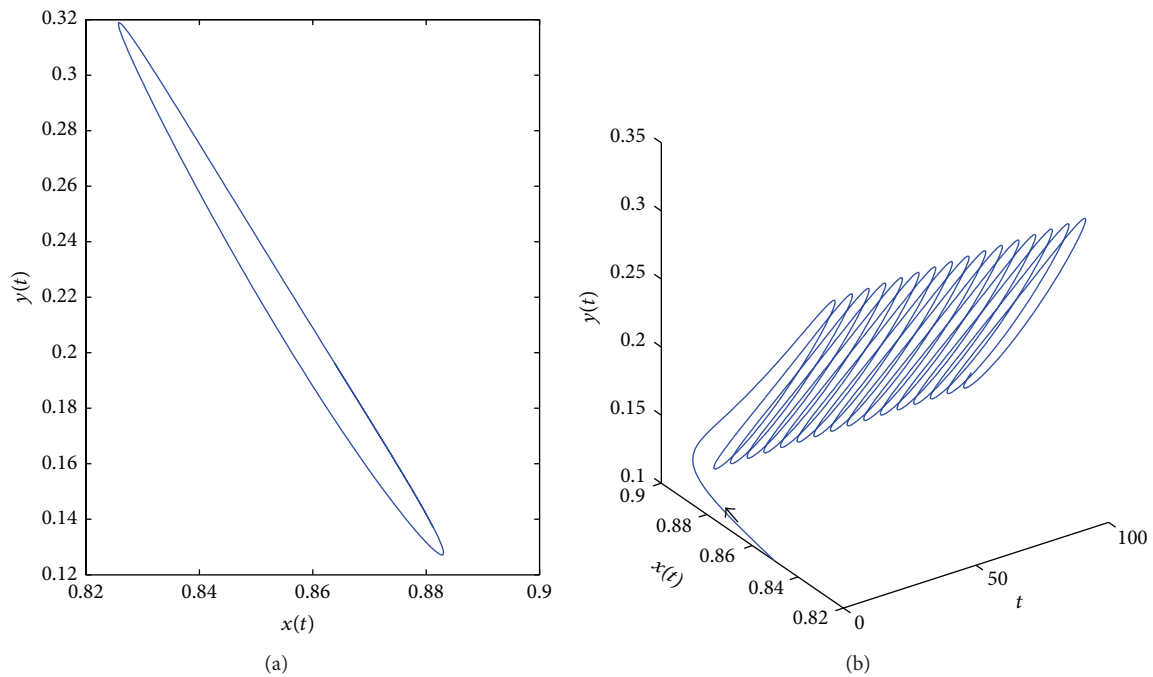


FIGURE 2: The orbits of prey-predator and time-prey-predator.

In this paper, we analyze the existence and global attractivity of positive periodic solutions of a delayed impulsive Lotka-Volterra model with Holing III type functional response. We propose two delays and impulses to describe the model. From Theorem 5, we can conclude that the positive periodic solutions of system (4) are delay dependent. This is different from these results that the positive periodic solutions are delay independent, and our conclusion is more

general. Furthermore, we have shown the permanence and global attractivity of system (4) under certain conditions. We have found that system (4) has a unique and globally attractive periodic solution, but how can we prove it? We leave it as our work in the future. In addition to delayed and impulsive biological systems, we hope that our analysis can provide valuable design insights and supports to future biological works.

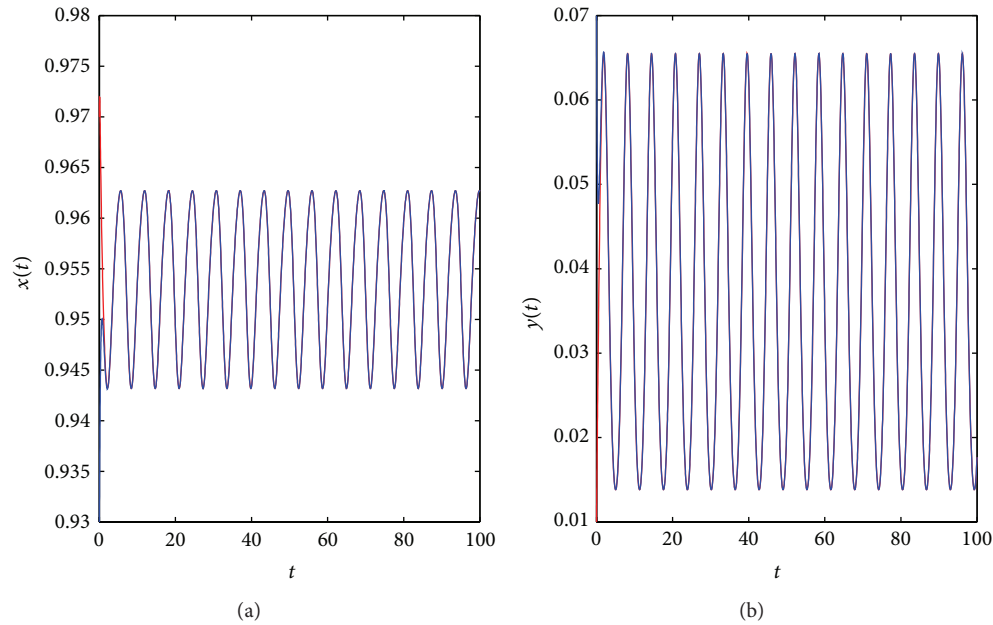


FIGURE 3: The integral curves of prey-time and predator-time.

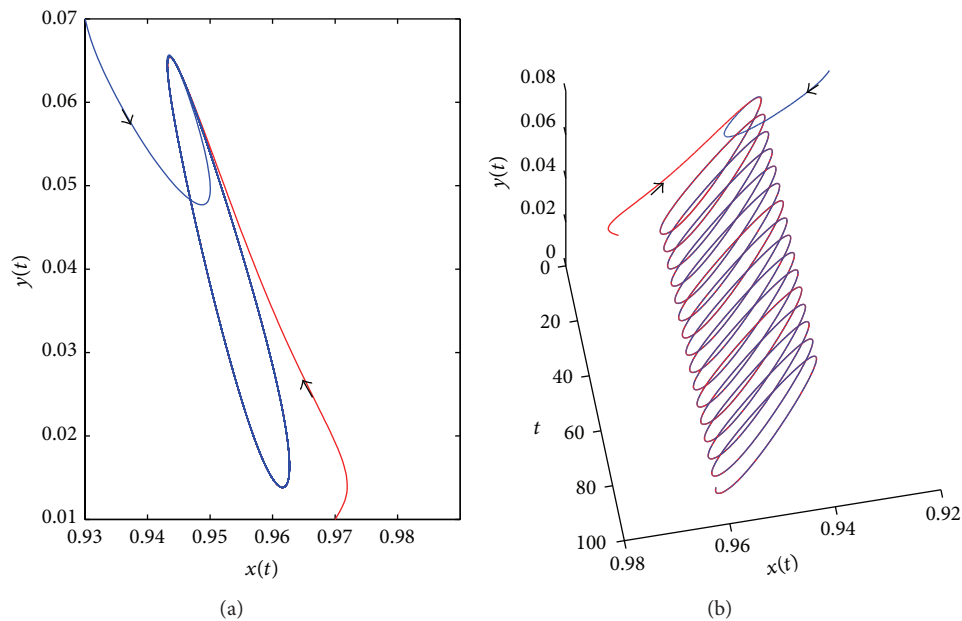


FIGURE 4: The orbits of prey-predator and time-prey-predator.

Conflict of Interests

The authors declare that there is no conflict of interests regarding the publication of this paper.

Acknowledgments

This work was supported by the National Natural Science Foundation of China (61174209) and the Basic Theory Research Foundation for Engineering Research Institute of USTB (YJ2012-001).

References

- [1] X. X. Liu, "Impulsive periodic oscillation for a predator-prey model with Hassell-Varley-Holling functional response," *Applied Mathematical Modelling*, vol. 38, no. 4, pp. 1482–1494, 2014.
- [2] Y. S. Lv and Z. J. Du, "Existence and global attractivity of a positive periodic solution to a Lotka-Volterra model with mutual interference and Holling III type functional response," *Nonlinear Analysis: Real World Applications*, vol. 12, no. 6, pp. 3654–3664, 2011.

- [3] X. Song and Y. Li, "Dynamic behaviors of the periodic predator-prey model with modified Leslie-Gower Holling-type II schemes and impulsive effect," *Nonlinear Analysis: Real World Applications*, vol. 9, no. 1, pp. 64–79, 2008.
- [4] K. Wang and Y. Zhu, "Periodic solutions, permanence and global attractivity of a delayed impulsive prey-predator system with mutual interference," *Nonlinear Analysis: Real World Applications*, vol. 14, no. 2, pp. 1044–1054, 2013.
- [5] Z. Yao, S. Xie, and N. Yu, "Dynamics of cooperative predator-prey system with impulsive effects and Beddington-DeAngelis functional response," *Journal of the Egyptian Mathematical Society*, vol. 21, no. 3, pp. 213–223, 2013.
- [6] G. Zhang, Y. Shen, and B. Chen, "Positive periodic solutions in a non-selective harvesting predator-prey model with multiple delays," *Journal of Mathematical Analysis and Applications*, vol. 395, no. 1, pp. 298–306, 2012.
- [7] M. P. Hassell, "Density dependence in single-species population," *The Journal of Animal Ecology*, vol. 44, no. 1, pp. 283–295, 1975.
- [8] Z. J. Du and Y. S. Lv, "Permanence and almost periodic solution of a Lotka-Volterra model with mutual interference and time delays," *Applied Mathematical Modelling*, vol. 37, no. 3, pp. 1054–1068, 2013.
- [9] R. E. Gaines and J. L. Mawhin, *Coincidence Degree and Nonlinear Differential Equations*, Springer, Berlin, Germany, 1977.
- [10] C. Shen, "Permanence and global attractivity of the food-chain system with Holling IV type functional response," *Applied Mathematics and Computation*, vol. 194, no. 1, pp. 179–185, 2007.
- [11] S. Lu, "On the existence of positive periodic solutions to a Lotka Volterra cooperative population model with multiple delays," *Nonlinear Analysis: Theory, Methods & Applications*, vol. 68, no. 6, pp. 1746–1753, 2008.
- [12] I. Barbalat, "Systems dequations differential doscillations nonlinearities," *Revue Roumaine de Mathématique Pures et Appliquées*, vol. 4, no. 2, pp. 267–270, 1959.

Review Article

Modeling and Analysis in Marine Big Data: Advances and Challenges

Dongmei Huang, Danfeng Zhao, Lifei Wei, Zhenhua Wang, and Yanling Du

College of Information, Shanghai Ocean University, Shanghai 201306, China

Correspondence should be addressed to Dongmei Huang; dmhuang@shou.edu.cn

Received 12 August 2014; Revised 5 September 2014; Accepted 15 September 2014

Academic Editor: L. W. Zhang

Copyright © 2015 Dongmei Huang et al. This is an open access article distributed under the Creative Commons Attribution License, which permits unrestricted use, distribution, and reproduction in any medium, provided the original work is properly cited.

It is aware that big data has gathered tremendous attentions from academic research institutes, governments, and enterprises in all aspects of information sciences. With the development of diversity of marine data acquisition techniques, marine data grow exponentially in last decade, which forms *marine big data*. As an innovation, marine big data is a double-edged sword. On the one hand, there are many potential and highly useful values hidden in the huge volume of marine data, which is widely used in marine-related fields, such as tsunami and red-tide warning, prevention, and forecasting, disaster inversion, and visualization modeling after disasters. There is no doubt that the future competitions in marine sciences and technologies will surely converge into the marine data explorations. On the other hand, marine big data also brings about many new challenges in data management, such as the difficulties in data capture, storage, analysis, and applications, as well as data quality control and data security. To highlight theoretical methodologies and practical applications of marine big data, this paper illustrates a broad view about marine big data and its management, makes a survey on key methods and models, introduces an engineering instance that demonstrates the management architecture, and discusses the existing challenges.

1. Introduction

Recently, the data volume all over the world is growing at an overwhelming speed, which is acquired by various devices with regard to Internet of Things and Social Networks. In this context, big data emerges and has been investigated extensively so far. In terms of marine field, countries around the world have launched several observing projects, for example, Argo [1], NEPTUNE-Canada [2], GOOS [3], OOI [4], IOOS [5], and so forth, and numerous marine observation satellites [6, 7]. Acquiring marine data by various observing techniques leads to a sharp increase in data volume. For example, Argo [1] has set up four data centers and deployed up to 10231 buoys all over the world, for real-time acquiring marine data like temperature, salinity, acidity, density, and carbon dioxide. Even one data center alone has to process 21954 profile data with 657 active buoys over the whole of last year [8, 9]. The different data collection devices result in various data as well as their format. We denote the diverse data provisions. A marine observation satellite emitted by NASA, named as *Aquarius* [6], records all the element of ocean circulation,

temperature, and ingredient and sea surface height every 7 days. Statistically, the data volume collected by *Aquarius* within every 2 months amounts to that collected by survey ships and buoys in 125 years [6]. By the end of year 2012, the annual data volume had been up to 30 PB (1 PB = $1024 * 1024$ GB) maintained by NOAA and over 3.5 billion observational files would be gathered together from satellites, ships, aircrafts, buoys, and other sensors each day [7]. As all-round marine observation systems and multiple observing techniques are widely put into service, data volume sharply increases, data type is greatly diversified, and data value is highly delivered, which forms *marine big data*.

Marine big data contains great values and embodies giant academic appeal, which can be transformed into a rich set of information for people to learn, exploit, and maintain the marine. For example, after analyzing the Argo data, it is found that the earth is seeking an intensification of global hydrological cycle [10]. Communities and species distribution can be determined by analysis of acoustic remote sensing data, which works as powerful scientific supporting

evidence to maintain the marine ecological balance [11]. In addition, researches on forecasting and warning of under-sea earthquake and tsunami can be successfully preceding, by analyzing observation data concerning seismic activity, faulting activity and midoceanic ridges acquired by Neptune project [12, 13]. In summary, marine big data supports forecasting and warning potential problems in the field of ecology, climate, and disasters and helps decision making.

In order to maximally exploit the value in marine data, it is of great realistic and theoretical significance to study on the management of marine big data concerning data storage, data analysis, quality control, and data security.

At present, almost all the existing researches concentrate on solving general issues about big data management. As a kind of typical big data, marine big data features massiveness, diverse data provisions, high-dimension besides temporality, and spatiality, which brings exceptional challenges and problems. In terms of data storage, there are problems like weak scalability in storage system and dissatisfaction on timeliness. In terms of data analysis, there are still problems like slow processing speed and failure in real-time response. Furthermore, the data available and data security are two features for the marine big data management. In terms of data available, there are some emerging problems like difference of data quality, diversity of data error, and unfixed schema of quality inspection. Additionally, as data security involves in all the process of marine big data management, security in data storage, data access, data computation, data sharing, and data supervision must be considered all over marine big data management. If the above problems cannot be well solved, the value of marine big data would not be fully exploited.

To our best of knowledge, this paper is the first survey on marine big data management. Our contribution is to study on marine big data management architecture, summarize the related methods and models, introduce a practical application to demonstrate the architecture of marine big data management, discuss the facing challenges, and ultimately prospect the research directions of marine big data management.

Organization of the rest paper is arranged as follows. Section 2 covers the source and informal definition of marine big data and provides an overview of the data characteristics. Related methods and models in marine big data management are summarized in Section 3. The project about marine big data management is presented in Section 4. Section 5 describes the facing challenges of marine big data management. Finally, we draw a conclusion.

2. Marine Big Data Management Architecture

2.1. Marine Big Data. There has been no consensus concerning the definition of marine big data. Given *4V* (*volume*, *variety*, *velocity*, and *value*) characters of big data [14], marine big data is informally described as large amount of data which is collected by satellite, aerial remote sensing, stations, ships, and buoys and serving in the marine-related fields. According to corresponding profiles [15–17], we summarize the significant characteristics of marine big data as follows.

(1) *Diverse Data Provisions.* Marine big data is acquired from widespread sources, such as satellites, aerial remote sensing, stations, ships, buoys, and undersea sensing. Different data sources take diverse data acquisition technologies to capture marine data; however, varieties in data acquisition technology specification, data format, arguments, and observation region make marine big data reveal its characteristic of data type diversity. Data with different diverse data provisions, as well as the various data types, is a significant characteristic of marine big data.

(2) *Temporality and Spatiality.* Marine big data features strong timeliness and spatial correlation. Only those marine data who contain specific spatial and temporal information will show significant values. The data storage and the data analysis are based on these two attributes. Without these two features, the marine data will be useless.

(3) *High Dimension.* The marine science involves several disciplines such as physical oceanography, chemical oceanography, biological oceanography, marine environment, and marine economy. Besides temporality and spatiality, every marine data still contains multiple attributes like water temperature, salinity, acidity, density, and velocity according to the various demands. As a result, it is known as high dimension data.

(4) *Huge Volume.* Since marine data grows at an overwhelming speed, due to its high dimension and real-time (or periodically) data acquisition by existing marine observation projects all over the world, all of these factors form the huge volume of marine big data.

(5) *Data Availability.* Marine big data also needs the techniques to keep the data's reliability. Once some illegal data injects in the system, we need some techniques to find out using data sampling technique, data quality inspection technique, and automatic restoration technique.

(6) *Data Security.* Marine big data involves privileged, confidential and strategic data, like long-cycle meteorology and hydrology data helping disaster evaluation and forecasting, marine fisheries and oil-gas distribution data helping marine resource utilization, large-scale reef data, and off-coast data helping military decision making.

2.2. Marine Big Data Management Architecture. Marine big data comes from various data provisions, and its application requirement and data type differ in each other. By analysis of marine big data, the architecture of marine big data management can be illustrated: data provision, data preprocessing, data storage, data analysis, and data application as well as quality control and data security throughout the whole process, specific as Figure 1.

The management architecture of marine big data involves several parts. Marine big data derives from various sources such as satellite, aerial remote sensing, stations, ships, buoys, and undersea sensing. Due to extra complex data structure

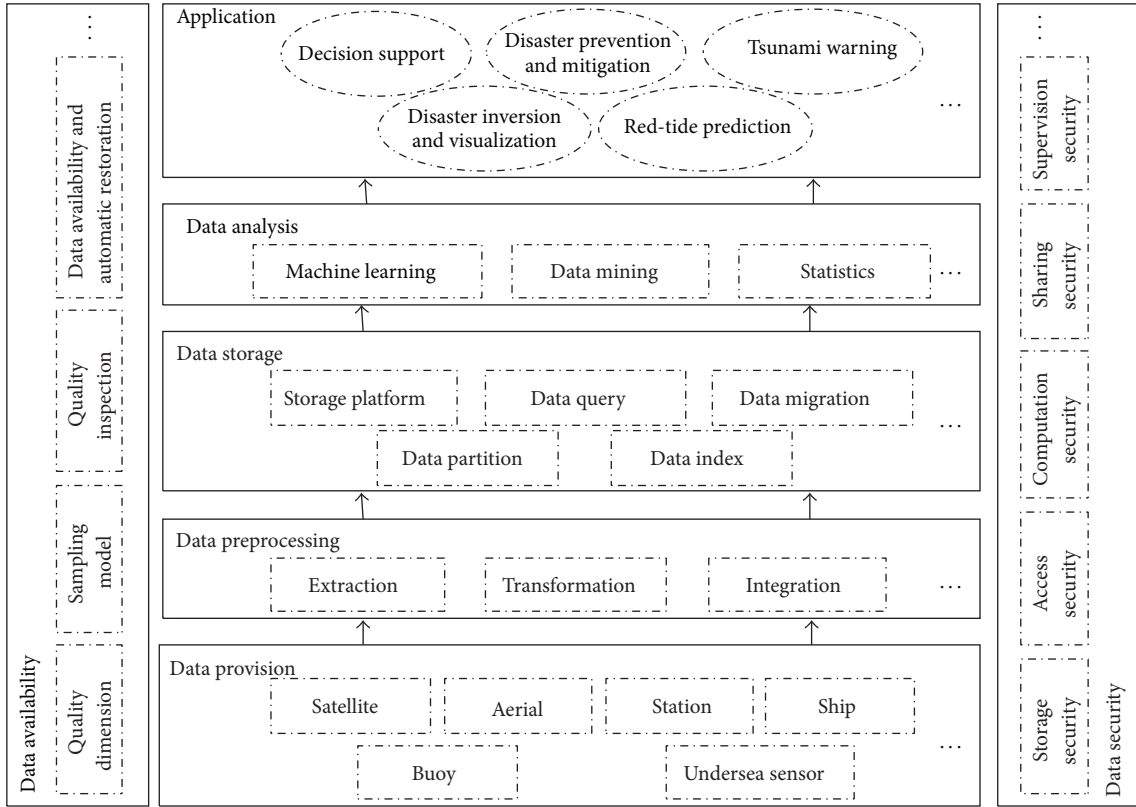


FIGURE 1: Marine big data management architecture.

and data type characteristics of marine big data, it is essential to perform preprocessing operations, such as data extraction, data transformation, and data integration. At data storage stage, aspects like storage platform, data classification, index building, query, and data migration should be properly taken into account. At data analysis stage, techniques like machine learning, data mining, and statistics are introduced to provide the reliable theoretical basis on applications, including decision support, disaster prevention and mitigation, disaster inversion and visualization modeling, tsunami warning, and red-tide forecasting. Data quality and data security are perceived as the assurance for the whole architecture. Data quality involves quality dimension, sampling model, quality inspection, and data availability and automatic restoration, while data security involves storage security, access security, computation security, sharing security, and supervision security.

3. Methods and Models in Marine Big Data Management

Nowadays, there are a great many of researches on big data management, and a few general technologies have been launched. This section discusses the methods and technologies, with regard to data storage, data analysis, data quality control, and data security in marine big data management.

3.1. Data Storage and Analysis. With the advent and development of cloud computing, new processing frameworks, computing models, and analytical methods emerge as required, which provide technical supports for storage and analysis in big data management. From the view of data storage and data analysis, this section analyzes these key technologies, which are applicable to marine big data with significant characteristics.

3.1.1. Data Storage. Cloud storage is widely applied in big data. Currently there are several cloud storage platforms, including Google Store [18], Amazon S3 [19], Microsoft Azure [20], and IBM Blue Cloud [21, 22]. To make cloud storage play better applicability in sensitive and spatial marine big data, operations like partitioning marine big data by security classification and building suitable index structure should be carried out to raise query efficiency. With the continual accumulation of observing data in data storage system, data should be dynamically migrated, in consideration of characteristics of marine big data. All the above contributes to maximum use of storage system.

Data partition helps to increase execution efficiency of index [23]. In terms of data security, current researches fasten on taking data sensitivity calculation [17], physical isolation [24], and user access restriction [25, 26], to partition data to the corresponding node. Besides, there are some partition methods based on statistical theory, such as clustering-based

data partition [27], sampling-based data partition [28, 29], and adaptive partition based on data distribution [30, 31]. These above methods aims to relieve processing pressure of massive data, avoid data skew, and achieve stable and dynamic data distribution. Data partitioning is a process that a dataset is divided into several fragments according to certain rules and there is no intersection among the various fragments. After the data is divided into a number of data fragments which are stored in clouds, assume that cloud storage is large enough. When a dataset D is uniformly fragmented stored into the n clouds, the information entropy requires

$$I(s_1, s_2, \dots, s_n) = - \sum_{i=1}^n \frac{s_i}{s} \log_2 \frac{s_i}{s}, \quad (1)$$

where s is the total number of fragments of dataset D and s_i is the number assigned to the Cloud_i fragments. When the value of n is greater, indicating that data is split into more fragments, the greater its entropy.

Index is a powerful technique to improve query efficiency. Cloud storage is a widely accepted distributed storage platform on marine big data. In this case, current researches mainly falls into several classes: hash index [32], tree structure index [33, 34], time-led composite index [35, 36], index dynamically adjusted with data migration [37, 38], and index optimized with parallel processing [39].

To improve query efficiency on cloud storage, it is essential to study on query optimization techniques, so as to relieve computing pressure and improve transmission speed. From the view of algorithm implementation, there are a few improvements, such as sharing history query result as intermediate result [40], adaptively sampling based on data characteristics [41], and extracting representative tuples according to relation compactness [42]. Zadeh introduced the notion of possibility distributions, which acts as a fuzzy restriction on the values that may be assigned to a variable. Given a fuzzy set F and a variable X on U , then the possibility of $X = u$, denoted by $\pi_X(u)$, is defined to be equal to $\mu_F(u)$. The possibility distribution of X on U with respect to F is denoted by

$$\pi_X = \left\{ \frac{\pi_X(u)}{u} \mid u \in U, \pi_X(u) = \mu_F(u) \in [0, 1] \right\}. \quad (2)$$

Additionally, relevant studies still focus on hardware performance improvement, adopting task scheduling [43, 44] to realize efficient parallel processing.

Dynamic data migration on storage platform ensures optimal utilization of storage resource. There are two kinds of traditional data migration methods: one is based on high and low water level method of storage space [44], and the other is based on cache replacement migration algorithm of data access frequency [45, 46]. With the development of storage technology, several different storage patterns have been created. In hierarchical storage, migration model is introduced to support automatic data migration [47]. In multistage storage, CuteMig migration method [48] is involved to realize data migration. In hybrid cloud storage, calculation

of data sensitivity and migration function contributes to dynamic data migration [17]. Dremel [49] successes in analyzing massive data in short time and supports data analysis platform over the cloud.

3.1.2. Data Analysis. Considering characteristics like real-time and diversity in data type of marine big data, data analysis should be performed according to data type and analysis target. Hence, adaptive algorithm and model should be taken to ensure the request for real-time data analysis. MapReduce is widely used in numerous big data applications to accelerate the data analysis process. As a result, there is no exception in marine big data application. The paragraph below briefly introduces some representative big data analysis models.

MapReduce is the earliest computing model that Google proposed, which applies to batch processing [50]. MapReduce can be divided into two phase: map phase and reduce phase. Graph is an effective data structure in representing relationships or connections between objects in the real world. Hence, graph computing is a normal computing pattern. Since graph computing involves continuously data updating and numerous message passing, it might impose lots of unnecessary serialization and deserialization overhead using MapReduce. Pregel [51] is another computing model proposed by Google after MapReduce, which is mainly devised to serve graph computing. Its core idea derives from distinguished BSP [52] computing model. Additionally, there exists a PageRank algorithm to reflect the computing quality. The formula is given as follows:

$$\text{PR}(A) = (1 - d) + d \left(\frac{\text{PR}(T_1)}{C(T_1)} + \dots + \frac{\text{PR}(T_n)}{C(T_n)} \right), \quad (3)$$

where T_1, \dots, T_n = Pages that point to page A (citations) and $C(T)$ = number of links going out of T . Dremel [49] successes in analyzing massive data in short time and supports data analysis platform over the cloud, that is, BigQuery [53]. As to its data model, it is based on strongly typed nested records. Its abstract syntax is given by

$$\tau = \text{dom} \mid \langle A_1 : \tau[*?] , \dots, A_n : \tau[*?] \rangle, \quad (4)$$

where τ is an atomic type or a record type. Field i in a record has a name A_i and an optional multiplicity label. Repeated fields (*) may occur multiple times in a record. Optional fields (?) may be missing from the record. Analysis tool, PowerDrill [54], adopts column storage and compress technique to load as much as data into memory. Both PowerDrill and Dremel are big data analysis tools of Google, but they fit into different application scenarios, respectively, and differ in implementation techniques. Dremel is mostly used in analysis of multidatasets, and it can handle up to PB data in several seconds. PoweDrill is mostly applied in analysis of core subset of massive data, and it disposes less data types than Dremel. Since PowerDrill resides data in the memory buffer as much as possible, its processing speed is higher. Microsoft proposed a data analysis model named Dryad [55], which supports applications of Directed

Acycline Graph (DAG), the same as Cascading on Hadoop [56]. The singleton graph is generated from a vertex v as $G = \langle \{v\}, \emptyset, \{v\}, \{v\} \rangle$. A graph can be cloned into a new graph containing k copies of its structure using the \wedge operator where $C = G \wedge k$ is defined as

$$C = \langle V_G^1 \oplus \dots \oplus V_G^K, E_G^1 \cup \dots \cup E_G^K, I_G^1 \cup \dots \cup I_G^K, O_G^1 \cup \dots \cup O_G^K \rangle, \quad (5)$$

where $G^n = \langle V_G^n, E_G^n, I_G^n, O_G^n \rangle$ is a “clone” of G containing copies of all of G 's vertices and edges, \oplus denotes sequence concatenation, and each cloned vertex inherits the type and parameters of its corresponding vertex in G .

3.2. Data Availability. Facing the quality problems of the uncertainty and inconsistency of marine big data, a scheme of data quality control throughout data management is highly on-demand. So far, academic study on data quality control involves several aspects, including selection of data quality dimensions, design of quality inspection scheme, regulation of quality control standard, and theories of the data usability and data autorestitution.

Quality Dimensions. In essence, data quality is considered as the applicability of data in applications [57] and can be described from five dimensions, including consistency, integrity, timeliness, usability, and credibility [58]. As for spatial data, existing researches put forward five important aspects of data quality evaluation, including spatial accuracy, thematic accuracy, logical consistency, completeness, and lineage [59]. In terms of various quality evaluation methods, spatial data quality is measured as such in ISO/TC211:

$$R = \sum_{i=1}^k (C_i \cdot W_i), \quad (6)$$

where R is the result of data quality, $R \in (0.0, 1.0)$; C_i is the accuracy of the i th object, $C_i \in (0.0, 1.0)$; W_i is the weight of the i th object, $W_i \in (0.0, 1.0)$; k is the amount of all kinds of ground objects [60].

Sampling Schemes for Spatial Data. Sampling method is an effective way for processing of massive information, by choosing a small amount of sample to represent the population. The sampling method is efficient with low cost. When spatial samples are not independent, the Bootstrap algorithm introduces two-time sampling technique [61], using the Bag of Little Bootstraps (BLB) functions as follows:

$$s^{-1} \sum_{j=1}^a \xi(Q_n(P_{n,b}^j)), \quad (7)$$

which has greatly improved the efficiency of data quality evaluation under parallel or distributed computing circumstance. In spatial data sampling, the “Sandwich” sampling model solves the problem of spatial heterogeneity, based on stratified sampling [62, 63] by considering autocorrelation of the spatial objects.

Quality Inspection Schemes for Spatial Data. During the past several years, efforts have been made on quality inspection of marine big data. These studies have put forward an available quality inspection scheme for marine big data, especially for one or a few dimensions. Marine dataset is usually composed of multidimension, multiscale, and multisource. Thus, it is required to propose a quality inspection scheme to inspect the quality of marine big data as a complete, indivisible set [64].

The purpose of quality inspection is to judge whether the data reach the quality levels required by data analysis or data utilization [65]. The principal goal of designing an optimal sampling scheme is to obtain high accuracy of product inspection and to reduce the inspection cost [66]. Current studies have proposed many sampling schemes of quality inspection for industrial product based on statistical theory [67–72]; based on hypergeometric distribution, the accepting probability is calculated as follows:

$$L(p) = \sum_{d=0}^c h(d, n, D, N), \quad (8)$$

where d is the actual number of unaccepted data products in the sample, n is the sample size, D is the total number of unaccepted data products in the lot, and N is the lot size.

Thus, the inspection model of marine big data is also brought up:

$$\begin{aligned} \min_n \quad & \varepsilon \\ \text{s.t.} \quad & \varepsilon = \varepsilon_\varepsilon = \sum_{d=0}^c \frac{\binom{N-D}{n-d} \binom{D}{d}}{\binom{N}{n}} - (1 - \alpha), \quad (9) \\ & (0 < c < n - 1, \varepsilon > 0), \end{aligned}$$

where ε is the residual of the accepting probability and α represents the quality demand of data user.

Data Usability. The usability of dataset includes data consistency, data integrity, data accuracy, timeliness, and entity identity [73]. Studies on data consistency are mainly based on description of semantic rules [74] and statistics [75]. The most classic resolution dealing with data integrity is an incomplete data expression system based on conditional table [76]. There are few researches on data accuracy. The most common one is a description method of data accuracy based on possible world semantics. In terms of timeliness, researches mainly fasten on autodetection and autorestitution [77]. Studies on entity identity are based on the detection of entity identity error, including semantic rules and similarity measurement [78].

Data Autodetection and Autorestitution. Studies on data error detection include two aspects, data consistency and entity identity. As for data consistency, studies mainly focus on designing on autodetection algorithm [79] and distributed database detecting method [80]. The purpose of entity identity detection is to maximize the identification accuracy [81] and the recognition efficiency [82]. In terms of studies on

data restoration, traditional functional dependency is used to solve the problem of data inconsistency [83], while data fusion techniques are mostly used for data entity identity issues [84].

3.3. Data Security. According to the challenges in marine big data security, the related researches and development techniques are summarized in the following five aspects as secure data storage, secure data access, secure data computation, secure data sharing, and secure data supervision.

Secure Data Storage. Since the existing data storage security depends on the credibility of the cloud servers, we need to study the ciphertext-based data storage techniques [85], to resist the administrators of the storage servers and adversary from the server side exposing and tampering data. Besides, it is also necessary to research on the multiauthorities in the access control to reduce the loss due to a single authority compromised by the malicious adversary. In addition, the techniques for data integrity checking [86] and data storage proofing [87] are also essential in the ciphertext-based storage.

Secure Data Access. Marine big data are used for different scenarios and accessed by different users with different roles and different security levels. Traditional access control is no longer suitable for the ciphertext-based storage platform. It is necessary to research the techniques of ciphertext-support data retrieval [88], the fine-grained data access control [89], and supporting the flexible functions such as “and,” “or,” and “not” logical connectives data access control [90], indexing [91], keyword searching and ranking [92], and similarity searching [93] on the encrypted data to realize the access security.

Secure Data Computation. Since the servers cannot be fully trusted and computation services are often in an outsourcing way, it requires that the input/output should be in an encrypted form for data calculation and data analysis, rather than that the storage ciphertext is decrypted before computation and analysis [94]. In the marine big data computation and analysis, it requires the techniques involving solving the ciphertext-based large scale linear equations [95], analyzing and mining the knowledge from the encrypted data, processing the ciphered images [96], and fully homomorphic encryption/decryption [97] to realize the computation security.

Secure Data Sharing. The marine data sharing security depends on the user's secret key. To keep the data secure sharing and data dissemination in the cloud environment [98], it is inevitable to research the techniques of leakage key tracing like white-box traceability [99, 100] and black-box traceability [101] and access ability revocation [102]. Meanwhile, faced to marine data, it also requires efficient encrypted data sharing and dissemination techniques [103], marine data privacy-preserving techniques [104], and

optimized implementation techniques [105] to improve the batch processing ability of marine big data.

Secure Data Supervision. In the data storage, computation, sharing, and dissemination, it needs secure data supervision techniques [106] such as removing illegal data [107], reducing the cost of redundant data [105], checking the completeness of the storage content [87], verifying the correctness of the calculation results [95], and mining the sensitive information and knowledge in the marine data usage. Furthermore, it also requires rules from the government to coordinate the personal privacy preserving and marine big data analyzing [108].

4. Application in Marine Big Data

In terms of the marine big data management architecture, we introduce a practical application of the marine big data—a disaster inversion visualization instance that reproduces a marine disaster happened in Chinese Yellow Sea to show our marine big data.

The disaster results, including latitude and longitude, flow velocity, flow direction, water depth, and height, produced every 10 minutes, involve over 40000 inversion grids. Each monitoring of disaster lasts 5 days, and the disaster data amount alone is up to 4.5 GB. (If we employ more precise data, the data volume will be much huger.) Thus, we choose it as an application since it satisfies all of the characteristics of marine big data. Furthermore, to achieve authenticity and quasireal-time of disaster process, massive data about the geographic locations and continuously rising water level need to be loaded in the disaster visualization, which leads to higher requirements for data transmission, data storage, data analysis, and rendering efficiency.

In this project, we apply hybrid cloud storage architecture, including public cloud and private cloud shown in Figure 2. The project partitions the marine big data in terms of the difference between spatial and temporal attributes. The data with strong timeliness attribute and location related attribute are stored in the private cloud. Public cloud assists to store the rest of the marine data.

Meanwhile, data migration is the key problem in such hybrid cloud storage architecture. Things like data sensitivity, data access frequency, data time length, and data size should be fully considered when performing data migration. To improve query efficiency in the cloud, we use the query optimization technique and improve transmission speed. We take the migration algorithm [17] to help to lower the management cost without sacrificing to slow down the data access speed. The migration function is the key of migration algorithm shown as follows:

$$M(D) = \sum_{i=1}^n \frac{1}{T_i} \times \sum_{k=1}^n f_k \times \frac{1}{S}, \quad (10)$$

where T_i represents time-length of the i th access of the marine dataset D , f_k represents access frequency of marine dataset D over the period of T_k , and S is the size of marine dataset D .

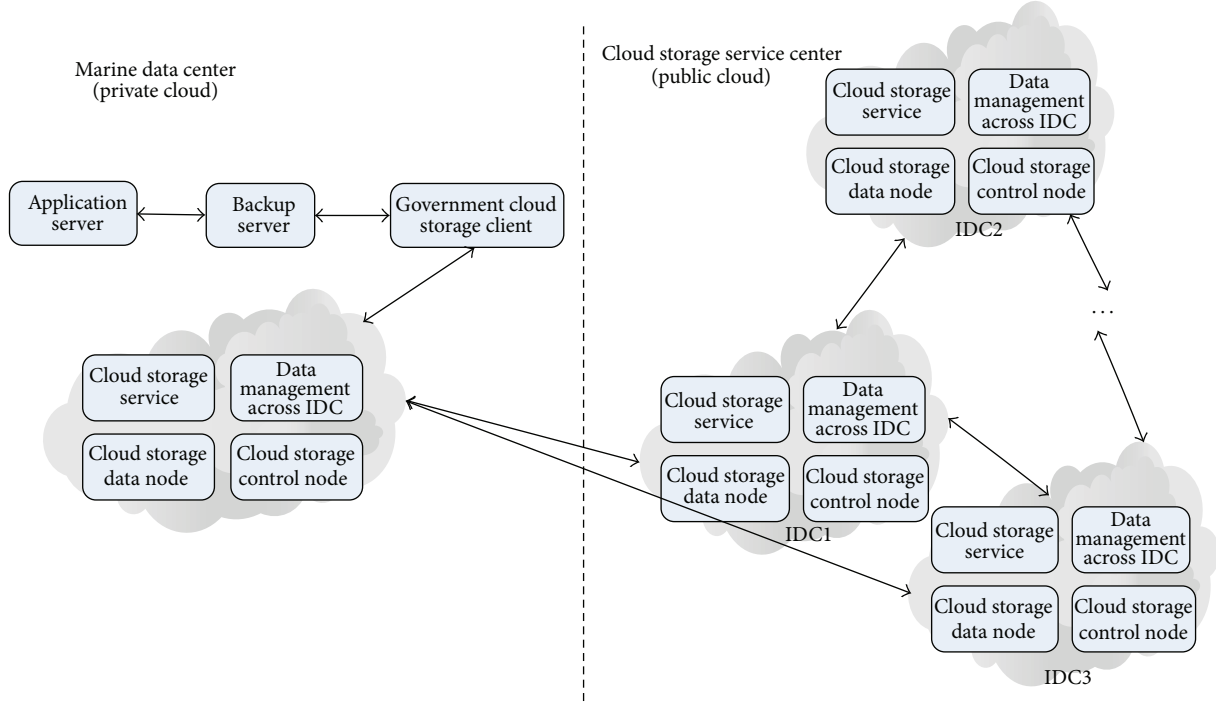


FIGURE 2: Hybrid cloud storage architecture.

The system performs migration by judging the value of the formula (10).

In this hybrid cloud storage platform, to keep the data availability, we set the data quality inspection model [68] to fit in marine big data and improve the data usage and reliability. The acceptance number c directly affects the inspection result. Given a sample size n , we can obtain c from the formula shown as follows:

$$c = -\frac{1}{2} + \frac{n}{\log(p_2/p_1) / \log(q_1/q_2) + 1}, \quad (11)$$

where p_1 represents accepting probability and p_2 is rejecting probability. And $q_1 = 1 - p_1$, $q_2 = 1 - p_2$.

We also use the data security technique to encrypt data in the cloud and keep the data confidential in the private cloud and to distribute the access right for cloud users and provide an effective access to the cloud data.

Along with data storage, data analysis and quality control finishing their works, the loaded disaster data would be cached on cloud, to facilitate demonstration fluency of disaster inversion process. The visualization cases of 3D terrain representation, water level rising process, and detail disaster situation are shown in Figures 3, 4, and 5, respectively.

In belief, the disaster inversion visualization has made significant contributions for marine big data.

(1) *Terrain Reconstruction.* The project has visualized the disaster of sea terrain in the form of 3-dimension style, which could help to analyze the causes of the disasters based on terrain conditions.

(2) *Disaster Reproduction.* The project, in a quasireal-time way, has reproduced multiple dataset involved in disaster process, including velocity, flow direction, and water depth, which could further help to fleetly evacuate victims.

(3) *Disaster Evaluation.* The project has reconstructed the postdisaster scene, which helps to evaluate the economic losses and human victims of the disaster area. (The project (Grant number 20905014-06) is finished by Digital Ocean Institute, College of Information, Shanghai Ocean University in May, 2014.)

5. Challenges in Marine Big Data Management

Prominent characteristics of marine big data have brought about new issues. In this case, this section discusses practical and theoretical challenges in the existence of marine big data management: data storage, data analysis, quality control, and data security.

5.1. *Data Storage.* Data storage underpins and sustains the efficient application of data. Under storage platform, rational data partition and suitable index building assist to realize efficient data queries. It has to be noted that there are some present situations in traditional storage system, mainly including lack in supporting dynamic scalability, simplified data storage method, relatively fixed data structure, controllable data size, and aware data type.

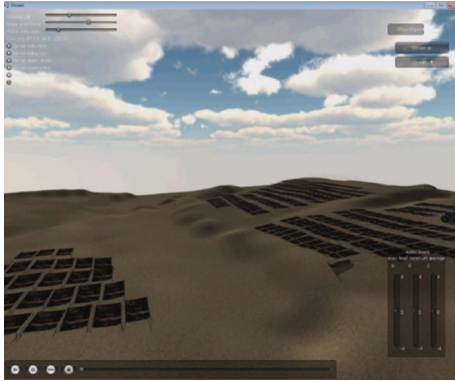


FIGURE 3: 3D terrain graph.



FIGURE 4: Water rising graph.



FIGURE 5: Postdisaster graph.

However, characteristics of marine big data, including large-volume, sensitivity, real-time, high dimension, diversity in data provision, and type, pose new challenges for data storage, mainly in two aspects.

(1) *Scalability Requirement for Storage Space.* Due to huge-volume and real-time characteristics of marine big data, it poses new challenges towards hardware architecture and file system, which requires data storage to be more scalable. Along with real-time acquisition of observing data, data storage should be more flexible.

(2) *Diversity Requirement for Storage System and Storage Model.* Multisource characteristic of marine big data imposes a great diversity in data type. Marine big data basically falls into three catalogs: structured attribute data (*.MDB, *.dbf, *.bak, *.dmp, etc.), spatial data (*.shp, *.adf, *.tif, *.jpg, etc.), and unstructured data (*.doc, *.xls, *.pdf, *.txt, *.xml, etc.). Diversity in data type puts forward higher request for database consistency, database usability, and partition tolerance.

5.2. Data Analysis. The purpose of data analysis is to find patterns and extract information from complex and vast data, which is the key to effectively exploit the value of marine big data. The object in traditional data analysis tends to be small datasets, which are structured dataset and single objects.

Data analysis and data mining prefer to build models by manual in advance according to priori knowledge and then analyze based on the selected data model. Diversity in data provision and heterogeneous characteristics of marine big data has raised some new issues, such as huge data amount, nonunified data type, and low data quality. Additionally, traditional analysis techniques like data mining, machine learning, and statistical analysis should be adjusted to make it adaptive to marine big data. Marine big data brings along with some analytical challenges, specific as follows.

(1) *Effectiveness Requirement.* Marine big data contains its unique characteristics, such as huge data amount, complex data type, and uncertain data distribution. Therefore, adaptive algorithm and model should be selected according to its data type and analysis target, to fleetly process marine data. This further leads to some challenges towards hardware and software, especially on data analysis algorithms.

(2) *Efficiency Requirement.* The application with marine data requires a higher demand on real-time response. Under such circumstances as Snow Dragon's expedition on extreme conditions in polar, it is essential to make a comprehensive analysis of real-time information on weather, sea ice, seabed, ship, and so forth. However, massive data processing and analyzing in real-time consumes huge computing resources, while traditional computing technologies are insufficient to that. Basically, it performs better in cooperation with cloud computing but proposes new challenges towards the scalability and real-time of its algorithm.

5.3. Data Availability. Quality of marine big data is the foundation of the development of marine Geographic Information Science. Due to the restriction of the acquisition and processing method, there exist a large number of random errors in marine big data, which leads to the unreliability of the marine data products. The existing theory of quality management is mainly used to control the quality of traditional industrial product, which is not quite suitable for the quality control marine big data with characteristics of multisource, massiveness, spatial relativity, and so forth. Therefore, development of quality control theories based on

characteristics of marine big data is one of the key issues in data management. The challenges are combining conventional quality control theory with marine big data management.

(1) *Quality Inspection Plan Designing.* Considering the characteristics of marine big data, it has become a priority issue to take the required precision into account, to design the optimal the sampling number and the acceptance number.

(2) *Spatial Sampling Method Deducing.* Due to the spatial autocorrelation characteristic of marine big data, the method of selecting marine data samples is different from the classical sampling method. The distance between data restricts the information redundancy between the sample points. Both considering the spatial autocorrelation of marine big data and achieving the maximum of information under the same inspection cost guarantee the implementation of the quality control of marine big data.

(3) *Theory of Usability and Autorestitution.* In terms of the quality inspection result, marine big data can be divided into usable data and risk data. Due to various data acquisition methods, most of marine big data are irreversible, which makes it significant to study on the usability of marine data products and data autorestitution.

5.4. *Data Security.* Compared to the traditional data security, marine data's security and privacy protection appear significantly different and show the typical structure-based characteristics including "one to many" structure (one user stores the data, multiple users access), "many to one" structure, and "many to many" structure. From the data processing perspective, the service of marine big data can be divided into data storage service, data access service, data computation service, data share service, and data supervision service. In short, the challenges in marine big data security can be also summarized as "secure data storage, secure data access, secure data computation, secure data sharing, and secure data supervision."

(1) *Secure Data Storage Requirement.* From the case of Snowden, people all over the world have realized that the users' privacy as well as the sensitive data will be greatly harmed if the data are not in a properly secure storage. The storage of marine data often relies on the credibility of the servers/nodes, which could not resist the servers' administrators and the inside adversary wiretapping and tampering the data. If the data is not discriminated and used directly, the factual data also cheat the users; in particular forgery or deliberately manufacturing data often leads to the incorrect and incomplete conclusions.

(2) *Secure Data Access Requirement.* Data access control is an effective way to realize the data sharing. Marine big data are used for different scenarios and accessed by different users with different roles and different security levels. The access control requirements are very prominent since the

traditional access control techniques mainly depend on the security of the database and cloud service providers. Once the database administrators and cloud service providers take malicious behaviors, the data are no longer secure in the database and data sharing, which results in violation of the data confidentiality and the users' privacy.

(3) *Secure Data Computation Requirement.* Data computation such as calculation and analysis of marine data is another important application. Since marine big data service providers cannot be fully trusted and computation services are often in an outsourcing way, it is an important requirement that how to achieve the data confidentiality and realize the data calculation and analysis simultaneously. In addition, it is also important to improve the efficiency of data calculation and analysis as well as ensure the effectiveness of the storage data.

(4) *Secure Data Sharing Requirement.* In the marine data sharing and dissemination, the data are often shared among the authored users. Thus, the security is based on the users' secret keys. The data will be given away if the user's secret keys were leaked intentionally or unintentionally, which is unable to realize the secure data sharing and dissemination mechanism in the cloud. Furthermore, since the security of modern cryptographic systems depends only on the secret keys, the whole security systems would collapse if there is no technique to trace and revoke leaked secret keys.

(5) *Secure Data Supervision Requirement.* Data supervision is a guarantee to marine data security. In the processing stages of data storage, computation, sharing, and dissemination, malicious adversaries may insert false data intentionally and unintentional users may insert error data if there is a lack of the techniques of data supervision and monitoring. It is also important to remove illegal information, reduce the redundancy cost, check the content completeness, and verify the correctness of the calculation results in the marine data supervision.

6. Conclusions

As we have entered an era of marine big data, it is of great realistic and theoretical significance to study on the marine big data management. Unfortunately, existing techniques and theories are very limited to solve the real problems completely in the marine big data. To tackle above issues, this paper has analyzed the existing challenges in data storage, data analysis, quality control, and data security, summarized the marine big data models, algorithms, methods, and techniques in field of marine big data management, and finally presented a practical engineering instance that demonstrates the management architecture. There is no doubt that study on marine big data management is still in the initial stage of development; thereby more scientific investments from both academy and industry should be poured into this scientific paradigm to capture huge values from marine big data.

Conflict of Interests

Dongmei Huang, Danfeng Zhao, Lifei Wei, Zhenhua Wang, and Yanling Du declare that there is no conflict of interests regarding the publication of this paper.

Acknowledgments

This work was supported by the National Natural Science Foundation of China (Grant no. 61272098 and 61402282) and the National 973 Program (Grant no. 2012CB316206). The authors would like to thank anonymous reviewers who helped us in giving comments to this paper.

References

- [1] "The International ARGO Project," <http://www.argo.net/>.
- [2] Ocean Networks Canada, <http://www.neptunecanada.ca/>.
- [3] "Ocean Observatories Initiative," <http://oceanobservatories.org/>.
- [4] The Global Ocean Observing System, <http://www.ioc-goos.org/>.
- [5] Integrated Ocean Observing System, <http://www.ioos.noaa.gov>.
- [6] National Aeronautics and Space Administration, <http://www.nasa.gov/>.
- [7] National Oceanic and Atmospheric Administration, <http://www.noaa.gov/>.
- [8] China Argo Data Center, <http://www.argo.gov.cn/>.
- [9] "News in brief of Argo," China Argo Real-time Data Center, China, 2014, (Chinese), <http://www.argo.org.cn/>.
- [10] P. J. Durack, S. E. Wijffels, and R. J. Matear, "Ocean salinities reveal strong global water cycle intensification during 1950 to 2000," *Science*, vol. 336, no. 6080, pp. 455–458, 2012.
- [11] C. J. Brown, S. J. Smith, P. Lawton, and J. T. Anderson, "Benthic habitat mapping: a review of progress towards improved understanding of the spatial ecology of the seafloor using acoustic techniques," *Estuarine, Coastal and Shelf Science*, vol. 92, no. 3, pp. 502–520, 2011.
- [12] G. C. Rogers, R. Meldrum, R. Baldwin et al., "The NEPTUNE Canada seismograph network," *Seismological Research Letters*, vol. 81, no. 2, p. 369, 2009.
- [13] A. B. Rabinovich, R. E. Thomson, and I. V. Fine, "The 2010 chilean tsunami off the west coast of Canada and the northwest coast of the United States," *Pure and Applied Geophysics*, vol. 170, no. 9–10, pp. 1529–1565, 2013.
- [14] X. Meng and X. Ci, "Big data management: concepts, techniques and challenges," *Computer Research and Development*, vol. 50, no. 1, pp. 146–169, 2013 (Chinese).
- [15] National Oceanographic Data Center, <http://www.nodc.noaa.gov/access/allproducts.html>.
- [16] <http://en.wikipedia.org/wiki/Oceanography>.
- [17] D. Huang, Y. Du, and Q. He, "Migration algorithm for big data in hybrid cloud storage," *Journal of Computer Research and Development*, vol. 51, no. 1, pp. 199–205, 2014 (Chinese).
- [18] Google Cloud Storage Overview, <https://developers.google.com/storage/docs/overview?csw=1>.
- [19] <http://aws.amazon.com/cn/s3/>.
- [20] "Windows Azure General Availability," <http://blogs.microsoft.com/blog/2010/02/01/windows-azure-general-availability/>.
- [21] "Cloud computing strategy and Blue Cloud of IBM," <ftp://ftp.software.ibm.com/software/cn/smsp/4.0/cloudstrategy-IBMbluecloud.pdf>.
- [22] D. Zhao, *The architecture of artifact-centric business process management system on the cloud computing platform [Ph.D. thesis]*, Yanshan University, Qinhuangdao, China, 2012.
- [23] X.-M. Zhou and G.-R. Wang, "Key dimension based high-dimensional data partition strategy," *Journal of Software*, vol. 15, no. 9, pp. 1361–1374, 2004 (Chinese).
- [24] P. Ren, W. Liu, and D. Sun, "Partition-based data cube storage and parallel queries for cloud computing," in *Proceedings of the 9th International Conference on Natural Computation (ICNC '13)*, pp. 1183–1187, July 2013.
- [25] C. Selvakumar, G. J. Rathanam, and M. R. Sumalatha, "PDDS—improving cloud data storage security using data partitioning technique," in *Proceedings of the 3rd IEEE International Advance Computing Conference (IACC '13)*, pp. 7–11, 2013.
- [26] D. Zhao, S. Jin, G. Liu, F. Gao, and N. Wang, "A cryptograph index technology based on query probability in DAS model," *Journal of Yanshan University*, vol. 32, no. 6, pp. 477–482, 2008 (Chinese).
- [27] B.-R. Dai and I.-C. Lin, "Efficient map/reduce-based DBSCAN algorithm with optimized data partition," in *Proceedings of the IEEE 5th International Conference on Cloud Computing (CLOUD '12)*, pp. 59–66, June 2012.
- [28] L. Han, X. Sun, and Z. Wu, "Optimization study on sample based partition on mapreduce," *Journal of Computer Research and Development*, vol. 50, pp. 77–84, 2013 (Chinese).
- [29] Y. Xu, P. Zou, W. Qu, Z. Li, K. Li, and X. Cui, "Sampling-based partitioning in mapreduce for skewed data," in *Proceedings of the 7th ChinaGrid Annual Conference (ChinaGrid '12)*, pp. 1–8, September 2012.
- [30] D. Huang, L. Sun, D. Zhao et al., "An efficient hybrid index structure for temporal marine data," in *Proceedings of Conference on Web-Age Information Management*, 2014.
- [31] S. Shi and B. Lei, *Theory and Practice on China Digital Ocean*, Ocean Press, Beijing, China, 2011.
- [32] A. Fox, C. Eichelberger, J. Hughes, and S. Lyon, "Spatio-temporal indexing in non-relational distributed databases," in *Proceedings of the IEEE International Conference on Big Data*, pp. 291–299, October 2013.
- [33] B. Stantic, R. Topor, J. Terry, and A. Sattar, "Advanced indexing technique for temporal data," *Computer Science and Information Systems*, vol. 7, no. 4, pp. 679–703, 2010.
- [34] B. Stantic, J. Terry, R. Topor et al., "Indexing temporal data with virtual structure," in *Proceedings of the 14th East European Conference on Advances in Databases and Information Systems*, pp. 591–594, 2010.
- [35] T. Emrich, H.-P. Kriegel, N. Mamoulis, M. Renz, and A. Züfle, "Indexing uncertain spatio-temporal data," in *Proceedings of the 21st ACM International Conference on Information and Knowledge Management (CIKM '12)*, pp. 395–404, November 2012.
- [36] Y. Zhong, J. Fang, and X. Zhao, "VegaIndexer: a distributed composite index scheme for big spatio-temporal sensor data on cloud," in *Proceedings of the 33rd IEEE International Geoscience and Remote Sensing Symposium (IGARSS '13)*, pp. 1713–1716, July 2013.

- [37] S. Chen, B. C. Ooi, K.-L. Tan, and M. A. Nascimento, "ST2B-tree: a self-tunable spatio-temporal B+-tree index for moving objects," in *Proceedings of the ACM SIGMOD International Conference on Management of Data (SIGMOD '08)*, pp. 29–42, June 2008.
- [38] S. Chen, B. C. Ooi, K.-L. Tan, and M. A. Nascimento, "ST2B-tree: a self-tunable spatio-temporal B+-tree index for moving objects," in *Proceedings of the ACM SIGMOD International Conference on Management of Data*, pp. 29–42, June 2008.
- [39] M. Kaufmann, A. A. Manjili, P. Vagenas et al., "Timeline index: a unified data structure for processing queries on temporal data in SAP HANA," in *Proceedings of the ACM SIGMOD Conference on Management of Data (SIGMOD '13)*, pp. 1173–1184, June 2013.
- [40] X. Hu, M. Qiao, and Y. Tao, "Independent range sampling," in *Proceedings of the 33rd ACM Special Interest Group Conference on Management of Data*, pp. 246–255, 2014.
- [41] J. Zhang, G. Chen, and X. Tang, "Extracting representative information to enhance flexible data queries," *IEEE Transactions on Neural Networks and Learning Systems*, vol. 23, no. 6, pp. 928–941, 2012.
- [42] S. Thomas and L. Kevin, "MapReduce optimization using regulated dynamic prioritization," in *Proceedings of the 11th international joint conference on Measurement and modeling of computer systems (SIGMETRICS '09)*, pp. 299–310, June 2009.
- [43] W. Gharibi and A. Mousa, "Query optimization based on time scheduling approach," in *Proceedings of the 11th IEEE East-West Design & Test Symposium (EWDTS '13)*, pp. 1–7, September 2013.
- [44] T. Miller and T. Gibson, "An improved long-term file usage prediction algorithm," <http://users.soe.ucsc.edu/~elm/Papers/cmg99.pdf>.
- [45] J. Jeong and M. Dubois, "Cost-sensitive cache replacement algorithms," in *Proceedings the 9th International Symposium on High-Performance Computer Architecture (HPCA-9 '03)*, vol. 1, pp. 327–337, Anaheim, Calif, USA, 2003.
- [46] B. Reed and D. D. E. Long, "Analysis of caching algorithms for distributed file systems," in *Proceedings of the ACM SIGOPS Operating Systems Review*, pp. 12–21, July 1996.
- [47] D. He, X. Zhang, D. H. C. Du, and G. Grider, "Coordinating parallel hierarchical storage management in object-based cluster file system," <http://wiki.lustre.org/images/f/fc/MSST-2006-paper.pdf>.
- [48] L. Ao, D. Yu, J. Shu, and W. Xue, "A tiered storage system for massive data: TH-TS," *Journal of Computer Research and Development*, vol. 48, no. 6, pp. 1089–1100, 2011 (Chinese).
- [49] S. Melnik, A. Gubarev, J. J. Long et al., "Dremel: interactive analysis of web-scale datasets," *Proceedings of the VLDB Endowment*, vol. 3, no. 1-2, pp. 330–339, 2010.
- [50] F. Li, B. C. Ooi, M. T. Ozsu et al., "Distributed data management using mapReduce," *ACM Computing Surveys (CSUR)*, vol. 46, no. 3, pp. 1–41, 2014.
- [51] G. Malewicz, M. H. Austern, A. J. C. Bik et al., "Pregel: a system for large-scale graph processing," in *Proceedings of the International Conference on Management of Data (SIGMOD '10)*, pp. 135–146, June 2010.
- [52] L. G. Valiant, "Bridging model for parallel computation," *Communications of the ACM*, vol. 33, no. 8, pp. 103–111, 1990.
- [53] "Google BigQuery," <https://cloud.google.com/products/big-query/>.
- [54] A. Hall, O. Bachmann, R. Bussow et al., "Processing a trillion cells per mouse click," *PVLDB*, vol. 5, no. 11, pp. 1436–1446, 2012.
- [55] M. Isard, M. Budiu, Y. Yu, A. Birrell, and D. Fetterly, "Dryad: distributed data-parallel programs from sequential building blocks," in *Proceedings of the 2nd ACM SIGOPS/EuroSys European Conference on Computer Systems (EuroSys '07)*, vol. 41, pp. 59–72, March 2007.
- [56] "Cascading," <http://www.cascading.org/>.
- [57] G. Shank, R. Y. Wang, and Z. Mostapha, "IP-map: representing the manufacture of an information product," in *Proceedings of the Information Quality Conference*, pp. 1–16, 2000.
- [58] Y. Wand and R. Y. Wang, "Anchoring data quality dimensions in ontological foundations," *Communications of the ACM*, vol. 39, no. 11, pp. 86–95, 1996.
- [59] A. Zargar and R. Devillers, "An operation-based communication of spatial data quality," in *Proceedings of the International Conference on Advanced Geographic Information Systems and Web Services (GEOWS '09)*, pp. 140–145, February 2009.
- [60] "ISO 19113: Geographic Information Quality Principles," <http://www.statkart.no/isot211/>, 2001.
- [61] A. Kleiner, A. Talwalkar, P. Sarkar, and M. I. Jordan, "A scalable bootstrap for massive data," *Journal of the Royal Statistical Society B: Statistical Methodology*, vol. 76, no. 4, pp. 795–816, 2014.
- [62] J. Wang, J. Liu, D. Zhuan, L. Li, and Y. Ge, "Spatial sampling design for monitoring the area of cultivated land," *International Journal of Remote Sensing*, vol. 23, no. 2, pp. 263–284, 2002.
- [63] J. Wang, R. Haining, and Z. Cao, "Sample surveying to estimate the mean of a heterogeneous surface: reducing the error variance through zoning," *International Journal of Geographical Information Science*, vol. 24, no. 4, pp. 523–543, 2010.
- [64] Z. Wang, X. N. Zhou, and D. M. Huang, "A sampling model for the quality inspection of uncertain ocean data," to appear in *Computer Science*.
- [65] E. G. Schilling and D. V. Neubauer, *Acceptance Sampling and Quality Control*, CRC Press, New York, NY, USA, 2012.
- [66] ISO 2859.0, *Sampling Procedures for Inspection by Attributes—Part 0: Introduction to the ISO 2859 Attribute Sampling System*, International Organization for Standardization, 1995.
- [67] A. Golub, "Designing single-sampling inspection plans when the sample size is fixed," *Journal of the American Statistical Association*, vol. 48, no. 262, pp. 278–288, 1953.
- [68] A. Hald, "The determination of single sampling attribute plans with given producer's and consumer's risk," *Technometrics*, vol. 9, no. 3, pp. 401–415, 1967.
- [69] B. P. M. Duarte and P. M. Saraiva, "An optimization-based approach for designing attribute acceptance sampling plans," *International Journal of Quality and Reliability Management*, vol. 25, no. 8, pp. 824–841, 2008.
- [70] S. T. A. Niaki and M. S. F. Nezhad, "Designing an optimum acceptance sampling plan using Bayesian inferences and a stochastic dynamic programming approach," *ScientiaIranica Transaction E: Industrial Engineering*, vol. 16, no. 1, pp. 19–25, 2009.
- [71] E. B. Jamkhaneh and B. S. Gildeh, "AOQ and ATI for double sampling plan with using fuzzy binomial distribution," in *Proceedings of the International Conference on Intelligent Computing and Cognitive Informatics (ICICCI '10)*, pp. 45–49, June 2010.
- [72] C. A. J. Klaassen, "Credit in acceptance sampling on attributes," *Technometrics*, vol. 43, no. 2, pp. 212–222, 2001.

- [73] J. Li and X. Liu, "An important aspect of big data: data usability," *Computer Research and Development*, vol. 50, no. 6, pp. 1147–1162, 2012.
- [74] W. Fan, F. Geerts, J. Li, and M. Xiong, "Discovering conditional functional dependencies," *IEEE Transactions on Knowledge and Data Engineering*, vol. 23, no. 5, pp. 683–698, 2011.
- [75] L. Golab, F. Korn, and D. Srivastava, "Efficient and effective analysis of data quality using pattern tableaux," *IEEE on Data Engineering*, vol. 34, no. 3, pp. 26–33, 2011.
- [76] G. Grahne, *The Problem of Incomplete Information in Relational Databases*, Springer, Berlin, Germany, 1991.
- [77] W. Fan, F. Geerts, and J. Wijzen, "Determining the currency of data," *ACM Transactions on Database Systems*, vol. 37, no. 4, article 25, 2012.
- [78] L. W. Ferreira Chaves, E. Buchmann, and K. Böhm, "Finding misplaced items in retail by clustering RFID data," in *Proceedings of the 13th International Conference on Extending Database Technology (EDBT '10)*, pp. 501–512, March 2010.
- [79] W. Fan, F. Geerts, X. Jia, and A. Kementsietsidis, "Conditional functional dependencies for capturing data inconsistencies," *ACM Transactions on Database Systems*, vol. 33, no. 2, Article ID 1366103, pp. 1–48, 2008.
- [80] W. Fan, F. Geerts, S. Ma, and H. Müller, "Detecting inconsistencies in distributed data," in *Proceedings of the 26th IEEE International Conference on Data Engineering (ICDE '10)*, pp. 64–75, March 2010.
- [81] W. Fan, J. Li, N. Tang, and W. Yu, "Incremental detection of inconsistencies in distributed data," in *Proceedings of the IEEE 28th International Conference on Data Engineering (ICDE '12)*, pp. 318–329, April 2012.
- [82] S. E. Whang, D. Menestrina, G. Koutrika, M. Theobald, and H. Garcia-Molina, "Entity resolution with iterative blocking," in *Proceedings of the 35th SIGMOD Conference on Management of Data*, pp. 219–231, July 2009.
- [83] J. Chomicki and J. Marcinkowski, "Minimal-change integrity maintenance using tuple deletions," *Information and Computation*, vol. 197, no. 1–2, pp. 90–121, 2005.
- [84] J. Bleiholder, S. Szott, M. Herschel, F. Kaufer, and F. Naumann, "Subsumption and complementation as data fusion operators," in *Proceedings of the 13th International Conference on Extending Database Technology (EDBT '10)*, pp. 513–524, March 2010.
- [85] H. Lin, Z. Cao, X. Liang, and J. Shao, "Secure threshold multi authority attribute based encryption without a central authority," *Information Sciences*, vol. 180, no. 13, pp. 2618–2632, 2010.
- [86] K. Yang and X. Jia, "Data storage auditing service in cloud computing: challenges, methods and opportunities," *World Wide Web*, vol. 15, no. 4, pp. 409–428, 2012.
- [87] C. Wang, S. S. Chow, Q. Wang, K. Ren, and W. Lou, "Privacy-preserving public auditing for secure cloud storage," *IEEE Transactions on Computers*, vol. 62, no. 2, pp. 362–375, 2013.
- [88] M. Li, S. Yu, K. Ren, W. Lou, and Y. Hou, "Toward privacy-assured and searchable cloud data storage services," *IEEE Network*, vol. 27, no. 4, pp. 56–62, 2013.
- [89] X. Liang, Z. Cao, H. Lin, and D. Xing, "Provably secure and efficient bounded ciphertext policy attribute based encryption," in *Proceedings of the 4th International Symposium on ACM Symposium on Information, Computer and Communications Security (ASIACCS '09)*, pp. 343–352, March 2009.
- [90] K. Yang, X. Jia, K. Ren et al., "Enabling efficient access control with dynamic policy updating for big data in the cloud," in *Proceedings of the IEEE Conference on Computer Communications (INFOCOM '13)*, pp. 2013–2021, 2013.
- [91] H. Wang and L. V. S. Lakshmanan, "Efficient secure query evaluation over encrypted XML databases," in *Proceedings of the 32nd International Conference on Very Large Data Bases (VLDB '06)*, pp. 127–138, September 2006.
- [92] N. Cao, C. Wang, L. Ming et al., "Privacy-preserving multi-keyword ranked search over encrypted cloud data," *IEEE Transactions on Parallel and Distributed Systems*, vol. 25, no. 1, pp. 222–233, 2014.
- [93] C. Wang, K. Ren, S. Yu, and K. M. R. Urs, "Achieving usable and privacy-assured similarity search over outsourced cloud data," in *Proceedings of the IEEE Conference on Computer Communications (INFOCOM '12)*, pp. 451–459, March 2012.
- [94] E. Shen, E. Shi, and B. Waters, "Predicate privacy in encryption systems," in *Proceedings of the 6th Theory of Cryptography Conference (TCC '09)*, pp. 457–473, San Francisco, Calif, USA, March 2009.
- [95] C. Wang, K. Ren, J. Wang, and Q. Wang, "Harnessing the cloud for securely outsourcing large-scale systems of linear equations," *IEEE Transactions on Parallel and Distributed Systems*, vol. 24, no. 6, pp. 1172–1181, 2013.
- [96] Z. Xu, C. Wang, K. Ren et al., "Proof-carrying cloud computation: the case of convex optimization," *IEEE Transactions on Information Forensics and Security*, vol. 9, no. 11, pp. 1790–1803, 2014.
- [97] J. H. Cheon, J. S. Coron, J. Kim et al., "Batch fully homomorphic encryption over the integers," in *Proceedings of the Annual International Conference on the Theory and Applications of Cryptographic Techniques (EUROCRYPT '13)*, pp. 315–335, 2013.
- [98] M. Li, S. Yu, Y. Zheng, K. Ren, and W. Lou, "Scalable and secure sharing of personal health records in cloud computing using attribute-based encryption," *IEEE Transactions on Parallel and Distributed Systems*, vol. 24, no. 1, pp. 131–143, 2013.
- [99] Z. Liu, Z. Cao, and D. S. Wong, "White-box traceable ciphertext-policy attribute-based encryption supporting any monotone access structures," *IEEE Transactions on Information Forensics and Security*, vol. 8, no. 1, pp. 76–88, 2013.
- [100] J. Ning, Z. Cao, X. Dong et al., "Large universe ciphertext-policy attribute-based encryption with white-box traceability," in *Proceedings of the European Symposium on Research in Computer Security (ESORICS '14)*, Wroclaw, Poland, September 2014.
- [101] Z. Liu, Z. Cao, and D. S. Wong, "Blackbox traceable CP-ABE: how to catch people leaking their keys by selling decryption devices on eBay," in *Proceedings of the ACM SIGSAC Conference on Computer and Communications Security (CCS '13)*, pp. 475–486, November 2013.
- [102] K. Yang, X. Jia, and K. Ren, "Attribute-based fine-grained access control with efficient revocation in cloud storage systems," in *Proceedings of the 8th ACM SIGSAC Symposium on Information, Computer and Communications Security (ASIACCS '13)*, pp. 523–528, May 2013.
- [103] Z. Cao, *New Directions of Modern Cryptography*, CRC Press, Boca Raton, Fla, USA, 2012.
- [104] K. Yang, X. Jia, K. Ren, B. Zhang, and R. Xie, "DAC-MACS: effective data access control for multiauthority cloud storage systems," *IEEE Transactions on Information Forensics and Security*, vol. 8, no. 11, pp. 1790–1801, 2013.

- [105] L. Wei, H. Zhu, Z. Cao et al., “Security and privacy for storage and computation in cloud computing,” *Information Sciences*, vol. 258, pp. 371–386, 2014.
- [106] Q. Wang, K. Ren, and X. Meng, “When cloud meets eBay: towards effective pricing for cloud computing,” in *Proceedings of the IEEE Conference on Computer Communications (INFOCOM '12)*, pp. 936–944, March 2012.
- [107] D.-G. Feng, M. Zhang, and H. Li, “Big data security and privacy protection,” *Chinese Journal of Computers*, vol. 37, no. 1, pp. 1–13, 2014 (Chinese).
- [108] G.-H. Kim, S. Trimi, and J.-H. Chung, “Big-data applications in the government sector,” *Communications of the ACM*, vol. 57, no. 3, pp. 78–85, 2014.

Research Article

Computational Fluid Dynamics Simulation of Oxygen Seepage in Coal Mine Goaf with Gas Drainage

Guo-Qing Shi,¹ Mao-xi Liu,¹ Yan-Ming Wang,² Wen-Zheng Wang,¹ and De-Ming Wang¹

¹School of Safety Engineering, China University of Mining and Technology, Xuzhou 221116, China

²Department of Mechanical and Aerospace Engineering, Rutgers, The State University of New Jersey, Piscataway, NJ 08854, USA

Correspondence should be addressed to Yan-Ming Wang; cumtwangym@163.com

Received 7 August 2014; Revised 17 October 2014; Accepted 27 October 2014

Academic Editor: Shaofan Li

Copyright © 2015 Guo-Qing Shi et al. This is an open access article distributed under the Creative Commons Attribution License, which permits unrestricted use, distribution, and reproduction in any medium, provided the original work is properly cited.

Mine fires mainly arise from spontaneous combustion of coal seams and are a global issue that has attracted increasing public attention. Particularly in China, the closure of coal workfaces because of spontaneous combustion has contributed to substantial economic loss. To reduce the occurrence of mine fires, the spontaneous coal combustion underground needs to be studied. In this paper, a computational fluid dynamics (CFD) model was developed for coal spontaneous combustion under goaf gas drainage conditions. The CFD model was used to simulate the distribution of oxygen in the goaf at the workface in a fully mechanized cave mine. The goaf was treated as an anisotropic medium, and the effects of methane drainage and oxygen consumption on spontaneous combustion were considered. The simulation results matched observational data from a field study, which indicates CFD simulation is suitable for research on the distribution of oxygen in coalmines. The results also indicated that near the workface spontaneous combustion was more likely to take place in the upper part of the goaf than near the bottom, while further from workface the risk of spontaneous combustion was greater in the lower part of the goaf. These results can be used to develop firefighting approaches for coalmines.

1. Introduction

Spontaneous combustion of coal is an issue that threatens the development of the coal industry worldwide. Among China's state-owned collieries, 56% of the mines have been jeopardized by spontaneous combustion, and the combustion incidents in these mines account for 90–94% of all coalmine fires [1]. Since the 1990s, the coalmines operating in China have mainly been fully mechanized cave mines. This type of mining leaves a large amount coal in the goaf. The production efficiency is increased compared to nonmechanized mining, but fully mechanized mining results in high air leakage, high rock fall, and more loose coal. These factors increase the probability of coal spontaneous combustion. Furthermore to reduce the risks of gas explosion and improve utilization of methane, especially in mines with high gas content, at some coalmines gas is drained from the mine goaf and coal with high negative pressure technology. These practices increase the air leakage volume and disturb mine ventilation, which elevates the risk of coal spontaneous combustion.

Spontaneous combustion of coal underground takes place mainly in the goaf and occurs through a complex system of thermal, hydraulic, chemical, and mechanical processes [2–6]. The combustion of coal underground is closely related to the concentration and distribution of oxygen in the goaf [7]. Consequently, study of the oxygen concentration and distribution is important to understand coal spontaneous combustion. To date, the oxygen distribution in coal mine goaf has typically been approximated from either a minimal number of actual gas measurements in the goaf or model test results obtained in the laboratory. These two methods have many disadvantages, one of which is the heavy workload required. Although laboratory results are valuable, their extrapolation to the mining environment is not entirely successful because scaling is complicated, and small-scale experiments do not accurately replicate the large-scale environment. Scaling issues typically arise when the coal temperature is high enough that radiative heat transfer cannot be neglected. In these cases, there are problems with scaling of the radiative heat transfer from the small-scale

spontaneous combustion results to large-scale mining. For small-scale tests when the coal temperature is low, radiative heat transfer can be neglected but the test results have not been validated [7, 8]. Consequently, it is necessary to establish a new method to study coal spontaneous combustion.

In this paper, to study coal spontaneous combustion, we developed a three-dimensional CFD model of the oxygen concentration under conditions of gas drainage from the goaf. The distribution of oxygen in the goaf was simulated, and the results used to evaluate the coal spontaneous combustion hazard in specific areas of the goaf. The influence of goaf gas drainage on oxygen distribution was also studied using numerical methods. The results could be used for prevention of coal spontaneous combustion and to establish fire-fighting protocols.

2. Theory

2.1. Oxygen Diffusion in the Goaf. In order to simulate the oxygen distribution in goaf under gas drainage conditions, numerical modeling was performed with CFD theories. The finite volume method with the second-order upwind scheme was used to solve the coupled flow, mass transfer, and energy equations using the CFD solver. CFD simulations require solving the Navier-Stokes (N-S) equations, which are formed from a series of partial differential equations governing mass, momentum, and energy conservation. If mass transfer and mixing are part of the process under investigation, then a conservation equation for the components must also be included [9]. The mathematical model for flow of mixed gas in the mine goaf is developed using these equations, along with specific boundary conditions and initial conditions. The following equations apply to gas flow in goaf [10]. The mass conservation equation can be expressed as

$$\frac{\partial \rho}{\partial t} + \frac{\partial (\rho u_i)}{\partial x_i} = s_m, \quad (1)$$

where ρ is the density the mixed gas, i represents the x , y , z coordinates in three-dimensional space, x_i is the distance, t is the time, u_i is the velocity, and s_m is the source of mass loss of gas in goaf.

The momentum conservation equation is

$$\frac{\partial}{\partial t} (\rho u_i) + \frac{\partial}{\partial x_j} (\rho u_i u_j) = -\frac{\partial p}{\partial x_i} + \frac{\partial \tau_{ij}}{\partial x_j} + \rho g_i + s_i, \quad (2)$$

where p is the gas pressure of cube i , j represents the x , y , z coordinates in three-dimensional space, x_j is the distance, τ_{ij} is the viscous stress tensor which is caused by the viscous effect, g_i is the gravity component in direction i , and s_i is source of momentum loss. The momentum loss is caused by fluid flow in porous media and can be expressed as

$$s_i = \sum_{j=1}^3 D_{ij} \mu v_j + \sum_{j=1}^3 C_{ij} \frac{1}{2} \rho |v_j| v_j, \quad (3)$$

where μ is the gas viscosity in the goaf; D_{ij} is the matrix of the viscous loss coefficient; C_{ij} is the matrix of the inertia

loss coefficient; and v_j is the velocity component in direction j , where j represents the x , y , z coordinates in three-dimensional space. This equation indicates that when the velocity is low in comparison to the viscous loss coefficient, the inertia loss coefficient will be infinitely small.

Equation (3) is equivalent to Darcy's equation. Convection and diffusion of the multicomponent gas is mainly considered when air transfer occurs in the goaf. From the component mass conservation law, the following conservation equation is obtained:

$$\frac{\partial (\rho c_S)}{\partial t} + \text{div} (\rho \vec{u} c_S) = \text{div} (D_S \text{grad} (\rho c_S)) + s_S, \quad (4)$$

where c_S is the fraction of component S and ρ is its density, D_S is the diffusion coefficient of component S , s_S is the source term of S , and $\text{div} (*) = \partial a_x / \partial x + \partial a_y / \partial y + \partial a_z / \partial z$ is a scalar quantity. The source term includes events such as methane and CO release and oxygen consumption.

The energy transport equation is formulated under the assumption of thermal equilibrium between the solid matrix and gas. Coal oxidation is an exothermic process, and to provide an accurate description of oxygen concentration, the link between heat production and oxygen consumption must be considered. Therefore, the mathematical model should contain energy conservation equations such as

$$\frac{\partial (\rho T)}{\partial t} + \text{div} (\rho \vec{u} T) = \text{div} \left(\frac{k}{c_p} \text{grad} T \right) + s_T, \quad (5)$$

where c_p is the specific heat capacity, T is the thermodynamic temperature, k is the thermal conductivity of gas in the goaf, and s_T is energy source term. For CFD simulation, the geometry, material properties, and boundary conditions need to be specified.

2.2. CFD Model of Oxygen for the Fully Mechanized Cave Mine Workface. The distribution of oxygen was modeled using the widely used CFD software FLUENT. CFD analysis generally involves the following key steps: field studies to obtain basic information on goaf geometry and other parameters; meshing of the established geometric model to a finite element grid by automatic mesh generation software such as Gambit; establishment of flow models and boundary conditions through user-defined functions (UDFs) as described in [11]; model simulations with basic conditions; model calibration and validation with field measured data; and study of the influence of various parameters on the oxygen distribution using the CFD model.

The main factors influencing the distribution of oxygen in mine goaf are viscous flow, which is caused by a pressure gradient, and diffusion, which is caused by a concentration gradient. The longwall goaf permeability and oxygen consumption and diffusion coefficients are the main parameters in a mathematical model of oxygen distribution. Goaf permeability is largely affected by the distribution of pressure in the goaf. Creedy and Clarke highlighted that the permeability at the edge of the goaf is significantly different from that in the middle, and the permeability in these areas

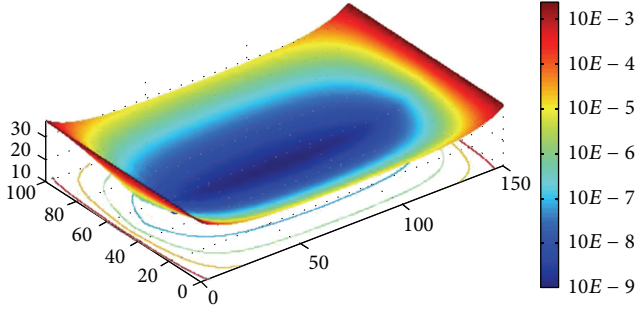


FIGURE 1: Permeability distributions in the goaf.

can range from 10^{-2} m^2 to 10^{-7} m^2 [12]. In the simulation in the present study, goaf permeability was varied from 10^{-2} m^2 to 10^{-9} m^2 , and the permeability was expressed by a hyperbolic tangent function [13, 14], and the characteristics of permeability distribution can be seen as in Figure 1.

With Fick's Law of diffusion, the diffusion flux can be expressed by the following equation [15]:

$$J_i = \rho D_{im} \frac{\partial X_i}{\partial x_i} - \frac{D_i^T}{T} \frac{\partial T}{\partial x_i}, \quad (6)$$

where J_i is diffusion flow volume of gas i and is mainly caused by concentration and thermal gradients; D_{im} is the diffusion coefficient of the mixed gas; x_i is mass fraction of gas i ; D_i^T is the thermal diffusion, and T is the temperature.

For a nonrarefied gas, (5) can be replaced by the following equation:

$$J_i = \rho \frac{M_i}{M_{\min}} \sum_{j,j \neq i} D_{ij} \left(\frac{\partial X_j}{\partial x_i} + \frac{X_j}{M_{\min}} \frac{\partial M_{\min}}{\partial x_i} \right) - \frac{D_i^T}{T} \frac{\partial T}{\partial x_i}, \quad (7)$$

where M_i is the molecular weight of gas i , M_{\min} is the molecular weight of the mixed gas, and D_{ij} is the diffusion coefficient of gas i mixed with gas j .

The chemical reaction between coal and oxygen at low temperatures is complex. Generally, the following three types of processes are believed to occur [16]: (i) physical adsorption; (ii) chemical adsorption, which leads to the formation of coal-oxygen complexes and oxygenated carbon species; and (iii) oxidation, in which the coal and oxygen react and release gaseous products such as carbon monoxide (CO), carbon dioxide (CO₂), and water vapor (H₂O). Of the above processes, oxidation is by far the most exothermic. At low temperatures, oxygen consumption can be expressed by the following equation [17]:

$$\text{Rate} = A [\text{O}_2]^n \exp\left(\frac{-E}{RT}\right), \quad (8)$$

where E is the activation energy, which for different coals can vary from 12 to 95 kJ/mol; A is the preexponential factor, which is typically between 1 and $7 \times 10^5/\text{s}$ and depends on the coal rank and measurement method; R is the gas constant; n is the apparent order of reaction; T is the absolute temperature; and $[\text{O}_2]$ is the oxygen concentration.

TABLE 1: Physical and chemical parameters of the coal.

Density of the coal (kg·m ³)	1300
Activation energy (KJ/(mol·K))	90.0
Thermal conductivity of coal W/(m·K)	0.1998
Heat release when coal absorbs one Moore oxygen (Kj)	310
Preexponential factor (s ⁻¹)	64
Initial temperature (K)	300
Specific heat capacity (J·kg ⁻¹ ·K)	1003

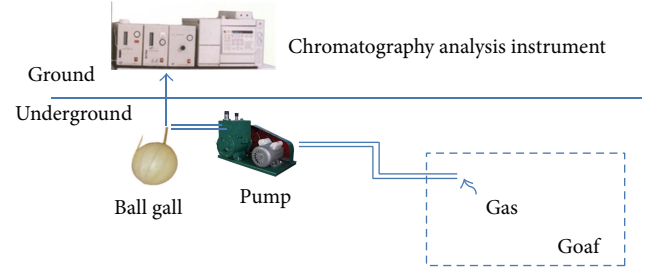


FIGURE 2: Collection of gas from the goaf for oxygen concentration analysis.

According to the Arrhenius equation (Equation (8)), the temperature will have a large influence on oxygen consumption. Therefore, to accurately describe the oxygen consumption, the heat of the coal oxidation reaction at low temperatures must be considered. This heat can be expressed by $Q = Vq$, where Q is the exothermic velocity, which is closely related to the oxygen consumption, and q is total heat release for consumption of one mole of oxygen at low temperature by coal oxidation. In this paper these chemical reaction parameters of the coal can be seen as in Table 1.

3. In Situ Measurement and Model Configuration

3.1. Field Experiment on Oxygen Concentration in Goaf. For calibration and to validate the simulation results, mixed gas samples were collected from the goaf (Figure 2) in an actual coal mine and analyzed by gas chromatography (GC) to obtain the oxygen concentration. To collect these samples, multiple sample collection tubes were placed in the goaf behind the scraper conveyor.

The gas from the goaf was collected through these tubes using a pump and pumped into a ball sample vessel. This full sample vessel was transferred to the laboratory for analysis.

The pump system to remove gas from the goaf using suction was an electric rotary vane vacuum pump (Figure 3) with an explosion-proof motor and power of 0.75 kW. The gas collection tubes were composed of rigid plastic (ø8 mm) that could withstand negative pressure. The tubes were also placed in a seamless steel tube for further protection against damage from falling rocks in the goaf (Figure 4(a)). A sealant of latex clay was placed between the tubes and the protective sleeve

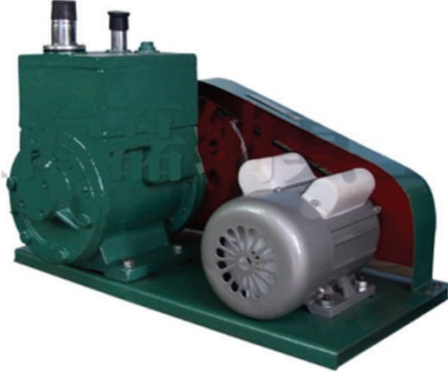


FIGURE 3: Electric rotary vane vacuum.

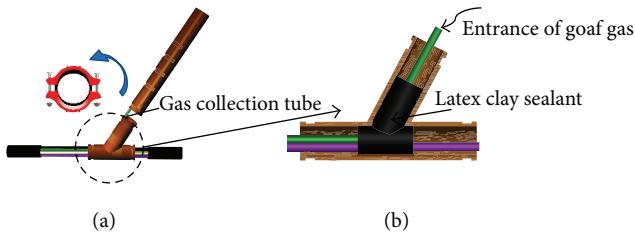


FIGURE 4: (a) Protective sleeve around gas collection tube. (b) Placement of latex clay sealant in protective sleeve.

(Figure 4(b)), to ensure that the extracted gas originated from the goaf and not from the protective sleeve.

Gas samples were collected at three different points in the mine (Figure 5). Collection tubes were placed in the goaf near the air return, air inlet, and 60 m from the air return. The workplace in this area is ventilated at $1400 \text{ m}^3/\text{min}$ with fresh air with the following composition (percentage by volume): oxygen (20.7%), and nitrogen (80.6%). The gas samples were analyzed using a KSS-200 chromatograph. This system can be used to analyze the following gases (volume fraction ranges): O_2 (0–25%); N_2 (70–98%); CO , C_2H_4 , C_2H_6 , and C_2H_2 (0–50%); and CH_4 and CO_2 (0–80%). This system has an accuracy of $\leq 1 \text{ ppm}$ and relative error of $\leq 1.5\%$.

3.2. Model for Simulation of Oxygen Concentration in the Goaf under Gas Drainage Conditions. Boundaries for the model were based on a workplace in Dafosi coalmine (China), which has a U-type ventilation mode. Figure 6 shows the layout for the CFD model based on the Dafosi coalmine workplace. The intake airflow and return airflow are shown in red on the right and left, respectively, of the front of this model. A gas drainage system was established in the model, which included a gas drainage pipe near the return airflow (Point 1 in Figure 6) and gas drainage boreholes in the goaf (Point 2 in Figure 6). The length of the workplace which is also the goaf width in the model was 200 m, and the distance from the starting point of the longwall to the workplace was 500 m. The height of the goaf flow field was 20 m, the coal seam pitch was 0° , the pitch in the strike direction was 2° , and the workplace was ventilated in U + L-mode. Air ventilation was at a rate of $1400 \text{ m}^3/\text{min}$ with

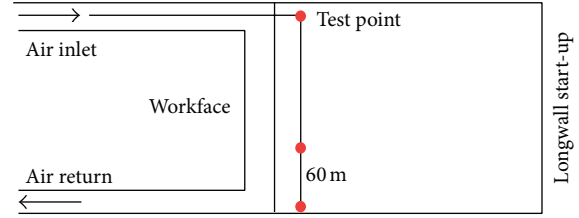


FIGURE 5: Gas collection points in the coalmine.

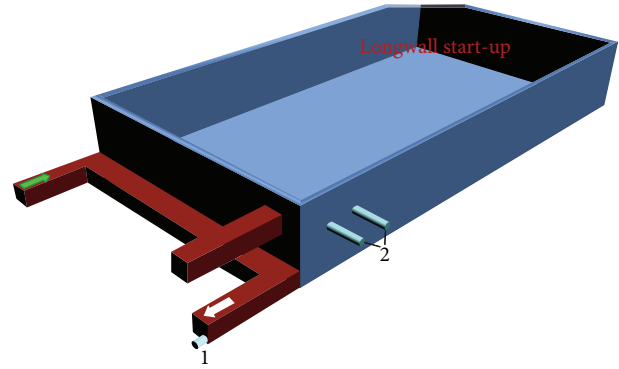


FIGURE 6: Model for gas drainage from the goaf through (1) a gas drainage tube in the area of the return airflow and (2) gas drainage boreholes in the goaf.

TABLE 2: Parameters of the workplace and goaf.

Goaf size (m)	$500(L) \times 200(W) \times 20(H)$
Section size of workplace (m×m)	$3(H) \times 8(W)$
Wind volume of workplace (m^3/min)	1400
Oxygen concentration of the wind	20.7%
Coal seam pitch ($^\circ$)	0
Strike pitch ($^\circ$)	2
Section size of laneway (m×m)	$4(W) \times 3(H)$
Diameter of drainage pipe 1 and pipe 2 (mm)	325
Gas drainage rate of pipe 1 (m^3/h)	200
Gas drainage rate of pipe 2 (m^3/h)	180

an oxygen volume fraction of 20.7%. The gas drainage pipe at Point 1 had a diameter of 325 mm, and the gas drainage rate was $200 \text{ m}^3/\text{h}$. Gas drainage from the boreholes in the goaf was at a rate of $180 \text{ m}^3/\text{h}$. The gas that was drained from the goaf main mainly came from the workplace and bottom and roof of the goaf. Assuming that gas emission had a linear relationship, the gas release from the goaf was predicted to be about $21\text{--}24 \text{ m}^3/\text{min}$ in this model. Main parameters of this model can be seen as in Table 2.

The model was meshed using an unstructured grid containing about 84000 cells and 179000 faces (Figure 7(a)). For the model to converge easily during the solving process, the mesh was increased around where the gas drainage boreholes were located (Figure 7(b)).

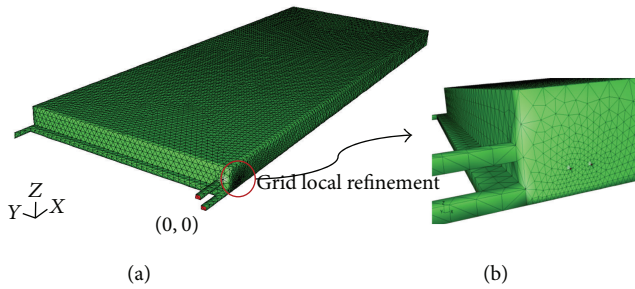


FIGURE 7: CFD model geometry and computational grid of a longwall panel.

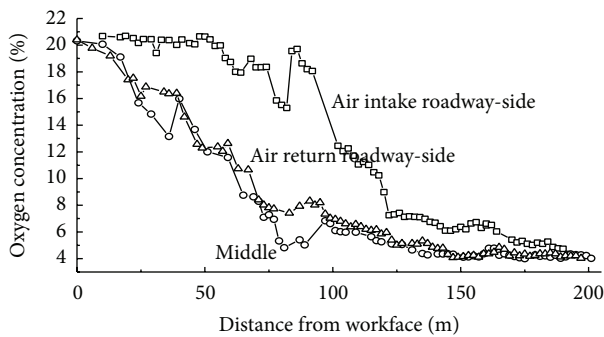


FIGURE 8: Percentage by volume of oxygen in the goaf.

4. Results and Discussion

4.1. Oxygen Concentrations in the Mine Goaf from Field Study.

The oxygen concentration in the goaf was very high beside the air inlet (Figure 8). In this area the volume fraction of oxygen in the goaf remained $>18\%$ until 70 m behind the long-wall workface and $>8\%$ until 120 m behind the longwall workface. In the middle of the goaf, 60 m from the air-return, the volume fraction of oxygen in the goaf remained at $>18\%$ until 20 m behind the workface and at $>8\%$ until 75 m behind the longwall workface. The trends in the reduction of oxygen in the goaf were very similar in these two areas.

4.2. Simulation Results and Discussion

4.2.1. Oxygen Concentration in the Goaf under Gas Drainage Conditions. The distribution patterns of oxygen in the goaf obtained with the model are illustrated in Figures 9 and 10. The gas at higher levels above the bottom of the goaf has a lower oxygen concentration (Figure 10). The oxygen concentration at different distances from the workface was also obtained with the model (Figure 11). It presented similar trends in the oxygen concentration as observed in the field study (Figure 8). This suggests that the simulation can reflect the actual gas distribution in goaf. Comparison of temperature anomalies between the presented simulation results and *in situ* measurements is only possible when the overlying beds are assumed to be homogeneous on a macroscopic scale.

Consequently, the results do not necessarily apply to all fire sites.

At 20 m above the bottom of the goaf, the air inlet region was the only area where the volume fraction of oxygen was $>20\%$. At this height, the volume fraction of oxygen was only 15% near the air return.

Figure 12 shows the oxidation zone or coal spontaneous combustion zone obtained from the model. This zone is defined as the area where the oxygen volume fraction is 8–18%. On the air inlet-side, float coal dust 75 m from the workface will be in the spontaneous combustion zone, and that at 130 m from the workface will be in the suffocation zone. In the middle area of the goaf, the float coal dust will be in the spontaneous combustion zone at only 30 m from the workface and in the suffocation zone at 67 m from the workface. Near the air return, float coal dust is in the spontaneous combustion and suffocation zones at 26 m and 72 m, respectively, from the workface. Because fully mechanized caving mining creates large quantities of float coal dust in the goaf, the thickness of float coal dust will always be sufficient for coal spontaneous combustion. Therefore, the spontaneous combustion zone in the model is equivalent to the hazard zone for the mine. The maximum width of the spontaneous combustion hazard zone is 55 m near the intake airflow. The simulation showed that there is a serious air leak at the workface of the goaf in this mine; even with high methane release, high oxygen concentrations were widespread.

Figure 13 presents a three-dimensional representation of the spontaneous combustion zone. In this figure, blue represents an oxygen volume fraction of 8%, and orange represents an oxygen volume fraction of 18%.

Because oxygen density is higher than air density, the oxygen concentration near the bottom of the goaf was higher than that in the upper part of the goaf close to the workface (Figures 14 and 15). This suggests the possibility of coal spontaneous combustion is higher in the upper part of the goaf than near the bottom. Further from the workface, the possibility of coal spontaneous combustion was lower in the upper part of goaf than near the bottom.

The CFD simulation indicated that the high oxygen region was widespread in the goaf, which could increase coal spontaneous combustion. To prevent this, the fire control measures for the mine must be improved. Consequently, three-phase foam was used during backfilling of the goaf. Three-phase foam has a large flow volume, excellent fluidity, and low density, is durable, and provides uniform coverage.

4.2.2. Effect of Gas Drainage Volume on Oxygen Distribution.

In order to study the effect of gas drainage parameters on spontaneous combustion, the gas drainage volume was changed and the oxygen distribution in goaf was simulated again. Gas drainage from three points was investigated. These points were (1) 5 m behind the workface and 5 m from the goaf boundary near the air return, (2) 5 m behind the workface and 5 m from the goaf boundary near the air intake,

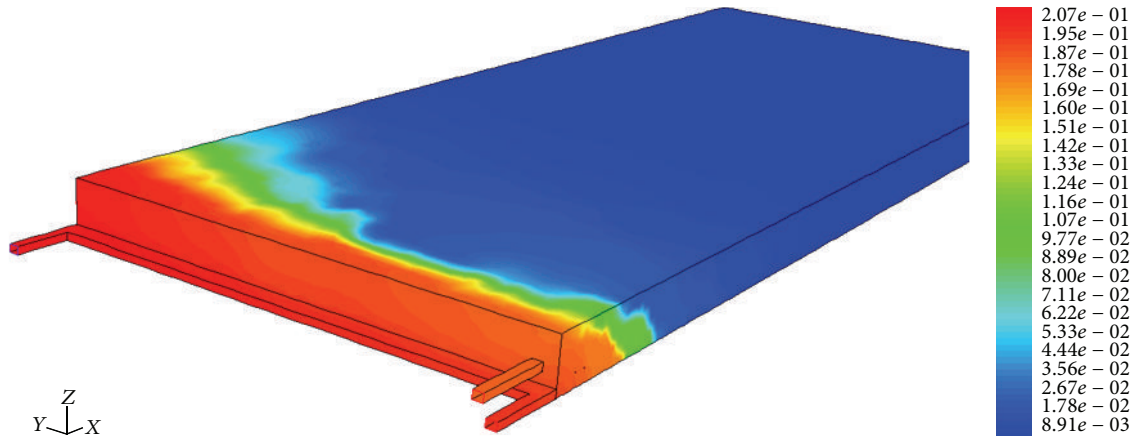


FIGURE 9: Oxygen on the surface of the model.

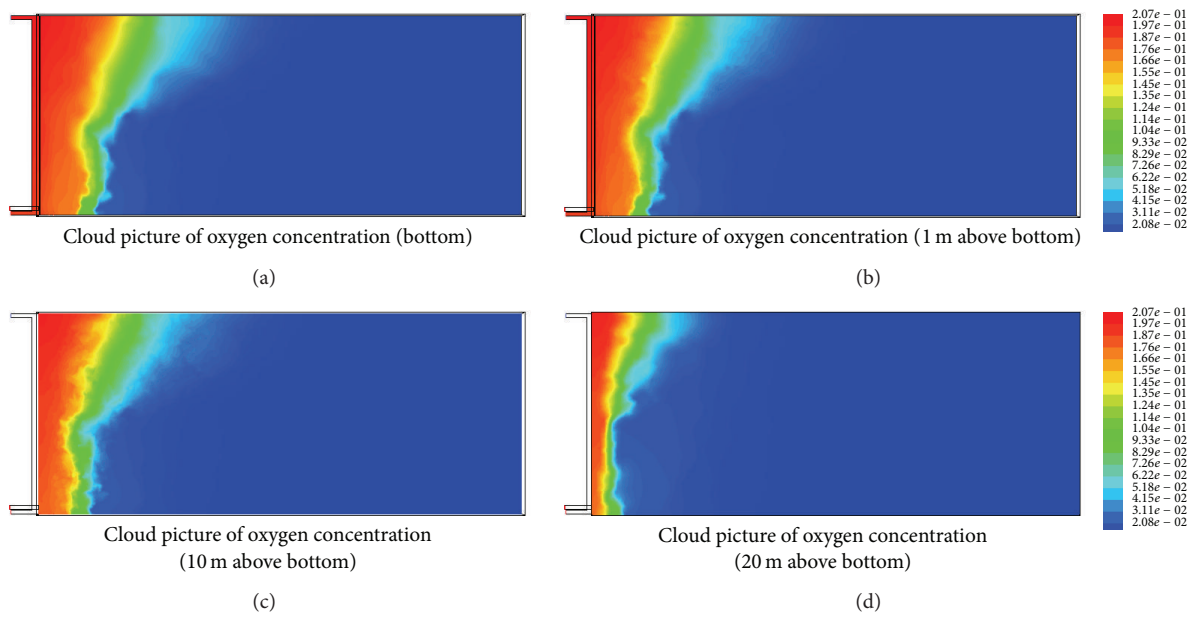


FIGURE 10: Oxygen distribution at different levels in the goaf: (a) the bottom, (b) 1 m above the bottom, (c) 10 m above the bottom, and (d) 20 m above the bottom.

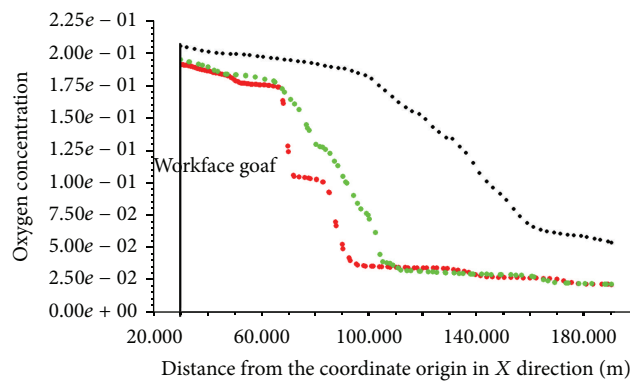


FIGURE 11: Oxygen concentration at different distances from the workplace.

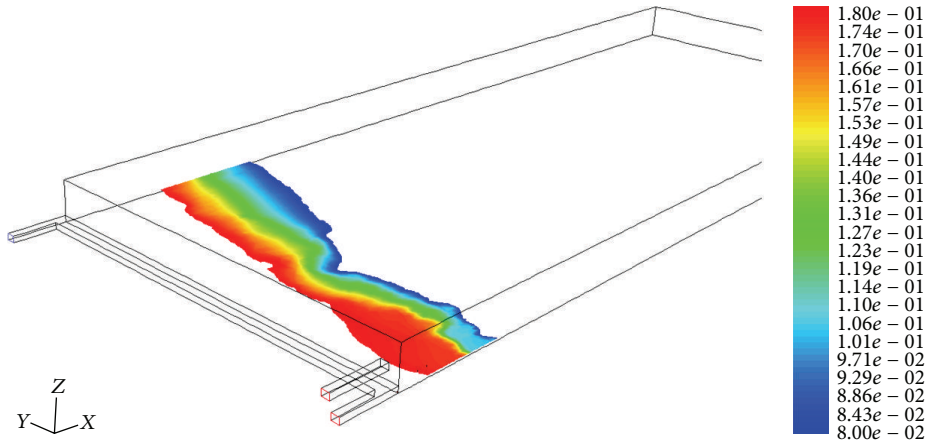


FIGURE 12: Oxidation zone or coal spontaneous combustion zone.

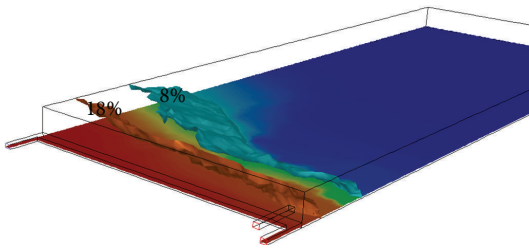


FIGURE 13: Three-dimensional distribution of spontaneous combustion zone.

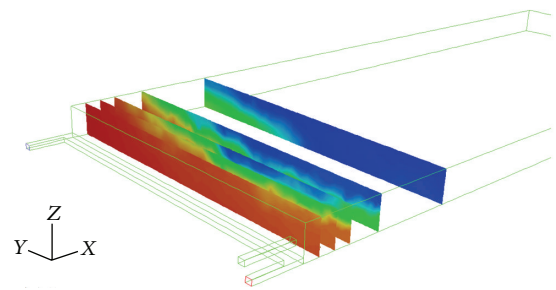


FIGURE 15: Location of longitudinal sections.

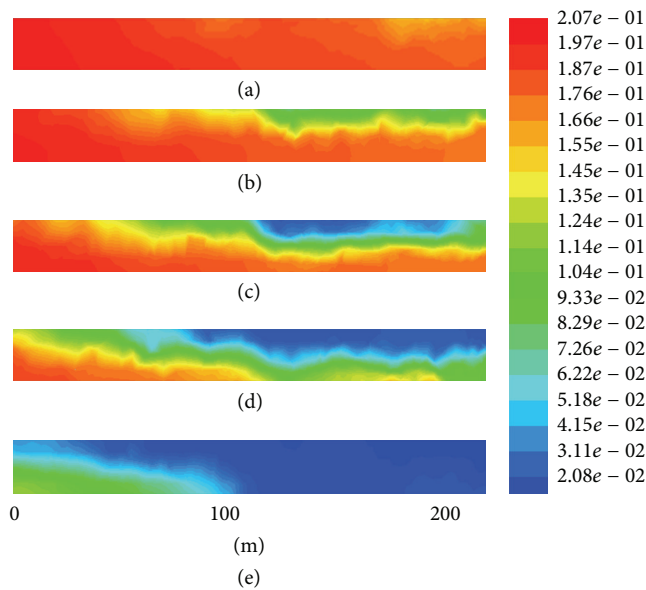


FIGURE 14: The oxygen distribution in section planes (a) 10 m, (b) 20 m, (c) 30 m, (d) 50 m and (e) 80 m behind the workface.

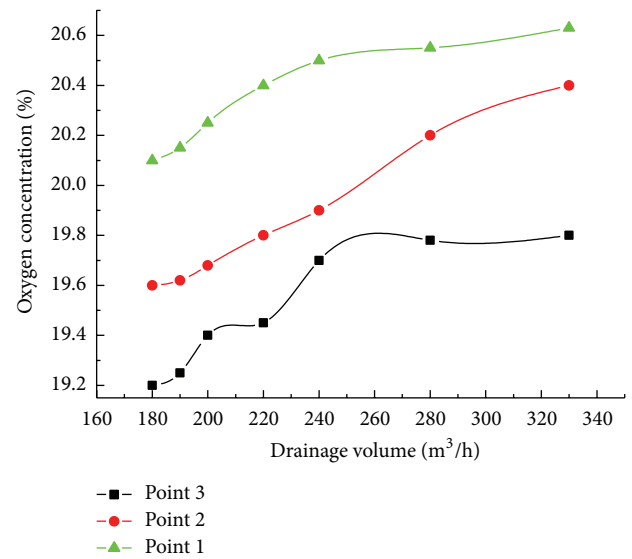


FIGURE 16: Effect of the gas drainage volume in pipe 1 on the concentration of oxygen at Point 1, Point 2, and Point 3.

and (3) 50 m behind the workface and 100 m from the goaf boundary, and all of these points are on the goaf bottom.

Figure 16 shows the changes in the volume fraction of oxygen at Points 1–3 with different drainage volumes for

gas drainage pipe 1. The variation in the volume fraction of oxygen was dependent on the goaf gas drainage volume. Larger gas drainage volumes resulted in increased leakage that is why volume fractions of oxygen at the three points

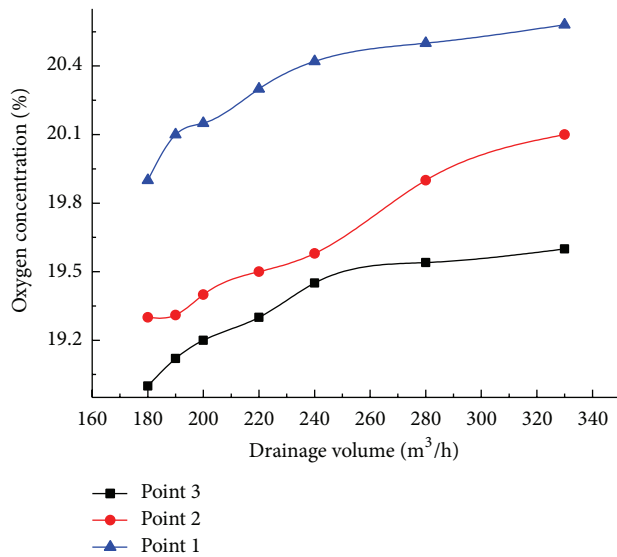


FIGURE 17: Effect of the gas drainage volume in pipe 2 on the concentration of oxygen at Point 1, Point 2, and Point 3.

become higher. However, the oxygen concentration at Point 3 increased slightly faster than at Point 1 or 2. This suggests that increases in the gas drainage volume create greater risk of coal spontaneous combustion on the air return side than on the air intake side or in the middle of the goaf.

Figure 17 shows the changes in the volume fraction of oxygen at Points 1–3 with different drainage volumes for gas drainage pipe 2. From this figure we can also find that the variation in the volume fraction of oxygen was dependent on the goaf gas drainage volume. Larger gas drainage volumes resulted in higher oxygen concentration. Besides, from the contradistinction between Figures 16 and 17, we can find that, with the same drainage volume, when there is drainage of the gas from the pipe 1, oxygen concentration is higher; it means that drainage from the pipe 1 may lead to higher possibility of coal spontaneous combustion. So if we must use drainage of gas from the goaf, we would better use drainage of gas at the location of pipe 2 rather than pipe 1.

5. Conclusions

In combination with detailed field studies, extensive CFD modeling was conducted to investigate the oxygen distribution in longwall goaf under gas drainage conditions. The results of these studies greatly improve the fundamental understanding of the distribution of oxygen and other gases in coalmines. The high oxygen region in the mine was widespread in the goaf under gas drainage conditions. Near the air inlet, the maximum width of the spontaneous combustion zone was about 70 m. The gas drainage volume influenced the oxygen concentration in the goaf, with greater volumes of gas drainage increasing the volume fraction of oxygen. The oxygen was more concentrated near the air return than near the air intake or the middle of the goaf. In comparison to field study results, the CFD simulation

of the oxygen distribution in the mine was an accurate representation of the actual situation in the goaf under gas drainage conditions. This method is flexible and simple to conduct and can be used to numerically simulate various complex situations of spontaneous combustion. The results provide a means for control of spontaneous combustion and establishment of firefighting measures in coalmines.

Conflict of Interests

The authors declare that there is no conflict of interests regarding the publication of this paper.

Acknowledgments

This research was supported by the National Natural Science Foundation of China (Grant nos. 51106175, 51134020, and 51104154), Fundamental Research Funds for the Central Universities(2011QNA05) and China Postdoctoral Science Foundation funded project.

References

- [1] X. C. Li, *Coal Mine Safety in China*, China Coal Industry Press, Beijing, China, 1998 (Chinese).
- [2] A. K. Singh, R. V. K. Singh, M. P. Singh, H. Chandra, and N. K. Shukla, "Mine fire gas indices and their application to Indian underground coal mine fires," *International Journal of Coal Geology*, vol. 69, no. 3, pp. 192–204, 2007.
- [3] A. Saghafi, N. W. Bainbridge, and J. N. Carras, "Modelling of spontaneous heating in a longwall goaf," in *Proceedings of the 7th US Mine Ventilation Symposium*, pp. 167–172, June 1995.
- [4] A. Saghafi and J. N. Carras, "Modeling of spontaneous combustion in underground coal mines: application to a gassy longwall panel," in *Proceedings of the 27th International Conference of Safety in Mines Research Institute*, pp. 573–579, 1997.
- [5] R. Balusu, G. Deguchi, R. Holland et al., "Goaf gas flow mechanics and development of gas and Sponcom control strategies at a highly gassy mine," *Coal and Safety*, vol. 20, no. 3, pp. 35–45, 2002.
- [6] A. C. Smith and C. P. Lazzara, "Spontaneous combustion studies of US coals," Report of Investigations 9079, US Bureau of Mines, 1987.
- [7] L. Yuan and A. C. Smith, "Numerical study on effects of coal properties on spontaneous heating in longwall gob areas," *Fuel*, vol. 87, no. 15-16, pp. 3409–3419, 2008.
- [8] A. C. Smith, Y. Miron, and C. P. Lazzara, "Large-scale studies of spontaneous combustion of coal," Report of Investigations 9346, US Bureau of Mines, Washington, DC, USA, 1991.
- [9] J. Bear, *Fluid Dynamics in Porous Medium*, Press of China Building Industry, Beijing, China, 1983.
- [10] F. J. Wang, *Principle and Application of CFD Software*, Tsinghua University Press, Beijing, China, 2004.
- [11] Z. Wen, L. C. Shi, and Y. R. REN, *Course Book of Fluid Calculation by FLUENT*, Tsinghua University Press, Beijing, China, 2004.
- [12] D. P. Creedy and R. D. C. Clarke, "Minimizing firedamp risks on high production coalfaces: a computational modelling approach," in *Proceedings of the International Symposium: Safety, Hygiene and Health in Mining*, pp. 192–203, 1992.

- [13] T. X. Ren, J. S. Edwards, and R. R. Jozefowicz, "CFD modeling of methane flow around Longwall coal faces," in *Proceedings of the 6th International Mine Ventilation Congress*, pp. 17–22, 1997.
- [14] T. X. Ren and J. S. Edwards, "Three-dimensional computational fluid dynamics modelling of methane flow through permeable strata around a longwall face," *Mining Technology*, vol. 109, no. 1, pp. 41–48, 2000.
- [15] Q. T. Hu, Y. P. Liang, and J. Z. Liu, "CFD simulation of methane flow in goaf," *Journal of Coal science and Engineering*, vol. 32, no. 7, pp. 719–724, 2007.
- [16] J. N. Carras and B. C. Young, "Self-heating of coal and related materials: models, application and test methods," *Progress in Energy and Combustion Science*, vol. 20, no. 1, pp. 1–15, 1994.
- [17] L. Yuan and A. C. Smith, "Computational fluid dynamics modeling of spontaneous heating in Longwall gob areas," *Transactions of the Society for Mining, Metallurgy, and Exploration*, vol. 322, p. 37, 2007.

Research Article

A Practical Method of Nonprobabilistic Reliability and Parameter Sensitivity Analysis Based on Space-Filling Design

Xin-dang He, Wen-xuan Gou, Yong-shou Liu, and Zong-zhan Gao

Department of Engineering Mechanics, Institute of Aircraft Reliability Engineering, Northwestern Polytechnical University, Xi'an 710129, China

Correspondence should be addressed to Xin-dang He; xindanghe@163.com

Received 21 July 2014; Revised 29 October 2014; Accepted 10 November 2014

Academic Editor: Shaofan Li

Copyright © 2015 Xin-dang He et al. This is an open access article distributed under the Creative Commons Attribution License, which permits unrestricted use, distribution, and reproduction in any medium, provided the original work is properly cited.

Using the convex model approach, the bounds of uncertain variables are only required rather than the precise probability distributions, based on which it can be made possible to conduct the reliability analysis for many complex engineering problems with limited information. In this paper, three types of convex model including interval, ellipsoid, and multiellipsoid convex uncertainty model are investigated, and a uniform model of nonprobabilistic reliability analysis is built. In the reliability analysis process, an effective space-filling design is introduced to generate representative samples of uncertainty space so as to reduce the computational cost and provide an accurate depiction of possible model outcome. Finally, Spearman's rank correlation coefficient is used to perform parameters global sensitivity analysis. Three numerical examples are investigated to demonstrate the feasibility and accuracy of the presented method.

1. Introduction

In practical engineering problems, uncertainty is often unavoidable due to the lack of knowledge, assumptions made by model builders, variations of physical properties of materials, geometric dimensions, and operating environments and other reasons. Therefore, these uncertainties involved in structure should be taken into account for a proper design process [1]. With the ever-increasing demands of structure security, the structural reliability analysis has received considerable attention in the last decades and is becoming increasingly important in the structural design [2].

The aim of reliability analysis is to assess the probability of structural survival or the probability of structural failure when the uncertainties involved in the structures are taken into account [3]. In the area of reliability analysis, probability model is one of the most commonly used uncertainty models, in which the uncertainties involved in structures are described as random variables. This reliability model has been intensively studied in the last decades and a variety of important analysis techniques have been established, such as the first order reliability method (FORM) [4, 5], second order

reliability method (SORM) [6, 7], Monte-Carlo method (MC) [8], and system reliability method [9, 10].

It is important to point out that the aforementioned reliability method requires precise probabilistic distribution characteristics, which come from a large number of input samples. However, in real world engineering design problems, probabilistic reliability model is often hindered due to the lack of samples information. For instance, in the conceptual design stage of structures, it is difficult to provide sufficient experimental samples to describe the distribution of uncertainty input variables [11]. As revealed by Ben-Haim [12] and Elishakoff [13], probabilistic reliability model is very sensitive to small inaccuracy of input quantities, which means that misleading results may be yielded due to the unjustified assumption in constructing a probabilistic model.

This challenge thus raised the interest of the alternative nonprobabilistic approach for uncertainty description, namely, the set theory-based convex model [14–18]. At present, interval, ellipsoid, and multiellipsoid convex model are three widely studied convex models [19]. Based on interval model, Guo et al. [20] proposed a robust reliability index to estimate structural nonprobability reliability and

presented three solution methods of the reliability index. Tao et al. [21] proposed a semianalytic method to solve the nonprobabilistic reliability index. Chen et al. [22] suggested an enhanced semianalytic method based on monotonicity analysis. Qiu and Elishakoff studied the structural optimal design method using the interval set model [23, 24]. With multiellipsoid convex model, Kang et al. [25] and Luo et al. [26] constructed a nonprobabilistic reliability optimization design method.

This paper aims to develop a practical nonprobability reliability global sensitivity analysis technique based on optimal Latin hypercube sampling (OLHS) and Monte Carlo simulation. The method proposed in this paper has wider applicability. It can be used in solving more general problems with interval model, ellipsoid model, or multiellipsoid convex model. The proposed method has some very attractive advantages, such as the following: its analysis process is simple, computational cost is regardless with variables dimension and the nonlinear degree of the performance function. Hence it is particularly suitable for implementing the nonprobabilistic reliability analysis for some complicated structure.

This paper is organized as follows. Firstly, three uncertain information description methods, including interval model, ellipsoid model, and multiellipsoid convex model, are introduced. The nonprobabilistic reliability model and its physical meaning are then discussed in detail in Section 3. Based on OLHS, a Monte Carlo simulation and global sensitivity analysis method for structural nonprobabilistic reliability is proposed in Section 4. The feasibility and accuracy of the presented method are demonstrated through three numerical examples in Section 5. Conclusions are given in Section 6.

2. The Description of Structural Uncertainty with Convex Model

In this paper, three types of ellipsoid-bound convex models, including interval model, ellipsoid model, and multiellipsoid convex model, are introduced for the description of uncertainty variables [14, 27].

(1) In interval uncertain model, an uncertain variable can be described by an interval set, which can be expressed as

$$x = [x^L, x^U] = \{x \in R \mid x^L \leq x \leq x^U\}, \quad (1)$$

where variable $x \in R$ belongs to a bounded closed interval, x^L denotes the lower bound of interval variable, x^U stands for the upper bound of interval variable, and $x^L \leq x^U$.

For easy expression, the variable x can also be expressed by

$$x = (1 + \delta) \cdot \bar{x}, \quad (2)$$

where δ denotes a dimensionless variable and \bar{x} denotes the nominal value of the uncertain variable; it can be expressed by

$$\bar{x} = \frac{x^L + x^U}{2}. \quad (3)$$

(2) In ellipsoid uncertain model, the uncertain variables are assumed to fall into a multidimensional (hyper-) ellipsoid. The uncertainty domain can be expressed by

$$\delta = \{\delta : \delta^T \mathbf{W} \delta \leq \varepsilon^2\}, \quad (4)$$

where \mathbf{W} is the characteristic matrix of the ellipsoid and ε is real number standing for the magnitude of the parameter variability.

(3) In multiellipsoid uncertain model, the uncertain variables are assumed to fall into several ellipsoid sets. Supposing k ellipsoid sets are employed, the vector of the grouped uncertain variables can be expressed by

$$\mathbf{x}^T = \{\mathbf{x}_1^T, \mathbf{x}_2^T, \dots, \mathbf{x}_k^T\}, \quad (5)$$

where each group of variables is bounded by an ellipsoid set as follows:

$$\delta_i = \{\delta_i : \delta_i^T \mathbf{W}_i \delta_i \leq \varepsilon_i^2\} \quad (i = 1, 2, \dots, k), \quad (6)$$

where δ_i denotes the dimensionless vector of \mathbf{x}_i , \mathbf{W}_i denotes the characteristic matrix of the i th ellipsoid, and ε_i ($i = 1, 2, \dots, k$) are real numbers.

For illustrative purpose, we provide a problem with three uncertain variables. Its dimensionless vector is expressed by $\delta = \{\delta_1, \delta_2, \delta_3\}^T$. We describe it with interval model, ellipsoid model, and multiellipsoid convex model, respectively.

(a) Interval model:

$$\delta_1^2 \leq \varepsilon_1^2, \quad \delta_2^2 \leq \varepsilon_2^2, \quad \delta_3^2 \leq \varepsilon_3^2. \quad (7)$$

(b) Single-ellipsoid model:

$$\{\delta_1, \delta_2, \delta_3\} \begin{bmatrix} 3 & 0 & 1 \\ 0 & 3 & 1 \\ 1 & 1 & 1 \end{bmatrix} \begin{Bmatrix} \delta_1 \\ \delta_2 \\ \delta_3 \end{Bmatrix} \leq \varepsilon^2. \quad (8)$$

(c) Multiellipsoid uncertain model:

$$\{\delta_1, \delta_2\} \begin{bmatrix} 1 & 0 \\ 0 & 1 \end{bmatrix} \begin{Bmatrix} \delta_1 \\ \delta_2 \end{Bmatrix} \leq \varepsilon_1^2, \quad \delta_3^2 \leq \varepsilon_2^2. \quad (9)$$

The above three types of convex model are schematically shown in Figures 1(a)–1(c).

3. A Reliability Model with Convex Uncertainty

During the reference review, we found that Jiang et al. [28] proposed a desirable structural nonprobabilistic reliability model, in which reliability is defined as a ratio of the multidimensional volume falling into the reliability domain to the one of whole convex model. This reliability model has a very intuitional and easily understandable mathematical form and can be used to deal with some complex engineering problems. In this reference, ellipsoid convex model is intensively discussed, while, in this paper, this reliability model

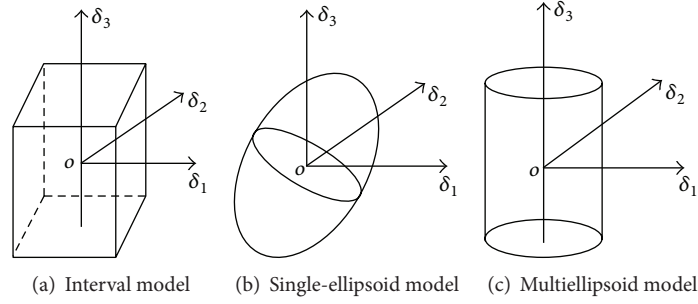


FIGURE 1: Convex models for three uncertain variables.

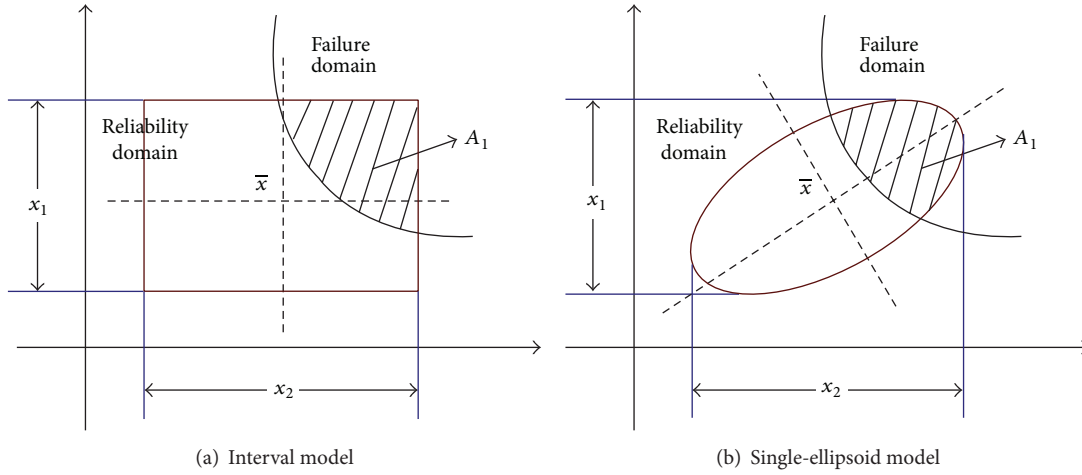


FIGURE 2: Nonprobabilistic reliability for 2D problem.

will be expanded to interval model, ellipsoid model, and multiellipsoid convex model, which will be able to deal with more general convex model problems. Assume a structural performance function is expressed by

$$Y = g(\mathbf{x}), \quad (10)$$

where \mathbf{x} stands for an n -dimensional vector of input parameters.

Firstly, a two-dimensional problem is considered. As shown in Figure 2

From Figure 2, the whole uncertainty domain is divided into two regions by the failure surface. One is in the reliability region, which is denoted by $g(\mathbf{x}) \geq 0$. The other one is in the failure region, which is denoted by $g(\mathbf{x}) < 0$. The reliability can be evaluated as follows:

$$R_c = \frac{A - A_1}{A}, \quad (11)$$

where A stands for the region of the whole convex model, A_1 stands for the failure region, and $A - A_1$ stands for the reliability region.

When a three-dimensional problem is taken into account, the domain of whole convex model will extend to corresponding volumes as shown in Figure 3.

The definition of the nonprobabilistic reliability formulated by (11) can easily be extended to an n -dimensional problem, in which the domain will become a multidimensional

volume. The value of R_c is in the range of $[0, 1]$, which can well describe the safety extent of a structure. Correspondingly, the dangerous degree f_c can be expressed by

$$f_c = \frac{A_1}{A}. \quad (12)$$

Obviously, we can find that the relationship of dangerous degree f_c with reliability R_c can be expressed by

$$R_c + f_c = 1. \quad (13)$$

4. Reliability and Variables Global Sensitivity Solution Method Based on Optimal Latin Hypercube Sampling

It should be pointed out that the reliability model mentioned above is based on areas or volumes. However, the magnitude of reliability domain in the whole uncertainty domain is difficult to be computed analytically for some complex engineering problems. Thus, a Monte Carlo simulation method has been developed in [28] to deal with this problem. However, the Monte Carlo simulation present in this reference can not assure the samples are uniformly scattered in the uncertainty space. Hence the number of samples falling into reliability domain can not effectively represent the magnitude

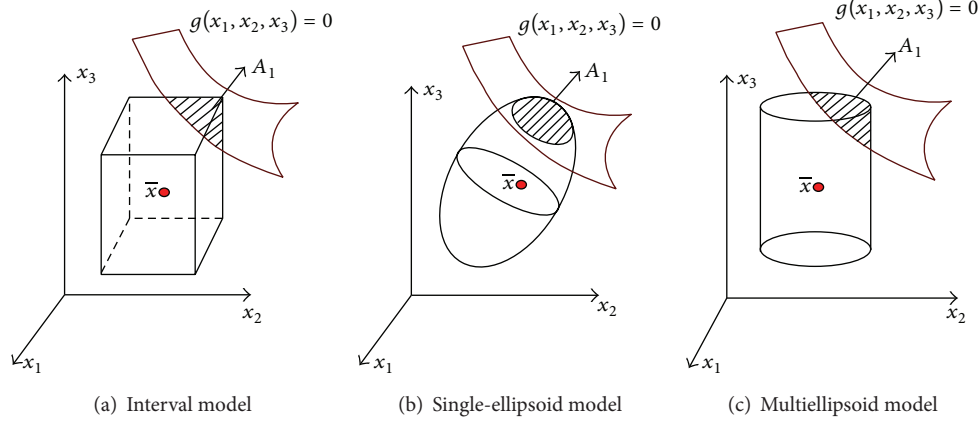


FIGURE 3: Nonprobabilistic reliability for 3D problem.

of reliability domain. The precision of analysis result can not be ensured even though a lot of samples are used.

In this study, we approached the problem by a space-filling design of computer experiment. This method is proposed by Jin et al. [29] and named as optimal Latin hypercube sampling (OLHS). Because OLHS can evenly spread out sample points over the entire design space, people also named it as space-filling design [30]. After samples of structural uncertainty variables are generated readily by the OLHS in Section 4.1, an efficient nonprobabilistic reliability and global sensitivity analysis method will be proposed in Sections 4.2 and 4.3, respectively.

4.1. Generate the Samples of Convex Model Uncertainty Variables Based on Uniform Design. When the uncertain variables are defined as (tolerances) intervals with given lower and upper bounds, failure analysis methods are needed to consider the complete range of uncertain domain. Theoretically, every point within the interval has some unknown probability of occurrence. Therefore, all the possible combinations of these uncertain intervals must be considered in the analysis.

In this section, we will use optimal Latin hypercube sampling (OLHS) to solve structural nonprobabilistic reliability index. OLHS is one of the space-filling designs and it seeks experimental points to be uniformly scattered in the experimental domain, which is proposed by Jin et al. [29, 30].

OLHS has several advantages. It can explore relationships between the response and the factors with a reasonable number of runs and is shown to be robust to the situation where little knowledge is known about the function to be modeled. In the past decade, it has been successfully applied in industry, system engineering, pharmaceuticals, and natural sciences. Its practical success is due to its economical and flexible experimental runs to study many factors with high levels simultaneously.

In order to verify the space-filling capability of OLHS, a graphical comparison of Monte Carlo sampling (MCS), Halton sequence, Latin square sampling (LHS), Maximin Latin hypercube sampling (Maximin LHS), and Optimal Latin

hypercube (Optimal LHS) for two independent variables is presented in Figure 4.

As shown in Figure 4, among these sampling methods, the OLHS method has been shown to be capable of space-filling uniformity. It can uniformly scatter samples in the 2D space and obviously is better than the other methods in terms of space-filling capability. Hence, in this paper, OLHS will be introduced to solve the nonprobabilistic index. Concerning how to carry out the optimal Latin hypercube sampling, this content is discussed detailedly in [25]. So we will not repeat it in this paper.

Consider that a structure contains S variables that can be realized N times. The samples of input variables can be arranged as an input matrix with N row and S columns. Using OLHS to generate $N \times S$ uniform numbers r_i in $[0, 1]$, arrange these values into a $N \times S$ matrix, which has the smallest discrepancy and excellent space-filling capability. After the matrix $N \times S$ in $[0, 1]$ has been generated, we will construct the sampling matrix $N \times S$ for three types of uncertainty convex model including interval model, ellipsoid model, and multiellipsoid convex model.

(1) Interval Model. For interval model, uncertain variables can be described by an interval set with upper and lower bounds (Figure 5). The uncertain domain can be expressed by

$$\Omega_1 = \{x = (x_1, \dots, x_S) : x_i^L \leq x_i \leq x_i^U, i = 1, \dots, S\}, \quad (14)$$

where variable $x_i \in R$ and belong to a bounded closed interval, x_i^L is the lower bound of interval variable, x_i^U is the upper bound of interval variable, and $x_i^L \leq x_i^U$.

Consider a computer model requiring S variables that can be realized N times. After a matrix $N \times S$ in $[0, 1]$ has been generated, we will construct the sampling matrix by

$$x_i^* = x_i^L - r_i^* (x_i^U - x_i^L), \quad (15)$$

where x_i^* is the sample of interval variable and r_i^* is the sample of matrix $N \times S$ in $[0, 1]$.

(2) Ellipsoid Model. For ellipsoid convex model, it is difficult to obtain the samples directly. Hence we can make the n

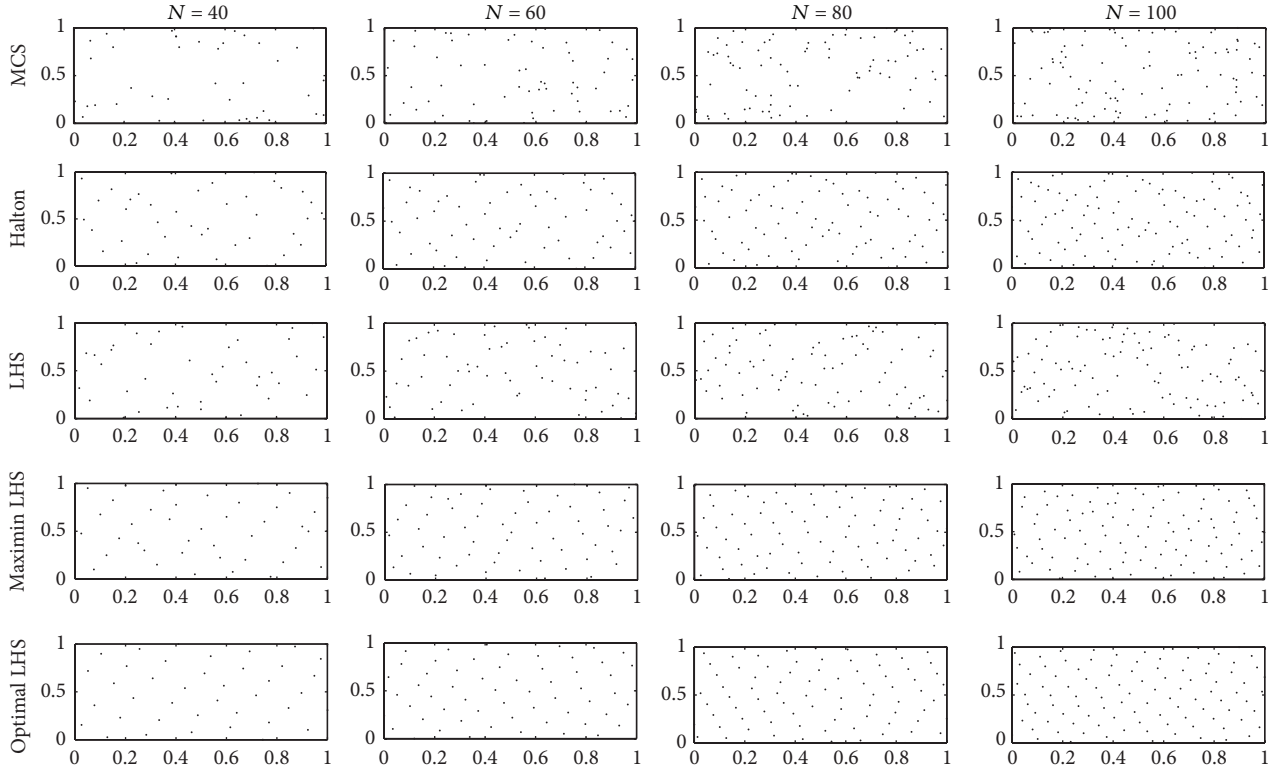


FIGURE 4: Comparison of realization sets generated by MCS, Halton, LHS, Maximin LHS, and OLHS.

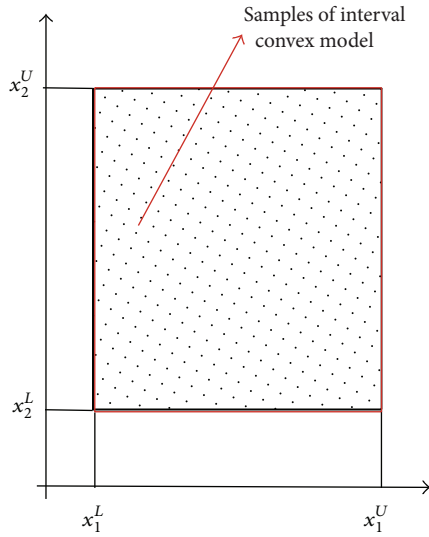


FIGURE 5: Samples of interval model variables in 2D space.

uncertain parameters as independent random variables and obtain samples by interval model at first. Then we substitute the samples into the ellipsoidal function and obtain a pile of samples \mathbf{X}_e^* satisfying

$$\Omega_2 = \{\mathbf{X}_e^* : \boldsymbol{\delta}^T \mathbf{W} \boldsymbol{\delta} \leq \varepsilon^2\}. \quad (16)$$

By this treatment, we can get a pile of samples, which can be uniformly scattered in the n -dimensional ellipsoidal convex model. This principle is shown in Figure 6.

(3) *Multiellipsoid Model*. Similarly to ellipsoid convex model, we can make the n uncertain parameters as independent random variables and obtain samples by interval model at first. Then we substitute the samples into the multiellipsoidal function and obtain a pile of samples \mathbf{X}_{me}^* satisfying

$$\Omega_3 = \{\mathbf{X}_{me}^* : \boldsymbol{\delta}_i^T \mathbf{W}_i \boldsymbol{\delta}_i \leq \varepsilon_i^2, i = 1, 2, \dots, k\}. \quad (17)$$

By this treatment, we can get a pile of samples \mathbf{X}_{me}^* , which can be uniformly scattered in the n -dimensional multiellipsoidal convex model.

4.2. Reliability Solution Method of Convex Models Based on Monte Carlo Simulation. In the process of reliability solution, we calculate the number of samples instead of the magnitude of failure region. The proposed reliability method can be outlined as follows.

Step 1. Consider a computer model containing S variable; we first generate the input variables samples matrix by the method mentioned in Section 4.1. Suppose the number of generated samples is N ; the samples of input variables can be viewed as an input matrix with N row and S columns,

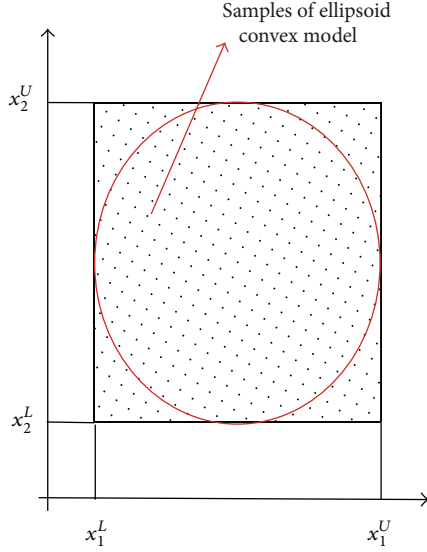


FIGURE 6: Samples of ellipsoid convex model variables in 2D space.

which has the smallest discrepancy and excellent space-filling capability.

Step 2. Sequentially substitute the samples into the performance function. Then we can obtain the number of samples satisfying the $g(\mathbf{x}) = g(x_1, x_2, \dots, x_n) > 0$. We denoted it by N_s . Through this step, the samples falling into the reliability domain can be captured.

Step 3. Finally, calculate structural reliability through the equation $R_c = N_s/N$.

4.3. Global Sensitivity Analysis Method of Convex Uncertainty Model. Compared with the researches on solving nonprobabilistic reliability index, the nonprobabilistic reliability sensitivity analysis is less available. Sensitivity analysis can quantitatively assess the impact of inputs on the output, which can be used to identify significant inputs and thereby to help you to improve design toward a more reliable and better quality product.

In this paper, we will present a global sensitivities analysis approach, different from local sensitivities [31]. Local sensitivities are mostly only local gradient information. It usually calculates structural variables sensitivity by finite-differencing scheme. Local sensitivities cannot globally reflect the impact of the variability of inputs on the output. It also neglects the influence of interactions between inputs [32]. The global approach proposed in this paper cannot only consider the slope at a particular location, but also study the global variability of an output induced by inputs over the entire range of values of inputs. Hence it can provide an overall view on the influence of inputs on the outputs.

In this paper, OLHS and Spearman's rank correlation coefficient [33] will be introduced to quantitatively assess the influence of the inputs on the output performance function.

Suppose the samples of input variables are denoted by x_1, x_2, \dots, x_n , and simulation results of output are denoted by y_1, y_2, \dots, y_n . Then we can calculate Spearman's rank correlation coefficient r_s as follows:

$$r_s = \frac{\sum_{i=1}^n (R_{x_i} - \bar{R}_x)(R_{y_i} - \bar{R}_y)}{\sqrt{\sum_{i=1}^n (R_{x_i} - \bar{R}_x)^2} \sqrt{\sum_{i=1}^n (R_{y_i} - \bar{R}_y)^2}}, \quad (18)$$

where R_{x_i} is the rank of x_i within the set of samples x_1, x_2, \dots, x_n . R_{y_i} is the rank of y_i within the set of samples y_1, y_2, \dots, y_n . \bar{R}_x denotes the average ranks of R_{x_i} , and it can be calculated by $\bar{R}_x = \sum_{i=1}^n R_{x_i}/n = (n+1)/2$. \bar{R}_y denotes the average ranks of R_{y_i} , and it can be calculated by $\bar{R}_y = \sum_{i=1}^n R_{y_i}/n = (n+1)/2$. Equation (18) can be rewritten in a simple manner as follows:

$$r_s = 1 - \frac{6 \left[\sum_{i=1}^n (R_{y_i} - R_{x_i})^2 \right]^2}{n(n^2 - 1)}, \quad -1 \leq r_s \leq 1. \quad (19)$$

The range of the value r_s is in the range of -1 to 1 . Its magnitude stands for the extent of closeness between the input variable and output. A positive value will be obtained if the variables are directly positively related, while a negative value will be obtained if they are inversely related.

Consider a computer model containing S variables. We generate N samples by uniform design. Then the Monte Carlo simulation will be performed to obtain the sampling results of performance function, which can be denoted by $\{y_1, y_2, \dots, y_N\}$. We can organize the input parameter and output parameter as follows:

$$\begin{bmatrix} x_{11} & x_{12} & \dots & x_{1S} \\ x_{21} & x_{22} & \dots & x_{2S} \\ \vdots & \vdots & \vdots & \vdots \\ x_{N1} & x_{N2} & \dots & x_{NS} \end{bmatrix} \begin{bmatrix} y_1 \\ y_2 \\ \vdots \\ y_N \end{bmatrix}. \quad (20)$$

By the definition of Spearman's rank correlation coefficient, we can divide the input parameter and output parameter into S groups as follows:

$$\begin{bmatrix} x_{11} \\ x_{21} \\ \vdots \\ x_{N1} \end{bmatrix} \begin{bmatrix} y_1 \\ y_2 \\ \vdots \\ y_N \end{bmatrix}, \begin{bmatrix} x_{12} \\ x_{22} \\ \vdots \\ x_{N2} \end{bmatrix} \begin{bmatrix} y_1 \\ y_2 \\ \vdots \\ y_N \end{bmatrix}, \dots, \begin{bmatrix} x_{1S} \\ x_{2S} \\ \vdots \\ x_{NS} \end{bmatrix} \begin{bmatrix} y_1 \\ y_2 \\ \vdots \\ y_N \end{bmatrix}. \quad (21)$$

By performing nonparametric Spearman's rank correlation coefficient analysis, we can obtain the sensitivity information of variables about structural performance function. The advance of this method is that it does not increase the computation cost. After the reliability analysis is implemented, the sensitivity results can be obtained readily.

5. Engineering Examples and Discussion

5.1. Case Study 1. In order to expound the analysis process of the proposed method easily, a simple finite element analysis (FEA) model is investigated.

TABLE 1: Uncertainty variables of plate structure.

Variable name	Mean value	Minimum	Maximum
Length A (mm)	95	93	97
Width B (mm)	40	38	42
Height H (mm)	6	5	7
Young's modulus E (MPa)	71700	71600	71800
External load F (N)	2000	1900	2100

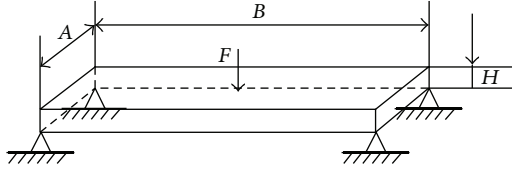


FIGURE 7: A plate structure.

This model is a simple plate structure as shown in Figure 7. Its length, width, and height are denoted by A , B , and H , respectively. In this model, an external load denoted by F is acted at the center of the upper surface, and four corners of the lower surface are fixed. Young's modulus of the plank is denoted by E , and Poisson's ratio is 0.33. The uncertainties related to geometrical dimensions, material properties, and external loads can be described with interval model and are listed in Table 1.

The FEA model of the plate structure is initially built with the mean value of variables, and structural response (maximum strain) is shown in Figure 8.

Suppose the maximum strain of the plate is denoted by $d(A, B, H, E, F)$ and the allowable strain of the plane is $d_m = 0.5$ mm; we can define structural performance function as follows:

$$g(A, B, H, E, F) = d_m - d(A, B, H, E, F). \quad (22)$$

To perform Monte Carlo analysis with 1000 samples generated by uniform design, the plane structural reliability can be readily obtained by $R_c = (1000 - 9)/1000 = 0.991$. The sampling results of performance function are shown in Figure 9.

To implement the sensitivity analysis by the method mentioned in Section 4.3, the bar chart of sensitivity results is shown in Figure 10.

As shown in Figure 10, the variable H is a main factor that influences the magnitude of structural strain. Compared with other variables, Young's modulus E has less impact on the magnitude of structural strain.

5.2. Case Study 2. A practical 25-bar steel truss (Figure 11) is investigated, which is modified from [28].

In this model, Young's modulus is 199949.2 MPa and Poisson's ratio is 0.3. Horizontal bars and the vertical bars have the same length denoted by L . The cross-sectional area of bars (1)–(4) is A_1 , the cross-sectional area of bars (16)–(25) is A_2 , the cross-sectional area of bars (11)–(15) is A_3 , and the cross-sectional area of bars (5)–(10) is A_4 . The joints 6, 8, and

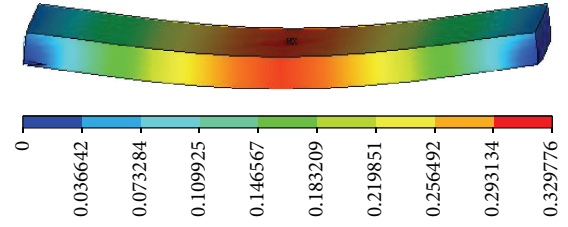


FIGURE 8: Strain of the plate structure.

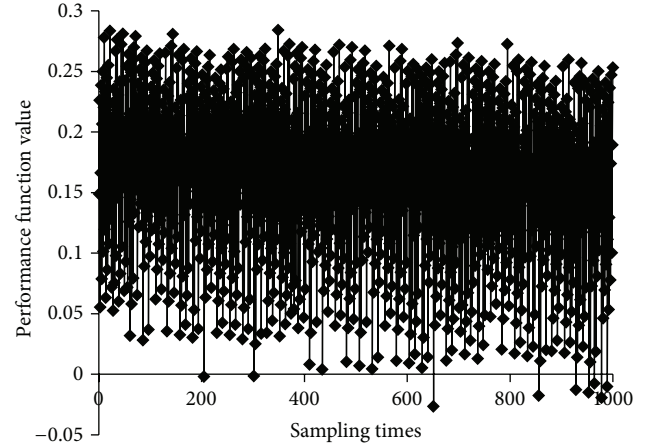


FIGURE 9: Sampling results of performance function.

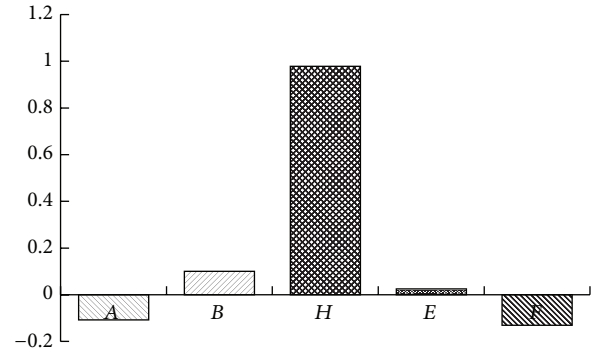


FIGURE 10: Bar chart of sensitivity analysis results.

10 are roller-supported, and joint 12 is hinge-supported. The vertical loads are denoted by F_3 , F_2 , and F_1 and are acted at the joints 7, 9, and 10, respectively. A horizontal load is denoted by F_4 and is acted at the joint 1. The horizontal displacement of joint 6 is denoted by d , and its allowable maximum value is d_m . The five inputs (cross-sectional area A_i , $i = 1, 2, 3, 4$, and the length L) in this example are treated as uncertain variables. The performance function of the structure can then be expressed as

$$g(A_1, A_2, A_3, A_4, L) = d_m - d(A_1, A_2, A_3, A_4, L). \quad (23)$$

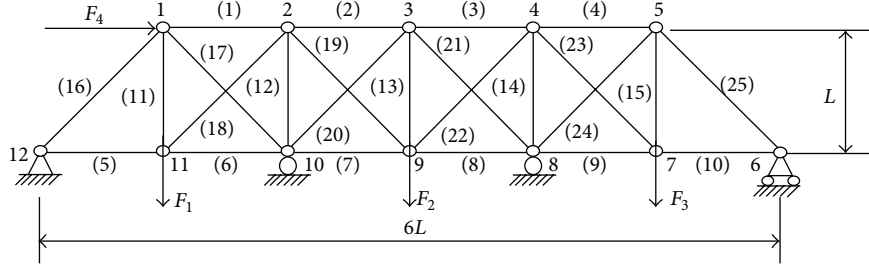


FIGURE 11: A 25-bar truss.

The uncertain intervals of the five input variables are

$$\begin{aligned} A_1 &= [630 \text{ mm}^2; 770 \text{ mm}^2], \\ A_2 &= [5580 \text{ mm}^2; 6820 \text{ mm}^2], \\ A_3 &= [4770 \text{ mm}^2; 5830 \text{ mm}^2], \\ A_4 &= [7920 \text{ mm}^2; 9680 \text{ mm}^2], \\ L &= [13500 \text{ mm}; 16500 \text{ mm}^2]. \end{aligned} \quad (24)$$

The uncertainty domain of the design problem can be represented as an ellipsoidal convex model:

$$\begin{bmatrix} A_1 - \bar{A}_1 \\ A_2 - \bar{A}_2 \\ A_3 - \bar{A}_3 \\ A_4 - \bar{A}_4 \\ L - \bar{L} \end{bmatrix}^T \times \begin{bmatrix} 225.0492 & -3.7576 & -4.3957 & -2.6474 & 0 \\ -3.7576 & 2.8687 & -0.4963 & -0.2989 & 0 \\ -4.3957 & -0.4963 & 3.9257 & -0.3497 & 0 \\ -2.6474 & -0.2989 & -0.3497 & 1.4240 & 0 \\ 0 & 0 & 0 & 0 & 0.4444 \end{bmatrix} \times \begin{bmatrix} A_1 - \bar{A}_1 \\ A_2 - \bar{A}_2 \\ A_3 - \bar{A}_3 \\ A_4 - \bar{A}_4 \\ L - \bar{L} \end{bmatrix} \leq 10^6. \quad (25)$$

In this problem, the ANSYS software is used to solve to the horizontal displacement d of joint 6. In order to observe the difference between interval model and ellipsoidal model for reliability analysis results, different values of the maximum allowable displacement d_m are taken into account. We calculated the structural reliability with interval model and ellipsoidal model by Monte Carlo simulation with 1000 samples, respectively. The reliability analysis results are given in Figure 12.

As shown in Figure 12, with increasing of d_m , the non-probabilistic reliability R_c also has an increasing trend. From Figure 12, it is noted that interval model is more conservative than results of ellipsoidal model.

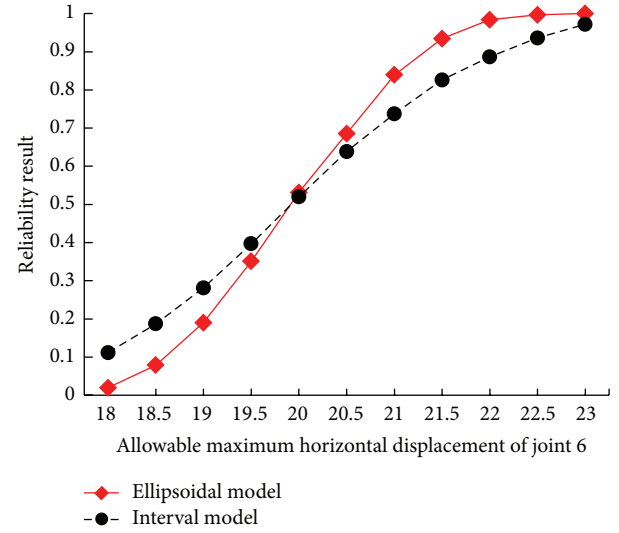


FIGURE 12: Reliability analysis results with interval model and ellipsoidal model.

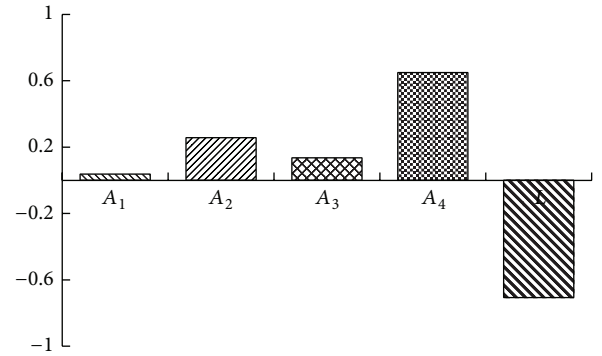


FIGURE 13: Sensitivity analysis result with interval model and ellipsoidal model.

Set the maximum allowable horizontal displacements $d_m = 22$; perform sensitivity analysis with ellipsoidal model; the structural sensitivity can be obtained readily as shown in Figure 13.

As shown in Figure 13, increasing the value of cross-sectional area A_i , $i = 1, 2, 3, 4$, will enhance the structural rigidity and increase the structural reliability, while increasing the input variable L will decrease the structural reliability.

TABLE 2: Uncertainty variables of piccolo tube structure.

Variable name	Nominal value	Convex model description
Pipeline diameter A (m)	0.060	$\delta_A^2 \leq 0.01^2$
Pipeline wall thickness B (m)	0.002	$\{\delta_B, \delta_C\} \begin{bmatrix} 1 & 0 \\ 0 & 1 \end{bmatrix} \begin{Bmatrix} \delta_B \\ \delta_C \end{Bmatrix} \leq 0.1^2$
Hole diameter C (m)	0.002	
Hole side distance D (m)	0.040	$\{\delta_D, \delta_E\} \begin{bmatrix} 1 & 0 \\ 0 & 1 \end{bmatrix} \begin{Bmatrix} \delta_D \\ \delta_E \end{Bmatrix} \leq 0.1^2$
Hole interval length E (m)	0.04	
Hole angle F ($^\circ$)	45	$\delta_F^2 \leq 0.01^2$
Young's modulus M	2.1E11	$\delta_M^2 \leq 0.02^2$
Density ρ (kg/m ³)	7800	$\delta_\rho^2 \leq 0.1^2$
External vibration frequency λ (Hz)	1700	$\delta_\lambda^2 \leq 0.1^2$

TABLE 3: Anterior four mode frequencies of piccolo tube structure.

Mode number	1	2	3	4
Natural frequency (Hz)	1538.4	1613.8	1819.0	1827.5

This sensitivity analysis results are in accordance with the engineering practice.

5.3. Case Study 3. An anti-ice piccolo structure is the core component part of a wing anti-ice system. It is close to aircraft engines, subject to random excitation generated by the engine. So there exists the potential possibility of structural resonances. In this paper, we take a part of anti-ice piccolo structure to perform the resonance reliability and variables sensitivity analysis. The finite element model (FEM) of anti-ice piccolo structure is shown in Figure 14, which is built with ANSYS software. The local meth model is shown in Figure 15.

The uncertain parameters of piccolo are described with multiellipsoid convex model and are listed in Table 2.

Firstly, we take the mean value of variables as input parameters. By mode analysis, the anterior four natural frequencies of anti-ice piccolo structure can be obtained. The anterior four mode frequencies are shown in Table 3. The anterior four vibration modes are shown in Figure 16.

As shown in Table 3, the first natural frequency denoted by η is close to external excitation frequency. According to the requirement of antiresonance design, the performance function of structural resonance failure can be expressed by

$$g(\eta, \lambda) = \eta - \lambda, \quad (26)$$

where λ is the external excitation frequency and η is the first natural frequency. When $|\eta - \lambda| \leq \delta$, the structure will cause resonance damage; when $|\eta - \lambda| > \delta$, structure is safe. In practical engineering, we usually set $\delta = 0.05\lambda$; here $\delta = 60$ Hz.

To perform Monte Carlo analysis with 365 samples generated by the method mentioned in Section 4.3, the sampling results of performance function are shown in Figure 17.

As shown in Figure 17, there are only 6 samples falling into the structural resonance failure; the pipeline structural reliability can be readily obtained by $R_c = 350/365 = 0.9863$. To implement the sensitivity analysis by the method

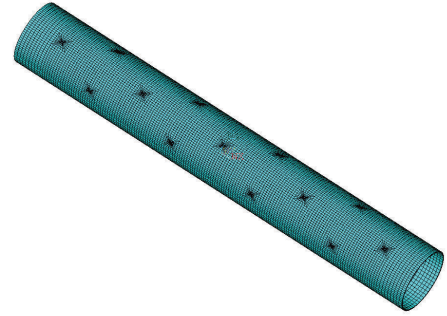


FIGURE 14: FEM of piccolo structure.

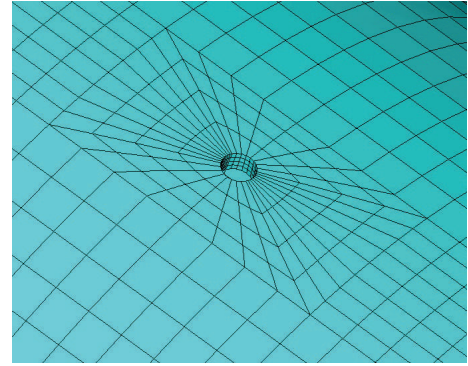


FIGURE 15: Local meth model of piccolo structure.

mentioned in Section 4.3, the bar chart of sensitivity analysis results is shown in Figure 18.

Figure 18 provides a graphical illustration of the impact of structural input variables on output. A positive sensitivity indicates that increasing the value of input variable will increase the structural reliability. Likewise, a negative sensitivity indicates that increasing the value of input variable will reduce the structural reliability.

6. Conclusions

In this paper, a practical nonprobability reliability and global sensitivity analysis method for interval, ellipsoid, and multiellipsoid convex uncertainty model is constructed. In order

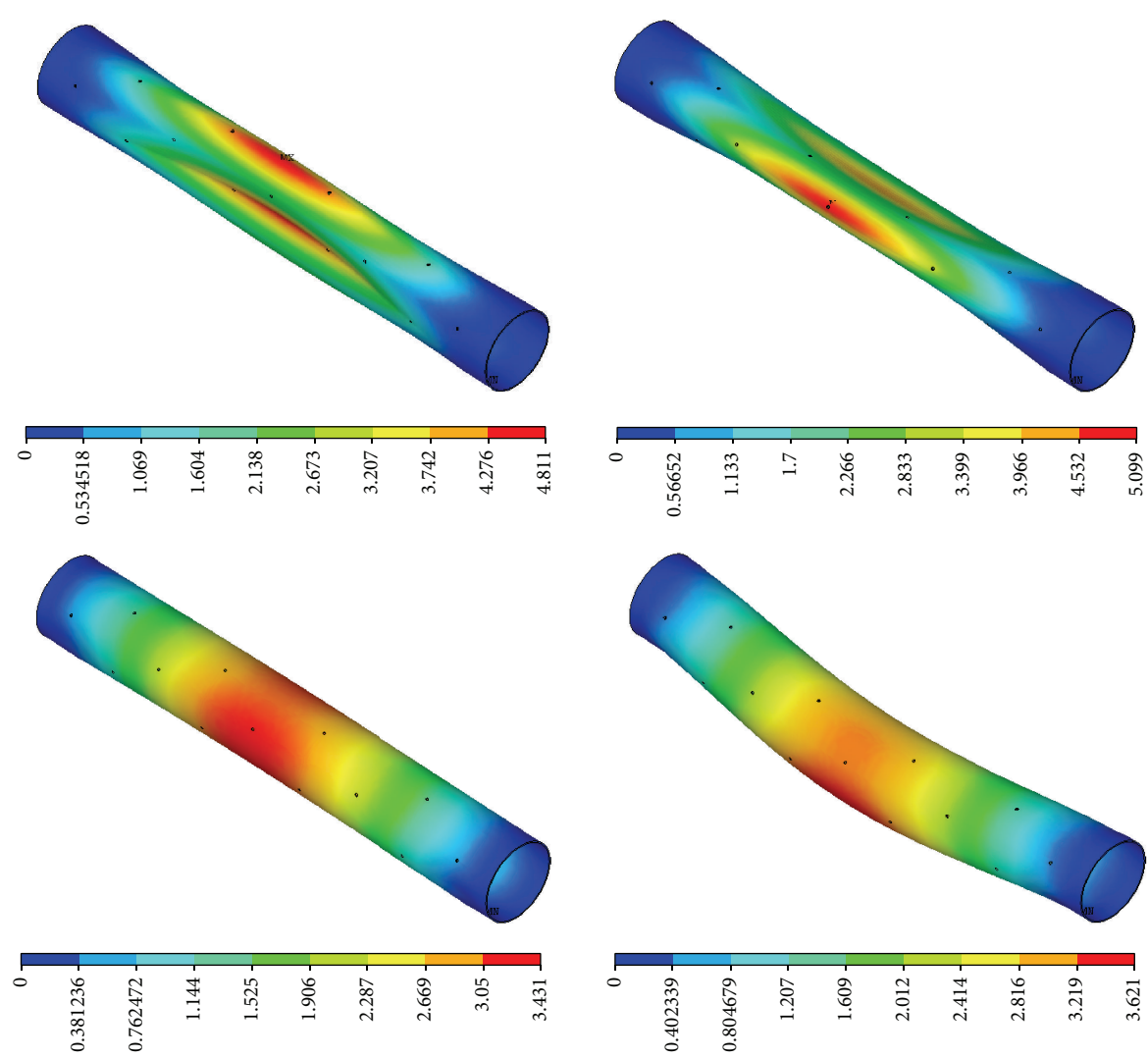


FIGURE 16: The diagram of anterior four vibration modes.

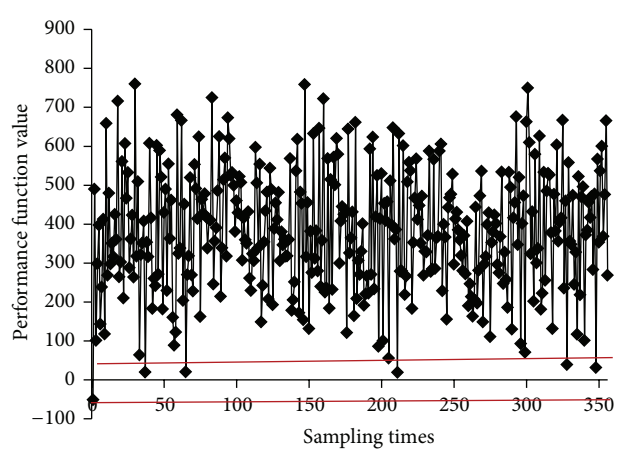


FIGURE 17: Sampling results of performance function.

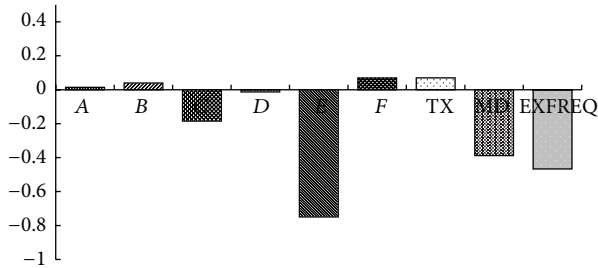


FIGURE 18: Bar chart of sensitivity analysis results.

to provide an accurate depiction of possible model outcome, uniform design, an effective space-filling design, is used to generate representative samples for input variables. As the computation of reliability index proposed in this paper is based on Monte Carlo simulation, it is very suitable for more general engineering problem, like some problems with black-box performance function.

The global sensitivities analysis method present in this paper is based on Spearman's rank correlation coefficient, which is different from local sensitivities analysis. The advance of this method is that it does not increase the computation cost. After the reliability analysis is implemented, the sensitivity results can be obtained readily. These examples demonstrated the feasibility of the presented method.

Conflict of Interests

The authors declare that there is no conflict of interests regarding the publication of this paper.

Acknowledgments

Authors gratefully acknowledge the support of the National Natural Science Foundation of China (E050401) and the Foundation of G2015KY0103.

References

- [1] G. Stefanou, "The stochastic finite element method: past, present and future," *Computer Methods in Applied Mechanics and Engineering*, vol. 198, no. 9–12, pp. 1031–1051, 2009.
- [2] Z. Qiu, D. Yang, and I. Elishakoff, "Probabilistic interval reliability of structural systems," *International Journal of Solids and Structures*, vol. 45, no. 10, pp. 2850–2860, 2008.
- [3] A. D. Kiureghian and O. Ditlevsen, "Aleatory or epistemic? Does it matter?" *Structural Safety*, vol. 31, no. 2, pp. 105–112, 2009.
- [4] A. M. Hasofer and N. C. Lind, "Exact and invariant second-moment code format," *ASCE Journal of the Engineering Mechanics Division*, vol. 100, no. 1, pp. 111–121, 1974.
- [5] R. Rackwitz and B. Flessler, "Structural reliability under combined random load sequences," *Computers and Structures*, vol. 9, no. 5, pp. 489–494, 1978.
- [6] K. Breitung, "Asymptotic approximations for multinormal integrals," *Journal of Engineering Mechanics*, vol. 110, no. 3, pp. 357–366, 1984.
- [7] D. C. Polidori, J. L. Beck, and C. Papadimitriou, "New approximations for reliability integrals," *Journal of Engineering Mechanics*, vol. 125, no. 4, pp. 466–475, 1999.
- [8] R. Y. Rubinstein and D. P. Kroese, *Simulation and the Monte-Carlo Method*, Wiley Series in Probability and Statistics, Wiley-Interscience, New York, NY, USA, 2nd edition, 2007.
- [9] C. Thoft and M. Yoshisuda, *Application of Structural Systems Reliability Theory*, Springer, Berlin, Germany, 1986.
- [10] F. Tonon, "Using random set theory to propagate epistemic uncertainty through a mechanical system," *Reliability Engineering & System Safety*, vol. 85, no. 1–3, pp. 169–181, 2004.
- [11] C. Jiang, X. Han, and G. R. Liu, "Optimization of structures with uncertain constraints based on convex model and satisfaction degree of interval," *Computer Methods in Applied Mechanics and Engineering*, vol. 196, no. 49–52, pp. 4791–4800, 2007.
- [12] Y. Ben-Haim, "A non-probabilistic concept of reliability," *Structural Safety*, vol. 14, no. 4, pp. 227–245, 1994.
- [13] I. Elishakoff, "Essay on uncertainties in elastic and viscoelastic structures: from A. M. Freudenthal's criticisms to modern convex modeling," *Computers and Structures*, vol. 56, no. 6, pp. 871–895, 1995.
- [14] Y. Ben-Haim and I. Elishakoff, *Convex Models of Uncertainties in Applied Mechanics*, Elsevier Science, Amsterdam, The Netherlands, 1990.
- [15] G. J. Klir, "Generalized information theory: aims, results, and open problems," *Reliability Engineering and System Safety*, vol. 85, no. 1–3, pp. 21–38, 2004.
- [16] C. Jiang, X. Han, G. Y. Lu, J. Liu, Z. Zhang, and Y. C. Bai, "Correlation analysis of non-probabilistic convex model and corresponding structural reliability technique," *Computer Methods in Applied Mechanics and Engineering*, vol. 200, no. 33–36, pp. 2528–2546, 2011.
- [17] Y. Ben-Haim and I. Elishakoff, "Discussion on: a non-probabilistic concept of reliability," *Structural Safety*, vol. 17, no. 3, pp. 195–199, 1995.
- [18] Y. Ben-Haim, "Uncertainty, probability and information-gaps," *Reliability Engineering & System Safety*, vol. 85, no. 1–3, pp. 249–266, 2004.
- [19] Y. Luo, Z. Kang, and Z. Yue, "Maximal stiffness design of two-material structures by topology optimization with nonprobabilistic reliability," *AIAA Journal*, vol. 50, no. 9, pp. 1993–2003, 2012.
- [20] S. X. Guo, Z. Y. Lu, and Y. S. Feng, "Non-probabilistic model of structural reliability based on interval analysis," *Chinese Journal of Computational Mechanics*, vol. 18, no. 1, pp. 56–60, 2001.
- [21] J. Tao, C. Jian-Jun, and X. Ya-Lan, "A semi-analytic method for calculating non-probabilistic reliability index based on interval models," *Applied Mathematical Modelling*, vol. 31, no. 7, pp. 1362–1370, 2007.
- [22] X. Chen, C.-Y. Tang, C.-P. Tsui, and J. Fan, "Modified scheme based on semi-analytic approach for computing non-probabilistic reliability index," *Acta Mechanica Solida Sinica*, vol. 23, no. 2, pp. 115–123, 2010.
- [23] Z. Qiu and I. Elishakoff, "Antioptimization of structures with large uncertain-but-non-random parameters via interval analysis," *Computer Methods in Applied Mechanics and Engineering*, vol. 152, no. 3–4, pp. 361–372, 1998.
- [24] I. Elishakoff, R. T. Haftka, and J. Fang, "Structural design under bounded uncertainty—optimization with anti-optimization," *Computers and Structures*, vol. 53, no. 6, pp. 1401–1405, 1994.

- [25] Z. Kang, Y. Luo, and A. Li, "On non-probabilistic reliability-based design optimization of structures with uncertain-but-bounded parameters," *Structural Safety*, vol. 33, no. 3, pp. 196–205, 2011.
- [26] Y. Luo, A. Li, and Z. Kang, "Reliability-based design optimization of adhesive bonded steel-concrete composite beams with probabilistic and non-probabilistic uncertainties," *Engineering Structures*, vol. 33, no. 7, pp. 2110–2119, 2011.
- [27] Y. Ben-Haim, "A non-probabilistic measure of reliability of linear systems based on expansion of convex models," *Structural Safety*, vol. 17, no. 2, pp. 91–109, 1995.
- [28] C. Jiang, R. G. Bi, G. Y. Lu, and X. Han, "Structural reliability analysis using non-probabilistic convex model," *Computer Methods in Applied Mechanics and Engineering*, vol. 254, pp. 83–98, 2013.
- [29] R. Jin, W. Chen, and A. Sudjianto, "An efficient algorithm for constructing optimal design of computer experiments," *Journal of Statistical Planning and Inference*, vol. 134, no. 1, pp. 268–287, 2005.
- [30] R. C. Jin, *Enhancements of Metamodeling Techniques in Engineering Design*, Graduate College, University of Illinois at Chicago, Chicago, Ill, USA, 2004.
- [31] A. Saltelli and J. Marivoet, "Non-parametric statistics in sensitivity analysis for model output: a comparison of selected techniques," *Reliability Engineering and System Safety*, vol. 28, no. 2, pp. 229–253, 1990.
- [32] I. M. Sobol', "Global sensitivity indices for nonlinear mathematical models and their Monte Carlo estimates," *Mathematics and Computers in Simulation*, vol. 55, no. 1–3, pp. 271–280, 2001.
- [33] E. B. Niven and C. V. Deutsch, "Calculating a robust correlation coefficient and quantifying its uncertainty," *Computers and Geosciences*, vol. 40, pp. 1–9, 2012.

Research Article

Numerical Simulation of Interaction between Hall Thruster CEX Ions and SMART-1 Spacecraft

Kang Shan,¹ Yuchuan Chu,¹ Qingyu Li,¹ Liang Zheng,² and Yong Cao¹

¹Department of Mechanical Engineering and Automation, Harbin Institute of Technology Shenzhen Graduate School, Shenzhen, Guangdong 518055, China

²Department of Natural Sciences and Humanities (Mathematics/Mechanics/Humanities), Harbin Institute of Technology Shenzhen Graduate School, Shenzhen, Guangdong 518055, China

Correspondence should be addressed to Yong Cao; yongc@hitsz.edu.cn

Received 11 June 2014; Accepted 13 September 2014

Academic Editor: Junuthula N. Reddy

Copyright © 2015 Kang Shan et al. This is an open access article distributed under the Creative Commons Attribution License, which permits unrestricted use, distribution, and reproduction in any medium, provided the original work is properly cited.

The interaction between the plume of Hall thruster and the surface of the SMART-1 spacecraft is investigated by developing a three-dimensional IFE-PIC-MCC code, with the emphasis on the effect of the disturbance force and thermal loading caused by charge exchange ions (CEX) impingement on the surface of the spacecraft. The parameters such as heat flux and forces of CEX ions which impinge on SMART-1 and solar arrays are obtained. The disturbance force of CEX ions to the spacecraft is calculated for different divergence angles and different solar array rotation cases. The simulation results show that the disturbance force and heat flux on spacecraft change very little as the divergence angle changes. The effect of maximum disturbance force can be neglected since it is so small comparing with the nominal value of the main thrust. Solar arrays receive the least thermal heating from the CEX ions when the beam ions flow is perpendicular to the solar array plane.

1. Introduction

The motion of the satellite is usually controlled by the ejection of the plume from the thruster into the space. Then, the interaction between the plume and the spacecraft surface may cause undesirable effects such as causing the disturbance force and thermal loads and contaminating sensitive equipment and sensors. The disturbance force can be a fraction of the total thrust, while thermal loads on the surface of spacecraft body result in the heating of the surface and affect the working status of electronic components which can only function properly in a range of temperatures. So the accurate modeling and predictions of these effects are very crucial to the design of a satellite [1–3].

The interaction between the exhausted plume of thrusters and the satellite components has been studied by some researchers for both chemical thrusters and electric propulsion thrusters [2, 4]. Park et al. [2] used three-dimensional discrete simulation Monte Carlo (DSMC) to investigate the interaction of the chemical thruster (a 4.45N MRE-1

monopropellant hydrazine liquid rocket engine) plume with satellite components in KOMPSAT-II. The results showed a negligible disturbance force/torque and thermal loading compared with its nominal thrust/torque and solar heating. Xiao et al. [5] analyzed molecules adsorption and transmission on the surface of satellite by using numerical simulation and ground experiment method. Also, the motion of plume pollutants which leads to performance degradation of satellite key functional surfaces (optical systems, solar panels, thermal control object surface, etc.) is calculated. Different from the plume of the chemical thrusters, the plume of electric propulsion is plasma which consists of a large number of ions and electrons except neutral atoms. In addition, charge exchange collisions will occur between the high-speed ions and neutral atoms which result in the generation of low-speed CEX ions that have significant impact on the plume characteristics. These charged particles are affected heavily by their self-consistent electric fields. Therefore, compared with the plume of the chemical thrusters, the plume of the electric propulsion thruster is different in not only the ingredients

of the plume but also the flow characteristics of the plume. A number of simulation models or numerical methods have been developed for the plume in the electric propulsion thruster to investigate the interaction with the spacecraft surface and the results from these numerical models were verified through the comparison with the experiment data in recent years [6–13]. Yan et al. [10] used particle in cell (PIC) code with DSMC techniques to model Hall thruster plume and sputtering erosion on SPT-70. Kafafy and Cao [11] investigated plume effects from indirect plume impingement on formation flying satellites using ion propulsion by developing an immersed-finite-element PIC (IFE-PIC) algorithm on parallel computers. Tajmar et al. [12] developed a hybrid PIC code with Monte Carlo collision (MCC) to study spacecraft-environment interaction. Boyd [13] studied the ion current density profile and ion energy distribution by using a detailed particle-fluid PIC-DSMC model, which was compared with the experimental measurements taken in space. However, most of them were concerned about CEX ions sputtering erosion or the accuracy of simulation model, but few of them were concerned about the disturbance force and thermal loading on the spacecraft which are caused by the impinging of the backflow CEX ions on the surface of the spacecraft.

Therefore, in this paper, the study of the force and thermal loads on the spacecraft caused by backflow CEX ions is performed by using a three-dimensional IFE-PIC-MCC code. The PIC-MCC [12] code is used to simulate the generation and movement of CEX ions. The DSMC method [14] is applied to model neutral atoms. Electric field in the plume is obtained by solving Poisson's equation which is calculated by IFE-PIC [15, 16] method which is designed to handle complex boundary conditions accurately while maintaining the computational speed of the standard PIC code. The code is then applied to the numerical simulations of the SMART-1 spacecraft which had traveled to the moon using a PPS-1350 Hall thruster with the maximum thrust of 70 mN [17].

Section 2 describes the interaction model between the plume of Hall thruster and the surface of the spacecraft. The numerical method is presented in Section 3. The simulation results are then shown in Section 4 and some discussions on these results are carried out. Finally, the summary and conclusions are presented at the end of this paper.

2. SMART-1 Spacecraft-Plume Interactions Model

The geometry and dimensions of SMART-1 spacecraft model are illustrated in Figure 1. The main body of SMART-1 can be considered as the cubic shape with the dimensions of $l \times w \times h = 1100 \text{ mm} \times 1100 \text{ mm} \times 900 \text{ mm}$. In this model, the Hall thruster is simplified as a cylinder with the diameter of 100 mm and the height of 50 mm; two thin rectangles with 5400 mm length and 1000 mm width are utilized to represent the solar arrays which can rotate around the satellite.

The PPS-1350 Hall thruster emits an ion beam out of a ring-shaped anode with a divergence angle $\theta = 45^\circ$. Typical operating parameters of PPS-1350 Hall thruster are

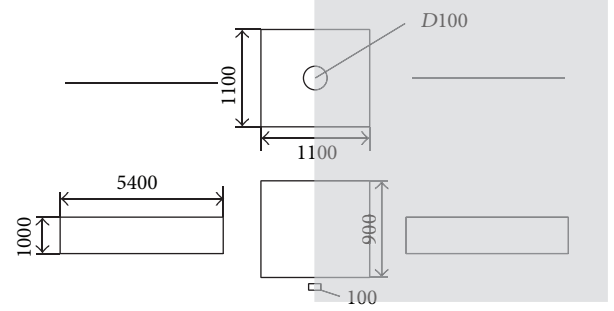


FIGURE 1: The geometry and dimensions of SMART-1 (in mm).

TABLE 1: Operating parameters of PPS-1350 Hall thruster.

Parameter	Value
Thrust	70 mN
Voltage U_{acc}	350 V
Ion current I_i	3.8 A
Mass flow rate	4.2 mg/s
Specific impulse	164 s
Total efficiency η	51%
Outer insulator diameter r_o	100 mm
Inner insulator diameter r_i	56 mm
Neutral temperature	750 K
Electron temperature T_e	2 eV

summarized in Table 1 [13]. At the exit of the thruster, the densities and temperatures are assumed to be radically uniform, and the velocity vectors vary uniformly from -45° at the lower edge of the channel exit to $+45^\circ$ at the upper edge. The temperatures of the electrons and neutrals are assumed to be 2 eV and 750 K, respectively. The heavy particle densities and velocities are subsequently obtained from the mass flow rate and integrated ion current. The plume in the PPS-1350 Hall thruster assumingly consists of the following components:

- (i) propellant beam ions,
- (ii) unionized propellant neutrals,
- (iii) slow propellant ions created by CEX reaction collisions,
- (iv) neutralising electrons.

The plasma in the beam of the Hall thruster typically has a number density of more than 10^{15} m^{-3} . The widely used PIC approach is applied in this research. The so-called super particle representing a number of 10^9 real particles is introduced here. As a result, the total number of simulated entities of Xe and Xe^+ is kept below 10^7 ; therefore the simulations can be carried out on standard workstations [17].

Xe^+ particles are given a constant velocity at the thruster exit as

$$v_i = \sqrt{\frac{2eU_{acc}}{m_i}}, \quad (1)$$

where U_{acc} is accelerating voltage, m_i is xenon ion mass, and v_i denotes the ion velocity.

Initially the ions are uniformly distributed across the thruster opening between the inner radius r_i and the outer radius r_o . The direction of the velocity \mathbf{v}_i is determined in spherical coordinates $(v_i; \alpha_1; \alpha_2)$ [17], where α_1 is randomly chosen in $0 < \alpha_1 < 2\pi$ and α_2 is varied in accordance with the radial position between the inner and outer beam-spreading angles α_i and α_o by

$$\alpha_2(r) = \frac{\alpha_o - \alpha_i}{r_o - r_i} (r - r_i) + \alpha_i, \quad (2)$$

where r_o and r_i are the outer and inner radii at the exit of the thruster, respectively.

During the simulations, the number of ejected Xe^+ beam ions by the Hall thruster at each time-step is obtained by the ion current:

$$\Delta n_i = I_i \Delta t, \quad (3)$$

where I_i denotes ion current, Δn_i is number of ions generated at each time step, and Δt represents the time of each step.

The electrons are assumed to be collisionless, currentless, isothermal, and unmagnetized. The plasma is quasineutral and electrons satisfy the Boltzmann [12] relation as

$$n_e = n_{e0} \exp \left[\frac{e(\phi - \phi_0)}{kT_{e0}} \right], \quad (4)$$

where n_e is electron number density, ϕ is potential, and n_{e0} , ϕ_0 represent the reference parameters.

The electric field surrounding the spacecraft is solved from Poisson equation

$$-\nabla \cdot \epsilon \nabla \phi = e(n_i - n_e), \quad (5)$$

where ϵ denotes permittivity of vacuum, n_e is electron number density, n_i represents ion number density, and ϕ is the potential.

Charged particles in the simulation area are accelerated due to the electric field. Their movement can be determined by the integration of the equation of motion, which can be described with Newton's second law:

$$\frac{d}{dt}(m\mathbf{v}) = \mathbf{F} = q\mathbf{E}, \quad \mathbf{v} = \frac{d\mathbf{x}}{dt}. \quad (6)$$

Neutral Xe propellant atoms are introduced with no drift velocity but the thermal velocity related to the temperature of the neutral Xe propellant atom. As neutral Xe atoms move, the DSMC method is applied to simulate collisions of neutral Xe propellant atoms since neutral propellant can be considered as a rarefied gas flow. In this method, each unit cell, containing many particles, has the dimensions on the order of a mean free path. Pairs of these particles are then randomly selected and a collision probability is evaluated which is proportional to the product of the relative velocity and cross section of the collision for each pair. The probability is compared with a random number to determine if that collision occurs.

Let us consider a single simulation cell containing a number of simulation macroparticles. Bird [14] gives the probability of a collision for a macroparticle in this cell:

$$P = F_N \sigma_T c_r \frac{\Delta t}{V_c}, \quad (7)$$

where F_N is the macroparticle weight, σ_T is the total collision cross section, c_r is the relative velocity, Δt is the simulation time step, and V_c is the cell volume.

One order to check for collisions would be to iterate over all N particles and compute probability with all remaining particles. This would result in $N(N-1)/2 \sim (N^2)/2$ pairs. For a large number of particles, this method clearly becomes very computationally inefficient. Bird's no time counter (NTC) method was designed to provide help with this issue. It allows us to estimate ahead of time the maximum number of pairs that need to be checked. The maximum collision probability is

$$P_{\text{max}} = F_N (\sigma_T c_r)_{\text{max}} \frac{\Delta t}{V_c}, \quad (8)$$

where $(\sigma_T c_r)_{\text{max}}$ is a parameter chosen ahead of time using approximate predictions of cross section and velocity. As Bird points out in his book, the actual value is not all that important since it ends up getting cancelled out. The number of pairs to check is then

$$\left(\frac{1}{2}\right) N \bar{N} F_N (\sigma_T c_r)_{\text{max}} \frac{\Delta t}{V_c}. \quad (9)$$

Here the second \bar{N} is the average particle count. The average is used to reduce the statistical time-step to time-step oscillations. For each pair, we then compute the probability as follows:

$$P = \frac{\sigma_T c_r}{(\sigma_T c_r)_{\text{max}}}. \quad (10)$$

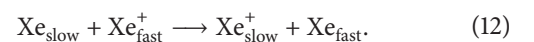
This value is compared to a random number and the collision occurs if $P > R$.

For atom-atom elastic collisions, the variable hard sphere collision model is employed. For xenon, the collision cross section is

$$\sigma_{\text{EL}}(\text{Xe}, \text{Xe}) = \frac{2.12 \times 10^{-18}}{g^{2\omega}} \text{ m}^2, \quad (11)$$

where g is the relative velocity and ω denotes the viscosity temperature exponent for xenon which has the value of 0.12 [14].

Charge-exchange collisions occur between the fast beam Xe^+ ions and the slow neutral Xe atoms. After these collisions, the fast beam Xe^+ ions turn to be neutral and keep the fast speed; and the slow neutral Xe atoms change into ions which are accelerated due to the effect of the electric field. These changes can be expressed as follows:



To model the CEX process, we use the MCC method. For each Xe^+ ion we calculate the collision probability. This probability is then compared to a random number. If the probability is larger than the random number, the collision occurs and a process-specific collision handler is called. The collision probability is given by Birdsall [18] as

$$P = 1 - \exp(-\nu\Delta t) = 1 - \exp(-n_n\sigma g\Delta t). \quad (13)$$

n_n is the density of the target gas at the location of the particle, σ is the collision cross section, g is the relative velocity, and Δt is the time difference between collision checks. This time-step may correspond to the time-step used to move the ions in the PIC method.

In this research, the transfer of only one electron between an atom and an ion is considered during the charge-exchange process. For singly charged ions, the following cross section measured by Pullins et al. and Miller et al. [19, 20] is used:

$$\sigma_{\text{CEX}}(\text{Xe}, \text{Xe}^+) = [-23.30\log_{10}(g) + 142.21] \times 0.8423 \times 10^{-20} \text{ m}^2, \quad (14)$$

where g is the relative velocity between the beam ion and neutral atom.

Boundary conditions for computing of the Hall thruster plume are presented as follows. Both field and particle boundary conditions are required at the outer boundary of the computational domain. The field condition is simply set as the electric field normal to the boundary edges equal to zero. The particle boundary condition is set to be that any particle crossing the boundary is simply removed and will no longer be calculated in the model. The solid surfaces of the Hall thruster and the satellite are also considered during the simulations. Along these surfaces, the potential of surfaces is set to be at a certain given value (-2 V). Any ions colliding onto the surfaces are absorbed by the surfaces.

3. Numerical Method

A particle simulation code using the IFE-PIC-MCC algorithm is developed to solve the plume interaction problem. The IFE-PIC-MCC code solves the generating of CEX ions and their trajectories and the electric field surrounding the spacecraft.

The simulation is run in three phases: modeling beam Xe^+ ions, neutral Xe, and CEX ions, respectively. The reason that these different species particles can be simulated asynchronously is as follows.

- (1) Beam Xe^+ ions have so high energy that they are hardly affected by self-consistent electric field.
- (2) Neutral Xe atoms do not get charged so that they are not affected by electric field.
- (3) CEX ions are in small numbers in plasma plume and their generation affects the plume character very little.

In the first phase, we run the PIC code to generate and trace beam Xe^+ ions and neutral Xe until steady-state

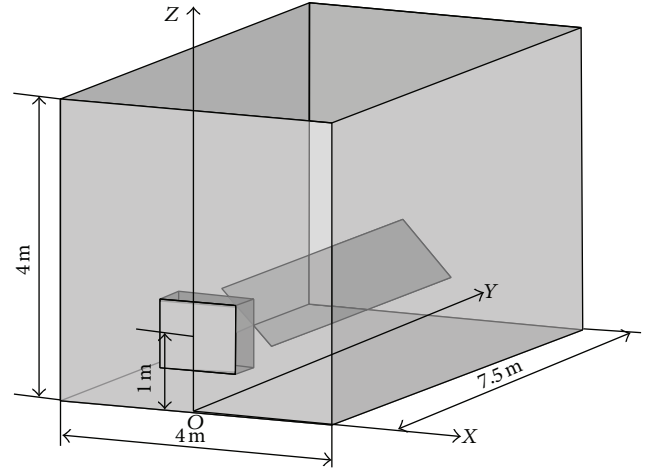


FIGURE 2: The dimensions of the simulation region.

trajectories are obtained. In this phase, we use a simplified approach to model beam Xe^+ ions. Those beam Xe^+ ions are accelerated in the Hall thruster channel with the velocities on the order of 10 km/s . So most high-energy beam Xe^+ ions are unaffected by self-consistent electric field and follow straight trajectories. The DSMC method is used in the computation of Xe-Xe collisions. After this phase, the distribution of beam Xe^+ ions and neutral Xe is gotten in the computation region, respectively.

In the second phase, the IFE-PIC-MCC code is used to trace CEX ions until steady-state trajectories are obtained. CEX ions are generated from the collision of steady-state beam Xe^+ ions and neutral Xe by MCC at each time step. The initial velocity of CEX ions is given a uniform velocity distribution with a temperature corresponding to that of the neutral propellant. That is to say, initial CEX ions only have thermal velocity with no drift velocity which is relatively small and is affected heavily by electric field. Using IFE-PIC, the electric field is calculated which pushes the movement of CEX ions at each time step. Those processes are cycled until steady-state CEX ions trajectories are obtained.

In the final phase, CEX ions are collected which impinge on SMART-1 and solar arrays; then all those CEX ions are used to calculate the flux density of CEX ions, the energy distribution, and pressure distribution on SMART-1 and solar arrays.

4. Simulations Results

Due to the symmetry of SMART-1 (as illustrated in Figure 1), a half-symmetry model is employed to simulate the interaction between the plume and the surface of SMART-1, as shown in Figure 2. The position of SMART-1 in the simulation region is also shown in Figure 2. The simulation domain has a size of $4.0 \text{ m} \times 7.5 \text{ m} \times 4.0 \text{ m}$ with $81 \times 151 \times 81$ grid points. During the simulations, approximately 8 million simulation particles are employed. The time-step is on the order of 10^{-6} s . The simulation reaches a steady state for CEX ions after about 800 iterations, and solutions are then averaged over further 200

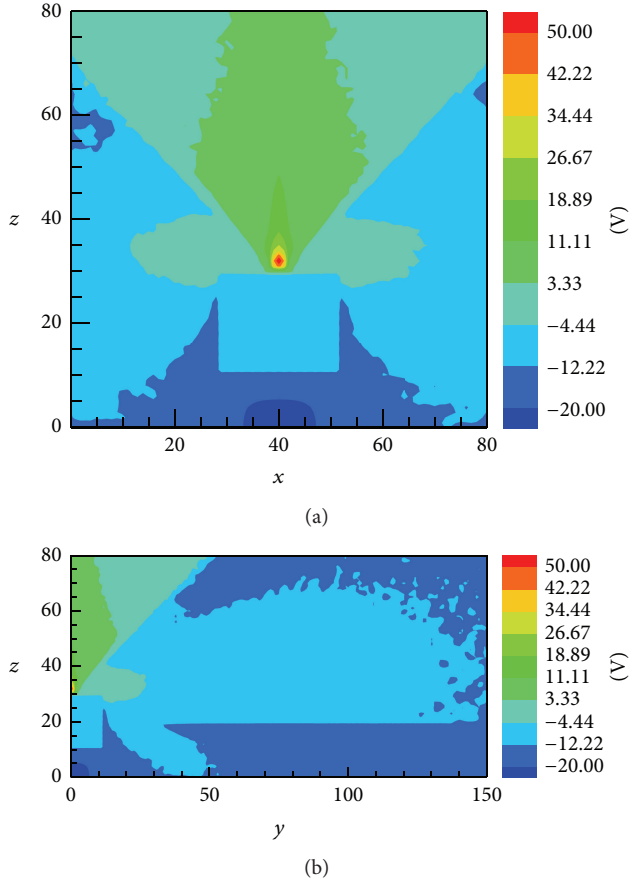


FIGURE 3: Plasma potential distribution (at $\theta = 45^\circ$, $\gamma = 0^\circ$).

iterations. The total computation time is about 24 h on an HP computer server.

Figure 3 illustrates the distribution of the potential under the conditions of $\theta = 45^\circ$ and $\gamma = 0^\circ$ (here γ is the angle between the normal of the solar array plane and the center line of the beam flow). As shown in Figure 3, the backflow of the CEX ions results in the fact that the isopotential surface expands toward a direction opposite to the ion beam movement. It makes the pattern of the distribution look like a mushroom.

Figures 4 and 5 present the pressure and energy distribution of CEX ions on solar arrays, respectively. As solar arrays can rotate around the axis to change their direction, the effect of the angle between the normal of solar array plane and the beam flow center line is investigated. As illustrated in Figures 4 and 5, three different angles are chosen as $\gamma = 0^\circ$, 45° , and 90° and their effects are presented. It is clear to see that the solar arrays receive more CEX ions and bear much more pressure at $\gamma = 0^\circ$ than at $\gamma = 90^\circ$.

Figures 6 and 7 present the energy and pressure distribution about CEX ions impinging on the surface of SMART-1 main body. CEX impingement on main body and CEX ions distribution on main body are almost the same for different solar array rotation angles, since different solar array positions can hardly affect the electric field distribution in

TABLE 2: Parameter values on main body for different solar array rotation angle cases (at $\theta = 45^\circ$).

Solar array rotation angle γ (in deg)	Average energy (in W/m^2)	Disturbance normal force (in mN)
0	2.46513	0.5652
45	2.46513	0.5652
90	2.46513	0.5652

the vicinity of the main body. Also, it can be observed that the less backflow CEX ions on the main body can be obtained along with the increasing of the distance to the location of the Hall thruster. The maximum energy of CEX ions reaching onto the main body of the spacecraft is 17.056 W/m^2 .

Tables 2 and 3 list the values of the disturbance normal force and thermal loading on the SMART-1 spacecraft for different solar array rotation angle cases, which are calculated based on the backflow CEX ions energy and pressure distribution. It can be seen that the values of the average energy and disturbance force on the main body of the spacecraft are the same under different solar array rotation angle, while the values of the average energy and disturbance force on solar arrays decrease as the solar array rotation angle γ increases. The maximum value of disturbance force onto spacecraft can reach 0.7 mN when $\gamma = 0^\circ$. The tangential force acting on the main body is symmetric due to the symmetric distribution of the pressure on the main body (as shown in Figure 7). Although tangential force on the half main body can reach a value of 0.1512 mN , the total tangential force on main body is counteracted and can be neglected. As the rotation angle of the solar array increases, the tangential force in the direction of array plane length direction decreases due to less CEX impingement on solar arrays. But the total effect of the tangential force on the solar arrays is limited, since the total tangential force on both solar arrays is mostly counteracted with each other.

Figure 8 presents the distribution of the plasma potential for different divergence angle. It can be seen in Figure 8 that the distributions of the plasma potential are quite different under the condition of the same rotating angle but different divergence angle. The divergence angle also affects the CEX ions impinging on the spacecraft. The effects of three different divergence angles are studied for the same mass flow rate (4.2 mg/s). The solar arrays are set in the position that solar arrays are perpendicular to ion beam ($\gamma = 0^\circ$), and the parameters of CEX ions impingement are recorded for the three divergence angles: $\theta = 15^\circ$, 30° , and 45° .

As listed in Table 4, the average energy on both the main body and solar arrays does not change much when the divergence angle changes. As divergence angle increases, the disturbance force on the main body increases very little. The disturbance force to solar arrays is relatively small comparing to the disturbance force on the main body, since solar arrays are far from the flux beam flow and receive less CEX ions. The maximum disturbance force is less than 0.1% of the nominal value of the main thrust. Thus, the disturbance force has little influence on the dynamic system of the satellite, as well as the propellant budget.

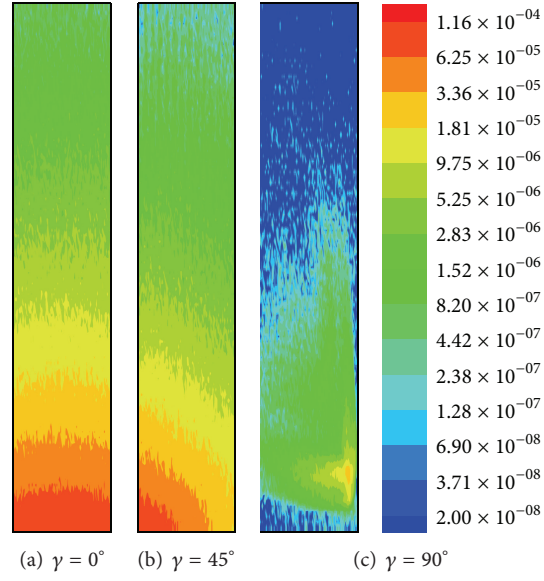


FIGURE 4: Pressure distribution of CEX ions on the solar array of SMART-1 (at $\theta = 45^\circ$) (in N/m^2).

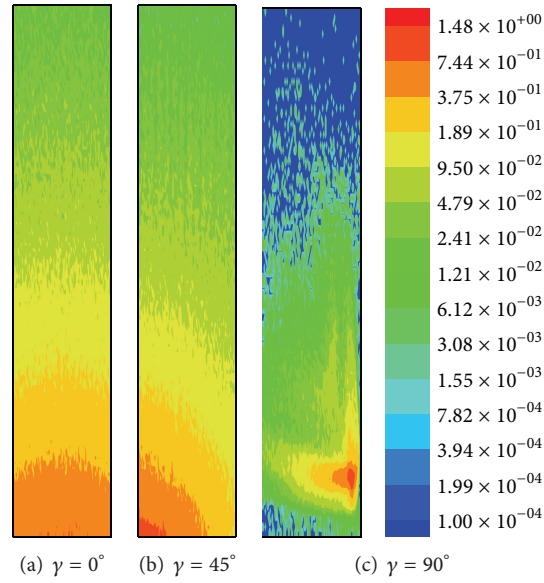


FIGURE 5: Energy distribution of CEX ions on the solar array of SMART-1 (at $\theta = 45^\circ$) (in W/m^2).

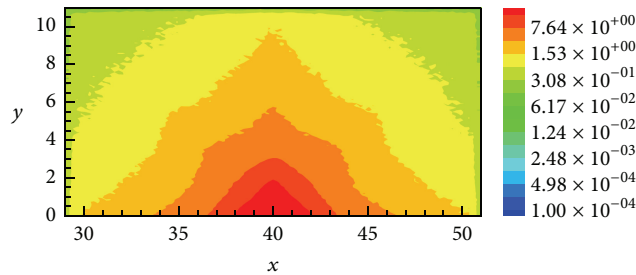


FIGURE 6: CEX ions energy distribution on the surface of SMART-1 main body (at $\theta = 45^\circ$) (in W/m^2).

TABLE 3: Parameter values on one of solar arrays for different solar array rotation angle cases (at $\theta = 45^\circ$).

Solar array rotation angle γ (in deg)	Average energy (in W/m^2)	Disturbance normal force (in mN)	Tangential force in array width direction (in mN)	Tangential force in array length direction (in mN)
0	0.16692	0.09449	0	0.2071
45	0.12463	0.05512	0.0354	0.1562
90	0.02903	0.01105	0.00732	0.0748

TABLE 4: Parameter values for different divergence angle cases (at $\gamma = 0^\circ$).

Divergence angle θ (in deg)	Average energy on main body (in W/m^2)	Average energy on solar arrays (in W/m^2)	Disturbance force to main body (in mN)	Disturbance force to solar arrays (in mN)
15	2.43187	0.18829	0.54366	0.17317
30	2.42073	0.19279	0.54532	0.19483
45	2.46513	0.16692	0.56523	0.18897

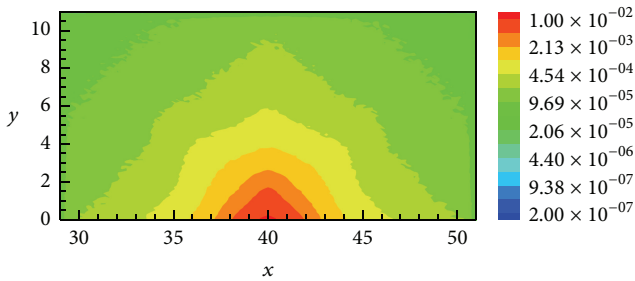
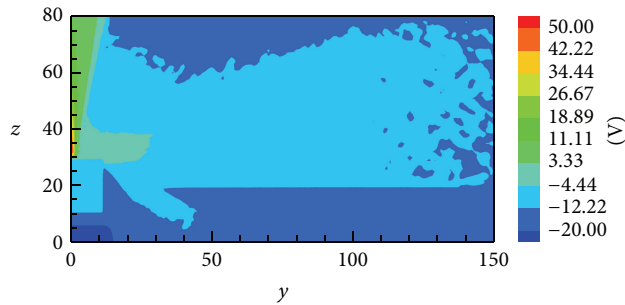
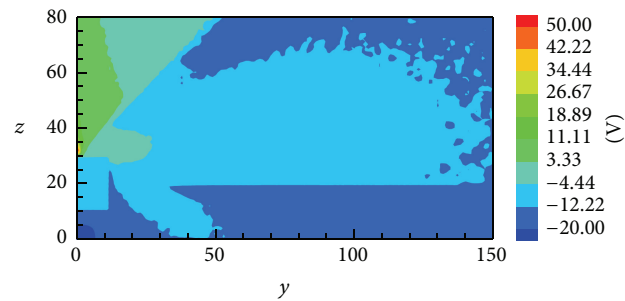
FIGURE 7: CEX ions pressure distribution on the surface of SMART-1 main body (at $\theta = 45^\circ$) (in N/m^2).(a) At $\theta = 15^\circ$, $\gamma = 0^\circ$ (b) At $\theta = 45^\circ$, $\gamma = 0^\circ$

FIGURE 8: Distribution of plasma potential for different divergence angles.

5. Summary and Conclusion

In summary, the interaction between the plume of the Hall thruster and the SMART-1 spacecraft has been investigated using a three-dimensional IFE-PIC-MCC code. In this research, the backflow CEX ions impingement on the SMART-1 is investigated, and the effects of the disturbance force and the thermal loading due to the impingement are studied. The effects of different divergence angles and solar array rotation angles on the disturbance force are considered. Simulation results revealed that the maximum disturbance normal force can only reach a value of 0.7 mN, which is relatively small comparing with the main thrust (70 mN). As the solar array rotation angle increases, both the disturbance force on the spacecraft and the average energy on solar arrays decrease substantially. With the increment of the divergence angle, both the disturbance force and the average energy on the surface of spacecraft are slightly changed under the same solar array rotation angle conditions, whereas the disturbance force in the main body has a slight rise. But the maximum disturbance force is less than 0.1% of the nominal value of the main thrust, which means the effect of the disturbance force can be ignored.

Conflict of Interests

The authors declare that there is no conflict of interests regarding the publication of this paper.

Acknowledgment

This work was supported by the National Natural Science Foundation of China under Contract nos. 10875034, 11175052, and 11275034.

References

- [1] I. D. Boyd and J. P. W. Stark, "Modeling of a small hydrazine thruster plume in the transition flow regime," *Journal of Propulsion and Power*, vol. 6, no. 2, pp. 121–126, 1990.

- [2] J. H. Park, S. W. Back, and J. S. Kim, "Direct simulation Monte Carlo analysis of thruster plumes/satellite base region interaction," *AIAA Journal*, vol. 42, no. 8, pp. 1622–1632, 2004.
- [3] I. D. Boyd and A. Ketsdever, "Interactions between spacecraft and thruster plumes," *Journal of Spacecraft and Rockets*, vol. 38, no. 3, p. 380, 2001.
- [4] F. E. Lumpkin III, J. Marichalar, and B. D. Stewart, "High fidelity simulations of plume impingement to the international space station," in *Proceedings of the 33rd JANNAF Exhaust Plume and Signatures Subcommittee Meeting*, Monterey, Calif, USA, December 2012.
- [5] Z.-J. Xiao, H.-E. Cheng, and H.-L. Zhou, "Plume interaction in parallel multi-thrusters propulsion system and the effect on backflow," in *Proceedings of the 9th AIAA/ASME Joint Thermophysics and Heat Transfer Conference*, pp. 1963–1972, San Francisco, Calif, USA, June 2006.
- [6] G. Markelov and E. Gengembre, "Modeling of plasma flow around SMART-1 spacecraft," *IEEE Transactions on Plasma Science*, vol. 34, no. 5, pp. 2166–2175, 2006.
- [7] I. D. Boyd and J. T. Yim, "Modeling of the near field plume of a Hall thruster," *Journal of Applied Physics*, vol. 95, no. 9, pp. 4575–4584, 2004.
- [8] A. Passaro, A. Vicini, F. Nania, and L. Biagioni, "Numerical rebuilding of smart-1 plasma plumespacecraft interaction," IEPC Paper IEPC-2005-174, 2005.
- [9] V. A. S. Y. A. Bondar, "Modeling of plume of stationary plasma thruster by particle method," *Thermophysics and Aeromechanics*, vol. 38, no. 3, pp. 373–392, 2001.
- [10] L. Yan, P.-Y. Wang, Y.-H. Ou, and X.-L. Kang, "Numerical study of hall thruster plume and sputtering erosion," *Journal of Applied Mathematics*, vol. 2012, Article ID 327021, 16 pages, 2012.
- [11] R. Kafafy and Y. Cao, "Modelling ion propulsion plume interactions with spacecraft in formation flight," *Aeronautical Journal*, vol. 114, no. 1157, pp. 417–426, 2010.
- [12] M. Tajmar, J. González, and A. Hilgers, "Modeling of spacecraft-environment interactions on SMART-1," *Journal of Spacecraft and Rockets*, vol. 38, no. 3, pp. 393–399, 2001.
- [13] I. D. Boyd, "Numerical simulation of hall thruster plasma plumes in space," *IEEE Transactions on Plasma Science*, vol. 34, no. 5, pp. 2140–2147, 2006.
- [14] G. A. Bird, *Molecular Gas Dynamics and the Direct Simulation of Gas Flows*, Oxford University Press, Oxford, UK, 1994.
- [15] R. Kafafy, T. Lin, Y. Lin, and J. Wang, "Three-dimensional immersed finite element methods for electric field simulation in composite materials," *International Journal for Numerical Methods in Engineering*, vol. 64, no. 7, pp. 940–972, 2005.
- [16] J. Wang, Y. Cao, R. Kafafy, J. Pierru, and V. K. Decyk, "Simulations of ion thruster plume-spacecraft interactions on parallel supercomputer," *IEEE Transactions on Plasma Science*, vol. 34, no. 5, pp. 2148–2158, 2006.
- [17] M. Tajmar, R. Sedmik, and C. Scharlemann, "Numerical simulation of SMART-1 Hall-thruster plasma interactions," *Journal of Propulsion and Power*, vol. 25, no. 6, pp. 1178–1188, 2009.
- [18] C. K. Birdsall, "Particle-in-cell charged-particle simulations, plus Monte Carlo collisions with neutral atoms, PIC-MCC," *IEEE Transactions on Plasma Science*, vol. 19, no. 2, pp. 65–85, 1991.
- [19] S. Pullins, R. Dressler, Y. Chiu, and D. Levandier, "Thrusters: $\text{Xe}^+ + \text{Xe}$ symmetric charge transfer," in *Proceedings of the 38th AIAA Aerospace Sciences Meeting and Exhibit*, Reno, Nev, USA, January 2000.
- [20] J. S. Miller, S. H. Pullins, D. J. Levandier, Y.-H. Chiu, and R. A. Dressler, "Xenon charge exchange cross sections for electrostatic thruster models," *Journal of Applied Physics*, vol. 91, no. 3, pp. 984–991, 2002.

Research Article

Fractional Dynamics in Calcium Oscillation Model

Yoothana Suansook and Kitti Paithoonwattanakij

Faculty of Engineering, King Mongkut's Institute of Technology Ladkrabang, Chalongkrung Road, Ladkrabang, Bangkok 10520, Thailand

Correspondence should be addressed to Yoothana Suansook; yoothana@gmail.com

Received 20 April 2014; Revised 8 June 2014; Accepted 1 July 2014

Academic Editor: Shaofan Li

Copyright © 2015 Y. Suansook and K. Paithoonwattanakij. This is an open access article distributed under the Creative Commons Attribution License, which permits unrestricted use, distribution, and reproduction in any medium, provided the original work is properly cited.

The calcium oscillations have many important roles to perform many specific functions ranging from fertilization to cell death. The oscillation mechanisms have been observed in many cell types including cardiac cells, oocytes, and hepatocytes. There are many mathematical models proposed to describe the oscillatory changes of cytosolic calcium concentration in cytosol. Many experiments were observed in various kinds of living cells. Most of the experimental data show simple periodic oscillations. In certain type of cell, there exists the complex periodic bursting behavior. In this paper, we have studied further the fractional chaotic behavior in calcium oscillations model based on experimental study of hepatocytes proposed by Kummer et al. Our aim is to explore fractional-order chaotic pattern in this oscillation model. Numerical calculation of bifurcation parameters is carried out using modified trapezoidal rule for fractional integral. Fractional-order phase space and time series at fractional order are present. Numerical results are characterizing the dynamical behavior at different fractional order. Chaotic behavior of the model can be analyzed from the bifurcation pattern.

1. Introduction

The behaviors of many physical systems are nonlinear. The study of complexity arising from nonlinear systems is an intrigue subject for scientific research. Nonlinear systems have demonstrated a wide range of strange behaviors; the small change in initial conditions or system parameters result in long-term unpredictable behavior known as chaos.

Nonlinear dynamical systems have many interesting behaviors to study. The research in this field starts from the discovery of chaos in atmospheric convection model by Lorenz [1]. The equations that described the dynamical system are differential equations which yield different type of solutions [2] such as limit cycle, periodic, periodic doubling, nonperiodic, and chaotic solutions. Further studies in this field are chaos synchronization [3] and fractional-order dynamical system [4–17].

The biological systems are examples of nonlinear system where chaos arises including cardiac rhythms and bursting patterns of excited neural and intracellular chemical oscillation [18]. Nonlinear dynamical systems in living organisms are examples of complex system which evolved far from

equilibrium conditions [19]. Many biological phenomena can now be understood with mathematical modeling [18]. The studies biological systems via nonlinear dynamics are feasible to discover new explanation in biological sciences and emerging applications for clinical diagnosis and therapy [19]. The examples of nonlinear dynamics in living organism include respiratory burst, glycolysis, peroxidase reaction, and Ca^{2+} oscillations [18, 19].

Biorhythms are example of nonlinear dynamics in living organism, usually associated with excitable cells, but there is growing evidence that nonexcitable cells may also exhibit periodic behavior [20]. Much of this periodic activity is driven by regular oscillations in intracellular calcium [19, 20]. The experimental studies show that Ca^{2+} oscillations are the changing in free cytosolic Ca^{2+} concentration, which are found in various cell types [21].

A nonlinear dynamical system is a deterministic system that is feasible to explain by set of differential equations [2]. Recently, studies on theory of fractional calculus have been applied to describe the dynamical system where the derivative can be fractional order [4–17].

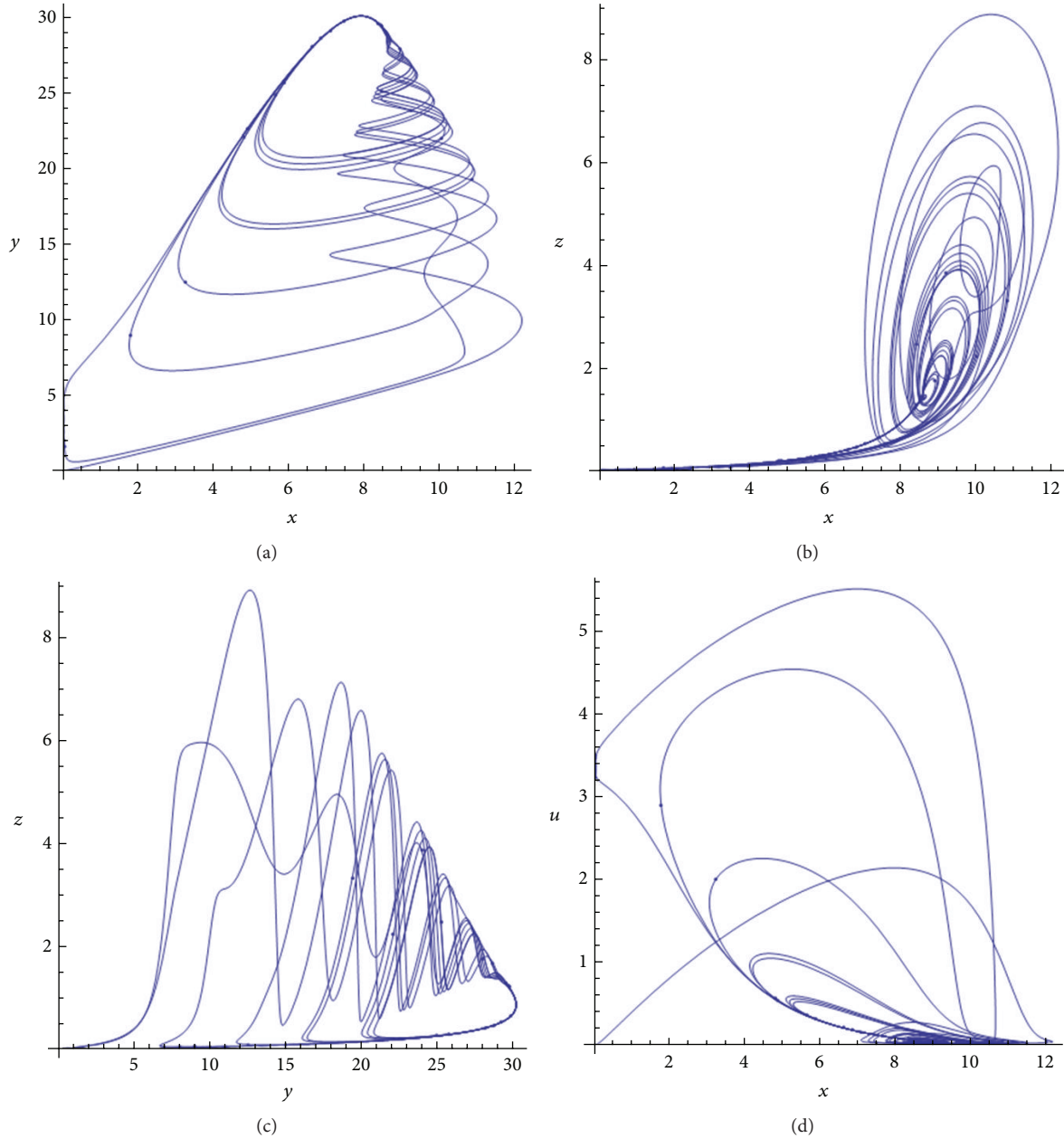


FIGURE 1: Phase space of Ca^{2+} oscillation at $q = 1$.

The fractional chaotic dynamical systems have attracted increasing attention, for example, chaos in a fractional-order Rössler system [4], chaotic dynamics of fractional-order Arneodo's systems [3], fractional Chen system [5], chaos in a fractional order modified Duffing system [6], chaos in the Newton–Leipnik system with fractional order [7], fractional order Chua's system [8], fractional-order Volta's system [9], fractional model for malaria transmission under control strategies [10] and fractional order logistic [11], and discrete chaos in fractional sine and standard maps [12].

The aim of this paper is to investigate the complex dynamics of fractional-order Ca^{2+} oscillation model purposed by Kummer et al. [21]. The model is obtained from experimental study of hepatocyte. This mathematical model is exhibiting

various dynamical behaviors, such as periodic and periodic doubling, quadrupling, and chaos. The numerical calculation of bifurcation parameters is carried out using modified trapezoidal rule for fractional integral.

2. Role of Calcium Oscillations

The biological system provided good examples of nonlinear dynamical system to study including the population of living things in ecosystem and biochemical oscillation and spread of epidemic diseases [19]. Oscillations in living thing are an important biological rhythmic [22]. These phenomena play an important role in many aspects of biological order and function, which involve many systems ranging from

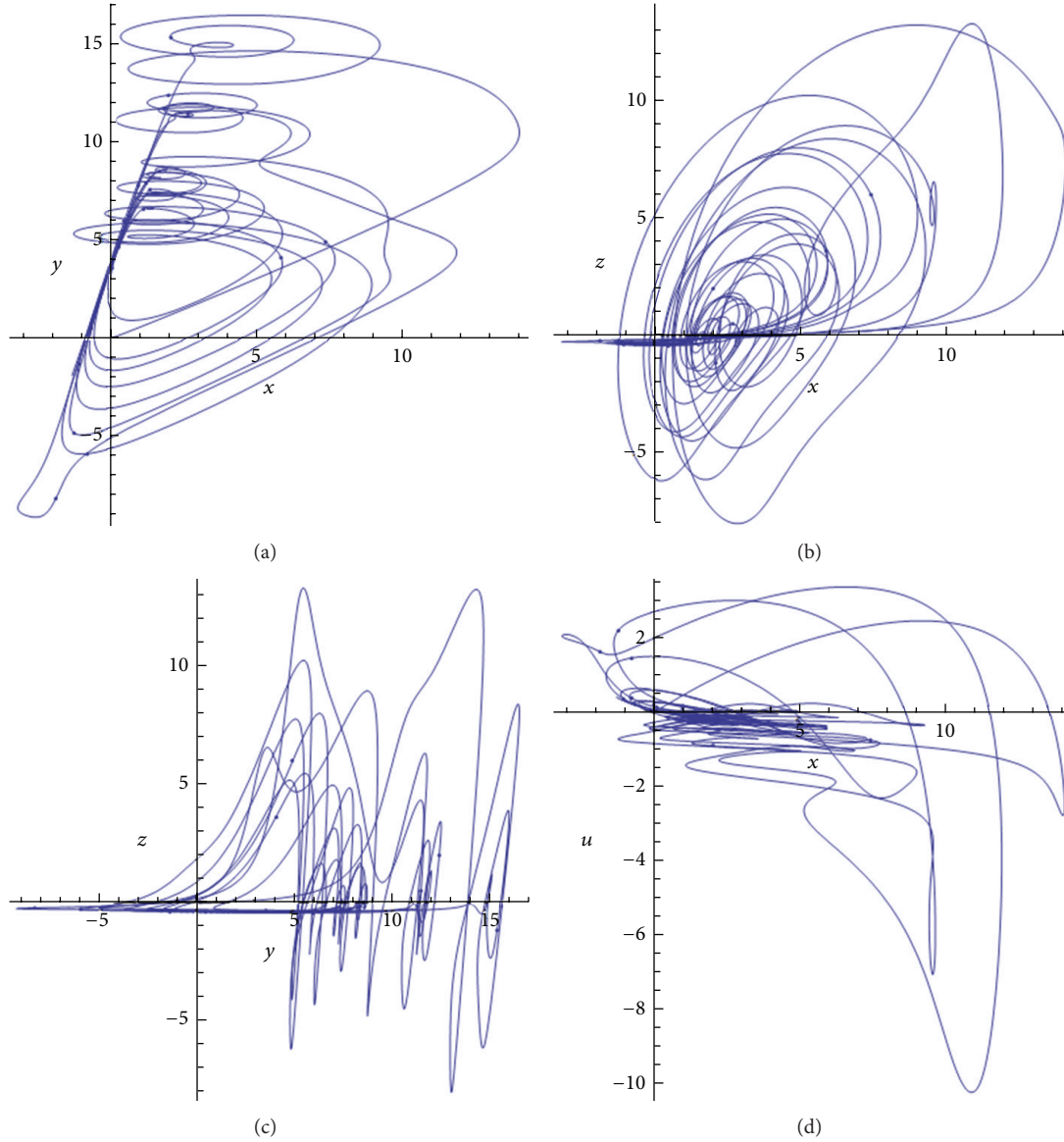


FIGURE 2: Fractional-order phase space of Ca^{2+} oscillation $q = 0.6$.

the molecular to the macroscopic scale. The rhythmic cycles may range from microsecond to hours (molecular and cellular oscillations) or days (circadian rhythms) and even months (population growth cycles) [18]. Dynamical behaviors range from sustained autonomous oscillations with periodic cycles to periodic doubling and nonperiodic cycles or chaos [22]. Calcium oscillations are important oscillations at cellular level. It has many important roles to perform many specific functions ranging from fertilization to cell death [23]. There are many mathematical models proposed to describe the oscillatory changes on cytosolic calcium concentration in intracellular [8, 9]. Many of experiments on different kinds of living cells are observed [21]. Most of the experimental data show simple periodic oscillations [24].

Woods et al. [25] discovered the calcium oscillations experimentally in 1986 and large numbers of cells show

calcium oscillations after simulation by an extracellular agonist [21]. Later, the role in calcium signaling by inositol triphosphate (IP_3) was discovered by Berridge from studies of the control fluid secretion by an insect salivary gland [26]. The signaling pathway of $\text{IP}_3/\text{Ca}^{2+}$ has been adapted to control processes as diverse as fertilization, proliferation, cell contraction, secretion, and information processing in neuronal cells [26]. Many activities of living cells are controlled by calcium from both intracellular and extracellular sources to generate signals that transduce exogenous stimulation into physiological output [23]. The important role of calcium oscillations has been confirmed by many experimental works [18, 22, 23].

The difference in Ca^{2+} oscillations frequency regulates different functions. The high frequency cytosolic Ca^{2+} oscillations regulate fast responses, such as synaptic transmission

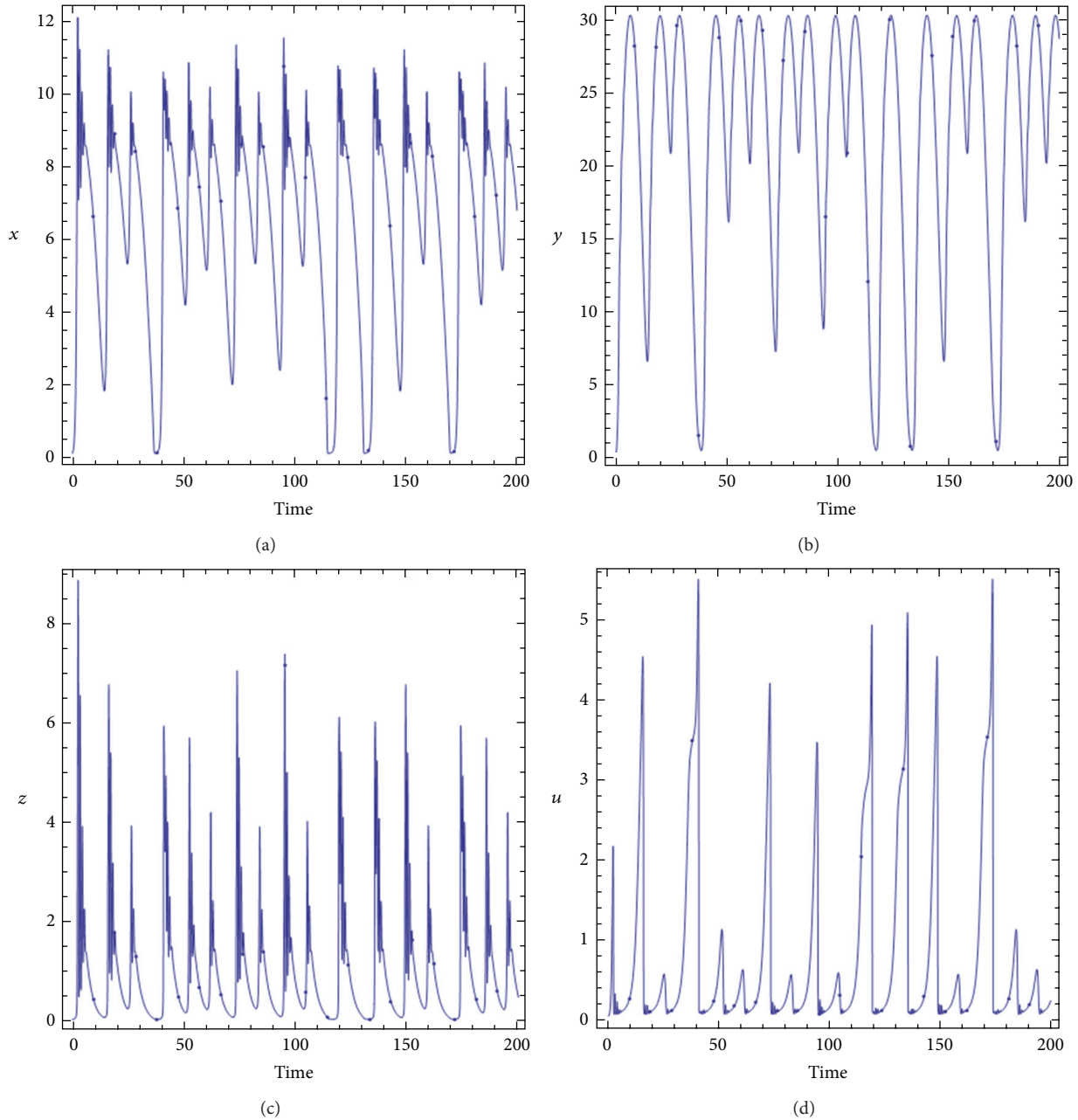


FIGURE 3: Integer-order time series with chaotic parameters.

and secretion, whereas low frequency oscillations regulate slow processes, such as fertilization and gene transcription [27]. Ca^{2+} oscillations have essential role in intracellular signaling [21]. The oscillating signal can have different frequency and amplitude depending upon the encoding of specific message that triggers the functions [28]. There are many mathematical models proposed to describe the mechanism of calcium oscillations but most of them present only simple periodic oscillations which are characterized by a single frequency [10].

There exist non-periodic complex bursting types of calcium oscillations found in some experimental study [21]. The models were proposed; that is, Borghans et al. [24] proposed

calcium-induced calcium release (CICR) based on model focusing on the effect of cytosolic calcium on the degradation of inositol triphosphate. Shen and Larter [29] proposed theoretical study of complex calcium oscillations model based on both the calcium-induced calcium release (CICR) and the inositol triphosphate (IP_3) cross-coupling (ICC). The model has demonstrated regular bursting and a transition to chaos which involves differential equations for cytosolic Ca^{2+} , endoplasmic Ca^{2+} , and IP_3 . Dupont and Goldbeter [30] have developed some mathematical models; one of them is related to the activation and autophosphorylation of the multifunctional Ca^{2+} -calmodulin-dependent protein kinase II (CaMKII) by Ca^{2+} and calmodulin (CaM) which is able

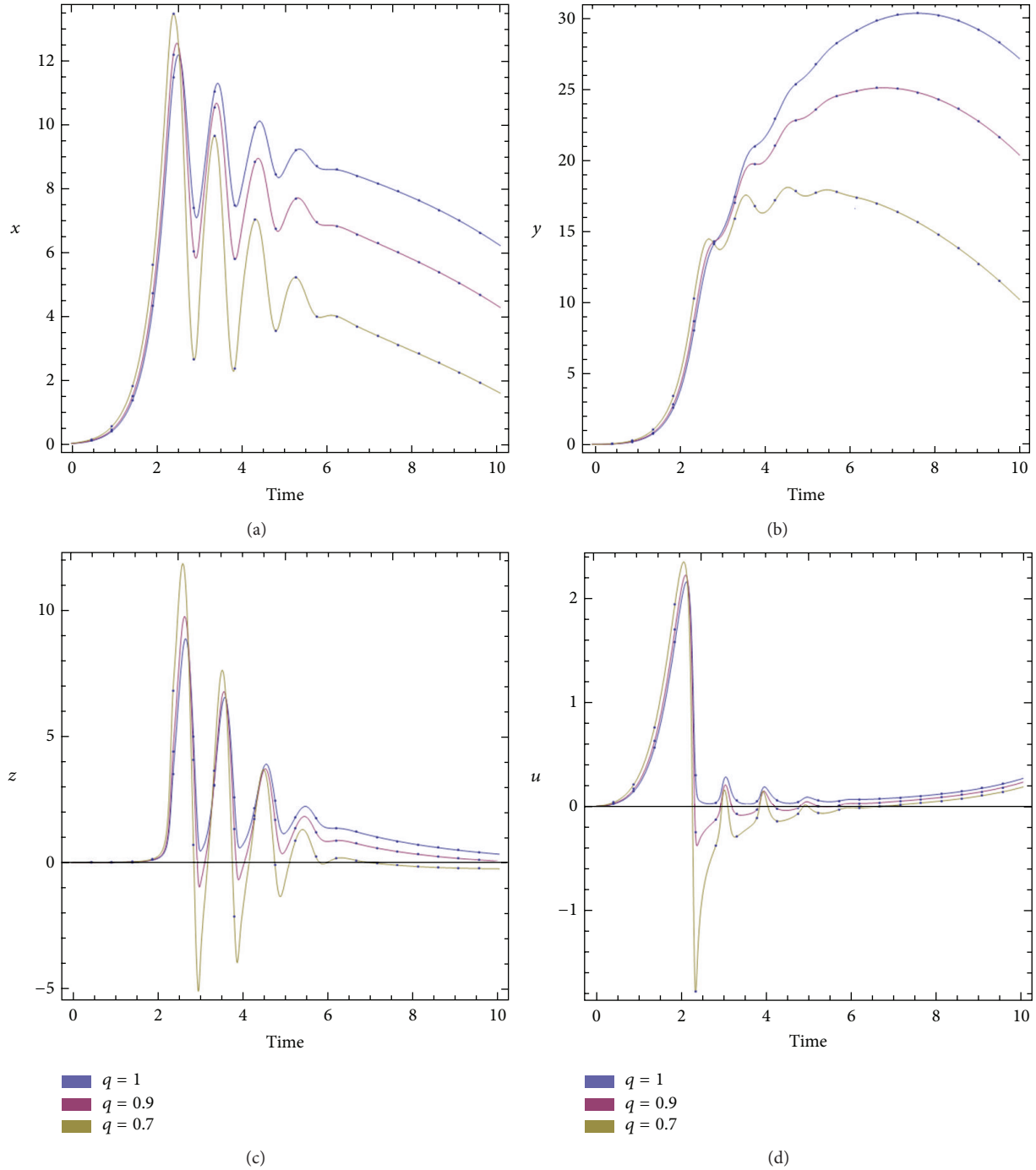


FIGURE 4: Fractional-order time series with chaotic parameters.

through underlying its ability to decode Ca^{2+} oscillations and to control multiple cellular functions.

Meyer and Stryer [31] proposed the inositol trisphosphate- (IP_3 -) Ca^{2+} cross coupling model (ICC) in which the cooperative release of Ca^{2+} from an IP_3 -sensitive store results in positive feedback by Ca^{2+} on phospholipase C (PLC). Borghans et al. [24] proposed the calcium-induced calcium release (CICR) mechanism based on the processes originally described in skeletal triggered by calcium itself via a positive

feedback loop. de Young and Keizer IP_3 R model [32] has one IP_3 and two Ca^{2+} binding sites on the cytosolic side. Kummer et al. [21] proposed calcium oscillation in hepatocytes on the basis of qualitative experimental results. This mathematical model consists of the four variables as follows: cytosolic Ca^{2+} , endoplasmic Ca^{2+} , concentrations of active subunits of a G protein, and active PLC [21]. The model shows good agreement with experimental observations in two respects. First, each oscillation period starts with a large, steep spike

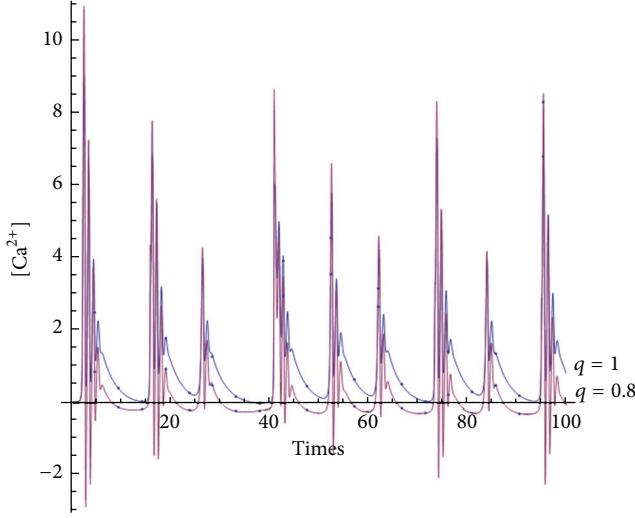


FIGURE 5: Fractional-order time series of Ca^{2+} oscillations.

followed by a number of pulses of decreasing amplitude around an elevated mean value. Second, varying the model parameters, one finds that the difference in stimulation nature can induce (periodic or aperiodic) bursting or regular oscillations [33].

Calcium has many roles for controlling numerous cellular functions. Intracellular signaling pathways are often regulated by the Ca^{2+} and cAMP [19]. Many physiological processes such as egg fertilization, short-term memory, neurotransmission, and gene transduction and triggering cell to death are controlled by Ca^{2+} oscillation [28]. The Ca^{2+} oscillation can be explained by change in cytosolic Ca^{2+} concentration.

A comprehensive review of the calcium modeling is provided by Schuster et al. [34]. Calcium has important role in information processing. It has functions as messengers. Proteins within the cell have the capacity to decode the information from the Ca^{2+} signals to perform different functions [19].

3. Fractional Calculus

Fractional calculus is the theory of differential and integral operator of non-integer order. This old mathematical topic has origin date back to the day that Leibnitz replies to L'Hospital about the meaning of half order derivative [35]. Theory is not known to scientists and engineers much until the last few decades. The theory has been applied to model many physical processes successfully with fractional differential equations including theory of viscoelasticity, heat diffusion, and nonlinear dynamics. The comprehensive discussions of this theory are presented by Oldham and Spanier [35], Miller and Ross [36], and Podlubny [37]. There are many approaches for solving the fractional-order differential equation (FDE) including series expansion, numerical approximation, Laplace transform [38], Adomian decomposition [39], predictor corrector scheme [40], Galerkin approximation [41], and Adam Moulton algorithm [42].

The applications of fractional calculus in physics are better in describing the diffusion phenomena in inhomogeneous media with non-integer derivative [37], modeling of ultracapacitors [43], the fractional derivatives model of viscoelastic material [44], thermal modeling and temperature estimation of a transistor junction [45], fractional-order impedance in electric circuit [37], dynamical process of heat conduction, and chaotic dynamical system [4–17].

In classical calculus, the meaning of integer-order derivative is the rate of change, direction of decline, or slope in the geometric interpretation. The meaning of fractional-order derivative is different. It has no obvious geometric meaning or physical interpretation [37]. Recently, Podlubny has proposed a new physical interpretation based on general convolution integrals of the Volterra type [46]. Tenreiro Machado gives a geometric and probabilistic interpretation based on Grunwald-Letnikov definition of the fractional derivative [47]. Du et al. explain physical meaning of the fractional order which is an index of memory [48]. Sabatier et al. impose physically coherent initial conditions to a fractional system [42]. Recently, this mathematical theory gains more attention in biological science, that is, low frequency constant-phase behavior in the respiratory impedance [49], front dynamics in fractional-order epidemic models [15], fractional derivatives in Dengue epidemics [14], and dynamical characteristics of the fractional-order FitzHugh-Nagumo model neuron [13].

The advantage of fractional derivatives in comparison with classical integer-order calculus is description of memory properties. In the last few decades many authors show that derivatives and integral of noninteger order are very suitable for describing properties of various real materials, for example, polymers; Bagley and Torvik show that the fractional-order models are more adequate than integer-order models [44].

4. Definition

Definition 1. The Riemann-Liouville fractional integral of order $q > 0$ of a function $f : \mathbb{R}^+ \rightarrow \mathbb{R}$ is given by

$$I^q f(x) = \frac{1}{\Gamma(q)} \int_0^x (x-t)^{q-1} f(t) dt \quad (1)$$

provided the right side is pointwise defined on \mathbb{R}^+ [37].

Where $\Gamma(\cdot)$ is Gamma function define by

$$\Gamma(x) = \int_0^\infty e^{-u} u^{x-1} du. \quad (2)$$

Definition 2. The Caputo fractional derivative of order $q \in (n-1, n)$ of a continuous function $f : \mathbb{R}^+ \rightarrow \mathbb{R}$ is given by [37]

$$D^q f(x) = I^{n-q} D^n f(x), \quad D = \frac{d}{dt}. \quad (3)$$

Definition 3. Grunwald-Letnikov definition for fractional derivative of order q is given by [37]

$${}_a D_t^q f(t) = \lim_{h \rightarrow 0} \frac{1}{h^q} \sum_{j=0}^{[t-a/h]} (-1)^j \binom{q}{j} f(t-jh), \quad (4)$$

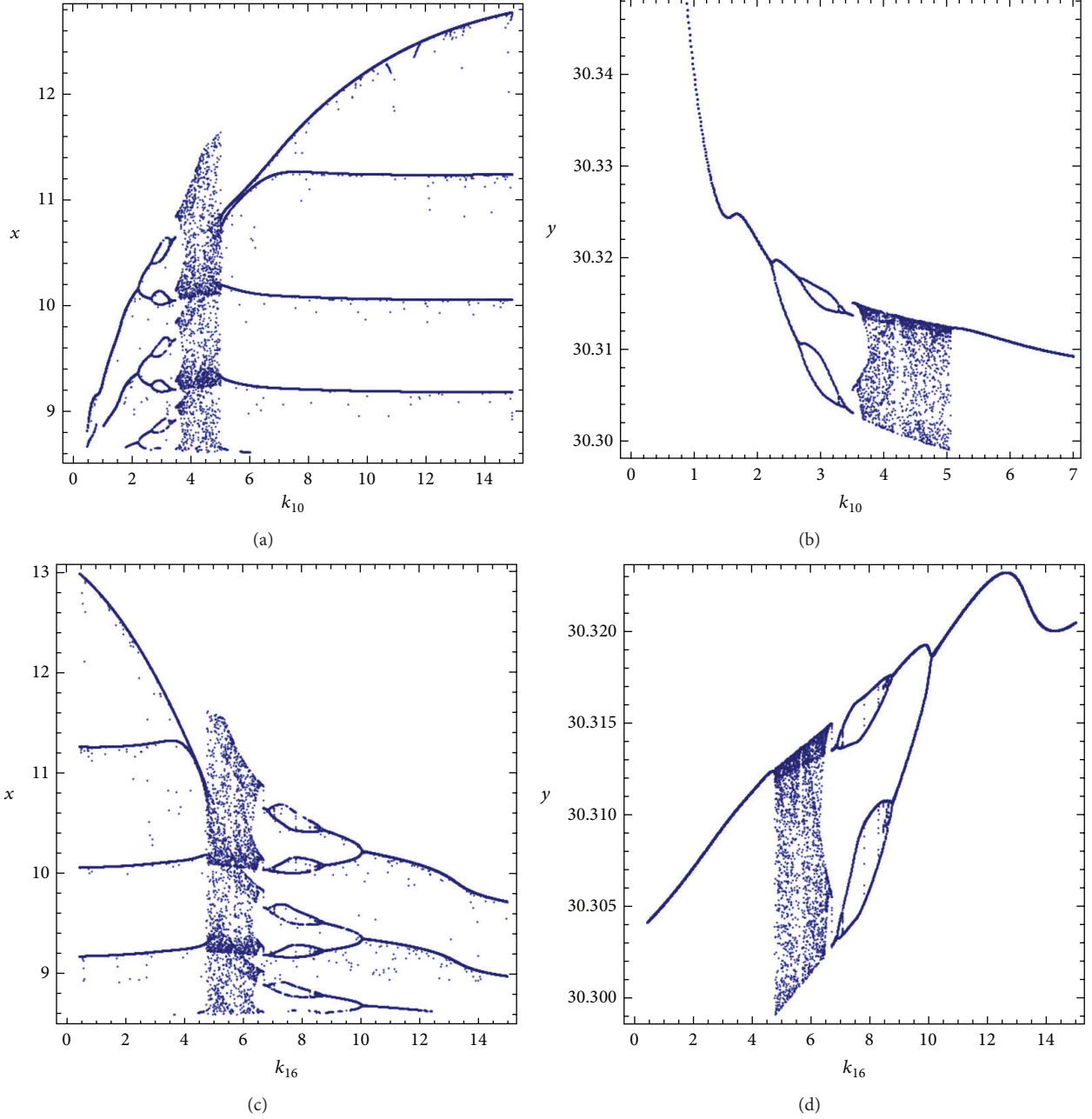


FIGURE 6: The bifurcation diagram of Ca^{2+} oscillations model with different control parameters.

where

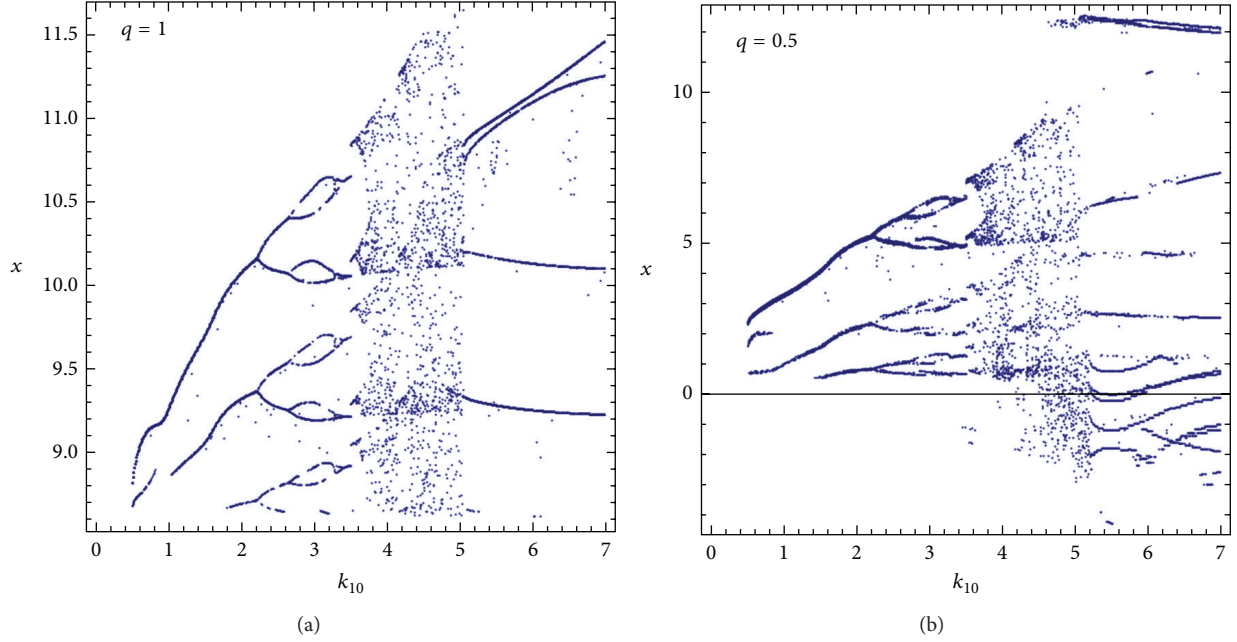
$$\begin{aligned} \binom{n}{r} &= \frac{n!}{r!(n-r)!} = \frac{n(n-1)(n-2)\cdots(n-r+1)}{r!} \\ &= \frac{\Gamma(n+1)}{\Gamma(r+1)\Gamma(n-r+1)}. \end{aligned} \quad (5)$$

There are many definitions in fractional calculus. Two mostly used definitions are Riemann-Liouville and Grunwald-Letnikov. The Riemann-Liouville definition for the fractional integral and derivative is used for solving the analytical

solution while the Grunwald-Letnikov definition is more appropriate in numerical calculation [35–37].

5. Mathematical Model

The model proposed by Kummer et al. [21] focuses on the feedback inhibition on the initial agonist receptor complex by Ca^{2+} and activated phospholipase C (PLC) and receptor type-dependent self-enhanced behavior of the activated G_α subunit. So the four main variables are the free Ca^{2+} concentration in the cytosol (Ca_{cyt}), the concentration of the active

FIGURE 7: Fractional-order bifurcation of Ca^{2+} oscillation model.

G_α subunit, the concentration of active PLC (PLC), and the concentration of Ca^{2+} in endoplasmic reticulum.

Kummer et al. [21] assume that IP_3 is in a quasi-stationary state where the concentration of inositol triphosphate (IP_3) follows the dynamics of active PLC. The model can be described by the four differential equations as follows:

$$\begin{aligned} x' &= k_1 + k_2x - k_3 \frac{xy}{x + k_4} - k_5 \frac{xz}{x + k_6}, \\ y' &= k_7x - k_8 \frac{y}{y + k_9}, \\ z' &= k_{10}yz \frac{u}{u + k_{11}} + k_{12}y + k_{13}x - k_{14} \frac{z}{z + k_{15}} - k_{16} \frac{z}{z + k_{17}}, \\ u' &= -k_{10}yz \frac{u}{u + k_{11}} + k_{16} \frac{z}{z + k_{17}}, \end{aligned} \quad (6)$$

where

x is the change in the concentration of the active G_α subunit;

y is the concentration of active phospholipase C (PLC);

z is the concentration of free calcium in the cytosol (Ca_{cyt});

u is the concentration of calcium in the intracellular stores such as endoplasmic reticulum (ER) and k_1 to k_{17} are constant values.

We have used the same initial values as Kummer et al. [21] as follows:

$$\begin{aligned} k_1 &= 0.09, \quad k_2 = 2.7738, \quad k_3 = 0.64, \\ k_4 &= 0.19, \quad k_5 = 4.88, \quad k_6 = 1.18, \\ k_7 &= 2.08, \quad k_8 = 32.24, \\ k_9 &= 29.09, \quad k_{10} = 5.0, \quad k_{11} = 2.67, \quad k_{12} = 0.7, \\ k_{13} &= 13.58, \quad k_{14} = 153, \quad k_{15} = 0.16, \\ k_{16} &= 4.85, \quad k_{17} = 0.05. \end{aligned} \quad (7)$$

6. Fractional-Order Model

We consider the commensurate order where the orders are all equal. The fractional-order calcium oscillation model is simply represented by replacing the integer derivative with fractional-order derivative as follows:

$$\begin{aligned} D^q x &= k_1 + k_2x - k_3 \frac{xy}{x + k_4} - k_5 \frac{xz}{x + k_6}, \\ D^q y &= k_7x - k_8 \frac{y}{y + k_9}, \\ D^q z &= k_{10}yz \frac{u}{u + k_{11}} + k_{12}y + k_{13}x \\ &\quad - k_{14} \frac{z}{z + k_{15}} - k_{16} \frac{z}{z + k_{17}}, \\ D^q u &= -k_{10}yz \frac{u}{u + k_{11}} + k_{16} \frac{z}{z + k_{17}}, \end{aligned} \quad (8)$$

where q is commensurate fractional order.

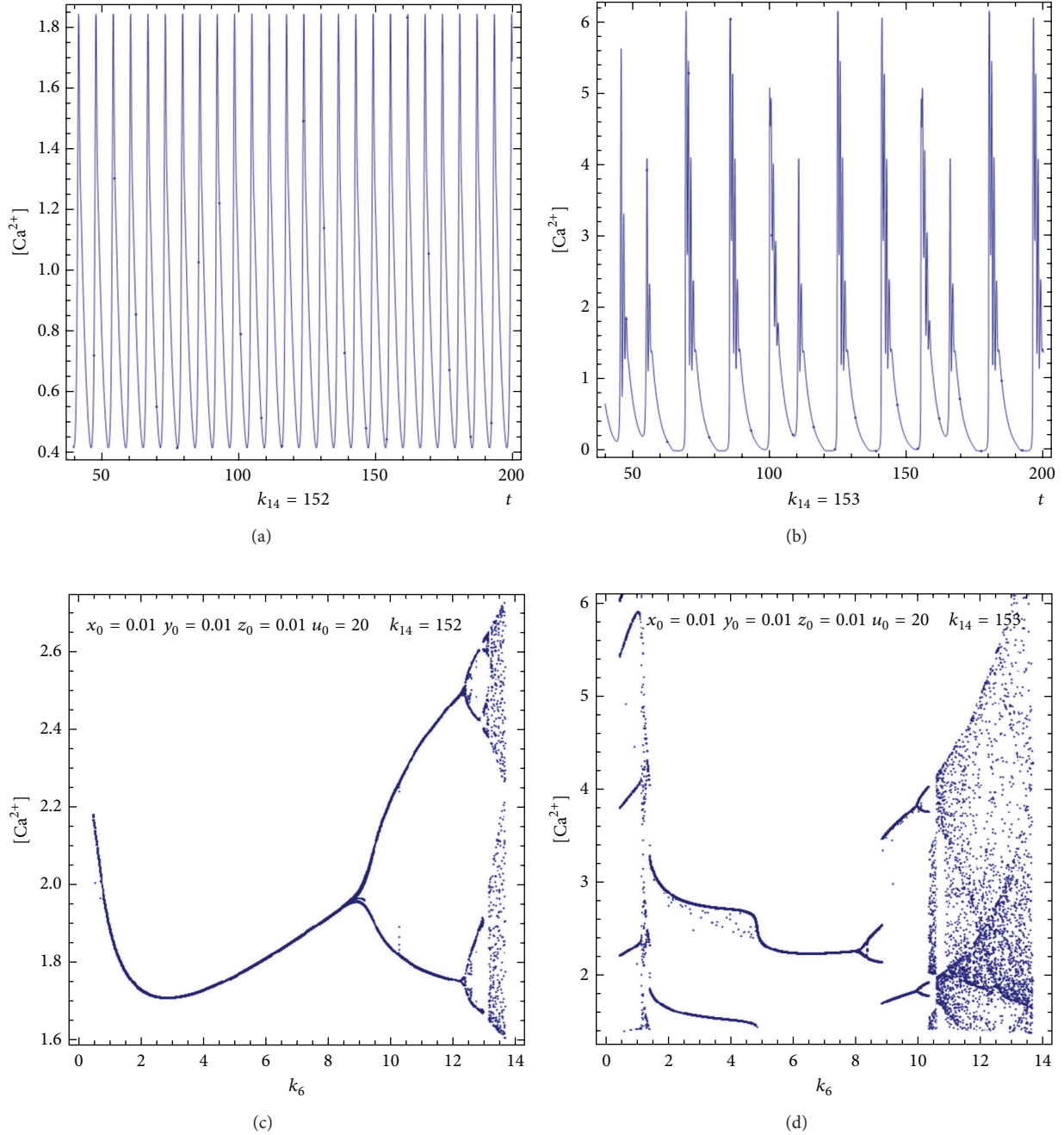


FIGURE 8: Spikes change in Ca^{2+} concentration for different k_{14} and bifurcation diagram of Ca^{2+} concentration and k_6 .

7. Numerical Method

There are many approaches in fractional-order numerical calculation. There are two main approaches for numerical calculation: the frequency domain and time domain. The study of Tavazoei and Haeri shows that the frequency domain approach can lead to the fake chaotic results [38]. The numerical method that we utilize in this paper is time domain approach of the modified trapezoidal rule proposed by Odibat and Momani [50]. This method is a simple calculation

scheme that is derived from the area of trapezoidal shape.

Consider $y = f(x)$ over $[a, b]$ and suppose that the interval $[a, b]$ is subdivided into m subintervals $\{[x_{k-1}, x_k]\}_{k=1}^m$ of equal width $h = (b - a)/m$ by using the equally spaced nodes $x_k = x_0 + kh$ for $k = 1, 2, \dots, m$.

The composite trapezoidal rule for m subinterval is

$$T(f, h) = \frac{h}{2} (f(a) + f(b)) + h \sum_{k=1}^m f(x_k). \quad (9)$$

The formula can extend to use with fractional-order differential as follows [50]:

$$T(f, h, q) = \left((k-1)^{q+1} - (k-q-1)k^q \right) \frac{h^q f(0)}{\Gamma(q+2)} + \sum_{j=1}^{k-1} \left((k-j+1)^{q+1} - 2(k-j)^{q+1} + (k-j-1)^{q+1} \right) \times \frac{h^q f(x_j)}{\Gamma(q+2)}. \quad (10)$$

The formula in (10) is used for approximating the integral function of arbitrary order. According to the classical theory of ordinary differential equations, to produce a unique solution for the problem, we need to specify initial conditions [50].

The equation is an approximation to fractional integral at order q

$$(I^q f(x)(a)) = T(f, h, q) - E(f, h, q), \quad (11)$$

where $a > 0$ and $q > 0$.

Odiat and Momani [50] show that the error is function of parameter h

$$|E(f, h, q)| = O(h^2). \quad (12)$$

It is obvious that if the order $q = 1$, then the modified trapezoidal rule reduces to the classical trapezoidal rule

$$\lim_{q \rightarrow 1} D^q f(x) = \frac{df(x)}{dx}. \quad (13)$$

8. Stability at Fractional Order

In this section, we discuss the stability condition for fractional-order systems and a necessary condition for chaos to exist. Consider the following fractional differential equation [6]:

$$D^q x_i = f_i(x_1, x_2, x_3), \quad i = 1, 2, 3. \quad (14)$$

The equilibrium points x_i^{eq} of the fractional-order differential system can be obtained by solving the following equation:

$$D^q x_i = 0, \quad (15)$$

and δ_i a small deviation can be obtained from the following equilibrium:

$$f_i(x_1^{\text{eq}} + \delta_1(t), x_2^{\text{eq}} + \delta_2(t), x_3^{\text{eq}} + \delta_3(t)) = f_i(x_1^{\text{eq}}, x_2^{\text{eq}}, x_3^{\text{eq}}) + \left. \frac{\partial f_1}{\partial x_1} \right|_{\text{eq}} \delta_1 + \left. \frac{\partial f_1}{\partial x_2} \right|_{\text{eq}} \delta_2 + \left. \frac{\partial f_1}{\partial x_3} \right|_{\text{eq}} \delta_3, \quad (16)$$

and then

$$D^q(\delta_i) \cong + \left. \frac{\partial f_1}{\partial x_1} \right|_{\text{eq}} \delta_1 + \left. \frac{\partial f_1}{\partial x_2} \right|_{\text{eq}} \delta_2 + \left. \frac{\partial f_1}{\partial x_3} \right|_{\text{eq}} \delta_3, \quad (17)$$

Therefore, we will have a linear system

$$D^q(\delta_i) = A\delta, \quad (18)$$

where

$$A = \begin{bmatrix} \frac{\partial f_1}{\partial x_1} & \frac{\partial f_1}{\partial x_2} & \frac{\partial f_1}{\partial x_3} \\ \frac{\partial f_2}{\partial x_1} & \frac{\partial f_2}{\partial x_2} & \frac{\partial f_2}{\partial x_3} \\ \frac{\partial f_3}{\partial x_1} & \frac{\partial f_3}{\partial x_2} & \frac{\partial f_3}{\partial x_3} \end{bmatrix}. \quad (19)$$

The following autonomous system:

$$D^q x = Ax, \quad x(0) = x_0, \quad (20)$$

where $0 < q < 1$, $x \in R^n$, and $A \in R^{n \times n}$, is asymptotically stable if and only if $|\arg(\lambda_i(A))| > q\pi/2$. In this case, each component of the states decays towards 0 like t^{-q} . Also; this system is stable if and only if $|\arg(\lambda_i(A))| \geq q\pi/2$ and those critical eigenvalues that satisfy $|\arg(\lambda_i(A))| = q\pi/2$ have geometric multiplicity one [17].

9. Commensurate Fractional Order

Consider that the commensurate fractional-order system with the order is all equal to q . In this case, a system shows regular behavior if it satisfies [51]

$$q < \frac{2}{\pi} \min_i |\arg(\lambda_i)|. \quad (21)$$

The equilibrium points of the system at the given parameters set are as follows:

$$\begin{aligned} E_1 & (10.0544, 53.7091, -1.3183, -0.0374864), \\ E_2 & (-1.24025, -2.15522, -0.0171356, -2.4883), \\ E_3 & (-0.352276, -0.64645, -0.00529478, -2.59275), \\ E_4 & (-0.0299949, -0.0561849, -0.000465736, -2.66236), \\ E_5 & (7.81412, 29.5754, 0.775014, 0.110537), \\ E_6 & (19.1242, -153.502, 32.7238, -0.000514706). \end{aligned} \quad (22)$$

From the initial condition in [10],

$$\begin{aligned} k_1 &= 0.09, & k_2 &= 2.7738, & k_3 &= 0.64, & k_4 &= 0.19, \\ k_5 &= 4.88, & k_6 &= 1.18, & k_7 &= 2.08, & k_8 &= 32.24, \\ k_9 &= 29.09, & k_{10} &= 5.0, & k_{11} &= 2.67, & k_{12} &= 0.7, \\ k_{13} &= 13.58, & k_{14} &= 153, \\ k_{15} &= 0.16, & k_{16} &= 4.85, & k_{17} &= 0.05. \end{aligned} \quad (23)$$

The Jacobian determinant is

$$J = \begin{vmatrix} k_2 - \frac{k_3 k_4 (k_6 + x)^2 y + k_5 k_6 (k_4 + x)^2 z}{(k_4 + x)^2 (k_6 + x)^2} & -\frac{k_3 x}{k + x} & -\frac{k_5 x}{k_6 + x} & -\frac{k_5 x}{k_6 + x} \\ k_7 & -\frac{k_8 k_9}{(k_9 + y)^2} & 0 & 0 \\ k_{13} & k_{12} + \frac{k_{10} u z}{k_{11} + u} & \frac{k_{10} u z}{k_{11} + u} - \frac{k_{14} k_{15}}{(k_{15} + z)^2} - \frac{k_{16} k_{17}}{(k_{17} + z)^2} & \frac{k_{10} u y}{k_{11} + u} - \frac{k_{14} k_{15}}{(k_{15} + z)^2} - \frac{k_{16} k_{17}}{(k_{17} + z)^2} \\ 0 & \frac{k_{10} u z}{k_{11} + u} & -\frac{k_{10} u y}{k_{11} + u} + \frac{k_{16} k_{17}}{(k_{17} + z)^2} & -\frac{k_{10} u y}{k_{11} + u} + \frac{k_{16} k_{17}}{(k_{17} + z)^2} \end{vmatrix}. \quad (24)$$

The characteristic equation is

$$\begin{aligned} \lambda^4 + 15.6113\lambda^3 + 12.1598\lambda^2 + 31.393\lambda - 4.07004 \times 10^{-16} \\ \text{Arg}(\lambda_1) = \pi, \quad \text{Arg}(\lambda_2) = -1.80517, \\ \text{Arg}(\lambda_3) = 1.80517, \quad \text{Arg}(\lambda_4) = 0. \end{aligned} \quad (25)$$

From (21) system shows regular behavior if it satisfies $q < 1.14921$.

We have calculated the values of each argument that correspond to the equilibrium point's results in either 0 or π which means that all equilibrium points are unstable.

10. Fractional-Order Phase Space

The constructing fractional-order phase space can assist in understanding the fractional change in dynamical system. Chaotic behavior of the calcium oscillation in liver cell can be viewed in phase space of the calcium concentration and other system variables. The geometric meaning of the single closed loop of phase space represents the periodic system, two closed loops of phase space represent the periodic doubling, and so on [49]. For chaotic system, the phase space appears as a multiple loop. According to the given values of the constants chaotic parameters k_1 to k_{17} , the phase spaces of Kummer model are presented in Figures 1 and 2, respectively.

11. Fractional-Order Time Series

Nonlinear dynamics are time dependent system. The change from periodic behavior to periodic doubling and then route to chaos can be analyzed from the time series. Time series represent are sequence of points which describe the behavior of dynamical system. The calcium oscillation model is characterized by four different variables: the change in the concentration of the active G_α subunit (x), the concentration of active phospholipase C (PLC) (y), concentration of free calcium in the cytosol (Ca_{cyt}) (z), and concentration of calcium in the intracellular stores (u). The integer-order time series of the Ca^{2+} model are shown in Figure 3 and

the numerical results of fractional-order time series obtained by numerical integration of the modified trapezoidal rule are shown in Figures 4 and 5, respectively. The complexities at fractional-order are present as the bursting of the Ca^{2+} signal.

12. Fractional-Order Bifurcation Diagram

Generally, the bifurcation diagram represents the behavior of dynamical system when varying certain parameter values. Single lines represent the stable periodic system, while branching represents the periodic doubling or quadrupling or higher. The band of dots represents the chaotic region. The integer-order bifurcation diagram of the model for parameter k_{10} and k_{16} is presented in Figure 6. The comparison between integer-order bifurcation diagram and fractional order bifurcation of the parameter k_{10} is presented in Figure 7. The numerical result shows the existence of chaos at fractional order for the same control parameter and initial condition. The two diagrams look resemble but slightly different in scales.

13. Numerical Results

The model proposed by Kummer et al. [10] show that there exists chaotic behavior at the given parameters. We have examined further different ranges with fractional calculus for the parameters that show periodic doubling and route to chaos. The corresponding bursting fractional-order time series are also present. The numerical integration at fractional order is accomplished by applying the modified trapezoidal rule to the fractional differential equation. The numerical errors are related to the time step of numerical integration. To reduce the numerical errors, the time step is set to $h = 3000$.

The numerical results with fractional order are provided by huge variations in the number of solutions. This would be able to fit to the experimental data. According to the literature, the functions of calcium are in numerous areas ranging from fertilization and muscle movement. The variation in solutions outcome would be feasible to describe certain functions caused from the oscillations.

We have chosen the order $q = 0.8$ to examine the fractional-order time series of the Ca^{2+} concentration as presented in Figure 5. The constant values are as follows:

$$\begin{aligned} k_1 &= 0.09, & k_2 &= 2.7738, & k_3 &= 0.64, & k_4 &= 0.19, \\ k_5 &= 4.88, & k_6 &= 1.18, & k_7 &= 2.08, & k_8 &= 32.24, \\ k_9 &= 29.09, & k_{10} &= 5.0, & k_{11} &= 2.67, & & \\ k_{12} &= 0.7, & k_{13} &= 13.58, & k_{14} &= 153, & & \\ k_{15} &= 0.16, & k_{16} &= 4.85, & k_{17} &= 0.05. & & \end{aligned} \quad (26)$$

The initial values are $x_0 = 0.01$, $y_0 = 0.01$, $z_0 = 0.01$, and $u_0 = 20$.

The bifurcation diagrams are obtained by varying certain control parameter and take the highest values from iteration. The constant values in the model that show the periodic doubling and route to chaos are k_6 , k_{10} , k_{11} , and k_{16} .

We choose the parameter k_{10} to study the fractional-order bifurcation in Figure 7. The integer-order shows that there exist period-3 ($k_{10} < 2.2$), period-6 ($2.2 < k_{10} < 2.6$), and period-10 ($2.6 < k_{10} < 3.4$) and then route to chaos ($3.6 < k_{10} < 5$). The fractional-order bifurcation diagram is slightly different and there still exists the chaotic region at different scale.

14. Discussion and Conclusions

We have shown that cytosolic Ca^{2+} oscillations can change the concentration very rapidly when the constant variable k_{14} changes from 152 to 153 as present with time series and bifurcation diagram in Figure 8. There are many mathematical models proposed to explain the calcium oscillations. Kummer's model of calcium oscillations in hepatocytes is able to display simple oscillatory and chaotic bursting. The slight change in certain variable can cause the abruptly change in Ca^{2+} concentration.

The Poincare-Bendixson theorem states that continuous dynamical systems cannot exhibit chaotic attractor if dimension is less than three. We have presented the example of biological model of Ca^{2+} oscillation that exhibits chaotic behavior at order less than three. In this paper, we have applied the theory of fractional calculus to study chaotic property in mathematical model of calcium oscillation proposed by Kummer et al. There exists the irregularity behavior in the model. The complex behaviors are exhibited as bursting during the oscillation. The fractional-order time series of bursting signal are present. The bifurcation diagrams show that there exists chaos with the order less than three. In conclusion, the numerical results are able to yield insight into an intermediate change in fractional order numerical integration. The variation of the solutions by fractional order integration would be feasible to describe certain functions of the Ca^{2+} oscillations when compared with the experimental data.

Conflict of Interests

The authors declare that there is no conflict of interests regarding the publication of this paper.

References

- [1] E. N. Lorenz, "Deterministic non-periodic flow," *Journal of the Atmospheric Sciences*, vol. 20, pp. 130–141, 1963.
- [2] S. H. Strogatz, *Nonlinear Dynamics and Chaos*, Westview, 2000.
- [3] J. G. Lu, "Chaotic dynamics and synchronization of fractional-order Arneodo's systems," *Chaos, Solitons and Fractals*, vol. 26, no. 4, pp. 1125–1133, 2005.
- [4] W. Zhang, S. Zhou, H. Li, and H. Zhu, "Chaos in a fractional order Rössler system," *Chaos, Solitons and Fractals*, vol. 42, no. 3, pp. 1684–1691, 2009.
- [5] J. G. Lu and G. Chen, "A note on the fractional-order Chen system," *Chaos, Solitons and Fractals*, vol. 27, no. 3, pp. 685–688, 2006.
- [6] Z.-M. Ge and C.-Y. Ou, "Chaos in a fractional order modified Duffing system," *Chaos, Solitons and Fractals*, vol. 34, no. 2, pp. 262–291, 2007.
- [7] X. Wang and L. Tian, "Bifurcation analysis and linear control of the Newton-Leipnik system," *Chaos, Solitons and Fractals*, vol. 27, no. 1, pp. 31–38, 2006.
- [8] I. Petráš, "A note on the fractional-order Chua's system," *Chaos, Solitons and Fractals*, vol. 38, no. 1, pp. 140–147, 2008.
- [9] I. Petráš, "A note on the fractional-order Volta's system," *Communications in Nonlinear Science and Numerical Simulation*, vol. 15, no. 2, pp. 384–393, 2010.
- [10] C. M. A. Pinto and J. A. T. Machado, "Fractional model for malaria transmission under control strategies," *Computers & Mathematics with Applications*, vol. 66, no. 5, pp. 908–916, 2013.
- [11] Y. Suansook and K. Paithoonwattanakij, "Dynamic of logistic model at fractional order," in *Proceeding of the International Symposium on Industrial Electronics (IEEE ISIE '09)*, pp. 718–723, Seoul, Republic Korea, July 2009.
- [12] G.-C. Wu, D. Baleanu, and S.-D. Zeng, "Discrete chaos in fractional sine and standard maps," *Physics Letters A*, vol. 378, no. 5–6, pp. 484–487, 2014.
- [13] Y. Liu, Y. Xie, Y. Kang et al., "Dynamical characteristics of the fractional-order fitzHugh-Nagumo model neuron," in *Advances in Cognitive Neurodynamics (II)*, pp. 253–258, 2011.
- [14] S. Poosheh, H. S. Rodrigues, and D. F. M. Torres, "Fractional derivatives in dengue epidemics," in *Proceedings of the International Conference on Numerical Analysis and Applied Mathematics (ICNAAM '11)*, vol. 1389, pp. 739–742, September 2011.
- [15] E. Hanert, E. Schumacher, and E. Deleersnijder, "Front dynamics in fractional-order epidemic models," *Journal of Theoretical Biology*, vol. 279, pp. 9–16, 2011.
- [16] V. Daftardar-Gejji and S. Bhalekar, "Chaos in fractional ordered Liu system," *Computers and Mathematics with Applications*, pp. 1117–1127, 2010.
- [17] I. Petráš, "Method for simulation of the fractional order chaotic system," *Acta Montanistica Slovaca*, vol. 11, pp. 273–277, 2006.
- [18] A. Goldbeter, *Biochemical Oscillations and Cellular Rhythms: The Molecular Bases of Periodic and Chaotic Behavior*, Cambridge University Press, 1996.

- [19] M. Falcke and D. Malchow, *Understanding Calcium Dynamics: Experiments and Theory*, vol. 623 of *Lecture Notes in Physics*, 2003.
- [20] M. J. Berridge, "Calcium oscillations," *The Journal of Biological Chemistry*, vol. 265, no. 17, pp. 9583–9586, 1990.
- [21] U. Kummer, L. F. Olsen, C. J. Dixon, A. K. Green, E. Bornberg-Bauer, and G. Baier, "Switching from simple to complex oscillations in calcium signaling," *Biophysical Journal*, vol. 79, no. 3, pp. 1188–1195, 2000.
- [22] A. Goldbeter, "Computational approaches to cellular rhythms," *Nature*, vol. 420, no. 6912, pp. 238–245, 2002.
- [23] M. D. Bootman, M. J. Berridge, and H. L. Roderick, "Calcium signalling: more messengers, more channels, more complexity," *Current Biology*, vol. 12, no. 16, pp. R563–R565, 2002.
- [24] J. A. M. Borghans, G. Dupont, and A. Goldbeter, "Complex intracellular calcium oscillations. A theoretical exploration of possible mechanisms," *Biophysical Chemistry*, vol. 66, no. 1, pp. 25–41, 1997.
- [25] N. M. Woods, K. S. R. Kuthbertson, and P. H. Cobbold, "Agonist-induced oscillations in hepatocytes," *Cells Calcium*, vol. 8, pp. 79–100, 1987.
- [26] M. J. Berridge, "Unlocking the secrets of cell signaling," *Annual Review of Physiology*, vol. 67, pp. 1–21, 2005.
- [27] P. Uhlén and N. Fritz, "Biochemistry of calcium oscillations," *Biochemical and Biophysical Research Communications*, vol. 396, no. 1, pp. 28–32, 2010.
- [28] M. Perc and M. Marhl, "Sensitivity and flexibility of regular and chaotic calcium oscillations," *Biophysical Chemistry*, vol. 104, no. 2, pp. 509–522, 2003.
- [29] P. Shen and R. Larter, "Chaos in intracellular Ca^{2+} oscillations in a new model for non-excitable cells," *Cell Calcium*, vol. 17, no. 3, pp. 225–232, 1995.
- [30] G. Dupont and A. Goldbeter, "One-pool model for Ca^{2+} oscillations involving Ca^{2+} and inositol 1,4,5-trisphosphate as co-agonists for Ca^{2+} release," *Cell Calcium*, vol. 14, no. 4, pp. 311–322, 1993.
- [31] T. Meyer and L. Stryer, "Transient calcium release induced by successive increments of inositol 1,4,5-trisphosphate," *Proceedings of the National Academy of Sciences of the United States of America*, vol. 87, no. 10, pp. 3841–3845, 1990.
- [32] G. W. de Young and J. Keizer, "A single-pool inositol 1,4,5-trisphosphate-receptor-based model for agonist-stimulated oscillations in Ca^{2+} concentration," *Proceedings of the National Academy of Sciences of the United States of America*, vol. 89, no. 20, pp. 9895–9899, 1992.
- [33] Y. Timofeeva, *Oscillations and waves in single and multi-cellular system with free calcium [Ph.D. thesis]*, Loughborough University, 2003.
- [34] S. Schuster, M. Marhl, and T. Höfer, "Modelling of simple and complex calcium oscillations from single-cell responses to intercellular signalling," *European Journal of Biochemistry*, vol. 269, no. 5, pp. 1333–1355, 2002.
- [35] K. B. Oldham and J. Spanier, *The Fractional Calculus*, Academic Press, New York, NY, USA, 1974.
- [36] K. S. Miller and B. Ross, *An Introduction to the Fractional Calculus and Fractional Differential Equations*, John Wiley & Sons, New York, NY, USA, 1993.
- [37] I. Podlubny, *Fractional Differential Equations*, vol. 198, Academic Press, San Diego, Calif, USA, 1999.
- [38] M. S. Tavazoei and M. Haeri, "Limitations of frequency domain approximation for detecting chaos in fractional order systems," *Nonlinear Analysis: Theory, Methods & Applications*, vol. 69, no. 4, pp. 1299–1320, 2008.
- [39] V. Daftardar-Gejji and H. Jafari, "Adomian decomposition: a tool for solving a system of fractional differential equations," *Journal of Mathematical Analysis and Applications*, vol. 301, no. 2, pp. 508–518, 2005.
- [40] J. Sabatier, O. P. Agrawal, and J. A. T. Machado, *Advances in Fractional Calculus: Theoretical Developments and Applications in Physics and Engineering*, Springer, Dordrecht, The Netherlands, 2007.
- [41] S. J. Singh and A. Chatterjee, "Three classes of FDEs amenable to approximation using a Galerkin technique," in *Advances in Fractional Calculus*, Springer, 2007.
- [42] J. Sabatier, M. Merveillaut, R. Malti, and A. Oustaloup, "How to impose physically coherent initial conditions to a fractional system?" *Communications in Nonlinear Science and Numerical Simulation*, vol. 15, no. 5, pp. 1318–1326, 2010.
- [43] N. Bertrand, J. Sabatier, O. Briat, and J.-M. Vinassa, "Fractional non-linear modelling of ultracapacitors," *Communications in Nonlinear Science and Numerical Simulation*, vol. 15, no. 5, pp. 1327–1337, 2010.
- [44] R. L. Bagley and P. J. Torvik, "A theoretical basis for the application of fractional calculus to viscoelasticity," *Journal of Rheology*, vol. 27, no. 3, pp. 201–210, 1983.
- [45] J. Sabatier, H. C. Nguyen, C. Farges et al., "Fractional models for thermal modeling and temperature estimation of a transistor junction," *Advances in Difference Equations*, vol. 201, Article ID 687363, 12 pages, 2011.
- [46] I. Podlubny, "Geometric and physical interpretation of fractional integration and fractional differentiation," *Fractional Calculus & Applied Analysis*, vol. 5, no. 4, pp. 367–386, 2002.
- [47] J. A. Tenreiro Machado, "A Probabilistic Interpretation of the fractional-order differentiation," *Fractional Calculus & Applied Analysis*, vol. 6, no. 1, pp. 73–80, 2003.
- [48] M. Du, Z. Wang, and H. Hu, "Measuring memory with the order of fractional derivative," *Scientific Reports*, vol. 3, article 3431, 2013.
- [49] C. Ionescu, R. de Keyser, J. Sabatier, A. Oustaloup, and F. Levron, "Low frequency constant-phase behavior in the respiratory impedance," *Biomedical Signal Processing and Control*, vol. 6, no. 2, pp. 197–208, 2011.
- [50] Z. Odibat and S. Momani, "An Algorithm for the numerical solution of differential equations of fractional order," *Journal of Applied Mathematics & Informatics*, vol. 26, no. 1-2, pp. 15–27, 2008.
- [51] D. Matignon, "Stability results for fractional differential equations with applications to control processing," in *Proceedings of the Computational Engineering in Systems Applications*, vol. 2, pp. 963–968, Lille, France, 1996.

Research Article

Ship Electric Propulsion Simulation System Reliability Evaluation Based on Improved D-S Expert Weight Calculation Method

Bing Li, Guoliang Gu, Bowen Xing, and Lihong Li

College of Automation, Harbin Engineering University, Harbin, Heilongjiang 150001, China

Correspondence should be addressed to Bowen Xing; bwheu@outlook.com

Received 12 August 2014; Revised 21 September 2014; Accepted 5 October 2014

Academic Editor: Shaofan Li

Copyright © 2015 Bing Li et al. This is an open access article distributed under the Creative Commons Attribution License, which permits unrestricted use, distribution, and reproduction in any medium, provided the original work is properly cited.

In order to have a better evaluation process to determine the experts weight in the evaluation process, this paper proposes a new expert weight calculation method. First of all to establish electric propulsion simulation evaluation system, use AHP method to calculate the initial weight principle of index. Then use the D-S to fuse the experts evaluation information, combined with the weight vector, structure of the expert weight objective function, and through the genetic algorithm to solve the expert weight size. According to the expert weight vector, calculate the final weight vector. Not only can it greatly make use of the experts information and analyze the similarity of information effectively but also it calculates the weight of each expert objectively. At the same time the evaluation subjective factors have been reduced by the adoption of this new method.

1. Introduction

Regarding ship electric propulsion system as a modern ship career development direction, its safety and reliability are more and more concerned about [1]. The simulation technology is one of the important means for people to study ship electric propulsion system [2]. But the results of simulation credibility are worth considering, and incorrect results could lead to major events. So analyzing the credibility in the system simulation results, determining the relative weight of each subsystem, has great significance for studying the mechanism of ship electric propulsion system.

In the system simulation credibility analysis, we need to make sure of the mutual importance of the systems, namely, the weight. Analytic hierarchy process (AHP) is a comprehensive evaluation method used in research of complicated system [3]. The basic idea of using analytic hierarchy process to determine weight is to invite more related experts to compare each subsystem and to identify and analyse the judgment matrix. As a result of difference between each expert in knowledge, experience, ability, and level, different experts have different result to weight evaluation system. How

to make better use of the evaluation experts has always been about the topic of comparison.

The D-S evidence theory is a method widely used in information fusion technology [4]. Chen et al. propose making use of the Markov random fields (MRFs) and D-S evidence theory to interactive color image segmentation method [5]. Si et al. proposed a novel prediction approach through information fusion of improved D-S evidence theory and neural network to forecast the distribution of coal seam terrain [6]. Li and Pang use D-S evidence theory to solve vessel collision risk assessment [7]. Experimental results show that the proposed approach confirms the validity and is reasonable for real application. But D-S evidence theory cannot solve the conflict evidence problem.

To solve this problem, according to the multiple experts judgment matrix by using analytic hierarchy process method and D-S evidence theory, avoid the conflict in information on the expert information synthesis from the actual case. According to the weight of the fusion, establish an expert weight target function and determine the weight of experts using genetic algorithms. Finally, determine the weight of final system by weighting. This algorithm is effective to

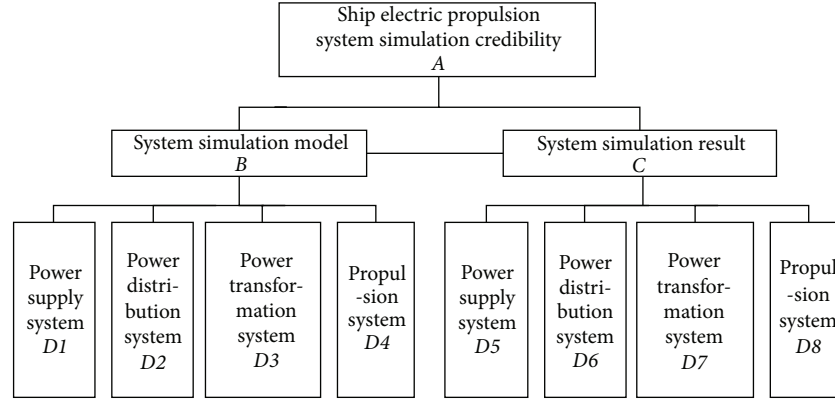


FIGURE 1: Structure diagram for ship electric propulsion simulation system reliability evaluation index system.

solve the synthesis expert information conflict problems and improve the system of the objectivity of the judgment.

2. The Simulation System Reliability Evaluation Index System

For the ship electric propulsion simulation system reliability evaluation study, according to user requirements and the characteristics of the system itself, first of all we need to establish the ship electric propulsion simulation system reliability evaluation index system. Based on the key indicators in research process, investigate subsystem one by one, and establish the system equivalence evaluation index system. In the process of building evaluation system, according to the target layer, criterion layer, and measures layer sequence, decompose the system step by step hierarchically and make a complicated problem decomposed into several elements. For ship electric propulsion simulation system is concerned about, target layer is ship electric propulsion simulation system reliability. Criterion layer, from the system simulation model to system based on the simulation results, determines the level of index measures step by step [8]. For system simulation model and system simulation results are concerned about, the reliability is analyzed from the power supply system, power distribution system, power transformation system, and propulsion system, respectively. Finally ship electric propulsion simulation system reliability evaluation system is shown in Figure 1.

3. Expert Evaluation Weight Analysis

3.1. The Steps to Calculate the Index Weight

Step 1. According to many experts' relative judgment matrix, use the principle of AHP to calculate the index of the initial weight.

Step 2. Determine the index weight fusion through the modified D-S fusion initial index weight, and determine the absolute judgment matrix through the expert judgment.

Step 3. According to each index fusion weight and absolute judgment matrix, determine the expert weight, the objective function and a genetic algorithm is adopted to calculate the optimal solution to determine the expert weight.

Step 4. Weigh the initial weight and expert weight, and determine the weights of the index.

3.2. Based on the AHP Analysis of Initial Weights. Initial weight can be calculated by AHP to carry out. Compared with the previous expert scoring method, fuzzy evaluation method, the grey correlation method, Pressure-State-Response method (PSR), and artificial neural network algorithm, AHP is a kind of qualitative analysis and quantitative analysis and systematic and hierarchical multiple factors of decision analysis method; this method will be the decision maker's experience quantitative judgment. It is very convenient in the condition of the multiobjective and lack of necessary data [9].

Ship electric propulsion simulation system reliability evaluation index system calculation generally can be divided into the following four steps [10].

Step 1. Each element value in judgment matrix is relative to a certain element in a previous level, associated with the each elements in the layer pairwise comparison judgment importance. In the judge process, use 1–9 scale method to show, specific as is shown in Table 1.

Step 2. The element's relative weight for the criterion is calculated by judgment matrix.

Step 3. Compute synthetic weight of each of the layer elements to system target.

Step 4. Consistency check: consistency includes absolute consistency (or complete consistency) and order consistency. The so-called absolute consistency means that the judgment matrix A , If matrix A meet

$$a_{ij} = a_{ik}a_{jk} \quad i, j, k = 1, 2, \dots, n. \quad (1)$$

We called matrix A meet absolute consistency.

TABLE 1: The scale method of 1~9.

Scale	Meaning
1	Two factors have the same importance
3	A factor relative to another factor a little important
5	A factor relative to another obvious important factors
7	A factor relative to another important factor strongly
9	A factor relative to another extremely important factor
2, 4, 6, 8	Median in two adjacent judgments
Reciprocal	Factors i and j are to judge b_{ij} ; the factors j and i compare judgment $b_{ji} = 1/b_{ij}$

It says A is absolute consistency matrix (or complete consistency matrix); at the same time there is

$$a_{ij} = \frac{W_i}{W_j} \quad i, j, k = 1, 2, \dots, n, \quad (2)$$

$$AW = nW.$$

Sort consistency is to point to the following: if factor a is important than factor b and factor b is important than factor c , then a factor is important than factor c . And the consistency check index C.I. is as follows:

$$\text{C.I.} = \frac{\lambda_{\max} - n}{n - 1}. \quad (3)$$

The n is the order number of judgment matrix A and λ_{\max} is the biggest characteristic root of judgment matrix A .

Calculation consistency ratio C.R. is as follows:

$$\text{C.R.} = \frac{\text{C.I.}}{\text{R.I.}}. \quad (4)$$

When $\text{C.R.} < 0.1$, consider the consistency of judgement matrix is acceptable [11] (Table 2).

3.3. The Construction of Expert Weight Objective Function Based on D-S Method. For the ship electric propulsion system concerned about, setting the index set $B = \{b_1, b_2, \dots, b_n\}$, experts set $D = \{d_1, d_2, \dots, d_m\}$, and matrix $A = (a_{ij})_{m \times n}$ ($0 < a_{ij} < 1$) is absolute judgment matrix coming from experts to marking index weight. Set index fusion weight vector $W = \{w_1, w_2, \dots, w_n\}$, expert weight vector is $R = \{r_1, r_2, \dots, r_m\}$, and meet $\sum_{j=1}^n w_j = 1$, $\sum_{i=1}^m r_i = 1$.

For absolute judgment matrix, if evaluation from expert d_i has no difference with other experts' evaluation, the expert d_i has a higher similarity with other experts. That is to say, expert d_i has higher credibility. $F_{ij}(r)$ show the index judgment deviation from experts d_i and other experts:

$$F_{ij}(r) = \sum_{k=1}^m |a_{ij}r_i - a_{kj}r_k| * w_j. \quad (5)$$

TABLE 2: The average random consistency targets R.I.

Matrix order number	R.I.
1	0
2	0
3	0.52
4	0.89
5	1.12
6	1.26
7	1.36
8	1.41
9	1.46
10	1.19

$F_j(r)$ show the total index judgment deviation from m experts:

$$F_j(r) = \sum_{i=1}^m \sum_{k=1}^m |a_{ij}r_i - a_{kj}r_k| * w_j. \quad (6)$$

For index b_j , deviation value $F_j(r)$ is smaller; credibility of the judge from experts is higher. For the system in the index, total deviation value is smaller; credibility of the judge from experts is higher. According to the calculation of the system integration indicators weight, structural expert weight target optimization function

$$\begin{aligned} \min \quad & F(r) = \sum_{j=1}^n \sum_{i=1}^m \sum_{k=1}^m |a_{ij}r_i - a_{kj}r_k| * w_j \\ \text{s.t.} \quad & \sum_{i=1}^m r_i = 1 \\ & 0 < r_i < 1 \quad (i = 1, \dots, m). \end{aligned} \quad (7)$$

3.4. Solve the Objective Function. Formula (7) belongs to non-linear optimization problem, the genetic algorithm suitable for processing this kind of problem. With the increase of matrix dimension, parameters in formula (7) will increase sharply, in order to find the optimal solution under multivariate conditions, introducing the concept of niche to enhance the diversity of population [12, 13]. Algorithm flow chart is shown in Figure 2.

4. Ship Electric Propulsion Simulation System Expert Evaluation Weight Calculation Conclusion

Based on the analysis of the weight of each subsystem, invite three authoritative experts to score evaluation. Relative to

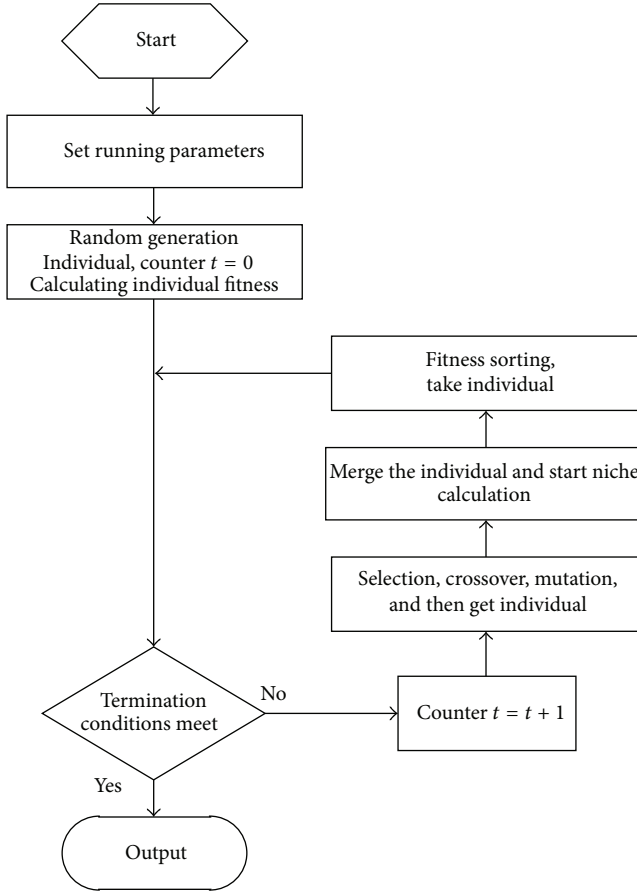


FIGURE 2: Flow chart for the niche genetic algorithm of AHP calculation.

the subsystem B , three experts are given, respectively, $D1$, $D2$, $D3$, and $D4$ judgment matrix, specific as follows:

$$\begin{aligned}
 B_1 &= \begin{bmatrix} 1 & \frac{1}{6} & \frac{1}{3} & 3 \\ 6 & 1 & 2 & 7 \\ 3 & \frac{1}{2} & 1 & 5 \\ \frac{1}{3} & \frac{1}{7} & \frac{1}{5} & 1 \end{bmatrix}, \\
 B_2 &= \begin{bmatrix} 1 & \frac{1}{2} & \frac{1}{1} & 3 \\ 2 & \frac{1}{1} & \frac{1}{1} & 4 \\ 2 & 1 & 1 & 4 \\ \frac{1}{3} & \frac{1}{4} & \frac{1}{4} & 1 \end{bmatrix}, \\
 B_3 &= \begin{bmatrix} 1 & 1 & \frac{1}{5} & 3 \\ 1 & 1 & \frac{1}{5} & 3 \\ 5 & 1 & 1 & 7 \\ \frac{1}{3} & \frac{1}{3} & \frac{1}{7} & 1 \end{bmatrix}.
 \end{aligned} \tag{8}$$

According to the principle of AHP calculate the corresponding initial weights of each subsystem, and check the consistency of judge matrix. If they do not meet the requirements for consistency, give the judge matrix again. Get three experts to $D1$, $D2$, $D3$, and $D4$ judgment weight: $W_{b1} = \{0.1176, 0.5345, 0.2904, 0.0578\}$, $W_{b2} = \{0.2004, 0.3587, 0.3583, 0.0816\}$, and $W_{b3} = \{0.1953, 0.1953, 0.5324, 0.0771\}$.

According to the calculation of the initial weight, using the improved D-S to fuse evaluation information, get $D1$, $D2$, $D3$, and $D4$ fusion weight to subsystem $BW_b = \{0.0633, 0.3941, 0.5334, 0.0091\}$.

For ship electric propulsion system simulation model credibility analysis, the purpose is to determine whether the model is accurate. In this criterion, the three experts give $D1$, $D2$, $D3$, and $D4$ weight fuzzy evaluation matrix: $B = [0.1 \ 0.5 \ 0.3 \ 0.1; 0.2 \ 0.35 \ 0.35 \ 0.1; 0.2 \ 0.2 \ 0.5 \ 0.1]$. According to each subsystem fusion weight and expert fuzzy evaluation matrix, by the algorithm to determine the expert weight objective function, and through the genetic algorithm optimization, determine the expert weight optimal solution. Get three subsystems $D1$, $D2$, $D3$, $D4$ weight evaluation of its own weight $R_B = \{0.401, 0.36, 0.238\}$.

According to the expert weight and the initial weight of the subsystem, using the weighted method to calculate the weight of each subsystem, get $D1$, $D2$, $D3$, $D4$ weight to subsystem $BW_b = \{0.1654, 0.3886, 0.3732, 0.0706\}$.

Similarly, the three experts give the judgment matrix of each subsystem for objectives A and C and calculate the weight of each subsystem according to the above method. In view of the space reasons, give only the expert weight and the weight of each subsystem.

For the three experts grade evaluation for $D5$, $D6$, $D7$, $D8$, get the weight in the evaluation process of evaluation: $R_C = \{0.48, 0.218, 0.3\}$, and the subsystem $D5$, $D6$, $D7$, $D8$ weight $W_C = \{0.1666, 0.1758, 0.2974, 0.3582\}$.

Analyzing subsystem B and C against overall goal A , get evaluation weight $R_A = \{0.44, 0.259, 0.3\}$ and the weight subsystem B , C to A : $W_A = \{0.5108, 0.4882\}$.

According to the calculation of the W_A , W_B , W_C weight vector, use the weighted method to calculate the total target:

$$\begin{aligned}
 W &= [W'_B \ W'_C] \cdot W'_A \\
 &= \begin{bmatrix} 0.1653 & 0.1666 \\ 0.3887 & 0.1758 \\ 0.3731 & 0.2974 \\ 0.0708 & 0.3582 \end{bmatrix} \cdot \begin{bmatrix} 0.5108 \\ 0.4882 \end{bmatrix} \\
 &= [0.1658 \ 0.2844 \ 0.3358 \ 0.2110]'.
 \end{aligned} \tag{9}$$

From the calculation results above, it is known that, in the ship electric propulsion system, the simulation credibility is the greatest impacted by power conversion subsystem, secondly they were distribution subsystem, propulsion subsystem, and power subsystem. Power transformation simulation subsystem in energy conversion and harmonic aspects affect the credibility of the system. Distribution system simulation subsystem produces certain effect to management and distribution of electricity. Propulsion system simulation subsystem is aimed at mutation load. For power subsystem

main consideration of its power quality, the other modules produce small amount of influence.

5. Conclusions

By using D-S theory and AHP, study the ship electric propulsion simulation system for the credibility evaluation expert weight. Through the inspection of the similarity between the experts, determine the expert weight objective function, and the genetic algorithm was used to calculate the expert weight optimal solution. This method not only can fuse the advantages of other methods, but also make better use of the expert advice in the evaluate process greatly. It can make subjective judgments of experts more united and avoid the one-sidedness when considering only one expert, and various judgments from different experts on reliability of ship electric propulsion simulation system can be treated; particularly evidence of conflict is no longer blindly negated. At the same time, this method can optimize the indexes and enhance the veracity and reliability for scientific decision-making, which has better comprehensive assessment evaluation and is more meaningful.

Conflict of Interests

The authors declare that there is no conflict of interests regarding the publication of this paper.

Acknowledgments

This work is supported by National Natural Science Foundation (NNSF) of China under Grant 51307026, Natural Science Foundation of Heilongjiang Province under Grant E201347, Fundamental Research Funds for the Central Universities under Grant HEUCFX41305, and the China Postdoctoral Funds (no. 2012M510924).

References

- [1] L. Sheng and L. Lihong, "Application of FCE for credibility of simulation of ship electric propulsion system," *Techniques of Automation & Applications*, vol. 32, no. 4, pp. 52–77, 2012.
- [2] S. Ya-feng, W. Chao-yang, and H. Zhi-ping, "Research on simulation credibility," *Electronic Measurement Technology*, vol. 32, no. 11, pp. 8–11, 2009.
- [3] H. Chen and W. Yong, "Credibility research of the simulation of the integrative avionics electronic system which based on cloud focus judgement," *Electronic Measurement Technology*, vol. 32, no. 10, pp. 69–72, 2009.
- [4] B. Chen and J. Feng, "Multisensor information fusion of pulsed GTAW based on improved D-S evidence theory," *International Journal of Advanced Manufacturing Technology*, vol. 71, no. 1–4, pp. 91–99, 2014.
- [5] Y. Chen, A. B. Cremers, and Z. Cao, "Interactive color image segmentation via iterative evidential labeling," *Information Fusion*, vol. 20, no. 1, pp. 292–304, 2014.
- [6] L. Si, Z. Wang, C. Tan, and X. Liu, "A novel approach for coal seam terrain prediction through information fusion of improved D-S evidence theory and neural network," *Measurement: Journal of the International Measurement Confederation*, vol. 54, pp. 140–151, 2014.
- [7] B. Li and F.-W. Pang, "An approach of vessel collision risk assessment based on the D-S evidence theory," *Ocean Engineering*, vol. 74, pp. 16–21, 2013.
- [8] I.-S. Jung and C.-S. Lee, "Fuzzy inference and AHP-based alternative evaluation tool in the development of sustainable residential land," *KSCE Journal of Civil Engineering*, vol. 16, no. 3, pp. 273–282, 2012.
- [9] C.-C. Sun, "A performance evaluation model by integrating fuzzy AHP and fuzzy TOPSIS methods," *Expert Systems with Applications*, vol. 37, no. 12, pp. 7745–7754, 2010.
- [10] G.-Z. Li, N.-L. Tan, and J.-B. Zhang, "Criticality analysis of subway train equipment based on improved analytical hierarchy process," *Journal of Electronic Measurement and Instrument*, vol. 26, no. 6, pp. 503–507, 2012.
- [11] W. Shi, Y. Li, C. Deng, M. Fan, and Z. Cai, "Design and implementation of water environment safety risk assessment model based on AHP," *Chinese Journal of Scientific Instrument*, vol. 30, no. 5, pp. 1009–1013, 2009.
- [12] Z.-Y. Yang, J.-B. Qu, and C.-K. Huang, "Bridge safety evaluation based on fuzzy synthetic evaluation method and analytic hierarchy process," *Journal of Tianjin University Science and Technology*, vol. 38, no. 12, pp. 1063–1067, 2005.
- [13] S. Liu, Y. Zhang, and D. Yu, "Correctinn consistency of fuzzy judgment matrix using niche genetic algorithm," *Journal of Huazhong University of Science and Technology*, vol. 38, no. 7, pp. 126–129, 2010.

Research Article

Simulation of Cavitation Water Flows

Piroz Zamankhan^{1,2}

¹*Institute of Geothermal Energy, Dedan Kimathi University of Technology, 101000 Nyeri, Kenya*

²*Chemical Engineering Department, School of Engineering, Collage of Agriculture, Engineering and Science, University of KwaZulu-Natal, 4041 Durban, South Africa*

Correspondence should be addressed to Piroz Zamankhan; qpz002000@yahoo.com

Received 20 July 2014; Revised 4 September 2014; Accepted 13 September 2014

Academic Editor: Junuthula N. Reddy

Copyright © 2015 Piroz Zamankhan. This is an open access article distributed under the Creative Commons Attribution License, which permits unrestricted use, distribution, and reproduction in any medium, provided the original work is properly cited.

The air-water mixture from an artificially aerated spillway flowing down to a canyon may cause serious erosion and damage to both the spillway surface and the environment. The location of an aerator, its geometry, and the aeration flow rate are important factors in the design of an environmentally friendly high-energy spillway. In this work, an analysis of the problem based on physical and computational fluid dynamics (CFD) modeling is presented. The numerical modeling used was a large eddy simulation technique (LES) combined with a discrete element method. Three-dimensional simulations of a spillway were performed on a graphics processing unit (GPU). The result of this analysis in the form of design suggestions may help diminishing the hazards associated with cavitation.

1. Introduction

In spillway engineering there are numerous challenging obstacles. One of the most determining factors is the geological geometry in which the dam and its spillway have to be built in. The geometry, such as length and slope of the spillway, can range from short and steep to long and flat or vice versa. Generally, the longer and steeper is the spillway the higher is the gradient of the energy head of the flowing water. In some cases the velocity of the water might exceed 30 m/s and cavitation might occur. Used as an illustrative example, the high-energy spillway of the Kárahnjúkar Dam which supports the Hálsson Reservoir in eastern Iceland displays numerous problems in spillway engineering. An aerial perspective of this spillway can be seen in Figure 1.

When a fluid changes state from liquid to vapor, its volume increases by orders of magnitude and cavities (or bubbles) can form. Indeed, cavities, which are filled with water vapor, are formed by boiling at the local pressure which equals the water vapor pressure. If the cavity is filled with gases other than water vapor, then the process is named gaseous cavitation [1].

There is a technical difference between boiling and cavitation. On the one hand, boiling is defined as the process of phase change from the liquid state to the vapor state by

changing the temperature at constant pressure. On the other hand, cavitation is the process of phase change from the liquid state to the vapor state by changing the local pressure at constant temperature.

Cavitation is a consequence of the reduction of the pressure to a critical value, due to a flowing liquid or in an acoustical field. Spillways are subject to cavitation. Inertial cavitation is the process in which voids or bubbles rapidly collapse, forming shock waves. This process is marked by intense noise. The shock waves formed by cavitation can significantly damage the spillway face [1]. Cavitation damage on the spillway face is a complex process [2]. Richer concrete mixes are used to increase the resistance to cavitation damage and erosion [3].

Falvey [1] suggested that impurities and microscopic air bubbles in the water are necessary to initiate cavitation. As can be seen from Figure 1, the color of water accumulated behind the dam indicates that it may contain various types of impurities including suspended fine solid particles. The density of the water accumulated behind the dam was determined from a sample using a hydrometer. The relative density of the sample with respect to water has been found to be approximately 1.08.

The melting water which transports suspended clay particles flows into the side channel and then follows an

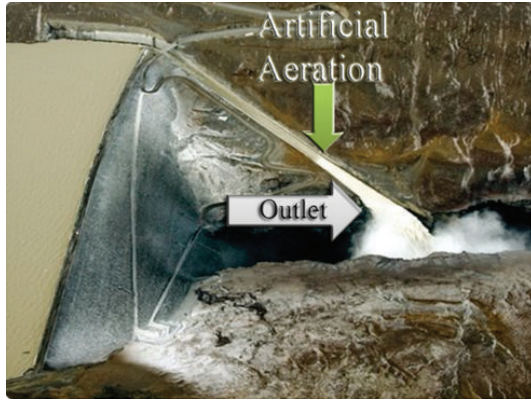


FIGURE 1: Aerial view of Kárahnjúkar spillway with bottom aerator, eastern Iceland.

approximately 414 m long chute with a transition bend and a bottom aerator.

The most important task is to reduce the energy head of the flowing water until it enters the river. In this example the jet should not hit the opposite canyon wall where it increases erosion. An artificial aeration device “cushions” the water; the widening at the chute’s end reduces the flow velocity and increases the impact area in the plunge pool which in turn decreases rock scouring. Additionally, seven baffles and lateral wedges at the main throw lip abet the jet disintegration. In general, every high-energy spillway has to be analyzed for cavitation risk.

The water in spillways contains air bubbles and impurities, such as suspended particles, in a range of sizes. As discussed later these air bubbles and impurities induce cavitation. Vaporization is the most important factor in bubble growth. At a critical combination of flow velocity, water pressure, and the vapor pressure of the flowing water, cavitation starts. The cavitation number is used to define this starting point. The equation for this parameter is derived from the Bernoulli equation for a steady flow between two points. In dimensionless terms, the comparable equation results in a pressure coefficient, C_p . The value of this parameter is a constant at every point until the minimum pressure at a certain location is greater than the vapor pressure of water. The pressure at a certain location will not decrease any further once the vapor pressure is reached. Taking everything into account, such as temperature, clarity of the water, and safety reasons, the pressure coefficient is set to a minimum value and then called cavitation number σ . The cavitation number is a dimensionless number which expresses the relationship between the difference of a local absolute pressure from the vapor pressure and the kinetic energy per volume. It may be used to characterize the potential of the flow to cavitate.

It has been suggested that no cavitation protection for a spillway would be needed if the cavitation number is larger than 1.8. If the cavitation number is in the range of 0.12–0.17, then the spillway should be protected by additional aeration grooves. In Figure 2 the cavitation indices for different discharges have been calculated.

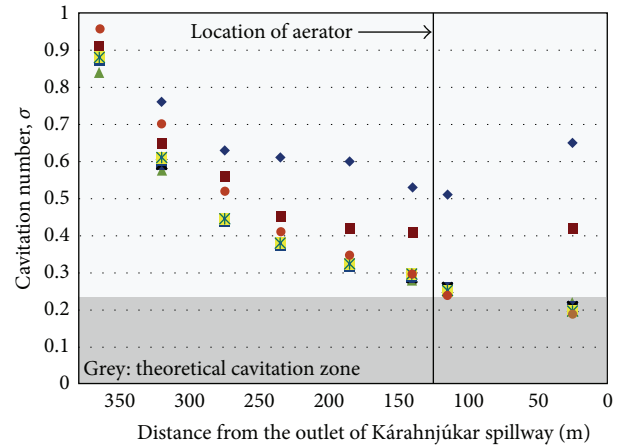


FIGURE 2: Cavitation numbers at different discharges on the Kárahnjúkar spillway [4]. The location of the outlet is shown in Figure 1. Here, blue diamonds: 200 m³/s; red squares: 400 m³/s; green triangle: 800 m³/s; blue squares: 950 m³/s; yellow square with green star: 1350 m³/s; and orange dot: 2250 m³/s.

As a precaution the cavitation zone has been set to $\sigma = 0.25$ because of the lower atmospheric pressure, low water temperature, and overall safety reasons. Thus, as a precaution, the aerator was placed 125 m before the end of the chute. Nevertheless, incipient white water far upstream from the aerator allows the assumption that in such a long spillway fully self-aerated flow may have already been developed. Therefore, the purpose of this aerator is mainly to reduce the impact energy in the plunge pool.

The main idea is to develop a fully 3D simulation of an aerated spillway in the future. But to achieve that the physics of bubble growth due to cavitation and aeration and the formation and distribution of the bubbles have to be understood and simulations have to be validated. In this work it is shown that LES combined with a discrete element method on GPUs yields promising results. Cavitation is defined as the formation of the vapor phase and the subsequent immediate implosion of small liquid-free zones in a liquid, called voids or bubbles [1].

The first section deals with forced cavitation and the dynamics of cavitation bubbles. An experiment was carried out in which cavitation was forced to develop with clear water in glass and galvanized steel pipes. These findings were compared to computational simulations. The mathematical model and simulation results of the cavitation bubble dynamics will be described.

In the second part of the paper the flow behavior of an aerated spillway is computed. In this section, the reliability of the predicted cavitation zone as shown in Figure 2 is examined.

2. Experimental Methods and Observations

Cavitation occurs when the fluid pressure is lower than the local vapor pressure [5]. In the cavities, the vapor phase replaces the liquid phase. The surrounding liquid then experiences evaporative cooling. For water these thermal effects

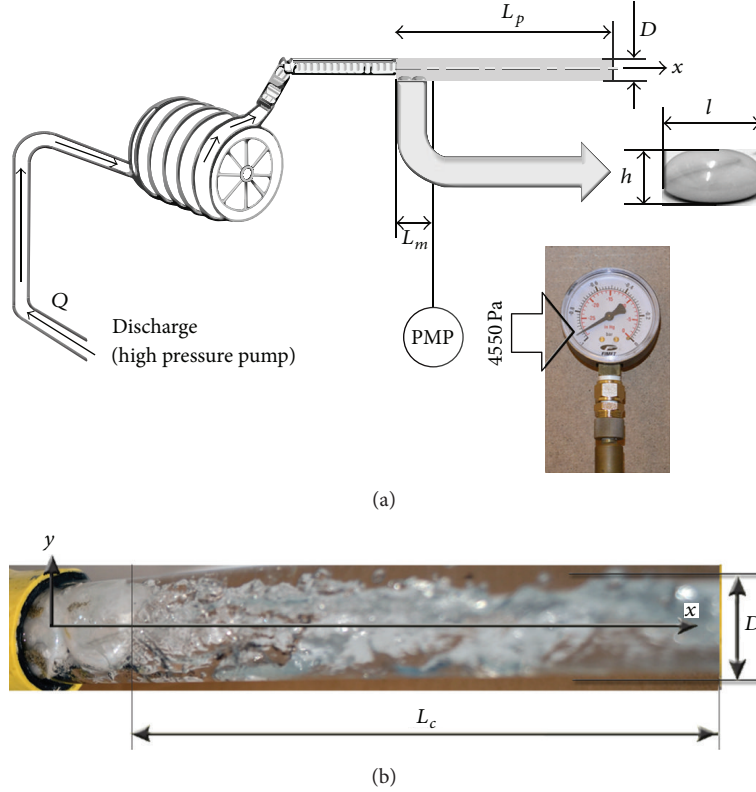


FIGURE 3: The experimental setup for investigating cavitation. (a) Schematic of the experimental setup. Inset (on the right-hand side): an image of the aquarium stone used in the cavitation test. Inset (lower): the minimum pressure measured was 4.55 kPa (absolute). (b) An image of sheet cavitation at the discharge $Q = 12.5$ L/s.

can have a significant influence on the dynamics of bubbles in the cavitation process. However, for simplicity, in this paper the isothermal problem will be investigated which retains a number of interesting qualitative features of the cavitation process.

For water flow over a uniform roughness in a spillway, incipient cavitation will occur randomly over the spillway surface. If the cavitation number is lowered below incipient conditions, then cavitation will occur in sheets whose locations are influenced by the magnitude and spectrum of turbulent fluctuation within the boundary layer [1].

To enhance the predictive reliability of computational models for cavitation, which are still considered to be immature, further validation based on experimental data is required. Figure 3 shows a simple system in which sheet cavitation may be observed.

Surface roughness, cracks, and offsets may initiate cavitation. The local pressure on the step's surfaces or directly at the step in a high velocity spillway can reach the vapor pressure. This may result in sheet cavitation similar to that shown in Figure 3. As stated earlier, cavitation can cause severe damage to the spillway concrete. The extent of cavitation damage is a function of the local cavitation number in the spillway chute and the duration of the flow.

In brief, experiments were conducted in a test setup as illustrated in Figure 3(a). The tests were performed in a horizontal galvanized steel pipe with an outer diameter of

TABLE 1: Physical properties.

Material	Dynamic viscosity (Pa s)	Density (kg/m^3)	Vaporization pressure (mmHg) [18]
Water (liquid)	0.001	996.4	$\log_{10} P = 8.07131$
Water (vapor)	1.34×10^{-5}	0.5542	$-1730.63/T - 39.724$
Air	1.79×10^{-5}	1.175	

$D = 0.0254$ m and the length of $L_p = 0.3$ m. Two very similar aquarium stones with a length of $l = 0.0215$ m and a height of $h = 0.01$ m were attached to the bottom of the pipe in the entrance section. The stones produced a sudden offset whose leading edge is approximately an ellipse. The dimensions of one of the stones are depicted in the inset of Figure 3(a).

Clear water was used in the experiments; its physical properties are given in Table 1. The discharge $Q = 12.5$ L/s was provided with a heavy-duty high-pressure wash-down pump with a pressure range of 2.5 bar to 140 bars (maximum pressure). A high-pressure hose was used to connect the test tube to the high-pressure pump.

The average pressure at the pipe inlet was approximately 2.5 bars (absolute) and the minimum measured pressure was 4.55 kPa (absolute). Figure 3(b) shows the monometer connected to the pressure measuring port (PMP) as shown in the second inset of Figure 3(a). The port was located $L_m = 0.048$ m downstream from the inlet of the test tube.

Here, L_c represents the length of the sheet. The low pressure measured at the sampling port indicates that cavitation may have occurred in the test tube.

The above-mentioned test with the same discharge of $Q = 12.5$ L/s and the same average inlet pressure of 2.5 bar (absolute) was repeated in a cylindrical borosilicate glass pipe with a diameter of $D = 0.026$ m. The pipe wall thickness was 0.001 m. A camera was used to take images of sheet cavitation from the underside of the test tube.

Figure 3(b) shows an image of sheet cavitation with an average inlet channel pressure of approximately 2.5 bars (absolute). As can be seen from Figure 3(b), the sheet appears to be attached to the stone with a length of $L_c > 5D$. The sheet consists of a number of fuzzy white clouds. A flash photograph reveals that a cloud consists of individual small bubbles [1].

In the following section, simulation results will be presented, giving a more detailed insight and showing an ongoing process of cavity formation and deformation.

It is difficult to obtain accurate measurements using the simple setup as shown in Figure 3. The stones attached to the bottom of the pipes may not be stable over long periods of time.

Additional experimental studies in cavitation tunnels are required to supply a more reliable and convincing data basis for the validation of computational approaches to model cavitation.

3. Mathematical Model and Simulation Results

If sheet cavitation, as described in the experiments in the preceding section, occurs in the spillway chute, it can produce extensive damage to its concrete linings [1]. Note that cavitation damage in tunnels and conduits is less likely to result in dam failure.

Experimental observations such as those shown in Figure 3(b) are indispensable for investigating cavitation problems. However, numerical simulation can provide possibilities to study cavity formation and deformation in greater detail than what is affordable by experiments.

3.1. Bubble Dynamics in a Quiescent Fluid. The importance of microscopic bubbles as cavitation nuclei has been known for a long time [1]. Consider a single bubble, which contains the vapor of the liquid, in equilibrium in an incompressible, Newtonian fluid that is at rest at infinity. In this case, the bubble radius R_E must satisfy the following condition [6]:

$$(p_v - p_\infty^{(0)}) R_E^3 - 2\gamma R_E^2 + G = 0. \quad (1)$$

The bubble radius at the limit point, where $(p_v - p_\infty^{(0)}) = (32\gamma^3/27G)^{1/2}$, can be expressed in terms of material parameters as [5]

$$R_{\text{critical}} = \left(\frac{3G}{2\gamma} \right)^{1/2}. \quad (2)$$

If $R_E \leq R_{\text{critical}}$, then the bubble is *stable* against infinitesimal changes in its radius. The bubble becomes unstable if $R_E >$

R_{critical} . Note that the bubble may contain a “contaminant” gas which dissolves very slowly compared to the time scales associated with changes in its size.

Apparently small bubbles whose radii are smaller than the critical radius behave like rigid spheres in accelerated flows [7].

3.2. Bubble Dynamics in Accelerated Flows. For the present study the interaction of a small bubble whose size is characterized by the critical bubble radius with its neighboring bubbles is assumed to be subjected to the Lennard-Jones (LJ) condition [8]. Figure 5(a) shows the Lennard-Jones 12-6 pair potential. The force between two bubbles with diameter d_B located at r_i and r_j is given as

$$\mathbf{F}_{ij} = \frac{48\epsilon}{r_{ij}^2} \left[\left(\frac{d_B}{r_{ij}} \right)^{12} - \frac{1}{2} \left(\frac{d_B}{r_{ij}} \right)^6 \right] \mathbf{r}_{ij}. \quad (3)$$

A simplified momentum equation for the i th spherical bubble may be given as

$$\begin{aligned} & \underbrace{\frac{\pi}{6} \rho_v d_B^3 \frac{d\mathbf{v}_B^i}{dt}}_{\text{momentum transfer}} \\ &= \underbrace{\frac{\pi}{6} \rho_w d_B^2 C_D (\text{Re}_B, \text{Ac}) |\mathbf{v}_B^i - \mathbf{v}_w| (\mathbf{v}_B^i - \mathbf{v}_w)}_{\text{viscous}} \\ &+ \underbrace{\frac{\pi}{12} \rho_w d_B^3 \left(\frac{D\mathbf{v}_w}{Dt} - \frac{d\mathbf{v}_B^i}{dt} \right)}_{\text{added mass}} + \underbrace{\frac{3}{2} \rho_w d_B^2 (\pi v_w)^{1/2}}_{\text{Basset}} \\ &\times \underbrace{\int_{-\infty}^t \left(\frac{D\mathbf{v}_w}{Dt} - \frac{d\mathbf{v}_B^i}{dt} \right) \frac{d\tau}{(t-\tau)^{1/2}}}_{\text{history term}} + \underbrace{\frac{\pi}{6} \rho_w d_B^3 \frac{D\mathbf{v}_w}{Dt}}_{\text{pressure term}} \\ &- \underbrace{\frac{\pi}{6} d_B^3 (\rho_v - \rho_w) \mathbf{g}}_{\text{buoyancy}} + \underbrace{\sum_{j=1}^N \mathbf{F}_{ij}}_{\text{bubble-bubble interaction}}. \end{aligned} \quad (4)$$

In the current effort the aim is to combine the Lagrangian (bubble-based) model (4) and large eddy simulation (LES) in order to achieve more accurate simulations of cavitation water flows. The filtered continuity momentum for an isothermal 3D flow of water may be given as

$$\frac{\partial \bar{\rho}}{\partial t} + \nabla \cdot (\bar{\rho} \bar{\mathbf{v}}_w) = -S_v, \quad (5)$$

$$\begin{aligned} \frac{\partial \bar{\rho} \bar{\mathbf{v}}_w}{\partial t} + \nabla \cdot (\bar{\rho} \bar{\mathbf{v}}_w \bar{\mathbf{v}}_w) = & -\frac{1}{\rho_w} \nabla (\bar{\rho} \bar{p}) + \frac{1}{\rho_w} \nabla \cdot (\bar{\rho} \bar{\boldsymbol{\sigma}}) + \nabla \cdot \boldsymbol{\tau} \\ & + \bar{f}_{bw} + \bar{\rho} \mathbf{g}. \end{aligned} \quad (6)$$

The viscous stress tensor in (6) is defined as

$$\boldsymbol{\sigma} = -\frac{2}{3} \mu_w \nabla \cdot \mathbf{v}_w \mathbf{I} + \mu_w (\nabla \mathbf{v}_w + (\nabla \mathbf{v}_w)^T). \quad (7)$$

In (6), τ may be given as

$$\tau = -\bar{\rho}(\widetilde{\mathbf{v}_w \mathbf{v}_w} - \widetilde{\mathbf{v}_w} \widetilde{\mathbf{v}_w}) - \bar{\rho}(\widetilde{\mathbf{v}_w'' \mathbf{v}_w} + \widetilde{\mathbf{v}_w} \widetilde{\mathbf{v}_w''}) - \bar{\rho}(\widetilde{\mathbf{v}_w'' \mathbf{v}_w''}). \quad (8)$$

The SGS stress tensor, τ , is required to close the equations for the large-scale fields on a grid small enough (but much larger than the Kolmogorov scale) to provide reasonable resolutions. In contrast to the filtered single-phase equations, a conceptual restriction arising in the present approach is that the filter width, Δ , should strictly be larger than the length scale characteristic of the small bubbles. Thus, an appropriate choice of Δ should provide a sufficiently large-scale resolution while not violating the aforementioned restriction.

Following Sauer and Schnerr [9], the mass flow rate through the surface of a bubble with the radius of R , S_v , may be given as

$$S_v = 4\pi n_B R^2 \left(1 + \frac{4}{3}\pi n_B R^3\right)^{-2} \frac{\rho_w \rho_v}{\rho} \dot{R}. \quad (9)$$

Here, the changes in the bubble radius may be calculated using the famous Rayleigh-Plesset equation [6]

$$\frac{p_v + GT/R^3 - p_\infty}{\rho_w} - \frac{1}{\rho_w} \left(\frac{2\gamma}{R} + \frac{4\mu_w}{R} \dot{R} \right) = R\ddot{R} + \frac{3}{2}\dot{R}^2. \quad (10)$$

The vapor transport equation may be given as

$$\frac{\partial}{\partial t} (\phi_v \rho_v) + \nabla \cdot (\phi_v \rho_v \mathbf{V}_B) = S_v. \quad (11)$$

It is known that the presence of bubbles contributes to the processes of energy removal from the resolved scales of the liquid phase. This two-way coupling effect may be modeled by superposing bubble-induced SGS energy dissipation to that induced by shear. A tentative first attempt at closure, the momentum equation (6), may be closed with an SGS model for, τ , given as [10]

$$\begin{aligned} \tau_{\text{mod}} = & -\bar{\rho}(\widetilde{\mathbf{v}_w \mathbf{v}_w} - \widetilde{\mathbf{v}_w} \widetilde{\mathbf{v}_w}) \\ & + \bar{\rho} \left[2(C_s \Delta)^2 (\tilde{\mathbf{S}} : \tilde{\mathbf{S}})^{1/2} + (C_s \Delta) |\widetilde{\mathbf{v}_{\text{slip}}}| \right] \\ & \times \left(\tilde{\mathbf{S}} - \frac{1}{3} \text{tr} \tilde{\mathbf{S}} \mathbf{I} \right). \end{aligned} \quad (12)$$

Here, the value of the backscatter parameter, C_{b0} , is set to $C_{b0} = 0.2$. The model for τ has been validated for dense gas-particle flows [11–13].

During each time step of the simulation, the forces acting on each particle should be calculated. This requires knowledge of the local values of the fluid velocity components at the position of the bubbles. These variables are only known at spatial grid points in the computational domain. A tricubic interpolation has been used for calculating the fluid velocity components at the centers of the bubbles. The bubbles are propagated using the generalized Verlet algorithm, whose parallelization for the GPU is described in detail in [10].

3.3. Simulation Results

3.3.1. Air Bubbles. Figures 4(b) and 4(c) show a computed large bubble in an aerated tank [7]. The bubble is a cluster of small bubbles with a size of the critical air bubble radius. Figure 4(d) depicts the denoised version of the bubble using multiscale image denoising based on a multiscale representation of the images [14]. The denoised version of the bubble-like structure in Figure 4(b) is very similar to the small bubbles observed in an aerated tank [7].

Figures 4(e) and 4(f) are snapshots of bubbles separated by $t = 0.3$ sec. As can be seen from Figure 4(f), three bubbles in Figure 4(e) coalesce to form one large bubble. The denoised version depicted in Figure 4(g) is very similar to the bubbles with complex geometries shown in [7].

To further assess the quality of the model described in the preceding section, the cavitation water flow in Figure 3 is simulated in the following section.

3.3.2. 3D Model Using 2D Images. Apparently, it is not possible to reconstruct a 3D model from a single image of the stone as shown in the inset of Figure 5(a). To get around this limitation, an optical processing algorithm can be developed that employs multiple photographs taken at every 15 degrees, from the above and from the side to create a 3D model of the stone. Figure 5(a) illustrates the positions of the camera for taking about 40 photographs of the stone. The images acquired are the input of the Autodesk 123D Catch 3D scanning software [15].

Figure 5(b) shows the basics of the stitching process for the accurate creation of a 3D model of the stone. Figure 5(c) represents a medium quality 3D mesh of the stone which is used to simulate sheet cavitation in the following section.

3.3.3. Sheet Cavitation

Aspects of the Simulation. As mentioned earlier, turbulence modeling has a critical role in cavitation prediction. Cavitation flow in the liquid-vapor region is locally compressible [9, 16]. To capture the shedding dynamics and the unsteadiness of cavitation the modified form of LES as detailed in the preceding section would be required. Note that (5) and (6) look like the equations of motion of a fluid with variable density $\rho = \rho_w(1 - \phi_v)$.

In this section, the mathematical model described in the preceding section will be used to analyze sheet cavitation in a pipe flow as shown in Figure 3. The discharge was set to $Q = 12.5$ L/s. The tube inner diameter was $D = 0.024$ m and its length was $L = 0.3$ m.

The length and the height of the stones in the simulations are exactly the same as those used in the experiments. The model of the stone is shown in Figure 5(c). It is likely that cavitation as shown in Figure 3(b) starts at minute cracks on the otherwise smooth surface of the stones. The aforementioned system may be characterized as belonging to the singular roughness category [1].

In brief, the Lagrangian (bubble-based) and the Eulerian (grid-based) methods are used to simulate the cavitation

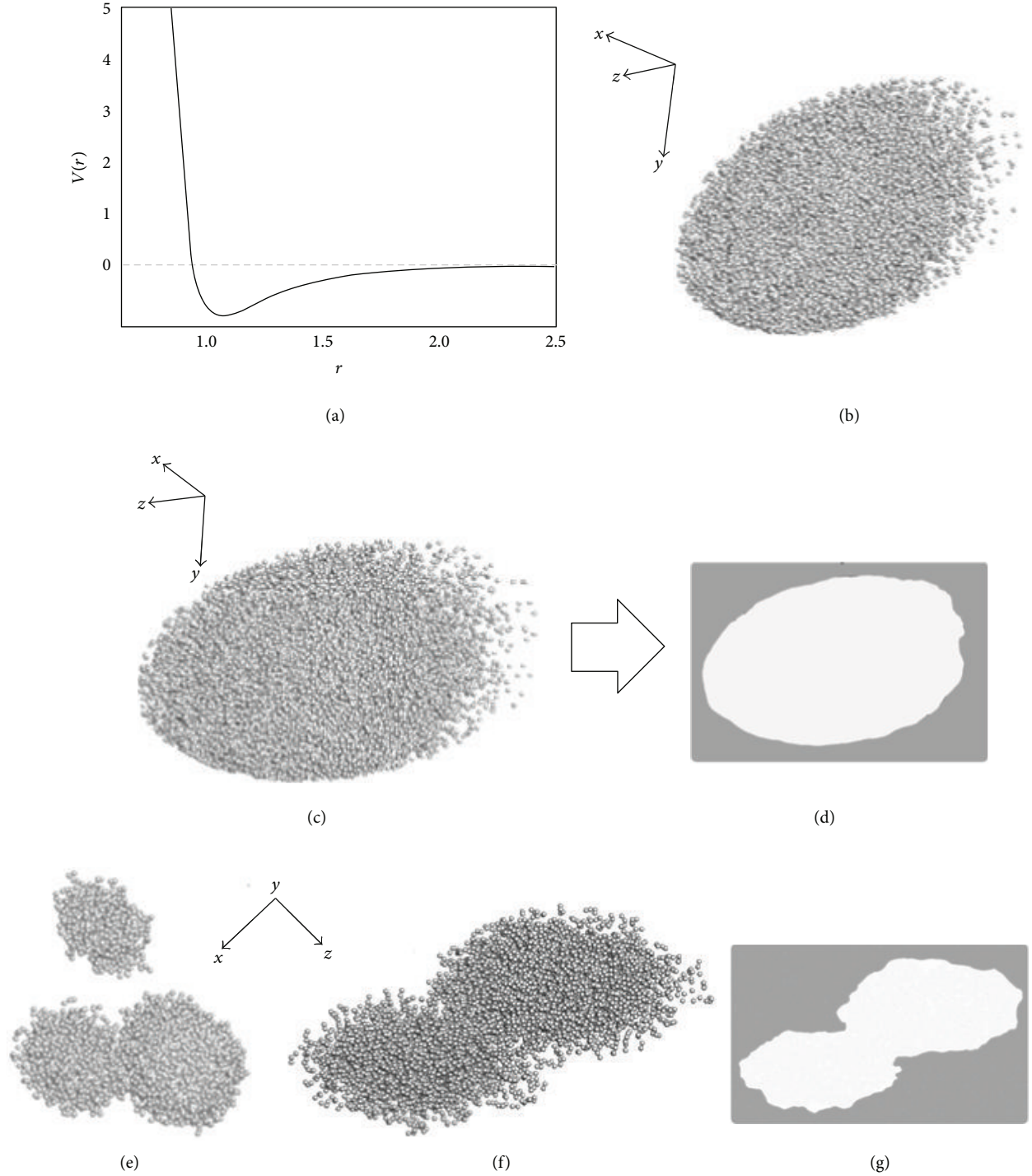


FIGURE 4: The interaction of small bubbles in an aerated tank. (a) The Lennard-Jones 12-6 pair potential. (b) Computed bubble-like structure in an aerated tank at the Reynolds number of 29500. (c) A different view of (b). (d) The denoised version of (c). The length of the bubble is approximately 1 cm and its height is 0.65 cm. (e) Configuration of a three bubble-like structure in an aerated tank. (f) The bubbles in (e) coalesce to form a larger bubble after 0.3 sec. (g) The denoised version of (f).

singular roughness in a tube flow. Figure 6(a) illustrates the model used in the simulations. Here, the dimensions are $L_p = 0.3$ m, $D = 0.024$ cm, and $h_s = 0.004$ m. Figure 6(b) depicts a top view of the entrance region of the pipe in which the positions of the stones are clearly shown. The total length

of the pipe covered by stones is $l_2 = 0.037$ m, and the pipe's length covered by the first stone is $l_1 = 0.0185$ m. The length and height of the stones are exactly the same as those shown in Figure 3(a). Figure 6(c) shows the grid which consists of more than 5×10^6 tetrahedral meshes.

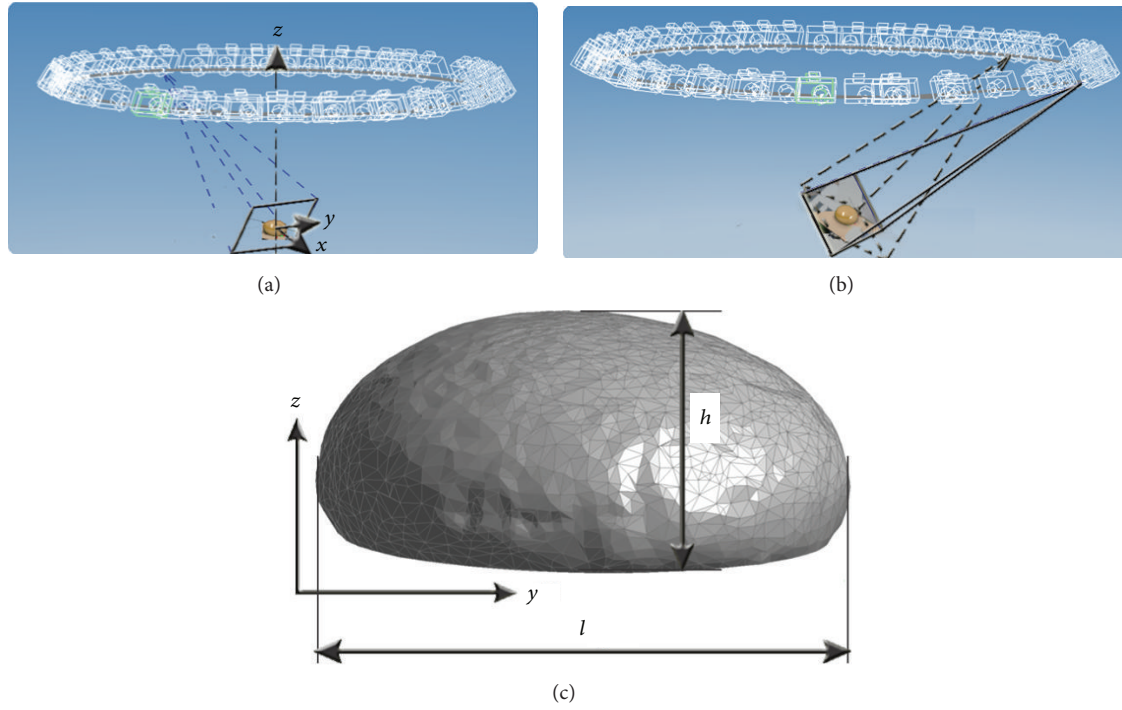


FIGURE 5: A CFD model for a stone in Figure 3. (a) Taking 2D images of the stone by moving camera's position at regular intervals. (b) Automatically aligning the images with the others. (c) Reconstruction of a 3D model from 2D image.

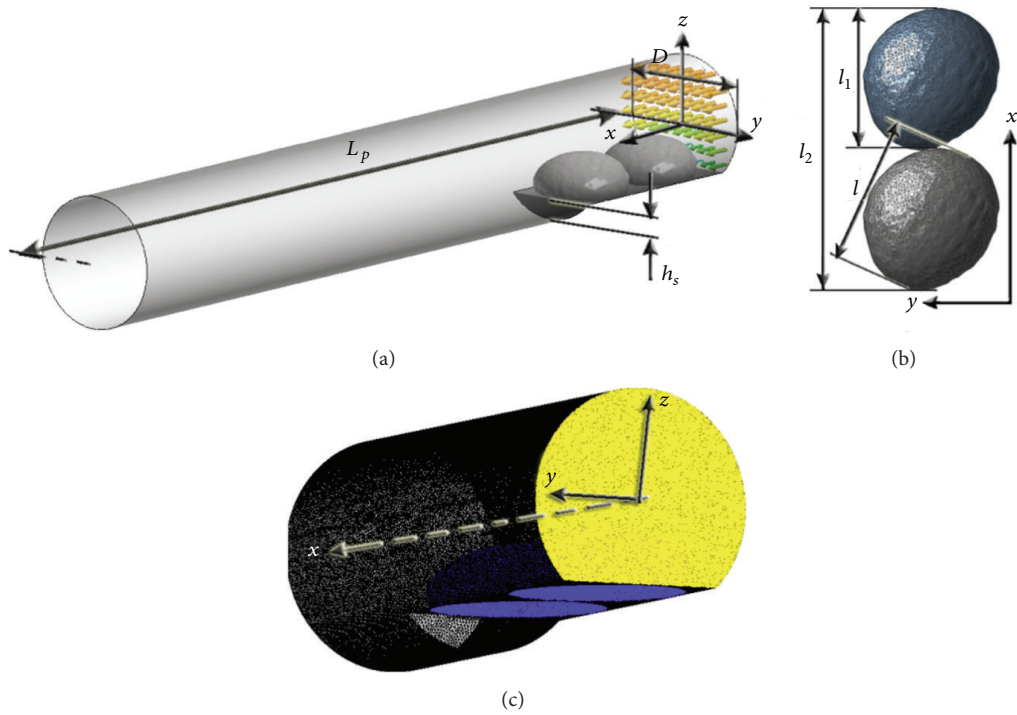


FIGURE 6: A CFD model for the tube in Figure 3. (a) Schematic of the pipe used in sheet cavitation simulations with some nomenclatures. (b) A top view of the entrance region of the pipe. (c) The grid used in the cavitation simulations. Insets: the grid is magnified and replotted.

The filtered Navier-Stokes equations (5) and (6) are discretized with the finite-volume method on a staggered Cartesian grid. Convective and diffusive fluxes are approximated with central differences of second-order accuracy and time advancement is achieved by a second-order, explicit Adams-Bashforth scheme. The equation for coupling the pressure to the velocity field is solved iteratively using the SIP method [17]. The subgrid-scale stresses appearing in the filtered Navier-Stokes equations are computed using (12). No-slip boundary conditions are employed on the surface of the stone and the tube walls. The physical properties used in the simulations are listed in Table 1. The temperature was assumed to be constant and it was set to $T = 302$ K. Note that the vaporization pressure [18] at that temperature is 4500 Pa (absolute). The acceleration due to gravity is $g = 9.81$ m/s².

The Lagrangian (bubble-based) simulation was performed to calculate the motion of bubbles in the liquid using (4). In brief, equivalent spherical bubbles were determined from irregular vapor structure by marking the cells with $\phi_w < 0.95$. Equation (4) was integrated using the generalized Verlet algorithm. The time step used in the simulation was $\Delta t = 5 \times 10^{-7}$ s. The linear interpolation routines were used to communicate the information from grid nodes to particle positions and vice versa. The simulations were performed by using GPU computing [10].

Results. Obviously, a single parameter such as the cavitation number cannot describe many of the complexities of cavitation. Falvey [1] suggested that for flow past stones as shown in Figure 7(a), cavitation will not occur if the cavitation number is greater than about 1.8. Figure 7(a) shows that cavitation bubbles form within the flow at the discharge $Q = 12.5$ L/s. This indicates that the cavitation number was below 1.8. Figure 7(b) represents a view from below of an instantaneous configuration of bubbles in the cavitation water flow. In this case, a sheet consists of a large number of small bubbles which are extensively developed downstream of the step formed by the stones in the pipe. Here, cavitation is formed by turbulence in the shear zone which is produced by the sudden change of flow direction at the stone face. Figure 7(b) also shows large nonspherical cavities with patterns similar to those shown in Figure 3(b).

Following Falvey [1], it may be estimated that the system in Figure 7(a) operates at a cavitation number of $\sigma_h = 0.9$. For this case, the reference location is immediately upstream of the first stone and at its maximum height. The computed length of the sheet is quite comparable with that shown in Figure 3(b). It would be expected that for even lower values of the cavitation number, the clouds form one long supercavitating pocket.

Figure 7(c) depicts the computed instantaneous contours of the averaged vapor volume fraction in the xz -plane. In this figure, the locations at which cavitation occurred on the surfaces of the stones are presented by the use of color coding. As can be seen from Figure 7(c), the process starts with the occurrence of swarm of bubbles in the small regions of the first stone at sampling port 3 located at $x = 0.015$ m. However, no evidence of cavitation can be found at sampling port 4 located at $x = 0.022$ m in a narrow cleft between the stones

where the local pressure is much higher than that of the vapor pressure. This figure also shows that a large number of small bubbles are extensively produced on the trailing edge of the second stone close to sampling port 8 located at $x = 0.045$ m. Sampling ports 1 through 16 are all located in the xz -plane. The distances of these ports from the inlet of the pipe are $x = 5 \times 10^{-5}$, 0.0077, 0.015, 0.022, 0.025, 0.029, 0.035, 0.045, 0.055, 0.065, 0.09, 0.12, 0.2, 0.25, 0.29, and 0.298 m, respectively.

Figure 7(d) illustrates the averaged vapor volume fraction, $\bar{\phi}_v$, as a function of the vertical distance from the pipe wall, l_w , at sampling ports 1 through 4. Here, the squares, circles, diamonds, and left triangles represent the computed vapor volume fraction at ports 1, 2, 3, and 4, respectively. This figure indicates the occurrence of a swarm of bubbles at sampling port 3.

The squares, circles, diamonds, and left triangles in Figure 7(e) represent variations of $\bar{\phi}_v$ as a function of l_w at sampling ports 5, 6, 7, and 8, respectively. This figure indicates that cavitation reoccurred at sampling port 7 and became extensive at port 8. These complexities cannot be described with a single parameter such as cavitation number.

Figure 7(f) shows variations of $\bar{\phi}_v$ as a function of l_w at sampling ports 9, 10, 11, and 12 using the squares, circles, diamonds, and left triangles, respectively. As can be seen from Figure 7(f), the vapor bubbles roll up into a larger volume and become cloudy as they are transported further downstream and leave the entrance region of the pipe.

Figure 7(g) represents the final stage of the process which is an ongoing process of bubble formation and deformation. This figure depicts variations of $\bar{\phi}_v$ as a function of l_w at sampling ports 13, 14, 15, and 16 using the squares, circles, diamonds, and left triangles, respectively.

In brief, the appearance of visible cavitation in the flowing water in the pipe as shown in Figure 7 was preceded by the occurrence of small bubbles in the small area on the surface of the stones. This observation highlights the importance of bubbles as cavitation nuclei which has been known for a long time [6].

Figure 7(d) indicated that a swarm of small bubbles occurred at sampling port 3. However, no evidence of cavitation was found at sampling port 4 which was located further downstream from port 3. To address this issue, the pressure field is illustrated in the xz -plane in Figure 8(a). Here, the dimensionless pressure Π^* is defined as $\ln(p)/\ln(p_v)$, where p represents the local pressure. Figure 8(b) depicts variations of the dimensionless pressure p^* (defined as p/p_v) as a function of l_w at sampling ports 1, 2, 3, and 4 using the squares, circles, diamonds, and left triangles, respectively. This figure indicates that the local pressure in the narrow cleft between the stones is approximately 50 times higher than that of the vapor pressure.

Figure 8(c) illustrates variations of the dimensionless pressure, p^* , as a function of l_w at sampling ports 5, 6, 7, and 8 using squares, circles, diamonds, and left triangles, respectively. As can be seen from this figure, the local pressure at port 7 on the surface of the second stone reached the vapor pressure. Consequently, the small bubbles were formed on the trailing edge of the second stone as shown in Figure 7(e). The

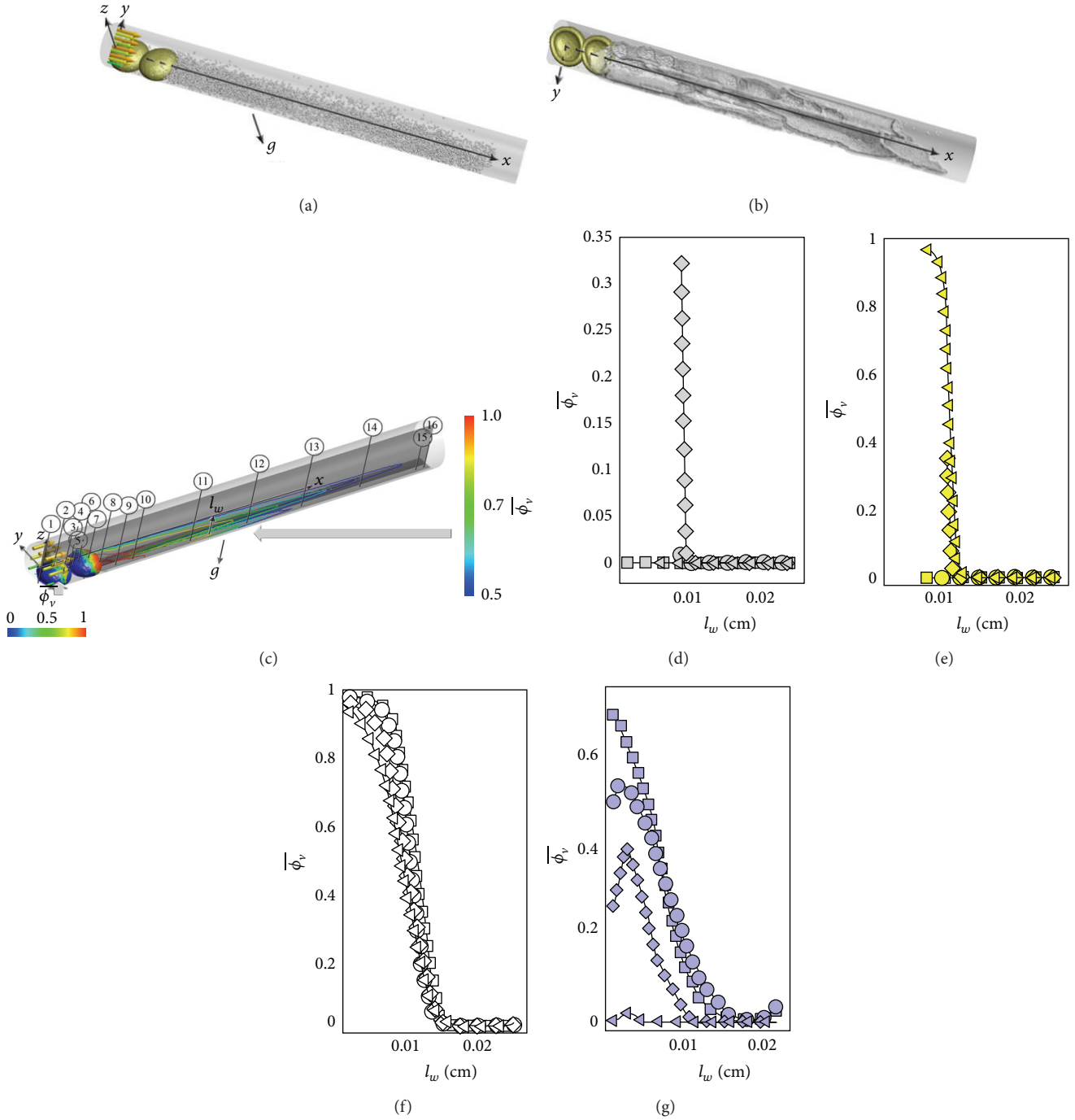


FIGURE 7: Computer experiments at a cavitation number of $\sigma_h = 0.9$ in a duct. (a) A top view of the instantaneous configuration of bubbles in a cavitating water flow of water through a pipe with inner diameter of $D = 0.024$ m at the discharge of $Q = 12.5$ L/s and at the cavitation number of $\sigma_h = 0.9$. (b) A view from below of the bubbles in the cavitating flow of water through the pipe. Here, the large cavities consisting of small individual bubbles are illustrated. (c) Computed contours of the averaged vapor volume fraction on the xz -plane for the cavitating water flow in (a). Here, a color code as illustrated below the stones is used to indicate the values of the averaged vapor volume fraction on the surfaces of the stones. (d)–(g) Variations of $\bar{\phi}_v$ as a function of l_w at the sampling ports 1 through 16, respectively.

appearance of visible cavitation as shown in Figure 7(a) was preceded by the occurrence of these bubbles in the small area around sampling port 5 on the surface of the second stone. The computed low pressure at port 8 (which is the same as

that measured at the PMP in Figure 3(a)) provides a favorable situation for a sheet, which consists of a large number of small bubbles, to be developed and transported downstream as depicted in Figures 7(a) and 7(b). The low pressure condition

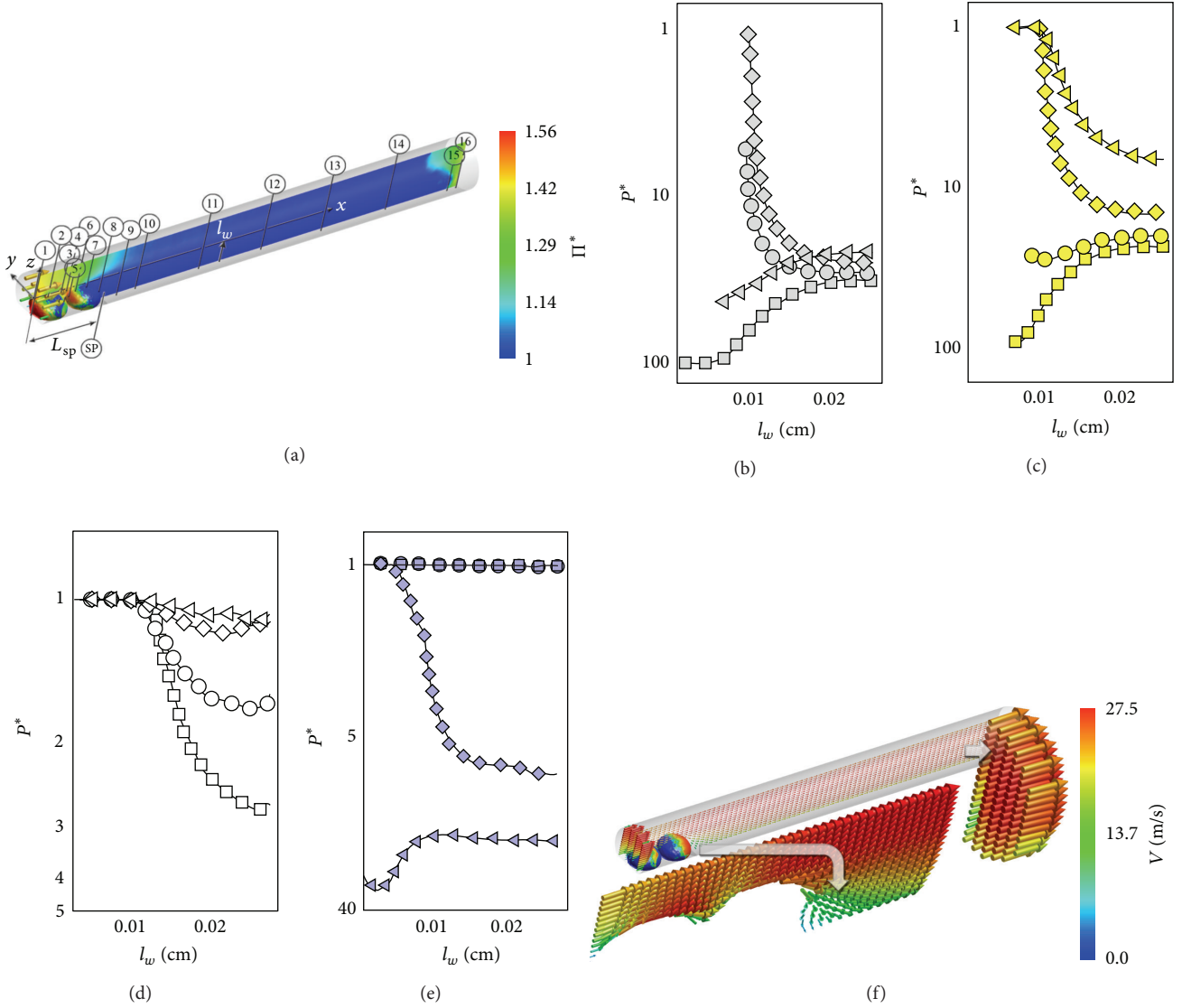


FIGURE 8: Cavitation in a tube. (a) The instantaneous computed contours of the dimensionless pressure Π^* on the xz -plane bubbles in a cavitation flow of water at the cavitation number of $\sigma_h = 0.9$. The locations of the sampling ports are the same as those in Figure 7(c). (b)–(e) Variations of the dimensionless pressure p^* as a function of l_w . (f) The instantaneous computed velocity field of a cavitating water flow through the pipe with inner diameter of $D = 0.024$ m at the discharge of $Q = 12.5$ L/s.

extends from sampling port 9 to sampling port 14 as shown in Figures 8(d) and 8(e). The squares, circles, diamonds, and left triangles in Figure 8(d) represent variations of p^* as a function of l_w at sampling ports 9, 10, 11, and 12, respectively.

In the aforementioned region the vapor bubbles roll up into a larger volume and become less extensive as they are transported further downstream. The volume fraction of the vapor bubble is lower at the upper part of the pipe between ports 9 and 14 due to the fact that the pressure slightly increases with l_w .

The squares, circles, diamonds, and left triangles in Figure 8(e) represent variations of p^* as a function of l_w at sampling ports 13, 14, 15, and 16, respectively. This figure indicates that the pressure increased from ports 14 to 16 and

reached the atmospheric pressure at the pipe outlet at which the vapor bubbles vanished.

The area-weighted average pressure at the inlet of the pipe was found to be 257 kPa. The results show agreement between simulation and experiment. The model is therefore deemed to be sufficiently flexible to capture a number of the interesting qualitative features of the cavitation process.

Figure 8(f) shows the computed velocity vector field in the xz -plane. This figure indicates a complex shearing flow around sampling port 8 at which cavitation was formed. As stated earlier, the system in Figure 7(a) operates at a cavitation number of $\sigma_h = 0.9$. Note that the computed pressure at sampling port 1 immediately upstream of the first stone and at its maximum height is approximately 300 kPa. In this case,

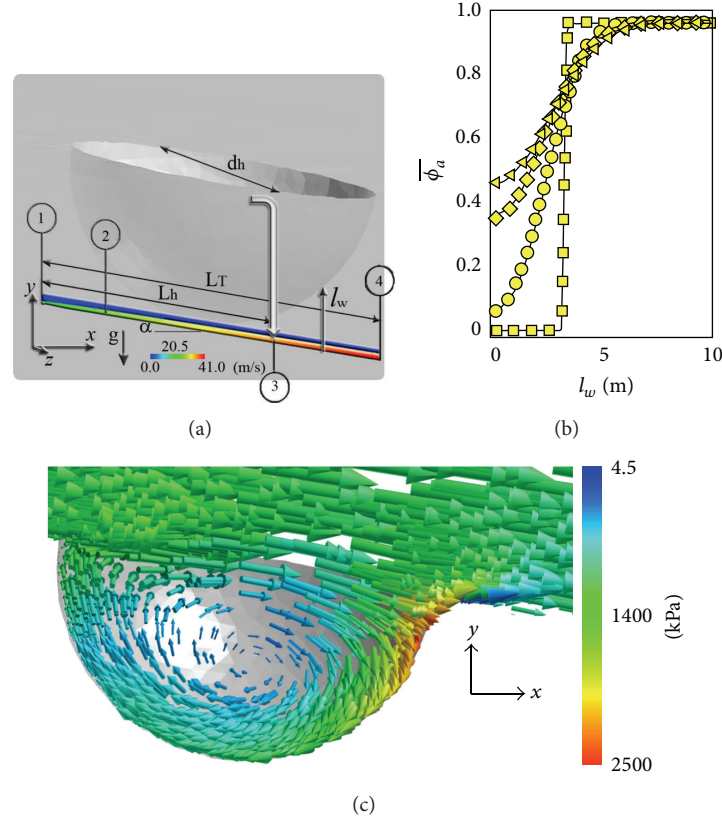


FIGURE 9: Cavitation in a spillway chute. (a) Schematic of a hypothetical hole with a diameter $d_h = 0.02$ on the surface of a model of Kárahnjúkar spillway at a distance from the inlet of $L_h = 300$ m. The total length of the spillway is $L_T = 414$ m and its slope is $\alpha = 11^\circ$. Inset: the computed contours of velocity in the spillway. The distances of the sampling ports 1, 2, 3, and 4 from the inlet are 0, 107, 300, and 414 m, respectively. (b) The averaged air volume fraction as a function of l_w at the sampling ports 1, 2, 3, and 4. Here, the squares, circles, diamonds, and left triangles represent the air volume fraction at the sampling ports 1 through 4, respectively. (c) The computed velocity vector field around the hole at the sampling port 3. Here, a color code as illustrated on the left-hand side of the hole is used to indicate the values of the local pressure.

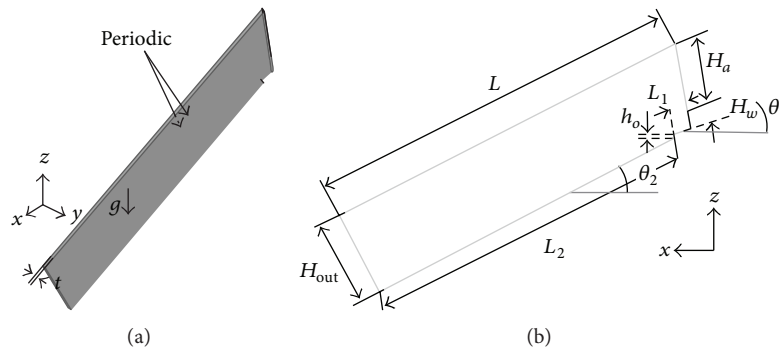


FIGURE 10: A CFD model for the Kárahnjúkar bottom aerator. (a) Perspective view of the simulation model and selected nomenclature. (b) The front view of the spillway with bottom aerator. Here, $\delta = 0.02$ m, $L = 2.42$ m, $H_a = 0.44$ m, $H_w = 0.11$ m, $L_1 = 0.11$ m, $L_2 = 2.15$ m, $h_0 = 0.022$, $H_{out} = 0.55$ m, $\theta_1 = 20^\circ$, and $\theta_2 = 30^\circ$.

the computed average water velocity is 25 m/s. The area-weighted average pressure at the inlet of the pipe was found to be 257 kPa.

In the following section, the model is employed to check the reliability of the predicted cavitation zone as shown in Figure 2.

3.3.4. Cavitation in a Spillway Chute. The previous section described the complexity of the occurrence of cavitation. As stated earlier, Figure 2 indicates that the cavitation number should be quite low at approximately 135 m from the end of the chute of Kárahnjúkar spillway. Apparently, the designers of the Kárahnjúkar spillway decided to use an aerator at that

location (as shown in Figure 1) in order to protect the spillway surface from cavitation.

Recall that Semenov and Saranchev [19] suggested that the beginning of the spillway is the cavitation-hazardous section. Particularly for large discharges, natural air entrainment is absent in more than 60 m from the inlet [19]. The bottom turbulent layer is shielded above by the undisturbed potential flow core, which reduces diffusion air entrainment [19]. Consequently, on the entire length of the cavitation-hazardous section of the spillway passage the volume air concentration in the boundary layer with thickness 0.2–0.25 m would be less than 7–8%. In this case, artificial air entrainment is needed to protect the surface of the spillway [20].

In this section, the usefulness of using artificial air at 125 m from the end of the chute of the Kárahnjúkar spillway is investigated using the mathematical model as detailed in the preceding section. To this end, a simplified model of Kárahnjúkar spillway with a hypothetical hole with diameter of 0.02 m is used in the simulation. Figure 9(a) shows the hypothetical hole which is essential to initiate cavitation at the cavitation number of 0.25. The simplified model of Kárahnjúkar spillway is 414 m long with a slope of approximately $\alpha = 11^\circ$.

The inlet boundary condition at $x = 0$ was set to $V = 20$ m/s. The height of the water at the inlet was 3 m. Furthermore, it was assumed that the top surface of the model is open to the atmosphere. The outlet boundary condition was set to $p = p_{\text{atm}}$. Periodic boundary conditions were used in the z -direction. The no-slip boundary condition was applied on the walls of the model. To capture the effects of viscous boundary layers, a wall-function was used to specify velocity at the forcing points as [21]

$$\frac{u}{u_*} = \begin{cases} y^+ & y^+ \leq 5 \\ -1.15576 + 1.47869y^+ & 5 < y^+ \leq 30 \\ -0.0527848y^{+2} + 0.000655444y^{+3} & 5 < y^+ \leq 30 \\ \frac{\ln(y^+)}{K} + 5.1 & y^+ > 30, \end{cases} \quad (13)$$

where y^+ represents dimensionless, sublayer-scaled distance, and K is the von Kármán constant (typically the value 0.41 is used).

The inset of Figure 9(a) represents the computed velocity contours in the model of the Kárahnjúkar spillway. The computed bubble volume fraction as a function of vertical distance from the wall l_w at four sampling ports is illustrated in Figure 9(b). In this case, the bubble is an air bubble which may contain vapor. As can be seen from Figure 9(a), the hypothetical hole is located at 135 m from the outlet of the model. Figure 9(b) indicates that the thickness of the air-water mixture increases with x . Here, the squares, circles, diamonds, and left triangles represent the bubble volume fraction at sampling ports 1, 2, 3, and 4, respectively. As can be seen from Figure 9(b), the bubble volume fraction at

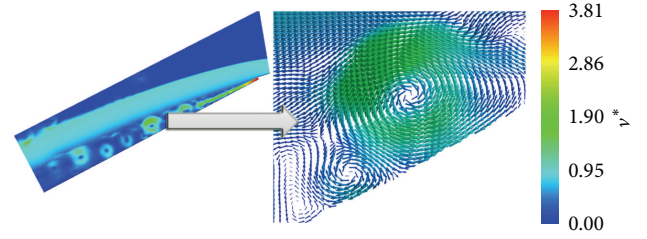


FIGURE 11: Computed contours of the velocity field for the bottom aerator of Kárahnjúkar spillway. Inset: a pair of vortices in the ventilation zone.

sampling port 2 is lower than 7%. This finding highlights the need of artificial aerators between sampling ports 1 and 2 in order to protect the surface of the spillway.

Figure 9(b) indicates that the bubble volume fraction at the hypothetical hole (i.e., at sampling port 3) is approximately 38% which is in accordance with Semenov and Saranchev [19] and very much above the “cavitation safe” value of 7% of entrained air. In this case, the vapor volume fraction is quite low.

Figure 9(c) illustrates the computed velocity vector field. A color code as illustrated on the left hand side of the hole in Figure 9(c) is used to indicate the values of the local pressure. This figure indicates that the water flows mainly over the hole. A small part of the water stream hits the hole’s face and reticulates inside the hole. As can be seen from Figure 9(c), the pressure reaches a maximum of 2500 kPa and diverts the flow to an upward direction over a little edge and in a downward direction which initiates the water swirl in the hole. The local pressure in the center of the hole is slightly lower than 5 kPa. This finding indicates that cavitation might occur at 125 m from the end of the chute of the Kárahnjúkar spillway. Indeed, cavitation will occur for the flow past the sudden into-the-flow offset introduced by the hypothetical hole as noted in Figure 9(c). This figure indicates a low-pressure region and thus potential cavitation might also occur shortly after passing the hole’s edge. However, the air volume fraction at the hole as shown in Figure 9(b) is approximately 38%. This finding suggests that the use of an aerator at port 3 in order to protect the surface of the spillway might not be needed. Adding extra air at sampling port 3 would produce a very thick air-water mist flow at the outlet of the spillway. This will be further analyzed in the following section.

Figure 9(b) also indicates that in the absence of an artificial aerator the computed thickness of the air-water mixture at the outlet of the spillway is approximately 8 m. In addition, the average bubble volume fraction is higher than 50%.

3.3.5. Artificial Aeration. The designers of the Kárahnjúkar spillway were challenged in their task due to the lack of literature on air entrainment for spillways. As mentioned in the preceding section, an aerator must be introduced to prevent cavitation in the Kárahnjúkar spillway at high discharges. The air volume fraction in the spillway downstream from sampling port 2 in Figure 9(b) is well above the 7%

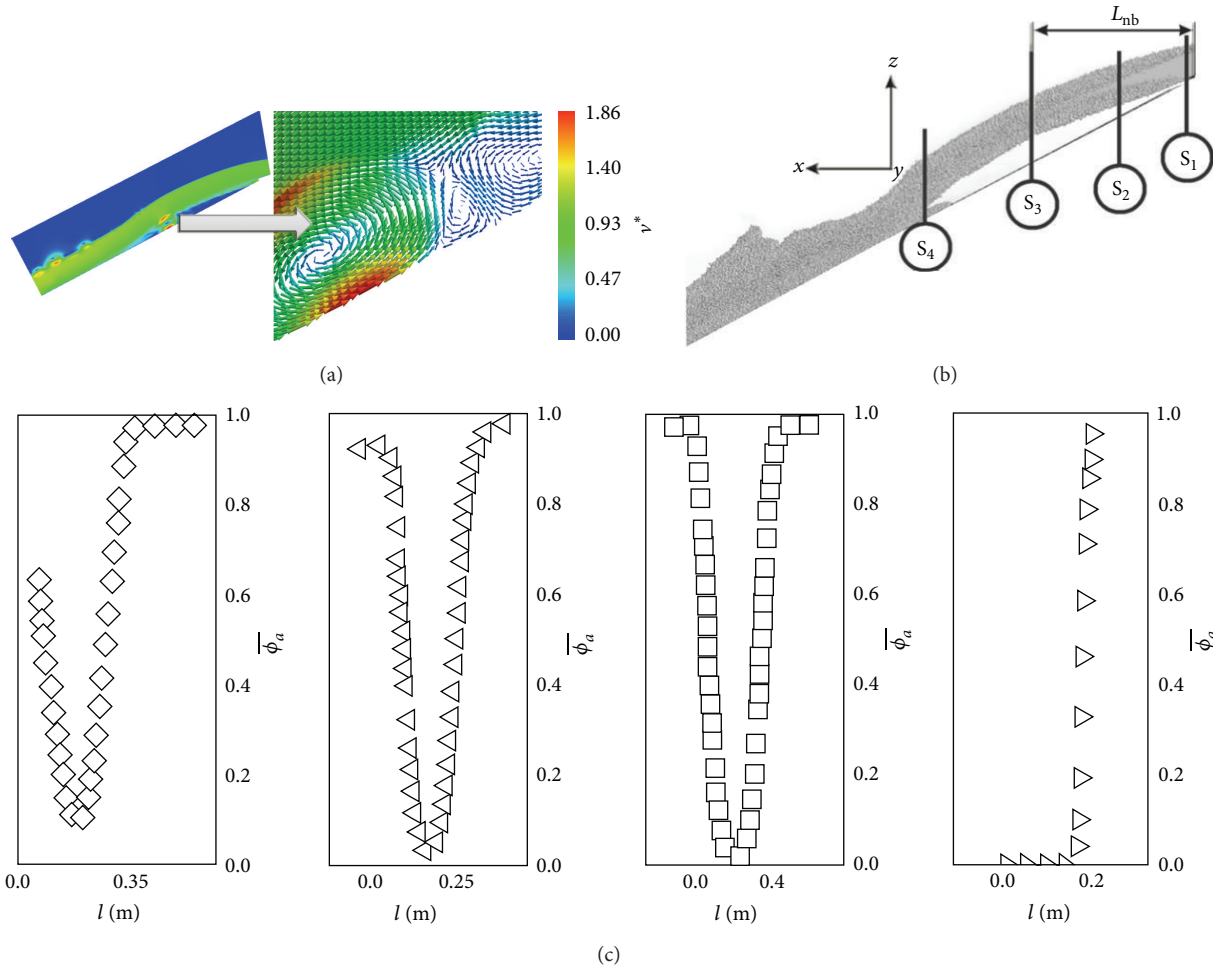


FIGURE 12: The computed flow field for the aerator of Kárahnjúkar spillway. (a) Computed contours of velocity field of a more optimized design for the aerator of Kárahnjúkar spillway. Inset: vortical structures in the ventilation zone. (b) Instantaneous configuration of bubbles in a spillway with ski jump aerator. Here, $L_{nb} = 0.62$ m. (c) Air concentration distribution versus z in the aeration region. Here, right triangles, squares, left triangles, and diamonds represent the air concentration at the sampling ports S_1 , S_2 , S_3 , and S_4 , respectively.

minimum requirement of its protection against cavitation. Hence, artificial aeration would only be needed between sampling ports 1 and 2 illustrated in Figure 9(a).

In this section, the mathematical model described in the preceding section will be used to analyze the Kárahnjúkar spillway with a bottom aerator. Figure 10 illustrates a CFD model which can be imagined as a 1:15 Froude scale of the Kárahnjúkar bottom aerator. Figure 1 shows an aerial view of the Kárahnjúkar spillway and its bottom aerator located in eastern Iceland.

By implementing periodic boundary conditions in the y -direction, a small part of the system that is far from the vertical side walls was simulated. The model flow rate was set to $v_{w0} = 20$ m/s at the inlet with a size of $H_w = 0.11$ m, corresponding to $Q = 2250$ m³/s.

As can be seen from Figure 11, the water stream is deflected by a deflector in order to ventilate the nappe to the atmosphere. The connection to the atmosphere is made via a channel under the ski jump of the aerator. Note that the air entraining capacity of the aerator depends on the take-off

distance from the free flow. The air pressure is atmospheric at the inlets and the outlet.

Figure 12(a) and its insets illustrate the computed contours and vector velocity field of a more optimized design for the aerator of the Kárahnjúkar spillway. Here, vortices can be seen to be created at the ventilation gate and to detach periodically from its other side. A pair of vortices is magnified and replotted in the inset. The air enters the ventilation zone with a normalized velocity of $v^* = 3.81$. Here, the velocity is normalized with the water velocity at inlet v_{w0} . Figure 12(b) represents an instantaneous configuration of bubbles in the spillway with an optimized bottom aerator. The high stream of air tends to move the water stream up. In this case, the air concentration in the ventilated zone appears to be more than that needed to prevent cavitation. Figure 1 shows a highly aerated water stream which is likely to serve as a source for an intense canyon erosion.

When water flows over a spillway, vortex sheet instability at the air-water interface known as Kelvin-Helmholtz instability can occur. The instability will be in the form of

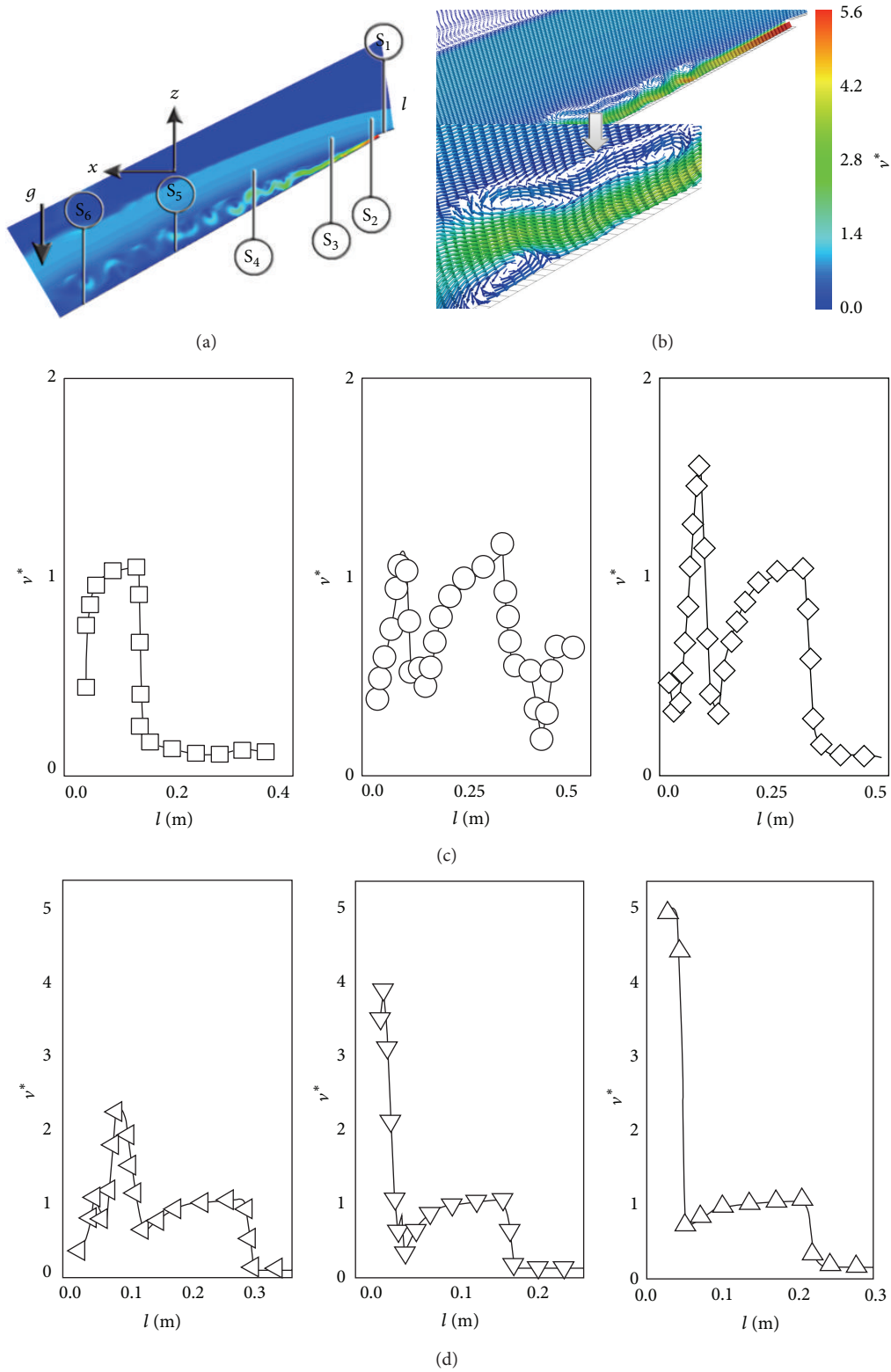


FIGURE 13: The computed flow field for a hypothetical case with a discharge of $Q = 3150 \text{ m}^3/\text{s}$. (a) Computed contours of velocity field. (b) Computed vector plot of vertical structures in the ventilation zone. (c) and (d) Variations of the normalized velocity v^* as a function of z . Squares, circles, diamonds, left triangles, gradients, and deltas represent the normalized velocity at the sampling ports S_1 , S_6 , S_5 , S_2 , S_3 , and S_4 , respectively.

waves being generated on the water surface which can initiate natural air entrainment.

The air entrainment process is strengthened when a growing boundary layer in the water flow reaches the free surface. In this case, the entrained air from the free surface can reach the spillway surface to minimize the danger of cavitation. As can be seen from Figure 12, the details of air entrainment through the upper air-water interface of the jet can be predicted by the model. In addition, the details of air entrainment through the lower interface are very similar to those presented in [10]. Here, L_{nb} represents the length at which the air entrainment through the lower interface reaches that through the upper interface. Figure 12(c) depicts the variations of air concentration as a function of z at four different sampling ports as shown in (b).

The region at which the natural air entrainment effectively eliminates the risk of damage due to cavitation is called the fully aerated region. The artificial aeration process discussed above would not be needed in the fully aerated region.

Figure 13(a) illustrates the computed contours of the velocity field for a hypothetical case in which the discharge of the Kárahnjúkar spillway is $Q = 3150 \text{ m}^3/\text{s}$. Figure 13(b) indicates that the air enters the ventilation zone with a normalized velocity of $v^* = 5.6$. The vortex shedding of the aeration gate is quite intense. Therefore, the air-water mixture entering the canyon could cause extensive erosion. Recall that the canyon shown in Figure 1 suffered a disastrous erosion in 2009.

4. Conclusions

A previous study revealed that the cavitation number of the Kárahnjúkar spillway is below 0.25 at a discharge of $2250 \text{ m}^3/\text{s}$. Hence, the spillway was protected by additional aeration grooves located some 300 m from its inlet. In this work, an analysis of the problem based on physical and computational fluid dynamics (CFD) modeling is presented. The numerical modeling is based on the large eddy simulation technique (LES) combined with the discrete element method.

A three-dimensional simulation of a cavitation tube flow at cavitation number of ca. 0.9 was performed to highlight the importance of artificial aeration for protecting a spillway. More simulations were performed using a CFD model which is a 1:15 Froude scale of the Kárahnjúkar bottom aerator in order to gain insights into how to diminish the hazards associated with cavitation and minimize canyon erosion. It is recommended to use the artificial aerators only at the distances less than 100 m from the inlet in order to minimize canyon erosion.

The main finding was that the design of the aerator of the Kárahnjúkar spillway should be improved. It is highly unlikely that the artificial aerators would be needed at the distances of 300 m from the inlet of the spillway.

Nomenclature

Ac : Archimedes number
 C_{b0} : Backscatter parameter

C_D : Drag coefficient of the bubble, which is a function of the Reynolds number of the bubble
 C_p : Pressure coefficient
 C_s : Smagorinsky constant, given as $C_s = 2\pi/3\sqrt{3}(-R(1 + C_{b0}R^2)/K^3)^{1/2}$
 D : Pipe diameter
 d_B : Bubble diameter
 d_h : Hole diameter
 F : Force between two bubbles
 f_{bw} : Forces exerted by the liquid on the bubbles per unit volume
 h : Height of aquarium stone
 h_s : Step height
 G : Gas constant
 g : Gravitational acceleration
 \mathbf{I} : Second-order identity tensor
 K : Kolmogorov constant
 L_c : Length of the sheet
 L_h : Distance of the hole from the inlet
 L_m : Axial distance of the pressure measuring port for the pipe inlet
 L_p : Pipe length
 L_t : Total length of spillway chute
 l : Length of aquarium stone
 l_1 : Length of the stone in the axial direction
 l_2 : Total length of the region covered by stones
 l_w : Vertical distance from the pipe wall
 n_B : Bubble number density
 P^* : Dimensionless pressure defined as $P^* = \bar{p}/p_v$
 p_v : Vapor pressure at ambient temperature
 $p_{\infty}^{(0)}$: Constant in (1)
 p_{∞} : Ambient pressure in the fluid at a large distance from the bubble
 \bar{p} : Filtered pressure
 Q : Discharge
 R_{critical} : Bubble critical radius
 r_i : Location of the i th bubble
 r_{ij} : Distance between the centers of two bubbles
 R_E : Bubble equilibrium radius
 Re_B : Bubble Reynolds number defined as $Re_B = |\mathbf{v}_B^i - \mathbf{v}_w|d/\nu_w$
 R_k : Ratio of the mesh spacing and the Kolmogorov length scale, so that $R_k = -1 + (\eta/\Delta)^{4/3}$
 R : Bubble radius
 \dot{R} : Bubble interface velocity
 \bar{S} : Resolved rate of strain tensor
 S_v : Source term in (5) to account for the mass transfer between liquid and vapor phase
 T : Temperature
 t : Time
 V : Mixture velocity
 \mathbf{v}_B^i : Velocity of the i th bubble with a diameter d_B

- v_w : Water velocity in absence of the bubble
 \mathbf{v}_w'' : Subgrid-scale part of \mathbf{v}_w based on Favre filtering
 $\widetilde{\mathbf{v}_w}$: Density-weighted Favre filter velocity defined as $\widetilde{\mathbf{v}_w} = \overline{\rho \mathbf{v}_w} / \bar{\rho}$
 \mathbf{v}_{slip} : Slip velocity
 v^* : Normalized velocity.

Greek Symbols

- α : Chute angle for chute slope
 Δ : Filter width
 ε : Constant in (3)
 γ : Surface tension
 μ_w : Dynamic viscosity of water
 Π^* : Dimensionless pressure defined as $\Pi^* = \text{Ln}P / \text{Ln}P_v$
 $\bar{\rho}$: Filtered density defined as $\bar{\rho} = \rho_w \overline{\phi_w}$
 ϕ : Bubble volume fraction
 ϕ_v : Vapor volume fraction defined as $\phi_v = (4/3)\pi n_B R^3 / (1 + (4/3)\pi n_B R^3)$
 ϕ_a : Air volume fraction
 ϕ_w : Water volume fraction
 ρ_a : Air density
 ρ_v : vapor density
 ρ_w : Water density
 σ : Cavitation number
 σ_h : Cavitation number
 τ : Subgrid scale (SGS) stress tensor.

Conflict of Interests

The author declares that there is no conflict of interests regarding the publication of this paper.

References

- [1] H. T. Falvey, *Cavitation in Chutes and Spillways*, U.S. Department of the Interior, Bureau of Reclamation, 1990.
- [2] W. Lee and J. A. Hoopes, "Prediction of cavitation damage for spillways," *Journal of Hydraulic Engineering*, vol. 122, no. 9, pp. 481–488, 1996.
- [3] P. Novak, A. I. B. Moffat, C. Nalluri, and R. Narayanan, *Hydraulic Structures*, Spon Press, London, UK, 2004.
- [4] Landsvirkjun, *Kárahnjúkar HEP Iceland, Physical Model Investigation on the Kárahnjúkar Dam Spillway*, VAW, Laboratory of Hydraulics and Glaciology of the Swiss Federal Institute of Technology Zurich, 2006, http://www.vaw.ethz.ch/people/wb/archive/wb_251_karahnjukar_dam_spillway.
- [5] D. D. Joseph, "Cavitation in a flowing liquid," *Physical Review E*, vol. 51, Article ID R1649(R), 1995.
- [6] L. G. Leal, *Advanced Transport Phenomena*, Cambridge University Press, Cambridge, UK, 2007.
- [7] P. Zamankhan, "Large eddy simulation and PIV experiments of air-water mixing tanks," *Communications in Nonlinear Science and Numerical Simulation*, vol. 15, no. 6, pp. 1511–1525, 2010.
- [8] M. P. Allen and D. J. Tildesley, *Computer Simulations of Liquids*, Oxford University Press, Oxford, UK, 1987.
- [9] G. H. Sauer and J. Schnerr, "Physical and numerical modeling of unsteady cavitation dynamics," in *Proceedings of the 4th International Conference on Multiphase Flow*, New Orleans, La, USA, 2001.
- [10] P. Zamankhan, "Solid structures in a highly agitated bed of granular materials," *Applied Mathematical Modelling*, vol. 36, no. 1, pp. 414–429, 2012.
- [11] P. Zamankhan, "Formation patterns at the air-grain interfaces in spinning granular films at high rotation rates," *Communications in Nonlinear Science and Numerical Simulation*, vol. 17, no. 11, pp. 4224–4240, 2012.
- [12] P. Zamankhan, "Simulation of self-segregation of a low density spherical particle in a bubbling bed," *Chemical Engineering Journal*, vol. 181–182, pp. 842–845, 2012.
- [13] P. Zamankhan, "Sinking and recirculation of large intruders in vertically vibrated granular beds," *Advanced Powder Technology*, vol. 24, no. 6, pp. 1070–1085, 2013.
- [14] C. Chaux, L. Duval, A. Benazza-Benyahia, and J.-C. Pesquet, "A nonlinear Stein-based estimator for multichannel image denoising," *IEEE Transactions on Signal Processing*, vol. 56, no. 8, pp. 3855–3870, 2008.
- [15] <http://labs.autodesk.com/technologies/123d/>.
- [16] O. Coutier-Delgosha, R. Fortes-Patella, and J. L. Reboud, "Evaluation of the turbulence model influence on the numerical simulations of unsteady cavitation," *Journal of Fluids Engineering*, vol. 125, no. 1, pp. 38–45, 2003.
- [17] H. L. Stone, "Iterative solution of implicit approximations of multidimensional partial differential equations," *SIAM Journal on Numerical Analysis*, vol. 5, pp. 530–558, 1968.
- [18] C. Antoine, "Tensions des vapeurs, nouvelle relation entre les tensions et les températures," *Comptes Rendus des Séances de l'Académie des Sciences*, vol. 107, p. 681, 1888.
- [19] V. M. Semenov and V. O. Saranchev, "Computer program for hydraulic calculation of structures for controlling aeration of the flow on spillways," *Hydrotechnical Construction*, vol. 30, no. 5, pp. 234–242, 1996.
- [20] R. S. Gal'perin, A. G. Oskolkov, V. M. Semenov, and G. N. Tsedrov, *Cavitation on Hydraulic Structures*, Énergiya, Moscow, Russia, 1977, (Russian).
- [21] P. Zamankhan, "Rollers in low-head dams—challenges and solutions," *Communications in Nonlinear Science and Numerical Simulation*, vol. 17, no. 12, pp. 5273–5285, 2012.

Research Article

Evolutionary Game Analysis of Competitive Information Dissemination on Social Networks: An Agent-Based Computational Approach

Qing Sun^{1,2} and Zhong Yao¹

¹*School of Economics and Management, Beihang University, Beijing 100191, China*

²*School of Computer Science and Engineering, Beihang University, Beijing 100191, China*

Correspondence should be addressed to Zhong Yao; iszhyao@buaa.edu.cn

Received 22 August 2014; Accepted 5 December 2014

Academic Editor: L. W. Zhang

Copyright © 2015 Q. Sun and Z. Yao. This is an open access article distributed under the Creative Commons Attribution License, which permits unrestricted use, distribution, and reproduction in any medium, provided the original work is properly cited.

Social networks are formed by individuals, in which personalities, utility functions, and interaction rules are made as close to reality as possible. Taking the competitive product-related information as a case, we proposed a game-theoretic model for competitive information dissemination in social networks. The model is presented to explain how human factors impact competitive information dissemination which is described as the dynamic of a coordination game and players' payoff is defined by a utility function. Then we design a computational system that integrates the agent, the evolutionary game, and the social network. The approach can help to visualize the evolution of % of competitive information adoption and diffusion, grasp the dynamic evolution features in information adoption game over time, and explore microlevel interactions among users in different network structure under various scenarios. We discuss several scenarios to analyze the influence of several factors on the dissemination of competitive information, ranging from personality of individuals to structure of networks.

1. Introduction and Prior Work

The emergent and rapid development of online social networking applications has changed the way in which both consumers and enterprises interact and collaborate with each other. Online social networking applications provide the engaged individuals with collaborative environment to share information or ideas with their neighbors, where the total effect is greater than the sum of individual effects. In social commerce, the dissemination of product-related information is affected by individuals' actions, which are strongly determined by their characteristics and often influenced by the decisions of other individuals. This kind of information diffusion on the social network, including social advertisements, word-of-mouth, and comments, finally influences the buying behavior of the potential consumers. The features and patterns of competitive information dissemination will affect the product-related information spreading, such as competitive advertisement and positive or negative word-of-mouth because of their commercial feature. Therefore, it is

important to study how to model and analyze the competitive diffusion through social network.

Epidemic models have been widely adopted by researchers for information dissemination due to the analogy between epidemics and the spread of information. The underlying assumption of these models is that individuals adopt a new behavior with a probability when they interact with others who have already adopted it [1]. Gruhl et al. [2] investigate the adoption of the classic Susceptible-Infected-Removed (SIR) model for information dissemination. Yang and Leskovec [3] developed a linear influence model to focus on influence of individual node on the rate of dissemination through the implicit network. Lü et al. [4] propose a modified SIR model to describe the information diffusion in the small-world network, proposing three different spreading rules from the standard SIR model: memory effects, social reinforcement, and nonredundancy of contacts, in which the influence of social network structure is considered and analyzed. These studies have macroscopically committed

to the description of information diffusion through social networks.

In recent years, researchers gradually observe that game behaviors between individuals in social network, being the foundation of the social group behavior, raise social diffusions, which were always discussed in the microlevel in prior related research. Micronodes in network constantly adjust their strategy according to the behavior of other nodes, through the dynamic game with other nodes to maximize their own interests, and all the behaviours of individual node finally form the social network group behavior. Therefore, game-theoretic models, as a new perspective of interpreting social diffusion, are increasingly adopted by computer scientists for analyzing network behaviors. Game theory is a set of analytical tools and solution concepts, which provides explanatory and predicting power in interactive decision situations, when the aims, goals, and preferences of the participating players are potentially in conflict [5]. Unlike the classic game theory, which assumes that gaming exists between two individuals and happens only one-off, the evolutionary game theory has opened up related hypothesis limitations. It introduces the concept of time and space, considering the game as the summary of historical experience and individual learning, which makes it advantageous for social network study. Several papers have applied evolutionary game theory method to explain social diffusion. Kostka et al. [6] examined the dissemination of competing rumors in social network, using concepts of game theory and location theory, modelling the selection of starting nodes for the rumors as a strategy game. Meier et al. [7] presented a virus propagation game model, finding that the Windfall of Friendship does not increase monotonically with stronger relationships. Zinoviev et al. [8, 9] adopted game theoretic models to understand human aspects of information dissemination in which personalities of individuals are considered. Jiang et al. [10] examined the evolutionary process of knowledge sharing among users in social network and designed a computational experimental system, developing a mixed learning algorithm based on individual's historical game strategy, neighbors' strategy, and information noise.

Applying evolutionary game theory in social diffusion study presumes that the game process between individuals is not only determined by a single rival or individual, but also all individuals in the neighborhood. Meanwhile, it takes the historical game experience for future game behavior into consideration. The benefit of each individual is evaluated by the accumulated result of gaming many times. Individuals benefit from the game with its neighbors; at the same time, the benefit can be observed with comparisons to adjust their game strategies, trying to achieve optimum benefits and reach the overall game equilibrium. Evolutionary game theory also has advantages on competitive social behaviors and social diffusions. Alon et al. [11] introduced a game-theoretic model of competitive dissemination of technologies, advertisements, or influence through a social network. Wang et al. [12] proposed the stochastic game net model for analyzing competitive network behaviors. Takehara et al. [13] introduced and studied a deterministic model for competitive information diffusion on social networks. In contrast to many

other game theoretic models for the diffusion of information and innovation [14, 15], the model considered competition between different innovations spreading instead of discussing a single one.

This paper is an extension of recent works, including the method suggested by Jiang et al. [16] and the results described by Yu et al. [17]. The dissemination of information is modeled as the dynamic of coordination game, in which player's payoff is defined by a utility function and several cases are analyzed to reach the conclusion that the spreading rate is influenced by characteristics of individuals and several other factors. Different from the models of competitive information diffusion introduced in prior work, we adopt a framework for describing competitive information dissemination based on a game-theoretic model and multiagent-based dynamics. In this framework, we target several similar product-related pieces of information that competes with each other. Consumers may participate in discussing, adopting, and spreading one of them. Totally different from news or opinions dissemination that is always described as the spreading of the virus, consumers always make product-related decision for the utility motivation. In general, the utility is dynamically determined by factors from the environment or from his personal reasons. Meanwhile, prior research has shown that different network structures topology has great impact on social commerce. Therefore, both sociological and psychological characteristics are explicitly considered in our model as the novelty. In this model, information passing intrinsically involves both sides considering their characteristics: self-perceived knowledge, brand loyalty, and social conformity, which further determine their decisions of whether or not to forward the information. The decisions are also based on the global properties of the network, such as the knowledge dynamic all through the network. These factors finally bring different results of disseminations of different information that compete with each other. Based on the dynamic game model and strategy updating rules, we analyze competitive information propagation and the affecting factors.

The remainder of this paper is organized as follows. Section 2 presents the overview of competitive dissemination model based on evolutionary game theory, social network, and multiagent theory and introduces the individual's utility function. Section 3 discusses the dynamics and updating rules for the model we build, proposes the assumptions, and explains the model. In Section 4 we use an agent-based computational approach for simulation.

2. Problem Statement

We propose a different, global point of view regarding the incentives that govern the diffusion process. Suppose we have several firms that would like to advertise competitive products via "viral marketing." Each firm initially targets a small subset of users, in the hope that the social advertisements about their product would spread throughout the network. However, a user that participates in discussing and spreading product-related information is reluctant to participate in another one.

TABLE 1: Game payoff matrix.

	Player i	
	a	b
Player j		
a	U_{aa}, U_{aa}	U_{ab}, U_{ba}
b	U_{ba}, U_{ab}	U_{bb}, U_{bb}

For simplicity, we consider two pieces of information competing over the social network, represented by information A or B . They are about the same kind of product with different brands (e.g., Smartphones of iPhone or Samsung). Which information is adopted by the individual is determined by his self-perceived knowledge and herd mentality. Information dissemination is caused by individuals' interaction with his neighbours for sharing knowledge and opinion. This interaction, which arouses changes of individuals' acceptance and preference, could be considered as a game based on information exchange. Individuals update their strategies according to their payoff and the influence of their neighbours. The change of individual's information level for the product affects the individual's preference and accordingly affects his choice of consumption.

2.1. Evolutionary Game Model. In the classic game-theoretic model, the consumers are defined as players and each player has only one state. We take each node in online social network as players in game. The game is played in period $t = \{n, n = 1, 2, 3, \dots\}$ in online social networks that could be described as an undirected graph.

First of all, we assume that all players engaged in the evolutionary game are pure strategists, and each player could choose only one of the strategies; strategy a is participating in discussion and spreading of information for information A (corporation) and strategy b is participating in discussion and spreading of information B (defection). Then the set of available strategies for node i could be described as two-dimensional vectors:

$$S_i = \begin{pmatrix} 1 \\ 0 \end{pmatrix} \quad \text{or} \quad \begin{pmatrix} 0 \\ 1 \end{pmatrix}, \quad (1)$$

where S_i is the strategy of node i . In each round, the node games with all of its neighbours (friends) and profit. The payoff matrix M is defined by the utility function $U(i)$ illustrated in Table 1.

In Table 1, U_{ij} , $i, j \in (a, b)$, represents the utility for the player according to what strategy he chooses. The evolutionary game equilibrium can be detected by the dynamic replication method [5, 18] that can provide theoretical support for macroscopic decisions on information dissemination, ignoring network structure and environmental factors. Then, the expected cooperation (defection) benefit from knowledge sharing can be expressed as

$$\begin{aligned} U_i(C) &= p * U_{aa} + (1 - p) * U_{ab}, \\ U_i(D) &= p * U_{ba} + (1 - p) * U_{bb}, \end{aligned} \quad (2)$$

where p is the percentage of nodes holding a cooperative attitude (strategy a). $U_i(C)$ and $U_i(D)$, respectively, stand for the benefit that node i get in current round of game.

From the dynamic replication, the average benefit of the whole group is

$$\bar{U} = p * U_i(C) + (1 - p) U_i(D). \quad (3)$$

The state of the evolutionary system over time for different initial value of p can be evaluated by the diffusion rate $F(p)$:

$$\begin{aligned} F(p) &= \frac{dp}{dt} = p(U_i(C) - \bar{U}) \\ &= p(1 - p)[(U_{aa} - U_{ab} - U_{ba} + U_{bb}) * p + (U_{ab} - U_{bb})]. \end{aligned} \quad (4)$$

Therefore, the game has three possible solutions to reach equilibrium:

$$\begin{aligned} p &= 0, 1, \frac{U_{ab} - U_{bb}}{U_{aa} - U_{ab} - U_{ba} + U_{bb}}, \\ p^* &= \frac{U_{ab} - U_{bb}}{U_{aa} - U_{ab} - U_{ba} + U_{bb}}, \end{aligned} \quad (5)$$

where p^* is the value with which the group evolutionary will get the game equilibrium. This method can get the evolutionary equilibrium independent of environmental factors and network structure. However, the competitive dissemination we discuss in this paper is more complex. The historical game path, the impacts of environment, and the interactive users' decision should be taken into consideration comprehensively. In this context, the equilibrium cannot be simply and solely determined by the traditional dynamic replication method. In this paper, we choose the method of computational simulation approach so as to get a more reasonable explanation and description for competitive information dissemination over the social networks.

2.2. Utility Definition. The impact of other individuals' behavior has been extensively studied in social psychology and marketing. In general, many early past findings (Asch [19] and Schachter [20]) suggest that individuals have a tendency to behave in accordance with group or social norms and behave negatively toward opinions that deviate from these norms. Based upon this premise, Deutsch and Gerard [21] further developed the distinction between normative social influence (pressure to conform to the expectations of others) and informational influence (individual's acceptance of persuasive argument(s) of others). Meanwhile, other researches [22, 23] (McQuail [22] and Flanagan and Metzger [23]) proved that people expect two types of value to engage in community: information value and social support. We refer to the conclusion and define the utility function when game continues as follows.

(1) *Self-Perceived Knowledge Model.* People feel that the message they spread can help others make informed decision

of purchase. Product-related information is now being overwhelmed from a constantly increasing amount of advertising. Meanwhile, it can also be obtained by interpersonal sources (Feick and Price [24]). Self-perceived knowledge level helps to reduce the risk when making adopting and purchasing decision. In this paper, we define $k_i \in [0, 1]$ ($i = A$ or B) as the quantitative measure of self-perceived knowledge for the product of brand i . This kind of knowledge can either be gained from mass media or word-of-mouth prevalent in the social network. The quantity of 1 represents full knowledge of the product, which means the player knows everything about the background of the product. The quantity of 0 represents no prior knowledge of the product, which means the product is totally new to the player. A value of $k \in (0, 1)$ represents partial background knowledge of the product, which means the player knows something about the product (such as “I know something about the Smartphone of this brand”). We describe the self-perceived knowledge level for both the two brands of play i as a vector $K_i = \begin{pmatrix} k_A \\ k_B \end{pmatrix}$. The consistent conclusion can easily be reached in the real social commerce circumstance, because the more self-perceived knowledge a consumer has, the lower risk and cost he will pay for consumptions.

Moreover, we observe that knowledge will transfer within players as game continues; under some situations even new knowledge will be created. In order to describe the knowledge dynamics during the game process, we assume that there are two independent kinds of knowledge, each kind corresponding to one of the competitive pieces of information of product. For example, k_i and k_j are referring to different products. They interact as the following rules.

- (1) Interacting with a player having different kinds of knowledge does not increase knowledge; k_i and k_j are different kinds of knowledge.
- (2) Interacting with a player having no knowledge increases knowledge; k_i and k_j are the same kind of knowledge.
- (3) Interacting with a player having full knowledge creates full knowledge; k_i , k_j are the same kind of knowledge.

The combined knowledge (marked as $k_{(i,j)}$) is generated by the following equation:

$$k_{(i,j)} = \frac{\max(k_i, k_j) + \min(1, \max(k_i + k_j))}{2}. \quad (6)$$

We define a transferring operator \oplus to describe the knowledge transferring process among players when the game is going. The transferring equation is given below:

$$K_{ij,t+1} = K_{i,t} \oplus K_{j,t}. \quad (7)$$

The above method was observed by Szabó and Fáth [5] and Yu et al. [17], with a slightly different definition.

(2) *Brand Commitment Model*. In marketing, applications of social or group influence can be found across a wide

range of contexts [25]. For example, scholars (Arndt [26] and Gatignon and Robertson [27]) have often relied on social influence as a theoretical basis for studying WOM dynamics in the adoption of new products, for understanding reference-group's influence on product and brand choice (Bearden and Etzel [28]) as well as polarization phenomenon in group decision-making (Ward and Reingen [29]). Social identity theory, explained by Ellermers et al. [30] and Tajfel [31], indicates that some people care about the success of the company they identify with. Dutton et al. [32] found that people always voluntarily promote the company on which they have a positive view and become loyal to the brand once they develop to self-identity. Brand commitment is an enduring desire to maintain a relationship with a brand. It can be perceived as a condition in which consumers are firmly enchanted with a certain brand to the extent that there is no second choice. In other words, it implies brand loyalty.

Therefore, if an actor has a high level of commitment to a brand, he or she will tend to keep a stable relationship with the brand. The actions of person with high or low commitment will be different when they receive a negative message talking about a target brand. For the sake of simplicity, we define b_i ($i=a$ or b) as the quantitative measure of brand commitment of the product. This kind of commitment can bring bias when choosing strategy. A value of $b \in [0, 1]$ represents player's preference or bias on some brand of product, which means the player will definitely choose certain brand of the product and reject others, no matter which one his neighbours choose. Under some situations we can even infer that they are spokesman or discommender of particular brand. We describe the brand preference level of the two products for player i as a vector $B_i = \begin{pmatrix} b_A \\ b_B \end{pmatrix}$.

(3) *The Rational Choice Model of Conformity*. In social commerce, applications of social or group influence can be found across a wide range of contexts; prior results found by Ryu and Han [25] and Arndt [26] suggest that individuals are susceptible to social influence and that they often behave in ways that conform to social norms or pressure. The same conclusion is also observed by Gatignon and Robertson [27] and Bearden and Etzel [28]. Conformity is often meant to represent a solution to the problem and attain or maintain social order that requires cooperation. These studies generally focus on modelling the dynamics of norms in the perspective of cooperation. With reference to the prior research, we assume that the need for social conformity is associated with popularity. Popularity measures player i 's social influence and dominance. It is one of the components in his utility function. For the sake of simplicity, we evaluate it with the number of his neighbours, which is modified from the method suggested by Yu et al. [17]:

$$P_i = \alpha \frac{n_i}{n_{\max}}. \quad (8)$$

In this equation, n_{\max} is the maximum number of neighbours of all players in the network, and n_i represents the number of neighbours of player i . $\alpha = [0, 1]$ is a controlling

parameter and describes the probability the player will choose to assimilate. For example, if $\alpha = 1$, keeping conformity with his neighbours brings benefit to the player; $\alpha = 0$ indicates that the two players' choice conflicts with each other and the total benefit for both two players is 0. In that case he is more reasonable when making purchase decision.

(4) *The Utility Function.* Sociologists believe that how human beings interpret and accept things could be summarized to more than one way [33]. The first way is personal experience and findings; another one is the established agreements or beliefs; also some people rely on the behaviours of people in groups, for they insist that believing what others say is a very useful quality that can make people easily get along and contributes a lot to stable social relations. In actual social activities, these three ways are often combined. However giving different weights on them reflects different personalities of people and different characteristics of social behaviour. We believe that the purpose of a rational actor i is to maximize her utility U_i . Therefore, U_i can be defined as a convex combination of information contribution and social norm contribution with coefficients $0 \leq \rho, \pi, k \leq 1$:

$$U_i = \rho K_i + \pi B_i + k P_i. \quad (9)$$

With reference to the method and the experienced data recommended by Zinoviev and Duong [8], we use a set of coefficients $\{\rho, \pi, k\}$ to characterize a particular type of actors. For example, $\rho = 0, \pi = 1$, and $k = 0$ describe a type of actors who have high loyalty to a special brand or those who represent the benefit of certain brand. We call them "sworn followers." $\pi = 0, \rho = 1$, and $k = 0$ probably correspond to a community of actors who believe that different self-perceived knowledge level will uniquely determine the strategy-making process; we call them "experts." $\pi = 0, \rho = 0$, and $k = 1$ probably correspond to a community of actors who care more about their reputation and conformity with the whole community; we call them "conformists." Meanwhile, j is the neighbour of i in the network. According to the utility definition we can calculate the payoff matrix in detail.

3. Analysis of Model

3.1. *Assumption of the Model.* Product-related information is a kind of public information that can be got from various channels; therefore we modify public goods game model and make the following assumptions:

- (1) In social network, the nodes are bounded rational. We agreed that each node only interacts with its neighbour nodes.
- (2) Benefit is defined by the payoff matrix. Each node is trying to obtain maximum benefit by enhancing the significance of its activities to improve the social capital in the community.
- (3) The evolution process of nodes in the network is influenced by various social factors. Each node has to constantly adjust their strategy, imitating the behaviours of its neighbours to improve the sociability within community.

Strategies in the evolutionary game tend to be influenced by other nodes' opinion in the public information environment. Therefore, the strategy for node i could be described as a dimensional vector S_i . This kind of game is carried out over certain kinds of social network structures; node i interacts with all of his neighbors in each round, and its payoff (P_i) can be described as

$$P_i = \sum_{j \in \Omega_i} s_i^T M s_j, \quad (10)$$

where Ω_i is the set of neighbors of node i in the network and M is the payoff matrix defined in Section 2.

3.2. *Learning and Updating.* Each node in the network evolution needs to constantly adjust its strategy to imitate the behaviors of its neighbors to improve sociability, referring to various social factors. Nodes i and j may also change their strategies because they contact public social media or they are influenced by other environment factors. Whether to keep the old strategy or change to the new one is defined by updating rules. At the end of each stage of the evolutionary game, all nodes can adjust their strategy according to the features and benefits of its neighbours. This kind of imitation processes formed a wide class of microscopic update rules. The essence of the imitation is that the node who has the opportunity to revise her strategy takes over one of her neighbor's strategy with some probability. The imitation process covers two respects: whom to imitate and with what probability.

There are several common strategy update rules described in the dynamics of evolutionary games. [5] (Majority rules, Best Response Dynamic, etc.). Among them, this paper considers the typical rule of imitation: Imitate If Better. The standard procedure of the rule is to choose the node to imitate at random from the neighbourhood. In the mean-field case this can be interpreted as a random partner from the whole population. The imitation probability may depend on the information available for the node. The rule can be different if only the strategies used by the neighbours are known, or if both the strategies and their resulting last-round (or accumulated) payoffs are available for inspection. Node i with strategy S_i takes over the strategy S_j of another node j , which is chosen randomly from i 's neighbourhood, if j 's strategy has yielded higher payoff. Otherwise the original strategy S_i is maintained. If we denote the set of neighbours of node i who hold the strategy S_i by $\Omega_i(s_i) \subseteq \Omega_i$ ($\Omega_i(a) + \Omega_i(b) = \Omega_i$). The individual's strategy transition rate from strategy s_i to strategy s'_i could be written as

$$\omega(s_i \rightarrow s'_i) = \frac{\lambda}{|\Omega_i|} \sum_{j \in \Omega_i(s'_i)} \theta[U_j - U_i], \quad (11)$$

where θ is the Heaviside function, $\lambda > 0$ is an arbitrary constant, and $|\Omega_i|$ is the number of neighbors. Imitation rules are more realistic if they take into consideration the actual payoff difference between the original and the imitated strategies. Proportional imitation does not allow for an inferior strategy to replace a more successful one. Update rules which forbid this are usually called payoff monotone.

However, payoff monotonicity is frequently broken in case of bounded rationality. Therefore, a possible general form of imitation more realistic could be described as follows:

$$P_{r_{i \rightarrow j}} = \frac{1}{1 + \exp[(U_i - U_j)/K]}, \quad (12)$$

where $P_{r_{i \rightarrow j}}$ represents the probability node i and imitates the strategy of its neighbour j finally. U_j is the benefit generated by node j and it is the maximum among those accrued by its neighbours, while U_i is the accumulated benefits of node i , and K is the information noise [34], representing the rational level of the nodes.

The smaller K value is, the more rational of the behaviour is. If $K = 0$, then the whole process can be described as a completely rational game, in which there is no error when making decision; $K = +\infty$ indicates that game strategies choosing can be depicted as a pure random process, which is completely irrational; $0 < K < +\infty$ indicates a limited rational game process; namely, the gamers adjust their strategies according to rules, but there is a certain error.

4. Computational Simulations

In this section, we design the computational system, simulate the virtual community and evolutionary process, collect numerical results under different scenarios, and make comparisons through statistical analysis. The simulation and experiments are implemented by NetworkX 1.7. NetworkX is a graph theory and complex network modelling tool, developed with Python language, containing built-in algorithms figure and complex network analysis modules, which can be conveniently imported and executed for complex network data analysis, simulation modelling, and so forth.

4.1. Formalize the Model Definition. Let each node in the virtual network be an agent and there are n agents. We define the community network N as $N = \{X, NT, U, F, t\}$, in which

- (1) X is the set of agents and $X = \{\text{agent1}, \text{agent2}, \dots, \text{agent}n\}$. Each agent is a node in the network.
- (2) NT is the set of network types and $NT = \{\text{smallworld}, \text{random}, \text{scalefree}\}$.
- (3) U is the set of benefits derived by all agents in each game round; it is the accumulated value while gaming with all its neighbours, $U = \{U_1, U_2, \dots, U_n\}$.
- (4) F is the state transfer function. The state of agent i at time $t + 1$ is a function of parameters as stated in (12).

4.2. Experimental System and the Default Parameters. In our study, a node in the network is either in a cooperation (strategy a) or defection (strategy b) state. We describe the diffusion of information for product A (information A for simplicity in the later paper) in the network as

$$\begin{aligned} &\text{diffusion of information } A \text{ (\%)} \\ &= \frac{\text{sum of the nodes holding strategy } a}{\text{total number of nodes}} * 100\%. \end{aligned} \quad (13)$$

And we describe the diffusion of information for product B (information B for simplicity) as

$$\begin{aligned} &\text{diffusion of information } B \text{ (\%)} \\ &= \frac{\text{sum of the nodes holding strategy } b}{\text{total number of nodes}} * 100\%. \end{aligned} \quad (14)$$

In the model, we simulate individual strategy evolution. The evolutions of the information spreading and accepting conditions are studied, trying to find out how to promote or hinder certain preference of strategy from winning. We conduct several experiments on the competitive information dissemination in a social network. There are some familiar and natural models of social networks, which could be applied in these experiments: random graph, scale-free network, and small-world network. We applied the latter two different networks for case study. A scale-free network is a random graph whose degree distribution follows a power law, while a small-world network follows a random graph model in which most nodes can be reached from every other node by a small number of hops, which is generally known as small-world phenomenon. Many empirical networks are well-modelled by small-world networks, such as social networks, wikis, and gene networks.

We explore the interaction among all individuals over time (100 simulation rounds in our case). The simulation is divided into five procedures.

- (1) Set up the network structure; define the game parameters and the model parameters.
- (2) Graphically illustrate the network evolution and show how the nodes change dynamically in the network.
- (3) In each step, each participating individual updates the strategy according to the rules of replication dynamic view (strategy).
- (4) In each simulation time period, take the evolutionary steps in the periodic system that all the individuals or a fixed percentage of them reach or maintain a stable state as the equilibrium of the evolution.
- (5) Display the simulation result and show the characteristics of the network.

4.3. Experimental Results. The population of our experiments is set to 1000. The small-world network applied for our experiments is set as follows: the number of connections per node is set to 5, and the probability of connection to link neighbours per node is set to 0.2. For the scale-free network, the number of edges being added to the network each step is set as 5. k_a , k_b , b_a , and b_b are initialized using uniform distribution on $[0, 1)$ throughout the experiment with slight difference under different scenarios.

(1) Results for Different Network Structures. At the start of the experiments, the two pieces of product information has been equally adopted. k_a , k_b , b_a , and b_b are initialized using uniform distribution, with the condition that A dominate in dissemination during gaming. We assume that the maximum

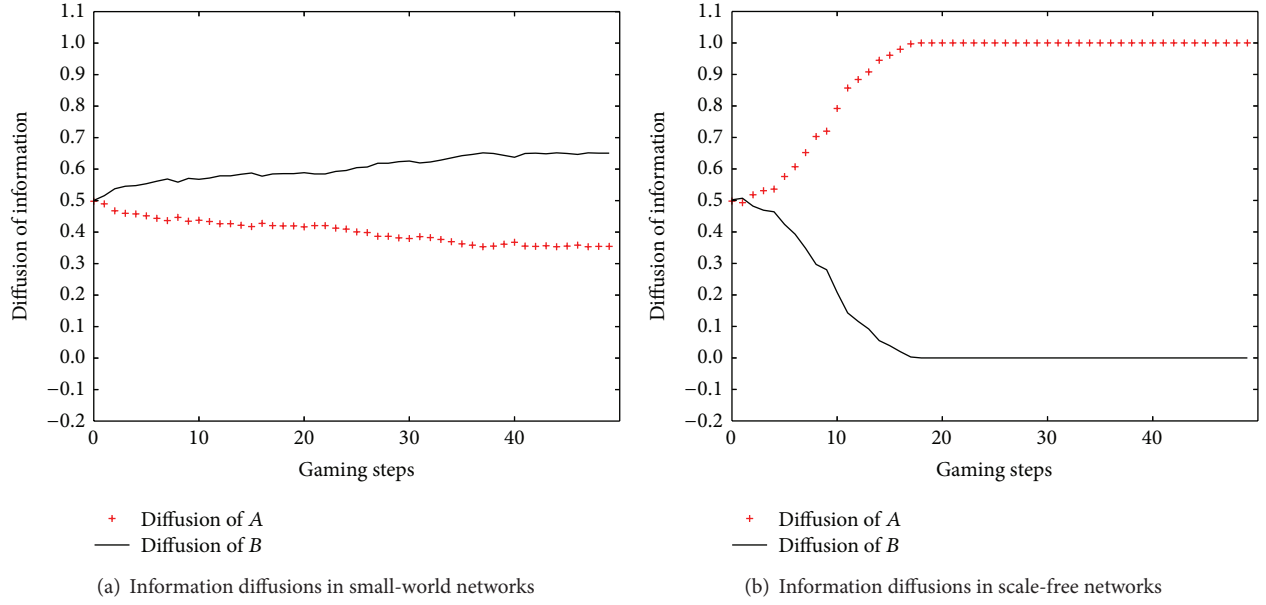


FIGURE 1: % of adoption for competitive product-related information under different network structure.

value of k_a is larger than the one of k_b ; for simplicity, to guarantee the condition, k_a and k_b are initialized on $[0.2, 0.7]$ and $[0, 0.2]$ and vary following the knowledge dynamic rules defined in Section 2. b_a and b_b follow uniform distribution on the interval $[0, 1]$. $\pi = 0.3$, $\rho = 0.3$, $k = 0.4$, and $K = 0.8$. The evolutionary steps in each round are set to 50.

Following the conditions of this scenario, we find the dominant strategy reaches the whole population or reaches a stable dominant winning status (the equilibrium), in different gaming steps over different network structure (see Figure 1). In the scale-free network, the dynamic can reach a stable status more easily.

Compared to the small-world networks, in scale-free network, the majority of individuals have only one high-degree neighbour. There will be more references for him to evaluate his neighbours' payoff, providing him with a higher probability to successfully imitate a better strategy. Then the neighbours of him are apt to imitate his strategy because of his high-degree status in the social networks. After several game rounds, the individual game is changed to group game with several high-degree players as the core nodes. It is obvious that the number of groups is much less than the number of nodes who participate in the game; thus the Scale-free networks can reach equilibrium faster than small-world model and meanwhile shows higher sensitivity, assumed by a larger amplitude around the equilibrium.

(2) *Results for Different Personalities.* Our analysis continues with how the spreading of competitive information differs according to the weight of acceptance change that affects agents' utility function. In the prior model, we classify the cases into different personalities.

(a) *The Influence of Individual Personality Differences on Game Equilibrium.* We use a particular set of coefficients

$\{\rho, \pi, k\}$ to characterize different types of agents. At the start of experiments, k_A , k_B , b_A , and b_B are initialized using uniform distribution on the interval $[0, 1]$ and they evolve according to the knowledge dynamic rules described in Section 2. Referring to the empirical data [17] (Yu et al., 2012), $K = 0.01$. We ran the experiment in three different cases which cover population with different personalities. In the first case (Figure 2), the agents have high desire for knowledge and low desire for brand loyalty and reputation; we set the parameters (π, ρ, k) distinguishing personalities as $(0.8, 0.1, 0.1)$, which we called "experts." In the second case, the agents have low expectation for reputation and knowledge and strong desire for loyalty to a certain brand; we set the parameter (π, ρ, k) as $(0.1, 0.8, 0.1)$, and we called them "sworn followers." In the last case, the agents have great desire for social conformity and influence; we set the parameter (π, ρ, k) as $(0.1, 0.1, 0.8)$ and call them "conformist."

In this experiment, the gaming steps are set to 50 in each simulation round and the initial % of information A is set to 80% to get a more definite comparison. We carry out experiments in 100 simulating rounds totally for the two different kinds of network structure.

Comparing experimental results under three different scenarios, a phenomenon could be observed in common, that the average steps before reaching the equilibrium in scale-free network is generally less than that in the small-world network, which get the consistent conclusion with experiment (a). The convergence of dynamic in scale-free network is more obvious with slight fluctuation, while the dissemination in the small-world network distribute more scattered.

As one can see from the figures, in all scenarios the whole network rapidly converges to a stable distribution. In the network of "experts" the average full convergence takes more time than in the network of "sworn followers" and

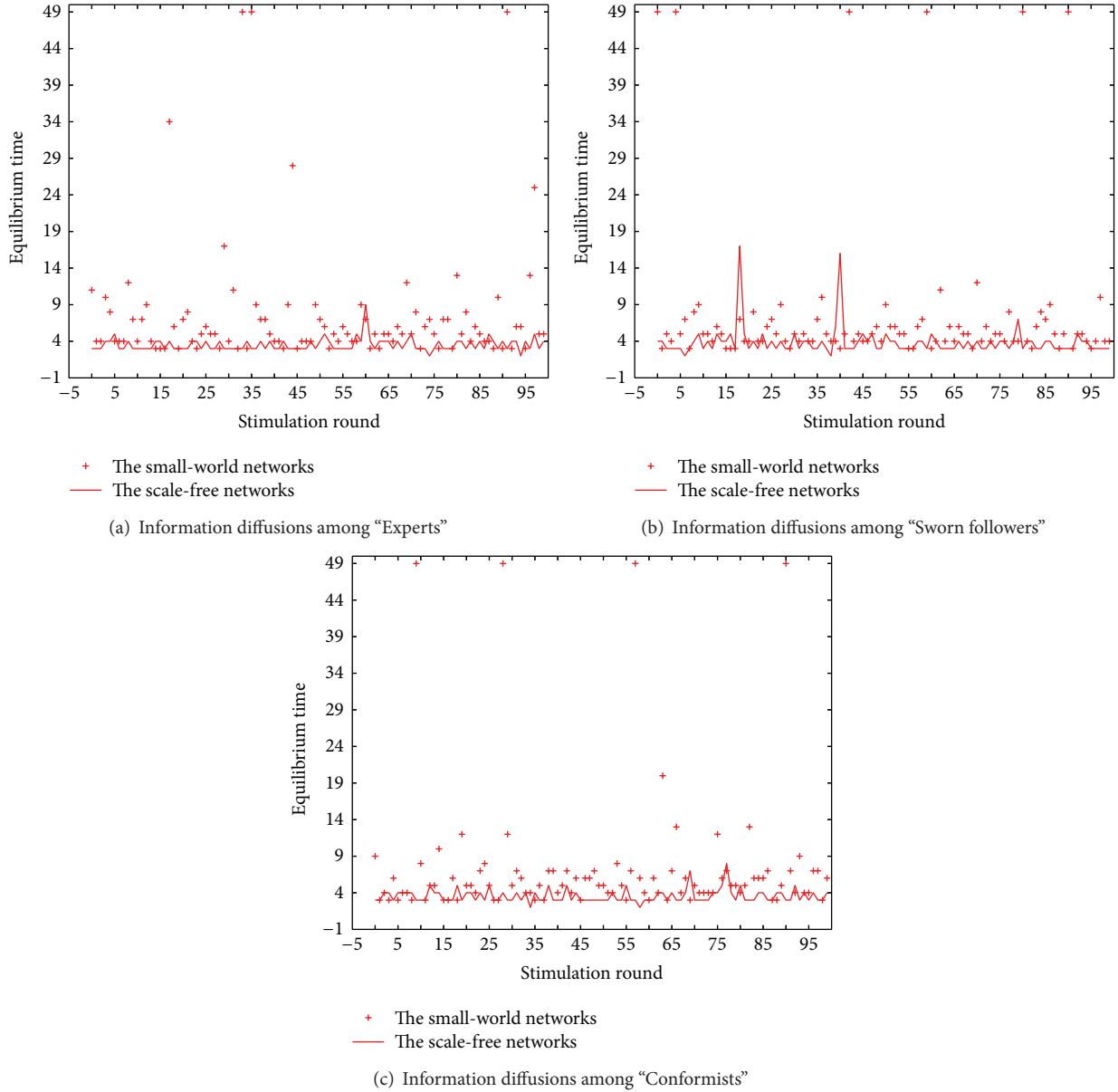


FIGURE 2: Different convergence times due to different settings of (π, ρ, k) , k_A , k_B , b_A , and b_B are initialized on $[0, 1)$. The values of (π, ρ, k) are, from (a) to (c), $(0.8, 0.1, 0.1)$, $(0.1, 0.8, 0.1)$, and $(0.1, 0.1, 0.1)$, representing experts, sworn followers, and conformists.

“conformist.” Also, the “expert” network always has some unsubstantial numbers of people doubting the diffused facts, performance in the sharp fluctuations. Generally speaking, information dissemination will proceed to the stable state most quickly in the scale-free network with “conformist” in the majority.

Local heterogeneity behaviour preference can explain the phenomenon, which could be sharply reduced over the network of “sworn followers” and “conformist.” A compatible opinion or preference could be more easily reached, being explained by fewer steps before the equilibrium during evolution. Each agent considers all the strategies their neighbours take and keep consistent with the overall opinion easily. However, when “experts” take a strategy, accidental shadows

have more chance to happen, which increase the uncertainty of spreading result.

(b) The Influence of Preference Benefit on Information Dissemination. Large proportion of a particular personality dominant in the population indicates a certain psychological tendency in social networks. For example, the psychology of “First Impression” leads to a majority of “sworn followers” to a special brand or product. The psychology of “Herd effect” leads to plenty of “conformists.” Meanwhile, the psychology of “Experientialism” makes most agents in the network more rational and specialistic.

In addition, a piece of information has its own life cycle, experiencing the process of production, diffusion, decay, and

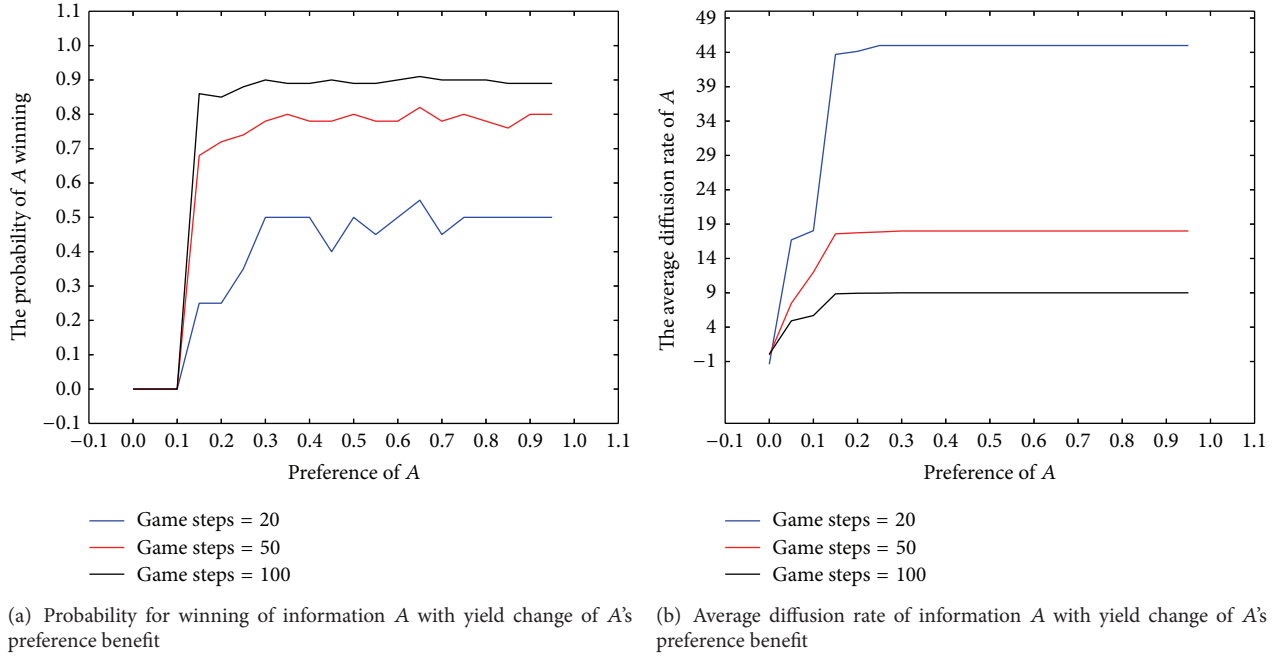


FIGURE 3: Under different evolutionary time, the diffusion states of information A with yield change of A's preference benefit. The values of b_A and b_B are well-distributed on $[0, 1)$ with step size 0.05. k_A, k_B are initialized using uniform distribution on the interval $[0, 1)$.

death, which cannot be absolutely fixed. Therefore, each round of evolutionary game cannot continue without time limiting. Thus, we simulate the winning probability of certain information for evolutionary process in limited time periods, trying to reveal the dissemination of competitive information from a more practical perspective.

As is shown in Figure 3, the gaming steps are, the gaming steps are, respectively, set to 20, 50, and 100; the initial % of information A is set to relatively low rate as 1%. Taking the small-world network under the psychological state of "First Impression" for instance, we carry out experiments in 100 rounds for different evolution time, trying to observe the change on winning probability and diffusion rate of information A due to different information preference benefits.

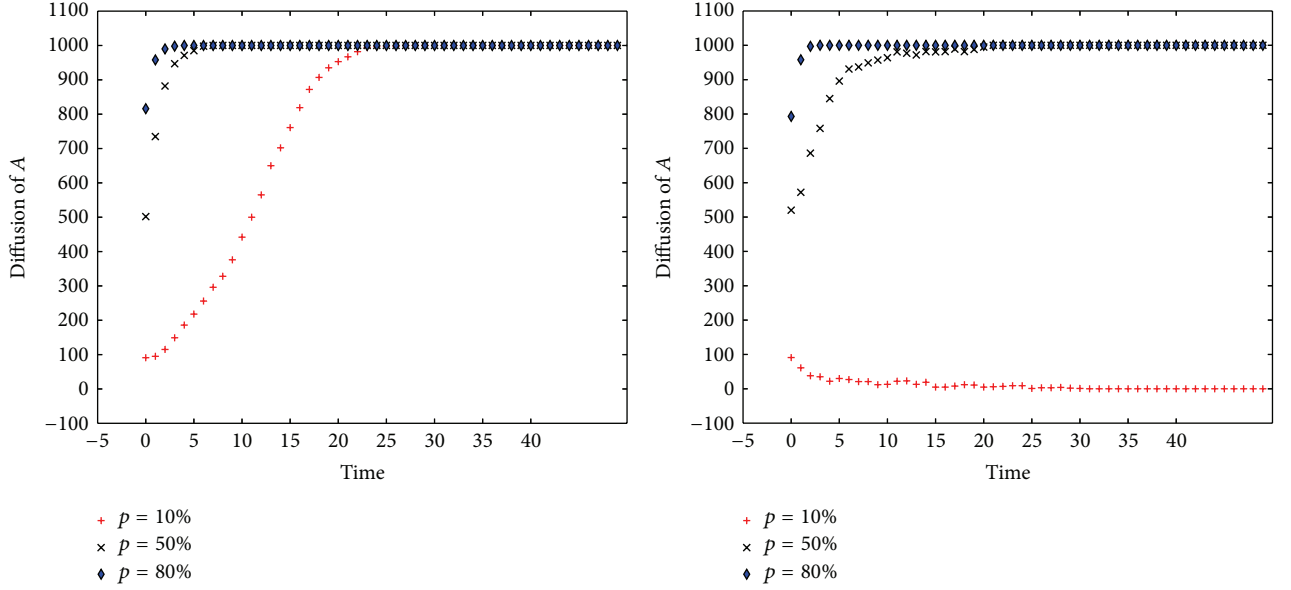
The winning probability of A generally increases with its preference benefit and the evolution time. When the benefit is lower than 0.1 comparing to B, there is no advantage for A to win. There is a sharp rising between the preference values 0.1 and 0.2. After that, the probability fluctuates at a relatively high level. Following the rule of "Imitate If Better," a very small group of initial adoption can get a high win probability. The diffusion rate of A also shows an ascending trend along with the preference benefit increasing when the benefit is lower than 0.2. Then the average diffusion rate keeps stable. Meanwhile, it can be concluded that information diffuse becomes lower after 50 game steps, which means, in most rounds of simulation, the minority of population for information A will quickly occupy the whole population because of the enough preference benefit and knowledge dynamic.

(3) *Results with Different Initial Settings.* We now discuss the impact of the initial % of information settings. The initial

percentage of people adopting information A is set at 0.1, 0.5, and 0.8, respectively. k_a and k_b are initialized on $[0.2, 0.7]$ and $[0, 0.2)$, varied by the knowledge dynamic rules defined in Section 2. b_a and b_b follow uniform distribution on the interval $[0, 1)$. $\pi = 0.3$, $\rho = 0.3$, $k = 0.4$, and $K = 0.8$. The evolution steps in each round are set to 50. The simulation round is set to 100 and the value gained at each step is calculated to the average.

The results indicate that the initial support of information will also have a major impact on the diffusion process. If information A in the initial state of the system has a higher adoptive rating ($p > 0.5$), the chance of information A wins will be further enhanced. As to the lower initial adoptive rating of information A ($p < 0.5$), the network will take much more time to reach an equilibrium as shown in Figure 4. In the network structure of small-world, information A will fail to win when its initial adoptive rating is set to 0.1. When information A's initial adoptive rating is increasing, the diffusion rate of A raises sharply, indicating that information A is more likely to reach the whole population. Under the structure of scale-free network, the phase change process is much smoother. It can be inferred that scale-free networks provide more heterogeneous topology structure, in which information A has a higher probability of winning. Thus scale-free networks could be seen as a factor which decreases with the winning odds of preferred information for a certain product.

(4) *Results with Incomplete Information.* We finally examine the impact of information noise on the probability of A's adoption and dissemination. The information noise levels are set at $k = 0.01, 10$, and $10,000$, respectively.



(a) Diffusion of information A under different initial % setting in small-world networks (b) Diffusion of information A under different initial % setting in scale-free networks

FIGURE 4: Diffusion of information under different initial % setting through different network structure. The value of p is 0.1, 0.5, and 0.8.

The initial percentage of people adopting information A is set at 0.1 to make a more significant comparison. k_a and k_b are initialized on $[0.2, 0.7]$ and $[0, 0.2)$ and vary following the knowledge dynamic rules defined in Section 2. b_a and b_b follow uniform distribution on the interval $[0, 1)$. $\pi = 0.3$, $\rho = 0.3$, and $k = 0.4$. The evolution steps in each simulation time period are set to 50. The simulation round is set to 100 and in each simulation period the mean value is referred.

The results in Figure 5 reveal that individual's irrational selection of strategies will also affect the results of dissemination. The smaller K 's value is, the more rational behaviour can be observed. The preferred information will take the advantage more easily over the network. It indicates that, for a limited rational game process, namely the game players adjust their strategies according to certain rules, the evolution will reach an equilibrium under the circumstance of low knowledge noise. Therefore, in the process of irrational game, it is hard for a certain piece of information to win more audience than the other, even though the former one has an obvious advantage of initial share. The reason is that the increasing of noise brings uncertainty of strategy evolution when "Imitate If Better" updating rule plays a role. It can also easily reach the conclusion again that scale-free networks structure could weaken the winning probability of preferred information.

5. Conclusion and Future Work

An evolutionary game model based on stochastic strategy updating dynamic for competitive product-related information dissemination in social network is presented in this paper. Several important implications can be drawn from the work.

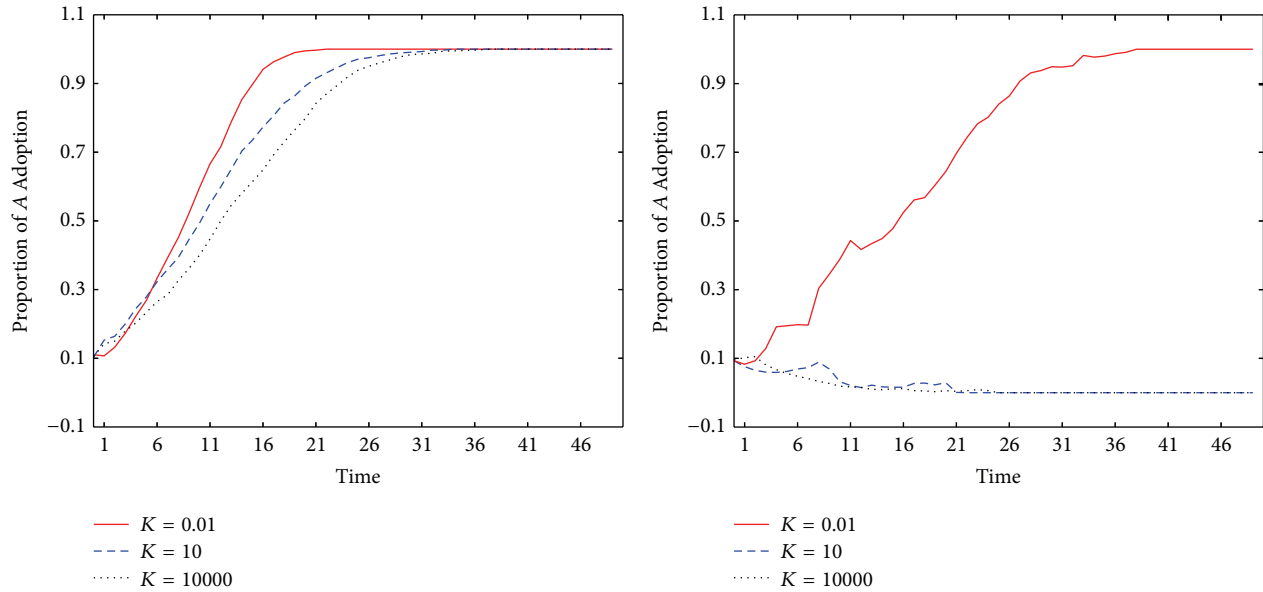
Firstly, compared with the Small-world networks, Scale-free networks are a kind of better structure for information dissemination. In the case that the overall average knowledge level is relatively high, the advantageous information in scale-free networks more easily defeat the others because of the less difference between individuals in this network structure.

Secondly, different virtual communities (with different network structures) should adopt different macrolevel managerial strategies, for instance customized rewarding and penalty mechanisms. Different incentives and penalties can influence user's choice of product-related information spreading decision and affect the performance of information sharing.

Furthermore, results of the competitive information dissemination are affected by the initial self-perceived knowledge distribution of products and brand preference among individuals, which means that, in order to make more individuals prefer a brand than the other, the company should provide more information to indirectly promote individuals' acceptance of the product, for example, through the mass media.

Finally, different personalities and mentalities in the virtual community lead to different dissemination process of competitive product-related information. Individuals' irrational selection of strategies also affects the results of dissemination.

Other models as we know, including SIR Model, Markov Model, and Random Petri-Net Model, only explain the information spreading in individual behaviour level. They could not preferably reflect the individual spreading behavior evolution in the context of time change, network structure, and interaction with others. Game theory is powerful tool in information dissemination behavior description. Our work



(a) The trend of change for information A adoption in evolution over small-world networks

(b) The trend of change for information A adoption in evolution over scale-free networks

FIGURE 5: The impact of information noise on the % of information adoption in evolutionary process, the value of K is 0.01, 10, and 1000.

reveals several interesting conclusions as to the nature of competitive information dissemination, employing an agent-based simulation method to explore the evolution of information adoption and dissemination behavior in social networks. We hope that this paper would provide some new insights into the research of competitive information.

This paper has some limitations and we will improve our model from the aspects as follows.

- (1) We assume that the network structure is fixed and did not consider the evolution of the network structures themselves, including not only homogeneous network, but also heterogeneous network containing several different types of players.
- (2) The utility parameters are endogenous to some extent. To evaluate how the endogeneity impacts the personality and to what extent it will influence the choice of information adoption is a problem we will discuss in the future work.
- (3) Large number of real data should be used to support the model, as a supplement of the simulation.

Conflict of Interests

The authors declare that there is no conflict of interests regarding the publication of this paper.

Acknowledgment

This work is supported by the National Natural Science Foundation of China (NSFC: 71271012 and NSFC: 71332003).

References

- [1] A. Montanaria and A. Saberi, "The spread of innovations in social networks," *Proceedings of the National Academy of Sciences of the United States of America*, vol. 107, no. 47, pp. 20196–20201, 2010.
- [2] D. Gruhl, R. Guha, D. L. Nowell, and A. Tomkins, "Information diffusion through blogspace," in *Proceedings of the 13th International Conference on World Wide Web (WWW '04)*, pp. 491–501, 2004.
- [3] J. Yang and J. Leskovec, "Modeling information diffusion in implicit networks," in *Proceedings of the 10th IEEE International Conference on Data Mining (ICDM '10)*, pp. 599–608, IEEE, Sydney, Australia, December 2010.
- [4] L. Lü, D.-B. Chen, and T. Zhou, "The small world yields the most effective information spreading," *New Journal of Physics*, vol. 13, Article ID 123005, 10 pages, 2011.
- [5] G. Szabó and G. Fáth, "Evolutionary games on graphs," *Physics Reports A*, vol. 446, no. 4–6, pp. 97–216, 2007.
- [6] J. Kostka, Y. A. Oswald, and R. Wattenhofer, "Word of mouth: rumor dissemination in social networks," in *Structural Information and Communication Complexity*, vol. 5058 of *Lecture Notes in Computer Science*, pp. 185–196, Springer, Berlin, Germany, 2008.
- [7] D. Meier, Y. A. Oswald, S. Schmid, and R. Wattenhofer, "On the windfall of friendship: inoculation strategies on social networks," in *Proceedings of the 9th ACM Conference on Electronic Commerce (EC '08)*, pp. 294–301, July 2008.
- [8] D. Zinoviev and V. Duong, "A game theoretical approach to broadcast information diffusion in social networks," in *Proceedings of the 44th Annual Simulation Symposium*, pp. 47–52, 2011.
- [9] D. Zinoviev, V. Duong, and H. G. Zhang, "A game theoretical approach to modeling information dissemination in social networks," in *Proceedings of the SUMMER 4th International*

- Conference on Knowledge Generation, Communication and Management*, vol. 1, pp. 407–412, 2010.
- [10] G. Jiang, F. Ma, J. Shang, and P. Y. Chau, "Evolution of knowledge sharing behavior in social commerce: an agent-based computational approach," *Information Sciences*, vol. 278, pp. 250–266, 2014.
 - [11] N. Alon, M. Feldman, A. D. Procaccia, and M. Tennenholtz, "A note on competitive diffusion through social networks," *Information Processing Letters*, vol. 110, no. 6, pp. 221–225, 2010.
 - [12] Y. Wang, J. Li, K. Meng, C. Lin, and X. Cheng, "Modeling and security analysis of enterprise network using attack-defense stochastic game Petri nets," *Security and Communication Networks*, vol. 6, no. 1, pp. 89–99, 2013.
 - [13] R. Takehara, M. Hachimori, and M. Shigeno, "A comment on pure-strategy Nash equilibria in competitive diffusion games," *Information Processing Letters*, vol. 112, no. 3, pp. 59–60, 2012.
 - [14] J. R. Davis, Z. Goldman, E. N. Koch et al., "Equilibria and efficiency loss in games on networks," *Internet Mathematics*, vol. 7, no. 3, pp. 178–205, 2011.
 - [15] A. Galeotti, S. Goyal, M. O. Jackson, F. Vega-Redondo, and L. Yarov, "Network games," *The Review of Economic Studies*, vol. 77, no. 1, pp. 218–244, 2010.
 - [16] G. Jiang, B. Hu, and Y. Wang, "Agent-based simulation of competitive and collaborative mechanisms for mobile service chains," *Information Sciences*, vol. 180, no. 2, pp. 225–240, 2010.
 - [17] J. Yu, Y. Wang, J. Li, H. Shen, and X. Cheng, "Analysis of competitive information dissemination in social network based on evolutionary game model," in *Proceedings of the 2nd International Conference on Cloud and Green Computing (CGC '12)*, pp. 748–753, Xiangtan, China, November 2012.
 - [18] J. Hofbauer and K. Sigmund, "Evolutionary game dynamics," *Bulletin of the American Mathematical Society*, vol. 40, no. 4, pp. 479–519, 2003.
 - [19] S. E. Asch, "Opinions and social pressure," *Scientific American*, vol. 193, no. 5, pp. 31–35, 1955.
 - [20] S. Schachter, "Deviation, rejection, and communication," *Journal of Abnormal and Social Psychology*, vol. 46, no. 2, pp. 190–207, 1951.
 - [21] M. Deutsch and H. B. Gerard, "A study of normative and informational social influences upon individual judgment," *Journal of Abnormal and Social Psychology*, vol. 51, no. 3, pp. 629–636, 1955.
 - [22] D. McQuail, *Mass Communication Theory: An Introduction*, Sage Publications, Thousand Oaks, Calif, USA, 2nd edition, 1987.
 - [23] A. J. Flanagin and M. J. Metzger, "Internet use in the contemporary media environment," *Human Communication Research*, vol. 27, no. 1, pp. 153–181, 2001.
 - [24] L. F. Feick and L. L. Price, "The market maven: a diffuser of marketplace information," *Journal of Marketing*, vol. 51, pp. 83–97, 1987.
 - [25] G. Ryu and J. K. Han, "Word-of-mouth transmission in settings with multiple opinions: the impact of other opinions on WOM likelihood and valence," *Journal of Consumer Psychology*, vol. 19, no. 3, pp. 403–415, 2009.
 - [26] J. Arndt, "Role of product-related conversations in the diffusion of a new product," *Journal of Marketing Research*, vol. 4, no. 3, pp. 291–295, 1967.
 - [27] H. Gatignon and T. S. Robertson, "A propositional inventory for diffusion research," *Journal of Consumer Research*, vol. 11, pp. 849–867, 1985.
 - [28] W. O. Bearden and M. J. Etzel, "Reference group influences on product and brand purchase decisions," *Journal of Consumer Research*, vol. 9, no. 2, pp. 183–194, 1982.
 - [29] J. C. Ward and P. H. Reingen, "Sociocognitive analysis of group decision making among consumers," *Journal of Consumer Research*, vol. 17, pp. 245–265, 1990.
 - [30] N. Ellermers, R. Spears, and B. Doosje, *Social Identity*, Blackwell, Oxford, UK, 1999.
 - [31] H. E. Tajfel, *Differentiation between Social Groups: Studies in the Social Psychology of Intergroup Relations*, Academic Press, Oxford, UK, 1978.
 - [32] J. E. Dutton, J. M. Dukerich, and C. V. Harquail, "Organizational images and member identification," *Administrative Science Quarterly*, vol. 39, no. 2, pp. 239–263, 1994.
 - [33] E. R. Babbie, *The Practice of Social Research*, Wadsworth Publishing Co Inc., 11th edition, 2007.
 - [34] W.-B. Du, X.-B. Cao, M.-B. Hu, H.-X. Yang, and H. Zhou, "Effects of expectation and noise on evolutionary games," *Physica A: Statistical Mechanics and its Applications*, vol. 388, no. 11, pp. 2215–2220, 2009.

Research Article

Modeling and Querying Business Data with Artifact Lifecycle

Danfeng Zhao,¹ Wei Zhao,² Le Sun,¹ and Dongmei Huang¹

¹ College of Information, Shanghai Ocean University, Shanghai 201306, China

² Information & Telecommunication Branch, Heilongjiang Electric Power Company Ltd., State Grid Corporation of China, Heilongjiang 150090, China

Correspondence should be addressed to Danfeng Zhao; dfzhao@shou.edu.cn and Dongmei Huang; dmhuang@shou.edu.cn

Received 28 August 2014; Accepted 11 September 2014

Academic Editor: L. W. Zhang

Copyright © 2015 Danfeng Zhao et al. This is an open access article distributed under the Creative Commons Attribution License, which permits unrestricted use, distribution, and reproduction in any medium, provided the original work is properly cited.

Business data has been one of the current and future research frontiers, with such big data characteristics as high-volume, high-velocity, high-privacy, and so forth. Most corporations view their business data as a valuable asset and make efforts on the development and optimal utilization on these data. Unfortunately, data management technology at present has been lagging behind the requirements of business big data era. Based on previous business process knowledge, a lifecycle of business data is modeled to achieve consistent description between the data and processes. On this basis, a business data partition method based on user interest is proposed which aims to get minimum number of interferential tuples. Then, to balance data privacy and data transmission cost, our strategy is to explore techniques to execute SQL queries over encrypted business data, split the computations of queries across the server and the client, and optimize the queries with syntax tree. Finally, an instance is provided to verify the usefulness and availability of the proposed method.

1. Introduction

With the advent of Big Data, attentions from all walks of life gradually focus on exploiting their controllable data so as to realize a satisfactory profit. Against this background, data resource is widely recognized to be equal in status and value to mineral resource. In enterprise-led dataspace, data generated in business process are the most significant factor which will affect the performance of process execution. As business process is closely related to enterprise's business strategy and market competitiveness, researches on business data will benefit enterprises in coping with the challenges brought by Big Data and are significant in predicting and responding to potential business risks in a timely way as well as offering business opportunities. Recently, research work on data management in business process has gradually become a research hotspot.

During business process execution, there is usually a large data transfer, which falls into the scope of Big Data. For example, currently China Unicom monthly stores more than 2 trillion records, data volume is over 525 TB, and the highest data volume has reached a peak of 5 PB [1]. China UnionPay daily handles more than 60 billion transactions; thereby the

generated data are exceptionally large. Google supports such a great many of services as both processing over 20 petabytes (10^{15} bytes) of data and monitoring 7.2 billion pages per day [2]. Starting from 2005, NTDB (National Trauma Data Bank) has tracked more than half a million trauma patients by now and stored their records, and many service retailers collect data from multiple sales channels, catalogs, stores, and online interaction, such as Client-Side Click-to-Action [3]. Hence, Big Data is ubiquitous (business process data arises in enterprises (large or small)) and grows exponentially, which poses huge challenges in data management. To address this, the first priority is to build an adaptive data model, which provides basis and direction for efficient data acquisition. Secondly, we see it as the next big issue about devising a suitable query strategy for business data which is a prerequisite for data processing and analysis.

Data modeling is the foundation for dataspace building. The research work in the early days focused on dataspace modeling where its subject is individual [4, 5]. iDM (iMeMex data model) [6] is the first model which is able to represent all heterogeneous personal information into a single model. This data model uses database approach so easy to understand but introduce a new query language iQL, which is a little hard

for normal users to learn. UDM (unified data model) [7] uses the integrated IR-DB approach, which is able to represent the partial sections of a file but is also not able to support relational data query. Triple model [8] represents heterogeneous data in triple form, which is a simple and flexible solution but does not support the path expression queries, uncertainty, and lineage queries. PDM (probabilistic semantic model) [9] supports top-k query answering but it is difficult to obtain reliable probability functions. The methods above are based on personal dataspace. Unfortunately, in enterprise-led data space scenarios today there is rare research works on data modeling.

Query ability is the basis of the exploitation of Big Data's value. Query language iQL [6] realizes rules-based query optimization but ignores the evaluation of optimization cost. UDM [7] introduces a new query language, which is based on SQL query language with some extended core operations, called TALZBRA operation. Triple model [8] supports subject predicate object (SPO) query language that can be enhanced by RDF-based query language. DSSP (dataspace support platforms) supports some useful services on dataspace, helps to recognize the correlation among sources of dataspace, and provides a basic query schema upon these data sources. In enterprise-led dataspace, business process data is the key element in data modeling, which has such characteristics as large-volume, strong temporal correlation and stable lifecycle. These characteristics make it an extreme challenge for current query schemes.

Business data realistically records the whole execution process of a single task, including execution status, resource status and real-time usage, and correlation with other business process instances. Executing a business process would generate additional data for a variety of reasons such as monitoring for performance or business concerns, auditing, and compliance checking. Even business process schemas and enactments can be viewed as data so that they can be managed, queried, mined for process schemas, and analyzed [10]. An artifact is a kind of widely recognized business process data, representing key business entities. Artifact-centric approach [11] is the representative method in data-centric business process management and has been applied in various client engagements, including financial [12], supply chain, retailer [13], bank, pharmaceutical research [14], and cooperative work [15]. In this paper we firstly adopt artifact as a basic element, analyze its evolution process, and then model business data through corresponding artifact lifecycle. Secondly, we make efforts on devising a safe and quick query strategy in consideration of the privacy and storage distribution of artifacts.

The rest of the paper is organized as follows. In Section 2 we introduce the concept of artifact in field of workflow management and model business data with its lifecycle from the perspective of process. In Section 3 we propose a business data partition method concerning user interest, based on which we further present a cryptograph query for off-site storage data. Then, we give a detailed instance to verify the proposed method in Section 4. In the last section, we draw a conclusion.

2. Business Data Modeling

As before, artifacts describe the business-relevant data and their lifecycles which is an important property of business data and describes the whole dynamic process of business data. It also contains specific time information. To take advantage of these characteristics, our strategy is to model business data with its lifecycle, which aims to realize the completed description of dynamic business data. In this section, we introduce artifact-relevant notions and take artifact-centric process description method to model business data with artifact lifecycle. Furthermore, we adopt business process logic model to illustrate the lifecycle of business data and then measure the quality of above model.

2.1. Basic Definition

Definition 1. Artifact [16] is an objective data entity which records the business process. Artifact comprises both a unique immutable identity and self-describing mutable content.

Definition 2. An artifact lifecycle captures the end-to-end process of a specific artifact, from creation to completion and archiving.

Definition 3. Artiflow model (artifact logical flow) [17] is 5-tuple (N, S, R, C, Ru) , where N is the name of model, S is a finite set of services, R is a finite set of repositories, C is a finite set of transport channels, and Ru is a finite set of business rules.

Definition 4. The states of artifact are a set, $\bigwedge_{i=1}^m IsDefine(A_i)$ (conjunction expression), where $IsDefine(A_i)$ is a mapping function that assigns a Boolean value $\{0, 1\}$ to each single attribute A_i in attribute set A , $A_i \in A$, $i \in \{1, m\}$, and m is the number of attributes in artifact. If the attribute is defined and has value, it will return 1; else it will return 0.

Definition 5. Service is 5-tuple (n, V_r, V_w, P, E) , where n is the name of a certain service, $n \in S$; V_r, V_w are the finite set of artifact classes, where V_r is a set of artifacts which the service is about to read and V_w is a set of artifacts which the service is about to rewrite; P is the description of artifact states inputted by V ; E is the description of activities on V .

Definition 6. Repository is 4-tuple $R = (re, R_a, R_r, C_t)$, where re is the name of repository; R_a, R_r are the set of stored and read artifacts, respectively; C_t is the reading condition for R_r .

Definition 7. Transport channel is 2-tuple (Cn, Cs) where Cn is the name of the channel; Cs is 3-tuple (prior service/repository name, rear service/repository name, channel type). $Cs \in R \times S \times \{Read, ReadOnly\} \cup S \times R \times \{Write\}$, where R, S are the finite set of repository elements and service elements in Artiflow, respectively, and the set of transport channel types is described as $\{Read, ReadOnly, Write\}$.

2.2. Data Modeling with Artifact Lifecycle. As suggested in Definitions 2 and 3, Artiflow is a logical model that records

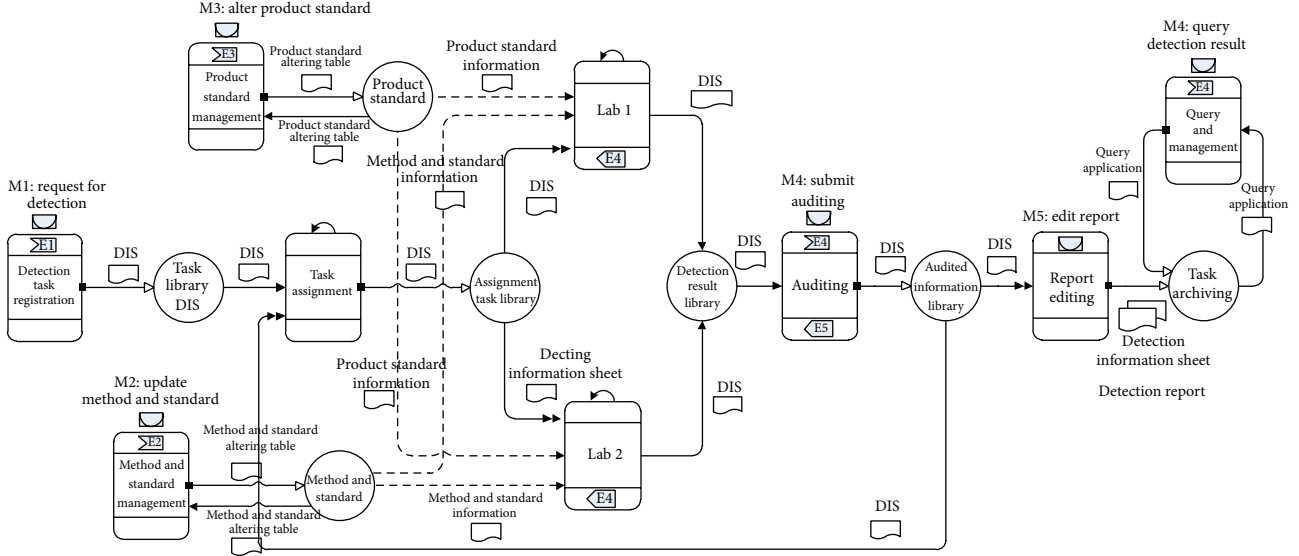


FIGURE 1: Lifecycle of business data in “monitoring information.”

the artifact lifecycle, in which elements of repository, service, artifact type, and transport channel are abstracted to represent a realistic business process. Artiflow views business process as a graph, where nodes are either “service” or “repository.” We formalize Artiflow to facilitate data analysis and illustrate it to facilitate process analysis. Figure 1 illustrates a quality inspection process instance of a certain enterprise where the main artifact is the “monitoring information sheet.” The artifact captures the detected product’s evolvement from creation to archiving, which includes all the business-relevant data in this process. The whole process comprises detection task registration, task assignment, task inspection, task audition, and so forth. Note that artifact “monitoring information sheet” is inseparable from the coordinate with such other artifacts as “product standard” and “method & standard” within its lifecycle. When “monitoring information sheet” completes its lifecycle, it will serve as a reference to form a new artifact—“detection information sheet (DIS, for short).”

In this figure, there are nine services (“task assignment,” “auditing,” etc.), seven repositories (“assignment task library,” etc.), and serial transport channels between these repositories and services.

2.3. Model Quality Evaluation. Exactly, one business object can be achieved by implementing different business processes, while different business process corresponds to a different Artiflow model. However, we will measure the Artiflow based on two factors: (1) the number of services determines the flexibility of model. (2) The repository services read and update artifacts. It is in this context that we define following theorem to measure the quality of artifact models.

Theorem 8. Given an Artiflow (N, S, R, C, Ru) , it has j Artifacts where the number of attributes in any Artifact $_i$ is n_i . Suppose $|S^i|$ and $|R^i|$ represent the service amount and repository amount of corresponding Artifact $_i$, respectively; formula (1) is defined to calculate Artiflow’s web service granularity and

repository service proportion, so as to measure the quality of models:

$$\pi = \frac{\sum_{i=1}^j \rho_i (\alpha (|S^i|/n_i) + \beta (1 - |R^i|/(|S^i| + |R^i|)))}{\sum_{i=1}^j \alpha (|S^i|/n_i) + \beta (1 - |R^i|/(|S^i| + |R^i|))}, \quad (1)$$

where α , β , and ρ_i are known.

Theorem Proving. For a given Artiflow (N, S, R, C, Ru) , each Artifact $_i$ comprises both a service sequence and a repository sequence, marked as $(S_x, R_u, \dots, S_y, R_v)$, where service sequence is described as $S^i = (S_x, \dots, S_y)$ and repository sequence is described as $R^i = (R_u, \dots, R_v)$. Each Artifact $_i$ also contains m attributes.

Suppose $|S^i|$ and $|R^i|$ represent the service amount and repository amount, respectively, then $|S^i|/m$ represents the granularity of services when dividing the whole lifecycle of artifact by its attribute number m . A larger value indicates there are more blocks that are divided and the granularity is less, which contributes to building a more flexible model.

In Artiflow, normally each artifact has a following repository to store its intermediate state, but there is exception that some services can directly communicate with each other and do not need intermediate repositories. Therefore, for the same Artifact, the few the repository elements are, the less the redundancy would be. $|R^i|/(|S^i| + |R^i|)$ represents the proportion of repository elements in both service and repository elements within its corresponding artifact lifecycle. The shorter the value is, the better the designed lifecycle would be.

The quality of Artifact $_i$ is computed by the following formula:

$$\pi = \alpha \left(\frac{|S^i|}{n_i} \right) + \beta \left(1 - \frac{|R^i|}{|S^i| + |R^i|} \right), \quad (2)$$

where α and β are predefined constants, which is used to balance the different magnitude between values both before and after the plus.

Each Artiflow comprises multiple Artifacts, so the quality measurement formula for the whole Artiflow is $\pi = \frac{\sum_{i=1}^j \rho_i \pi_i}{\sum_{i=1}^j \pi_i}$, where j is the number of artifacts and $\sum_{i=1}^j \rho_i = 1$; ρ_i represents the importance of Artifact _{i} . The optimization of key Artifacts has a great impact on the whole model to great extent, while the optimization of less-valuable artifact does not contribute too much to the model efficiency. Note that ρ_i can be either given by user or obtained by data analysis.

By integrating with both repository element redundancy and service element granularity,

$$\begin{aligned} \pi &= \frac{\sum_{i=1}^j \rho_i \pi_i}{\sum_{i=1}^j \pi_i} \\ &= \frac{\sum_{i=1}^j \rho_i (\alpha (|S^i|/n_i) + \beta (1 - |R^i| / (|S^i| + |R^i|)))}{\sum_{i=1}^j \alpha (|S^i|/n_i) + \beta (1 - |R^i| / (|S^i| + |R^i|))} \end{aligned} \quad (3)$$

can be deduced and taken to measure the model quality.

3. Business Data Querying

Enterprises like Google, Amazon have provided plenty of cloud services, which provide an open storage solution for data like process data all over the world. But off-site storage is unsafe due to data privacy, even public cloud. In this case, these data need to be encrypted and then stored in database. But it is hard to make a trade-off between data security and query speed, which is because process data need to be frequent queried, modified, and transmitted. In this section we make study on partitioning encrypted artifacts and coming up with a superior query plan for cryptograph query that minimizes the execution cost.

3.1. Business Data Partition. In order to ensure the efficiency of business process, a superior data partition is on-demand. When using Bucket partition method, query result on cryptograph is actually a superset of true results generated by relevant operators and then filtered at the client after decryption. Thus, superior partition method is of great help and aims to minimize the work done as much as possible, such as minimizing the number of interferential results.

3.1.1. Data Analysis

Definition 9 (Bucket [18]). Mapping the domain of attribute A into another partitions set $\{p_1, \dots, p_M\}$, where $p_i \cup p_j = \emptyset$, $1 \leq i, j \leq M$, each partition p_i is named as a Bucket; M is the Bucket number.

Definition 10 (the user interest on artifact). Querying on Artifact's attribute A of n times, respectively, while $q(a_i)$ represents any single result of queries q that contains value a_i , suppose $f(q(a_i))$ is the frequency of $q(a_i)$ occurring in n trials, as n increases, the frequency stabilizes at a certain value, which is expressed as $p(q(a_i))$. In other words, $p(q(a_i))$ is the probability of artifact attribute a_i emerged in query result dataset, called user interest.

Definition 11 (interferential artifact). (Intf-Artifact) is an artifact which is incorrect result but belong to cryptograph query result $q^*(a_i)$, named as INTFA($q^*(a_i)$).

3.1.2. Min-Interference Partition. All Artifacts in each Bucket correspond to a given index number in Bucket-based cryptograph partition. Cryptograph query returns all the encrypted Artifacts in Bucket where true result exists. The rest in Bucket would be transmitted to users as Intf-Artifact, and then it should be deciphered and further filtered. Hence, Bucket partition method determines the number of Intf-Artifacts, which further effects the query processing cost.

Suppose a cryptograph relation contains n tuples $\{\text{Artifact}_1, \text{Artifact}_2, \dots, \text{Artifact}_n\}$ and k is a large integer; then we pose k random queries. Totally, there are k_i queries where their final query results are Artifact _{i} , and other l_i tuples are returned as the provisional result. In this case the expectation of Intf-Artifact is $l_i * (k_i/k)$.

There are n tuples in the relation at all, and then the expectation of total Intf-Artifacts is

$$l_1 * \left(\frac{k_1}{k}\right) + l_2 * \left(\frac{k_2}{k}\right) + \dots + l_n * \left(\frac{k_n}{k}\right). \quad (4)$$

As for each Bucket containing n different attribute values, its user interest is $p(q(B)) = p(q(a_1)) + p(q(a_2)) + \dots + p(q(a_n))$.

If the user interest on i th artifact in a given Bucket is $p(q(a_i)/p(q(B)))$, ($1 \leq i \leq n$), then the number of Intf-Artifacts brought by above query is $|\text{INTFA}(q^*(a_i))| = f_1 + f_2 + \dots + f_{i-1} + f_{i+1} + \dots + f_n$.

As for Bucket j ($1 \leq j \leq k$), based on the user interest on artifact and the number of Intf-Artifacts in each Bucket, we can describe Bucket Intf-Artifact as follows:

WINTFA

$$\begin{aligned} &= \sum_{j=1}^M \left[p(q(B_j)) \right] * |\text{INTFA}(\text{Bucket}_j)| \\ &= \sum_{j=1}^M \left[p(q(B_j)) * \sum_{i=1}^n \left(\frac{p(q(a_i))}{p(q(B_j))} |\text{INTFA}(q^*(a_i))| \right) \right] \\ &= \sum_{j=1}^M \left[p(q(B_j)) * \sum_{i=1}^n \left(\frac{p(q(a_i))}{p(q(B_j))} \left(\sum_{i=1}^n f_i^j - f_i^j \right) \right) \right] \\ &= \sum_{j=1}^M \left[\sum_{i=1}^n p(q(a_i)) \sum_{i=1}^n f_i^j - \sum_{i=1}^n p(q(a_i)) f_i^j \right] \\ &= \sum_{j=1}^M \left[\sum_{i=1}^n p(q(a_i)) F_j - \sum_{i=1}^n p(q(a_i)) f_i^j \right]. \end{aligned} \quad (5)$$

From here we see that in the case of a fixed Bucket number, the smaller the value of formula (5) is, the more excellent the index would be. A larger value brings a heavy cost when querying and renders a low efficiency of Bucket partition. From the probability angle, Bucket where artifact with higher user interest exists should contain fewer Artifacts. Therefore, user interest on each artifact should be viewed as the weight

in the whole process. Moreover, when the index is being built, formula (5) is used to determine which Bucket we store each artifact in, which helps to obtain an optimal partition result.

3.2. Business Data Query. Cloud service stores encrypted artifact information and corresponding index information, while such other information as the partitioning of attributes, mapping function, and so forth are stored at client. When a user issues a query request, query q should be rewritten to its server-side cryptograph query q^* , which is then executed on cloud. The purpose of rewriting SQL queries is to split the query computation across the client and cloud.

3.2.1. Basic Definitions

Definition 12. $\xi_{(*,a]}(x)$ is a function which returns a set of all the Bucket ID where its right boundary value $B_{*}^j.\text{right}$ is not greater than x when once partitioning Bucket; that is, $\xi_{(*,a]}(x) = \{ \text{BID}_{*}^j \mid B_{*}^j.\text{right} \leq x \}$.

Definition 13. $\xi_{[a,*)}(x)$ is a function which returns a set of all the Bucket ID where its left boundary value $B_{*}^j.\text{left}$ is greater than x when once partitioning Bucket; that is, $\xi_{[a,*)}(x) = \{ \text{BID}_{*}^j \mid B_{*}^j.\text{left} \geq x \}$.

Definition 14. $\xi_{(*,p(q(v_i)))}(x)$ is a function which returns a set of all the Bucket ID where its maximum artifact query probability $B_{*}^j.\text{pright}$ is not greater than x when twice partitioning Bucket; that is, $\xi_{(*,p(q(v_i)))}(x) = \{ \text{BID}_{*}^j \mid B_{*}^j.\text{pright} \leq x \}$.

Definition 15. $\xi_{[p(q(a_i)),*)}(x)$ is a function which returns a set of all the Bucket ID where its minimum artifact query probability $B_{*}^j.\text{pleft}$ is not less than x when twice partitioning Bucket; that is, $\xi_{[p(q(a_i)),*)}(x) = \{ \text{BID}_{*}^j \mid B_{*}^j.\text{pleft} \geq x \}$.

Definition 16. $\delta_{\text{cond}}(C)$ is a function that translates specific query conditions to encrypted ones.

Definition 17. Query rewriting function is described as $\delta_{\text{query}}(q) \Rightarrow q^*$, where q is the original query and q^* is the cryptograph query.

3.2.2. Query Rewriting Rules. In view of grammatical rules, query condition cond includes: $v, A : A, \text{cond}_1 \vee \text{cond}_2, \text{cond}_1 \wedge \text{cond}_2$, where “:” is the operator, such as equal, less than, not greater than, greater than, and not less than. We list the rewrite formulas for various query conditions as shown in Formulas (6) to (8).

(1) $A : v$:

$$\begin{aligned} \delta_{\text{cond}}(x = e) &\Rightarrow^1 A^* = \xi_e(x) \\ \delta_{\text{cond}}(x < e) &\Rightarrow^2 A^* \leq \xi_e(x) \\ \delta_{\text{cond}}(x < e) &\Rightarrow^3 A^* \in \xi_{(*,e]}(x) \\ \delta_{\text{cond}}(x > e) &\Rightarrow^4 A^* \geq \xi_e(x) \\ \delta_{\text{cond}}(x > e) &\Rightarrow^5 A^* \in \xi_{[e,*)}(x), \end{aligned} \quad (6)$$

where both Map 2 and Map 4 are order preserving, and both Map3 and Map 5 are random.

(2) $A : A$:

$$\begin{aligned} \delta_{\text{cond}}(A_i < A_j) &\Rightarrow^1 \vee (A_i^* = \text{Bid}_{A_i}(p_k) \wedge A_j^* \geq \xi_{A_i}(p.\text{left})) \\ \delta_{\text{cond}}(A_i < A_j) &\Rightarrow^2 \vee (A_j^* = \text{Bid}_{A_j}(p_l) \wedge A_i^* \geq \xi_{A_j}(p.\text{right})) \\ \delta_{\text{cond}}(A_i < A_j) &\Rightarrow^3 \vee (\xi_{A_i}(p_k.\text{left}) \leq \xi_{A_j}(p_l.\text{right})) \\ \delta_{\text{cond}}(A_i < A_j) &\Rightarrow^4 \vee (A_i^* = \text{Bid}_{A_i}(p_k) \wedge A_j^* = \text{Bid}_{A_j}(p_l)), \end{aligned} \quad (7)$$

where $p_k \in \text{partition}(A_i)$, $p_l \in \text{partition}(A_j)$, and $p_l.\text{high} \geq p_k.\text{low}$.

When the condition is $A_i < A_j$, in Map 1 A_i is order preserving, while in Map 3 both A_i and A_j are order preserving. Meanwhile, in Map 2 A_j is order preserving, and in Map 4 both A_i and A_j are random.

(3) $\text{cond}_1 \vee \wedge \text{cond}_2$:

$$\begin{aligned} \delta_{\text{cond}}(\text{cond}_1 \vee \text{cond}_2) &\Rightarrow \delta_{\text{cond}}(\text{cond}_1) \vee \delta_{\text{cond}}(\text{cond}_2), \\ \delta_{\text{cond}}(\text{cond}_1 \wedge \text{cond}_2) &\Rightarrow \delta_{\text{cond}}(\text{cond}_1) \wedge \delta_{\text{cond}}(\text{cond}_2). \end{aligned} \quad (8)$$

For instance, suppose there are two artifact plaintext tables in cloud database, which are app (aid, aname, time, content, cid) check (cid, aid, result), respectively, where the range of attribute *aid* is divided into 6 partitions, including $\text{id}_{\text{app.aid}}([0, 100]) = 3$; $\text{id}_{\text{app.aid}}((100, 200]) = 7$; $\text{id}_{\text{app.aid}}((200, 300]) = 5$; $\text{id}_{\text{app.aid}}((300, 400]) = 1$; $\text{id}_{\text{check.aid}}([0, 200]) = 2$; $\text{id}_{\text{check.aid}}((200, 400]) = 6$.

Given above partition results, we rewrite the following query conditions based on above formulas:

$$\begin{aligned} \delta_{\text{cond}}(\text{aid} = 256) &\Rightarrow \text{aid}^* = 5, \\ \delta_{\text{cond}}(\text{aid} < 180) &\Rightarrow \text{aid}^* \in \{3, 7\}, \\ \delta_{\text{cond}}(\text{aid} > 240) &\Rightarrow \text{aid}^* \in \{5, 1\}. \end{aligned} \quad (9)$$

$\delta_{\text{cond}}(\text{app.did} = \text{check.did}) \Rightarrow (\text{app}^*.\text{did}^* = 3 \wedge \text{check}^*.\text{did}^* = 2) \vee (\text{app}^*.\text{did}^* = 7 \wedge \text{check}^*.\text{did}^* = 2) \vee (\text{app}^*.\text{did}^* = 5 \wedge \text{check}^*.\text{did}^* = 6) \vee (\text{app}^*.\text{did}^* = 1 \wedge \text{check}^*.\text{did}^* = 6)$.

$\delta_{\text{cond}}(\text{app.did} < \text{check.did}) \Rightarrow (\text{app}^*.\text{did}^* = 3 \wedge \text{check}^*.\text{did}^* = 2) \vee (\text{app}^*.\text{did}^* = 3 \wedge \text{check}^*.\text{did}^* = 6) \vee (\text{app}^*.\text{did}^* = 7 \wedge \text{check}^*.\text{did}^* = 2) \vee (\text{app}^*.\text{did}^* = 7 \wedge \text{check}^*.\text{did}^* = 6) \vee (\text{app}^*.\text{did}^* = 5 \wedge \text{check}^*.\text{did}^* = 6) \vee (\text{app}^*.\text{did}^* = 1 \wedge \text{check}^*.\text{did}^* = 6)$.

3.2.3. Query Optimization Principles. Because data is encrypted and stored in various places, in order to reduce the transmission cost and improve the query efficiency, we

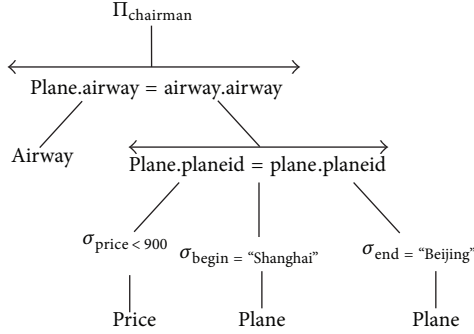


FIGURE 2: Initial syntax tree.

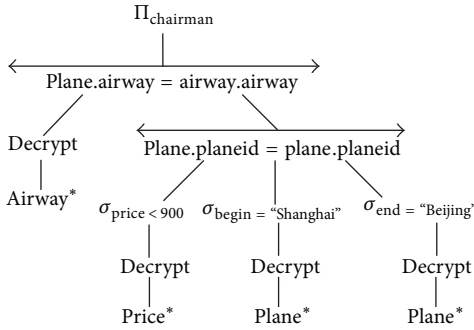


FIGURE 3: Syntax tree applied to cloud DB.

should run operations on cloud services as much as possible, and the answers can be computed with little effort by the client.

For clear expression, operation procedure is expressed by using the syntax tree. The decryption operation splits the tree into cryptograph operations and plaintext operations. Because any single operation on the original tree ends with the selection after decryption; thereby the principle of query optimization by using syntax tree is to iteratively pull up the selection.

For example, given a selection “SELECT chairman FROM Airway, Price, Plane WHERE price < 900 AND begin = ‘shanghai’ AND end = ‘beijing’ AND Price.planeid = Plane.planeid AND Plane.airway = Airway.airway”, we take query tree to illustrate how to optimize this query and describe its detailed procedures.

In Figure 2 the SQL statement is converted into an initial syntax tree. If the enterprise use cloud services or other off-site storage platforms, we need to first decrypt the cryptograph then query the data at client, as shown in Figure 3, where cryptograph database on cloud is bounded by the dotted line. Query objects (Price, Plane, and Airway) are converted to cryptograph tables (Price*, Plane* and Airway*) in the cloud database.

Operations on syntax tree are performed from bottom to up. In Figure 3 the first step is to execute selection, while the following steps include rewriting the condition of selection operations, converting it to a selection on cryptograph in cloud database and then decrypting and further filtering the result at client. A new syntax tree is derived as shown in Figure 4.

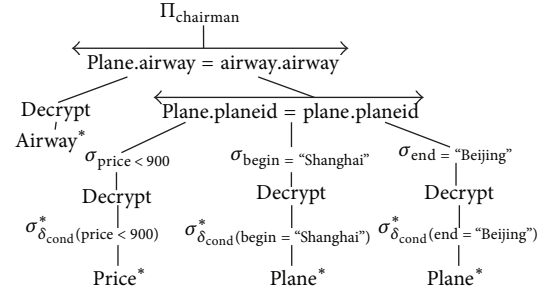


FIGURE 4: Rewriting syntax tree.

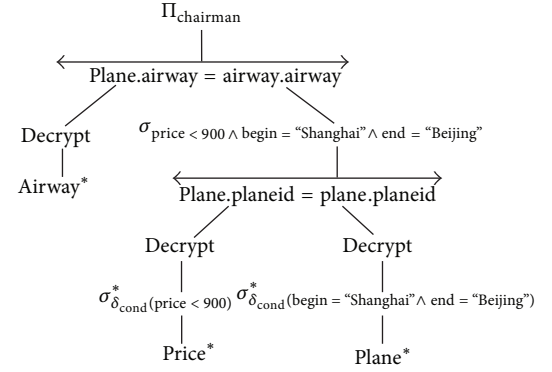


FIGURE 5: Moving selections in syntax tree.

According to optimization principles described above, we should iteratively pull up selections. Therefore, by both exchanging the positions between selection operations (price < 900, begin = ‘shanghai’ and end = ‘beijing’) and join operation and then combining corresponding conditions, we obtain a new syntax tree, as shown in Figure 5.

Moreover, based on operation rewriting rules, join operation in Figure 5 should be converted into two parts, including the join on cryptograph in the cloud database and the selection on decrypted provisional results, as shown in Figure 6. Repeat the above steps, rewrite all kinds of operations, and continuously exchange the positions between selection operations and other operations, till all the selections cannot be pulled up. As a result, we get the ultima syntax tree as shown in Figure 7. Operations within dotted line would be executed on cloud service, whereas user only needs to execute the last selection. From here we see that the above method takes full advantage of cloud service to reduce the cost of transmitting and postprocessing and improve the efficiency of artifact querying in business process.

4. Case Study

In this section, we will introduce a business instance of a certain enterprise. Based on the method in Section 2, we complete the data modeling with artifact lifecycle from a given process instance and illustrate the query process through query tree mentioned in Section 3.

An enterprise’s process of equipment purchase/scrap involves the following steps. At first equipment division fills out the equipment purchase/scrap application and hands it to

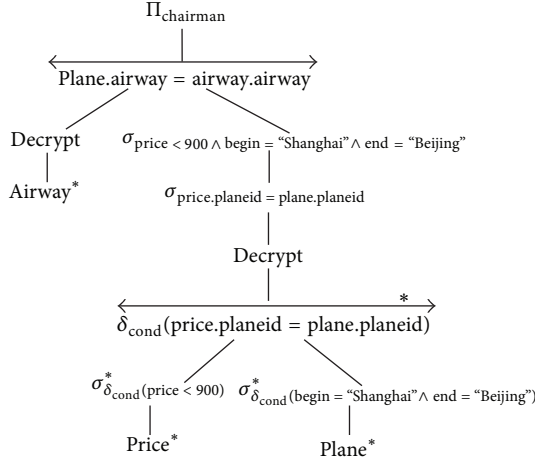


FIGURE 6: Rewriting syntax tree.

department managers and company's leadership for approval. If the application is consented, then we should archive it; else we withdraw it. Purchasing department does purchase according to a copy of application, and when the purchase is completed, documents should be archived. Equipment division scraps the equipment based on specific methods and standards and then archives the processing results. Assets department regularly verifies company's assets based on purchase/scrap equipment information. Archive department has permission to query all the archived information.

This process involves multiple departments and multiple sets of information. If we manage the data alone, as business data are complicated, and even one attribute has difference value in different event, thereby it is difficult to manage. If we manage the process alone, only the department activities will be involved while business data in the process will be ignored. In this context, we analyze the process concerning both data and process and describe this instance with an Artiflow (N, S, R, C, Ru) , where

N : "EP/S";

S : {FilloutEPA, Audit1, Audit2, Query, Purchase, Asset Verification...};

R : {NewEPA, PrimaryEPA, FinalEPA, Unapro-ved EPA, PO, FAL...};

C : {FtoN, NtoA,...};

Ru : {constraint (EPA) = (FilloutEPA, Audit1, Audit2)...}.

The model contains multiple artifacts: "EPA" is for describing equipment purchase application, while its lifecycle starts from filling, auditing to archiving. When having been archived, it will provide asset verification and support query processing. "ESA" is for describing equipment scrap application, while its lifecycle starts from filling, auditing to archiving. It is associated with another artifact, called "method & standard." The lifecycle of "PO"/"SL" captures process from

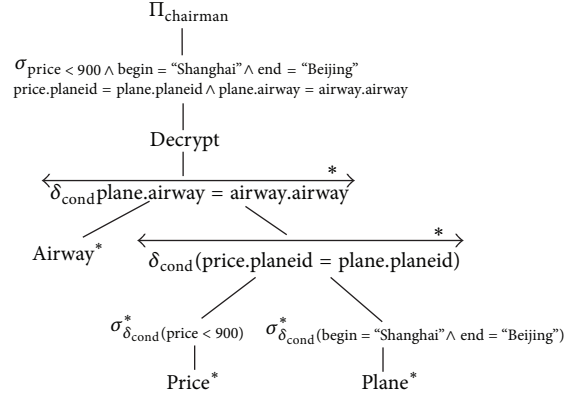


FIGURE 7: The ultima syntax tree.

purchase/scrap to application archive. The whole process is shown in Figure 8.

Artifact Example.

Artifact: (C, A, τ, Q, s, F)

C = "EPA";

A : {EquipmentName, PurchaseAmount, UnitPrice, ApplicationDate, Applicant, AuditingComment, AuditingDate};

Q : {empty table (initial state s), basic information filling, delivery auditing, auditing completion, audited application archiving (terminate state F)};

τ : EquipmentName: verchar; PurchaseAmount: In; UnitPrice: Int; ApplicationDate: Date; Applicant: Verchar; AuditingComment: Verchar; AuditingDate: Date.

Service Example.

service = (n, V_r, V_w, P, E) , where:

n = "Audit2";

V_r : {EPA};

V_w : {EPA};

P : DEFINED (EquipmentName) \wedge DEFINED (PurchaseAmount) \wedge DEFINED (UnitPrice) \wedge DEFINED (ApplicationDate) \wedge DEFINED (Applicant) \wedge \neg DEFINED (AuditingComment) \wedge \neg DEFINED (AuditingDate).

E : DEFINED (EquipmentName) \wedge DEFINED (PurchaseAmount) \wedge DEFINED (UnitPrice) \wedge DEFINED (ApplicationDate) \wedge DEFINED (Applicant) \wedge DEFINED (AuditingComment) \wedge DEFINED (AuditingDate).

Repository Example.

$R = (re, R_a, R_r, C_t)$.

re: "FinalEPA";

R_a : {EPA};

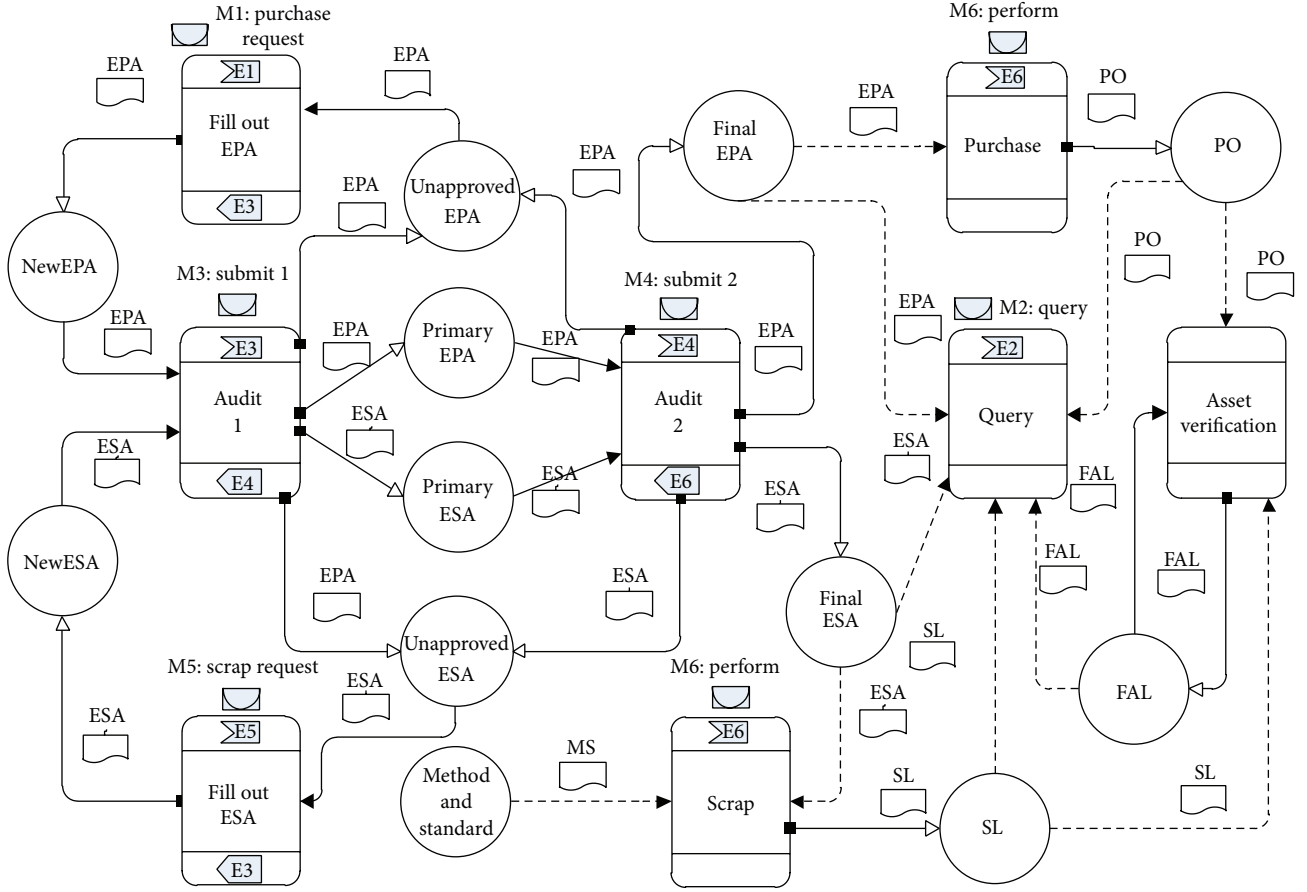


FIGURE 8: Lifecycle of business data in equipment purchase/scrap process.

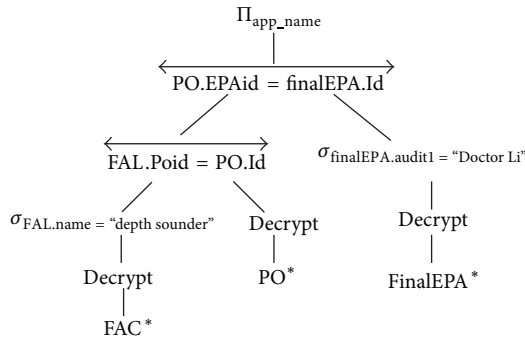


FIGURE 9: Initial query on EP/S.

 $R_r: \{EPA\};$
 $C_t: IsDefine(AuditingComment).$

There is a repository named “FinalEPA,” which reads and stores artifact “EPA” only if “AuditingComment” has been assigned.

Given a query “SELECT app_name FROM FAL, PO, FinalEPA WHERE Fal.name = ‘depthsounder’ AND FAL.Poid = PO.Id AND PO.EPAId = FinalEPA.Id AND FinalEPA.Audit2 = ‘Doctor Li’”, it can be converted into a syntax tree as shown in Figure 9, which can be further converted into a new syntax tree shown in Figure 10. Queries will be issued on this syntax tree.

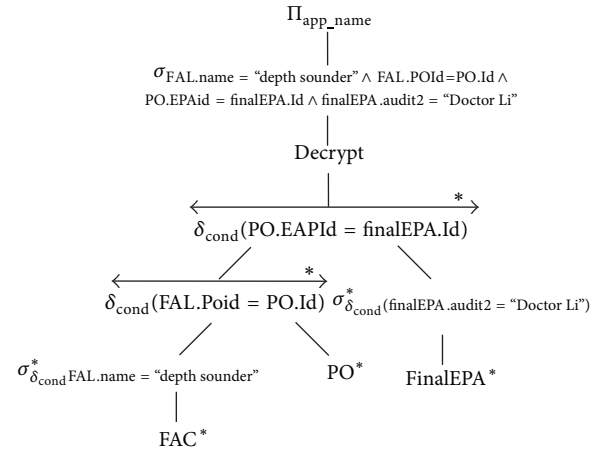


FIGURE 10: Ultima query on EP/S.

5. Conclusion

There is no doubt that more and more large datasets will be poured out during business process execution; meanwhile, these business data are extremely valuable. In this case, we modeled business data through its lifecycle from the perspective of process, which ensures the integrity of dynamic business data. Furthermore, we present the notion of user interest on business data, which has a superior function in

counting minimum interferential tuples during data partition and ensuring a lower cost of postprocessing brought by data partition. Considering current business data are mostly stored on cloud, we proposed a query rewriting strategy for off-site encrypted data which has a significant advantage in reducing the postprocessing cost. Currently there is little research on business data modeling and querying in the true sense. Our research lays great foundation for business data's application in enterprise. That is the initial step of business data management architecture, and we will further research on business data analysis with its lifecycle, to fully dig the significant value of business data.

Conflict of Interests

The authors declare that there is no conflict of interests regarding the publication of this paper.

Acknowledgments

This work is supported by National Natural Science Foundation of China (61272098) and Science and Technology Development Foundation of Shanghai Ocean University.

References

- [1] W. Huang, Z. Chen, W. Dong, H. Li, B. Cao, and J. Cao, "Mobile internet big data platform in china unicom," *Tsinghua Science and Technology*, vol. 19, no. 1, pp. 95–101, 2014.
- [2] S. Sagirolu and D. Sinanc, "Big data: a review," in *Proceedings of the International Conference on Collaboration Technologies and Systems (CTS '13)*, pp. 42–47, San Diego, Calif, USA, May 2013.
- [3] M. Chui, B. Brown, J. Bughin et al., *Big Data: The Next Frontier for Innovation, Competition, and Productivity*, McKinsey Global Institute, 2011.
- [4] M. Singh and S. K. Jain, "A survey on dataspace," in *Advances in Network Security and Applications*, vol. 196 of *Communications in Computer and Information Science*, pp. 608–621, Springer, 2011.
- [5] K. Belhajjame, N. W. Paton, S. M. Embury, A. A. A. Fernandes, and C. Hedeler, "Incrementally improving dataspace based on user feedback," *Information Systems*, vol. 38, no. 5, pp. 656–687, 2013.
- [6] J.-P. Dittrich and M. A. Vaz Salles, "IDM: a unified and versatile data model for Personal Dataspace Management," in *Proceedings of the 32nd International Conference on Very Large Data Bases (VLDB '06)*, pp. 367–378, September 2006.
- [7] S. Pradhan, "Towards a novel desktop search technique," in *Database and Expert Systems Applications*, pp. 192–201, Springer, Berlin, Germany, 2007.
- [8] M. Zhong, M. Liu, and Q. Chen, "Modeling heterogeneous data in dataspace," in *Proceedings of the IEEE International Conference on Information Reuse and Integration (IEEE IRI '08)*, pp. 404–409, Las Vegas, Nev, USA, July 2008.
- [9] A. Sarma, X. Dong, and A. Halevy, "Data modeling in dataspace support platforms," in *Conceptual Modeling: Foundations and Applications*, pp. 122–138, Springer, Berlin, Germany, 2009.
- [10] R. Hull and J. Su, *Report on NSF Workshop on Data-Centric Workflows*, 2012, <http://dcw2009.cs.ucsb.edu/report.pdf>.
- [11] R. Hull, J. Su, and R. Vaculin, "Data management perspectives on business process management," in *Proceedings of the ACM SIGMOD Conference on Management of Data (SIGMOD '13)*, pp. 943–947, June 2013.
- [12] K. Bhattacharya, N. S. Caswell, S. Kumaran, A. Nigam, and F. Y. Wu, "Artifact-centered operational modeling: lessons from customeengagements," *IBM Systems Journal*, vol. 46, no. 4, pp. 703–721, 2007.
- [13] K. Bhattacharya, R. Guttman, K. Lyman et al., "A model-driven approach to industrializing discovery processes in pharmaceutical research," *IBM Systems Journal*, vol. 44, no. 1, pp. 145–162, 2005.
- [14] R. Vaculin, R. Hull, T. Heath, C. Cochran, A. Nigam, and P. Sukaviriya, "Declarative business artifact centric modeling of decision and knowledge intensive business processes," in *Proceedings of the 15th IEEE International EDOC Enterprise Computing Conference (EDOC '11)*, pp. 151–160, September 2011.
- [15] R. Vaculin, R. Hull, M. Vuković, T. Heath, N. Mills, and Y. Sun, "Supporting collaborative decision processes," in *Proceedings of the IEEE 10th International Conference on Services Computing (SCC '13)*, pp. 651–658, July 2013.
- [16] A. Nigam and N. S. Caswell, "Business artifacts: an approach to operational specification," *IBM Systems Journal*, vol. 42, no. 3, pp. 428–445, 2003.
- [17] G. Liu, X. Liu, H. Qin et al., "Automated realization of business workflow specification," in *Proceedings of the 1st International Workshop on SOA, Globalization, People, and Work (SG-PAW '09)*, pp. 8–9, 2009.
- [18] H. Hacigümüş, B. Iyer, C. Li, and S. Mehrotra, "Executing SQL over encrypted data in the database-service-provider model," in *Proceedings of the ACM SIGMOD International Conference on Management of Data*, pp. 216–227, June 2002.

Research Article

Seismic Stability Time-Frequency Analysis Method of Reinforced Retaining Wall

Yang Changwei,¹ Zhang Shixian,^{1,2} Zhang Jianjing,¹ and Bi Junwei¹

¹School of Civil Engineering, Key Laboratory of Transportation Tunnel Engineering, Ministry of Education, Southwest Jiaotong University, Chengdu 610031, China

²School of Civil Engineering, Panzhihua University, Panzhihua 617000, China

Correspondence should be addressed to Yang Changwei; 1209732335@qq.com

Received 16 April 2014; Revised 27 June 2014; Accepted 8 July 2014

Academic Editor: Kim M. Liew

Copyright © 2015 Yang Changwei et al. This is an open access article distributed under the Creative Commons Attribution License, which permits unrestricted use, distribution, and reproduction in any medium, provided the original work is properly cited.

The first-order differential equation of the seismic active earth pressure is established by horizontal slices analysis method, based on the elastic wave theory, with the summarized dynamic analysis model of the reinforced retaining wall and the plane of fracture assumed as linear type. And then this paper proposes a time-frequency analysis method for the internal antiseismic stability analysis on the retaining wall. The reasonability of this method is verified by the results from other methods, for example, rule. The internal frictional angle of filling earth, the seismic intensity, and the frequency of the input earthquake wave have a predominant effect on the needed total tensile force of the lacing wires, which shows that (1) the needed total tensile force of the lacing wires goes up with the increase of the PGA and the internal frictional angle; (2) the needed total tensile force of the expandability lacing wires is bigger than that of the nonexpandability lacing wires; (3) the needed total tensile force of lacing wires is saddle distributed and the force achieves maximum value when the frequency of input wave equals the natural frequency of reinforced retaining wall. Besides, if the reinforced retaining wall is designed in compliance with the rules, the emergency capacity of reinforced retaining wall is reduced. At last, this paper not only takes into account the effect of three factors of the seismic wave (PGA, frequency, and duration) on the internal antiseismic stability analysis of reinforced retaining wall but also provides some valuable references for the time-frequency seismic design of other retaining structures.

1. Introduction

In Wenchuan earthquake, only one type of destruction of reinforced retaining wall caused by earthquake ground motion results in the rigid-plastic complex reinforcement's fracture. This phenomenon fully shows that reinforced retaining wall is applicable in high intensity earthquake area [1]. The earthquake stability analysis methods for reinforced retaining wall are usually pseudostatic method, limit displacement method, and numerical method [2–7]. The pseudostatic method only considers the effect of PGA on the stability of retaining wall and ignores the duration and frequency of seismic wave; while duration and frequency are not considered in limit displacement method, the method is not convenient in engineering practice with poor precision. The progress of computer techniques promotes the numerical

analysis methods development in practical engineering analysis. The methods contain the finite element method, boundary element method, the meshless method, and so forth [8, 9]. Among those analysis methods, the meshless method is suitable in resolving practical problems, and another problem as mesh distortion in the finite element method and boundary element method can be generally avoided. Now, there are dozens of meshless methods, and each method uses different weighted residuals and approximate functions [10], which might be the direction of development in numerical analysis methods. As for the design of the reinforced retaining wall, results are more precise than pseudostatic method, finite element method, and boundary element method. It can consider the effect of PGA likewise, duration, and frequency of seismic wave, and nonlinear behavior of backfill earth on the stability of retaining wall. However, the meshless method

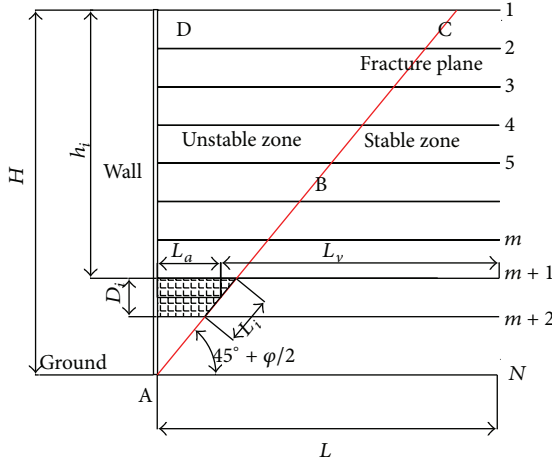


FIGURE 3: Reinforcement with ductility.

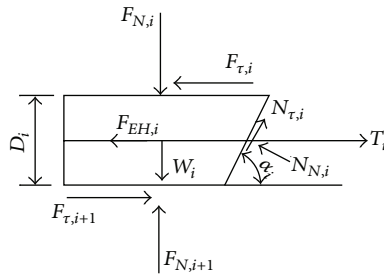


FIGURE 4: Analysis model of horizontal soil layer.

In the inclined section, the height is $h_2 = H/2$ and the dip angle is $45^\circ + \Phi/2$. If the reinforcement is nonductile, field test results show that this rupture plane is close to the real failure plane. Therefore, according to the characteristics of rods, this paper simplifies the rupture plane to two kinds. (2) In the real reinforced earth retaining wall engineering, the backfill soil is placed in layers, while not every layer is proper continuous, homogeneous, and isotropic. As a theoretical study, this paper assumes that the backfill soil meets the above characteristics. A number of research results indicate that the above assumptions of backfill soil cannot produce bigger effect on the calculated results. (3) When the seismic wave spreads from the bottom of the retaining wall to the top, the internal material damping will dissipate major seismic energy, the seismic wave will produce waveform transformation, and the seismic wave will be transformed into surface wave, behaving in the elliptical polarization movement. The reflective seismic wave on the upper surface of soil carries a small amount of energy of downpropagation, which has been verified by the same results. In this paper, ignoring the influence of surface reflective seismic wave is reasonable.

2.1.2. Generalized Model. For the cases of expandable and nonexpandable lacing wires, one can establish mechanical balance equations of the selective microelement by horizontal slice method, respectively. Figure 4 shows the parameters of unit-volume selected out as follows: the self-weight of

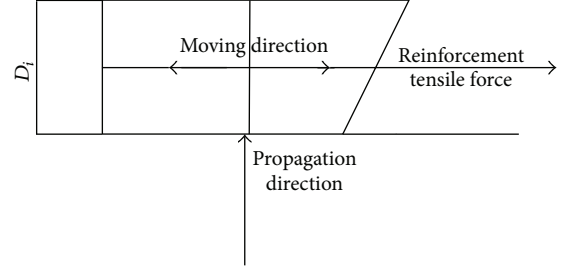


FIGURE 5: Wave-force model of horizontal soil layer.

the slice is W_i ; the normal and shear interaction forces of the upper individual horizontal slice are $F_{N,i}$, $F_{t,i}$, respectively, and those of the lower slice are $F_{N,i+1}$, $F_{t,i+1}$; tensile force of the geosynthetic at layer i is T_i ; the horizontal inertial force on the slice is $F_{EH,i}$; the angle between rupture plane and horizontal plane is α_i . The free-body diagram of wave force on the horizontal slice is shown in Figure 5.

2.1.3. Calculated Tension of Reinforcement. In Figure 4, when the force of slice i reached a balance, the total of all vertical components is zero:

$$F_{N,i+1} - F_{N,i} - W_i + N_{t,i} \sin \alpha_i + N_{N,i} \cos \alpha_i = 0, \quad (1)$$

$$N_{t,i} = cl_i + N_{N,i} \tan \phi, \quad (2)$$

where c is the cohesion of the filling earth and ϕ is the internal frictional angle.

Bring (2) into (3); the normal force of the horizontal slice $F_{N,i}$ can be derived:

$$N_{N,i} = \frac{F_{N,i} - F_{N,i+1} + W_i - cl_i \sin \alpha_i}{\tan \phi \sin \alpha_i + \cos \alpha_i}. \quad (3)$$

When the whole sliding mass reached a balance, the sum of all horizontal components is zero:

$$\sum_{i=1}^n T_i + \sum_{i=1}^n N_{t,i} \cos \alpha_i - \sum_{i=1}^n N_{t,i} \sin \alpha_i - \sum_{i=1}^n F_{EH,i} = 0. \quad (4)$$

Bringing (2) and (3) into (4), we can get that

$$\begin{aligned} & \sum_{i=1}^n T_i + \sum_{i=1}^n (cl_i + N_{N,i} \tan \phi) \cos \alpha_i \\ & - \sum_{i=1}^n \frac{F_{N,i} - F_{N,i+1} + W_i - cl_i \sin \alpha_i}{\tan \phi \sin \alpha_i + \cos \alpha_i} \sin \alpha_i \\ & - \sum_{i=1}^n F_{EH,i} = 0. \end{aligned} \quad (5)$$

The potential function of SV-wave can be formulated uniformly by elastic displacements [20], as follows:

$$u(z, t) = U(z) e^{i\omega t}, \quad (6)$$

where $U(z, t)$ is the displacement function of microunit i ; $U(z)$ is the amplitude of the elastic displacement of microunit i ; ω is the vibrational frequency of microunit i .

Then, the inertial force which is generated by SV-wave of microunit i is as follows:

$$F_{EH,i} = \left| w_i \cdot \frac{\partial^2 u / \partial t^2}{g} \right| = \frac{W_i w^2 U(z)}{g}. \quad (7)$$

Hence, the needed total tensile force of the expandability and nonexpandability lacing wires in reinforced retaining wall can be obtained, respectively, by bringing (7) into (5), as follows:

$$\sum_{i=1}^n T_i = \rho V w^2 U(z) - \frac{cH \cos \alpha}{\sin \alpha} - \frac{[\cos \alpha \tan \varphi - \sin \alpha] [F_{N,0} + W - cH]}{\tan \varphi \sin \alpha + \cos \alpha}, \quad (8)$$

$$\begin{aligned} \sum_{i=1}^n T_i &= \rho V w^2 U(z) - 0.3cH \\ &+ \frac{0.3(1 - 0.3 \tan \alpha) \gamma H^2 - [c(1 - 0.3 \tan \alpha) H]}{\tan \varphi} \\ &\times ([\cos \alpha \tan \varphi - \sin \alpha] [F_{N,0} + 0.045 \gamma H^2 \tan \alpha] \\ &- 0.3cH \tan \alpha) \\ &\times (\tan \varphi \sin \alpha + \cos \alpha)^{-1}, \end{aligned} \quad (9)$$

where $F_{N,0}$ is the overload at the top surface of the retaining wall; ω is the instantaneous frequency of SV-wave, which changes over time; ρ is the density of the filling earth behind retaining wall; V is the volume of the sliding mass ABCD; α is the angle between the rupture plane inclined part of retaining wall and the horizontal plane.

The needed total tensile force ($\sum_{i=1}^n T_i$) of the lacing wires in reinforced retaining wall can be transformed into the dimensionless value K , which is equal to the coefficient of soil pressure with the traditional design method for retaining wall. And then the formulation of K is that

$$K = \sum_{i=1}^n \frac{T_i}{\gamma H^2}. \quad (10)$$

The tensile force of lacing wires at layer i is T_i , as follows:

$$T_i = \gamma h_i D_i K. \quad (11)$$

2.2. Analysis Mentality of Time-Frequency Effect. Time-frequency effect of seismic wave is mainly manifested in the elastic amplitude $U(z)$ and frequency ω of input seismic excitation. The analysis procedures of time-frequency effect proposed in this paper are as follows. (1) Decompose the seismic wave to several intrinsic mode functions (IMF)

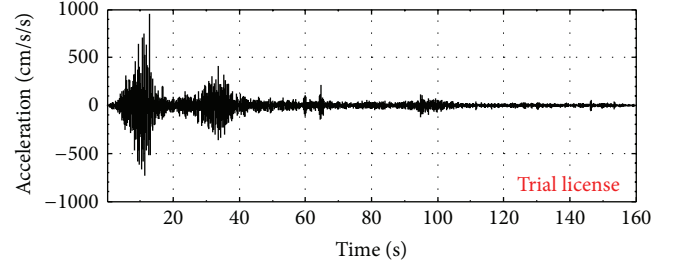


FIGURE 6: Time history of Wenchuan-Wolong wave.

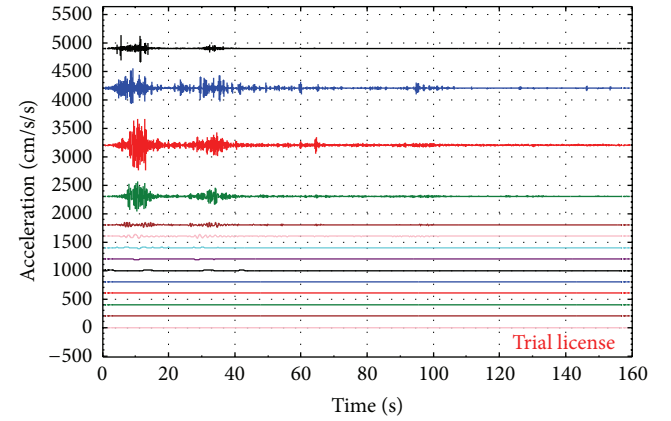


FIGURE 7: Acceleration time history of IMF.

by the empirical mode decomposition (EMD) method. (2) Convert the multiple-channel multiple signals which consist of IMF to several single-channel single signals by conducting channel switch. (3) Solve instant frequency of each channel and plot the frequency time history curve. (4) The needed total tensile force of lacing wires can be obtained by bringing every IMF and its instant frequency into (8) and (9).

From the above analysis, we know that time-frequency effect method of the antiseismic stability of reinforced retaining wall proposed in this paper can offset the drawbacks of pseudostatic method and limited displacement method. Moreover, it considers the effects of PGA, frequency, and duration primly for the stability of reinforced retaining wall under earthquake.

2.3. Application of Time-Frequency Effect for Seismic Wave. In order to illustrate the application of time-frequency effect for seismic wave particularly, authors chose Wolong seismic waves input to carry out time-frequency analysis. (1) Input the Wolong seismic wave (Figure 6). (2) Disintegrate the seismic wave into multiple IMF by conducting EEMD method (Figure 7). (3) Solve the instant frequency of each IMF (Figure 8).

Note that owing to sustenance over long periods of time for Wolong seismic wave, in Figures 7 and 8, the time history is only chosen from zero to eighty seconds, including peak ground acceleration.

TABLE 1: Comparison of tensile force of reinforcement between time-frequency and other calculated methods.

PGA	Tensile force (kN) $\varphi = 20^\circ$			Tensile force (kN) $\varphi = 25^\circ$			Tensile force (kN) $\varphi = 30^\circ$		
	<i>T-F</i>	Shahgholi et al. [21]	Code	<i>T-F</i>	Shahgholi et al. [21]	Code	<i>T-F</i>	Shahgholi et al. [21]	Code
0.1	151	159	156	137	147	144	123	118	117
0.2	161	171	169	146	157	154	145	138	136
0.4	177	189	184	161	173	169	157	150	145

Note: PGA means peak ground acceleration; *T-F* means time-frequency method presented in this paper; Sha means method presented by Shahgholi et al., 2001 [21].

TABLE 2: Error analysis of tensile force of reinforcement between time-frequency and other calculated methods.

PGA	Tensile force (%) $\varphi = 20^\circ$		Tensile force (%) $\varphi = 25^\circ$		Tensile force (%) $\varphi = 30^\circ$	
	Shahgholi et al. [21]	Code	Shahgholi et al. [21]	Code	Shahgholi et al. [21]	Code
0.1	5.30	3.14	7.30	4.76	-4.07	-5.08
0.2	6.21	4.68	7.53	5.10	-4.83	-6.52
0.4	6.78	3.70	7.45	4.62	-4.46	-8.00

Note: error = (the results of Shahgholi et al. [21] or Code - that of *T-F*) * 100% / the results of *T-F*.

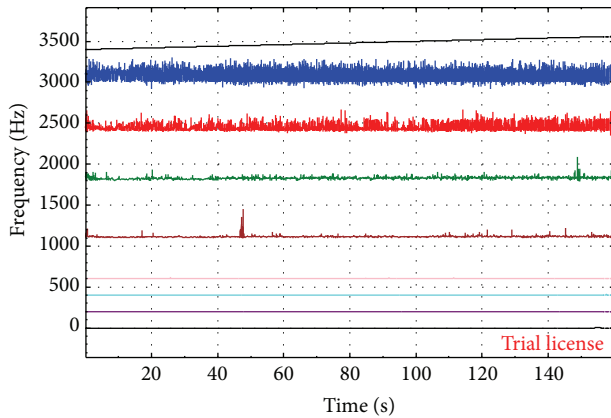


FIGURE 8: Frequency time history of IMF.

3. Solution Procedures of Time-Frequency Analysis Method for the Antiseismic Stability of Reinforced Retaining Wall

The solution procedures of time-frequency analysis method for the antiseismic stability of reinforced retaining wall proposed in this paper are as follows.

- (1) Summarize the analysis model, based on the panel, filling earth, geosynthetics of reinforced retaining wall, and actual site condition.
- (2) Judge the place of fracture plane and bar spacing in accordance with the physical characteristic of soil and the type of reinforcement.
- (3) Determine the design response spectra according to the "Code for Seismic Design of Buildings," and then synthesize the acceleration time history by the method detailed in [22].

- (4) Generate displacement time history curve according to acceleration time history curve; then, with Hilbert-Huang transform, solve all the intrinsic mode functions of seismic wave and corresponding frequency time history curves.
- (5) Bring the results above into (8) or (9) to obtain the needed total tensile force of the lacing wires; moreover, in alliance with (10), acquire the tension of reinforcement in each layer.
- (6) Based on the above calculations and the position of rupture plane, we can get the requisite sectional area and the length of any reinforcement.

4. Verification of Time-Frequency Analysis Method for the Antiseismic Stability of Reinforced Retaining Wall

In order to verify the correctness of time-frequency analysis method for the antiseismic stability of reinforced retaining wall, we consider the effect of the PGA, however, regardless of the frequency of seismic wave. For example, the unit weight of the backfill is 20 kN/m^3 and the height of retaining wall is 5 m, to arrange 18 layers of expandability lacing wires with constant spacing, and the antipull friction coefficient is 0.75; characteristic values of the shear strength parameters for the backfill are $c = 0$ and $\varphi = 20^\circ, 25^\circ, 30^\circ$, respectively, PGA of the input sinusoidal wave is 0.1, 0.2, 0.4 (g), and the frequency is 15 Hz which is beyond the incidence of frequency about seismic wave by part 3. The results of the total tensile force are shown in Tables 1 and 2.

In general, the maximum error is 8.0%, and the minimum error is 3.14%, which can show that the results by time-frequency analysis method when ignoring the effect of frequency which are shown in Tables 1 and 2 are consistent with that by the current standard method and reference.

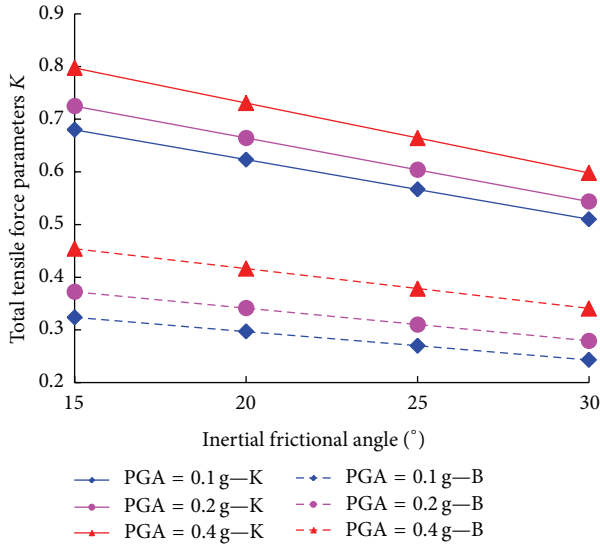


FIGURE 9: Relationship between total tensile force parameter K and internal friction angle of fill under frequency of 0.2 Hz.

Hence, the comparing simulation results proves the reliability and effectiveness of the new method proposed in this paper.

5. Parametric Study of Time-Frequency Analysis Method for the Antiseismic Stability of Reinforced Retaining Wall

For the time-frequency analysis method of reinforced retaining wall, the internal frictional angle of the filling earth, the seismic intensity, and the frequency of the input earthquake wave in different types of geosynthetics have a predominant effect on the parameter K . For example, the unit weight of the backfill is 20 kN/m^3 and the height of retaining wall is 5 m; arrange 18 layers of reinforcements with a constant spacing and the antipull friction coefficient is 0.75; characteristic values of the shear strength parameters for the backfill are $c = 0$ and $\varphi = 15^\circ, 20^\circ, 25^\circ, 30^\circ$, respectively, and PGA of the input sinusoidal wave is 0.1, 0.2, 0.4 (g) with the frequency change among 0.1, 0.2, 0.4, 0.8, 1.0, 2, 4, 5, 6, 8, and 10 (HZ).

The values of the parameter K are shown in Figures 9, 10, 11, and 12, and as well K and B represent the expandable and nonexpandable facing wires separately.

Analyzing Figure 9 to Figure 12 comprehensively, we can reach that the parameter K of the total tensile force of the facing wires decreases with the increase of the internal frictional angle, and it may be because of the following reasons: the frictional resistance on the surface of facing wires increases with the frictional angle, which improves the pulling resistance of facing wires, and then the total tensile force reduces. However, the inertia force of backfill earth increases with the increase of the PGA, and then the total tensile force of facing wires also increases significantly; the parameter K of the total tensile force of the expandability facing wires is bigger than that of the nonexpandability facing wires, and it may be because of the following reasons: if

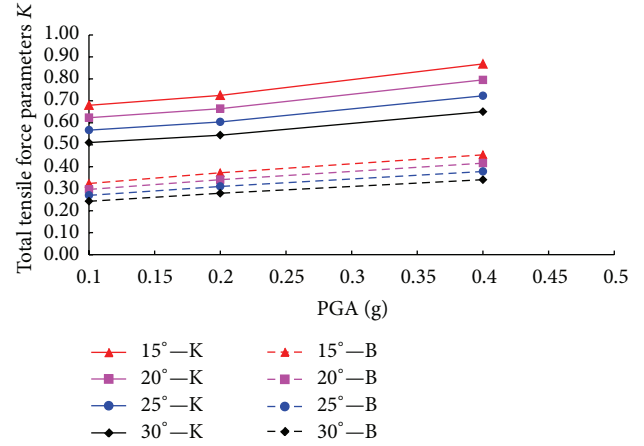


FIGURE 10: Relationship between total tensile force parameter K and PGA under frequency of 0.2 Hz.

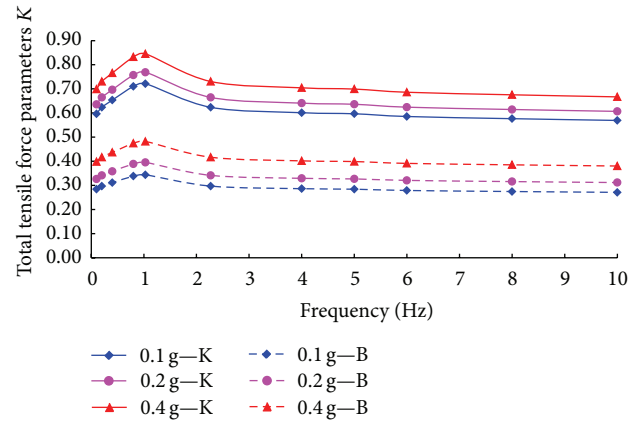


FIGURE 11: Relationship between total tensile force parameter K and frequency under internal friction angle of 20 degrees.

the reinforcement is ductility, the rupture plane is linear. On the contrary, the rupture is bending rupture plane that the reinforcement is nonductility. However, the wedge formed by the linear type plane is bigger than that formed by the bend linear type plane, and then the inertia force of the former is bigger than the latter, so the parameter K of the total tensile force of the expandability facing wires is bigger than that of the nonexpandability facing wires; the needed total tensile force of facing wires is distributed in the shape of saddle and the force achieves the maximum value when the frequency of the input wave is 1 Hz. This phenomenon is because the instant frequency (1 Hz) of the input seismic wave is close to the natural frequency (1.16 Hz) of the retaining wall, causing the resonance effect to be enhanced; for the expandability and nonexpandability facing wires, the calculations of K with the method that is proposed in this paper range from 1.0 to 1.25, while that value with normative methodologies between 1.02 and 1.35 (both inclusive), which indicate seismic safety reserve of retaining wall, may be lowered by formal methods for the design of antiseismic stability of the reinforcement retaining wall.

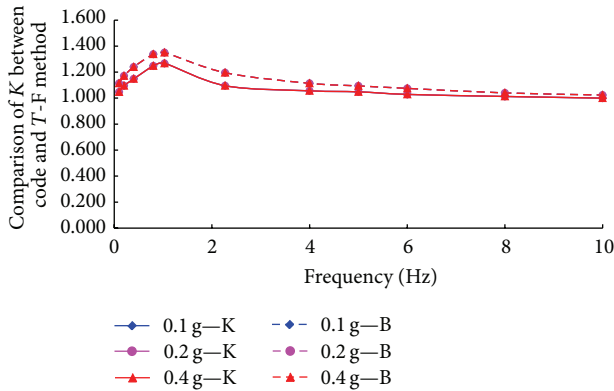


FIGURE 12: Relationship between different total tensile force parameter K and frequency under internal friction angle of 20 degrees.

From the above analysis, one can know that the type of geosynthetic, the internal frictional angle of the filling earth, the seismic intensity, and the frequency of the input earthquake wave have a predominant effect on the antiseismic stability of the reinforced retaining wall. Therefore, the effect of the above factors should be given due considerations in the earthquake-resistant design.

6. Conclusions

Based on the above analysis, the following conclusions can be concluded.

First, for the expandability and nonexpandability facing wires, based on the elastic wave theory, we summarize the dynamic analysis model of the reinforced retaining wall and establish time-frequency analysis method of the antiseismic stability with HHT method by horizontal slices analysis method. And then the reasonability of this method is verified by the results of the other methods, for example, normative methodologies. The new method not only considers the effect of three factors of the seismic wave (PGA, frequency, and duration) on the internal antiseismic stability analysis of reinforced retaining wall and improves the seismic design accuracy greatly but also provides some valuable references for the seismic design of the other retaining structures.

Second, the type of geosynthetic, the internal frictional angle of the filling earth, the seismic intensity, and the frequency of the input earthquake wave have a predominant effect on the antiseismic stability of the reinforced retaining wall, which should be given due considerations in the earthquake-resistant design. Likewise, for the expandability and nonexpandability facing wires, seismic safety reserve of retaining wall may be lowered by formal methods for the design of antiseismic stability of the reinforcement retaining wall when considering the effect of the PGA, while ignoring the frequency.

Third, the needed total tensile force of the facing wires decreases with the increase of the internal frictional angle; on the contrary, it increases significantly with the increase of the PGA; the total tensile force of the expandability facing wires is bigger than that of the nonexpandability facing wires, and it

is distributed in the shape of saddle and the force achieves the maximum value when the frequency of the input wave is the same as the natural frequency of reinforced retaining wall.

Conflict of Interests

The authors of this paper do not have any conflict of interests regarding the publication of this paper.

Acknowledgments

This study is supported in part by NSF of China (Contract no. 51408510), Construction and Science and Technology Project of Ministry of Transport (2013 318800 020), Guangxi Science Foundation, the Program for Science and Technology of Henan Province in China (Grant no. 142300410200), and Science Foundation of Key Laboratory of High-speed Railway Engineering, Ministry of Education, School of Civil Engineering, Southwest Jiaotong University (Grant no. 2014-HRE-05).

References

- [1] L. haiguang and Z. Depei, *Design of the New Retaining Structure and Engineering Practice*, Monographs, Communications Press, Beijing, China, 2004.
- [2] J. Jianqing, "Interior stability analysis of reinforced earth retaining wall under complicated dynamical loads," *Central South Highway Engineering*, vol. 32, no. 1, pp. 51–54, 2007.
- [3] J. Yingchun, "Internal stability calculation of reinforced retaining wall subjected to seismic load," *Chinese Journal of Highway*, vol. 10, no. 5, pp. 43–47, 1991.
- [4] H. B. Liu, "Internal stability analysis of segmental geosynthetic-reinforced soil retaining walls subjected to seismic loading," *Chinese Journal of Geotechnical Engineering*, vol. 30, no. 2, pp. 278–279, 2008.
- [5] M. M. El-Emam, *Behaviour of reinforced soil walls under earthquake loading [Ph.D. thesis]*, Queen's University of Canada, Kingston, Canada, 2003.
- [6] Y. Youhai, "Stability analysis on the reinforced earth retaining wall under earthquake loadings," *Journal of Lanzhou Railway University*, vol. 21, no. 4, pp. 9–11, 2007.
- [7] P. Cui, Y.-Y. Zhu, Y.-S. Han, X.-Q. Chen, and J.-Q. Zhuang, "The 12 May Wenchuan earthquake-induced landslide lakes: distribution and preliminary risk evaluation," *Landslides*, vol. 6, no. 3, pp. 209–223, 2009.
- [8] L. W. Zhang, Z. X. Lei, K. M. Liew, and J. L. Yu, "Static and dynamic of carbon nanotube reinforced functionally graded cylindrical panels," *Composite Structures*, vol. 232, no. 111, pp. 205–212, 2014.
- [9] L. W. Zhang, P. Zhu, and K. M. Liew, "Thermal buckling of functionally graded plates using a local Kriging meshless method," *Composite Structures*, vol. 108, pp. 472–492, 2014.
- [10] X. Zhang, X.-H. Liu, K.-Z. Song, and M.-W. Lu, "Least-squares collocation meshless method," *International Journal for Numerical Methods in Engineering*, vol. 51, no. 9, pp. 1089–1100, 2001.
- [11] C. B. Burke, *Full-scale shaking table tests and finite element analysis of reinforced soil retaining walls [Ph.D. thesis]*, Columbia University, New York, NY, USA, 2004.

- [12] Y. Shengming, "Experimental study on reinforced soil retaining wall and analysis of deformation mechanism," in *Monographs*, pp. 9–11, Dalian University of Technology Press, Dalian, China, 2009.
- [13] C. Hua, *The experimental study on mechanical characteristics of geogrid-reinforced soil retaining wall [Ph.D. thesis]*, China Academy of Railway Sciences, 2011.
- [14] J. Liang, *Seismic response and dynamic stability analysis of reinforced retaining wall [Ph.D. thesis]*, Lanzhou University of Technology, Lanzhou, China, 2011.
- [15] X. Du, *Theories and Methods of Wave Motion for Engineering*, Science Press, Beijing, China, 2009.
- [16] N. E. Huang, Z. Shen, S. R. Long et al., "The empirical mode decomposition and the Hilbert spectrum for nonlinear and non-stationary time series analysis," *The Royal Society of London A*, vol. 454, no. 1971, pp. 903–995, 1998.
- [17] C. Yang, J. Zhang, and D. Zhou, "Research on time-frequency analysis method for seismic stability of rock slope subjected to SV wave," *Chinese Journal of Rock Mechanics and Engineering*, vol. 32, no. 3, pp. 483–491, 2013.
- [18] Ministry of Transport of the People's Republic of China, *JTJ015-91 Specifications for Design of Highway Reinforced Earth Engineering*, Standard, China Communications Press, Beijing, China, 1999.
- [19] U. S. Department of Transportation and Federal Highway Administration, *FHWA2N HI2002043 Mechanically Stabilized Earth Walls and Reinforced Soil Slopes Design & Construction Guidelines*, Standard, National Highway Institute Office of Bridge Technology, Washington, D.C., USA, 2002.
- [20] D. Xiuli, *Theories and Methods of Wave Motion for Engineering*, Monographs; Science Press, Beijing, China, 2008.
- [21] M. Shahgholi, A. Fakher, and C. J. F. P. Jones, "Horizontal slice method of analysis," *Geotechnique*, vol. 51, no. 10, pp. 881–885, 2001.
- [22] H. Yuxian and X. Xun, "Phase angle consideration in generating response spectrum-compatible ground motion," *Earthquake Engineering & Engineering Vibration*, vol. 6, no. 2, pp. 37–51, 1986.

Research Article

Solving the Maximum Weighted Clique Problem Based on Parallel Biological Computing Model

Zhaocai Wang,¹ Jiangfeng Qin,² Zuwen Ji,³ Dongmei Huang,¹ and Lei Li⁴

¹*School of Information Sciences, Shanghai Ocean University, Shanghai 201306, China*

²*Guangxi Institute of Water Resources Research, Nanning 530023, China*

³*State Key Laboratory of Simulation and Regulation of River Basin Water Cycle, China Institute of Water Resources and Hydropower Research, Beijing 100048, China*

⁴*Department of Civil Engineering, Xi'an University of Architecture & Technology, Xi'an 710055, China*

Correspondence should be addressed to Zuwen Ji; zuwenji70@163.com

Received 2 July 2014; Revised 15 September 2014; Accepted 20 September 2014

Academic Editor: L. W. Zhang

Copyright © 2015 Zhaocai Wang et al. This is an open access article distributed under the Creative Commons Attribution License, which permits unrestricted use, distribution, and reproduction in any medium, provided the original work is properly cited.

The maximum weighted clique (MWC) problem, as a typical NP-complete problem, is difficult to be solved by the electronic computer algorithm. The aim of the problem is to seek a vertex clique with maximal weight sum in a given undirected graph. It is an extremely important problem in the field of optimal engineering scheme and control with numerous practical applications. From the point of view of practice, we give a parallel biological algorithm to solve the MWC problem. For the maximum weighted clique problem with m edges and n vertices, we use fixed length DNA strands to represent different vertices and edges, fully conduct biochemical reaction, and find the solution to the MVC problem in certain length range with $O(n^2)$ time complexity, comparing to the exponential time level by previous computer algorithms. We expand the applied scope of parallel biological computation and reduce computational complexity of practical engineering problems. Meanwhile, we provide a meaningful reference for solving other complex problems.

1. Introduction

DNA computing, as a comprehensive discipline, can use DNA biological technologies to solve complex practical engineering problems. In 1994, Adleman [1] made use of DNA molecule operations to solve the Hamiltonian path problem with n vertices in $O(n)$ time complexity; simultaneously, he also demonstrated the strong parallel ability of DNA computing. In 1995, Lipton [2] figured out the NP-complete satisfiability problem utilizing Adleman's biochemical experiment. Since then, DNA biological computing attracted more and more interest from different disciplinary scholars. DNA biological computing has three advantages: high parallelism, low energy consumption, and large memory capacity. Many research scholars, designing DNA procedures and algorithms, succeed in solving multifarious kinds of complicated NP-complete problems [3–21], which promoted development of DNA computing. In order to better apply DNA computing

theory to more practical engineering science broad, it is worth trying to solve more intractable problems using the DNA molecular computing. Furthermore, most previous works, relating to DNA computing, focused on how to solve the path search problems that the solutions are continuous head-to-tail ligation edge or vertex sets, so that the possible solutions can be relatively easily represented by DNA strands, while some practical engineering problems, such as maximum weighted clique problem, are discrete set problems without sequentially connected path. So how to represent discrete data on DNA strands is an important key to expand the applied scope of DNA computing.

The maximum weighted clique problem has a wide range of applications in optimal engineering scheme and computational mathematics. In this paper, DNA algorithm, based on the research foundation of Adleman [1] and Lipton [2], is used to get solution of the maximum weighted clique problem. The rest dissertation is organized as follows.

In Section 2, the parallel biological computing model is introduced with detailed description. Section 3 uses DNA molecular algorithm to solve the maximum weighted clique problem. Section 4 proves DNA algorithm correctness and feasibility and gets the computation complexity. We come to the conclusions in Section 5.

2. The Parallel Biological Computing Model

DNA is the material basis of biological genetics, which is strung together from deoxyribonucleotides. DNA is formed by four kinds of base composition. These bases are, respectively, called adenine (A), guanine (G), cytosine (C), and thymine (T). The permutation and combination of bases store genetic information. An important feature of DNA is that two single strands can form a double strand through complementary base pairing. Moreover, the pairing has high specificity: A can only match T; C can only be paired with G. The length of a DNA single strand is counted by the number of bases. For example, a single strand (ATTCTG) includes 5 bases; then it is called a 5 *mer*.

Based on Adleman [1] and Lipton's [2] research, DNA biological algorithm operations are described as follows. Corresponding biological operations can be used to get solution of the maximum weighted clique problem. In the parallel biological computing model, we can perform the following operations with given tubes which contain a list of DNA strands.

- (1) *Copy*(P_1, P_2): given a test tube P_1 , it can get another test tube P_2 with the same strands as P_1 .
- (2) *Merge*(P_1, P_2): given two test tubes P_1 and P_2 , it can get the compound strands P_1 and P_2 in P_1 and leave P_2 empty.
- (3) *Annealing*(P): given a test tube P , it can generate all feasible double strands in P by annealing. The products and residues are still stored in P after annealing.
- (4) *Separation*(P_1, Z, P_2): given a test tube P_1 and a list strands set Z , it can remove all single strands in Z from P_1 and get an another tube P_2 with the removed strands.
- (5) *Ligation*(T): given a tube P , it is used to ligate together the strands in P .
- (6) *Sort*(P_1, P_2, P_3): it picks out the shortest length strands into tube P_2 from tube P_1 , the longest strands into P_3 , and the surplus strands are still kept in P_1 .
- (7) *Denaturation*(P): given a test tube P , it can dissociate every double strand in P to couple of single strands.
- (8) *Read*(P): given a tube P , it can be used to describe each single strand in P .
- (9) *Append-tail*(P, z): given a test tube P and a single strand z , it can append z at back of each strand in the tube P .
- (10) *Discard*(P): given a test tube P , it discards the strands in tube P and leave P empty.

Since above operations are realized through the limited biological experimental procedures with DNA strands [18], we can reasonably conclude that each operation is in $O(1)$ time complexity.

3. Biological Algorithm for the Maximum Weighted Clique Problem

An undirected simple graph $G = (V, E, W)$ is a pair of vertex set $V = \{v_1, v_2, \dots, v_n\}$ with corresponding vertex positive weight value $\{w_1, w_2, \dots, w_n\}$ and edge set $E = \{e_{i,j} \mid 1 \leq i < j \leq n\}$. For a vertex subset $T_1 \subseteq V$, if $\forall v_i, v_j \in T_1$, v_i and v_j can be linked by edge $e_{i,j}$ in the graph, then T_1 is called a clique of the graph G , and simultaneously the clique weight is the sum of vertex weight in the T_1 . The solution of maximum weighted clique problem aims to seek a vertex clique T of graph G with maximal weight sum. For example, the undirected simple graph in Figure 1 is defined as the MVC problem.

In succession, the symbols A_k, B_k ($k = 1, 2, \dots, n$), 1, 0, #, # are composed by different single strands having same length, as t *mer*. Certainly, t would be best to choose a small integer which can be determined by the scale of the problem. Then in the following algorithms, we use DNA single strands symbols $A_k 0 B_k, A_k 1 B_k$ to indicate the vertex v_k , with strands symbol $A_k 1 B_k$ for vertex v_k in the vertex subset while $A_k 0 B_k$ for not. Simultaneously, the symbols #, # are the signal of division between different vertex subsets. We denote DNA singled strands y_k to encode the vertex v_k weight value with length of w_k *mer*. For distinguishing some edges belonging to the graph G or not, we meantime design DNA strings $B_i A_j$ in the tube R if $e_{i,j} \in E$. Let

$$\begin{aligned} T_1 &= \{\#, \overline{A_k 0 B_k}, \overline{A_k 1 B_k} \mid k = 1, 2, \dots, n\}, \\ T_2 &= \{\#A_1, B_n\#, 0, 1, B_{k-1}A_k \mid k = 2, 3, \dots, n\}, \\ R &= \{B_i A_j \mid e_{i,j} \in E\}, \\ Y &= \{y_k \mid k = 1, 2, \dots, n\}. \end{aligned} \quad (1)$$

For a n -vertex graph, every vertex subset can be expressed by a n -bit binary value. The k th bit set to 1 means the vertex v_k in the subset; on the contrary, the k th bit set to 0 shows the vertex v_k out of the subset. Taking Figure 1, for example, the vertex subset $\{v_2, v_3, v_5\}$ can be expressed by the binary value 01101. Using the same method, we can represent the vertex subsets of a n -vertex simple graph as a series of n -bit binary numbers.

- (1) We generate all possible vertex subsets in graph G ;

- (1) *Merge*(T_1, T_2);
- (2) *Annealing*(T_1);
- (3) *Ligation*(T_1);
- (4) *Denaturation*($T_1, \{\#A_1\}, T_3$);
- (5) *Discard*(T_1);
- (6) *Denaturation*($T_3, \{B_n\# \}, T_1$).

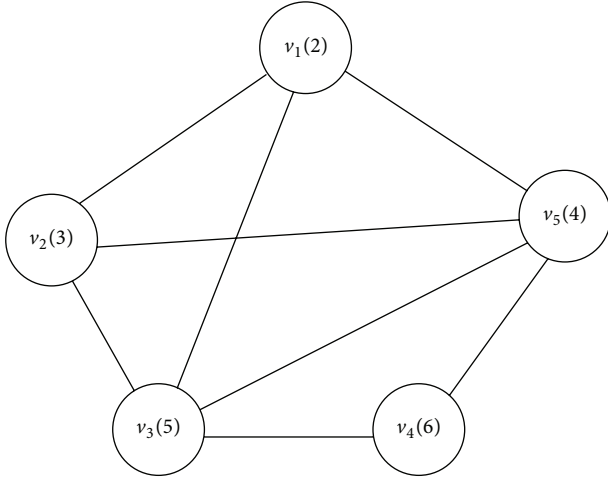


FIGURE 1: An undirected simple graph G with 5 vertices and 8 edges.

After the above six manipulations, the single strands in tube T_1 mean all kinds of vertex subsets. For example, in Figure 1, we have single strands:

$$\#A_11B_1A_21B_2A_30B_3A_41B_4A_51B_5\# \in T_1 \quad (2)$$

which denote the vertex subset $\{v_1, v_2, v_4, v_5\}$ corresponding to binary value 11011. These operations can be executed with $O(1)$ time complexity since every operation can be finished in $O(1)$.

- (2) Every strand in tube T_1 denotes one kind of vertex subset. For the maximum weighted clique problem, solution is one kind of vertex subset that arbitrary two vertices in the subset can be connected by one edge included in the graph G . Therefore, we check whether all vertex subsets in T_1 are in line with the condition or not. If $e_{i,j} \notin E$, we discard the strands indicating that both vertices v_i and v_j are in the same subset. For example, in Figure 1, the singled strands $\#A_10B_1A_21B_2A_30B_3A_41B_4A_51B_5\#$ representing the vertex subset $\{v_2, v_4, v_5\}$ should be discarded for not including the edge $e_{2,4}$ in graph G to connect vertices v_2 and v_4 . We choose all possible vertex cliques in graph.

For $i = 1$ to $i = n$,

- (1) *Separation*($P, \{A_i1B_i\}, T_2$);
For $j = 1$ and $j \neq i$ to $j = n$
- (2) *Separation*($R, \{B_iA_j\}, T_3$);
- (3) If(*Detect*(T_3));
Then
- (4) *Discard*(T_3);
- (5) *Separation*($T_2, \{A_j1B_j\}, T_4$);
- (6) *Merge*(P, T_2);

End for

End for

Through the above operations, all the single strands in tube T_1 represent different vertex clique subsets.

Meanwhile, the algorithm includes two “For” clauses, this step is executed in $O(n^2)$ time complexity since each operation can be finished in $O(1)$.

- (3) The maximum weighted clique problem should be a maximal vertex clique subset in which arbitrary two vertices should be linked by certain edge of the graph G . So we select the maximal vertex subset from all kinds of vertex clique subsets. If the vertex v_k is included in the vertex subset, we append additional strand y_k at the end of previous subset strand in order to find the optimum solution strand. For the singled strand (representing the vertex subset $\{v_2, v_3, v_5\}$)

$$\#A_10B_1A_21B_2A_31B_3A_40B_4A_51B_5\# \in T_1, \quad (3)$$

we append strands $\{y_2, y_3, y_5\}$ at end of the previous strand to

$$\#A_10B_1A_21B_2A_31B_3A_40B_4A_51B_5\#y_2y_3y_5. \quad (4)$$

This step can be carried out as follows.

For $k = 1$ to $k = n$,

- (1) *Separation*(T_1, A_k1B_k, T_7);
- (2) *Append-tail*(T_7, y_k);
- (3) *Merge*(T_1, T_7);
- (4) *Discard*(T_7).

End for

This step includes one “For” clause; thus it can be finished in $O(n)$ time complexity.

- (4) We select single strands with the longest length from T_1 , which represent the solutions of maximum weighted clique problem. For example, in Figure 1, single strands in T_1 with the largest length are

$$\#A_10B_1A_20B_2A_31B_3A_41B_4A_51B_5\#y_3y_4y_5. \quad (5)$$

Consequently, solution of maximum weighted clique problem for Figure 1 is vertex subset $\{v_3, v_4, v_5\}$ with weight sum 15.

- (1) *Sort*(T_1, T_8, T_9);
- (2) *Read*(T_9).

4. The Feasibility and Computational Complexity of the Parallel Biological Computing Algorithm

Theorem 1. *The maximum weighted clique problem for a n -vertex graph can be solved by the biological computing algorithm.*

Proof. At first, we get all kinds of the vertex combinational subset in the test tube after Step (1). For the maximum weighted clique problem, if $e_{i,j} \notin E$, vertices v_i and v_j should be not in the same subset. Therefore, basic biological manipulations remove illegal combinations and seek legal

TABLE 1: Sequences chosen to represent $\#, A_k, B_k, y_k (k = 1, 2, \dots, n)$ in the example of Figure 1.

Symbol	3'-5' DNA sequence	Symbol	3'-5' DNA sequence
A_1	CCT	B_1	ACT
A_2	CAC	B_2	TAT
A_3	CTA	B_3	TAA
A_4	TTC	B_4	ATC
A_5	AAC	B_5	CTT
0	CAA	1	AAT
#	TAC	y_1	GG
y_2	GGG	y_3	GGGGG
y_4	GGGGG	y_5	GGGG

ones from solution space strands through the Step (2). At Step (3), we append a series of “tails” y_k at the end of the strands which imply the vertex v_k included in the vertex subset. Owing to the length of strands $\|y_k\| = w_k$, the longest length strands in the pool mean the solutions of maximum weighted clique problem. Besides, we can search and get the solution at the last step. \square

Theorem 2. *The solutions of maximum weighted clique problem for a n -vertex graph can be solved in $O(n^2)$ time complexity using DNA molecules computing.*

Proof. The parallel biological computing algorithm can be entirely executed in finite time complexity such as Steps (1) and (4) in $O(1)$, Step (3) in $O(n)$, and simultaneously Step (2) in $O(n^2)$ time complexity. The total algorithm complexity T is as below:

$$\begin{aligned}
T(\text{Step (1)}) &= O(1); \\
T(\text{Step (2)}) &= O(n); \\
T(\text{Step (3)}) &= O(n^2); \\
T(\text{Step (4)}) &= O(1); \\
T &= T(\text{Step (1)}) + T(\text{Step (2)}) \\
&\quad + T(\text{Step (3)}) + T(\text{Step (4)}); \\
&= O(1) + O(n^2) + O(n) + O(1); \\
&= O(n^2).
\end{aligned} \tag{6}$$

In conclusion, we can get the solutions of maximum weighted clique problems with n -vertices in $O(n^2)$ time complexity. \square

Theorem 3. *Solution strands to the maximum weighted clique problem with n -vertices can be found in the finite length range.*

Proof. After Step (1), the singled strands in tube T_1 denote all possible vertex subsets. These strands can be described as follows:

$$\#A_1x_1B_1A_2x_2B_2 \cdots A_kx_kB_k \cdots A_nx_nB_n \# \quad x_k = 0 \text{ or } 1. \tag{7}$$

At Step (2), the single strands in T_1 mean all possible vertex clique subsets. We design the fixed length strands of $\#, A_k, B_k$, and x_k , for

$$\|A_k\| = \|B_k\| = \|\#\| = \|x_k\| = t \text{ mer}. \tag{8}$$

S is defined as strands assemblage after Step (3). Then S can be described:

$$\#A_1x_1B_1A_2x_2B_2 \cdots A_kx_kB_k \cdots A_nx_nB_n \# y_{i_1} \cdots y_{i_n}. \tag{9}$$

Appending the strands y_{i_j} or not is decided whether there exists vertex v_{i_j} information strands $A_{i_j}1B_{i_j}$ on the previous strands. Due to the fact that the number of vertex v_k in sunset is between 1 and n , so after “append” operation, the strands is also in a finite length range:

$$\begin{aligned}
\|S\| &= \|\#\| + \|A_1\| + \|x_1\| + \|B_1\| \\
&\quad + \cdots + \|A_k\| + \|x_k\| + \|A_k\| + \cdots \\
&\quad + \|A_n\| + \|x_n\| + \|A_n\| + \|\#\| \\
&\quad + \|y_{i_1}\| + \cdots + \|y_{i_n}\| \\
&= 2\|\#\| + \sum_{k=1}^n \|A_k\| + \sum_{k=1}^n \|x_k\| \\
&\quad + \sum_{k=1}^n \|B_k\| + \sum_{x_k=1}^n \|y_k\| \\
&= (3n+2)t + \sum_{x_k=1}^n \|y_k\|
\end{aligned} \tag{10}$$

$$\because 0 \leq \sum_{x_k=1}^n \|y_k\| \leq \sum_{k=1}^n \|y_k\|$$

$$\text{Let } \sum_{k=1}^n \|y_k\| = m$$

$$\therefore (3n+2)t \leq \|S\| \leq (3n+2)t + m.$$

For the maximum vertex clique problem, the length of solution strands is between $(3n+2)t$ and $(3n+2)t + m$. Therefore, we can get the solution in appropriate length range at Step (4). \square

TABLE 2: Sequences chosen to represent all kinds of vertex subsets for the example of Figure 1.

Vertex subset	Symbols sequence	3'-5' DNA sequence
$\{v_1\}$	$\#A_10B_1A_21B_2A_30B_3A_40B_4A_50B_5\#$	TACCCTAATACTCACCA ATATCTACAATAATTCC AAATCAACCAACTTTAC
$\{v_2\}$	$\#A_10B_1A_21B_2A_30B_3A_40B_4A_50B_5\#$	TACCCTCAAACCTCACAA TTATCTACAATAATTCC AAATCAACCAACTTTAC
$\{v_3\}$	$\#A_10B_1A_21B_2A_30B_3A_40B_4A_50B_5\#$	TACCCTCAAACCTCACCA ATATCTAAATTAATTCC AAATCAACCAACTTTAC
$\{v_4\}$	$\#A_10B_1A_21B_2A_30B_3A_40B_4A_50B_5\#$	TACCCTCAAACCTCACCA ATATCTACAATAATTCA ATATCAACCAACTTTAC
$\{v_5\}$	$\#A_10B_1A_21B_2A_30B_3A_40B_4A_50B_5\#$	TACCCTCAAACCTCACCA ATATCTACAATAATTCC AAATCAACAATCTTTAC
$\{v_1, v_2\}$	$\#A_10B_1A_21B_2A_30B_3A_40B_4A_50B_5\#$	TACCCTAATACTCACAA TTATCTACAATAATTCC AAATCAACCAACTTTAC
$\{v_1, v_3\}$	$\#A_10B_1A_21B_2A_30B_3A_40B_4A_50B_5\#$	TACCCTAATACTCACCA ATATCTAAATTAATTCC AAATCAACCAACTTTAC
$\{v_1, v_4\}$	$\#A_10B_1A_21B_2A_30B_3A_40B_4A_50B_5\#$	TACCCTAATACTCACCA ATATCTACAATAATTCA ATATCAACCAACTTTAC
$\{v_1, v_5\}$	$\#A_10B_1A_21B_2A_30B_3A_40B_4A_50B_5\#$	TACCCTAATACTCACCA ATATCTACAATAATTCC AAATCAACAATCTTTAC
$\{v_2, v_3\}$	$\#A_10B_1A_21B_2A_30B_3A_40B_4A_50B_5\#$	TACCCTCAAACCTCACAA TTATCTAAATTAATTCC AAATCAACCAACTTTAC
$\{v_2, v_4\}$	$\#A_10B_1A_21B_2A_30B_3A_40B_4A_50B_5\#$	TACCCTCAAACCTCACAA TTATCTACAATAATTCA ATATCAACCAACTTTAC
$\{v_2, v_5\}$	$\#A_10B_1A_21B_2A_30B_3A_40B_4A_50B_5\#$	TACCCTCAAACCTCACAA TTATCTACAATAATTCCA AATCAACAATCTTTAC
$\{v_3, v_4\}$	$\#A_10B_1A_21B_2A_30B_3A_40B_4A_50B_5\#$	TACCCTCAAACCTCACCA ATATCTAAATTAATTCA ATATCAACCAACTTTAC
$\{v_3, v_5\}$	$\#A_10B_1A_21B_2A_30B_3A_40B_4A_50B_5\#$	TACCCTCAAACCTCACCA ATATCTAAATTAATTCC AAATCAACAATCTTTAC
$\{v_4, v_5\}$	$\#A_10B_1A_21B_2A_30B_3A_40B_4A_50B_5\#$	TACCCTCAAACCTCACCA ATATCTACAATAATTCA ATATCAACAATCTTTAC
$\{v_1, v_2, v_3\}$	$\#A_10B_1A_21B_2A_30B_3A_40B_4A_50B_5\#$	TACCCTAATACTCACAA TTATCTAAATTAATTCC AAATCAACCAACTTTAC
$\{v_1, v_2, v_4\}$	$\#A_10B_1A_21B_2A_30B_3A_40B_4A_50B_5\#$	TACCCTAATACTCACAA TTATCTACAATAATTCA ATATCAACCAACTTTAC

TABLE 2: Continued.

Vertex subset	Symbols sequence	3'-5' DNA sequence
$\{v_1, v_2, v_5\}$	$\#A_10B_1A_21B_2A_30B_3A_40B_4A_50B_5\#$	TACCCTAATACTCACAA TTATCTACAATAATTCC AAATCAACAATCTTTAC
$\{v_1, v_3, v_4\}$	$\#A_10B_1A_21B_2A_30B_3A_40B_4A_50B_5\#$	TACCCTAATACTCACCA ATATCTAAATTAATTCA ATATCAACCAACTTTAC
$\{v_1, v_3, v_5\}$	$\#A_10B_1A_21B_2A_30B_3A_40B_4A_50B_5\#$	TACCCTAATACTCACCA ATATCTAAATTAATTCC AAATCAACAATCTTTAC
$\{v_1, v_4, v_5\}$	$\#A_10B_1A_21B_2A_30B_3A_40B_4A_50B_5\#$	TACCCTAATACTCACCA ATATCTACAATAATTCA ATATCAACAATCTTTAC
$\{v_2, v_3, v_4\}$	$\#A_10B_1A_21B_2A_30B_3A_40B_4A_50B_5\#$	TACCCTCAAACTCACAA TTATCTAAATTAATTCA ATATCAACCAACTTTAC
$\{v_2, v_3, v_5\}$	$\#A_10B_1A_21B_2A_30B_3A_40B_4A_50B_5\#$	TACCCTCAAACTCACA ATTATCTAAATTAATTCC AAATCAACAATCTTTAC
$\{v_2, v_4, v_5\}$	$\#A_10B_1A_21B_2A_30B_3A_40B_4A_50B_5\#$	TACCCTCAAACTCACAA TTATCTACAATAATTCA ATATCAACAATCTTTAC
$\{v_3, v_4, v_5\}$	$\#A_10B_1A_21B_2A_30B_3A_40B_4A_50B_5\#$	TACCCTCAAACTCACCA ATATCTAAATTAATTCA ATATCAACAATCTTTAC
$\{v_1, v_2, v_3, v_4\}$	$\#A_10B_1A_21B_2A_30B_3A_40B_4A_50B_5\#$	TACCCTAATACTCACAA TTATCTAAATTAATTCA ATATCAACCAACTTTAC
$\{v_1, v_2, v_3, v_5\}$	$\#A_10B_1A_21B_2A_30B_3A_40B_4A_50B_5\#$	TACCCTAATACTCACAA TTATCTAAATTAATTCC AAATCAACAATCTTTAC
$\{v_1, v_2, v_4, v_5\}$	$\#A_10B_1A_21B_2A_30B_3A_40B_4A_50B_5\#$	TACCCTAATACTCACAA TTATCTACAATAATTCA ATATCAACAATCTTTAC
$\{v_1, v_3, v_4, v_5\}$	$\#A_10B_1A_21B_2A_30B_3A_40B_4A_50B_5\#$	TACCCTAATACTCACCA ATATCTAAATTAATTCA ATATCAACAATCTTTAC
$\{v_2, v_3, v_4, v_5\}$	$\#A_10B_1A_21B_2A_30B_3A_40B_4A_50B_5\#$	TACCCTCAAACTCACAA TTATCTAAATTAATTCA ATATCAACAATCTTTAC
$\{v_1, v_2, v_3, v_4, v_5\}$	$\#A_10B_1A_21B_2A_30B_3A_40B_4A_50B_5\#$	TACCCTAATACTCACAA TTATCTAAATTAATTCA ATATCAACAATCTTTAC

5. The Detailed Approach and Walkthrough of the Biological Computing Algorithm

Taking Figure 1 as example, we describe operation result of each step. Due to the fact that biological computing algorithm depends on basic biochemical DNA molecules reactions which may cause errors in the process, it is an important matter to make biological computing more reliable by means of the DNA molecular sequence design. To have a better performance in hybridization reactions, we follow

[22] to accomplish the sequence design. For the problem of Figure 1, the program generates 3-base random sequences to represent symbols $\#$, A_k , B_k , and y_k . If the generated DNA sequence fails to pass any of the constraints, the program will regenerate a new DNA sequence. If the constraints are satisfied, the new DNA sequences are accepted. If all the DNA strands satisfy the constraints, the program has then succeeded and these sequences would be the outputs. The corresponding vertex symbol sequences are shown in Table 1. In accordance with the above design, we can get all kinds of

TABLE 3: Symbols sequences chosen to represent the different vertex cliques for the example of Figure 1.

Vertex cliques	Symbols sequence
$\{v_1, v_2\}$	$\#A_11B_1A_21B_2A_30B_3A_40B_4A_50B_5\#$
$\{v_1, v_3\}$	$\#A_11B_1A_20B_2A_31B_3A_40B_4A_50B_5\#$
$\{v_1, v_4\}$	$\#A_11B_1A_20B_2A_30B_3A_41B_4A_50B_5\#$
$\{v_1, v_5\}$	$\#A_11B_1A_20B_2A_30B_3A_40B_4A_51B_5\#$
$\{v_2, v_3\}$	$\#A_10B_1A_21B_2A_31B_3A_40B_4A_50B_5\#$
$\{v_2, v_4\}$	$\#A_10B_1A_21B_2A_30B_3A_41B_4A_50B_5\#$
$\{v_2, v_5\}$	$\#A_10B_1A_21B_2A_30B_3A_40B_4A_51B_5\#$
$\{v_3, v_4\}$	$\#A_10B_1A_20B_2A_31B_3A_41B_4A_50B_5\#$
$\{v_3, v_5\}$	$\#A_10B_1A_20B_2A_31B_3A_40B_4A_51B_5\#$
$\{v_4, v_5\}$	$\#A_10B_1A_20B_2A_30B_3A_41B_4A_51B_5\#$
$\{v_1, v_2, v_3\}$	$\#A_11B_1A_21B_2A_31B_3A_40B_4A_50B_5\#$
$\{v_1, v_2, v_5\}$	$\#A_11B_1A_21B_2A_30B_3A_41B_4A_50B_5\#$
$\{v_1, v_3, v_5\}$	$\#A_11B_1A_21B_2A_30B_3A_40B_4A_51B_5\#$
$\{v_2, v_3, v_5\}$	$\#A_11B_1A_20B_2A_31B_3A_41B_4A_50B_5\#$
$\{v_3, v_4, v_5\}$	$\#A_11B_1A_20B_2A_31B_3A_40B_4A_51B_5\#$
$\{v_1, v_2, v_3, v_5\}$	$\#A_11B_1A_20B_2A_30B_3A_41B_4A_51B_5\#$

TABLE 4: Symbols sequences chosen to represent the vertex weighted cliques for the example of Figure 1.

Vertex set	Symbols sequence
$\{v_1, v_2\}$	$\#A_11B_1A_21B_2A_30B_3A_40B_4A_50B_5\#y_1y_2$
$\{v_1, v_3\}$	$\#A_11B_1A_20B_2A_31B_3A_40B_4A_50B_5\#y_1y_2$
$\{v_1, v_4\}$	$\#A_11B_1A_20B_2A_30B_3A_41B_4A_50B_5\#y_1y_4$
$\{v_1, v_5\}$	$\#A_11B_1A_20B_2A_30B_3A_40B_4A_51B_5\#y_1y_5$
$\{v_2, v_3\}$	$\#A_10B_1A_21B_2A_31B_3A_40B_4A_50B_5\#y_2y_3$
$\{v_2, v_4\}$	$\#A_10B_1A_21B_2A_30B_3A_41B_4A_50B_5\#y_2y_4$
$\{v_2, v_5\}$	$\#A_10B_1A_21B_2A_30B_3A_40B_4A_51B_5\#y_2y_5$
$\{v_3, v_4\}$	$\#A_10B_1A_20B_2A_31B_3A_41B_4A_50B_5\#y_3y_4$
$\{v_3, v_5\}$	$\#A_10B_1A_20B_2A_31B_3A_40B_4A_51B_5\#y_3y_5$
$\{v_4, v_5\}$	$\#A_10B_1A_20B_2A_30B_3A_41B_4A_51B_5\#y_4y_5$
$\{v_1, v_2, v_3\}$	$\#A_11B_1A_21B_2A_31B_3A_40B_4A_50B_5\#y_1y_2y_3$
$\{v_1, v_2, v_5\}$	$\#A_11B_1A_21B_2A_30B_3A_41B_4A_50B_5\#y_1y_2y_5$
$\{v_1, v_3, v_5\}$	$\#A_11B_1A_21B_2A_30B_3A_40B_4A_51B_5\#y_1y_3y_5$
$\{v_2, v_3, v_5\}$	$\#A_11B_1A_20B_2A_31B_3A_41B_4A_50B_5\#y_2y_3y_5$
$\{v_3, v_4, v_5\}$	$\#A_11B_1A_20B_2A_31B_3A_40B_4A_51B_5\#y_3y_4y_5$
$\{v_1, v_2, v_3, v_5\}$	$\#A_11B_1A_20B_2A_30B_3A_41B_4A_51B_5\#y_1y_2y_3y_5$

symbol representations of vertex subsets in Table 2 after Step (1). Step (2) discards the inappropriate vertex combinatorial sequences and retains the vertex clique sequences in Table 3. At Step (4), we append the corresponding weighted sequences which are showed in Table 4. Through the “Sort” operation at Step (4), we find the optimal solution to the maximum weighted clique problem of Figure 1 in Table 5.

TABLE 5: DNA sequences chosen to represent the solution of the maximum weighted clique problem.

$\{v_3, v_4, v_5\}$	3'-TACCCTCAAACCTCACCAATAT CTAAATTAATTCAATATCAACAATC TTTACGGGGGGGGGGGGGGG-5'
---------------------	---

6. Conclusions

In this paper, we present a parallel computing algorithm to solve the maximum weighted clique problem based on biological operations. Due to the fact that DNA biological computing has some advantages including high parallelism, low energy consumption, and large memory capacity, comparing to electronic computers low speed and limited memory, the method of DNA computing has attracted more and more attention. Besides, compared with the previous algorithms, our proposed algorithm has the following features: (1) we utilize fixed length DNA strands to generate the solution strands of the problem, the algorithm actually has lower error rate in hybrid operations; (2) the time cost of algorithm and solution strands length increase in linear proportion with the expansion of instance scale. For an undirected simple n -vertex graph, the parallel biological computing algorithm executes in $O(n^2)$ time complexity for the maximum weighted clique problem, having lower computational complexity than previous algorithms in exponential level. Although operations in our paper are on the basis of a theoretical model, the capacity to executive complicated operations in algorithm could help us understand more about the nature of computing and promote the better and faster development of biocomputing, more conducive for us to solve complex practical engineering problems.

Conflict of Interests

The authors declare that there is no conflict of interests regarding the publication of this paper.

Acknowledgments

This research was supported by the Open Research Fund of State Key Laboratory of Simulation and Regulation of Water Cycle in River Basin, China Institute of Water Resources and Hydropower Research (Grant no. 2014ZY05), and “12th Five-Year Plan” to Support Science and Technology Project (Grant no. 2012BAB04B02). The project was also supported by CNSF (Grant nos. 61272098, 51409050, and 51108376), SSF (Grant no. 2014JQ7231), and Doctor fund of Shanghai Ocean University (A-2400-12-0000351).

References

- [1] L. M. Adleman, “Molecular computation of solutions to combinatorial problems,” *Science*, vol. 266, no. 5187, pp. 1021–1024, 1994.
- [2] R. J. Lipton, “DNA solution of hard computational problems,” *Science*, vol. 268, no. 5210, pp. 542–545, 1995.

- [3] A. Fujiwara, K. Matsumoto, and W. Chen, "Procedures for logic and arithmetic operations with DNA molecules," *International Journal of Foundations of Computer Science*, vol. 15, no. 3, pp. 461–474, 2004.
- [4] W. X. Li, D. M. Xiao, and L. He, "DNA ternary addition," *Applied Mathematics and Computation*, vol. 182, no. 2, pp. 977–986, 2006.
- [5] F. Guarnieri, M. Fliss, and C. Bancroft, "Making DNA add," *Science*, vol. 273, no. 5272, pp. 220–223, 1996.
- [6] X. C. Liu, X. F. Yang, S. L. Li, and Y. Ding, "Solving the minimum bisection problem using a biologically inspired computational model," *Theoretical Computer Science*, vol. 411, no. 6, pp. 888–896, 2010.
- [7] G. Paun, G. Rozenberg, and A. Salomaa, *DNA Computing*, Springer, New York, NY, USA, 1998.
- [8] J. Y. Lee, S.-Y. Shin, T. H. Park, and B.-T. Zhang, "Solving traveling salesman problems with DNA molecules encoding numerical values," *BioSystems*, vol. 78, no. 1–3, pp. 39–47, 2004.
- [9] X. L. Wang, Z. M. Bao, J. J. Hu, S. Wang, and A. Zhan, "Solving the SAT problem using a DNA computing algorithm based on ligase chain reaction," *BioSystems*, vol. 91, no. 1, pp. 117–125, 2008.
- [10] Z. Wang, D. Xiao, W. Li, and L. He, "A DNA procedure for solving the shortest path problem," *Applied Mathematics and Computation*, vol. 183, no. 1, pp. 79–84, 2006.
- [11] A. Brennenman and A. Condon, "Strand design for biomolecular computation," *Theoretical Computer Science*, vol. 287, no. 1, pp. 39–58, 2002.
- [12] M. Y. Guo, W.-L. Chang, M. Ho, J. Lu, and J. N. Cao, "Is optimal solution of every NP-complete or NP-hard problem determined from its characteristic for DNA-based computing," *BioSystems*, vol. 80, no. 1, pp. 71–82, 2005.
- [13] Y. Wang, T. Yang, Y. Ma et al., "Mathematical modeling and stability analysis of macrophage activation in left ventricular remodeling post-myocardial infarction," *BMC Genomics*, vol. 13, supplement 6, article S21, 2012.
- [14] Y. Wang, H.-C. Han, J. Y. Yang, M. L. Lindsey, and Y. Jin, "A conceptual cellular interaction model of left ventricular remodelling post-MI: dynamic network with exit-entry competition strategy," *BMC Systems Biology*, vol. 4, supplement 1, article S5, 2010.
- [15] W.-L. Chang, "Fast parallel DNA-based algorithms for molecular computation: quadratic congruence and factoring integers," *IEEE Transactions on Nanobioscience*, vol. 11, no. 1, pp. 62–69, 2012.
- [16] Z. C. Wang, D. M. Huang, H. J. Meng, and C. P. Tang, "A new fast algorithm for solving the minimum spanning tree problem based on DNA molecules computation," *BioSystems*, vol. 114, no. 1, pp. 1–7, 2013.
- [17] Y. Xu and Z. Wang, "Genetic algorithm optimized CCEM for complex topology," *Mathematical Problems in Engineering*, vol. 2012, Article ID 383248, 14 pages, 2012.
- [18] W.-L. Chang, M. S.-H. Ho, and M. Guo, "Fast parallel molecular algorithms for DNA-based computation: factoring integers," *IEEE Transactions on Nanobioscience*, vol. 4, no. 2, pp. 149–163, 2005.
- [19] Z. C. Wang, Y. M. Zhang, W. H. Zhou, and H. F. Liu, "Solving traveling salesman problem in the Adleman-Lipton model," *Applied Mathematics and Computation*, vol. 219, no. 4, pp. 2267–2270, 2012.
- [20] T. Yang, Y. A. Chiao, Y. Wang et al., "Mathematical modeling of left ventricular dimensional changes in mice during aging," *BMC Systems Biology*, vol. 6, supplement 3, article S10, 2012.
- [21] Z. C. Wang, J. Tan, D. M. Huang, Y. C. Ren, and Z. W. Ji, "A biological algorithm to solve the assignment problem based on DNA molecules computation," *Applied Mathematics and Computation*, vol. 244, pp. 183–190, 2014.
- [22] R. S. Braich, C. Johnson, P. W. K. Rothmund, D. Hwang, N. Chelyapov, and L. M. Adleman, "Solution of a satisfiability problem on a gel-based DNA computer," in *Proceedings of the 6th International Conference on DNA Computation (DNA '00)*, vol. 2054 of *Lecture Notes in Computer Science*, pp. 27–42, 2000.

Research Article

Global Quasi-Minimal Residual Method for Image Restoration

Jun Liu, Ting-Zhu Huang, Xiao-Guang Lv, Hao Xu, and Xi-Le Zhao

School of Mathematical Sciences/Institute of Computational Science, University of Electronic Science and Technology of China, Chengdu, Sichuan 611731, China

Correspondence should be addressed to Ting-Zhu Huang; tingzhuhuang@126.com

Received 13 August 2014; Accepted 14 October 2014

Academic Editor: Shaofan Li

Copyright © 2015 Jun Liu et al. This is an open access article distributed under the Creative Commons Attribution License, which permits unrestricted use, distribution, and reproduction in any medium, provided the original work is properly cited.

The global quasi-minimal residual (QMR) method is a popular iterative method for the solution of linear systems with multiple right-hand sides. In this paper, we consider the application of the global QMR method to classical ill-posed problems arising from image restoration. Since the scale of the problem is usually very large, the computations with the blurring matrix can be very expensive. In this regard, we use a Kronecker product approximation of the blurring matrix to benefit the computation. In order to reduce the disturbance of noise to the solution, the Tikhonov regularization technique is adopted to produce better approximation of the desired solution. Numerical results show that the global QMR method outperforms the classic CGLS method and the global GMRES method.

1. Introduction

In the area of remote sensing, materials science, medical and astronomical imaging, and so on, image restoration plays an important role in preprocessing and postprocessing the image [1]. Many image restoration tasks can be posed as problems of the form

$$\iint_{\Omega} h(x, y; s, t) f(s, t) ds dt = g(x, y), \quad (1)$$

where the functions f , g represent the original and blurred images, respectively. The kernel h is a *point spread function* (PSF) which is a function that specifies the degree of blurring. PSFs are often classified as either spatially variant or spatially invariant [2, 3]. For simplicity, we take into account spatially variant PSF in this paper. By means of discretization methods such as the Galerkin method or quadrature method [4], (1) can be discretized to the following linear equations:

$$Ax = \tilde{b}, \quad A \in \mathbb{R}^{n^2 \times n^2}, \quad x, \tilde{b} \in \mathbb{R}^{n^2}, \quad (2)$$

where x is a vector representing the true image and \tilde{b} is a vector representing the blurred image, which are the discretized versions of f and g in (1), respectively. The matrix

A is the blurring matrix constructed from the discretized version of the PSF h . It should be noted that the PSF is assumed to be known here. In fact, if the PSF is unknown, there are a variety of means of techniques available for estimating it [5, 6]. In real applications, the right-hand side error-free vector \tilde{b} is not accessible. Instead, the vector

$$b = \tilde{b} + \eta \quad (3)$$

is known, where the vector η represents the additive noise. That is, the observed image is not only blurred but also contaminated with noise. Commonly, η is assumed to be the white Gaussian noise, and its Euclidean vector norm is considered to be a priori but the noise vector itself is not.

In this work, we aim to obtain an approximation of the original image x by computing a solution of the linear system of equations

$$Ax = b, \quad A \in \mathbb{R}^{n^2 \times n^2}, \quad x, b \in \mathbb{R}^{n^2}. \quad (4)$$

If the observed image array has dimension $n \times n$, then f and g are vectors of length n^2 , and A is an $n^2 \times n^2$ matrix. Typical values of n are 256, 512, and 1024, so the dimensions of the matrix A can be extremely large [7]. Then the computations with A can be very expensive.

Fortunately, the matrix A has a special structure when an appropriate boundary condition is imposed. Then the computational cost of matrix-vector multiplication can be alleviated to some extent. For large-scale problems, such as image restoration problems, the direct regularization method cannot always obtain good solutions, but the iterative method is a better choice. Krylov subspace iterative methods are the most commonly used approaches that can be employed for solving (4). In [8], the authors proposed to employ the well known BiCG and QMR methods for image restoration. They also considered using a popular iterative method GMRES which was first proposed by Saad and Schultz for image restoration in [9].

Equation (4) can be replaced by new ones involving matrix equations, if the matrix A can be decomposed as Kronecker products, and then the computations with A can be reduced. In [10], the authors first proposed the global Krylov subspace methods to solve the matrix equations. The methods were proved to be very effective for large-scale matrix equations. Later in [11], Bouhamidi and Jbilou applied the global GMRES method to image restoration problems. Their numerical tests demonstrated that the global GMRES method was better than the GMRES method.

Due to the error in the right-hand side and the severe ill-conditioning property of the matrix A , the straightforward solution of (4) typically does not yield a meaningful approximation [4, 12, 13]. Therefore, instead of solving the system (4) directly, we replace it by a nearby linear system with a less ill-conditioned matrix and solve the corresponding new linear system. This replacement is commonly referred to as regularization [9]. Probably the most renowned regularization approach to overcome ill-conditioning dates back to Tikhonov and Arsenin [14].

In this paper, we consider the implementation of the global quasi-minimal residual (QMR) method for image restoration problems. The approach discussed here can be considered as an extension and a specific real application of the method introduced in [15] where the authors applied this method to solve the general Sylvester equation. This approach is motivated by the work of Bouhamidi and Jbilou in [11]. The numerical experiments show that the global QMR method is very effective compared with the global-GMRES method and the classic conjugate gradient method for least square (CGLS) problem.

The outline of this paper is as follows. In the next section, we give some notations and definitions that will be used throughout this paper. Section 3 introduces the global QMR method for image restoration problems. We present some numerical experiments to show the efficiency of the global QMR method in Section 4. Finally concluding remarks can be found in Section 5.

2. Preliminaries

As shown in [7], some blurring operators (e.g., Gaussian) are separable and therefore can be factored as Kronecker product of two matrices. The computation for the solution of (4) can be reduced if the Kronecker product approximation of A is employed.

Suppose that $P \in \mathbb{R}^{n \times n}$ is the discretized PSF. If the PSF is separable, that is, P can be decomposed as

$$P = \mathbf{a}\mathbf{b}^T, \quad (5)$$

where \mathbf{a} and \mathbf{b} are $n \times 1$ vectors, the matrix A constructed from P has block structure of the form

$$A = A_r \otimes A_c = \begin{pmatrix} a_{11}^r A_c & a_{12}^r A_c & \cdots & a_{1n}^r A_c \\ a_{21}^r A_c & a_{22}^r A_c & \cdots & a_{2n}^r A_c \\ \vdots & \vdots & \ddots & \vdots \\ a_{n1}^r A_c & a_{n2}^r A_c & \cdots & a_{nn}^r A_c \end{pmatrix}, \quad (6)$$

where the matrices A_r and A_c have parameters \mathbf{a} and \mathbf{b} , respectively, with the specific structures depending on the imposed boundary condition [6, 16], and “ \otimes ” denotes Kronecker product. We refer the readers to [17] for details about the properties of Kronecker product.

If the PSF P is inseparable, then the corresponding matrix A is inseparable. However, we can find the Kronecker product approximation of A by using SVD technique so that A can be approximately decomposed as the following form:

$$A \approx \sum_{i=1}^r A_{\mathbf{a}_i} \otimes A_{\mathbf{b}_i}, \quad (7)$$

where $P = \sum_{i=1}^r \mathbf{b}_i \mathbf{a}_i^T$ with a given integer $r \leq \text{rank}(P)$. In particular, the authors in [2, 16] pointed out that $A_{\mathbf{a}_1} \otimes A_{\mathbf{b}_1}$ is the best (as measured by the Frobenius norm) Kronecker approximation of A .

According to the properties of Kronecker product, (4) can be rewritten as

$$A_c X A_r^T = B, \quad (8)$$

where $x = \text{vec}(X)$ and $b = \text{vec}(B)$. Note that $z = \text{vec}(Z)$ with $Z \in \mathbb{R}^{n \times n}$ is the $n^2 \times 1$ vector obtained by stacking n columns of the matrix Z . Define an operator $\mathcal{A} : X \in \mathbb{R}^{n \times n} \rightarrow A_c X A_r^T$ and $\mathcal{A}^T : X \in \mathbb{R}^{n \times n} \rightarrow A_r X A_c^T$; then (4) can be rewritten as

$$\mathcal{A}X = B. \quad (9)$$

We use the notation

$$\mathcal{K}_m(\mathcal{A}, V) = \text{span}\{V, \mathcal{A}V, \mathcal{A}^2V, \dots, \mathcal{A}^{m-1}V\}, \quad (10)$$

for the global Krylov subspace of $\mathbb{R}^{n \times n}$ generated by the matrix $V \in \mathbb{R}^{n \times n}$ and the operator \mathcal{A} . Note that

$$Z \in \mathcal{K}_m(\mathcal{A}, V) \iff Z = \sum_{i=1}^m \alpha_i \mathcal{A}^{i-1}V, \quad \alpha_i \in \mathbb{R}. \quad (11)$$

Let $X, Y \in \mathbb{R}^{n \times n}$; we define the inner matrix product $\langle X, Y \rangle_F = \text{tr}(X^T Y)$, where $\text{tr}(Z)$ denotes the trace of the square matrix Z and X^T the transpose of the matrix X . The associated norm is the Frobenius norm $\|\cdot\|_F$. The matrices X, Y are said to be F-orthonormal if $\text{tr}(X^T Y) = 0$.

In the following, we will introduce an algorithm of the global Lanczos biorthogonal process, which has been

(1) Given \mathcal{A} , V_1 and W_1 such that $\langle V_1, W_1 \rangle_F = 1$;
 (2) Set $\beta_1 = \delta_1 = 0$ and $V_0 = W_0 = O_{n \times n}$;
 (3) For $i = 1, 2, \dots, m$
 $\alpha_j = \text{tr}(W_j^T \mathcal{A} V_j)$;
 $\widehat{V}_{j+1} = \mathcal{A} V_j - \alpha_j V_j - \beta_j V_{j-1}$;
 $\widehat{W}_{j+1} = \mathcal{A}^T W_j - \alpha_j W_j - \delta_j W_{j-1}$;
 $\delta_{j+1} = |\text{tr}(\widehat{V}_{j+1}^T \widehat{W}_{j+1})|^{1/2}$, if $\delta_{j+1} = 0$, stop;
 $\beta_{j+1} = \text{tr}(\widehat{V}_{j+1}^T \widehat{W}_{j+1}) / \delta_{j+1}$;
 $V_{j+1} = \widehat{V}_{j+1} / \delta_{j+1}$;
 $W_{j+1} = \widehat{W}_{j+1} / \beta_{j+1}$;
 End

ALGORITHM 1: The global Lanczos biorthogonal process.

elaborately discussed in [15, 18]. This process is used to construct a pair of biorthogonal basis V_1, V_2, \dots, V_m and W_1, W_2, \dots, W_m of the two Krylov subspaces $\mathcal{K}_m(\mathcal{A}, V_1)$ and $\mathcal{K}_m(\mathcal{A}^T, W_1)$, respectively, such that

$$\begin{aligned} \langle V_i, W_j \rangle &= \text{tr}(V_i^T W_j) = \delta_{ij} \\ &= \begin{cases} 1, & i = j, \\ 0, & i \neq j. \end{cases} \quad \text{for } i, j = 1, 2, \dots, m. \end{aligned} \quad (12)$$

The construction process can be summarized as in Algorithm 1.

For convenience, we denote by \mathcal{V}_m and \mathcal{W}_m the $n \times nm$ block matrix, that is, $\mathcal{V}_m = [V_1, V_2, \dots, V_m]$ and $\mathcal{W}_m = [W_1, W_2, \dots, W_m]$; two matrices are of dimension $n \times mn$. Suppose that the tridiagonal matrix T_m is denoted by

$$T_m = \begin{pmatrix} \alpha_1 & \beta_2 & & & \\ \delta_2 & \alpha_2 & & & \\ & \ddots & \ddots & & \\ & & \ddots & \beta_{m-1} & \\ & & & \delta_m & \alpha_m \end{pmatrix}, \quad (13)$$

where α_i, β_i , and δ_i ($i = 1, 2, \dots, m$) are the scalars defined in Algorithm 1.

To derive the relation between $\mathcal{A}\mathcal{V}_m$ and T_m , we define the matrix $\tilde{T}_m = \begin{pmatrix} T_m \\ \delta_{m+1} e_m^T \end{pmatrix}$, where $e_m = (0, \dots, 0, 1)^T \in \mathbb{R}^m$.

Recall the notation $*$ in [10]:

$$\mathcal{V}_m * y = \sum_{i=1}^m y^i V_i = \mathcal{V}_m (y \otimes I_n), \quad (14)$$

where $y = (y_1, y_2, \dots, y_m)^T$ is a vector of \mathbb{R}^m , I_n is the $n \times n$ identity matrix, and

$$\mathcal{V}_m * T_m = [\mathcal{V}_m * T_{:,1}, \dots, \mathcal{V}_m * T_{:,m}], \quad (15)$$

where $T_{:,i}$ denotes the i th column of the matrix T_m . Then, for $j = 1, 2, \dots, m-1$, we have the following relations:

$$\begin{aligned} \mathcal{V}_m * T_{:,j} &= \alpha_j V_j + \delta_{j+1} V_{j+1} + \beta_j V_{j-1} = \mathcal{A} V_j, \\ \mathcal{V}_m * T_{:,m} &= \beta_m V_{m-1} + \alpha_m V_m \\ &= \mathcal{A} V_m + \delta_{m+1} V_{m+1}. \end{aligned} \quad (16)$$

Then we get

$$\begin{aligned} \mathcal{A}\mathcal{V}_m &= \mathcal{V}_m * T_m + \delta_{m+1} [O_{n \times n}, \dots, O_{n \times n}, V_{m+1}] \\ &= \mathcal{V}_m * T_m + \delta_{m+1} e_m^T V_{m+1} \\ &= [\mathcal{V}_m, V_{m+1}] * \tilde{T}_m. \end{aligned} \quad (17)$$

That is, by the global Lanczos biorthogonal process, we can obtain

$$\mathcal{A}\mathcal{V}_m = \mathcal{V}_{m+1} * \tilde{T}_m. \quad (18)$$

It was pointed out in [15] that the global Lanczos algorithm had significant advantages over the Arnoldi method for its fewer matrices of storage.

3. The Global QMR Method for Image Restoration

The quasi-minimal residual (QMR) method was first introduced by Freund and Nachtigal [19] to solve the linear equation $Ax = b$. The main idea of this algorithm is to solve the reduced tridiagonal system in a least squares sense. Additionally, the QMR method uses the look-ahead technique to avoid breakdowns in the underlying Lanczos process, which makes it more robust than the BiConjugate Gradient method (BiCG) [20], and when BiCG makes no progress at all, QMR may still show slow convergence. Since the linear system is usually of large scale in applications such as image restoration, it needs enormous computation.

Fortunately, by applying the Kronecker product approximation of the matrix A [16, 17], the large-scale problems such as image restoration could be simplified intensively. In [10], the authors first introduced a global approach for solving matrix equations and derived the global FOM and the global GMRES methods. These methods are generalizations of the global MINRES method proposed by Saad [20]. The authors proved that these methods were effective when applied for matrix equations of large scale and low rank [21]. More recently, Wang and Gu [15] applied the global QMR method to solve the Sylvester equations. In this work, we will focus on the global QMR method for image restoration.

Suppose that the operator $\mathcal{A} = A_r \otimes A_c$ is a good approximation of A , $x = \text{vec}(X)$ and $b = \text{vec}(B)$. In the following, we give details of the global QMR method for image restoration. Let $X_0 \in \mathbb{R}^{n \times n}$ be the initial solution of (9) and let $R_0 = B - \mathcal{A}X_0$ be the corresponding residual. Usually we set the black image to be the initialization. By using Algorithm 1 for (9), the iterate X_m at step m satisfies that

$$X_m - X_0 \in \mathcal{K}_m(\mathcal{A}, R_0). \quad (19)$$

Define $V_1 = R_0 / \rho$, $\rho = \|R_0\|_F$ and W_1 such that $\langle V_1, W_1 \rangle_F = 1$. Suppose that the matrix Krylov subspaces $\mathcal{K}_m(\mathcal{A}, R_0)$ and $\mathcal{K}_m(\mathcal{A}^T, W_1)$ are generated by the sets of matrices $\{V_1, V_2, \dots, V_m\}$ and $\{W_1, W_2, \dots, W_m\}$ constructed by Algorithm 1. Then according to (19), we can obtain an approximate solution of (9):

$$X_m = X_0 + \mathcal{V}_m * y_m, \quad (20)$$

where $\mathbf{y}_m = (y_1, y_2, \dots, y_m)^T$. Consequently, we can get the associated residual matrix

$$\begin{aligned} R_m &= B - \mathcal{A}X_m \\ &= B - \mathcal{A}(X_0 + \mathcal{V}_m * \mathbf{y}_m) \\ &= R_0 - \mathcal{A}\mathcal{V}_m * \mathbf{y}_m \\ &= \rho V_1 - \mathcal{V}_{m+1} * \tilde{T}_m \mathbf{y}_m \\ &= \mathcal{V}_{m+1} * (\rho e_1 - \tilde{T}_m \mathbf{y}_m), \end{aligned} \quad (21)$$

where $e_1 = (1, 0, \dots, 0)^T$. Hence, the norm of the residual matrix is

$$\|R_m\|_F = \|\mathcal{V}_{m+1} * (\rho e_1 - \tilde{T}_m \mathbf{y}_m)\|_F. \quad (22)$$

An approximate solution of (9) can be obtained by computing the minimizer from (22) with respect to \mathbf{y}_m . Generally, the V_i 's obtained by Algorithm 1 are not F-orthonormal. However, as shown in [20], it is still reasonable to obtain that

$$\hat{\mathbf{y}}_m = \arg \min_{\mathbf{y}_m \in \mathbb{R}^m} \|\rho e_1 - \tilde{T}_m \mathbf{y}_m\|_F. \quad (23)$$

What has been shown above is the key idea of the global QMR method; hence the approximated solution by the global QMR method can be given as

$$X_m = X_0 + \mathcal{V}_m * \hat{\mathbf{y}}_m, \quad (24)$$

where $\hat{\mathbf{y}}_m = \arg \min_{\mathbf{y}_m \in \mathbb{R}^m} \|\rho e_1 - \tilde{T}_m \mathbf{y}_m\|_F$. We refer the readers to see [15, 20] for the details on how to compute $\hat{\mathbf{y}}_m$.

To sum up, the algorithm for obtaining the approximate solution of (9) arising from image restoration can be described as in Algorithm 2.

We note that the discrepancy principle can be used as the stopping criterion in Algorithm 2; that is, the computations will be terminated if the associated residual error corresponds to the approximate solution X_m

$$\|\mathcal{A}X_m - B\| \leq \mu\epsilon, \quad \|\mathcal{A}X_{m-1} - B\| > \mu\epsilon, \quad (25)$$

where ϵ is the noise's Frobenius Norm which is supposed to be a priori and $\mu \geq 1$ is a fixed constant. For details on the discrepancy principle, we refer to [22] and references therein for more details.

Since the matrix A is usually ill-conditioned, the solution is sensitive to the noise in the observed image. In the following, in order to improve the accuracy of the solution, we consider combining the global QMR method with Tikhonov regularization technique. Motivated by the work in [11], we can obtain the following algorithm which is named as the global Tik-QMR method.

In Algorithm 3, the regularization parameter λ can be determined by the L-curve criterion or the GCV method. We choose the latter here. Note that the regularization step in our work is different from the work in [11], since we adopt the regularization after Lanczos process while the authors in [11] used the regularization before the Lanczos process. Then our method needs fewer computations than theirs.

```
(1) Given  $\mathcal{A}$ , and  $B, X_0$ ;
(2) Set  $R_0 = \hat{B} - \mathcal{A}X_0, \rho = \|R_0\|_F, W_1 = V_1 = R_0/\rho$ ;
(3) For  $m = 1, 2, \dots$ 
    Compute  $\tilde{T}_m, V_m, W_m$  using Algorithm 1;
     $\hat{\mathbf{y}}_m = \arg \min_{\mathbf{y}_m \in \mathbb{R}^m} \|\rho e_1 - \tilde{T}_m \mathbf{y}_m\|_2$ ;
     $X_m = X_0 + \mathcal{V}_m * \hat{\mathbf{y}}_m$ ;
End
```

ALGORITHM 2: The global QMR method for image restoration.

```
(1) Given  $\mathcal{A}, \hat{B}, X_0, \mu$  and  $\epsilon$ ;
(2) Set  $R_0 = \hat{B} - \mathcal{A}X_0, \rho = \|R_0\|_F, W_1 = V_1 = R_0/\rho$ ;
(3) For  $m = 1, 2, \dots$ 
    Compute  $\tilde{T}_m, V_m, W_m$  using Algorithm 1;
     $\hat{\mathbf{y}}_m = \arg \min_{\mathbf{y}_m \in \mathbb{R}^m} \|\rho e_1 - \tilde{T}_m \mathbf{y}_m\|_2^2 + \lambda^2 \|\mathbf{y}_m\|_2^2$ ;
     $X_m = X_0 + \mathcal{V}_m * \hat{\mathbf{y}}_m$ ;
     $R_m = \mathcal{V}_{m+1} * (\rho e_1 - \tilde{T}_m \mathbf{y}_m)$ ;
    if  $\|R_m\|_F$  satisfies the discrepancy principle, stop
    else
         $X_0 = X_m, \rho = \|R_m\|_F, V_1 = R_m/\rho$ ;
End
```

ALGORITHM 3: The global Tik-QMR method for image restoration.

4. Numerical Experiments

In this section, we report some numerical examples to illustrate the performance of the global QMR method for image restoration problems. The results show that the quality of images restored by the global QMR method is better than those obtained by other methods of the same kind, such as the classic CGLS method [23] and the global GMRES method proposed by Jbilou et al. [10]. The experiments are carried out in Matlab 7.0 on a PC equipped with a 2.93 GHz Intel Core Duo CPU, with 2 GB of RAM, under Microsoft Windows XP.

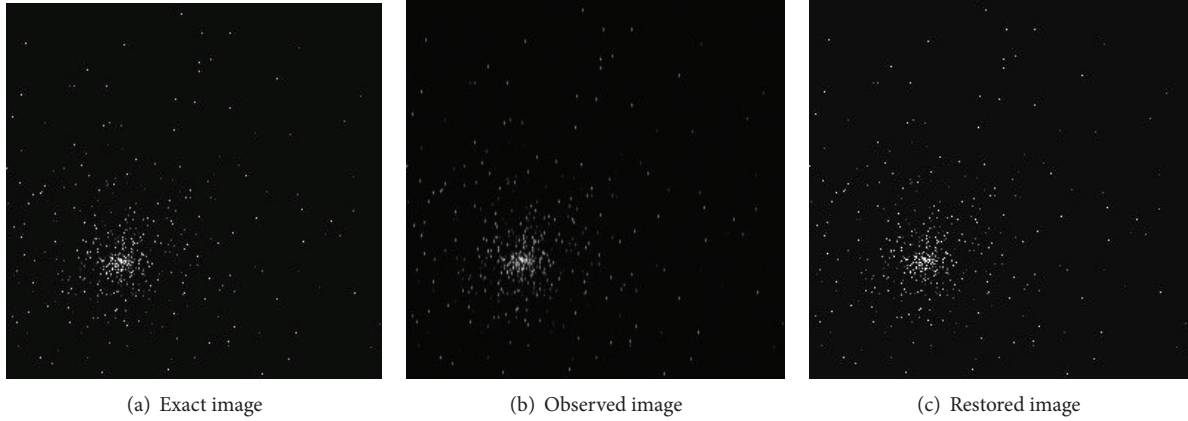
Example 1. Our first example is to show the practical efficiency of the global QMR method. The original image X of size 256×256 is shown in Figure 1(a), which can be obtained from the *Telescope Science Institute*, and intended to simulate a star cluster image taken by the Hubble space telescope before its defective mirror was replaced [24]. Let X denote the exact star cluster. The PSF used in this example is the so-called Moffat function [6]. The PSF is given by

$$P_{ij} = \begin{cases} \left((i-16)^2 + \left(\frac{j-16}{2} \right)^2 \right)^{-5} & \text{if } 1 \leq i, j \leq 30, \\ 0, & \text{otherwise.} \end{cases} \quad (26)$$

This PSF P is nonsymmetric and unseparable, so the blurring matrix A constructed from P is nonsymmetric and unseparable. If the zero boundary condition is imposed, the matrix A can be represented as the Kronecker product approximation of Toeplitz matrices A_r and A_c ; that is, $A = A_r \otimes A_c$. We add 1% white Gaussian noise to the blurred image

TABLE 1: Numerical results for the experiments, in terms of PSNR (dB) and CPU time (second).

Test problem	Method	restored PSNR	CPU time	observed PSNR
starcluster	global QMR	41.16	0.25 s	30.82
MRI	global QMR	20.61	0.156 s	17.95
	global Tik-QMR	22.16	0.344 s	
Indian man	global Tik-QMR	25.69	8.078 s	23.51
	CGLS	25.05	1.7 s	
bridge	global Tik-QMR	19.91	49.42 s	15.66
	global GMRES	20.05	67.95 s	

FIGURE 1: *Example 1*: (a) original image. (b) Observed image contaminated with blur and noise. (c) Image restored by the global QMR method.

to simulate the observed image (Figure 1(b)). The PSNR of the observed image is 30.82 dB. We set the parameter $\mu = 1.05$ for the discrepancy principle. Using the global QMR method, we obtained the estimated image after 4 iterations when the discrepancy principle of its associated residual is satisfied. The numerical results in terms of PSNR are reported in Table 1. From the table, we see that the PSNR of the restored image by the global QMR method is 41.16 dB and the consumed CPU time is 0.25 s. The restored image is shown in Figure 1(c).

Example 2. In order to suppress the sensitivity of solution to noise, we employ Tikhonov regularization technique to get a more accurate solution. In this example, we compared the performance of the global Tik-QMR method and the global QMR method. We consider the problem of restoring the image of the MRI data from Matlab (Figure 2(a)). The data size is 128×128 . The blurred and noisy image is shown in Figure 2(b). The PSF for blurring in this test is the truncated separable Gaussian function, and the variance of the Gaussian blur is 3 and 1% white Gaussian noise is added.

The restored images obtained by the global QMR method and the global Tik-QMR method are shown in Figure 3, respectively. From Figure 3, it is easy to see that the image restored by the global Tik-QMR method has higher visual quality than that by the global QMR method. The numerical results are shown in Table 1, and it is not difficult to see that

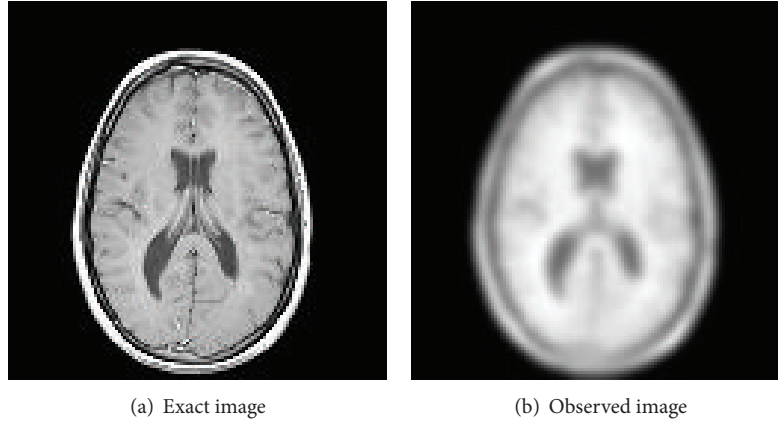
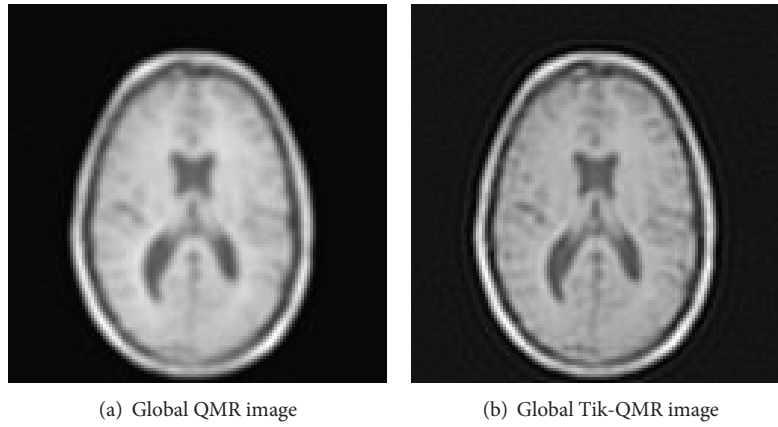
the global Tik-QMR method outperforms the global QMR method.

Example 3. The third example consists in restoring the image of 512×512 “Indian man” degraded by the Gaussian blur and 0.1% additive noise. The true image and degraded image are shown in Figure 4. We compare the global Tik-QMR method with the classic CGLS. The PSNR of the restored images by the two methods and computational CPU time are given in Table 1. The restored images are shown in Figure 5.

From Figure 5 and Table 1, we see that the global Tik-QMR method is quite competitive with the CGLS method.

Example 4. In the last experiment, the 256×256 bridge image has been contaminated by a nonsymmetric wavefront blur [25] and 0.1% additive noise. The true image, the wavefront PSF, and the degraded image are shown in Figure 6. The PSF is also unseparable. Then the corresponding blurring matrix A is approximated by the Kronecker product of two small matrices. We compared the behavior of the global Tik-QMR method and the global GMRES method [11] in this experiment.

The numerical results are given in Table 1. From the table, we see that the PSNR of the restored image by the global GMRES method is slightly higher than the global Tik-QMR method, but the CPU time by using the global Tik-QMR method is much less than the global GMRES method.

FIGURE 2: *Example 2*: exact and observed images.FIGURE 3: *Example 2*: restored images by the global QMR method and the global Tik-QMR method.FIGURE 4: *Example 3*: exact and observed images.

The visual quality of restored images is very close. The restored images by using the two methods are displayed in Figure 7.

At the end of this section, a general comment about the presented numerical experiments is worth mentioning. The first example illustrates efficiency of the proposed method for image restoration problems. In general, the global Tik-QMR

method behaves better than the classic CGLS method and the global GMRES method.

5. Conclusion

In [10], Jbilou et al. first introduced the global methods. In this paper, we take the advantage of the global QMR method



FIGURE 5: *Example 3*: exact and observed images.

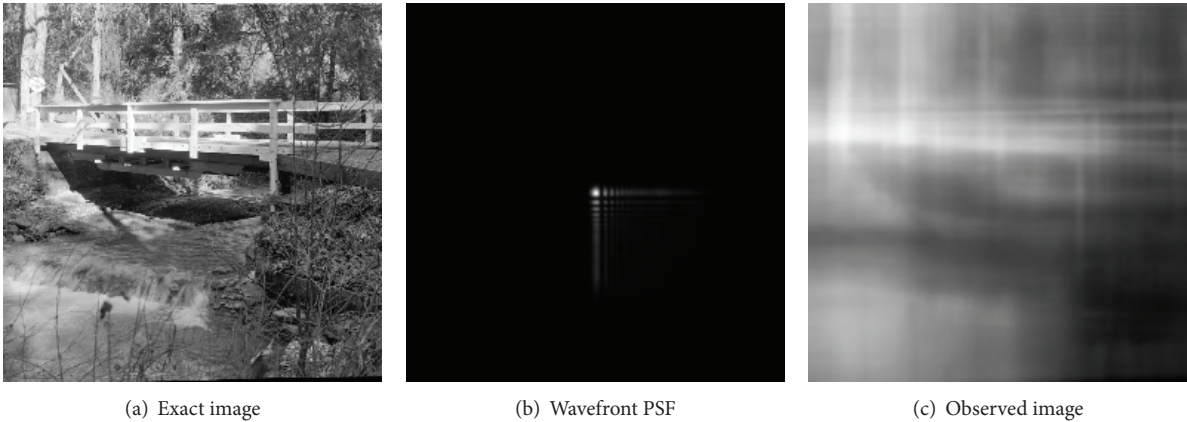


FIGURE 6: *Example 4*: exact image, wavefront PSF, and observed image.

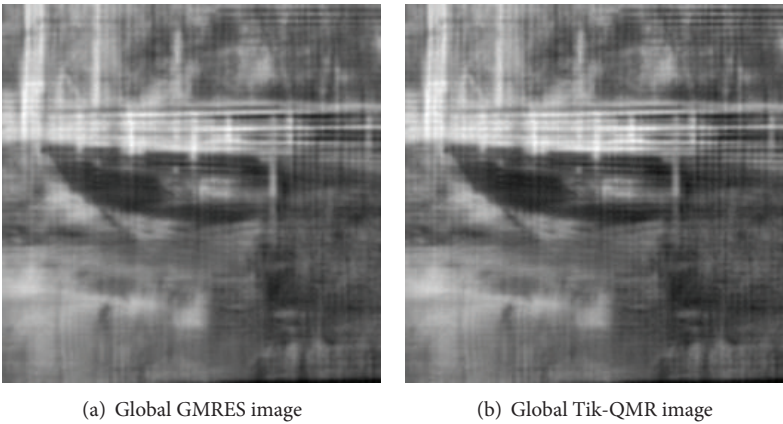


FIGURE 7: *Example 4*: restored images using the global GMRES method and the global Tik-QMR method.

for image restoration and compare it with other popular methods. Numerical results show that the global QMR method is very efficient and is competitive with the classic CGLS method and the global GMRES method in [11]. In addition, when combining with the Tikhonov regularization, the global QMR method can behave much better.

Conflict of Interests

The authors declare that there is no conflict of interests regarding the publication of this paper.

Acknowledgments

This work is supported by NSFC (61370147, 61170311), 973 Program (2013CB329404), and Sichuan Province Sci. & Tech. Research Project (2012GZX0080).

References

- [1] M. R. Banham and A. K. Katsaggelos, "Digital image restoration," *IEEE Signal Processing Magazine*, vol. 14, no. 2, pp. 24–41, 1997.
- [2] J.-G. Nagy, M.-K. Ng, and L. Perrone, "Kronecker product approximations for image restoration with reflexive boundary conditions," *SIAM Journal on Matrix Analysis and Applications*, vol. 25, no. 3, pp. 829–841, 2003.
- [3] J. G. Nagy, K. Palmer, and L. Perrone, "Iterative methods for image deblurring: a Matlab object-oriented approach," *Numerical Algorithms*, vol. 36, no. 1, pp. 73–93, 2004.
- [4] P. C. Hansen, *Rank-Deficient and Discrete Ill-Posed Problems*, SIAM Monographs on Mathematical Modeling and Computation, Society for Industrial and Applied Mathematics (SIAM), Philadelphia, Pa, USA, 1997.
- [5] K. T. Lay and A. K. Katsaggelos, "Identification and restoration based on the expectation-maximization algorithm," *Optical Engineering*, vol. 29, no. 5, pp. 436–445, 1990.
- [6] P. C. Hansen, J. G. Nagy, and D. O'Leary, *Deblurring Images: Matrices, Spectra, and Filtering*, SIAM, Philadelphia, Pa, USA, 2006.
- [7] J. Kamm and J. G. Nagy, "Kronecker product and SVD approximations in image restoration," *Linear Algebra and Its Applications*, vol. 284, no. 1–3, pp. 177–192, 1998.
- [8] D. Calvetti, B. Lewis, and L. Reichel, "Krylov subspace iterative methods for nonsymmetric discrete ill-posed problems in image restoration," in *Advanced Signal Processing Algorithms, Architectures, and Implementations XI*, vol. 4474 of *Proceedings of SPIE*, pp. 224–233, San Diego, Calif, USA, 2001.
- [9] D. Calvetti, B. Lewis, and L. Reichel, "GMRES, L-curves, and discrete ill-posed problems," *BIT. Numerical Mathematics*, vol. 42, no. 1, pp. 44–65, 2002.
- [10] K. Jbilou, A. Messaoudi, and H. Sadok, "Global FOM and GMRES algorithms for matrix equations," *Applied Numerical Mathematics*, vol. 31, no. 1, pp. 49–63, 1999.
- [11] A. Bouhamidi and K. Jbilou, "Sylvester Tikhonov-regularization methods in image restoration," *Journal of Computational and Applied Mathematics*, vol. 206, no. 1, pp. 86–98, 2007.
- [12] P.-C. Hansen, *Discrete Inverse Problems: Insight and Algorithms*, SIAM, Philadelphia, Pa, USA, 2010.
- [13] X.-G. Lv, T.-Z. Huang, Z.-B. Xu, and X.-L. Zhao, "Kronecker product approximations for image restoration with whole-sample symmetric boundary conditions," *Information Sciences*, vol. 186, pp. 150–163, 2012.
- [14] A. Tikhonov and V. Arsenin, *Solution of Ill-Posed Problems*, V. H. Winston & Sons, Washington, DC, USA, 1977.
- [15] Y. Wang and G.-D. Gu, "Global quasi-minimal residual method for the Sylvester equations," *Journal of Shanghai University (English Edition)*, vol. 11, no. 1, pp. 52–57, 2007.
- [16] J. G. Nagy and L. Perrone, "Kronecker products in image restoration," in *13th Advanced Signal Processing Algorithms, Architectures, and Implementations*, vol. 5205 of *Proceedings of SPIE*, pp. 369–379, San Diego, Calif, USA, August 2003.
- [17] C.-F. van Loan and N. P. Pitsianis, "Approximation with Kronecker product," in *Linear Algebra for Large Scale and Real Time Applications*, M. S. Moonen and G. H. Golub, Eds., pp. 293–314, Kluwer Publications, 1993.
- [18] K. Jbilou, H. Sadok, and A. Tinzeft, "Oblique projection methods for linear systems with multiple right-hand sides," *Electronic Transactions on Numerical Analysis*, vol. 20, pp. 119–138, 2005.
- [19] R. W. Freund and N. M. Nachtigal, "QMR: a quasi-minimal residual method for non-Hermitian linear systems," *Numerische Mathematik*, vol. 60, no. 3, pp. 315–339, 1991.
- [20] Y. Saad, *Iterative Methods for Sparse Linear Systems*, Philadelphia, Pa, USA, 2nd edition, 2003.
- [21] Y.-Q. Lin, "Implicitly restarted global FOM and GMRES for nonsymmetric matrix equations and Sylvester equations," *Applied Mathematics and Computation*, vol. 167, no. 2, pp. 1004–1025, 2005.
- [22] D. Calvetti, B. Lewis, and L. Reichel, "On the regularizing properties of the GMRES method," *Numerische Mathematik*, vol. 91, no. 4, pp. 605–625, 2002.
- [23] M. Hanke, *Conjugate Gradient Type Methods for Ill-Posed Problems*, Longman Scientific & Technical, Essex, UK, 1995.
- [24] D. Calvetti, G. Landi, L. Reichel, and F. Sgallari, "Non-negativity and iterative methods for ill-posed problems," *Inverse Problems*, vol. 20, no. 6, pp. 1747–1758, 2004.
- [25] E.-R. Dowski and W.-T. Cathey, "Extended depth of field through wave-front coding," *Applied Optics*, vol. 34, no. 11, pp. 1859–1866, 1995.

Research Article

An Extended Assessment of Fluid Flow Models for the Prediction of Two-Dimensional Steady-State Airfoil Aerodynamics

José F. Herbert-Acero,¹ Oliver Probst,¹ Carlos I. Rivera-Solorio,²
Krystel K. Castillo-Villar,³ and Santos Méndez-Díaz⁴

¹Wind Energy Group, Department of Physics, Instituto Tecnológico y de Estudios Superiores de Monterrey, Eugenio Garza Sada 2501 Sur, 64849 Monterrey, NL, Mexico

²Solar Energy and Thermosciences Group, Department of Mechanical Engineering, Instituto Tecnológico y de Estudios Superiores de Monterrey, Eugenio Garza Sada 2501 Sur, 64849 Monterrey, NL, Mexico

³Department of Mechanical Engineering, The University of Texas at San Antonio, One UTSA Circle, San Antonio, TX 78249, USA

⁴School of Mechanical and Electrical Engineering, Universidad Autónoma de Nuevo León, Avenida Universidad s/n, Ciudad Universitaria, 66451 San Nicolás de los Garza, NL, Mexico

Correspondence should be addressed to José F. Herbert-Acero; jf.herbert.phd.mty@itesm.mx

Received 30 August 2014; Revised 13 January 2015; Accepted 13 January 2015

Academic Editor: Shaofan Li

Copyright © 2015 José F. Herbert-Acero et al. This is an open access article distributed under the Creative Commons Attribution License, which permits unrestricted use, distribution, and reproduction in any medium, provided the original work is properly cited.

This work presents the analysis, application, and comparison of thirteen fluid flow models in the prediction of two-dimensional airfoil aerodynamics, considering laminar and turbulent subsonic inflow conditions. Diverse sensitivity analyses of different free parameters (e.g., the domain topology and its discretization, the flow model, and the solution method together with its convergence mechanisms) revealed important effects on the simulations' outcomes. The NACA 4412 airfoil was considered throughout the work and the computational predictions were compared with experiments conducted under a wide range of Reynolds numbers ($7e5 \leq Re \leq 9e6$) and angles-of-attack ($-10^\circ \leq \alpha \leq 20^\circ$). Improvements both in modeling accuracy and processing time were achieved by considering the RS LP-S and the Transition SST turbulence models, and by considering finite volume-based solution methods with preconditioned systems, respectively. The RS LP-S model provided the best lift force predictions due to the adequate modeling of the micro and macro anisotropic turbulence at the airfoil's surface and at the nearby flow field, which in turn allowed the adequate prediction of stall conditions. The Transition-SST model provided the best drag force predictions due to adequate modeling of the laminar-to-turbulent flow transition and the surface shear stresses. Conclusions, recommendations, and a comprehensive research agenda are presented based on validated computational results.

1. Introduction

The measurement and prediction of aerodynamic forces on two-dimensional airfoils is a problem that has been widely investigated since the early 1930s and its development has produced important improvements in the aerospace, automotive, and wind-based sciences, among others [1–4]. Prior to the experimental assessment of aerodynamic forces, the state-of-the-art procedures [1, 2] impose major prerequisites such as the detailed manufacture of the tested airfoil [5], the setup of expensive wind tunnel facilities [6], and the

use of special sensing equipment to characterize both the aerodynamic behavior of the airfoil and the disturbances it produces on the free stream (e.g., streamlines, flow attachment/detachment, flow compression dynamics, and wake aerodynamics). In addition, correction factors [1, 4, 6–10] are often applied to account for nonideal inflow conditions (e.g., buoyancy, solid blockage, wake blockage, or streamline curvature corrections). These prerequisites and issues, together with the overall propagation of uncertainty, turn the experimentation procedures into daunting tasks. A useful, inexpensive, and faster alternative to perform aerodynamic

characterizations involves the implementation of computational methods for the theoretical estimation of aerodynamic forces, which are predicted through the numerical solution of the governing equations of fluid mechanics. This approach is formally known as Computational Fluid Dynamics (CFD).

It is generally acknowledged that there is no universal model/method that ultimately describes the complete characteristics of a fluid flow and its interactions with objects with reasonable accuracy while employing a reasonable amount of computational resources. This modeling problem becomes more complex as more physical phenomena are considered (e.g., if turbulent, compressible, and multiphase flows are considered, among other relevant conditions). Therefore, depending on the case study conditions and the assumptions made, different CFD-based approaches with different levels of sophistication can be employed. Some of the most important fluid flow modeling techniques are briefly presented next: (1) the potential flow theory [11], considered the coarsest modeling approach, does not account for turbulence or vorticity effects in its basic formulations. Nonetheless, recent advances in potential flow theory and Boundary Layer (BL) modeling have led to the development of the vortex modeling approach [12], in which viscous and vorticity effects have been successfully integrated into the fluid flow modeling, resulting in improved aerodynamic predictions. (2) The turbulence modeling approach, considered as the industry standard approach for design purposes, is much more complex and computationally demanding since both small-scale and large-scale turbulence effects are modeled by solving either the Reynolds-Averaged Navier-Stokes (RANS) or the Favre-Averaged Navier-Stokes (FANS) equations complemented with turbulence models [13, 14]. (3) Advanced techniques that solve large-scale turbulence effects and model only the small-scale turbulence effects are based on large eddy simulations (LES) complemented with subgrid-scale models [15]. Finally, (4) more advanced techniques based on Direct Numerical Simulations (DNS) [16], which are typically implemented for theoretical research purposes, have the ability to solve the whole range of spatial and temporal scales of the turbulence and predict all the effects and interactions between fluids and solids at the cost of an extraordinary large amount of computational resources.

Currently, there is no consensus regarding the minimum level of flow modeling required to accurately predict airfoil aerodynamics, while considering different flow regimes/states (e.g., laminar, transitional, and turbulent flows) and different inflow conditions (e.g., Reynolds numbers and angles of attack). Despite this issue, in works mainly focused on airfoil shape development and optimization [3, 17] it is often considered sufficient to solve the compressible Euler equations [18] or solve a set of potential flow equations that are coupled with integral BL formulations, some of which are implemented in popular public domain and commercial codes such as XFOIL [19, 20] or VisualFoam [21], respectively, to estimate aerodynamic forces under subsonic, transonic, or supersonic flows. The selection of these approaches, however, was mostly based on the convenient amount of computational resources they require rather than their performance for predicting aerodynamic forces.

Only a limited number of research works have attempted to determine the accuracy of different fluid flow modeling techniques for predicting the aerodynamic behavior of two-dimensional airfoils undergoing different inflow conditions. Wolfe and Ochs [22] presented a laminar/turbulent flow analysis, considering an airflow at a Reynolds number (Re) of $2e6$ and the range of angles of attack (α , AOA) $0^\circ \leq \alpha \leq 20.5^\circ$, to determine the asymmetric S809 airfoil aerodynamics. They employed the commercial code CFD-ACE, which solves the FANS equations coupled with the Standard $k-\epsilon$ turbulence model. Wolfe and Ochs contrasted the computed pressure coefficient distributions and the computed aerodynamic coefficients with experimental measurements obtained under laminar inflow conditions and observed a drag force overprediction when fully turbulent computations were considered. To address the issue of simulating transitional flows, they developed a mixed laminar/turbulent calculation method, in which the computational domain was split into one laminar and one turbulent region at a guessed transition point, which in turn improved the drag force predictions. They concluded that more research on both the determination of the laminar-to-turbulent flow transition point [23] and the accurate modeling of turbulent effects under stall conditions was necessary to reduce observed discrepancies.

Some of the discrepancies observed by Wolfe and Ochs are related to BL modeling issues. In their work, the modeled dimensionless wall distance ($y^+ = u^* y / \nu$ [24], which is a parameter typically used to determine what sublayers of the BL are solved) was of the order of $y^+ \geq 30$, thus limiting the probed sample volume of the BL to the logarithmic and outer layers. Therefore, the modeling of the near-wall flow dynamics and the calculation of wall shear stresses depended on the use of wall functions. The standard wall functions [24, 25], such as the ones used by Wolfe and Ochs, have proven to be inaccurate while modeling BLs subject to large adverse pressure gradients (like the ones encountered on airfoils undergoing inflow conditions at large AOA), which in turn induce flow detachment conditions. The appropriate description of the complex BL, from which aerodynamic forces are calculated, requires the accurate modeling of the viscous, turbulent, and rotational properties of the flow found within the airfoil's vicinity. Therefore, the better the airfoil's BL is modeled, with special emphasis on the viscous sublayer (or laminar sublayer, which is located at the inner part of the BL), the better the agreement between the computed and the measured aerodynamic forces and the observed flow dynamics. In order to model the viscous sublayer, a solved $y^+ \cong 1$ is required over the entire airfoil surface [24, 26]. The interested reader is directed to [1, 2, 27] for additional and comprehensive descriptions of the physics of airfoil aerodynamics.

Eleni et al. [28] presented a work focused on determining which turbulence model, among the Spalart-Allmaras, the Realizable $k-\epsilon$, and the SST $k-\omega$ turbulence models, was the best performer for predicting the symmetric four-digit National Advisory Committee for Aeronautics (NACA) 0012 airfoil aerodynamics, while considering an airflow at a $Re = 3e6$ and for the range of AOA $-12^\circ \leq \alpha \leq 20^\circ$. Similar to the study performed by Wolfe and Ochs, Eleni et al.

found drag overpredictions when comparing fully turbulent computations with experimental measurements that considered laminar inflow conditions. To improve the drag force predictions, they conducted mixed laminar/turbulent simulations, similar to the procedure proposed by Wolfe and Ochs. However, in order to determine the laminar-to-turbulent flow transition point, Eleni et al. developed an iterative method that depends on already measured data. In addition, they conducted simulations, considering five different Reynolds numbers ($1e6 \leq Re \leq 5e6$), at a zero AOA by assuming both fully turbulent and mixed laminar/turbulent conditions. In such simulations, the laminar-to-turbulent flow transition took place at the same axial point at both the top and the bottom surfaces of the airfoil due to its symmetry. The resultant drag coefficients were compared satisfactorily with the experimental measurements. They concluded that for both fully turbulent and mixed laminar/turbulent flows the best performer turbulence model was the SST $k-\omega$.

Kumar et al. [29] presented a work in which the asymmetric NACA 4412 airfoil was simulated in a turbulent airflow, at a $Re = 3.42e6$ and for the range of AOA $-18^\circ \leq \alpha \leq 18^\circ$, while considering the Spalart-Allmaras and the Standard $k-\omega$ turbulence models. The computed predictions were contrasted with the experimental data (at a $Re = 3e6$) provided by Abbott and von Doenhoff [1]. Kumar et al. reached the same conclusions as Wolfe and Ochs about the importance of the accurate determination of the laminar-to-turbulent flow transition points at both the upper and the lower surfaces of the airfoil, since a notable overprediction of the drag coefficient was observed by simulating a fully turbulent flow over the airfoil's vicinity. They concluded that the Standard $k-\omega$ model was the best performer turbulence model.

Villalpando et al. [30] presented an assessment of the ability of different turbulence models to predict the asymmetric NACA 63-415 airfoil aerodynamics, while considering an airflow at a $Re = 1.6e6$, the range of AOA $0^\circ \leq \alpha \leq 28^\circ$, and an inlet turbulence intensity (TI) of 1%. The contrasted turbulence models were the Spalart-Allmaras, the RNG $k-\epsilon$, the SST $k-\omega$, and the Reynolds Stress Low-Re $S-\omega$. The computational results were compared with experimental measurements performed under laminar inflow conditions, which were provided by the Risø National Laboratory for Sustainable Energy. Unlike the observations of the previously described works, the contrasted turbulence models accurately predicted the experimental drag coefficient for $\alpha \leq 17^\circ$. Only at large AOA (i.e., under stall conditions) all the tested models overpredicted both the lift and drag coefficients. Villalpando et al. did not report the numerical convergence criteria of their finite-volume-based solution method but reported oscillatory convergence, an observation pointing to numerical instabilities, for moderately large AOA (e.g., $\alpha \geq 8^\circ$). In such cases, an averaging procedure was performed to estimate the aerodynamic forces. The approach, however, is believed to be inadequate since such convergence issues are often related to the quality of the domain discretization and/or to the numerical approach used to solve the problem.

They concluded that the SST $k-\omega$ model was the best performer model, with the Reynolds Stress Low-Re $S-\omega$ being the worst performer model.

Other studies related to the prediction of airfoil aerodynamics (e.g., [31–34]), in which laminar/transitional flows are involved, may be affected by the already noted overprediction of the drag coefficient, which is an issue directly related to the lacking ability of full-turbulent models to simulate the laminar-to-turbulent flow transition. In order to deal with this issue, improved turbulence models, named Transition-based models [24, 26, 35], have been developed to accurately estimate the laminar-to-turbulent flow transition zones and solve the flow as turbulent at downstream locations. So far, improved drag predictions have been obtained as described by Yuhong and Congming [36], Yao et al. [37], Aranake et al. [38], and Khayatzadeh and Nadarajah [26].

Yuhong and Congming [36] presented a work in which the asymmetric S814 airfoil aerodynamics was predicted using the Transition SST model, considering an airflow at a $Re = 1e6$ and for the range of AOA $0^\circ \leq \alpha \leq 30^\circ$. They concluded that the Transition SST model predicts the lift and drag coefficients more accurately than full-turbulent models only in prestall conditions. Under stall conditions, both tested turbulence models (the Transition SST and the SST $k-\omega$) failed to predict the aerodynamic behavior of the tested airfoil.

Yao et al. [37] performed a similar work by predicting the symmetric NACA 0018 airfoil aerodynamics for an airflow at a $Re = 5e5$, a relative Mach number of 0.023, and for the range of AOA $-8^\circ \leq \alpha \leq 13^\circ$. The contrasted turbulence models were the Standard $k-\epsilon$, the RNG $k-\epsilon$, the four-equation Transition SST model, and a five-equation Reynolds Stress model. For all the considered inflow conditions, all turbulence models overpredicted the drag coefficient, as concluded in previous works. The magnitude of the lift coefficient was systematically underpredicted for both large negative AOA and large positive AOA. The Reynolds Stress model was the top performer in that study.

Aranake et al. [38] presented an evaluation of the RANS-based Transition $\gamma - \overline{Re}_{\theta t}$ model, which was coupled with the Spalart-Allmaras turbulence model (named the Transition $\gamma - \overline{Re}_{\theta t} - SA$ model), for predicting the asymmetric S827 and the S809 airfoil aerodynamics. For the S827 airfoil aerodynamics prediction, an airflow at a $Re = 3e6$, a Mach number of 0.1, an inlet TI = 0.05%, and the range of AOA $0^\circ \leq \alpha \leq 20^\circ$ were considered. The same conditions, but considering a $Re = 2e6$, were assumed for the evaluation of the S809 airfoil aerodynamics. After comparing fully turbulent computations performed with the Spalart-Allmaras model, laminar/transitional computations performed with the Transition $\gamma - \overline{Re}_{\theta t} - SA$ model, and experimental measurements conducted under laminar inflow conditions, Aranake et al. found improved lift, drag, and pressure coefficients predictions under both prestall and stall conditions. Nevertheless, significant discrepancies were found at intermediary AOA, where a characteristic double-stall condition arises for both tested airfoils. They concluded that in situations for which the flow remains completely attached or massively separated,

the Transition $\gamma - \overline{Re}_{\theta t}$ - SA model qualitatively and quantitatively exhibits the same behavior as the fully turbulent SA model. But when moderate flow separation occurs, the coupled model significantly improves the quality of the predictions.

Khayatzaheh and Nadarajah [26] presented a comprehensive evaluation of the RANS-based Transition $\gamma - \overline{Re}_{\theta t}$ model, which was coupled with the SST $k-\omega$ turbulence model, for predicting the asymmetric NLF(1)-0416 and the S809 airfoil aerodynamics. They provided modifications for both the SST $k-\omega$ and the Transition $\gamma - \overline{Re}_{\theta t}$ models in order to allow an appropriate gradual activation of the SST $k-\omega$ model along the BL upon the onset of transition from laminar-to-turbulent flow conditions. The proposed modifications improved the aerodynamic predictions of the original models, which were compared with experimental measurements performed under laminar inflow conditions. The improved model predicted the laminar-to-turbulent transition locations, the skin friction coefficient distribution, the pressure coefficient distribution, and the lift, drag, and moment coefficients with reasonable accuracy for different inflow conditions, which included the ranges $2e6 \leq Re \leq 4e6$ and $-10^\circ \leq \alpha \leq 15^\circ$. Khayatzaheh and Nadarajah highlighted the importance of using an adequate domain discretization (considering average y^+ values below 1) and the importance of developing robust and well-calibrated relations for the prediction of the laminar-to-turbulent flow transition, which were shown to be very sensitive to the considered inflow condition.

The evidence presented in the above-described works indicates that by employing Transition-based models, or by performing mixed laminar/turbulent procedures, improved predictions can be obtained when comparing computational results with experiments conducted under laminar/transitional inflow conditions. However, for the mixed laminar/turbulent procedures proposed in [22, 28], three unsolved issues have been identified: (1) no insights of the boundary conditions used between the split regions were provided; thus, the procedure may have resulted in an unphysical representation of the flow field in the vicinity of that boundary, (2) the determination of the transition point was guessed or computed from already measured data, and (3) the laminar/turbulent domain segmentation must be changed for different scenarios, resulting in a complex task when considering asymmetric airfoils undergoing nonhomogeneous inflow conditions. Moreover, grid-independence tests must be performed for each considered scenario. If a mixed laminar/turbulent procedure is to be implemented, instead of guessing the transition location, the authors of the present work recommend computing the airfoil's top transition point (x_{tr}^T) and bottom transition point (x_{tr}^B) by first using specialized software such as XFOIL that incorporates the e^n method for transition prediction [39], which has proven to be accurate [40], thus avoiding possible metastability issues. It should be noted that one of the key advantages of employing Transition-based turbulence models is that they implicitly solve the three above-described issues, at the expense of increased computational requirements and the incorporation

of complex formulations for the accurate prediction of the laminar-to-turbulent flow transition [24, 26, 35].

As it becomes apparent from this literature review, most of the research works have focused on validating the effectiveness of a limited number of fluid flow models for predicting two-dimensional airfoil aerodynamics, while considering a limited range of inflow conditions. None of them provided a justification for the selection of specific full-turbulence models (e.g., while coupling with Transition models [26, 38]) during the validation process and their scope was limited mainly due to the availability of experimental measurements. Moreover, only a few works have investigated the sensitivity of the simulations' outcomes to the different free parameters, and the majority of the works have not provided detailed descriptions of the numerical solution process and its convergence mechanisms. As consequence, only limited conclusions can be drawn about the performance of the tested models due to the impossibility of extrapolating the findings to situations different from the original case studies. It should be noted that a wide range of conflicting findings arise in the literature with regard to which models, or combination of models, are the most effective in terms of solution quality and computational efficiency. Thus, in order to overcome these issues, this work reports on an extended assessment of the accuracy of thirteen state-of-the-art fluid flow models applied to the problem of quantifying aerodynamic forces on two-dimensional airfoils for a wide range of inflow conditions. The outcomes of the assessment allowed to (1) identify the best performing fluid flow models, (2) understand the modeling pitfalls for different conditions (e.g., stall conditions), (3) determine which free parameters are the most important during the computational evaluation, (4) identify strategies for improved numerical convergence, and (5) identify key research needs and provide a comprehensive research agenda.

A full comparison of two different CFD-based methodologies was performed; the first one is based on the potential flow modeling approach [11, 41] complemented with an e^n transition model and a set of integral BL formulations, which are implemented in the XFOIL 6.96 software. The second methodology is based on the turbulence modeling approach, where twelve different turbulence models were tested. Transition-based turbulence models were adopted when laminar/transitional inflow conditions were considered. For the remaining turbulence models, the free-stream flow was considered to be turbulent (i.e., no attempts were made to separate the laminar and the turbulent regions within the computational domain) and, therefore, an overprediction of the drag coefficient was expected when comparing the computational outputs with experimental measurements that were typically conducted under laminar inflow conditions. The asymmetric four-digit NACA 4412 airfoil was considered as a test case. The rationale for selecting this airfoil is twofold: on the one hand, abundant information of the NACA 4412 airfoil can be found in the literature [1, 42–45], containing experimental measurements for up to 23 different Reynolds numbers ranging from $4.21e4 \leq Re \leq 9e6$. On the other hand, the asymmetric features of the NACA 4412 airfoil pose a reasonable challenge to the flow modeling techniques.

The remainder of this work is structured as follows: Section 2 presents the different setups of the computational study. Section 3 presents the computational results, their validation, and the corresponding physical interpretations. Finally, Section 4 presents the overall conclusions and outlines future research.

2. Computational Study

The NACA 4412 is an airfoil that has a maximum camber of 4%, which is located at 40% from the leading edge, and has a maximum thickness of 12%, all percentages measured with respect to the airfoil's chord length. The NACA 4412 ordinates were obtained from [20, 45]. The airfoil's trailing edge was smoothed, with the aid of the XFOIL 6.96 software, on the last 5% of the chord to produce a sharp closed profile since the original ordinates had an open section at the tip of the trailing edge (i.e., blunt shape). This is a common issue for analytically developed airfoils and affects all the NACA four-digit airfoils.

The present work reproduced the experimental tests reported in [1, 10, 42, 43, 45] in which transonic and supersonic flows were avoided since the experiments were performed in the Langley two-dimensional low-turbulence pressure tunnel [6], which compressed the airflow up to an absolute pressure of 4 atmospheres in order to increase the air density. Therefore, the simulated airflow was considered to be incompressible and standard sea level air properties ($\rho = 1.225 \text{ (kg/m}^3\text{)}$, $\mu = 1.7894 \times 10^{-5} \text{ (kg/m-s)}$, $T = 288.15 \text{ (K)}$, and $p = 101.325 \text{ (kPa)}$) were considered in all case studies. Furthermore, the earth's gravitational force was neglected.

The computer used to perform the computational assessment was a customized machine containing a water-cooled Intel Core i7-2600k processor operating at 5.2 GHz, 16 GB of memory DDR3 @1600 MHz, a Corsair Force GT solid state drive operating at 6 Gb/s, and an ASUS Maximus IV GENE-Z motherboard based on the Intel Z68 chipset. Double-precision parallelized simulations were performed for all case studies using an Intel 64 Message Passing Interface (MPI-2).

2.1. Computation of the NACA 4412 Airfoil Aerodynamics Using XFOIL 6.96. XFOIL [19, 20] is Fortran-based software, created by Drela in 1986 at the Massachusetts Institute of Technology (MIT) during the MIT Daedalus project, for the analysis of the subsonic aerodynamics of isolated airfoils. The XFOIL computations are based on the panel method [11, 19, 41, 46], which is combined with an e^n laminar-to-turbulent transition method [35, 39] and a set of integral boundary layer formulations. Given an initial inflow condition, the flow velocity distribution around the airfoil is computed from the panel method while accounting for viscous forces and the induced vorticity from the airfoil surface. The resultant boundary layer and wake are interacted with a surface transpiration model. The resultant flow field is incorporated into the fluid mechanics viscous equations, yielding a nonlinear elliptic system of equations which is solved by a Newton-Raphson algorithm, resulting in both a complete pressure and velocity distributions in the airfoil vicinity. The lift force coefficient (C_L) is calculated by direct

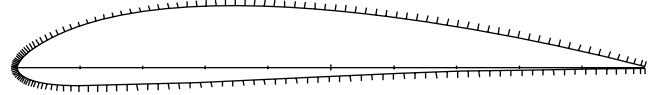


FIGURE 1: Panel node distribution over the NACA 4412 airfoil.

surface pressure integration, as viscous contributions to the lift force are often neglected, and the pressure coefficient (C_p) is calculated using the Karman-Tsien compressibility correction. The drag force coefficient (C_D) is determined from the wake momentum thickness at a location far downstream of the airfoil and calculated with use of the Squire-Young formulation. The methods, corrections, and the boundary layer formulation used in XFOIL are extensively described in [19, 46].

For panel-based methods, the first set of free parameters is related to the discretization of the airfoil's geometry. In all the XFOIL-based simulations, a constant number of panel nodes (160) were considered. The panel nodes were concentrated towards both the leading and the trailing edges of the airfoil, as shown in Figure 1, with the aim of increasing the density of nodes in these sensitive zones. The trailing edge to the leading edge panel density ratio was 0.15. The panel density ratio at the leading edge was 0.2 and the maximum panel angle was 7.87° . The second set of free parameters is related to the definition of the specific inflow conditions to be studied. In XFOIL, the laminar-to-turbulent flow transition begins when one of the following two scenarios occur: (1) a free transition occurs when the e^n criterion is met or (2) a forced transition occurs when a trip or the airfoil's trailing edge is encountered. For this Transition-based model, a free parameter named the critical amplification factor (N_{crit}), which affects the laminar-to-turbulent flow transition location, must be defined. A suitable value of this parameter depends on the ambient disturbance, or Turbulence Intensity (TI), in which the airfoil operates and mimics the effect of such disturbances on the flow state transition. A value of $N_{\text{crit}} = 2.6232$ was set to simulate a free-stream TI of 1%, which was the same flow condition of the experimental measurements obtained from the literature. Finally, it was observed that the XFOIL computations were usually very fast, in the order of milliseconds for one simulated case, and consume almost negligible computational resources.

2.2. Computation of the NACA 4412 Airfoil Aerodynamics through Turbulence Modeling. Two-dimensional, incompressible, steady-state, turbulence modeling-based simulations were performed for predicting the NACA 4412 airfoil aerodynamics using the specialized commercial package ANSYS Fluent 13.0. On the preprocessing stage, the geometry, the boundary topology, and the finite volume domain discretization were set/performed as described in next subsections.

2.2.1. Boundary Topology. The first set of free parameters on finite volume-based simulations refers to the definition of the boundary topology, which is strongly dependent on the geometric complexity of the tested object/system. The main

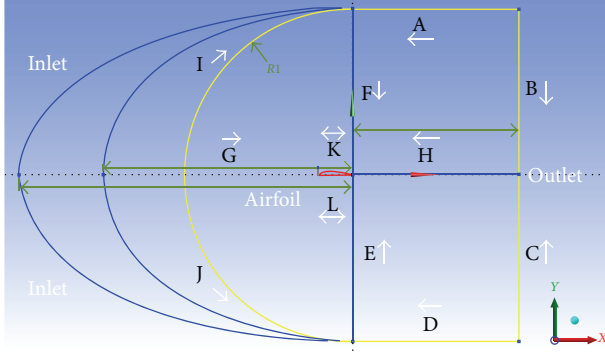


FIGURE 2: Boundary topologies and edge labels.

concern is related to the requirement of allowing enough free space between the tested object/system and the simulation's boundary so that no blockage effects occur. Blockage effects may produce significant side effects on the modeled physics, even if numerical convergent simulations are obtained. Different boundary topologies have been considered in the literature within the context of two-dimensional airfoil aerodynamics prediction. Most of them are based on the two-dimensional immersed boundary method [47], which is an approach used for solving external fluid flow problems (i.e., problems in which the fluid flows through the external surface of the tested object). Therefore, the geometry of interest is immersed in a uniform or nonuniform nonboundary-conforming Cartesian grid; thus the flow and its interactions with the tested object are modeled.

In the present work, three different boundary topologies based on the C-type shape, as shown in Figure 2, were studied with the aim of improving the quality of the numerical solutions and reducing the resources spent during the computational assessment. Type 1 topology consisted in an upwind semicircular boundary (denoted by the letters I and J) of radius equal to 10 times the chord length of the airfoil and a downwind rectangle of total height and axial length of 20 and 10 times the chord length of the airfoil, respectively. Type 2 and 3 topologies consisted of upwind semielliptical boundaries with semimajor axis of 15 and 20 times the chord length of the airfoil and a semiminor axis of 10 times the chord length of the airfoil. The boundaries were extended at least 10 times the chord length of the airfoil in all directions in order to avoid flow blockage effects, thus properly encompassing all the relevant zones of the simulation (e.g., the wake zone and the zones where the pressure, velocity, and main turbulence variables distributions still affected the computation of aerodynamic forces). Elliptical-based topologies enabled discretizing the domain using structured quadrilateral elements (e.g., see Section 2.2.2) without significantly affecting the final grid quality and its use can be advantageous when highly asymmetric and/or sharper airfoils are considered. However, elliptical topologies often require more quadrilateral elements and require finer grid refinements towards the airfoil surface in order to obtain acceptable values of dimensionless wall distance (y^+). In the boundary topology analysis performed for the NACA 4412

airfoil, it was found that the use of any of the proposed topologies is suitable as it was easy to get enough grid quality to get quality-converged results, considering any of the studied inflow conditions. However, type 1 topology was used in the rest of this work as it requires fewer discretized elements in the final refined grid. In cases where the grid quality is low due to the geometric features of the tested airfoil, the use of cubic splines or the airfoil shape itself can provide a guideline for the construction of the upwind boundaries (i.e., edges I and J in Figure 2).

2.2.2. Spatial Discretization. The finite volume-based domain discretization consisted of structured quadrilateral elements that were refined towards airfoil's surface. The use of high-quality structured quadrilateral grids allows numerical algorithms to converge faster, thus requiring less computational resources. The grid quality is commonly measured in terms of the cell aspect ratio, cell Jacobian ratio, cell parallel deviation, cell maximum corner angle, cell skewness, and cell orthogonal quality, among other measures. Each edge of the boundary topology (labeled with a specific letter, as shown in Figure 2) contained a different number of nodal points and different nodal refinements (e.g., arrows in Figure 2 define the refinement direction in which the average quality of the grid is enhanced). In previous studies [28, 48], 80,000 quadrilateral elements formed the total grid and were considered sufficient since successful grid-independence tests were performed, and, therefore, the same grid was used for all the computational experiments. In the present work, it was found that the use of a unique grid was not sufficient to properly test the different fluid flow models and thus several grid-independence tests were performed for each model. This fact can be understood in terms of BL modeling; since each model predicts different results in the converged solution, as described in Section 3, different grids are required to obtain suitable values of the dimensionless wall coordinate (y^+), hence adequately modeling the complete airfoil's BL. The grids were constructed in such a way that the converged y^+ varied along the airfoil's surface with an approximated maximum value of 1 for cases considering a Reynolds number of $9e6$ and below 1 for cases considering lower Reynolds numbers. The first nodal point was typically located at a distance of $7.35e-7$ m from the airfoil's surface. The best nodal distributions, determined through grid-independence tests (as discussed in Section 3.1), are summarized for each turbulence model in Table 1. The bias factor, or refinement factor, is defined as the ratio of the largest distance between two adjacent nodes in the discretized edge to the smallest distance between two adjacent nodes in the discretized edge, so the distance between nodes increased linearly towards the nonrefined section of the edge.

2.2.3. Turbulence Models, Numerical Schemes, Boundary Conditions, and Convergence Criteria. In ANSYS Fluent 13.0, the set of RANS equations [13, 14, 24], complemented with turbulence models, are solved. A total of 12 different turbulence models were tested and are summarized in Table 2. A complete description of each turbulence model can be found in [24].

TABLE 1: Best performing grids for each turbulence model.

Edge/turbulence models	(1) SA VB	(3) Standard $k-\varepsilon$	(4) RNG $k-\varepsilon$	(10) RS LP-S							
	(2) SA S-VB	(5) Realizable $k-\varepsilon$	(7) SST $k-\omega$	(8) Transition $k-kl-\omega$	(11) RS QP-S						
		(6) Standard $k-\omega$	(9) Transition SST		(12) RS Low-Re S- ω						
A	66	78	84	72	96						
B	110	130	140	90	120						
C	110	130	140	90	120						
D	66	78	84	72	96						
E	110	130	140	90	120						
F	110	130	140	90	120						
G	110	130	140	90	120						
H	66	78	84	72	96						
I	770	910	980	720	960						
J	770	910	980	720	960						
K	770	910	980	720	960						
L	770	910	980	720	960						
Total elements	183,920	256,880	297,920	142,560	253,440						
Refinement factor											
A	B	C	D	E	F	G	H	I	J	K	L
500	5e5	5e5	500	5e5	5e5	5e5	3400	50	50	10	10

TABLE 2: Contrasted turbulence models.

#	Turbulence model	Formulation and/or wall functions	Reference [24] chapter theory
(1)	Spalart-Allmaras V-B (vorticity-based formulation for turbulent production)	Low Reynolds damping.	4.2
(2)	Spalart-Allmaras SV-B (strain/vorticity-based formulation for turbulent production)	Low Reynolds damping.	4.2
(3)	Standard $k-\varepsilon$	Enhanced wall treatment.	4.3.1
(4)	Renormalization group (RNG) $k-\varepsilon$	Enhanced wall treatment.	4.3.2
(5)	Realizable $k-\varepsilon$	Enhanced wall treatment.	4.3.3
(6)	Standard $k-\omega$	Low-Reynolds corrections. Shear Flow corrections.	4.4.1
(7)	Shear stress transport (SST) $k-\omega$	Low-Reynolds corrections.	4.4.2
(8)	Transition $k-kl-\omega$	NA.	4.5
(9)	Transition SST	NA.	4.6
(10)	Reynolds stress LP-S (linear pressure-strain model)	Enhanced wall treatment, wall boundary conditions from k equation, wall reflection effects were considered.	4.8
(11)	Reynolds Stress QP-S (quadratic pressure-strain model)	Enhanced wall treatment, wall boundary conditions from k equation.	4.8
(12)	Reynolds Stress Low-Re S- ω (Low-Reynolds Stress- ω model)	Low-Reynolds corrections. Shear flow corrections.	4.8

The models' characteristic constants were maintained at their default values. Enhanced wall functions were considered instead of standard wall functions, although no meaningful differences in flow modeling were observed while considering standard wall functions [24, 49] for cases in which the grid was sufficiently refined towards the airfoil surface, so a value of $y^+ \cong 1$ was obtained. In all cases, a density-based solver with an absolute velocity formulation was considered. The

solution method considered an implicit formulation and a Roe flux-difference splitting (FDS) convective flux type scheme. The gradients and derivatives were computed using the least squares cell-based method and the flow variables (i.e., the x and y velocities, the pressure, and all the turbulence variables) were solved and interpolated using second-order upwind discretization schemes. A full description of such methods and schemes can be found in [24, 25]. The edges A,

I, J, and D in Figure 2 were prescribed with an inlet-velocity boundary condition in which the magnitude and direction of the free-stream airflow varied with the Reynolds number and the AOA. The values of the inlet turbulence variables were calculated as a function of the free-stream TI (1%), which was reported in the experimental data found in the literature, and the eddy length scale, which was defined as 1% of the length of the airfoil (0.01 m) [24] since the experiments were conducted in a low turbulence wind tunnel where larger free-stream eddies were hardly found. The edges B and C were prescribed with a pressure-outlet condition, where the gauge pressure was set to 0 Pa and the backflow turbulence intensity and backflow turbulence length scale were set to 1% and 0.01 m, respectively. The edges K and L (the airfoil's top and bottom surfaces) were prescribed as stationary walls with a no-slip shear condition. The airfoil was considered to be solid and made of aluminum with a density of $\rho_{\text{Airf}} = 2,719 \text{ kg/m}^3$. The wall roughness height and the roughness constant were defined as 0 m and 0.5, respectively, as no other information was available from the literature results. A zero wall roughness height (smooth wall) means that no roughness effects [27, 50] were included during the work development.

The numerical convergence definition is based on the computation of double-precision residuals. In ANSYS Fluent 13.0, the residual of a variable being solved, considering a density-based solver, is defined as the time rate of change of the conserved variable (W). Equation (1) shows the unscaled root-mean-square residual definition, which is used for all the variables being solved:

$$R(W) = \sqrt{\sum_{i=1}^n \frac{(\partial W_i / \partial t)^2}{n}}, \quad (1)$$

where n is the number of nodal points in the spatial discretization. In order to properly judge the numerical convergence, the scaled residual definition presented in (2) was considered:

$$R(W)_S = \frac{R(W)_N}{R(W)_5}, \quad (2)$$

where $R(W)_N$ is the unscaled residual of the N th iteration and $R(W)_5$ is the largest absolute residual value found within the first five iterations. In the present work, an absolute convergence criterion of $R(W)_S \leq 5e - 7$ was considered for all the solved variables. This value was considered adequate as no significant improvements in the solution's precision (e.g., up to 5 significant digits when computing aerodynamic coefficients) were obtained when considering lower convergence criteria values.

In ANSYS Fluent 13.0, the coupled set of governing equations are discretized in time, for both steady-state and unsteady-state computations, and are solved with the use of an explicit or an implicit time-marching algorithm. The present work adopted a Euler-type implicit discretization in time of the governing equations, which was combined with a Newton-type linearization of the flow fluxes, to produce

the following preconditioned linearized system in delta form [24]:

$$\left[D + \sum_j^{N_{\text{faces}}} S_{jk} \right] \Delta \mathbf{Q}^{N+1} = -\mathbf{R}^N, \quad (3)$$

where the center and off-diagonal coefficient matrices D and S_{jk} are given by

$$D = \frac{V}{\Delta t} \Gamma + \sum_j^{N_{\text{faces}}} S_{ji}, \quad (4)$$

$$S_{jk} = \left(\frac{\partial \mathbf{F}_j}{\partial Q_k} - \frac{\partial \mathbf{G}_j}{\partial Q_k} \right) A_j, \quad (5)$$

where the residual vector \mathbf{R}^N and the time step Δt , computed from the Courant number (CFL), are defined as

$$\mathbf{R}^i = \sum_{f=1}^{N_{\text{faces}}} (\mathbf{F}(Q^i) - \mathbf{G}(Q^i)) \cdot \mathbf{A} - V \mathbf{H}, \quad (6)$$

$$\Delta t = \frac{2(\text{CFL}) V}{\sum_f \lambda_f^{\max} A_f},$$

where V is the cell volume with surface area \mathbf{A} , A_f is the cell face area, Q^i is an intermediate solution, Q_k is a spatial coordinate in the simulation domain, Γ is a preconditioned matrix, whose aim is to help in reducing numerical divergence issues at the beginning of the simulations [24], λ_f^{\max} is the maximum of the local eigenvalues of the preconditioned system, \mathbf{F} is a vector containing the convective variables to solve, \mathbf{G} is a vector that contains the viscous stress tensor terms, and \mathbf{H} contains source terms such as body forces and energy sources:

$$\mathbf{F} = \begin{Bmatrix} \rho \mathbf{v} \\ \rho \mathbf{v} u + p \hat{i} \\ \rho \mathbf{v} v + p \hat{j} \\ \rho \mathbf{v} w + p \hat{k} \\ \rho \mathbf{v} E + p \mathbf{v} \end{Bmatrix}, \quad \mathbf{G} = \begin{Bmatrix} 0 \\ \tau_{xi} \\ \tau_{yi} \\ \tau_{zi} \\ \tau_{ij} v_j + \mathbf{q} \end{Bmatrix}, \quad (7)$$

where ρ , \mathbf{v} , E , p , and \mathbf{q} are the density, velocity, total energy per unit mass, pressure, and heat flux, respectively. In the present work, the energy equation is not solved, since the flow is considered to be subsonic and incompressible, so the last term of \mathbf{F} and \mathbf{G} is not considered.

During computations, the variation of the values of the explicit underrelaxation factors (URFs) was crucial to get quality-converged results and to speed up convergence [24, 51]. When oscillatory convergence on the monitored residuals was observed, the URFs values (which typically range around $0 \leq \text{URFs} \leq 1$) were decreased to almost a fifth of its default values and later, after numerical oscillations were reduced, they were increased to almost the unity. Nonetheless, the variation of the CFL number provided the best speed-up improvements. By increasing the CFL number an increased

time step is computed; on the one hand, the increased time step develops the steady-state solution faster through the time-marching algorithm and on the other hand makes the first term of (4) less important and therefore \mathbf{D} more dependent on the computed linear strain rate tensor S_{ji} , thus reducing the effects of the preconditioned system on the Euler-type implicit scheme. From the linear stability theory, it is well known that the implicit formulations are unconditionally stable (e.g., the Courant-Friedrichs-Lewy condition [25]) in contrast to explicit formulations. This fact provides the ability to propose any desired time step to the problem being solved. However, nonlinearities in the governing equations will often limit the numerical stability at the beginning of the simulations (e.g., first 300–500 iterations) and thus the CFL number was maintained low (e.g., $0.1 \leq \text{CFL} \leq 5$) to avoid numerical divergences. Later, the CFL number was slowly increased (e.g., up to a value of 200) until the convergence criterion was met. This simple procedure accelerated the numerical convergence at least three times in contrast with constant CFL number simulations. However, numerical convergence is often difficult unless a good initial solution is provided. In ANSYS Fluent 13.0 three different initialization procedures are available. The first type of initialization (or standard initialization) assigns the same value, which is typically determined from the inlet condition, to all the variables being solved within the discretized domain. The second type of initialization, named the “hybrid initialization” [24, 51], solves the Laplace equation (i.e., is based on a potential flow procedure) in a preprocessing stage to produce a velocity field and a pressure field which smoothly connects high and low pressure values in the computational domain. The third type of initialization consists in incorporating a solution from a previous simulation by using solution interpolations (multigridding approach). The present work considered a multigridding technique in which solutions computed using coarser grids (i.e., having less quadrilateral elements and where the converged y^+ values were larger than 30) were used as initial solutions to solve refined cases, which had grids such as the ones reported in Table 1. Nonetheless, the hybrid initialization procedure was considered while conducting simulations using coarser grids. Even after these considerations, in some cases numerical convergence could not be obtained if a proper multigrid initialization and a proper variation of the URFs and the CFL number are not provided/performed.

The computation of aerodynamic forces employing turbulence modeling approaches is very slow in contrast with the XFOIL computations, requiring execution times in the scale of tens of minutes per simulated case and consuming significant computational resources as a function of grid size and considered turbulence model.

2.2.4. Test Cases. In order to properly determine the performance of the tested models while predicting two-dimensional airfoil aerodynamics, more than 1,200 CFD-based simulations, considering the range of $\text{AOA } -10^\circ \leq \alpha \leq 20^\circ$ and five different Reynolds numbers ($5.5e5$, $8e5$, $3e6$, $6e6$, and $9e6$), were performed and the outputs were contrasted with experimental measurements reported in the literature. Some

of the literature results were not reported in a tabular fashion; thus the data was digitized using the commercial software GetData Graph Digitizer [52]. In addition, most of the drag-based characteristics are commonly reported as a function of the lift coefficient. In order to express the drag coefficient as function of the AOA, the MATLAB 2012a Piecewise Cubic Hermite Interpolating Polynomial (PCHIP) function was used. Finally, in order to compare the CFD-based computations with the experimental measurements provided in the literature, bicubic interpolations were performed using the MATLAB R2012a `griddata` function, which is based on the Boris Delaunay triangulation method, which in turn fits a surface of the form $C_L = f(\alpha, \text{Re})$ and $C_D = f(\alpha, \text{Re})$ to the set of experimental data.

3. Results and Discussion

3.1. Grid-Independence Tests. The case chosen for the determination of the minimum amount of quadrilateral elements required to compute grid-independent values of the aerodynamic coefficients was an airflow having the properties described in Section 2, a Reynolds number of $9e6$, and the AOA 12.22° . The selection of this inflow condition posed a reasonable challenge during the grid-independence characterization due to the required flow modeling complexity, as opposed to previous works [26, 30, 47] in which a prestall condition was considered. The experimental values of the lift and drag coefficients for this test case are $C_L^{12.22^\circ} = 1.5742$ and $C_D^{12.22^\circ} = 0.01511$ [1, 45]. For this case, XFOIL predicts a $C_L^{12.22^\circ} = 1.7077$ and $C_D^{12.22^\circ} = 0.01504$. Figure 3 summarizes the grid-independence test results for all the considered models. From the figure three important findings can be highlighted: (1) it can be noted that the different models differ quite substantially in their predictions of both the lift and the drag coefficients values. (2) At least 120,000 quadrilateral elements are required (with their corresponding refinements towards the airfoil's surface) to obtain stable values of the computed aerodynamic coefficients and to reach a maximum y^+ value of approximately 1 along the airfoil surface. Note, however, that the y^+ values are highly dependent on the refinement factor described in Section 2.2.2. (3) In all cases, a drag coefficient overprediction is observed when comparing with the experimental measurement.

3.2. Boundary Layer Modeling Effects. After performing multigridding techniques, as described in Section 2.2.3, insights into how the different solved layers of the BL affect the computation of aerodynamic coefficients were obtained. Figure 4 shows the difference between the absolute values of the aerodynamic coefficients computed using grids with converged maximum values of $y^+ \cong 1$ along the airfoil's surface and grids with converged maximum values of $y^+ \gg 30$ (i.e., $\Delta C_{L,D} = |C_{L,D}(y^+ \cong 1)| - |C_{L,D}(y^+ \gg 30)|$) for different AOA, Reynolds numbers, and five turbulence models (for the sake of brevity). It can be observed that there is an important effect in both the lift and the drag coefficients predictions as stall conditions are reached. The magnitude of the effect is partially attributed to the change of the wall shear

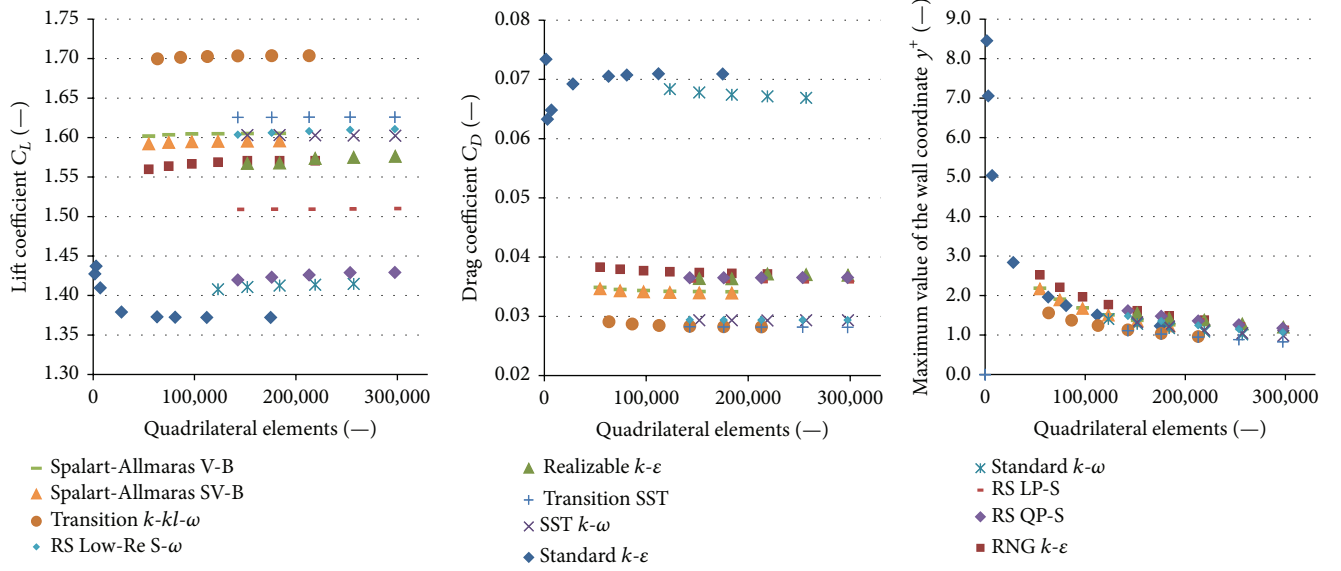


FIGURE 3: Grid-independence tests.

stresses magnitudes, which substantially increase in near-stall and stall conditions. These changes were captured differently in grids that do not solve the inner parts of the BL and depended on the considered wall models [24, 49]. Moreover, the effect varied in magnitude depending on the considered turbulence model; it can be observed that the effect is lower for the Standard k - ε and the Standard k - ω models (note that, for all the k - ε turbulence models, enhanced wall functions were considered for both cases showing converged $y^+ \approx 1$ and $y^+ \gg 30$). However, the predictions of other turbulence models (e.g., the Transition-based models and all the Reynolds Stress models) were substantially affected. In particular, the RS LP-S model showed a maximum difference in the lift coefficient magnitude of 0.3275 and a maximum difference in drag coefficient magnitude of 0.0326.

The ability of the Transition-based models to predict the laminar-to-turbulent flow transition is strongly influenced by the converged y^+ value [24, 26], and therefore an erratic behavior was obtained when characterizing the effects of not explicitly modeling all the layers of the BL. The side effect of not meeting a value of $y^+ \approx 1$ (e.g., $y^+ > 5$) is that the transition onset location moves upstream with increasing y^+ , resulting in higher drag and lower lift forces predictions. However, it must be noted that this effect can be confused with modeling performance since the comparison between the computed lift coefficients (e.g., considering $y^+ \gg 30$) and the experimental measurements performed under laminar inflow conditions tends to improve. It has been observed (not shown) that lift predictions typically improve as larger y^+ values are considered, but drag predictions worsen even more.

Figure 5 shows the evolution of the converged maximum y^+ along the airfoil's surface, for both the coarse (e.g., $y^+ \gg 30$) and the refined (e.g., $y^+ \approx 1$) grids, as a function of the Reynolds number and AOA while considering the RS LP-S model. The converged maximum y^+ value increased as

both the Reynolds number and the magnitude of the AOA increased. It can be observed that the magnitude of the slope decreases in the range $16^\circ \leq \alpha \leq 20^\circ$ as the maximum wall shear stresses are reached (stall condition). It is expected, as shown in the coarse grid results, that at larger AOA this slope will tend to zero and/or become negative, as no larger wall shear stresses would result in deep stall conditions, consequence of the massive flow separation observed in such conditions.

Not unexpectedly, the variation of the converged maximum y^+ value as a function of Reynolds number, for a given AOA, is linear, as shown in Figure 6. It should be noted that the obtained linear regressions are a function of the grid, the considered turbulence model, and the airfoil's shape. A similar behavior was observed for the results of the remaining turbulence models. The graph provided in Figure 6 is a very useful tool to determine up to which Reynolds number the grid will be able to simulate the viscous sublayer. When the maximum y^+ value, evaluated at the first grid layer along the airfoil's surface, is much larger than 1, the grid will not be able to simulate the viscous sublayer and the resultant airfoil aerodynamics could be questionable, even if the simulations were numerically convergent.

3.3. Validation of the Computational Predictions. It has been experimentally observed [1, 27, 53] that as the Reynolds number increases the lift coefficient will increase but the drag coefficient will decrease for a given AOA. Nonetheless, the net effects of varying the Reynolds number are higher at large AOA. Through the simulation of flows with different free-stream velocities, the ability of the different turbulence models to predict prestall and stall conditions can be quantified. Figure 7 illustrates the Reynolds number effects predictions of each turbulence model on the computed lift-to-drag ratio (direct comparisons of the individual predicted coefficients against experimental measurements performed

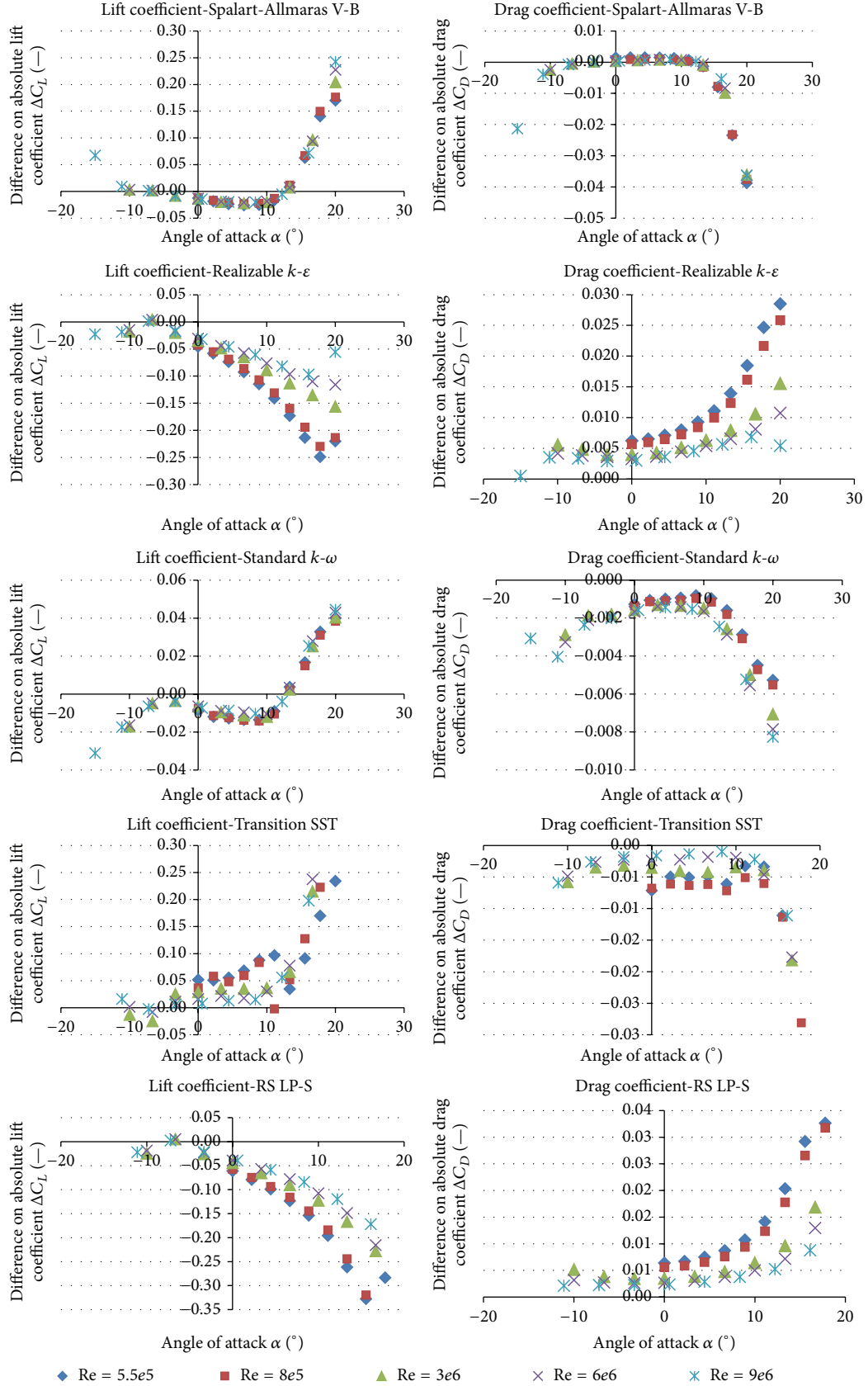


FIGURE 4: Boundary layer modeling effects on the computation of the NACA 4412 airfoil aerodynamics.

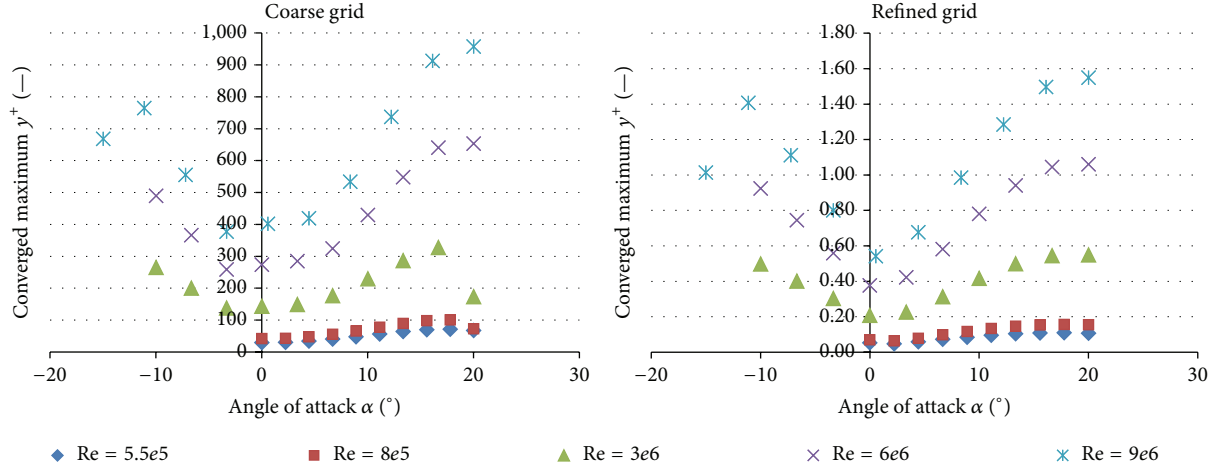


FIGURE 5: Variation of the converged maximum y^+ as a function of the AOA, considering the RS LP-S turbulence model.

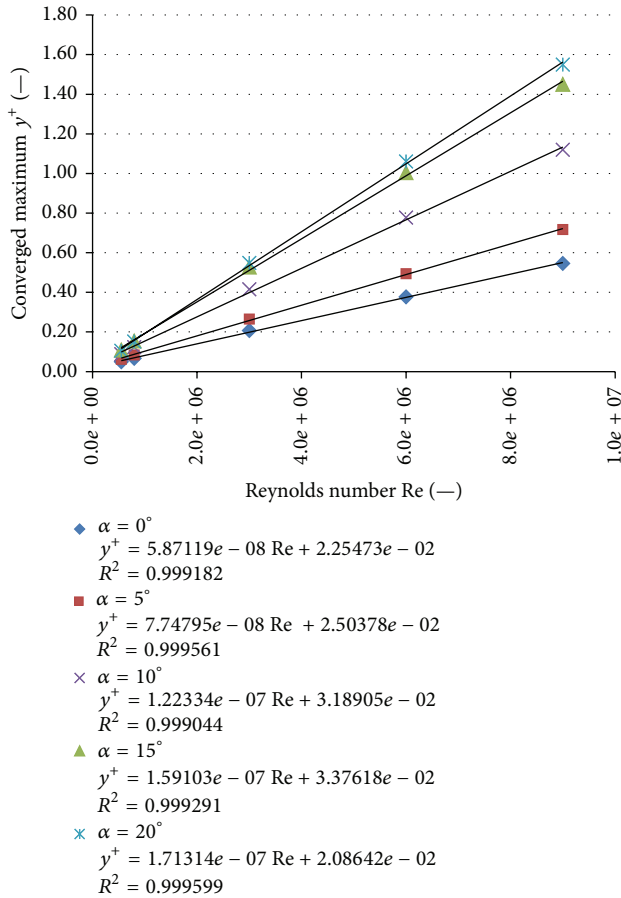


FIGURE 6: Variation of the converged maximum y^+ as a function of the Reynolds number, considering the RS LP-S turbulence model.

under laminar inflow conditions [1, 42, 45] can be found in Figures 11, 12, 13, 14, 15, 16, and 17). It can be observed that both Spalart-Allmaras formulations predicted similar results for the lift and drag coefficients as a function of Reynolds number and AOA. The different $k-\epsilon$ and $k-\omega$ turbulence

models predicted quite different results for both the lift and the drag coefficients, as previously noted from the grid-independence tests. In particular, the Standard $k-\epsilon$, the Standard $k-\omega$, and the Transition $k-kl-\omega$ models could not capture the lift and the drag forces dependence on the Reynolds number since almost identical values were obtained for each computational experiment. However, the remaining models were able to capture a Reynolds number effect but in different magnitude.

Interestingly, the drag coefficient predictions of the Standard $k-\omega$ model are almost the double in magnitude as compared with the SST $k-\omega$ model predictions, while considering large Reynolds numbers (e.g., see Figures 15–17). This behavior is similar to the one observed when contrasting the outputs of the Standard $k-\epsilon$ and the Realizable $k-\epsilon$ turbulence models. It should be noted that the drag predictions of the Transition-based models are substantially lower when comparing with the outputs of full-turbulence turbulence models and are in better agreement with the experimental measurements (e.g., see Figures 11–17). This behavior is consistent with the findings observed in previous works [26, 36, 38]. However, despite the improvements in the drag coefficient estimation, the predictions of the lift coefficient by the Transition-based models tend to be larger as the AOA increases and differ when comparing with the outputs of any other full-turbulence model or when comparing with the experimental measurements. In the following sections, separated descriptions and interpretations of this problematic and the accuracy of the remaining flow models on the prediction of aerodynamic forces are provided.

3.3.1. Description of the Accuracy of the Tested Flow Models for Predicting the Lift Coefficient. Based on the results shown in Figures 11 to 17, it can be observed that at the highest simulated Reynolds number (i.e., $\text{Re} = 9e6$) the agreement between the experimental data and all the flow models predictions is relatively good for nonstall conditions. However, as the Reynolds number becomes smaller, the discrepancy becomes larger, except for the RS LP-S model

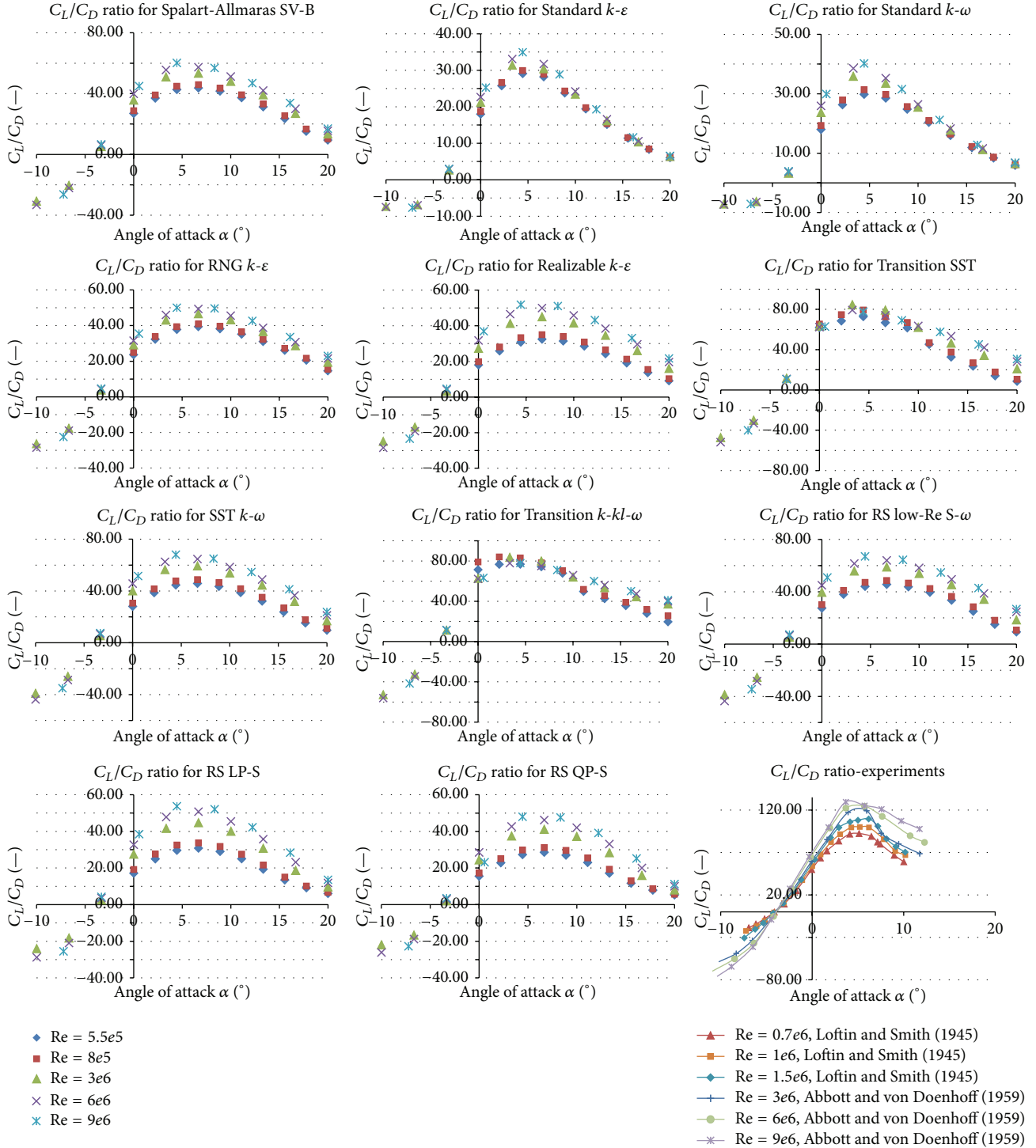


FIGURE 7: Predicted Reynolds number effects on the lift-to-drag ratio by different turbulence models.

whose predictions remain close to the experimental data for all Reynolds numbers. The RS QP-S model predicted the lowest lift coefficient values on prestall conditions among all the tested models and at all Reynolds numbers, while XFOIL and the Transition $k-kl-\omega$ models predicted the largest lift coefficient values.

When stall conditions were considered, the Transition $k-kl-\omega$ model failed to predict stall at all. Both XFOIL and the Transition SST model performed somewhat better but significantly overpredicted the lift coefficient for AOA beyond the experimental stall angle, similar to the observations provided by Yuhong and Congming [36]. Out of the Standard

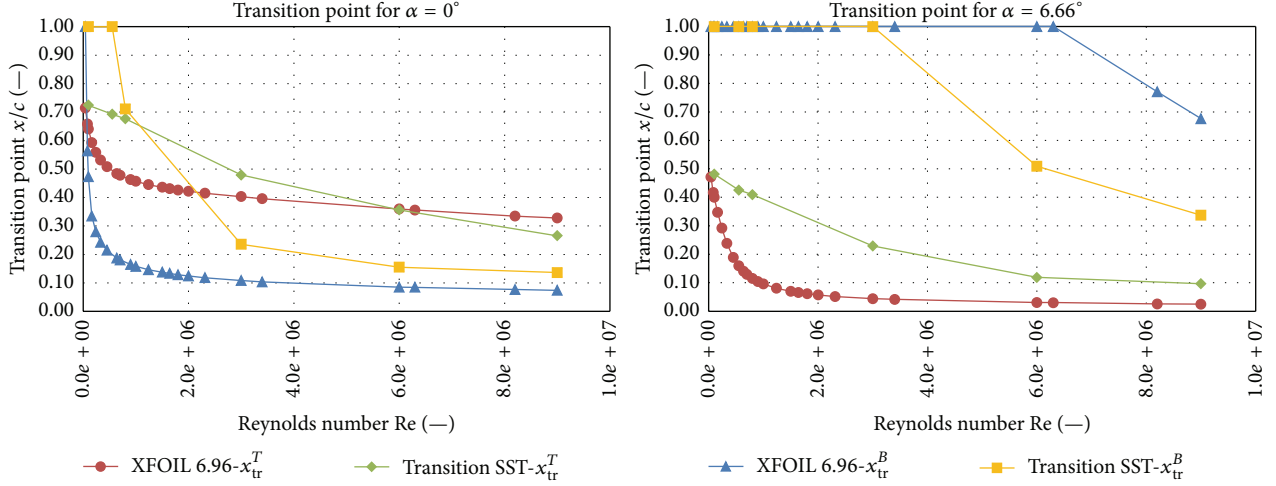


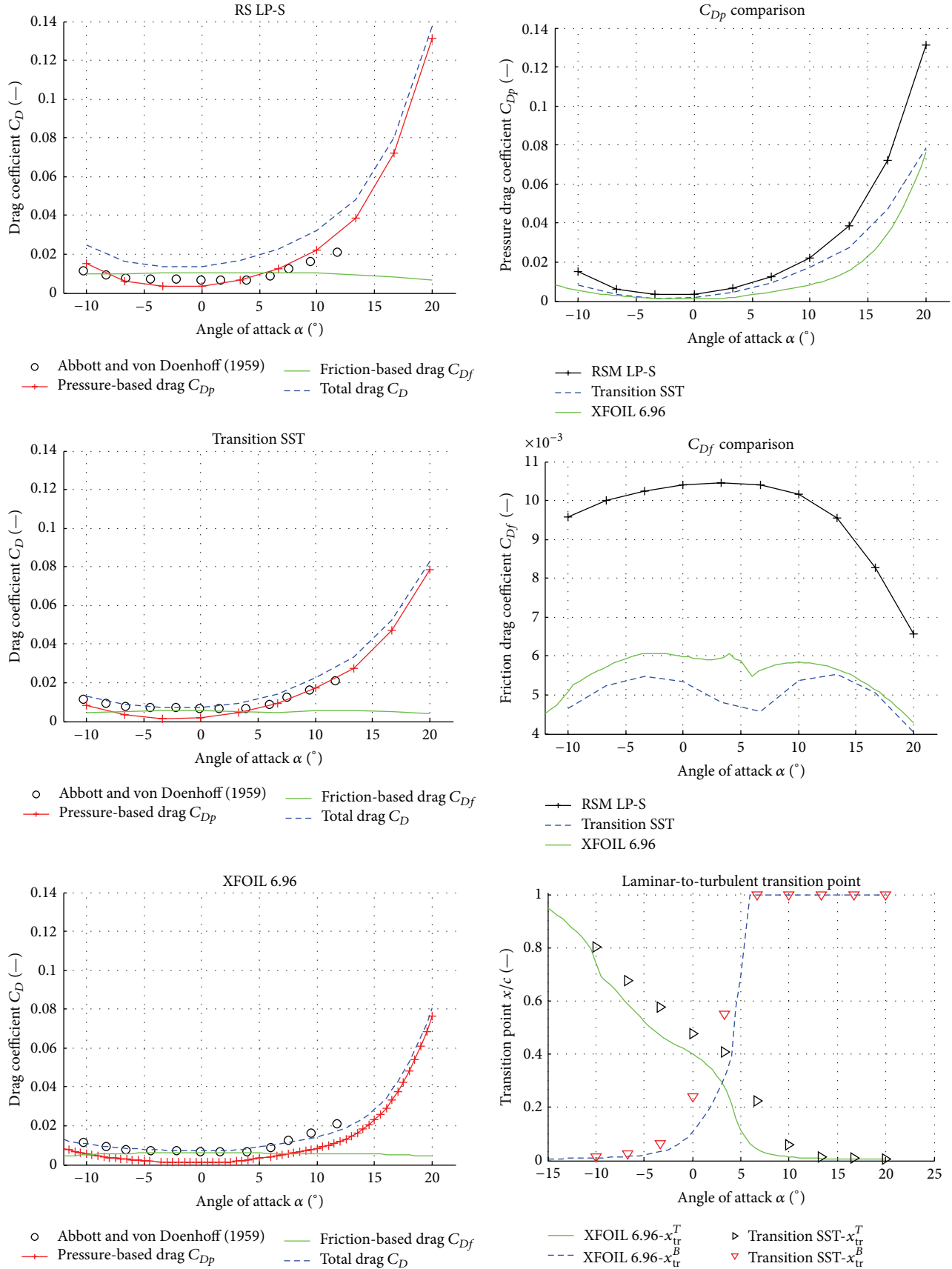
FIGURE 8: Evolution of the top and bottom superficial transition points as a function of Reynolds number.

models, both Spalart-Allmaras models, the NRG k - ε , the Realizable k - ε , the SST k - ω , and the RS Low-Re S - ω models overpredicted the poststall lift at all Reynolds numbers. For the Standard k - ε and the k - ω models, the poststall lift is somewhat overpredicted at low Reynolds numbers, while for high Reynolds numbers the poststall lift is underpredicted, with good agreement at intermediate Reynolds numbers (e.g., $1e6 < Re < 6e6$). The RS LP-S model comes out the best in lift prediction for all the considered inflow conditions. The remarkable aspect of this model is that it predicts the lift coefficient with reasonable accuracy even in stall states. The RS QP-S and the RS Low-Re S - ω underpredict and overpredict lift, respectively, at stall conditions and at all Reynolds numbers.

3.3.2. Discussion of the Lift Coefficient Predictions by Different Fluid Flow Models. The prestall lift coefficient overprediction observed at low Reynolds numbers (e.g., see Figures 11–14) can be largely attributed to the inadequate prediction of the laminar-to-turbulent flow transition (i.e., not only close the airfoil surface) and the inadequate turbulence modeling at the outer layers of the BL. Both factors affect the pressure distribution around the airfoil, thus directly affecting the prestall lift force computation, as discussed next. The differences observed while contrasting the prestall lift predictions of the different Transition-based models, which showed the largest discrepancies in the prediction of the experimentally observed prestall lift, are due to their differences while predicting the laminar-to-turbulent flow transition, as exemplified in Figure 8. It can be observed that the laminar-to-turbulent flow transition predictions of XFOIL and the Transition SST model differ quite substantially at low Reynolds numbers. Moreover, an inadequate modeling of turbulent forces in the outer layers of the BL, together with an inadequate laminar-to-turbulent flow transition prediction, can lead to an inadequate modeling of the local flow speed, which in turn affects the pressure distribution around the airfoil, thus affecting the computation of the main component of the lift force. It was observed that

Transition-based models typically predict higher flow speeds close to the top surface of the airfoil (e.g., see Figure 21), thus resulting in larger lift forces as compared to full-turbulence models or the experimental data. An extended description of this issue is given in Section 3.4, where a validation study of the predicted pressure coefficient distributions is presented.

As the Reynolds number increased, the airfoil's superficial laminar-to-turbulent transition locations moved towards the leading edge in a nonlinear fashion, as shown in Figure 8. An increased agreement between the models' predictions of the laminar-to-turbulent flow transition locations, as well as an increased concordance while predicting the experimental prestall lift force (e.g., see Figures 15–17), was observed as the Reynolds number increased. In such cases, a large part of the airfoil's BL was turbulent and the effects of the laminar-to-turbulent flow transition were less relevant in the prediction of the lift force since turbulent forces were the most important mechanism regulating the transversal diffusion of momentum between the different layers of the airfoil's BL, hence affecting the flow speed magnitude in most of the airfoil's vicinity and, thus, the pressure distribution along the airfoil's surface. Therefore, the increased agreement between the prestall lift force predictions by all tested models and the experimental measurements at large Reynolds numbers is understood given that the experimental laminar flow became turbulent sooner at the airfoil's surface (i.e., closer to the leading edge of the airfoil) as the Reynolds number increased. The differences between the predictions of the prestall lift by the different models at large Reynolds numbers essentially depended on the way turbulent forces were modeled. Nonetheless, since all the models' predictions of the prestall lift were similar in those conditions and showed good agreement with the experimental data, it can be inferred that almost negligible changes on the prestall lift predictions occur at large Reynolds numbers when considering either turbulent inflow conditions (i.e., when employing full-turbulence models) or laminar inflow conditions (i.e., when employing Transition-based models).

FIGURE 9: NACA 4412 drag components for $Re = 3e6$.

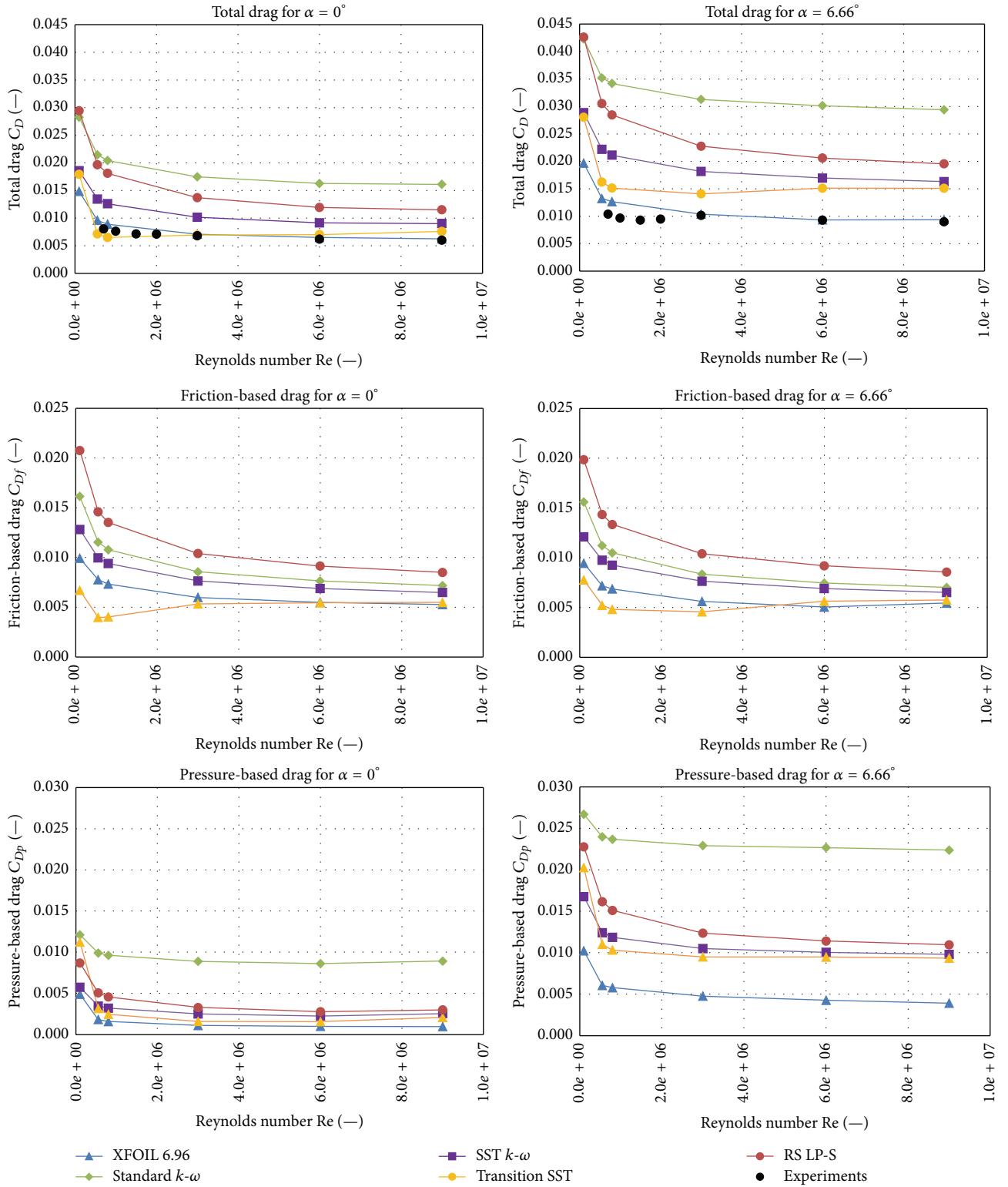
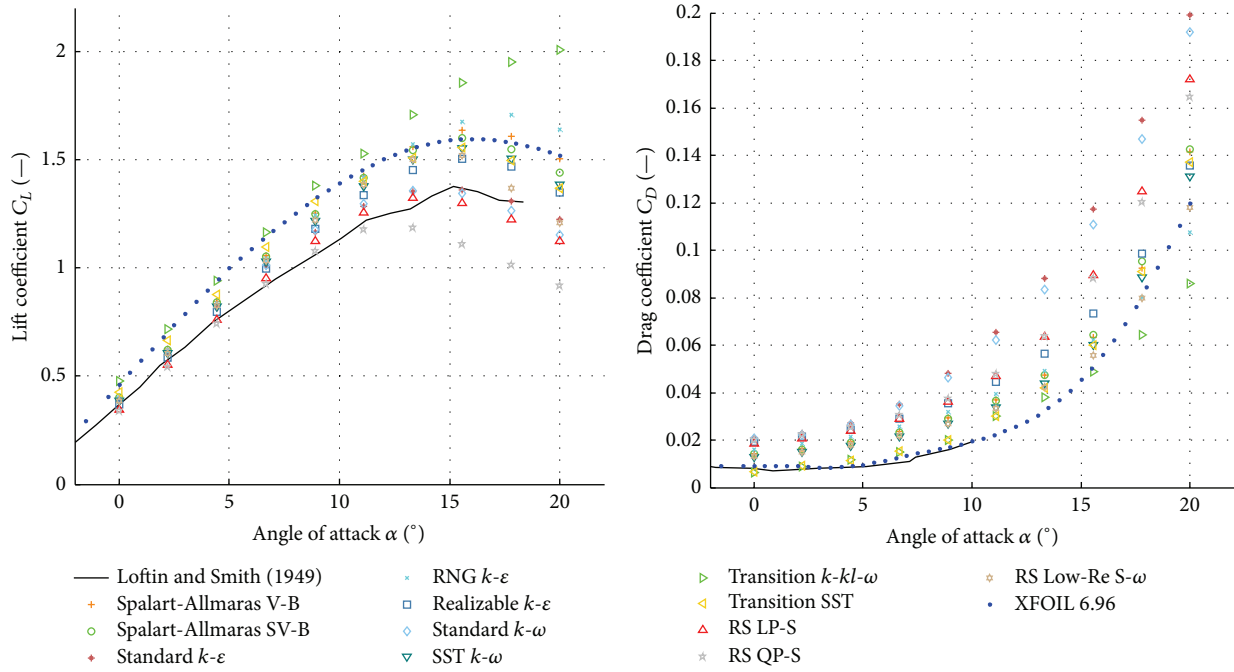
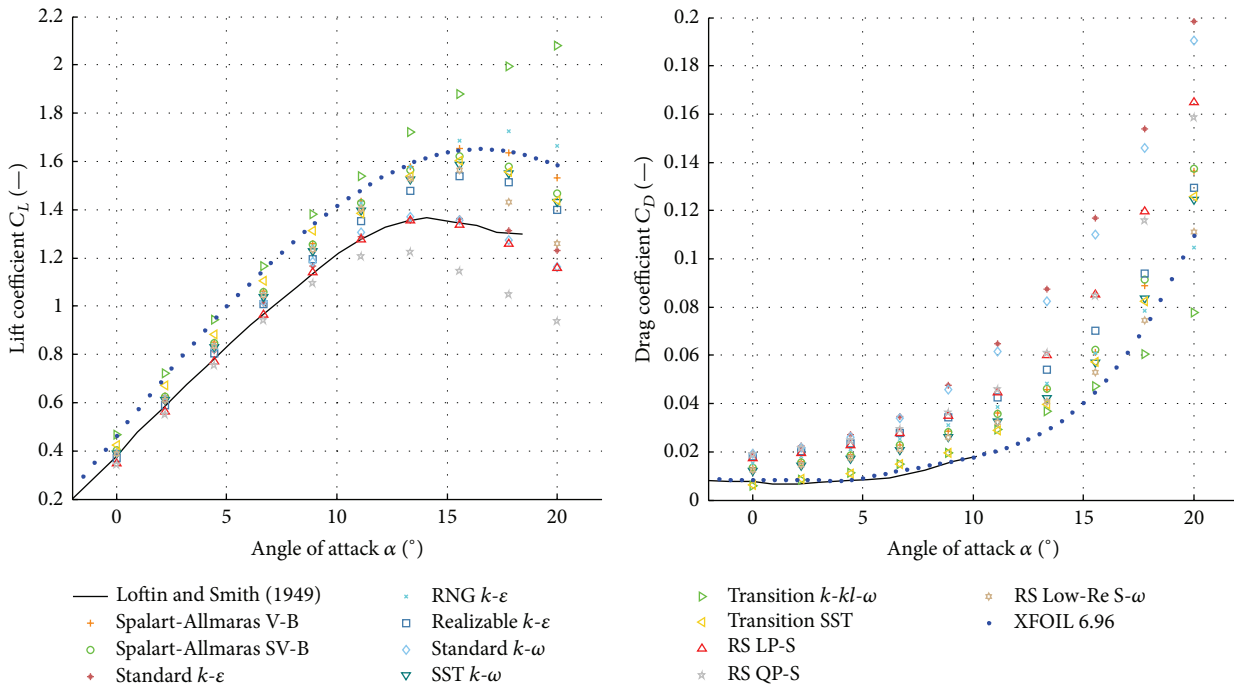
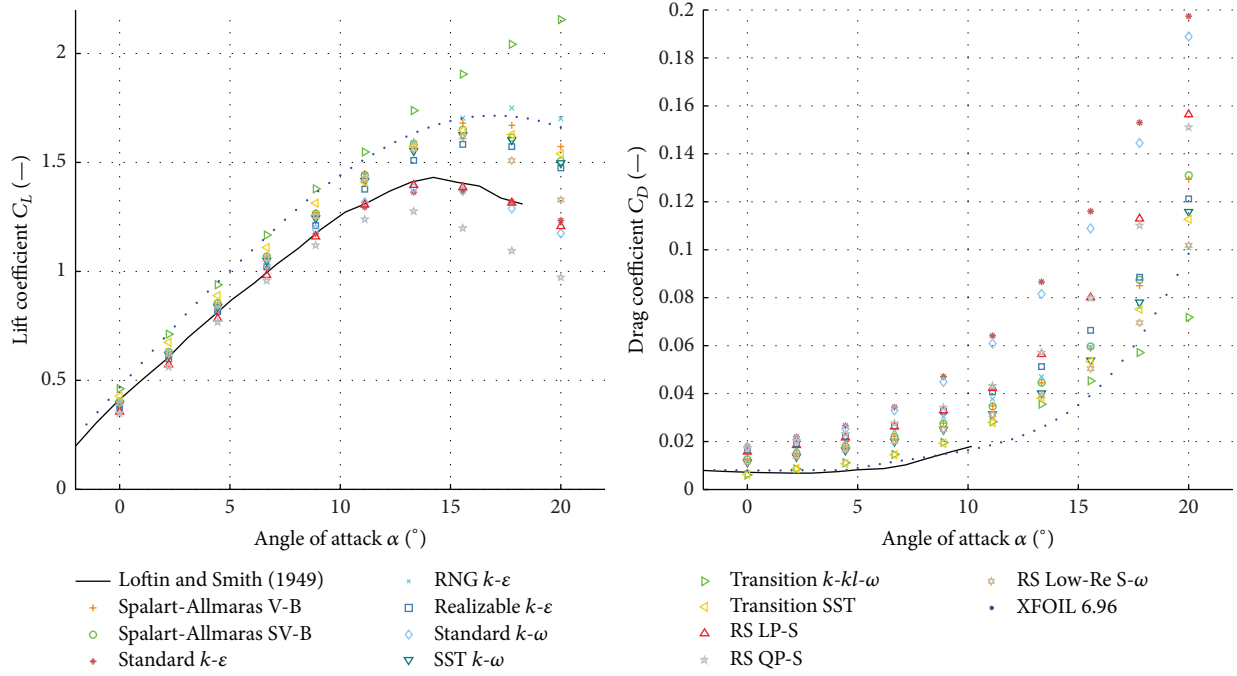
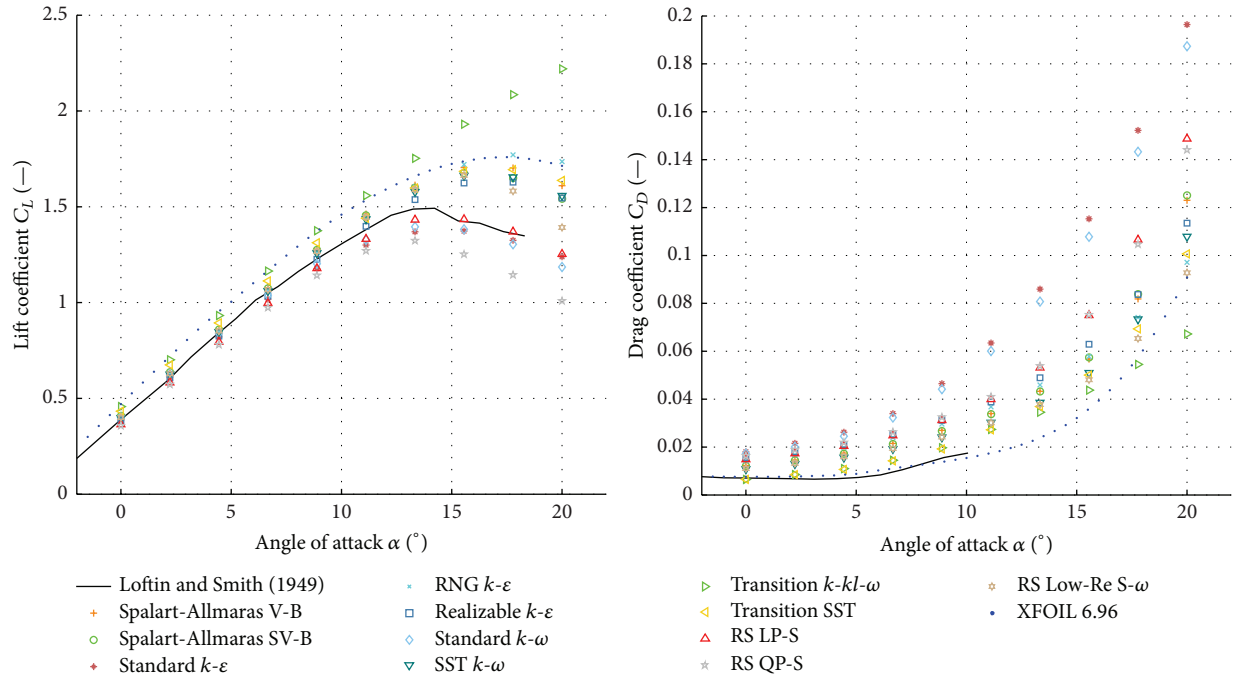


FIGURE 10: Evolution of the predicted NACA 4412 drag components for different Reynolds numbers.

FIGURE 11: NACA 4412 performance characteristics for $Re = 0.7e6$.FIGURE 12: NACA 4412 performance characteristics for $Re = 1e6$.

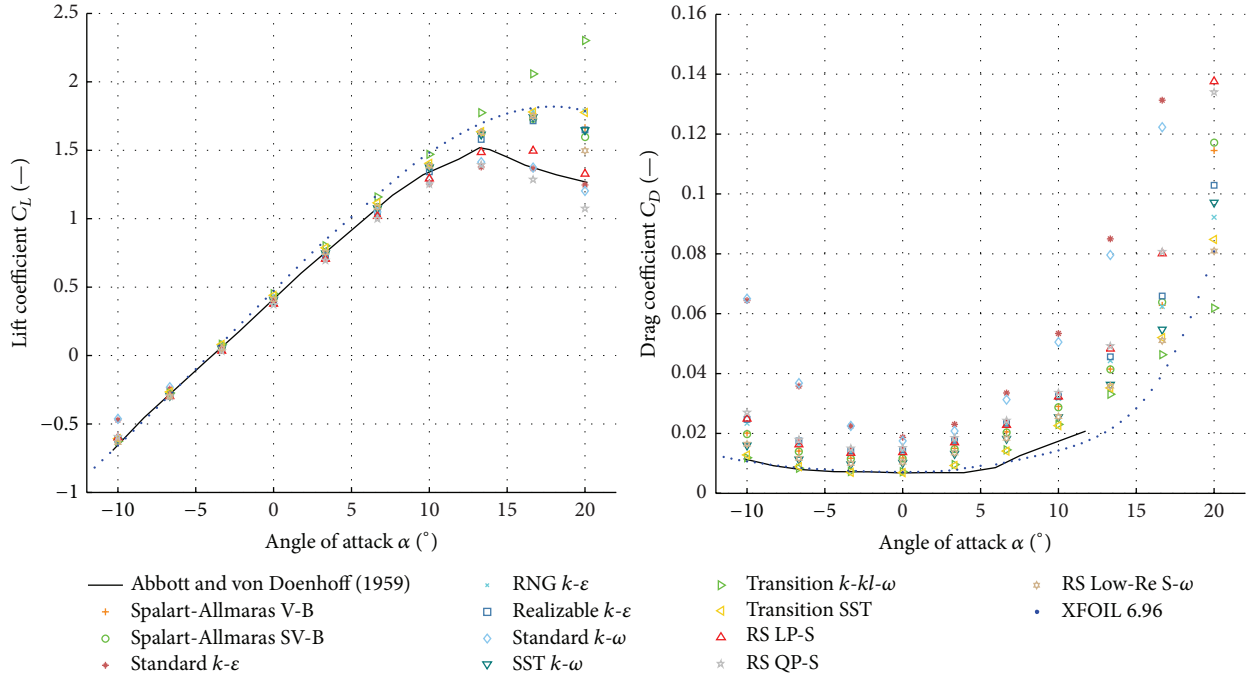
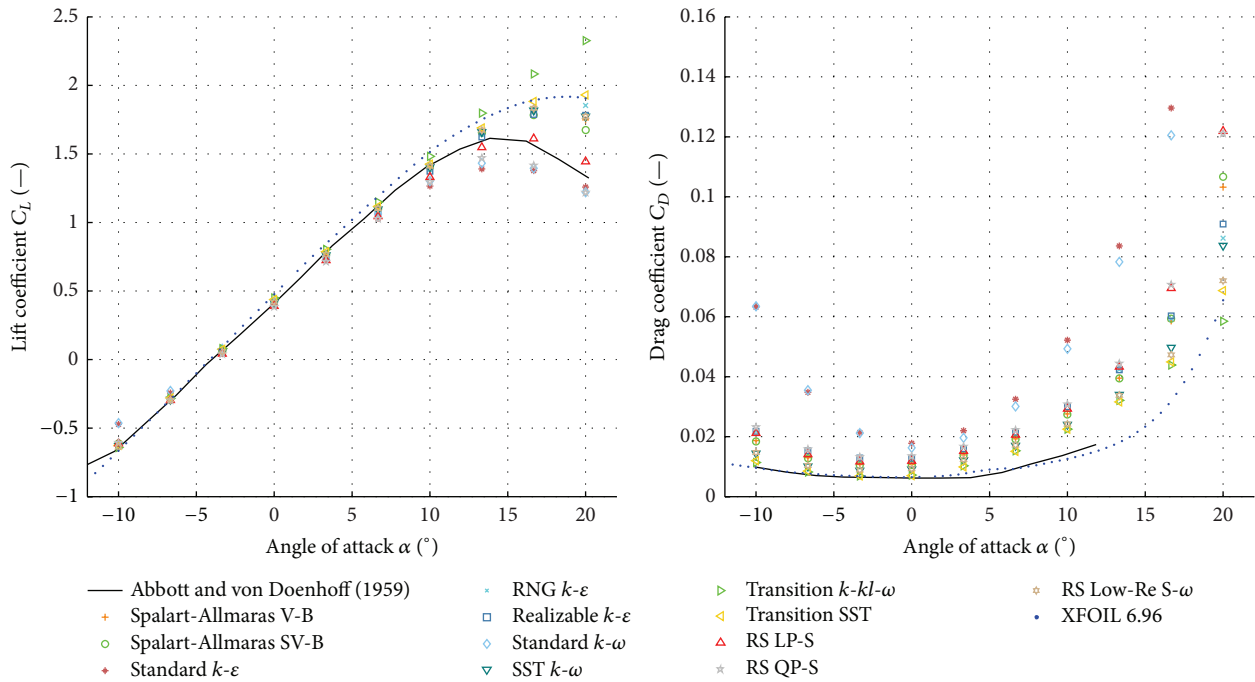
When the AOA increases, the laminar-to-turbulent flow transition location moves towards the leading edge (i.e., upstream) at the airfoil's top surface whereas at airfoil's bottom surface it moves towards the trailing edge (i.e., downstream), as shown in Figure 8. Moreover, opposite effects occur when the AOA is decreased to negative values.

As the absolute value of the AOA increases, a stall condition is reached independently of the considered Reynolds number. Nonetheless, the AOA at which the stall condition occurs depend on the Reynolds number and the geometric complexity of the airfoil. Under stall conditions, almost half of the experimental airfoil's BL was turbulent, and the

FIGURE 13: NACA 4412 performance characteristics for $Re = 1.5e6$.FIGURE 14: NACA 4412 performance characteristics for $Re = 2e6$.

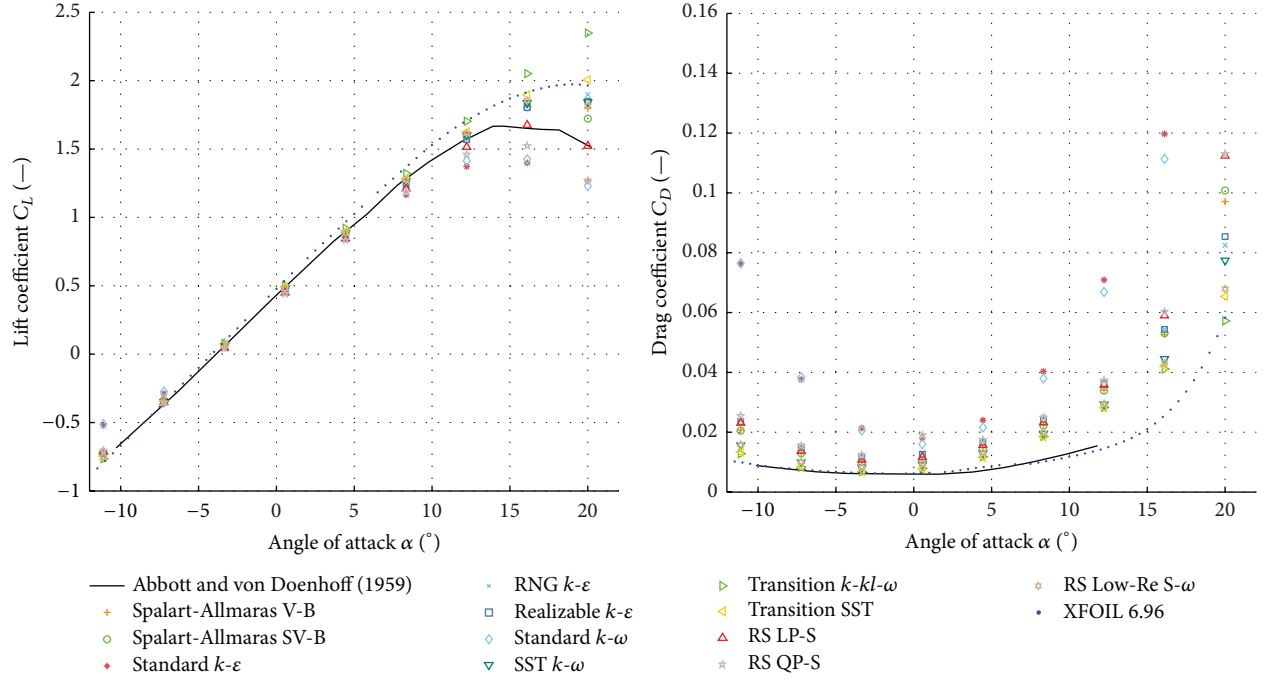
flow detachment condition occurred on the turbulent side (e.g., see Figures 21–24). Therefore, the flow detachment modeling is strongly dependent on the modeled turbulent effects. Following this line of reasoning, the most important deviations in the prediction of the lift force by the different turbulence models were found in stall conditions.

The overprediction of the lift force under stall conditions by full-turbulence models can be understood since free-stream turbulence promotes the earlier formation of turbulent BLs, which typically prevent flow detachment conditions (i.e., surface flow attachment/reattachment is enhanced in turbulent BL). Therefore, the modeled delay on the onset

FIGURE 15: NACA 4412 performance characteristics for $Re = 3e6$.FIGURE 16: NACA 4412 performance characteristics for $Re = 6e6$.

of stall was a consequence of the modeled turbulent BL, as opposed to the partial laminar BL of the experimental data. However, the simulated free-stream turbulence intensity was rather low (1%) and the magnitude of the computed delay on the onset of stall seems to be unrealistic and it is not expected in real free-stream turbulent experiments, which unfortunately were not available in the literature. In this

regard, the RS LP-S model properly regulates the delay on the onset of stall, as shown in Figures 11–17, due to the proper modeling of anisotropic turbulent forces. Moreover, since the RS LP-S model considered a fully turbulent inflow condition, the effects of the laminar-to-turbulent flow transition and the modeling of a turbulent BL at the bottom surface of the airfoil played a minor role in the prediction of the poststall lift force.

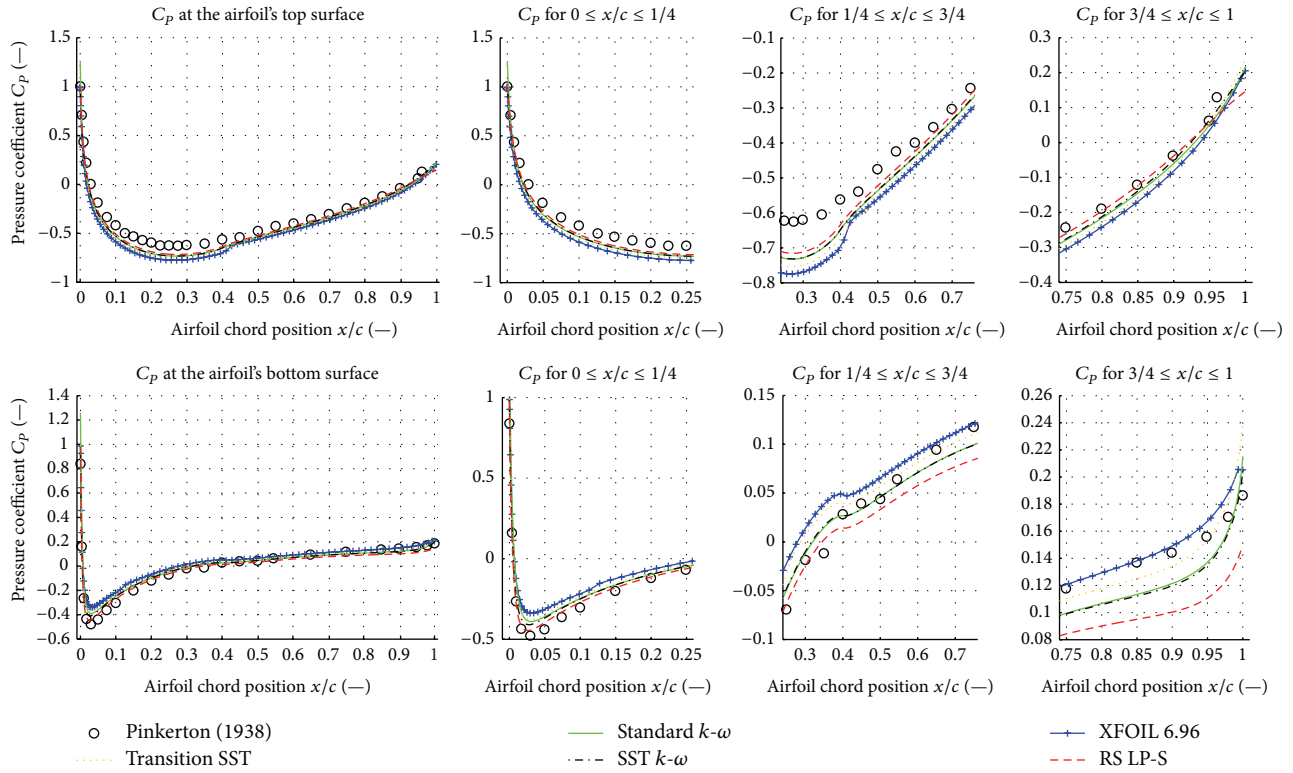
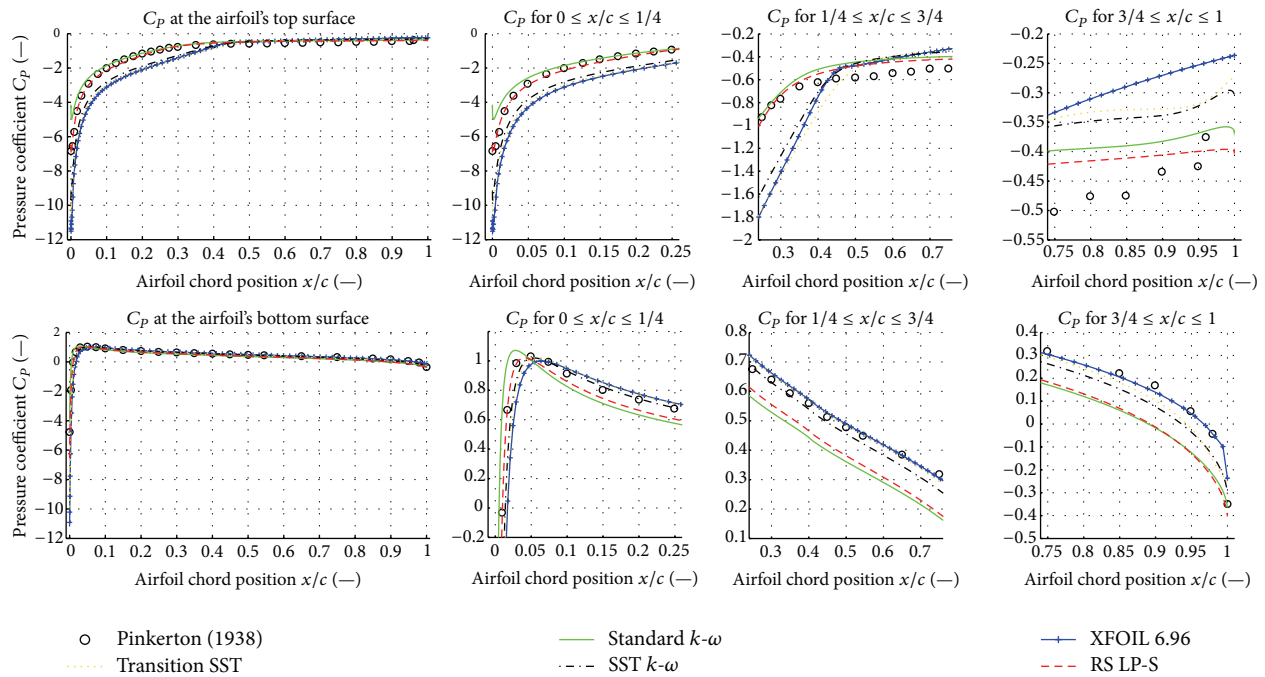
FIGURE 17: NACA 4412 performance characteristics for $Re = 9e6$.

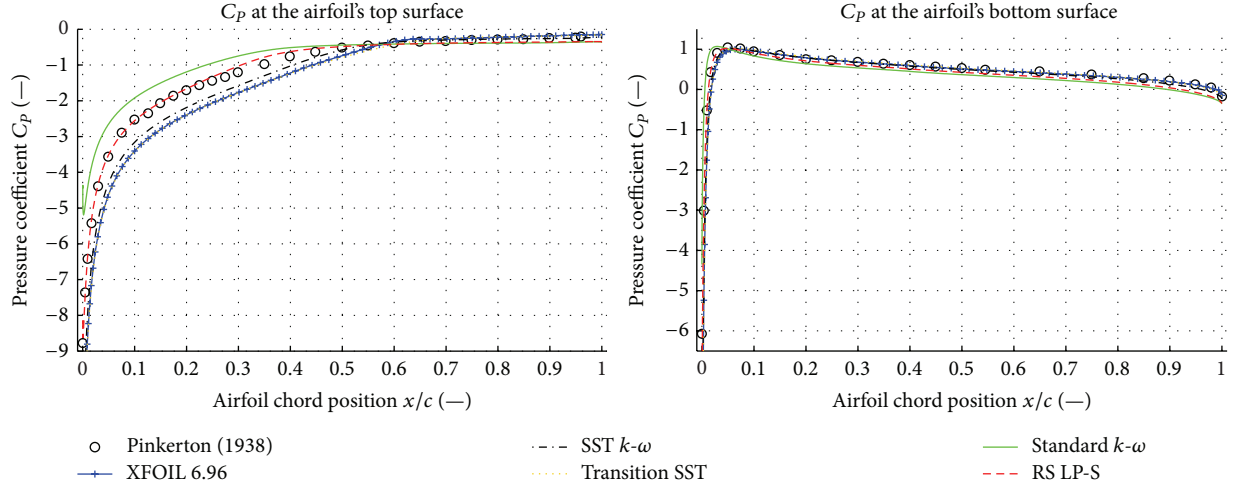
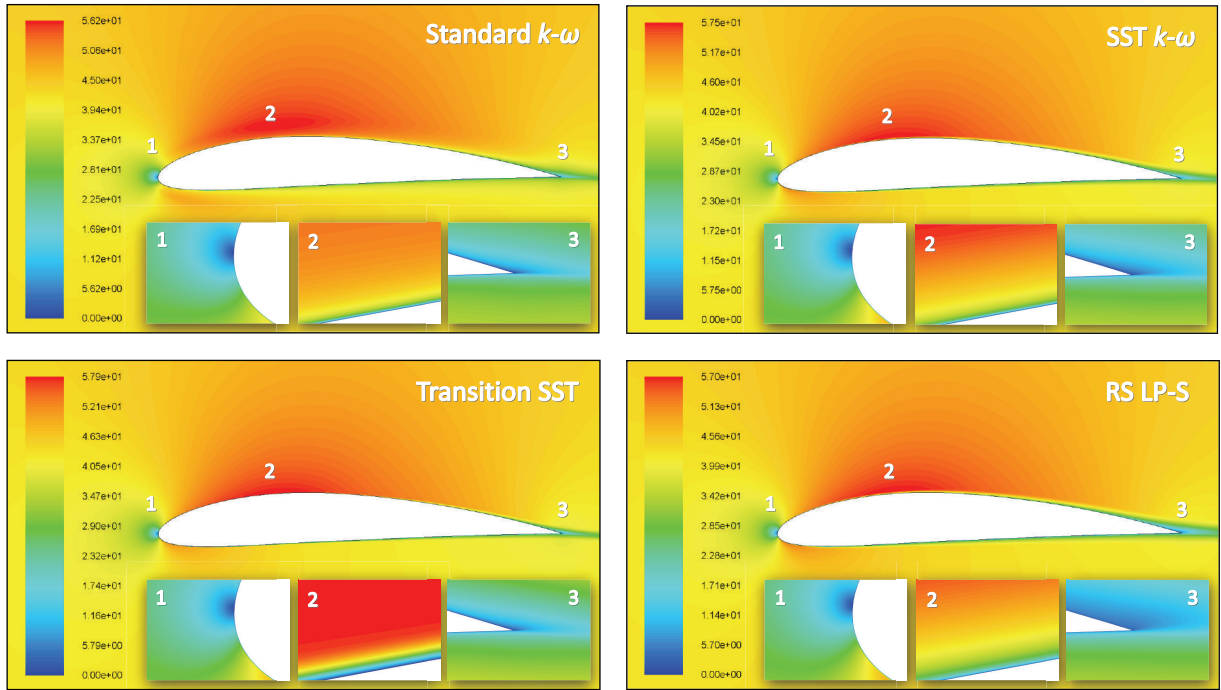
It should be noted that the performance of the Standard $k-\epsilon$ and the Standard $k-\omega$ models for predicting lift coefficients can be good at certain Reynolds numbers, but the agreement can be shown to be fortuitous. As illustrated in Figures 7 and 11–17, their predictions are literally independent of the Reynolds number, whereas the experimental lift and drag coefficients increased and decreased with increasing Reynolds numbers, respectively. Therefore, the observed agreement can be regarded as an occasional coincidence. This observation contradicts with the findings of Kumar et al. [29] who, for a fixed Reynolds number of $3.42e6$, concluded that the Standard $k-\omega$ model provided the best predictions of the NACA 4412 airfoil aerodynamics.

3.3.3. Description of the Accuracy of the Tested Flow Models for Predicting the Drag Coefficient. The drag coefficient was overpredicted by all the RANS-based approaches, being the Transition-based models the best performers at all Reynolds numbers. The best drag predictions occurred at low Reynolds numbers and at low absolute AOA, with the discrepancy monotonically increasing towards higher Reynolds numbers and higher AOA, as shown in Figures 11 to 17.

In all cases, the Standard $k-\epsilon$ and the Standard $k-\omega$ models predicted the largest drag coefficients. Similar predictions were found for the SST $k-\omega$ and the RS Low-Re S- ω models; both models perform poorly at lower Reynolds numbers and when stall conditions were considered. All Reynolds stress models overpredicted the experimental drag coefficient values with the RS Low-Re S- ω predicting the lowest drag values among the three different models. Both the RS LP-S and the RS QP-S predicted similar drag values at all Reynolds numbers and AOA. XFOIL comes out best, quite accurately predicting the drag for all the considered inflow conditions.

3.3.4. Discussion of the Drag Coefficient Predictions by Different Fluid Flow Models. In prestall conditions, the friction-based drag is the dominant component of the total drag force; thus any increase in the magnitude of the wall shear stresses will significantly affect the total drag force. Figure 9 shows the drag components predicted by one full-turbulence model (the RS LP-S) and two Transition-based models (the Transition SST and XFOIL) at a Reynolds number of $3e6$. The friction-based drag prediction of the RS LP-S model is significantly larger when compared to the other models' predictions at any given AOA. This is because the RS LP-S model predicts a fully turbulent BL around the airfoil, similarly to other full-turbulence models. Therefore, the overprediction of the prestall drag force by the different full-turbulence models can be attributed to the modeled small-scale turbulence found near the surface of the airfoil (i.e., the airfoil's full-turbulent BL), which produces larger wall shear stresses and therefore larger values of the skin friction coefficient (C_f), as shown in Figure 25. As described in [1, 27], it is well known that free-stream turbulence increases the total drag force and in some cases doubles the drag force compared to laminar cases. Therefore, in prestall conditions, Transition-based models do a better job in predicting drag because they consider a laminar inflow condition, predict a laminar-to-turbulent flow transition, and solve the flow as turbulent in the airfoil's downstream vicinity and in the resultant wake. From Figure 9, it can be observed that important discrepancies between XFOIL and the Transition SST model predictions of the laminar-to-turbulent flow transition occur only at prestall conditions, which in turn result in the observed discrepancy of both models for predicting the same values of the friction-based drag. The Transition SST model predicted a lower friction-based drag component

FIGURE 18: Pressure coefficient distributions for a $Re = 3e6$ and $\alpha = 0^\circ$.FIGURE 19: Pressure coefficient C_p for a $Re = 3e6$ and $\alpha = 20^\circ$.

FIGURE 20: Pressure coefficient C_p for a $Re = 9e6$ and $\alpha = 20^\circ$.FIGURE 21: Contours of wind speed magnitude (m/s) for $Re = 3e6$ and $\alpha = 0^\circ$.

(consequence of predicting a delayed laminar-to-turbulent flow transition), resulting in a slight underprediction of the drag coefficient at low AOA when compared with the XFOIL predictions or the experimental measurements, as shown in Figures 11 to 17.

As the Reynolds number increases, the laminar-to-turbulent flow transition points at both the top and the bottom surfaces of the airfoil move towards the leading edge, as shown in Figure 8. However, as opposed to intuition, the relocation of the laminar-to-turbulent flow transition

locations does not lead to larger prestall total drag coefficients. Figure 10 shows the evolution of the predicted drag components by various models, while considering different Reynolds numbers. It can be observed that both the friction-based drag coefficient and the pressure-based drag coefficient decreased as the Reynolds number increased and hence the total drag coefficient decreased. This fact can be understood since the rate of increase of the net drag force was lower compared to the rate of increase of the free-stream dynamic pressure at different Reynolds numbers. Moreover,

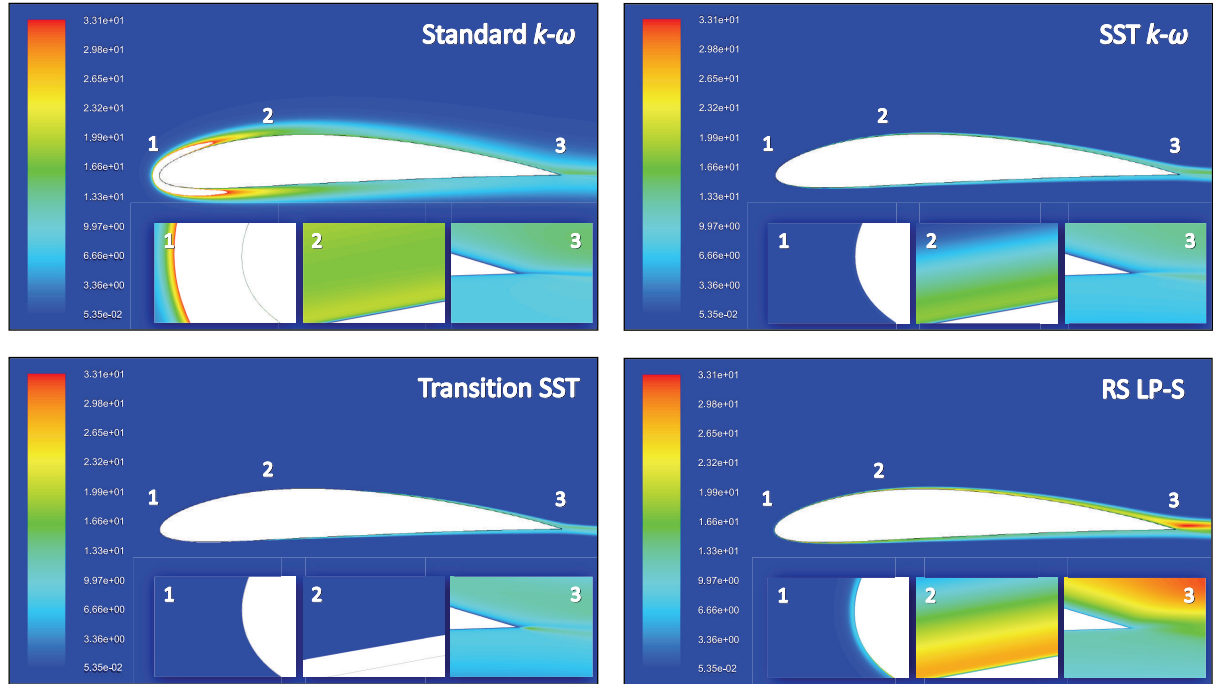


FIGURE 22: Contours of turbulent kinetic energy (m^2/s^2) for $\text{Re} = 3e6$ and $\alpha = 0^\circ$.

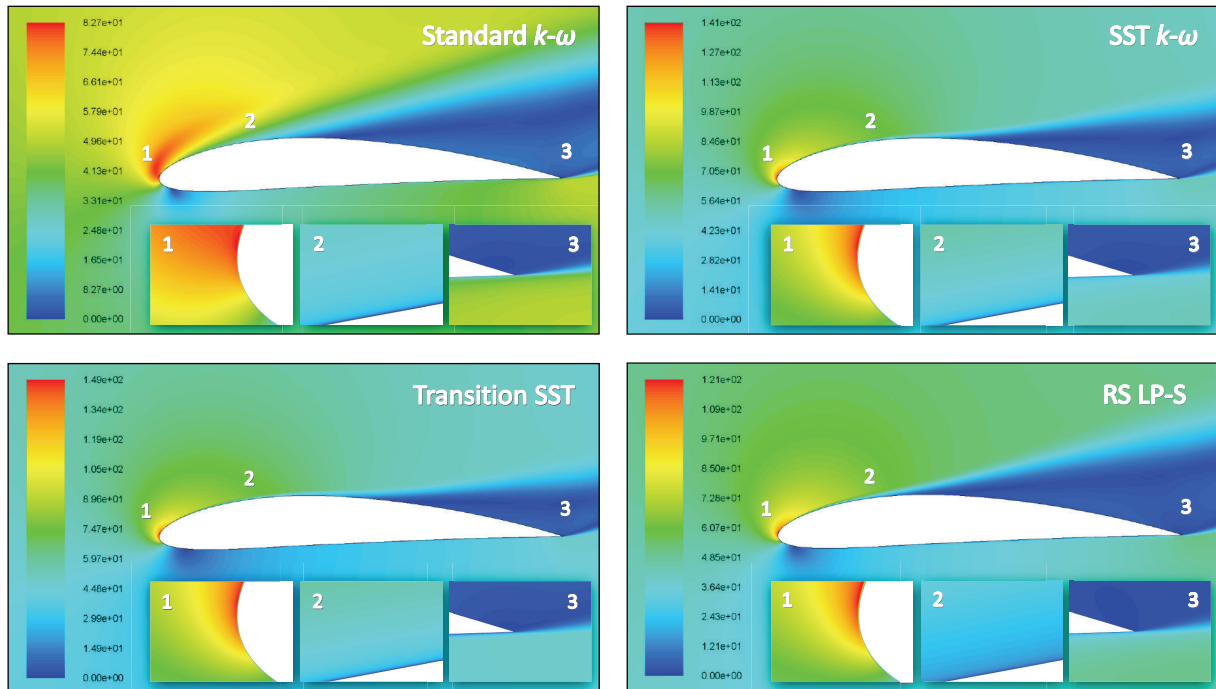


FIGURE 23: Contours of wind speed magnitude (m/s) for $\text{Re} = 3e6$ and $\alpha = 20^\circ$.

the observed reduction of the pressure-based drag was also a consequence of the modeled turbulence, which prevented the formation of adverse pressure gradients in prestall conditions. The predictions of the pressure-based drag at low AOA were similar among all the different models.

The discrepancies observed in prestall conditions between the Transition-based models' predictions and the experimental measurements, as the Reynolds number increased, were due to the modeling of the pressure-based drag, which was heavily influenced by the AOA and the

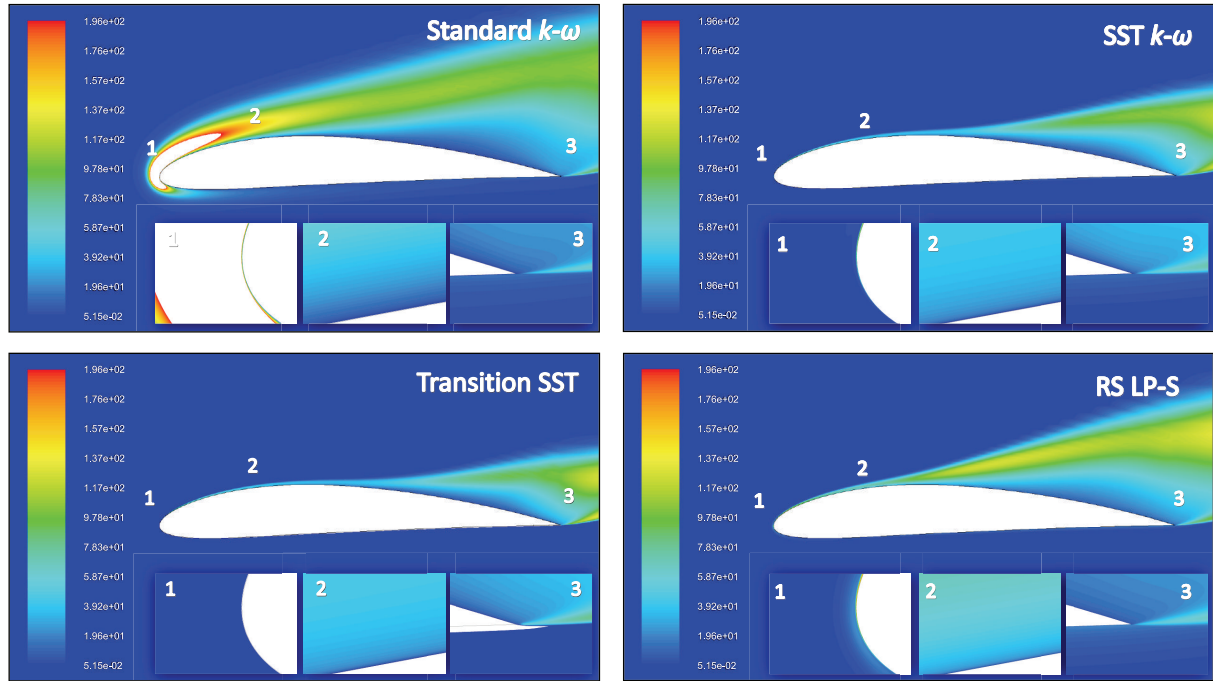


FIGURE 24: Contours of turbulent kinetic energy (m^2/s^2) for $\text{Re} = 3\text{e}6$ and $\alpha = 20^\circ$.

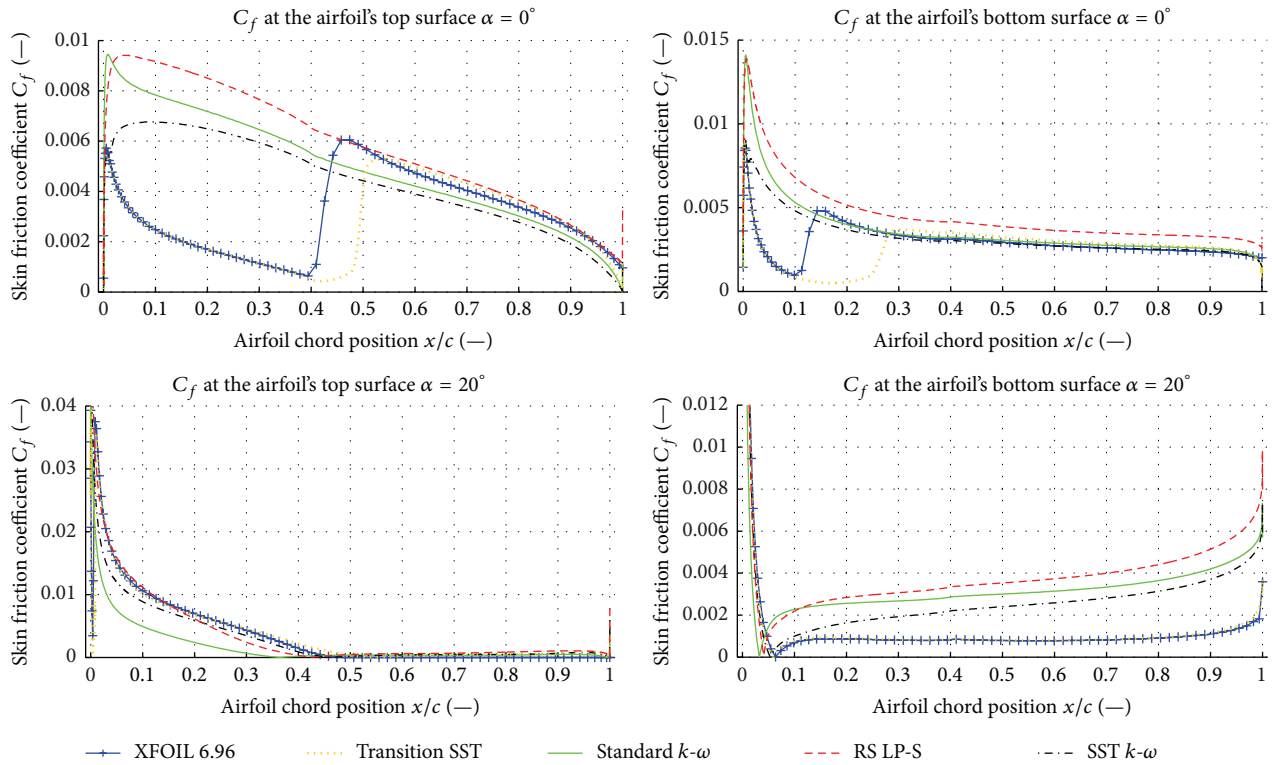


FIGURE 25: NACA 4412 skin friction coefficient (C_f) for $\text{Re} = 3\text{e}6$.

modeled turbulence effects, as shown in Figure 10 and as discussed in detail in Section 3.4. Equivalently, the differences between the full-turbulence models' predictions of the prestall drag were due to the modeling of the pressure-based drag, since almost no changes in the friction-based drag values were found when varying the AOA, as shown in Figures 9 and 10.

When stall conditions were reached, the pressure-based drag coefficient became the dominant component of the total drag coefficient (e.g., see Figure 9) and the friction-based drag coefficient decreased due to the flow detachment conditions. Thus, the growth rate of the total drag force increased dramatically in stall conditions. As it can be observed from Figures 11 to 17, the drag discrepancies between the full-turbulence models' predictions and the experimental measurements increased more rapidly when the AOA increased, as compared to the discrepancies observed between the Transition-based models and the experimental measurements. This fact implies that the drag force is very sensitive to the modeled turbulence effects. Therefore, under stall conditions, the laminar-to-turbulent flow transition becomes less relevant and the proper modeling of the turbulent effects and the flow detachment/reattachment conditions becomes crucial in the prediction of the total drag force.

The large discrepancies of the drag coefficient predictions by the different full-turbulence models, observed at large AOA, depended on the modeled medium-to-large-scale turbulence, which induced larger values of the pressure-based drag (C_{Dp}), which in turn produced a premature flow detachment, as discussed in detail in Section 3.4. Moreover, their predictions were influenced by the lift force overprediction described above, which created an induced drag component (or lift-induced drag C_{Di}), consequence of the modification on the pressure distribution around the airfoil due to the trailing vortex system that accompanies the lift generation.

Based on the findings presented before, the common modeling pitfalls are related to the inadequate modeling of the laminar-to-turbulent flow transition, the turbulent effects, and the flow detachment conditions. Moreover, there appears to be no current methodology that yields accurate results for both aerodynamic forces for any given inflow condition. On the one hand, the turbulence modeling approach (with the RSM LP-S model as the top performer) is capable of predicting the experimental lift force with reasonable accuracy but tends to overpredict drag force, as the flow is considered turbulent in the entire spatial domain. On the other hand, Transition-based models (as exemplified by XFOIL or the Transition SST model) are able to accurately predict the experimental drag characteristics but tend to overpredict lift forces. The main difference between the RANS-based full-turbulence models and the RANS-based Reynolds stress models is the way in which Reynolds stresses are approximated (e.g., the Boussinesq isotropic eddy viscosity assumption is considered in most k - ϵ -based models [32]). Moreover, the difference between the Reynolds stress models is the way they model the pressure-strain term in the equations for the transport of the Reynolds stresses ($\rho \overline{u_i' u_j'}$), which models transport due to pressure and the

mean turbulent strain rate interactions [24]. Since the best lift force predictions were achieved by the RS LP-S model in contrast with the predictions of both the RS QP-S and the RS Low-Re S- ω models, it can be inferred that the pressure-strain term plays an important role in the prediction of lift coefficient in stall conditions.

In order to enhance the level of understanding of the effects that the modeled turbulence produces on the airfoil aerodynamics, the next section contrasts the main flow variables solved within the airfoil's vicinity.

3.4. Main Differences between the Flow Models' Predictions.

In order to understand what mechanisms are driving the modeling procedures, a comparison of the main variables solved (i.e., the local flow speed, the pressure coefficient distributions, and the turbulent variables) was conducted. The test cases used for such comparison are (1) an airflow at a $Re = 3e6$ and $\alpha = 0^\circ$ and (2) an airflow at a $Re = 3e6$ and $\alpha = 20^\circ$. Based on the observed agreements and disagreements with the experimental measurements, the contrasted models were XFOIL, the Standard k - ω , the SST k - ω , the Transition SST, and the RS LP-S models.

3.4.1. Test Case 1 ($Re = 3e6$ and $\alpha = 0^\circ$). The first test case was reasonably well predicted by all models in terms of the lift coefficient. In this case, XFOIL and the Transition SST model slightly overpredict the lift coefficient while the RS LP-S slightly underpredicts it. The best lift coefficient prediction is given by the Standard k - ω and the SST k - ω models. The drag coefficient is accurately predicted by XFOIL and the Transition SST models. The worst drag predictions are given by the Standard k - ω and the RS LP-S models (e.g., see Figure 15).

As expected, the predicted pressure coefficient profiles along the airfoil's surface are very similar among all the considered models and are similar to the experimental measurements, as shown in Figure 18. In this case, both XFOIL and the Transition SST model underpredict the pressure coefficient at all chord positions at the top surface and conversely at the bottom surface. This is consistent with the already noted lift coefficient overprediction. The transition point predicted by XFOIL differs slightly from the one predicted by the Transition SST model, as noted in Figures 8 and 9, where XFOIL predicts the transition point sooner than the Transition SST model. The pressure coefficient shape profiles for both the Standard k - ω and the SST k - ω models are almost identical. At the top surface and in most of the bottom surface, the best performer model is the RS LP-S. The disagreement between the full-turbulence models' predictions and the experimental measurements is mostly observed within the range $0 \leq x/c \leq 0.40$ at the top surface and is understood given that the experimental flow was laminar in that section. An increased agreement between the full-turbulence models' predictions and the experimental measurements is observed after $x/c \approx 0.40$, as the experimental flow became turbulent. Furthermore, an increased agreement between all the flow models' predictions and the experimental measurements is observed at both surfaces close to the trailing edge of the airfoil.

3.4.2. Test Case 2 ($Re = 3e6$ and $\alpha = 20^\circ$). The second test case is challenging to solve because it considers a stall condition. The best lift force predictors are the RS LP-S and the Standard $k-\omega$ models; however, they overpredict the drag force when compared with the remaining flow models' predictions. From Figure 19, it can be observed that the predictions of the pressure coefficient distribution along the top surface of the airfoil are substantially different between flow models. Interestingly, the pressure coefficient distributions from XFOIL and the Transition SST turbulence model are very similar in both surfaces. However, XFOIL and the Transition SST models overpredicted the absolute value of the pressure coefficient at most of the airfoil's top surface. This is consistent with the fact that both models predicted similar values for the lift and drag coefficients, as shown in Figures 9 and 15. It is conspicuous that the Standard $k-\omega$ model predicted large values of the pressure coefficient (i.e., lower absolute values of the pressure coefficient) along the leading edge of the airfoil, which led to the already observed discrepancy in the predicted aerodynamic forces, as shown in Figures 10 and 15. The overprediction of the pressure coefficient by the Standard $k-\omega$ model increased with increasing Reynolds number, as shown in Figure 20, which presents the resultant pressure coefficient distributions for the case of simulating an airflow at a $Re = 9e6$ and at an $\alpha = 20^\circ$. This behavior was also found in the predictions of the Standard $k-\epsilon$ and NRG $k-\epsilon$ models. The best performer turbulence model is, again, the RS LP-S showing the best agreement with the experimental pressure coefficient distributions.

3.4.3. Discussion of the Pressure Coefficient Predictions by Different Flow Models. The pressure coefficient and the lift coefficient overprediction of XFOIL has been noted previously [40, 54] and it is attributed to (1) the inadequate prediction of the local flow speed within the laminar section, close to the airfoil surface, and (2) the lacking ability of XFOIL to simulate the turbulent BL development, rotational effects, and the proper flow attachment/detachment conditions. Equivalently, the Transition SST model typically overpredicts the local flow speed at the airfoil's top surface, close to leading edge, compared to other models that predict more accurate aerodynamics (e.g., see Figures 21 and 23).

The overprediction of the pressure coefficient (or the underprediction of the absolute value of the pressure coefficient) by full-turbulence models (e.g., Standard $k-\omega$) is a direct consequence of the modeled turbulent forces found near the leading edge of the airfoil, as shown in Figures 22 and 24 which illustrate the contours of turbulent kinetic energy, which in turn are limited to the range of values found for the same situation but considering the RS LP-S model (i.e., the uncolored zones represent zones where the magnitude of the turbulent kinetic energy is larger or lower than the maximum or minimum values found for the same situation but considering the RS LP-S model). The large turbulent kinetic energy and the large turbulent viscosity (not shown) predicted by the Standard $k-\omega$ model within the airfoil's vicinity produce an enhanced transversal diffusion of momentum, mostly noted at the upper surface of the airfoil, resulting in both a substantial reduction of the flow speed

magnitude and an affection of the resultant flow direction, as shown in Figures 21 and 23, when compared to the RS LP-S, SST $k-\omega$, and the Transition SST models' results. The induced disturbances on the wind field, product of the large modeled turbulent forces, lead to premature flow detachment conditions, thus producing thicker and larger wakes and promoting the prediction of large values of pressure-based drag coefficient. This is observed phenomenon is consistent with the already studied drag predictions of each full-turbulence model, as shown in Figure 10. Therefore, the prediction large pressure-based drag coefficient values by most full-turbulence models, with the exception of the Transition models, can be partially attributed to the large modeled turbulent forces, which produced premature flow detachment conditions. Nonetheless, proper premature flow detachment conditions are required for the adequate prediction of the lift reduction that accompanies the stall regime, which is well described by the RS LP-S model.

The prediction of large turbulent forces within the airfoil's vicinity is mostly observed when employing turbulence models that are based on the Boussinesq isotropic eddy viscosity hypothesis [55]. Nonetheless, this modeling issue does not affect the predictions of the Reynolds stress-based models as they solve additional transport equations for the six independent Reynolds stresses and the eddy viscosity isotropic assumption is avoided, thus denoting the main reason why the turbulent forces are better described by the Reynolds Stress-based models compared to the Standard $k-\epsilon$ or the Standard $k-\omega$ models.

In order to improve the level of understanding of the already noted drag coefficient overpredictions, an illustration of the skin friction coefficient (C_f) is shown in Figure 25. It is worth noting that in the frontal top and bottom surfaces of the airfoil the skin friction coefficient is larger when considering full-turbulence models. As previously discussed, these larger values are expected since the airfoil's BL is turbulent. Both XFOIL and the Transition SST models predicted lower values of the skin friction coefficient since the flow was laminar in that section. When the laminar-to-turbulent flow transition occurred, the computed C_f increased and became comparable to the predicted C_f values by full-turbulence models. Interestingly, there is reasonable agreement between the predictions of XFOIL, the Transition SST, and the RS LP-S models of the C_f at the airfoil's top surface. It can be observed that the skin friction coefficient tends to decay rapidly at the top forward half of the airfoil surface, when considering the case $\alpha = 20^\circ$. The observed reduction is attributed to a flow detachment condition. Interestingly, as already discussed, full-turbulence models predict total flow detachment sooner than XFOIL or the Transition SST models, the Standard $k-\omega$ being the one that predicts more turbulent kinetic energy in the airfoil's vicinity and the one that predicts total flow detachment sooner. Equivalent to C_f , the friction-based drag tends decay due to the flow detachment experienced at larger AOA, as previously shown in Figure 9.

Figure 26 shows the magnitude and the shape profile of the solved independent superficial Reynolds stresses, considering the RS LP-S model. In 2D cases, four independent stresses are solved, corresponding to the normal stresses

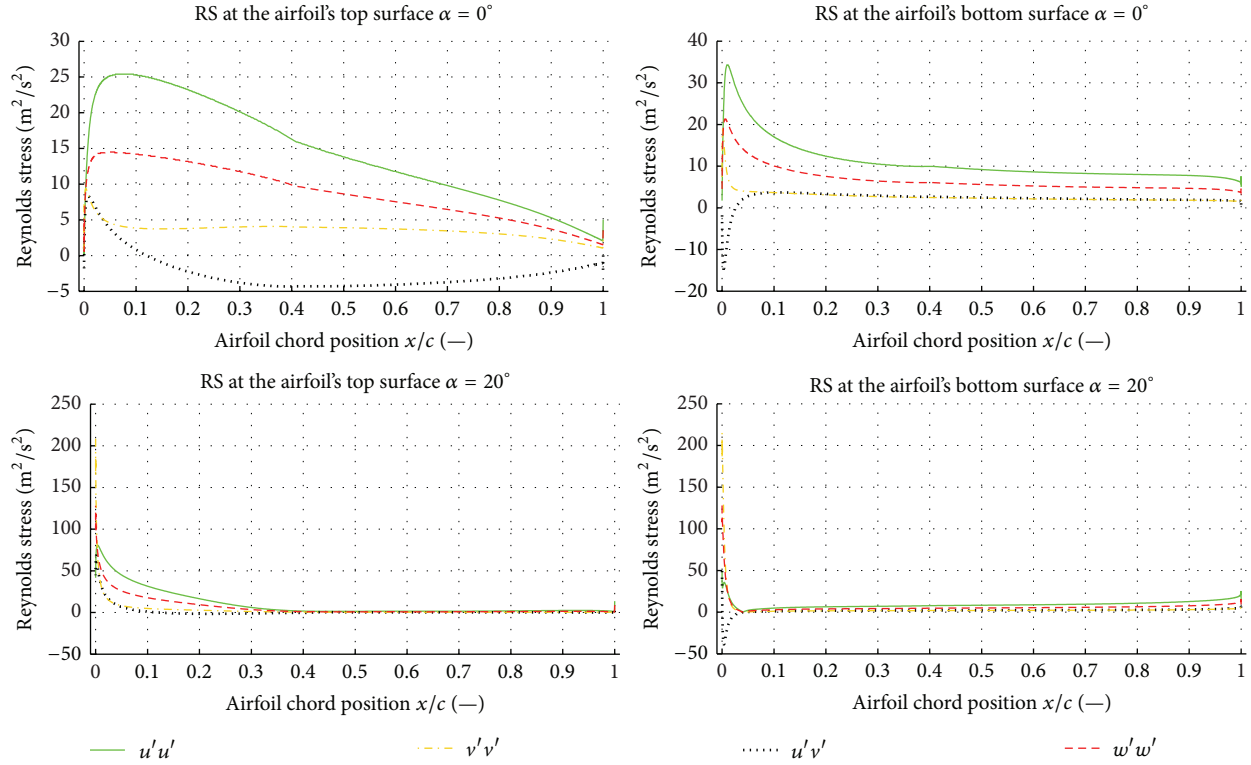


FIGURE 26: Computed airfoil's surface Reynolds stresses from the RS LP-S model.

$\overline{u_i u_i}$ and the off-diagonal Reynolds stresses $\overline{u_i u_j}$. It should be noted from this figure that the normal stresses are, in magnitude, more important than the off-diagonal Reynolds stresses at both surfaces of the airfoil and for both studied cases. However, the off-diagonal Reynolds stress cannot be neglected. For both test cases ($\alpha = 0^\circ$ and $\alpha = 20^\circ$) the superficial Reynolds stresses tend to decay rapidly towards the tip of the airfoil, with the exception of the tip zone at the airfoil's bottom surface for the $\alpha = 20^\circ$ case, where the formation of vortices takes place. Furthermore, the Reynolds stresses shape profiles are significantly affected by flow detachment conditions, as noted from the case $\alpha = 20^\circ$. It was observed that the magnitude of all the Reynolds stresses decayed rapidly in the near wake as a result of the turbulent dissipation rate found in such zone. Finally, as mentioned before, the modeling of such independent stresses is important to get accurate predictions of the lift coefficient in the stall regime, thus denoting the importance of modeling anisotropic turbulent flows during the airfoil aerodynamics prediction.

4. Conclusions and Future Research

This work presented a comprehensive assessment of the accuracy of thirteen state-of-the-art fluid flow models applied to the problem of predicting aerodynamic forces on two-dimensional airfoils. The primary aims of the work were to (1) extend previous literature conclusions by considering additional flow models and a wide range of inflow conditions, (2) identify the best performer models and their key modeling

features, (3) study the effects of different free parameters on the simulations' outcomes, (4) provide a complete set of physical interpretations based on validated computational results, and (5) provide recommendations for future work regarding the modeling of two-dimensional airfoil aerodynamics. The specific improvements achieved during the work development are summarized next.

- (i) One of the main concerns in previous literature works results is related to the quality of the numerical solutions. During the development of the present computational assessment, it was possible to achieve an adequate numerical convergence, while considering any of the tested turbulence models and even while considering stall conditions. This was possible due to the proper setup of the computational experiments, which considered model-tailored spatial domain discretizations. In this regard, extensive guidelines of the procedures and calculations were provided to allow the reader to replicate them in different scenarios. Furthermore, additional recommendations, based on a boundary topology analysis and on a set of grid-independence tests, were given with the aim of improving the quality and the computational efficiency of the solution process. Through the extensive study of the effects of different free parameters, it was possible to spare computational resources without compromising the modeling accuracy. The grid-independence tests revealed that at least 120,000 elements, with their corresponding refinements towards

the airfoil's surface, are required to simulate stable airfoil aerodynamics at large Reynolds numbers and at large AOA. Moreover, among the most relevant strategies for improved numerical convergence, it was found that the use of finite volume-based solution methods incorporating preconditioned systems, together with the proper variation of the under-relaxation factors and the Courant number values, was crucial to significantly speed up the numerical convergence process.

- (ii) Contradictory findings were distinguished in the literature with regard to which models, or combination of models, are the most effective in terms of solution quality and computational efficiency while predicting two-dimensional airfoil aerodynamics. Through the development and validation of a variety of computational experiments that encompassed a wide range of inflow conditions, the best modeling approaches were objectively identified. However, it was found that the prediction of aerodynamic forces considering laminar inflow conditions is complex and there is still no methodology that by itself provides accurate predictions of both the lift and the drag forces. On the one hand, the turbulence modeling approach (with the RSM LP-S model as the top performer) was able to predict lift forces that agreed with the experimental results, even when stall conditions were considered, but drag forces were substantially overpredicted. By assuming a free-stream turbulent inflow condition, it was demonstrated that the frictional (or viscous) component of the drag was larger in the frontal zone of the airfoil, since the airfoil's BL was turbulent, as opposed to the partially laminar BL layer found in the experimental measurements. In addition, premature flow detachment conditions were observed when considering free-stream turbulent inflow conditions in contrast with considering free-stream laminar inflow conditions, which were modeled with the aid of XFOIL and the Transition SST models. The premature flow detachment conditions predicted by full-turbulence models were a consequence of the large turbulent forces predicted at the leading edge of the airfoil, which produced a substantial modification of the local flow speed magnitude and its direction within the airfoil's vicinity, which in turn produced larger values of the pressure-based drag due to the induced adverse pressure gradients. It was observed that as the magnitude of the turbulent kinetic energy found close to the airfoil's surface increased the absolute value of the pressure coefficient decreased. This modeled effect increased the drag force predictions discrepancy between the full-turbulence models predictions and the experimental results. On the other hand, XFOIL and the Transition SST turbulence models predicted near identical drag forces as compared to the literature results but overpredicted lift forces even in prestall conditions. This is because both XFOIL and the Transition SST models predicted large flow

speed magnitudes within the airfoil's vicinity, thus affecting the prediction of the pressure coefficient at all chord positions. The overprediction of the flow speed magnitude by XFOIL is believed to be due its lacking ability to properly simulate turbulent BLs, rotational effects, and flow detachment conditions. Furthermore, the overprediction of the flow speed magnitude by the Transition SST model is related to the prediction of the laminar-to-turbulent flow transition in the outer layers of the BL (i.e., not only close to the airfoil's surface). Important differences were found when contrasting the laminar-to-turbulent flow transition predictions of XFOIL and the Transition SST models in prestall conditions.

- (iii) The worst performance was observed when full-turbulence models based on the Boussinesq isotropic eddy viscosity hypothesis were employed, which include all the k - ϵ -based models, as they were unable to model a Reynolds number dependence while predicting both aerodynamic coefficients. Moreover, they predicted the largest drag coefficients, which differed with the literature results at all AOA and Reynolds numbers. For these full-turbulence models, large values of the turbulent kinetic energy and the turbulent viscosity were found in the airfoil's vicinity, which led to a greatly underpredicted absolute value of the pressure coefficient.
- (iv) During the computational assessment, it was found that significant variations in all the model's predictions occur by not explicitly modeling the inner layers of the airfoil's BL. The proper modeling of the complete airfoil's BL leads to the accurate estimation of wall shear stresses and flow detachment conditions, which are required to match the experimental results. The modeling of anisotropic turbulence employing RANS-based approaches complemented with Reynolds stress turbulence models, considering a linear pressure-strain term in the equations for the transport of the Reynolds stresses, was crucial to obtain accurate predictions of the lift coefficient in the stall regime since the prediction of flow detachment conditions is heavily influenced by the modeled turbulent diffusion of momentum across the airfoil's vicinity. However, detailed experimental studies on flow detachment/reattachment and its relation with the pressure-based drag coefficient and the free-stream turbulence intensity are required in order to improve the lift predictions in the stall regime.

Based on the validated computational results, the most important modeling pitfalls, which still provide room for improvement and define fertile areas of inquiry, as well as the main research needs, were identified and are presented in summary form.

- (i) Since the performance of the RS LP-S and the Transition-based models for predicting lift and drag forces was good, respectively, coupling the Transition $\gamma - \bar{Re}_{\theta t}$ model with the RS LP-S model could result

in a model capable of predicting accurate airfoil aerodynamics when considering laminar/transitional inflow conditions.

- (ii) Important differences in the laminar-to-turbulent flow transition prediction were found when contrasting the outputs of XFOIL and the outputs of the Transition SST model. A recalibration of the Transition SST model constants could enhance the performance of the model while predicting prestall aerodynamics at different Reynolds numbers.
- (iii) One important unaddressed question is related to quantification of the effects that different free-stream turbulent conditions have on the prediction of aerodynamic forces (i.e., the determination of the effects of varying the inlet turbulence intensity and the eddy length scale on the aerodynamic predictions), while considering different inflow conditions (e.g., different Reynolds numbers and AOA). In many real applications (e.g., aircrafts flying within the earth's BL, automobiles or wake-affected wind turbines, etc.), free-stream turbulent conditions are experienced and their aerodynamics should be studied assuming fully turbulent conditions, while considering different turbulence intensities and eddy length scales. In order to validate the outputs of the cases that considered free-stream turbulent inflow conditions, it is required to perform wind tunnel tests over the NACA 4412 airfoil considering free-stream turbulent flows containing different levels of turbulent intensity. Such experimental information is not available in the literature.
- (iv) Other relevant cases to be studied are (1) the computation of the two-dimensional airfoil aerodynamics up to $0^\circ \leq \alpha < 360^\circ$, (2) assessment of the ability of different turbulence models for predicting transonic and supersonic aerodynamics, (3) assessment of the accuracy of advanced techniques based on LES and different subgrid-scale models for the prediction of two-dimensional airfoil aerodynamics, (4) evaluation of the ability of the Transition-based models for predicting airfoil aerodynamics at very low Reynolds numbers (e.g., the prediction of laminar separation bubbles), and (5) assessment of the net effects the superficial roughness produces on the lift and drag forces prediction.

Although RANS-based and FANS-based approaches are often used for comparison purposes during the development of alternative flow models, it is clear that these approaches still exhibit deficiencies while predicting two-dimensional airfoil aerodynamics. The findings of this work, together with the provided physical interpretations, are believed to be useful and can be considered as a building block for the development of alternative flow models.

Nomenclature

A_f : Cell face area (m^2)
 c : Airfoil chord (m)

C_D : Drag coefficient (—)
 C_{Df} : Friction-based drag coefficient (—)
 C_{Dp} : Pressure-based drag coefficient (—)
 C_f : Skin friction coefficient (—)
 C_L : Lift coefficient (—)
 C_p : Pressure coefficient (—)
 N_{Crit} : Critical amplification factor for the e^n transition prediction method (—)
 P : Pressure (kPa)
 Re : Reynolds number [—]
 T : Temperature (K)
 TI : Turbulence intensity (%)
 $u'_i u'_j$: Reynolds stress (m^2/s^2)
 u^* : Friction velocity (m/s)
 ν : Local kinematic viscosity (m^2/s)
 v : Velocity (m/s)
 V : Cell volume (m^3)
 x : Axial distance from the airfoil leading edge (m)
 x_{tr}^T : Normalized transition point at the top surface of the airfoil (—)
 x_{tr}^B : Normalized transition point at the bottom surface of the airfoil (—)
 y : Distance to the nearest wall (m)
 y^+ : Dimensionless wall distance (—)
 α : Angle of attack ($^\circ$)
 μ : Dynamic viscosity (kg/m-s)
 ρ : Fluid density (kg/m^3)
 ρ_{Airf} : Airfoil density (kg/m^3)
 τ : Shear stress (Pa)
 ΔC_D : Difference of absolute drag coefficient (—)
 ΔC_L : Difference of absolute lift coefficient (—)
 Δt : Time step (s).

Conflict of Interests

The authors declare that there is no conflict of interests regarding the publication of this paper.

Acknowledgments

Support from the Research Chair for Wind Energy at Instituto Tecnológico y de Estudios Superiores de Monterrey de Monterrey (ITESM), under Contract CAT158, and support from the Mexican Council for Science and Technology (CONACYT) are gratefully acknowledged. Special thanks are due to José Santiago Martínez Torres for his valuable aid while conducting computational experiments.

References

- [1] I. H. Abbott and A. E. von Doenhoff, *Theory of Wing Sections*, Dover Publications, New York, NY, USA, 1959.
- [2] E. L. Houghton, P. W. Carpenter, S. H. Collicott, and D. T. Valentine, *Aerodynamics for Engineering Students*, Elsevier, Waltham, Mass, USA, 6th edition, 2013.
- [3] A. Filippone, "Airfoil inverse design and optimization by means of viscous-inviscid techniques," *Journal of Wind Engineering and Industrial Aerodynamics*, vol. 56, no. 2-3, pp. 123–136, 1995.

- [4] M. S. Selig and B. D. McGranahan, "Wind tunnel aerodynamic tests of six airfoils for use on small wind turbines," *Journal of Solar Energy Engineering, Transactions of the ASME*, vol. 126, no. 4, pp. 986–1001, 2004.
- [5] Z. Zhou, D. Li, Z. Zhang, and J. Zeng, "Design and fabrication of a hybrid surface-pressure airfoil model based on rapid prototyping," *Rapid Prototyping Journal*, vol. 14, no. 1, pp. 57–66, 2008.
- [6] A. E. von Doenhoff and F. T. Abbott, "The langley two-dimensional low-turbulence pressure tunnel," Technical Note 1293, National Advisory Committee for Aeronautics, Washington, DC, USA, 1947.
- [7] H. Glauert, "Wind tunnel interference on wings, bodies and airscrews in a two-dimensional-flow wind tunnel with consideration of the effect of compressibility," R. & M. No. 1566, British A. R. C., 1938.
- [8] P. Dube and V. Damodaran, "Numerical approach to determine wind tunnel blockage correction for the external aerodynamics of a vehicle," SAE Technical Paper 2007-01-3462, 2007.
- [9] F. Riegels, "Correction factors for wind tunnels of elliptic section with partially open and partially closed test section," Tech. Rep. TM-1310, National Advisory Committee for Aeronautics, Washington, DC, USA, 1951.
- [10] I. H. Abbott, A. E. von Doenhoff, and L. S. Stivers, "Summary of airfoil data," Tech. Rep. 824, National Advisory Committee for Aeronautics, Washington, DC, USA, 1945.
- [11] R. L. Panton, "Stream functions and velocity potential," in *Incompressible Flow*, pp. 251–270, John Wiley & Sons, Hoboken, NJ, USA, 3rd edition, 2005.
- [12] A. Zanon, P. Giannattasio, and C. J. S. Ferreira, "A vortex panel model for the simulation of the wake flow past a vertical axis wind turbine in dynamic stall," *Wind Energy*, vol. 16, no. 5, pp. 661–680, 2013.
- [13] R. L. Panton, "Introduction to turbulent flows," in *Incompressible Flow*, pp. 732–774, John Wiley & Sons, Hoboken, NJ, USA, 3rd edition, 2005.
- [14] Z. U. A. Warsi, "Development of averaged equations," in *Fluid Dynamics: Theoretical and Computational Approaches*, pp. 559–585, Taylor & Francis Group, Boca Raton, Fla, USA, 3rd edition, 2006.
- [15] M. Lesieur and O. Metais, "New trends in large eddy simulations of turbulence," *Annual Reviews of Fluid Mechanics*, vol. 28, pp. 45–82, 1996.
- [16] R. Friedrich, T. J. Hüttl, M. Manhart, and C. Wagner, "Direct numerical simulation of incompressible turbulent flows," *Computers and Fluids*, vol. 30, no. 5, pp. 555–579, 2001.
- [17] X. Maucière, *Automatic 2D airfoil generation, evaluation and optimisation using MATLAB and XFOIL [M.S. thesis]*, Department of Mechanical Engineering, Section of Fluid Mechanics, Technical University of Denmark, Lyngby, Denmark, 2009.
- [18] Z. U. A. Warsi, "The Navier-Stokes equations: equations of inviscid flow (Euler's equations)," in *Fluid Dynamics: Theoretical and Computational Approaches*, pp. 83–85, Taylor & Francis, 3rd edition, 2006.
- [19] M. Drela, "XFOIL: an analysis and design system for low reynolds number airfoils," in *Low Reynolds Number Aerodynamics: Proceedings of the Conference Notre Dame, Ind, USA, 5–7 June*, vol. 54 of *Lecture Notes in Engineering*, pp. 1–12, Springer, Berlin, Germany, 1989.
- [20] M. Drela and H. Youngren, *XFOIL 6.96 User Guide*, Massachusetts Institute of Technology, Cambridge, Mass, USA, 2001, <http://web.mit.edu/drela/Public/web/xfoil/>.
- [21] Accurate Lift, Drag & Moments for Airfoil Shapes, Software Package, Ver. 5.0, ©Hanley Innovations, Ocala, Fla, USA, VisualFoam, 2013, http://www.hanleyinnovations.com/air_16.html.
- [22] W. P. Wolfe and S. S. Ochs, "CFD calculations of S809 aerodynamic characteristics," in *Proceedings of the 35th AIAA Aerospace Sciences Meeting and Exhibit*, AIAA-97-0973, Reno, Nev, USA, 1997.
- [23] F. R. Menter, R. Langtry, and S. Völker, "Transition modelling for general purpose CFD codes," *Flow, Turbulence and Combustion*, vol. 77, no. 1–4, pp. 277–303, 2006.
- [24] ANSYS, *ANSYS FLUENT Theory Guide*, ANSYS, Canonsburg, Pa, USA, 2014, <http://www.ansys.com/>.
- [25] J. H. Ferziger and M. Peric, *Computational Methods for Fluid Dynamics*, Springer, Berlin, Germany, 3rd edition, 1996.
- [26] P. Khayatizadeh and S. Nadarajah, "Laminar-turbulent flow simulation for wind turbine profiles using the γ - $Re_{\theta t}$ transition model," *Wind Energy*, vol. 17, no. 6, pp. 901–918, 2014.
- [27] S. J. Miley, "A catalog of low Reynolds number airfoil data for wind turbine applications," RFP-3387 VC-60, Rockwell International, USA Department of Energy, Wind Energy Technology Division, Federal Wind Energy Program, 1982.
- [28] D. C. Eleni, T. I. Athanasios, and M. P. Dionissios, "Evaluation of the turbulence models for the simulation of the flow over a national advisory committee for aeronautics (NACA) 0012 airfoil," *Journal of Mechanical Engineering Research*, vol. 4, no. 3, pp. 100–111, 2012.
- [29] A. Kumar, M. Singh, and A. Kumar, "Analysis of the Spalart-Allmaras and k - ω standard models for the simulation of the flow over a National Advisory Committee for Aeronautics (NACA) 4412 airfoil," *International Journal of Scientific & Engineering Research*, vol. 3, no. 8, pp. 881–887, 2012.
- [30] F. Villalpando, M. Reggio, and A. Ilinca, "Assessment of turbulence models for flow simulation around a wind turbine airfoil," *Modelling and Simulation in Engineering*, vol. 2011, Article ID 714146, 8 pages, 2011.
- [31] A. Firooz and M. Gadami, "Turbulence flow for NACA 4412 in unbounded flow and grounded effect with different turbulence models and two ground conditions: fixed and moving ground condition," in *Proceedings of the International Conference on Boundary and Interior Layers*, Göttingen, Germany, 2006.
- [32] X. Hua, R. Gu, J.-F. Jin et al., "Numerical simulation and aerodynamic performance comparison between seagull aerofoil and NACA 4412 aerofoil under low-reynolds," *Advances in Natural Science*, vol. 3, no. 2, pp. 244–250, 2010.
- [33] C. S. Jang, J. C. Ross, and R. M. Cummings, "Numerical investigation of an airfoil with a Gurney flap," *Aircraft Design*, vol. 1, no. 2, pp. 75–88, 1998.
- [34] F. Villalpando, M. Reggio, and A. Ilinca, "Numerical study of flow around iced wind turbine airfoil," *Engineering Applications of Computational Fluid Mechanics*, vol. 6, no. 1, pp. 39–45, 2012.
- [35] D. D. Pasquale, A. Rona, and S. J. Garrett, "A selective review of CFD transition models," in *Proceedings of the 39th AIAA Fluid Dynamics Conference*, AIAA, San Antonio, Tex, USA, June 2009.
- [36] L. Yuhong and L. Congming, "A numerical simulation of flow around a wind turbine airfoil based on transition model," in *Proceedings of the 1st World Non-Grid-Connected Wind Power and Energy Conference (WNWEC '09)*, pp. 1–5, Nanjing, China, September 2009.
- [37] J. Yao, W. Yuan, J. Wang et al., "Numerical simulation of aerodynamic performance for two dimensional wind turbine

- airfoils,” in *Proceedings of the International Conference on Advances in Computational Modeling and Simulation*, vol. 31, pp. 80–86, Procedia Engineering, 2012.
- [38] A. C. Aranake, V. K. Lakshminarayan, and K. Duraisamy, “Assessment of transition model and CFD methodology for wind turbine flows,” in *Proceedings of the 42nd AIAA Fluid Dynamics Conference and Exhibition*, AIAA 2012-2720, New Orleans, La, USA, June 2012.
- [39] J. L. Van Ingen, “The e^+ method for transition prediction. Historical review of work at TU Delft,” in *Proceedings of the 38th Fluid Dynamics Conference and Exhibit*, AIAA 2008-3830, Seattle, Wash, USA, 2008.
- [40] P. Bæk and P. Fuglsang, “Experimental detection of transition on wind turbine airfoils,” in *Proceedings of the European Wind Energy Conference and Exhibition (EWEC '09)*, pp. 1628–1652, European Wind Energy Association, Marseille, France, March 2009.
- [41] R. L. Fearn, “Airfoil aerodynamics using panel methods,” *The Mathematica Journal*, vol. 10, no. 4, p. 15, 2008.
- [42] E. N. Jacobs and A. Sherman, “Airfoil section characteristics as affected by variations of the Reynolds number,” NASA Technical Reports Server 586, National Advisory Committee for Aeronautics, Washington, DC, USA, 1937.
- [43] R. M. Pinkerton, “The variation with reynolds number of pressure distribution over an airfoil section,” National Advisory Committee for Aeronautics, Technical Report 613, NASA Technical Reports Server, Washington, DC, USA, 1938.
- [44] A. J. Wadcock, “Investigation of low-speed turbulent separated flow around airfoils,” NASA CR-177450, NASA, Washington, DC, USA, 1987.
- [45] L. K. Loftin and H. A. Smith, “Aerodynamic characteristics of 15 NACA airfoil sections at seven Reynolds numbers from 0.7×10^6 to 9×10^6 ,” National Advisory Committee for Aeronautics, Technical Note 1945, NASA, Washington, DC, USA, 1949.
- [46] M. Drela and M. B. Giles, “Viscous-inviscid analysis of transonic and low reynolds number airfoils,” *AIAA Journal*, vol. 25, no. 10, pp. 1347–1355, 1987.
- [47] J. P. Johnson, G. Iaccarino, K.-H. Chen, and B. Khalighi, “Simulations of high reynolds number air flow over the NACA-0012 airfoil using the immersed boundary method,” *Journal of Fluids Engineering*, vol. 136, no. 4, Article ID 040901, 2014.
- [48] W. A. Bacha and W. S. Ghaly, “Drag prediction in transitional flow over two-dimensional airfoils,” in *Proceedings of the 44th Aerospace Sciences Meeting and Exhibit*, AIAA 2006-248, Reno, Nev, USA, January 2006.
- [49] G. Kalitzin, G. Medic, G. Iaccarino, and P. Durbin, “Near-wall behavior of RANS turbulence models and implications for wall functions,” *Journal of Computational Physics*, vol. 204, no. 1, pp. 265–291, 2005.
- [50] J. Quinn, “Effects of Reynolds number and leading-edge roughness on lift and drag characteristics of the NACA 653-418, $a=1.0$ airfoil section,” Confidential Bulletin L5J04, National Advisory Committee for Aeronautics, Washington, DC, USA, 1945.
- [51] ANSYS, “Excellence in engineering simulation. Tips and tricks: accelerating CFD solutions,” *ANSYS Advantage*, vol. 5, no. 1, p. 47, 2011.
- [52] GetData Graph Digitizer, Software Package, Ver. 2.26, 2013, <http://getdata-graph-digitizer.com/index.php>.
- [53] H. Qu, J. Hu, and X. Gao, “The impact of Reynolds number on two-dimensional aerodynamic airfoil flow,” in *Proceedings of the 1st World Non-Grid-Connected Wind Power and Energy Conference (WNWEC '09)*, pp. 121–124, Nanjing, China, September 2009.
- [54] M. D. Maughmer and J. G. Coder, “Comparisons of theoretical methods for predicting airfoil aerodynamic characteristics,” U.S. Army Aviation Research, Development and Engineering Command RDECOM TR 10-D-106, 2010.
- [55] F. G. Schmitt, “About Boussinesq’s turbulent viscosity hypothesis: historical remarks and a direct evaluation of its validity,” *Comptes Rendus Mécanique*, vol. 335, no. 9-10, pp. 617–627, 2007.

Research Article

Parallel Numerical Simulations of Three-Dimensional Electromagnetic Radiation with MPI-CUDA Paradigms

Bing He, Long Tang, Jiang Xie, XiaoWei Wang, and AnPing Song

High Performance Computing Centre, Shanghai University, Shanghai 200436, China

Correspondence should be addressed to Bing He; hebing@shu.edu.cn

Received 28 August 2014; Accepted 15 December 2014

Academic Editor: L. W. Zhang

Copyright © 2015 Bing He et al. This is an open access article distributed under the Creative Commons Attribution License, which permits unrestricted use, distribution, and reproduction in any medium, provided the original work is properly cited.

Using parallel computation can enhance the performance of numerical simulation of electromagnetic radiation and get great runtime reduction. We simulate the electromagnetic radiation calculation based on the multicore CPU and GPU Parallel Architecture Clusters by using MPI-OpenMP and MPI-CUDA hybrid parallel algorithm. This is an effective solution comparing to the traditional finite-difference time-domain method which has a shortage in the calculation of the electromagnetic radiation on the problem of inadequate large data space and time. What is more, we use regional segmentation, subregional data communications, consolidation, and other methods to improve procedures nested parallelism and finally verify the correctness of the calculation results. Studying these two hybrid models of parallel algorithms run on the high-performance cluster computer, we draw the conclusion that both models are suitable for large-scale numerical calculations, and MPI-CUDA hybrid model can achieve higher speedup.

1. Introduction

Finite-difference time-domain (FDTD) method has become a common method for solving Maxwell's equations [1]. It is a full vector method and can be naturally given time-domain and frequency-domain information user need. This is the unique advantage in electromagnetic and photonic application. FDTD algorithm is discrete in terms of time and space. Therefore, the structure of the electromagnetic field must be described on the grid by the Yee cellular composition. Maxwell's equation is discrete in time factor; therefore, time step is closely related to the mesh size. When mesh size tends to zero in the limit case, the discrete model accurately describes Maxwell's equations.

Recently, general-purpose computing on a graphics processing unit (GPGPU) has received considerable attention in many scientific fields [2–4] because a GPGPU offers high computational performance at low cost. What is more, Intel Xeon Phi coprocessor, based on the Many Integrated Core (MIC) architecture, packs up to 1 TFLOP of double precision performance in one chip. It runs a Linux operations system and provides x86 compatibility and also supports several popular programming models including MPI, OpenMP,

Thread Building Blocks, and others that are used on multicore architectures. High-performance computer architecture tends to hybrid system, and this corresponds to the software program design requirements mixed programming model. GPGPU and MIC accelerated computing components which appeared in recent years provide the opportunity to improve the performance of FDTD parallel algorithm. Therefore, we achieved the parallel three-dimensional FDTD algorithm based MPI-CUDA model.

The FDTD algorithm obtains a wide range of applications in many fields of electromagnetic radiation, such as radiation antenna analysis, scattering calculations, electronic packaging, and radar. With the development of high-performance computing, the MPI has solved a weakness that the computing time of the FDTD parallel algorithm [5, 6] is too long. However, increasing amount of computation, the MPI process in a single node increases computational burden. When we use two different hybrid models which are MPI-OpenMP model and MPI-CUDA model to solve this problem, we can use the distributed shared memory features to improve the parallel speedup and scalability [7, 8].

The rest of the paper is organized as follow. We present the FDTD algorithm with uniaxial perfectly matched layer

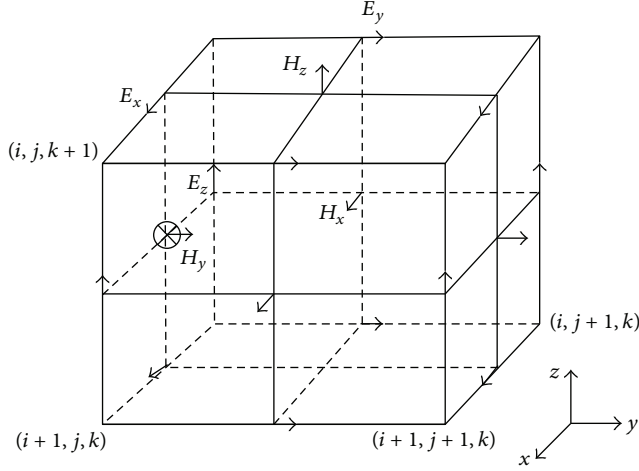


FIGURE 1: The structure of Yee cell.

(UPML) in Section 2. Then we describe the procedure and present basic steps for the method acceleration by means of MPI-OpenMP paradigms and MPI-CUDA paradigms in Sections 3 and 4. In Section 5, the performance of parallel computing of the two methods was compared and analyzed the factor that affects performance. The conclusions are given in Section 6 finally.

2. FDTD Algorithm

FDTD algorithm is a numerical method based on Maxwell's equations. The algorithm uses leapfrog calculation method and alternating electric field and magnetic field distribution in space within a half step sampling by Yee cellular composition [9].

From Figure 1, we can see that the Yee cell has the following characteristics: each magnetic field component was surrounded by four electric field components and each electric field component was surrounded by the four components of the magnetic field, and these field components placement relative position in the Yee cell and automatically satisfy the continuity conditions in the interface. This sampling method not only meets Maxwell's equations difference calculation but also meets Faraday's law of electromagnetic induction and the natural Ampere's law [10]. Therefore, this method gradually completes recursive entire electromagnetic fields. First, the explicit equations for the E_x and H_x are given by

$$\begin{aligned}
 E_x^{n+1} \left(i + \frac{1}{2}, j, k \right) &= CA \left(i + \frac{1}{2}, j, k \right) + CD \cdot CB \left(i + \frac{1}{2}, j, k \right) \\
 &\cdot \left[H_z^{n+1/2} \left(i + \frac{1}{2}, j + \frac{1}{2}, k \right) - H_z^{n+1/2} \left(i + \frac{1}{2}, j - \frac{1}{2}, k \right) \right. \\
 &\quad \left. - H_y^{n+1/2} \left(i + \frac{1}{2}, j, k + \frac{1}{2} \right) \right. \\
 &\quad \left. + H_y^{n+1/2} \left(i + \frac{1}{2}, j, k - \frac{1}{2} \right) \right]
 \end{aligned} \quad (1)$$

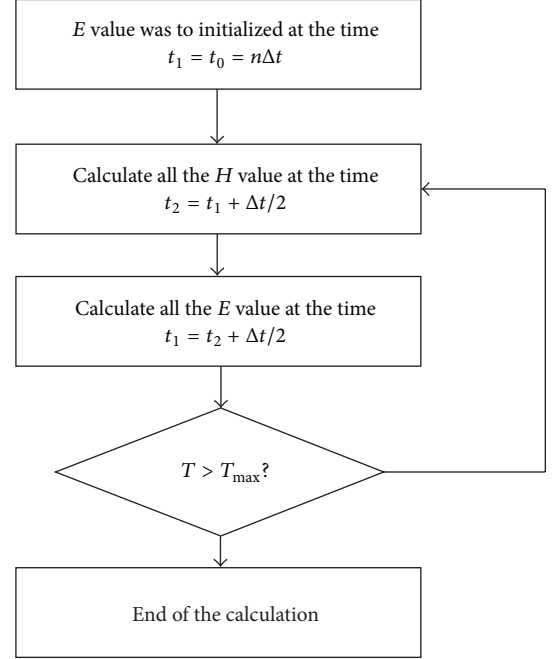


FIGURE 2: The workflow of the FDTD method.

$$\begin{aligned}
 H_x^{n+1/2} \left(i, j + \frac{1}{2}, k + \frac{1}{2} \right) &= H_x^{n-1/2} \left(i, j + \frac{1}{2}, k + \frac{1}{2} \right) + CD \\
 &\cdot \left[E_y^n \left(i, j + \frac{1}{2}, k + 1 \right) - E_y^n \left(i, j - \frac{1}{2}, k \right) \right. \\
 &\quad \left. - E_z^n \left(i, j + 1, k + \frac{1}{2} \right) + E_z^n \left(i, j, k - \frac{1}{2} \right) \right],
 \end{aligned} \quad (2)$$

where

$$\begin{aligned}
 CA(i, j, k) &= \frac{(1 - \sigma(i, j, k) \Delta t / 2\epsilon(i, j, k))}{(1 + \sigma(i, j, k) \Delta t / 2\epsilon(i, j, k))}; \\
 CB(i, j, k) &= \frac{\epsilon_0}{\epsilon(i, j, k)} + \frac{\sigma(i, j, k) \Delta t}{2\epsilon(i, j, k)}; \\
 CD &= \frac{\Delta t}{\delta \sqrt{\epsilon_0 \mu_0}},
 \end{aligned} \quad (3)$$

where ϵ is the relative permittivity, σ is the conductivity of the tissue [S/m], δ is the mesh size, and Δt is the time step. Figure 2 shows the workflow of the FDTD method.

The explicitly iterative process of FDTD algorithm requires initial field values and boundary conditions. The traditional definition of initial field values put all the space field values which are defined as 0, then the field values of two successive time steps are stored as the initial field value of the next step. There are a variety of the boundary conditions, such as Mur absorbing boundary, perfectly matched layer (PML), and uniaxial perfectly matched layer [11] (UMPL). With the improvement of FDTD algorithm these three matching layers have good effect on absorption.

In our experiments, we use uniaxial perfectly matched layer (UPML) as absorbing boundary condition. UPML inherited the PML absorbing layers good absorption characteristics, but the UPML absorbing layer is directly based on Maxwell's equations which is different from PML absorbing layer. This ensures that the form of FDTD algorithm calculation model has good consistency with Maxwell's equations, which makes it easier to understand and program.

3. FDTD Algorithm Based on MPI-OpenMP

3.1. MPI-OpenMP Hybrid Model. MPI programming model is a parallel programming interface for developing standards based messaging, acting on a heterogeneous network environment. It provides a reliable transport mechanism, and it uses security channel to achieve the communication between all the tasks within a process group, data exchange and processing. However, MPI is calculated by parallel interprocess communication, which results in a lower efficiency, the parallel memory overhead, programming problems, and other shortcomings. The OpenMP programming model utilizes fork-join execution mode and shared memory model where a process can be divided into several parallel task execution threads. In a single node, when the main thread is running into OpenMP parallel region, it will produce different thread queue to achieve a parallel effect. However, since OpenMP parallel programming model can only be a single node, computing power of the CPU has been greatly restricted.

MPI-OpenMP programming model is the combination of these two models, which is between multiple machines using MPI distributed memory and each MPI process uses multithreaded OpenMP shared memory model to parallel computing [12]. This model can reduce the number of MPI processes in parallel, thereby reducing the number of messages passing. What is more, OpenMP parallel on each node can save memory overhead. So this parallel hybrid model has certain advantage over a single model.

3.2. The Division of MPI Model. According to the different regional calculation scale, each division way has different characteristics. Common area includes one-dimensional, two-dimensional, and three-dimensional division. In the cube model, each section of the communication direction is all the same, which means that the communication traffic is proportionate to the number of communication surfaces. Three-dimensional method produces the minimal communication surface. Therefore, we should select the three-dimensional division in the balanced scales calculating. But when the area which you calculated is dominant in one direction or in both directions, the communication traffic is not proportional to the number of communication surfaces. The one-dimensional or two-dimensional division can get better results. For example, long waveguide will be divided one-dimensional along the waveguide direction. In addition wing aircraft is usually divided two-dimensional along its width direction.

In this paper, the computational model which is similar to the phone box is an extreme rectangular model. We

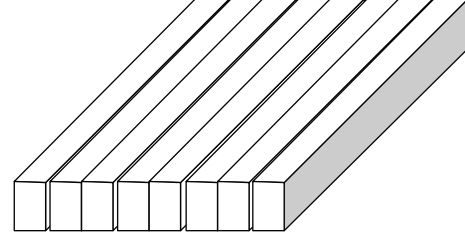


FIGURE 3: The division of rectangular computational model.

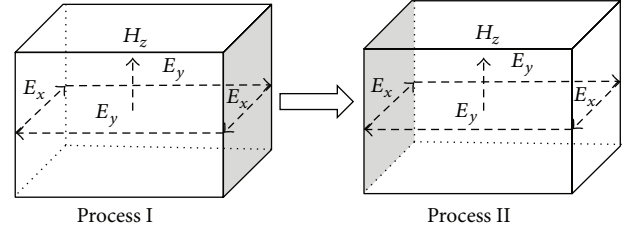


FIGURE 4: Data communication between processes.

performed a one-dimensional division by the meshing and each process is assigned to one node on average to obtain high efficiency. This division can be reduced communication time between nodes in the rectangular model (Figure 3).

3.3. MPI Parallel Communication Design. As shown in (1), FDTD field value for each step of the algorithm depends only on the value of magnetic field intensity and the circumference value of the grid, which means that it has significantly localized. Therefore, MPI algorithm just calculates the area into a plurality of subregions, and each subregion is allocated MPI node in the mesh to ensure the exchange data in the each time step. Finally, we synchronize data of each node at end of the step. In order to obtain high efficiency of parallel speedup, we partition the process by X direction and put the processes average assigned to each node. This partitioning can reduce the communication between nodes time in the X direction dominant of the rectangular parallelepiped model.

After the calculate area is divided into a number of subregions. The data communication is shown in Figure 4. If we want to calculate H_z which is in process II, we should require the value of electric fields E_x and E_y which is in process I. Then process I transfers the values to process II. H_z can begin calculating when data exchange is completed. Obviously, the data in the other direction can communicate with each other in this way.

3.4. OpenMP Threaded Design and Optimization. The electric field and magnetic field strength only depends on the electromagnetic field data of the former step in the electromagnetic computing. Therefore, it has the natural parallelism. In the multicore computing, the program uses OpenMP model to increase program parallelism.

For better memory utilization, the load balancing may not be very good; therefore, when considering performance optimization, we should have a compromise between the

```
#pragma omp parallel for schedule(static)
for (i = 1; i < ie_tot; i++)
  for (j = 0; j < je_tot; j++)
    for (k = 0; k < ke_tot; k++)
      ...
```

In order to increase OpenMP load balance and get better scalability, we merge the nested loops and reduce from 3 nest layers to 2 layers.

```
_end = je_tot;
ij_end = (ie_tot) * (je_tot);
ij_start = j_end + 1;
#pragma omp parallel for schedule(static)
for (ij = ij_start; ij < ij_end; ij++)
{
  i = ij / j_end;
  j = ij;
  if (!i) continue;
  for (k = 0; k < ke_tot; k++)
    ...
}
```

ALGORITHM 1

need to optimize memory utilization and load balancing. In OpenMP model, there are four kinds of commonly used scheduling, such as static, dynamic, guided, and runtime. The commonly used scheduling is static where iterations are divided into chunks of size `chunk_size` while chunks are assigned to threads in the team in round-robin fashion in order of thread number and dynamic where each thread executes a chunk of iterations and then requests another chunk until no chunks remain to be distributed.

From the definitions of the schedule, we can see that static scheduling applies to the situation that all CPU functions are similar due to the complexity of balancing reasons, while the dynamic scheduling applies to the situation of the ability to run large differences between the CPUs. Due to the experimental environment that each CPU computing power is not very different, we use static scheduling so that each thread can average computing tasks [13] (see Algorithm 1).

Its obvious that x , y , and z directions have similar calculation.

3.5. MPI-OpenMP Hybrid Programming. With the increasing scale of operation, the shared storage processor overhead of process limits parallel performance. We can solve this problem by OpenMP and MPI hybrid model where each node is calculated by MPI processes and each node uses the optimal number of threads. Thus the amount of computation is shared by multiple threads, thereby reducing communication overhead and easing the process workload on each node.

When FDTD algorithm based on MPI-OpenMP model allocates a process for each compute node, each node is assigned a process. Passing MPI initialization and calculation parameters initialization, the process starts OpenMP parallel computing. In this phase, the program should update cycle electric field value and the electric field value with adjacent nodes exchanges the date. After the communication is completed, CPUs use OpenMP programming model to

update the value of the magnetic field. When the programs achieve the maximum time step, MPI processes and the main procedures will end. As for the border absorption treatment, process calculation is carried out in a single process in every time step. Therefore, it can also improve program parallelism through OpenMP model.

The pseudocode is as shown in Algorithm 2.

4. MPI + GPU Programming Model Design

4.1. FDTD Parallel Algorithm Based on GPU Model. FDTD is the most popular method of computational electromagnetic simulation because of its simple algorithm and high computational efficiency. Figure 5 shows the flow of the three-dimensional FDTD method for a single GPU computation [14]. There are four tasks within each time step for the GPU side in this figure: electric field computation (e_field), uniaxial perfectly matched layers (UPML) computation for electric field (e_upml) as the absorbing boundary condition, magnetic field computation (h_field), and PML for magnetic field (h_upml). All field updates in each time step can be parallelized and are offloaded to the GPU [15].

Our GPU implementation of the FDTD method is based on the C++ code that runs on the ZiQiang4000 high-performance computer clusters of Shanghai University. Since all the magnetic and electric field computations can be vectored and parallelized, these computations are also candidates for GPU computation with a CUDA kernel. The CUDA kernel including e_field , e_pml , h_field , and h_pml follows. And our GPU three-dimensional FDTD program requires no data transfer for field updates because of all computations within each time. The CUDA kernel function [16] would be in Algorithm 3.

4.2. The Optimized Memory of Access Patterns. The kernel code which can be called by the GPU has role similar to

```

MPI_Init(&argc, &argv); //MPI parallel environment initialization
MPI_Comm_rank(MPI_COMM_WORLD, &rank);
MPI_Comm_size(MPI_COMM_WORLD, &size);
MPI_Get_processor_name(processor_name, &namelen);
MPI_Barrier(MPI_COMM_WORLD);
node.init(x_size/size, y_size/size, z_size/size); //Grid data initialization
UPMLcompute(); //Set up the absorbing boundary
for (int i = 0; i < max_step; i++) //Iterating over the time step
{
#pragma omp parallel for schedule(static)
    for (i = 1; i < ie_tot; i++)
    {
        ...Compute; //Calculating the electric field and magnetic field values
    }
    MPI_Send(datasend_right, data_size, MPI_DOUBLE, NodeRank + 1, 1,
    MPI_COMM_WORLD); //Send data to the neighboring node
    MPI_Recv(datarecv_right, data_size, MPI_DOUBLE, NodeRank + 1, 1, MPI_COMM_WORLD,
    &status); //Accept the adjacent node data
    MPI_Barrier(MPI_COMM_WORLD);
}
MPI_Finalize();
Out(EHdate); //Output the results

```

ALGORITHM 2

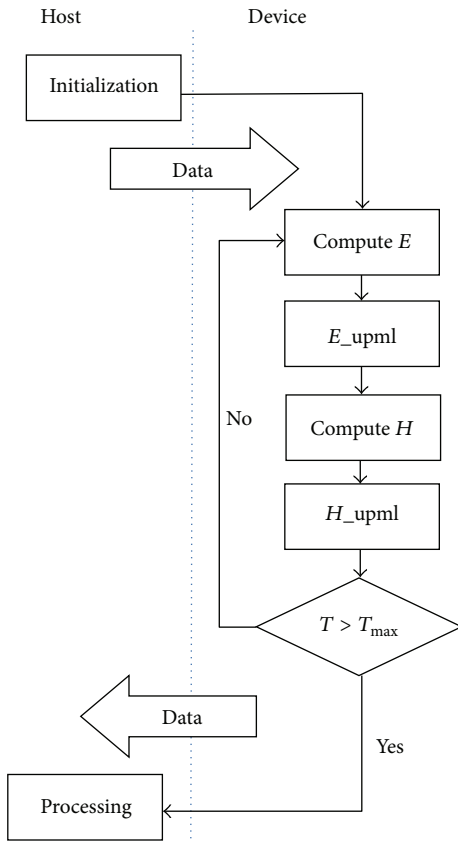


FIGURE 5: The workflow of the three-dimensional FDTD method for a single GPU computation.

caluH C function. The kernel variable threadIdx, blockIdx, and blockDim can calculate the array indexes ix , iy , and iz . Host-side code then uses caluH «grid, block» (arguments) function to call the kernel code, where grid and block specify the division of thread blocks and the number of threads in the each block.

As the internal memory of GPU, registers and shared memory have a high access speed and a small data latency. Therefore, the data is loaded into the global memory so that shared memory can improve the efficiency of GPU parallel. Consider

```

_shared_double new_hx[];
new_hx [hx_size] = hx [hx_size].

```

The first line of code is carried in the shared memory array definition. Since the shared memory space is very limited, programmer should choose dynamically allocated arrays or static allocation based on the data size. The second line was to load the data into the global memory shared memory which can increase memory access speed by data sharing. Obviously, other data should also do the same optimization.

4.3. MPI-CUDA Hybrid Programming. In the MPI programming model, a problem will be divided into multiple subtasks so that each process to execute a task. But with the growth of the scale, MPI communication overhead increases at the same time; thereby this will reduce the parallel efficiency. However, the model is just coarse-grained parallelism between the nodes, and computing capacity of CPU is not fully utilized. Then the CUDA model is just to make up the deficiency of this section. The use of multithreaded shared memory

```

__global__ void caluH(arguments)
{
    ix = threadIdx.x + blockIdx.x * blockDim.x;
    iy = threadIdx.y + blockIdx.y * blockDim.y;
    iz = threadIdx.z + blockIdx.z * blockDim.z;
    if (ix < ex_size && iy < ey_size && iz < ez_size)
    {
        int i = ix * ez_size * ey_size + iy * ez_size + iz;
        double tmp = _bx[i];
        _bx[i] = D1 * _bx[i] - D2 * ((_ez[i + ez_size] - _ez[i]) - (_ey[i + 1] - _ey[i]))/delta;
        _hx[i] = D3 * _hx[i] + D4 * (D5 * _bx[i] - D6 * tmp)
    }
}
}
The host:
dim3 block(BlockDim[0], BlockDim[1], BlockDim[2]);
Grid[0] = nx/blockDim[0];
Grid[1] = ny/blockDim[1];
Grid[2] = nz/blockDim[2];
dim3 grid (Grid[0], Grid[1], Grid[2]);
caluH <<<grid, block>>> (arguments);

```

ALGORITHM 3

mechanism on the GPU achieves data sharing fine-grained parallelism, which can achieve higher speedup [17].

In order to reduce the computational load of the GPU, we use a single node in a multi-GPU programming model [18], which means that each process is calculated by calling the function `cudaSetDevice()` to get two GPUs in a single node.

Workflow of three-dimensional FDTD program based MPI-CUDA model is as follows.

- (1) Initialize calculation parameter GPU and MPI environment.
- (2) Divide the regional calculation and allocate GPU memory and copy initial data to GPU.
- (3) Time step for-loop Use MPI model.
 - (a) execute electric field computation on GPU
 - (b) execute magnetic field computation on GPU.
- (5) Process output results.

5. Experiments and Analysis

5.1. Experimental Environment. ZiQiang4000 normal cluster is constituted of 40-unit IBM X240 server blade, which contains two intel E5-2680, 64 G shared memory, and 16 core components in each blade. The GPU computing cluster node contains 11 sets of IBM DX360, which has two intel E5-2680, 64 G shared memory, and plus two Nvidia M2090 GPU constitution. The software environment of the system includes Centos Linux 6.3 operating system, NVCC compiler supports OpenMP guided C/C++ compiler, and MPICH2 parallel environment.

5.2. Model Validation and Analysis. Verifying the correctness of parallel programs is a prerequisite for its performance analysis. In order to verify the correctness of the program

TABLE 1: The result of FDTD algorithm based on MPI.

Process	Overall time(s)	Speedup ratio	Communication area ($\times 10^3$)	Efficiency (%)
1	17146	1	0	100
2	8956	1.9144	32	95.72
4	4632	3.7012	99	92.59
8	2306	7.4353	230	92.9
16	1188	14.4327	482	90.21
32	623	27.5217	1017	86.01
48	422	40.6303	1540	84.64
64	338	50.7221	2066	79.25

and UMPL absorbing boundary absorption effect, this paper makes use of three-dimensional point source radiation to have a situation analysis. we compared the run time between GPUs and CPUs in the case of Gaussian incidence at 900 MHz. What is more, the grid size is 0.02 mm and the calculation scale is of $100 \times 100 \times 100$. We use UPML absorbing layer which is set to 10-mesh size and the maximum time step 1000. Figure 6 shows the 50 layers and 65 layers of XY section of the electric field strength calculations at the 1000 steps. As we can see in the figure, electromagnetic waves shape was diffusion, and the further the cross-sectional layer of electric field away from the excitation source, the smaller the value you get. The excitation source is at the center of the field map and gradually spreads to the electromagnetic field borders, which fits the propagation of electromagnetic waves.

5.3. Parallel Analysis. In order to obtain intuitive results, we expand the calculated scale to $1024 \times 256 \times 128$, and the absorbing boundary UMPL mesh size is set to 16. The results were as follows after 1000 steps calculation using MPI model.

Table 1 shows the result of point source radiation calculation time based on the MPI model, such as speedup

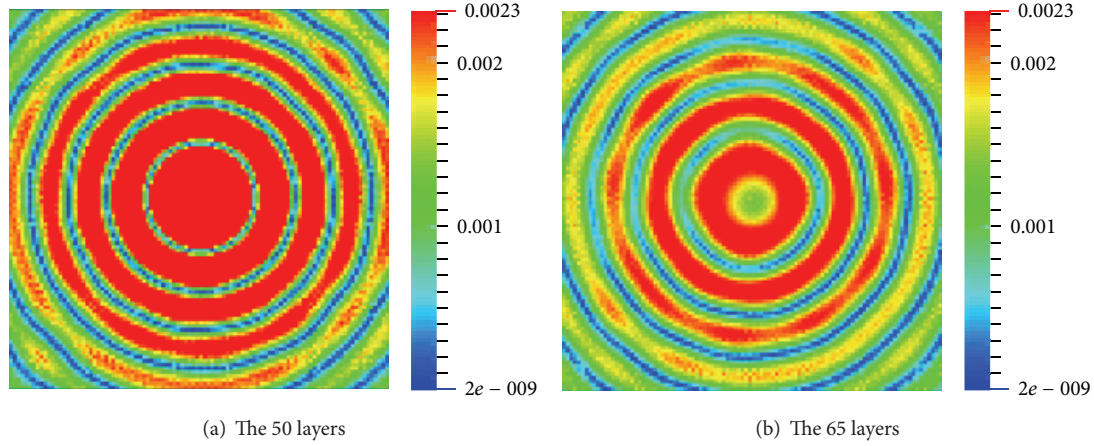
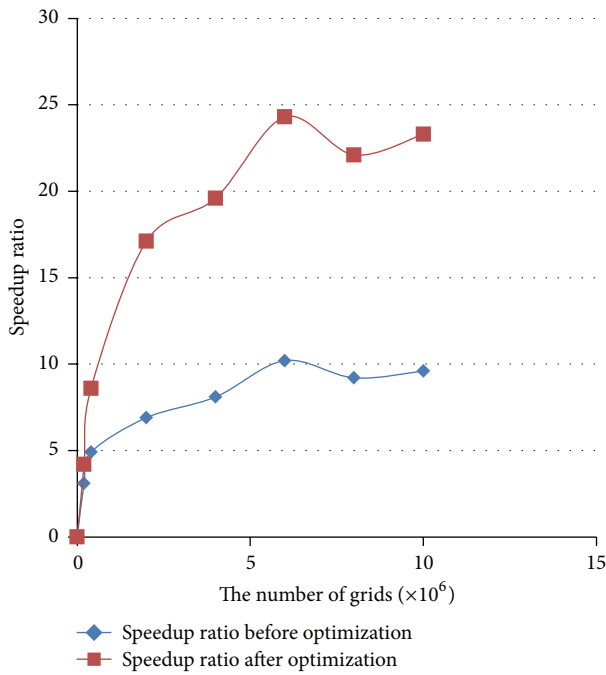
FIGURE 6: The electric field strength calculations of sectional x - y at 1000 steps.

FIGURE 7: GPU/CPU speed ratio.

and efficiency of the communication area. In this paper, we performed 16 processes on each node. It can be seen from the table that, as the number of processes increases, the computing time significantly reduced for linear speedup. And the electromagnetic radiation program has good scalability and parallelism in a distributed process parallel environment. But with the increase in the number of processes, the parallel efficiency becomes more and more low. This is because the increase in the number of processes leading to the communication area is increasing. It will increase the communication overhead and cause the load between nodes to be not balanced.

From Figure 7, we can see that, when calculating small scale, the acceleration effect of GPU is not obvious. This is

due to the number of threads too little to create enough block to make SM concurrent execution, reducing GPU occupancy rate. With the increasing of the calculation size, GPU computing resources gradually are called and the speed of computation is improved. Therefore, when calculating a smaller scale, GPU speed increase is limited, and in the large-scale electromagnetic calculations, GPU-accelerated effects model is very impressive, which is reaching about 9 times the CPU. After optimizing memory access patterns by shared storage, the max speed ratio achieves 23 when the number of grids is 6×10^6 . The reason is segmentation of data blocks fit in GPU memory.

MPI-OpenMP hybrid programming model combines two kinds of models, which can take advantage of shared memory and message passing model and improve FDTD algorithm parallelism. FDTD program is mainly calculated by the parameter initialization, the time step, absorbing boundary calculated, updating the electric field, and data processing. However, over 98% of the total time is conducted in two stages which are absorbed electromagnetic boundaries update phase and calculating electromagnetic fields. We can utilize OpenMP programming model to improve program parallelism at this two stages. In this paper, each node runs two processes, and the number of parallel threads is 8. Similarly, MPI-CUDA models use shared memory and message passing mechanism to calculate the electric field value performed on the GPU. Each block is divided into $16 \times 16 \times 16$, and the calculation results are shown in Table 2.

From Columns 2 and 3 of Table 2, it can be seen that pure MPI program is better than MPI-OpenMP model when the calculating cores is small. This is because MPI communication is very small when the number of processes is small, and OpenMP program will be a corresponding increase in the thread overhead. But with the increase of the number of the GPUs, the growth rate of MPI model will decline as MPI process communication and synchronization overhead increases, while MPI-OpenMP program obtains a better parallelism for saving offset cost of the thread. By comparing the two parallel methods, we can see MPI application performance superior to MPI-OpenMP program

TABLE 2: The result of FDTD algorithm based on all models.

Process	MPI model		MPI-OpenMP model		MPI-CUDA model	
	Overall time(s)	Speedup ratio	Overall time(s)	Speedup ratio	Overall time(s)	Speedup ratio
1	17146	1	17146	1	803	21.3524
4	4632	3.7012	4697	3.6504	217	79.0138
8	2306	7.4353	2376	7.2163	109	157.3028
16	1188	14.4327	1210	14.1702	79	217.0378
32	623	27.5217	615	27.8797	68	252.1471
48	422	40.6303	407	42.7581	61	281.082

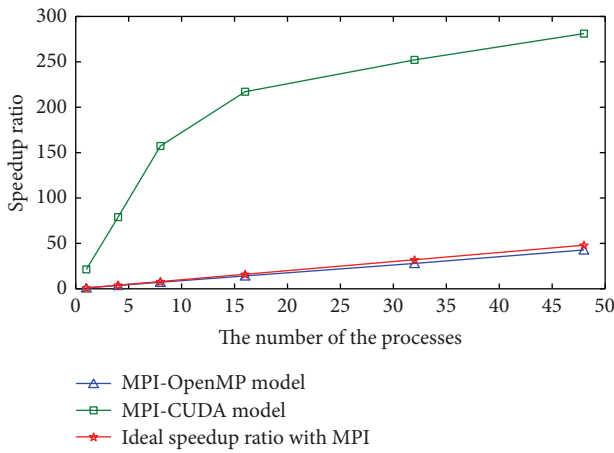


FIGURE 8: The result of FDTD algorithm based on two hybrid models.

when calculating the cores is less than 32. But with the increase in the number of cores, the advantage of MPI-OpenMP program will gradually be revealed and get better speedup.

From Columns 2 and 4 of Table 2, it can be seen that pure MPI-CUDA program is better than pure MPI model, and it has a linear increase when the number of processes is small. But with the increase in the number of processes, the efficiency of the program decreased very significantly. MPI communication overhead is increased in the proportion of the total time. As the overall calculation region is divided into a plurality of subregions, the size of each process significantly reduced to GPU parallel efficiency. We can find that the speedup of MPI-CUDA programming model is about 20 times the pure MPI program, which effectively improved the parallelism of the program.

Figure 8 shows the result of FDTD algorithm based on two hybrid models. Due to the GPU's high-speed floating-point operations, MPI-CUDA parallel model clearly has a better effect. However, this model is limited by memory and is device-dependent. MPI-OpenMP program can save communication costs and have better scalability. These two kinds of parallel models are suitable for mass-scale electromagnetic calculations which conform the actual electromagnetic calculations. Therefore, the programmer should be

selected by different hybrid models according to the different circumstances.

6. Conclusions

With the development of high-performance computing, the new technology provides a better use of space for FDTD algorithm. The various parallel models make hybrid programming model become the mainstream of high-performance computing. In this study, we implemented the three-dimensional FDTD method by MPI-OpenMP model. What is more, we also implemented FDTD method on multi-GPU cluster environment with CUDA and MPI and fulfilled the simulation of three-dimensional numerical electromagnetic radiation. The results indicate that hybrid programming model can better take advantage of distributed shared memory in order to improve parallel performance.

Conflict of Interests

The authors declare that there is no conflict of interests regarding the publication of this paper.

Acknowledgments

This work was supported by the Major Research Plan of NSFC [no. 91330116], the National Science Foundation of China [no. 71203135], Key Project of Science and Technology Commission of Shanghai Municipality [no. 11510500300], and the Research Fund for the Doctoral Program of Higher Education [no. 20113108120022].

References

- [1] R. F. Harrington, *Time-Harmonic Electromagnetic Fields*, McGraw-Hill Electrical and Electronic Engineering Series, McGraw-Hill, 1961.
- [2] M. de Greef, J. Crezee, J. C. van Eijk, R. Pool, and A. Bel, "Accelerated ray tracing for radio-therapy dose calculations on a gpu," *Medical Physics*, vol. 36, no. 9, pp. 4095–4102, 2009.
- [3] S. Adams, J. Payne, and R. Boppana, "Finite difference time domain (FDTD) simulations using graphics processors," in *Proceedings of the DoD High Performance Computing Modernization Program Users Group Conference*, pp. 334–338, June 2007.

- [4] N. Takada, T. Shimobaba, N. Masuda, and T. Ito, "High-speed FDTD simulation algorithm for GPU with compute unified device architecture," in *Proceedings of the IEEE Antennas and Propagation Society International Symposium (APSURSI '09)*, pp. 1–4, Charleston, SC, USA, June 2009.
- [5] C. Guiffaut and K. Mahdjoubi, "A parallel FDTD algorithm using the MPI library," *IEEE Antennas and Propagation Magazine*, vol. 43, no. 2, pp. 94–103, 2001.
- [6] Z. Yu, D. Wei, and L. Changhong, "Analysis of parallel performance of MPI based parallel FDTD on PC clusters," in *Proceedings of the Asia-Pacific Conference Proceedings and Microwave Conference Proceedings (APMC '05)*, vol. 4, p. 3, IEEE, December 2005.
- [7] P. Micikevicius, "3D finite difference computation on GPUs using CUDA," in *Proceedings of the 2nd Workshop on General Purpose Processing on Graphics Processing Units (GPGPU '09)*, pp. 79–84, ACM, 2009.
- [8] T. Nagaoka and S. Watanabe, "A GPU-based calculation using the three-dimensional FDTD method for electromagnetic field analysis," in *Proceedings of the Annual International Conference of the IEEE Engineering in Medicine and Biology Society (EMBC '10)*, pp. 327–330, IEEE, September 2010.
- [9] A. Taflov and S. C. Hagness, *Computational Electromagnetics: The Finite-Difference Time-Domain Method*, Artech House, London, UK, 3rd edition, 2005.
- [10] W. Yu, "A novel hardware acceleration technique for high performance parallel fdtd method," in *Proceedings of the 2nd IEEE International Conference on Microwave Technology and Computational Electromagnetics (ICMTCE '11)*, pp. 441–444, May 2011.
- [11] S. D. Gedney, "An anisotropic perfectly matched layer-absorbing medium for the truncation of FDTD lattices," *IEEE Transactions on Antennas and Propagation*, vol. 44, no. 12, pp. 1630–1639, 1996.
- [12] M. F. Su, I. El-Kady, D. A. Bader, and S.-Y. Lin, "A novel FDTD application featuring OpenMP-MPI hybrid parallelization," in *Proceedings of the International Conference on Parallel Processing (ICPP '04)*, pp. 373–379, August 2004.
- [13] J. Li, J. Shu, Y. Chen, D. Wang, and W. Zheng, "Analysis of factors affecting execution performance of openMP programs," *Tsinghua Science & Technology*, vol. 10, no. 3, pp. 304–308, 2005.
- [14] Nvidia Corporation Technical Staff, *Nvidia Cuda C Programming Guide*, Chapter 12, NVIDIA Corporation, 2012.
- [15] T. Nagaoka and S. Watanabe, "Multi-GPU accelerated three-dimensional FDTD method for electromagnetic simulation," in *Proceedings of the 33rd Annual International Conference of the IEEE Engineering in Medicine and Biology Society (EMBS '11)*, pp. 401–404, IEEE, September 2011.
- [16] D. S. Cai, Y. Li, K.-I. Nishikawa, C. Xiao, and X. Yan, "Three-dimensional electromagnetic particle-in-cell code using high performance fortran on PC cluster," in *High Performance Computing*, vol. 2327 of *Lecture Notes in Computer Science*, pp. 515–525, Springer, Berlin, Germany, 2002.
- [17] V. Demir and A. Z. Elsherbeni, "Programming finite-difference time-domain for graphics processor units using compute unified device architecture," in *Proceedings of the IEEE Antennas and Propagation Society International Symposium (APSURSI '10)*, pp. 1–4, Toronto, Canada, July 2010.
- [18] D. A. Jacobsen, J. C. Thibault, and I. Senocak, "An MPI-CUDA implementation for massively parallel incompressible flow computations on multi-GPU clusters," in *Proceedings of*

the 48th AIAA Aerospace Sciences Meeting Including the New Horizons Forum and Aerospace Exposition, vol. 16, January 2010.

Research Article

Development of Fast-Time Stochastic Airport Ground and Runway Simulation Model and Its Traffic Analysis

Ryota Mori

Air Traffic Management Department, Electronic Navigation Research Institute, 7-42-23 Jindaiji-Higashimachi, Chofu, Tokyo 182-0012, Japan

Correspondence should be addressed to Ryota Mori; r-mori@enri.go.jp

Received 28 August 2014; Accepted 18 October 2014

Academic Editor: Kim M. Liew

Copyright © 2015 Ryota Mori. This is an open access article distributed under the Creative Commons Attribution License, which permits unrestricted use, distribution, and reproduction in any medium, provided the original work is properly cited.

Airport congestion, in particular congestion of departure aircraft, has already been discussed by other researches. Most solutions, though, fail to account for uncertainties. Since it is difficult to remove uncertainties of the operations in the real world, a strategy should be developed assuming such uncertainties exist. Therefore, this research develops a fast-time stochastic simulation model used to validate various methods in order to decrease airport congestion level under existing uncertainties. The surface movement data is analyzed first, and the uncertainty level is obtained. Next, based on the result of data analysis, the stochastic simulation model is developed. The model is validated statistically and the characteristics of airport operation under existing uncertainties are investigated.

1. Introduction

Airport ground congestions are becoming a critical problem at many airports in the world. Since the bottleneck of airport operations exists on the runway, there are long waiting queues of aircraft both on the ground taxiway and in the air, which increase the fuel burn and emissions. Arrival aircraft are often considered in research targeting airport congestions decrease because any additional flight time obviously requires extra fuel. Even if not so apparent, departure aircraft burn sufficient amount of fuel during taxiing, too, so departure queue management can help to reduce fuel burn. Although there are some researches regarding the taxi-out time saving of the departure aircraft [1–5], these researches focus on taxi-out time saving and do not investigate its negative effect. One such possible negative effect caused by departure queue management is take-off delay.

The main reason for increased taxi-out time is that many departure aircraft wait in a queue before the runway due to runway congestion, so taxi-out time reduction is achieved by shifting the pushback time later intentionally. If the aircraft waits in the spot instead of waiting in a queue near the runway, the aircraft can turn its engines off and therefore

save fuel. However, if this shift is too large, the aircraft cannot take off at the expected time. If all airport operations were estimated without errors, the reduction of taxi-out time would be maximized without imposing any take-off time delay, but this is impossible due to various uncertainties. Even if large margins are set to absorb uncertainties, the expected delay will be close to 0, but not definitely 0. Besides, setting of a large margin leads to decrease the reduction of taxi-out time as well. Therefore, to evaluate uncertainty effects, stochastic simulation model is necessary. The main focus of this paper is the development of such a stochastic simulation model.

There are numerous airport simulation models proposed by many researchers already. However, this paper focuses on a stochastic model, which should also be appropriate to run a simulation fast enough. Most existing simulation models account for detailed aircraft movement but are also deterministic and slow, thus not suitable for the purpose of this paper [6–13]. Although some airport models consider uncertainty effect, such as the variance of taxiing speed or the take-off separation [14, 15], there are few researches considering uncertainties. In addition, uncertainty parameters are usually obtained via actual airport operation data, but only specific parameters are used in the simulation, and

no stochastic simulation model has been verified whether it accurately models the airport operation. For example, even when the variation of taxiing speed is assumed, the model does not estimate the take-off time well unless the model handles variation of take-off separation. Therefore, this paper aims at developing a sufficiently accurate stochastic airport simulation model to account for the uncertainty effect. The stochastic parameters are obtained based on the actual operation data in each phase of the aircraft movement, and, using these parameters, the taxi-out of each departure aircraft is simulated. The simulated take-off time is then compared to the actual take-off time. Using the developed simulation model, the characteristics of the airport operation are also investigated, and the importance of the uncertainty is revealed.

2. Stochastic Airport Simulation Model at Tokyo International Airport

Tokyo International Airport is the target airport of this research. First, the airport operation is briefly explained in Section 2.1, and a stochastic simulation model is developed. To conduct sufficient number of simulations to account for uncertainty effects, a single simulation run time should be short enough, so the model itself should be simplified. Error distribution models for stochastic components are introduced in Section 2.2, and taxi-out time of departure aircraft and taxi-in time of arrival aircraft are stochastically modeled in Section 2.3. Additional simulation constraints are explained in Section 2.4, and the take-off separation is stochastically modeled in Section 2.5. Finally, the simulation flow is shown and the model limitations are described in Section 2.6.

2.1. Tokyo International Airport and Its Runway Operation.

Tokyo International Airport is the busiest airport in Japan and is mostly used for domestic flights. In 2010, the traffic volume was 303,000 flights per year and increases to 447,000 flights per year in 2014 with the opening of the new runway. Figure 1 shows the airport map and typical operation under north wind. There are four runways at the airport. A runway is used for arrival and D runway is used for departure, but C runway is shared by both departure and arrival aircraft. Due to the runway location, aircraft departing from D runway cannot take off while a landing aircraft is approaching C runway. B runway is usually not used under north wind.

In order to model taxiing correctly, knowledge of the procedures preceding take-off is necessary. The air traffic control (ATC) flow of departure aircraft is summarized in Figure 2. First, about 5 minutes before the aircraft is ready for starting the engines, the pilot calls clearance delivery. If the flight plan is approved, the pilot will get a departure clearance from ATC. When the aircraft is ready for block-off, the pilot requests pushback to ATC. Once the pilot gets pushback approval, the aircraft starts pushback. During or after the pushback, the pilot requests taxiing to the runway. If the taxiing is approved and the aircraft is ready for taxiing, the aircraft will start taxiing. When the aircraft approaches

the runway, the pilot requests runway clearance. Only after the runway clearance is approved, the aircraft can take off.

Here, several variables are defined. The time when the pilot starts pushback is AOBT (actual off-block time), and actual take-off time is defined as ATOT. The difference between ATOT and AOBT is defined as AXOT (actual taxi-out time). Airport operation is not completely deterministic, and there are probabilistic factors. Therefore, considering certain uncertainty, AXOT is determined probabilistically in the simulation. The distribution of AXOT is examined in Section 2.3.

As for arrival aircraft, the aircraft lands at ALDT (actual landing time). After landing, the aircraft goes taxiing to the spot and block in at AIBT (actual in-block time). The duration of taxiing (AIBT-ALDT) is defined as AXIT (actual taxi-in time).

This time, the data used to determine the simulation parameters in this research are obtained based on the smoothened airport surface movement data for 20 days between 2012 and 2014 (called Day 1 to Day 20), when north wind operation was conducted throughout a day.

2.2. Error Distribution Model. To consider the error factor, several error distribution models are applied. In this research, normal distribution and Erlang distribution are used. Normal distribution, also known as Gaussian distribution, is a symmetric distribution. Detailed explanation is not given here, but it has two parameters: average μ and standard deviation (SD) σ . The probability density function of normal distribution is given by the following equation:

$$N(x; \mu, \sigma) = \frac{1}{\sqrt{2\pi}\sigma} \exp\left(-\frac{(x - \mu)^2}{2\sigma^2}\right). \quad (1)$$

Furthermore, to account for error's asymmetry, Erlang distribution is also introduced. This distribution is asymmetric and is defined only when x is greater than 0. This function is often used in the field of stochastic processes. There are two parameters: average μ and shape n (positive integer). The probability density function of Erlang distribution is given by the following equation. This distribution approaches the normal distribution as n increases:

$$E(x; \mu, n) = \frac{n^n x^{n-1} e^{-nx/\mu}}{\mu^n (n-1)!} \quad (x > 0). \quad (2)$$

2.3. Distribution of Taxi-Out Time (AXOT) and Taxi-In Time (AXIT). Taxi-out time is defined as the time between pushback start and take-off. To determine the taxi-out time, it is divided into several stages, and the duration of each stage is determined. Figure 3 shows the taxi-out flow. First, the aircraft has to complete pushback, defined as "pushback time" ($\Delta t_{\text{pushback}}$). Next, the aircraft has to be released from the pushback truck and prepare for taxiing, defined as "preparation time" ($\Delta t_{\text{prepare}}$). Then, the aircraft goes taxiing to the runway, defined as "taxiing time." If there is a queue before the runway, the aircraft will need to wait extra. The minimum time which an aircraft needs to cover the distance

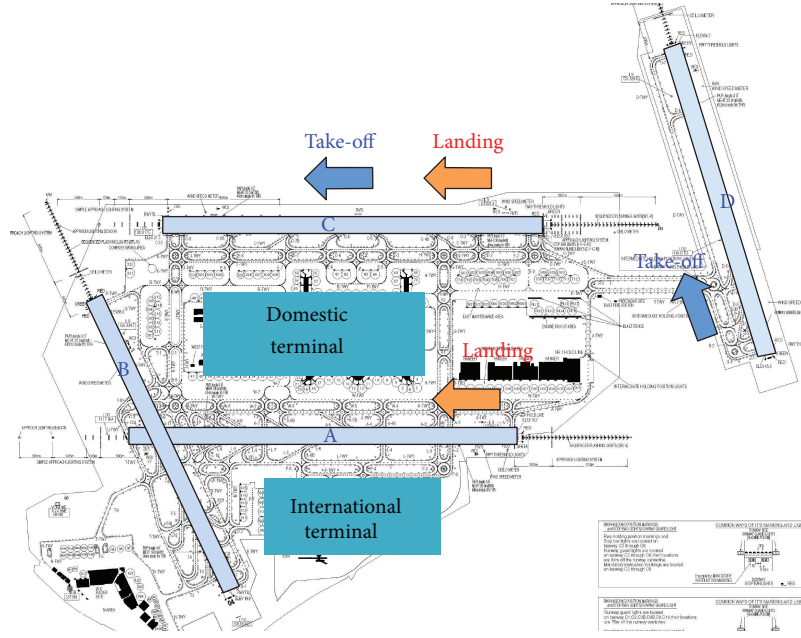


FIGURE 1: The airport map and runway operation under north wind.

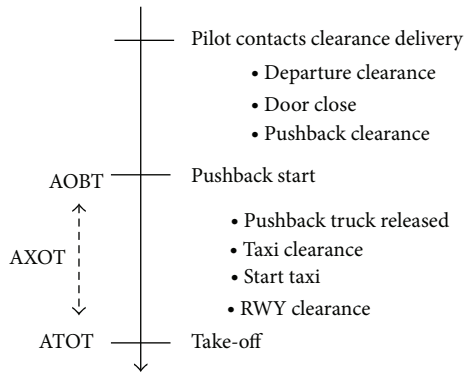


FIGURE 2: Flow of departure.

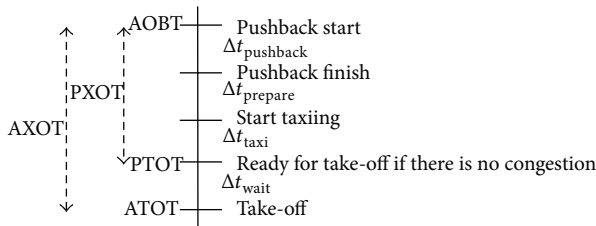


FIGURE 3: Taxi-out flow.

between its spot and the runway even when no congestion is observed is defined as “minimum taxiing time” (Δt_{taxi}). The difference between total taxiing time and minimum taxiing time is defined as “additional waiting time” (Δt_{wait}). Finally, taxi-out time (AXOT) is calculated by the following equation. Each time is estimated based on the data available:

$$AXOT = \Delta t_{\text{pushback}} + \Delta t_{\text{prepare}} + \Delta t_{\text{taxi}} + \Delta t_{\text{wait}} \quad (3)$$

Here, some variables are defined. PTOT (earliest possible take-off time) is defined as the time when the aircraft is ready for take-off assuming there is no congestion. PTOT is calculated by the following equation:

$$PTOT = ATOT - \Delta t_{\text{wait}} \quad (4)$$

PXOT (earliest possible taxi-out time) is also defined in the same way by the following equation:

$$PXOT = AXOT - \Delta t_{\text{wait}} = \Delta t_{\text{pushback}} + \Delta t_{\text{prepare}} + \Delta t_{\text{taxi}} \quad (5)$$

As for the pushback time ($\Delta t_{\text{pushback}}$), it is expected to depend on the pushback distance. The pushback distance and thus the pushback time are usually determined by the spot position. Another variable defined in this research is the preparation time ($\Delta t_{\text{prepare}}$). It includes the time for the pilot to receive a taxiing clearance and the time needed to release the pushback truck from the aircraft. This preparation time is assumed to be the same in all situations, so the sum of the pushback time and the preparation time ($\Delta t_{\text{pushback}} + \Delta t_{\text{prepare}}$) is assumed to depend on the spot position, and this variable (called setup time) is used for the data analysis. Figure 4 shows the average and standard deviation of setup time in each spot position. As seen in the figure, the average of setup time varies with spot position, but the standard deviation of setup time does not change significantly with spot positions. Therefore, the setup time is assumed to depend on the spot position only. Here, the difference between the average setup time and the actual setup time is denoted by the residual of the setup time, and it is fitted by the combination of normal distribution and Erlang distribution as shown in Figure 5.

The probability density function of setup time is calculated by the following function:

$$0.0959N(\Delta t_{\text{pushback}} + \Delta t_{\text{prepare}} - \bar{t}_{\text{setup}}(\text{spot}); 46.07, 78.72) \\ + 0.9041E(\Delta t_{\text{pushback}} + \Delta t_{\text{prepare}} - \bar{t}_{\text{setup}}(\text{spot}) \\ + 117.0; 122.0, 13), \quad (6)$$

where $\bar{t}_{\text{setup}}(\text{spot})$ is the average setup time in each spot obtained by data.

The next element needed to be defined in order to determine the earliest possible taxi-out time is the taxiing time (Δt_{taxi}). The taxiing time is basically related to taxiing distance, so it is modeled with the parameter of the taxiing distance. Of course, the taxiing time varies with each pilot, and some aircraft go faster taxiing while others go slower. In addition, if two aircraft are conflicted along the taxiing route, additional taxiing time is required. Here, these effects are included in uncertainty. When obtaining the data of taxiing time, only the value of the sum of taxiing time and waiting time ($\Delta t_{\text{taxi}} + \Delta t_{\text{wait}}$) is available, because the data of start taxiing time and take-off time is obtained based on the surface movement data. Here, only the data where the aircraft goes taxiing smoothly and is not stuck in the waiting queue are used to calculate the taxiing time, because the waiting time is assumed to be zero for such aircraft.

Figure 6 shows the relationship between taxiing distance and taxiing time for noncongested aircraft departing from D runway. Note that the red points indicate the aircraft whose spot is at the international terminal. The figure shows that there is a correlation between taxiing distance and taxiing time, and the residual tends to increase with the taxiing distance. Therefore, the distribution of the normalized residual (residual per 1km taxiing distance) is fitted by an Erlang distribution. In addition, the aircraft from the international terminal tends to have longer taxiing time, but that is because these aircraft have to cross A runway along the taxiing route and often wait due to passing landing aircraft. Therefore, it is assumed that these aircraft require additional taxiing time. Finally, the probability density function of taxiing time is calculated based on the following equations:

$$\text{C RWY: } E\left(\Delta t_{\text{taxi}} - 0.1090d_{\text{taxi}} - 68.03 - \Delta x; \frac{37.3d_{\text{taxi}}}{1000, 5}\right), \quad (7)$$

$$\text{D RWY: } E\left(\Delta t_{\text{taxi}} - 0.1002d_{\text{taxi}} - 71.60 - \Delta x; \frac{75.2d_{\text{taxi}}}{1000, 30}\right), \quad (8)$$

$$\Delta x = \begin{cases} 120, & \text{spot is in the international terminal.} \\ 0, & \text{otherwise.} \end{cases} \quad (9)$$

Taxiing route and route structure differ between C and D runways, so minimum taxiing time is calculated in a different manner. Once the spot position and the departure runway are determined, the taxiing distance and time are easily obtained.

TABLE 1: Prohibited departure time relative to the landing time on C runway.

	Prohibited start	Prohibited end
Departure from C runway	-65 s	+85 s
Departure from D runway	-80 s	+0 s

As for the arrival aircraft, the result of RWY C is well fitted, so the taxiing time is calculated based on (7).

Finally, the additional waiting time (Δt_{wait}) is considered. The additional waiting time is caused by the waiting queue at the runway, so it is strongly affected by take-off separation. Since only one aircraft can use the runway at the same time, a minimum separation (called take-off separation) is set. The take-off is usually operated based on first-come-first-served policy. If many aircraft come to the runway at the same time, a departure queue is made and the aircraft has to wait before the runway. In addition, the departure and arrival traffic are mutually dependent due to the arrangement of the runways at this airport, so the runway interaction should also be considered. The runway interaction is explained in Section 2.4. The take-off separation is affected by many parameters, so it is explained in Section 2.5.

As for taxi-in time of arrival aircraft, the arrival aircraft only goes taxiing to the spot. If the spot is not occupied by other aircraft, the aircraft can block in. Therefore, uncertainty is found only in the taxiing phase. As mentioned before, the distribution of taxiing of arrival aircraft almost follows the one of departure aircraft on C runway, so (7) is used to estimate the taxiing time from the runway to the spot. The spot occupancy problem is described in Section 2.4.

2.4. Constraints at the Airport. In Section 2.3, the normal operation of departure and arrival aircraft was explained. However, there are many constraints at the airport, such as (1) take-off separation, (2) mutual interaction between runways, (3) the spot occupancy problem, and (4) conflict of two aircraft on the taxiway. The run time of the simulation should be small, so this time only the constraints (1), (2), and (3) are considered, and the constraint (4) is not explicitly considered and is assumed to be included in "uncertainty." The constraint (1) take-off separation will be explained in Section 2.5, so here the constraints (2) and (3) are explained.

As for mutual interaction between runways, as shown in Figure 1, the runway interaction is observed between take-off and landing aircraft on C runway and between take-off aircraft on D runway and landing aircraft on C runway. In addition, due to the departure and arrival route structure, C runway traffic and D runway traffic are mutually affected. However, this effect is complicated and its influence is relatively small so it is not considered here. Considering the runway operation, the landing time of arrival aircraft is currently not controlled, and the take-off time is controlled in accordance with the landing aircraft. Therefore, it is reasonable that the "no take-off time" relative to the landing time on C runway is set. According to the data analysis, the following constraints are set as shown in Table 1.

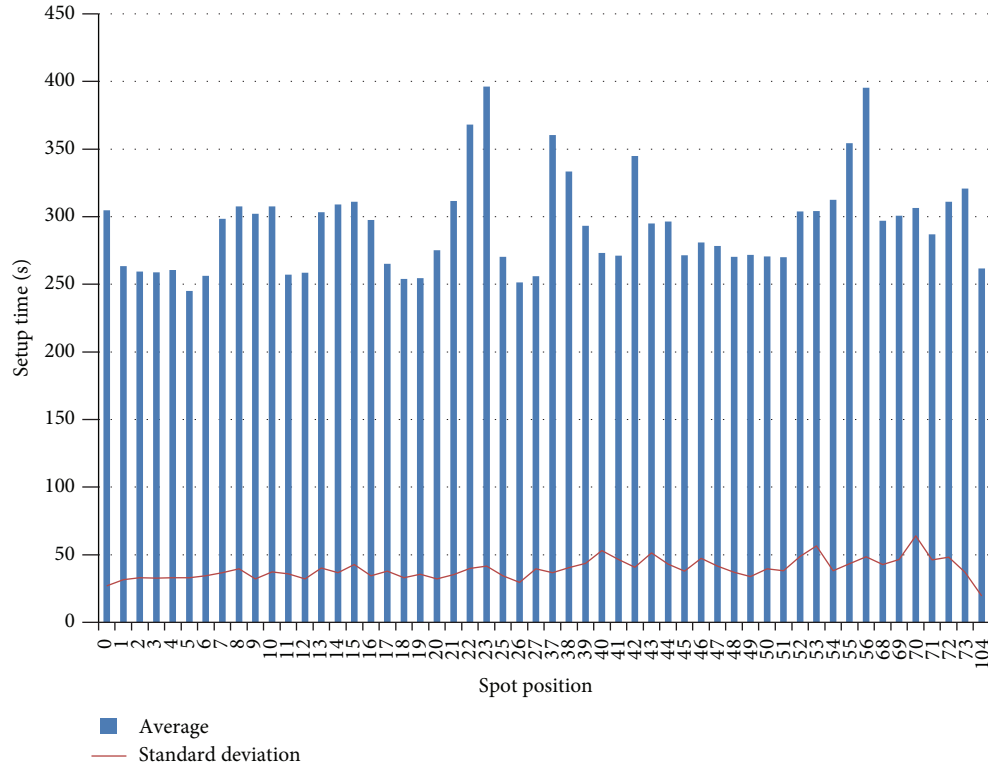


FIGURE 4: Average and standard deviation of setup time in each spot position. (Spot number does not correspond to the actual spot number.)

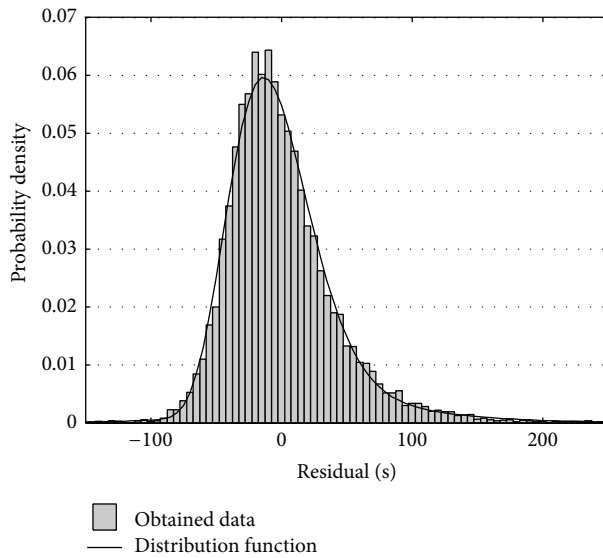


FIGURE 5: Residual of the setup time and fitted function.

As for the spot occupancy problem, obviously a single spot contains a single aircraft only. If the spot is already occupied by another aircraft, the arrival aircraft cannot block in until the aircraft leaves the spot, which is implemented in the simulation. In addition, paths near the spots are often shared among several spots, so arrival aircraft sometimes cannot get into the spot during the pushback of departure

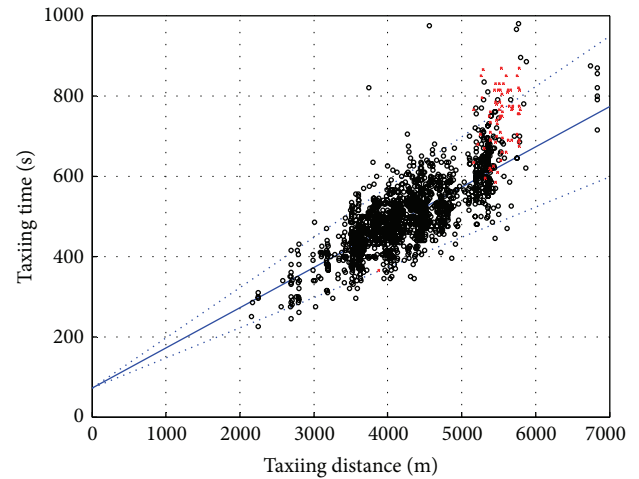


FIGURE 6: Taxiing time versus taxiing distance of aircraft departing from runway D.

aircraft from a nearby spot. Therefore, based on the surface movement data, the conflict path of pushback and block-in is investigated in each spot, and the conflict effect between block-in path and pushback path is also implemented in the simulation.

2.5. Distribution of Take-Off Separation. The take-off separation is the key to determine the waiting time of departure

TABLE 2: Average take-off separation in each combination of wake turbulence category [s] (data size = 4144).

Preceding/following	Heavy	Medium
Heavy	99.92	106.06
Medium	90.28	91.31

aircraft. The take-off procedure is operated by a pilot, so the take-off separation should include uncertainty effect. However, the take-off separation is also affected by the following two factors: wake turbulence and weather condition.

As for the wake turbulence, ICAO determines the minimum take-off separation based on the aircraft size of the current aircraft and the aircraft ahead [16]. There are four categories of aircraft: super, heavy, medium, and light (denoted by “S,” “H,” “M,” and “L”). Note that super and light aircraft are not operated at Tokyo International Airport, so only heavy and medium aircraft are considered in this research.

Table 2 shows the average take-off separation in each combination of wake turbulence category. Note that the standard deviation of take-off separation is about 20 s for each category. This table shows that the take-off separation differs by the wake turbulence category, and it is reflected in the calculation. The take-off separation between M-H and M-M is almost the same, so it is treated as the same value (90.75 s). From now, the take-off separation of “M-H” and “M-M” is treated as the nominal take-off separation, and the separation of “H-H” and “H-M” is reduced by the difference of the average to fit the nominal separation. The uncertainty of take-off separation is assumed to be the same for all wake turbulence categories.

Regarding weather conditions, it is said that wind and visibility affect the take-off separation. According to the data analysis, only visibility statistically affects the take-off separation, and here only the visibility effect is explained. The visibility information is provided by METAR (METeological Airport Report) usually every thirty minutes. If the visibility is more than 10 km, it is recorded as 9999 m. Figure 7 shows the relationship between the visibility and take-off separation (wake turbulence effect is already considered). Note that 80% of data is obtained when the visibility is more than 10 km, so low visibility data is relatively less. As shown in the figure, the take-off separation increases with smaller visibility, but it jumps up around 4000 m of visibility. Therefore, this is modeled by sigmoid function and linear regression as shown in the following expression:

$$95.64 - 0.0005356v + \frac{7.235}{1 + \exp(0.0604(v - 4000))}, \quad (10)$$

where v is the visibility in m. When the visibility of 10 km is treated as the nominal take-off separation, the separation data of another visibility is reduced to fit the nominal separation.

Now, the nominal take-off separation is defined as the data where the visibility is 10 km and “M-H” or “M-M” of wake turbulence category is applied. Even if these effects are considered, there is still a large residual, which is modeled

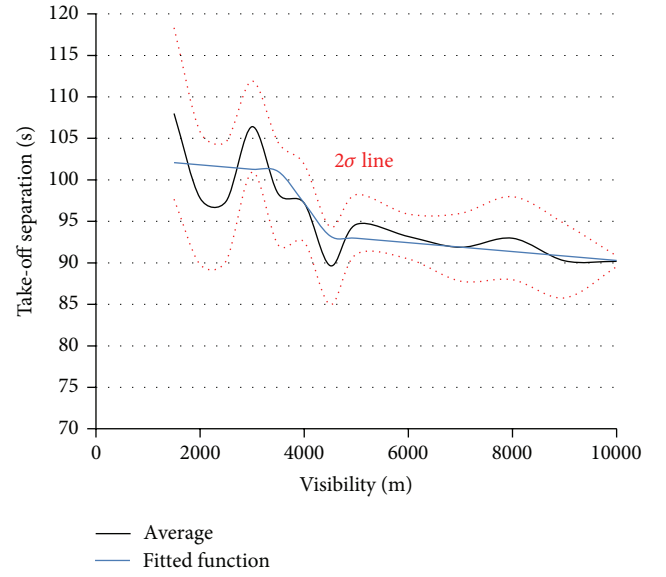


FIGURE 7: Take-off separation versus visibility.

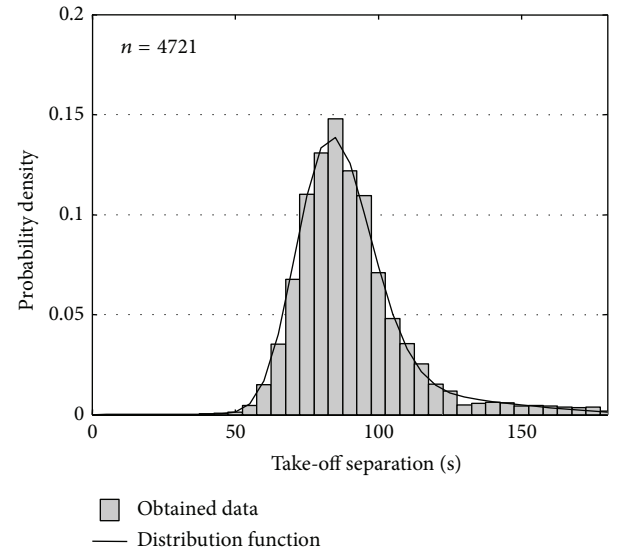


FIGURE 8: Distribution of take-off separation.

by the combination of normal distribution and Erlang distribution. Figure 8 shows the distribution of obtained take-off separation and probability density function of the fitted distribution of the nominal take-off separation ($t_{\text{sep-nom}}$) is described by the following equation:

$$0.890E(t_{\text{sep-nom}} - 13.56; 72.47, 30) + 0.110N(t_{\text{sep-nom}}; 122.47, 30.03). \quad (11)$$

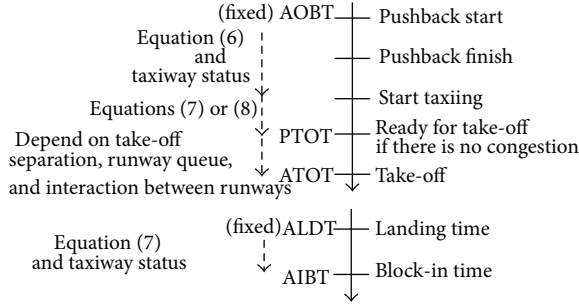


FIGURE 9: Simulation flow.

The take-off separation should include the wake turbulence effect and visibility effect. Finally, the take-off separation (t_{sep}) is calculated in the following equation:

$$t_{sep} = t_{sep_nom} - 0.0005356\nu + \frac{7.235}{1 + \exp(0.0604(\nu - 4000))} + 5.35 + \Delta t_{wake},$$

$$\Delta t_{wake} = \begin{cases} 9.17, & \text{H-H} \\ 15.31, & \text{H-M} \\ 0, & \text{M-H or M-M.} \end{cases} \quad (12)$$

2.6. Flow of the Simulation and Limitations of the Simulation Model. In order to conduct a simulation, initial conditions must be specified. As for the departure aircraft, once AOBT is obtained, the PTOT can be calculated considering the uncertainty explained before. In the simulation, each departure aircraft is assumed to come to the runway at PTOT, and ATOT is decided based on the runway status and first-come-first-served basis. For arrival aircraft, once ALDT is obtained, AIBT is obtained based on (7) and taxiway status. The flow of the calculation of each variable is summarized in Figure 9.

In order to simulate the actual airport operation, AOBT and ALDT are set the same as the data obtained on each day. Furthermore, the spot position, the taxiing distance, the wake turbulence category, and the departure/arrival runway of each aircraft are also set based on each day's data. These data are called each day's scenario data. This scenario data includes each day's traffic volume and the distribution of traffic. Even if the traffic volume is the same, the congestion level at the airport might differ between days. By using the scenario data, the daily fluctuation can also be investigated.

In order to appropriately evaluate the results, the limitations of the simulation model should be carefully considered. First, this model does not take into account the conflict on taxiway between aircraft in any areas apart from the spot areas. It is assumed that the additional taxiing time by the conflict includes uncertainty. Second, in the real world, there are cases when the runway operation does not necessarily follow the first-come-first-served basis. The air traffic controllers are in charge of the operations, so the take-off sequence is sometimes changed. In addition, EDCT

(expected departure clearance time) is sometimes set to the departure aircraft. This is the take-off time restriction due to the congestion in airspace or destination airport, and the aircraft cannot take off before EDCT, which is not considered in the simulation. EDCT also changes the departure sequence. Finally, nonstandard operation might be included in the data. It is confirmed in advance that the data do not include the long runway close, but short runway close might be included in data, which is difficult to exclude. Considering these limitations, the simulation accuracy will be evaluated.

3. Verification of Proposed Simulation Model and Daily Data Analysis

3.1. Characteristics of Daily Data. Before evaluating the simulation model, the characteristics of the daily traffic are investigated first. The proposed simulation model is to be used to evaluate uncertainty effect, especially important in congestions, so the model performance in such cases is of the utmost importance. Therefore, first, the congestion level throughout a day at the airport is investigated.

When the airport is not congested, the take-off is operated smoothly; that is, the waiting time of take-off aircraft is zero. Therefore, the congestion level at the airport closely relates to the waiting time of take-off aircraft. To investigate the actual congestion level at the airport, the actual waiting time of take-off aircraft is calculated. Since the actual waiting time is difficult to obtain directly, it is estimated based on the difference between AXOT and PXOT. AXOT can be obtained directly from the data. PXOT can be estimated as the nominal PXOT. PXOT is usually stochastically calculated as explained in the last section, but the nominal PXOT can be estimated if the uncertainty is assumed to be zero. Even if the uncertainty is zero, the nominal PXOT includes the taxiing distance effect and the spot position effect. In this way, the waiting time is estimated for each aircraft, and this waiting time based on actual data is called estimated waiting time. Figure 10 shows the estimated waiting time of each aircraft throughout a day on Day 1. The waiting time is not distributed evenly throughout a day, because the traffic volume in each time range differs. Some data include negative waiting time, which occurs because the estimated waiting time is calculated based on the estimated PXOT. Now, the time is split into three hours each, and the congestion is considered in each time range. The traffic volume and scheduled traffic distribution are almost the same within the time range between days, so the waiting time can be compared in each time range.

Figure 11 shows the total estimated waiting time in each time range on each day. Table 3 shows the average of estimated total waiting time for 20 days and the average number of departure and arrival aircraft. According to the figure and the table, the largest total waiting time is observed at PM6–PM9, and the smallest waiting time is observed at PM3–PM6, but the daily fluctuation is also large. On the other hand, both departure and arrival traffic are the largest at AM9–AM12. Although more traffic potentially causes longer

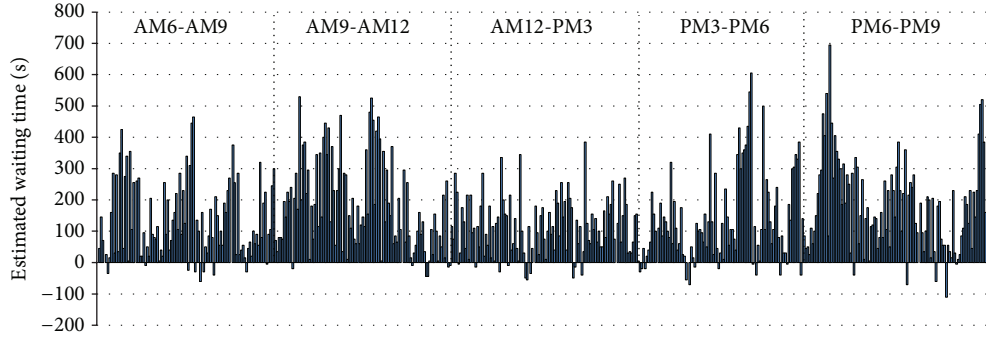


FIGURE 10: Estimated waiting time on Day 1 (ordered by actual take-off sequence).

TABLE 3: Average estimated waiting time and traffic volume in each time range for 20 days.

Time range	Estimated waiting time [minutes]	Number of departure aircraft	Number of arrival aircraft
AM6-AM9	174.5	105.5	44.0
AM9-AM12	178.3	105.8	104.4
AM12-PM3	158.3	99.6	98.8
PM3-PM6	133.4	93.8	102.1
PM6-PM9	281.9	98.4	104.2

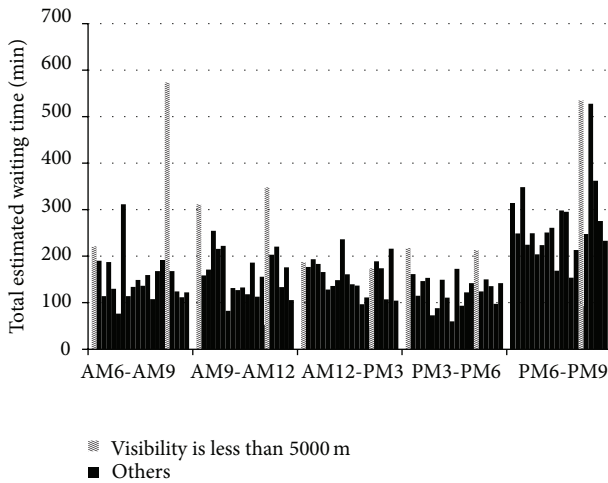


FIGURE 11: Total estimated waiting time in each time range on each day.

waiting time, there seems to be other factors as well. The waiting time increases if the runway waiting queue gets longer. The length of the runway queue is heavily affected by the traffic concentration. If many aircraft approach the runway at the same time, the runway queue becomes long and therefore the waiting time gets long and vice versa. Actually, at PM6-PM9, the departure traffic is not evenly distributed for these 3 hours, and it is concentrated between PM7 and PM8 and the waiting time is also long. Therefore, the effect of the traffic concentration seems to be more important than the traffic volume itself. Each day's scenario fixes AOBT, which

includes the actual distribution of off-block time, so the traffic concentration effect can also be evaluated in the simulation.

In addition, the take-off separation can also affect the total waiting time. According to Figure 7 and (11), the visibility affects the take-off separation. When the take-off separation is large, large total waiting time is expected. In Figure 11, the cases where the visibility is less than 5000 m are shown separately. When the visibility is less than 5000 m, large total waiting time is observed at all times. However, the cases where the large total waiting time is observed are not necessarily on a low visibility day. The visibility, that is, the take-off separation, is an important factor, but it is not the only one.

3.2. Validation of the Proposed Simulation Model. Next, the proposed simulation model is evaluated. The model considers the uncertainty effect, so it should be evaluated by a sufficient number of simulation runs. This time, 10,000 runs of simulations are conducted and the result is discussed. The program is made by C++ language and run with Intel Core i7-3770. It takes about 20 s to complete 10,000 runs of simulation on each day, and it is sufficiently fast to evaluate the uncertainty effect.

When evaluating the simulation model, it is important to decide what is expected in the simulation model. The main purpose of the simulation model is to evaluate the uncertainty effect, and the modeling of the congestion phenomena is the most important. On the other hand, the runway operation is assumed to follow the first-come-first-served basis, so the take-off time of individual aircraft (i.e., waiting time of individual aircraft) might not be necessarily well modeled.

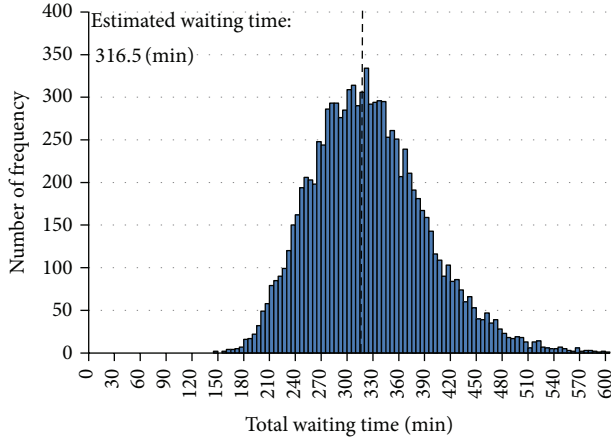


FIGURE 12: The distribution of total waiting time based on 10,000 runs of simulation and the estimated waiting time on Day 1 PM6–PM9.

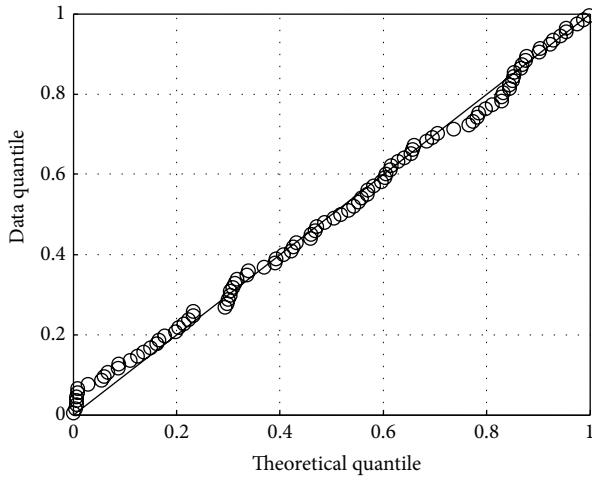


FIGURE 13: Q-Q plot of the total estimated waiting time on each day and each time range.

Here, the total waiting time and the take-off time of each aircraft are used as an index of the simulation accuracy.

First, the total waiting time is discussed. Figure 12 shows the distribution of the total waiting time on Day 1 PM6–PM9 based on 10,000 times of simulation. The estimated waiting time based on the actual data is 316.5 minutes, and the peak of the distribution by the simulation and the estimated waiting time almost match. The estimated waiting time corresponds to 47.49 percentile of the distribution. However, only this result by itself does not indicate that the proposed simulation model works well. The actual operation can be considered a single sample set of simulations. If so, it is expected that the actual operation is the same as one of the simulations. To evaluate it, the percentile of the waiting time is used. If the uncertainty of the simulation is underestimated, the percentile will be observed often around 0 and 100. If the uncertainty is overestimated, the percentile will be observed often around 50. Therefore, if the uncertainty of the simulation is well modeled, the percentile of the estimated

TABLE 4: Statistical tests results.

	P value	
	KS test	AD test
AM6–AM9	0.8247	0.8443
AM9–PM12	0.2684	0.1409
PM12–PM3	0.7513	0.6186
PM3–PM6	0.4026	0.0693
PM6–PM9	0.3282	0.5481
All	0.8211	0.4698

waiting time should be uniformly distributed between 0 and 100. As shown in Figure 11, a whole day is split into 5 time ranges for all 20 days; the percentile of the total estimated waiting time of 100 data is obtained. To investigate that the obtained percentile is evenly distributed, Q-Q plot is often used. Q-Q plot is a probability plot, where one axis shows the data quantile and the other axis shows the theoretical quantile. If the actual data completely follow the theoretical distribution, the plot is observed on the line “ $y = x$.” Figure 13 shows the Q-Q plot of the total waiting time.

This figure shows that the theoretical quantile and data quantile match very well, which infers that the uncertainty is well modeled, and therefore the proposed simulation model works well. The uniformity of the distribution is also examined via a statistical test. This time, Kolmogorov-Smirnov test (KS test) [17] and Anderson-Darling test (AD test) [18] are used. Both tests are statistical tests to verify whether a given sample of data is made from a given probability distribution (this time, uniform distribution). Both tests show a P value, which is the probability of a test result being at least as extreme as the one that is actually obtained. A small P value means that the actual data is more extreme, and usually if the P value is less than 0.05, it is concluded that the actual data do not come from a given probability distribution. The main difference between KS test and AD test is that AD test weights much more on the tail probability. However, these tests are usually done to reject the null hypothesis, that is, to prove that the obtained data do not come from the given probability distribution. Therefore, even if the P value is greater than 0.05, it does not directly mean that the obtained data follow the given probability distribution, but such a result leaves open the probability that the obtained data do not come from the given probability distribution.

The statistical test results are shown in Table 4. The statistical test is also done with data of each time range only. According to the result, the P value of all data is much greater than 0.05 for both tests, and no P value being less than 0.05 is observed for any time range.

Next, the take-off time is considered. The take-off time in the simulation is also distributed, and the percentile of the actual take-off time is obtained. However, as mentioned before, the take-off sequence is not modeled in the simulation, so the percentile of the take-off time might not be uniformly distributed. Figure 14 shows the Q-Q plot of the take-off time of all aircraft for 20 days. In total, 10,226 departure aircraft data are used.

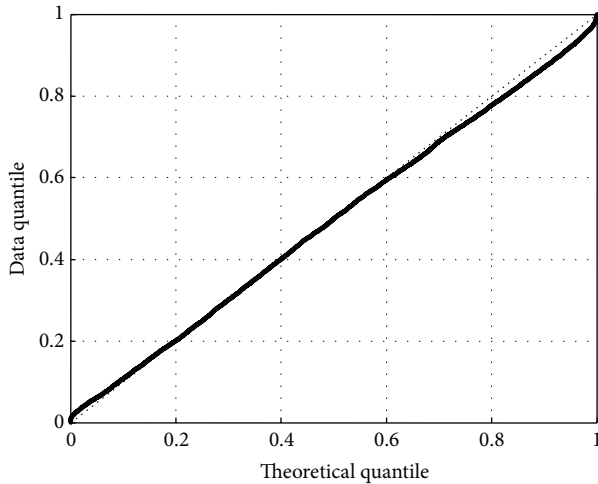


FIGURE 14: Q-Q plot of take-off time.

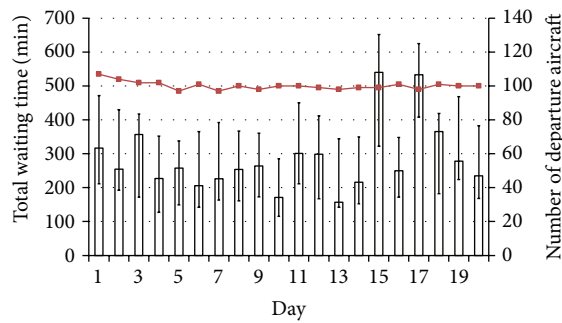


FIGURE 15: Total estimated waiting time and 95% range of total simulated waiting time at PM6-PM9 on each day.

The data quantile slightly differs from the theoretical quantile around the edge of the quantile. KS test is also conducted, and the P value here is $1.385E - 9$, which means that the actual percentile is not uniformly distributed. However, as mentioned in the last section, this simulation model does not include all effects of airport operation, and it is expected that the percentile of take-off time is not completely uniformly distributed. However, according to Figure 14, the data quantile and theoretical quartile almost match each other, and also considering the result of total waiting time, it is concluded that the proposed simulation model is sufficiently accurate as an airport-runway statistical simulation model.

3.3. Uncertainty Effect Based on the Simulation. Since the simulation model is developed successfully, several aspects of uncertainty effects in airport operations are examined. The congestion in a runway queue is observed every day, but the congestion level changes every day. There are many possible factors related to the total waiting time, such as the number of departure aircraft, the initial condition (how much traffic is concentrated on a specific time slot, here also called scenario uncertainty), uncertainties of taxi-in, taxi-out, and take-off separation (called traffic uncertainty), and meteorological

conditions. The effects of the number of departure aircraft and meteorological conditions can be associated with each day. The traffic uncertainty effect can be evaluated with a large number of simulations under the same initial condition. The scenario uncertainty can be investigated between days. It is interesting to understand how much each factor affects the congestion level.

First, the variation of the congestion within a day is examined. An example is shown in Figure 12 on Day PM6-PM9, which shows the distribution of total waiting time based on 10,000 simulations. According to additional calculations, the similar shape of distribution is obtained on other days and other time ranges. This variation of the total waiting time stems from traffic uncertainty effects. On this day, the estimated total waiting time based on the actual data is 316.5 minutes, but the distribution of the total waiting time between about 150 minutes and 600 minutes is observed. Even between 2.5 percentile and 97.5 percentile, the total waiting time varies between 211 and 472 minutes. This infers that the congestion level changes more than twice even if the scenario involves no uncertainty. In addition, the distribution of the total waiting time is not symmetric, and the large waiting time is observed slightly more often.

Next, Figure 15 shows the daily fluctuation of the total waiting time at PM6-PM9. The bar indicates the estimated total waiting time based on actual data (the same data shown in Figure 11), and the error bar indicates the 95% range of the total waiting time in the simulation. The red line shows the number of departure aircraft within this time range. On Day 15, visibility was low. From this figure, there are many interesting points found.

First, the number of departure aircraft is almost constant in this time range, and only a small difference among the days is observed. However, like the result obtained in Table 3, there is no clear relationship between the number of departure aircraft and the total waiting time. Second, even though the flight schedule is almost the same on each day in each time range, the range of the total waiting time in the simulation varies. The simulation scenario includes the initial condition of the off-block time, so it does not include the uncertainty between actual off-block time and scheduled off-block time, that is, scenario uncertainty. On Days 15 and 17, large estimated waiting time is observed, but the simulated total waiting time is also large. The low visibility seems to be a reason for large total waiting time on Day 15, but that is not the case on Day 17, maybe due to the traffic concentration. Therefore, on these days, the large total waiting time is caused not because of the traffic uncertainty effect, but because of either visibility or the scenario uncertainty, that is, the uncertainty of the off-block time compared to the scheduled time. If so, the total waiting time in the simulation varies very much with only traffic uncertainty, which means that the further large distribution will be obtained if the scenario uncertainty is considered. Therefore, the uncertainty affects the airport congestion very much, and it is almost impossible to estimate the airport congestion level on a specific day in advance, though the average congestion level can be estimated.

However, this result does not directly mean that congestion cannot be relieved. If the scheduled departure or arrival time is optimally decided, the average congestion level might be reduced with keeping the traffic volume. The better spot allocation might also decrease the congestion level. However, since we understand that the uncertainty in airport traffic is significant, the uncertainty effect cannot be ignored when considering the airport operation. Otherwise, even if the taxi-out time is reduced, the uncertainty might cause the delay of take-off time or reduce the runway capacity.

4. Conclusions

This paper evaluated the uncertainty effect in the airport operation. The uncertainty level was obtained in each phase based on the surface movement data, and a fast-time airport traffic simulation model was developed. The validation of the simulation model was also done, and the simulation model seemed to model the uncertainty effect appropriately. Based on the developed simulation model, the characteristics of the airport traffic were investigated. The results inferred that the airport traffic congestion seemed to be mostly affected by the uncertainty of taxi-out or taxi-in and the traffic concentration, not by the traffic volume and weather conditions. Since the uncertainty effect was significant in airport traffic, it was difficult to estimate the congestion level on a specific day in advance. The developed airport simulation model would help to evaluate the airport operation with existing uncertainties.

Conflict of Interests

The author declares that there is no conflict of interests regarding the publication of this paper.

Acknowledgments

The author would like to thank Japan Civil Aviation Bureau for providing the airport surveillance data at Tokyo International Airport. Also, this work was supported by JSPS KAKENHI Grant no. 25871210.

References

- [1] N. Pujet, B. Delcaire, and E. Feron, "Input-output modeling and control of the departure process of congested airports," in *Proceedings of the AIAA Guidance, Navigation and Control Conferences and Exhibit*, AIAA-1999-4299, 1999.
- [2] I. Simaiakis, H. Khadilkar, H. Balakrishnan, T. G. Reynolds, and R. J. Hansman, "Demonstration of reduced airport congestion through pushback rate control," *Transportation Research Part A: Policy and Practice*, vol. 66, 2014.
- [3] C. Brinton, C. Provan, S. Lent, T. Prevost, and S. Passmore, "Collaborative departure queue management: an example of airport collaborative decision making," in *Proceedings of the 9th USA/Europe Air Traffic Management Research and Development Seminar*, 2011.
- [4] S. H. Kim and E. Feron, "Impact of gate assignment on gate-holding departure control strategies," in *Proceedings of the 31st Digital Avionics Systems Conference: Projecting 100 Years of Aerospace History into the Future of Avionics (DASC '12)*, pp. E31–E38, IEEE, October 2012.
- [5] G. Gupta, W. Malik, and Y. C. Jung, "An integrated Collaborative Decision Making and tactical advisory concept for airport surface operations management," in *Proceedings of the 12th AIAA Aviation Technology, Integration, and Operations Conference (ATIO '12)*, Indianapolis, Ind, USA, September 2012.
- [6] Jeppesen, "Total Airspace and Airport Modeler," <http://www.jeppesen.com/industry-solutions/aviation/government/total-airspace-airport-modeler.jsp>.
- [7] Airtopsoft, AirTOp, <http://www.airtopsoft.com/index.html>.
- [8] S. Atkins, Y. Jung, C. Brinton, L. Stell, T. Carniol, and S. Rogowski, "Surface management system field trial results," AIAA 4th Aviation, Technology, Integration and Operations Forum AIAA-2004-6241, 2004.
- [9] G. J. Couluris, R. K. Fong, M. B. Downs et al., "A new modeling capability for airport surface traffic analysis," in *Proceedings of the 27th IEEE/AIAA Digital Avionics Systems Conference (DASC '08)*, pp. 3.E.4-1–3.E.4-11, St. Paul, Minn, USA, October 2008.
- [10] G. J. Couluris, P. C. Davis, N. C. Mittler, A. P. Saraf, and S. D. Timar, "Aces terminal model enhancement," in *Proceedings of the 28th Digital Avionics Systems Conference: Modernization of Avionics and ATM-Perspectives from the Air and Ground (DASC '09)*, October 2009.
- [11] L. Meyn, R. Windhorst, K. Roth et al., "Build 4 of the airspace concept evaluation system," in *Proceedings of the AIAA Modeling and Simulation Technologies Conference*, AIAA-2006-6110, 2006.
- [12] Z. Wood, M. Kistler, S. Rathinam, and Y. Jung, "A simulator for modeling aircraft surface operations at airports," in *Proceedings of the AIAA Modeling and Simulation Technologies Conference*, AIAA-2009-5912, 2009.
- [13] R. Mori, "Aircraft ground-taxiing model for congested airport using cellular automata," *IEEE Transactions on Intelligent Transportation Systems*, vol. 14, no. 1, pp. 180–188, 2013.
- [14] J. B. Gotteland, N. Durand, J. M. Alliot, and E. Page, "Aircraft ground traffic optimization," in *Proceedings of the 4th USA/Europe Air Traffic Management Research and Development Seminar*, 2001.
- [15] F. R. Carr, *Stochastic modeling and control of airport surface traffic [Doctoral dissertation]*, Massachusetts Institute of Technology, 2001.
- [16] International Civil Aviation Organization, "Procedures for Air Navigation Service—Air Traffic Management (PANS-ATM)," Doc 4444.
- [17] F. J. Massey Jr., "The Kolmogorov-Smirnov test for goodness of fit," *Journal of the American statistical Association*, vol. 46, no. 253, pp. 68–78, 1951.
- [18] T. W. Anderson and D. A. Darling, "A test of goodness of fit," *Journal of the American Statistical Association*, vol. 49, pp. 765–769, 1954.

Research Article

An Analytical Solution of Partially Penetrating Hydraulic Fractures in a Box-Shaped Reservoir

He Zhang,^{1,2} Xiaodong Wang,^{1,2} and Lei Wang^{1,2}

¹*School of Energy Resources, China University of Geosciences, Beijing 100083, China*

²*Beijing Key Laboratory of Unconventional Natural Gas Geology Evaluation and Development Engineering, Beijing 100083, China*

Correspondence should be addressed to Lei Wang; wanglei1986sp@foxmail.com

Received 19 August 2014; Revised 8 December 2014; Accepted 8 December 2014

Academic Editor: Shaofan Li

Copyright © 2015 He Zhang et al. This is an open access article distributed under the Creative Commons Attribution License, which permits unrestricted use, distribution, and reproduction in any medium, provided the original work is properly cited.

This paper presents a new method to give an analytical solution in Laplace domain directly that is used to describe pressure transient behavior of partially penetrating hydraulic fractures in a box-shaped reservoir with closed boundaries. The basic building block of the method is to solve diffusivity equation with the integration of Dirac function over the distance that is presented for the first time. Different from the traditional method of using the source solution and Green's function presented by Gringarten and Ramey, this paper uses Laplace transform and Fourier transform to solve the diffusivity equation and the analytical solution obtained is accurate and simple. The effects of parameters including fracture height, fracture length, the position of the fracture, and reservoir width on the pressure and pressure derivative are fully investigated. The advantage of the analytical solution is easy to incorporate storage coefficient and skin factor. It can also reduce the amount of computation and compute efficiently and quickly.

1. Introduction

Hydraulic fracturing technology has been a common application in the oil and gas industry during the last two decades. More and more attentions were focused on the study of pressure transient behavior of hydraulically fractured wells. In most published literatures, hydraulic fractures were assumed to be fully penetrating the formation. Limited efforts have been made to investigate the effects of partially penetrating fracture height on the performance of wells. In practice, fully penetrating fractures may lead to an early or immediate water or gas breakthrough in a reservoir with bottom water or gas cap in contact, whereas partially penetrating fractures may be the only way to prevent the early breakthrough [1–3].

No matter the problem of wells with or without hydraulic fractures, most scholars considered the fully penetrating wells or fully penetrating hydraulic fractures. However the issue of partial penetration is always ignored. In the early time, some scholars presented some methods to study partially penetrating wells. Muskat, Nisile, Brons and Marting, and Papatzacos used the method of images [4], Streltsova-Adams [5] used Laplace and Hankel transformations, and Buhidma

and Raghavan [6] used Green's function to solve the problem to partial penetration well in a reservoir. Later Yeh and Reynolds [7] used a numerical simulator to present some type curves for partial penetration, multilayered reservoirs with transient crossflow. In the late time, Ozkan and Raghavan [8] proposed a solution for a limited-entry slanted well in an infinite reservoir with closed top and bottom boundaries using the Laplace transformation and Bui et al. [9] used the double-porosity formulation of Warren and Root for naturally fractured reservoir. Fuentes-Cruz and Camacho-Velazquez [10] obtained the pressure transient behavior for partially penetrating wells completed in naturally fractured-vuggy reservoir by combination of Laplace transformation and finite Fourier transformation.

To solve the unsteady-state flow problem of fractures in the reservoir, most solutions were presented based on the using of the source solution and Green's function provided by Gringarten and Ramey [11] which can be used in combination with Newman's product method to generate solutions for different reservoir flow problem. At first, the pressure behavior of the partially penetrating fractures was presented by Gringarten and Ramey Jr. [12] using Green's function. But

the physical model only considered the closed upper and lower boundaries. Raghavan et al. [13] presented an analytical model that researched the effect of the vertical fracture height on the pressure transient behavior of a partially penetrated uniform-flux fractured well by evaluating the uniform-flux solution at a point in the fracture which was assumed to yield the infinite-conductivity solution. This model was an extension of the case of fully penetrating vertical fracture previously found by Gringarten et al. Rodriguez et al. [14, 15] presented semianalytical solution of the pressure transient behavior in a homogeneous and isotropic reservoir with a well intersected by a partially penetrating single vertical fracture of finite or infinite conductivity. However they did not investigate the effect of vertical fracture position on the wellbore pressure.

These previous solutions were quite significant to the later analysis of the pressure behavior of the partially penetrating fractures. Valkó and Amini [16] presented a method of distributed volume sources (DVS) to investigate a horizontal well with multiple transverse fractures in a box-shaped reservoir. The diffusivity equation considered a source term to calculate the pressure distribution and compute the production rate from a fracture. But it was only an approximate approach. Alpheus and Tiab [3] presented the analysis of the solution to the effect of partial penetration of an infinite conductivity hydraulic fracture on the pressure behavior of horizontal well extending in naturally fractured reservoirs. They founded that the duration of early linear flow regime is a function of the hydraulic fractures height. Although the mathematical model was obtained in Laplace domain with elliptical flow model, the method was complex and unclear because of the model that was obtained indirectly. Al Rbeawi and Tiab [1, 2] presented an analytical model in real time domain for the pressure behavior of a horizontal well with multiple vertical and inclined partially penetrating hydraulic fractures in an infinite homogenous reservoir to explain the pressure transient tests and forecast productivity of the well by using the instantaneous source function in three principal directions. Moreover, Lin and Zhu [17] developed a slab source method to evaluate performance of horizontal wells with or without fractures with consideration of the three-dimensional fracture geometry. However, the solution was also derived in real time domain, making it difficult to incorporate storage coefficient and skin factor that are usually obtained from the Laplace domain solution.

This study attempts to give some new insights in understanding the partially penetrating hydraulic fractures in a box-shaped reservoir. This paper presents an analytical solution that describes pressure transient behavior of partially penetrating fractures in a box-shaped reservoir and is successfully applied to examine effects of fracture half height, fracture half length, and reservoir width on performance of a fracture in a reservoir with closed boundaries based on pressure and pressure derivative concepts. Moreover the effect of the vertical position of the fracture on the pressure and pressure derivative is fully investigated. More specifically, the diffusivity equation is presented for the first time and the analytical solution of pressure transient behavior in Laplace domain is derived by using Laplace transform and Fourier

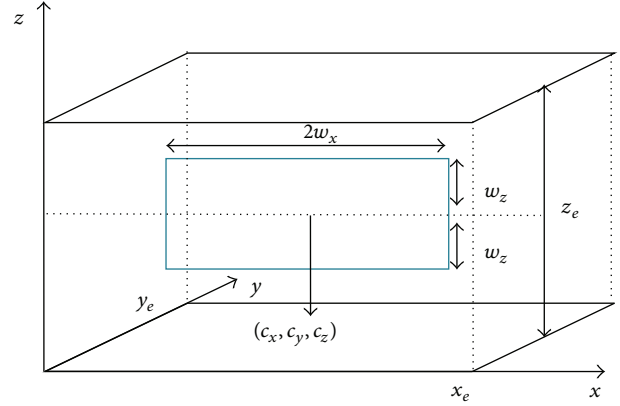


FIGURE 1: Schematic diagram of partially penetrating fracture.

transform. Then the bottomhole pressure in the real time domain can be obtained by using the inverse Laplace algorithm as proposed by Stehfest [18] subsequently. The result is validated accurately by comparing with previous results in the literature. The advantages of Laplace domain solution are that it can make it easy to incorporate storage coefficient and skin factor, can reduce the amount of computation, and improve the computational efficiency because it is unnecessary to scatter time.

2. Mathematical Model

Consider a partially penetrating hydraulic fracture in a closed homogenous box-shaped reservoir as shown in Figure 1. If we assume that all fluid withdrawal will be through the fracture, the fracture is partially penetrating the formation and the fracture can be simulated as plane source [2].

As shown in Figure 1, a partially penetrating fracture is placed in a reservoir with height (z direction) z_e , length (x direction) x_e , and width (y direction) y_e , having its dimension $2w_x$ in x direction and $2w_z$ in z direction. The formation has horizontal and vertical permeability k_h and k_z , respectively. The fracture is assumed to be infinitely conductive and its position is (c_x, c_y, c_z) . The pressure is uniform initially throughout the reservoir and equal to p_i .

The analytical model for the pressure behavior of a fracture in a box-shaped reservoir can be derived based on the solution for the diffusivity equation in the porous media. The diffusivity equation that governs the flow is

$$\eta_h \frac{\partial^2 P}{\partial x^2} + \eta_h \frac{\partial^2 P}{\partial y^2} + \eta_z \frac{\partial^2 P}{\partial z^2} + \frac{QB}{\phi c_t} H_1 \times H_2 \times H_3 = \frac{\partial P}{\partial t}, \quad (1)$$

where ϕ is porosity, c_t is total compressibility, t is the time, p is reservoir pressure, and B is formation volume factor. The well produces slightly compressible fluid with constant viscosity μ at the total flow rate of Q , where

$$\eta_h = \frac{k_h}{\phi \mu c_t} \quad \eta_z = \frac{k_z}{\phi \mu c_t}. \quad (2)$$

We should notice that

$$QB = q2w_x2w_z, \quad (3)$$

where q is the fluid withdraw per unit fracture surface area.

Reservoir pressure is initially constant

$$p(x, y, z, 0) = p_i. \quad (4)$$

The outer boundaries are assumed to be closed so that

$$\left. \frac{\partial p}{\partial x} \right|_{x=0, x_e} = 0 \quad \left. \frac{\partial p}{\partial y} \right|_{y=0, y_e} = 0 \quad \left. \frac{\partial p}{\partial z} \right|_{z=0, z_e} = 0, \quad (5)$$

H_1 , H_2 , and H_3 can be written, respectively, as

$$\begin{aligned} H_1 &= \int_{c_x - w_x}^{c_x + w_x} \frac{1}{2w_x} \delta(x - c_x) dc_x \\ H_2 &= \delta(y - c_y) \\ H_3 &= \int_{c_z - w_z}^{c_z + w_z} \frac{1}{2w_z} \delta(z - c_z) dc_z, \end{aligned} \quad (6)$$

where δ is Dirac function.

To simplify the problem we define dimensionless variables as the follows:

$$\begin{aligned} P_D &= \frac{2\pi k_h z_e (p_i - p)}{QB\mu} & t_D &= \frac{k_h t}{\phi \mu c_i L^2} & k_h &= \sqrt{k_x k_y} \\ L_D &= \frac{z_e}{L} \sqrt{\frac{k_h}{k_z}} \\ x_D &= \frac{x}{L} & y_D &= \frac{y}{L} & z_D &= \frac{z}{z_e} \\ x_{eD} &= \frac{x_e}{L} & y_{eD} &= \frac{y_e}{L} & z_{eD} &= \frac{z_e}{z_e} = 1 \\ w_{xD} &= \frac{w_x}{L} & w_{zD} &= \frac{w_z}{z_e} \\ c_{xD} &= \frac{c_x}{L} & c_{yD} &= \frac{c_y}{L} & c_{zD} &= \frac{c_z}{z_e}, \end{aligned} \quad (7)$$

where L is the reference length.

Using the dimensionless variables (1) can be written as

$$\frac{\partial^2 P_D}{\partial x_D^2} + \frac{\partial^2 P_D}{\partial y_D^2} + \frac{\partial^2 P_D}{L_D^2 \partial z_D^2} + 2\pi H_{1D} \times H_{2D} \times H_{3D} = \frac{\partial P_D}{\partial t_D}, \quad (8)$$

where H_1 , H_2 , and H_3 can be written as

$$\begin{aligned} H_{1D} &= \int_{c_{xD} - w_{xD}}^{c_{xD} + w_{xD}} \frac{1}{2w_{xD}} \delta(x_D - c_{xD}) dc_{xD} \\ H_{2D} &= \delta(y_D - c_{yD}) \\ H_{3D} &= \int_{c_{zD} - w_{zD}}^{c_{zD} + w_{zD}} \frac{1}{2w_{zD}} \delta(z_D - c_{zD}) dc_{zD} \end{aligned} \quad (9)$$

with

$$\text{I.C.: } p_D(x_D, y_D, z_D, 0) = 0$$

$$\text{B.C.s: } \left. \frac{\partial p_D}{\partial x_D} \right|_{x_D=0, x_{eD}} = 0 \quad \left. \frac{\partial p_D}{\partial y_D} \right|_{y_D=0, y_{eD}} = 0 \quad (10)$$

$$\left. \frac{\partial p_D}{\partial z_D} \right|_{z_D=0, z_{eD}} = 0.$$

The Laplace transform with respect to time is defined as

$$\tilde{p}_D(r_D, s) = \int_0^\infty p_D(r_D, s) e^{-st_D} dt_D. \quad (11)$$

By applying Laplace transform to (8), we obtain

$$\frac{\partial^2 \tilde{p}_D}{\partial x_D^2} + \frac{\partial^2 \tilde{p}_D}{\partial y_D^2} + \frac{\partial^2 \tilde{p}_D}{L_D^2 \partial z_D^2} + 2\pi \frac{H_{1D} \times H_{2D} \times H_{3D}}{s} = s \tilde{p}_D. \quad (12)$$

Outer boundary conditions in Laplace space are

$$\begin{aligned} \left. \frac{\partial \tilde{p}_D}{\partial x_D} \right|_{x_D=0, x_{eD}} &= 0 & \left. \frac{\partial \tilde{p}_D}{\partial y_D} \right|_{y_D=0, y_{eD}} &= 0 \\ \left. \frac{\partial \tilde{p}_D}{\partial z_D} \right|_{z_D=0, z_{eD}} &= 0. \end{aligned} \quad (13)$$

Fourier cosine transform with respect to x_D can be defined as

$$\bar{p}_D(u_n) = \int_0^{x_{eD}} p_D \cos(u_n x_D) dx_D. \quad (14)$$

The characteristic equation is defined as

$$\sin(u_m x_{eD}) = 0. \quad (15)$$

By solving (15), the characteristic number is obtained as follows:

$$u_m = \frac{m\pi}{x_{eD}}. \quad (16)$$

Based on the concept of Fourier cosine transform, the Fourier transform of the H_{1D} , H_{2D} , and H_{3D} function, respectively, is

$$\begin{aligned}\bar{H}_{1D} &= \int_0^{x_{eD}} \int_{c_{xD}-w_{xD}}^{c_{xD}+w_{xD}} \frac{1}{2w_{xD}} \delta(x_D - c_{xD}) dc_{xD} \\ &\quad \cdot \cos(u_m x_D) dx_D \\ &= \frac{\{\sin[u_m(c_{xD} + w_{xD})] - \sin[u_m(c_{xD} - w_{xD})]\}}{2u_m w_{xD}}\end{aligned}\quad (17a)$$

$$\bar{H}_{2D} = \int_0^{y_{eD}} \delta(y_D - c_{yD}) \cos(v_n y_D) dy_D = \cos(v_n c_{yD}) \quad (17b)$$

$$\begin{aligned}\bar{H}_{3D} &= \int_0^{z_{eD}} \int_{c_{zD}-w_{zD}}^{c_{zD}+w_{zD}} \frac{1}{2w_{zD}} \delta(z_D - c_{zD}) dc_{zD} \\ &\quad \cdot \cos(w_p z_D) dz_D \\ &= \frac{\{\sin[w_p(c_{zD} + w_{zD})] - \sin[w_p(c_{zD} - w_{zD})]\}}{2w_p w_{zD}}.\end{aligned}\quad (17c)$$

The first Fourier cosine transform of (12) on the variable x_D is

$$-u_m^2 \bar{\bar{P}}_D + \frac{\partial^2 \bar{\bar{P}}_D}{\partial y_D^2} + \frac{\partial^2 \bar{\bar{P}}_D}{L_D^2 \partial z_D^2} + 2\pi \frac{\bar{H}_{1D} \times H_{2D} \times H_{3D}}{s} = s \bar{\bar{P}}_D. \quad (18)$$

The second Fourier cosine transform of (18) on the variable y_D is

$$-u_m^2 \bar{\bar{\bar{P}}}_D - v_n^2 \bar{\bar{\bar{P}}}_D + \frac{\partial^2 \bar{\bar{\bar{P}}}_D}{L_D^2 \partial z_D^2} + 2\pi \frac{\bar{H}_{1D} \times \bar{H}_{2D} \times H_{3D}}{s} = s \bar{\bar{\bar{P}}}_D. \quad (19)$$

For the third Fourier cosine transform of (19) on the variable z_D , we obtain

$$-u_m^2 \bar{\bar{\bar{\bar{P}}}}_D - v_n^2 \bar{\bar{\bar{\bar{P}}}}_D - \frac{w_p^2 \bar{\bar{\bar{\bar{P}}}}_D}{L_D^2} + 2\pi \frac{\bar{H}_{1D} \times \bar{H}_{2D} \times \bar{H}_{3D}}{s} = s \bar{\bar{\bar{\bar{P}}}}_D, \quad (20)$$

where

$$u_m = \frac{m\pi}{x_{eD}} \quad v_n = \frac{n\pi}{y_{eD}} \quad w_p = \frac{p\pi}{z_{eD}}. \quad (21)$$

According to the following equation

$$P_D(x_D) = \sum_{m=1}^{\infty} \frac{\cos(u_m x_D)}{N(n)} \bar{P}_D(u_m) \quad (22)$$

taking the first Fourier inverse transform of (20) on the variable z_D , the solution can be expressed as follows:

$$\begin{aligned}\bar{\bar{\bar{P}}}_D &= 2\pi \frac{1}{z_{eD}} \bar{H}_{1D} \times \bar{H}_{2D} \times \frac{1}{(s + u_m^2 + v_n^2)} \\ &\quad + 2\pi \bar{H}_{1D} \times \bar{H}_{2D} \\ &\quad \times \frac{2}{z_{eD}} \sum_{p=1}^{\infty} \cos(w_p z_D) \bar{H}_{3D} \frac{1}{(s + u_m^2 + v_n^2 + w_p^2/L_D^2)}.\end{aligned}\quad (23)$$

The second Fourier inverse transform of (19) on the variable y_D is

$$\begin{aligned}\bar{\bar{\bar{P}}}_D &= 2\pi \frac{1}{y_{eD}} \frac{1}{z_{eD}} \frac{\bar{H}_{1D}}{(s + u_m^2)} \\ &\quad + 2\pi \frac{2}{y_{eD}} \bar{H}_{1D} \sum_{n=1}^{\infty} \frac{1}{z_{eD}} \cos(v_n y_D) \frac{\bar{H}_{2D}}{(s + u_m^2 + v_n^2)} \\ &\quad + 2\pi \frac{1}{y_{eD}} \bar{H}_{1D} \frac{2}{z_{eD}} \sum_{p=1}^{\infty} \cos(w_p z_D) \frac{\bar{H}_{3D}}{(s + u_m^2 + w_p^2/L_D^2)} \\ &\quad + 2\pi \frac{2}{y_{eD}} \frac{2}{z_{eD}} \bar{H}_{1D} \\ &\quad \times \sum_{n=1}^{\infty} \sum_{p=1}^{\infty} \cos(v_n y_D) \cos(w_p z_D) \\ &\quad \cdot \frac{\bar{H}_{2D} \bar{H}_{3D}}{(s + u_m^2 + v_n^2 + w_p^2/L_D^2)}.\end{aligned}\quad (24)$$

The third Fourier inverse transform of (18) on the variable x_D is

$$\begin{aligned}s \bar{\bar{\bar{P}}}_D &= \frac{2\pi}{x_{eD} y_{eD} z_{eD} s} \\ &\quad + \frac{4\pi}{x_{eD} y_{eD} z_{eD}} \sum_{m=1}^{\infty} \cos(u_m x_D) \frac{\bar{H}_{1D}}{(s + u_m^2)} \\ &\quad + \frac{4\pi}{x_{eD} y_{eD} z_{eD}} \sum_{n=1}^{\infty} \cos(v_n y_D) \frac{\bar{H}_{2D}}{(s + v_n^2)} \\ &\quad + \frac{8\pi}{x_{eD} y_{eD} z_{eD}} \\ &\quad \cdot \sum_{n=1}^{\infty} \sum_{m=1}^{\infty} \cos(v_n y_D) \cos(u_m x_D) \frac{\bar{H}_{1D} \bar{H}_{2D}}{(s + u_m^2 + v_n^2)} \\ &\quad + \frac{4\pi}{x_{eD} y_{eD} z_{eD}} \sum_{p=1}^{\infty} \cos(w_p z_D) \frac{\bar{H}_{3D}}{(s + w_p^2/L_D^2)} \\ &\quad + \frac{8\pi}{x_{eD} y_{eD} z_{eD}}\end{aligned}$$

$$\begin{aligned}
& \cdot \sum_{m=1}^{\infty} \sum_{p=1}^{\infty} \cos(w_p z_D) \cos(u_m x_D) \frac{\bar{H}_{1D} \bar{H}_{3D}}{(s + u_m^2 + w_p^2/L_D^2)} \\
& + \frac{8\pi}{x_{eD} y_{eD} z_{eD}} \\
& \cdot \sum_{n=1}^{\infty} \sum_{p=1}^{\infty} \cos(v_n y_D) \cos(w_p z_D) \frac{\bar{H}_{2D} \bar{H}_{3D}}{(s + v_n^2 + w_p^2/L_D^2)} \\
& + \frac{16\pi}{x_{eD} y_{eD} z_{eD}} \\
& \cdot \sum_{m=1}^{\infty} \sum_{n=1}^{\infty} \sum_{p=1}^{\infty} \cos(v_n y_D) \cos(w_p z_D) \cos(u_m x_D) \\
& \cdot \frac{\bar{H}_{1D} \bar{H}_{2D} \bar{H}_{3D}}{(s + u_m^2 + v_n^2 + w_p^2/L_D^2)}. \quad (25)
\end{aligned}$$

Applying (17b) and following equation

$$\begin{aligned}
& 2 \cos(v_n c_{yD}) \cos(v_n w_{yD}) \\
& = \cos(v_n (c_{yD} - w_{yD})) + \cos(v_n (c_{yD} + w_{yD})) \\
& = \cos\left(\frac{n\pi}{y_{eD}} (c_{yD} - w_{yD})\right) + \cos\left(\frac{n\pi}{y_{eD}} (c_{yD} + w_{yD})\right) \\
& \sum_{k=1}^{\infty} \frac{\cos kx}{k^2 + \alpha^2} = \frac{\pi}{2\alpha} \frac{\cosh \alpha (\pi - x)}{\sinh \alpha \pi} - \frac{1}{2\alpha^2} \quad (26)
\end{aligned}$$

we can obtain

$$\begin{aligned}
& \sum_{n=1}^{\infty} \frac{2 \cos(v_n y_D) \cos(v_n c_{yD})}{s + v_n^2} \\
& = \frac{y_{eD}}{2\sqrt{s}} \left(\cosh \sqrt{s} (y_{eD} - (y_D - c_{yD})) \right. \\
& \quad \left. + \cosh \sqrt{s} (y_{eD} - (y_D + c_{yD})) \right) \\
& \cdot (\sinh(\sqrt{s} y_{eD}))^{-1} - \frac{1}{s}. \quad (27)
\end{aligned}$$

Using the same method, the following formulas can be written as

$$\begin{aligned}
& \sum_{n=1}^{\infty} \frac{2 \cos(v_n y_D) \cos(v_n c_{yD})}{s + u_m^2 + v_n^2} \\
& = \frac{y_{eD}}{2\varepsilon_m} \left(\cosh \varepsilon_m (y_{eD} - (y_D - c_{yD})) \right. \\
& \quad \left. + \cosh \varepsilon_m (y_{eD} - (y_D + c_{yD})) \right) \\
& \cdot (\sinh(\varepsilon_m y_{eD}))^{-1} - \frac{1}{\varepsilon_m^2}
\end{aligned}$$

$$\begin{aligned}
& \sum_{p=1}^{\infty} \frac{2 \cos(v_n y_D) \cos(v_n c_{yD})}{s + v_n^2 + w_p^2/L_D^2} \\
& = \frac{y_{eD}}{2\varepsilon_p} \left(\cosh \varepsilon_p (y_{eD} - (y_D - c_{yD})) \right. \\
& \quad \left. + \cosh \varepsilon_p (y_{eD} - (y_D + c_{yD})) \right) \\
& \cdot (\sinh(\varepsilon_p y_{eD}))^{-1} - \frac{1}{\varepsilon_p^2} \\
& \sum_{p=1}^{\infty} \frac{2 \cos(v_n y_D) \cos(v_n c_{yD})}{s + u_m^2 + v_n^2 + w_p^2/L_D^2} \\
& = \frac{y_{eD}}{2\varepsilon_{mp}} \left(\cosh \varepsilon_{mp} (y_{eD} - (y_D - c_{yD})) \right. \\
& \quad \left. + \cosh \varepsilon_{mp} (y_{eD} - (y_D + c_{yD})) \right) \\
& \cdot (\sinh(\varepsilon_{mp} y_{eD}))^{-1} - \frac{1}{\varepsilon_{mp}^2}, \quad (28)
\end{aligned}$$

where

$$\begin{aligned}
\varepsilon_m^2 &= s + u_m^2 = s + \frac{m^2 \pi^2}{x_{eD}^2} \\
\varepsilon_p^2 &= s + w_p^2 = s + \frac{p^2 \pi^2}{L_D^2} \quad (29) \\
\varepsilon_{mp}^2 &= s + u_m^2 + w_p^2 = s + \frac{m^2 \pi^2}{x_{eD}^2} + \frac{p^2 \pi^2}{L_D^2}.
\end{aligned}$$

Substitute (27)–(29) in (25) and simplify the equation is calculated as

$$\begin{aligned}
& s \tilde{p}_D = \frac{\pi}{x_{eD} z_{eD}} \\
& \cdot \left(\left[\cosh \sqrt{s} (y_{eD} - y_D + c_{yD}) \right. \right. \\
& \quad \left. \left. + \cosh \sqrt{s} (y_{eD} - y_D - c_{yD}) \right] \right) \\
& \cdot (\sqrt{s} \sinh \sqrt{s} y_{eD})^{-1} \\
& + \frac{2\pi}{x_{eD} z_{eD}} \sum_{m=1}^{\infty} \cos(u_m x_D) \frac{\cos(u_m c_{xD}) \sin(u_m w_{xD})}{u_m w_{xD}} \\
& \times \left[(\cosh \varepsilon_m (y_{eD} - (y_D - y_{wD})) \right. \\
& \quad \left. + \cosh \varepsilon_m (y_{eD} - (y_D + y_{wD}))) \right. \\
& \quad \left. \cdot (\varepsilon_m \sinh \varepsilon_m y_{eD})^{-1} \right] \\
& + \frac{2\pi}{x_{eD} z_{eD}} \sum_{p=1}^{\infty} \cos(w_p z_D) \frac{\cos(w_p c_{zD}) \sin(w_p w_{zD})}{w_p w_{zD}}
\end{aligned}$$

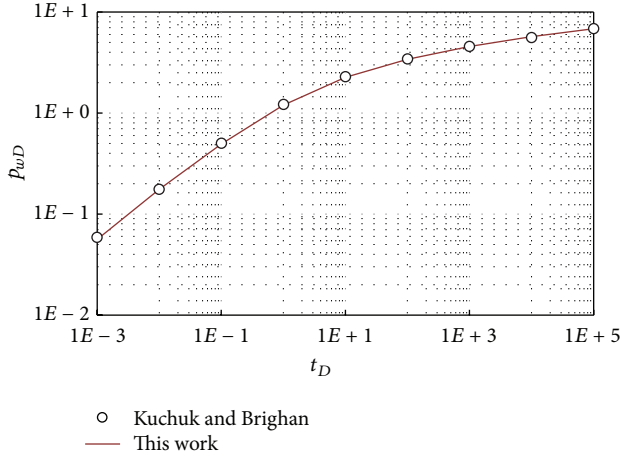


FIGURE 2: Model validation between this study and literature results.

$$\begin{aligned}
 & \times \left[\left(\cosh \varepsilon_p (y_{eD} - (y_D - y_{wD})) \right) \right. \\
 & \quad \left. + \cosh \varepsilon_p (y_{eD} - (y_D + y_{wD})) \right) \\
 & \quad \cdot (\varepsilon_p \sinh \varepsilon_p y_{eD})^{-1} \Big] \\
 & + \frac{4\pi}{x_{eD} z_{eD}} \sum_{m=1}^{\infty} \sum_{p=1}^{\infty} \cos(w_p z_{eD}) \cos(u_m x_{eD}) \\
 & \cdot \frac{\cos(u_m c_{xD}) \sin(u_m w_{xD})}{u_m w_{xD}} \frac{\cos(w_p c_{zD}) \sin(w_p w_{zD})}{w_p w_{zD}} \\
 & \times \left[\frac{y_{eD}}{2} \left(\cosh \varepsilon_{mp} (y_{eD} - (y_D - y_{wD})) \right) \right. \\
 & \quad \left. + \cosh \varepsilon_{mp} (y_{eD} - (y_D + y_{wD})) \right) \\
 & \quad \cdot (\varepsilon_{mp} \sinh \varepsilon_{mp} y_{eD})^{-1} \Big].
 \end{aligned} \tag{30}$$

Equation (30) is the mathematical model for pressure response of a partially penetrating hydraulic fracture in Laplace domain in dimensionless form. The solution in the real time domain can be obtained by using the inverse Laplace algorithm as proposed by Stehfest [18].

3. Validation of the Method

Kuchuk and Brigham [19] presented analytical solutions that are applicable to infinite-conductivity vertically fractured wells, elliptically shaped reservoirs, and anisotropic reservoirs producing at a constant rate or pressure. In order to validate the solution, we considered a special case that the fracture is full penetration; that is, $w_{zD} = 0.5$. We obtained some data from the literature presented by Kuchuk and Brigham. Figure 2 shows a comparison between the results from Kuchuk and Brigham and this work for the fully penetrating infinite-conductivity isotropic case. We can see a very

TABLE 1: Basic data of the system.

Dimensionless parameter	Value
Reservoir length x_{eD}	4000
Reservoir width y_{eD}	4000
Reservoir height z_{eD}	1
Half fracture length w_{xD}	1
Half fracture height w_{zD}	0.5
Variable L_D	1
Fracture position c_{xD}, c_{yD}, c_{zD}	(2000, 2000, 0.5)

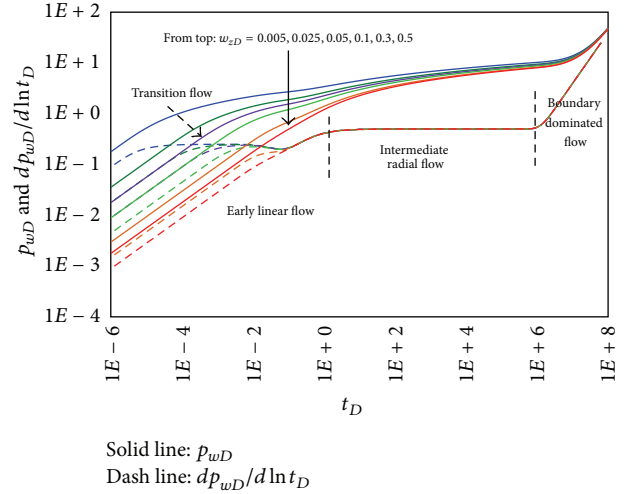


FIGURE 3: The effect of fracture height for fracture in the center.

good agreement between the solution in this paper and the literature, showing that the method in this study produces reliable transient pressure.

4. Sensitivity Analysis

Based on the analytical solution for a partially penetrating fracture in a box-shaped reservoir presented in the previous part, a sensitivity study for the parameters affecting the pressure and pressure derivative in the model is carried out. The intention of this study is to show the effect of each of these parameters on the dynamic behavior of a partially penetrating fracture in a box-shaped reservoir. We evaluate the pressure transient solution by varying the values of four parameters including the fracture half height, the fracture half length, the fracture position, and the reservoir width. As shown on the plots, the pressure and pressure derivative have different shapes for each combination of fracture height, fracture length, fracture position, and reservoir width. Dimensionless basic parameters used for simulating pressure transient response are presented in Table 1.

4.1. The Effect of Fracture Half Height and Off Center Fracture. Figure 3 depicts pressure and pressure derivative curves versus time for $w_{zD} = 0.005, 0.025, 0.05, 0.1, 0.3, 0.5$ with a fracture in the center of the reservoir, respectively (see

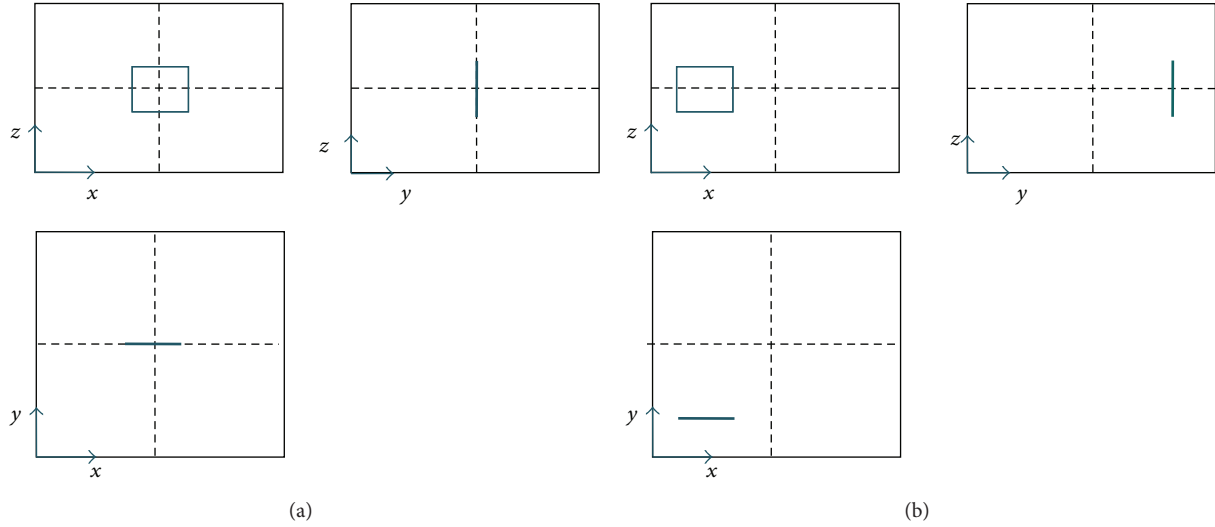


FIGURE 4: Schematic diagram of partially penetrating fracture.

Figure 4(a)). Other parameters are not changed in Table 1. Obviously, the pressure drop becomes larger as the fracture half height is decreased, which means that small fracture height will cause big pressure drop mainly in the early time period. The pressure drop for different w_{zD} tends to be consistent as time goes on. As shown in the pressure derivative curves, the fracture height mainly influences the early linear flow and transition flow and has no effect on the intermediate radial flow and boundary dominated flow. The fluids which take place in the direction of the upper and lower boundaries towards the fracture because of the effect of the partially penetrating fracture could produce the transition flow. As shown in Figure 3, when the $w_{zD} = 0.5$ (fully penetrating fracture), the transition flow cannot be seen from the pressure derivative curve. The end time of the early linear flow of the smaller w_{zD} is shorter than that of larger w_{zD} . All pressure derivative curves for different w_{zD} value are also parallel in early linear flow regime.

Figure 5 depicts pressure and pressure derivative curves versus time for $w_{zD} = 0.005, 0.025, 0.05, 0.1, 0.3, 0.5$ with a fracture in the off center of the reservoir, respectively (see Figure 4(b)). The fracture is located at (500, 500, 0.5) and other parameters are not changed as shown in Table 1. Comparing to the fracture in the center of the reservoir, the only difference is the number of the boundary dominated flows. The fluids flowing from the nearer boundaries and further boundaries towards the fracture cause first boundary dominated flow and second boundary dominated flow, respectively, because the distance of the off center fracture to each boundary (x -direction boundary and y -direction boundary) is different at late time. According to the boundary dominated flow which occurs twice as seen from the pressure derivative curve we can judge the fracture is off the center.

4.2. The Effect of Fracture Half Length and Off Center Fracture

4.2.1. Small Half Penetration Ratio ($2w_{zD} < 0.5$). Figure 6 shows the type curves for different value of fracture half

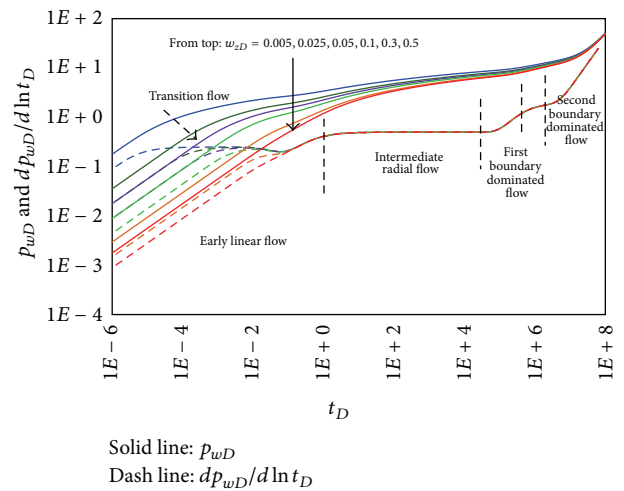


FIGURE 5: The effect of fracture height for fracture not in the center.

length ($w_{xD} = 2, 4, 6, 8$, resp.). The fracture is in the center of the reservoir while remaining other parameters are unchanged as shown in Table 1. As expected, the smaller the fracture half length, the higher the dimensionless pressure drop, which implies that small fracture length will cause great pressure drop at the early time. As shown in the pressure derivative curves, the fracture length mainly influences the early linear flow and transition flow and has no effect on the radial flow and boundary dominated flow. Comparing with the type curves for a fully penetrating fracture, the pressure derivative of a partially penetrating fracture has higher values during early time period. Before the intermediate radial flow regime, the pressure derivative becomes larger when the fracture length (w_{xD}) is decreased. For the same fracture height and reservoir thickness, the larger the dimensionless fracture half length w_{xD} is, the longer it takes to reach radial flow regime in the reservoir.

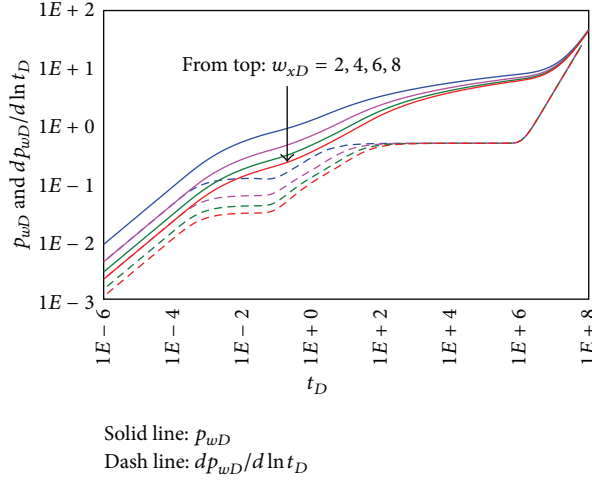


FIGURE 6: The effect of fracture length at $w_{zD} = 0.05$ for fracture in the center.

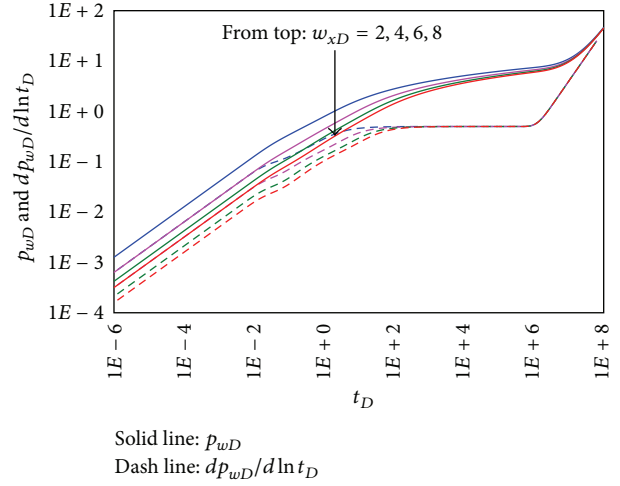


FIGURE 8: The effect of fracture length at $w_{zD} = 0.35$ for fracture in the center.

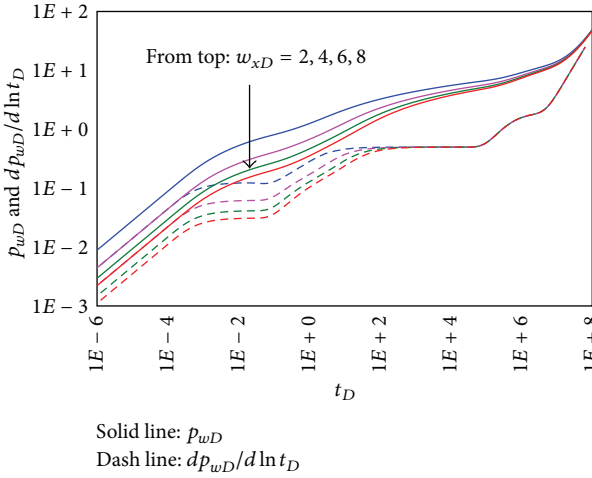


FIGURE 7: The effect of fracture length at $w_{zD} = 0.05$ for fracture not in the center.

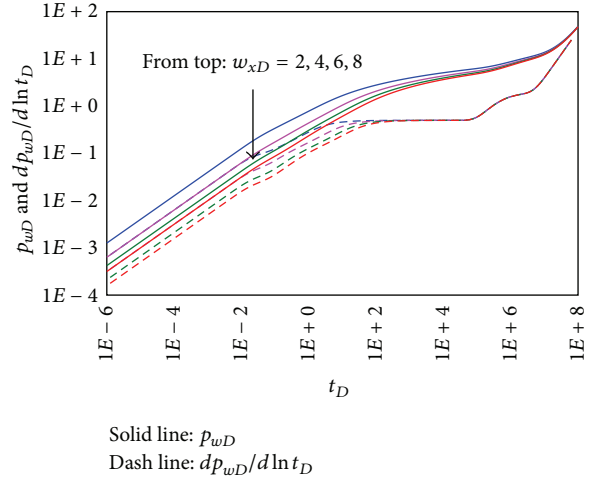


FIGURE 9: The effect of fracture length at $w_{zD} = 0.35$ for fracture not in the center.

Figure 7 depicts pressure and pressure derivative curves versus time for $w_{xD} = 2, 4, 6, 8$ with a fracture in the off center of the reservoir, respectively. The fracture is located at $(500, 500, 0.5)$ and other parameters are not changed as shown in Table 1. Comparing to Figure 6, the off center fracture mainly affects the boundary dominated flow. The boundary dominated flow regime appears twice followed by the intermediate radial flow.

4.2.2. Large Half Penetration Ratio ($2w_{zD} > 0.5$). The effect of the fracture half length on pressure and pressure derivative when the fracture with large half penetration ratio is in the center of the reservoir is shown in Figure 8. Because of the large half penetration ratio, the pressure behavior in this case tends to be similar to the fully penetrating fractures ($w_{zD} = 0.5$) where other factors such as fracture dimension have the main influence. A slight transition regime appears at the initial production time followed by the early linear flow regime.

Comparing with the type curves for a fully penetrating fracture, the pressure derivative of a partially penetrating fracture has higher values during early time period. The pressure drop is larger as the fracture length is decreased and the pressure derivative has the same rule before the radial flow regime.

Figure 9 depicts pressure and pressure derivative curves for $w_{xD} = 2, 4, 6, 8$ with a fracture in the off center of the reservoir, respectively. The position of the fracture is $(c_{xD} = 500, c_{yD} = 500, c_{zD} = 0.5)$, and other parameters are not changed as shown in the Table 1. We notice that the pressure and pressure derivative values for the case of partially penetrating fractures in the off center of the reservoir are very similar to that case of fully penetrating fractures. The only difference is that the boundary dominated flow regime appears twice. As such, the boundary dominated flow can be used to distinguish whether the fracture in the center of the reservoir.

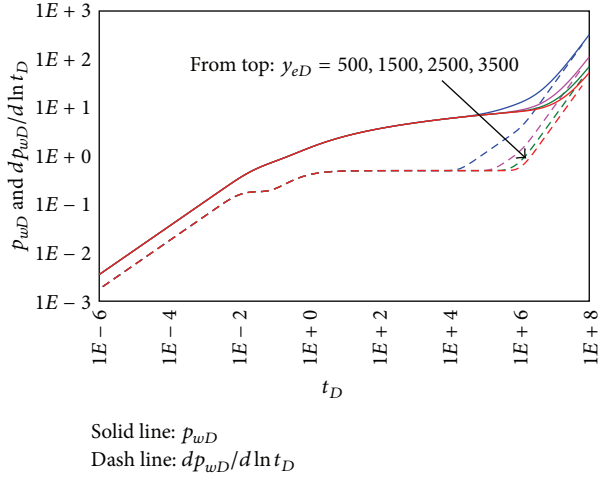


FIGURE 10: The effect of reservoir width.

4.3. The Effect of the Reservoir Width. Figure 10 depicts pressure derivative curves versus time for $y_{eD} = 500, 1500, 2500, 3500$ with a fracture in the center of the reservoir, respectively, while other parameters are not changed. Reservoir width mainly affects the boundary dominated flow regime. As seen in Figure 10, the starting time of the boundary dominated flow regime is affected by the dimensionless reservoir width. It is observed that the dimensionless pressure drop becomes larger as the dimensionless reservoir width is decreased, which means that a small reservoir will cause big pressure drop in the boundary dominated flow regime.

5. Application of Type Curve Matching

Type-curve matching is a quick method to estimate reservoir and fracture parameters. The following procedures illustrate how type curve matching is used to calculate reservoir and fracture characteristics such as permeability, fracture half length, and fracture half height.

Step 1. Plot pressure change (Δp) and pressure derivative ($t \times \Delta p'$) values versus test time on a log-log graph.

Step 2. Obtain the best match of the data with one of the type curves.

Step 3. Read from an match point: $t_M, t_{DM}, \Delta p_M, p_{DM}, w_{zD}, w_{xD}, L_D$.

Step 4. Calculate k_h :

$$k_h = \frac{141.2QB\mu p_D}{z_e \Delta p}. \quad (31)$$

Step 5. Calculate L :

$$L = \sqrt{\frac{0.0002637 t_M k_h}{\phi \mu c_t t_{DM}}}. \quad (32)$$

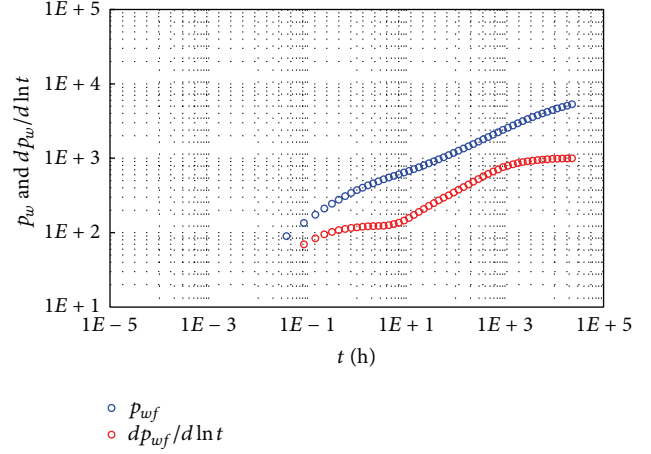


FIGURE 11: Pressure and pressure derivative plot for example.

Step 6. Calculate k_z :

$$k_z = \frac{k_h}{(L_D L / z_e)^2}. \quad (33)$$

Step 7. Calculate the fracture half height:

$$w_z = w_{zD} z_e. \quad (34)$$

Step 8. Calculate the fracture half length:

$$w_x = w_{xD} L. \quad (35)$$

Example 1. Giving the reservoir and well data,

$$\begin{aligned} Q &= 500 \text{ STB/D} & \phi &= 0.3 & \mu &= 4 \text{ cp} \\ B_o &= 1.4 \text{ bbl/STB} & z_e &= 100 \text{ ft} \\ c_t &= 4 \times 10^{-6} \text{ psi}^{-1} & r_w &= 0.25 \text{ ft} \\ p_i &= 6000 \text{ psi.} \end{aligned} \quad (36)$$

Fracture position is in the center of the reservoir.

Step 1. Plot pressure change (Δp) and pressure derivative ($t \times \Delta p'$) values versus test time on a log-log graph as shown in Figure 11.

Step 2. Obtain the best match of the data with one of the type curves as shown in Figure 12.

Step 3. Read from an match point: $t_M, t_{DM}, \Delta p_M, p_{DM}, w_{zD}, w_{xD}, L_D$:

$$\begin{aligned} t_M &= 10 & t_{DM} &= 0.11 & \Delta p_M &= 100 \\ p_{DM} &= 0.05 & w_{zD} &= 0.1 & w_{xD} &= 4 & L_D &= 1. \end{aligned} \quad (37)$$

Step 4. Calculate k_h from (31):

$$k_h = \frac{141.2 \times 500 \times 1.4 \times 4 \times 0.05}{100 \times 100} = 2 \text{ md.} \quad (38)$$

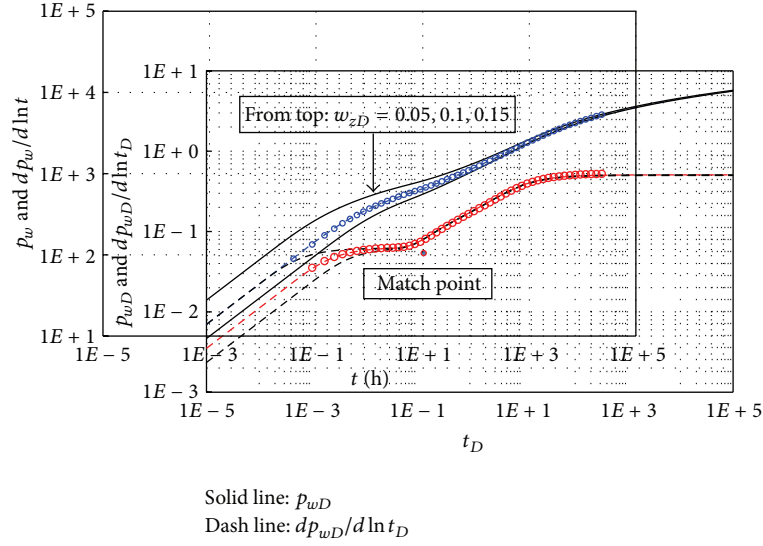
FIGURE 12: Type-curve matching plot for example ($w_{xD} = 4, L_D = 1$).

TABLE 2: Results of example.

Parameter	Input value	Calculated value by type curve matching technique
Horizontal permeability k_h , md	2	2
Vertical permeability k_z , md	2	2
Fracture half length w_x , ft	400	400
Fracture half height w_z , ft	10	10

Step 5. Calculate L from (32):

$$L = \sqrt{\frac{0.0002637 \times 10 \times 2}{0.3 \times 4 \times 4 \times 10^{-6} \times 0.11}} = 100 \text{ ft.} \quad (39)$$

Step 6. Calculate k_z from (33):

$$k_z = \frac{2}{((100 \times 1)/100)^2} = 2 \text{ md.} \quad (40)$$

Step 7. Calculate the fracture half height from (34):

$$w_z = 0.1 \times 100 = 10 \text{ ft.} \quad (41)$$

Step 8. Calculate the fracture half length from (35):

$$w_x = 4 \times 100 = 400 \text{ ft.} \quad (42)$$

Table 2 compares the input data and the resulting values of the example.

6. Conclusions

A detailed step by step procedure for solving the analytical solution of a partially penetrating hydraulic fracture in

a box-shaped reservoir by using Fourier cosine transform and Laplace transform is presented. The solution can be used to investigate the pressure transient behavior. In this paper, we validated it available with the published analytical solution for a relative simple system. Sensitivity analyses about the effects of the main parameters including fracture height, fracture length, and reservoir width on type curves are also presented in detail. Moreover the effect of the vertical position of the fracture on the pressure and pressure derivative is fully investigated. And an example is used to illustrate that the type curves can be used to analyze transient well test analysis for partially penetrating fracture in closed reservoirs. The merit of the solution is that it can also reduce the amount of computation and compute efficiently and quickly. The solution can be further developed as its great applicability.

Conflict of Interests

The authors declare that there is no conflict of interests regarding the publication of this paper.

References

- [1] S. Al Rbeawi and D. Tiab, "Effect of penetrating ratio on pressure behavior of horizontal wells with multiple-inclined hydraulic fractures," in *Proceedings of the SPE Western Regional Meeting Aeld in Bakersfield*, pp. 1–20, San Diego, Calif, USA, March 2012, SPE paper No. 153788.
- [2] S. Al Rbeawi and D. Tiab, "Partially penetrating hydraulic fractures: pressure responses and flow dynamics," in *Proceedings of the SPE Production and Operations Symposium*, SPE paper no. 164500, pp. 333–360, Oklahoma City, Okla, USA, March 2013.
- [3] O. Alpheus and D. Tiab, "Pressure transient analysis in partially penetrating infinite conductivity hydraulic fracture in naturally fractured reservoirs," in *Proceedings of the SPE Annual Technical Conference and Exhibition*, SPE Paper no. 116733, pp. 1–19, Denver, Colo, USA, September 2008.

- [4] E. Gomes and A. K. Ambastha, "Analytical expressions for pseudoskin for partially penetrating wells under various reservoir conditions," in *Proceedings of the 68th Annual Technical Conference and Exhibition of the Society of Petroleum Engineers*, pp. 691–706, Houston, Tex, USA, October 1993, SPE Paper No. 26484.
- [5] T. D. Streltsova-Adams, "Pressure drawdown in a well with limited flow entry," *Journal of Petroleum Technology*, vol. 31, no. 11, pp. 1469–1476, 1979, SPE-7486-PA.
- [6] I. M. Buhidma and R. Raghavan, "Transient pressure behavior of partially penetrating wells subject to bottomwater drive," *Journal of Petroleum Technology*, vol. 32, no. 7, pp. 1251–1261, 1980.
- [7] N. Yeh and A. C. Reynolds, "Analysis of pressure data from a restricted-entry well in a multilayer reservoir," *SPE Formation Evaluation*, vol. 4, no. 1, pp. 81–15584, 1989.
- [8] E. Ozkan and R. Raghavan, "A computationally efficient, transient-pressure solution for inclined wells," in *SPE Reservoir Evaluation & Engineering*, pp. 414–425, October 2000, SPE Paper No. 49085.
- [9] T. D. Bui, D. D. Mamora, and W. J. Lee, "Transient pressure analysis for partially penetrating wells in naturally fractured reservoirs," in *Proceedings of the SPE Rocky Mountain Regional/Low Permeability Reservoirs Symposium and Exhibition*, SPE Paper No. 60289, pp. 1–8, Denver, Colo, USA, March 2000.
- [10] G. Fuentes-Cruz and R. Camacho-Velazquez, "Pressure transient and decline curve behaviors for partially penetrating wells completed in naturally fractured-vuggy reservoirs," in *Proceedings of the SPE International Petroleum Conference in Mexico*, SPE Paper 92116, pp. 1–14, Puebla, Mexico, November 2004.
- [11] A. C. Gringarten and H. J. Ramey, "The use of source and Green's function in solving unsteady-flow problem in reservoir," SPE Paper 3818, Society of Petroleum Engineers, 1973.
- [12] A. C. Gringarten and H. J. Ramey Jr., "Unsteady-state pressure distributions created by a well with a single horizontal fracture, partial penetration, or restricted entry," SPE Paper No. 3819, SPE, 1974.
- [13] R. Raghavan, A. Uraiet, and G. W. Thomas, "Vertical fracture height: effect on transient flow behavior," in *Proceedings of the SPE-AIME Annual Fall Technical Conference and Exhibition*, pp. 265–277, August 1978, SPE Paper No. 6016.
- [14] F. Rodriguez, R. N. Horne, and H. Cinco-Ley, "Partially penetrating fractures: pressure transient analysis of an infinite conductivity fracture," in *Proceedings of the California Regional Meeting*, SPE Paper no. 12743, pp. 163–177, Long Beach, Calif, USA, April 1984.
- [15] F. Rodriguez, R. N. Horne, and H. Cinco-Ley, "Partially penetrating vertical fractures: pressure transient behavior of a finite-conductivity fracture," in *Proceedings of the 59th Annual Technical Conference and Exhibition*, SPE Paper no. 13057, pp. 1–4, Houston, Tex, USA, September 1984.
- [16] P. P. Valkó and S. Amini, "The method of distributed volumetric sources for calculating the transient and pseudosteady-state productivity of complex well-fracture configurations," in *Proceedings of the SPE Hydraulic Fracturing Technology Conference*, SPE paper 106279, pp. 1–14, January 2007.
- [17] J. Lin and D. Zhu, "Predicting well performance in complex fracture systems by slab source method," in *Proceedings of the SPE Hydraulic Fracturing Technology Conference*, SPE Paper 151960, pp. 1–15, The Woodlands, Tex, USA, February 2012.
- [18] H. Stehfest, "Algorithm 368: numerical inversion of laplace transforms," *Communications of the ACM*, vol. 13, no. 1, pp. 47–49, 1970.
- [19] F. Kuchuk and W. E. Brigham, "Transient flow in elliptical systems," Tech. Rep. SPE-7488-PA, Society of Petroleum Engineers, December 1979.

Research Article

Generalized Finite Difference Time Domain Method and Its Application to Acoustics

Jianguo Wei,¹ Song Wang,¹ Qingzhi Hou,² and Jianwu Dang^{2,3}

¹School of Computer Software, Tianjin University, Tianjin 300072, China

²Tianjin Key Laboratory of Cognitive Computing and Application, Tianjin University, Tianjin 300072, China

³Japan Advanced Institute of Science and Technology, Ishikawa 923-1292, Japan

Correspondence should be addressed to Qingzhi Hou; qhou@tju.edu.cn

Received 28 August 2014; Revised 11 January 2015; Accepted 11 January 2015

Academic Editor: Shaofan Li

Copyright © 2015 Jianguo Wei et al. This is an open access article distributed under the Creative Commons Attribution License, which permits unrestricted use, distribution, and reproduction in any medium, provided the original work is properly cited.

A meshless generalized finite difference time domain (GFDTD) method is proposed and applied to transient acoustics to overcome difficulties due to use of grids or mesh. Inspired by the derivation of meshless particle methods, the generalized finite difference method (GFDM) is reformulated utilizing Taylor series expansion. It is in a way different from the conventional derivation of GFDM in which a weighted energy norm was minimized. The similarity and difference between GFDM and particle methods are hence conveniently examined. It is shown that GFDM has better performance than the modified smoothed particle method in approximating the first- and second-order derivatives of 1D and 2D functions. To solve acoustic wave propagation problems, GFDM is used to approximate the spatial derivatives and the leap-frog scheme is used for time integration. By analog with FDTD, the whole algorithm is referred to as GFDTD. Examples in one- and two-dimensional domain with reflection and absorbing boundary conditions are solved and good agreements with the FDTD reference solutions are observed, even with irregular point distribution. The developed GFDTD method has advantages in solving wave propagation in domain with irregular and moving boundaries.

1. Introduction

Partial differential equations (PDEs) modeling problems in science and engineering, such as electromagnetics, acoustics, and hydrodynamics, are usually solved by numerical methods that discretize the computational domain with mesh or grids. Grid-based methods such as finite difference method (FDM), finite element method (FEM), and boundary element method (BEM) [1, 2] have had much achievements and still dominate the field of scientific computing. However, numerical difficulties originating from usage of grids often emerge. For complicated and irregular geometry, implementation of boundary conditions could be a big challenge for FDM. Generation of grids with high quality is not an easy task in FEM and BEM. Moreover, when free surface and moving boundary/interface have to be treated, the transformation of grids will turn the conventional grid-based methods into a difficult, time-consuming process. Numerical accuracy often degenerates and divergence problem occurs.

In recent 20 years, to overcome numerical difficulties due to use of grids or mesh, meshless methods (MMs) based on

different techniques have been proposed and widely used in many fields such as hydrodynamics [3], astrophysics [4], and solid mechanics [3, 5]. Among the MMs, generalized finite difference method (GFDM) is the one that evolved from traditional FDM [6, 7] and many different forms have been developed [8]. Benito and his coauthors made great contribution to its recent development [9–11]. For heat conduction problem, it has been compared with the element-free Galerkin (EFG) method (one of the most used MMs in solid mechanics) and better performance has been observed [10]. Recently, GFDM was used to solve the wave equations [11] and Burgers' equations [12] and simulate seismic wave propagation problems in heterogeneous media [13]. An application to the detonation shock dynamics [14] was also carried out. Nevertheless, few work on computational acoustics has been reported.

For acoustic wave propagation problems, the concentration is on the ones in confined domain, for which grid-based methods like FDTD and TDFEM (time-domain finite-element methods) [15], are mostly used. However, moving

boundary exists in many acoustic problems like sound wave propagation inside a deforming vocal tract. This problem is hardly solved by conventional grid-based methods and MMs provide a possibility. As one of the MMs, GFDM is extended to transient acoustics in this paper, which is helpful to solve wave propagation problems with moving boundary in the future.

Inspired by the derivation of meshless particle methods, we firstly formulated the GFDM in a way different from the original one that minimizes an energy norm. Such that the relationship between GFDM and meshless particle methods like smoothed particle hydrodynamics (SPH) and its improvements can be conveniently examined. Comparison with the modified dmoothed particle hydrodynamics (MSPH) method, which has better performances than SPH and its corrections [16], shows higher approximation accuracy of the GFDM, especially at the boundary region. By analog with FDTD, a method referred to as generalized finite difference time domain (GFDTD) is proposed, in which GFDM is used to discretize the spatial operators and the leap-frog algorithm is used for time integration. To show its good performance and efficiency, the GFDTD method is applied to transient acoustics. Comparison with conventional FDTD solutions is presented and discussed.

2. Generalized Finite Difference Method (GFDM)

Other than conventional derivation of GFDM by minimizing an energy norm [10], a different derivation of GFDM is presented in this section. Taylor series expansion of $f(x, y)$ around point (x_0, y_0) remaining up to second-order terms yields

$$f \approx f_0 + h \frac{\partial f_0}{\partial x} + k \frac{\partial f_0}{\partial y} + \frac{h^2}{2} \frac{\partial^2 f_0}{\partial x^2} + \frac{k^2}{2} \frac{\partial^2 f_0}{\partial y^2} + hk \frac{\partial^2 f_0}{\partial x \partial y}, \quad (1)$$

where $f = f(x, y)$, $f_0 = f(x_0, y_0)$, $h = x - x_0$, and $k = y - y_0$.

By multiplying both sides of (1) with $w^2 h$ and $w^2 k$ (w is a weighting function with compact support) and integrating

the resulted equations over the support domain Ω , we get two equations, and the following, as an example, is the result for $w^2 h$:

$$\begin{aligned} \int_{\Omega} f w^2 h \, dv &\approx \int_{\Omega} f_0 w^2 h \, dv + \int_{\Omega} \frac{\partial f_0}{\partial x} w^2 h^2 \, dv \\ &+ \int_{\Omega} \frac{\partial f_0}{\partial y} w^2 h k \, dv + \frac{1}{2} \int_{\Omega} \frac{\partial^2 f_0}{\partial x^2} w^2 h^3 \, dv \\ &+ \frac{1}{2} \int_{\Omega} \frac{\partial^2 f_0}{\partial y^2} w^2 h k^2 \, dv + \int_{\Omega} \frac{\partial^2 f_0}{\partial x \partial y} w^2 h^2 k \, dv, \end{aligned} \quad (2)$$

where dv is a volume measure.

Repeating the same procedure with $w^2 h^2/2$, $w^2 k^2/2$, and $w^2 h k$ instead of $w^2 h$ and $w^2 k$, we get other three equations and the following is the result for $w^2 h^2/2$:

$$\begin{aligned} \int_{\Omega} f \frac{w^2 h^2}{2} \, dv &\approx \int_{\Omega} f_0 \frac{w^2 h^2}{2} \, dv + \int_{\Omega} \frac{\partial f_0}{\partial x} \frac{w^2 h^3}{2} \, dv \\ &+ \int_{\Omega} \frac{\partial f_0}{\partial y} \frac{w^2 h^2 k}{2} \, dv + \frac{1}{2} \int_{\Omega} \frac{\partial^2 f_0}{\partial x^2} \frac{w^2 h^4}{2} \, dv \\ &+ \frac{1}{2} \int_{\Omega} \frac{\partial^2 f_0}{\partial y^2} \frac{w^2 h^2 k^2}{2} \, dv + \int_{\Omega} \frac{\partial^2 f_0}{\partial x \partial y} \frac{w^2 h^3 k}{2} \, dv. \end{aligned} \quad (3)$$

To approximate the integrations by Riemann sum, the volume of the support domain Ω is divided into N points with associated volumes dv_i , ($i = 1, 2, \dots, N$). Equations (2), (3), and the other three constitute a system of five equations written in matrix form as

$$\mathbf{A}_p \mathbf{D}_{fp} = \mathbf{b}_p, \quad (4)$$

with

$$\mathbf{A}_p = \begin{pmatrix} \sum_{i=1}^N w_i^2 h_i^2 \, dv_i & \sum_{i=1}^N w_i^2 h_i k_i \, dv_i & \sum_{i=1}^N w_i^2 \frac{h_i^3}{2} \, dv_i & \sum_{i=1}^N w_i^2 \frac{h_i k_i^2}{2} \, dv_i & \sum_{i=1}^N w_i^2 h_i^2 k_i \, dv_i \\ \sum_{i=1}^N w_i^2 h_i k_i \, dv_i & \sum_{i=1}^N w_i^2 k_i^2 \, dv_i & \sum_{i=1}^N w_i^2 \frac{h_i^2 k_i}{2} \, dv_i & \sum_{i=1}^N w_i^2 \frac{k_i^3}{2} \, dv_i & \sum_{i=1}^N w_i^2 h_i k_i^2 \, dv_i \\ \sum_{i=1}^N w_i^2 \frac{h_i^3}{2} \, dv_i & \sum_{i=1}^N w_i^2 \frac{h_i^2 k_i}{2} \, dv_i & \sum_{i=1}^N w_i^2 \frac{h_i^4}{4} \, dv_i & \sum_{i=1}^N w_i^2 \frac{h_i^2 k_i^2}{4} \, dv_i & \sum_{i=1}^N w_i^2 \frac{h_i^3 h_i}{2} \, dv_i \\ \sum_{i=1}^N w_i^2 \frac{h_i k_i^2}{2} \, dv_i & \sum_{i=1}^N w_i^2 \frac{k_i^3}{2} \, dv_i & \sum_{i=1}^N w_i^2 \frac{h_i^2 k_i^2}{4} \, dv_i & \sum_{i=1}^N w_i^2 \frac{k_i^4}{4} \, dv_i & \sum_{i=1}^N w_i^2 \frac{h_i k_i^3}{2} \, dv_i \\ \sum_{i=1}^N w_i^2 h_i^2 k_i \, dv_i & \sum_{i=1}^N w_i^2 h_i k_i^2 \, dv_i & \sum_{i=1}^N w_i^2 \frac{h_i^3 k_i}{2} \, dv_i & \sum_{i=1}^N w_i^2 \frac{h_i k_i^3}{2} \, dv_i & \sum_{i=1}^N w_i^2 h_i^2 k_i^2 \, dv_i \end{pmatrix},$$

$$\mathbf{D}_{\text{fP}} = \begin{Bmatrix} \frac{\partial f_0}{\partial x} \\ \frac{\partial f_0}{\partial y} \\ \frac{\partial^2 f_0}{\partial x^2} \\ \frac{\partial^2 f_0}{\partial y^2} \\ \frac{\partial^2 f_0}{\partial x \partial y} \end{Bmatrix}, \quad \mathbf{b}_{\text{P}} = \begin{pmatrix} -f_0 \sum_{i=1}^N w_i^2 h_i dv_i + \sum_{i=1}^N f_i w_i^2 h_i dv_i \\ -f_0 \sum_{i=1}^N w_i^2 k_i dv_i + \sum_{i=1}^N f_i w_i^2 k_i dv_i \\ -f_0 \sum_{i=1}^N w_i^2 \frac{h_i^2}{2} dv_i + \sum_{i=1}^N f_i w_i^2 \frac{h_i^2}{2} dv_i \\ -f_0 \sum_{i=1}^N w_i^2 \frac{k_i^2}{2} dv_i + \sum_{i=1}^N f_i w_i^2 \frac{k_i^2}{2} dv_i \\ -f_0 \sum_{i=1}^N w_i^2 h_i k_i dv_i + \sum_{i=1}^N f_i w_i^2 h_i k_i dv_i \end{pmatrix}, \quad (5)$$

where $w_i = w(d_i, d_m)$ with $d_i = \sqrt{(x_i - x_0)^2 + (y_i - y_0)^2}$, $h_i = x_i - x_0$, and $k_i = y_i - y_0$, and d_m is a measure of the support size.

The conventional derivation of GFDM is presented in appendix. It is clear that the difference between the conventional and the current derivation is not only the procedure but also the final form. The conventional derivation loses term dv_i (see (A.5)). If all the points in the domain have the same volume, dv_i at both sides of (4) will be cancelled, and the two final forms will be the same. However, dv_i can hardly be the same when points are irregularly spaced. From this point of view, our derived final form is more general and takes point irregularity into account.

3. Modified Smoothed Particle Hydrodynamics (MSPH)

As a modification to SPH, the MSPH method improves the accuracy of the approximations especially at points near the boundary of the domain [16]. It uses Taylor series expansion of function $f(x, y)$ as in (1). Similar to the derivations of (2) and (3), but with different weight functions $\partial w/\partial x$, $\partial w/\partial y$,

$\partial w^2/\partial x^2$, $\partial w^2/\partial y^2$, and $\partial^2 w/\partial x \partial y$, the following equations, as examples, for $\partial w/\partial x$ and $\partial w^2/\partial x^2$, are obtained:

$$\begin{aligned} \int_{\Omega} f \frac{\partial w}{\partial x} dv &= \int_{\Omega} f_0 \frac{\partial w}{\partial x} h dv + \frac{\partial f_0}{\partial x} \int_{\Omega} \frac{\partial w}{\partial x} h dv \\ &\quad + \frac{\partial f_0}{\partial y} \int_{\Omega} \frac{\partial w}{\partial x} k dv + \frac{1}{2} \frac{\partial^2 f_0}{\partial x^2} \int_{\Omega} \frac{\partial w}{\partial x} h^2 dv \\ &\quad + \frac{1}{2} \frac{\partial^2 f_0}{\partial y^2} \int_{\Omega} \frac{\partial w}{\partial x} k^2 dv + \frac{\partial^2 f_0}{\partial x \partial y} \int_{\Omega} \frac{\partial w}{\partial x} h k dv, \\ \int_{\Omega} f \frac{\partial w^2}{\partial x^2} dv &= \int_{\Omega} f_0 \frac{\partial w^2}{\partial x^2} dv + \frac{\partial f}{\partial x} \int_{\Omega} \frac{\partial w^2}{\partial x^2} h dv \\ &\quad + \frac{\partial f}{\partial y} \int_{\Omega} \frac{\partial w^2}{\partial x^2} k dv + \frac{1}{2} \frac{\partial^2 f_0}{\partial x^2} \int_{\Omega} \frac{\partial w^2}{\partial x^2} h^2 dv \\ &\quad + \frac{1}{2} \frac{\partial^2 f_0}{\partial y^2} \int_{\Omega} \frac{\partial w^2}{\partial x^2} k^2 dv + \frac{\partial^2 f_0}{\partial x \partial y} \int_{\Omega} \frac{\partial w^2}{\partial x^2} h k dv. \end{aligned} \quad (6)$$

Again the Riemann sum over the support domain Ω is used to approximate the integrations and a system of five equations is obtained as

$$\begin{pmatrix} \sum_{i=1}^N \frac{\partial w_i}{\partial x} h_i dv_i & \sum_{i=1}^N \frac{\partial w_i}{\partial x} k_i dv_i & \sum_{i=1}^N \frac{\partial w_i}{\partial x} \frac{h_i^2}{2} dv_i & \sum_{i=1}^N \frac{\partial w_i}{\partial x} \frac{k_i^2}{2} dv_i & \sum_{i=1}^N \frac{\partial w_i}{\partial x} h_i k_i dv_i \\ \sum_{i=1}^N \frac{\partial w_i}{\partial y} h_i dv_i & \sum_{i=1}^N \frac{\partial w_i}{\partial y} k_i dv_i & \sum_{i=1}^N \frac{\partial w_i}{\partial y} \frac{h_i^2}{2} dv_i & \sum_{i=1}^N \frac{\partial w_i}{\partial y} \frac{k_i^2}{2} dv_i & \sum_{i=1}^N \frac{\partial w_i}{\partial y} h_i k_i dv_i \\ \sum_{i=1}^N \frac{\partial w_i^2}{\partial x^2} h_i dv_i & \sum_{i=1}^N \frac{\partial w_i^2}{\partial x^2} k_i dv_i & \sum_{i=1}^N \frac{\partial w_i^2}{\partial x^2} \frac{h_i^2}{2} dv_i & \sum_{i=1}^N \frac{\partial w_i^2}{\partial x^2} \frac{k_i^2}{2} dv_i & \sum_{i=1}^N \frac{\partial w_i^2}{\partial x^2} h_i k_i dv_i \\ \sum_{i=1}^N \frac{\partial w_i^2}{\partial y^2} h_i dv_i & \sum_{i=1}^N \frac{\partial w_i^2}{\partial y^2} k_i dv_i & \sum_{i=1}^N \frac{\partial w_i^2}{\partial y^2} \frac{h_i^2}{2} dv_i & \sum_{i=1}^N \frac{\partial w_i^2}{\partial y^2} \frac{k_i^2}{2} dv_i & \sum_{i=1}^N \frac{\partial w_i^2}{\partial y^2} h_i k_i dv_i \\ \sum_{i=1}^N \frac{\partial w_i^2}{\partial x \partial y} h_i dv_i & \sum_{i=1}^N \frac{\partial w_i^2}{\partial x \partial y} k_i dv_i & \sum_{i=1}^N \frac{\partial w_i^2}{\partial x \partial y} \frac{h_i^2}{2} dv_i & \sum_{i=1}^N \frac{\partial w_i^2}{\partial x \partial y} \frac{k_i^2}{2} dv_i & \sum_{i=1}^N \frac{\partial w_i^2}{\partial x \partial y} h_i k_i dv_i \end{pmatrix} \begin{Bmatrix} \frac{\partial f_0}{\partial x} \\ \frac{\partial f_0}{\partial y} \\ \frac{\partial^2 f_0}{\partial x^2} \\ \frac{\partial^2 f_0}{\partial y^2} \\ \frac{\partial^2 f_0}{\partial x \partial y} \end{Bmatrix}$$

$$= \begin{pmatrix} -f_0 \sum_{i=1}^N \frac{\partial w_i}{\partial x} dv_i + \sum_{i=1}^N f_i \frac{\partial w_i}{\partial x} dv_i \\ -f_0 \sum_{i=1}^N \frac{\partial w_i}{\partial y} dv_i + \sum_{i=1}^N f_i \frac{\partial w_i}{\partial y} dv_i \\ -f_0 \sum_{i=1}^N \frac{\partial w_i^2}{\partial x^2} dv_i + \sum_{i=1}^N f_i \frac{\partial w_i^2}{\partial x^2} dv_i \\ -f_0 \sum_{i=1}^N \frac{\partial w_i^2}{\partial y^2} dv_i + \sum_{i=1}^N f_i \frac{\partial w_i^2}{\partial y^2} dv_i \\ -f_0 \sum_{i=1}^N \frac{\partial w_i^2}{\partial x \partial y} dv_i + \sum_{i=1}^N f_i \frac{\partial w_i^2}{\partial x \partial y} dv_i \end{pmatrix}. \quad (7)$$

Compared with formula (4), the only difference is the terms multiplied to both sides of (1). In GFDM, $w^2 h$, $w^2 k$, $w^2 h^2/2$, $w^2 k^2/2$, and $w^2 hk$ are used instead of $\partial w/\partial x$, $\partial w/\partial y$, $\partial w^2/\partial x^2$, $\partial w^2/\partial y^2$, and $\partial^2 w/\partial x \partial y$ in MSPH. As a result, GFDM avoids computing the derivatives of the weight function and hence saves computational efforts and leads to more choice of the weight function.

4. Numerical Tests for Approximation of Derivatives

In previous sections the deviation of GFDM and MSPH is presented. In this section, to compare the performance of the two methods, they are used to approximate the derivatives of certain 1D and 2D functions. For the convenience of evaluation, a global error measure is defined as follows:

$$\text{Error}_u = \frac{1}{|u|_{\max}} \sqrt{\frac{1}{N} \sum_{i=1}^N (u_i^{(e)} - u_i^{(n)})^2}, \quad (8)$$

where u can be $\partial f/\partial x$, $\partial f/\partial y$, $\partial^2 f/\partial x^2$, and $\partial^2 f/\partial y^2$ and the superscripts (e) and (n) refer to the exact and numerical solutions, respectively.

The quartic spline function is used as the weight function w_i :

$$w_i(d) = \begin{cases} 1 - 6\left(\frac{d}{d_m}\right)^2 + 8\left(\frac{d}{d_m}\right)^3 - 3\left(\frac{d}{d_m}\right)^4, & d \leq d_m, \\ 0, & d > d_m, \end{cases} \quad (9)$$

where d_m is the kernel radius taken as $2.1\Delta x$ (Δx is the space interval) which is usually used in meshless methods.

4.1. One-Dimensional Case. Consider the following function:

$$f(x) = (x - 0.5)^4, \quad x \in [0, 1]. \quad (10)$$

Figure 1 shows the first- and second-order derivatives estimated by GFDM and MSPH and the exact results when

the domain is discretized into 21 equally spaced points. It is seen that GFDM has better performance in both derivatives especially for the points near boundaries. When the number of points increases to 51, the results are similar as exhibited in Figure 2. Error analysis shown in Table 1 indicates that GFDM has higher accuracy. With increasing number of points, the global error decreases.

4.2. Two-Dimensional Case. For the function

$$f(x, y) = \sin \pi x \sin \pi y, \quad x, y \in [0, 1] \times [0, 1], \quad (11)$$

its first- and second-order derivatives together with estimations by GFDM and MSPH are shown in Figure 3. In each direction 21 points are employed. As expected, GFDM has higher approximation accuracy than MSPH for both first- and second-order derivatives as shown in Table 2.

5. Generalized Finite Difference Time Domain Method for Computational Acoustics

For computational acoustics, the mostly used approach is the FDTD method, which was originally designed for the simulation of electromagnetics [1, 2]. As a finite difference scheme, its applicability to complex problems suffers from aforementioned difficulties, for which the generalized finite difference can be a good alternative. In this section, together with the basics of computational acoustics, a meshless method is proposed, in which GFDM is used to discretize the spatial derivatives and the leap-frog algorithm is used to discretize the temporal derivatives. By analog with FDTD, it is referred to as generalized finite difference time domain (GFDTD) method and is expected to have advantages due to its meshless property.

The governing equations for acoustic wave propagation problems are

$$\begin{aligned} \rho_0 \frac{\partial \mathbf{v}}{\partial t} &= -\nabla p, \\ \frac{1}{c_0^2} \frac{\partial p}{\partial t} &= -\rho_0 \nabla \cdot \mathbf{v}, \end{aligned} \quad (12)$$

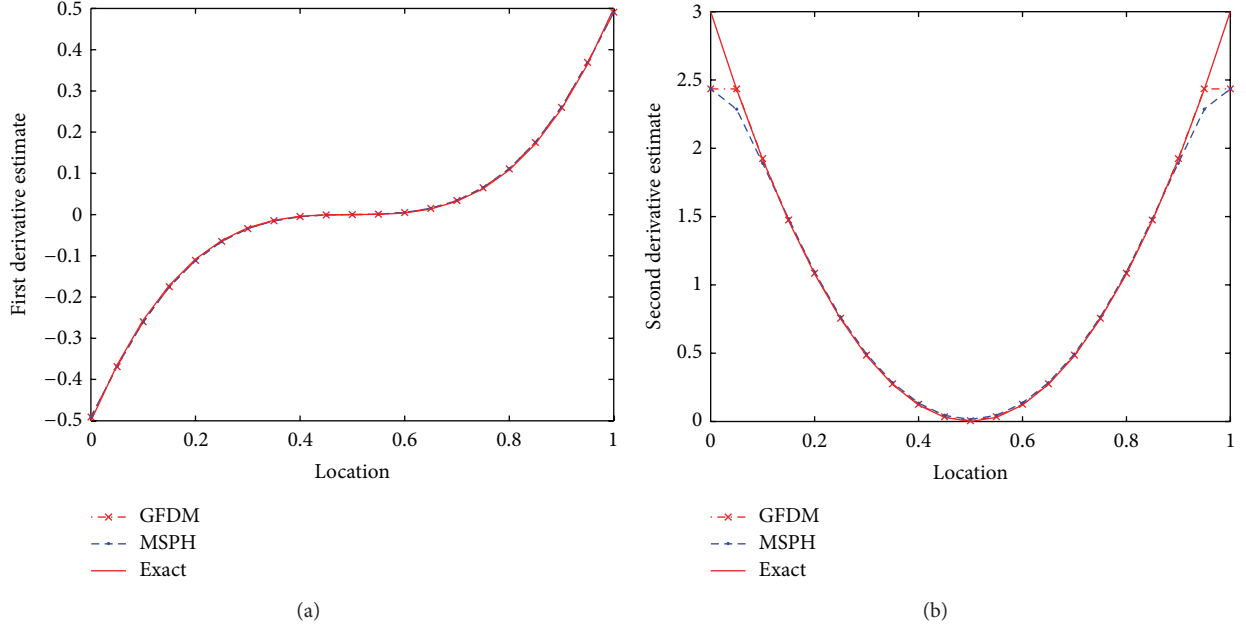


FIGURE 1: Estimates of the first derivative (a) and second derivative (b) of function $f(x) = (x - 0.5)^4$ with 21 equally spaced points on $[0, 1]$.

TABLE 1: Approximation errors in the derivatives of the function $f(x) = (x - 0.5)^4$.

Error (%)	$\partial f / \partial x$	$\partial^2 f / \partial x^2$
GFDM with 21 points	0.77	5.81
MSPH with 21 points	0.77	6.02
GFDM with 51 points	0.11	1.55
MSPH with 51 points	0.11	1.61

TABLE 2: Approximation errors in the derivatives of the function $f(x, y) = \sin \pi x \sin \pi y$.

Error (%)	$\partial f / \partial x$	$\partial f / \partial y$	$\partial^2 f / \partial x^2$	$\partial^2 f / \partial y^2$
GFDM	0.29	0.29	2.87	2.87
MSPH	0.47	0.47	4.71	4.71

where p is pressure, \mathbf{v} is particle velocity, ρ_0 is the density of the medium, and c_0 is the speed of sound.

5.1. Spatial Derivative Approximations by GFDM. The spatial derivatives on the right-hand side of (12) are approximated by GFDM. By solving (4) we get the approximations of $\partial f / \partial x$ and $\partial f / \partial y$. That is, the derivatives of variable f at point (x_0, y_0) can be approximated by function values at points inside the support domain centered at (x_0, y_0) as

$$\begin{aligned} \frac{\partial f_0}{\partial x} &= -m_0 f_0 + \sum_{i=1}^N f_i m_i, \\ \frac{\partial f_0}{\partial y} &= -\eta_0 f_0 + \sum_{i=1}^N f_i \eta_i, \end{aligned} \quad (13)$$

where m_0 and η_0 are the difference coefficients for center point and m_i and η_i are coefficients for other points in the support domain. As GFDM can reproduce constant functions [4], we have

$$m_0 = \sum_{i=1}^N m_i, \quad \eta_0 = \sum_{i=1}^N \eta_i. \quad (14)$$

By taking both p and \mathbf{v} in (12) as f , the approximated spatial operators in (12) are accordingly obtained.

5.2. Explicit Leap-Frog Scheme in GFDTD. Generally, the temporal derivatives on the left-hand side of (12) can be integrated by any time marching algorithms. Inspired by the conventional FDTD method, the second-order accurate explicit leap-frog scheme is used herein, in which two variables p and \mathbf{v} are alternatively calculated. The velocity is computed at the half time step and the pressure is calculated at the integer time step [2]. After temporal approximations the semi-discretization of (12) becomes

$$\begin{aligned} \rho_0 \frac{\mathbf{v}^{n+1/2} - \mathbf{v}^{n-1/2}}{\Delta t} &= -\nabla p^n, \\ \frac{1}{c_0^2} \frac{p^{n+1} - p^n}{\Delta t} &= -\rho_0 \nabla \cdot \mathbf{v}^{n+1/2}, \end{aligned} \quad (15)$$

where superscript n represents the time step. The leap-frog scheme is conditionally stable and the time step Δt should satisfy the Courant-Friedrichs-Lewy (CFL) condition; that is, $\Delta t \leq \Delta x / (\sqrt{\text{dim}} \cdot c_0)$, where dim is the dimension of the problem.

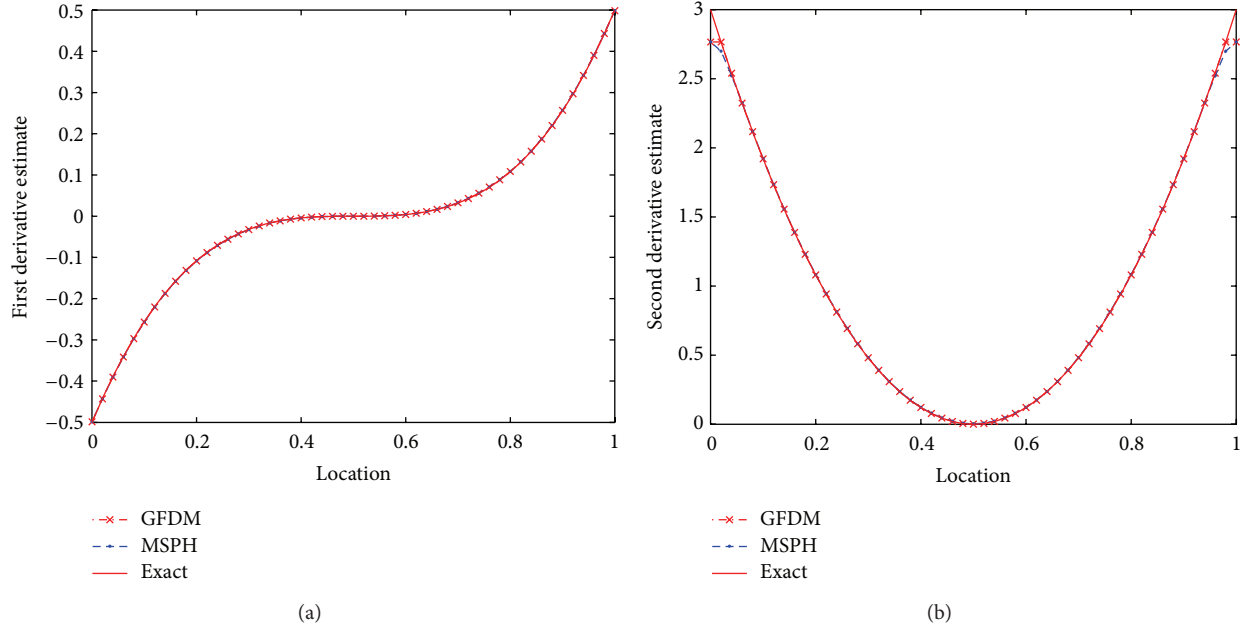


FIGURE 2: Estimates of the first derivative (a) and second derivative (b) of function $f(x) = (x - 0.5)^4$ with 51 equally spaced points on $[0, 1]$.

Substituting (13) into the right-hand side of (15) as the approximation of the first-order spatial derivatives, the full discretized system of equations becomes

$$\begin{aligned}
 \mathbf{v}_0^{n+1/2} &= \mathbf{v}_0^{n-1/2} + \frac{\Delta t}{\rho_0} \\
 &\cdot \left[\left(m_0 p_0^n - \sum_{i=1}^N m_i p_i^n \right), \left(\eta_0 p_0^n - \sum_{i=1}^N \eta_i p_i^n \right) \right]^T, \\
 p_0^{n+1} &= p_0^n + \Delta t \rho_0 c_0^2 \\
 &\cdot \left[\left(m_0 u_0^{n+1/2} - \sum_{i=1}^N m_i u_i^{n+1/2} \right) \right. \\
 &\quad \left. + \left(\eta_0 v_0^{n+1/2} - \sum_{i=1}^N \eta_i v_i^{n+1/2} \right) \right],
 \end{aligned} \tag{16}$$

where the particle velocity is a 2D vector $\mathbf{v} = [u, v]^T$.

By analog with FDTD, the full discretization scheme is referred to as generalized finite difference time domain (GFDTD) method.

6. Numerical Results

To validate the proposed GFDTD method, it is applied to one- and two-dimensional wave propagation problems. Three cases are presented. The first two examine the acoustic wave propagation in one- and two-dimensional domain, respectively, and the third one is a real case with different types of boundary conditions. All the cases use (9) as the weight function. The other parameters are $\rho_0 = 1 \text{ kg/m}^3$ and $c_0 = 346.4 \text{ m/s}$ and the time interval Δt is set to be $1 \mu\text{s}$ to

satisfy the CFL condition. FDTD solutions are chosen as the reference.

6.1. One-Dimensional Case. In this case 501 points are equally spaced in the domain $[0, 1]$. In the middle of it, there is a wave source in Gaussian pulse form:

$$gp(x) = e^{-25|x-0.5|}. \tag{17}$$

As shown in Figure 4, the simulated results at two time levels $t = 250 \mu\text{s}$ and $500 \mu\text{s}$ have good agreement with the FDTD solutions. Compared with FDTD, the relative errors concerning the pressure P^{FDTD} and P^{GFDTD} are

$$\begin{aligned}
 \text{Error}_{250} &= \frac{\|P^{\text{FDTD}} - P^{\text{GFDTD}}\|_2}{\|P^{\text{FDTD}}\|_2} = 0.267 \cdot 10^{-2}, \\
 \text{Error}_{500} &= \frac{\|P^{\text{FDTD}} - P^{\text{GFDTD}}\|_2}{\|P^{\text{FDTD}}\|_2} = 0.519 \cdot 10^{-2}.
 \end{aligned} \tag{18}$$

6.2. Two-Dimensional Case. The Gaussian wave propagation in two-dimensional domain is simulated in this section. The length of the square domain is 0.1 m and 101 points are uniformly distributed in each direction. The wave source starts from the middle of the domain. Figure 5 compares the solutions of FDTD and GFDTD at $t = 20 \mu\text{s}$. The results along $y = 0.05 \text{ m}$ are shown in Figure 5(c). Again, good agreement is observed and the relative error is less than 2%.

To show the advantage of the proposed GFDTD over the conventional FDTD, irregular point distribution is examined. All the points used above are allowed to have $\pm 10\%$ perturbation around their original locations to make the distribution irregular, part of which is shown in Figure 6(a) and

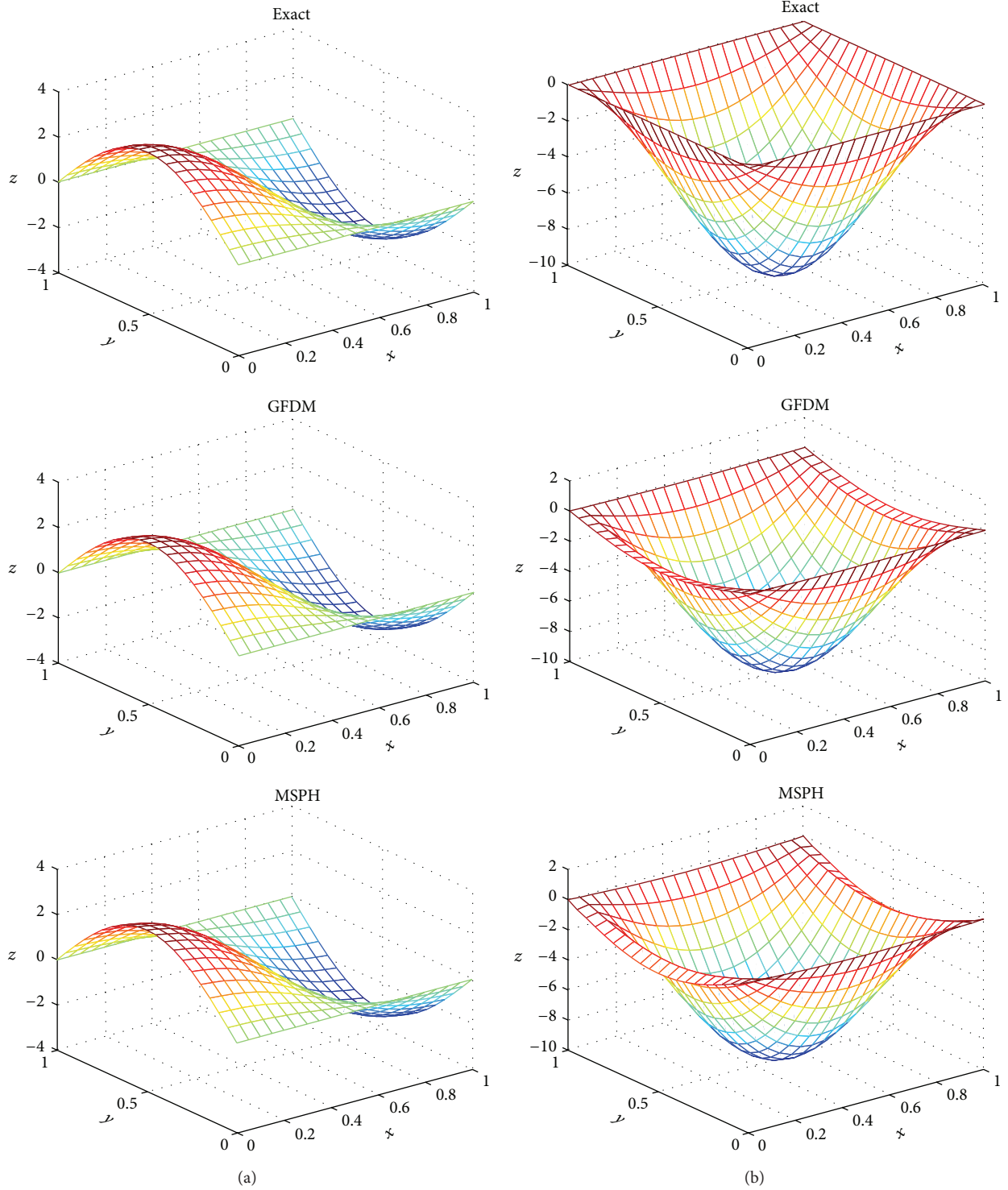


FIGURE 3: Exact (top) and estimated (a) $\partial f/\partial x$ and (b) $\partial^2 f/\partial x^2$ of function $f(x, y) = \sin \pi x \sin \pi y$ by GFDm (middle) and MSPH (bottom).

the result is shown in Figure 6(b). The comparison of the result along $y = 0.05$ m shown in Figure 6(c) indicates that, with irregular distribution of computational points, the Gaussian wave propagates as well as before.

In the GFDm simulation of wave propagation with irregular point distribution, the volume associated to each

point had better to be considered as analyzed at the end of Section 2. In 2D case, the volume associated with a given point is the area that the point dominates. Here we use Delaunay triangulation and Voronoi diagram [17] to calculate the area and the results are shown in Figure 7. The volume of each point is shown in Figure 7(a). Due to the designed $\pm 10\%$

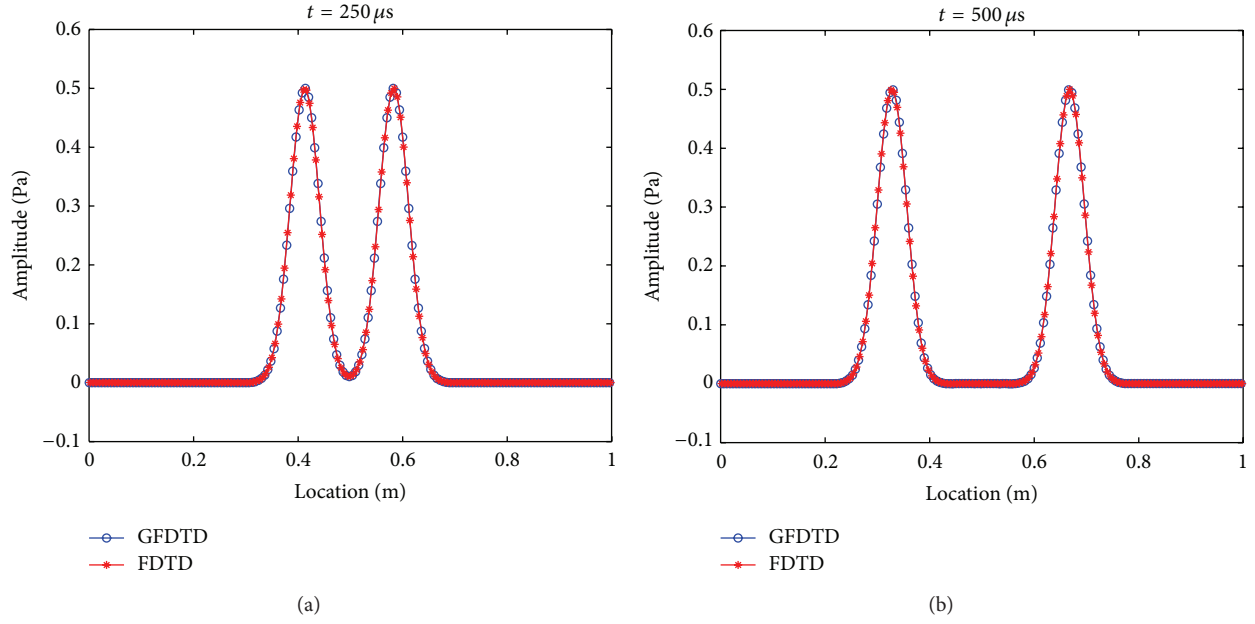


FIGURE 4: Gaussian wave propagation at two time points: (a) $t = 250 \mu s$ and (b) $500 \mu s$.

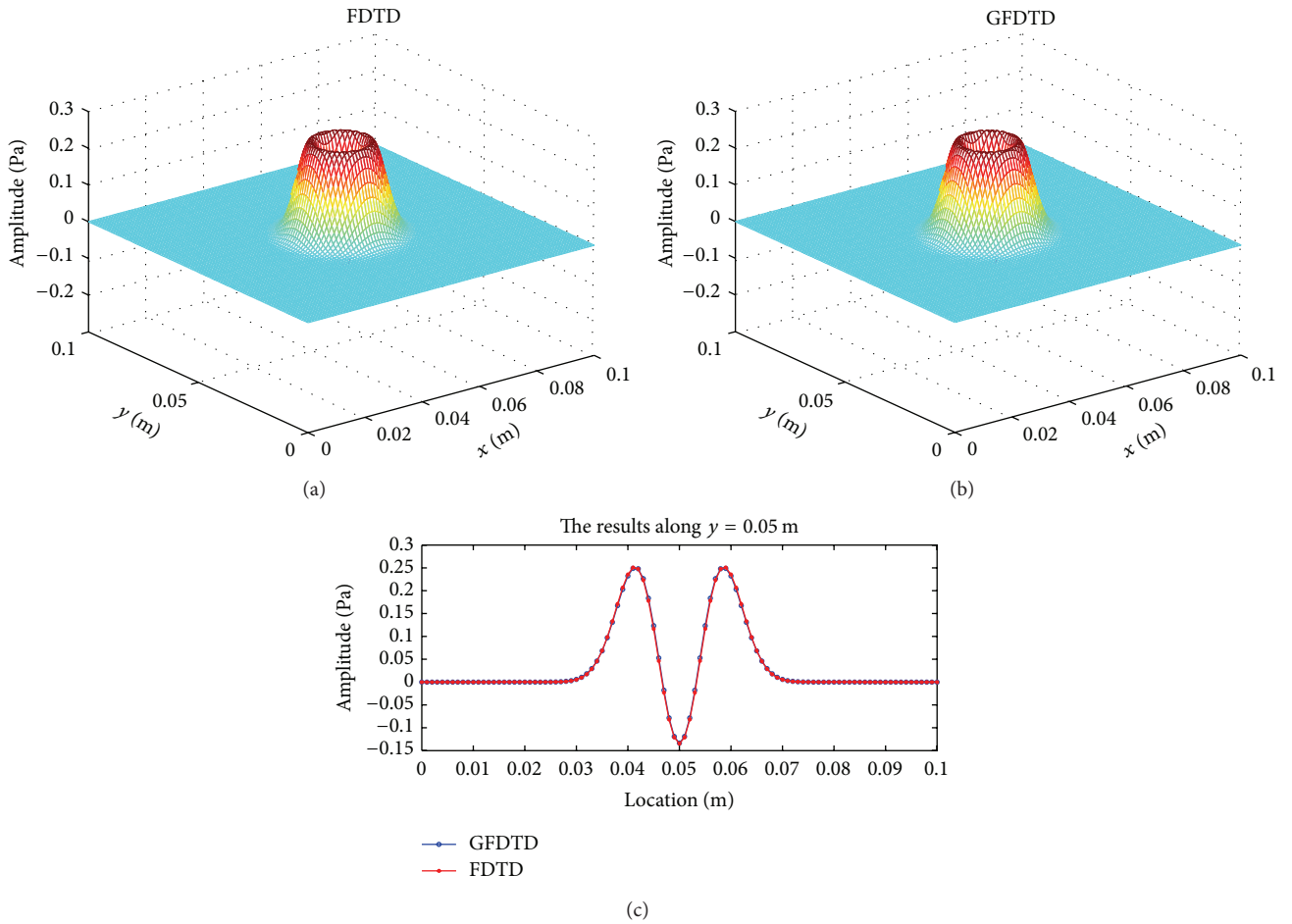


FIGURE 5: Gaussian wave propagation in a square domain at time $t = 20 \mu s$. (a) The FDTD result, (b) the GFDTD result, and (c) the comparison along $y = 0.05$ m.

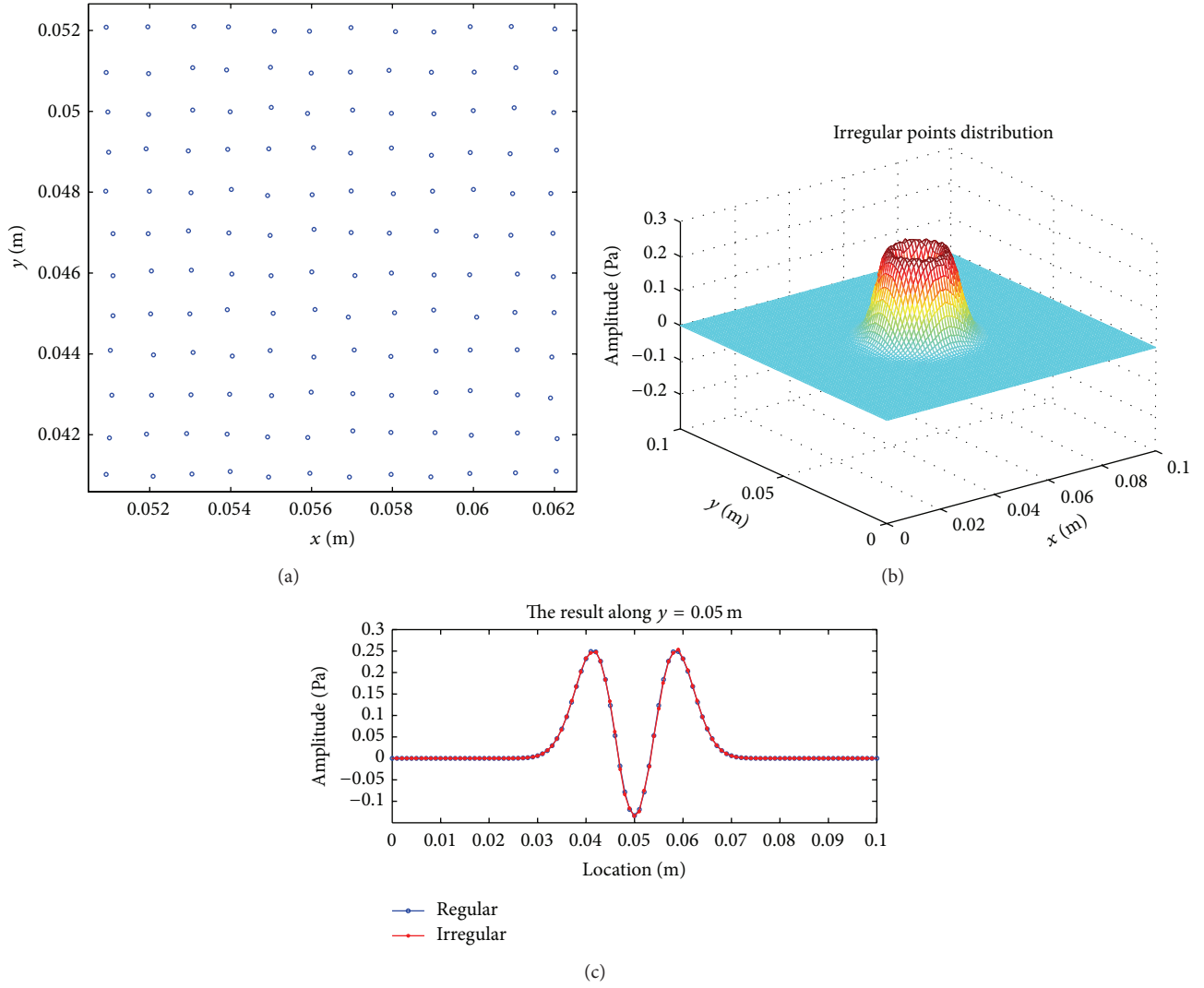


FIGURE 6: Gaussian wave propagation in a square domain with irregular point distribution. (a) Part of the irregular distribution, (b) simulated results, and (c) comparison with regular point distribution after $20 \mu\text{s}$.

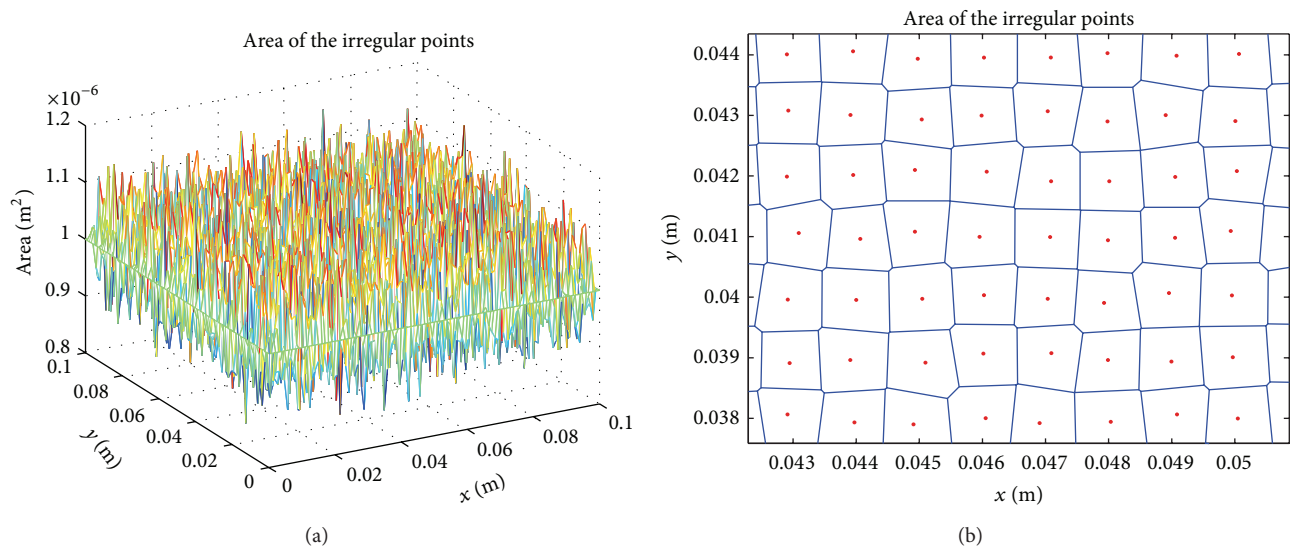


FIGURE 7: (a) Area associated with irregular distributed points and (b) Voronoi diagram.

perturbation, the volume fluctuates around 1^{-6} m^2 . Based on Delaunay triangulation and Voronoi diagram, the area associated with a red point is indicated by the area surrounded by the blue lines as shown in Figure 7(b). To compare the results with regular and irregular point distributions, the values on regularly distributed points have to be firstly interpolated by the calculated results with irregularly spaced points. The third-order accurate cubic interpolation method [17] is used herein. The relative error is

$$\text{Error} = \frac{\|P^{\text{irregular}} - P^{\text{regular}}\|_2}{\|P^{\text{regular}}\|_2} = 1.58 \cdot 10^{-2}. \quad (19)$$

The relatively small error is due to the gentle irregular point distribution. That is, if the point irregularity is small, the effect of dv_i is negligible. This is consistent with Benito's results [9–11].

6.3. Two-Dimensional Case with Effect of Boundary Conditions. In Sections 6.1 and 6.2, wave propagation inside a domain is simulated. In this section, to show the effect of boundaries, which is of high importance in transient acoustics, sound wave propagation in a rectangular tube is studied. Two different kinds of boundary conditions including reflection and absorbing boundary are considered. At the left edge of the computational domain there is a Gaussian pulse as the source term. The upper and bottom boundaries are reflection layers and the second-order Mur's absorbing boundary condition [18] exists at the right side boundary. In this case, the same ρ_0 and c_0 are used as before and the time interval Δt is $1 \mu\text{s}$. Inside the computational domain 64×100 points with spatial interval $\Delta x = \Delta y = 1 \text{ mm}$ are evenly spaced.

6.3.1. Source Term. The left is a wave source with pressure given by the Gaussian pulse:

$$\text{gp}(t) = e^{-\{(t-T)/0.29T\}^2}, \quad (20)$$

where $T = 0.646/f_0$ and $f_0 = 10 \text{ KHz}$.

6.3.2. Reflection Boundary Condition. To simulate reflections at the upper and bottom wall boundaries, the model proposed by Yokota et al. [19, 20] and widely used in room acoustics is employed herein. In this model, the normal component of particle velocity and the pressure of the points on the boundary are supposed to satisfy the following condition:

$$\mathbf{v}_{\text{norm}} = \frac{P}{Z_{\text{norm}}}, \quad (21)$$

where Z_{norm} is the normal acoustic impedance on the boundary given by

$$Z_{\text{norm}} = \rho_0 c_0 \frac{1 + \sqrt{1 - \alpha_{\text{norm}}}}{1 - \sqrt{1 - \alpha_{\text{norm}}}}. \quad (22)$$

Here the normal sound absorption coefficient α_{norm} is taken as 0.2 as in [19].

6.3.3. Absorbing Boundary Condition. At the right boundary, second-order Mur's absorbing boundary condition [18] is applied:

$$\frac{1}{c_0} \frac{\partial^2 p}{\partial x \partial t} + \frac{1}{c_0^2} \frac{\partial^2 p}{\partial t^2} + \frac{1}{2} \frac{\partial^2 p}{\partial y^2} = 0. \quad (23)$$

By applying (12) to (23) and performing time integration, (23) degenerates to

$$\frac{\partial p}{\partial x} + \frac{1}{c_0} \frac{\partial p}{\partial t} - \frac{c_0 \rho_0}{2} \frac{\partial u}{\partial y} = 0. \quad (24)$$

When GFDTD is used, the discrete form of (24) is obtained as

$$\begin{aligned} \frac{p_0^{n+1} - p_0^n}{\Delta t} &= \frac{c_0^2 \rho_0}{2} \left(\eta_0 u_0^{n+1/2} - \sum_{i=1}^N \eta_i u_i^{n+1/2} \right) \\ &\quad - c_0 \left(m_0 p_0^n - \sum_{i=1}^N m_i p_i^n \right). \end{aligned} \quad (25)$$

6.3.4. Results. After applying the source term and the two boundary conditions into our case, the wave is considered to be propagating from left to right inside a tube and gets absorbed at the end of it. Figure 8 shows the simulated results after $200 \mu\text{s}$ with a color map image that clearly depicts the pressure distribution. In Figure 9, the results after $350 \mu\text{s}$ are depicted and the absorbing boundary at the right edge leads to no reflection.

7. Conclusion

A new derivation of the generalized finite difference method (GFDM) with Taylor series expansion generates the same formulation as its conventional derivation and clearly demonstrates its relationship with meshless particle methods. GFDM has better performance in derivative approximations than the particle methods. The proposed generalized finite difference time domain (GFDTD) method has been successfully applied to one- and two-dimensional acoustic wave propagation problems with reflection and absorbing boundary conditions. The numerical results are in line with the FDTD reference solutions even with irregular point distribution. The GFDTD method has high potentials in solving transient acoustic problems with moving boundaries, which deserves further studies.

Appendix

Conventional Derivation of GFDM

Considering the 2D case, for the same Taylor expansion in (1), we consider an energy norm B :

$$\begin{aligned} B = \sum_{i=1}^N \left[\left[f_0 - f_i + h_i \frac{\partial f_0}{\partial x} + k_i \frac{\partial f_0}{\partial y} + h_i^2 \frac{\partial^2 f_0}{\partial x^2} + k_i^2 \frac{\partial^2 f_0}{\partial y^2} \right. \right. \\ \left. \left. + h_i k_i \frac{\partial^2 f_0}{\partial x \partial y} \right] w_i \right]^2, \end{aligned} \quad (A.1)$$

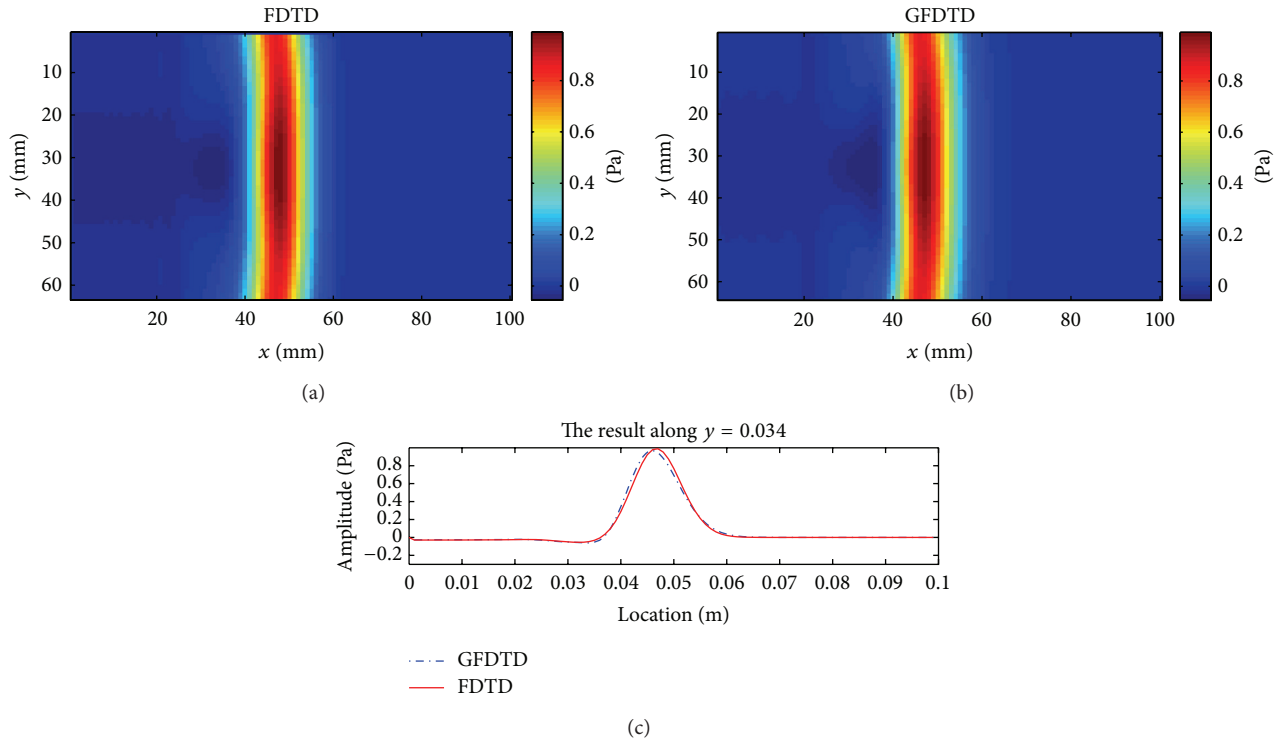


FIGURE 8: Sound wave propagation in a two-dimension tube. (a) FDTD results, (b) GFDTD results, and (c) the comparison along $y = 0.034$ m at $t = 200 \mu\text{s}$.

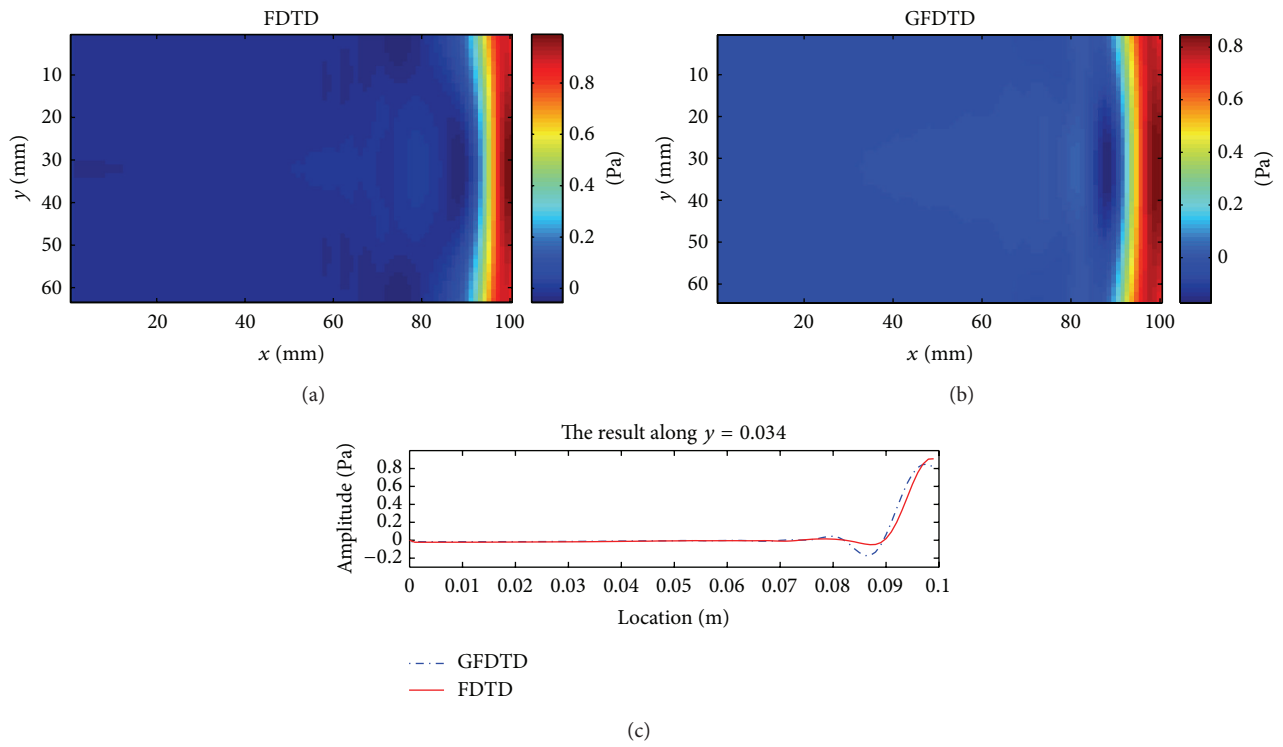


FIGURE 9: Sound wave propagation in a two-dimension tube. (a) FDTD results, (b) GFDTD results, and (c) the comparison along $y = 0.034$ m at $t = 350 \mu\text{s}$.

where $f_i = f(x_i, y_i)$, $f_0 = f(x_0, y_0)$, $h_i = x_i - x_0$, $k_i = y_i - y_0$, and w_i is weighing function with compact support.

The solution of the derivatives is obtained by minimizing the norm B , that is,

$$\frac{\partial B}{\partial \{Df\}} = 0, \quad (\text{A.2})$$

with

$$\{Df\}^T = \left\{ \frac{\partial f_0}{\partial x}, \frac{\partial f_0}{\partial y}, \frac{\partial^2 f_0}{\partial x^2}, \frac{\partial^2 f_0}{\partial y^2}, \frac{\partial^2 f_0}{\partial x \partial y} \right\}. \quad (\text{A.3})$$

For example, the first equation is

$$\begin{aligned} f_0 \sum_{i=1}^N w_i^2 h_i - \sum_{i=1}^N f_i w_i^2 h_i + \frac{\partial f_0}{\partial x} \sum_{i=1}^N w_i^2 h_i^2 + \frac{\partial f_0}{\partial y} \sum_{i=1}^N w_i^2 h_i k_i \\ + \frac{\partial^2 f_0}{\partial x^2} \sum_{i=1}^N w_i^2 \frac{h_i^3}{2} + \frac{\partial^2 f_0}{\partial y^2} \sum_{i=1}^N w_i^2 \frac{k_i^3}{2} \\ + \frac{\partial^2 f_0}{\partial x \partial y} \sum_{i=1}^N w_i^2 h_i^2 k_i = 0. \end{aligned} \quad (\text{A.4})$$

Equation (A.4) and the other four give the following system:

$$\begin{bmatrix} \sum_{i=1}^N w_i^2 h_i^2 & \sum_{i=1}^N w_i^2 h_i k_i & \sum_{i=1}^N w_i^2 \frac{h_i^3}{2} & \sum_{i=1}^N w_i^2 \frac{k_i^3}{2} & \sum_{i=1}^N w_i^2 h_i^2 k_i \\ \sum_{i=1}^N w_i^2 h_i k_i & \sum_{i=1}^N w_i^2 k_i^2 & \sum_{i=1}^N w_i^2 \frac{h_i^2 k_i}{2} & \sum_{i=1}^N w_i^2 \frac{k_i^3}{2} & \sum_{i=1}^N w_i^2 h_i k_i^2 \\ \sum_{i=1}^N w_i^2 \frac{h_i^3}{2} & \sum_{i=1}^N w_i^2 \frac{h_i^2 k_i}{2} & \sum_{i=1}^N w_i^2 \frac{h_i^4}{4} & \sum_{i=1}^N w_i^2 \frac{h_i^2 k_i^2}{4} & \sum_{i=1}^N w_i^2 \frac{h_i^3 k_i}{2} \\ \sum_{i=1}^N w_i^2 \frac{k_i^3}{2} & \sum_{i=1}^N w_i^2 \frac{k_i^3}{2} & \sum_{i=1}^N w_i^2 \frac{h_i^2 k_i^2}{4} & \sum_{i=1}^N w_i^2 \frac{k_i^4}{4} & \sum_{i=1}^N w_i^2 \frac{h_i k_i^3}{2} \\ \sum_{i=1}^N w_i^2 h_i^2 k_i & \sum_{i=1}^N w_i^2 h_i k_i^2 & \sum_{i=1}^N w_i^2 \frac{h_i^3 k_i}{2} & \sum_{i=1}^N w_i^2 \frac{h_i k_i^3}{2} & \sum_{i=1}^N w_i^2 h_i^2 k_i^2 \end{bmatrix} \begin{bmatrix} \frac{\partial f_0}{\partial x} \\ \frac{\partial f_0}{\partial y} \\ \frac{\partial^2 f_0}{\partial x^2} \\ \frac{\partial^2 f_0}{\partial y^2} \\ \frac{\partial^2 f_0}{\partial x \partial y} \end{bmatrix} = \begin{bmatrix} -f_0 \sum_{i=1}^N w_i^2 h_i + \sum_{i=1}^N f_i w_i^2 h_i \\ -f_0 \sum_{i=1}^N w_i^2 k_i + \sum_{i=1}^N f_i w_i^2 k_i \\ -f_0 \sum_{i=1}^N w_i^2 \frac{h_i^2}{2} + \sum_{i=1}^N f_i w_i^2 \frac{h_i^2}{2} \\ -f_0 \sum_{i=1}^N w_i^2 \frac{k_i^2}{2} + \sum_{i=1}^N f_i w_i^2 \frac{k_i^2}{2} \\ -f_0 \sum_{i=1}^N w_i^2 h_i k_i + \sum_{i=1}^N f_i w_i^2 h_i k_i \end{bmatrix}. \quad (\text{A.5})$$

Conflict of Interests

The authors declare that there is no conflict of interests regarding the publication of this paper.

Acknowledgment

This work is supported in part by the National Natural Science Foundation of China (nos. 51478305 and 61175016) and Key Program (no. 61233009). The authors thank the anonymous reviewers for their most useful suggestions.

References

- [1] M. N. O. Sadiku, *Numerical Techniques in Electromagnetics*, CRC Press, 2000.
- [2] D. M. Sullivan, *Electromagnetic Simulation Using the FDTD Method*, John Wiley & Sons, 2013.
- [3] J. W. Sweigle and S. W. Attaway, "On the feasibility of using Smoothed Particle Hydrodynamics for underwater explosion calculations," *Computational Mechanics*, vol. 17, no. 3, pp. 151–168, 1995.

- [4] T. Belytschko, Y. Krongauz, D. Organ, M. Fleming, and P. Krysl, "Meshless methods: an overview and recent developments," *Computer Methods in Applied Mechanics and Engineering*, vol. 139, no. 1-4, pp. 3-47, 1996.
- [5] G. R. Johnson, R. A. Stryk, and S. R. Beissel, "SPH for high velocity impact computations," *Computer Methods in Applied Mechanics and Engineering*, vol. 139, no. 1-4, pp. 347-373, 1996.
- [6] N. Perrone and R. Kao, "A general finite difference method for arbitrary meshes," *Computers & Structures*, vol. 5, no. 1, pp. 45-57, 1975.
- [7] P. S. Jensen, "Finite difference techniques for variable grids," *Computers & Structures*, vol. 2, no. 1-2, pp. 17-29, 1972.
- [8] T. Liszka and J. Orkisz, "The finite difference method at arbitrary irregular grids and its application in applied mechanics," *Computers and Structures*, vol. 11, no. 1-2, pp. 83-95, 1980.
- [9] J. J. Benito, F. Urea, and L. Gavete, "Influence of several factors in the generalized finite difference method," *Applied Mathematical Modelling*, vol. 25, no. 12, pp. 1039-1053, 2001.
- [10] L. Gavete, M. L. Gavete, and J. J. Benito, "Improvements of generalized finite difference method and comparison with other meshless method," *Applied Mathematical Modelling*, vol. 27, no. 10, pp. 831-847, 2003.
- [11] J. J. Benito, F. Urena, and L. Gavete, "Solving parabolic and hyperbolic equations by the generalized finite difference method," *Journal of Computational and Applied Mathematics*, vol. 209, no. 2, pp. 208-233, 2007.
- [12] C.-M. Fan and P.-W. Li, "Generalized finite difference method for solving two-dimensional Burgers' equations," *Procedia Engineering*, vol. 79, pp. 55-60, 2014.
- [13] J. J. Benito, F. Ureña, L. Gavete, E. Salete, and A. Muelas, "A GFDM with PML for seismic wave equations in heterogeneous media," *Journal of Computational and Applied Mathematics*, vol. 252, pp. 40-51, 2013.
- [14] Y. L. Chen, K. B. Huang, and X. Yu, "Numerical study of detonation shock dynamics using generalized finite difference method," *Science China: Physics, Mechanics and Astronomy*, vol. 54, no. 10, pp. 1883-1888, 2011.
- [15] J. F. Lee, R. Lee, and A. Cangellaris, "Time-domain finite-element methods," *IEEE Transactions on Antennas and Propagation*, vol. 45, no. 3, pp. 430-442, 1997.
- [16] G. M. Zhang and R. C. Batra, "Modified smoothed particle hydrodynamics method and its application to transient problems," *Computational Mechanics*, vol. 34, no. 2, pp. 137-146, 2004.
- [17] M U Guide, The mathworks Inc., Natick, Mass, USA, 2013.
- [18] G. Mur, "Absorbing boundary conditions for the finite-difference approximation of the time-domain electromagnetic-field equations," *IEEE Transactions on Electromagnetic Compatibility*, vol. 23, no. 4, pp. 377-382, 1981.
- [19] T. Yokota, S. Sakamoto, and H. Tachibana, "Visualization of sound propagation and scattering in rooms," *Acoustical Science and Technology*, vol. 23, no. 1, pp. 40-46, 2002.
- [20] S. Sakamoto, H. Nagatomo, A. Ushiyama, and H. Tachibana, "Calculation of impulse responses and acoustic parameters in a hall by the finite-difference time-domain method," *Acoustical Science and Technology*, vol. 29, no. 4, pp. 256-265, 2008.

Research Article

Active Learning Algorithms for the Classification of Hyperspectral Sea Ice Images

**Yanling Han,¹ Jing Ren,¹ Zhonghua Hong,¹ Yun Zhang,¹
Long Zhang,² Wanting Meng,¹ and Qiming Gu¹**

¹College of Information, Shanghai Ocean University, Shanghai 201306, China

²College of Information Engineering, Shanghai Maritime University, Shanghai 201306, China

Correspondence should be addressed to Zhonghua Hong; zhhong@shou.edu.cn

Received 29 August 2014; Accepted 9 December 2014

Academic Editor: L. W. Zhang

Copyright © 2015 Yanling Han et al. This is an open access article distributed under the Creative Commons Attribution License, which permits unrestricted use, distribution, and reproduction in any medium, provided the original work is properly cited.

Sea ice is one of the most critical marine disasters, especially in the polar and high latitude regions. Hyperspectral image is suitable for monitoring the sea ice, which contains continuous spectrum information and has better ability of target recognition. The principal bottleneck for the classification of hyperspectral image is a large number of labeled training samples required. However, the collection of labeled samples is time consuming and costly. In order to solve this problem, we apply the active learning (AL) algorithm to hyperspectral sea ice detection which can select the most informative samples. Moreover, we propose a novel investigated AL algorithm based on the evaluation of two criteria: uncertainty and diversity. The uncertainty criterion is based on the difference between the probabilities of the two classes having the highest estimated probabilities, while the diversity criterion is based on a kernel k -means clustering technology. In the experiments of Baffin Bay in northwest Greenland on April 12, 2014, our proposed AL algorithm achieves the highest classification accuracy of 89.327% compared with other AL algorithms and random sampling, while achieving the same classification accuracy, the proposed AL algorithm needs less labeling cost.

1. Introduction

As a member of the global marine and atmospheric system, sea ice with the high albedo has impacted the marine, power between the atmospheres, and heat and material exchange. Also sea ice plays a key role in the radiation balance, energy balance, and mass balance on the ocean surface [1]. Expect for the influence on marine hydrology, atmospheric circulation, and ecosystems, sea ice has a great threat to the shipping and the facilities of marine resource development and has become one of the most prominent oceanic disasters in the polar and high latitude regions.

For the prevention and mitigation of the ice disasters and the hazard assessment, we not only need to obtain real-time sea ice area and the outer line information, but also need more detailed data about types, thickness, and distribution of sea ice. However, for the traditional methods of sea ice detection, it is very difficult to get the continuous and large-area sea ice condition, while, remote sensing is

an effective mean that can get the large area of sea ice data rapidly. Currently, the main research areas of sea ice detection with the remote sensing are in the polar and high latitude regions. Furthermore, the countries carrying out the relevant research include America, Canada, Norway, Australia, and German. These researches mainly aimed at the moderate-resolution remote sensing detections, such as airborne remote sensing, moderate-resolution imaging spectrometer (MODIS) [2], and synthetic aperture radar (SAR). Shi et al. [3] extracted the information of sea ice by the surface temperature based on NOAA/AVHRR and got the relation between ice thickness and reflectivity by empirical formula; Meyer et al. [4] introduced an approach to map landfast ice extent based on L-band SAR data; Ozsoy-Cicek et al. [5] verified that active microwave can depart the ice edge and floating ice by field survey; Hong [6] proposed to use passive microwave for the inversion of small-scale roughness on ice surface and refractive index of sea ice. In contrast with the traditional remote sensing technology,

the hyperspectral remote images contain nearly continuous spectral information and the abundant spatial information, which has a higher capability of the target recognition and can greatly improve the accuracy of target detection. From the published literatures, the researches on sea ice detection with hyperspectral technology are rarely involved by far.

Many methods have been developed in the classification of hyperspectral images, which can be mainly concluded in two types [7, 8]: the unsupervised classification and supervised classification. Unsupervised classification does not need priori knowledge and can classify the primary hyperspectral images directly, which is simple and easy to implement, but the classification accuracy is low; the supervised classification needs some priori knowledge in advance and to get the classifier by training the labeled samples; finally we can use the trained classifier to categorize the unlabeled samples, which can get accurate classification accuracies. The classifier based on supervised classification can be obtained by the following ways: probabilistic model, empirical risk minimization (ERM) and structural risk minimization (SRM) [9, 10]. The most classic method based on probabilistic model is maximum likelihood classifier (MLC), which has higher computational complexity and requires a large number of training samples in order to get better classification results [11]; the commonly used methods based on ERM theory include the decision tree and neural network, which are easier to face the problems of “Hughes” and “overfitting” in the case of high dimension and small sample; the SRM principle considers the ERM and SRM simultaneously and increases the generalization capabilities for future samples, where the classic method based on the SRM principle is support vector machine (SVM). At present, SVM has got great progress in the way of theory research and algorithm realization and has obtained better classification results compared with traditional classifiers [12–16]. For example, Melgani and Bruzzone [17] compared the different SVM methods with the k -means and neural network based on radial basis function (RBF) in the original feature space and the feature subspace. Camps-Valls et al. [18] put forward to classify the crop by SVM and compare with other neural network methods, such as a multilayer perception neural network and RBF. Pal and Mather [19] compared the SVM with MLC and multilayer perception neural network and verified the results with Landsat-7.

The classification of hyperspectral remote sensing image often applies the supervised classification techniques, which require a large amount of labeled samples. The quality and the number of the available training samples are important for the accurate classification images. Because of the limitations of environment and conditions, the measured data used in the sea ice detection are very rare. The interpretation of hyperspectral images need to be analyzed by traditional remote sensing images with the higher spatial resolution at the same time and scene. But the available training samples are usually not enough for adequate learning of the classifier. How to mark as few samples as possible artificially and obtain better classification performance becomes the key issues of sea ice detection. In order to solve the classification problems, active learning (AL) approaches are proposed based on SVM

which have got remarkable success in the real-world learning. The SVM classifier is fit for AL because its classification rule can be characterized by a small number of support vectors that can be easy to update over the successive iterations [20]. At each iteration, the classifiers do not passively accept the training samples provided by the user but actively select the most valuable samples for the current classification model. The obtained labeled samples by the user are incorporated in the training set and the classifiers is retrained and updated. In this way, we can greatly reduce the labeling time and improve the classification accuracy. In recent years, researchers have conducted a large number of studies on the active learning and proposed many AL methods. Tong et al. [21, 22] proposed the margin sampling (MS), which selects the samples closest to the current separating hyperplane as the most uncertainty and informative samples. Another popular strategy is given by committee-based active learners. A set of unlabeled samples are trained by different classifiers. The approach selects the examples where the disagreement is maximal between the classifiers. Afterward, the method based on entropy is proposed. Examples with the highest value of entropy are selected to query the user. In [23], Joshi et al. put forward the best versus second-best (BvSB) approach, which is based on the difference between the probabilities of the two classes having the highest estimated probabilities as a measure of uncertainty. In addition, there are many other AL algorithms, such as the Fisher information matrix method. In this paper, we propose a novel investigated AL technology on the classification of hyperspectral sea ice images, which can select the most informative samples and get good classification results.

2. AL Algorithms

2.1. AL Process Model. AL was put forward by professor Angluin from Yale University in the paper of “Queries and concept learning” [24]. Currently, the AL algorithms are widely used in the text classification and image retrieval. However, AL can be applied to the classification of remote sensing images by considering the specific features of this area. In the remote sensing problems, the land-cover types of the area are selected by the three methods, such as photo interpretation, ground survey and mixed strategies. But, these strategies are implemented with high costs and much time. So we expect that the AL process can be conducted with few labeled training samples without reducing the convergence capability. The classification framework based on AL is described as shown as the Figure 1.

The active learning process is conducted according to an iterative process that can be described by the form (C, Q, E, T, U) [25], in which, C is a supervised classifier trained; T is the labeled training set; Q is the query function, in order to select the most informative unlabeled samples from the unlabeled sample pool U ; E is an human expert who can label the selected samples with the above mentioned three strategies.

The iterative process of AL can be described as follows. First, the classifier C is trained on the initial training set T which made up of few labeled samples. After

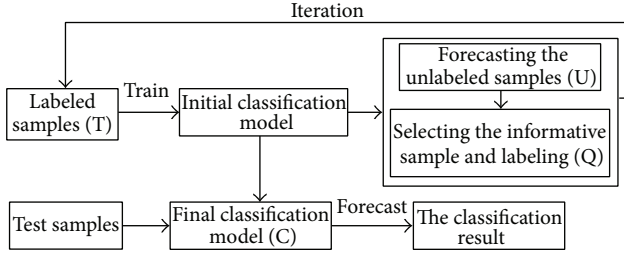


FIGURE 1: The classification framework based on AL.

the initialization, the set of samples are selected by Q query function from the pool U and query the expert E . Then, these labeled samples are included into T and the classifier C is retained by the updated training set. The retrained process continues until a stopping criterion (e.g., the labeling costs or the generalization accuracy reached some standard) is satisfied. The algorithm is described as follows.

Algorithm 1 (active learning).

Inputs. The inputs are labeled sample set T , unlabeled sample set U , classifier C (Initial), and query function Q .

Output. the output is updated classifier C .

- (1) Train the initial classifier C on labeled sample set T .
- (2) Classify the unlabeled samples U by classifier C .
- (3) Repeat.
- (4) Select the unlabeled samples with the query function Q from the unlabeled sample pool U .
- (5) Label the unlabeled samples by human expert E .
- (6) Add the new labeled samples to the training set T .
- (7) Retrain the classifier C .
- (8) Until the stopping criteria is satisfied.

From the above mentioned descriptions, the selection of classifier and sampling strategy are two important components of AL.

2.2. The Classification Model. Because SVM shows the outstanding performance in solving small sample, nonlinear and high-dimensional pattern recognitions, we choose the SVM classifier in this paper. SVM is only directly applicable for two-class tasks. Aiming at solving the multiclass classification problems of hyperspectral sea ice images, the implementation of SVM is approached by multiclass strategy.

Supposing that the training sample set T is made up of N independent samples, which can be described $(x_i, y_i)_{i=1}^N$, where x_i denotes the training samples and $y_i \in \{+1, -1\}$ denotes the associated labels. The basic thought of SVM is to map the data through a proper nonlinear transformation into a higher dimensional feature space, in order to find an optimal hyperplane which maximizes the margin between the two classes.

The classification problem can be transformed into a typical convex programming problem [5] on the basis of Kuhn-Tucker theorem. Accordingly, the convex programming problem can be converted into the following the dual linear programming problem by Lagrange multipliers α_i associated with the original training patterns x_i :

$$\text{Max } J(a) = \text{Max} \left\{ \sum_{i=1}^N \alpha_i - \frac{1}{2} \sum_{i=1}^N \sum_{j=1}^N \alpha_i \alpha_j y_i y_j K(x_i, x_j) \right\} \quad (1)$$

$$\text{s.t. } \sum_{i=1}^N \alpha_i y_i = 0 \quad \alpha_i \geq 0; \quad i = 1, \dots, N.$$

The dual linear problem has global optimization. The α_i values corresponding with the nonsupport vectors are zero, so the optimal classification decision function used for binary problem is obtained by solving above problems:

$$f(x) = \text{sgn} \left(\sum_{SV} \alpha_i y_i K(x_i \cdot x) + b \right), \quad (2)$$

where SV is the set of support vectors, α_i and b are the parameters used to define the optimal hyperplane, and $K(\cdot, \cdot)$ is the kernel function (we adopt the radial basis kernel function with better classification performance).

The multiclass classification problems depend on the binary classification, which can be transformed into multiple binary classification problems to solve. The construction of multiclass SVM classifier can be approached in two methods [26, 27]. Firstly, by constructing a series of binary classifiers, the decision is taken by combining the partial decisions of the single members of the ensemble [26, 27]. There are two common techniques, namely, the one-against-all (OAA) strategy and one-against-one (OAO) strategy. Secondly, the method is represented by SVM formulated directly as a multiclass optimization problem. The second method has poor stability and can affect the classification accuracy for the multiclass optimization. The OAO method for SVM is computationally efficient and shows good classification performance [28]. So we use OAO approach for multiclass classification in the paper. If there are k classes of data, then we need to construct $k(k-1)/2$ binary classifiers in total. In this case, the binary classifier can separate class i from class j by means of a discriminant function $f_{ij}(x)$:

$$f_{ij}(x) = \text{sgn} [w^{ij} \cdot x + b^{ij}] \quad (3)$$

$$(i = 1, \dots, k; j = 1, \dots, k; i < j),$$

where w^{ij} is the normal vector of the hyperplane discriminant the class i and the class j . The final decision in the OAO strategy is taken on the basis of the “winner-takes-all” rule, which corresponds to the following maximization:

$$M = \text{argmax} \left(\sum_{j=1, j \neq i}^k \text{sgn} (f_{ij}(x)) \right). \quad (4)$$

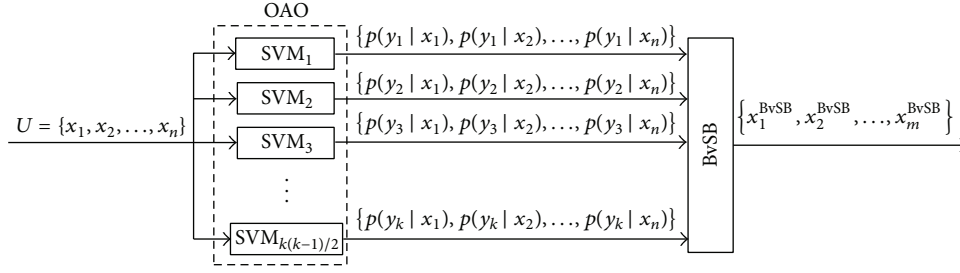


FIGURE 2: Architecture of the BvSB method.

Sometimes, conflict situations may occur between two different classes characterized by the same score. Such ambiguities can be solved by selecting the class with the smaller index value of the class.

2.3. The Sampling Strategy. The sampling strategy is crucial to distinguish the pros and cons of different AL algorithms. The selection of unlabeled samples with different strategies depends on the information content of the samples (i.e., the influence of the unlabeled samples on the generalization capabilities of classifier). Currently, the sampling strategy is widely used on the basis of uncertainty. In which, MS is one of the popular and effective measure for active SVM learning, but this method is only applicable to binary SVM classification problem. Although the entropy method is suitable for multiclass classification, it has a drawback. A major shortcoming of the entropy method is that its value is heavily affected by probability values of unimportant classes, which make the classifier confused [23]. In order to solve the aforementioned problems, the BvSB method was proposed which can achieve better performance in the multiclass classification.

It is very important to observe that the above mentioned strategies consider only the uncertainty. In the way, the selected samples may have the same label after querying the user. It means that there will be a lot of redundant samples selected, which do not provide additional information and are unfavorable for the algorithm convergence. In order to address the shortcomings, we adopted the enhanced clustering-based diversity criterion (ECBD) based on the diversity distribution of the samples. In the following sections, we will introduce the BvSB method and the ECBD method, respectively.

3. AL Algorithm Based on Uncertainty and Diversity

3.1. The BvSB Method Based on the Uncertainty. Let us assume that the unlabeled sample set is $U = \{x_1, \dots, x_n\}$ and the associated labels are denoted by $Y = \{y_1, \dots, y_k\}$, where $p(y_i | x_i)$ denotes the membership probability [29]. Under the BvSB criterion, we only consider the difference as a measure of uncertainty between the probabilities of the two classes having the highest estimated probability. The optimal label and the suboptimal label are denoted by y_{Best} and $y_{\text{Second-best}}$, respectively, but the other classes are ignored.

The probabilities of the optimal label and the suboptimal label for sample x_i are represented by $p(y_{\text{Best}} | x_i)$ and $p(y_{\text{Second-best}} | x_i)$; then the criterion can be described as

$$c_{\text{uncertainty}}(x_i) = \arg \min_{x_i \in U} (p(y_{\text{Best}} | x_i) - p(y_{\text{Second-best}} | x_i)). \quad (5)$$

The BvSB method is taken as a more greedy approach as a measure of uncertainty. We use the OAO strategy for multiclass classification. We assume that $C_{i,j}$ ($i, j \in Y$) is the classifier used to discriminate the sample x between the class i and class j . If the true class label of an unlabeled sample x is l , once its label is marked and added to the training set, which will modify the boundary of the classifiers that separate class l from the other classes. We denote these classifiers by $C_l = \{C_{l,i} \mid (i, l \in Y, i \neq l)\}$. Because the true label of the sample x is unknown, we use the optimal label y_{best} as the evaluation of the true label. Thus, the classification set in contention is called $C_{y_{\text{best}}} = \{C_{y_{\text{best}}, y_i} \mid (y_{\text{best}} \in Y, y_i \neq y_{\text{best}})\}$. For the classifier set $C_{y_{\text{best}}}$, the uncertainty degree of sample x can be denoted by the difference in the estimated class probability value $p_{y_{\text{best}}} - p_i$, which can be taken as an indicator describing the information content of sample x . By minimizing the value of $p_{y_{\text{best}}} - p_{y_i}$, that is maximizing the classification uncertainty, the BvSB criterion is obtained:

$$\begin{aligned} c_{\text{uncertainty}}(x) &= \arg \min_{x_i \in U} \left(\min_{y \in Y, y_i \neq y_{\text{Best}}} (p(y_{\text{best}} | x) - p(y_i | x)) \right) \quad (6) \\ &= \arg \min_{x_i \in U} (p(y_{\text{best}} | x) - p(y_{\text{second-best}} | x)). \end{aligned}$$

According to formula (6), m samples with lower $c_{\text{uncertainty}}$ are selected as uncertainty samples. From the view of changing the classification boundaries, the BvSB criterion can be considered an efficient approximation for selecting the informative samples. Figure 2 shows the architecture based on the BvSB method.

3.2. The ECBD Method Based on the Diversity. Considering the distribution of uncertain samples at the diversity step, clustering is an effective solution to select the most diverse samples. In the previous section, the similar samples may be selected as the informative samples by the BvSB method. So we consider combining the sampling strategy with unsupervised clustering. In this case, the representative samples

are selected to label from different clusters. That is to say, the $h < m$ samples are selected by clustering, where m samples are obtained in the uncertainty step. The standard k -means clustering algorithm is applicable to original feature space, while the SVM classification hyperplane works in the kernel space. Therefore, the selected samples in the original space may not be fit for the kernel space. To overcome this shortcoming, we adopt the enhanced clustering-based diversity method (ECBD) by clustering in kernel space, which is improved based on the standard k -means clustering. The ECBD is described as follows [20].

Assuming that m samples (x_1, x_2, \dots, x_m) are selected at the uncertainty step, the idea of kernel k -means is to divide m samples into h clusters (C_1, C_2, \dots, C_h) in the kernel space, then the most uncertainty samples of each cluster is taken as the representative sample. The center of each cluster is denoted by $(\rho_1, \rho_2, \dots, \rho_h)$. We suppose that sample x_i mapped into the kernel space is indicated by $\varphi_i = \theta(x_i)$. The Euclidean distance between the sample φ_i and the sample φ_j is written as

$$\begin{aligned} D^2(\varphi_i, \varphi_j) &= \|\theta(x_i) - \theta(x_j)\|^2 \\ &= \theta^2(x_i) - 2\theta(x_i) \cdot \theta(x_j) + \theta^2(x_j) \\ &= K(x_i, x_i) - 2K(x_i, x_j) + K(x_j, x_j). \end{aligned} \quad (7)$$

Let ∇_k be the cluster center in the kernel space that

$$\nabla_k = \frac{1}{|C_k|} \sum_{i=1}^m \delta(\varphi_i, C_k) \varphi_i, \quad (8)$$

where $|C_k|$ denotes the total number of samples in the cluster C_k and is computed as $|C_k| = \sum_{i=1}^m \delta(x_i, C_k)$. $\delta(x_i, C_k)$ ($1 \leq k \leq h$) shows the indicator function:

$$\delta(x_i, C_k) = \begin{cases} 1 & D(x_i, m_k) < D(x_i, m_j) \quad \forall j \neq k \\ 0 & \text{otherwise.} \end{cases} \quad (9)$$

The distance between φ_i and ∇_k can be expressed as

$$\begin{aligned} D^2(\varphi_i, \nabla_k) &= \left\| \varphi_i - \frac{1}{|C_k|} \sum_{j=1}^m \delta(\varphi_j, C_k) \varphi_j \right\|^2 \\ &= K(x_i, x_i) + f(x_i, C_k) + g(C_k), \end{aligned} \quad (10)$$

where

$$f(x_i, C_k) = -\frac{1}{|C_k|} \sum_{j=1}^m \delta(\varphi_j, C_k) K(x_i, x_j), \quad (11)$$

$$g(C_k) = \frac{1}{|C_k|^2} \sum_{j=1}^m \sum_{s=1}^m \delta(\varphi_j, C_k) \delta(\varphi_s, C_k) K(x_j, x_s).$$

By applying (10) to the standard k -means clustering, we obtain the kernel-based k -means algorithm described as follows:

- (1) Assign the initial value of $\delta(x_i, C_k)$ ($i = 1, 2, \dots, m$, $k = 1, 2, \dots, h$), and h initial clusters C_1, C_2, \dots, C_h are obtained.
- (2) For each cluster C_k , compute $|C_k|$, $f(x_i, C_k)$ and $g(C_k)$.
- (3) For each training sample x_i and cluster C_k , assign x_i to the closest cluster:

$$\begin{aligned} \delta(x_i, C_k) &= \begin{cases} 1 & f(x_i, C_k) + g(C_k) < f(x_i, C_j) + g(C_j) \quad \forall j \neq k \\ 0 & \text{otherwise} \end{cases} \end{aligned} \quad (12)$$

- (4) Repeat step (2) and step (3) until converge.
- (5) For each cluster C_k , select the sample that is closest to the center in the kernel space as the pseudocenter of C_k :

$$m_k = \arg \min_{x_i \text{ that } \delta(x_i, C_k)=1} (D^2(\theta(x_i), \nabla_k)). \quad (13)$$

After C_1, C_2, \dots, C_h are obtained, the most informative sample is selected as the representative sample of each cluster. This sample is defined as follows:

$$\begin{aligned} x_k^{\text{BvSB} + \text{ECBD}} &= \arg \min_{x_i \text{ that } \delta(x_i, C_k)=1} \{c_{\text{uncertainty}}(x_i^{\text{BvSB}})\} \\ k &= 1, 2, \dots, h, \end{aligned} \quad (14)$$

where $x_k^{\text{BvSB} + \text{ECBD}}$ represents the k th sample chosen by the sampling strategy (i.e., BvSB + ECBD), and it is the most uncertain sample of the k th cluster (i.e., the sample that has minimum $c_{\text{uncertainty}}(x)$ in the k th cluster). Totally, h samples are selected using (14), one for each cluster.

3.3. AL Algorithm Based on BvSB + ECBD. Based on the considerations of the uncertainty of the current classifier and the diversity of the sample distribution, we design the multiclass classification algorithm based on the BvSB + ECBD method. The BvSB criterion aims at selecting the most informative samples; ECBD criterion is used to select the diversity samples by clustering in the kernel space. In this case, the most representative samples are selected to query the user for sample labels. Then the obtained samples and the corresponding labels are together incorporated into the training samples and the classifier is retrained. The algorithm can be summarized as follows.

Algorithm 2 (Proposed BvSB + ECBD).

Inputs

m is the number of samples selected based on the BvSB method

h is the number of samples selected to add to training set at each iteration

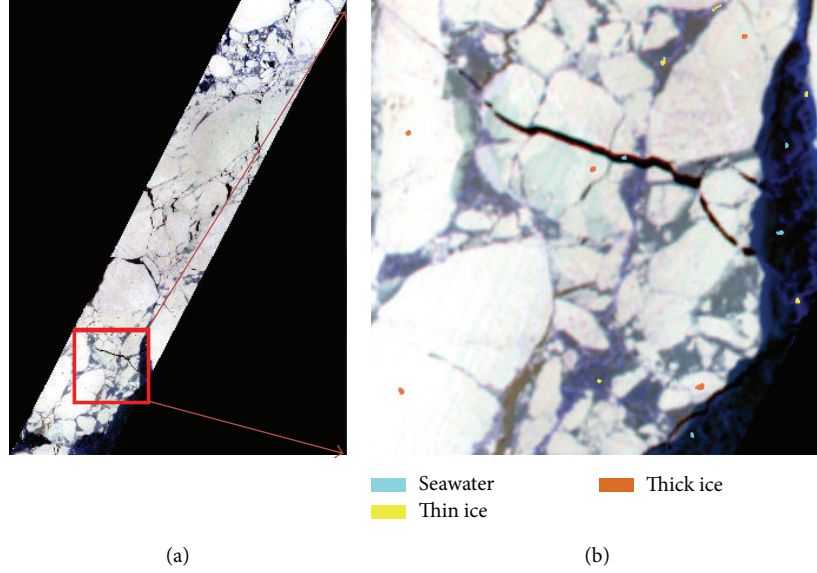


FIGURE 3: (a) Hyperspectral image marked with labeled samples (a false color image composed of R: 84, G: 49, and B: 25). (b) Partial hyperspectral image taken from (a).

K_{ini} is the number of samples selected as initial training samples

Output

X is set of unlabeled samples added in the training set

(1) *The Selection of Training Samples and the Classifier.* The training set and the unlabeled pool are marked as T and U , respectively. In the initial classification, K_{ini} samples from the pool U are selected and labeled by the user, and the sample set is denoted by S_{ini} . The training sample set T and the unlabeled pool U are updated: $T = S_{\text{ini}}$, $U \rightarrow U \setminus S_{\text{ini}}$. The SVM classifier is trained by the training set T , then we compute the probabilities of all unlabeled samples in the pool U belonging to each class, which is denoted by $p(y_i | x)$, $y_i \in Y$, and $x \in U$.

Repeat

(2) *AL Based on the BvSB Method.* According to aforeobtained probabilities $p(y_i | x)$ of each unlabeled samples, m samples are chosen from U by formula (5), which is marked as $X_{\text{BvSB}} = \{x_1^{\text{BvSB}}, x_2^{\text{BvSB}}, \dots, x_m^{\text{BvSB}}\}$.

(3) *The Clustering Based on ECBD in the Kernel Space.* The m samples are clustered in the kernel space, and detailed description is shown in Section 3.2. The h samples are selected according to formula (14), which is marked as $X_{\text{BvSB} + \text{ECBD}} = \{x_1^{\text{BvSB} + \text{ECBD}}, x_2^{\text{BvSB} + \text{ECBD}}, \dots, x_h^{\text{BvSB} + \text{ECBD}}\}$. These selected samples are marked as the representative samples by the user and denote them by $X = X_{\text{BvSB} + \text{ECBD}}$.

(4) *Updating the Training Sample Set and Retraining the Classifier.* Renew the training sample set and unlabeled

sample set with new selected sample $T = T \cup X$, $U \rightarrow U \setminus X$, then the SVM classifier are retrained with the novel training sample set.

Until algorithm converges or satisfies the number of iterations.

4. Experiment Analysis

4.1. *Data set Description.* Hyperion sensor is mounted on the Earth observation satellite which was launched by NASA in November 2000. Hyperspectral image has a total of 242 bands and spatial resolution of 30 m. There are 220 unique spectral channels collected with a complete spectrum covering from 357–2576 nm. Because it is being in the experimental stage, the coverage of hyperspectral image is small, only $7.7 \text{ km} \times 44 \text{ km}$ [30]. Because hyperspectral images have the high resolution and continuous spectrums, it has been widely used in vegetation studies, geological surveys, fine agriculture, marine remote sensing and so on.

The data set is a hyperspectral image acquired on a marine area of Baffin Bay in northwest Greenland on April 12, 2014. The data are L1Gst level through geometric correction, projection registration and topographic correction. This image consists of 2395×1769 pixels (which include background pixels). The number of bands is initially reduced to 176 by removing the bands with low signal-to-noise and water absorption. The available labeled samples (1678 samples) are collected by Landsat-8 image interpretation, which are illustrated in Figure 3(a). Figure 3(b) is a subset of the entire image in Figure 3(a). As can be seen from the image, there are three different classes available, namely seawater, thin ice and thick ice. All labeled samples are randomly divided to derive a pool U and the validation set V . Here we use Landsat-8 data with a spatial resolution of 15 m as the test set at the same time and same scene. The final classification performance is

TABLE 1: Number of samples of each class in U, V for the data set.

Class	U	V
Seawater	343	200
Thin ice	339	200
Thick ice	396	200
Total	1078	600

evaluated by calculating the Kappa coefficient and the overall classification accuracy. The classes and the related number of samples used in the experiments are shown in Table 1.

4.2. Design of Experiments. In our experiments, without losing generality, we adopt an SVM classifier with radial basis function (RBF) kernel. The values for the regularization parameter C and the spread γ of the RBF kernel parameters are acquired by the cross validation grid search method on the basis of the validation set. Finally, the best value of the parameter C is 32; the optimal kernel width parameter γ is found equal to 16.

The experiments are designed in order to compare the classification accuracy with different AL algorithms that are, respectively, BvSB and the investigated and proposed techniques (BvSB + k -means and BvSB + ECBD). In the experiments with AL algorithms, three samples of each class are randomly chosen from the pool U as initial training samples, and the rest are considered as unlabeled samples. All experimental results are referred to the average classification accuracies obtained in ten trials because of ten initial randomly selected training samples. At each round of active learning in the following, firstly, in the uncertainty step, we select m samples on the basis of uncertainty (the difference between the highest estimated probability values of the two classes, i.e., BvSB) to query the user for labels. In the diversity step, the most diverse $h < m$ samples are chosen based on either standard k -means or ECBD to query the user for labels. Then the selected samples and the corresponding labels are together incorporated in the training set. Finally, the classifier is retrained. The related number of samples chosen by the different methods is shown in Table 2.

4.3. Experimental Results. This section reports experimental results with the random sampling and AL algorithms, that are respectively BvSB, BvSB + k -means, and BvSB + ECBD. Results are presented as learning rate curves, which show the relation between the average overall classification accuracies and the active learning rounds used to train the SVM classifier. By analyzing Figure 4, we can observe that three AL algorithms are generally better than random sampling. The results show that our proposed BvSB + ECBD technique shows the highest accuracies in most of the iterations. Furthermore, given the same size of training samples, as indicated by the same point on the x -axis, BvSB + ECBD shows significantly improved classification accuracy. From another perspective, in order to achieve the same value of classification accuracy (same point on the y -axis), our proposed active learning algorithm needs far fewer training

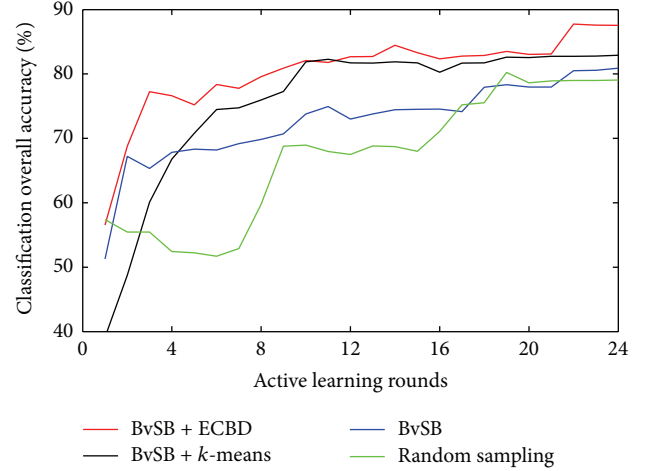


FIGURE 4: Classification of overall accuracy obtained with different AL algorithms and sampling.

TABLE 2: Number of samples chosen by the different methods.

Method	m	h
BvSB	3	—
BvSB + K -means	12	3
BvSB + ECBD	12	3

TABLE 3: Percentage reduction in the number of training samples.

BvSB + ECBD selection rounds	Random selection rounds	%Reduction in training samples
1	8	63.64
2	9	58.33
5	17	60
8	19	50

samples than random selection from Table 3. The result indicates that the proposed method selects the most useful samples at each iteration, so that user input can be effectively utilized on the most relevant samples [23].

From Figure 4, one can know that the BvSB + ECBD method provides more informative samples compared to BvSB and BvSB + k -means methods and achieves higher accuracies with the same active learning rounds. Figures 5 and 6 show the distribution of the chosen training samples and the pool (considering bands 49 and 84 of the hyper-spectral image) after six iterations of the AL process with the BvSB method and BvSB + ECBD method, respectively. Note that, since the BvSB method considers only the uncertainty of samples, it may result in the selection of similar samples which can only provide redundant information. We can also find that performing the clustering in the kernel space can improve the classification accuracy compared with the standard k -means clustering. Indeed, because of the kernel mapping, the set of most diverse sample in the original space may not be the most diverse in the kernel space [20].

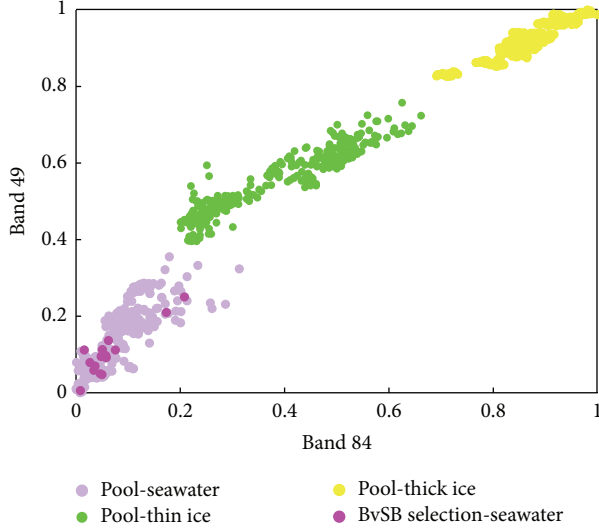


FIGURE 5: Distribution of the chosen training samples by the BvSB method and pool samples considering bands 49 and 84 of the hyperspectral image.

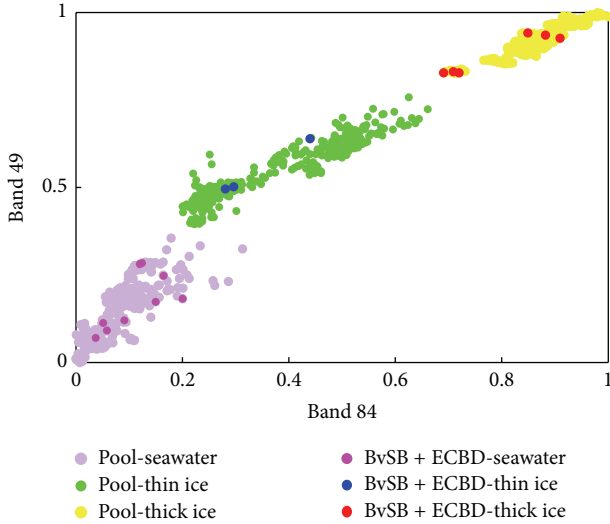


FIGURE 6: Distribution of the chosen training samples by the BvSB + ECBD method and pool samples considering bands 49 and 84 of the hyperspectral image.

In Figure 7, we demonstrate the original hyperspectral image and the classification results, in which, Figure 7(a) is an original hyperspectral image composed of band 25, 49 and 84. Figure 7(b) is the classification image of the Landsat-8 data obtained by the standard SVM classifier, which used as a reference image for evaluating the classification performance. Further, Figure 7(c) is the classification image of the hyperspectral image with the BvSB + ECBD method.

In order to assess the classification performance of our proposed method, in Table 4, we also report the confusion matrix, the accuracy per class and Kappa coefficient at the last iteration of the BvSB + ECBD method. It is important to observe that the accuracies of seawater and thin ice are low.

TABLE 4: Confusion matrix for the classification with the proposed BvSB + ECBD method.

Class	Seawater	Thin ice	Thick ice	Total
Seawater	45476	9967	2450	57893
Thin ice	21741	139924	39873	201538
Thick ice	3729	59508	963416	1026653
Total	70946	209399	1005739	1286084
%Accuracy per class	64.099	66.822	95.792	—
Kappa = 0.693			Overall accuracy = 89.327%	

Since hyperspectral image was acquired in April, 2014, thin ice began to melt with the increasing temperature. So there are lots of pixels of seawater and thin ice that were confused and wrongly classified.

Finally, we carry out an analysis of the sensibility of our proposed BvSB + ECBD method with different number of initial training samples. In Figure 8, n denotes the total number of initial training samples of three classes, where, the selected number of samples of each class is the same. One can see that, selecting different n values results in similar classification accuracies. The experiment result indicates that the different initial training samples do not provide a large benefit in the BvSB + ECBD method, that is to say, the classification accuracy is not sensitive to the selection of initial training samples [23]. Furthermore, we can also observe that, when using high n values, convergence is easily achieved than when using small n values. That is because the greater n values, the more the number of training samples, when given the same number of rounds.

5. Conclusions

In this paper, AL algorithms in the classification of hyperspectral image have been addressed, which can reduce the number of labeled samples added to training set and improve the classification accuracy with respect to traditional passive techniques. Query function based on BvSB in the uncertainty step, and standard k -means clustering and ECBD in the diversity step have been generalized to multiclass problems. Moreover, our proposed novel BvSB + ECBD method is compared with BvSB, BvSB + k -means and random sampling in the classification accuracy. By analyzing the experiment results, we can summarize as follows: (1) The proposed BvSB + ECBD method gets the best performance in terms of classification accuracy and can reduce a large amount of labeled samples compared with random sampling; (2) the BvSB + k -means method provides slightly lower classification accuracies than the BvSB + ECBD technique. At the diversity step, because of kernel mapping, the most diverse samples in the original space by the standard k -means clustering may not be the most diverse in the kernel space, which means that the most informative samples cannot be selected for the current classifier; (3) the BvSB method leads to poorer classification accuracies with respect to other AL algorithms. Therefore, we can conclude that obtained uncertainty samples based on

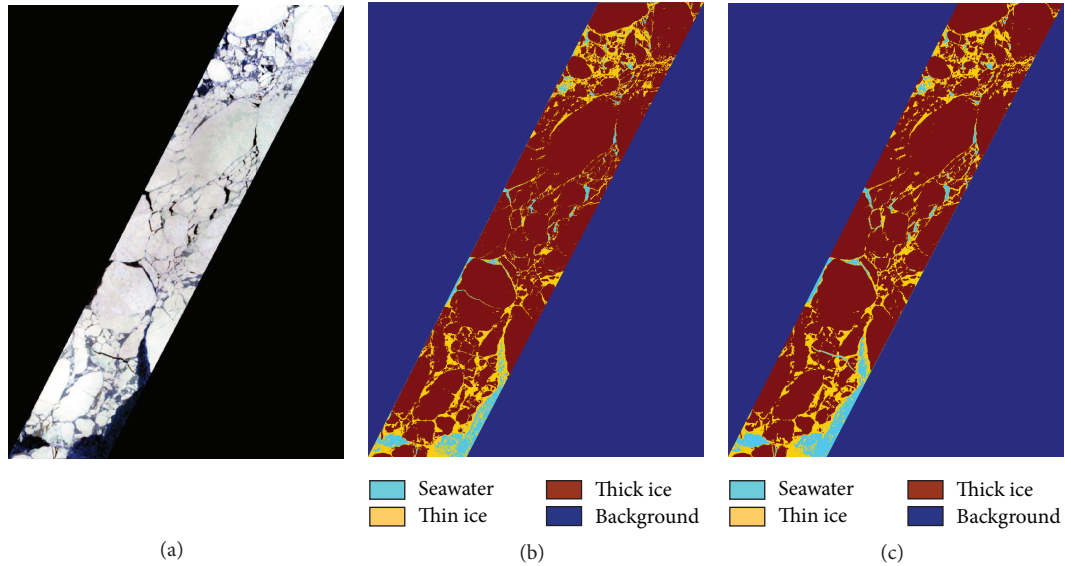


FIGURE 7: (a) Hyperspectral image (a false color image composed of R: 84, G: 49, and B: 25). (b) Result of the classification of the Landsat-8 data. (c) Result of the classification of the hyperspectral image.

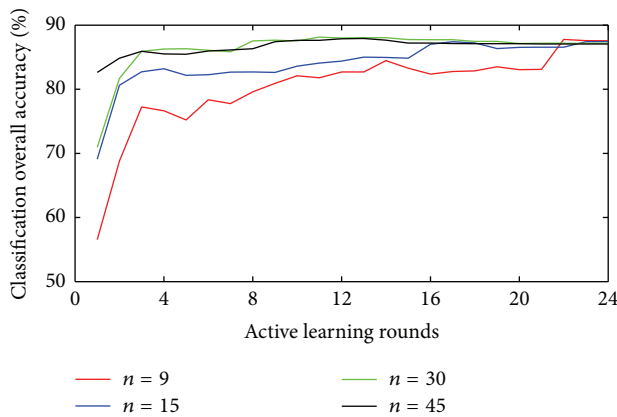


FIGURE 8: Classification overall accuracy obtained by the BvSB + ECBD method with different n values.

the BvSB technique may be the similar samples and cannot provide available information; (4) our proposed BvSB + ECBD method is not sensitive to the selection of initial training samples.

As a future development, we consider to extend our proposed AL technique by integrating the semisupervised method in the classification of hyperspectral image. During the iterative process, we can also make full use of abundant spectral information to select the more respective samples and more accurately identify the types of ice.

Conflict of Interests

The authors declare that there is no conflict of interests regarding the publication of this paper.

Acknowledgments

This research is supported by National Natural Science Foundation of China (Grant nos. 41376178 and 41401489), the Program for Professor of Special Appointment (Eastern Scholar) at Shanghai Institutions of Higher Learning, Shanghai Science and Technology Committee (Project 11510501300), and Shanghai Foundation for University Youth Scholars (ZZHY13033), and special funding for the development of science and technology of Shanghai Ocean University (A2-0209-14-200070).

References

- [1] C. Deser, J. E. Walsh, and M. S. Timlin, "Arctic sea ice variability in the context of recent atmospheric circulation trends," *Journal of Climate*, vol. 13, no. 3, pp. 617–633, 2000.
- [2] C. Drüe and G. Heinemann, "Accuracy assessment of sea-ice concentrations from MODIS using in-situ measurements," *Remote Sensing of Environment*, vol. 95, no. 2, pp. 139–149, 2005.
- [3] J. Shi, J. Guo, T. Zheng, Q. Wang, and J. Zhu, "Monitoring sea ice based on NOAA/AVHRR data," in *Earth Observing Systems XVII*, vol. 8510 of *Proceedings of SPIE*, August 2012.
- [4] F. J. Meyer, A. R. Mahoney, H. Eicken, C. L. Denny, H. C. Druckenmiller, and S. Hendricks, "Mapping arctic landfast ice extent using L-band synthetic aperture radar interferometry," *Remote Sensing of Environment*, vol. 115, no. 12, pp. 3029–3043, 2011.
- [5] B. Ozsoy-Cicek, S. F. Ackley, A. Worby, H. Xie, and J. Lieser, "Antarctic sea-ice extents and concentrations: comparison of satellite and ship measurements from International Polar Year cruises," *Annals of Glaciology*, vol. 52, no. 57, pp. 318–326, 2011.
- [6] S. W. Hong, "Detection of small-scale roughness and refractive index of sea ice in passive satellite microwave remote sensing," *Remote Sensing of Environment*, vol. 114, no. 5, pp. 1136–1140, 2010.

- [7] F. A. Mianji and Y. Zhang, "Robust hyperspectral classification using relevance vector machine," *IEEE Transactions on Geoscience and Remote Sensing*, vol. 49, no. 6, pp. 2100–2112, 2011.
- [8] B. C. Kuo and D. A. Landgrebe, "A robust classification procedure based on mixture classifiers and nonparametric weighted feature extraction," *IEEE Transactions on Geoscience and Remote Sensing*, vol. 40, no. 11, pp. 2486–2494, 2002.
- [9] N. Cristianini and J. Shawe-Taylor, *An Introduction to Support Vector Machines and Other Kernel-Based Learning Methods*, Cambridge University Press, Cambridge, UK, 2000.
- [10] V. N. Vapnik, *Statistical Learning Theory*, Wiley, New York, NY, USA, 1998.
- [11] X. Jia and J. A. Richards, "Efficient maximum likelihood classification for imaging spectrometer data sets," *IEEE Transactions on Geoscience and Remote Sensing*, vol. 32, no. 2, pp. 274–281, 1994.
- [12] J. Chen, C. Wang, and R. S. Wang, "Using stacked generalization to combine SVMs in magnitude and shape feature spaces for classification of hyperspectral data," *IEEE Transactions on Geoscience and Remote Sensing*, vol. 47, no. 7, pp. 2193–2205, 2009.
- [13] M. Marconcini, G. Camps-Valls, and L. Bruzzone, "A composite semisupervised SVM for classification of hyperspectral images," *IEEE Geoscience and Remote Sensing Letters*, vol. 6, no. 2, pp. 234–238, 2009.
- [14] J. Chen, C. Wang, and R. Wang, "Fusion of SVMs in wavelet domain for hyperspectral data classification," in *Proceedings of the IEEE International Conference on Robotics and Biomimetics (ROBIO '09)*, pp. 1372–1375, December 2009.
- [15] R. S. Hosseini and S. Homayouni, "A SVMs-based hyperspectral data classification algorithm in a similarity space," in *Proceedings of the 1st Workshop on Hyperspectral Image and Signal Processing: Evolution in Remote Sensing (WHISPERS '09)*, pp. 1–4, Grenoble, France, August 2009.
- [16] B. Demir and S. Erturk, "Accurate SVM classification using border training patterns," in *Proceedings of the 1st Workshop on Hyperspectral Image and Signal Processing: Evolution in Remote Sensing (WHISPERS '09)*, pp. 1–4, Grenoble, France, August 2009.
- [17] F. Melgani and L. Bruzzone, "Classification of hyperspectral remote sensing images with support vector machines," *IEEE Transactions on Geoscience and Remote Sensing*, vol. 42, no. 8, pp. 1778–1790, 2004.
- [18] G. Camps-Valls, L. Gómez-Chova, J. Calpe-Maravilla et al., "Robust support vector method for hyperspectral data classification and knowledge discovery," *IEEE Transactions on Geoscience and Remote Sensing*, vol. 42, no. 7, pp. 1530–1542, 2004.
- [19] M. Pal and P. M. Mather, "Support vector machines for classification in remote sensing," *International Journal of Remote Sensing*, vol. 26, no. 5, pp. 1007–1011, 2005.
- [20] B. Demir, C. Persello, and L. Bruzzone, "Batch-mode active-learning methods for the interactive classification of remote sensing images," *IEEE Transactions on Geoscience and Remote Sensing*, vol. 49, no. 3, pp. 1014–1031, 2011.
- [21] S. Tong and E. Chang, "Support vector machine active learning for image retrieval," in *Proceedings of the 9th ACM International Conference on Multimedia*, pp. 107–118, October 2001.
- [22] S. Tong and D. Koller, "Support vector machine active learning with applications to text classification," *The Journal of Machine Learning Research*, vol. 2, pp. 45–66, 2002.
- [23] A. J. Joshi, F. Porikli, and N. Papanikolopoulos, "Multi-class active learning for image classification," in *Proceedings of the IEEE Computer Society Conference on Computer Vision and Pattern Recognition Workshops (CVPR '09)*, pp. 2372–2379, June 2009.
- [24] D. Angluin, "Queries and concept learning," *Machine Learning*, vol. 2, no. 4, pp. 319–342, 1988.
- [25] M. Li and I. K. Sethi, "Confidence-based active learning," *IEEE Transactions on Pattern Analysis and Machine Intelligence*, vol. 28, no. 8, pp. 1251–1261, 2006.
- [26] J. A. Gualtieri and R. F. Crompt, "Support vector machines for hyperspectral remote sensing classification," in *The 27th AIPR Workshop Advances in Computer-Assisted Recognition*, vol. 3584 of *Proceedings of SPIE*, pp. 221–232, Washington, DC, USA, January 1999.
- [27] D. J. Sebald and J. A. Bucklew, "Support vector machines and the multiple hypothesis test problem," *IEEE Transactions on Signal Processing*, vol. 49, no. 11, pp. 2865–2872, 2001.
- [28] C.-W. Hsu and C.-J. Lin, "A comparison of methods for multiclass support vector machines," *IEEE Transactions on Neural Networks*, vol. 13, no. 2, pp. 415–425, 2002.
- [29] R. Zhang and A. I. Rudnicky, "A large scale clustering scheme for kernel k-means," in *Proceedings of the 16th International Conference on IEEE Pattern Recognition*, vol. 4, pp. 289–292, IEEE, 2002.
- [30] P. Barry, C. Segal, and S. Carman, *EO-1/Hyperspectral Science Data User's Guide*, 2001.

Research Article

A Numerical Study on the Improvement of Suction Performance and Hydraulic Efficiency for a Mixed-Flow Pump Impeller

Sung Kim, Kyoung-Yong Lee, Jin-Hyuk Kim, and Young-Seok Choi

Thermal & Fluid System R&D Group, Korea Institute of Industrial Technology, 89 Yangdaegiro-gil, Ipjang-myeon, Seobuk-gu, Cheonan-si, Chungcheongnam-do 331-822, Republic of Korea

Correspondence should be addressed to Jin-Hyuk Kim; jinhuk@kitech.re.kr

Received 28 April 2014; Revised 11 September 2014; Accepted 16 September 2014; Published 8 October 2014

Academic Editor: Shaofan Li

Copyright © 2014 Sung Kim et al. This is an open access article distributed under the Creative Commons Attribution License, which permits unrestricted use, distribution, and reproduction in any medium, provided the original work is properly cited.

This paper describes a numerical study on the improvement of suction performance and hydraulic efficiency of a mixed-flow pump by impellers. The design of these impellers was optimized using a commercial CFD (computational fluid dynamics) code and DOE (design of experiments). The design variables of meridional plane and vane plane development were defined for impeller design. In DOE, variables of inlet part were selected as main design variables in meridional plane, and incidence angle was selected in vane plane development. The verification of the experiment sets that were generated by 2^k factorial was done by numerical analysis. The objective functions were defined as the NPSH_{re} (net positive suction head required), total efficiency, and total head of the impellers. The importance of the geometric design variables was analyzed using 2^k factorial designs. The interaction between the NPSH_{re} and total efficiency, according to the meridional plane and incidence angle, was discussed by analyzing the 2^k factorial design results. The performance of optimally designed model was verified by experiments and numerical analysis and the reliability of the model was retained by comparison of numerical analysis and comparative analysis with the reference model.

1. Introduction

The mixed-flow pump is a typical instrument of mass energy consumption although it also has important roles in water resource development and various industrial plants. The importance of design engineering of the mixed-flow pump with high total efficiency and suction performance and energy saving as a consequence is increasing as oil price increases. The advanced enterprises in developed countries like the US, Germany, and Japan have competitiveness through their own technologies and know-how in pump designing that has been accumulated for more than a hundred years.

Specifically for the pumps that are used in higher value added business such as desalination or extraction of petroleum, the total efficiency and suction performance are a main issue giving advanced enterprises possessing accumulated technologies absolute advantage. For that reason, there have been researches going on regarding pumps including mixed-flow pump and the results have been reported several times by different companies and research agencies [1, 2].

When it comes to impeller designing of the mixed-flow pump, two main objectives of the research, namely, high total efficiency and improved suction performance, have conflicting directions of the design [3, 4]. The design technique that could improve suction performance maintaining high total efficiency at the same time is very important but more design experiences are required at this stage.

Suction performance correlate with cavitation. In case where the flow level changes by time when the pump is operating, unusual phenomena such as cavitation happen as the pressure of pump inlet part changes. Because of the nature of the fluid, the suction performance of a pump decreases creating bubbles when the pressure is low. Thus, securing design technology for pump with high suction performance is very important [5–7].

In order to improve total efficiency and suction performance of the impeller by selecting impeller shape variables appropriately, an analysis that can determine the importance of the design variables and the effect of chosen variables on pump performance is required. In order to perform the study, numerical analysis and bench marking via experiments were

done on the reference model and the results of them were used as criteria for the comparison.

Recently, the application of computational fluid dynamics (CFD) in the performance analysis of fluid machinery is common, and many studies have conducted for validating its usefulness in predicting the performance of pumps. For instance, Goto and Zangeneh [8] applied their optimization methodology based on an inverse design method and three-dimensional numerical analysis to design low specific speed pump diffusers with high efficiency performance. Bing and Cao [9] also improved the total hydraulic efficiency of a mixed-flow pump impeller by a combined approach using numerical simulation, inverse design, and a genetic algorithm. J. H. Kim and K. Y. Kim [10] tried the single-objective numerical optimization to enhance the total efficiency of a mixed-flow pump with two design variables related to vaned diffuser geometry.

In design engineering, the importance of the mixed-flow pump with high total efficiency and suction performance has been increasing, which has made it necessary to improve hydrodynamic design techniques in order to develop a mixed-flow pump with high total efficiency and optimal suction performance. Because the most important component of the pump is the impeller, its hydrodynamic design determines the pump design technique.

The two main objectives in designing the impeller of the mixed-flow pump, namely, high total efficiency and improved suction performance, can be realized using contrasting techniques. A design technique that could improve suction performance and maintain high total efficiency at the same time is desirable but remains in the experimental stage.

In this study, the design variables of the impeller meridional plane and vane plane development were defined for the improvement of suction performance. The design variables were then rated in importance by systematically analyzing them in relation to the response variables of the impeller. First, an impeller with high total efficiency, which satisfies the head at the design flow rate, was designed by using database (D/B).

The impeller was designed using D/B , 2^k factorial designs, which were applied to analyze the effect on suction performance and total efficiency of the design variables. The tendency to change performance according to each variation in shape was studied by numerical analysis. By applying response optimization, the main design variables determined by the 2^k factorial design were used to create the optimal shape.

The performance of optimized impeller was verified by numerical analysis and experiments. Numerical analysis and experiment of the reference model were used to compare the optimal impeller with the reference model.

2. Mixed-Flow Pump Impeller Design Method

2.1. Traditional Design Method. The traditional design for the meridional plane and the front plane of the impeller is done easily by applying pump theory. When design specifications are given, the diameters of the inlet/outlet of the meridional

plane are determined by basic pump theory. The shroud and hub curve of the inlet/outlet of the meridional plane are easily connected by drawing an arc.

In designing the blade shape, the inlet/outlet angles of the blade are mainly determined by the flow angles of the inlet/outlet using the given meridional plane, according to pump design theory. The sweep angle, which is relevant to the blade length, is determined by the inlet/outlet angles because it is designed such that it connects the inlet/outlet angles smoothly when the angles are determined.

As shown in Figure 1, the shape of the impeller is presented in the meridional and front planes; Figure 1(a) shows the meridional view of the blade shape and presents information on the direction of axis and radius; Figure 1(b) shows the front plane representing the radius and rotational direction; and Figure 1(c) shows the vane plane development of the impeller. The vane plane development includes the blade angle distribution. Axis x of the vane plane development indicates the total length of the arc at each radius from the front view. Axis y indicates the total length of the blade in the meridional view. Hence, the distribution of the blade angles is easily seen in the vane plane development and is usually achieved by the smooth connection of the inlet blade angle and the outlet blade angle. The inlet and outlet angles of the blade are mainly derived using pump design theory [11, 12].

The head can be satisfied by a traditionally designed impeller but, in order to improve total efficiency and suction performance, a detailed definition of the design variables and subsequent analysis of performance variations according to different impeller design variables are required.

The meridional plane shows the shape and size of blade. The impeller meridional shape was designed using our own D/B . Figure 2 shows the newly designed impeller shape. As shown in Figure 2, consequentially, the axis direction of the newly designed shape is approximate 24% shorter than that of the reference model.

2.2. Design Variables in a Meridional Plane. The typical shape of the meridional plane is shown in Figure 1(a), and the design variables for this meridional plane are defined in Figure 3. On the inlet of the impeller, R_1h is the hub, R_1s is the inlet radius of shroud, and Φ_1 indicates the inclined angle of the impeller's leading edge. On the outlet of the impeller, R_2 is the outlet radius, B_2 is the blade width of the impeller's trailing edge, and Φ_2 indicates the inclined angle of the trailing edge. The outlet hub of the impeller and the straight line of the shroud are defined as $\%L_h$ and $\%L_s$, respectively. Because it can express smooth curves, a Bezier curve was used to connect the inlet to the outlet of the impeller. When using Bezier curves, two reference points with set inclination levels are connected smoothly using a control point, and the shape of the curve varies depending on the location of the control point. When the control point is determined, the curve is connected smoothly in accordance with the inlet/outlet angles. When the impeller hub curve meets the horizontal and vertical lines, θ_1_h and θ_2_h indicate the inlet angle and outlet angle, respectively. θ_1_s and θ_2_s

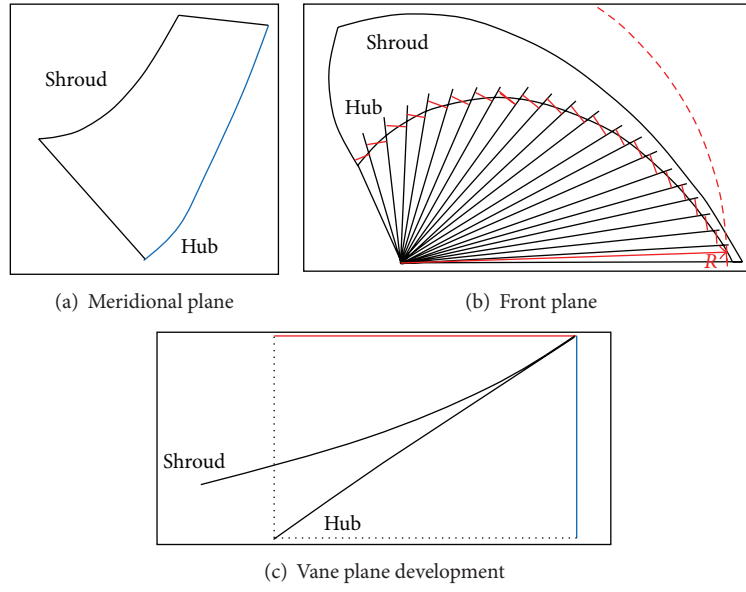


FIGURE 1: Traditional impeller design method.

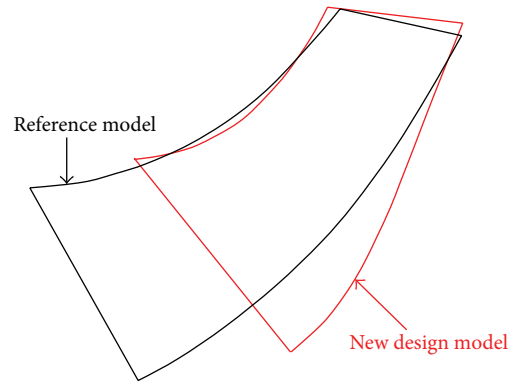


FIGURE 2: Comparison of meridional planes.

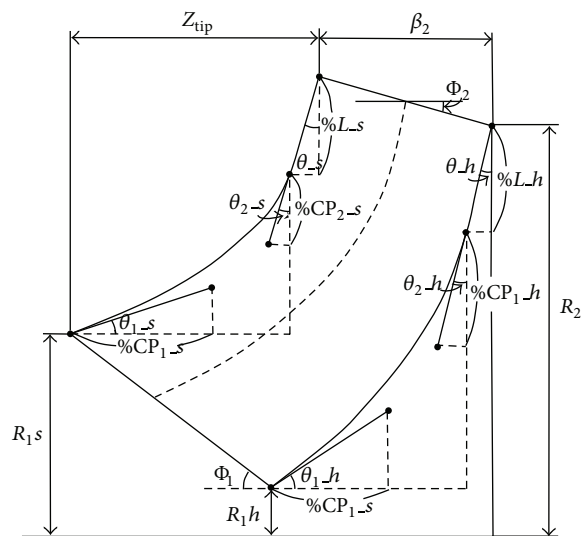


FIGURE 3: Design variable of meridional plane [11, 12].

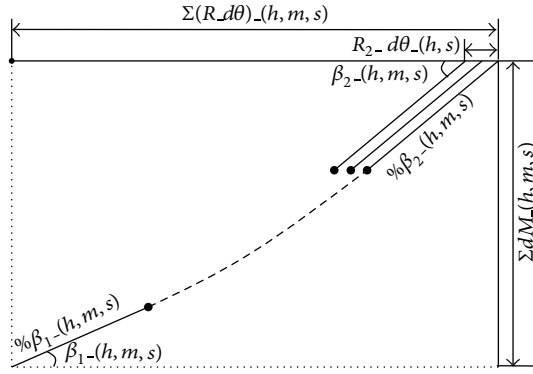


FIGURE 4: Design variable of vane plane development [13, 14].

indicate those of the shroud. θ_h and θ_s indicate the angles of the outlet hub and the shroud, respectively, when $\%L_h$ and $\%L_s$ of the straight lines meet the vertical axis. The control points of the hub inlet and outlet are shown as $\%CP_{1h}$ and $\%CP_{2h}$, respectively, and $\%CP_{1s}$ and $\%CP_{2s}$ indicate those of the shroud. Z_{tip} indicates the length of the axial direction from inlet/outlet parts of the shroud [11, 12].

2.3. Design Variables in a Vane Plane Development. A typical shape of vane plane development is shown in Figure 1(c), and the design variables for this vane plane development are defined in Figure 4. In the diagram, “ h ” means hub, “ m ” means midspan, and “ s ” means shroud. $\Sigma(R \cdot d\theta)_-(h, m, s)$ indicates the total length of the arc at each radius from the front view. $\Sigma dM_-(h, m, s)$ represents the total values of blade length in the meridional view; $\% \beta_{1-}(h, m, s)$ and $\% \beta_{2-}(h, m, s)$ show the portion of the blade having the same blade angle at the leading edge and trailing edge, respectively, and they are presented as a percentage of the whole length of the y -axis. $\beta_{1-}(h, m, s)$ is the inlet angle of the blade from the impeller, and $\beta_{2-}(h, m, s)$ is the outlet angle of the blade from the impeller. $R_2 \cdot d\theta_-(h, s)$ shows the inclination level toward the circumference from the hub and shroud at the outlet of the impeller. The inlet and outlet sections are connected by a smooth curved line, the angle of which changed linearly. Figure 5 shows the three-dimensional geometry of the impeller using the variables of the meridional plane and the vane plane development [13, 14].

3. Numerical Analysis Methods

The three-dimensional shape of the impeller was generated using the ANSYS CFX-BladeGen program. The structured grid system was generated using ANSYS CFX-TurboGrid, a program that generates a fluid machinery grid [15].

Although the impeller has five blades, we carried out the numerical analysis on only one blade passage using a periodic condition. Figure 6 shows the boundary conditions for the impeller calculation. Water with ambient temperature of 25°C was specified as the working fluid. We set the atmospheric pressure of 1 atm with the turbulence intensity of 5% on the inlet section of the impeller and gave the mass flow rate of

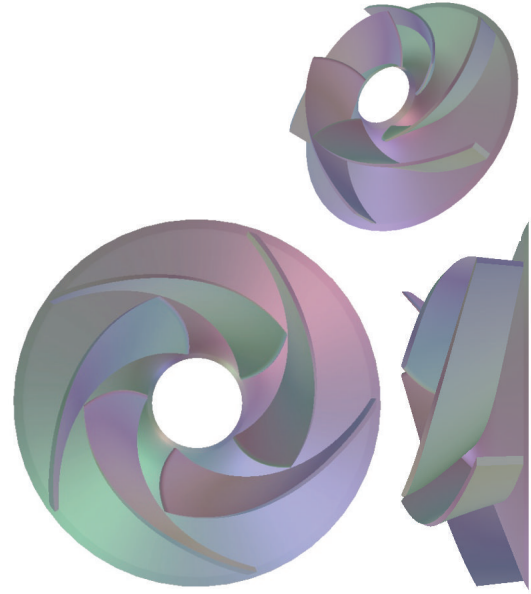


FIGURE 5: Three-dimensional geometry of the impeller.

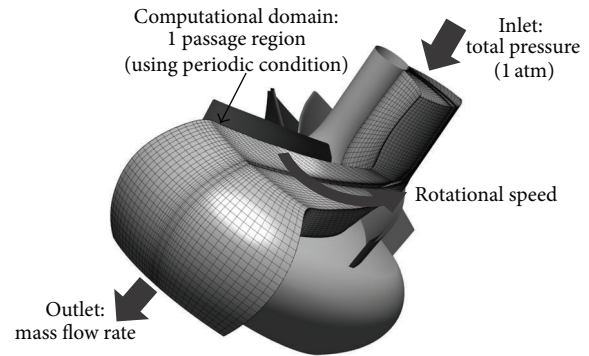


FIGURE 6: Boundary conditions for the impeller calculation.

665.33 kg/s of one blade passage at the design point on the exit section as a boundary condition. The solid surfaces in the computational domain were considered to be hydraulically smooth with adiabatic and no-slip conditions. The rotational speed of the impeller was 580 r/min. When the numerical analysis was performed for the impeller only, the inlet was simplified as a straight pipe and the outlet was expressed as the same meridional shape without the diffuser vane.

A structured grid system was constructed in the computational domain, with O-type grids near the main blade and vane surfaces and H-type grids in the other regions. Figure 7 shows the results of the grid dependency test for the total head and total efficiency of the reference impeller model. The total head and total efficiency values of the reference impeller did not change as the grid size was varied from approximately 90,000 to 110,000. Thus, about 90,000 grid points were used to define the computational domain encompassing the main

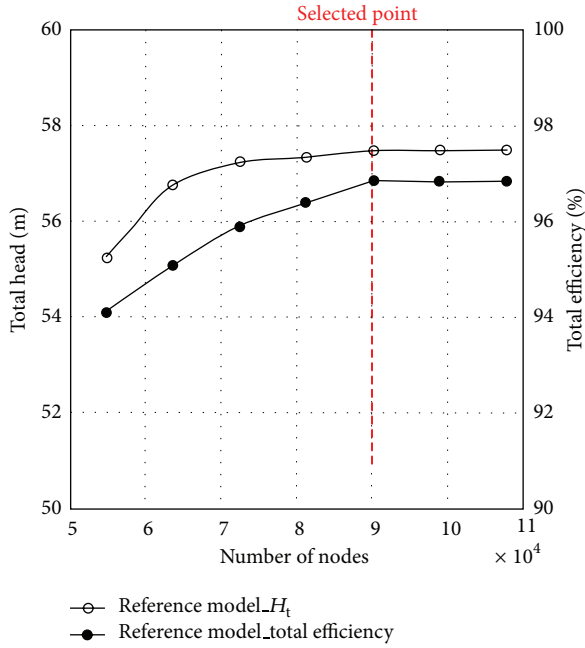


FIGURE 7: Results of the grid dependency test.

impeller passage. Figure 8 shows a typical example of the grid system used for the mixed-flow pump impeller in this work.

The ANSYS CFX-11, which is a commercial computational fluid dynamics (CFD) code, was used for the numerical analysis. A three-dimensional Reynolds average Navier-Stokes equation was used to analyze incompressible turbulence flow inside the pump. The governing equation was discretized using a finite volume method. A high-resolution scheme, which has more than a second degree of accuracy, was used to solve the convection-diffusion equations. For the turbulent model, the shear stress transport $k-\omega$ model [16–19], which is appropriate for the prediction of flow separation, was used to analyze turbulent flow through the impeller.

We used water as a working fluid. Disk friction losses, mechanical losses, leakage losses, and the tip clearance effect were not included in this calculation. The specific speed (r/\min , m^3/\min , m) of the pump was 380, the flow rate was $12,000 m^3/hr$, and the total head was 60 m.

4. Design of Experiments

The experiments design was based on the modern analysis of statistics, which helps select the main cause of abnormal fluctuations from many possible causes. In this study, 2^k factorial designs of the design of experiment (DOE) were used as numerical optimization methods [21–23]. Minitab 14, a commercial program, was used for the analysis of DOE.

Figure 9 shows the flow chart of this study. The performance of the reference model with same specific speed was analyzed and drawbacks that reduce pump performance could be identified based on the result of the analysis. Impeller design variables for the improvement of pump performance were defined using D/B . Response variables

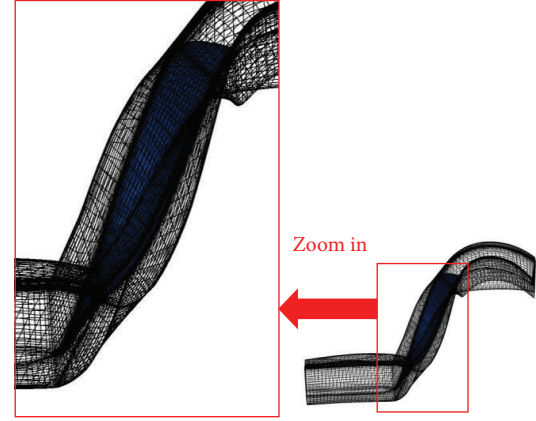


FIGURE 8: Grid system for numerical analysis of the impeller.

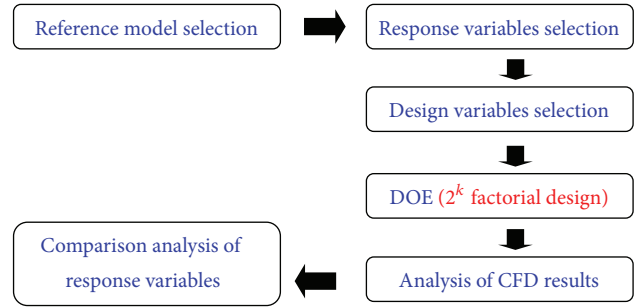


FIGURE 9: Optimization process flowchart.

were defined as total head, total efficiency, and suction performance. Tendencies of the response variables according to the identified design variables were analyzed by using 2^k factorial. The response variables of experiment sets generated by 2^k factorial were verified by using numerical analysis. Impeller shape was deduced by response optimization with the result of 2^k factorial. The performance of the optimized model was compared to that of the reference model using comparative analysis.

In DOE, a response variable should be defined in order to analyze the performance of the impeller according to the design variables. The actual response variables are defined in the total head curve, the total efficiency curve, and the NPSH curve, as shown in Figures 10 and 11. The design flow-rate is considered ideal if the flow rate at maximum total efficiency corresponds to the required flow rate.

In the case where the flow level changes over time when the pump is operating, unusual phenomena, such as cavitation, happen as the pressure of the pump inlet changes. Because of the nature of the fluid, the suction performance of the pump decreases, creating bubbles when the pressure is low. Thus, securing a design technology for a pump with high suction performance is very important. The graph of the results shows that net positive suction head (NPSH) value, which is represented as the x -axis, is determined by the set

TABLE 1: Design target (real), design specifications, and CFD results of the reference model.

	Design target (real)	Design specifications	Reference model
		CFD	
Q (m ³ /hr)	12,000	12,000	12,000
Total head (m)	60	More than 63 m	57.48
Total efficiency (%)	To be maximized	To be maximized	96.84
NPSHre (m)	To be minimized	To be minimized	6.7

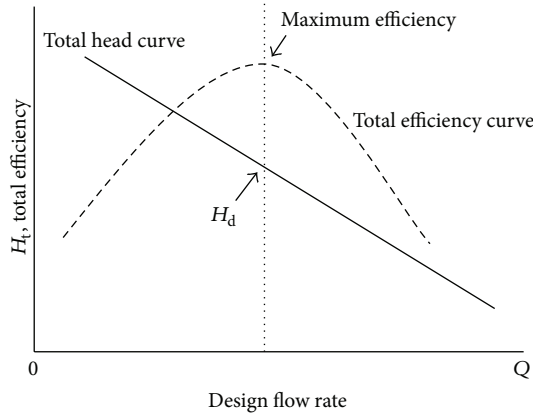


FIGURE 10: Total head and total efficiency curve.

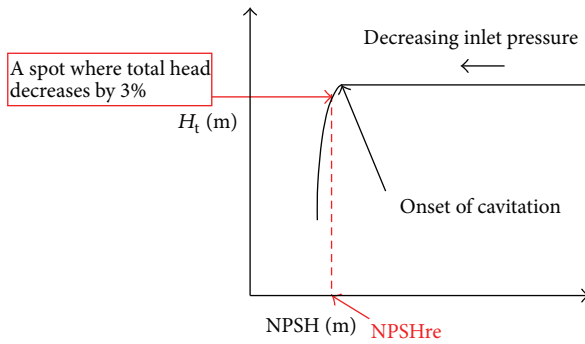


FIGURE 11: NPSH curve.

inlet pressure (P_{in}) and saturation vapor pressure (P_v), and it is calculated by the following equation:

$$NPSH = \frac{P_{in} - P_v}{\rho g}. \quad (1)$$

Different NPSH values are generated as the inlet pressure decreases and NPSH required (NPSHre) represents an area with more than 3% of loss in the total head [24–26].

5. Optimal Mixed-Flow Pump Impeller Design

Table 1 shows the real design target and the modified design specifications for the CFD cases and the CFD results for the reference model. The specific speed (r/min, m³/min, m) of the pump is 380, the flow rate is 12,000 m³/hr, the total head is 60 m, the total efficiency should be maximized, and

the NPSHre should be minimized at the design flow-rate. According to the numerical analysis of the reference model, however, the numerical analyses for the impeller do not satisfy 60 m. As a result, a new design model that satisfies the specifications is needed.

Because of the simplified flow domain, without including tip clearance and roughness, the results of the numerical analysis are expected to be higher than those of the design target. Thus, we modified the design specifications for the CFD results. Design specifications for the numerical analysis are shown in Table 1. The total head was defined to be higher than 63 m from the impeller. The total efficiency should be maximized and the NPSHre should be minimized at the design flow rate.

5.1. 2^k Factorial Designs. 2^k factorial designs are usually represented as n^k . In this DOE, the number of factors is k and the number of levels is n . The experiments are performed in every possible combination of all factors. The number of performed experiments should be at least n^k , without repetition. The advantage of factorial designs is that we can assume the main effect (the sole effect of the factor) and interaction effect (the effect between factors) of all factors. This convenient screening method can be used to find the core factor when there are many factors involved at the beginning of the experiment. In this study, considering the number of factors involved and the number of possible experiments, in addition to cost and time, we used fractional factorial designs in which the number of experiments is reduced by deleting less meaningful interactions.

5.2. Effect of Impeller Design Variables. To analyze the influence of the impeller design variables on the performance of the mixed-flow pump, the 2^k factorial designs were applied after defining the design variables of the meridional plane and the vane plane development. We therefore generated nine experimental conditions for the numerical analysis, including a center point using four design variables. As the various impeller design variables, the selected design variables for the 2^k factorial designs are $i\beta_{1-h}$ and $i\beta_{1-s}$, which are related to the incidence angle of the design variables of the vane plane development, and R_1 s and Z_{tip} , which are the meridional plane design variables. Here, the $i\beta_{1-h}$ and $i\beta_{1-s}$ are the incidence angles at the leading edge of the blade on the hub and shroud, respectively. The incidence angles are the design variables showing the difference between flow angle and the inlet angle.

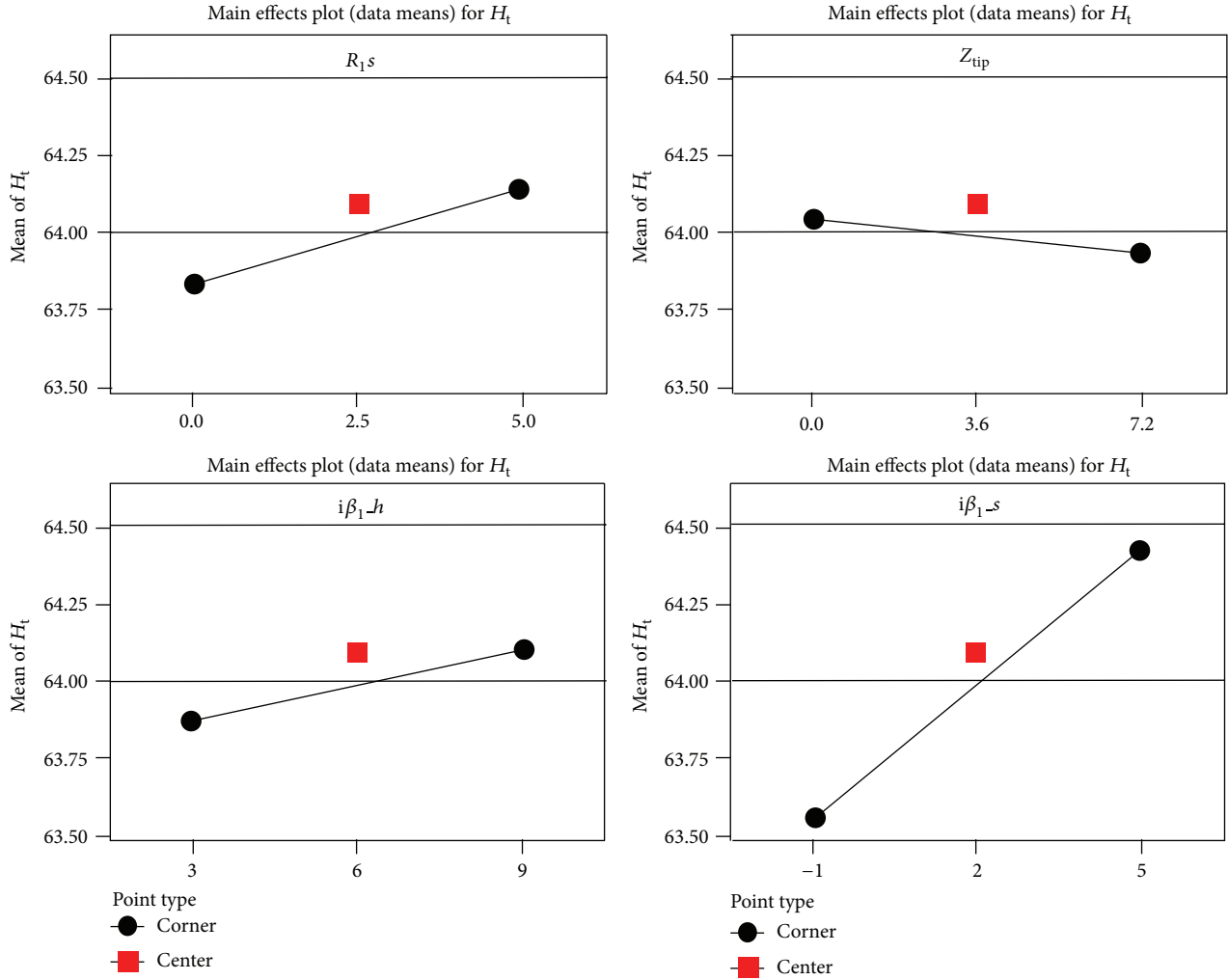


FIGURE 12: Main effects plot for total head.

TABLE 2: 2^k factorial designs set.

Set	A	B	C	D (A × B × C)
1	–	–	–	–
2	+	–	–	+
3	–	+	–	+
4	+	+	–	–
5	–	–	+	+
6	+	–	+	–
7	–	+	+	–
8	+	+	+	+
Center	0	0	0	0

Table 2 shows the set arrangement of 2^k factorial designs for nine experimental conditions. Here, the symbols of “+” and “–” mean the maximum and minimum levels of each design variable, respectively. In Table 2, the variables of A, B,

and C are defined by the orthogonal design and the D variable is decided by the combination of $A \times B \times C$.

The base model applied in 2^k factorial designs was the shape used in a previous study, and it satisfied maximum total efficiency at the design flow rate. Variation ranges of $i\beta_{1-h}$ and $i\beta_{1-s}$ are $\pm 3^\circ$, and those of R_{1s} and Z_{tip} were $\pm 2.5\%$ and $\pm 3.6\%$, respectively. The rest of the design variables of the meridional plane and vane plane development were fixed as base design value. Table 3 shows the numerical analysis sets of 2^k factorial designs.

Figures 12 and 13 show plots of the main effects and a Pareto chart of the total head, respectively. In the main effects plot, the tendency to increase the total head can be identified as increases in R_{1s} , $i\beta_{1-h}$, and $i\beta_{1-s}$. In Pareto chart, the total head is influenced by $i\beta_{1-s}$, R_{1s} , and $i\beta_{1-h}$ in the order of most to least.

Figures 14 and 15 show plots of the main effects and Pareto chart of total efficiency, respectively. In the main effects plot, total efficiency tends to increase as R_{1s} and Z_{tip} decrease, but $i\beta_{1-h}$ and $i\beta_{1-s}$ increase. It is clear that the tendency of the meridional plane design variables is

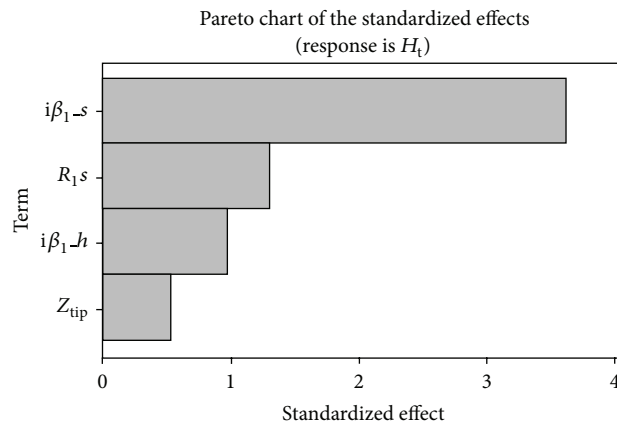


FIGURE 13: Pareto chart for total head.

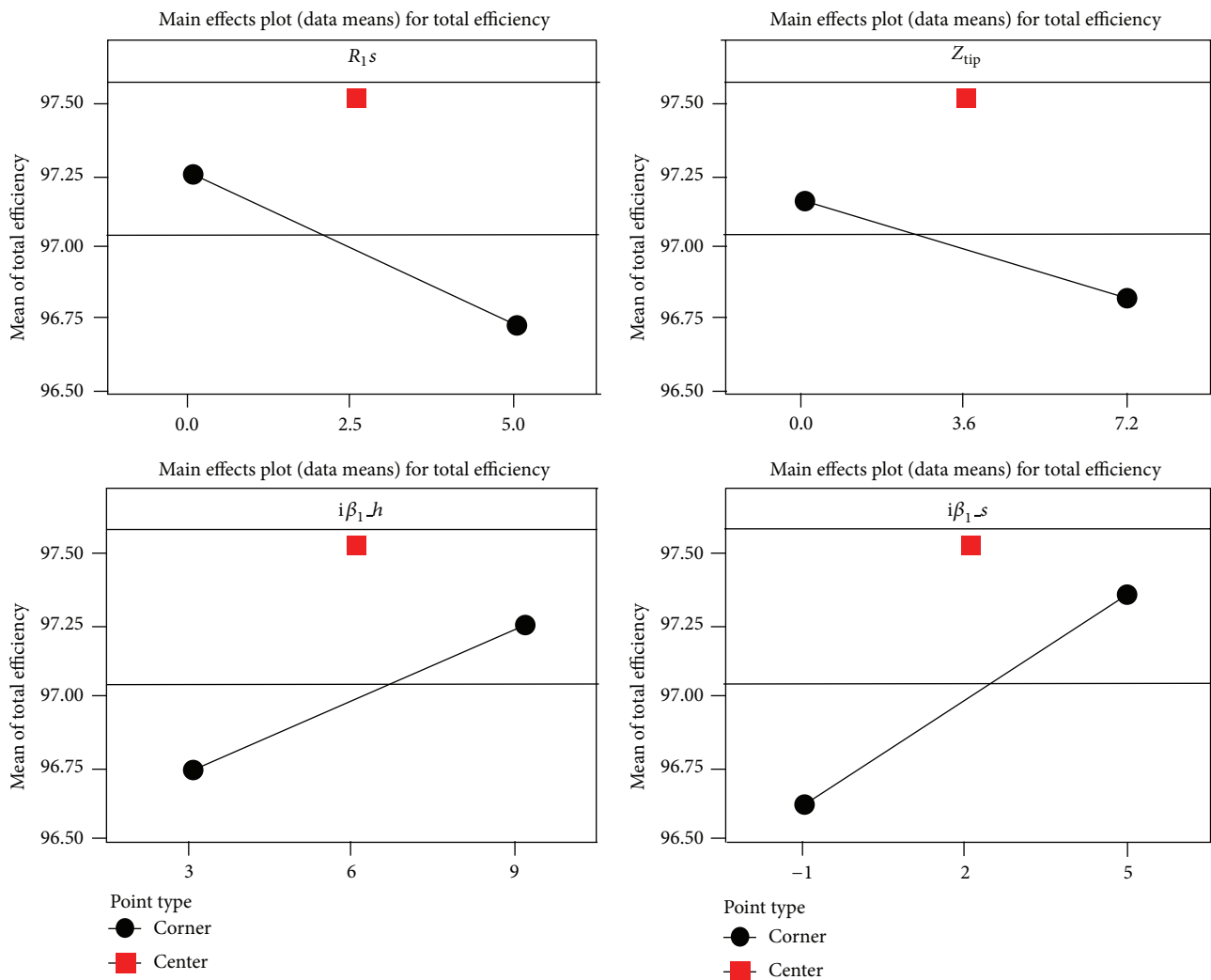


FIGURE 14: Main effects plot for total efficiency.

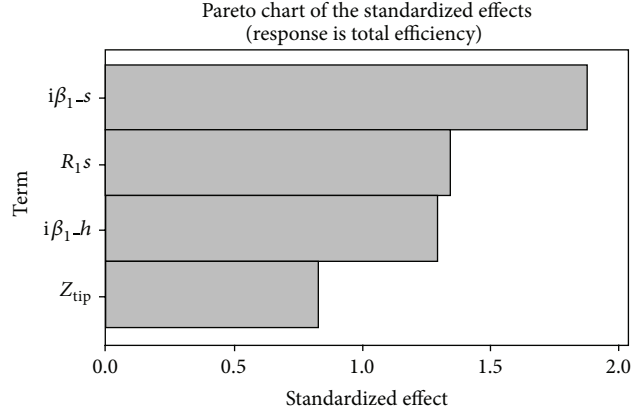


FIGURE 15: Pareto chart for total efficiency.

TABLE 3: Numerical analysis set of 2^k factorial designs for the impeller design.

Set	R_1s (m)	Z_{tip} (m)	$i\beta_{1-h}$ (°)	$i\beta_{1-s}$ (°)	Total head (m)	Total efficiency (%)	NPSHre (m)
1	0	0	3	-1	63.24	96.65	6.36
2	5	0	3	5	64.92	97.21	5.23
3	0	7.2	3	5	64.07	97.61	5.64
4	5	7.2	3	-1	63.25	95.47	8.09
5	0	0	9	5	64.18	97.55	6.15
6	5	0	9	-1	63.86	97.19	5.28
7	0	7.2	9	-1	63.83	97.18	5.74
8	5	7.2	9	5	64.55	97.04	5.28
Center	2.5	3.6	6	2	64.10	97.54	5.48

opposite to that of the vane plane development. In the Pareto chart, $i\beta_{1-s}$, R_1s , and $i\beta_{1-h}$ are variables affecting total efficiency; $i\beta_{1-s}$ shows the most influence and $i\beta_{1-h}$ shows the least.

Figures 16 and 17 show plots of the main effects and a Pareto chart of NPSHre. In the main effects plot, NPSHre tends to increase as Z_{tip} decreases, but $i\beta_{1-h}$ and $i\beta_{1-s}$ increase. Compared to other design variables, R_1s does not have a significant effect on NPSHre. Apart from R_1s , it is clear that the tendency of the meridional plane design variables is opposite to that of the vane plane development. In the Pareto chart, $i\beta_{1-s}$, $i\beta_{1-h}$, and Z_{tip} are variables affecting total efficiency; $i\beta_{1-s}$ shows the most influence and Z_{tip} shows the least.

To summarize the 2^k factorial designs, it was identified that the tendencies of total efficiency and NPSHre were opposite, depending on the design variables. The analysis of the tendencies of the response variables was important in order to draw a shape with improved NPSHre in high total efficiency, depending on the changing design variables. In order to create an impeller shape with improved NPSHre in high total efficiency, a response optimization method was

applied. In Table 3, most of the 2^k factorial sets satisfy 63 m of total head. Thus, the response variables were defined to improve total efficiency and NPSHre at the design flow rate, except for the total head as the objective function.

Response optimization was performed by regression analysis. Regression analysis is assuming mathematical model based on data in order to investigate the relevance among variables. Generally, the estimated model is used to make necessary prediction or statistical inference. Multiple regression analysis is a type of regression analysis where the relation between two or more predictors and one dependent variable is estimated linearly on straight line. Estimation equation for multiple regression analysis is as follows:

$$\hat{Y} = \hat{\beta}_0 + \hat{\beta}_1 \times X_1 + \hat{\beta}_2 \times X_2 + \cdots + \hat{\beta}_n \times X_n, \quad (2)$$

where X indicates the design variables from 2^k factorial. \hat{Y} and $\hat{\beta}$ are established by regression analysis. The regression model with consideration of multiple regression models is as (3) and (4).

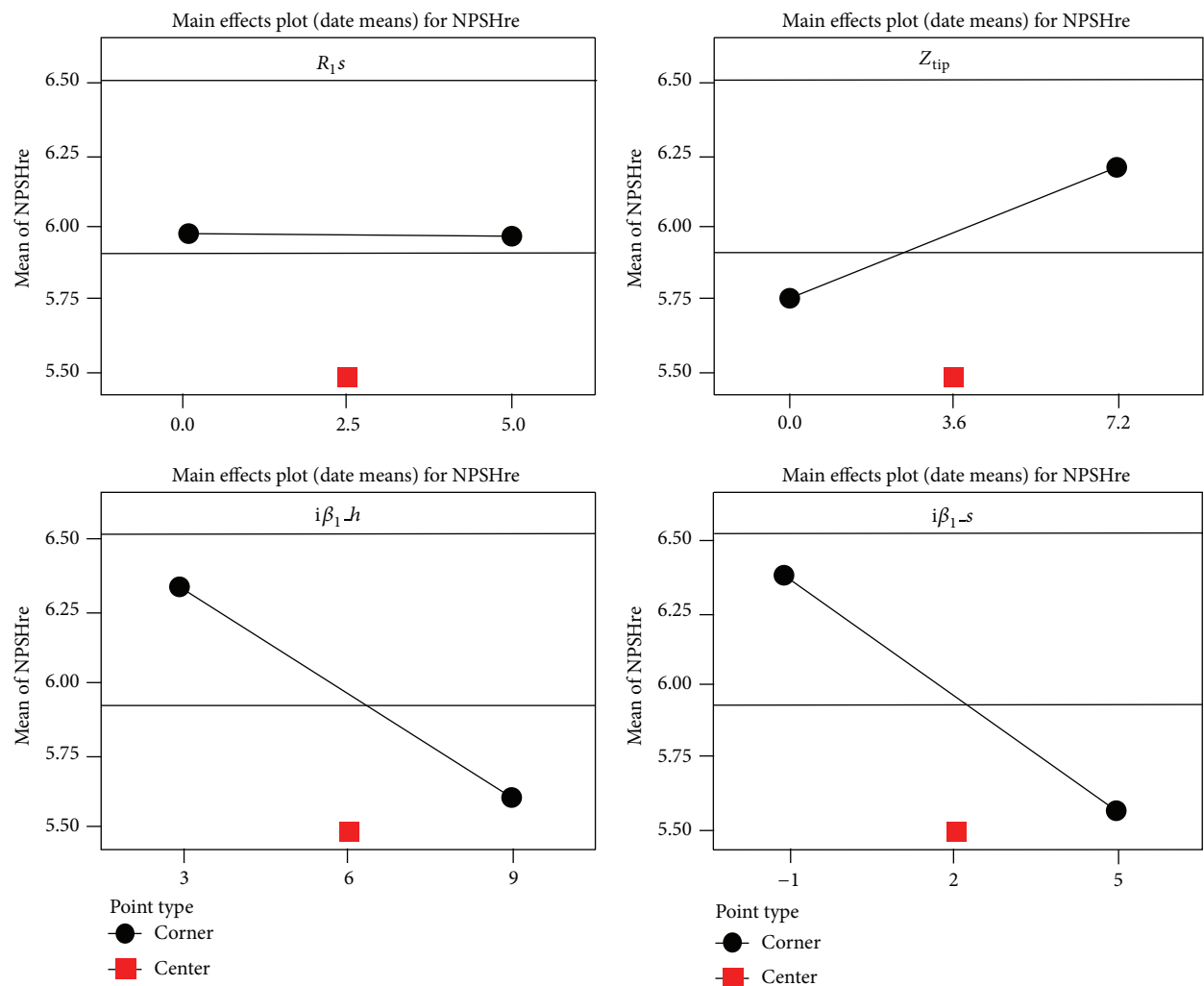


FIGURE 16: Main effects plot for NPSHre.

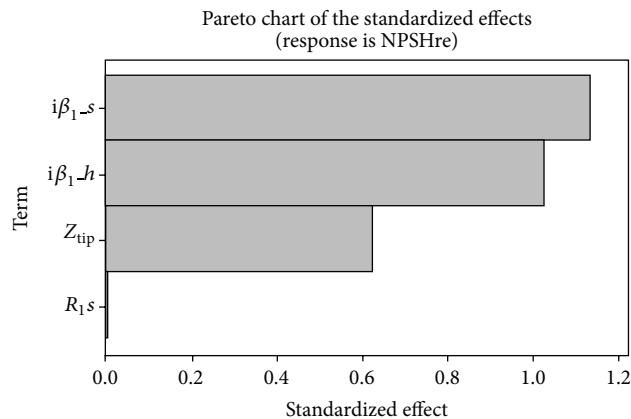
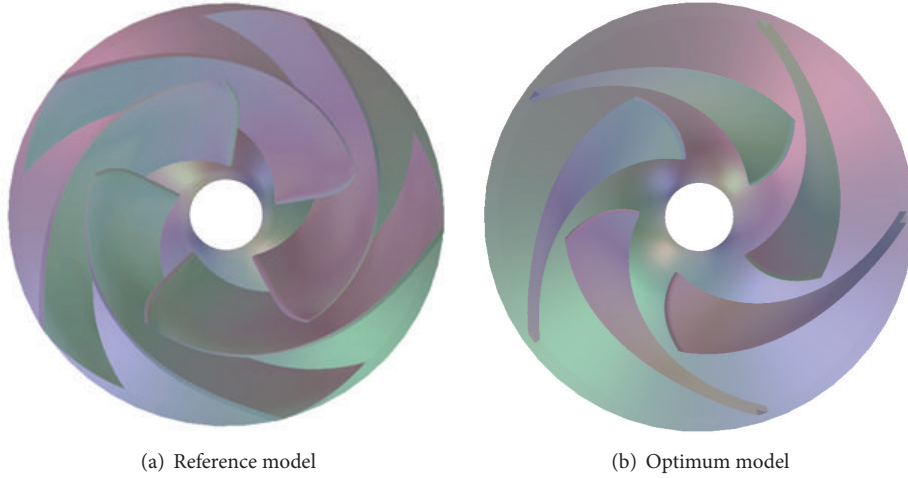


FIGURE 17: Pareto chart for NPSHre.

New	Hi	R_1s	Z_{tip}	$i\beta_1h$	$i\beta_1s$
D		5.0	7.2	9.0	5.0
0.79	Cur	[0.0]	[7.2]	[9.0]	[5.0]
	Lo	0.0	0.0	3.0	-1.0
Total efficiency Maximum $Y = 97.77$ $d = 0.77$					
NPSHre Minimum $Y = 5.38$ $d = 0.81$					

FIGURE 18: Plot for response optimization.



(a) Reference model

(b) Optimum model

FIGURE 19: Comparison of three-dimensional geometry impeller.

The regression equations for total efficiency and NPSHre are as follows, respectively:

$$\begin{aligned} \text{Total efficiency} = & 96.7 - 0.104 \times R_1s - 0.0447 \times Z_{tip} \\ & + 0.0839 \times i\beta_1h + 0.121 \times i\beta_1s, \end{aligned} \quad (3)$$

$$\begin{aligned} \text{NPSHre} = & 6.68 - 0.000 \times R_1s + 0.0604 \times Z_{tip} \\ & - 0.119 \times i\beta_1h - 0.132 \times i\beta_1s. \end{aligned} \quad (4)$$

The regression models in (2) and (3) were produced considering each design variable and thereby applicable as reliable optimization and predictive models. In response optimization, the objective function was defined as maximum total efficiency and minimum NPSHre. The total head was excluded because it showed little change as the design variables changed. Figure 18 shows the plot of response optimization. As shown in Figure 18, the optimum model that satisfies the objective value can be drawn when R_1s is 0%, Z_{tip} is 7.2%, $i\beta_1s$ is 9°, and $i\beta_1h$ is 5°. Figure 19 shows the

three-dimensional geometry impeller of reference model and optimum model.

6. Analyses of Numerical Analysis and Experiment Results

The selected optimum model was verified by numerical analysis. Figure 20 shows total head and total efficiency curves according to the result of numerical analysis. Figure 20(a) shows total head curves of the reference and optimum models. The tendencies of total head curves from the reference and optimum models are same but total head curve of optimum model has higher value than that of reference model. Especially, the total head at design flow rate from the reference model is expected to be under 60 m not meeting the requirement of design specification. Optimum model was designed to have total head higher than 60 m which is design specification considering disk friction losses, mechanical losses, leakage losses, tip clearance effect, machine loss, roughness loss, and diffuser loss. Figure 20(b) shows the total

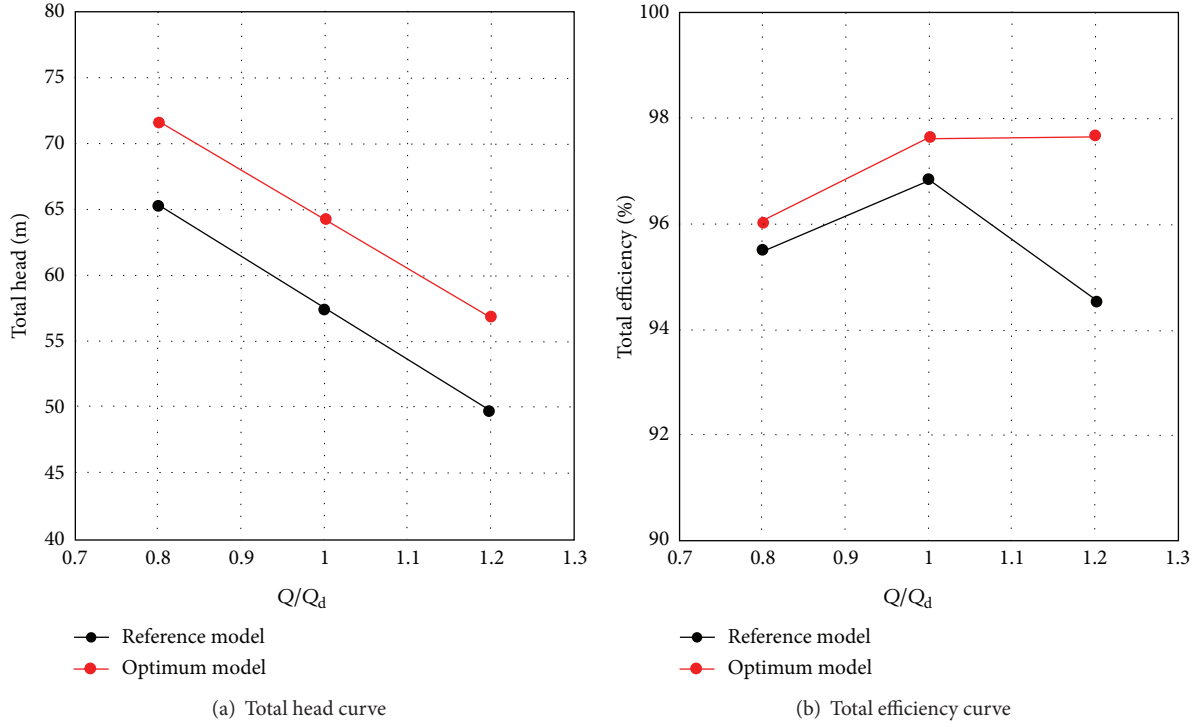


FIGURE 20: Comparison of total head and total efficiency curve.

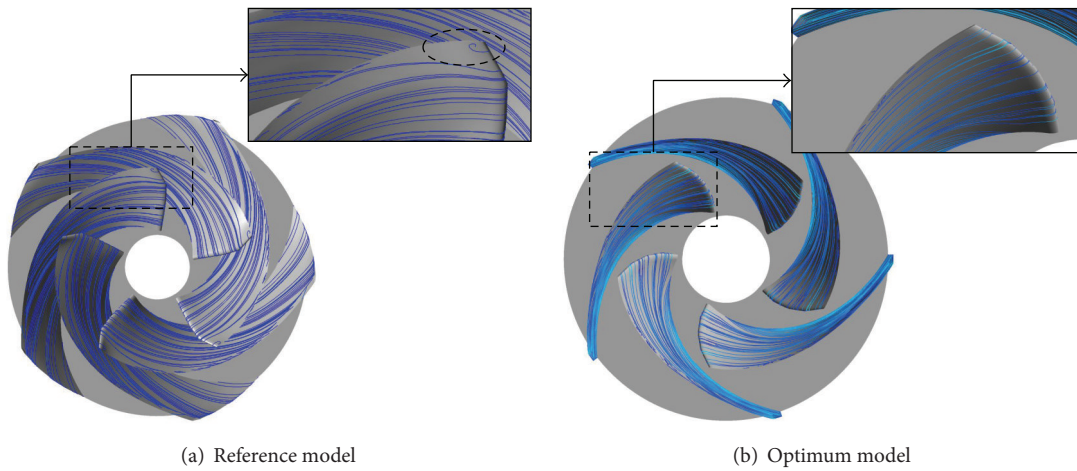


FIGURE 21: Comparison of streamline at design flow rate.

efficiency curves of the reference and optimum models. In Figure 20(b), the total efficiency of optimum model is higher not only from the design flow rate but also from low and high flow rates than that of the reference model.

Figure 21 shows the comparison between reference and optimum models regarding streamline at impeller blades. In Figure 21(a), there is a section side with flow separation at inlet shroud of the reference model. The total efficiency seems to decrease as a result of this flow separation at impeller blades. In Figure 21(b), the streamline is stabilized at inlet shroud of the optimum model increasing total efficiency compared to reference model.

The NPSH curves for the reference and optimum models are shown in Figure 22. In Figure 22, the NPSH_{res} for the reference and optimum models are 6.7 m and 5.7 m, respectively. Consequently, the optimum model was improved as 1 m compared to the reference model. On the other hand, Figures 23 and 24 show the isosurfaces of vapor pressures of -20 kPa and -40 kPa at the NPSH = 8.0 m (design flow rate) and NPSH = 5.9 m, respectively. It seems that the quantity of vapor in both the models is similar as shown in Figure 23. In Figure 24, the dramatic decrease of the vapor in the optimum model is observed at the NPSH = 5.9 m in comparison with the reference model. It is thought

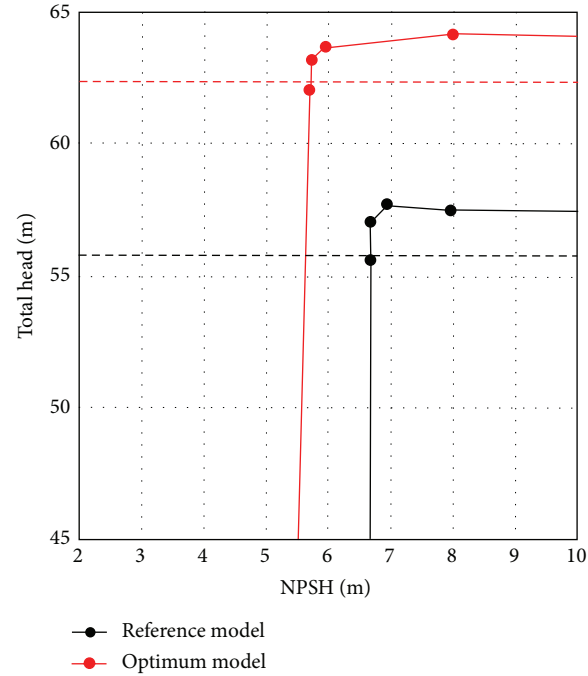


FIGURE 22: Comparison of NPSH curve at design flow rate.

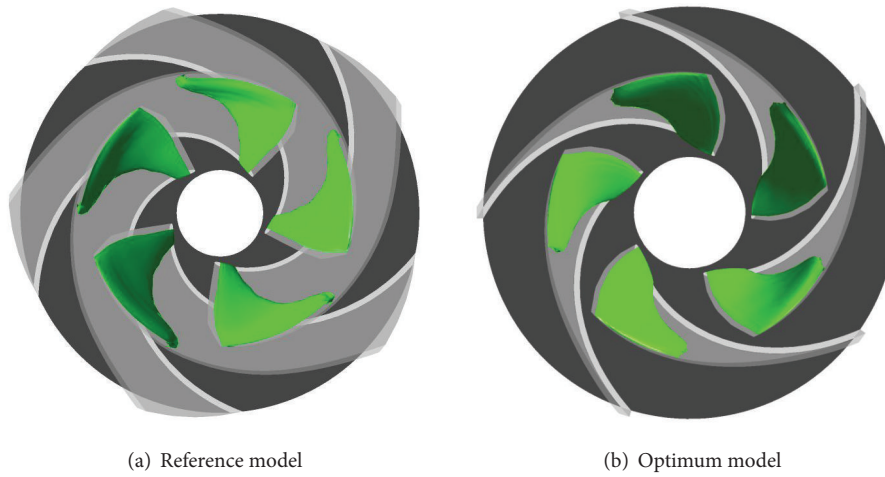


FIGURE 23: Comparison of isosurface of vapor pressure at NPSH = 8.0 m.

that the suction performance of the optimum model is improved by the considerable decrease of vapor in the suction side.

Figure 25 shows the NPSHre curves for the reference and optimum models. In Figure 25, it is apparent that the suction performance of the optimum model is improved in the entire flow rate, compared to the reference model. Table 4 shows the numerical results of the efficiency and NPSHre for the reference and optimum models at the design flow rate. According to the result of numerical analysis in Table 4, total head of optimum model is improved by the approximate 6 m than that of reference model. Moreover, it has shown 1 m and 0.81% improvements in the NPSHre and total efficiency, respectively, compared to the reference

TABLE 4: Comparison of total head, total efficiency, and NPSHre (CFD results).

	Total head (m)	Total efficiency (%)	NPSHre (m)
Reference model	57.48	96.84	6.7
Optimum model	64.25	97.65	5.7

model. Therefore, the optimum design produced mostly stable flows in the impeller passage.

The overall experimental apparatus used in the performance test is illustrated in Figure 26, which shows the installation of the test pump [20]. The test pump is connected

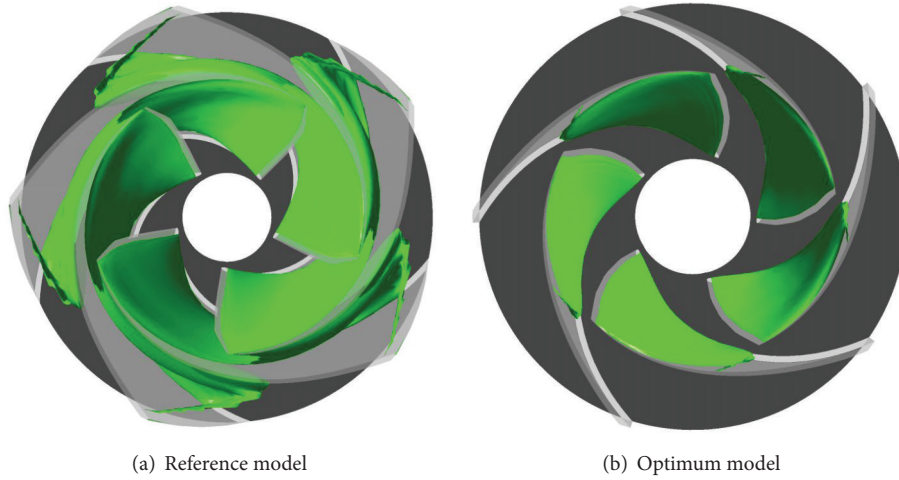


FIGURE 24: Comparison of isosurface of vapor pressure at NPSH = 5.9 m.

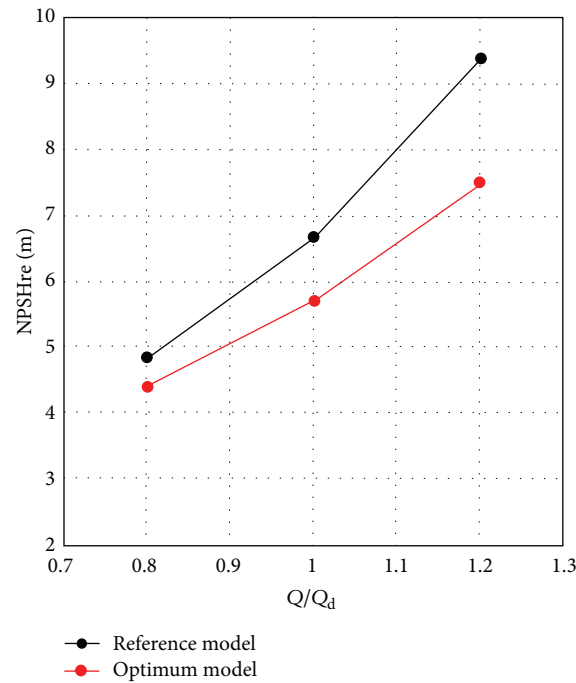


FIGURE 25: Comparison of NPSHre curve.

to the electric motor which is controlled by an inverter and a data acquisition system. As shown in Figure 26, the main component devices for the experimental apparatus consist of the flow meter, control valve, heat exchanger, booster pump, thermometer, damping valve, and pressure gauge. The measuring instruments and their uncertainties used for the performance test are tabulated in Table 5.

The numerical and experimental results for the total head, total efficiency, and NPSHre of the optimum model are compared in Figure 27. As shown in Figures 27(a) and 27(b), although the numerical and experimental results are different in terms of quantitative value, they are similar in tendency.

TABLE 5: Specifications of a measurement device.

Measurement device	Uncertainty (%)
Torque meter	± 2
Flow meter	± 2
Rotational sensor	± 0.3
Absolute pressure transducer	± 2
Differential pressure transducer	± 2
Thermocouple	± 2

In Figure 27(c), they are also similar in tendencies in the NPSHre curves but show the bigger difference at especially

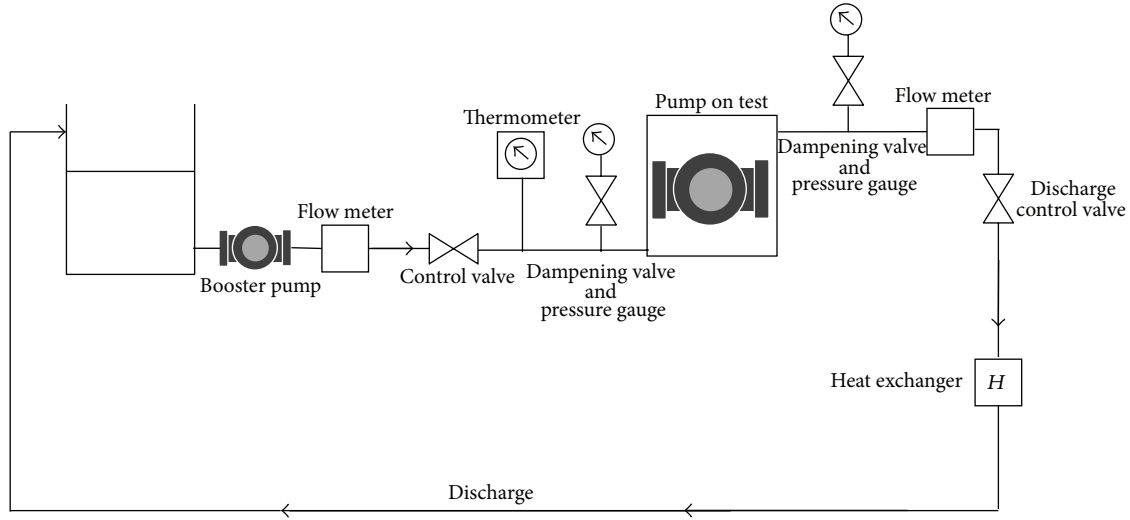


FIGURE 26: Schematic diagram of experimental apparatus for a mixed-flow pump [20].

the high flow rate. This is probably explained by the fact that bell mouth of inlet part, disk friction losses, mechanical losses, leakage losses, tip clearance effect, machine loss, roughness loss, and diffuser loss were not considered for the numerical analysis. First of all, the main effect on a relatively large error between the CFD and experiment results is due to no consideration of the tip clearance. These results illustrate the enhancement of the pump impeller's performances as a result of the optimization.

7. Conclusion

A numerical optimization on the improvement of suction performance and hydraulic efficiency of a mixed-flow pump impeller was conducted in this work. The main conclusions of this work are summarized as follows.

- (1) In this work, the impeller's meridional plane and vane plane development were employed as the design variables to improve the suction performance and total efficiency of the mixed-flow pump. According to the result of 2^k factorial, it showed that the suction performance and total efficiency had an opposite trend with the selected design variables.
- (2) In the analyses of the main effects plot and Pareto chart, the $i\beta_1$ s was more sensitive than other variables in terms of the NPSHre and total efficiency. On the other hand, the R_1 s affected considerably to total efficiency, whereas it did not affected absolutely to the NPSHre.
- (3) As a result of the optimization, the total head of the optimum model was numerically improved by the approximate 6 m, and moreover its numerical result showed 1 m and 0.81% improvements in the NPSHre and total efficiency, respectively, in comparison with the reference model.

- (4) The numerical and experimental results for the total head, total efficiency, and NPSHre of the optimum model were compared. Although the numerical and experimental results for the total head, total efficiency, and NPSHre were different in terms of quantitative value, they were similar in tendency. Therefore, the numerical optimization method based on the impeller's meridional plane and vane plane development can be effectively used for improving hydraulic performance of the mixed-flow pump.

Nomenclature

CFD:	Computational fluid dynamics
DOE:	Design of experiments
h :	Hub
H_d :	Designed total head (m)
H_t :	Total head (m)
M :	Meridional length (m)
N :	Rotational speed (r/min)
NPSH:	Net positive suction head (m)
NPSHre:	Net positive suction head required (m)
N_s :	Specific speed (r/min, m^3/min , m)
P_{in} :	Inlet pressure (pa)
P_v :	Vapor pressure (pa)
Q :	Flow rate (m^3/hr)
Q_d :	Design flow rate (m^3/hr)
R_1 :	Radius of inlet part (m)
R_2 :	Radius of outlet part (m)
s :	Shroud
Z_{tip} :	Axial direction from inlet/outlet parts of the shroud (m)
Φ_1 :	Inclined angle of the leading edge ($^\circ$)
Φ_2 :	Inclined angle of the trailing edge ($^\circ$)

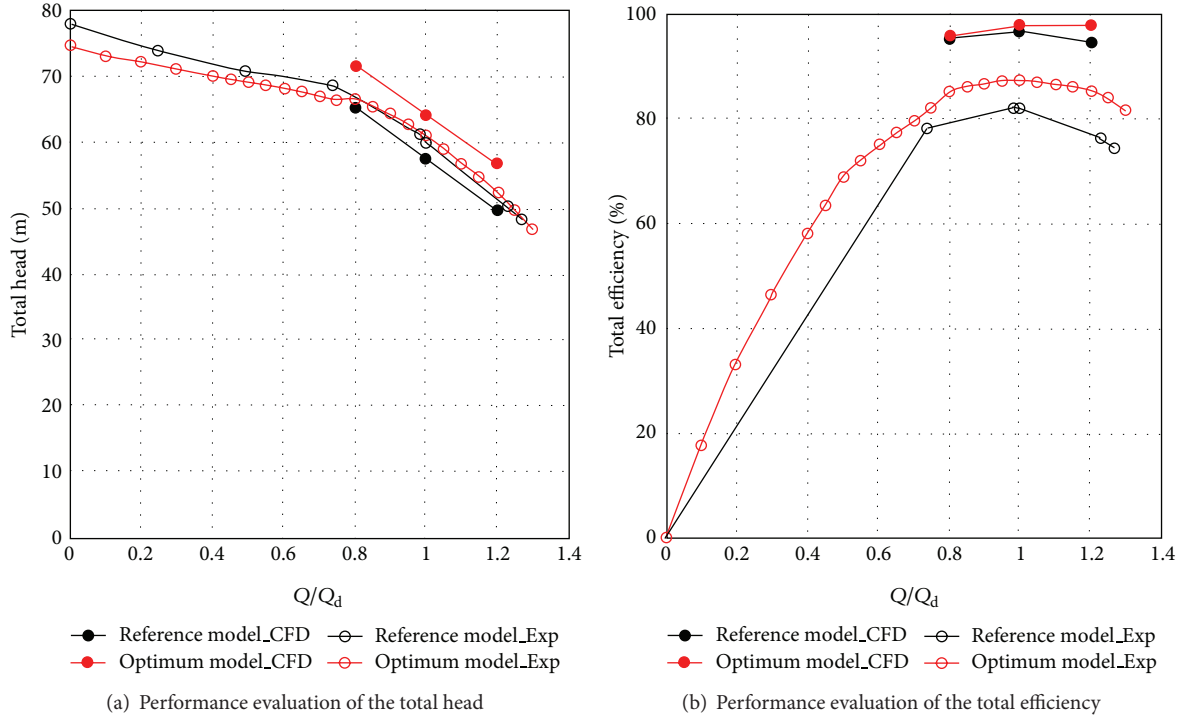


FIGURE 27: Comparative analysis of the performance evaluation (experimental versus numerical analysis).

β_1 : Inlet angle of the impeller ($^\circ$)
 $i\beta_1$: Incidence angle ($^\circ$)
 θ_1 : Inlet angle from meridional curve ($^\circ$)
 θ_2 : Outlet angle from meridional curve ($^\circ$)
 $\%L$: Straight line from outlet part (%)

$\%CP_1$: Control points of inlet part (%)
 $\%CP_2$: Control points of outlet part (%)
 $\%\beta_1$: Portion of same inlet blade angle (%)
 $\%\beta_2$: Portion of same outlet blade angle (%)
 ω : Angular velocity (m/s).

Conflict of Interests

The authors declare that there is no conflict of interests regarding the publication of this paper

Acknowledgments

This research was supported by a grant (no. 10044860) from the Korea Institute of Industrial Technology Evaluation and Planning (ITEP) that is funded by the Ministry of Science, ICT and Future Planning.

References

- [1] N. Nariman-Zadeh, N. Amanifard, A. Hajiloo, P. Ghalandari, and B. Hoseinpoor, "Multi-objective pareto optimization of centrifugal pump using genetic algorithms," in *Proceedings of the 11th WSEAS International Conference on Computers*, pp. 135–139, Crete Island, Greece, 2007.
- [2] R. K. Ursem, "Centrifugal pump design: three benchmark problems for many-objective optimization," Grundfos Management Technical Report 2010-01, 2010.
- [3] J. Kurokawa, K. Matsumoto, J. Matsui, and T. Kitahora, "Performances of centrifugal pumps of very low specific speed," in *Proceedings of the 19th IAHR Symposium on Hydraulic Machinery and Cavitation*, pp. 833–842, Singapore, 1998.
- [4] J. Kurokawa, K. Matsumoto, J. Matsui, and H. Imamura, "Development of high efficiency volute pump of very low specific speed," in *Proceedings of the 6th Asian International Conference on Fluid Machinery*, pp. 250–255, Johor, Malaysia, 2000.
- [5] J. F. Gulich, *Centrifugal Pumps Second Edition*, Springer, Heidelberg, Germany, 2010.
- [6] L. Bachus and A. Custodio, *Know and Understand Centrifugal Pumps*, Elsevier, New York, NY, USA, 2006.
- [7] E. Grist, *Cavitation and the Centrifugal Pump: A Guide for Pump Users*, Taylor & Francis, 1998.
- [8] A. Goto and M. Zangeneh, "Hydrodynamic design of pump diffuser using inverse design method and CFD," *Journal of Fluids Engineering*, vol. 124, no. 2, pp. 319–328, 2002.
- [9] H. Bing and S. Cao, "Optimal design of mixed-flow pump impeller based on direct inverse problem iteration and genetic algorithm," in *Proceedings of the ASME-JSME-KSME Joint Fluids Engineering Conference (AJK '11)*, vol. 8, pp. 803–810, Shizuoka, Japan, July 2011.
- [10] J. H. Kim and K. Y. Kim, "Optimization vane diffuser in a mixed-flow pump for high efficiency design for high efficiency design," *International Journal of Fluid Machinery and Systems*, vol. 4, no. 1, pp. 172–178, 2011.
- [11] J. Stepanoff, *Centrifugal and Axial Flow Pumps*, John Wiley & Sons, New York, NY, USA, 1957.
- [12] B. Neumann, "The interaction between geometry and performance of a centrifugal pump," in *Mechanical Engineering*, pp. 74–87, Publications Limited, London, UK, 1991.
- [13] S. Kim, Y. S. Choi, K. Y. Lee, and J. Y. Yoon, "Design optimization of centrifugal pump impellers in a fixed meridional geometry using DOE," *International Journal of Fluid Machinery and Systems*, vol. 2, no. 2, pp. 172–178, 2009.
- [14] S. Kim, Y. S. Choi, K. Y. Lee, and J. H. Kim, "Design optimization of mixed-flow pump in a fixed meridional shape," *International Journal of Fluid Machinery and Systems*, vol. 4, no. 1, pp. 14–24, 2011.
- [15] Help Navigator, ANSYS CFX, Release 11.0, ANSYS CFX-Solver Theory Guide.
- [16] J.-H. Kim, J.-W. Kim, and K.-Y. Kim, "Axial-flow ventilation fan design through multi-objective optimization to enhance aerodynamic performance," *ASME Journal of Fluids Engineering*, vol. 133, no. 10, Article ID 101101, 2011.
- [17] F. R. Menter, "Zonal two equation κ - ω turbulence models for aerodynamic flows," in *Proceedings of the AIAA 24th Fluid Dynamics Conference*, pp. 789–792, 1993.
- [18] Help Navigator, "ANSYS CFX, Release 11.0, ANSYS CFX-Solver Modeling Guide, Multiphase Flow Modeling, Interphase Mass Transfer, Cavitation Model".
- [19] Help Navigator, ANSYS CFX, Release 11.0, ANSYS CFX-Solver Theory Guide, Turbulence and Wall Function Theory, Eddy Viscosity Turbulence Models, Two Equation Turbulence Models.
- [20] ANSI/HI 1.6, *American National Standard for Centrifugal Pump Tests*, Hydraulic Institute, Parsippany, NJ, USA, 2000.
- [21] U. H. Jung, Y. S. Choi, and K. Y. Lee, "Optimum design of volute configuration in a sirocco fan using CFD and DOE," *International Journal of Air-Conditioning and Refrigeration*, vol. 17, no. 2, pp. 68–73, 2007.
- [22] R. H. Myers and D. C. Montgomery, *Response Surface Methodology: Process and Product Optimization Using Designed Experiments*, A Wiley-Interscience Publication, New York, NY, USA, 2nd edition, 2002.
- [23] C. R. Hick and K. V. Turner, *Fundamental Concepts in the Design of Experiments*, Oxford University Press, New York, NY, USA, 5th edition, 1999.
- [24] V. S. Lobanoff and R. R. Ross, *Centrifugal Pumps Design & Application*, Gulf Publishing, London, UK, 2nd edition, 1992.
- [25] T. Wright, *Fluid Machinery Performance, Analys, and Design*, CRC Press, New York, NY, USA, 1999.
- [26] M. Volk, *Pump Characteristics and Applications*, Taylor & Francis Group, Columbus, Ohio, USA, 2nd edition, 2005.

Research Article

A Comparative Assessment of Spalart-Shur Rotation/Curvature Correction in RANS Simulations in a Centrifugal Pump Impeller

Ran Tao, Ruofu Xiao, Wei Yang, and Fujun Wang

College of Water Resources and Civil Engineering, China Agricultural University, Beijing 100083, China

Correspondence should be addressed to Ruofu Xiao; xrf@cau.edu.cn

Received 10 June 2014; Accepted 29 August 2014; Published 30 September 2014

Academic Editor: Shaofan Li

Copyright © 2014 Ran Tao et al. This is an open access article distributed under the Creative Commons Attribution License, which permits unrestricted use, distribution, and reproduction in any medium, provided the original work is properly cited.

RANS simulation is widely used in the flow prediction of centrifugal pumps. Influenced by impeller rotation and streamline curvature, the eddy viscosity models with turbulence isotropy assumption are not accurate enough. In this study, Spalart-Shur rotation/curvature correction was applied on the SST $k-\omega$ turbulence model. The comparative assessment of the correction was proceeded in the simulations of a centrifugal pump impeller. CFD results were compared with existing PIV and LDV data under the design and low flow rate off-design conditions. Results show the improvements of the simulation especially in the situation that turbulence strongly produced due to undesirable flow structures. Under the design condition, more reasonable turbulence kinetic energy contour was captured after correction. Under the low flow rate off-design condition, the prediction of turbulence kinetic energy and velocity distributions became much more accurate when using the corrected model. So, the rotation/curvature correction was proved effective in this study. And, it is also proved acceptable and recommended to use in the engineering simulations of centrifugal pump impellers.

1. Introduction

Reynolds-averaged Navier-Stokes (RANS) simulation provides effective solutions for numerical simulations in engineering. By solving the time-averaged N-S equations, RANS simulation reduces the consumption of computing resources on the premise of keeping sufficient accuracy. Based on the Boussinesq assumption [1, 2], eddy viscosity models (EVM) directly established the relationship between Reynolds stress tensor and the traceless mean strain rate tensor. Because of the simplicity and stability, EVMs are widely used in engineering simulations. However, because of the coordinate invariance, EVMs are insensitive to streamline curvature and system rotation [3]. Moreover, with the turbulence isotropy assumption, the rotation effect on turbulent flow is difficult to describe. However, under the influences of the nonlinear wave induced by the Coriolis force, the flow structure will change [4]. So, a proper correction for EVM is necessary in the RANS simulation of rotating and swirling flow.

To describe the effects of rotation or streamline curvature on a turbulent flow, Bradshaw [5] first proposed the gradient

Richardson number Ri . Combined with the low-Reynolds-number $k-\epsilon$ model, Khodak and Hirsch [6] introduced a new form of Ri number which allows including the influence of curvature and rotation on the three-dimensional turbulent flow. It improved the prediction accuracy of mean velocity and Reynolds stresses in verification cases. On the basis of Galilean invariance, Spalart and Shur [3] differentiated the property between streamline curvature and system rotation and also introduced a new Ri number. By establishing intermediate variables, this new Ri number was used to correct the turbulence production term of EVM. This correction method was applied to Spalart-Allmaras model by Shur et al. [7] and proved to be much more accurate than the original S-A model. Moreover, Dufour et al. [8, 9] corrected the $k-\epsilon$ model and compared it with the Spalart-Shur corrected S-A model through a compressor case. Improvements were obtained after the rotation and curvature correction for the corrected $k-\epsilon$ model. Smirnov and Menter [10] also applied the Spalart-Shur correction to SST $k-\omega$ model that is known as the SST-RC model. The computational accuracy was proved to be significantly improved with just a little increase of the

time costs. Then, Dhakal and Walters [11] corrected the SST k - ω model based on the correction method by York et al. [12]. The new model was compared with the SST-RC model and was proved accurate without compromising stability and efficiency. With the modified mean-flow time scale, Hellsten [13] also introduced a new Ri number to correct the ω equation of SST k - ω model. This new corrected model, which is called SST-RC-Hellsten model, was sensitized on the effects of system rotation and streamline curvature with slight improvement on the numerical behavior. Based on Spalart-Shur correction method and Hellsten's time scale, Zhang and Yang [14] corrected the S-A model and got reasonable results in a U-turn duct case.

In general, all the correction methods mentioned above were theoretically feasible for swirling turbulent flow. For centrifugal pumps, the internal flow regime varies with the operating condition [15]. Under off-design conditions, the turbulent flow in the impeller is much more complicated due to the vortex, backflow, and other secondary flow structures. Hence, it is necessary to ensure the simulation accuracy of centrifugal pumps under the influence of system rotation and streamline curvature. However, in the vast majority of RANS simulations of centrifugal pumps, the rotation and curvature effects are not considered when using EVM. In order to evaluate the Spalart-Shur rotation/curvature correction in the centrifugal pump cases, RANS simulations were conducted with both the original and the corrected SST k - ω models. The simulation results were compared with the experimental data by particle image velocimetry and laser Doppler velocimetry [16, 17].

2. Turbulence Modeling

As mentioned above, the SST-RC turbulence model [10] was used in the turbulent flow simulation. Compared with the original SST k - ω model [18], in consideration of the turbulence anisotropy, the rotation/curvature correction coefficient f_{r1} was introduced as a multiplier of the turbulence production term P in the turbulence kinetic energy k equation and specific dissipation rate ω equation. So, the production term P is defined as follows:

$$P = f_{r1} \tau_{ij} \frac{\partial u_i}{\partial x_j}, \quad (1)$$

where f_{r1} is given empirically with specific limiters as follows:

$$f_{r1} = \max [\min (f_{\text{rot}}, 1.25), 0], \quad (2)$$

$$f_{\text{rot}} = (1 + C_{r1}) \frac{2r^*}{1 + r^*} [1 - C_{r3} \tan^{-1} (C_{r2} \hat{r})] - C_{r1},$$

where C_{r1} , C_{r2} , and C_{r3} are constants valued as 1.0, 2.0, and 1.0 respectively. The remaining functions are defined as follows:

$$r^* = \frac{S}{W},$$

$$\hat{r} = \frac{2W_{ik}S_{jk}}{WD^3} \left[\frac{DS_{ij}}{D_t} + (\epsilon_{imn}S_{jn} + \epsilon_{jmn}S_{in}) \Omega_m^{\text{rot}} \right],$$

$$S^2 = 2S_{ij}S_{ij},$$

$$W^2 = 2W_{ij}W_{ij},$$

$$D^2 = \max (S^2, 0.09\omega^2), \quad (3)$$

where Ω^{rot} is the rotation rate of the reference frame and the term DS_{ij}/D_t represents the Lagrangian derivative of the strain rate tensor. S_{ij} is the strain rate tensor and W_{ij} is the rotation rate tensor by

$$S_{ij} = \frac{1}{2} \left(\frac{\partial u_i}{\partial x_j} + \frac{\partial u_j}{\partial x_i} \right)$$

$$W_{ij} = \frac{1}{2} \left(\frac{\partial u_i}{\partial x_j} - \frac{\partial u_j}{\partial x_i} \right) + \epsilon_{mji} \Omega_m^{\text{rot}}. \quad (4)$$

The τ_{ij} in (1) is the Reynolds stress tensor. In the Boussinesq assumption [2], τ_{ij} is proportional to the strain rate tensor S_{ij} by

$$\tau_{ij} = \mu_t \left(2S_{ij} - \frac{2}{3} \frac{\partial u_k}{\partial x_k} \delta_{ij} \right), \quad (5)$$

where μ_t is the turbulent eddy viscosity. By applying the rotation/curvature correction, anisotropic effects were considered in the simulation when solving the turbulence equations.

3. Numerical Simulation

To assess the Spalart-Shur rotation/curvature correction in RANS simulation of centrifugal pump, the internal flow in the impeller was numerically simulated. Based on the numerical results and available experimental data [16], the flow details were comparatively investigated under both the design and low flow rate off-design conditions.

3.1. Pump Impeller Model. The scheme of the investigated centrifugal pump impeller is shown in Figure 1. The specific speed N_s of this impeller is about 26.3 calculated by

$$N_s = 3.65 \frac{n\sqrt{Q_d}}{H_d^{3/4}}, \quad (6)$$

where n is the rotational speed of 725 r/min, Q_d is the design flow rate of $3.06 \times 10^{-3} \text{ m}^3/\text{s}$, and H_d is the design head of 1.75 m. The geometrical parameters of impeller are shown in Table 1 and illustrated in Figure 1. Two operating conditions including $Q = 1.0Q_d$ and $Q = 0.25Q_d$ were simulated and performed in this study.

3.2. Flow Domain Discretization. The flow domain consisted of the impeller only. For a better geometric adaptability, tetrahedral mesh elements were used to discretize the impeller domain. For the usage of wall functions, y^+ of the first element outside the walls should be set in the log-layer. So, prism boundary layers were used in the near wall region.

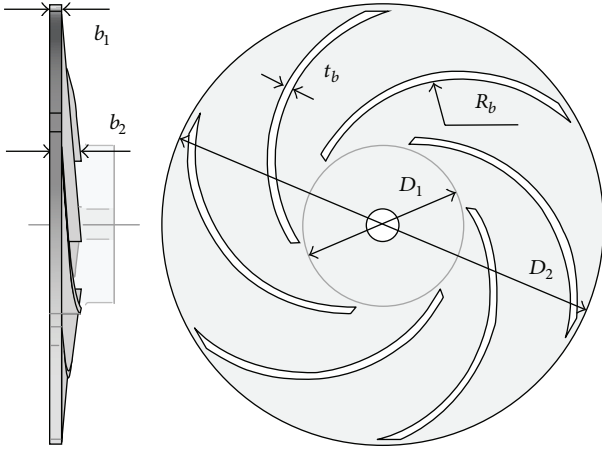


FIGURE 1: Scheme of the investigated centrifugal pump impeller.

TABLE 1: Geometrical parameters of impeller.

Parameter	Value
Inlet diameter D_1	71.0 mm
Outlet diameter D_2	190.0 mm
Inlet height b_1	13.8 mm
Outlet height b_2	5.8 mm
Number of blades Z	6
Blade thickness t_b	3.0 mm
Inlet blade angle β_1	19.7 degrees
Outlet blade angle β_2	18.4 degrees
Blade curvature radius R_b	70.0 mm

TABLE 2: Detailed parameters of mesh scheme.

Parameter	Value
Nodes	406012
Elements	2046670
Prism boundary layers	5
The first layer height	0.1 mm
Boundary layer growth rate	1.2

Then, a mesh-size independence check was conducted to compromise the accuracy and costs in the simulation. By modifying the mesh size, the residuals of head and hydraulic efficiency was ensured to be less than 1×10^{-3} . By modifying the boundary layer height, the y^+ values were controlled within the range from 1.53 to 26.97 so that the near-wall region could be solved with wall functions. The final mesh scheme is shown in Table 2 and Figure 2.

3.3. Simulation Settings. In this study, transient numerical simulations were conducted. Three dimensional incompressible N-S equations were solved in the simulation process. The fluid medium was set as water at 25 degree centigrade (density $\rho = 997 \text{ kg/m}^3$ and dynamic viscosity $\mu = 8.899 \times 10^{-4} \text{ kg/m}\cdot\text{s}$). The reference frame was set as rotational with the speed of 725 r/min. The reference pressure was 1 Atm. Mass flow inlet was set at the impeller inflow with the

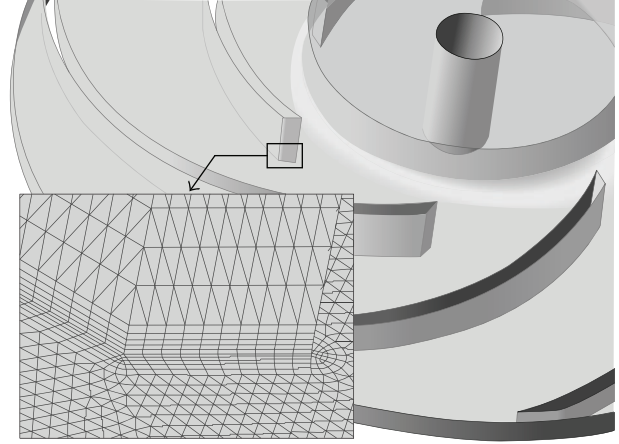


FIGURE 2: Schematic map of the mesh.

velocity normal to the boundary. Pressure outlet was set at the impeller outflow with a value of 0 Pa. No-slip wall condition was given on the solid wall boundaries including hub, shroud and blades.

4. Results and Discussion

In order to fully assess the impacts of Spalart-Shur correction, as mentioned above, the simulations were proceeded under the design ($1.0Q_d$) and off-design ($0.25Q_d$) conditions. The design condition is the most important operating condition of pump. A correct simulation of the flow details is obviously significant. The off-design condition is also crucial. Undesirable flow structures make the flow hard to predict. For this reason, the improvements of simulation accuracy are necessary. Hence, based on the CFD results, the comparative assessment of the rotation/curvature correction and discussions are given as follows.

4.1. Flow under the Design Condition. Under the design condition ($1.0Q_d$), the velocity field on the spanwise 50% surface was simulated and compared with the LDV data [16] as shown in Figure 3. It can be seen that the flow regime is smooth, stable, and uniform among all the impeller passages.

The correction coefficient f_r contour on the spanwise 50% surface is shown in Figure 4. It indicates the enhancement or reduction of local turbulence production under the influence of rotation and curvature. As the multiplier of turbulence production term, the value of f_r was almost 1.0 in the vast majority of impeller domain. However, small scale of reduction was detected at the blade leading edge (LE) and in the near suction surface (SS) region.

Figure 5 shows the comparison map of turbulence kinetic energy k_{2D} . In the impeller, fluid separated from the blade surface while flowing around the LE. High k_{2D} region occurred due to the small scale local separation. Also, in the near SS region, high turbulence occurred due to the local unattached flow. After the rotation/curvature correction, the range of high k_{2D} region became smaller than before because

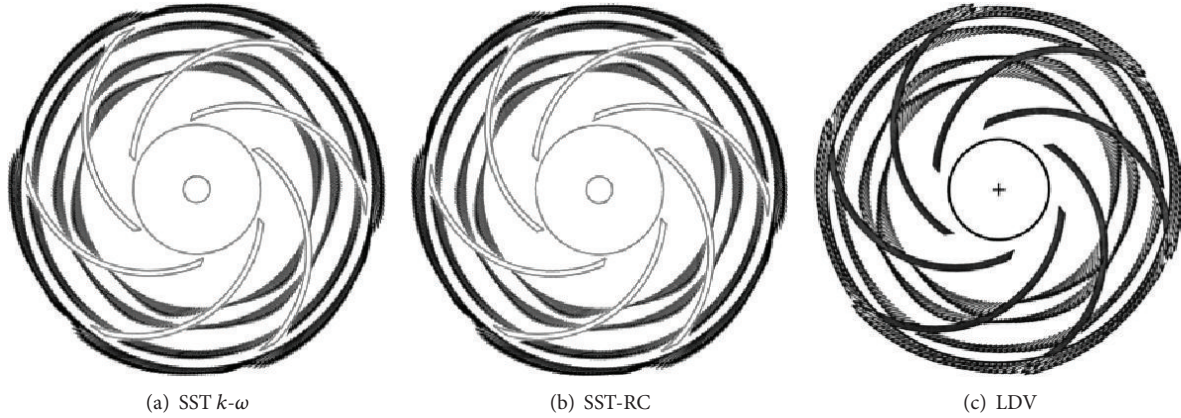


FIGURE 3: Velocity field on spanwise 50% surface under $1.0Q_d$.

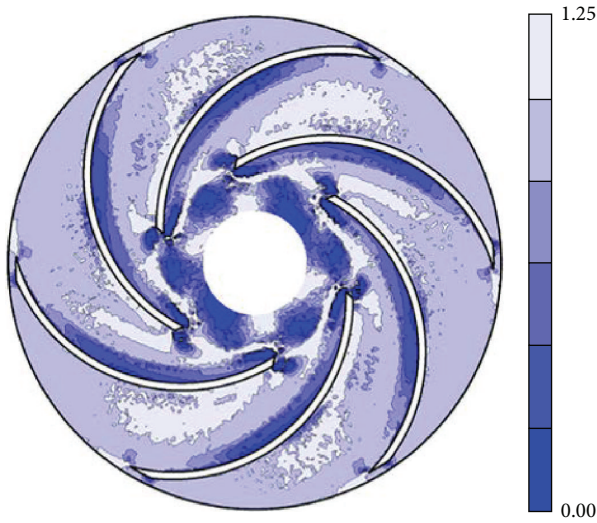


FIGURE 4: Correction coefficient f_r on spanwise 50% surface at $1.0Q_d$.

of the turbulence reduction. As shown in Figure 5, by comparing the k_{2D} value and pattern, the result by SST-RC model was more consistent with the PIV data [16].

Additionally, the relative velocity distributions on the spanwise 50% surface are analyzed and shown as follows. The radial component (W_r) and tangential component (W_t) in three different radius' positions were plotted, respectively, in Figure 6 ($R_2 = 0.5D_2$). Considering the flow uniformity among all the passages, the velocity distributions were compared based on just a single passage. Seen from the velocity curves, the velocities magnitude by SST-RC model was just slightly bigger than that by SST $k-\omega$ model. In consideration of the deviations between the PIV and LDV data [16], both the original and the corrected turbulence models get the similar velocity distribution regularities.

In general, the impact of rotation/curvature correction on the simulation accuracy was not obvious under $1.0Q_d$. Nevertheless, there was no obvious extra time cost when using SST-RC model instead of SST $k-\omega$ model. So, it would

be reasonable to use the SST-RC model in the simulation of centrifugal pump under the design condition.

4.2. Flow under the Low Flow Rate Off-Design Condition.

Under the low flow rate off-design condition ($0.25Q_d$), the velocity field on the spanwise 50% surface was also simulated and compared with the LDV data [16] as shown in Figure 7. With the flow rate decreasing, flow regime in the impeller became undesirable with secondary flow structures. As shown in the velocity field map, fluid did not flow along the direction of blade geometry. Back flow from outlet to inlet occurred in the passage. Lateral secondary flow from blade pressure surface (PS) to suction surface (SS) also occurred. Under the influence of all the disordered flow structures, the flow uniformity among all the passages disappeared. Some passages were blocked by secondary flow, but some other passages were smoother. As shown in the LDV experiment, the blocked passage and unblocked passage occurred alternately in the impeller [16]. This phenomenon was also captured by numerical simulations. In this situation, the streamline curvature under $0.25Q_d$ became more obvious than that under $1.0Q_d$.

The correction details under $0.25Q_d$ are shown in Figure 8. As plotted in the f_r contour, reductions of turbulence production were detected in the vast majority of impeller domain. But influenced by the flow regime, the rotation/curvature correction was different in each passage. The passages marked "A" and "B" in Figure 8 represented the unblocked and blocked passages, respectively. In passage-A, the low f_r region occurred at the whole blade SS. The high f_r region occurred at the PS near LE and the midpassage near trailing edge (TE). In passage-B, the low f_r region occurred at SS near LE and midpassage near TE. The high f_r region occurred at SS near TE.

Influenced by the differences of coefficient f_r , the turbulence kinetic energy k_{2D} had also changed after the correction. Figure 9 shows the k_{2D} contour on the spanwise 50% surface under $0.25Q_d$. As shown in the contours, the turbulence kinetic energy was low in the unblocked "A" passages and was high in the blocked "B" passages. Due to the flow separation at LE and backflow at TE, the high k_{2D} region

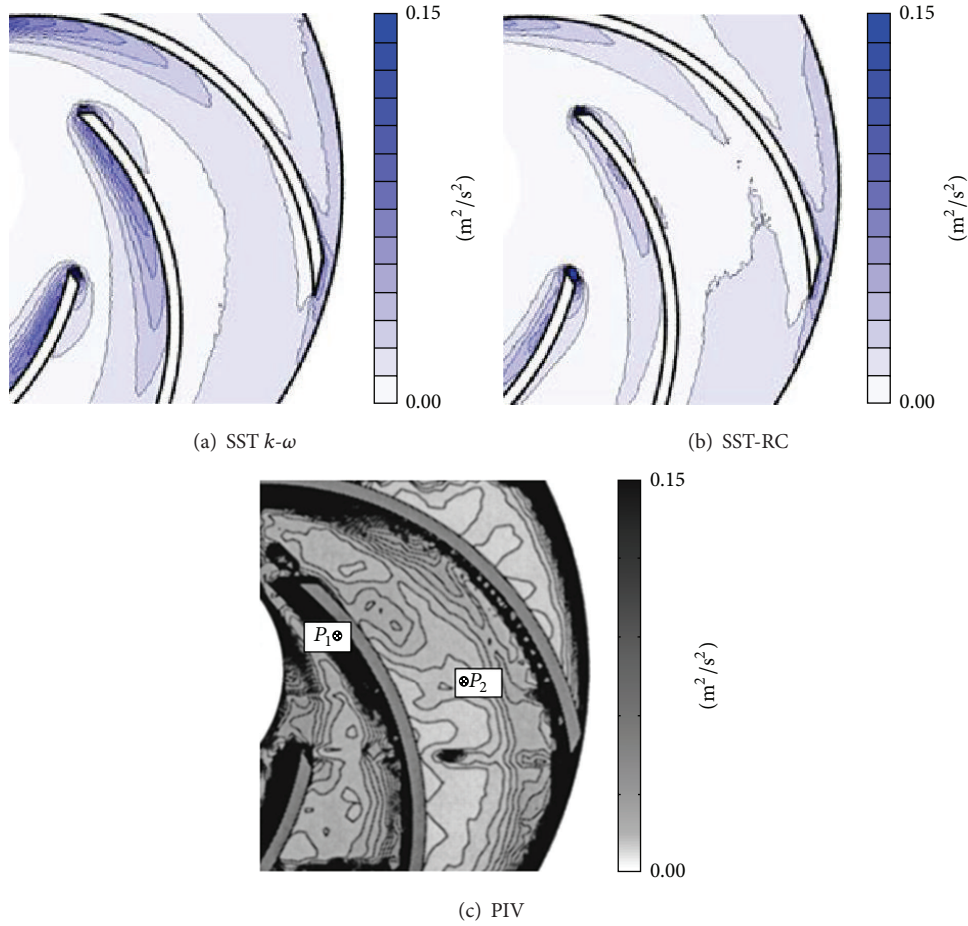


FIGURE 5: Contour of turbulence kinetic energy k_{2D} on the spanwise 50% surface under $1.0Q_d$.

occurred at LE and TE in “B” passages. On the contrary, because of the well-behaved flow regime, the k_{2D} value was lower in “A” passages. Compared with the PIV data [16], the location and intensity of k_{2D} were more reasonable after correction. Moreover, the alternately blocked phenomena were more obvious by using the SST-RC model.

To assess in details, the relative velocity distributions on the spanwise 50% surface are also plotted in Figure 10. Considering the differences of flow regime among all the passages, two adjacent passages (“A” and “B”) were analyzed. The distributions of velocity components changed after correction. Compared with the experimental data [16], it can be seen that the results became more accurate. In particular, flow severely separated at blade LE with a stronger streamline curvature and higher turbulence. So, corrected by reducing the production of turbulence, radial and tangential velocities became more consistent with experiments especially at $0.5R_2$.

All in all, the correction impact was obvious under $0.25Q_d$. So, it is strongly recommended to use the corrected model under the low flow rate off-design condition.

5. Conclusions

By comparatively assessing the Spalart-Shur correction in the RANS simulations in centrifugal pump impeller under

different operating conditions, conclusions can be drawn as follows.

- (1) In the RANS simulations, the isotropous description of turbulence model is not perfect enough. The flow in a centrifugal pump impeller is strongly affected by the system rotation and streamline curvature. With the pump rotation, separation flow occurred at blade leading edge. Under different operating conditions, the scale of separation is also different. Particularly under low flow rate off-design conditions, fluid does not flow along the blade geometry; secondary flow structures become more and more obvious and occurred everywhere in the pump impeller passages.
- (2) By the supplements of descriptions of turbulence anisotropy, turbulence production term is corrected. Verified by comparing the CFD results with experimental data, improvements are found after correction. Under the design condition, the impact of correction is not obvious but theoretically reasonable. Under the low flow rate off-design condition, simulation accuracy is significantly improved especially in the strong separation region. Moreover, there is no obvious extra time cost when using the corrected model. Hence, in the RANS simulations of centrifugal

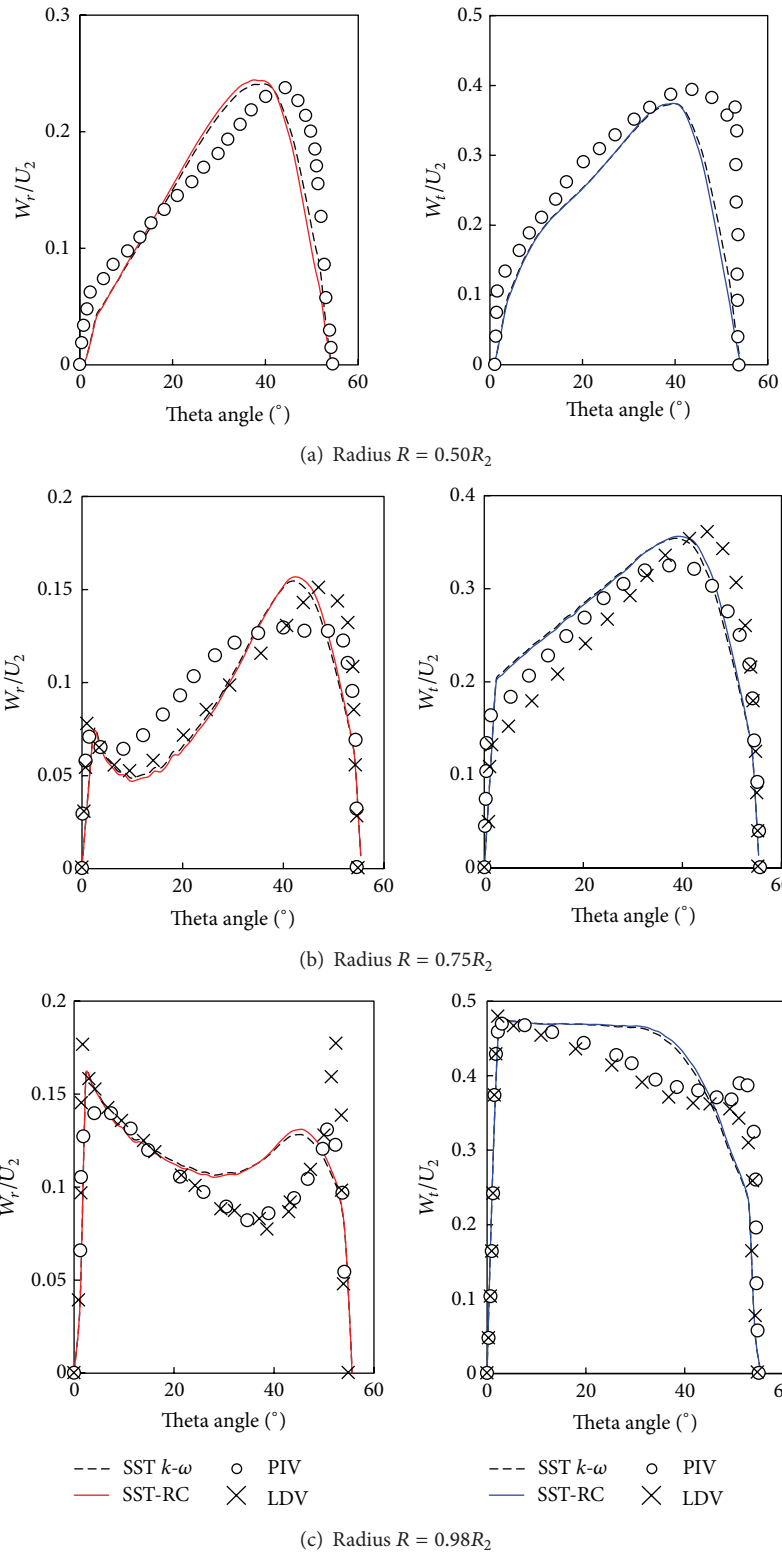


FIGURE 6: Relative velocity distributions on the spanwise 50% surface at radius of 0.50, 0.75, and $0.98R_2$ under $1.0Q_d$.

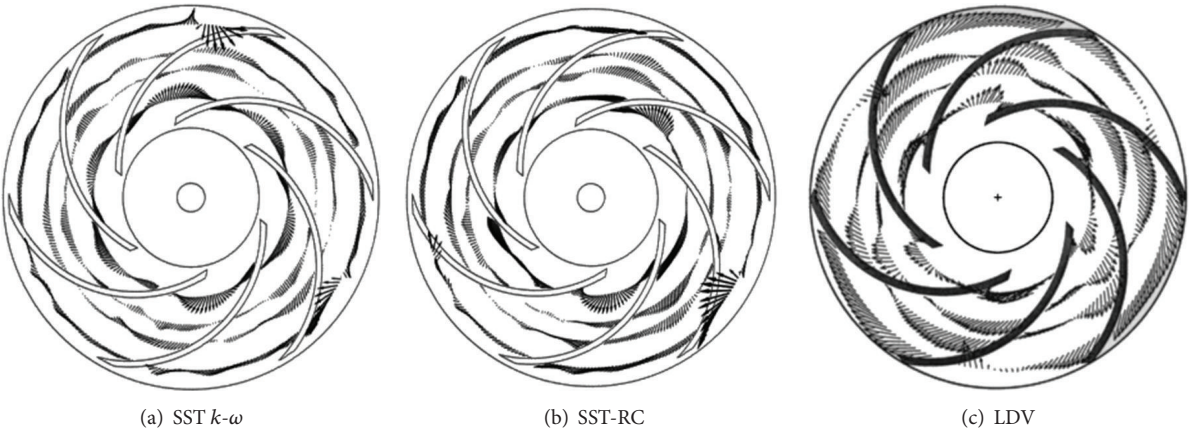


FIGURE 7: Velocity field on spanwise 50% surface under $0.25Q_d$.

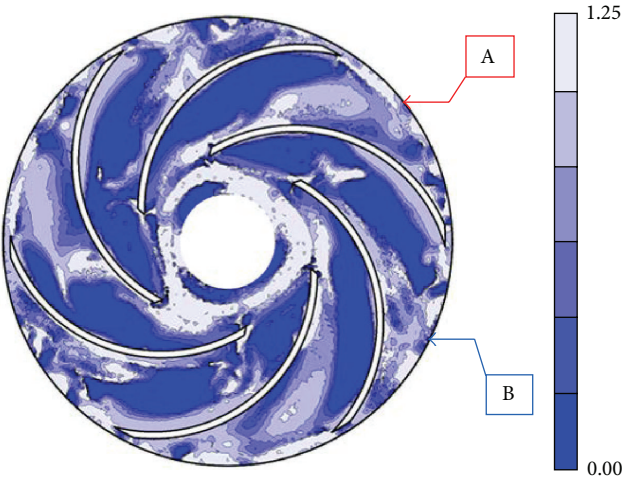


FIGURE 8: Correction coefficient f_r on spanwise 50% surface at $0.25Q_d$.

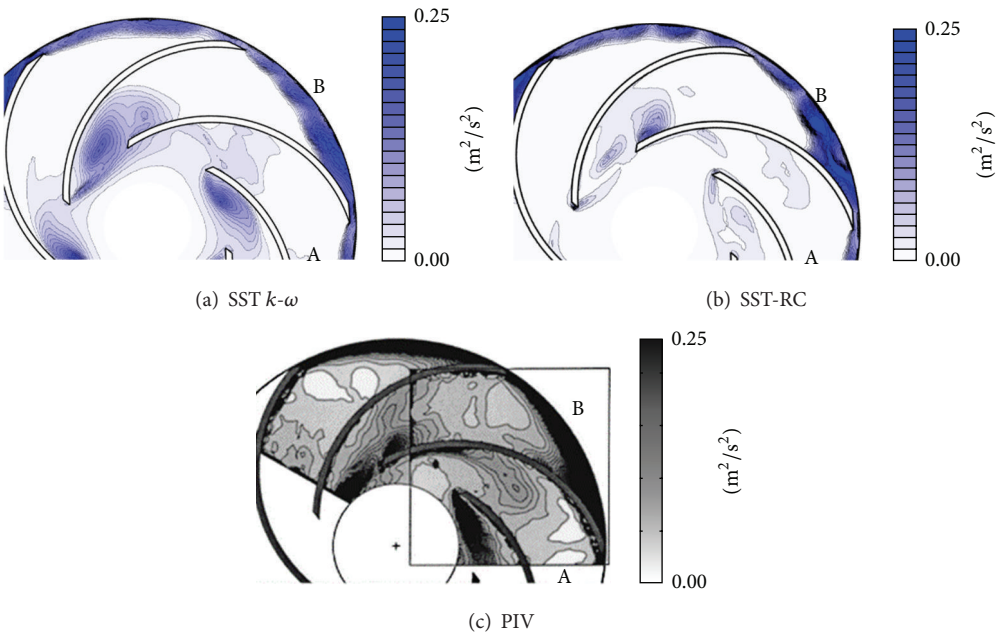


FIGURE 9: The contour of turbulence kinetic energy k_{2D} on the spanwise 50% surface under $0.25Q_d$.

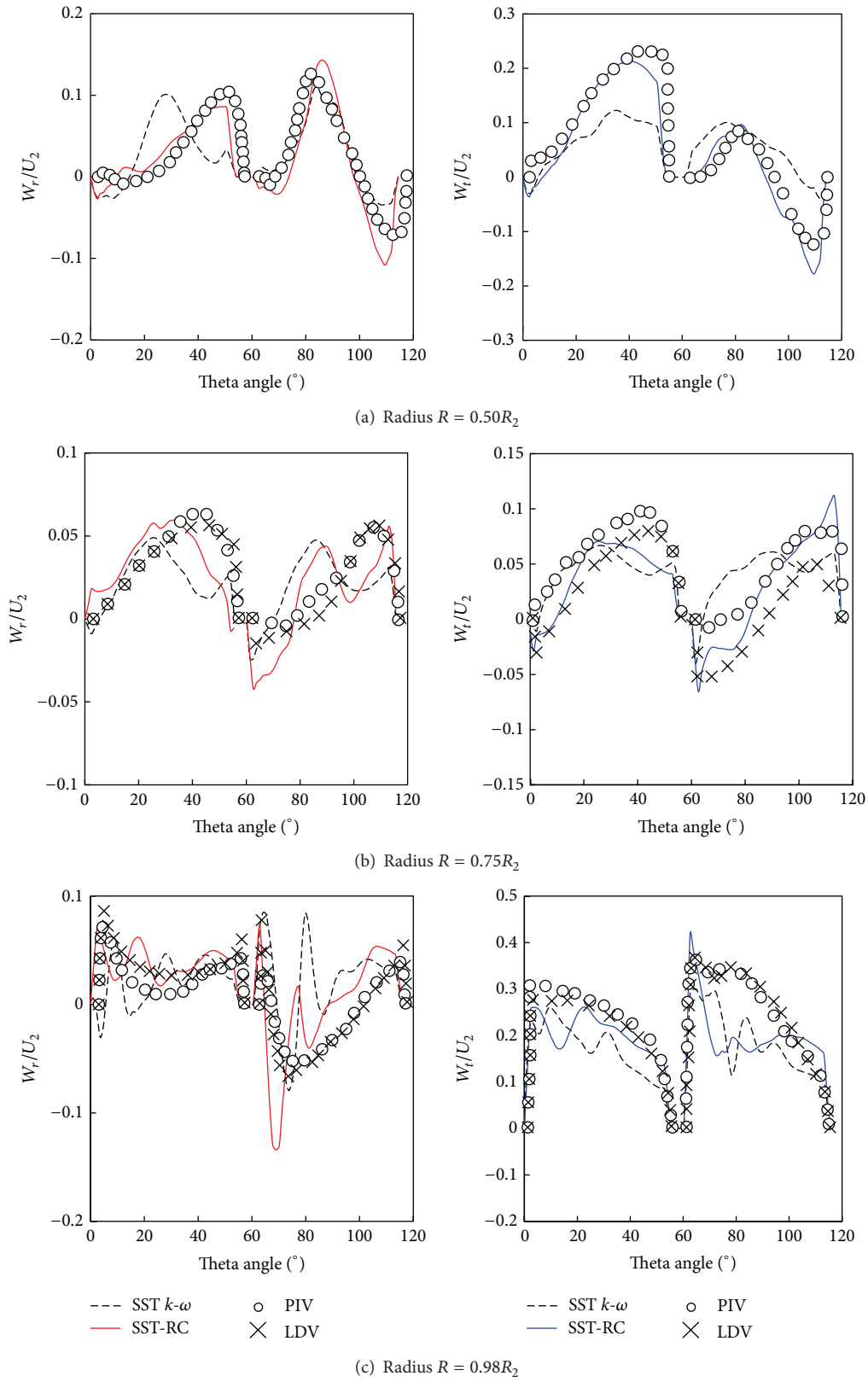


FIGURE 10: Relative velocity distributions on the spanwise 50% surface at radius of 0.50, 0.75, and $0.98R_2$ under $0.25Q_d$.

pumps, if the flow regime is undesirable with strong secondary flow structures, it will be very appropriate to apply the Spalart-Shur rotation/curvature correction to the SST k - ω model and other eddy viscosity turbulence models.

Conflict of Interests

The authors declare that there is no conflict of interests regarding the publication of this paper.

Acknowledgments

The authors would like to acknowledge the financial support given by the National Natural Science Foundation of China (no. 51139007) and National “Twelfth Five-Year” Plan for Science & Technology Support (no. 2012BAD08B03).

References

- [1] J. Boussinesq, *Essai sur la Théorie des Eaux Courantes*, Imprimerie Nationale, Paris, France, 1877.
- [2] F. G. Schmitt, “About Boussinesq’s turbulent viscosity hypothesis: historical remarks and a direct evaluation of its validity,” *Comptes Rendus Mécanique*, vol. 335, no. 9-10, pp. 617–627, 2007.
- [3] P. R. Spalart and M. Shur, “On the sensitization of turbulence models to rotation and curvature,” *Aerospace Science and Technology*, vol. 1, no. 5, pp. 297–302, 1997.
- [4] Y.-N. Huang and H.-Y. Ma, “Extended intrinsic mean spin tensor for turbulence modelling in non-inertial frame of reference,” *Applied Mathematics and Mechanics*, vol. 29, no. 11, pp. 1463–1475, 2008.
- [5] P. Bradshaw, “The analogy between streamline curvature and buoyancy in turbulent shear flow,” *Journal of Fluid Mechanics*, vol. 36, no. 1, pp. 177–191, 1969.
- [6] A. Khodak and C. Hirsch, “Second-order non-linear k - ϵ models with explicit effect of curvature and rotation,” in *Proceedings of the 3rd ECCOMAS Computational Fluid Dynamics Conference*, pp. 690–696, 1996.
- [7] M. L. Shur, M. K. Strelets, A. K. Travin, and P. R. Spalart, “Turbulence modeling in rotating and curved channels: assessing the Spalart-Shur correction,” *AIAA Journal*, vol. 38, no. 5, pp. 784–792, 2000.
- [8] G. Dufour, J.-B. Cazalbou, X. Carbonneau, and P. Chassaing, “Assessing rotation/curvature corrections to eddy-viscosity models in the calculations of centrifugal-compressor flows,” *Journal of Fluids Engineering, Transactions of the ASME*, vol. 130, no. 9, 2008.
- [9] J.-B. Cazalbou, P. Chassaing, G. Dufour, and X. Carbonneau, “Two-equation modeling of turbulent rotating flows,” *Physics of Fluids*, vol. 17, no. 5, Article ID 055110, 2005.
- [10] P. E. Smirnov and F. R. Menter, “Sensitization of the SST turbulence model to rotation and curvature by applying the Spalart-Shur correction term,” *Journal of Turbomachinery*, vol. 131, no. 4, Article ID 041010, 2009.
- [11] T. P. Dhakal and D. K. Walters, “A Three-equation variant of the SST k - ω model sensitized to rotation and curvature effects,” *Journal of Fluids Engineering*, vol. 133, no. 11, Article ID 111201, 2011.
- [12] W. D. York, D. K. Walters, and J. H. Leylek, “A simple and robust linear eddy-viscosity formulation for curved and rotating flows,” *International Journal of Numerical Methods for Heat & Fluid Flow*, vol. 19, no. 6, pp. 745–776, 2009.
- [13] A. Hellsten, “Some improvements in Menter’s SST k - ω turbulence model,” in *Proceedings of the 29th AIAA Fluid Dynamics Conference*, AIAA 98-2554, Albuquerque, NM, USA, June 1998.
- [14] Q. Zhang and Y. Yang, “A new simpler rotation/curvature correction method for Spalart-Allmaras turbulence model,” *Chinese Journal of Aeronautics*, vol. 26, no. 2, pp. 326–333, 2013.
- [15] C. E. Brennen, *Hydrodynamics of Pumps*, Cambridge University Press, Cambridge, UK, 2011.
- [16] N. Pedersen, P. S. Larsen, and C. B. Jacobsen, “Flow in a centrifugal pump impeller at design and off-design conditions—part I: particle image velocimetry (PIV) and laser Doppler velocimetry (LDV) measurements,” *Journal of Fluids Engineering*, vol. 125, no. 1, pp. 61–72, 2003.
- [17] R. K. Byskov, C. B. Jacobsen, and N. Pedersen, “Flow in a centrifugal pump impeller at design and off-design conditions—part II: large eddy simulations,” *Journal of Fluids Engineering, Transactions of the ASME*, vol. 125, no. 1, pp. 73–83, 2003.
- [18] F. R. Menter, M. Kuntz, and R. Langtry, “Ten years of industrial experience with the SST turbulence model,” *Turbulence, Heat and Mass Transfer*, vol. 4, pp. 625–632, 2003.

Research Article

Element-Free Approximation of Generalized Regularized Long Wave Equation

Dong-Mei Huang and L. W. Zhang

College of Information Technology, Shanghai Ocean University, Shanghai 201306, China

Correspondence should be addressed to L. W. Zhang; lwzhang@shou.edu.cn

Received 3 July 2014; Accepted 24 August 2014; Published 29 September 2014

Academic Editor: Kim M. Liew

Copyright © 2014 D.-M. Huang and L. W. Zhang. This is an open access article distributed under the Creative Commons Attribution License, which permits unrestricted use, distribution, and reproduction in any medium, provided the original work is properly cited.

The generalized regularized long wave (GRLW) equation is an important nonlinear equation for describing a large number of physical phenomena, for examples, the shallow water waves and plasma waves. In this study, numerical approximation of the GRLW using the element-free improved moving least-squares Ritz (IMLS-Ritz) method is performed. In the solution procedure, the IMLS approximation is employed to reduce the number of unknown coefficients in the trial functions. The Ritz minimization procedure is then used to derive the final algebraic equation system through discretizing the constructed energy formulation of the nonlinear GRLW equation. Time difference technique and Newton-Raphson method are adopted to solve the nonlinear equation system. Numerical experiments are conducted on the final form of the governing equation system to demonstrate the accuracy and efficiency of the element-free IMLS-Ritz method by comparing the computed IMLS-Ritz results with the existing available analytical solutions.

1. Introduction

The damped GRLW equation is established as a model for small-amplitude long waves on the surface of water [1, 2]. For some special cases, such as the regularized long wave (RLW) or the Benjamin-Bona-Mahony equation [3] which is used to describe a large number of physical phenomena with weak nonlinearity and dispersion waves.

The GRLW equation has been extensively studied for generating its solutions by analytical and approximate methods. Unlike the RLW and the Benjamin-Bona-Mahony equations, the stability of solutions to the GRLW equation depends on the solitary wave velocity [4]. Due to its potentially high nonlinearity, many efforts have been made to generate its solutions accurately and efficiently by means of, for examples, the finite difference method [5], the Adomian decomposition method [6, 7], the finite element method [8–14], and the element-free method [15–18]. Moreover, the separation of temporal and spatial derivatives was also used to study the wave interactions [19, 20].

The element-free or meshless method has become a popular numerical tool in recent years. It has been developed

and successfully applied to obtain accurate solutions for PDEs deriving from the physical and engineering fields [21–26]. These include the element-free Galerkin method [27, 28], smooth particle hydrodynamics method [29], radial basis function method [30], element-free kp-Ritz method [31–36], and meshless local Petrov-Galerkin method [37]. The major advantage of the element-free method for solving partial differential equations (PDEs) is that it does not require domain or boundary discretization. With this advantage together with its flexibility and simplicity in implementation [38–40], element-free methods have also been employed for solving many mathematical models of wave equation [17–20, 41, 42], such as the kp-Ritz method [17], the radial basis functions method [41], and the element-free Galerkin method [20, 42].

In this paper, we present an element-free computational framework to predict numerical solutions for the nonlinear GRLW equation using an improved moving least square Ritz (IMLS-Ritz) method. This novel IMLS-Ritz method consists of two essential parts: (i) the improved moving least-squares (IMLS) approximation and (ii) the Ritz procedure. The IMLS

technique is employed for construction of the shape functions. An energy formulation for the nonlinear GRLW equation is formulated and discretized by the Ritz minimization procedure to obtain its final algebraic equation system. In the solution procedure, the penalty method is adopted to impose the essential boundary conditions. Time difference technique and Newton-Raphson method are employed to solve the nonlinear system equations. Computational simulations for several numerical examples are presented to examine the affectivity and efficiency of the IMLS-Ritz method on the nonlinear GRLW equation.

2. Theoretical Formulation

2.1. Equivalent Functional of GRLW Equation. The general form of the GRLW equation can be written as

$$u_t + \alpha u_x + \varepsilon u^{p-1} u_x = \gamma u_{xx} + \mu u_{xxt}, \quad (1)$$

$$x \in \Omega = [a, b] \subset \mathbf{R}, \quad 0 < t \leq T,$$

where $a = 1$, $\gamma = 0$, p is a known positive integer, ε and μ are two known positive parameters. The subscripts x and t denote space and time derivatives, respectively. The function $u(x, t)$ will be determined when functions f , g_1 , and g_2 are given. Ω is the computational domain with boundary Γ .

The corresponding initial condition for the problem is

$$u(x, 0) = f(x), \quad a \leq x \leq b, \quad (2)$$

and the boundary conditions are

$$u(a, t) = g_1(t), \quad u(b, t) = g_2(t). \quad (3)$$

The functional $\Pi(u)$ is constructed from the weak form of (1), that is,

$$\begin{aligned} \Pi(u) = & \int_{\Omega} u^T u_t d\Omega + \int_{\Omega} u^T u_x d\Omega \\ & + \varepsilon \int_{\Omega} u^T u^{p-1} u_x d\Omega + \mu \int_{\Omega} u_x^T u_{xt} d\Omega. \end{aligned} \quad (4)$$

2.2. IMLS Shape Functions. The IMLS approximation was proposed for construction of the shape functions [21] in the element-free method. In one-dimensional IMLS approximation, for $\forall f(x), g(x) \in \text{span}(\mathbf{p})$, we define

$$(f, g) = \sum_{I=1}^n w(x - x_I) f(x_I) g(x_I), \quad (5)$$

where (f, g) is an inner product, and $\text{span}(\mathbf{p})$ is the Hilbert space.

In $\text{span}(\mathbf{p})$, for the set of points $\{x_i\}$ and weight functions $\{w_i\}$, if functions $p_1(x), p_2(x), \dots, p_m(x)$ satisfy the conditions

$$\begin{aligned} (p_k, p_j) &= \sum_{i=1}^n w_i p_k(x_i) p_j(x_i) \\ &= \begin{cases} 0, & k \neq j, \\ A_k, & k = j, \end{cases} \quad (k, j = 1, 2, \dots, m), \end{aligned} \quad (6)$$

we furnish the function set $p_1(x), p_2(x), \dots, p_m(x)$ as a weighted orthogonal function set with a weight function $\{w_i\}$ about points $\{x_i\}$. If $p_1(x), p_2(x), \dots, p_m(x)$ are polynomials, the function set $p_1(x), p_2(x), \dots, p_m(x)$ is called a weighted orthogonal polynomials set with a weight function $\{w_i\}$ about points $\{x_i\}$.

Consider an equation system from MLS approximation as follows:

$$\mathbf{A}(x) \mathbf{a}(x) = \mathbf{B}(x) \mathbf{u}, \quad (7)$$

where \mathbf{A} is the moment matrix. Equation (7) can be expressed as

$$\begin{bmatrix} (p_1, p_1) & (p_1, p_2) & \cdots & (p_1, p_m) \\ (p_2, p_1) & (p_2, p_2) & \cdots & (p_2, p_m) \\ \vdots & \vdots & \ddots & \vdots \\ (p_m, p_1) & (p_m, p_2) & \cdots & (p_m, p_m) \end{bmatrix} \begin{bmatrix} a_1(\mathbf{x}) \\ a_2(\mathbf{x}) \\ \vdots \\ a_m(\mathbf{x}) \end{bmatrix} = \begin{bmatrix} (p_1, u_I) \\ (p_2, u_I) \\ \vdots \\ (p_m, u_I) \end{bmatrix}. \quad (8)$$

If the basis function set $p_i(x) \in \text{span}(\mathbf{p})$, $i = 1, 2, \dots, m$, is a weighted orthogonal function set about points $\{x_i\}$, that is, if

$$(p_i, p_j) = 0, \quad (i \neq j), \quad (9)$$

then (8) becomes

$$\begin{bmatrix} (p_1, p_1) & 0 & \cdots & 0 \\ 0 & (p_2, p_2) & \cdots & 0 \\ \vdots & \vdots & \ddots & \vdots \\ 0 & 0 & \cdots & (p_m, p_m) \end{bmatrix} \begin{bmatrix} a_1(\mathbf{x}) \\ a_2(\mathbf{x}) \\ \vdots \\ a_m(\mathbf{x}) \end{bmatrix} = \begin{bmatrix} (p_1, u_I) \\ (p_2, u_I) \\ \vdots \\ (p_m, u_I) \end{bmatrix}. \quad (10)$$

Subsequently, coefficients $a_i(x)$ can be determined accordingly:

$$a_i(x) = \frac{(p_i, u_I)}{(p_i, p_i)}, \quad i = 1, 2, \dots, m; \quad (11)$$

that is,

$$\mathbf{a}(x) = \widetilde{\mathbf{A}}(x) \mathbf{B}(x) \mathbf{u}, \quad (12)$$

where

$$\widetilde{\mathbf{A}}(x) = \begin{bmatrix} \frac{1}{(p_1, p_1)} & 0 & \cdots & 0 \\ 0 & \frac{1}{(p_2, p_2)} & \cdots & 0 \\ \vdots & \vdots & \ddots & \vdots \\ 0 & 0 & \cdots & \frac{1}{(p_m, p_m)} \end{bmatrix}. \quad (13)$$

From (7) and (11), the expression of approximation function $u^h(x)$ is

$$u^h(x) = \widetilde{\Phi}(x) \mathbf{u} = \sum_{I=1}^n \widetilde{\Phi}_I(x) u_I, \quad (14)$$

where $\tilde{\Phi}(x)$ is the shape function and

$$\tilde{\Phi}(x) = (\tilde{\Phi}_1(x), \tilde{\Phi}_2(x), \dots, \tilde{\Phi}_n(x)) = \mathbf{p}^T(x) \tilde{\mathbf{A}}(x) \mathbf{B}(x). \quad (15)$$

The abovementioned formulation details an IMLS approximation in which coefficients $a_i(x)$ are obtained directly. It is, therefore, avoiding forming an ill-conditioned or singular equation system.

From (15), we have

$$\tilde{\Phi}_I(x) = \sum_{j=1}^m p_j(x) [\tilde{\mathbf{A}}(x) \mathbf{B}(x)]_{jI}, \quad (16)$$

which represents the shape function of the IMLS approximation corresponding to node I . From (16), the partial derivatives of $\tilde{\Phi}_I(x)$ lead to

$$\tilde{\Phi}_{I,i}(x) = \sum_{j=1}^m [p_{j,i}(\tilde{\mathbf{A}}\mathbf{B})_{jI} + p_j(\tilde{\mathbf{A}}_i\mathbf{B} + \tilde{\mathbf{A}}\mathbf{B}_i)_{jI}]. \quad (17)$$

The weighted orthogonal basis function set $\mathbf{p} = (p_i)$ is formed by using the Schmidt method as

$$\begin{aligned} p_1 &= 1, \\ &\vdots \\ p_i &= r^{i-1} - \sum_{k=1}^{i-1} \frac{(r^{i-1}, p_k)}{(p_k, p_k)} p_k, \quad i = 2, 3, \dots \end{aligned} \quad (18)$$

Moreover, using the Schmidt method, the weighted orthogonal basis function set $\mathbf{p} = (p_i)$ can be formed from the monomial basis function. For example, for the monomial basis function

$$\tilde{\mathbf{p}} = (\tilde{p}_i) = (1, x_1, x_2, x_3, x_1x_2, x_1x_3, x_2x_3, x_1^2, x_2^2, x_3^2, \dots), \quad (19)$$

the weighted orthogonal basis function set can be generated by

$$p_i = \tilde{p}_i - \sum_{k=1}^{i-1} \frac{(\tilde{p}_i, p_k)}{(p_k, p_k)} p_k, \quad i = 1, 2, 3, \dots \quad (20)$$

Using the weighted orthogonal basis functions described in (19) and (20), fewer coefficients existed in the trial function.

3. Ritz Minimization Procedure for the GRLW Equation

In the present element-free IMLS-Ritz method, the shape functions do not possess the Kronecker delta property, yielding to special techniques to impose the Dirichlet boundary conditions to the method. Lagrange's multiplier approach, the penalty method, and modified variational principles are those techniques which are often adopted for imposition of boundary conditions. In the present work, we employ the penalty method to modify the constructed functional in

implementing the specified Dirichlet boundary conditions. The variational form of the penalty function is described as follows:

$$\Pi_B = \frac{\alpha}{2} \int_{\Gamma_u} (u - \bar{u})^2 d\Gamma, \quad (21)$$

where \bar{u} is the specified function on the Dirichlet boundary Γ_u and α is the penalty parameter; normally it is chosen as $10^3 \sim 10^7$ which is case-dependent.

The total functional involving the Dirichlet boundary conditions can be expressed as

$$\Pi^*(u) = \Pi(u) + \Pi_B. \quad (22)$$

Substituting (4) into (22), we have

$$\begin{aligned} \Pi^*(u) &= \int_{\Omega} u^T u_t d\Omega + \int_{\Omega} u^T u_x d\Omega + \varepsilon \int_{\Omega} u^T u^{p-1} u_x d\Omega \\ &\quad + \mu \int_{\Omega} u_x^T u_{xt} d\Omega + \frac{\alpha}{2} \int_{\Gamma_u} (u - \bar{u})^2 d\Gamma. \end{aligned} \quad (23)$$

The approximation of the field function can be obtained from (14) as follows:

$$\begin{aligned} u^h(x, t) &= \sum_{I=1}^n \Phi_I(x) u_I(t) = \Phi(x) \mathbf{U}(t), \\ \frac{\partial u^h(x, t)}{\partial t} &= \sum_{I=1}^n \Phi_I(x) \frac{\partial u_I(t)}{\partial t} = \Phi(x) \dot{\mathbf{U}}(t), \\ \frac{\partial u^h(x, t)}{\partial x} &= \sum_{I=1}^n \Phi_{I,x}(x) u_I(t) = \Phi_x(x) \mathbf{U}(t), \\ \frac{\partial^2 u^h(x, t)}{\partial x \partial t} &= \sum_{I=1}^n \Phi_{I,x}(x) \frac{\partial u_I(t)}{\partial t} = \Phi_x(x) \dot{\mathbf{U}}(t), \end{aligned} \quad (24)$$

where

$$\begin{aligned} \Phi(x) &= (\Phi_1(x), \Phi_2(x), \dots, \Phi_n(x)), \\ \Phi_x(x) &= (\Phi_{1,x}(x), \Phi_{2,x}(x), \dots, \Phi_{n,x}(x)), \\ \mathbf{U}(t) &= (u_1(t), u_2(t), \dots, u_n(t))^T, \\ \dot{\mathbf{U}}(t) &= \left(\frac{\partial u_1(t)}{\partial t}, \frac{\partial u_2(t)}{\partial t}, \dots, \frac{\partial u_n(t)}{\partial t} \right)^T. \end{aligned} \quad (25)$$

Substituting (24) into (23) and applying the Ritz minimization procedure to the maximum energy function Π^* , one has the following:

$$\frac{\partial \Pi^*}{\partial u_I(t)} = 0, \quad I = 1, 2, \dots, n. \quad (26)$$

That yields the following matrix form:

$$(\mathbf{C} + \mathbf{M}) \dot{\mathbf{U}}(t) + (\mathbf{K} + \bar{\mathbf{K}}) \mathbf{U}(t) + \varepsilon \mathbf{K} u^p = \mathbf{F}(t), \quad (27)$$

where

$$\begin{aligned}
C_{IJ} &= \int_{\Gamma} \Phi_I(x) \Phi_J(x) d\Gamma, \\
M_{IJ} &= \mu \int_{\Gamma} \Phi_{I,x}(x) \Phi_{J,x}(x) d\Gamma, \\
K_{IJ} &= \int_{\Gamma} \Phi_I(x) \Phi_{J,x}(x) d\Gamma, \\
\bar{K}_{IJ} &= \alpha \left(\Phi_I(x) \Phi_J(x) \Big|_{x=a} + \Phi_I(x) \Phi_J(x) \Big|_{x=b} \right), \\
F_I &= \alpha \left(\Phi_I(x) \bar{u} \Big|_{x=a} + \Phi_I(x) \bar{u} \Big|_{x=b} \right).
\end{aligned} \tag{28}$$

To solve the above system, time discretization of (27) is forming with the center difference method as follows:

$$\begin{aligned}
(\mathbf{C} + \mathbf{M}) \frac{\mathbf{U}^{n+1} - \mathbf{U}^n}{\Delta t} + (\mathbf{K} + \bar{\mathbf{K}}) \frac{\mathbf{U}^{n+1} + \mathbf{U}^n}{2} \\
+ \varepsilon \mathbf{K} \frac{(u^p)^{n+1} + (u^p)^n}{2} = \frac{\mathbf{F}^{n+1} + \mathbf{F}^n}{2},
\end{aligned} \tag{29}$$

where Δt is the time of the step and

$$\mathbf{U}^n = \mathbf{U}(n\Delta t) = (u_1(n\Delta t), u_2(n\Delta t), \dots, u_n(n\Delta t)). \tag{30}$$

Iteration with Newton-Raphson method is implemented to solve the above equation and the numerical solution of the GRLW equation will be obtained.

4. Numerical Examples and Discussion

Numerical analysis for three selected example problems is performed in order to demonstrate the applicability and examine the accuracy of the IMLS-Ritz method for the GRLW equation. The problems are solved using regular node arrangements.

The convergence study is carried out for the results of the GRLW equation for (i) a single solitary wave, (ii) an interaction of two solitary waves, and (iii) an interaction of three solitary waves. Accuracy of the numerical solutions by the IMLS-Ritz method is measured by using the following equations:

$$\begin{aligned}
L_2 &= \|u_{\text{exact}} - u_{\text{numerical}}\|_2 = \sqrt{\sum_{i=0}^N |u_{\text{exact}}^i - u_{\text{numerical}}^i|^2}, \\
L_{\infty} &= \|u_{\text{exact}} - u_{\text{numerical}}\|_{\infty} = \max_i |u_{\text{exact}}^i - u_{\text{numerical}}^i|,
\end{aligned} \tag{31}$$

where u_{exact} and $u_{\text{numerical}}$ denote the exact solution and numerical approximation, respectively.

4.1. Single Solitary Wave. The analytical solution of (1) is given in the general form of [1, 35] as follows:

$$u(x, t) = d \left\{ \text{sech}^2 [k(x + x_0 - vt)] \right\}^{1/(p-1)}, \quad a \leq x \leq b. \tag{32}$$

When $p = 3$, (32) can be simplified as

$$u(x, t) = d \text{sech}^2 [k(x + x_0 - vt)], \tag{33}$$

TABLE 1: Values of L_2 -norm errors and L_{∞} -norm errors and CPU time as functions of the number of nodes (N) for the solution of GRLW equation ($t = 0.1$, $\Delta t = 0.01$, and $d_{\max} = 3.5$).

N	L_2 -norm error	L_{∞} -norm error	CPU time (s)
11	2.4514×10^{-2}	1.3741×10^{-2}	0.11356
21	1.5578×10^{-2}	1.3473×10^{-2}	0.15316
51	1.6046×10^{-3}	9.2657×10^{-4}	0.23117
101	3.8300×10^{-4}	3.3494×10^{-4}	0.50029
201	3.5489×10^{-4}	3.2499×10^{-4}	1.05792

TABLE 2: Values of L_2 -norm errors and L_{∞} -norm errors and CPU time as functions of the time steps (Δt) for the solution of GRLW equation ($N = 100$ and $d_{\max} = 3.5$).

Δt	L_2 -norm error	L_{∞} -norm error	CPU time (s)
2	2.2253×10^{-3}	1.0837×10^{-3}	0.4448
1.5	1.4073×10^{-3}	5.0827×10^{-4}	0.4574
1	1.1937×10^{-3}	4.1598×10^{-4}	0.4962
0.1	4.1246×10^{-4}	3.3449×10^{-4}	0.4426
0.01	3.8300×10^{-4}	3.3494×10^{-4}	0.4025

TABLE 3: Values of L_2 -norm errors and L_{∞} -norm errors and CPU time as functions of the d_{\max} for the solution of GRLW equation ($N = 100$ and $t = 0.1$).

d_{\max}	L_2 -norm error	L_{∞} -norm error	CPU time (s)
2	3.4836×10^{-4}	3.3442×10^{-4}	0.5774
2.4	3.4911×10^{-4}	3.3456×10^{-4}	0.5658
2.8	3.5201×10^{-4}	3.3474×10^{-4}	0.5742
3	3.5504×10^{-4}	3.3483×10^{-4}	0.5827
3.5	3.8300×10^{-4}	3.3494×10^{-4}	0.4335
4	4.5051×10^{-4}	3.3498×10^{-4}	0.4465

where $k = (1/\mu)\sqrt{(v-1)/v}$, $d = \sqrt{4(v-1)/(2\varepsilon)}$, $\varepsilon = 1$, and $\mu = 1$ for all examples. The initial and boundary conditions are extracted from the exact solution. Equation (29) is solved numerically with $[a, b] = [-100, 100]$, $v = 1.01$, and $x_0 = 10$.

We examine the convergence of the element-free IMLS-Ritz method on this example by varying the number of nodes (N). The penalty factor is set as $\alpha = 10^3$ and $d_{\max} = 3.5$. The L_2 -norm and L_{∞} errors of u are computed with the number of nodes varied from 11 to 201. The results are tabulated in Table 1. It is apparent that both L_2 -norm and L_{∞} errors decrease as N increases, indicating convergent results are obtained by the IMLS-Ritz method. Subsequently, we investigated the influence of time steps (Δt) on the accuracy of the IMLS-Ritz method by keeping $N = 101$ and $d_{\max} = 3.5$ and varying Δt from 0.01 to 2. As illustrated in Table 2, it is obvious that a smaller time step leads to a more precise result for this example. Moreover, as shown in Table 3, by varying d_{\max} from 2 to 4, accurate results can be furnished when $d_{\max} = 2$.

Furthermore, the predicted results are compared with the analytical solutions at $t = 0.1$. As shown in Figure 1, these results and the absolute error are obtained when $N = 101$. A close agreement is obtained from the illustrated results. The computed results of $u(x, t)$ for a time history is also predicted

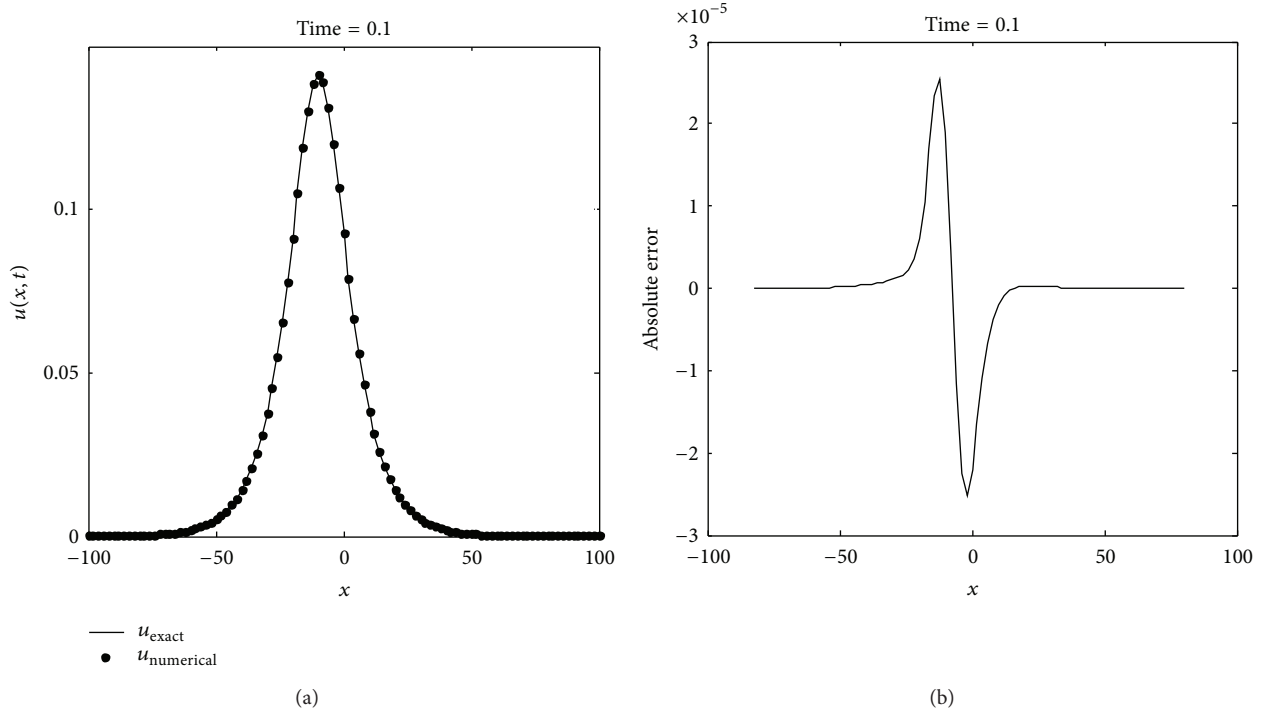


FIGURE 1: IMLS-Ritz and exact solutions of $u(x, t)$ at $N = 101$ (single solitary wave). (a) Solutions of $u(x, t)$; (b) absolute error.

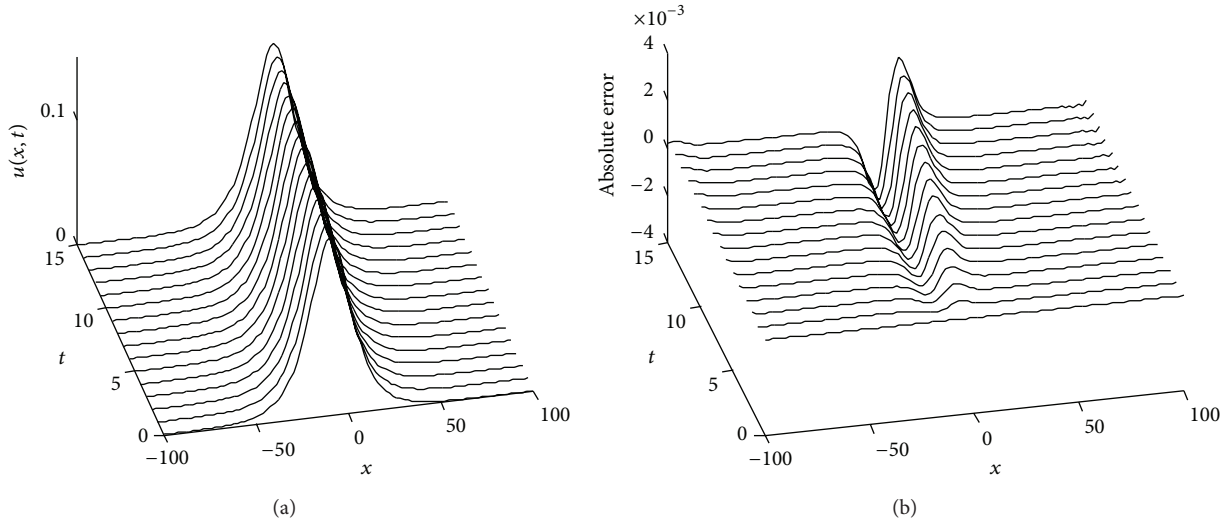


FIGURE 2: Numerical solutions of $u(x, t)$ at different times (single solitary wave). (a) Numerical solutions of $u(x, t)$; (b) absolute errors.

between $t = 0$ s and $t = 15$ s ($\Delta t = 1$) (Figure 2(a)). The corresponding absolute errors are plotted in Figure 2(b). To illustrate clearly the influence of number of nodes, we display L_2 -norm errors in a time period from 0 s to 0.01 s in Figure 3(a). Here we set $\Delta t = 0.001$ because when Δt is smaller than 0.001, the L_2 -norm errors will increase slightly, presumably due to the increase in round-off error. To further investigate the influence of different time steps, we examine the variation trend of the L_2 -norm errors as time step varies in different time period. As exhibited in Figure 3(b), generally, the L_2 -norm errors tend to decline linearly as time steps decreased. From the presented results in

the tables and figures, we can conclude that the approximate solutions generated by the IMLS-Ritz method are in close agreement with the analytical results.

4.2. Interaction of Two Solitary Waves. Consider an interaction of two solitary waves; we have the following exact solution [1, 35]:

$$u(x, 0) = \sum_{j=1}^2 d_j \operatorname{sech} [k_j (x + x_{0j} - v_j t)], \quad (34)$$

where $k_j = (1/\mu) \sqrt{(v_j - 1)/v_j}$ and x_{0j} are arbitrary constants.

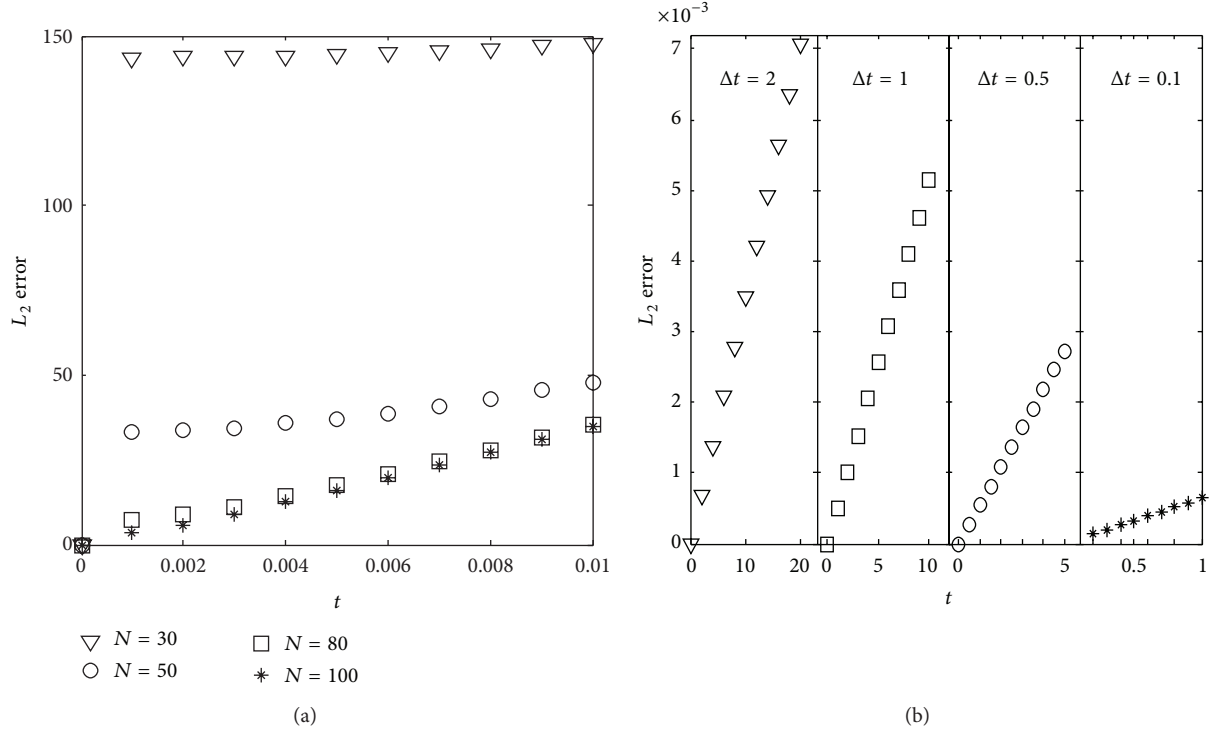


FIGURE 3: L_2 -norm errors of $u(x,t)$ (single solitary wave). (a) L_2 -norm errors at different number of nodes; (b) L_2 -norm errors at different time steps.

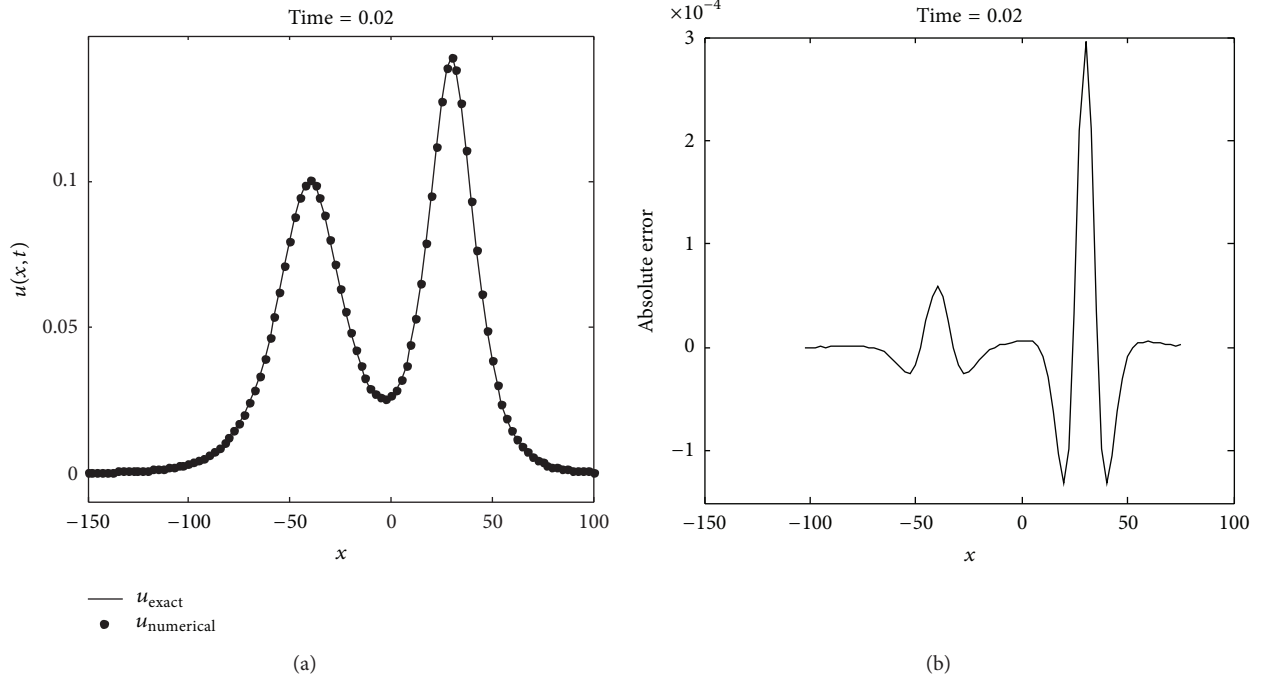


FIGURE 4: IMLS-Ritz and exact solutions of $u(x,t)$ at $N = 101$ (two solitary waves). (a) Solutions of $u(x,t)$; (b) absolute errors.

In this analysis, parameters are chosen to be $[a, b] = [-150, 100]$, $v_1 = 1.005$, $v_2 = 1.01$, $x_{01} = 45$, $x_{02} = -35$, and $\Delta t = 0.0001$. The problem is analyzed with 101 nodes. The numerical solutions are predicted and compared with the

analytical solutions at $t = 0.02$. As presented in Figure 4, the comparison study shows that the IMLS-Ritz method provides a very similar solution as the exact result. In Figure 5, the computed results and corresponding absolute errors of $u(x,t)$

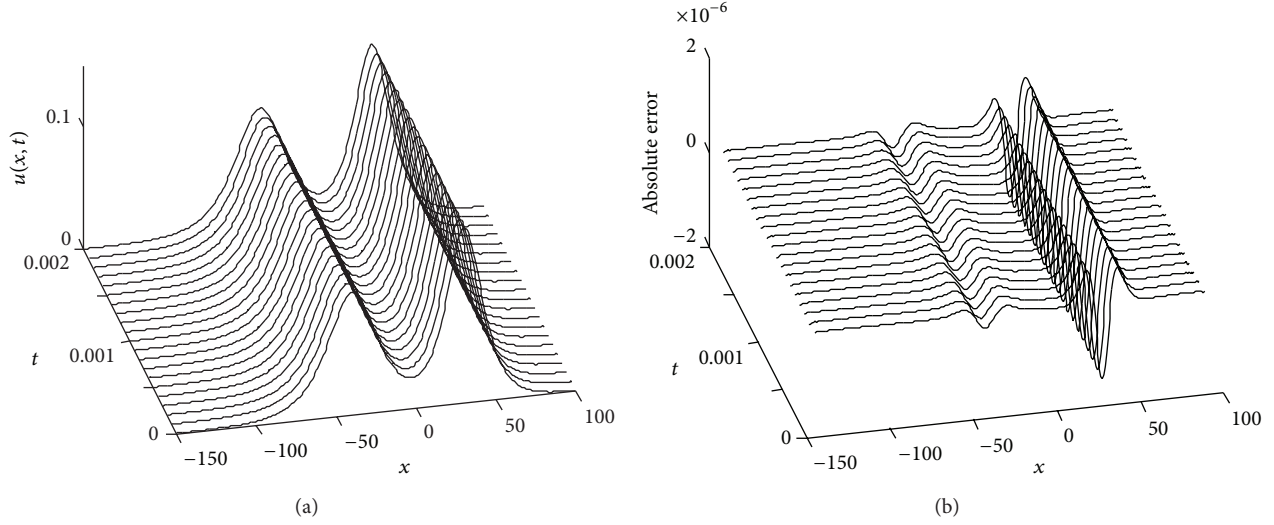


FIGURE 5: Numerical solutions of $u(x, t)$ at different times (two solitary waves). (a) Numerical solutions of $u(x, t)$; (b) absolute errors.

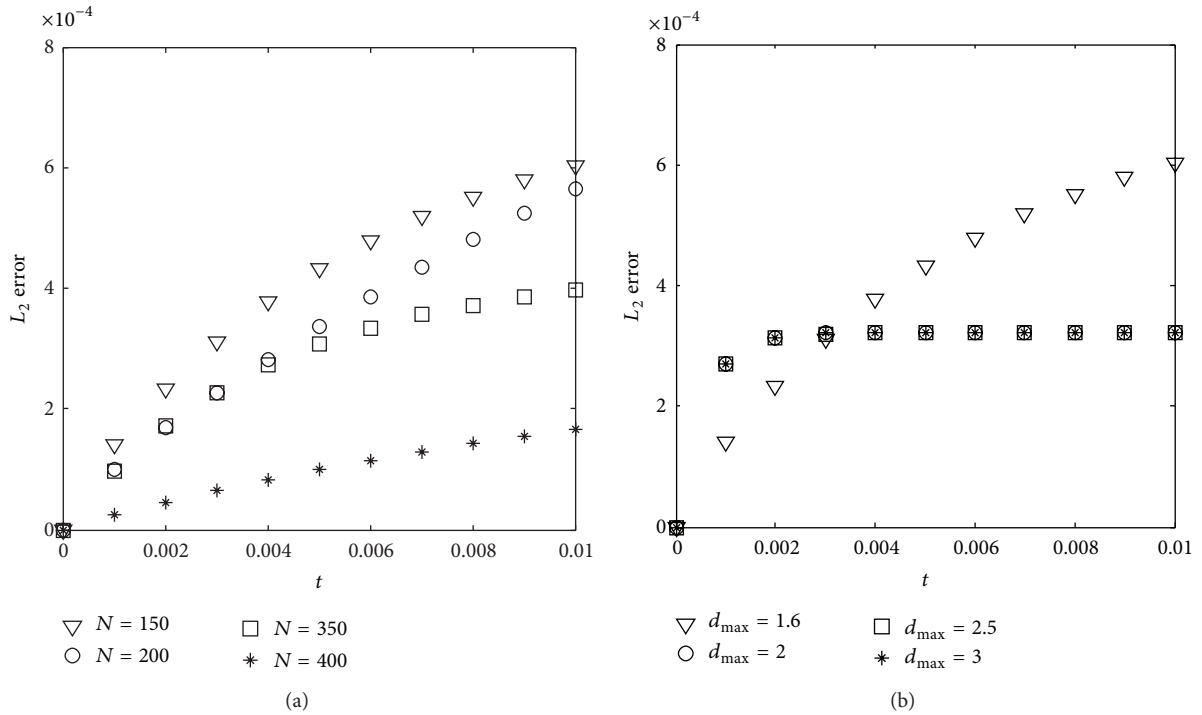


FIGURE 6: L_2 -norm errors of $u(x, t)$ (two solitary waves). (a) L_2 -norm errors at different number of nodes; (b) L_2 -norm errors at different d_{\max} .

for a time period from 0 s to 0.002 are displayed at $N = 301$. Again, further examination of the influence of number of nodes and d_{\max} in predicting the interaction between two solitary waves, we display the time history of L_2 -norm errors by varying time from 0 s to 0.01 s. As exhibited in Figure 6(a), the L_2 -norm errors decrease substantially as the arranged nodes increased while keeping the other variations as constants. Moreover, in this case, the results of numerical analysis suggested that satisfied accuracy can be achieved when $2 \leq d_{\max} \leq 3$.

4.3. Interaction of Three Solitary Waves. A third example considered the interaction of three waves of various amplitudes and traveling in the same direction. The analytical solutions has the same form as in Section 4.2, when choosing the following parameters: $[a, b] = [-30, 120]$, $c_1 = 7$, $c_2 = 3.25$, $c_3 = 1.6$, $x_{01} = -10$, $x_{02} = -45$, and $x_{03} = -65$.

Firstly, a regular 401 node is used in the IMLS-Ritz analysis with $d_{\max} = 2$, the penalty factor $\alpha = 10^5$, and $\Delta t = 0.001$. In Figure 7, the comparison results of IMLS-Ritz solutions and the analytical results are illustrated at $t = 0.15$ s.

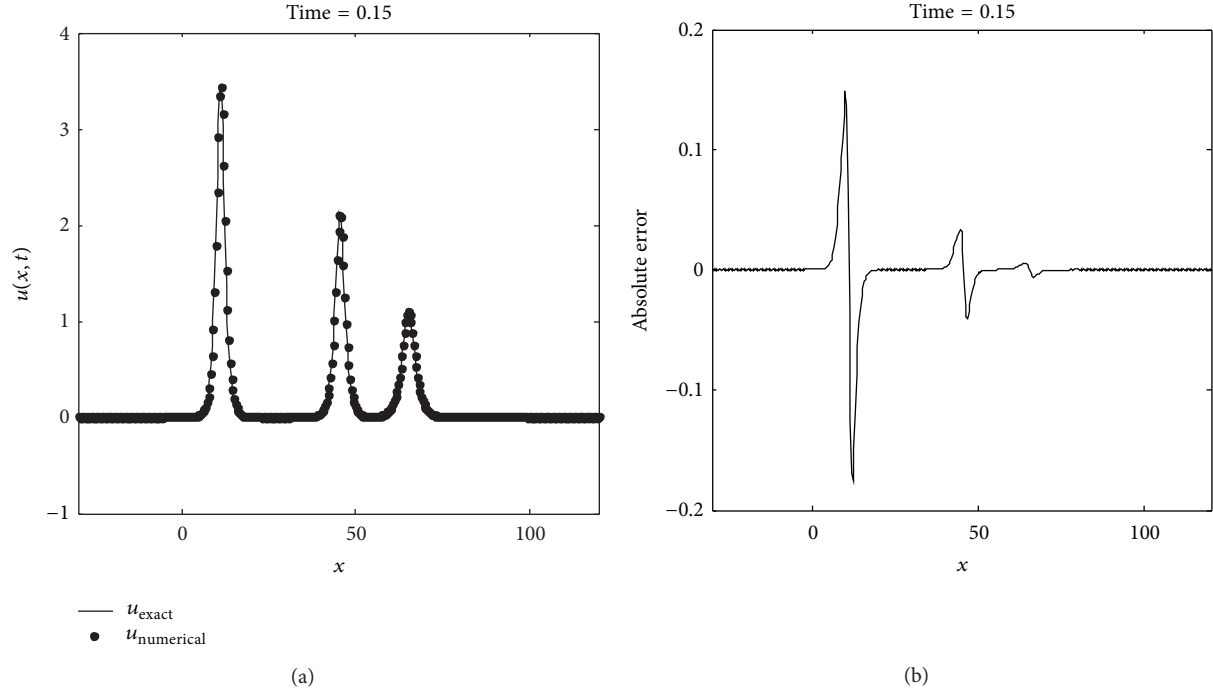


FIGURE 7: IMLS-Ritz and exact solutions of $u(x, t)$ at $N = 401$ (three solitary waves). (a) Solutions of $u(x, t)$; (b) absolute errors.

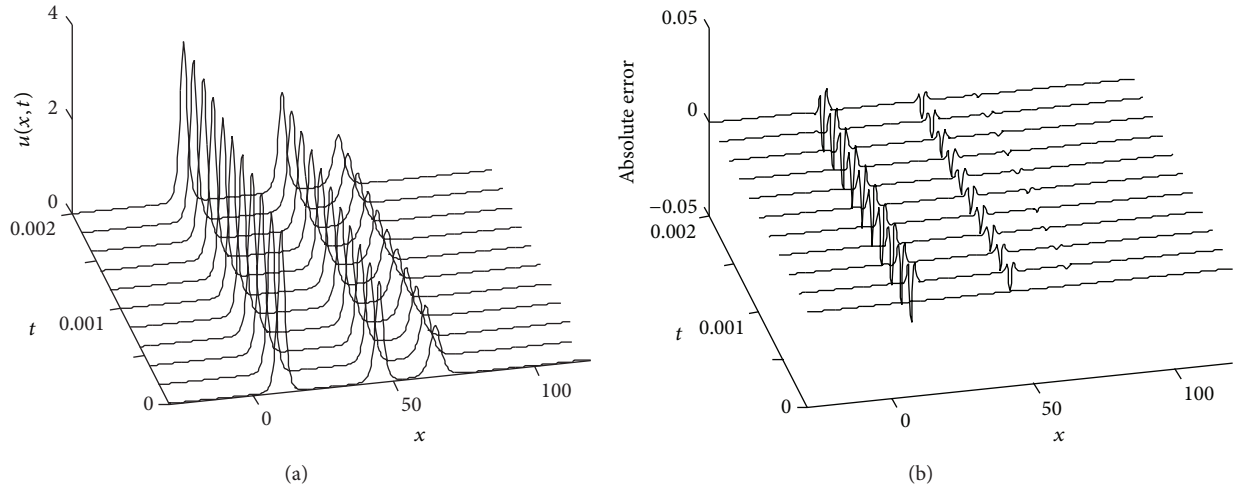


FIGURE 8: Numerical solutions of $u(x, t)$ at different times (three solitary waves). (a) Numerical solutions of $u(x, t)$; (b) absolute errors.

It is observed that the results obtained by implementing the IMLS-Ritz method are very close to the exact solutions. It is worth mentioning that the maximum error occurs near the peak position of the solitary wave, showing a good agreement with the results in [35]. Solutions at initial and different time levels are plotted in Figure 8(a), while Figure 8(b) gives the corresponding absolute error at $\Delta t = 0.0001$. To examine the influence of number of nodes and d_{\max} in predicting the interaction between three solitary waves, we display the time history of L_2 -norm errors by varying time from 0 s to 0.002 s. As observed from Figure 9, convergent results are obtained as

N increases up to 450 while keeping $\Delta t = 0.0001$, and smaller L_2 -norm errors are produced as d_{\max} increases.

5. Conclusion

An accurate numerical solution of the GRLW equation is important in investigating the creation of secondary solitary waves corresponding to particle physics. In this paper, the element-free IMLS-Ritz method is applied to provide an alternative solution for the GRLW equation. In this numerical

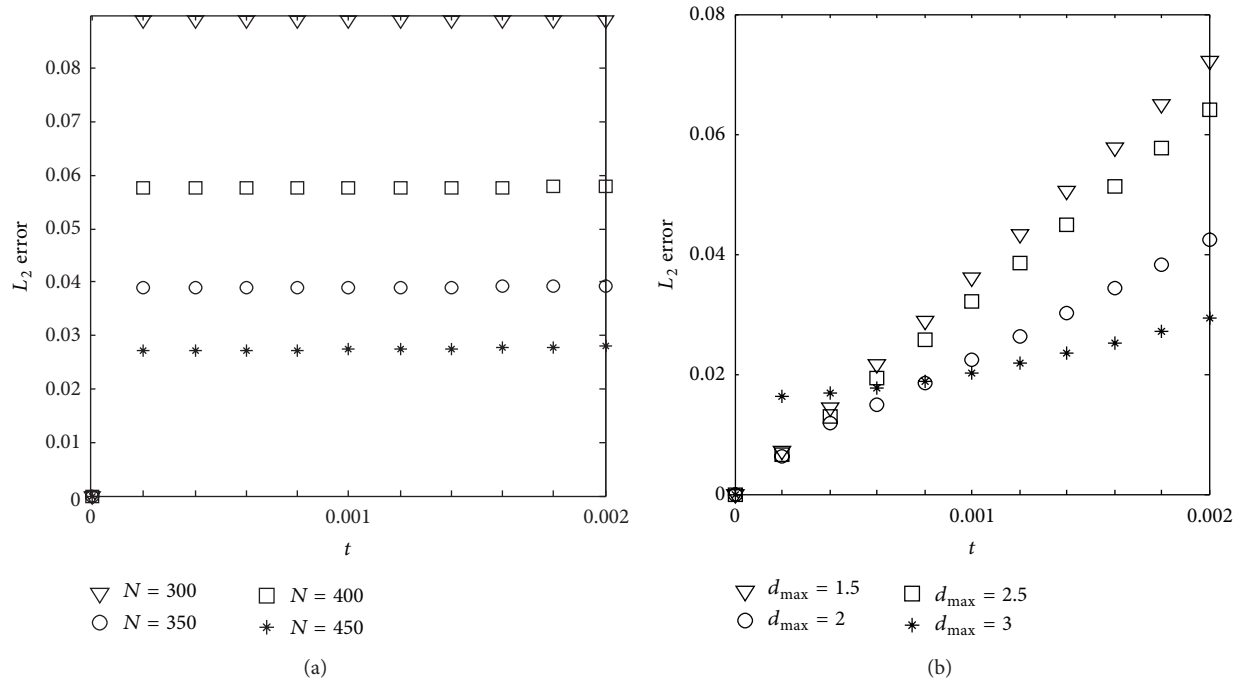


FIGURE 9: L_2 -norm errors of $u(x, t)$ (three solitary waves). (a) L_2 -norm errors at different number of nodes; (b) L_2 -norm errors at different d_{\max} .

solving process, IMLS approximation is employed to estimate the one-dimensional field function. The total functional is established by enforcement of Dirichlet boundary conditions using the penalty approach. The system of nonlinear discrete equations is furnished through Ritz minimization procedure. Time difference technique and Newton-Raphson method are used to solve the nonlinear equation system. The accuracy and efficiency of the IMS-Ritz method are examined through carefully selected numerical examples. From the computational results, it is concluded that the presented element-free method with satisfied performance can be extended to other PDEs in engineering problems.

Conflict of Interests

The authors declare that there is no conflict of interests regarding the publication of this paper.

Acknowledgments

The work described in this paper was fully supported by the National Natural Science Foundation of China (Grant no. 61272098 and Grant no. 11402142).

References

- [1] D. H. Peregrine, "Calculations of the development of an undular bore," *Journal of Fluid Mechanics*, vol. 25, pp. 321–330, 1966.
- [2] D. H. Peregrine, "Long waves on a beach," *Journal of Fluid Mechanics*, vol. 27, no. 4, pp. 815–827, 1967.
- [3] C. M. García-López and J. I. Ramos, "Effects of convection on a modified GRLW equation," *Applied Mathematics and Computation*, vol. 219, no. 8, pp. 4118–4132, 2012.
- [4] J. L. Bona and A. Soyeur, "On the stability of solitary-wave solutions of model equations for long waves," *Journal of Nonlinear Science*, vol. 4, no. 5, pp. 449–470, 1994.
- [5] L. M. Zhang, "A finite difference scheme for generalized regularized long-wave equation," *Applied Mathematics and Computation*, vol. 168, no. 2, pp. 962–972, 2005.
- [6] D. Kaya, "A numerical simulation of solitary-wave solutions of the generalized regularized long-wave equation," *Applied Mathematics and Computation*, vol. 149, no. 3, pp. 833–841, 2004.
- [7] D. Kaya and S. M. El-Sayed, "An application of the decomposition method for the generalized KdV and RLW equations," *Chaos, Solitons and Fractals*, vol. 17, no. 5, pp. 869–877, 2003.
- [8] I. Dağ, "Least-squares quadratic B-spline finite element method for the regularised long wave equation," *Computer Methods in Applied Mechanics and Engineering*, vol. 182, no. 1-2, pp. 205–215, 2000.
- [9] L. R. Gardner, G. A. Gardner, and I. Dag, "A B-spline finite element method for the regularized long wave equation," *Communications in Numerical Methods in Engineering*, vol. 11, no. 1, pp. 59–68, 1995.
- [10] L. R. T. Gardner, G. A. Gardner, and A. Dogan, "A least-squares finite element scheme for the RLW equation," *Communications in Numerical Methods in Engineering*, vol. 12, no. 11, pp. 795–804, 1996.
- [11] İ. Dağa, B. Saka, and D. Irk, "Application of cubic B-splines for numerical solution of the RLW equation," *Applied Mathematics and Computation*, vol. 159, no. 2, pp. 373–389, 2004.

- [12] A. A. Soliman and M. H. Hussien, "Collocation solution for RLW equation with septic spline," *Applied Mathematics and Computation*, vol. 161, no. 2, pp. 623–636, 2005.
- [13] A. K. Khalifa, K. R. Raslan, and H. M. Alzubaidi, "A collocation method with cubic B-splines for solving the MRLW equation," *Journal of Computational and Applied Mathematics*, vol. 212, no. 2, pp. 406–418, 2008.
- [14] L. R. Gardner, G. A. Gardner, F. A. Ayoub, and N. K. Amein, "Approximations of solitary waves of the MRLW equation by B-spline finite elements," *The Arabian Journal for Science and Engineering Section A: Sciences*, vol. 22, no. 2, pp. 183–193, 1997.
- [15] J.-F. Wang, F.-N. Bai, and Y.-M. Cheng, "A meshless method for the nonlinear generalized regularized long wave equation," *Chinese Physics B*, vol. 20, no. 3, Article ID 030206, 2011.
- [16] T. Roshan, "A Petrov-Galerkin method for solving the generalized regularized long wave (GRLW) equation," *Computers & Mathematics with Applications*, vol. 63, no. 5, pp. 943–956, 2012.
- [17] P. F. Guo, L. W. Zhang, and K. M. Liew, "Numerical analysis of generalized regularized long wave equation using the element-free kp-Ritz method," *Applied Mathematics and Computation*, vol. 240, pp. 91–101, 2014.
- [18] R. J. Cheng and K. M. Liew, "Analyzing modified equal width (MEW) wave equation using the improved element-free Galerkin method," *Engineering Analysis with Boundary Elements*, vol. 36, no. 9, pp. 1322–1330, 2012.
- [19] S. Hamdi, W. H. Enright, W. E. Schiesser, and J. J. Gottlieb, "Exact solutions and invariants of motion for general types of regularized long wave equations," *Mathematics and Computers in Simulation*, vol. 65, no. 4–5, pp. 535–545, 2004.
- [20] J. I. Ramos, "Solitary wave interactions of the GRLW equation," *Chaos, Solitons and Fractals*, vol. 33, no. 2, pp. 479–491, 2007.
- [21] L. X. Peng, Y.-P. Tao, H.-Q. Li, and G.-K. Mo, "Geometric nonlinear meshless analysis of ribbed rectangular plates based on the FSDT and the moving least-squares approximation," *Mathematical Problems in Engineering*, vol. 2014, Article ID 548708, 13 pages, 2014.
- [22] D. Huang, G. Zou, and L. W. Zhang, "Numerical approximation of nonlinear Klein-Gordon equation using an element-free approach," *Mathematical Problems in Engineering*, vol. 2014, Article ID 548905, 2014.
- [23] F. X. Sun, C. Liu, and Y. M. Cheng, "An improved interpolating element-free Galerkin method based on nonsingular weight functions," *Mathematical Problems in Engineering*, vol. 2014, Article ID 323945, 13 pages, 2014.
- [24] N. Zhao and H. Ren, "The interpolating element-free Galerkin method for 2D transient heat conduction problems," *Mathematical Problems in Engineering*, vol. 2014, Article ID 712834, 9 pages, 2014.
- [25] Q. Wei and R. Cheng, "The improved moving least-square Ritz method for the one-dimensional sine-Gordon equation," *Mathematical Problems in Engineering*, vol. 2014, Article ID 383219, 10 pages, 2014.
- [26] F. Li and X. Li, "The interpolating boundary element-free method for unilateral problems arising in variational inequalities," *Mathematical Problems in Engineering*, vol. 2014, Article ID 518727, 11 pages, 2014.
- [27] K. M. Liew, Y. Cheng, and S. Kitipornchai, "Boundary element-free method (BEFM) and its application to two-dimensional elasticity problems," *International Journal for Numerical Methods in Engineering*, vol. 65, no. 8, pp. 1310–1332, 2006.
- [28] T. Belytschko, Y. Y. Lu, and L. Gu, "Element-free Galerkin methods," *International Journal for Numerical Methods in Engineering*, vol. 37, no. 2, pp. 229–256, 1994.
- [29] J. J. Monaghan, "An introduction to SPH," *Computer Physics Communications*, vol. 48, no. 1, pp. 89–96, 1988.
- [30] W. Chen, "New RBF collocation methods and kernel RBF with applications," in *Meshfree Methods for Partial Differential Equations*, vol. 26 of *Lecture Notes in Computational Science and Engineering*, pp. 75–86, Springer, Berlin, Germany, 2000.
- [31] K. M. Liew, X. Zhao, and T. Y. Ng, "The element-free kp-Ritz method for vibration of laminated rotating cylindrical panels," *International Journal of Structural Stability and Dynamics*, vol. 2, pp. 523–558, 2002.
- [32] X. Zhao, Q. Li, K. M. Liew, and T. Y. Ng, "The element-free kp-Ritz method for free vibration analysis of conical shell panels," *Journal of Sound and Vibration*, vol. 295, no. 3–5, pp. 906–922, 2006.
- [33] X. Zhao, Y. Y. Lee, and K. M. Liew, "Free vibration analysis of functionally graded plates using the element-free kp-Ritz method," *Journal of Sound and Vibration*, vol. 319, no. 3–5, pp. 918–939, 2009.
- [34] X. Zhao and K. M. Liew, "Geometrically nonlinear analysis of functionally graded plates using the element-free kp-Ritz method," *Computer Methods in Applied Mechanics and Engineering*, vol. 198, no. 33–36, pp. 2796–2811, 2009.
- [35] L. W. Zhang, Z. X. Lei, K. M. Liew, and J. L. Yu, "Large deflection geometrically nonlinear analysis of carbon nanotube-reinforced functionally graded cylindrical panels," *Computer Methods in Applied Mechanics and Engineering*, vol. 273, pp. 1–18, 2014.
- [36] L. W. Zhang, Z. X. Lei, K. M. Liew, and J. L. Yu, "Static and dynamic of carbon nanotube reinforced functionally graded cylindrical panels," *Composite Structures*, vol. 111, no. 1, pp. 205–212, 2014.
- [37] S. N. Atluri and T. Zhu, "A new meshless local Petrov-Galerkin (MLPG) approach in computational mechanics," *Computational Mechanics*, vol. 22, no. 2, pp. 117–127, 1998.
- [38] K. M. Liew, T. Y. Ng, X. Zhao, and J. N. Reddy, "Harmonic reproducing kernel particle method for free vibration analysis of rotating cylindrical shells," *Computer Methods in Applied Mechanics and Engineering*, vol. 191, no. 37–38, pp. 4141–4157, 2002.
- [39] K. M. Liew, X. L. Chen, and J. N. Reddy, "Mesh-free radial basis function method for buckling analysis of non-uniformly loaded arbitrarily shaped shear deformable plates," *Computer Methods in Applied Mechanics and Engineering*, vol. 193, no. 3–5, pp. 205–224, 2004.
- [40] K. M. Liew, Z. X. Lei, J. L. Yu, and L. W. Zhang, "Postbuckling of carbon nanotube-reinforced functionally graded cylindrical panels under axial compression using a meshless approach," *Computer Methods in Applied Mechanics and Engineering*, vol. 268, pp. 1–17, 2014.
- [41] "A meshfree method for the numerical solution of the RLW equation," *Journal of Computational and Applied Mathematics*, vol. 223, no. 2, pp. 997–1012, 2009.
- [42] İ. Dağ, B. Saka, and D. Irk, "Galerkin method for the numerical solution of the RLW equation using quintic B-splines," *Journal of Computational and Applied Mathematics*, vol. 190, no. 1–2, pp. 532–547, 2006.

Research Article

A Mixed Element Method for the Desorption-Diffusion-Seepage Model of Gas Flow in Deformable Coalbed Methane Reservoirs

Lei Yang

School of Mathematics, Shandong University, Jinan 250100, China

Correspondence should be addressed to Lei Yang; yanglei1021@126.com

Received 5 July 2014; Revised 1 September 2014; Accepted 2 September 2014; Published 28 September 2014

Academic Editor: Kim M. Liew

Copyright © 2014 Lei Yang. This is an open access article distributed under the Creative Commons Attribution License, which permits unrestricted use, distribution, and reproduction in any medium, provided the original work is properly cited.

We present a desorption-diffusion-seepage model for the gas flow problem in deformable coalbed methane reservoirs. Effects of fracture systems deformation on permeability have been considered in the proposed model. A mixed finite element method is introduced to solve the gas flow model, in which the coalbed gas pressure and velocity can be approximated simultaneously. Numerical experiments using the lowest order Raviart-Thomas (RT_0) mixed element are carried out to describe the dynamic characteristics of gas pressure, velocity, and concentration. Error estimate results indicate that approximation solutions could achieve first-order convergence rates.

1. Introduction

Coalbed methane (CBM) is an abundant, low cost energy source, which has become a viable alternative source to conventional fuel. CBM reservoirs are dual porosity systems consisting of coal matrix and fracture network [1]. In CBM reservoirs, most of coalbed gas is stored in the coal matrix as adsorbed gas, and only a small amount is stored in fracture systems as free gas. Comparing with conventional natural gas reservoirs, the effect of fracture systems deformation on permeability is significant in CBM reservoirs [2–4]. Meanwhile, the gas flow in fracture systems is driven not only by pressure field but also by gas concentration field [5, 6], so we need to consider Darcy seepage and Fick diffusion simultaneously in multifield. As coalbed gas is released from CBM reservoirs, fracture system pressure reduces, resulting in gas diffusion in the coal matrix and gas desorption from coal matrix surface to fracture systems. Therefore, the gas flow process in CBM reservoirs includes gas desorption-diffusion in coal matrix and gas seepage in fracture systems [7–10]. Usually, the fracture systems are considered as the gas flow passage and the coal matrix is treated as the source for fracture systems.

Based on the above understandings about coalbed gas flow mechanism, a series of conventional mathematical and numerical models [5, 6, 11, 12] have been developed, obtaining

some useful computational and simulation results. Young [11] presented a computer model for CBM reservoirs to determine key data and to describe the variability in CBM reservoir properties. Unsal et al. [12] proposed a numerical model for multiphase flow in CBM reservoirs using a fracture-only model. Thararoop et al. [5, 6] developed a compositional dual porosity, dual permeability CBM numerical model to describe the pressure and concentration dynamic behaviors. Nevertheless, the existing CBM numerical simulation methods are based on finite difference scheme and mainly focus on gas pressure and concentration, ignoring gas flow velocity.

Mixed finite element method was initially introduced by engineers [13] in the 1960s and has been applied to many areas such as solid and fluid mechanics, which could approximate both vector variable (e.g., the fluid velocity) and scalar variable (e.g., the pressure) simultaneously and give a high order approximation of both variables. Comparing with the standard finite element method only employing a single finite element space, mixed finite element method need construct two different finite element spaces. Raviart and Thomas [14] introduced the first family of mixed finite element spaces for second-order elliptic problems. Nedelec [15] extended these spaces to three-dimensional problems. Then, Brezzi et al. [16, 17] and Chen and Douglas [18] presented many mixed finite element spaces.

In addition, the study about numerical method and numerical analysis for fluid flow problems in porous media has been a research hotspot for the past decades [19–24], due to its wide applications in various engineering areas. Douglas et al. [19–21] have done a lot of useful work for the fluid flow problem in porous media. For the incompressible miscible displacement problem in porous media, Wang [22] introduced ELLAM-MFEM to solve equation of the problem. A component-based Eulerian-Lagrangian method [23] was used to treat the multicomponent, multiphase flow problem in porous media. Li and Sun [24] presented an unconditional convergence Galerkin-mixed element approximation for the incompressible miscible flow problem. However, until now, we have not found any paper considering mixed element approximation scheme for the gas flow problem in deformable CBM reservoirs.

The aim of this paper is to study the gas flow problem in deformable CBM reservoirs using mixed element method. For this purpose, we introduce a mixed finite element method to approximate the coalbed gas pressure and velocity simultaneously. Another objective of this paper is to carry out some numerical experiments using the lowest order Raviart-Thomas mixed element, so as to show the convergence rate of the mixed element approximation method, and to analyze coalbed gas flow characteristics.

This paper is organized as follows. In Section 2, considering the effects of fracture system deformation, we present a desorption-diffusion-seepage model of gas flow in deformable CBM reservoirs for the two-dimensional problem. In Section 3 we introduce a mixed finite element approximation scheme for the coalbed gas flow model. In Section 4 numerical experiments using the lowest order Raviart-Thomas (RT₀) mixed element are carried out.

2. Coalbed Gas Flow Problem in Deformable CBM Reservoirs

In this section, considering the pressure dependence of permeability and porosity, we derive a mathematical model for the gas flow problem in deformable CBM reservoirs.

2.1. Basic Assumptions and Gas State Descriptions

- (i) CBM reservoirs are treated as dual porosity systems consisting of coal matrix and fracture network.
- (ii) CBM reservoirs are isothermal. When pressure variation is not significant, we can assume the gas viscosity is constant under isothermal conditions [25].
- (iii) The gas diffusion process in the coal matrix is pseudostatic and described by Fick's first diffusion law.
- (iv) Gas absorption/adsorption is described by Langmuir adsorption isotherm.

The equation of real gas state is

$$pV = nZRT = \frac{m}{M}ZRT, \quad (1)$$

where p is the gas pressure, V is the gas volume, n is the amount of substance, T is the gas temperature, m is the gas mass, M is the gas molar mass, Z is the gas deviation factor, and R is the universal gas constant. From (1) the gas density ρ can be written as

$$\rho = \frac{m}{V} = \frac{pM}{ZRT}. \quad (2)$$

According to the Langmuir isotherm and the state equation of real gas, the adsorbed gas concentration C_m in coal matrix and free gas concentration C_f in fracture systems can be written, respectively, as

$$C_m(p_m) = \frac{C_L p_m}{p_L + p_m}, \quad C_f = \phi_f \rho = \frac{\phi_f p_f M}{ZRT}, \quad (3)$$

where p_m is the gas pressure in coal matrix, C_L is the maximum adsorption concentration of the coal matrix, p_L is the Langmuir pressure, p_f is the gas pressure in fracture systems, and ϕ_f is the porosity of fracture systems.

2.2. Gas Flow Model. Considering the effects of fracture system deformation, fracture system permeability tensor $\mathbf{K}_f(x, p_f)$ can be written as

$$\mathbf{K}_f(x, p_f) = \mathbf{K}_0 e^{\beta(p_f - p_0)}, \quad (4)$$

where p_0 is the initial gas pressure in fracture systems, \mathbf{K}_0 is the fracture system permeability tensor under p_0 , and β is the permeability modulus with respect to gas pressure.

Coalbed gas flow in fracture systems is driven by pressure field and concentration field simultaneously. According to Darcy's law and Fick's diffusion law, the motion equation of gas flow in fracture systems can be written as

$$\mathbf{u} = - \left(\frac{\mathbf{K}_f(x, p_f)}{\mu_g} + \frac{\mathbf{D}_f \phi_f}{p_f} \right) \nabla p_f, \quad (5)$$

where \mathbf{u} is the total volume velocity of gas flow driven by multifield, μ_g is the gas viscosity, and \mathbf{D}_f is the gas diffusion coefficient in fracture systems.

Then, according to the mass conservation law, the continuity equation of gas flow in fracture systems is

$$\frac{\partial \rho \phi_f}{\partial t} + \nabla \cdot (\rho \mathbf{u}) = \rho q_m, \quad (6)$$

where q_m is the gas volume of interporosity flow from coal matrix to fracture systems. Using the state equation of real gas, the divergence term of (6) could be unfolded as the following form:

$$\nabla \cdot (\rho \mathbf{u}) = \rho \nabla \cdot \mathbf{u} + \mathbf{u} \cdot \nabla \rho = \rho \nabla \cdot \mathbf{u} + \frac{\rho}{p_f} \mathbf{u} \cdot \nabla p_f. \quad (7)$$

Similarly, the capacity term could be unfolded as the following form:

$$\begin{aligned} \frac{\partial \rho \phi_f}{\partial t} &= \phi_f \frac{\partial \rho}{\partial t} + \rho \frac{\partial \phi_f}{\partial t} \\ &= \frac{\phi_f \rho}{p_f} \frac{\partial p_f}{\partial t} - c_Z \phi_f \rho \frac{\partial p_f}{\partial t} + c_\phi \phi_f \rho \frac{\partial p_f}{\partial t}, \end{aligned} \quad (8)$$

where c_ϕ is the compressibility factor of ϕ_f and c_z is the compressibility factor of Z , defined as

$$c_\phi = \frac{1}{\phi_f} \frac{\partial \phi_f}{\partial p_f}, \quad c_z = \frac{1}{Z} \frac{\partial Z}{\partial p_f}. \quad (9)$$

For the expression brevity, define

$$\begin{aligned} \mathbf{K}(x, p_f) &= \frac{\mathbf{K}_f(x, p_f)}{\mu_g} + \frac{\mathbf{D}_f \phi_f}{p_f}, \\ c(x, p_f) &= \frac{\phi_f}{p_f} - c_z \phi_f + c_\phi \phi_f, \end{aligned} \quad (10)$$

and substitute motion equation (5) into (7); the continuity equation (6) can be rewritten as follows:

$$c(x, p_f) \frac{\partial p_f}{\partial t} - \nabla \cdot (\mathbf{K}(x, p_f) \nabla p_f) - \frac{\mathbf{K}(x, p_f)^{-1}}{p_f} \mathbf{u}^2 = q_m. \quad (11)$$

Since the seepage velocity \mathbf{u} is very low, the quadratic term \mathbf{u}^2 usually can be omitted in engineering application. Therefore, the more common form of continuity equation is as follows:

$$c(x, p_f) \frac{\partial p_f}{\partial t} - \nabla \cdot (\mathbf{K}(x, p_f) \nabla p_f) = q_m. \quad (12)$$

In addition, there are some other studies [26, 27] considering the influence of quadratic term \mathbf{u}^2 . For example, Ranjbar et al. [26] have considered the gas density variation in space and solved the nonlinear equations using semianalytical methods. However, they did not consider the effect of gas desorption and deformable media. But their method may form a basis for application of semianalytical methods for problem like the one studied here and it will be useful to the readers.

According to Fick's first diffusion law, the pseudosteady state equation of gas diffusion in coal matrix can be written as

$$\frac{dC_{am}}{dt} = D_m \sigma (C_E(p_f) - C_{am}), \quad (13)$$

where C_{am} is the average gas concentration of a coal matrix block, $C_E(p_f)$ is the adsorbed concentration on the coal matrix surface and is defined as $C_E(p_f) = C_L p_f / (p_L + p_f)$, D_m is the gas diffusion coefficient in coal matrix block, and σ is the geometrical factor.

Combining (11) and (13), with corresponding initial and boundary conditions, we have the coalbed gas flow model as follows:

$$(i) \quad c(x, p_f) \frac{\partial p_f}{\partial t} - \nabla \cdot (\mathbf{K}(x, p_f) \nabla p_f) = q_m, \quad x \in \Omega, \quad t \in [0, T],$$

$$(ii) \quad \frac{dC_{am}}{dt} = D_m \sigma (C_E(p_f) - C_{am}), \quad t \in [0, T],$$

$$(iii) \quad p_f = p_d, \quad x \in \partial\Omega, \quad t \in [0, T],$$

$$(iv) \quad p_f = p_0, \quad x \in \Omega, \quad t = 0,$$

$$(v) \quad C_{am} = C_0, \quad x \in V_m, \quad t = 0, \quad (14)$$

where Ω is the objective region for the two-dimensional problem with boundary $\partial\Omega$, $[0, T]$ is a time interval with $T \in (0, \infty]$, and V_m is the region of a coal matrix block.

3. Notations and Mixed Element Approximation Scheme

In this section, we will present the mixed element approximation scheme for the coalbed gas flow model and give some notations.

3.1. Some Notations and Basic Approximation Results. For the convenience of subsequent analysis, we first give notations and basic approximation results. Define the inner product on Ω and its norm:

$$(u, v) = \int_{\Omega} u(x) v(x) dx, \quad \|u\|_{L^2(\Omega)} = \left(\int_{\Omega} u^2 dx \right)^{1/2}. \quad (15)$$

Recall that the Sobolev space $H^k(\Omega)$ is the closure of $C^\infty(\Omega)$ in the norm

$$\|u\|_k^2 = \sum_{|\alpha| \leq k} \|D^\alpha u\|_{L^2(\Omega)}^2. \quad (16)$$

Define the function spaces W, V and their norms as follows:

$$W = L^2(\Omega),$$

$$V = H(\operatorname{div}, \Omega)$$

$$= \left\{ \mathbf{v} = (v_1, v_2) \in (L^2(\Omega))^2 \mid \nabla \cdot \mathbf{v} \in L^2(\Omega) \right\},$$

$$\|\omega\|_W = \left(\int_{\Omega} \omega^2 dx \right)^{1/2}, \quad \|\mathbf{v}\|_V = \left\{ \|\mathbf{v}\|^2 + \|\nabla \cdot \mathbf{v}\|^2 \right\}^{1/2}. \quad (17)$$

Let $W_h \times V_h \subset W \times V$ be the mixed element function spaces such as RT_k with index k and discretization parameter h . Now we define the RT projection $\Pi_h : V \rightarrow V_h$, satisfying

$$(\nabla \cdot (\mathbf{v} - \Pi_h \mathbf{v}), \omega_h) = 0, \quad \mathbf{v} \in V, \quad \omega_h \in W_h,$$

$$\|\mathbf{v} - \Pi_h \mathbf{v}\|_0 \leq C \|\mathbf{v}\|_s h^s,$$

$$1 \leq s \leq k+1, \quad \forall \mathbf{v} \in V \cap (H^s(\Omega))^2, \quad (18)$$

$$\|\nabla \cdot (\mathbf{v} - \Pi_h \mathbf{v})\|_0 \leq C \|\nabla \cdot \mathbf{v}\|_s h^s,$$

$$0 \leq s \leq k+1, \quad \forall \mathbf{v} \in V \cap H^s(\operatorname{div}, \Omega).$$

Define standard L^2 projection $P_h : W \rightarrow W_h$, satisfying

$$(P_h z - z, \omega_h) = 0, \quad z \in W, \quad \omega_h \in W_h,$$

$$\|z - P_h z\|_0 \leq C \|z\|_s h^s, \quad 0 \leq s \leq k+1, \quad \forall z \in W \cap H^s(\Omega). \quad (19)$$

3.2. Mixed Element Approximation Scheme. We consider the case that the seepage-diffusion tensor $\mathbf{K}(x, p_f)$ is a diagonal matrix and $k_{i,i} > 0$ ($i = 1, 2$) for the two-dimensional problem. That is to say, there exist positive constants k_m and k_M such that, for all $\xi \in R^2$,

$$k_m \xi' \xi \leq \xi' \mathbf{K}(x, p_f) \xi \leq k_M \xi' \xi. \quad (20)$$

For the practical situation, there exist c_m and c_M such that the scalar coefficient $c(x, p_f)$ satisfies

$$0 < c_m \leq c(x, p_f) \leq c_M < \infty. \quad (21)$$

Also, we can easily verify that the coefficients $k_{i,i}(p_f)$, $c(p_f)$, and $q_m(p_f)$ satisfy the Lipschitz continuity. Since $\mathbf{K}(x, p_f)$ is a diagonal and invertible matrix, from (5) we have that

$$\mathbf{K}(x, p_f)^{-1} \mathbf{u} + \nabla p_f = 0. \quad (22)$$

Using the integration by parts and applying the boundary condition, we can define the mixed weak formation, which is to find $p_f \in W$, $\mathbf{u} \in V$ such that

$$\begin{aligned} & (\mathbf{K}^{-1}(x, p_f) \mathbf{u}, \mathbf{v}) - (\nabla \cdot \mathbf{v}, p_f) = -(p_d, \mathbf{v} \cdot \mathbf{n})_{\partial\Omega}, \quad \forall \mathbf{v} \in V, \\ & \left(c(x, p_f) \frac{\partial p_f}{\partial t}, \omega \right) + (\nabla \cdot \mathbf{u}, \omega) = (q_m(p_f), \omega), \quad \forall \omega \in W, \end{aligned} \quad (23)$$

where \mathbf{n} is the unit exterior normal vector to the $\partial\Omega$.

Replacing the original pressure p_f and velocity \mathbf{u} by their approximations, we get the semidiscrete mixed element approximate problem, which is to find $p_h \in W_h$, $\mathbf{u}_h \in V_h$ such that

$$\begin{aligned} & (\mathbf{K}^{-1}(x, p_h) \mathbf{u}_h, \mathbf{v}_h) - (\nabla \cdot \mathbf{v}_h, p_h) \\ & = -(p_d, \mathbf{v}_h \cdot \mathbf{n})_{\partial\Omega}, \quad \forall \mathbf{v}_h \in V_h, \\ & \left(c(x, p_h) \frac{\partial p_h}{\partial t}, \omega_h \right) + (\nabla \cdot \mathbf{u}_h, \omega_h) \\ & = (q_m(t, p_h), \omega_h), \quad \forall \omega_h \in W_h. \end{aligned} \quad (24)$$

Let $\Delta t > 0$, $M = T/\Delta t$, an integer, and $t_n = n\Delta t$, $n = 0, 1, \dots, M$. We can define the full discrete mixed element approximate scheme with backward Euler time-discretization as follows:

$$\begin{aligned} & (\mathbf{K}^{-1}(p_h^{n-1}) \mathbf{u}_h^n, \mathbf{v}_h) - (\nabla \cdot \mathbf{v}_h, p_h^n) \\ & = -(p_d, \mathbf{v}_h \cdot \mathbf{n})_{\partial\Omega}, \quad \forall \mathbf{v}_h \in V_h, \\ & \left(c(p_h^{n-1}) \frac{p_h^n - p_h^{n-1}}{\Delta t}, \omega_h \right) + (\nabla \cdot \mathbf{u}_h^n, \omega_h) \\ & = (q_m(p_h^{n-1}), \omega_h), \quad \forall \omega_h \in W_h. \end{aligned} \quad (25)$$

Since gas diffusion equation (13) is an ordinary differential equation, when p_h^n is known, we can get $C_{am}(t_n)$ as follows:

$$C_{am}(t_n) = C_E(p_h^n) - (C_E(p_h^n) - C_0) e^{-D_m \sigma t_n}. \quad (26)$$

Then, the gas volume of interporosity flow from coal matrix to fracture systems could be calculated as follows:

$$q_m(p_h^n) = -\frac{1}{\rho} \frac{dC_{am}}{dt} \Big|_{t=t_n} = -\frac{1}{\rho} D_m \sigma (C_E(p_h^n) - C_0) e^{-D_m \sigma t_n}. \quad (27)$$

In practical calculation, alternative and iterative method is used to solve (25)–(27), and specific calculation procedure is listed as follows.

- (i) For $n = 1, 2, \dots, M$, when p_h^{n-1} is known, $q_m(p_h^{n-1})$ can be calculated using (27).
- (ii) Then, substituting $q_m(p_h^{n-1})$ into (25), (p_h^n, \mathbf{u}_h^n) can be approximated using (25).
- (iii) Lastly, when p_h^n is known, $C_{am}(t_n)$ can be calculated using (26).

Let τ_h be a quasiregular triangulation for the two-dimensional rectangular region Ω with mesh size h . For a triangular element $T(A_1 A_2 A_3)$, let $\mathbf{x}_i = (x_i, y_i)$ be the coordinate of vertex A_i and γ_i the edge opposite to vertex A_i . Let \mathbf{n}_i be the outward unit vector on the edge γ_i and h_i the length of the perpendicular dropped from the vertex A_i onto the edge γ_i , $i = 1, 2, 3$. We denote by F_h the set of all edges of the triangulation τ_h .

The pressure function space W_h is the space of piecewise constant functions:

$$W_h = \{\omega_h \mid \omega_h = \omega_k \equiv \text{constant}_k \text{ in } T_k, T_k \in \tau_h\} \quad (28)$$

and the dimension of the space W_h is equal to m_1 —the total number of elements T_k in the triangulation τ_h . Each function $\omega_h \in W_h$ can be represented as a linear combination:

$$\omega_h = \sum_{k=1}^{m_1} \omega_k \psi_k(\mathbf{x}), \quad (29)$$

where $\psi_k(\mathbf{x})$ is the basis function associated with the element T_k , satisfying

$$\psi_k(\mathbf{x}) = \begin{cases} 1, & \mathbf{x} \in T_k \\ 0, & \mathbf{x} \notin T_k \end{cases} \quad k = 1 \dots m_1. \quad (30)$$

The velocity function space V_h is chosen to be the $RT_0(\Omega, \tau_h)$, defined as

$$V_h = RT_0(\Omega, \tau_h) = \left\{ \mathbf{v}_h \mid \mathbf{v}_h = \begin{pmatrix} a_x + bx \\ a_y + by \end{pmatrix} \text{ in } T_k, T_k \in \tau_h \right\} \quad (31)$$

and the dimension of the space V_h is equal to m_2 —the total number of edges $\gamma_j \in F_h$. Each function $\mathbf{v}_h \in V_h$ can be represented as a linear combination

$$\mathbf{v}_h = \sum_{j=1}^{m_2} v_j \phi_j(\mathbf{x}), \quad (32)$$

where $v_j = \mathbf{v}_h \cdot \mathbf{n}_j$ and ϕ_j is the basis function associated with the edge $\gamma_j \in \mathcal{F}$, satisfying

$$\phi_j \cdot \mathbf{n}_{j'} = \begin{cases} 1, & j = j' \\ 0, & j \neq j'. \end{cases} \quad (33)$$

To be specific, for a triangle element T_k , the basis functions ϕ_i ($i = 1, 2, 3$) are determined by the following formulas:

$$\phi_i(\mathbf{x}) = \frac{1}{h_i} (\mathbf{x} - \mathbf{x}_i) \equiv \frac{|\gamma_i|}{2|T|} (\mathbf{x} - \mathbf{x}_i), \quad (34)$$

where $\mathbf{x}_i = (x_i, y_i)$ are the coordinates of the vertices A_i ($i = 1, 2, 3$) and $|T|$ is the area of triangle element T_k .

Now we use the basis functions $\psi_k(\mathbf{x})$ ($k = 1 \cdots m_1$) and $\phi_j(\mathbf{x})$ ($j = 1 \cdots m_2$) to represent p_h^n and \mathbf{u}_h^n :

$$p_h^n = \sum_{k=1}^{m_1} p_k^n \psi_k(\mathbf{x}), \quad \mathbf{u}_h^n = \sum_{j=1}^{m_2} u_j^n \phi_j(\mathbf{x}). \quad (35)$$

Substituting (35) into (25) and setting $\omega_h = \psi_k$ ($k = 1 \cdots m_1$) and $\mathbf{v}_h = \phi_j(\mathbf{x})$ ($j = 1 \cdots m_2$), full discrete mixed element approximation scheme (25) can be written as follows:

$$\begin{aligned} & \sum_{j=1}^{m_2} (\mathbf{K}^{-1} (p_h^{n-1}) \phi_j, \phi_t) u_j^n - \sum_{k=1}^{m_1} (\nabla \cdot \phi_t, \psi_k) p_k^n \\ & = -(p_d, \phi_t \cdot \mathbf{n})_{\partial\Omega}, \quad t = 1, 2 \cdots m_2, \\ & \Delta t \sum_{j=1}^{m_2} (\nabla \cdot \phi_j, \psi_l) u_j^n + \sum_{k=1}^{m_1} (c(p_h^{n-1}) \psi_k, \psi_l) p_k^n \\ & = \Delta t (q_m(p_h^{n-1}), \psi_l) + (c(p_h^{n-1}) p_h^{n-1}, \psi_l) \\ & \quad l = 1, 2 \cdots m_1. \end{aligned} \quad (36)$$

We introduce matrices and vectors as follows:

$$\begin{aligned} \mathbf{A} &= (A_{ij})_{m_2 \times m_2}, \quad \mathbf{B} = (B_{ij})_{m_2 \times m_1}, \quad \mathbf{C} = (C_{ij})_{m_1 \times m_1}, \\ \mathbf{U}^n &= (u_j^n)_{m_2 \times 1}, \quad \mathbf{P}^n = (p_k^n)_{m_1 \times 1}, \\ \mathbf{b}_1 &= (b_{1,i})_{m_2 \times 1}, \quad \mathbf{b}_2 = (b_{2,i})_{m_1 \times 1}, \end{aligned} \quad (37)$$

where

$$\begin{aligned} A_{ij} &= \int_{\Omega} \mathbf{K}^{-1} (p_h^{n-1}) \phi_j \phi_j dx, \quad B_{ij} = \int_{\Omega} \nabla \cdot \phi_i \psi_j dx, \\ C_{ij} &= \int_{\Omega} c(p_h^{n-1}) \psi_i \psi_j dx, \\ b_{1,i} &= - \int_{\partial\Omega} p_d (\phi_i \cdot \mathbf{n}) dx, \\ b_{2,i} &= \Delta t \int_{\Omega} q_m(p_h^{n-1}) \psi_i dx + \int_{\Omega} c(p_h^{n-1}) p_h^{n-1} \psi_i dx. \end{aligned} \quad (38)$$

TABLE 1: Relative errors and convergence rates for p_h .

Resolution	Error $\left(\frac{\ p_h^N - p_{1/128}^N\ _{L^2}}{\ p_{1/128}^N\ _{L^2}} \right)$	Rate
$h = \frac{1}{4}$	$6.67E-2$	—
$h = \frac{1}{8}$	$3.60E-2$	-0.8903
$h = \frac{1}{16}$	$1.91E-2$	-0.9131
$h = \frac{1}{32}$	$9.63E-3$	-0.9880
$h = \frac{1}{64}$	$4.81E-3$	-1.0015

Therefore, (36) can be written in a matrix form as follows:

$$\begin{pmatrix} \mathbf{A} & -\mathbf{B} \\ \Delta t \mathbf{B}^T & \mathbf{C} \end{pmatrix} \begin{pmatrix} \mathbf{U}^n \\ \mathbf{P}^n \end{pmatrix} = \begin{pmatrix} \mathbf{b}_1 \\ \mathbf{b}_2 \end{pmatrix}, \quad (39)$$

where \mathbf{B}^T is the transpose of \mathbf{B} . Solving linear algebra problem (39), we can get approximation solutions \mathbf{P}^n and \mathbf{U}^n at n th time step, simultaneously.

4. Numerical Examples

In this section, we carry out numerical experiments using the lowest order Raviart-Thomas mixed finite elements RT_0 for the gas flow problem in deformable CBM reservoirs.

Example 1. In order to verify the convergence, the test region is selected as unit square; that is, $\Omega = [0, 1] \times [0, 1]$, and 6 levels for $h = 1/4, 1/8, 1/16, 1/32, 1/64, 1/128$ are computed to estimate the convergence rate. Since we cannot get the analytical solution p_f , \mathbf{u} , and C_{am} for the problem (14), we use $\|p_h^N - p_{1/128}^N\|_{L^2} / \|p_{1/128}^N\|_{L^2}$, $\|\mathbf{u}_h^N - \mathbf{u}_{1/128}^N\|_{L^2} / \|\mathbf{u}_{1/128}^N\|_{L^2}$, and $\|C_{am,h}^N - C_{am,1/128}^N\|_{L^2} / \|C_{am,1/128}^N\|_{L^2}$ as the criterion of convergence for the pressure, velocity, and concentration. Error estimates in L^2 -norm and convergence rate estimates for p_h , \mathbf{u}_h , and $C_{am,h}$ are listed in Tables 1, 2, and 3, respectively. We can find that the approximation solutions p_h , \mathbf{u}_h , and $C_{am,h}$ could achieve first-order convergence rate (see Figure 1).

Example 2. For a simple application, the scale of objective region Ω is $100 \text{ m} \times 100 \text{ m}$ and the mesh size $h = 2.5 \text{ m}$. There is a production well at the center of region Ω with the production rate q_g . Simulation parameters are listed in Table 4.

Substituting the parameter value into calculation procedure, we can get the numerical solutions, so as to describe the dynamic characteristic of gas flow in deformable CBM reservoirs.

Since average pressure could reflect the decrement of reservoir driving energy during production process, Figures 2 and 3 illustrate the gas average pressure in fracture systems varying with time t and show the effects of D_m and β on average pressure, respectively. In Figure 2, the model

TABLE 2: Relative errors and convergence rates for \mathbf{u}_h .

Resolution	Error $\left(\frac{\ \mathbf{u}_h^N - \mathbf{u}_{1/128}^N\ _{L^2}}{\ \mathbf{u}_{1/128}^N\ _{L^2}} \right)$	Rate
$h = \frac{1}{4}$	$1.17E - 2$	—
$h = \frac{1}{8}$	$6.23E - 3$	-0.9092
$h = \frac{1}{16}$	$3.24E - 3$	-0.9432
$h = \frac{1}{32}$	$1.64E - 3$	-0.9823
$h = \frac{1}{64}$	$8.17E - 4$	-1.0053

TABLE 3: Relative errors and convergence rates for $C_{am,h}$.

Resolution	Error $\left(\frac{\ C_{am,h}^N - C_{am,1/128}^N\ _{L^2}}{\ C_{am,1/128}^N\ _{L^2}} \right)$	Rate
$h = \frac{1}{4}$	$4.77E - 2$	—
$h = \frac{1}{8}$	$2.54E - 2$	-0.9092
$h = \frac{1}{16}$	$1.31E - 2$	-0.9553
$h = \frac{1}{32}$	$6.59E - 3$	-0.9912
$h = \frac{1}{64}$	$3.29E - 3$	-1.0022

has the initial reservoir pressure of 10 MPa, and diffusion coefficient of coal matrix D_m is taken as 1×10^{-7} , 5×10^{-8} , 1×10^{-8} , and 5×10^{-9} m²/s, respectively, so as to analyze the effects of D_m on average pressure in fracture systems. In Figure 2, we have found that pressure variation curves could be divided into 3 stages. Firstly, at the initial stage, since coalbed gas could not desorb and diffuse from matrix into fracture systems instantly, average pressure in fracture systems declines rapidly. At this stage, we have found when D_m is increasing, the initial stage became shorter. It is because that larger D_m could make fracture systems get pressure compensation from coal matrix more quickly. Secondly, at the stable stage, with gas desorption increasing from the coal matrix into fracture systems, fracture systems could get more pressure compensation; thus, the average pressure drop speed slows down. We have also found, with a bigger D_m , fracture systems could maintain a higher average pressure, while the stable stage would be shorter. Lastly, at the last stage, due to the decline of gas concentration in matrix gas desorption rate decreases, resulting in the pressure drop speed becoming rapid once again. Meanwhile, when D_m is larger, the last stage appears at an earlier time. The double porosity characteristics of CBM reservoirs have been just shown through the pressure variation process presented above.

In Figure 3, the permeability modulus β is set as 1×10^{-1} , 1×10^{-3} , and 1×10^{-5} , respectively, so as to analyze the effects of β on average pressure. We have found that pressure drop curves with different β are almost coincident

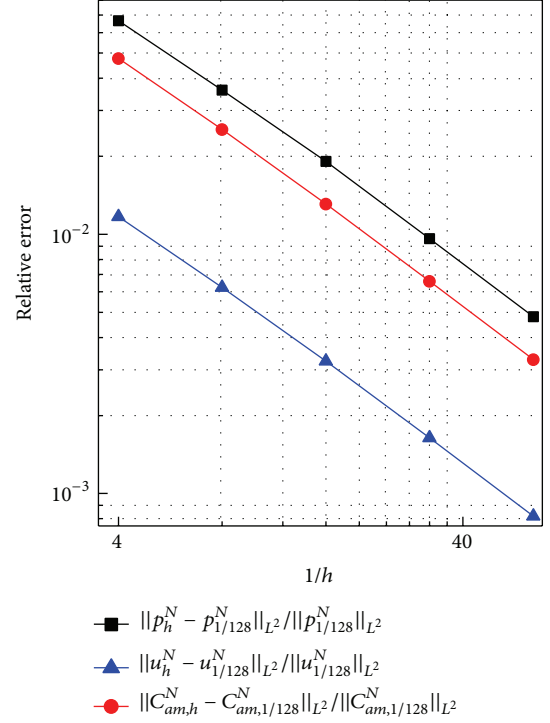
FIGURE 1: Convergence rates for $\|p_h^N - p_{1/128}^N\|_{L^2} / \|p_{1/128}^N\|_{L^2}$, $\|u_h^N - u_{1/128}^N\|_{L^2} / \|u_{1/128}^N\|_{L^2}$, and $\|C_{am,h}^N - C_{am,1/128}^N\|_{L^2} / \|C_{am,1/128}^N\|_{L^2}$.

TABLE 4: Parameters for simulation.

Coefficient	Value
Ω	100 m \times 100 m
ϕ_f	0.15
P_0	10 MPa
C_0	22.5 kg/m ³
D_m	10^{-8} m ² /s
P_L	6 MPa
c_Z	10^{-3}
q_g	180 m ³ /h
h	2.5 m
k_0	0.01 md
μ_g	0.65 mPa·s
D_f	10^{-6} m ² /s
C_L	36 kg/m ³
c_ϕ	5×10^{-2}
β	1.25×10^{-3}

at early time, which indicates that fracture deformation has no evident effects on permeability and pressure at this stage. Essentially, with the fracture pressure dropping, the effects of fracture deformation on permeability become significant, and, conversely, the permeability could also affect fracture pressure. That is to say, the effects of permeability and pore pressure are mutual. Subsequently, we have found pressure drop curves become apart in Figure 3. Also, we have found that the larger the β is, the lower the average pressure will be. From the definition of β , we know that β reflects

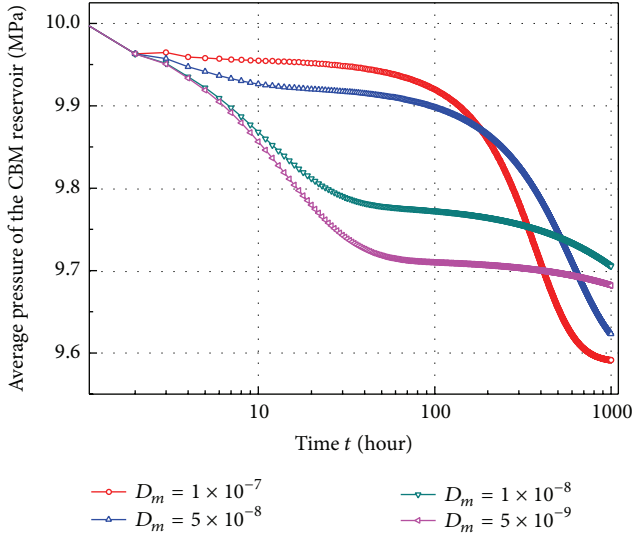


FIGURE 2: Gas average pressure of fracture systems with different D_m .

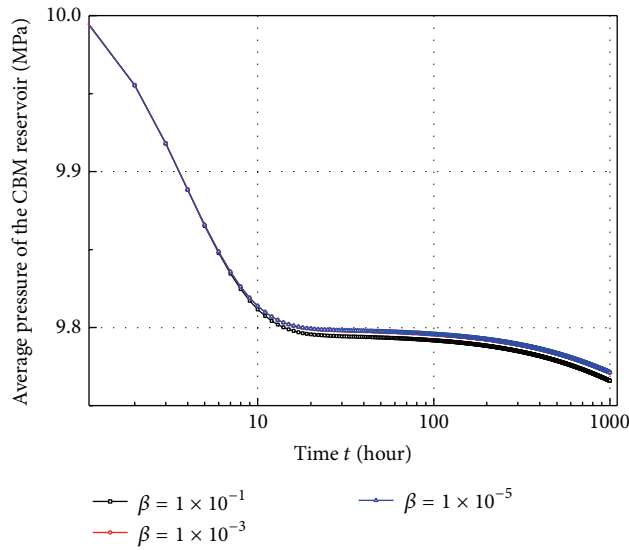


FIGURE 3: Gas average pressure of fracture systems with different β .

the effects of fracture system deformation on the permeability K_f . Thus, when β is larger, K_f decreases more significantly with p_f dropping, such that CBM reservoirs can only get less pressure compensation from outer boundary, resulting in a lower average pressure.

Figure 4 shows the bottom hole pressure varying with time t , and the diffusion coefficient D_m of coal matrix is taken as 1×10^{-7} , 5×10^{-8} , 1×10^{-8} , and 5×10^{-9} m²/s, respectively, so as to analyze the effects of D_m on bottom hole pressure. Since the bottom hole pressure is the direct reflection of production effects, the bottom hole pressure drops sharply from 10 MPa to about 4.25 MPa after starting production, and then there is a pressure recovery due to the gas desorption from coal matrix to fracture systems. Thus, this causes an early fluctuation before reaching a stable state.

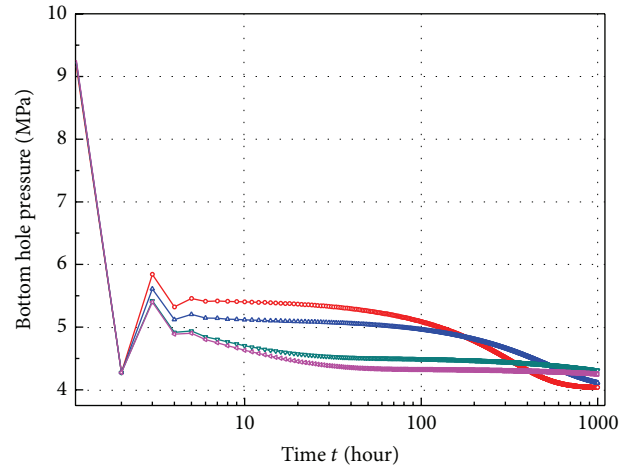


FIGURE 4: Bottom hole pressure of CBM reservoirs with different D_m .

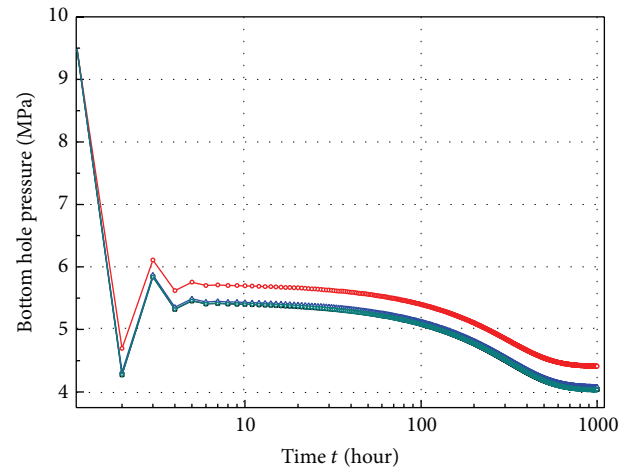


FIGURE 5: Bottom hole pressure of CBM reservoirs with different D_f .

In the subsequent stable stage, we have found that a bigger diffusion coefficient D_m could make more coalbed gas desorb into fracture systems and result in a higher bottom hole pressure. Then, at the last stage, due to the gas desorption decreasing, the effects of D_m become weak and bottom hole pressure curves tend to be close. Put simply, the effects of D_m are evident at stable stage, while they are not so evident at the early and last stage.

Coalbed gas flow in fracture systems is driven by pressure field and concentration field simultaneously; thus, the effects of gas diffusion in fracture systems need to be investigated. In Figure 5, we set fracture diffusion coefficient D_f as 0, 1×10^{-2} , 1×10^{-3} , and 1×10^{-5} m²/s, respectively, so as to analyze

the effects of gas diffusion in fracture systems. We have found that when D_f is larger, the bottom hole pressure is higher. Specifically, the pressure difference between $D_f = 1 \times 10^{-2}$ and $D_f = 0$ is about 0.35 MPa all through the stable stage in Figure 5. That is to say, existence of gas diffusion in fracture systems could make fracture systems get more pressure compensation from outer boundary, resulting in a higher bottom hole pressure. Thus, it is very meaningful to consider gas diffusion in fracture system.

In order to illustrate the gas desorption dynamic process from coal matrix into fracture systems, we show the gas average desorption rate varying with time t in Figures 6 and 7. In Figure 6, the diffusion coefficient D_m is taken as 1×10^{-7} , 5×10^{-8} , 1×10^{-8} , and 5×10^{-9} m²/s, respectively, so as to investigate the effects of matrix diffusion coefficient on gas desorption process. According to equilibrium desorption model, we know that gas desorption rate is affected by gas average concentration C_{am} in matrix, fracture pressure p_f , and diffusion coefficient D_m . During production process, as fracture pressure p_f and gas average concentration C_{am} decline, there are two stages in gas desorption process. At first half stage, due to quick drawdown of fracture pressure, gas concentration $C_E(p_f)$ on matrix surface declines sharply, and then the gas average desorption rate increased to the maximum. Then, at the second half stage, the desorption rate declines due to the reduction of gas average concentration C_{am} . In Figure 6, we have also found when D_m is larger, average desorption rate will be higher and peak desorption rate appears at an earlier moment. In Figure 7, the fracture diffusion coefficient D_f is taken as 0, 1×10^{-2} , 1×10^{-3} , and 1×10^{-5} m²/s, respectively. Since the effects of D_f on desorption rate are indirect and reflected by means of fracture pressure p_f , the effects of D_f are not evident at the starting and ending time. However, we have still found that the larger the D_f is, the higher the peak desorption rate will be.

In order to reflect the remaining reserves of coalbed gas in coal matrix, we show the gas average concentration in coal matrix varying with time t in Figures 8 and 9. In Figure 8, D_m is taken as 1×10^{-7} , 5×10^{-8} , 1×10^{-8} , and 5×10^{-9} m²/s, respectively. We have found that the gas average concentration declines slowly at the early stage on account of the existence of desorption delay phenomenon. Then, due to gas desorption increasing from coal matrix into fracture systems, the average concentration in coal matrix declines quickly at the later stage. At last stage, due to gas desorption rate decreasing, the concentration drop speed becomes slow once again. Also, in Figure 8, we have found concentration curves are almost coincident at early time. At subsequent stages, when D_m is larger, the average concentration is lower and the concentration drop speed is quicker. It is because that larger D_m could accelerate gas desorption rate. In Figure 9, we have found that the effects of initial permeability k_0 are not evident at the early stage, due to the existence of desorption delay phenomenon. And then, at the later half stage, the average concentration increases with k_0 increasing. It indicates that the CBM reservoir with higher permeability could get more pressure compensation from outer boundary, resulting in higher pore pressure and matrix concentration.

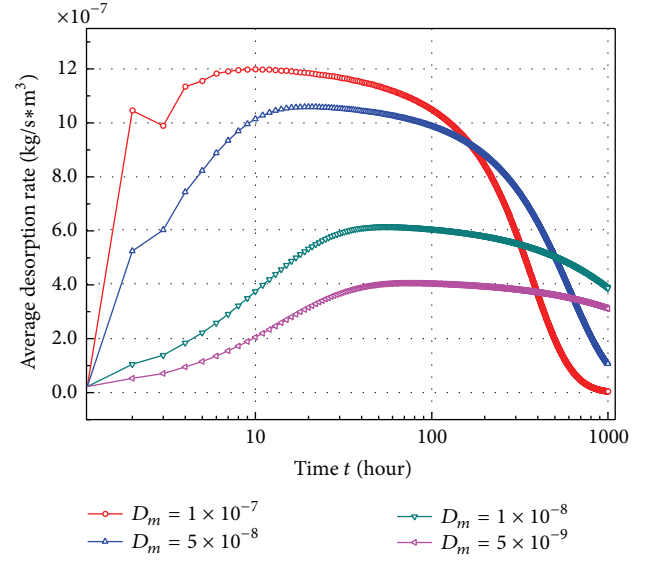


FIGURE 6: Gas average desorption rate with different D_m .

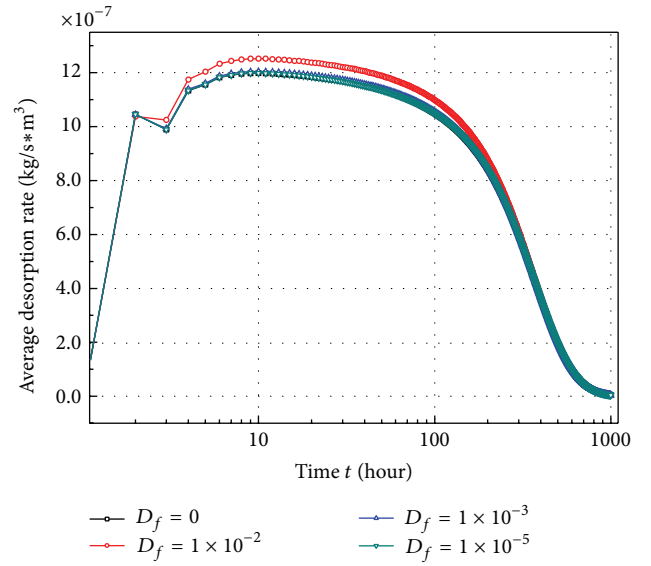


FIGURE 7: Gas average desorption rate with different D_f .

5. Conclusions

- (1) In this paper, we present a desorption-diffusion-seepage model of gas flow in deformable CBM reservoirs, in which the effects of fracture system deformation have been considered.
- (2) We introduce a mixed finite element method to approximate the coalbed gas pressure and velocity, simultaneously, and establish error estimates for the numerical solutions.
- (3) We carry out numerical experiments using the lowest order Raviart-Thomas mixed finite elements RT_0 . Numerical results in Example 1 indicate that the approximation solutions p_h , u_h , and $C_{am,h}$

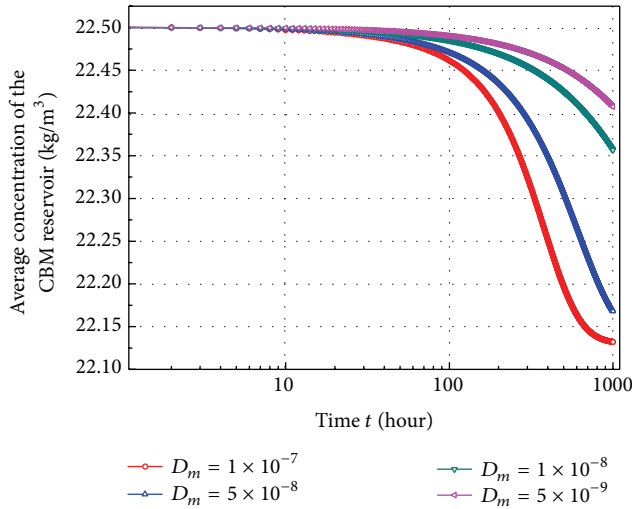


FIGURE 8: Gas average concentration in coal matrix with different D_m .

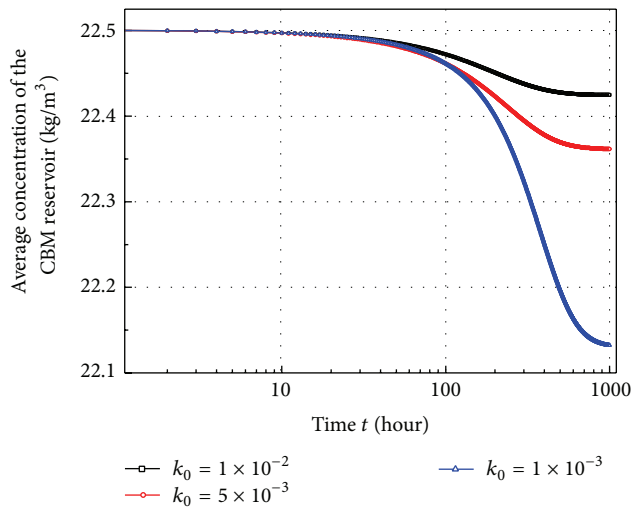


FIGURE 9: Gas average concentration in coal matrix with different k_0 .

could achieve first-order convergence rate. Numerical results in Example 2 have shown that the existence of fracture system deformation phenomenon will result in a lower gas average pressure.

Conflict of Interests

The author declares that there is no conflict of interests regarding the publication of this paper.

Acknowledgment

The work described in this paper was a part of research work of project supported by National Natural Science Foundation of China (Grant nos. 91330106 and 11171190).

References

- [1] M. Lu and L. D. Connell, "A dual-porosity model for gas reservoir flow incorporating adsorption behaviour. I. Theoretical development and asymptotic analyses," *Transport in Porous Media*, vol. 68, no. 2, pp. 153–173, 2007.
- [2] F. Gu and R. Chalaturnyk, "Permeability and porosity models considering anisotropy and discontinuity of coalbeds and application in coupled simulation," *Journal of Petroleum Science and Engineering*, vol. 74, no. 3-4, pp. 113–131, 2010.
- [3] H.-H. Liu and J. Rutqvist, "A new coal-permeability model: internal swelling stress and fracture-matrix interaction," *Transport in Porous Media*, vol. 82, no. 1, pp. 157–171, 2010.
- [4] Z. Pan and L. D. Connell, "A theoretical model for gas adsorption-induced coal swelling," *International Journal of Coal Geology*, vol. 69, no. 4, pp. 243–252, 2007.
- [5] P. Thararoop, Z. T. Karpyn, and T. Ertekin, "Development of a coal shrinkage swelling model accounting for water content in the micropores," *International Journal of Mining and Mineral Engineering*, vol. 1, pp. 346–364, 2009.
- [6] P. Thararoop, Z. T. Karpyn, and T. Ertekin, "Development of a multi-mechanistic, dual-porosity, dual-permeability, numerical flow model for coalbed methane reservoirs," *Journal of Natural Gas Science and Engineering*, vol. 8, pp. 121–131, 2012.
- [7] M. Pillalamarri, S. Harpalani, and S. Liu, "Gas diffusion behavior of coal and its impact on production from coalbed methane reservoirs," *International Journal of Coal Geology*, vol. 86, no. 4, pp. 342–348, 2011.
- [8] C. R. Clarkson and R. M. Bustin, "Coalbed methane: current field-based evaluation methods," *SPE Reservoir Evaluation and Engineering*, vol. 14, no. 1, pp. 60–75, 2011.
- [9] E. Ranjbar and H. Hassanzadeh, "Matrix-fracture transfer shape factor for modeling flow of a compressible fluid in dual-porosity media," *Advances in Water Resources*, vol. 34, no. 5, pp. 627–639, 2011.
- [10] K. Aminian and S. Ameri, "Predicting production performance of CBM reservoirs," *Journal of Natural Gas Science and Engineering*, vol. 1, no. 1-2, pp. 25–30, 2009.
- [11] G. B. C. Young, "Computer modeling and simulation of coalbed methane resources," *International Journal of Coal Geology*, vol. 35, no. 1-4, pp. 369–379, 1998.
- [12] E. Unsal, S. K. Matthäi, and M. J. Blunt, "Simulation of multi-phase flow in fractured reservoirs using a fracture-only model with transfer functions," *Computational Geosciences*, vol. 14, no. 4, pp. 527–538, 2010.
- [13] L. R. Herrmann, "Finite element bending analysis for plates," *Journal of Engineering Mechanics*, vol. 93, pp. 13–26, 1967.
- [14] R. Raviart and J. M. Thomas, "A mixed finite element method for second order elliptic problems," in *Lecture Notes in Mathematics*, vol. 606, pp. 292–315, 1977.
- [15] J. Nédélec, "Mixed finite elements in \mathbb{R}^3 ," *Numerische Mathematik*, vol. 35, no. 3, pp. 315–341, 1980.
- [16] F. Brezzi, J. Douglas, and L. D. Marini, "Two families of mixed finite elements for second order elliptic problems," *Numerische Mathematik*, vol. 47, no. 2, pp. 217–235, 1985.
- [17] F. Brezzi, J. Douglas, R. Durán, and M. Fortin, "Mixed finite elements for second order elliptic problems in three variables," *Numerische Mathematik*, vol. 51, no. 2, pp. 237–250, 1987.
- [18] Z. Chen and J. Douglas Jr., "Prismatic mixed finite elements for second order elliptic problems," *Calcolo*, vol. 26, pp. 135–148, 1989.

- [19] J. Douglas, F. Furtado, and F. Pereira, "On the numerical simulation of waterflooding of heterogeneous petroleum reservoirs," *Computational Geosciences*, vol. 1, no. 2, pp. 155–190, 1997.
- [20] J. Douglas Jr., F. Pereira, and L.-M. Yeh, "A locally conservative Eulerian-Lagrangian numerical method and its application to nonlinear transport in porous media," *Computational Geosciences*, vol. 4, no. 1, pp. 1–40, 2000.
- [21] J. Douglas Jr., D. Frías, N. Henderson, and F. Pereira, "Simulation of single-phase multicomponent flow problems in gas reservoirs by Eulerian-Lagrangian techniques," *Transport in Porous Media*, vol. 50, no. 3, pp. 307–342, 2003.
- [22] H. Wang, "An optimal-order error estimate for a family of ELLAM-MFEM approximations to porous medium flow," *SIAM Journal on Numerical Analysis*, vol. 46, no. 4, pp. 2133–2152, 2008.
- [23] H. Wang, W. Zhao, and M. S. a. Espedal, "A component-based Eulerian-Lagrangian formulation for multicomponent multiphase compositional flow and transport in porous media," *SIAM Journal on Scientific Computing*, vol. 35, no. 2, pp. B462–B486, 2013.
- [24] B. Li and W. Sun, "Unconditional convergence and optimal error estimates of a Galerkin-mixed FEM for incompressible miscible flow in porous media," *SIAM Journal on Numerical Analysis*, vol. 51, no. 4, pp. 1959–1977, 2013.
- [25] J. G. Wang, A. Kabir, J. Liu, and Z. Chen, "Effects of non-Darcy flow on the performance of coal seam gas wells," *International Journal of Coal Geology*, vol. 93, pp. 62–74, 2012.
- [26] E. Ranjbar, H. Hassanzadeh, and Z. Chen, "Semianalytical solutions for release of fluids from rock matrix blocks with different shapes, sizes, and depletion regimes," *Water Resources Research*, vol. 49, no. 4, pp. 2174–2196, 2013.
- [27] J. Yao, D. Fan, C. Wang, and K. Zhang, "Dynamic pressure analysis of horizontal wells in low permeability reservoirs with the effect of quadratic gradient term," *Acta Petrolei Sinica*, vol. 32, no. 3, pp. 479–483, 2011.

Research Article

Characteristic Value Method of Well Test Analysis for Horizontal Gas Well

Xiao-Ping Li,¹ Ning-Ping Yan,^{1,2} and Xiao-Hua Tan¹

¹ State Key Laboratory of Oil and Gas Reservoir Geology and Exploitation, Southwest Petroleum University, Xindu Road 8, Chengdu 610500, China

² No. 1 Gas Production Plant of PetroChina Changqing Oilfield Company, Yinchuan 750006, China

Correspondence should be addressed to Xiao-Hua Tan; xiaohua-tan@163.com

Received 16 May 2014; Accepted 28 July 2014; Published 25 September 2014

Academic Editor: Kim M. Liew

Copyright © 2014 Xiao-Ping Li et al. This is an open access article distributed under the Creative Commons Attribution License, which permits unrestricted use, distribution, and reproduction in any medium, provided the original work is properly cited.

This paper presents a study of characteristic value method of well test analysis for horizontal gas well. Owing to the complicated seepage flow mechanism in horizontal gas well and the difficulty in the analysis of transient pressure test data, this paper establishes the mathematical models of well test analysis for horizontal gas well with different inner and outer boundary conditions. On the basis of obtaining the solutions of the mathematical models, several type curves are plotted with Stehfest inversion algorithm. For gas reservoir with closed outer boundary in vertical direction and infinite outer boundary in horizontal direction, while considering the effect of wellbore storage and skin effect, the pseudopressure behavior of the horizontal gas well can manifest four characteristic periods: pure wellbore storage period, early vertical radial flow period, early linear flow period, and late horizontal pseudoradial flow period. For gas reservoir with closed outer boundary both in vertical and horizontal directions, the pseudopressure behavior of the horizontal gas well adds the pseudosteady state flow period which appears after the boundary response. For gas reservoir with closed outer boundary in vertical direction and constant pressure outer boundary in horizontal direction, the pseudopressure behavior of the horizontal gas well adds the steady state flow period which appears after the boundary response. According to the characteristic lines which are manifested by pseudopressure derivative curve of each flow period, formulas are developed to obtain horizontal permeability, vertical permeability, skin factor, reservoir pressure, and pore volume of the gas reservoir, and thus the characteristic value method of well test analysis for horizontal gas well is established. Finally, the example study verifies that the new method is reliable. Characteristic value method of well test analysis for horizontal gas well makes the well test analysis process more simple and the results more accurate.

1. Introduction

Recent years have seen the ever-growing application of horizontal wells technology, which aroused considerable interest in the exploration of horizontal well test analysis [1–4]. In order to surmount the challenges in estimating horizontal well productivity and parameters, analytical solutions for interpreting transient pressure behavior of horizontal wells have attracted great attention.

Numerous studies on the pressure transient analysis of horizontal wells have been documented extensively in the literature. Combined with Newman's product method, Gringarten and Ramey [5] found an access to solve the

unsteady-flow problems in reservoirs by means of the use of source and Green's function. Clonts and Ramey [6] presented an analytical solution for interpreting the transient pressure behavior of horizontal drain holes located in the heterogeneous reservoir. On the basis of finite Fourier transforms, Goode and Thambynayagam [7] addressed a solution for horizontal wells with infinite-conductivity in the semi-infinite reservoir. Ozkan and Rajagopal [8] demonstrated a derivative approach to analyze the pressure-transient behavior of horizontal wells, which revealed the relationship between the dimensionless well length and the horizontal-well pressure responses. Odeh and Babu [9] indicated that four significant flow periods could be

observed during the process of horizontal well transient pressure behavior, which was further consolidated by the buildup and drawdown equations. Thompson and Temeng [10] introduced the automatic type curve matching method in analyzing multirate horizontal well pressure transient data through nonlinear regression analysis techniques. Raha-van et al. [11] employed a mathematical model to identify the features of pressure responses of a horizontal well with multiple fractures. Equipped with Laplace transformation and boundary element method, Zerzar and Bettam [12] addressed an analytical model for horizontal wells with finite conductivity vertical fractures. By extrapolating the transient pressure data, a simplified approach to predict well production was presented by Whittle et al. [13].

Owing to the imperfection of common well test analysis methods including the semilog data plotting analysis technique [14, 15], type curve matching analysis method [16, 17], and automatic fitting analysis method [18], it is inconvenient to apply those methods during the process of analyzing and determining reservoir parameters. Therefore, this paper presents the characteristic value method of well test analysis for horizontal gas well for the sake of overcoming conventional limitations. This method involves two steps. The first step is to develop formulas to calculate gas reservoir fluid flow parameters according to the characteristic lines manifested by pseudopressure derivative curves of each flowing period. The next step is to utilize these formulas to complete the well test analysis for horizontal gas well by means of combining the measured pressure with the pseudopressure derivative curve. The characteristic value method of well test analysis for horizontal gas well enriches and develops the well test analysis theory and method.

2. Mathematical Models and Solutions of Well Test Analysis for Horizontal Gas Well

The hypothesis: the formation thickness is h , the initial formation pressure of gas reservoir is p_i and equal everywhere, the gas reservoir is anisotropic, the horizontal permeability is K_h , the vertical permeability is K_v , horizontal section length is $2L$, and the position of horizontal section in the gas reservoir which is parallel to the closed top and bottom boundary is z_w . The surface flow rate of horizontal gas well is q_{sc} and assumed to be constant. Single-phase compressible gas flow obeys Darcy law and the effect of gravity and capillary pressure is ignored. The physical model of horizontal gas well seepage is illustrated in Figure 1.

Considering the complexity of the seepage flow mechanism of horizontal gas well and in order to make the mathematical model's solving and calculation more simple, the establishment of mathematical models are divided into two parts: one is to ignore the effect of wellbore storage and skin effect; the other is to consider the effect of wellbore storage and skin effect [19, 20].

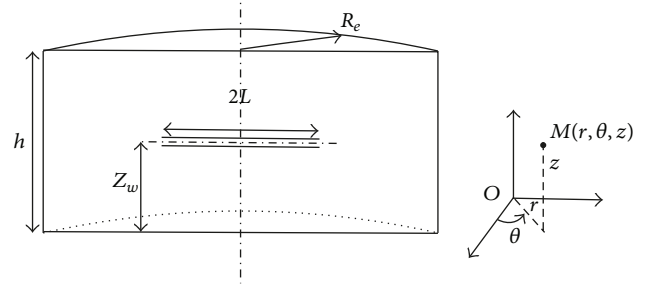


FIGURE 1: Physical model of horizontal gas well seepage.

2.1. The Mathematical Models without Considering the Effect of Wellbore Storage and Skin. The diffusivity equation is expressed by Ozkan and Raghavan [21]:

$$\frac{1}{r_D} \frac{\partial}{\partial r_D} \left(r_D \frac{\partial m_D}{\partial r_D} \right) + L_D^2 \frac{\partial^2 m_D}{\partial z_D^2} = (h_D L_D)^2 \frac{\partial m_D}{\partial t_D}. \quad (1)$$

Initial condition is

$$m_D(r_D, 0) = 0. \quad (2)$$

Inner boundary condition is

$$\lim_{\varepsilon \rightarrow 0} \left[\lim_{r_D \rightarrow 0} \int_{z_{wD}-\varepsilon/2}^{z_{wD}+\varepsilon/2} r_D \frac{\partial m_D}{\partial r_D} dz_{wD} \right] = \begin{cases} 0, & z_D > \left(z_{wD} + \frac{\varepsilon}{2} \right) \\ -\frac{1}{2}, & \left(z_{wD} + \frac{\varepsilon}{2} \right) \geq z_D \geq \left(z_{wD} - \frac{\varepsilon}{2} \right) \\ 0, & z_D < \left(z_{wD} - \frac{\varepsilon}{2} \right), \end{cases} \quad (3)$$

where ε is a tiny variable.

Infinite outer boundary condition in horizontal direction is

$$\lim_{r_D \rightarrow \infty} m_D(r_D, t_D) = 0. \quad (4)$$

Closed outer boundary condition in horizontal direction is

$$\left. \frac{\partial m_D}{\partial r_D} \right|_{r_D=r_{eD}} = 0. \quad (5)$$

Constant pressure outer boundary condition in horizontal direction is

$$m_D|_{r_D=r_{eD}} = 0. \quad (6)$$

Closed outer boundary conditions in vertical direction are

$$\left. \frac{\partial m_D}{\partial z_D} \right|_{z_D=1} = 0, \quad \left. \frac{\partial m_D}{\partial z_D} \right|_{z_D=0} = 0. \quad (7)$$

The dimensionless variables are defined as follows:

$$\begin{aligned} m_D &= \frac{78.489 K_h h}{q_{sc} T} (m_i - m), & t_D &= \frac{3.6 K_h t}{\phi \mu c_t r_w^2}, \\ L_D &= \frac{L}{h} \sqrt{\frac{K_v}{K_h}}, & h_D &= \frac{h}{r_w} \sqrt{\frac{K_h}{K_v}}, \\ z_D &= \frac{z}{h}, & z_{rD} &= z_{wD} + r_{wD} L_D, \\ z_{wD} &= \frac{z_w}{h}, & r_D &= \frac{r}{L}, \\ r_{eD} &= \frac{r_e}{L}, & r_{wD} &= \frac{r_w}{L}. \end{aligned} \quad (8)$$

The defined gas pseudopressure is

$$m(p) = 2 \int_{p_{ref}}^p \frac{p}{\mu(p) Z(p)} dp. \quad (9)$$

2.2. The Mathematical Model with Considering the Effect of Wellbore Storage and Skin. According to Duhamel's principle [22] and the superposition principle, while using the definition of dimensionless variables, the mathematical model of horizontal gas well with considering the effect of wellbore storage and skin is derived as follows:

$$\begin{aligned} m_{wD} &= m_D + \int_0^{t_D} C_D \frac{dm_{wD}}{d\tau_D} \frac{dm_{wD}(\tau_D - t_D)}{d\tau_D} d\tau_D \\ &+ \left(1 - C_D \frac{dm_{wD}}{d\tau_D}\right) h_D S, \end{aligned} \quad (10)$$

where

$$C_D = \frac{C}{2\pi\phi C_t h L^2}. \quad (11)$$

2.3. The Solutions of the Mathematical Models. The solutions of the mathematical models [23, 24] at various outer boundary conditions can be obtained by applying source function and integral transform and taking the Laplace transform to \bar{s} with respect to t_D .

For gas reservoir with closed outer boundary in vertical direction and infinite outer boundary in horizontal direction, according to (1), (2), (3), (4), and (7), the dimensionless bottomhole pseudopressure of horizontal gas well in the Laplace space can be obtained. This results in

$$\begin{aligned} \bar{m}_D &= \frac{1}{2\bar{s}} \left\{ \int_{-1}^1 K_0 \left(\sqrt{(x_D - \alpha)^2} \varepsilon_0 \right) d\alpha \right. \\ &+ 2 \sum_{n=1}^{\infty} \int_{-1}^1 K_0 \left(\sqrt{(x_D - \alpha)^2} \varepsilon_n \right) \cos(\beta_n z_{rD}) \\ &\quad \times \cos(\beta_n z_{wD}) d\alpha \Big\}, \end{aligned} \quad (12)$$

where

$$\begin{aligned} \beta_n &= n\pi, \\ \varepsilon_n &= \sqrt{\bar{s}(h_D L_D)^2 + \beta_n L_D^2}. \end{aligned} \quad (13)$$

For gas reservoir with closed outer boundary both in vertical and horizontal direction, according to (1), (2), (3), (5), and (7), the dimensionless bottomhole pseudopressure of horizontal gas well in the Laplace space can be obtained. This results in

$$\begin{aligned} \bar{m}_D &= \frac{1}{2\bar{s}} \left\{ \int_{-1}^1 K_0 \left(\sqrt{(x_D - \alpha)^2} \varepsilon_0 \right) d\alpha \right. \\ &+ \frac{K_1(r_{eD} \varepsilon_0)}{I_1(r_{eD} \varepsilon_0)} \int_{-1}^1 I_0 \left(\sqrt{(x_D - \alpha)^2} \varepsilon_0 \right) d\alpha \\ &+ 2 \sum_{n=1}^{\infty} \left[\int_{-1}^1 K_0 \left(\sqrt{(x_D - \alpha)^2} \varepsilon_n \right) d\alpha \right. \\ &+ \frac{K_1(r_{eD} \varepsilon_n)}{I_1(r_{eD} \varepsilon_n)} \int_{-1}^1 I_0 \left(\sqrt{(x_D - \alpha)^2} \varepsilon_n \right) d\alpha \\ &\quad \left. \left. \cdot \cos(\beta_n z_{rD}) \cos(\beta_n z_{wD}) \right] \right\}. \end{aligned} \quad (14)$$

For gas reservoir with closed outer boundary in vertical direction and constant pressure outer boundary in horizontal direction, according to (1), (2), (3), (6), and (7), the dimensionless bottomhole pseudopressure of horizontal gas well in Laplace space can be obtained. This results in

$$\begin{aligned} \bar{m}_D &= \frac{1}{2\bar{s}} \left\{ \int_{-1}^1 K_0 \left(\sqrt{(x_D - \alpha)^2} \varepsilon_0 \right) d\alpha \right. \\ &- \frac{K_0(r_{eD} \varepsilon_0)}{I_0(r_{eD} \varepsilon_0)} \int_{-1}^1 I_0 \left(\sqrt{(x_D - \alpha)^2} \varepsilon_0 \right) d\alpha \\ &+ 2 \sum_{n=1}^{\infty} \left[\int_{-1}^1 K_0 \left(\sqrt{(x_D - \alpha)^2} \varepsilon_n \right) d\alpha \right. \\ &- \frac{K_0(r_{eD} \varepsilon_n)}{I_0(r_{eD} \varepsilon_n)} \int_{-1}^1 I_0 \left(\sqrt{(x_D - \alpha)^2} \varepsilon_n \right) d\alpha \\ &\quad \left. \left. \cdot \cos(\beta_n z_{rD}) \cos(\beta_n z_{wD}) \right] \right\}. \end{aligned} \quad (15)$$

Making the Laplace transform to \bar{s} with respect to t_D/C_D , (10) can be solved for the dimensionless bottomhole pseudopressure of horizontal gas well considering the effect of wellbore storage and skin in the Laplace space. This results in

$$\bar{m}_{wD} = \frac{\bar{s} \bar{m}_D + h_D S}{\bar{s} + \bar{s}^2 (\bar{s} \bar{m}_D + h_D S)} = \frac{1}{\bar{s} (\bar{s} + 1/(\bar{s} \bar{m}_D + h_D S))}. \quad (16)$$

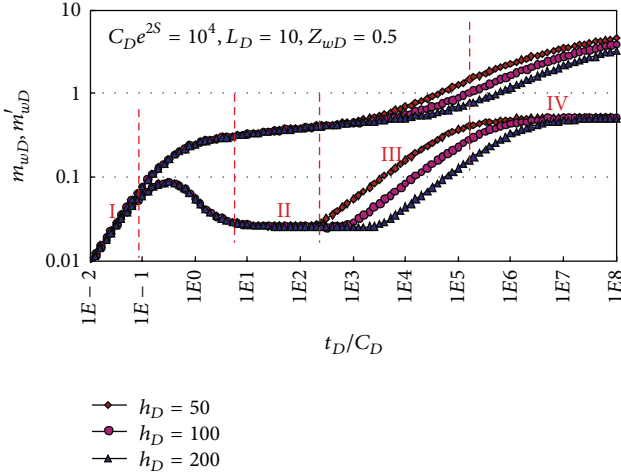


FIGURE 2: Well test analysis type curve of horizontal well in gas reservoir with infinite outer boundary.

3. Type Curves of Well Test Analysis for Horizontal Gas Well

3.1. Gas Reservoir with Infinite Outer Boundary in Horizontal Direction. For gas reservoir with infinite outer boundary in horizontal direction, according to (12) which is the solution of horizontal well seepage mathematical model, while combining with (16), the type curve of well test analysis for horizontal gas well can be plotted with Stehfest inversion algorithm, as shown in Figure 2.

As seen from Figure 2, for gas reservoir with infinite outer boundary in horizontal direction, the pseudopressure behavior of horizontal gas well can manifest four characteristic periods: pure wellbore storage period (I), early vertical radial flow period (II), early linear flow period (III), and late horizontal pseudoradial flow period (IV).

3.1.1. Pure Wellbore Storage Period. The characteristic of pure wellbore storage period of horizontal well is the same as vertical well, which is manifested as a 45° straight line segment on the log-log plot of m_{wD} , m'_{wD} versus t_D/C_D , and the duration of this period is affected by wellbore storage and skin effect.

Expressions of dimensionless bottomhole pseudopressure and pseudopressure derivative during this period can be obtained. This results in

$$m_{wD} = \frac{t_D}{C_D}, \quad (17)$$

$$m'_{wD} = \frac{dm_{wD}}{d \ln(t_D/C_D)} = \frac{t_D}{C_D}.$$

3.1.2. Early Vertical Radial Flow Period. The early vertical radial flow period appears after the effect of wellbore storage; the characteristic of this period is manifested as a horizontal straight line segment on the log-log plot of m'_{wD} versus t_D/C_D . The pseudopressure behavior of this period is affected by formation thickness, horizontal section length, and the

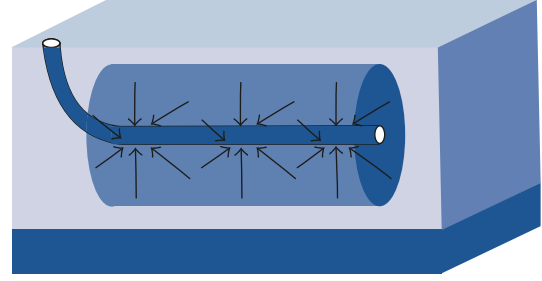


FIGURE 3: The schematic diagram of early vertical radial flow.

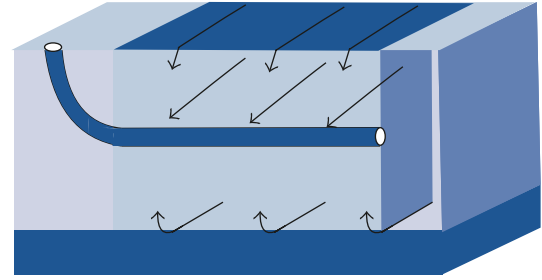


FIGURE 4: The schematic diagram of early linear flow.

position of horizontal section in the gas reservoir. The flow regime of this period is shown in Figure 3.

Expressions of dimensionless bottomhole pseudopressure and pseudopressure derivative during this period can be obtained. This results in

$$m_{wD} = \frac{1}{4L_D} \left[\ln 2.25 \left(\frac{t_D}{C_D} \right) + \ln C_D e^{2S} \right], \quad (18)$$

$$m'_{wD} = \frac{dm_{wD}}{d \ln(t_D/C_D)} = \frac{1}{4L_D}.$$

3.1.3. Early Linear Flow Period. The early linear flow period appears after the early vertical radial flow period. The characteristic of this period is manifested as a straight line segment with a slope of 0.5 on the log-log plot of m'_{wD} versus t_D/C_D . This characteristic describes the linear flow of fluid from formation to horizontal section. The pseudopressure behavior of this period is affected by dimensionless formation thickness h_D , dimensionless horizontal section length L_D , and the position of horizontal section in the gas reservoir z_{wD} . The flow regime of this period is shown in Figure 4.

Expressions of dimensionless bottomhole pseudopressure and pseudopressure derivative during this period can be obtained. This results in

$$m_{wD} = 2r_{wD} \sqrt{\pi t_D} + S, \quad (19)$$

$$m'_{wD} = \frac{dm_{wD}}{d \ln(t_D/C_D)} = r_{wD} \sqrt{\pi t_D}.$$

3.1.4. Late Horizontal Pseudoradial Flow Period. The late horizontal pseudoradial flow period appears after the early linear flow period. The characteristic of this period is manifested

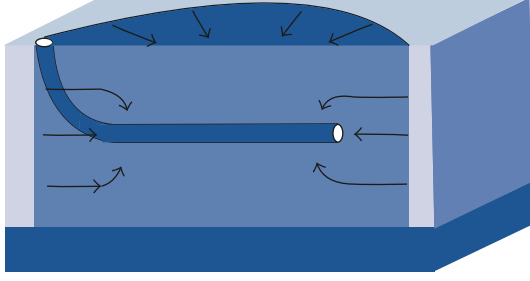


FIGURE 5: The schematic diagram of late horizontal pseudoradial flow.

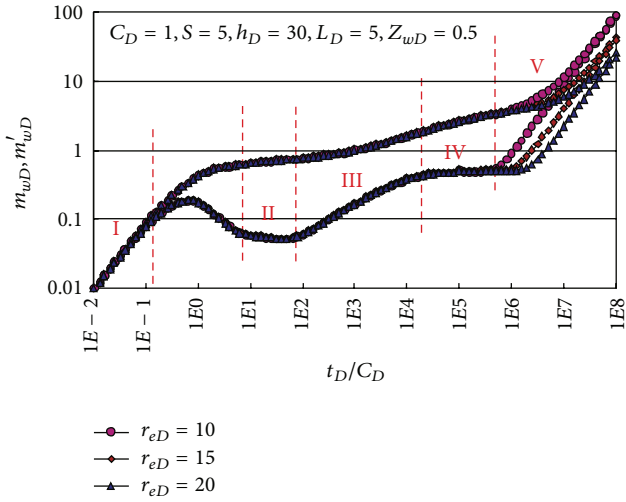


FIGURE 6: Well test analysis type curve of horizontal well in gas reservoir with closed outer boundary.

as a horizontal straight line segment with the value of 0.5 on the log-log plot of m'_{wD} versus t_D/C_D . This characteristic describes the horizontal pseudoradial flow of fluid from formation horizontal plane in the distance to horizontal section. The flow regime of this period is shown in Figure 5.

Expressions of dimensionless bottomhole pseudopressure and pseudopressure derivative during this period can be obtained. This results in

$$\begin{aligned} m_{wD} &= \frac{1}{2} \left[\ln \left(\frac{r_{wD} t_D}{C_D} \right) + \ln C_D e^{2S} \right], \\ m'_{wD} &= \frac{dm_{wD}}{d \ln(t_D/C_D)} = \frac{1}{2}. \end{aligned} \quad (20)$$

3.2. Gas Reservoir with Closed Outer Boundary in Horizontal Direction. For gas reservoir with closed outer boundary in horizontal direction, according to (14) which is the solution of horizontal well seepage mathematical model, while combining with (16), the type curve of well test analysis for horizontal gas well can be plotted with Stehfest inversion algorithm, as shown in Figure 6.

As seen from Figure 6, for gas reservoir with closed outer boundary in horizontal direction, the pseudopressure behavior of horizontal gas well can manifest five characteristic

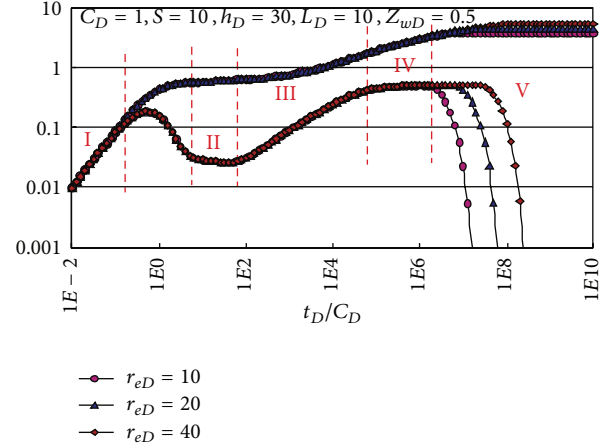


FIGURE 7: Well test analysis type curve of horizontal well in gas reservoir with constant pressure outer boundary.

periods. The previous four periods of gas reservoir with closed outer boundary are exactly the same as gas reservoir with infinite outer boundary, but the pseudopressure behavior of the horizontal gas well adds the pseudosteady state flow period (V) which appears after the boundary response. The characteristic of the pseudosteady state flow period is manifested as a straight line segment with a slope of 1 on the log-log plot of m_{wD} , m'_{wD} versus t_D/C_D . The greater the distance of the outer boundary, the later the appearance of the pseudosteady state flow period. The smaller the distance of the outer boundary, the sooner the appearance of the pseudosteady state flow period.

Expressions of dimensionless bottomhole pseudopressure and pseudopressure derivative during the pseudosteady state flow period can be obtained. This results in

$$\begin{aligned} m_{wD} &= 2\pi \left(\frac{r_{wD}}{r_{eD}} \right)^2 t_D + S, \\ m'_{wD} &= \frac{dm_{wD}}{d \ln(t_D/C_D)} = 2\pi \left(\frac{r_{wD}}{r_{eD}} \right)^2 t_D. \end{aligned} \quad (21)$$

3.3. Gas Reservoir with Constant Pressure Outer Boundary in Horizontal Direction. For gas reservoir with constant pressure outer boundary in horizontal direction, according to (15) which is the solution of horizontal well seepage mathematical model, while combining with (16), the type curve of well test analysis for horizontal gas well can be plotted with Stehfest inversion algorithm, as shown in Figure 7.

As seen from Figure 7, for gas reservoir with constant pressure outer boundary in horizontal direction, the pseudopressure behavior of horizontal gas well can manifest five characteristic periods; the previous four periods of gas reservoir with constant pressure outer boundary are exactly the same as gas reservoir with infinite outer boundary, but the pseudopressure behavior of the horizontal gas well adds the steady state flow period (V) which appears after the boundary response. The occurrence time of the steady state flow period is affected by the outer boundary distance

in horizontal direction. The smaller the distance of the outer boundary, the sooner the appearance of the steady state flow period. The greater the distance of the outer boundary, the later the appearance of the steady state flow period.

3.4. Characteristic Value Method of Well Test Analysis for Horizontal Gas Well. The characteristic value method of well test analysis for horizontal gas well can determine the gas reservoir fluid flow parameters according to the characteristic lines which are manifested by pseudopressure derivative curve of each flow period on the log-log plot.

3.4.1. Pure Wellbore Storage Period. The characteristic of pure wellbore storage period of horizontal well is manifested as a straight line segment with a slope of 1 on the log-log plot of m_{wD} , m'_{wD} versus t_D/C_D . The expression of dimensionless bottomhole pseudopressure during this period is

$$m_{wD} = \frac{t_D}{C_D}. \quad (22)$$

Equation (22) can be converted to dimensional form, and then according to the time and pressure data during pure wellbore storage period, the method to determine the wellbore storage coefficient can be obtained. By plotting the log-log plot of Δm , $\Delta m'$ versus t , the wellbore storage coefficient can be determined by the straight line segment with a slope of 1 on the log-log plot.

The following can be obtained from the definitions of dimensionless variables:

$$\frac{t_D}{C_D} = \frac{3.6K_h t / \phi \mu C_t r_w^2}{C / 2\pi \phi q_{sc} h L^2} = \frac{7.2\pi K_h h L^2}{\mu r_w^2} \frac{t}{C}. \quad (23)$$

According to (22), (23), and the definition of dimensionless pseudopressure, the wellbore storage coefficient can be obtained. This results in

$$C = \frac{0.288 q_{sc} T L^2}{\mu} \frac{t}{r_w^2 \Delta m}, \quad (24)$$

where $t/\Delta m$ represents the actual value on the log-log plot of Δm , $\Delta m'$ versus t during the pure wellbore storage period.

3.4.2. Early Vertical Radial Flow Period

The Determination of Geometric Mean Permeability. The dimensionless bottomhole pseudopressure derivative curve is manifested as a horizontal straight line segment with the value of $1/(4L_D)$ during the early vertical radial flow period. The expression of dimensionless bottomhole pseudopressure derivative during this period is

$$m'_{wD} = \frac{dm_{wD}}{d \ln(t_D/C_D)} = \frac{1}{4L_D}. \quad (25)$$

According to the definitions of dimensionless variables, the dimensional form of (25) can be obtained. This results in

$$\frac{78.489 K_h h}{q_{sc} T} (t \Delta m')_{er} = \frac{1}{4(L/h) \sqrt{K_v/K_h}}. \quad (26)$$

The geometric mean permeability of gas reservoir can be determined by (26). This results in

$$\sqrt{K_h K_v} = \frac{3.185 \times 10^{-3} q_{sc} T}{L(t \Delta m')_{er}}, \quad (27)$$

where $(t \Delta m')_{er}$ represents the actual value on the log-log plot of $\Delta m'$ versus t during the early vertical radial flow period.

The Determination of Skin Factor and Initial Reservoir Pressure. The expression of dimensionless bottomhole pseudopressure during the early vertical radial flow period is

$$m_{wD} = \frac{1}{4L_D} \left[\ln 2.25 \left(\frac{t_D}{C_D} \right) + \ln C_D e^{2S} \right]. \quad (28)$$

According to the definitions of dimensionless variables and (28), the skin factor can be obtained. This results in

$$S = 0.5 \left[\frac{\Delta m_{er}}{(t \Delta m')_{er}} - \ln \frac{K_h t_{er}}{\phi \mu C_t r_w^2} - 0.80907 \right], \quad (29)$$

where Δm_{er} and t_{er} represent the pseudopressure difference and time corresponding to the $(t \Delta m')_{er}$, respectively.

For pressure buildup analysis, when $\Delta t \rightarrow \infty$, the $\ln \Delta t / (\Delta t + t_p) \rightarrow 0$, (30) can be obtained through the use of the definitions of dimensionless variables and pseudopressure difference during the early vertical radial flow period:

$$\frac{m_i - m_{wf}}{t \Delta m'} = \ln t_{pD} + 0.80907 + 2S. \quad (30)$$

The initial reservoir pseudopressure can be determined by (30). This results in

$$m_i = m_{wf} + (t \Delta m')_{er} (\ln t_{pD} + 0.80907 + 2S), \quad (31)$$

where $(t \Delta m')_{er}$ represents the actual value on the pressure buildup log-log plot of $\Delta m'$ versus t during the early vertical radial flow period.

3.4.3. Early Linear Flow Period. The dimensionless bottomhole pseudopressure derivative curve is manifested as a straight line segment with the slope of 0.5 during the early linear flow period. According to the expression of dimensionless bottomhole pseudopressure derivative during this period and the definitions of dimensionless variables, the following can be obtained:

$$\frac{78.489 K_h h}{q_{sc} T} (t \Delta m')_l = \frac{r_w}{L} \sqrt{\frac{3.6\pi K_h t}{\phi \mu C_t r_w^2}}. \quad (32)$$

The horizontal permeability of gas reservoir can be determined by (32). This results in

$$\sqrt{K_h} = \frac{4.28 \times 10^{-2} q_{sc} T}{L h \sqrt{\phi \mu C_t}} \left[\frac{\sqrt{t}}{(t \Delta m')_l} \right], \quad (33)$$

where $(t\Delta m')_l$ represents the actual value on the log-log plot of $\Delta m'$ versus t during the early linear flow period.

Combining (27) with (33), the vertical permeability can be obtained. This results in

$$\sqrt{K_v} = 7.44 \times 10^{-2} h \sqrt{\phi \mu C_t} \frac{[(t\Delta m')/\sqrt{t}]_l}{(t\Delta m')_{er}}. \quad (34)$$

3.4.4. Late Horizontal Pseudoradial Flow Period. The dimensionless bottomhole pseudopressure derivative curve is manifested as a horizontal straight line segment with the value of 0.5 during the late horizontal pseudoradial flow period. According to the expression of dimensionless bottomhole pseudopressure derivative during this period and the definitions of dimensionless variables, (35) can be obtained:

$$\frac{78.489 K_h h}{q_{sc} T} (t\Delta m')_{lr} = 0.5. \quad (35)$$

The horizontal permeability of gas reservoir can be determined by (35). This results in

$$K_h = \frac{6.37 \times 10^{-3} q_{sc} T}{h(t\Delta m')_{lr}}, \quad (36)$$

where $(t\Delta m')_{lr}$ represents the actual value on the log-log plot of $\Delta m'$ versus t during the late horizontal pseudoradial flow period.

For pressure buildup analysis, when $\Delta t \rightarrow \infty$, the $\ln \Delta t / (\Delta t + t_p) \rightarrow 0$, (37) can be obtained through the use of the definitions of dimensionless variables and pseudopressure difference during the late horizontal pseudoradial flow period:

$$\frac{m_i - m_{wf}}{(t\Delta m')_{lr}} = \ln r_{wD} t_{pD} + 0.80907 + 2S. \quad (37)$$

The initial reservoir pseudopressure can be determined by (37). This results in

$$m_i = m_{wf} + (t\Delta m')_{lr} (\ln r_{wD} t_{pD} + 0.80907 + 2S), \quad (38)$$

where $(t\Delta m')_{lr}$ represents the actual value on the pressure buildup log-log plot of $\Delta m'$ versus t during the late horizontal pseudoradial flow period.

3.4.5. Pseudosteady Flow Period. The dimensionless bottomhole pseudopressure derivative curve is manifested as a straight line segment with the slope of 1 during the pseudosteady flow period. According to the expression of dimensionless bottomhole pseudopressure derivative during this period and the definitions of dimensionless variables, (39) can be obtained:

$$\frac{78.489 K_h h}{q_{sc} T} (t\Delta m')_{pp} = \frac{7.2 \pi K_h t_{pp}}{r_e^2 h \phi \mu C_t}. \quad (39)$$

The pore volume of gas reservoir can be determined by (39). This results in

$$\pi r_e^2 h \phi = \frac{0.905 q_{sc} T}{h \mu C_t} \frac{t_{pp}}{(t\Delta m')_{pp}}, \quad (40)$$

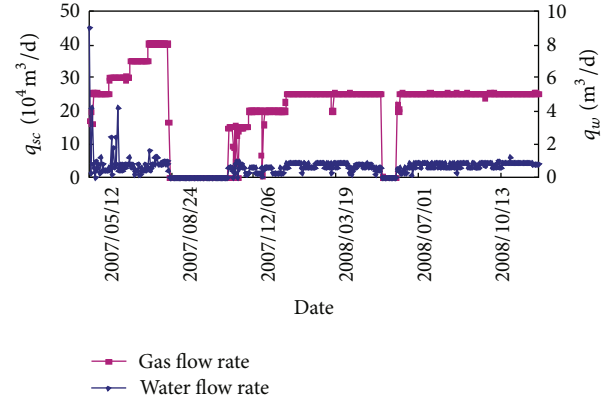


FIGURE 8: The gas flow rate and water flow rate curve of Longping 1 well.

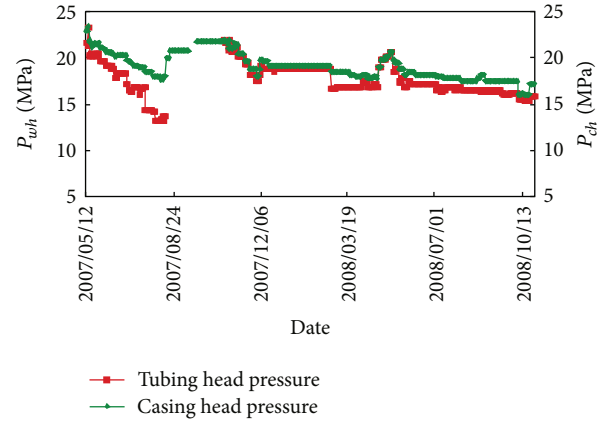


FIGURE 9: The tubing head pressure and casing head pressure curve of Longping 1 well.

where $(t\Delta m')_{pp}$ represents the actual value on the log-log plot of $\Delta m'$ versus t during the pseudosteady flow period.

4. Example Analysis

The Longping 1 well is a horizontal development well in JingBian gas field, the well total depth is 4672 m, the drilled formation name is Majiagou group, the mid-depth of reservoir is 3425.63 m, and the well completion system is screen completion. According to the deliverability test during 26–29 December, 2006, the calculated absolute open flow was $94.26 \times 10^4 \text{ m}^3/\text{d}$. The commissioning data of Longping 1 well was in 12 May, 2007, the initial formation pressure was 29.39 MPa, before production, and the surface tubing pressure and casing pressure were both 23.90 MPa. The production performance curves of Longping 1 well are shown in Figures 8 and 9, respectively.

Longping 1 well has been conducted pressure buildup test during 14 August, 2007, and 23 October, 2007. The gas flow rate of Longping 1 well was $40 \times 10^4 \text{ m}^3/\text{d}$ before the shut-in. The bottomhole pressure recovered from 22.38 MPa to 27.83 MPa during the pressure buildup test. Physical

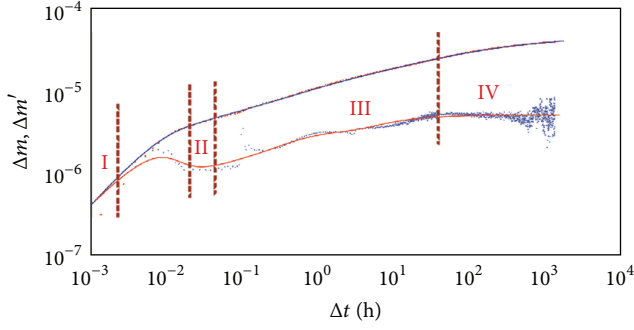


FIGURE 10: The pressure buildup log-log plot of Longping 1 well.

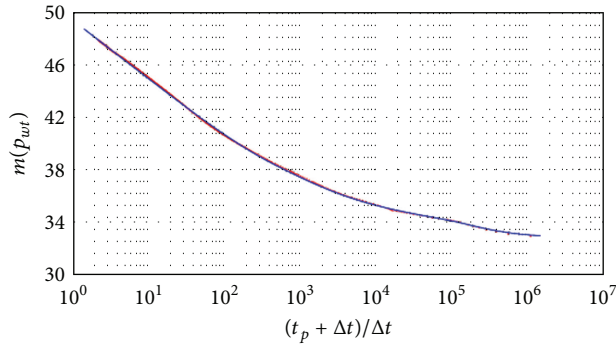


FIGURE 11: The pressure buildup semilog plot of Longping 1 well.

TABLE 1: Physical parameters of fluid and reservoir.

Parameter	Value
Initial formation pressure p_i (MPa)	29.39
Formation temperature T (°C)	95.80
Formation thickness h (m)	6.31
Porosity ϕ (%)	7.77
Initial water saturation S_{wi} (%)	13.60
Well radius r_w (m)	0.0797
Gas gravity γ_g	0.608
Gas deviation factor Z	0.9738
Gas viscosity μ_g (mPa·s)	0.0222

TABLE 2: Well test analysis results of Longping 1 well.

Parameter	Parameter values
Wellbore storage coefficient C (m ³ /MPa)	1.229
Horizontal permeability K_h (mD)	7.742
Vertical permeability K_v (mD)	0.039
Flow capacity $K_h h$ (mD·m)	48.857
Skin factor S	-2.49
Effective horizontal section length L (m)	198.37
Reservoir pressure p_R (MPa)	28.385

parameters of fluid and reservoir are shown in Table 1. The pressure buildup log-log plot of Longping 1 well is shown in Figure 10.

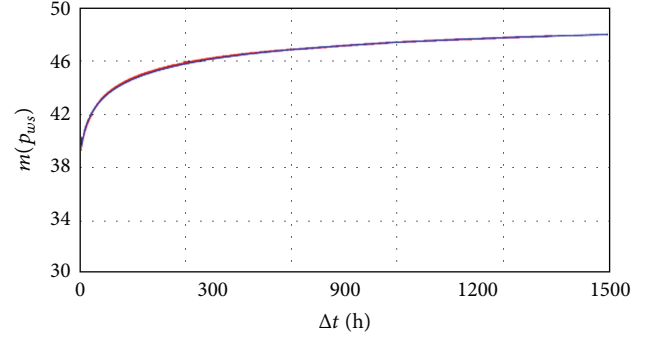


FIGURE 12: The pressure history matching plot of Longping 1 well.

As seen from the contrast between Figure 10 and well test analysis type curves of horizontal well, the pseudopressure behavior of Longping 1 well manifests four characteristic periods during the pressure buildup test: pure wellbore storage period (I), early vertical radial flow period (II), early linear flow period (III), and late horizontal pseudoradial flow period (IV).

Using the above characteristic value method of well test analysis for horizontal gas well, well test analysis results of Longping 1 well are shown in Table 2. The pressure buildup semilog plot and pressure history matching plot of Longping 1 well are shown in Figures 11 and 12, respectively.

5. Summary and Conclusions

The four main conclusions and summary of this study are as follows.

- (1) On the basis of establishing the mathematical models of well test analysis for horizontal gas well and obtaining the solutions of the mathematical models, several type curves which can be used to identify flow regime have been plotted and the seepage characteristic of horizontal gas well has been analyzed.
- (2) The expressions of dimensionless bottomhole pseudopressure and pseudopressure derivative during each characteristic period of horizontal gas well have been obtained; formulas have been developed to calculate gas reservoir fluid flow parameters.
- (3) The example study verifies that the characteristic value method of well test analysis for horizontal gas well is reliable and practical.
- (4) The characteristic value method of well test analysis, which has been included in the well test analysis software at present, has been widely used in vertical well. As long as the characteristic straight line segments which are manifested by pressure derivative curve appear, the reservoir fluid flow parameters can be calculated by the characteristic value method of well test analysis for vertical well. The proposed characteristic value method of well test analysis for

horizontal gas well enriches and develops the well test analysis theory and method.

Nomenclature

C :	Wellbore storage coefficient, m^3/MPa
C_D :	Dimensionless wellbore storage coefficient
C_t :	Total compressibility, MPa^{-1}
h :	Reservoir thickness, m
h_D :	Dimensionless reservoir thickness
I_n :	Modified Bessel function of first kind of order n
K_h :	Horizontal permeability, mD
K_n :	Modified Bessel function of second kind of order n
K_V :	Vertical permeability, mD
L :	Horizontal section length, m
L_D :	Dimensionless horizontal section length
$m(p)$:	Pseudopressure, $\text{MPa}^2/\text{mPa}\cdot\text{s}$
m_D :	Dimensionless pseudopressure
m_i :	Initial formation pseudopressure, $\text{MPa}^2/\text{mPa}\cdot\text{s}$
m_{wD} :	Dimensionless bottomhole pseudopressure
m_{wf} :	Flowing wellbore pseudopressure, $\text{MPa}^2/\text{mPa}\cdot\text{s}$
m'_{wD} :	Derivative of m_{wD}
\bar{m}_D :	Laplace transform of m_D
\bar{m}_{wD} :	Laplace transform of m_{wD}
Δm :	Pseudopressure difference, MPa
$\Delta m'$:	Derivative of Δm
p_{ch} :	Casing head pressure, MPa
p_i :	Initial formation pressure, MPa
p_R :	Reservoir pressure, MPa
p_{wh} :	Tubing head pressure, MPa
p_{ws} :	Flowing wellbore pressure at shut-in, MPa
q_{sc} :	Gas flow rate, $10^4 \text{ m}^3/\text{d}$
q_w :	Water production rate, m^3/d
r :	Radial distance, m
r_D :	Dimensionless radial distance
r_e :	Outer boundary distance, m
r_{eD} :	Dimensionless outer boundary distance
r_w :	Wellbore radius, m
r_{wD} :	Dimensionless wellbore radius
S :	Skin factor
\bar{s} :	Laplace transform variable
S_{wi} :	Initial water saturation, fraction
t :	Time, hours
t_D :	Dimensionless time
t_p :	Production time, hours
t_{pD} :	Dimensionless production time
Δt :	Shut-in time, hours
T :	Formation temperature, $^{\circ}\text{C}$
z :	Vertical distance, m
z_D :	Dimensionless vertical distance
z_w :	Horizontal section position, m
z_{wD} :	Dimensionless horizontal section position
Z :	Gas deviation factor
ε :	Tiny variable
ϕ :	Porosity, fraction
μ :	Gas viscosity, $\text{mPa}\cdot\text{s}$
γ_g :	Gas gravity.

Subscripts

D :	Dimensionless
er :	Early
erb :	Early of buildup
h :	Horizontal
i :	Initial
l :	Linear
lr :	Late horizontal pseudo-radial
lrb :	Late horizontal pseudo-radial of buildup
pp :	Pseudosteady flow period
t :	Total
v :	Vertical
wf :	Flowing wellbore
ws :	Shut-in wellbore.

Conflict of Interests

The authors declare that there is no conflict of interests regarding the publication of this paper.

References

- [1] R. S. Nie, J. C. Guo, Y. L. Jia, S. Q. Zhu, Z. Rao, and C. G. Zhang, "New modelling of transient well test and rate decline analysis for a horizontal well in a multiple-zone reservoir," *Journal of Geophysics and Engineering*, vol. 8, no. 3, pp. 464–476, 2011.
- [2] D. R. Yuan, H. Sun, Y. C. Li, and M. Zhang, "Multi-stage fractured tight gas horizontal well test data interpretation study," in *Proceedings of the International Petroleum Technology Conference*, March 2013.
- [3] M. Mavaddat, A. Soleimani, M. R. Rasaei, Y. Mavaddat, and A. Momeni, "Well test analysis of Multiple Hydraulically Fractured Horizontal Wells (MHFW) in gas condensate reservoirs," in *Proceedings of the SPE/LADC Middle East Drilling Technology Conference and Exhibition (MEDT '11)*, pp. 39–48, October 2011.
- [4] M. Mirza, P. Aditama, M. AL Raqmi, and Z. Anwar, "Horizontal well stimulation: a pilot test in southern Oman," in *Proceedings of the SPE EOR Conference at Oil and Gas West Asia*, April 2014.
- [5] A. C. Gringarten and H. J. Ramey Jr., "The use of source and green's function in solving unsteady-flow problem in reservoir," *Society of Petroleum Engineers Journal*, vol. 13, no. 5, pp. 285–296, 1973.
- [6] M. D. Clonts and H. J. Ramey, "Pressure transient analysis for wells with horizontal drainholes," in *Proceedings of the SPE California Regional Meeting*, Oakland, Calif, USA, April 1986, paper SPE 15116.
- [7] P. A. Goode and R. K. M. Thambynayagam, "Pressure drawdown and buildup analysis of horizontal wells in anisotropic media," *SPE Formation Evaluation*, vol. 2, no. 4, pp. 683–697, 1987.
- [8] E. Ozkan and R. Rajagopal, "Horizontal well pressure analysis," *SPE Formation Evaluation*, pp. 567–575, 1989.
- [9] A. S. Odeh and D. K. Babu, "Transient flow behavior of horizontal wells. Pressure drawdown and buildup analysis," *SPE Formation Evaluation*, vol. 5, no. 1, pp. 7–15, 1990.
- [10] L. G. Thompson and K. O. Temeng, "Automatic type-curve matching for horizontal wells," in *Proceedings of the Production Operation Symposium*, Oklahoma City, Okla, USA, 1993, paper SPE 25507.

- [11] R. S. Rahavan, C. C. Chen, and B. Agarwal, "An analysis of horizontal wells intercepted by multiple fractures," *SPE27652 (Sep)*, pp. 235–245, 1997.
- [12] A. Zerzar and Y. Bettam, "Interpretation of multiple hydraulically fractured horizontal wells in closed systems," in *Proceedings of the SPE International Improved Oil Recovery Conference in Asia Pacific (IIORC '03)*, pp. 295–307, Alberta, Canada, October 2003.
- [13] T. Whittle, H. Jiang, S. Young, and A. C. Gringarten, "Well production forecasting by extrapolation of the deconvolution of the well test pressure transients," in *Proceedings of the SPE EUROPEC/EAGE Conference*, Amsterdam, The Netherlands, June 2009, SPE 122299 paper.
- [14] C. C. Miller, A. B. Dyes, and C. A. Hutchinson, "The estimation of permeability and reservoir pressure from bottom-hole pressure buildup Characteristic," *Journal of Petroleum Technology*, pp. 91–104, 1950.
- [15] D. R. Horner, "Pressure buildup in wells," in *Proceedings of the 3rd World Petroleum Congress*, Hague, The Netherlands, May–June 1951, paper SPE 4135.
- [16] R. Raghavan, "The effect of producing time on type curve analysis," *Journal of Petroleum Technology*, vol. 32, no. 6, pp. 1053–1064, 1980.
- [17] D. Bourdet, "A new set of type curves simplifies well test analysis," *World Oil*, pp. 95–106, 1983.
- [18] T. M. Hegre, "Hydraulically fractured horizontal well simulation," in *Proceedings of the NPE/SPE European Production Operations Conference (EPOC '96)*, pp. 59–62, April 1996.
- [19] R. G. Agarwal, R. Al-Hussaing, and H. J. Ramey, "An investigation of wellbore storage and skin effect in unsteady liquid flow: I. Analytical treatment," *Society of Petroleum Engineers Journal*, vol. 10, no. 3, pp. 291–297, 1970.
- [20] H. J. J. Ramey and R. G. Agarwal, "Annulus unloading rates as influenced by wellbore storage and skin effect," *Society of Petroleum Engineers Journal*, vol. 12, no. 5, pp. 453–462, 1972.
- [21] E. Ozkan and R. Raghavan, "New solutions for well-test-analysis problems: part 1-analytical considerations," *SPE Formation Evaluation*, 1991.
- [22] L. G. Thompson, *Analysis of variable rate pressure data using duhamels principle [Ph.D. thesis]*, University of Tulsa, Tulsa, Okla, USA, 1985.
- [23] H. Stehfest, "Numerical inversion of laplace transforms," *Communications of the ACM*, vol. 13, no. 1, pp. 47–49, 1970.
- [24] N. Al-Ajmi, M. Ahmadi, E. Ozkan, and H. Kazemi, "Numerical inversion of laplace transforms in the solution of transient flow problems with discontinuities," in *Proceedings of the SPE Annual Technical Conference and Exhibition*, Paper SPE 116255, pp. 21–24, Denver, Colorado, 2008.

Research Article

A Smoothing Process of Multicolor Relaxation for Solving Partial Differential Equation by Multigrid Method

Xingwen Zhu^{1,2} and Lixiang Zhang¹

¹ Department of Engineering Mechanics, Kunming University of Science and Technology, Kunming, Yunnan 650500, China

² School of Mathematics and Computer, Dali University, Dali, Yunnan 671003, China

Correspondence should be addressed to Lixiang Zhang; zlxzcc@126.com

Received 24 June 2014; Accepted 26 August 2014; Published 25 September 2014

Academic Editor: Kim M. Liew

Copyright © 2014 X. Zhu and L. Zhang. This is an open access article distributed under the Creative Commons Attribution License, which permits unrestricted use, distribution, and reproduction in any medium, provided the original work is properly cited.

This paper is concerned with a novel methodology of smoothing analysis process of multicolor point relaxation by multigrid method for solving elliptically partial differential equations (PDEs). The objective was firstly focused on the two-color relaxation technique on the local Fourier analysis (LFA) and then generalized to the multicolor problem. As a key starting point of the problems under consideration, the mathematical constitutions among Fourier modes with various frequencies were constructed as a base to expand two-color to multicolor smoothing analyses. Two different invariant subspaces based on the $2h$ -harmonics for the two-color relaxation with two and four Fourier modes were constructed and successfully used in smoothing analysis process of Poisson's equation for the two-color point Jacobi relaxation. Finally, the two-color smoothing analysis was generalized to the multicolor smoothing analysis problems by multigrid method based on the invariant subspaces constructed.

1. Introduction

Multigrid methods [1–6] are generally considered as one of the fastest numerical methods for solving complex partial differential equations (PDEs), for example, Navier-Stokes equation in computational fluid dynamics (CFD). As we know, the speed of the multigrid computational convergence depends closely on the numerical properties of the underlying problem of PDEs, for example, equating type and discretizing stencil. Meanwhile, a variety of algorithms for the components in multigrid are of great importance, for example, the processing methods based on smoothing, restriction, prolongation processes, and so on. So, an appropriate choice for the available components has a great impact on the overall performance for specific problems.

Local Fourier analysis (LFA) [5, 7–12] is a very useful tool to predict asymptotic convergence factors of the multigrid methods for PDEs with high order accuracy. Therefore it is widely used to design efficient multigrid algorithms. In LFA an infinite regular grid needs to be considered and boundary conditions need to be ignored. On an infinite grid, the discrete solutions and the corresponding errors

are represented by linear combinations of certain complex exponential functions. Thus, Fourier modes are often used to form a unitary basis of the subspace of the grid functions with bounded norms [5, 7, 12]. The LFA monograph by Wienands and Joppich [11] provides an excellent background for experimenting with Fourier analysis. Recent advances in this context included LFA for triangular grids [13, 14], hexagonal meshes [15], semistructured meshes [16], multigrid with overlapping smoothers [17], multigrid with a preconditioner as parameters [18], and full multigrid method [19]. In [8], an LFA for multigrid methods on the finite element discretization of a 2D curl-curl equation with a quadrilateral grid was introduced.

A general definition on the multicolor relaxation was provided in [20]. Smoothing analysis of the two-color relaxation on LFA was given in [21–24], and the four-color relaxation with tetrahedral grids was presented in [16, 25]. In [26], a parallel multigrid method for solving Navier-Stokes equation was investigated and a multigrid Poisson equation solver was employed in [27]. A parallel successive overrelaxation (SOR) algorithm for solving the Poisson problem was discussed in [28], and multicolor SOR methods were studied in [29].

In the present paper, a novel smoothing analysis process of multicolor relaxation on LFA is provided with details. An important coupled relation among Fourier modes with various frequencies is constructed and expanded to the multicolor smoothing analysis. The roles of the Fourier modes with the high and low frequencies in the proposed method are well characterized. Thus, by the two invariant subspaces based on the $2h$ -harmonics the two-color smoothing analysis process is well generalized to the multicolor problems.

2. LFA in Multigrid

2.1. General Definition. A rigorous base of the local mode analysis in multigrid was elaborated [12]. Herein, we are following [11] as a starting point of our framework.

A generally linear scalar constant-coefficient system without boundary conditions is described with a discrete problem with infinite grid; that is,

$$L_h u_h(\vec{x}) = \sum_{\vec{n} \in J} l_{\vec{n}} u_h(\vec{x} + \vec{n} \cdot \vec{h}) = f_h(\vec{x}), \quad \vec{x} \in G_h \quad (1)$$

in which an infinite grid is stated as

$$G_h = \{ \vec{x} = (k_1 h_1, \dots, k_d h_d) \mid \vec{k} = (k_1, \dots, k_d) \in \mathbb{Z}^d \}, \quad (2)$$

where $\vec{h} = (h_1, h_2, \dots, h_d)$ is the mesh size, d denotes the dimension of \vec{x} , the discrete operator is given by

$$L_h := [l_{\vec{n}}]_h, \quad (3)$$

and $l_{\vec{n}} \in \mathbb{R}$ with $\vec{n} \in J$ is the stencil coefficients [3–5] of L_h for (2), $J \subset \mathbb{Z}^d$ containing $(0, 0, \dots, 0)$, and $\vec{n} \cdot \vec{h} \triangleq (n_1 h_1, n_2 h_2, \dots, n_d h_d)$. From [11, 20], the Fourier eigenfunctions of the constant-coefficient infinite grid operator L_h in (1) are given by

$$\varphi_h(\vec{\theta}, \vec{x}) := \prod_{j=1}^d \exp\left(\frac{i\theta_j x_j}{h_j}\right) = \exp(i\vec{\theta} \cdot \vec{k}), \quad (4)$$

where $\vec{x} \in G_h$, $\vec{\theta} = (\theta_1, \theta_2, \dots, \theta_d) \in \Theta = (-\pi, \pi]^d$ denotes the Fourier frequency, $\vec{\theta} \cdot \vec{k} \triangleq \theta_1 k_1 + \theta_2 k_2 + \dots + \theta_d k_d$, and $\varphi_h(\vec{\theta}, \vec{x})$ is called Fourier mode [3, 5, 20], which is orthogonal with respect to the scaled Euclidean inner product [3, 5, 10]. On grid (2), the corresponding eigenvalues of L_h are expressed by

$$L_h \varphi_h(\vec{\theta}, \vec{x}) = \tilde{L}_h(\vec{\theta}) \varphi_h(\vec{\theta}, \vec{x}) \quad (5)$$

with

$$\tilde{L}_h(\vec{\theta}) := \sum_{\vec{n} \in J} l_{\vec{n}} \exp(i\vec{\theta} \cdot \vec{n}) \quad (6)$$

called Fourier symbol of L_h . Further, a Fourier subspace with the bounded infinite grid function $V_h \in F(G_h)$, that is $F(G_h) \subseteq F_h$, is defined as

$$F_h := \text{span} \left\{ \varphi_h(\vec{\theta}, \vec{x}) \mid \vec{\theta} \in \Theta = (-\pi, \pi]^d \right\} \quad (7)$$

in which $\Theta_{\text{low}} = (-\pi/2, \pi/2]^d$ is referred to the low frequency and $\Theta_{\text{high}} = \Theta \setminus \Theta_{\text{low}}$ is referred to the high frequency. As a standard multigrid coarsening [11], a case of $\vec{H} = 2\vec{h}$ is considered, and infinite coarse grid G_H is stated as

$$G_H = \{ \vec{x} = (k_1 H_1, k_2 H_2, \dots, k_d H_d) \mid \vec{k} = (k_1, k_2, \dots, k_d) \in \mathbb{Z}^d \}. \quad (8)$$

2.2. Smoothing Analysis of Multigrid Relaxation. For multigrid relaxation S_h of discrete operator L_h on the infinite grid (2), if (4) are the eigenfunctions of S_h , then $\tilde{S}_h(\vec{\theta})$ is the Fourier symbol of S_h . For pattern relaxation [11], (4) are no longer the eigenfunctions of relaxation operator S_h . However, it leaves certain low-dimensional subspaces of (4) invariant yielding a block-diagonal matrix of smoothing operator consisting of small blocks. As presented in [10, 11], the $2h$ -harmonics of (4) is defined as

$$F_{2h}(\vec{\theta}) := \text{span} \left\{ \varphi_h(\vec{\theta}^{\vec{\alpha}}, \vec{x}) \mid \vec{\alpha} = (\alpha_1, \dots, \alpha_d), \alpha_m \in \{0, 1\}, m = 1, \dots, d \right\}, \quad (9)$$

where $\vec{\theta} = \vec{\theta}^{(0, \dots, 0)} \in \Theta_{\text{low}}$ and $\vec{\theta}^{\vec{\alpha}} = \vec{\theta}^{(0, \dots, 0)} - (\alpha_1 \text{sign}(\theta_1), \dots, \alpha_d \text{sign}(\theta_d))\pi$. If relaxation operator S_h satisfies

$$\begin{aligned} S_h \left(\varphi_h(\vec{\theta}^{(0, \dots, 0)}, \vec{x}), \dots, \varphi_h(\vec{\theta}^{(0, \dots, 1)}, \vec{x}) \right) \\ = \left(\varphi_h(\vec{\theta}^{(0, \dots, 0)}, \vec{x}), \dots, \varphi_h(\vec{\theta}^{(0, \dots, 1)}, \vec{x}) \right) \hat{S}_h(\vec{\theta}), \end{aligned} \quad (10)$$

that is, $S_h : F_{2h} \rightarrow F_{2h}$, the matrix $\hat{S}_h(\vec{\theta})$ is called Fourier representation of S_h . Furthermore, an idea coarse-grid correction operator Q_h^H is introduced [11] to drop out the low-frequency modes and to keep the high-frequency modes. So, it is clear that Q_h^H is a projection operator onto the subspace of the high-frequency modes

$$F_{\text{high}}(\vec{\theta}) := \text{span} \left\{ \varphi_h(\vec{\theta}, \vec{x}) \mid \vec{\theta} \in \Theta_{\text{high}} \right\}. \quad (11)$$

By the same way, a subspace of the low-frequency modes is defined as

$$F_{\text{low}}(\vec{\theta}) := \text{span} \left\{ \varphi_h(\vec{\theta}, \vec{x}) \mid \vec{\theta} \in \Theta_{\text{low}} \right\}. \quad (12)$$

Thus, a general coarsening strategy [11] is stated as

$$Q_h^H \varphi_h(\vec{\theta}, \vec{x}) := \begin{cases} \varphi_h(\vec{\theta}, \vec{x}) & \varphi_h(\vec{\theta}, \vec{x}) \in F_{\text{high}} \\ 0 & \varphi_h(\vec{\theta}, \vec{x}) \in F_{\text{low}} \end{cases} \quad (13)$$

Consequently, a smoothing factor [11] on the Fourier modes for the multigrid relaxation, $S_h(\omega)$ and Q_h^H , is yielded as

$$\rho(\nu, \omega) = \sup_{\vec{\theta} \in \Theta_{\text{low}}} \sqrt{\rho(\widehat{Q}_h^{2h} \widehat{S}_h^v(\vec{\theta}, \omega))}, \quad (14)$$

where ω is the relaxation parameter, $\nu = \nu_1 + \nu_2$ denotes the sum of pre- and postsmoothing steps, \widehat{Q}_h^H and $\widehat{S}_h(\vec{\theta}, \omega)$ are the Fourier representations of $S_h(\omega)$ and Q_h^H , respectively, and $\rho(M)$ denotes the spectral radius of the matrix M .

3. Smoothing Analysis of Two-Color Relaxation

To develop two different processes of LFA for the two-color relaxation, grid (2) is divided into two disjoint subsets G_h^R and G_h^B , referring to as the red and black points, respectively. Two process steps [11] are required to construct a complete two-color relaxation $S_h^{RB}(\omega)$. In the first step ($S_h^R(\omega)$), the unknowns located at the red points are only smoothed, whereas the unknowns at the black points remain to be unchanged. Then, in the second step ($S_h^B(\omega)$), the unknowns at the black points are changed by using the new values calculated with the red points in the first step. So, a complete red-black point process is obtained by iteration

$$S_h^{RB}(\omega) = S_h^B(\omega) S_h^R(\omega). \quad (15)$$

From the process mentioned above, it is noted that the Fourier modes (4) are no longer eigenfunctions of (15) on grid (2) because the relaxation operator is used.

3.1. Invariant Subspaces for Two-Color Relaxation. A new smoothing analysis process of the two-color relaxation is proposed with details. The proposed process is different with [11, 20–24]. A novel constitution among the Fourier modes with various frequencies is developed as a base of the smoothing analysis process. The analysis process is proved to be valuable.

The grid $G_h = \{\vec{x} = (k_1 h_1, k_2 h_2) \mid \vec{k} = (k_1, k_2) \in \mathbb{Z}^2\}$ is divided into two disjoint subsets G_h^0 and G_h^1 ; that is, $G_h = G_h^0 \cup G_h^1$ with

$$G_h^\beta = \{\vec{x} = (k_1 h_1, k_2 h_2) \mid k_1 + k_2 = \beta \bmod 2, \vec{k} \in \mathbb{Z}^2\}, \quad (16)$$

where $\beta = 0, 1$. According to (16), the subspace of the $2h$ -harmonics (9) is redefined as

$$F_{2h}^2(\vec{\theta}) := \text{span} \left\{ \varphi_h \left(\vec{\theta}^0, \vec{x} \right), \varphi_h \left(\vec{\theta}^1, \vec{x} \right) \right\} \quad (17)$$

with $\vec{\theta} = (\theta_1, \theta_2) \in \Theta_{\text{low}} = (-\pi/2, \pi/2]^2$, where $\vec{\theta}^\alpha = (\vec{\theta} + (\alpha, \alpha)\pi) \bmod 2\pi$, $\alpha = 0, 1$. Thus, the constitutions among the various Fourier modes defined by (16) and (17) are presented as follows.

Proposition 1. For $\forall \vec{x} \in G_h$, $\forall (k_1, k_2) \in \mathbb{Z}^2$, and $\forall \alpha \in \{0, 1\}$, if $\vec{\theta} \in \Theta_{\text{low}}$, then the following formulation holds:

$$\varphi_h \left(\vec{\theta}^\alpha, \vec{x} \right) = \exp[i\pi\alpha(k_1 + k_2)] \varphi_h \left(\vec{\theta}, \vec{x} \right). \quad (18)$$

Proof. From (4), for $\forall \vec{x} \in G_h$, it holds for $\varphi_h(\vec{\theta}^\alpha, \vec{x}) = \exp(i\vec{\theta}^\alpha \cdot \vec{k})$. From (17), $\exists \vec{n} = (n_1, n_2) \in \mathbb{Z}^2$ is subjected to $\vec{\theta}^\alpha = (\theta_1 + \alpha\pi, \theta_2 + \alpha\pi) + 2\pi\vec{n}$. Then

$$\vec{\theta}^\alpha \cdot \vec{k} = \vec{\theta} \cdot \vec{k} + \pi\alpha(k_1 + k_2) + 2\pi\vec{n} \cdot \vec{k} \quad (19)$$

holds. Thus,

$$\begin{aligned} \varphi_h \left(\vec{\theta}^\alpha, \vec{x} \right) &= \exp \left(i\vec{\theta}^\alpha \cdot \vec{k} \right) \\ &= \exp[i\pi\alpha(k_1 + k_2)] \exp \left(i\vec{\theta} \cdot \vec{k} \right) \\ &= \exp[i\pi\alpha(k_1 + k_2)] \varphi_h \left(\vec{\theta}, \vec{x} \right). \end{aligned} \quad (20)$$

Proposition 1 follows. \square

Proposition 2. For $\forall \alpha, \beta \in \{0, 1\}$, and $\forall \vec{x} \in G_h^\beta$, if $\vec{\theta} \in \Theta_{\text{low}}$, then the following formulation holds:

$$\varphi_h \left(\vec{\theta}^\alpha, \vec{x} \right) = \exp(i\pi\alpha\beta) \varphi_h \left(\vec{\theta}, \vec{x} \right). \quad (21)$$

Proof. By Proposition 1 and $G_h^\beta \subseteq G_h$, for $\forall \vec{x} \in G_h^\beta$, then

$$\varphi_h \left(\vec{\theta}^\alpha, \vec{x} \right) = \exp[i\pi\alpha(k_1 + k_2)] \varphi_h \left(\vec{\theta}, \vec{x} \right), \quad (22)$$

where $(k_1, k_2) \in \mathbb{Z}^2$. For $\vec{x} \in G_h^\beta$, from (16), $\exists p \in \mathbb{Z}$ is subjected to $k_1 + k_2 = \beta + 2p$; hence,

$$\begin{aligned} \varphi_h \left(\vec{\theta}^\alpha, \vec{x} \right) &= \exp[i\pi\alpha(\beta + 2p)] \varphi_h \left(\vec{\theta}, \vec{x} \right) \\ &= \exp(i\pi\alpha\beta) \varphi_h \left(\vec{\theta}, \vec{x} \right). \end{aligned} \quad (23)$$

Proposition 2 holds. \square

Subsequently, the smoothing analysis process of the two-color relaxation on the subspace of the $2h$ -harmonics (17) is conducted. By (15) and (16) and without loss of generality, let G_h^0 and G_h^1 correspond to G_h^R and G_h^B , respectively; thus (15) is rewritten as

$$S_h^{01}(\omega) = S_h^1(\omega) S_h^0(\omega). \quad (24)$$

Theorem 3. The iteration operator $S_h^{01}(\omega)$ for the two-color relaxation leaves the subspace of the $2h$ -harmonics (17) to be invariant.

Proof. From the process of the two-color relaxation, the operator $S_h^\beta(\omega)$ of grid (16) is

$$S_h^\beta(\omega) \varphi_h(\vec{\theta}, \vec{x}) = \begin{cases} \tilde{S}_h^\beta(\vec{\theta}, \omega) \varphi_h(\vec{\theta}, \vec{x}) & \forall \vec{x} \in G_h^\beta \\ \varphi_h(\vec{\theta}, \vec{x}) & \forall \vec{x} \notin G_h^\beta, \end{cases} \quad (25)$$

where $\tilde{S}_h^\beta(\vec{\theta}, \omega)$ is Fourier symbol of $S_h^\beta(\omega)$ on grid (16) with $\beta = 0, 1$. From (10) and (25), now it is proved that the subspace of the $2h$ -harmonics (17) is invariant for the iteration operator (24). Because of (17), we need to find out two complex numbers a_0 and a_1 with $\forall \alpha, \beta \in \{0, 1\}$ and make them subjected to

$$S_h^\beta(\omega) \varphi_h(\vec{\theta}^\alpha, \vec{x}) = a_0 \varphi_h(\vec{\theta}^0, \vec{x}) + a_1 \varphi_h(\vec{\theta}^1, \vec{x}). \quad (26)$$

From (25), the right hand side of (26) is written as

$$S_h^\beta(\omega) \varphi_h(\vec{\theta}^\alpha, \vec{x}) = \begin{cases} \tilde{S}_h^\beta(\vec{\theta}^\alpha, \omega) \varphi_h(\vec{\theta}^\alpha, \vec{x}) & \forall \vec{x} \in G_h^\beta \\ \varphi_h(\vec{\theta}^\alpha, \vec{x}) & \forall \vec{x} \notin G_h^\beta. \end{cases} \quad (27)$$

By Propositions 1 and 2, the right hand side of (27) is expressed as

$$S_h^\beta(\omega) \varphi_h(\vec{\theta}^\alpha, \vec{x}) = \begin{cases} \tilde{S}_h^\beta(\vec{\theta}^\alpha, \omega) \exp(i\alpha\beta\pi) \varphi_h(\vec{\theta}, \vec{x}) & \forall \vec{x} \in G_h^\beta \\ \exp[i\alpha(1-\beta)\pi] \varphi_h(\vec{\theta}, \vec{x}) & \forall \vec{x} \notin G_h^\beta. \end{cases} \quad (28)$$

Taking $A_\alpha^\beta = \tilde{S}_h^\beta(\vec{\theta}^\alpha, \omega)$, (28) is written as

$$S_h^\beta(\omega) \varphi_h(\vec{\theta}^\alpha, \vec{x}) = \begin{cases} A_\alpha^\beta \exp(i\alpha\beta\pi) \varphi_h(\vec{\theta}, \vec{x}) & \forall \vec{x} \in G_h^\beta \\ \exp[i\alpha(1-\beta)\pi] \varphi_h(\vec{\theta}, \vec{x}) & \forall \vec{x} \notin G_h^\beta. \end{cases} \quad (29)$$

From Propositions 1 and 2, the left hand side of (26) is written as

$$a_0 \varphi_h(\vec{\theta}^0, \vec{x}) + a_1 \varphi_h(\vec{\theta}^1, \vec{x}) = \begin{cases} (a_0 + a_1 \exp(i\beta\pi)) \varphi_h(\vec{\theta}, \vec{x}) & \vec{x} \in G_h^\beta \\ (a_0 + a_1 \exp[i(1-\beta)\pi]) \varphi_h(\vec{\theta}, \vec{x}) & \vec{x} \notin G_h^\beta. \end{cases} \quad (30)$$

Hence, from (26), (29), and (30), a set of two linear equations on a_0 and a_1 is given as

$$\begin{aligned} a_0 + a_1 \exp(i\beta\pi) &= A_\alpha^\beta \exp(i\alpha\beta\pi) \\ a_0 + a_1 \exp[i(1-\beta)\pi] &= \exp[i\alpha(1-\beta)\pi], \end{aligned} \quad (31)$$

where $\alpha, \beta \in \{0, 1\}$. Therefore, from (31), it is concluded that there exist two complex numbers a_0 and a_1 that are subjected to (26). From (10), (17), and (26), solving linear equation (31), the Fourier representations of the iteration operators $S_h^0(\omega)$ and $S_h^1(\omega)$ are obtained as

$$\begin{aligned} \tilde{S}_h^0(\vec{\theta}, \omega) &= \frac{1}{2} \begin{pmatrix} A_0^0 + 1 & A_1^0 - 1 \\ A_0^0 - 1 & A_1^0 + 1 \end{pmatrix}, \\ \tilde{S}_h^1(\vec{\theta}, \omega) &= \frac{1}{2} \begin{pmatrix} A_0^1 + 1 & -A_1^1 + 1 \\ -A_0^1 + 1 & A_1^1 + 1 \end{pmatrix}, \end{aligned} \quad (32)$$

where $A_\alpha^\beta = \tilde{S}_h^\beta(\vec{\theta}^\alpha, \omega)$ and $\alpha, \beta \in \{0, 1\}$. Furthermore, from (32), the Fourier representations of the two-color relaxation $S_h^{01}(\omega)$ are

$$\begin{aligned} \tilde{S}_h^{01}(\vec{\theta}, \omega) &= \tilde{S}_h^1(\vec{\theta}, \omega) \tilde{S}_h^0(\vec{\theta}, \omega) \\ &= \frac{1}{2} \begin{pmatrix} A_0^1 + 1 & -A_1^1 + 1 \\ -A_0^1 + 1 & A_1^1 + 1 \end{pmatrix} \\ &\quad \cdot \frac{1}{2} \begin{pmatrix} A_0^0 + 1 & A_1^0 - 1 \\ A_0^0 - 1 & A_1^0 + 1 \end{pmatrix}. \end{aligned} \quad (33)$$

From (10), Theorem 3 holds. \square

3.2. Invariant Subspaces on Four Fourier Modes for Two-Color Relaxation. We need to develop a Fourier representation of the two-color relaxation in the subspace of the $2h$ -harmonics with four Fourier modes. By following (9), for 2D system, another subspace of the $2h$ -harmonics is given as

$$F_{2h}^*(\vec{\theta}) := \text{span} \left\{ \varphi_h(\vec{\theta}^{\vec{\alpha}}, \vec{x}) \mid \vec{\alpha} = (\alpha_1, \alpha_2), \right. \quad (34)$$

$$\left. \alpha_m \in \{0, 1\}, m = 1, 2 \right\}$$

with $\vec{\theta} = (\theta_1, \theta_2) = \vec{\theta}^{(0,0)} \in \Theta_{\text{low}} = (-\pi/2, \pi/2]^2$, $\vec{\theta}^{\vec{\alpha}} = \vec{\theta}^{(0,0)} - (\alpha_1 \text{sign}(\theta_1), \alpha_2 \text{sign}(\theta_2))\pi$.

For the sake of convenient analysis, taking $\vec{\theta}^{\vec{\alpha}} = \vec{\theta}^{(\alpha_1, \alpha_2)} = \vec{\theta}^{\alpha_1 \alpha_2}$, for example, $\vec{\theta}^{(0,0)} = \vec{\theta}^{00}$, then $F_{2h}^*(\vec{\theta})$ is defined as

$$F_{2h}^*(\vec{\theta}) := \text{span} \left\{ \varphi_h(\vec{\theta}^{00}, \vec{x}), \varphi_h(\vec{\theta}^{11}, \vec{x}), \varphi_h(\vec{\theta}^{10}, \vec{x}), \varphi_h(\vec{\theta}^{01}, \vec{x}) \right\}. \quad (35)$$

Meanwhile, the grid G_h is divided into four subsets [11] as

$$G_h = G_h^{00} \cup G_h^{11} \cup G_h^{10} \cup G_h^{01}, \quad (36)$$

where $\vec{\eta} = \{\vec{x} = (k_1 h_1, k_2 h_2) \mid k_m = \eta_m \bmod 2, m = 1, 2\}$ and $\vec{\eta} = (\eta_1, \eta_2) \in \Lambda = \{00, 11, 10, 01\}$. The red and black grid points corresponding with G_h are thus obtained as

$$G_h^R = G_h^{00} \cup G_h^{11}, \quad G_h^B = G_h^{10} \cup G_h^{01}. \quad (37)$$

Therefore, a constitutive relationship among the various Fourier $2h$ -harmonics is constructed.

Proposition 4. For $\forall \vec{x} \in G_h, \forall \vec{k} = (k_1, k_2) \in \mathbb{Z}^2$, and $\forall \vec{\alpha} \in \Lambda$, if $\vec{\theta} \in \Theta_{low}$, the following equation is yielded as

$$\varphi_h \left(\vec{\theta}^{\vec{\alpha}}, \vec{x} \right) = \exp \left(-i\pi \vec{\alpha} \vec{k} \right) \varphi_h \left(\vec{\theta}, \vec{x} \right). \quad (38)$$

Proposition 5. For $\forall \vec{x} \in G_h^{\vec{\beta}}, \forall \vec{k} = (k_1, k_2) \in \mathbb{Z}^2$, and $\forall \vec{\alpha}, \vec{\beta} \in \Lambda$, if $\vec{\theta} \in \Theta_{low}$, the following equation is yielded as

$$\varphi_h \left(\vec{\theta}^{\vec{\alpha}}, \vec{x} \right) = \exp \left(-i\pi \vec{\alpha} \vec{\beta} \right) \varphi_h \left(\vec{\theta}, \vec{x} \right). \quad (39)$$

The proof of Propositions 5 and 4 is similar to Propositions 2 and 1.

Subsequently, a smoothing analysis process of the two-color relaxation on the subspace of the $2h$ -harmonics (35) is obtained.

Theorem 6. The iteration operator (15) for the two-color relaxation leaves the subspace of the $2h$ -harmonics (35) to be invariant 0.

Proof. Similar to the proof of Theorem 3, from process of the two-color relaxation and (15), operators $S_h^R(\omega)$ and $S_h^B(\omega)$ of the grid (37) are

$$S_h^R(\omega) \varphi_h \left(\vec{\theta}^{\vec{\alpha}}, \vec{x} \right) = \begin{cases} \tilde{S}_h^R \left(\vec{\theta}^{\vec{\alpha}}, \omega \right) \varphi_h \left(\vec{\theta}^{\vec{\alpha}}, \vec{x} \right) & \forall \vec{x} \in G_h^R \\ \varphi_h \left(\vec{\theta}^{\vec{\alpha}}, \vec{x} \right) & \forall \vec{x} \notin G_h^R \end{cases} \quad (40)$$

$$S_h^B(\omega) \varphi_h \left(\vec{\theta}^{\vec{\alpha}}, \vec{x} \right) = \begin{cases} \tilde{S}_h^B \left(\vec{\theta}^{\vec{\alpha}}, \omega \right) \varphi_h \left(\vec{\theta}^{\vec{\alpha}}, \vec{x} \right) & \forall \vec{x} \in G_h^B \\ \varphi_h \left(\vec{\theta}^{\vec{\alpha}}, \vec{x} \right) & \forall \vec{x} \notin G_h^B \end{cases} \quad (41)$$

where $\tilde{S}_h^R(\vec{\theta}^{\vec{\alpha}}, \omega)$ and $\tilde{S}_h^B(\vec{\theta}^{\vec{\alpha}}, \omega)$ are Fourier symbols of $S_h^R(\omega)$ and $S_h^B(\omega)$ with $\varphi_h(\vec{\theta}^{\vec{\alpha}}, \vec{x})$ on the corresponding grids (37), respectively, and $\vec{\alpha} \in \Lambda$. From (15), in order to prove

$S_h^{RB}(\omega) : F_{2h}^*(\vec{\theta}) \rightarrow F_{2h}^*(\vec{\theta})$ with $\vec{\theta} \in \Theta_{low}$, we need to find out four complex numbers a_{00}, a_{11}, a_{10} , and a_{01} subjected to

$$S_h^R(\omega) \varphi_h \left(\vec{\theta}^{\vec{\alpha}}, \vec{x} \right) = a_{00} \varphi_h \left(\vec{\theta}^{00}, \vec{x} \right) + a_{11} \varphi_h \left(\vec{\theta}^{11}, \vec{x} \right) + a_{10} \varphi_h \left(\vec{\theta}^{10}, \vec{x} \right) + a_{01} \varphi_h \left(\vec{\theta}^{01}, \vec{x} \right). \quad (42)$$

Meanwhile, we also need to find other four complex numbers b_{00}, b_{11}, b_{10} , and b_{01} and make them subjected to

$$S_h^B(\omega) \varphi_h \left(\vec{\theta}^{\vec{\alpha}}, \vec{x} \right) = b_{00} \varphi_h \left(\vec{\theta}^{00}, \vec{x} \right) + b_{11} \varphi_h \left(\vec{\theta}^{11}, \vec{x} \right) + b_{10} \varphi_h \left(\vec{\theta}^{10}, \vec{x} \right) + b_{01} \varphi_h \left(\vec{\theta}^{01}, \vec{x} \right). \quad (43)$$

Firstly, we prove (42) as follows.

From (36) and (40), as well as Propositions 5 and 4, the right and left hand sides of (42) are written as, respectively,

$$S_h^R(\omega) \varphi_h \left(\vec{\theta}^{\vec{\alpha}}, \vec{x} \right) = \begin{cases} A_{\vec{\alpha}}^R \varphi_h \left(\vec{\theta}, \vec{x} \right) & \forall \vec{x} \in G_h^{00} \\ A_{\vec{\alpha}}^R \exp \left[-i\pi (\alpha_1 + \alpha_2) \right] \varphi_h \left(\vec{\theta}, \vec{x} \right) & \forall \vec{x} \in G_h^{11} \\ \exp \left(-i\pi \alpha_1 \right) \varphi_h \left(\vec{\theta}, \vec{x} \right) & \forall \vec{x} \in G_h^{10} \\ \exp \left(-i\pi \alpha_2 \right) \varphi_h \left(\vec{\theta}, \vec{x} \right) & \forall \vec{x} \in G_h^{01} \end{cases}$$

$$\sum_{\vec{\alpha} \in \Lambda} a_{\vec{\alpha}} \varphi_h \left(\vec{\theta}^{\vec{\alpha}}, \vec{x} \right) = \begin{cases} (a_{00} + a_{11} + a_{10} + a_{01}) \varphi_h \left(\vec{\theta}, \vec{x} \right) & \forall \vec{x} \in G_h^{00} \\ (a_{00} + a_{11} - a_{10} - a_{01}) \varphi_h \left(\vec{\theta}, \vec{x} \right) & \forall \vec{x} \in G_h^{11} \\ (a_{00} - a_{11} - a_{10} + a_{01}) \varphi_h \left(\vec{\theta}, \vec{x} \right) & \forall \vec{x} \in G_h^{10} \\ (a_{00} - a_{11} + a_{10} - a_{01}) \varphi_h \left(\vec{\theta}, \vec{x} \right) & \forall \vec{x} \in G_h^{01} \end{cases}, \quad (44)$$

where $A_{\vec{\alpha}}^R = \tilde{S}_h^R(\vec{\theta}^{\vec{\alpha}}, \omega)$, $\vec{\alpha} = (\alpha_1, \alpha_2) \in \Lambda$. Hence, by using (42) and (44), linear equations with respect to the complex numbers a_{00}, a_{11}, a_{10} , and a_{01} are obtained as

$$\begin{aligned} a_{00} + a_{11} + a_{10} + a_{01} &= A_{\vec{\alpha}}^R \\ a_{00} + a_{11} - a_{10} - a_{01} &= A_{\vec{\alpha}}^R \exp \left[-i\pi (\alpha_1 + \alpha_2) \right] \\ a_{00} - a_{11} - a_{10} + a_{01} &= \exp \left(-i\pi \alpha_1 \right) \\ a_{00} - a_{11} + a_{10} - a_{01} &= \exp \left(-i\pi \alpha_2 \right). \end{aligned} \quad (45)$$

In the same way, equations with respect to the complex numbers b_{00} , b_{11} , b_{10} , and b_{01} are obtained as

$$\begin{aligned} b_{00} + b_{11} + b_{10} + b_{01} &= 1 \\ b_{00} + b_{11} - b_{10} - b_{01} &= \exp[-i\pi(\alpha_1 + \alpha_2)] \\ b_{00} - b_{11} - b_{10} + b_{01} &= A_{\alpha}^B \exp(-i\pi\alpha_1) \\ b_{00} - b_{11} + b_{10} - b_{01} &= A_{\alpha}^B \exp(-i\pi\alpha_2), \end{aligned} \quad (46)$$

where $A_{\alpha}^B = \widehat{S}_h^B(\vec{\theta}, \omega)$, $\vec{\alpha} = (\alpha_1, \alpha_2) \in \Lambda$. From (10), (35), (42), and (43), solving (45) and (46), the Fourier representations of the iteration operators $S_h^R(\omega)$ and $S_h^B(\omega)$ are obtained as

$$\begin{aligned} \widehat{S}_h^R(\vec{\theta}, \omega) &= \frac{1}{2} \begin{pmatrix} A_{00}^R + 1 & A_{11}^R - 1 & 0 & 0 \\ A_{00}^R - 1 & A_{11}^R + 1 & 0 & 0 \\ 0 & 0 & A_{10}^R + 1 & A_{01}^R - 1 \\ 0 & 0 & A_{10}^R - 1 & A_{01}^R + 1 \end{pmatrix} \\ \widehat{S}_h^B(\vec{\theta}, \omega) &= \frac{1}{2} \begin{pmatrix} A_{00}^B + 1 & -A_{11}^B + 1 & 0 & 0 \\ -A_{00}^B - 1 & A_{11}^B + 1 & 0 & 0 \\ 0 & 0 & A_{10}^B + 1 & -A_{01}^B + 1 \\ 0 & 0 & -A_{10}^B + 1 & A_{01}^B + 1 \end{pmatrix}. \end{aligned} \quad (47)$$

Furthermore, from (47), the Fourier representation of the iteration operators $S_h^{RB}(\omega)$ is

$$\begin{aligned} \widehat{S}_h^{RB}(\vec{\theta}, \omega) &= \widehat{S}_h^B(\vec{\theta}, \omega) \widehat{S}_h^R(\vec{\theta}, \omega) \\ &= \frac{1}{2} \begin{pmatrix} A_{00}^B + 1 & -A_{11}^B + 1 & 0 & 0 \\ -A_{00}^B - 1 & A_{11}^B + 1 & 0 & 0 \\ 0 & 0 & A_{10}^B + 1 & -A_{01}^B + 1 \\ 0 & 0 & -A_{10}^B + 1 & A_{01}^B + 1 \end{pmatrix} \\ &\quad \cdot \frac{1}{2} \begin{pmatrix} A_{00}^R + 1 & A_{11}^R - 1 & 0 & 0 \\ A_{00}^R - 1 & A_{11}^R + 1 & 0 & 0 \\ 0 & 0 & A_{10}^R + 1 & A_{01}^R - 1 \\ 0 & 0 & A_{10}^R - 1 & A_{01}^R + 1 \end{pmatrix}, \end{aligned} \quad (48)$$

where $A_{\alpha}^R = \widehat{S}_h^R(\vec{\theta}, \omega)$, $A_{\alpha}^B = \widehat{S}_h^B(\vec{\theta}, \omega)$, $\vec{\alpha} = (\alpha_1, \alpha_2) \in \Lambda$. Theorem 6 holds. \square

From Theorems 3 and 6, two ways to carry out smoothing analysis of the two-color relaxation are obtained.

4. Two-Color Jacobi Relaxation for 2D Poisson Equation

4.1. Poisson Equation and Optimal Smoothing Parameter. 2D Poisson equation to be considered is stated as

$$-\Delta u(x_1, x_2) = f(x_1, x_2). \quad (49)$$

For using uniform grids of mesh size h to solve this equation, a central discretization stencil is introduced as

$$L_h = -\Delta_h = \frac{1}{h^2} \begin{bmatrix} & -1 & \\ -1 & 4 & -1 \\ & -1 & \end{bmatrix}_h. \quad (50)$$

From (3)–(6), the Fourier symbol of (50) is

$$\tilde{L}_h(\vec{\theta}) = \frac{1}{h^2} (4 - 2 \cos \theta_1 - 2 \cos \theta_2). \quad (51)$$

From [1], the damped Jacobi relaxation S_h^{JAC} is defined as

$$S_h^{\text{JAC}}(\omega) = I_h - \omega D_h^{-1} L_h, \quad (52)$$

where $I_h = [1]_h$ is the identity operator, ω is the smoothing parameter, and $D_h = (1/h^2)[4]_h$ is the diagonal part of the discrete operator L_h . Thus, the Fourier symbol of (52) is given as

$$\widehat{S}_h^{\text{JAC}}(\vec{\theta}, \omega) = 1 - \omega \left(\sin^2 \frac{\theta_1}{2} + \sin^2 \frac{\theta_2}{2} \right). \quad (53)$$

For the operators $S_h(\omega)$ and Q_h^H in (14) with a relaxation parameter ω and according to the optimal one-stage relaxation [11], smoothing parameter and a related smoothing factor are given by

$$\omega_{\text{opt}} = \frac{2}{2 - S_{\max} - S_{\min}}, \quad \rho_{\text{opt}} = \frac{S_{\max} - S_{\min}}{2 - S_{\max} - S_{\min}}, \quad (54)$$

where S_{\max} and S_{\min} are the maximum and minimum eigenvalues of the matrix $\widehat{Q}_h^H \widehat{S}_h(\vec{\theta}, 1)$ for $\vec{\theta} \in \Theta_{\text{low}} = (-\pi/2, \pi/2)^2$ and $\widehat{S}_h(\vec{\theta}, 1)$ is the Fourier representation of $S_h(\omega)$ with $\omega = 1$.

4.2. Two-Color Relaxation on (17). According to (32), (33), and (53), for point Jacobi relaxation, A_{α}^{β} in (17) is expressed as

$$\begin{aligned} A_{\alpha}^0 &= A_{\alpha}^1 = \widehat{S}_h^0(\vec{\theta}^{\alpha}, \omega) = \widehat{S}_h^1(\vec{\theta}^{\alpha}, \omega) \\ &= \widehat{S}_h^{\text{JAC}}(\vec{\theta}^{\alpha}, \omega) = 1 - \omega \left(\sin^2 \frac{\theta_1^{\alpha}}{2} + \sin^2 \frac{\theta_2^{\alpha}}{2} \right) \end{aligned} \quad (55)$$

which denotes that both red and black points are swept by the Jacobi point relaxation method, where $\alpha, \beta = 0, 1$ and ω is the smoothing parameter. Further, when $\omega = 1$, (55) is rewritten as

$$A_{\alpha}^0 = A_{\alpha}^1 = \widehat{S}_h^{\text{JAC}}(\vec{\theta}^{\alpha}, 1) = 1 - \left(\sin^2 \frac{\theta_1^{\alpha}}{2} + \sin^2 \frac{\theta_2^{\alpha}}{2} \right), \quad (56)$$

where $\alpha = 0, 1$. For simplification, let

$$\begin{aligned} s_1 &= \sin^2 \frac{\theta_1^0}{2} = \sin^2 \frac{\theta_1}{2}, \\ s_2 &= \sin^2 \frac{\theta_2^0}{2} = \sin^2 \frac{\theta_2}{2}. \end{aligned} \quad (57)$$

By substituting (56) and (57) into (33), (56) is given as

$$\begin{aligned} A_0^0 &= A_0^1 = 1 - (s_1 + s_2), \\ A_1^0 &= A_1^1 = s_1 + s_2 - 1, \\ \widehat{S}_h^{01}(\vec{\theta}, 1) &= \begin{pmatrix} 1 - \frac{1}{2}(s_1 + s_2) & 1 - \frac{1}{2}(s_1 + s_2) \\ \frac{1}{2}(s_1 + s_2) & \frac{1}{2}(s_1 + s_2) \end{pmatrix} \\ &\quad \cdot \begin{pmatrix} 1 - \frac{1}{2}(s_1 + s_2) & \frac{1}{2}(s_1 + s_2) - 1 \\ -\frac{1}{2}(s_1 + s_2) & \frac{1}{2}(s_1 + s_2) \end{pmatrix}. \end{aligned} \quad (58) \quad (59)$$

Further, by using (13) and (17), the Fourier representation of Q_h^H is given as $\widehat{Q}_h^H = \text{diag}(0, 1)$. From (59), the product of \widehat{Q}_h^H and (59) is

$$\begin{aligned} \widehat{Q}_h^H \widehat{S}_h^{01}(\vec{\theta}, 1) &= \begin{pmatrix} 0 & 0 \\ \frac{1}{2}(s_1 + s_2)(1 - s_1 - s_2) & \frac{1}{2}(s_1 + s_2)(s_1 + s_2 - 1) \end{pmatrix}. \end{aligned} \quad (60)$$

Therefore, a unique nonzero eigenvalue of the matrix $\widehat{Q}_h^H \widehat{S}_h^{01}(\vec{\theta}, 1)$ is yielded as

$$\lambda(s_1, s_2) = \frac{1}{2}(s_1 + s_2)(s_1 + s_2 - 1). \quad (61)$$

Because of $\vec{\theta} \in \Theta_{\text{low}} = (-\pi/2, \pi/2]^2$, thus, from (57), we know $(s_1, s_2) \in [0, 1/2]^2$. So, by using (54), the optimal smoothing parameters for the two-color relaxation are given as

$$\begin{aligned} S_{\max} &= \max_{(s_1, s_2) \in [0, 1/2]^2} \lambda(s_1, s_2) \Big|_{\vec{\theta}=(\pi/2, \pi/2)} = 0, \\ S_{\min} &= \min_{(s_1, s_2) \in [0, 1/2]^2} \lambda(s_1, s_2) \Big|_{\vec{\theta}=(0, \pi/2)} = -\frac{1}{8}, \\ \omega_{\text{opt}} &= \frac{2}{2 - S_{\max} - S_{\min}} = \frac{16}{17}, \\ \rho_{\text{opt}} &= \frac{S_{\max} - S_{\min}}{2 - S_{\max} - S_{\min}} = \frac{1}{17}. \end{aligned} \quad (62) \quad (63)$$

4.3. *Two-Color Jacobi Relaxation on (35)*. By using (48) and (53), for point Jacobi relaxation, A_α^R and A_α^B for (35) are expressed as

$$\begin{aligned} A_\alpha^R &= A_\alpha^B = \widehat{S}_h^R(\vec{\theta}^\alpha, \omega) = \widehat{S}_h^B(\vec{\theta}^\alpha, \omega) \\ &= \widehat{S}_h^{\text{JAC}}(\vec{\theta}^\alpha, \omega) = 1 - \omega \left(\sin^2 \frac{\theta_1^{\alpha_1}}{2} + \sin^2 \frac{\theta_2^{\alpha_2}}{2} \right) \end{aligned} \quad (64)$$

which denotes that both red and black points are swept by the Jacobi point relaxation method, where $\vec{\alpha} = (\alpha_1, \alpha_2) \in \Lambda$. Further, substituting (57) into (64), when $\omega = 1$, (64) is written as

$$\begin{aligned} A_{00}^R &= A_{00}^B = 1 - (s_1 + s_2) \\ A_{11}^R &= A_{11}^B = s_1 + s_2 - 1 \\ A_{10}^R &= A_{10}^B = s_1 - s_2 \\ A_{01}^R &= A_{01}^B = -(s_1 - s_2). \end{aligned} \quad (65)$$

Substituting (65) into (48), the Fourier representation of $S_h^{RB}(\omega)$ with $\omega = 1$ is expressed as

$$\widehat{S}_h^{RB}(\vec{\theta}, 1) = \text{diag}(\widehat{S}_{11}, \widehat{S}_{22}), \quad (66)$$

where

$$\begin{aligned} \widehat{S}_{11} &= \begin{pmatrix} \frac{1}{2}(s_1 + s_2 - 1)(s_1 + s_2 - 2) & -\frac{1}{2}(s_1 + s_2 - 1)(s_1 + s_2 - 2) \\ -\frac{1}{2}(s_1 + s_2 - 1)(s_1 + s_2) & \frac{1}{2}(s_1 + s_2 - 1)(s_1 + s_2) \end{pmatrix}, \\ \widehat{S}_{22} &= \begin{pmatrix} \frac{1}{2}(s_1 + s_2 - 1)(s_1 + s_2) & -\frac{1}{2}(s_1 - s_2 + 1)(s_1 - s_2) \\ \frac{1}{2}(s_2 - s_1 + 1)(s_1 - s_2) & -\frac{1}{2}(s_2 - s_1 + 1)(s_1 - s_2) \end{pmatrix}. \end{aligned} \quad (67)$$

From (13) and (35), the Fourier representation of operator Q_h^H is given as

$$\widehat{Q}_h^H = \text{diag}(\widehat{Q}_{11}, \widehat{Q}_{22}), \quad (68)$$

where $\widehat{Q}_{11} = \text{diag}(0, 1)$, $\widehat{Q}_{22} = \text{diag}(1, 1)$. Therefore, the product of (66) and (68) is obtained as

$$\widehat{Q}_h^H \widehat{S}_h^{RB}(\vec{\theta}, 1) = \text{diag}(\widehat{Q}_{11} \widehat{S}_{11}, \widehat{Q}_{22} \widehat{S}_{22}), \quad (69)$$

in which the diagonal blocks are expressed as

$$\begin{aligned} \widehat{Q}_{11}\widehat{S}_{11} &= \begin{pmatrix} 0 & 0 \\ -\frac{(s_1+s_2)(s_1+s_2-1)}{2} & -\frac{(s_1+s_2)(s_1+s_2-1)}{2} \end{pmatrix}, \end{aligned} \quad (70)$$

$$\begin{aligned} \widehat{Q}_{22}\widehat{S}_{22} &= \begin{pmatrix} \frac{(s_1-s_2)(s_1-s_2+1)}{2} & -\frac{(s_1-s_2)(s_1-s_2+1)}{2} \\ \frac{(s_1-s_2)(s_2-s_1+1)}{2} & -\frac{(s_1-s_2)(s_2-s_1+1)}{2} \end{pmatrix}. \end{aligned} \quad (71)$$

The eigenvalues of the matrix (69) are obtained as

$$\begin{aligned} \lambda_1 &= 0, & \lambda_2 &= (s_1-s_2)^2, \\ \lambda_3 &= 0, & \lambda_4 &= \frac{(s_1+s_2)(s_1+s_2-1)}{2}. \end{aligned} \quad (72)$$

When $\vec{\theta} \in \Theta_{\text{low}}$, the maximum and minimum eigenvalues of the matrix $\widehat{Q}_h^H \widehat{S}_h^{RB}(\vec{\theta}, 1)$ are as follows:

$$\begin{aligned} \lambda_{\max}(\widehat{Q}_h^H \widehat{S}_h^{RB}(\vec{\theta}, 1)) &= \max_{(s_1, s_2) \in [0, 1/2]^2} \{\lambda_1, \lambda_2, \lambda_3, \lambda_4\} \\ &= \max_{(s_1, s_2) \in [0, 1/2]^2} \lambda_2 = \frac{1}{4}, \end{aligned} \quad (73)$$

$$\begin{aligned} \lambda_{\min}(\widehat{Q}_h^H \widehat{S}_h^{RB}(\vec{\theta}, 1)) &= \min_{(s_1, s_2) \in [0, 1/2]^2} \{\lambda_1, \lambda_2, \lambda_3, \lambda_4\} \\ &= \min_{(s_1, s_2) \in [0, 1/2]^2} \lambda_4 = -\frac{1}{8}. \end{aligned} \quad (74)$$

Therefore, by using (54), the values of the optimal smoothing parameters for the Poisson equation are obtained as

$$S_{\max} = \lambda_{\max}(\widehat{Q}_h^H \widehat{S}_h^{RB}(\vec{\theta}, 1)) \Big|_{\vec{\theta}=(0, \pi/2)} = \frac{1}{4}, \quad (75)$$

$$S_{\min} = \lambda_{\min}(\widehat{Q}_h^H \widehat{S}_h^{RB}(\vec{\theta}, 1)) \Big|_{\vec{\theta}=(\pi/2, 0)} = -\frac{1}{8},$$

$$\begin{aligned} \omega_{\text{opt}} &= \frac{2}{2 - S_{\max} - S_{\min}} = \frac{16}{15}, \\ \rho_{\text{opt}} &= \frac{S_{\max} - S_{\min}}{2 - S_{\max} - S_{\min}} = \frac{1}{5}. \end{aligned} \quad (76)$$

5. Extending Two-Color to Multicolor Relaxation

Herein, the proposed smoothing analysis process of two-color relaxation is generalized to a 3D system. The Fourier representation of the smoothing operator for two-color relaxation is still a 2-order square matrix in (17). The result in (35) for a 3D case is changed to a $2^3 \times 2^3$ diagonal block matrix.

For a m -color relaxation ($m > 2$), the infinite grid G_h is subdivided into m types of the grid points $G_h^0, G_h^1, \dots, G_h^{m-1}$ for presenting m different colors [11, 20]. Thus a complete analyzing step of the m -color relaxation consists of m substeps: at the β th step ($\beta = 0, 1, \dots, m-1$), the unknowns located at only $\vec{x} \in G_h^\beta$ are changed by using updated data at the previous step. For example, for the m -color relaxation of a 2D system, the infinite grid G_h is stated as

$$G_h = \bigcup_{\beta=0}^{m-1} G_h^\beta, \quad (77)$$

with

$$G_h^\beta = \{\vec{x} = (k_1 h_1, k_2 h_2) \mid k_1 + k_2 = \beta \bmod m, (k_1, k_2) \in \mathbb{Z}^2\}, \quad (78)$$

where $\beta \in \Lambda_m := \{0, 1, \dots, m-1\}$. In the subdivisions of the infinite grids G_h , there are $\forall j, n \in \Lambda_m, j \neq n$, and $G_h^j \cap G_h^n = \emptyset$.

For the standard coarsening [11, 20], the subspace of the $2h$ -harmonics is defined as

$$\begin{aligned} F_{2h}^m &:= \text{span} \left\{ \varphi_h \left(\vec{\theta}^0, \vec{x} \right), \varphi_h \left(\vec{\theta}^1, \vec{x} \right), \dots, \right. \\ &\quad \left. \varphi_h \left(\vec{\theta}^{m-1}, \vec{x} \right) \right\}, \end{aligned} \quad (79)$$

where $\vec{\theta} \in \Theta_{\text{low}}, \forall \alpha \in \Lambda_m$, and $\vec{\theta}^\alpha = (\vec{\theta} + (2\pi/m)(\alpha, \alpha)) \bmod 2\pi$.

In order to obtain a Fourier representation of the m -color point relaxation, let $S_h^{mc}(\omega)$ be the above complete m -color point relaxation operator and let $S_h^\beta(\omega)$ be the β th subrelaxation ($\beta \in \Lambda_m$); thus, the m -color point relaxation is expressed as

$$S_h^{mc}(\omega) = \prod_{\beta=0}^{m-1} S_h^\beta(\omega) \quad (80)$$

with

$$S_h^\beta(\omega) \varphi_h \left(\vec{\theta}^\alpha, \vec{x} \right) = \begin{cases} A_\alpha^\beta \varphi_h \left(\vec{\theta}^\alpha, \vec{x} \right) & \vec{x} \in G_h^\beta \\ \varphi_h \left(\vec{\theta}^\alpha, \vec{x} \right) & \vec{x} \notin G_h^\beta, \end{cases} \quad (81)$$

where $A_\alpha^\beta = \widehat{S}_h^\beta(\vec{\theta}^\alpha, \omega)$ denotes the Fourier symbol of $S_h^\beta(\omega)$, $\alpha, \beta \in \Lambda_m$. The proof of this process is analogous to the two-color case. In fact, as we know, the subspace of the $2h$ -harmonics F_{2h}^m with m Fourier modes remains to be invariant for m -color point relaxation operator $S_h^{mc}(\omega)$; that is, $S_h^{mc}(\omega) : F_{2h}^m \rightarrow F_{2h}^m$. So, the Fourier representation of the m -color point relaxation (80) is given as $\widehat{S}_h^{mc}(\omega) = \prod_{\beta=0}^{m-1} \widehat{S}_h^\beta(\omega)$, where $\widehat{S}_h^\beta(\omega)$ is a Fourier representation of $S_h^\beta(\omega)$ in F_{2h}^m .

Proposition 7. For $\forall \alpha, \beta \in \Lambda_m, \forall \vec{x} \in G_h^\beta$, if $\vec{\theta} \in \Theta_{low}$, the following equation holds:

$$\varphi_h(\vec{\theta}^\alpha, \vec{x}) = \exp\left(i \frac{2\pi}{m} \alpha \beta\right) \varphi_h(\vec{\theta}, \vec{x}). \quad (82)$$

The proof is similar to Proposition 1.

Theorem 8. The iteration operator (80) for m -color point relaxation makes the subspace of the $2h$ -harmonics (79) invariant.

The proof is similar to Theorem 3. In fact, in order to prove $S_h^{mc}(\omega) : F_{2h}^m \rightarrow F_{2h}^m$, one only needs to do $\forall \beta \in \Lambda_m, S_h^\beta(\omega) : F_{2h}^m \rightarrow F_{2h}^m$, which is equivalent to finding out m complex numbers $a_j, j \in \Lambda_m$, subject to

$$S_h^\beta(\omega) \varphi_h(\vec{\theta}^\alpha, \vec{x}) = \sum_{\alpha=0}^{m-1} a_\alpha \varphi_h(\vec{\theta}^\alpha, \vec{x}). \quad (83)$$

Being similar to the proof of Theorems 3 and 6 and according to (81), (83) and Proposition 7, m linear equations on a_j are obtained as

$$\begin{aligned} & a_0 + a_1 + a_2 + \dots + a_{m-1} = 1 & \vec{x} \in G_h^0 \\ & a_0 + a_1 \exp\left(i \frac{2\pi}{m}\right) + a_2 \exp\left(i \frac{2\pi \cdot 2}{m}\right) + \dots \\ & + a_{m-1} \exp\left[i \frac{2\pi(m-1)}{m}\right] = \exp\left(i \frac{2\pi\alpha}{m}\right) & \vec{x} \in G_h^1 \\ & a_0 + a_1 \exp\left(i \frac{2\pi \cdot 2}{m}\right) + a_2 \exp\left(i \frac{2\pi \cdot 4}{m}\right) \\ & + \dots + a_{m-1} \exp\left[i \frac{2\pi(m-1) \cdot 2}{m}\right] \\ & = \exp\left(i \frac{2\pi \cdot 2\alpha}{m}\right) & \vec{x} \in G_h^2 \\ & \vdots \\ & a_0 + a_1 \exp\left(i \frac{2\pi \cdot \beta}{m}\right) + a_2 \exp\left(i \frac{2\pi \cdot 2\beta}{m}\right) \\ & + \dots + a_{m-1} \exp\left[i \frac{2\pi(m-1) \cdot \beta}{m}\right] \\ & = A_\alpha^\beta \exp\left(i \frac{2\pi \cdot \alpha\beta}{m}\right) & \vec{x} \in G_h^\beta \\ & \vdots \\ & a_0 + a_1 \exp\left[i \frac{2\pi(m-1)}{m}\right] \\ & + a_2 \exp\left[i \frac{2\pi \cdot 2(m-1)}{m}\right] + \dots \\ & + a_{m-1} \exp\left[i \frac{2\pi(m-1) \cdot (m-1)}{m}\right] \\ & = \exp\left[i \frac{2\pi(m-1) \cdot \alpha}{m}\right] & \vec{x} \in G_h^{m-1}. \end{aligned} \quad (84)$$

Letting $\eta = 2\pi/m, \xi_n = \exp(in\eta)$ with $n \in \Lambda_m$, the equations are simplified as

$$N \vec{a} = \vec{b}_\beta, \quad (85)$$

where $\vec{a} = (a_0, a_1, \dots, a_{m-1})^T, \vec{b}_\beta = (\xi_0, \xi_1, \dots, A_\alpha^\beta \xi_1^{\alpha\beta}, \dots, \xi_{m-1}^{\alpha\beta})^T, T$ denotes transposition of matrix or vector, and N is the Vander monde matrix; namely,

$$N = \begin{pmatrix} 1 & 1 & \dots & 1 \\ \xi_0 & \xi_1 & \dots & \xi_{m-1} \\ \vdots & \vdots & \ddots & \vdots \\ \xi_0^{m-1} & \xi_1^{m-1} & \dots & \xi_{m-1}^{m-1} \end{pmatrix}. \quad (86)$$

Because of $\forall j \neq n \in \Lambda_m, \xi_j \neq \xi_n$, the determinant of the matrix N is nonzero. Therefore, from (83)–(86), for $\forall \alpha, \beta \in \Lambda_m$, the Fourier representation of the β th substep relaxation in F_{2h}^m is obtained as

$$\widehat{S}_h^\beta(\omega) = N^{-1} N_\beta \quad (87)$$

in which N_β is a square matrix which is obtained by substituting $\vec{\xi}_\beta = (A_\alpha^\beta \xi_0^\beta, A_\alpha^\beta \xi_1^\beta, \dots, A_\alpha^\beta \xi_{m-1}^\beta)$ for the β th row of the matrix N , and $A_\alpha^\beta = \widehat{S}_h^\beta(\vec{\theta}^\alpha, \omega)$. Therefore, from (80) and (87), the Fourier representation of the m -color point relaxation in the subspace of the $2h$ -harmonics F_{2h}^m is stated as

$$\widehat{S}_h^{mc}(\omega) = \prod_{\beta=0}^{m-1} N^{-1} N_\beta. \quad (88)$$

Theorem 8 holds.

6. Conclusions

A novel smoothing analysis process of the two-color point relaxation for a 2D system is presented. The results are generalized to the m -color point relaxation and extended to a 3D system. The applications to the 2D and 3D Poisson equations show that the computational domain over multigrids needs to be divided into the multisubsets to correspond with the different frequency modes in partial differential equations and to use the corresponding discretizing stencils. Meanwhile, the definition of the subspace based on the $2h$ -harmonics has to be agreeable to the subdomains of the multigrids. It is an important fact that establishes a mathematical constitution among the various Fourier modes with the different $2h$ -harmonics and constructs a usable Fourier representation of the m -color point relaxation in subspace of the $2h$ -harmonics.

Conflict of Interests

The authors declare that there is no conflict of interests regarding the publication of this paper.

Acknowledgments

The authors were supported by the National Natural Science Foundation of China (NSFC) (Grant no. 51279071) and the Doctoral Foundation of Ministry of Education of China (Grant no. 20135314130002).

References

- [1] W. L. Briggs, V. E. Henson, and S. McCormick, *A Multigrid Tutorial*, Society for Industrial and Applied Mathematics, 2nd edition, 2000.
- [2] W. Hackbusch, *Multigrid Methods and Applications*, Springer, Berlin, Germany, 1985.
- [3] U. Trottenberg, C. W. Oosterlee, and A. Schuller, *Multigrid*, Academic Press, New York, NY, USA, 2001.
- [4] P. Wesseling, *An Introduction to Multigrid Methods*, John Wiley, Chichester, UK, 1992.
- [5] K. Stüben and U. Trottenberg, "Multigrid methods: fundamental algorithms, model problem analysis and applications," in *Multigrid Methods*, W. Hackbusch and U. Trottenberg, Eds., vol. 960 of *Lecture Notes in Mathematics*, pp. 1–176, Springer, Berlin, Germany, 1982.
- [6] A. Brandt and O. E. Livne, *1984 Guide to Multigrid Development in Multigrid Methods*, Society for Industrial and Applied Mathematics, 2011.
- [7] A. Brandt, "Multi-level adaptive solutions to boundary-value problems," *Mathematics of Computation*, vol. 31, no. 138, pp. 333–390, 1977.
- [8] T. Boonen, J. van lent, and S. Vandewalle, "Local Fourier analysis of multigrid for the curl-curl equation," *SIAM Journal on Scientific Computing*, vol. 30, no. 4, pp. 1730–1755, 2008.
- [9] S. Vandewalle and G. Horton, "Fourier mode analysis of the multigrid waveform relaxation and time-parallel multigrid methods," *Computing*, vol. 54, no. 4, pp. 317–330, 1995.
- [10] R. Wienands and C. W. Oosterlee, "On three-grid Fourier analysis for multigrid," *SIAM Journal on Scientific Computing*, vol. 23, no. 2, pp. 651–671, 2001.
- [11] R. Wienands and W. Joppich, *Practical Fourier Analysis for Multigrid Methods*, CRC Press, 2005.
- [12] A. Brandt, "Rigorous quantitative analysis of multigrid—I: constant coefficients two-level cycle with ℓ_∞ -norm," *SIAM Journal on Numerical Analysis*, vol. 31, pp. 1695–1730, 1994.
- [13] C. Rodrigo, P. Salinas, F. J. Gaspar, and F. J. Lisbona, "Local Fourier analysis for cell-centered multigrid methods on triangular grids," *Journal of Computational and Applied Mathematics*, vol. 259, pp. 35–47, 2014.
- [14] F. J. Gaspar, J. L. Gracia, and F. J. Lisbona, "Fourier analysis for multigrid methods on triangular grids," *SIAM Journal on Scientific Computing*, vol. 31, no. 3, pp. 2081–2102, 2009.
- [15] G. Zhou and S. R. Fulton, "Fourier analysis of multigrid methods on hexagonal grids," *SIAM Journal on Scientific Computing*, vol. 31, no. 2, pp. 1518–1538, 2009.
- [16] B. Gmeiner, T. Gradl, F. Gaspar, and U. Rüde, "Optimization of the multigrid-convergence rate on semi-structured meshes by local Fourier analysis," *Computers & Mathematics with Applications*, vol. 65, no. 4, pp. 694–711, 2013.
- [17] S. P. MacLachlan and C. W. Oosterlee, "Local Fourier analysis for multigrid with overlapping smoothers applied to systems of PDEs," *Numerical Linear Algebra with Applications*, vol. 18, no. 4, pp. 751–774, 2011.
- [18] S. Cools and W. Vanroose, "Local Fourier analysis of the complex shifted Laplacian preconditioner for Helmholtz problems," *Numerical Linear Algebra with Applications*, vol. 20, no. 4, pp. 575–597, 2013.
- [19] C. Rodrigo, F. J. Gaspar, C. W. Oosterlee, and I. Yavneh, "Accuracy measures and Fourier analysis for the full multigrid algorithm," *SIAM Journal on Scientific Computing*, vol. 32, no. 5, pp. 3108–3129, 2010.
- [20] O. E. Livne and A. Brandt, "Local mode analysis of multicolor and composite relaxation schemes," *Computers & Mathematics with Applications*, vol. 47, no. 2–3, pp. 301–317, 2004.
- [21] C. J. Kuo and T. F. Chan, "Two-color Fourier analysis of iterative algorithms for elliptic problems with red/black ordering," *SIAM Journal on Scientific and Statistical Computing*, vol. 11, no. 4, pp. 767–793, 1990.
- [22] I. Yavneh, "On red-black SOR smoothing in multigrid," *SIAM Journal on Scientific Computing*, vol. 17, no. 1, pp. 180–192, 1996.
- [23] C. J. Kuo and B. C. Levy, "Two-color Fourier analysis of the multigrid method with red-black Gauss-Seidel smoothing," *Applied Mathematics and Computation*, vol. 29, no. 1, pp. 69–87, 1989.
- [24] I. Yavneh, "Multigrid smoothing factors for red-black Gauss-Seidel relaxation applied to a class of elliptic operators," *SIAM Journal on Numerical Analysis*, vol. 32, no. 4, pp. 1126–1138, 1995.
- [25] C. Rodrigo, F. J. Gaspar, and F. J. Lisbona, "Multicolor Fourier analysis of the multigrid method for quadratic FEM discretizations," *Applied Mathematics and Computation*, vol. 218, no. 22, pp. 11182–11195, 2012.
- [26] T. N. Venkatesh, V. R. Sarasamma, S. Rajalakshmy, K. C. Sahu, and R. Govindarajan, "Super-linear speed-up of a parallel multigrid Navier-Stokes solver on Flosolver," *Current Science*, vol. 88, no. 4, pp. 589–593, 2005.
- [27] K. C. Sahu and R. Govindarajan, "Stability of flow through a slowly diverging pipe," *Journal of Fluid Mechanics*, vol. 531, pp. 325–334, 2005.
- [28] L. M. Adams and H. F. Jordan, "Is SOR color-blind?" *SIAM Journal on Scientific and Statistical Computing*, vol. 7, no. 2, pp. 490–506, 1986.
- [29] Landon Boyd, Solving the Poisson Problem in Parallel with S.O.R., <http://www.cs.ubc.ca/~blandon/cpsc521/cpsc521boyd.pdf>.

Research Article

Effect of Rotation on Wave Propagation in Hollow Poroelastic Circular Cylinder

S. M. Abo-Dahab,^{1,2} A. M. Abd-Alla,^{1,3} and S. Alqosami¹

¹ Mathematics Department, Faculty of Science, Taif University, Taif 888, Saudi Arabia

² Mathematics Department, Faculty of Science, South Valley University, Qena 83523, Egypt

³ Mathematics Department, Faculty of Science, Sohag University, Egypt

Correspondence should be addressed to S. Alqosami; soo.s00@hotmail.com

Received 26 March 2014; Revised 10 May 2014; Accepted 11 May 2014; Published 25 September 2014

Academic Editor: Kim M. Liew

Copyright © 2014 S. M. Abo-Dahab et al. This is an open access article distributed under the Creative Commons Attribution License, which permits unrestricted use, distribution, and reproduction in any medium, provided the original work is properly cited.

The objective of this paper is to study the effect of rotation on the wave propagation in an infinite poroelastic hollow circular cylinder. The frequency equation for poroelastic hollow circular cylinder is obtained when the boundaries are stress free and is examined numerically. The frequency, phase velocity, and attenuation coefficient are calculated for a pervious surface for various values of rotation, wave number, and thickness of the cylinder which are presented for nonaxial symmetric vibrations for a pervious surface. The dispersion curves are plotted for the poroelastic elastic behavior of the poroelastic material. Results are discussed for poroelastic material. The results indicate that the effect of rotation, wave number, and thickness on the wave propagation in the hollow poroelastic circular cylinder is very pronounced.

1. Introduction

The study of wave propagation over a continuous medium is of practical importance in the fields of engineering, medicine, and bioengineering. Application of the poroelastic materials in medical fields such as orthopedic, dental, and cardiovascular is well known. In orthopedics, wave propagation over bone is used in monitoring the rate of fracture healing. There are two types of osseous tissue such as cancellous or trabecular and compact or cortical bone, which are of different materials, with respect to their mechanical behavior. In macroscopic terms, the percentage of porosity in the cortical bone is 3–5%, whereas, in the trabecular or cancellous, the percentage of porosity is up to 90% [1]. In fact, in a recent article, Ahmed and Abd-Alla [1] investigated the electromechanical wave propagation in a cylindrical poroelastic bone with cavity. Analytical solution of electromechanical wave propagation in long bones has been obtained by El-Naggar et al. [2]. Abd-Alla et al. [3] studied the wave propagation modeling in cylindrical human long wet bones with cavity. Hart [4] investigated the theoretical study of the influence of bone maturation rate on surface remodeling predictions. Qin et al. [5] studied

the thermoelectroelastic solutions for surface bone remodeling under axial and transverse loads. Martínez et al. [6] discussed the external bone remodeling through boundary elements and damage mechanics. Computational simulation of simultaneous cortical and trabecular bone change in human proximal femur during bone remodeling has been investigated by Jang and Kim [7]. Tsili [8] studied the theoretical solutions for internal bone remodeling of diaphyseal shafts using adaptive elasticity theory. Cowin and Firoozbakhsh [9] investigated the bone remodeling of diaphyseal surfaces under constant load: theoretical predictions, a contribution to the mechanics and thermodynamics of surface growth. Application to bone external remodeling has been studied by Ganghoffer [10]. Sims and Gooi [11] investigated bone remodeling: multiple cellular interactions required for coupling of bone formation and resorption. Zumsande et al. [12] discussed the general analysis of mathematical models for bone remodeling. Malachanne et al. [13] studied the numerical model of bone remodeling sensitive to loading frequency through a poroelastic behavior and internal fluid movements. A model for mechanical adaptation of trabecular bone incorporating cellular accommodation and effects of microdamage

and disuse has been studied by Vahdati and Rouhi [14]. Hazelwood et al. [15] investigated the mechanistic model for internal bone remodeling exhibiting different dynamic responses in disuse and overload. Qu et al. [16] studied the hypothetical mechanism of bone remodeling and modeling under electromagnetic loads. Papathanasopoulou et al. [17] investigated the poroelastic bone model for internal remodeling. Isotropic continuum damage/repair model for alveolar bone remodeling has been studied by Mengoni and Ponthot [18]. Boyle and Kim [19] investigated the three-dimensional microlevel computational study of Wolff's law via trabecular bone remodeling in the human proximal femur using design space topology optimization. Wang et al. [20] studied the theoretical analysis of alendronate and risedronate effects on canine vertebral remodeling and microdamage. A physiologically based mathematical model of integrated calcium homeostasis and bone remodeling has been discussed by Peterson and Riggs [21]. Qin and Ye [22] studied the thermoelectroelastic solutions for internal bone remodeling investigated under axial and transverse loads. Boyle and Kim [23] studied the comparison of different hip prosthesis shapes considering microlevel bone remodeling and stress-shielding criteria using three-dimensional design space topology optimization. Cowin and Van Buskirk [24] investigated surface bone remodeling induced by a medullary pin. Biot [25] explained the general theory of three-dimensional consolidation. Hegedus and Cowin [26] studied bone remodeling II, small strain adaptive elasticity. The extensive literature on the topic is now available and we can only mention a few recent interesting investigations in [27–33]. Recently, Abd-Alla and Abo-Dahab [34] investigated magnetic field effect on poroelastic bone model for internal remodeling.

In the present analysis, the free vibrations of an infinite hollow poroelastic circular cylinder are studied employing general displacement components in cylindrical polar coordinates, following Biot's [35] theory. The general frequency hollow cylinder is homogeneous and isotropic. Degenerate cases of the general frequency equation of pervious surfaces, when the longitudinal wave number k is considered. The numerical result displayed by figures and the physical meaning are explained. The results and discussions presented in this study may be helpful to further understand wave propagation in hollow poroelastic circular cylinder.

2. Governing Equations

Let us consider that the equations of motion of a homogeneous, isotropic poroelastic solid in the presence of dissipation b are

(A + N)

$$\times \left[\frac{\partial^2 u_r}{\partial r^2} + \frac{1}{r} \frac{\partial u_r}{\partial r} + \frac{1}{r} \frac{\partial^2 u_\theta}{\partial r \partial \theta} - \frac{1}{r^2} \frac{\partial u_\theta}{\partial \theta} + \frac{\partial^2 u_z}{\partial r \partial z} - \frac{1}{r} u_r \right]$$

$$\begin{aligned} & + N \left[\frac{\partial^2 u_r}{\partial r^2} + \frac{1}{r^2} \frac{\partial^2 u_r}{\partial \theta^2} + \frac{\partial^2 u_r}{\partial z^2} + \frac{1}{r} \frac{\partial u_r}{\partial r} - \frac{2}{r^2} \frac{\partial u_\theta}{\partial \theta} - \frac{2}{r} u_r \right] \\ & + Q \left[\frac{\partial^2 v_r}{\partial r^2} - \frac{v_r}{r^2} + \frac{1}{r} \frac{\partial^2 v_\theta}{\partial r \partial \theta} + \frac{\partial^2 v_z}{\partial r \partial z} - \frac{1}{r^2} \frac{\partial v_\theta}{\partial \theta} + \frac{1}{r} \frac{\partial v_r}{\partial r} \right] \\ & = \frac{\partial^2}{\partial t^2} (\rho_{11} u_r + \rho_{12} v_r) - \rho_{11} \Omega^2 u_r + b \frac{\partial}{\partial t} (u_r - v_r) \end{aligned}$$

(A + N)

$$\begin{aligned} & \times \left[\frac{1}{r} \frac{\partial^2 u_r}{\partial r \partial \theta} + \frac{1}{r} \frac{\partial^2 u_z}{\partial \theta \partial z} + \frac{1}{r^2} \frac{\partial u_r}{\partial \theta} + \frac{1}{r^2} \frac{\partial^2 u_\theta}{\partial r^2} \right] \\ & + N \left[\frac{2}{r^2} \frac{\partial u_r}{\partial \theta} + \frac{1}{r^2} \frac{\partial^2 u_\theta}{\partial \theta^2} + \frac{\partial^2 u_\theta}{\partial r^2} + \frac{1}{r} \frac{\partial u_\theta}{\partial r} - \frac{1}{r} u_\theta + \frac{\partial^2 u_\theta}{\partial z^2} \right] \\ & + \frac{Q}{r} \left[\frac{\partial^2 v_\theta}{\partial r \partial \theta} + \frac{1}{r^2} \frac{\partial^2 v_\theta}{\partial \theta^2} + \frac{1}{r} \frac{\partial v_r}{\partial \theta} + \frac{\partial^2 v_z}{\partial \theta \partial z} \right] \\ & = \frac{\partial^2}{\partial t^2} (\rho_{11} u_\theta + \rho_{12} v_\theta) + b \frac{\partial}{\partial t} (u_\theta - v_\theta) \\ & (A + N) \left[\frac{\partial^2 u_r}{\partial r \partial z} + \frac{1}{r} \frac{\partial^2 u_\theta}{\partial \theta \partial z} + \frac{1}{r} \frac{\partial u_r}{\partial z} + \frac{\partial^2 u_z}{\partial z^2} \right] \\ & + N \left[\frac{\partial^2 u_z}{\partial z^2} + \frac{\partial^2 u_z}{\partial r^2} + \frac{1}{r^2} \frac{\partial^2 u_z}{\partial \theta^2} + \frac{1}{r} \frac{\partial u_z}{\partial z} \right] \\ & + Q \left[\frac{\partial^2 v_r}{\partial r \partial z} + \frac{1}{r^2} \frac{\partial^2 v_\theta}{\partial \theta \partial z} + \frac{1}{r} \frac{\partial v_r}{\partial z} + \frac{\partial^2 v_z}{\partial z^2} \right] \\ & = \frac{\partial^2}{\partial t^2} (\rho_{11} u_z + \rho_{12} v_z) - \rho_{11} \Omega^2 u_z + b \frac{\partial}{\partial t} (u_z - v_z) \end{aligned}$$

$$\begin{aligned} & Q \left(\frac{\partial^2 u_r}{\partial r^2} + \frac{1}{r} \frac{\partial u_r}{\partial r} + \frac{1}{r} \frac{\partial^2 u_\theta}{\partial r \partial \theta} - \frac{1}{r^2} \frac{\partial u_\theta}{\partial \theta} + \frac{\partial^2 u_z}{\partial r \partial z} - \frac{1}{r} u_r \right) \\ & + R \left[\frac{\partial^2 v_r}{\partial r^2} - \frac{v_r}{r^2} + \frac{1}{r} \frac{\partial^2 v_\theta}{\partial r \partial \theta} + \frac{\partial^2 v_z}{\partial r \partial z} - \frac{1}{r^2} \frac{\partial v_\theta}{\partial \theta} + \frac{1}{r} \frac{\partial v_r}{\partial r} \right] \end{aligned}$$

$$\begin{aligned}
&= \frac{\partial^2}{\partial t^2} (\rho_{12} u_r + \rho_{22} v_r) - b \frac{\partial}{\partial t} (u_r - v_r), \\
&Q \left[\frac{1}{r} \frac{\partial^2 u_r}{\partial r \partial \theta} + \frac{1}{r} \frac{\partial^2 u_z}{\partial \theta \partial z} + \frac{1}{r^2} \frac{\partial u_r}{\partial \theta} + \frac{1}{r^2} \frac{\partial^2 u_\theta}{\partial r^2} \right] \\
&\quad + \frac{R}{r} \left[\frac{\partial^2 v_\theta}{\partial r \partial \theta} + \frac{1}{r} \frac{\partial^2 v_\theta}{\partial \theta^2} + \frac{1}{r} \frac{\partial v_r}{\partial \theta} + \frac{\partial^2 v_z}{\partial \theta \partial z} \right] \\
&= \frac{\partial^2}{\partial t^2} (\rho_{12} u_\theta + \rho_{22} v_\theta) - b \frac{\partial}{\partial t} (u_\theta - v_\theta), \\
&Q \left[\frac{\partial^2 u_r}{\partial r \partial z} + \frac{1}{r} \frac{\partial^2 u_\theta}{\partial \theta \partial z} + \frac{1}{r} \frac{\partial u_r}{\partial z} + \frac{\partial^2 u_z}{\partial z^2} \right] \\
&\quad + R \left[\frac{\partial^2 v_r}{\partial r \partial z} + \frac{1}{r^2} \frac{\partial^2 v_\theta}{\partial \theta \partial z} + \frac{1}{r} \frac{\partial v_r}{\partial z} + \frac{\partial^2 v_z}{\partial z^2} \right] \\
&= \frac{\partial^2}{\partial t^2} (\rho_{12} u_z + \rho_{22} v_z) - b \frac{\partial}{\partial t} (u_z - v_z),
\end{aligned} \tag{1}$$

where ∇^2 is the Laplace operator, $\vec{u} = (u_r, u_\theta, u_z)$, $\vec{v} = (v_r, v_\theta, v_z)$ are displacements of solid and liquid, respectively, e and ε are the dilatations of solid and liquid, A , N , Q , and R are all poroelastic constants, and ρ_{ij} ($i, j = 1, 2$) are the mass coefficients following Biot [35].

The stress-strain equations for an isotropic poroelastic material of solid and liquid are given as

$$\begin{aligned}
\sigma_{rr} &= 2NE_{rr} + AE + Q\varepsilon, \\
\sigma_{\theta\theta} &= 2NE_{\theta\theta} + AE + Q\varepsilon, \\
\sigma_{zz} &= 2NE_{zz} + AE + Q\varepsilon, \\
\tau_{\theta z} &= NE_{\theta z}, \\
\tau_{zr} &= NE_{zr}, \\
\tau_{r\theta} &= NE_{r\theta}, \\
s &= QE + R\varepsilon.
\end{aligned} \tag{2}$$

3. Solution of the Problem

Let us consider (r, θ, z) to be the cylindrical polar coordinates. Consider a homogeneous, isotropic, poroelastic cylinder with inner and outer radii being r_1 and r_2 , respectively, so that the thickness of poroelastic cylinder is $h = (r_2 - r_1) > 0$, whose axis is in the direction of z -axis; let

$$\begin{aligned}
\vec{v} &= \underline{\nabla} \phi_2 + \underline{\nabla} \wedge \vec{\psi}_2, \\
\vec{u} &= \underline{\nabla} \phi_1 + \underline{\nabla} \wedge \vec{\psi}_1,
\end{aligned} \tag{3}$$

where \vec{u} , \vec{v} are displacements of solid and liquid, respectively, ϕ_1 , ϕ_2 are scalar potentials, and $\vec{\psi}_1$, $\vec{\psi}_2$ are vector potentials.

Assuming that

$$\begin{aligned}
\vec{\Psi}_1 &= (h_r, h_\theta, h_z), \\
\vec{\Psi}_2 &= (H_r, H_\theta, H_z),
\end{aligned} \tag{4}$$

from (1) and (3), we get

$$\begin{aligned}
P\nabla^2 \theta_1 + Q\nabla^2 \theta_2 &= (\rho_{11} \ddot{\theta}_1 (1 + \Omega^2) + \rho_{12} \ddot{\theta}_2) + b (\dot{\theta}_1 - \dot{\theta}_2) \\
Q\nabla^2 \theta_1 + R\nabla^2 \theta_2 &= (\rho_{12} \ddot{\theta}_1 + \rho_{22} \ddot{\theta}_2) - b (\dot{\theta}_1 - \dot{\theta}_2) \\
0 &= (\rho_{12} \vec{\Psi}_1 + \rho_{22} \vec{\Psi}_2) - b (\vec{\Psi}_1 - \vec{\Psi}_2) \\
N\nabla^2 \vec{\Psi}_1 &= (\rho_{11} \vec{\Psi}_1 (1 + \Omega^2) + \rho_{12} \vec{\Psi}_2) + b (\vec{\Psi}_1 - \vec{\Psi}_2),
\end{aligned} \tag{5}$$

where $P = A + 2N$.

Assuming that

$$\begin{aligned}
\theta_1 &= f_1(r) \cos(n\theta) e^{i(kz+wt)}, \\
\theta_2 &= f_2(r) \cos(n\theta) e^{i(kz+wt)}, \\
h_r &= g_r(r) \sin(n\theta) e^{i(kz+wt)}, \\
h_\theta &= g_\theta(r) \cos(n\theta) e^{i(kz+wt)}, \\
h_z &= g_z(r) \sin(n\theta) e^{i(kz+wt)}, \\
H_r &= G_r(r) \sin(n\theta) e^{i(kz+wt)}, \\
H_\theta &= G_\theta(r) \cos(n\theta) e^{i(kz+wt)}, \\
H_z &= G_z(r) \sin(n\theta) e^{i(kz+wt)},
\end{aligned} \tag{6}$$

where k is the axial wave number, n is an integer number of waves around the circumference or also known as angular wave number, and w is circular frequency. From the second and third equations of (5) with (4), when the first two equations of (5) remain the same, they are reduced to

$$\begin{aligned}
P\nabla^2 \theta_1 + Q\nabla^2 \theta_2 &= (\rho_{11} \ddot{\theta}_1 (1 + \Omega^2) + \rho_{12} \ddot{\theta}_2) + b (\dot{\theta}_1 - \dot{\theta}_2), \\
Q\nabla^2 \theta_1 + R\nabla^2 \theta_2 &= (\rho_{12} \ddot{\theta}_1 + \rho_{22} \ddot{\theta}_2) - b (\dot{\theta}_1 - \dot{\theta}_2),
\end{aligned}$$

$$\begin{aligned}
& N \left(\nabla^2 h_r - \frac{h_r}{r^2} - \frac{2}{r^2} \frac{\partial h_\theta}{\partial \theta} \right) \\
&= \left((\rho_{11} + \Omega^2) \ddot{h}_r + \rho_{12} \ddot{H}_r \right) + b (\dot{h}_r - \dot{H}_r), \\
& N \left(\nabla^2 h_\theta - \frac{h_\theta}{r^2} + \frac{2}{r^2} \frac{\partial h_r}{\partial \theta} \right) \\
&= \left((\rho_{11} + \Omega^2) \ddot{h}_\theta + \rho_{12} \ddot{H}_\theta \right) + b (\dot{h}_\theta - \dot{H}_\theta), \\
& N (\nabla^2 h_z) \\
&= \left((\rho_{11} + \Omega^2) \ddot{h}_z + \rho_{12} \ddot{H}_z \right) + b (\dot{h}_z - \dot{H}_z), \\
& 0 = (\rho_{12} \ddot{h}_r + \rho_{22} \ddot{H}_r) - b (\dot{h}_r - \dot{H}_r), \\
& 0 = (\rho_{12} \ddot{h}_\theta + \rho_{22} \ddot{H}_\theta) - b (\dot{h}_\theta - \dot{H}_\theta), \\
& 0 = (\rho_{12} \ddot{h}_z + \rho_{22} \ddot{H}_z) - b (\dot{h}_z - \dot{H}_z).
\end{aligned} \tag{7}$$

From (7) and (6), we obtain

$$\begin{aligned}
p \Delta f_1 + Q \Delta f_2 &= -w^2 [k_{11} f_1 + k_{12} f_2], \\
Q \Delta f_1 + R \Delta f_2 &= -w^2 [k_{12} f_1 + k_{22} f_2], \\
N \left[\Delta g_r - \frac{g_r}{r^2} - \frac{2n}{r^2} g_\theta \right] &= -w^2 [k'_{11} g_r + k_{12} G_r], \\
N \left[\Delta g_\theta - \frac{g_\theta}{r^2} - \frac{2n}{r^2} g_r \right] &= -w^2 [k'_{11} g_\theta + k_{12} G_\theta], \\
N \Delta g_3 &= -w^2 [k'_{11} g_z + k_{12} G_z], \\
0 &= -w^2 [k_{12} g_r + k_{22} G_r], \\
0 &= -w^2 [k_{12} g_\theta + k_{22} G_\theta], \\
0 &= -w^2 [k_{12} g_z + k_{22} G_z],
\end{aligned} \tag{8}$$

where

$$\begin{aligned}
\Delta &= \frac{d^2}{dr^2} + \frac{1}{r} \frac{d}{dr} - \frac{n^2}{r^2} - k^2, \\
k_{11} &= \rho_{11} (1 - \Omega^2) - \frac{ib}{w}, \\
k_{12} &= \rho_{12} + \frac{ib}{w}, \quad k_{22} = \rho_{22} - \frac{ib}{w}, \\
k'_{11} &= \rho_{11} (1 + \Omega^2) - \frac{ib}{w}.
\end{aligned} \tag{9}$$

The general solution of (8) can be obtained in terms of the Bessel function of the first and second kind J and Y depending on its arguments $\alpha_1 r$, $\alpha_2 r$, $\alpha_3 r$.

From (8), we obtain

$$\begin{aligned}
f_1 &= c_1 J_n(\alpha_1 r) + c_2 Y_n(\alpha_1 r) + c_3 J_n(\alpha_2 r) + c_4 Y_n(\alpha_2 r), \\
g_3(r) &= A_3 J_n(\alpha_3 r) + B_3 Y_n(\alpha_3 r), \\
2g_1 &= g_r - g_\theta = 2A_1 J_{n+1}(\alpha_3 r) + 2B_1 Y_{n+1}(\alpha_3 r), \\
2g_2 &= g_r + g_\theta = 2A_2 J_{n-1}(r\alpha_3) + 2B_2 Y_{n-1}(r\alpha_3),
\end{aligned} \tag{10}$$

where J_n is Bessel function of the first kind and order n and Y_n is the Bessel function of the second kind and order n . Consider that

$$\begin{aligned}
\alpha_1^2 &= \zeta_1^2 - k^2 + \Omega^2, \\
\alpha_2^2 &= \zeta_2^2 - k^2 + \Omega^2, \\
\alpha_3^2 &= \zeta_3^2 - k^2 - \Omega^2
\end{aligned} \tag{11}$$

are positive or negative and

$$\omega^2 = \zeta_i^2 v_i^2 \quad (i = 1, 2, 3), \tag{12}$$

where v_r , v_θ are the dilatational wave velocities of first and second kind, respectively, and v_z is shear wave velocity.

The gauge invariance property, following the analysis of [36], is used to eliminate two integration constants from (10). Any one of the potential functions g_1 , g_2 , or g_3 can be set equal to zero, without loss of generality of the solution. Setting $g_2 = 0$, we can obtain

$$g_r = -g_\theta = g_1. \tag{13}$$

The displacement vector of solid $\vec{u} = (u_r, u_\theta, u_z)$ with the help of (3) and (4) is given by

$$\begin{aligned}
u_r &= \frac{\partial \theta_1}{\partial r} + \frac{1}{r} \frac{\partial h_z}{\partial \theta} - \frac{\partial h_\theta}{\partial z}, \\
u_\theta &= \frac{1}{r} \frac{\partial \theta_1}{\partial \theta} + \frac{\partial h_r}{\partial z} - \frac{\partial h_z}{\partial r}, \\
u_z &= \frac{\partial \theta_1}{\partial z} + \frac{\partial h_\theta}{\partial r} + \frac{h_\theta}{r} - \frac{1}{r} \frac{\partial h_r}{\partial \theta}.
\end{aligned} \tag{14}$$

Substituting from (6) into (14), the displacement components of solid are

$$\begin{aligned}
u_r &= \left[f'_1 + \frac{n}{r} g_z - ik g_\theta \right] \cos(n\theta) e^{i(kz + \omega t)}, \\
u_\theta &= \left[-\frac{n}{r} f_1 + ik g_r - g'_z \right] \sin(n\theta) e^{i(kz + \omega t)}, \\
u_z &= \left[ik f_1 + g'_\theta + g_\theta - \frac{n}{r} g_r \right] \cos(n\theta) e^{i(kz + \omega t)}.
\end{aligned} \tag{15}$$

Substituting from (13) into (15), the solid displacement is

$$u_r = \left[f'_1 + \frac{n}{r} g_3 - ik g_1 \right] \cos(n\theta) e^{i(kz + \omega t)},$$

$$\begin{aligned}
u_\theta &= \left[-\frac{n}{r} f_1 + i k g_1 - g'_3 \right] \sin(n\theta) e^{i(kz + \omega t)}, \\
u_z &= \left[i k f_1 + g'_1 - \frac{(n+1)}{r} g_1 \right] \cos(n\theta) e^{i(kz + \omega t)},
\end{aligned} \quad (16)$$

where “prime” over a quantity denotes differentiation with respect to r , $\beta_1, \beta_2, \beta_3$ being the absolute values of $\alpha_1, \alpha_2, \alpha_3$, respectively.

The dilatations of solid and liquid media are

$$\begin{aligned}
e &= \Delta f_1(r) \cos(n\theta) e^{i(kz + \omega t)}, \\
\epsilon &= \Delta f_2(r) \cos(n\theta) e^{i(kz + \omega t)}.
\end{aligned} \quad (17)$$

Substituting from (16) into strain displacement relations and then using (2), the stresses σ_{ij} and the liquid pressures are

$$\begin{aligned}
\sigma_{rr} + s &= [c_1 M_{11}(r) + c_2 M_{12}(r) \\
&+ c_3 M_{13}(r) + c_4 M_{14}(r) + A_3 M_{15}(r) \\
&+ B_3 M_{16}(r) + A_1 M_{17}(r) + B_1 M_{18}(r)] \\
&\times \cos(n\theta) e^{i(kz + \omega t)},
\end{aligned} \quad (18)$$

$$\begin{aligned}
\sigma_{r\theta} &= [c_1 M_{21}(r) + c_2 M_{22}(r) \\
&+ c_3 M_{23}(r) + c_4 M_{24}(r) + A_3 M_{25}(r) \\
&+ B_3 M_{26}(r) + A_1 M_{27}(r) + B_1 M_{28}(r)] \\
&\times \sin(n\theta) e^{i(kz + \omega t)},
\end{aligned} \quad (19)$$

$$\begin{aligned}
\sigma_{rz} &= [c_1 M_{31}(r) + c_2 M_{32}(r) \\
&+ c_3 M_{33}(r) + c_4 M_{34}(r) + A_3 M_{35}(r) \\
&+ B_3 M_{36}(r) + A_1 M_{37}(r) + B_1 M_{38}(r)] \\
&\times \cos(n\theta) e^{i(kz + \omega t)},
\end{aligned} \quad (20)$$

$$\begin{aligned}
s &= [c_1 M_{41}(r) + c_2 M_{42}(r) \\
&+ c_3 M_{43}(r) + c_4 M_{44}(r)] \\
&\times \cos(n\theta) e^{i(kz + \omega t)},
\end{aligned} \quad (21)$$

$$\begin{aligned}
\frac{\partial s}{\partial r} &= [c_1 M_{41}(r) + c_2 M_{42}(r) \\
&+ c_3 M_{43}(r) + c_4 M_{44}(r)] \\
&\times \cos(n\theta) e^{i(kz + \omega t)},
\end{aligned} \quad (22)$$

where the coefficients $M_{ij}(r)$ are given as

$$\begin{aligned}
M_{11}(r) &= \left\{ 2N \left[\frac{n(n-1)}{r^2} - \alpha_1^2 \right] \right. \\
&\quad \left. + [(Q+R)\delta_1^2 - (A+Q)](k^2 + \alpha_1^2) \right\} \\
&\quad \times J_n(\beta_1 r) + \frac{2N\beta_1}{r} J_{n+1}(\beta_1 r), \\
M_{12}(r) &= \left\{ 2N \left[\frac{n(n-1)}{r^2} - \alpha_1^2 \right] \right. \\
&\quad \left. + [(Q+R)\delta_1^2 - (A+Q)](k^2 + \alpha_1^2) \right\} \\
&\quad \times Y_n(\beta_1 r) + \frac{2N\beta_1}{r} Y_{n+1}(\beta_1 r), \\
M_{13}(r) &= \left\{ 2N \left[\frac{n(n-1)}{r^2} - \alpha_1^2 \right] \right. \\
&\quad \left. + [(Q+R)\delta_1^2 - (A+Q)](k^2 + \alpha_1^2) \right\} \\
&\quad \times J_n(\beta_1 r) + \frac{2N\beta_1}{r} J_{n+1}(\beta_1 r), \\
M_{14}(r) &= \left\{ 2N \left[\frac{n(n-1)}{r^2} - \alpha_1^2 \right] \right. \\
&\quad \left. + [(Q+R)\delta_1^2 - (A+Q)](k^2 + \alpha_1^2) \right\} \\
&\quad \times Y_n(\beta_1 r) + \frac{2N\beta_1}{r} Y_{n+1}(\beta_1 r), \\
M_{15}(r) &= \frac{2Nn(n-1)}{r^2} J_n(\beta_3 r) - \frac{2Nn\beta_3}{r} J_{n+1}(\beta_3 r), \\
M_{16}(r) &= \frac{2Nn(n-1)}{r^2} Y_n(\beta_3 r) - \frac{2Nn\beta_3}{r} Y_{n+1}(\beta_3 r), \\
M_{17}(r) &= 2Nik\beta_3 J_n(\beta_3 r) - \frac{2N(n+1)ik}{r} J_{n+1}(\beta_3 r), \\
M_{18}(r) &= 2Nik\beta_3 Y_n(\beta_3 r) - \frac{2N(n+1)ik}{r} Y_{n+1}(\beta_3 r), \\
M_{21}(r) &= \frac{2Nn(1-n)}{r^2} Y_n(\beta_1 r) + \frac{2Nn\beta_1}{r} J_{n+1}(\beta_1 r), \\
M_{22}(r) &= \frac{2Nn(1-n)}{r^2} Y_n(\beta_1 r) + \frac{2Nn\beta_1}{r} Y_{n+1}(\beta_1 r), \\
M_{23}(r) &= \frac{2Nn(1-n)}{r^2} J_n(\beta_2 r) + \frac{2Nn\beta_2}{r} J_{n+1}(\beta_2 r), \\
M_{24}(r) &= \frac{2Nn(1-n)}{r^2} Y_n(\beta_2 r) + \frac{2Nn\beta_2}{r} Y_{n+1}(\beta_2 r), \\
M_{25}(r) &= \left[\frac{2Nn(1-n)}{r^2} + N\alpha_3^2 \right] J_n(\beta_3 r) \\
&\quad - \frac{2N\beta_3}{r} J_{n+1}(\beta_3 r),
\end{aligned}$$

$$\begin{aligned}
M_{26}(r) &= \left[\frac{2Nn(1-n)}{r^2} + N\alpha_3^2 \right] Y_n(\beta_3 r) \\
&\quad - \frac{2N\beta_3}{r} Y_{n+1}(\beta_3 r), \\
M_{27}(r) &= ikN\beta_3 J_n(\beta_3 r) \\
&\quad - \frac{2N(n+1)ik}{r} J_{n+1}(\beta_3 r), \\
M_{28}(r) &= ikN\beta_3 Y_n(\beta_3 r) \\
&\quad - \frac{2N(n+1)ik}{r} Y_{n+1}(\beta_3 r), \\
M_{31}(r) &= \frac{2Nnik}{r} J_n(\beta_1 r) - 2Nik\beta_1 J_{n+1}(\beta_1 r), \\
M_{32}(r) &= \frac{2Nnik}{r} Y_n(\beta_1 r) - 2Nik\beta_1 Y_{n+1}(\beta_1 r), \\
M_{33}(r) &= \frac{2Nnik}{r} J_n(\beta_2 r) - 2Nik\beta_2 J_{n+1}(\beta_2 r), \\
M_{34}(r) &= \frac{2Nnik}{r} Y_n(\beta_2 r) - 2Nik\beta_2 Y_{n+1}(\beta_2 r), \\
M_{35}(r) &= \frac{Nnik}{r} J_n(\beta_3 r), \\
M_{36}(r) &= \frac{Nnik}{r} Y_n(\beta_3 r), \\
M_{37}(r) &= \frac{-Nn\beta_3}{r} J_n(\beta_3 r) - N(k^2 - \alpha_3^2) J_{n+1}(\beta_3 r), \\
M_{38}(r) &= \frac{-Nn\beta_3}{r} Y_n(\beta_3 r) - N(k^2 - \alpha_3^2) Y_{n+1}(\beta_3 r), \\
M_{41}(r) &= (R\delta_1^2 - Q)(k^2 + \alpha_1^2) J_n(\beta_1 r),
\end{aligned}$$

$$\begin{aligned}
M_{42}(r) &= (R\delta_1^2 - Q)(k^2 + \alpha_1^2) Y_n(\beta_1 r), \\
M_{43}(r) &= (R\delta_2^2 - Q)(k^2 + \alpha_1^2) J_n(\beta_2 r), \\
M_{44}(r) &= (R\delta_2^2 - Q)(k^2 + \alpha_2^2) Y_n(\beta_2 r), \\
M_{45}(r) &= 0, \quad M_{46}(r) = 0, \\
M_{47}(r) &= 0, \quad M_{48}(r) = 0.
\end{aligned} \tag{23}$$

In (23),

$$\begin{aligned}
\delta_i^2 &= \frac{1}{(Rk_{12} - Qk_{22})} \\
&\quad \times [(Rk_{11} - Qk_{12}) - V_i^{-2}(PR - Q^2)] \\
&\quad (i = 1, 2),
\end{aligned} \tag{24}$$

where we considered

$$|kv_1| < \omega. \tag{25}$$

4. Boundary Conditions and Frequency Equation

The boundary conditions for traction free inner and outer surfaces of the hollow poroelastic cylinder in case of a pervious surface are

$$\begin{aligned}
\sigma_{rr} + s &= 0, \quad \sigma_{r\theta} = 0, \quad \sigma_{rz} = 0, \\
s &= 0, \quad \text{at } r = r_1, \quad r = r_2.
\end{aligned} \tag{26}$$

Equations (18)–(21) together with (26) yield eight homogeneous equations for eight arbitrary constants $C_1, C_2, C_3, C_4, A_3, B_3, A_1$, and B_1 . A nontrivial solution can be obtained when the determinant of coefficients vanishes. Thus, the frequency equation for a pervious surface is

$$\begin{vmatrix}
M_{11}(r_1) & M_{12}(r_1) & M_{13}(r_1) & M_{14}(r_1) & M_{15}(r_1) & M_{16}(r_1) & M_{17}(r_1) & M_{18}(r_1) \\
M_{21}(r_1) & M_{22}(r_1) & M_{23}(r_1) & M_{24}(r_1) & M_{25}(r_1) & M_{26}(r_1) & M_{27}(r_1) & M_{28}(r_1) \\
M_{31}(r_1) & M_{32}(r_1) & M_{33}(r_1) & M_{34}(r_1) & M_{35}(r_1) & M_{36}(r_1) & M_{37}(r_1) & M_{38}(r_1) \\
M_{41}(r_1) & M_{42}(r_1) & M_{43}(r_1) & M_{44}(r_1) & 0 & 0 & 0 & 0 \\
M_{11}(r_2) & M_{12}(r_2) & M_{13}(r_2) & M_{14}(r_2) & M_{15}(r_2) & M_{16}(r_2) & M_{17}(r_2) & M_{18}(r_2) \\
M_{21}(r_2) & M_{22}(r_2) & M_{23}(r_2) & M_{24}(r_2) & M_{25}(r_2) & M_{26}(r_2) & M_{27}(r_2) & M_{28}(r_2) \\
M_{31}(r_2) & M_{32}(r_2) & M_{33}(r_2) & M_{34}(r_2) & M_{35}(r_2) & M_{36}(r_2) & M_{37}(r_2) & M_{38}(r_2) \\
M_{41}(r_2) & M_{42}(r_2) & M_{43}(r_2) & M_{44}(r_2) & 0 & 0 & 0 & 0
\end{vmatrix} = 0. \tag{27}$$

In (27), the element $M_{ij}(r)$ is defined in (23).

By ignoring the liquid effects in the frequency equation of a pervious surface (27), the results of purely elastic solid are

obtained as a special case considered by [36]. Now, we consider the particular cases of the general frequency equations (27) when the axial and angular wave numbers vanish.

4.1. *Motion Independent of z .* When the axial wave number k is taken to be equal to zero, that is, by considering zeroth azimuthal mode, the frequency equation of a pervious surface

(28) degenerates into the product of two determinants as follows:

$$D_1 D_2 = 0, \quad (28)$$

where

$$D_1 = \begin{vmatrix} M'_{11}(r_1) & M'_{12}(r_1) & M'_{13}(r_1) & M'_{14}(r_1) & M'_{15}(r_1) & M'_{16}(r_1) \\ M'_{21}(r_1) & M'_{22}(r_1) & M'_{23}(r_1) & M'_{24}(r_1) & M'_{25}(r_1) & M'_{26}(r_1) \\ M'_{41}(r_1) & M'_{42}(r_1) & M'_{43}(r_1) & M'_{44}(r_1) & 0 & 0 \\ M'_{11}(r_2) & M'_{12}(r_2) & M'_{13}(r_2) & M'_{14}(r_2) & M'_{15}(r_2) & M'_{16}(r_2) \\ M'_{21}(r_2) & M'_{22}(r_2) & M'_{23}(r_2) & M'_{24}(r_2) & M'_{25}(r_2) & M'_{26}(r_2) \\ M'_{41}(r_2) & M'_{42}(r_2) & M'_{43}(r_2) & M'_{44}(r_2) & 0 & 0 \end{vmatrix}, \quad (29)$$

$$D_2 = \begin{vmatrix} M'_{37}(r_1) & M'_{38}(r_1) \\ M'_{37}(r_2) & M'_{38}(r_2) \end{vmatrix}.$$

The terms $M_{ij}(r)$ appearing in D_1 and D_2 are given in Appendix A for $k = 0$. It clears that, for $k = 0$, $\alpha_1^2, \alpha_2^2, \alpha_3^2$ being all positive, Bessel functions of the first and second kind enter the solution. Equation (30) is satisfied, if either D_1 or D_2 is equal to zero. The case of $D_1 = 0$ corresponds to plane-strain vibrations of thick-walled hollow poroelastic cylinders for a pervious surface.

The case of $D_2 = 0$, corresponds to longitudinal vibrations which involve only longitudinal displacement w . Also, $D_2 = 0$ is the same for a pervious and an impervious surface; hence, it is clear that longitudinal shear vibrations are independent of the nature of the surface. From (27), it is clear that plane-strain vibrations and longitudinal shear vibrations are uncoupled for a pervious surface, when the motion is independent of longitudinal coordinated z , and these vibrations are coupled for nonzero longitudinal wave number k ; that is, $k \neq 0$. The frequency equation of

longitudinal shear vibrations $D_2 = 0$, when expanded, gives

$$J'_n(\alpha_3 r_1) Y'_n(\alpha_3 r_2) - J'_n(\alpha_3 r_2) Y'_n(\alpha_3 r_1) = 0. \quad (30)$$

And the amplitude ratio is given as

$$\frac{A_1}{B_1} = -\frac{Y'_n(\alpha_3 r_1)}{J'_n(\alpha_3 r_1)}, \quad (31)$$

the frequency equation of longitudinal shear vibrations of hollow poroelastic cylinders (31).

4.2. *Motion Independent of θ .* When the motion is independent of angular coordinated θ (i.e., $n = 0$), the frequency equation (27) for a pervious surface is reduced to the product of two determinants given by

$$D_3 D_4 = 0, \quad (32)$$

where

$$D_3 = \begin{vmatrix} M''_{11}(r_1) & M''_{12}(r_1) & M''_{13}(r_1) & M''_{14}(r_1) & M''_{17}(r_1) & M''_{18}(r_1) \\ M''_{31}(r_1) & M''_{32}(r_1) & M''_{33}(r_1) & M''_{34}(r_1) & M''_{37}(r_1) & M''_{38}(r_1) \\ M''_{41}(r_1) & M''_{42}(r_1) & M''_{43}(r_1) & M''_{44}(r_1) & 0 & 0 \\ M''_{11}(r_2) & M''_{12}(r_2) & M''_{13}(r_2) & M''_{14}(r_2) & M''_{17}(r_2) & M''_{18}(r_2) \\ M''_{31}(r_2) & M''_{32}(r_2) & M''_{33}(r_2) & M''_{34}(r_2) & M''_{37}(r_2) & M''_{38}(r_2) \\ M''_{41}(r_2) & M''_{42}(r_2) & M''_{43}(r_2) & M''_{44}(r_2) & 0 & 0 \end{vmatrix} \quad (33)$$

$$D_4 = \begin{vmatrix} M''_{25}(r_1) & M''_{26}(r_1) \\ M''_{25}(r_2) & M''_{26}(r_2) \end{vmatrix}.$$

The terms $M'_{ij}(r)$ in D_3 and D_4 are given in Appendix B for $n = 0$. From (33), now (32) is satisfied if $D_3 = 0$ or $D_4 = 0$. The case of $D_3 = 0$ gives the frequency equation of axial symmetric vibrations of an infinite hollow poroelastic cylinder for a pervious surface discussed by Ahmed Shah [37].

The case of $D_4 = 0$ when simplified yields the equation

$$J_2(\alpha_3 r_1) Y_2(\alpha_3 r_2) - J_2(\alpha_3 r_2) Y_2(\alpha_3 r_1) = 0, \quad (34)$$

which is the frequency of torsional vibrations of infinite hollow poroelastic cylinder studied by El-Naggar et al. [2] in the presence of dissipation. Moreover, the frequency equation (34) is independent of the nature of the surface, that is, pervious.

Also, it can be said that (34) is the same for pervious surfaces.

4.3. Equivoluminal Modes. For $n = 0$, the stress free boundary conditions on the inner and outer surfaces of the hollow poroelastic cylinder are satisfied if

$$\alpha_3^2 = k^2 > 0. \quad (35)$$

The dilatational and equivoluminal potentials f_1 and g_1 are coupled through the boundary conditions. In particular, to consider purely equivoluminal modes, we set

$$f_1 = f_2 = 0 \quad g_3 = 0. \quad (36)$$

Using (36) into (17), it is seen that the dilatations of solid and liquid media are zero. Hence, from (2), the liquid pressure is zero. Therefore, the equivoluminal modes are independent of the nature of surface, that is, pervious and impervious. Accordingly, no distinctions between pervious surfaces are seen. Therefore, from (35) and (36), we have

$$g'_1(\alpha_3 r_1) = g'_1(\alpha_3 r_2) = 0 \quad \sigma_{rr} + s = 0, \quad (37)$$

where

$$g_1(\alpha_3 r) = A_1 J_1(\alpha_3 r) + B_1 Y_1(\alpha_3 r). \quad (38)$$

Substituting from (38) into (37) and eliminating the constants A_1, B_1 , the frequency equation of purely equivoluminal modes is

$$J'_1(\alpha_3 r_1) Y'_1(\alpha_3 r_2) - J'_1(\alpha_3 r_2) Y'_1(\alpha_3 r_1) = 0, \quad (39)$$

with the amplitude ratio

$$\frac{A_1}{B_1} = -\frac{Y'_1(\alpha_3 r_1)}{J'_1(\alpha_3 r_1)}. \quad (40)$$

And the nonzero displacement and stress for equivoluminal modes are

$$\begin{aligned} U &= ik [A_1 J_1(\alpha_3 r_1) + B_1 Y_1(\alpha_3 r_2)] e^{i(kz+wt)} \\ W &= -\alpha_3 [A_1 J_0(\alpha_3 r) + B_1 Y_0(\alpha_3 r)] e^{i(kz+wt)} \\ \sigma_{rr} &= -2Nki [A_1 J'_1(\alpha_3 r) + B_1 Y'_1(\alpha_3 r)] e^{i(kz+wt)}. \end{aligned} \quad (41)$$

Equation (39) is the same as (34) of longitudinal shear vibrations for a case of $n = 1$.

4.3.1. For Thin Poroelastic Cylindrical Shell. When $h/r_1 \ll 1$, that is, for thin poroelastic cylindrical shell, the frequency equation (27) by using Hankel-Kirchhoff asymptotic approximations [38] is reduced to

$$\sin(\alpha_3 h) - \frac{7\alpha_3 h}{8\alpha_3 r_1 r_2} \cos(\alpha_3 h) + \frac{49}{64\alpha_3 r_1 r_2} \sin(\alpha_3 h) \approx 0. \quad (42)$$

As $\alpha_3 r_1 \rightarrow \infty$, $\alpha_3 r_2 \rightarrow \infty$, with the help of (41), (27) is simplified to

$$\omega \approx \sqrt{2} \frac{q\pi v_3}{h} \left[1 + \frac{7}{8q^2\pi^2} \left(\frac{h}{r_1} \right)^2 \right], \quad (q = 1, 2, 3, \dots). \quad (43)$$

Equation (43) determines the frequency of purely equivoluminal modes of a poroelastic plate of thickness h .

4.3.2. For Poroelastic Solid Cylinder. When $r_1/h \rightarrow 0$, that is, for the poroelastic solid cylinder, the frequency equation (39) is reduced asymptotically to

$$J'_1(\alpha_3 r) = 0, \quad (44)$$

which is the frequency equation of purely equivoluminal modes of a poroelastic solid cylinder of radius h .

5. Nondimensional Frequency Equation

For propagating modes in a nondissipative medium, the wave number k is real. To analyze the frequency equation of pervious and impervious surfaces, it is convenient to introduce the following nondimensional parameters:

$$\begin{aligned} P' &= \frac{P}{H}, & Q' &= \frac{Q}{H}, \\ R' &= \frac{R}{H}, & N' &= \frac{N}{H}, \\ \rho'_{11} &= \frac{\rho_{11}}{\rho}, & \rho'_{12} &= \frac{\rho_{12}}{\rho}, \\ \rho'_{22} &= \frac{\rho_{22}}{\rho}, & W &= \omega h C_0^{-1}, \\ \varepsilon_1 &= \frac{V_0^2}{V_1^2}, & \varepsilon_2 &= \frac{V_0^2}{V_2^2}, & \varepsilon_3 &= \frac{V_0^2}{V_3^2}, \\ \delta &= \frac{h}{L}, & \Omega' &= \frac{\Omega}{V_0^2 \rho}, \end{aligned} \quad (45)$$

where w is nondimensional frequency,

$$H = P + 2Q + R, \quad \rho = \rho_{11} + 2\rho_{12} + \rho_{22}, \quad (46)$$

where C_0 and V_0 are the reference velocities taking the following form

$$\left(C_0^2 = \frac{N}{\rho}, V_0^2 = \frac{H}{\rho} \right), \quad (47)$$

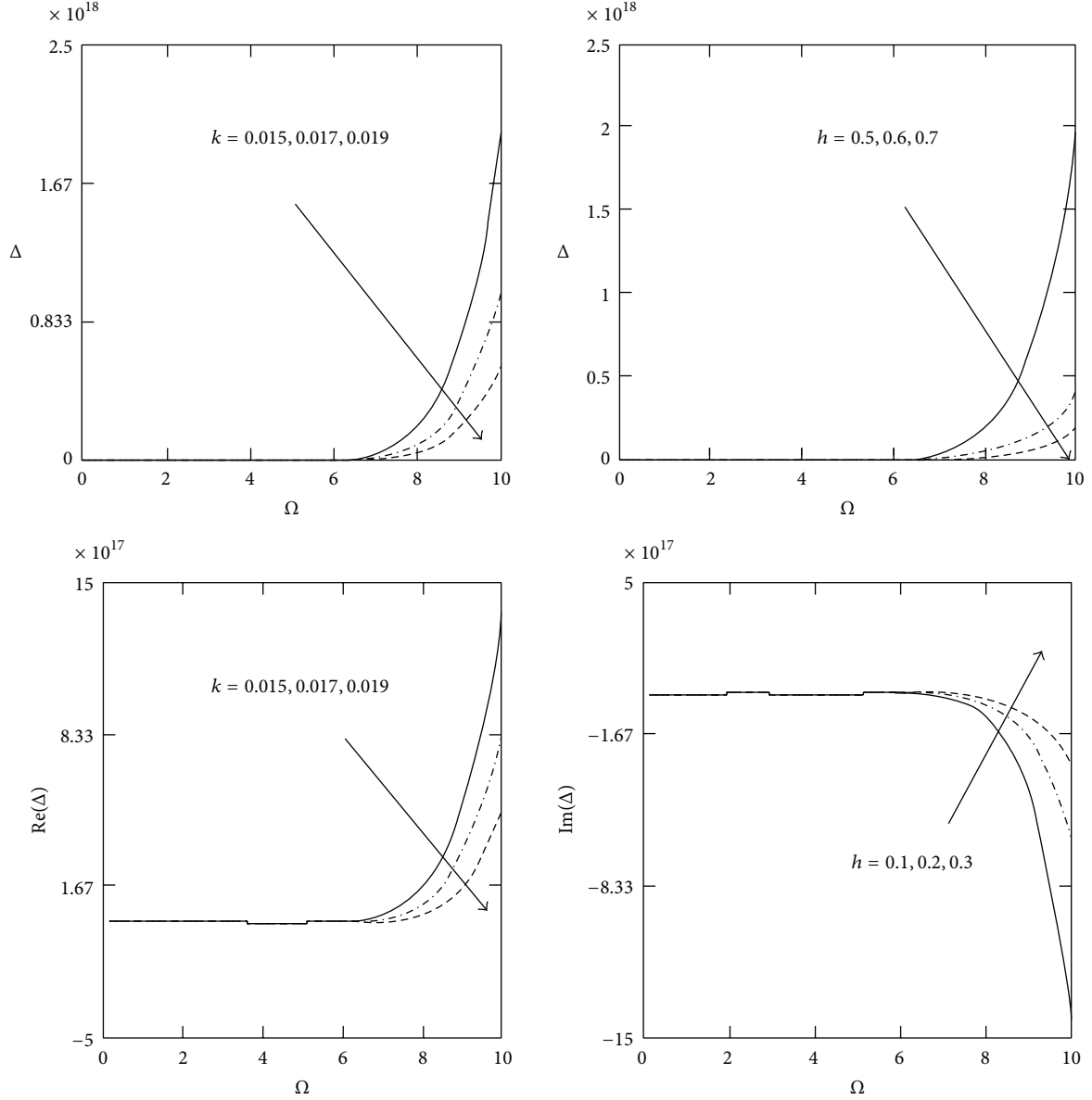


FIGURE 1: Effect of the frequency determinant Δ with respect to the rotation Ω for different values of k , h , and n .

where h is the thickness of the hollow poroelastic cylinder and L is the wavelength.

Let

$$g = \frac{r_2}{r_1} \quad \text{so that} \quad \frac{h}{r_1} = (g - 1). \quad (48)$$

6. Numerical Results and Discussion

The numerical results for frequency equations are computed for the poroelastic material. Since the frequency equation, phase velocity, and attenuation coefficient are transcendental in nature. The roots are obtained for $n = 0$, the axisymmetric mode, and for the flexural mode $n = 1$. The values of the elastic constants of poroelastic material, one being sandstone

saturated with kerosene [37] and the other one being sandstone with water [39], are as follows:

$$\begin{aligned} P' &= 0.843, & Q' &= 0.065, & R' &= 0.028, & N' &= 0.234 \\ \rho'_{11} &= 0.901, & \rho'_{12} &= 0.001, & \rho'_{22} &= 0.101, & \varepsilon_1 &= 0.999, \\ & & \varepsilon_2 &= 4.763, & \varepsilon_3 &= 3.851. \end{aligned} \quad (49)$$

The numerical technique outlined above was used to obtain frequency equation with respect to rotation Ω under the effect of wave number and thickness. For the sake of brevity, some computational results are being presented here. The variations are shown in Figures 1–5, respectively.

Figure 1 shows the variation of the frequency equation Δ , phase velocity $\text{Re}(\Delta)$, and attenuation coefficient $\text{Im}(\Delta)$

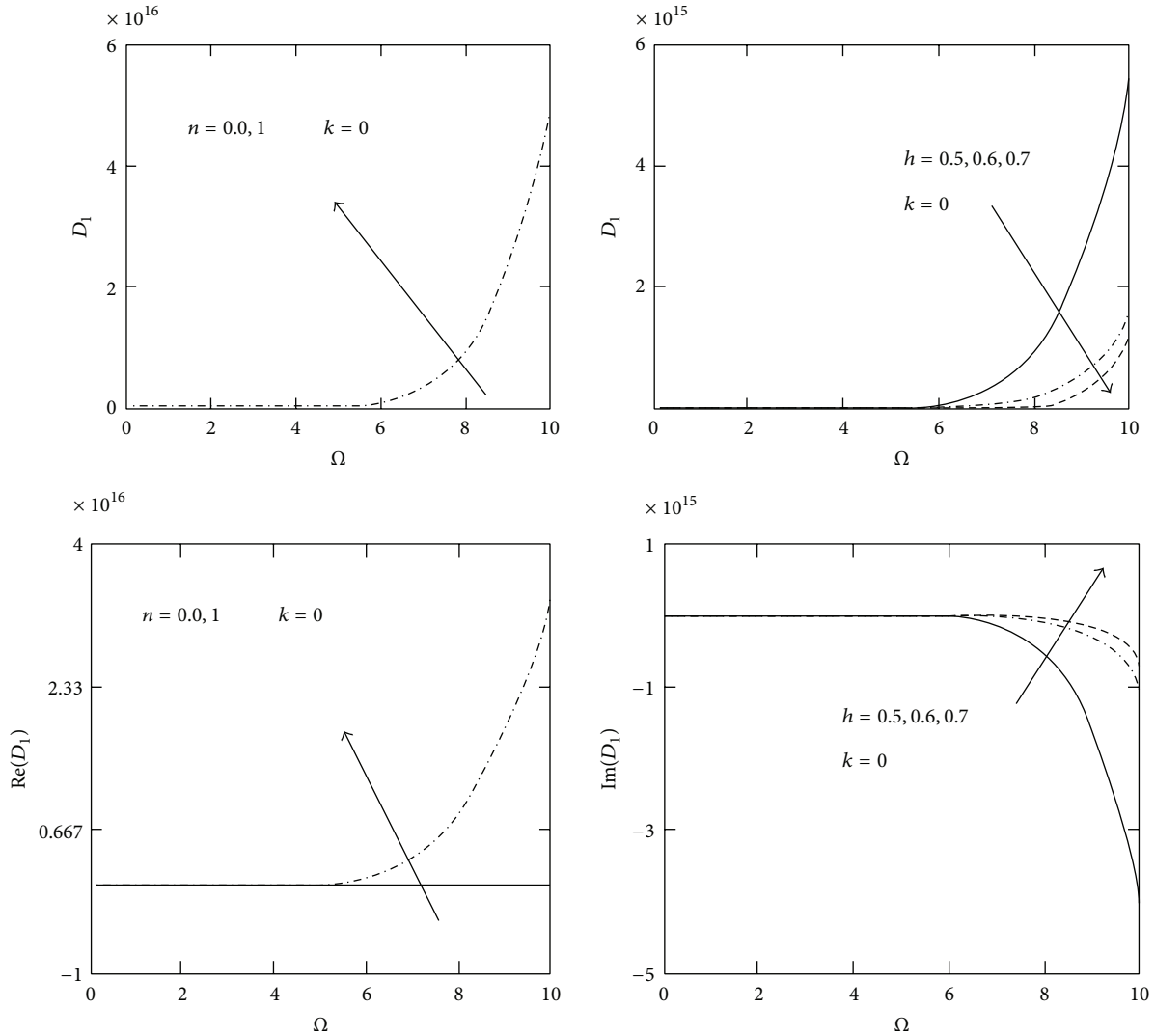


FIGURE 2: Effect of the frequency determinant D_1 with respect to the rotation Ω for different values of n and h .

of wave propagation in hollow poroelastic circular cylinders with respect to rotation Ω for different values of wave number k and thickness h . In both figures, it is clear that the frequency equation, phase velocity, and attenuation coefficient have a nonzero value only in a bounded region of space. It is observed that the frequency equation and phase velocity increase with increasing rotation, while it decreases with increasing wave number and thickness; as well, attenuation coefficient increases with increasing thickness, while it decreases with increasing of rotation.

Figure 2 shows the variation of the frequency equation D_1 , phase velocity $\text{Re}(D_1)$, and attenuation coefficient $\text{Im}(D_1)$ of wave propagation in hollow poroelastic circular cylinders with respect to rotation Ω subjected to motion independent of z for different values of longitudinal mode ($n = 0$), flexural mode ($n = 1$), and thickness h . In both figures, it is clear that the frequency equation, phase velocity, and attenuation coefficient have a nonzero value only in a bounded region of space. It is observed that the frequency equation and phase

velocity increase with increasing rotation, longitudinal mode, and flexural mode, while frequency equation increases with increasing rotation, while it decreases with increasing thickness; as well, attenuation coefficient increases with increasing thickness, while it decreases with increasing rotation.

Figure 3 shows the variation of the frequency equation D_2 of wave propagation in hollow poroelastic circular cylinders with respect to rotation Ω subjected to motion independent of z for different values of longitudinal mode ($n = 0$), flexural mode ($n = 1$), and thickness h . In both figures, it is clear that the frequency equation has a nonzero value only in a bounded region of space. It is observed that the frequency equation decreases with increasing rotation, while it increases with increasing longitudinal mode and flexural mode; as well, it decreases with increasing of thickness.

Figure 4 shows the variation of the frequency equation D_3 , phase velocity $\text{Re}(D_3)$, and attenuation coefficient $\text{Im}(D_3)$ of wave propagation in hollow poroelastic circular cylinders with respect to rotation Ω subjected to motion independent

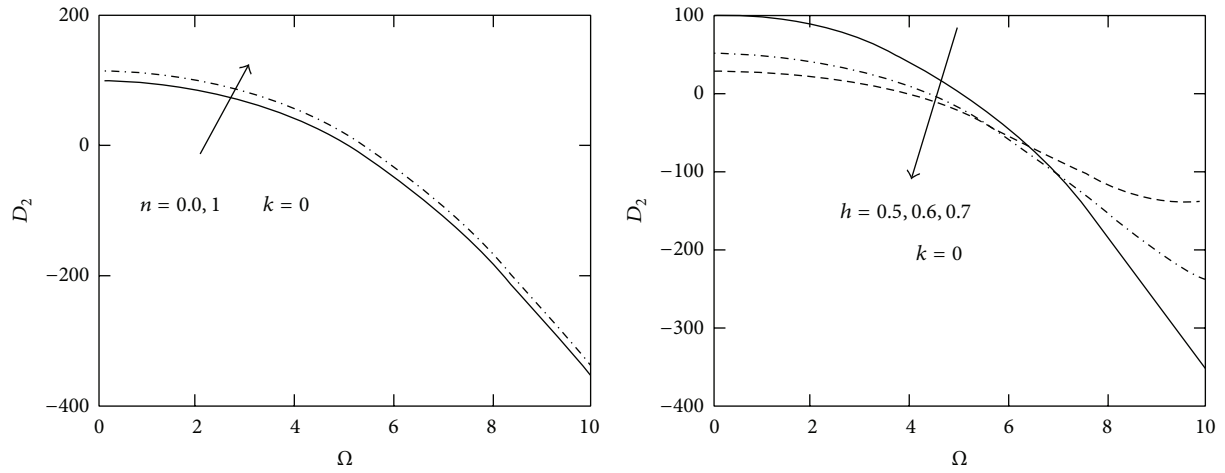


FIGURE 3: Effect of the frequency determinant D_2 with respect to the rotation Ω for different values of h and n .

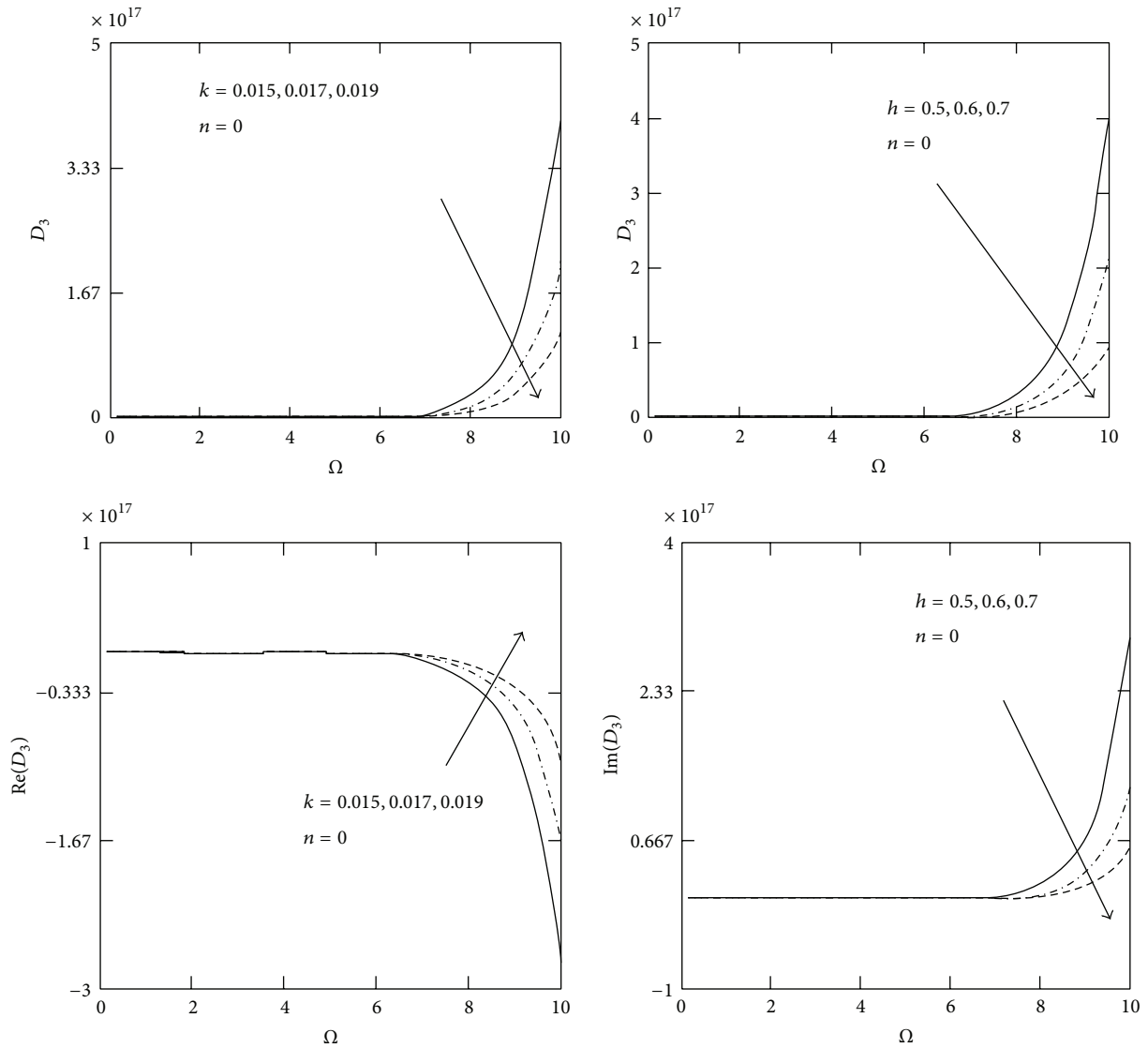


FIGURE 4: Effect of the frequency determinant D_3 with respect to the rotation Ω for different values of k and h .

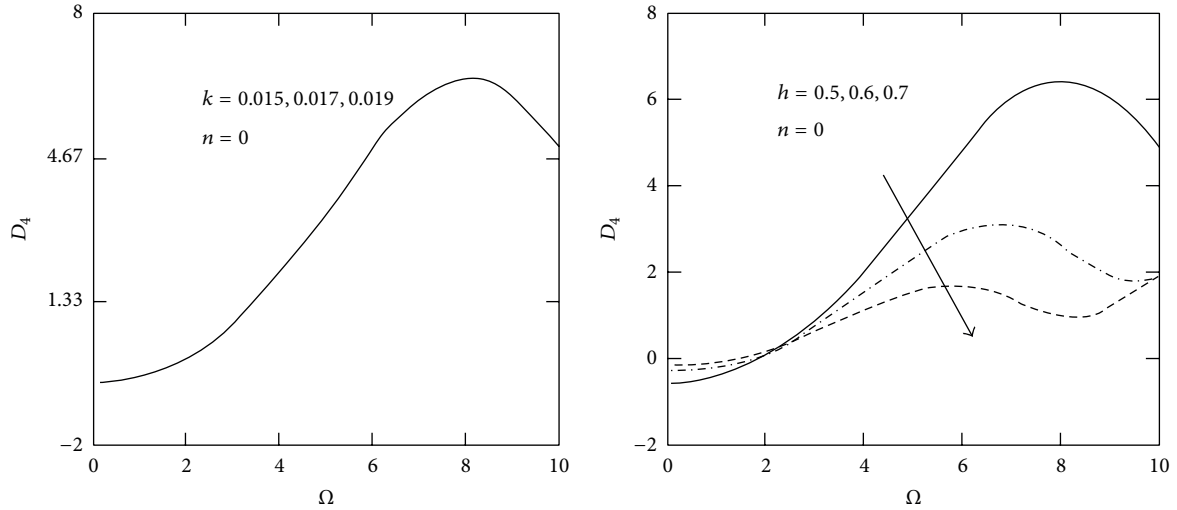


FIGURE 5: Effect of the frequency determinant D_4 with respect to the rotation Ω for different values of k and h .

of θ for different values of wave number k and thickness h . In both figures, it is clear that the frequency equation, phase velocity, and attenuation coefficient have a nonzero value only in a bounded region of space. It is observed that the frequency equation and attenuation coefficient decrease with increasing wave number and thickness, respectively, while it increases with increasing rotation; as well, attenuation coefficient decreases with increasing thickness, while it increases with increasing rotation.

Figure 5 shows the variation of the frequency equation D_4 of wave propagation in hollow poroelastic circular cylinders with respect to rotation Ω subjected to motion independent of θ for different values of wave number k and thickness h . In both figures, it is clear that the frequency equation has a nonzero value only in a bounded region of space. It is observed that the frequency equation decreases with increasing thickness and, while it has oscillatory behavior in the whole range of Ω -axis, there is no effect on the frequency equation.

Comparing with previous studies, we find that our results (shown in Figures 1–5) without rotation for the wave propagation of poroelastic bone with the results obtained by Ahmed Shah [37]. Also, these results agree with those of Kumar [40] by ignoring the liquid and rotation effect and, after rearrangement of terms, the results obtained agree with the purely elastic solid. In case of gravity $\Omega = 0$, our results are in agreement with those of Biot [36]. The analytical results obtained by Sharma and Gogna [41] can be considered as a limiting case (by taking $\Omega = 0$), which are in agreement with earlier results obtained by Fotiadis et al. [42].

7. Conclusion

In this paper, the wave propagation of poroelastic bone with circular cylinder subjected to traction free surfaces is considered. We adopted the analysis of [3], and the solution

of the problem was expressed in terms of a Bessel function of the first and second kind, respectively.

The resulting frequency equation has been solved numerically. The contribution of the fluid term to wave propagation is a well-established possible mechanism of wave propagation connected to many biological phenomena observed in bone. Although the prediction of the model cannot be trusted quantitatively at this stage, its qualitative behavior complies with the predictions of other theoretical and experimental models referred to in the literature. A calibration of the model and its verification with experimental data is in progress. Important phenomena are observed in all these computations as follows:

- (i) the frequency equation of axially symmetric vibrations is independent of the nature of surface, rotation, and presence of fluid in the poroelastic cylindrical;
- (ii) by comparing Figures 1–5, it was found that the frequency equation, phase velocity, and attenuation coefficient have the same behavior in both media; but, with the passage of rotation, wave number, and thickness, numerical values of frequency in the poroelastic cylinder are large in comparison due to the influences of rotation and fluid;
- (iii) special cases are considered as motion independent on z and motion independent on θ in poroelastic medium, as well as in the isotropic case for very large wave numbers and dispersion curves for longitudinal mode and flexural mode ($n = 0, 1$), respectively;
- (iv) the results presented in this paper should prove to be useful for researchers in material science and designers of new materials and bones;
- (v) the study of the phenomenon of rotation, wave number, and thickness is also used to improve the conditions of bones.

Appendices

A. Coefficients of $M'_{ij}(r_k)$

The coefficients $M'_{ij}(r_k)$ ($i, j = 1, 2, \dots, 8, k = 1, 2$) are given as follows:

$$\begin{aligned}
 M'_{11}(r_1) &= \left\{ 2N \left[\frac{n(n-1)}{r_1^2} - \alpha_1^2 \right] \right. \\
 &\quad \left. + [(Q+R)\delta_1^2 - (A+Q)](\alpha_1^2) \right\} \\
 &\quad \times J_n(\beta_1 r_1) + \frac{2N\beta_1}{r_1} J_{n+1}(\beta_1 r_1) \\
 M'_{12}(r_1) &= \left\{ 2N \left[\frac{n(n-1)}{r_1^2} - \alpha_1^2 \right] \right. \\
 &\quad \left. + [(Q+R)\delta_1^2 - (A+Q)](\alpha_1^2) \right\} \\
 &\quad \times Y_n(\beta_1 r_1) + \frac{2N\beta_1}{r_1} Y_{n+1}(\beta_1 r_1), \\
 M'_{13}(r_1) &= \left\{ 2N \left[\frac{n(n-1)}{r_1^2} - \alpha_1^2 \right] \right. \\
 &\quad \left. + [(Q+R)\delta_1^2 - (A+Q)](\alpha_1^2) \right\} \\
 &\quad \times J_n(\beta_1 r_1) + \frac{2N\beta_1}{r_1} J_{n+1}(\beta_1 r_1), \\
 M'_{14}(r_1) &= \left\{ 2N \left[\frac{n(n-1)}{r_1^2} - \alpha_1^2 \right] \right. \\
 &\quad \left. + [(Q+R)\delta_1^2 - (A+Q)](\alpha_1^2) \right\} \\
 &\quad \times Y_n(\beta_1 r_1) + \frac{2N\beta_1}{r_1} J_{n+1}(\beta_1 r_1), \\
 M'_{15}(r_1) &= \frac{2Nn(n-1)}{r_1^2} J_n(\beta_3 r_1) - \frac{2Nn\beta_3}{r_1} J_{n+1}(\beta_3 r_1), \\
 M'_{16}(r_1) &= \frac{2Nn(n-1)}{r_1^2} Y_n(\beta_3 r_2) - \frac{2Nn\beta_3}{r_1} Y_{n+1}(\beta_3 r_1), \\
 M'_{21}(r_1) &= \frac{2Nn(1-n)}{r_1^2} Y_n(\beta_1 r_1) + \frac{2Nn\beta_1}{r_1} J_{n+1}(\beta_1 r_1), \\
 M'_{22}(r_1) &= \frac{2Nn(1-n)}{r_1^2} Y_n(\beta_1 r_1) + \frac{2Nn\beta_1}{r_1} Y_{n+1}(\beta_1 r_1), \\
 M'_{23}(r_1) &= \frac{2Nn(1-n)}{r_1^2} J_n(\beta_2 r_1) + \frac{2Nn\beta_2}{r_1} J_{n+1}(\beta_2 r_1), \\
 M'_{24}(r_1) &= \frac{2Nn(1-n)}{r_1^2} Y_n(\beta_2 r_1) + \frac{2Nn\beta_2}{r_1} Y_{n+1}(\beta_2 r_1),
 \end{aligned}$$

$$\begin{aligned}
 M'_{25}(r_1) &= \left[\frac{2Nn(1-n)}{r_1^2} + N\alpha_3^2 \right] J_n(\beta_3 r_1) \\
 &\quad - \frac{2N\beta_3}{r_1} J_{n+1}(\beta_3 r_1), \\
 M'_{26}(r_1) &= \left[\frac{2Nn(1-n)}{r_1^2} + N\alpha_3^2 \right] Y_n(\beta_3 r_1) \\
 &\quad - \frac{2N\beta_3}{r_1} Y_{n+1}(\beta_3 r_1),
 \end{aligned}$$

$$M'_{37}(r_1) = \frac{-Nn\beta_3}{r_1} J_n(\beta_3 r_1) - N(\alpha_3^2) J_{n+1}(\beta_3 r_1),$$

$$M'_{38}(r_1) = \frac{-Nn\beta_3}{r_1} Y_n(\beta_3 r_1) - N(\alpha_3^2) Y_{n+1}(\beta_3 r_1),$$

$$M'_{37}(r_2) = \frac{-Nn\beta_3}{r_2} J_n(\beta_3 r_2) - N(\alpha_3^2) J_{n+1}(\beta_3 r_2),$$

$$M'_{38}(r_2) = \frac{-Nn\beta_3}{r_2} Y_n(\beta_3 r_2) - N(\alpha_3^2) Y_{n+1}(\beta_3 r_2),$$

$$M'_{41}(r_1) = (R\delta_1^2 - Q)(\alpha_1^2) J_n(\beta_1 r_1),$$

$$M'_{42}(r_1) = (R\delta_1^2 - Q)(\alpha_1^2) Y_n(\beta_1 r_1),$$

$$M'_{43}(r_1) = (R\delta_2^2 - Q)(\alpha_1^2) J_n(\beta_2 r_1),$$

$$M'_{44}(r_1) = (R\delta_2^2 - Q)(\alpha_2^2) J_n(\beta_2 r_1),$$

$$M'_{45}(r_1) = 0,$$

$$M'_{46}(r_1) = 0,$$

$$M'_{41}(r_2) = (R\delta_1^2 - Q)(\alpha_1^2) J_n(\beta_1 r_2),$$

$$M'_{42}(r_2) = (R\delta_1^2 - Q)(\alpha_1^2) Y_n(\beta_1 r_2),$$

$$M'_{43}(r_2) = (R\delta_2^2 - Q)(\alpha_1^2) J_n(\beta_2 r_2),$$

$$M'_{44}(r_2) = (R\delta_2^2 - Q)(\alpha_2^2) J_n(\beta_2 r_2),$$

$$M'_{45}(r_2) = 0,$$

$$M'_{46}(r_2) = 0.$$

(A.1)

B. Coefficients of $M''_{ij}(r_k)$

The coefficients $M''_{ij}(r_k)$ ($i, j = 1, 2, \dots, 8, k = 1, 2$) are given as follows:

$$\begin{aligned}
 M''_{11}(r_1) &= \left\{ -2N\alpha_1^2 + [(Q+R)\delta_1^2 - (A+Q)] \right. \\
 &\quad \left. \times (k^2 + \alpha_1^2) \right\} \\
 &\quad \times J_n(\beta_1 r_1) + \frac{2N\beta_1}{r_1} J_{n+1}(\beta_1 r_1),
 \end{aligned}$$

$$\begin{aligned}
M''_{12}(r_1) &= \{-2N\alpha_1^2 + [(Q+R)\delta_1^2 - (A+Q)] \\
&\quad \times (k^2 + \alpha_1^2)\} \\
&\quad \times Y_n(\beta_1 r_1) + \frac{2N\beta_1}{r_1} Y_{n+1}(\beta_1 r_1), \\
M''_{13}(r_1) &= \{-2N\alpha_2^2 + [(Q+R)\delta_2^2 - (A+Q)] \\
&\quad \times (k^2 + \alpha_2^2)\} \\
&\quad \times J_n(\beta_2 r_1) + \frac{2N\beta_2}{r_1} J_{n+1}(\beta_2 r_1), \\
M''_{14}(r_1) &= \{-2N\alpha_2^2 + [(Q+R)\delta_2^2 - (A+Q)] \\
&\quad \times (k^2 + \alpha_2^2)\} \\
&\quad \times Y_n(\beta_2 r_1) + \frac{2N\beta_2}{r_1} Y_{n+1}(\beta_2 r_1), \\
M''_{17}(r_1) &= 2Nik\beta_3 J_n(\beta_3 r_1) - \frac{2Nik}{r_1} J_{n+1}(\beta_3 r_1), \\
M''_{18}(r_1) &= 2Nik\beta_3 Y_n(\beta_3 r_1) - \frac{2Nik}{r_1} Y_{n+1}(\beta_3 r_1), \\
M''_{25}(r_1) &= -\frac{2N\beta_3}{r_1} J_{n+1}(\beta_3 r_1), \\
M''_{26}(r_1) &= [N\alpha_3^2] Y_n(\beta_3 r_1) - \frac{2N\beta_3}{r_1} Y_{n+1}(\beta_3 r_1), \\
M''_{25}(r_2) &= -\frac{2N\beta_3}{r_2} J_{n+1}(\beta_3 r_2), \\
M''_{26}(r_2) &= [N\alpha_3^2] Y_n(\beta_3 r_2) - \frac{2N\beta_3}{r_1} Y_{n+1}(\beta_3 r_2), \\
M''_{31}(r_1) &= -2Nik\beta_1 J_{n+1}(\beta_1 r_1), \\
M''_{32}(r_1) &= -2Nik\beta_1 Y_{n+1}(\beta_1 r_1), \\
M''_{33}(r_1) &= -2Nik\beta_2 J_{n+1}(\beta_2 r_1), \\
M''_{34}(r_1) &= -2Nik\beta_2 Y_{n+1}(\beta_2 r_1), \\
M''_{37}(r_1) &= -N(k^2 - \alpha_3^2) J_{n+1}(\beta_3 r_1), \\
M''_{38}(r_1) &= -N(k^2 - \alpha_3^2) Y_{n+1}(\beta_3 r_1), \\
M''_{41}(r_1) &= (R\delta_1^2 - Q)(k^2 + \alpha_1^2) J_n(\beta_1 r_1), \\
M''_{42}(r_1) &= (R\delta_1^2 - Q)(k^2 + \alpha_1^2) Y_n(\beta_1 r_1), \\
M''_{43}(r_1) &= (R\delta_2^2 - Q)(k^2 + \alpha_1^2) J_n(\beta_2 r_1), \\
M''_{44}(r_1) &= (R\delta_2^2 - Q)(k^2 + \alpha_2^2) J_n(\beta_2 r_1), \\
M''_{47}(r_1) &= 0, \\
M''_{48}(r_1) &= 0, \\
M''_{11}(r_2) &= \{-2N\alpha_1^2 + [(Q+R)\delta_1^2 - (A+Q)] \\
&\quad \times (k^2 + \alpha_1^2)\} \\
&\quad \times J_n(\beta_1 r_2) + \frac{2N\beta_1}{r_2} J_{n+1}(\beta_1 r_2), \\
M''_{12}(r_2) &= \{2N\alpha_1^2 + [(Q+R)\delta_1^2 - (A+Q)] \\
&\quad \times (k^2 + \alpha_1^2)\} \\
&\quad \times Y_n(\beta_1 r_2) + \frac{2N\beta_1}{r_2} Y_{n+1}(\beta_1 r_2), \\
M''_{13}(r_2) &= \{-2N\alpha_2^2 + [(Q+R)\delta_2^2 - (A+Q)] \\
&\quad \times (k^2 + \alpha_2^2)\} \\
&\quad \times J_n(\beta_2 r_2) + \frac{2N\beta_2}{r_2} J_{n+1}(\beta_2 r_2), \\
M''_{14}(r_2) &= \{-2N\alpha_2^2 + [(Q+R)\delta_2^2 - (A+Q)] \\
&\quad \times (k^2 + \alpha_2^2)\} \\
&\quad \times Y_n(\beta_2 r_2) + \frac{2N\beta_2}{r_2} J_{n+1}(\beta_2 r_2), \\
M''_{17}(r_2) &= 2Nik\beta_3 J_n(\beta_3 r_2) - \frac{2Nik}{r_2} J_{n+1}(\beta_3 r_2), \\
M''_{18}(r_2) &= 2Nik\beta_3 Y_n(\beta_3 r_2) - \frac{2Nik}{r_2} Y_{n+1}(\beta_3 r_2), \\
M''_{31}(r_2) &= -2Nik\beta_1 J_{n+1}(\beta_1 r_2), \\
M''_{32}(r_2) &= -2Nik\beta_1 Y_{n+1}(\beta_1 r_2), \\
M''_{33}(r_2) &= -2Nik\beta_2 J_{n+1}(\beta_2 r_2), \\
M''_{34}(r_2) &= -2Nik\beta_2 Y_{n+1}(\beta_2 r_2), \\
M''_{37}(r_2) &= -N(k^2 - \alpha_3^2) J_{n+1}(\beta_3 r_2), \\
M''_{38}(r_2) &= -N(k^2 - \alpha_3^2) Y_{n+1}(\beta_3 r_2), \\
M''_{41}(r_2) &= (R\delta_1^2 - Q)(k^2 + \alpha_1^2) J_n(\beta_1 r_2), \\
M''_{42}(r_2) &= (R\delta_1^2 - Q)(k^2 + \alpha_1^2) Y_n(\beta_1 r_2), \\
M''_{43}(r_2) &= (R\delta_2^2 - Q)(k^2 + \alpha_1^2) J_n(\beta_2 r_2), \\
M''_{44}(r_2) &= (R\delta_2^2 - Q)(k^2 + \alpha_2^2) J_n(\beta_2 r_2), \\
M''_{47}(r_2) &= 0, \\
M''_{48}(r_2) &= 0.
\end{aligned}$$

(B.1)

Conflict of Interests

The authors declare that there is no conflict of interests regarding the publication of this paper.

References

- [1] S. M. Ahmed and A. M. Abd-Alla, "Electromechanical wave propagation in a cylindrical poroelastic bone with cavity," *Applied Mathematics and Computation*, vol. 133, no. 2-3, pp. 257–286, 2002.
- [2] A. M. El-Naggar, A. M. Abd-Alla, and S. R. Mahmoud, "Analytical solution of electro-mechanical wave propagation in long bones," *Applied Mathematics and Computation*, vol. 119, no. 1, pp. 77–98, 2001.
- [3] A. M. Abd-Alla, S. M. Abo-Dahab, and S. R. Mahmoud, "Wave propagation modeling in cylindrical human long wet bones with cavity," *Meccanica*, vol. 46, no. 6, pp. 1413–1428, 2011.
- [4] R. T. Hart, "A theoretical study on the influence of bone maturation rate on surface remodeling predictions: idealized models," *Journal of Biomechanics*, vol. 23, no. 3, pp. 241–257, 1990.
- [5] Q.-H. Qin, C. Qu, and J. Ye, "Thermoelectroelastic solutions for surface bone remodeling under axial and transverse loads," *Biomaterials*, vol. 26, no. 33, pp. 6798–6810, 2005.
- [6] G. Martínez, J. M. García Aznar, M. Doblaré, and M. Cerrolaza, "External bone remodeling through boundary elements and damage mechanics," *Mathematics and Computers in Simulation*, vol. 73, no. 1–4, pp. 183–199, 2006.
- [7] I. G. Jang and I. Y. Kim, "Computational simulation of simultaneous cortical and trabecular bone change in human proximal femur during bone remodeling," *Journal of Biomechanics*, vol. 43, no. 2, pp. 294–301, 2010.
- [8] M. C. Tsili, "Theoretical solutions for internal bone remodeling of diaphyseal shafts using adaptive elasticity theory," *Journal of Biomechanics*, vol. 33, no. 2, pp. 235–239, 2000.
- [9] S. C. Cowin and K. Firoozbakhsh, "Bone remodeling of diaphyseal surfaces under constant load: the theoretical predictions," *Journal of Biomechanics*, vol. 14, no. 7, pp. 471–484, 1981.
- [10] J.-F. Ganghoffer, "A contribution to the mechanics and thermodynamics of surface growth. Application to bone external remodeling," *International Journal of Engineering Science*, vol. 50, no. 1, pp. 166–191, 2012.
- [11] N. A. Sims and J. H. Gooi, "Bone remodeling: multiple cellular interactions required for coupling of bone formation and resorption," *Seminars in Cell and Developmental Biology*, vol. 19, no. 5, pp. 444–451, 2008.
- [12] M. Zumsande, D. Stieffs, S. Siegmund, and T. Gross, "General analysis of mathematical models for bone remodeling," *Bone*, vol. 48, no. 4, pp. 910–917, 2011.
- [13] E. Malachanne, D. Dureisseix, and F. Jourdan, "Numerical model of bone remodeling sensitive to loading frequency through a poroelastic behavior and internal fluid movements," *Journal of the Mechanical Behavior of Biomedical Materials*, vol. 4, no. 6, pp. 849–857, 2011.
- [14] A. Vahdati and G. Rouhi, "A model for mechanical adaptation of trabecular bone incorporating cellular accommodation and effects of microdamage and disuse," *Mechanics Research Communications*, vol. 36, no. 3, pp. 284–293, 2009.
- [15] S. J. Hazelwood, R. Bruce Martin, M. M. Rashid, and J. J. Rodrigo, "A mechanistic model for internal bone remodeling exhibits different dynamic responses in disuse and overload," *Journal of Biomechanics*, vol. 34, no. 3, pp. 299–308, 2001.
- [16] C. Qu, Q.-H. Qin, and Y. Kang, "A hypothetical mechanism of bone remodeling and modeling under electromagnetic loads," *Biomaterials*, vol. 27, no. 21, pp. 4050–4057, 2006.
- [17] V. A. Papathanasopoulou, D. I. Fotiadis, G. Foutsitzi, and C. V. Massalas, "A poroelastic bone model for internal remodeling," *International Journal of Engineering Science*, vol. 40, no. 5, pp. 511–530, 2002.
- [18] M. Mengoni and J. P. Ponthot, "Isotropic continuum damage/repair model for alveolar bone remodeling," *Journal of Computational and Applied Mathematics*, vol. 234, no. 7, pp. 2036–2045, 2010.
- [19] C. Boyle and I. Y. Kim, "Three-dimensional micro-level computational study of Wolff's law via trabecular bone remodeling in the human proximal femur using design space topology optimization," *Journal of Biomechanics*, vol. 44, no. 5, pp. 935–942, 2011.
- [20] X. Wang, A. M. Erickson, M. R. Allen, D. B. Burr, R. B. Martin, and S. J. Hazelwood, "Theoretical analysis of alendronate and risedronate effects on canine vertebral remodeling and microdamage," *Journal of Biomechanics*, vol. 42, no. 7, pp. 938–944, 2009.
- [21] M. C. Peterson and M. M. Riggs, "A physiologically based mathematical model of integrated calcium homeostasis and bone remodeling," *Bone*, vol. 46, no. 1, pp. 49–63, 2010.
- [22] Q.-H. Qin and J.-Q. Ye, "Thermoelectroelastic solutions for internal bone remodeling under axial and transverse loads," *International Journal of Solids and Structures*, vol. 41, no. 9–10, pp. 2447–2460, 2004.
- [23] C. Boyle and I. Y. Kim, "Comparison of different hip prosthesis shapes considering micro-level bone remodeling and stress-shielding criteria using three-dimensional design space topology optimization," *Journal of Biomechanics*, vol. 44, no. 9, pp. 1722–1728, 2011.
- [24] S. C. Cowin and W. C. Van Buskirk, "Surface bone remodelling induced by a medullary pin," *Journal of Biomechanics*, vol. 12, no. 4, pp. 269–276, 1979.
- [25] M. A. Biot, "General theory of three-dimensional consolidation," *Journal of Applied Physics*, vol. 12, no. 2, pp. 155–164, 1941.
- [26] D. H. Hegedus and S. C. Cowin, "Bone remodeling II: small strain adaptive elasticity," *Journal of Elasticity*, vol. 6, no. 4, pp. 337–352, 1976.
- [27] L. W. Zhang, Z. X. Lei, K. M. Liew, and J. L. Yu, "Static and dynamic of carbon nanotube reinforced functionally graded cylindrical panels," *Composite Structures*, vol. 111, pp. 205–212, 2014.
- [28] L. W. Zhang, P. Zhu, and K. M. Lie, "Thermal buckling of functionally graded plates using a local Kriging meshless method," *Composite Structures*, vol. 108, pp. 472–492, 2014.
- [29] P. Zhu, L. W. Zhang, and K. M. Liew, "Geometrically nonlinear thermomechanical analysis of moderately thick functionally graded plates using a local Petrov-Galerkin approach with moving Kriging interpolation," *Composite Structures*, vol. 107, pp. 298–314, 2014.
- [30] K. M. Liew, Z. X. Lei, J. L. Yu, and L. W. Zhang, "Postbuckling of carbon nanotube-reinforced functionally graded cylindrical panels under axial compression using a meshless approach," *Computer Methods in Applied Mechanics and Engineering*, vol. 268, pp. 1–17, 2014.

- [31] L. W. Zhang, Z. X. Lei, K. M. Liew, and J. L. Yu, "Large deflection geometrically nonlinear analysis of carbon nanotube-reinforced functionally graded cylindrical panels," *Computer Methods in Applied Mechanics and Engineering*, vol. 273, pp. 1–18, 2014.
- [32] L. W. Zhang, Y. J. Deng, and K. M. Liew, "An improved element-free Galerkin method for numerical modeling of the biological population problems," *Engineering Analysis with Boundary Elements*, vol. 40, pp. 181–188, 2014.
- [33] R. J. Cheng, L. W. Zhang, and K. M. Liew, "Modeling of biological population problems using the element-free kp-Ritz method," *Applied Mathematics and Computation*, vol. 227, pp. 274–290, 2014.
- [34] A. M. Abd-Alla and S. M. Abo-Dahab, "Effect of magnetic field on poroelastic bone model for internal remodeling," *Applied Mathematics and Mechanics*, vol. 34, no. 7, pp. 889–906, 2013.
- [35] M. A. Biot, "Theory of elasticity and consolidation for a porous anisotropic solid," *Journal of Applied Physics*, vol. 26, no. 2, pp. 182–185, 1955.
- [36] M. A. Biot, "Theory of propagation of elastic waves in a fluid-saturated porous solid. I: low-frequency range," *Acoustical Society of America*, vol. 28, pp. 168–178, 1956.
- [37] S. Ahmed Shah, "Axially symmetric vibrations of fluid-filled poroelastic circular cylindrical shells," *Journal of Sound and Vibration*, vol. 318, no. 1-2, pp. 389–405, 2008.
- [38] A. Abramowitz and I. A. Stegun, *Handbook of Mathematical Functions*, National Bureau of Standards, Washington, DC, USA, 1956.
- [39] C. H. Yew and P. N. Jogi, "Study of wave motions in fluid-saturated porous rocks," *Journal of the Acoustical Society of America*, vol. 60, no. 1, pp. 2–8, 1976.
- [40] R. Kumar, "Dispersion of axially symmetric waves in empty and fluid-filled cylindrical shells," *Acustica*, vol. 27, no. 6, pp. 317–328, 1972.
- [41] M. D. Sharma and M. L. Gogna, "Propagation of elastic waves in a cylindrical bore in a liquid-saturated porous solid," *Geophysical Journal International*, vol. 103, no. 1, pp. 47–54, 1990.
- [42] D. I. Fotiadis, G. Foutsitzi, and C. V. Massalas, "Wave propagation modeling in human long bones," *Acta Mechanica*, vol. 137, no. 1, pp. 65–81, 1999.

Research Article

Unsteady Model for Transverse Fluid Elastic Instability of Heat Exchange Tube Bundle

Jun Liu,^{1,2} Chen Huang,¹ and Naibing Jiang³

¹ School of Mechanical and Electrical Engineering, Southwest Petroleum University, Chengdu 610500, China

² Modern Design and Simulation Lab for Oil and Gas Equipments, Southwest Petroleum University, Chengdu 610500, China

³ Science and Technology on Reactor System Design Technology Laboratory, Nuclear Power Institute of China, Chengdu 610041, China

Correspondence should be addressed to Jun Liu; 99803392@qq.com

Received 11 May 2014; Revised 11 August 2014; Accepted 12 August 2014; Published 26 August 2014

Academic Editor: Kim M. Liew

Copyright © 2014 Jun Liu et al. This is an open access article distributed under the Creative Commons Attribution License, which permits unrestricted use, distribution, and reproduction in any medium, provided the original work is properly cited.

From the viewpoint of practical application, based on the unsteady analytical model for transverse fluid elastic instability of tube array proposed by Yetisir and the linear attenuation function introduced by Li Ming, a new explicit model based on nonsteady state “streamtube” hypothesis is proposed and solved using complex number method. In the model, numerical integral is avoided and inappropriate aspects in Li Ming model are modified. Using the model, the fluid elastic instability analysis of a single flexible tube is made. The stability graphs for four typical types of tube array are plotted and contrasted with experimental results. It is found that the current explicit model is effective in the analysis of transverse fluid elastic instability of tube bundle.

1. Introduction

Among the various fluid excitation mechanisms of the tube bundle in heat exchange, fluid elastic instability can cause the most rapid deterioration of the tube supports and has received the most attention [1, 2]. Many efforts have been made to study this phenomenon. However the mechanism of instability is not fully understood. Connors [3] and Afshin [4] successively studied the fluid elastic instability of tube bundle induced by transverse flow with wind tunnel experiments. Based on their studies, a quasistatic model was proposed to describe fluid elastic instability and the judgment formula of critical velocity for single-phase fluid elastic instability was given. Then Blevins [5] proposed another quasistatic model for one-dimensional tube array. These models are just comprehensive analytical solutions with experimental data, not the real analytical solutions. Then Price and Paidoussis [6] and Blevins [7] put forward a quasisteady model in which the fluid influence on displacement of the tubes has been further considered. This model is the simplified form of unsteady flow model and is only suitable for high conversion velocity. Thereafter, based on the general equation of fluid mechanics, an unsteady flow model was proposed by Tanaka et al. [8, 9].

In the model, many parameters for the calculation of fluid elastic force need to be determined by experiment; therefore it was also known as the semiempirical theoretical model. Lever and Weaver [10] proposed a simplified elastic fluid system based on a large number of experimental observations and given analytical expressions of the fluid force used in one-dimension unsteady flow theory. Then Lai [11] used this method to study the dynamic characteristics of a heat exchange tube bundle. Potential function was also proposed by Paidoussis et al. [12] to solve the flow force and calculate the critical velocity. These models are called analytical model due to the advantages that they need less experimental data over semiempirical theory model. Furthermore, the flow force induced by the pipe movement in analytical model was derived by Yetisir and Weaver [13] using unsteady continuous and momentum equations. This method is essentially an unsteady analytical model with relatively few experimental data. The result based on the model is in good agreement with those from experiment. Consequently, many similar models were developed. However, the calculation of the flow force in this kind of model involves numerical integration. Therefore it is not very convenient in practical to use them.

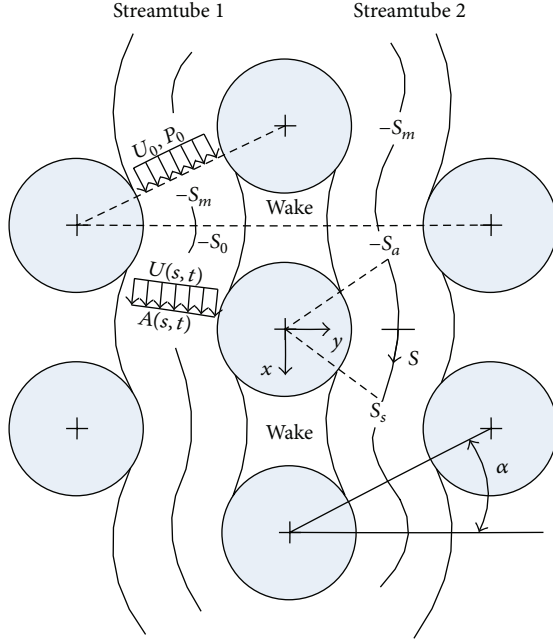


FIGURE 1: Idealized streamtube pattern [10].

In order to overcome the shortage, Li [14] attempted to give an explicit expression of flow force in Yetisir and Weaver's model by introducing a linear delay function. Nevertheless, there are several mistakes in his derivation such as coefficient A5. The final expression of the model is also not convenient for application.

The purpose of this paper is to present an explicit analytical model for transverse fluid elastic instability of standard array configurations which needs less experimental data and is convenient for application.

2. Theoretical Model

2.1. Physical Model. In Lever and Weaver's model (L-W model), "streamtube" concept is given. As shown in Figure 1, only an element of parallel triangle array is considered. On opposite sides of the centre pipe, there are two streamtubes with the sections changing with the motion of the pipe. Along the streamtubes, the curvilinear systems are set up. Meanwhile it is assumed that streamtubes began to attach to the centre flexible tube at position s_a and separate at position s_s .

In order to derive the eventual theoretical model, the mean area of the streamtube cross section along the streamtube length is assumed constant and determined by the minimum gap area at position $-s_l$. Consider

$$A_0 = \min \left(P \cos \alpha - \frac{D}{2}, P - D \right), \quad (1)$$

where P is tube spacing, D is tube diameter, α is geometric angle of tube array [13].

The instantaneous cross section area $A(s, t)$ of the streamtube changes with the vibration of the centre tube. Thus

$A(s, t)$ can be written as follows which contains average item A_0 and fluctuation item $a(s, t)$:

$$A(s, t) = A_0 + a(s, t). \quad (2)$$

Similarly, velocity and pressure of the streamtube can be expressed as follows:

$$U(s, t) = U_0 + u(s, t), \quad P(s, t) = P_0 + p(s, t), \quad (3)$$

where $u(s, t)$ and $p(s, t)$, respectively, represent the fluctuation parts of speed and velocity. On the upper position far enough from the vibrating tube $-s_l$, velocity and pressure can be seen as constants U_0 and P_0 .

Obviously, the vibration of the centre tube cannot immediately affect the flow at other position on the streamtube. Therefore upstream perturbation function $a(s, t)$ can be expressed as follows, based on the application of a phase function which considers the disturbance delayed effect:

$$a(s, t) = a(s_m, t) f(s) e^{i\varphi(s)}, \quad (4)$$

where $f(s)$ is artificial attenuation function which denotes the disturbance attenuation from the flexible tube position to upstream region and $a(s_m, t)$ is the area perturbation at the minimum clearance position and is the function of pipe geometry.

2.2. Continuity Equation, Momentum Equation, and Pressure Equation. The application of fluid continuity equation along the streamtube can yield the following formula:

$$\frac{\partial}{\partial t} A(s, t) + \frac{\partial}{\partial s} [A(s, t) U(s, t)] = 0. \quad (5)$$

Formula (5) can also be written as follows by using the following steps: introduce formulas (2) and (3) into formula (5) with a harmonic disturbance frequency ω adopted, integrate formula (5) along the coordinate s from the entrance $s = s_i$ to the exit $s = s_e$ of the streamtube, eliminate the steady state and high-order items, and normalize:

$$\begin{aligned} \frac{1}{U_r} \frac{\omega}{\omega_n} \int_{s_i}^{s_e} \frac{\partial a^*(s^*, t^*)}{\partial t^*} ds^* + l_0^* A_0^* [u^*(s_e^*, t^*) - u^*(s_i^*, t^*)] \\ + l_0^* [a^*(s_e^*, t^*) - a^*(s_i^*, t^*)] = 0, \end{aligned} \quad (6)$$

where U_r is reduced flow velocity and $U_r = U_0/\omega_n l_0$, ω_n is the natural frequency of the pipe in static water, ω is vibration complex frequency, $l_0 = 2s_1$ (s_1 is the distance between the vibrating tube and the position where pressure disturbance can be ignored), $t^* = \omega t$, $a^*(s, t) = a(s, t)/D$, $l_0^* = l_0/D$, $A_0^* = A_0/D$, $u^*(s, t) = u(s, t)/U_0$, $s^* = s/D$, and $p^*(s, t) = p(s, t)/P_0$.

Linear momentum equation of the fluid can be written as

$$\frac{\partial}{\partial t} \int_V \mathbf{U}(s, t) dV + \oint \rho \mathbf{U}(s, t) [\mathbf{U}(s, t) \cdot \mathbf{n}(s)] dA = \frac{1}{\rho} \sum \mathbf{F}, \quad (7)$$

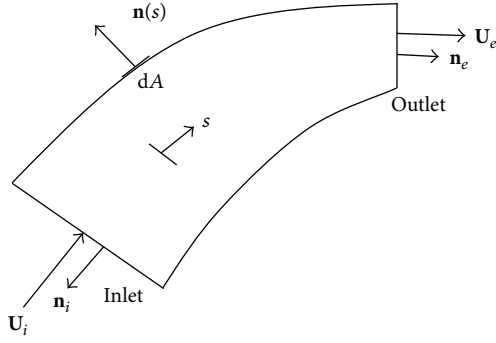


FIGURE 2: Control volume in streamtube.

where \forall denotes control volume (see Figure 2) and $\forall = Ad s$, ρ is the fluid density, and the right item denotes the sum of external forces on the control volume with unit length.

Using the derivation process similar to the above mentioned one, the momentum equation (7) can be further written as follows by substituting formulas (2) and (3) into it:

$$\begin{aligned} & \frac{\omega}{\omega_n} l_0^* U_r \int_{s_i}^{s_e} \frac{\partial u^*(s^*, t^*)}{\partial t^*} ds^* + \frac{\omega}{\omega_n} \frac{l_0^*}{A_0^*} U_r \int_{s_i}^{s_e} \frac{\partial a^*(s^*, t^*)}{\partial t^*} ds^* \\ & + \left[2l_0^* u^*(s_i^*, t^*) + \frac{l_0^*}{A_0^*} a^*(s_i^*, t^*) \right] l_0^* U_r^2 \\ & + \left[2l_0^* u^*(s_e^*, t^*) + \frac{l_0^*}{A_0^*} a^*(s_e^*, t^*) \right] l_0^* U_r^2 \\ & = -p^*(s_i^*, t^*) - p^*(s_e^*, t^*). \end{aligned} \quad (8)$$

It is worth noting that $p^* = p/(\rho d^2 \omega_n^2)$ which is not mentioned in Li's model. This is probably the main reason which leads to no density (ρ) existence in the final fluid force expression in Li's model.

Many studies have proved the fact that fluid elastic instability usually first occurs in the lift direction. Therefore, in the following part, only the fluid force calculation and fluid elastic analysis in the lift direction are made.

The force on the centre flexible tube can be obtained by integrating the pressure item on the pipe surface attached with fluid ($s_a^* \leq s \leq s_s^*$). Consider

$$F_y^* = \int_{s_a^*}^{s_s^*} p^*(s^*, t^*) \cos[\beta(s^*)] ds^*, \quad (9)$$

where $\beta(s^*)$ is the angle of the normal vector of the tube surface and $\beta(s^*) = 2s^*/Pr$. More detail about $\beta(s^*)$ is shown in literature [13].

2.3. Dynamic Equation. It is assumed that flexible tube vibrates in the lift and drags directions with the same harmonic oscillation

$$m\ddot{y} + c\dot{y} + ky = F_y a_1(s_m, t) - F_y a_2(s_m, t), \quad (10)$$

where $a_1(s_m, t)$ and $a_2(s_m, t)$, respectively, denote the area perturbations at the minimum clearances of streamtube 1 and streamtube 2.

The displacement mode of the centre pipe can be defined as follows:

$$y(t) = Y e^{i\omega t}, \quad (11)$$

where ω is vibration complex number frequency and Y is maximum vibration amplitude.

Substituting formula (11) into formula (10) and introducing the dimensionless variables, $y^* = Y/d$, $\bar{F}_y = F_y/\rho d^3 \omega_n$ can yield the following equation:

$$\begin{aligned} & \frac{m}{\rho d^2} \left[-\left(\frac{\omega}{\omega_n}\right)^2 + \frac{\delta}{\pi} \left(\frac{\omega}{\omega_n}\right) i + 1 \right] y^* \\ & = F_y^* a_1^*(s_m, t) - F_y^* a_2^*(s_m, t). \end{aligned} \quad (12)$$

Formula (12) can be further transformed as follows:

$$\frac{m}{\rho D^2} = \frac{F_y^*(U_r, \omega/\omega_n)}{1 - (\omega/\omega_n)^2 + i(\delta/\pi)(\omega/\omega_n)}, \quad (13a)$$

$$F_y^* = 2l_0^* U_r \cos \alpha F_y^*(s) = F_R^* \left(U_r, \frac{\omega}{\omega_n} \right) + i F_I^* \left(U_r, \frac{\omega}{\omega_n} \right), \quad (13b)$$

where m is the quality of the tube with unit length (including added fluid mass), ρ is fluid density, δ is damping logarithmic attenuation rate, F_y^* is the fluid resultant force applied on the unit length tube in the lift direction and is the function of frequency ratio ω/ω_n , and reduced speed $U_r = U_0/\omega_n l_0$. It is noted that the fluid resultant force F_y^* is a complex number and can be written as (13b) where F_R^* , F_I^* , respectively, represent real part and imaginary part.

According to the relation among the array geometry, fluid velocity at minimum interval U_0 , interval fluid velocity $U_p = [Pr/(Pr-1)]U_\infty$ (U_∞ is free flow velocity, Pr is tube pitch ratio, and $Pr = P/D$), and fluid continuity equation, formula (14) can be obtained:

$$U_r = \frac{U_p}{f_n D} \frac{1}{l_0^* A_0^*} \frac{\cos \alpha}{2\pi} (Pr-1). \quad (14)$$

2.4. Area Perturbation Equation. In order to obtain the explicit expression for the calculation of fluid force, the following linear attenuation function [14] is used, according to the requirement on it. For the convenience of introduction, superscript “*” will be ignored in the following derivation process:

$$f(s) = \frac{s-s_1}{s_a-s_1}, \quad s_1 \leq s \leq s_a, \quad (15)$$

$$f(s) = 1, \quad s_a \leq s \leq s_s.$$

Noting the fact that perturbation attenuation only takes place on “streamtube” path, two area perturbation equations for parallel triangular tube array are presented as follows:

$$\begin{aligned} a_1(s, U_r) &= f(s) e^{i\varphi(s, U_r)} \cos \alpha, \\ \varphi(s, U_r) &= \varphi(U_r) \frac{s - s_a}{s_1 - s_a}, \\ s_1 &\leq s \leq s_a, \\ a_2 &= \cos \alpha, \quad f(s) = 1.0, \quad \varphi(s, U_r) = 0, \\ s_a &\leq s \leq s_s. \end{aligned} \quad (16)$$

For other types of tube array, area perturbation equations are similar as the above equations except for the item $\cos \alpha$.

2.5. Solving Method. For the convenience of derivation, let $\bar{s} = (s - s_a)/(s_1 - s_a)$, so that attenuation function and (16) can be rewritten, respectively, as follows:

$$\begin{aligned} f(s) &= 1 - \bar{s}, \\ a_1(s, U_r) &= a(-s_m, t) f(s) e^{i\varphi(s)} \\ &= \frac{Y}{D} e^{i\omega t} \cos \alpha (1 - \bar{s}) e^{i\bar{s}\varphi(U_r)}, \\ s_1 &\leq s \leq s_a, \\ a_2 &= \frac{Y}{D} e^{i\omega t} \cos \alpha, \quad f(s) = 1.0, \quad \varphi(s, U_r) = 0, \\ s_a &\leq s \leq s_s. \end{aligned} \quad (17)$$

To further facilitate the derivation, $\varphi(U_r)$ is briefly written as φ in the following work.

Substituting (17) into (6) yields the following expression:

$$u_1(s, U_r) = (A_1 e^{i\varphi\bar{s}} + A_2 \bar{s} e^{i\varphi\bar{s}} + A_3) \frac{Y}{D} e^{i\omega t} \cos \alpha, \quad (18)$$

where

$$\begin{aligned} A_1 &= -\frac{1}{A_0} - \frac{\omega_r}{l_0 A_0 U_r} (s_l - s_a) \left(\frac{1}{\varphi} - \frac{i}{\varphi^2} \right), \\ A_2 &= \frac{1}{A_0} + \frac{\omega_r}{l_0 A_0 U_r} (s_l - s_a) \frac{1}{\varphi}, \\ A_3 &= -\frac{\omega_r i}{l_0 A_0 U_r} (s_1 - s_a) \frac{1}{\varphi^2} e^{i\varphi}. \end{aligned} \quad (19a)$$

In the same way we have

$$\begin{aligned} u_2(s, U_r) &= (A_4 \bar{s} + A_5) \frac{Y}{D} e^{i\omega t} \cos \alpha, \\ 0 &\leq \bar{s} \leq \frac{s_s - s_a}{s_1 - s_a}, \end{aligned} \quad (19b)$$

where

$$\begin{aligned} A_4 &= -\frac{\omega_r i}{l_0 A_0 U_r} (s_l - s_a), \\ A_5 &= -\frac{\omega_r}{l_0 A_0 U_r} (s_l - s_a) \left(\frac{1}{\varphi} - \frac{i}{\varphi^2} + \frac{i}{\varphi^2} e^{i\varphi} \right) - \frac{1}{A_0}. \end{aligned} \quad (20)$$

Substituting (18) and (19b) into the integral expression for unsteady pressure (8) yields the following formula:

$$p_2(s, U_r) = (C_1 \bar{s}^2 + C_2 \bar{s} + C_3) \frac{Y}{D} e^{i\omega t} \cos \alpha, \quad (21)$$

where

$$\begin{aligned} C_1 &= -\omega_r l_0 U_r i B_2, \\ C_2 &= -\omega_r l_0 U_r i B_3 - 2l_0^2 U_r^2 A_4 - \frac{\omega_r l_0 U_r i}{A_0} (s_1 - s_a), \\ C_3 &= -\omega_r l_0 U_r i B_1 - 2l_0^2 U_r^2 A_5 - \frac{l_0^2 U_r^2}{A_0} - \frac{\omega_r l_0 U_r}{A_0} B_4, \end{aligned} \quad (22)$$

where

$$\begin{aligned} B_1 &= (s_1 - s_a) \\ &\times \left(\frac{-iA_1}{\varphi} + \frac{iA_1}{\varphi} e^{i\varphi} + \frac{iA_2}{\varphi} e^{i\varphi} + \frac{A_2}{\varphi^2} - \frac{A_2}{\varphi^2} e^{i\varphi} - A_3 \right), \\ B_2 &= \frac{(s_1 - s_a) A_4}{2}, \\ B_3 &= (s_1 - s_a) A_5, \\ B_4 &= (s_1 - s_a) \left(-\frac{i}{\varphi} - \frac{1}{\varphi^2} + \frac{1}{\varphi^2} e^{i\varphi} \right). \end{aligned} \quad (23)$$

The explicit expression for the fluid force applied on the centre moving tube is obtained by substituting formula (21) into formula (9). Consider

$$\begin{aligned} F_y &= \frac{Y}{D} e^{i\omega t} \cos \alpha \int_{s_a}^{s_s} p_2(s, U_r) \cos \left(\frac{2s}{Pr} \right) ds \\ &= \frac{Y}{D} e^{i\omega t} \cos \alpha \int_{s_a}^{s_s} (C_1 \bar{s}^2 + C_2 \bar{s} + C_3) \cos \left(\frac{2s}{Pr} \right) ds \\ &= \frac{Y}{D} e^{i\omega t} \cos \alpha \sum_{i=1}^3 C_i D_i, \end{aligned} \quad (24)$$

TABLE 1: Numerical values of geometric parameters for test arrays [1].

Layout pattern	P/d	δ	ρ (kg/m ³)	A_0/d	s_0/d	s_1/d	l_0/d	x_1/d
Square (90°)	1.25	0.012	1.112	0.25	1.25	1.25	5.00	0.05
	1.32	0.015	1.125	0.32	1.32	1.32	5.28	0.05
	1.41	0.010	1.110	0.41	1.41	1.41	5.64	0.05
Rotated triangular (60°)	1.25	0.024	1.124	0.25	0.654	0.982	2.616	0.104
	1.32	0.021	1.110	0.32	0.691	1.037	2.764	0.0985
	1.41	0.030	1.110	0.41	0.738	1.107	2.952	0.092
Rotated square (45°)	1.25	0.019	1.110	0.25	0.981	1.472	3.925	0.155
	1.41	0.015	1.110	0.41	1.107	1.660	4.427	0.137
Triangular (30°)	1.25	0.014	1.110	0.125	1.249	1.874	4.996	0.203
	1.41	0.018	1.110	0.205	1.371	2.057	5.484	0.181

where

$$\begin{aligned}
D_1 &= \left(\frac{1}{s_1 - s_a} \right)^2 \left(\frac{2s}{b^2} \cos bs - \frac{2}{b^3} \sin bs + \frac{s^2}{b} \sin bs \right) \Big|_{s_a}^{s_s} \\
&\quad - \frac{2s_a}{(s_1 - s_a)^2} \left(\frac{1}{b^2} \cos bs + \frac{s}{b} \sin bs \right) \Big|_{s_a}^{s_s} \\
&\quad + \left(\frac{s_a}{s_1 - s_a} \right)^2 \frac{1}{b} \sin bs \Big|_{s_a}^{s_s}, \\
D_2 &= \frac{1}{s_1 - s_a} \left(\frac{1}{b^2} \cos bs + \frac{s}{b} \sin bs \right) \Big|_{s_a}^{s_s} \\
&\quad - \frac{s_a}{s_1 - s_a} \frac{1}{b} \sin bs \Big|_{s_a}^{s_s}, \\
D_3 &= \int_{s_a}^{s_s} \cos \left(\frac{2s}{\text{Pr}} \right) ds \\
&= \int_{s_a}^{s_s} \cos (bs) ds = \frac{1}{b} \sin bs \Big|_{s_a}^{s_s},
\end{aligned} \tag{25}$$

where

$$a = \frac{\varphi}{s_1 - s_a}, \quad b = \frac{2}{\text{Pr}}. \tag{26}$$

In formula (24), F_y is fluid force with complex number form and can be written as $F_y = F_R + F_I i$. By substituting the fluid force into formula (13a), the relation between the reduced fluid velocity $U_p/f_n D$ and quality-damping ratio $m\delta/\rho D^2$ can be obtained.

3. Example

Using the above explicit unsteady model, fluid elastic instability analyses on four standard tube arrays are carried out and the result is compared with those from experiment in order to verify the validity of the model. Geometric parameters of the four types of tube arrays are listed in Table 1. The diameter

and first order natural frequency of the tubes in experiment are, respectively, 0.022 m and 90 Hz.

The results from the explicit analytic method and experiment are presented in Figure 3 where vertical coordinate denotes reduced fluid velocity and horizontal coordinate denotes quality-damping parameter. It is shown in the figure that for the four typical tube arrays, the results from the explicit analytic method are consistent with those from Nie's experiment [1]. For $m\delta/\rho D^2 > 5$, the results based on current method tend to be more conservative than the result of experiment, whereas, for $m\delta/\rho D^2 < 5$, the result of experiment is more conservative. But the difference between the two types of results is not great. The influence of the pitch ratio (P/d) on the result is not obvious. This is consistent with the observed phenomenon by Lever and Weaver [10].

It is shown in the above analysis that the current explicit analytic method inherits the advantage of Y-W "streamtube" model which possesses good calculation precision and needs little experiment data. Moreover, comparing with Y-W model, the unsteady explicit model presented in this paper has another advantage that no numerical integral is needed in the calculation of fluid force due to its explicit expression. Therefore, the current method is more convenient for practical application.

4. Conclusion

This paper introduces an unsteady model in detail for fluid elastic instability analysis of standard array configuration in transverse flow. Complex number solving method is used to deduce the unsteady explicit analytical model with new area perturbation equation. In the model, numerical integration similar to Y-W model is avoided and inappropriate parameters presented in Li's model are corrected. Finally the explicit expression of the model which is convenient for application is presented.

Fluid elastic instability analysis on four standard array configurations is made and the stability maps based on current model are given. A comparison of the result between the current model and those from Nie's experiment data is

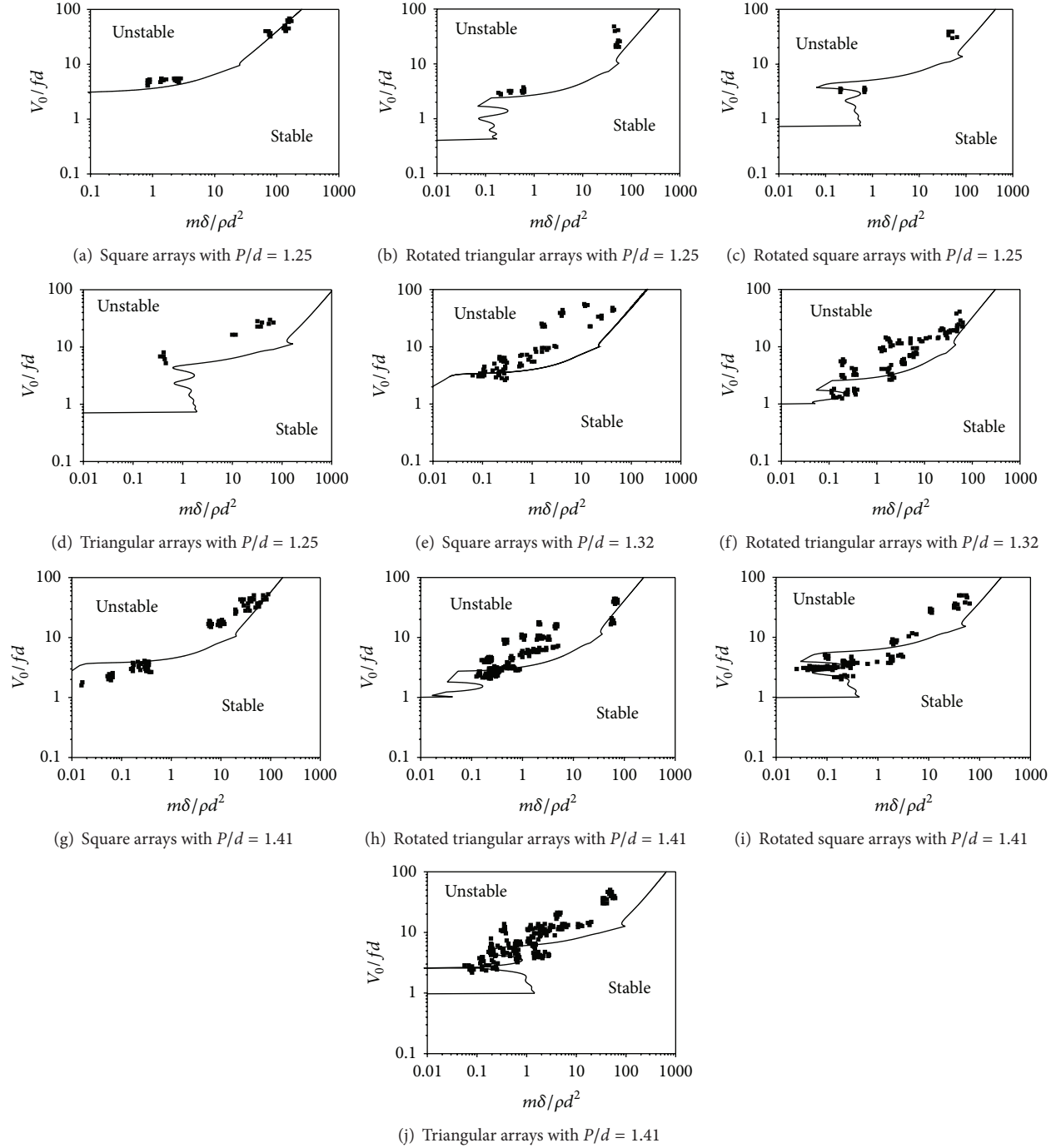


FIGURE 3: Stability maps for typical tube arrays (solid black points represent Nie's experiment result and black solid lines represent the result in this paper).

made to indicate the validity of current explicit fluid elastic analytical model.

Conflict of Interests

The authors declare that there is no conflict of interests regarding the publication of this paper.

Acknowledgments

This research has been supported by the National Natural Science Foundation of China (nos. 51105319 and 51274171), National Significant Science and Technology Special Sub-project of China (2011ZX05026-001-07), and National Key Laboratory of Nuclear Reactor System Design Technology Foundation of China.

References

- [1] Q. D. Nie, B. Y. Guo, and X. R. Ding, "Fluidelastic instability of tube bundle in heat exchanger," *Chinese Journal of Theoretical and Applied Mechanics*, vol. 28, no. 2, pp. 151–158, 1996.
- [2] D. L. Wen, "Study on the vibration design and improvement for tube bundle in tube-shell heat exchanger," *Refrigeration & Air-Condition*, vol. 10, no. 2, pp. 35–37, 2010.
- [3] H. Connors, *Fluidelastic Vibration of Tube Arrays Excited by Cross Flow, Flow-Induced Vibration in Heat Exchangers*, 1970, edited by D. D. Reiff, ASME, New York, NY, USA, 1970.
- [4] K. Afshin, *Effect of Preferential Flexibility Angle on Fluidelastic Instability of a Rotated Triangular Tube Bundle*, University De Montreal, 2007.
- [5] R. D. Blevins, *Vibration Induced by Fluid*, China Machine Press, 1982.
- [6] S. J. Price and M. P. Paidoussis, "Fluidealstic instability of an infinite double row of acoustics circular cylinders subjected to a uniform cross flow," *Journal of Vibration, Acoustics, Stress, and Reliability in Design*, vol. 105, no. 1, pp. 59–66, 1983.
- [7] R. D. Blevins, "Fluid damping and the whirling instability of tube arrays," in *Flow-Induced Vibrations*, pp. 35–39, ASME, New York, NY, USA, 1979.
- [8] H. Tanaka, S. Takahara, and K. Ohta, "Flow-induced vibration of tube arrays with various pitch-to diameter ratio," *Journal of Pressure Vessel Technology*, vol. 104, no. 3, pp. 168–174, 1982.
- [9] N. W. Mureithi, T. P. Sawadogo, and A. A. Grie, "Estimation of the fluid-elastic instability boundary for steam-generator tubes subjected to two-phase flows," in *Proceedings of the 18th International Conference on Nuclear Engineering (ICONE '10)*, Paper no. ICONE18-30241, pp. 679–690, Xi'an, China, May 2010.
- [10] J. H. Lever and D. S. Weaver, "On the stability of heat exchanger tube bundles, part I: modified theoretical model. Part II: numerical results and comparison with experiments," *Sound and Vibration*, vol. 107, no. 1, pp. 375–410, 1986.
- [11] Y. X. Lai, *Analysis on dynamic characteristic and flow induced vibration of heat exchanger tube bundles [Doctor thesis]*, Nanjing University of Technology, 2006.
- [12] M. P. Paidoussis, D. Mavriplis, and S. J. Price, "A potential flow theory for the dynamics of cylinder arrays in cross flow," *Journal of Fluid Mechanics*, vol. 146, pp. 227–252, 1984.
- [13] M. Yetisir and D. S. Weaver, "An unsteady theory for fluidelastic instability in an array of flexible tubes in cross-flow, Part I: theory," *Journal of Fluids and Structures*, vol. 7, no. 7, pp. 751–766, 1993.
- [14] M. Li, *An experimental and theoretical study of fluidelastic instability in cross flow multi-span heat exchanger tube arrays [Doctor thesis]*, McMaster University, 1997.

Research Article

Fingerprint Classification Combining Curvelet Transform and Gray-Level Cooccurrence Matrix

Jing Luo,^{1,2,3} Dan Song,^{1,2} Chunbo Xiu,^{1,2} Shuze Geng,^{1,2} and Tingting Dong^{1,2}

¹ Key Laboratory of Advanced Electrical Engineering and Energy Technology, Tianjin 300387, China

² College of Electrical Engineering and Automation, Tianjin Polytechnic University, Tianjin 300387, China

³ School of Electrical, Computer and Telecommunications Engineering, University of Wollongong, Wollongong, NSW 2522, Australia

Correspondence should be addressed to Dan Song; sweet0502@sina.com

Received 30 April 2014; Revised 25 June 2014; Accepted 1 July 2014; Published 17 August 2014

Academic Editor: L. W. Zhang

Copyright © 2014 Jing Luo et al. This is an open access article distributed under the Creative Commons Attribution License, which permits unrestricted use, distribution, and reproduction in any medium, provided the original work is properly cited.

Fingerprint classification is an important indexing scheme to reduce fingerprint matching time for a large database for efficient large-scale identification. The abilities of Curvelet transform capturing directional edges of fingerprint images make the fingerprint suitable to be classified for higher classification accuracy. This paper presents an efficient algorithm for fingerprint classification combining Curvelet transform (CT) and gray-level cooccurrence matrix (GLCM). Firstly, we use fast discrete Curvelet transform warping (FDCT_WARPING) to decompose the original image into five scales Curvelet coefficients and construct the Curvelet filter by Curvelet coefficients relationship at adjacent scales to remove the noise from signals. Secondly, we compute the GLCMs of Curvelet coefficients at the coarsest scale and calculate 16 texture features based on 4 GLCMs. Thirdly, we construct 49 direction features of Curvelet coefficients at the other four scales. Finally, fingerprint classification is accomplished by K -nearest neighbor classifiers. Extensive experiments were performed on 4000 images in the NIST-4 database. The proposed algorithm achieves the classification accuracy of 94.6 percent for the five-class classification problem and 96.8 percent for the four-class classification problem with 1.8 percent rejection, respectively. The experimental results verify that proposed algorithm has higher recognition rate than that of wavelet-based techniques.

1. Introduction

As a type of human biometrics, fingerprint has been widely used for personal recognition in forensic and civilian applications because of its uniqueness, immutability, and low cost. An automatic recognition of people based on fingerprints requires matching of an input fingerprint with a large number of fingerprints in a database. However, the database can be huge (e.g., the FBI database contains more than 70 million fingerprints), such a task can be very expensive in terms of computational burden and time. In order to reduce the search time and computational burden, fingerprints in the database are classified into several prespecified types or subclasses. When an input fingerprint is received, a coarse level matching is applied to determine which subclass the input belongs to, and then at a finer level, it is compared to samples within the subset of the database for recognition. While such a scheme is obviously more efficient, the first step, that is, fingerprint

classification, must be accurate and reliable and hence has attracted extensive research in recent years [1–13].

Fingerprints are classified based on their shapes, and in literature it is common to have five classes as shown in Figure 1 (x):(A) ($x = a, b, c, d, e$), including whorl (W), right loop (R), left loop (L), arch (A), and tent arch (T). Although these five classes appear very different to us as a person, automatically classifying a fingerprint by a machine is in fact a very challenging pattern recognition problem, due to the small interclass variability, the large intraclass variability and the difficulty for poor quality fingerprints. Fingerprint classification is carried out by analysis and comparison of the features. Over the past decade various approaches have been proposed by means of different types of features, such as singularities [1–3], orientation field [4–6], and statistical and frequency features [7–10]. The methods based on singularities [1–3] accomplish fingerprint classification according to the number and relative position of the core and delta points.

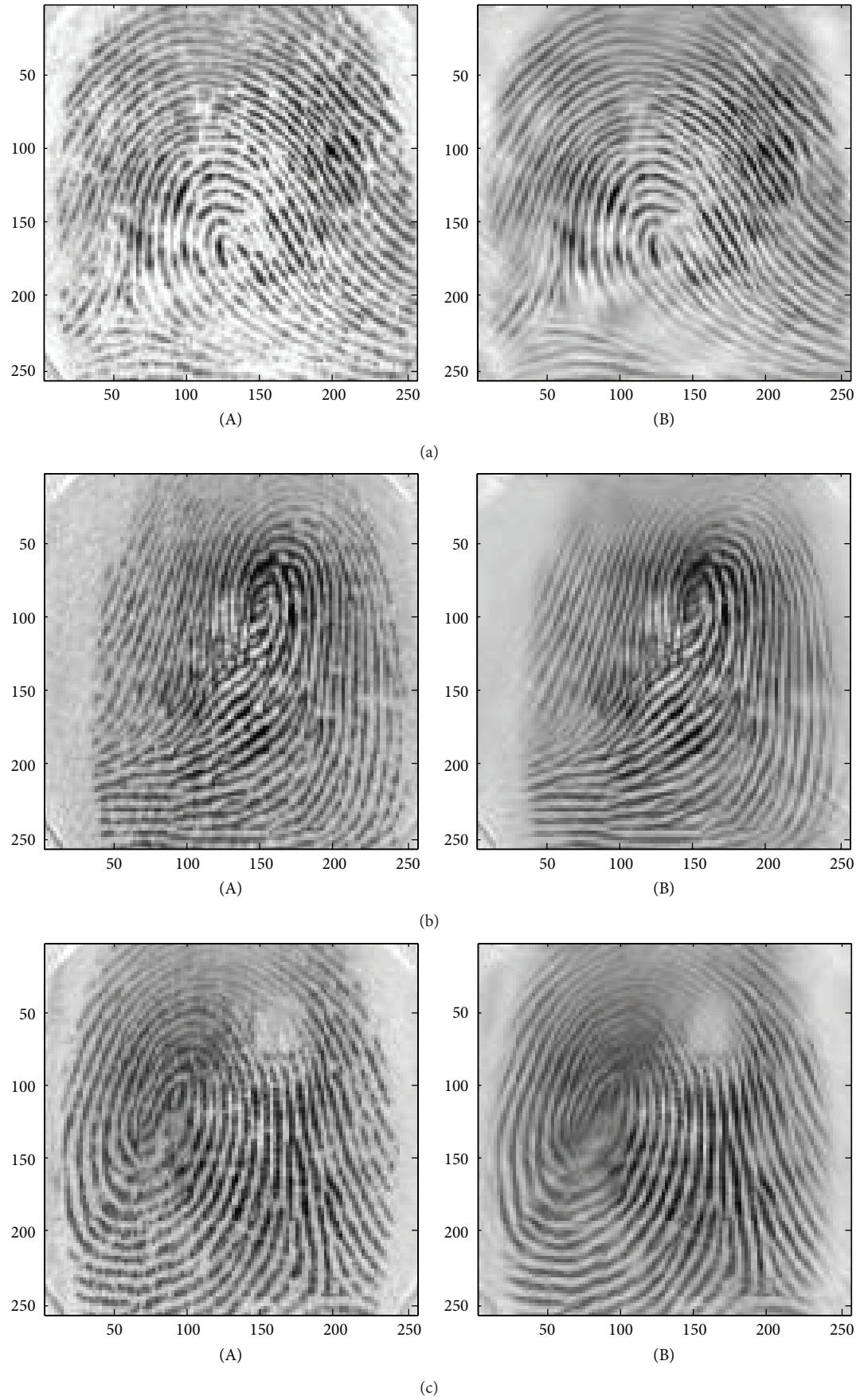


FIGURE 1: Continued.

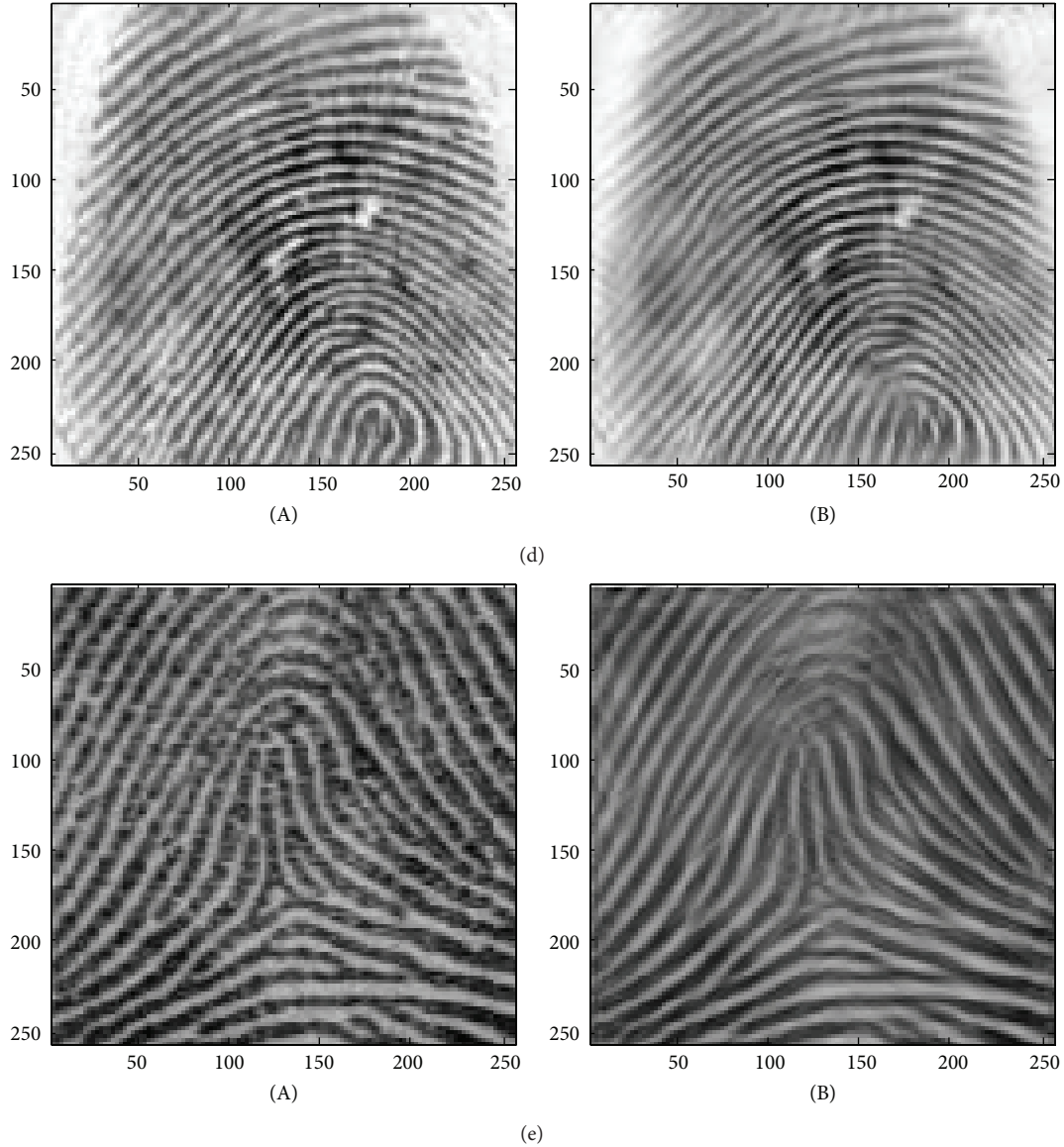


FIGURE 1: (a) (A) Original right loop image and (B) denoised right loop image. (b) (A) Original left loop image, (B) denoised left loop image. (c) (A) Original whorl image and (B) denoised whorl image. (d) (A) Original arch image and (B) denoised arch image. (e) (A) Original tented arch image and (B) denoised tented arch image.

The approaches using orientation field [4–6] partition the fingerprint orientation field into “homogeneous” orientation regions and the relational graphs of these regions are used to make fingerprint classification. Gabor filter [9] can also be used to extract the fingerprint features for classification where the input image is decomposed into four component images by four Gabor filters, and the standard deviation of the component images in each sector to generate the feature vector, and uses a K -nearest neighbor classifier to make fingerprint classification.

In 2001, Tico et al. [10] proposed an approach to use wavelet transform as features for fingerprint recognition. In [10], a wavelet decomposition on 6 octaves of each fingerprint image was performed, and the normalized l_2 -norm of each wavelet subimage is computed to extract a feature vector of

length 18. The experimental database contains 168 fingerprint images collected from 21 fingers (8 images per finger). The algorithm achieves the accuracy of 100% when wavelet basis Symmlet 6 or Symmlet 9 was employed. The work in [10] shows that the wavelet features are suitable for matching complex patterns of oriented texture such as fingerprints. However, wavelets are characterized by isotropic scaling (e.g., the standard orthogonal wavelet transform contains wavelets in the directions of primary vertical, primary horizontal, and primary diagonal only) and hence their abilities to resolve directional features are limited. So wavelets are not able to detect curved singularities effectively.

Inspired by the success of wavelets, a number of other multiresolution analysis tools have also been proposed with the aim to present better the edges and other singularities

along curves. These tools include contourlet, ridgelet, and Curvelet. In recent years, researchers have used Curvelets for fingerprint image enhancement [11, 12] and for fingerprint recognition [13]. Comparing to the limited directional features of wavelets, Curvelets are more powerful as they are able to describe a signal by a group of matrices at multiscale and multidirection. Furthermore, with the increase of the scale, the number of directions is much finer.

In 2008, Mandal and Wu [13] proposed to use Curvelet transform for fingerprint recognition and achieved the accuracy of 100%. However, the performance of the proposed algorithm was only tested on a small database of 120 fingerprint images (containing only 15 individuals). Furthermore, in order to ensure the accuracy, the technique requires manual detection of the core of the fingerprint image. Also, before extracting the Curvelet features, the technique needs complex image enhancement process which includes estimation of local ridge-orientation, estimation of local ridge-frequency across the fingerprint, filtering of the image, and binarization (conversion of a gray-scale fingerprint image to binary image).

In this paper, we present a novel fingerprint classification algorithm. Firstly, we use fast discrete Curvelet transform warping (FDCT_WARPING) to decompose the original image into five-scale Curvelet coefficients and construct the Curvelet filter by Curvelet coefficients relationship at adjacent scales to smooth the discontinuities of ridges and remove the noise in the fingerprint image. Secondly, we calculate four gray-level cooccurrence matrices (GLCMS) of Curvelet coefficients at the coarsest scale and calculate 16 texture features based on 4 GLCMS. Furthermore, we construct 49 direction features of Curvelet coefficients at the other four scales. Finally, these combined Curvelet-GLCM based features act as the feature set to a K -nearest neighbor classifier.

In the following sections, we will present the details of our fingerprint classification algorithm. Section 2 presents our noise filtration scheme and our feature extraction scheme. Section 3 presents some experimental results achieved on NIST-4 databases. Finally Section 4 draws the conclusions and outlines the open problems.

2. Fingerprint Classification

2.1. Fingerprint Alignments. Considering the translation and rotation between template images and probe images, this paper adopted the algorithm in [14] to accomplish the fingerprint image registration. The algorithm used the reference points of the central area to calculate the parameters of translation and rotation, which is much more general when there are no cores in the fingerprint images.

2.2. Fast Discrete Curvelet Transform (FDCT). Curvelets were proposed by Candès and Donoho [15], constituting a family of frames that are designed to represent the edges and other singularities along curves. Conceptually, the Curvelet transform is a multiscale pyramid with many orientations and positions at each length scale and needle-shaped elements

at fine scale. This pyramid is nonstandard, however. Indeed, Curvelets have useful geometric features that set them apart from wavelets and the likes. For instance, Curvelets present highly anisotropic behavior as it has both variable *length* and *width*. At fine scale, anisotropy increases with decreasing scale, in keeping with power law.

In 2006, Candès et al. proposed two fast discrete Curvelet transforms (FDCT) [16]. The first one is based on unequally spaced fast Fourier transforms (USFFT) [16], and the other is based on the wrapping of specially selected Fourier samples (FDCT_WARPING) [16]. Curvelets by warping have been used for this work, because this is the fastest Curvelet transform currently available [16].

After Curvelet transform, several groups of Curvelet coefficients are generated at different scales and angles. Curvelet coefficients at scale j and angle l are represented by a matrix $C_{j,l}$, and scale j is from finest to coarsest scale, and angle l starts at the top-left corner and increases clockwise.

Suppose that $f(t_1, t_2)$, $1 \leq t_1 \leq N_1$, $1 \leq t_2 \leq N_2$ denotes original image and $\hat{f}[n_1, n_2]$ denotes 2D discrete Fourier transform; N_1, N_2 is the size of original image.

The implementation of FDCT_WARPING is as follows.

Step 1. 2D FFT (fast Fourier transform) is applied on $f(t_1, t_2)$ to obtain Fourier samples $\hat{f}[n_1, n_2]$.

Step 2. Resample $\hat{f}[n_1, n_2]$ at each pair of scale and direction j, l in frequency domain, yielding the new sampling function:

$$\hat{f}[n_1, n_2 - n_1 \tan \theta_l], \quad (n_1, n_2) \in P_j, \quad (1)$$

where $P_j = \{(n_1, n_2), n_{1,0} \leq n_1 < n_{1,0} + L_{1,j}, n_{2,0} \leq n_2 < n_{2,0} + L_{2,j}\}$ and $n_{1,0}$ and $n_{2,0}$ are two initial positions of the window function $\tilde{u}_{j,l}[n_1, n_2]$.

$L_{1,j}$ and $L_{2,j}$ are relevant parameters of 2^j and $2^{j/2}$, respectively, and they are length and width components of window function support interval.

Step 3. Multiplication of the new sampling function $\hat{f}[n_1, n_2 - n_1 \tan \theta_l]$ with window function $\tilde{u}_{j,l}[n_1, n_2]$, and the result is [16]

$$\tilde{f}_{j,l}[n_1, n_2] = \hat{f}[n_1, n_2 - n_1 \tan \theta_l] \tilde{u}_{j,l}[n_1, n_2], \quad (2)$$

where

$$\begin{aligned} \tilde{u}_{j,l}[n_1, n_2] &= w_j(w_1, w_2) v_j \left(s_{\theta_l} \cdot \frac{(2^{l/2} w_2)}{w_1} \right), \\ w_j(w_1, w_2) &= \sqrt{\phi_{j+1}^2(w^2) - \phi_j^2(w^2)}, \\ \phi_j(w_1, w_2) &= \phi(2^{-j} w_1) \phi(2^{-j} w_2), \end{aligned} \quad (3)$$

$$s_{\theta_l} = \begin{bmatrix} 1 & 0 \\ -\tan \theta_l & 1 \end{bmatrix},$$

$$\tan \theta_l = l \times 2^{[-j/2]}, \quad l = -2^{[-j/2]}, \dots, 2^{[-j/2]} - 1.$$

Step 4. Apply the inverse 2D FFT to each $\tilde{f}_{j,l}$, hence collecting the discrete coefficients $C_{j,l}$.

2.3. Fingerprint Image FDCT and Noise Filtration Technique. Curvelet transform describes a signal by the power at each scale, angle, and position. Curvelets have variable length in addition to variable width. Curvelet transform has improved directional capability and better ability to represent edges and other singularities along curves compared to other multiscale transforms, for example, wavelet transform. Image like fingerprints often have two nearby regions (ridges and valleys) that differ in pixel values. These variations in pixel values between two consecutive regions are likely to form such “edges” and this edge information is eventually captured by digital Curvelet transform.

2.3.1. Acquisition of Curvelet Coefficients. In this paper, fingerprint images are from NIST-4 databases. Firstly, the size of all the images is normalized to 256×256 pixels. The proposed algorithm is implemented by using MATLAB 7.5 programming language and is executed under Windows XP Professional O.S. on a PC with AMD Dual-Core CPU E-350 at 1.28 GHz. The original image is decomposed by FDCT.WARPING [16].

Suppose that $f(t_1, t_2)$, $1 \leq t_1 \leq N_1$, $1 \leq t_2 \leq N_2$ denotes original fingerprint image and $\hat{f}[n_1, n_2]$ denotes 2D discrete Fourier transform; N_1 , N_2 is the size of original fingerprint image.

The number of scales can be calculated by

$$N_{\text{scales}} = \text{ceil}(\log_2(\min(N_1, N_2)) - 3), \quad (4)$$

where $\min(N_1, N_2)$ returns the minimum of N_1 and N_2 and $\text{ceil}(\cdot)$ rounds the input to the nearest integers greater than or equal to input.

The number of orientation at scale $2, 3, \dots, N_{\text{scales}} - 1$, is calculated by

$$l_j = 16 \times 2^{\text{ceil}((N_{\text{scales}} - i)/2)}, \quad (5)$$

where $i = N_{\text{scales}}$, $j = 2$; $i = N_{\text{scales}} - 1$, $j = 3; \dots; i = 3$, and $j = N_{\text{scales}} - 1$.

Noted that if FDCT.WARPING chooses the Curvelets for the coefficients at the finest level N_{scales} , the number of orientation at scale N_{scales} can be determined by (2). On the other hand, when choosing the wavelets for the coefficients at the finest level N_{scales} , there is only one angle at the finest level N_{scales} . In this paper, we adopt the wavelets for the coefficients at the finest level N_{scales} . As a result, there is only one angle at the finest level N_{scales} .

For scale $j = 2, 3, \dots, (N_{\text{scales}} - 1)$, all the Curvelet coefficients are divided into the four quadrants. The quadrant label of Curvelet coefficients is denoted by quad, and four quadrants are denoted by quad = 1, 2, 3, 4, respectively. At each quadrant, Curvelet coefficients are further subdivided in angular panels. The number of angular panels at each quadrant of each scale j , denoted by $n_{\text{quad}-j}$, can be calculated as follows:

$$n_{\text{quad}-j} = 4 \times 2^{\text{ceil}((N_{\text{scales}} - i)/2)}, \quad (6)$$

where $i = N_{\text{scales}}$, $j = 2$; $i = N_{\text{scales}} - 1$, $j = 3; \dots; i = 3$, and $j = N_{\text{scales}} - 1$.

In this paper, according to (4), we can get the number of scales $N_{\text{scales}} = 5$. According to (5), the number of angle at scale 4 is 32, at scale 3 is 32, and at scale 2 is 16. At scale 4, the number of angular panels of each quadrant is 8. At scale 3, the number of angular panels of each quadrant is 8. At scale 2, the number of angular panels of each quadrant is 4. After decomposition, the original image was divided into three levels: coarse, detail, and fine. The low-frequency coefficients were assigned to coarse. The high-frequency coefficients were assigned to fine. The middle-frequency coefficients were assigned to detail. According to FDCT.WARPING [16], the scale j is from finest to coarsest scale and angle l starts at the top-left corner and increases clockwise.

The acquisition of Curvelet coefficients is as follows.

Step 1. 2D FFT (fast Fourier transform) is applied on $f(t_1, t_2)$ to obtain Fourier samples $\hat{f}[n_1, n_2]$.

Step 2. Acquire the Curvelet coefficients at scale 5, denoted by matrix $C_{5,1}$.

Suppose that

$$M_1 = \frac{N_1}{6}, \quad M_2 = \frac{N_2}{6},$$

$$l_{N_{\text{scales}}-1} = \text{floor}(2 \times M_1) - \text{floor}(M_1) - 1, \quad (7)$$

$$l_{N_{\text{scales}}-2} = \text{floor}(2 \times M_2) - \text{floor}(M_2) - 1.$$

In this paper, $\text{floor}(\cdot)$ rounds the input to the nearest integers less than or equal to the input.

(1) Construct the right and left windows along the horizontal direction, denoted by row vector W_{r-1} and W_{l-1} , respectively. Consider

$$W_{r-1}(i) = \begin{cases} 1, & i = 0, \\ e^{(1-1/(1-e^{(1-1/i)}))}, & i = \frac{1}{l_{N_{\text{scales}}-1}}, \frac{2}{l_{N_{\text{scales}}-1}}, \dots, \frac{l_{N_{\text{scales}}-1}-1}{l_{N_{\text{scales}}-1}}, \\ 0, & i = 1, \end{cases}$$

$$W_{l-1}(i) = \begin{cases} 0, & i = 0, \\ e^{(1-1/(1-e^{(1-1/(1-i))})), & i = \frac{1}{l_{N_{\text{scales}}-1}}, \frac{2}{l_{N_{\text{scales}}-1}}, \dots, \frac{l_{N_{\text{scales}}-1}-1}{l_{N_{\text{scales}}-1}}, \\ 1, & i = 1. \end{cases} \quad (8)$$

- (2) Construct the right and left windows along the vertical direction, denoted by row vector W_{r-2} and W_{l-2} , respectively. Consider

$$W_{r-2}(i) = \begin{cases} 1, & i = 0, \\ e^{(1-1/(1-e^{(1-1/i)}))}, & i = \frac{1}{l_{N_{\text{scales}}-2}}, \frac{2}{l_{N_{\text{scales}}-2}}, \dots, \frac{l_{N_{\text{scales}}-2}-1}{l_{N_{\text{scales}}-2}}, \\ 0, & i = 1, \end{cases} \quad (9)$$

$$W_{l-2}(i) = \begin{cases} 0, & i = 0, \\ e^{(1-1/(1-e^{(1-1/(1-i))})), & i = \frac{1}{l_{N_{\text{scales}}-2}}, \frac{2}{l_{N_{\text{scales}}-2}}, \dots, \frac{l_{N_{\text{scales}}-2}-1}{l_{N_{\text{scales}}-2}}, \\ 1, & i = 1. \end{cases} \quad (10)$$

W_{r-1} , W_{l-1} , W_{r-2} , and W_{l-2} are normalized by

$$\begin{aligned} W_{r-1}(i) &= \frac{W_{r-1}(i)}{\sqrt{[W_{r-1}(i)]^2 + [W_{l-1}(i)]^2}}, \\ W_{l-1}(i) &= \frac{W_{l-1}(i)}{\sqrt{[W_{r-1}(i)]^2 + [W_{l-1}(i)]^2}}, \\ W_{r-2}(i) &= \frac{W_{r-2}(i)}{\sqrt{[W_{r-2}(i)]^2 + [W_{l-2}(i)]^2}}, \\ W_{l-2}(i) &= \frac{W_{l-2}(i)}{\sqrt{[W_{r-2}(i)]^2 + [W_{l-2}(i)]^2}}. \end{aligned} \quad (11)$$

- (3) Construct the two sub-low-pass filters, denoted by row vector $f_{\text{lowpasssub1}}$ and $f_{\text{lowpasssub2}}$, respectively. Consider

$$\begin{aligned} f_{\text{lowpasssub1}} &= \left[W_{l-1}, \underbrace{1, 1, \dots, 1}_{p_1}, W_{r-1} \right]_{1 \times [2 \times \text{floor}(2 \times M_1) + 1]}, \\ f_{\text{lowpasssub2}} &= \left[W_{l-2}, \underbrace{1, 1, \dots, 1}_{p_2}, W_{r-2} \right]_{1 \times [2 \times \text{floor}(2 \times M_2) + 1]}, \end{aligned} \quad (12)$$

where $p_1 = 2 \times \text{floor}(M_1) + 1$, $p_2 = 2 \times \text{floor}(M_2) + 1$.

- (4) Construct a low-pass filter at scale 5, denoted by matrix $(f_{\text{lowpass}_5})_{[2 \times \text{floor}(2 \times M_1) + 1] \times [2 \times \text{floor}(2 \times M_2) + 1]}$, and

$$f_{\text{lowpass}_5} = (f_{\text{lowpasssub1}})^T \times f_{\text{lowpasssub2}}, \quad (13)$$

where $(\cdot)^T$ is the transpose vector or matrix of the input vector or matrix.

- (5) Construct a high-pass filter at scale 5, denoted by matrix f_{hipass_5} , which has the same size as f_{lowpass_5} . Consider

$$f_{\text{hipass}_5} = \sqrt{1 - (f_{\text{lowpass}_5})^2}. \quad (14)$$

- (6) $\hat{f}[n_1, n_2]$ is filtered by f_{hipass_5} , hence generating the filtered high-pass signal at scale 5 f'_{hipass_5} , which has the same size of $N_1 \times N_2$ as $\hat{f}[n_1, n_2]$. Consider

$$\begin{aligned} f'_{\text{hipass}_5}(n_1, n_2) &= \begin{cases} \hat{f}(n_1, n_2) \times f_{\text{hipass}_5}(n_1, n_2), & a \leq n_1 \leq b, \quad c \leq n_2 \leq d, \\ \hat{f}(n_1, n_2), & \text{others,} \end{cases} \end{aligned} \quad (15)$$

where the filter at scale 5 has the following range:

$$\begin{aligned} a &= -\text{floor}(2 \times M_1) + \text{ceil}\left(\frac{(N_1 + 1)}{2}\right), \\ b &= \text{floor}(2 \times M_1) + \text{ceil}\left(\frac{(N_1 + 1)}{2}\right), \\ c &= -\text{floor}(2 \times M_2) + \text{ceil}\left(\frac{(N_2 + 1)}{2}\right), \\ d &= \text{floor}(2 \times M_2) + \text{ceil}\left(\frac{(N_2 + 1)}{2}\right). \end{aligned} \quad (16)$$

- (7) Inverse 2DFFT (inverse fast Fourier transform) is applied to f'_{hipass_5} , hence generating the discrete Curvelet coefficients at scale 5, $C_{5,1}$.

- (8) $\hat{f}[n_1, n_2]$ is filtered by f_{lowpass_5} , hence generating the filtered low-pass signal at scale 5, $(f'_{\text{lowpass}_5})_{[2 \times \text{floor}(2 \times M_1) + 1] \times [2 \times \text{floor}(2 \times M_2) + 1]}$ and

$$f'_{\text{lowpass}_5}(n_1, n_2) = \hat{f}(n_1, n_2) \times f_{\text{lowpass}_5}(n_1, n_2), \quad (17)$$

$$a \leq n_1 \leq b, \quad c \leq n_2 \leq d.$$

Step 3. Acquire the Curvelet coefficients at scale 4 and angle 1 to angle 32, $C_{4,l}$, $l = 1, 2, \dots, 32$.

Firstly, we acquire the Curvelet coefficients at scale 4 and angle 1, $C_{4,1}$.

Suppose that

$$M_1 = \frac{N_1}{(6 \times 2)}, \quad M_2 = \frac{N_2}{(6 \times 2)}. \quad (18)$$

The filter at scale 4 has the following range:

$$\begin{aligned} a_{N_{\text{scales}}-1} &= -\text{floor}(2 \times M_1) + \text{floor}(4 \times M_1) + 1, \\ b_{N_{\text{scales}}-1} &= \text{floor}(2 \times M_1) + \text{floor}(4 \times M_1) + 1, \\ c_{N_{\text{scales}}-1} &= -\text{floor}(2 \times M_2) + \text{floor}(4 \times M_2) + 1, \\ d_{N_{\text{scales}}-1} &= \text{floor}(2 \times M_2) + \text{floor}(4 \times M_2) + 1. \end{aligned} \quad (19)$$

- (1) Construct a low-pass filter at scale 4 and angle 1 in the same way as at scale 5, $(f'_{\text{lowpass}_4})_{[2 \times \text{floor}(2 \times M_1) + 1] \times [2 \times \text{floor}(2 \times M_2) + 1]}$.
- (2) Construct a high-pass filter at scale 4 and angle 1 in the same way as at scale 5, $(f'_{\text{hipass}_4})_{[2 \times \text{floor}(2 \times M_1) + 1] \times [2 \times \text{floor}(2 \times M_2) + 1]}$.
- (3) f'_{lowpass_5} is filtered by f_{lowpass_4} , hence generating the filtered low-pass signal at scale 4 $(f'_{\text{lowpass}_4})_{[2 \times \text{floor}(2 \times M_1) + 1] \times [2 \times \text{floor}(2 \times M_2) + 1]}$.
- (4) f'_{lowpass_5} is filtered by f_{hipass_4} , hence generating the filtered high-pass signal at scale 4 f'_{hipass_4} , which has the same size as that of f'_{lowpass_5} .
- (5) Determine the discrete locating window of wedge wave at scale 4 and angle 1.

The Curvelet coefficients at scale 4 are divided into the four quadrants. The quadrant label of Curvelet coefficients is denoted by quad, and four quadrants are denoted by quad = 1, 2, 3, 4, respectively. Each quadrant has 8 angles. In the first quadrant, quad = 1, angle ranges from 1 to 8, in the second quadrants, quad = 2, angle ranges from 9 to 16, in the third quadrants, quad = 3, angle ranges from 17 to 24, in the fourth quadrants, and quad = 4, angle ranges from 25 to 32.

Suppose that

$$\begin{aligned}
 M_{\text{horiz}} &= M_2, & \text{quad} &= 1 \text{ or } 3, \\
 M_{\text{vert}} &= M_1, \\
 M_{\text{horiz}} &= M_1, & \text{quad} &= 2 \text{ or } 4, \\
 M_{\text{vert}} &= M_2, \\
 p &= \frac{1}{2 \times n_{\text{quad}-4}}, \\
 q &= 2 \times \text{floor}(4 \times M_{\text{horiz}}),
 \end{aligned} \tag{20}$$

where $n_{\text{quad}-4}$ denotes the number of angle at each quadrant at scale 4; in this paper, $n_{\text{quad}-4} = 8$.

The left vector of wedge wave is denoted by $W_{\text{left}} = (a_{1,k+1})_{1 \times (n_{\text{quad}-4} + 1)}$, where $a_{1,k+1} = \text{round}(k \times p \times q + 1)$, $k = 0, 1, 2, \dots, n_{\text{quad}-4}$.

The right vector of wedge wave is denoted by $W_{\text{right}} = (a_{1,k+1})_{1 \times (n_{\text{quad}-4} + 1)}$, where $a_{1,k+1} = q + 2 - \text{round}(k \times p \times q + 1)$, $k = n_{\text{quad}-4}, n_{\text{quad}-4} - 1, \dots, 1$.

The combination wedge wave vector is denoted by $W = [W_{\text{left}}, W_{\text{right}}]_{1 \times (2 \times n_{\text{quad}-4} + 1)}$.

The endpoint vector of wedge wave is denoted by $W_{\text{end}} = (a_{1,k})_{1 \times (n_{\text{quad}-4})}$, where $a_{1,k} = W(2 \times k) \cdots k = 1, 2, \dots, n_{\text{quad}-4}$.

The first midpoint vector of wedge wave is denoted by $W_{\text{mid1}} = (a_{1,k})_{1 \times (n_{\text{quad}-4} - 1)}$, where $a_{1,k} = W_{\text{end}}(k) \cdots k = 1, 2, \dots, n_{\text{quad}-4} - 1$.

The second midpoint vector of wedge wave is denoted by $W_{\text{mid2}} = (a_{1,k})_{1 \times (n_{\text{quad}-4} - 1)}$, where $a_{1,k} = W_{\text{end}}(k) \cdots k = 2, 3, \dots, n_{\text{quad}-4}$.

The combination midpoint vector of wedge wave is denoted by $W_{\text{mid}} = (a_{1,k})_{1 \times (n_{\text{quad}-4} - 1)}$, where $a_{1,k} = (W_{\text{mid1}}(k) + W_{\text{mid2}}(k))/2 \cdots k = 1, 2, 3, \dots, n_{\text{quad}-4} - 1$.

The first wedge wave endpoint along the vertical orientation is denoted by

$$r_{\text{first_wedge_endpoint}} = \text{round}\left(\frac{2 \times \text{floor}(4 \times M_{\text{vert}})}{2 \times n_{\text{quad}-4}} + 1\right). \tag{21}$$

The length of the first wedge wave is denoted by

$$s_{\text{wedge}} = \text{floor}(4 \times M_{\text{vert}}) - \text{floor}(M_{\text{vert}}) + \text{ceil}\left(\frac{r_{\text{first_wedge_endpoint}}}{4}\right). \tag{22}$$

The width of the wedge wave is denoted by $W_{\text{wedge}} = W_{\text{end}}(2) + W_{\text{end}}(1) - 1$.

The slope of the first wedge wave is $s_{\text{slope}} = [\text{floor}(4 \times M_{\text{horiz}}) + 1 - W_{\text{end}}(1)]/\text{floor}(4 \times M_{\text{vert}})$.

The left line vector is denoted by $s_{\text{left_line}} = (a_{1,k})_{1 \times (s_{\text{wedge}})}$, where $a_{1,k} = \text{round}(2 - W_{\text{end}}(1) + s_{\text{slope}} \times (k - 1)) \cdots k = 1, 2, \dots, s_{\text{wedge}}$.

The first row coordinate is $r_{\text{first}} = \text{floor}(4 \times M_{\text{vert}}) + 2 - \text{ceil}((s_{\text{wedge}} + 1)/2)$.

The first column coordinate is $c_{\text{first}} = \text{floor}(4 \times M_{\text{horiz}}) + 2 - \text{ceil}((W_{\text{wedge}} + 1)/2)$.

Condition column vector is denoted by $V_{\text{col}} = (a_{1,k})_{1 \times W_{\text{wedge}}}$, where

$$\begin{aligned}
 a_{1,k} &= s_{\text{left_line}}(k + 1) \\
 &+ \text{mod}\left((k - s_{\text{left_line}}(k + 1) + c_{\text{first}}), W_{\text{wedge}}\right), \\
 k &= 0, 1, 2, \dots, W_{\text{wedge}} - 1,
 \end{aligned} \tag{23}$$

$$\text{mod}(x, y) = \begin{cases} x - n \times y & n = \text{floor}\left(\frac{x}{y}\right), y \neq 0, \\ x, & y = 0. \end{cases}$$

Thus, the discrete locating window of wedge wave is denoted by $W_{\text{data}} = (a_{n_1, n_2})_{s_{\text{wedge}} \times W_{\text{wedge}}}$, where

$$a_{n_1, n_2} = \begin{cases} f'_{\text{hipass}_4}(n_1, n_2), & V_{\text{col}}(n_2) > 0, \\ 0, & V_{\text{col}}(n_2) \leq 0, \end{cases} \tag{24}$$

where

$$n_1 = 1 + \text{mod}(k - r_{\text{first}}, s_{\text{wedge}}), \quad k = 1, 2, \dots, s_{\text{wedge}}, \tag{25}$$

$$\begin{aligned}
 n_2 &= 0.5 \times V_{\text{col}}(k) + 1 + |V_{\text{col}}(k) - 1|, \\
 k &= 1, 2, \dots, W_{\text{wedge}}.
 \end{aligned} \tag{26}$$

(6) The discrete locating window of wedge wave W_{data} is filtered and rotated, hence generating matrix $W_{\text{data}.2}$.

Suppose that

$$y_{\text{corner}} = (a_{1,k})_{1 \times s_{\text{wedge}}}, \tag{27}$$

where $a_{1,k} = k, k = 1, 2, 3, \dots, s_{\text{wedge}}$ and

$$x_{\text{corner}} = (a_{1,k})_{1 \times q}, \quad (28)$$

where $a_{1,k} = k, k = 1, 2, 3, \dots, q + 1$ and

$$X = \begin{bmatrix} x_{\text{corner}} \\ x_{\text{corner}} \\ x_{\text{corner}} \\ \vdots \\ x_{\text{corner}} \end{bmatrix}_{s_{\text{wedge}} \times q}, \quad (29)$$

$$Y^T = \begin{bmatrix} y_{\text{corner}} \\ y_{\text{corner}} \\ y_{\text{corner}} \\ \vdots \\ y_{\text{corner}} \end{bmatrix}_{q \times s_{\text{wedge}}},$$

$$X_{\text{wrap}} = (X(n_1, n_2))_{s_{\text{wedge}} \times W_{\text{wedge}}},$$

where n_1, n_2 are calculated by (25) and (26), respectively. Consider

$$Y_{\text{wrap}} = (Y(n_1, n_2))_{s_{\text{wedge}} \times W_{\text{wedge}}}, \quad (30)$$

where n_1, n_2 are calculated by (25) and (26), respectively.

The slope of right wedge wave is $s_{\text{slope-right}} = (\text{floor}(4 \times M_{\text{horiz}}) + 1 - W_{\text{mid}}(1)) / \text{floor}(4 \times M_{\text{vert}})$.

The middle line matrix $M_{\text{mid-line-right}} = (a_{n_1, n_2})_{s_{\text{wedge}} \times W_{\text{wedge}}}$, where $a_{n_1, n_2} = W_{\text{mid}}(1) + s_{\text{slope-right}} \times (Y_{\text{wrap}}(n_1, n_2) - 1)$.

The right coordinate matrix is $C_{\text{cord-right}} = (a_{n_1, n_2})_{s_{\text{wedge}} \times W_{\text{wedge}}}$, where

$$a_{n_1, n_2} = 0.5 + \frac{\text{floor}(4 \times M_{\text{vert}})}{W_{\text{end}}(2) - W_{\text{end}}(1)} \times \frac{X_{\text{wrap}}(n_1, n_2) - M_{\text{mid-line-right}}(n_1, n_2)}{\text{floor}(4 \times M_{\text{vert}}) + 1 - Y_{\text{wrap}}(n_1, n_2)},$$

$$c2 = 1$$

$$\times \left(\frac{1}{2 \times (\text{floor}(4 \times M_{\text{horiz}}) / (W_{\text{end}}(1) - 1)) - 1} - 1 \right. \\ \left. + 1 \times \left(2 \times \left(\frac{\text{floor}(4 \times M_{\text{vert}})}{r_{\text{first-wedge-endpoint}} - 1} \right) - 1 \right)^{-1} \right)^{-1},$$

$$c1 = \frac{c2}{2 \times ((\text{floor}(4 \times M_{\text{horiz}})) / (r_{\text{first-wedge-endpoint}} - 1)) - 1}. \quad (31)$$

The corner coordinate matrix $C_{\text{cord-corner}} = (a_{n_1, n_2})_{s_{\text{wedge}} \times W_{\text{wedge}}}$, where

$$a_{n_1, n_2} = c1 + c2 \times \left[\frac{X_{\text{wrap}}(n_1, n_2) - 1}{\text{floor}(4 \times M_{\text{horiz}})} - \frac{Y_{\text{wrap}}(n_1, n_2) - 1}{\text{floor}(4 \times M_{\text{vert}})} \right],$$

$$\times \left(2 - \left[\frac{X_{\text{wrap}}(n_1, n_2) - 1}{\text{floor}(4 \times M_{\text{horiz}})} - \frac{Y_{\text{wrap}}(n_1, n_2) - 1}{\text{floor}(4 \times M_{\text{vert}})} \right] \right)^{-1}. \quad (32)$$

The $C_{\text{cord-corner}}$ is wrapped, yielding the matrix $W_{l\text{-left}}$ and $W_{r\text{-right}}$:

$$W_{l\text{-left}}(n_1, n_2) = \begin{cases} 1, & C_{\text{cord-corner}}(n_1, n_2) = 0, \\ e^{(1-1/(1-e^{(1-1/(1-C_{\text{cord-corner}}(n_1, n_2))))}),} & 0 < C_{\text{cord-corner}}(n_1, n_2) < 1, \\ 0, & C_{\text{cord-lcorner}}(n_1, n_2) = 1, \end{cases} \quad (33)$$

$$W_{l\text{-right}}(n_1, n_2) = \begin{cases} 1, & C_{\text{cord-corner}}(n_1, n_2) = 0, \\ e^{(1-1/(1-e^{(1-1/(1-C_{\text{cord-corner}}(n_1, n_2))))}),} & 0 < C_{\text{cord-corner}}(n_1, n_2) < 1, \\ 0, & C_{\text{cord-corner}}(n_1, n_2) = 1. \end{cases}$$

In the same way, the $C_{\text{cord-right}}$ is wrapped, yielding the matrix $W_{wl\text{-left}}$ and $W_{wr\text{-right}}$.

The discrete locating window of wedge wave W_{data} is filtered, yielding the matrix $W_{\text{data-tran}} = (a_{n_1, n_2})_{s_{\text{wedge}} \times W_{\text{wedge}}}$, where

$$a_{n_1, n_2} = W_{\text{data}}(n_1, n_2) \times [W_{l\text{-left}}(n_1, n_2) \times W_{wr\text{-right}}(n_1, n_2)].$$

The matrix $W_{\text{data-tran}}$ is rotated, yielding the matrix $W_{\text{data.2}}$

$$W_{\text{data.2}} = \text{rot } 90(W_{\text{data-tran}}, -(\text{quad} - 1)), \quad (34)$$

where $\text{rot } 90(A, k)$ rotates matrix A counterclockwise by $k \times 90^\circ$ degrees.

(7) Inverse 2DFFT is applied to $W_{\text{data.2}}$, hence generating the Curvelet coefficient at scale 4 and angle 1, $C_{4,1}$.

(8) Repeat (5), (6), and (7) in Step 3, in the same way of acquiring $C_{4,1}$; Curvelet coefficients at scale 4 and angle from 2 to 8 are generated.

Noted that at angle from 2 to 32, the left line vector is denoted by $s_{\text{left-line}} = (a_{1,k})_{1 \times (s_{\text{wedge}})}$, where $a_{1,k} = \text{round}(W_{\text{end}}(l_{\text{sub}} - 1) + s_{\text{slope}} \times (k - 1)) \dots k = 1, 2, \dots, s_{\text{wedge}}$. Consider

$$l_{\text{sub}} = 2, 3, 4, \dots, 8. \quad (35)$$

TABLE 1: Structure of Curvelet transform coefficients.

Levels	Scales (j)	Orientation (l)	Matrix form $C_{j,l}$							
Coarse	1	1	21 × 21							
			18 × 22	16 × 22	16 × 22	18 × 22				
	2	16	22 × 18	22 × 16	22 × 16	22 × 18				
			18 × 22	16 × 22	16 × 22	18 × 22				
Details	3	32	22 × 18	22 × 16	22 × 16	22 × 18				
			34 × 22	32 × 22	32 × 22	32 × 22	32 × 22	32 × 22	32 × 22	34 × 22
			22 × 34	22 × 32	22 × 32	22 × 32	22 × 32	22 × 32	22 × 32	22 × 34
			34 × 22	32 × 22	32 × 22	32 × 22	32 × 22	32 × 22	32 × 22	34 × 22
	4	32	22 × 34	22 × 32	22 × 32	22 × 32	22 × 32	22 × 32	22 × 32	22 × 34
			67 × 44	64 × 43	64 × 43	64 × 44	64 × 44	64 × 43	64 × 43	67 × 44
			44 × 67	43 × 64	43 × 64	44 × 64	44 × 64	43 × 64	43 × 64	44 × 67
			67 × 44	64 × 43	64 × 43	64 × 44	64 × 44	64 × 43	64 × 43	67 × 44
	5	1	44 × 67	43 × 64	43 × 64	44 × 64	44 × 64	43 × 64	43 × 64	44 × 67
			256 × 256							
Fine	5	1								

(9) The Curvelet coefficients at scale 4 and other three quadrants, $C_{4,l}$, $l = 9, 10, \dots, 32$ are acquired in the same way as that in the first quadrants.

Finally, the Curvelet coefficients at scale 4, $C_{4,l}$, $l = 1, 2, \dots, 32$, are generated after Step 3.

Step 4. Repeat Step 3, hence generating the Curvelet coefficients at scale 3, $C_{3,l}$, $l = 1, 2, \dots, 32$.

Note that the discrete locating window of wedge wave at scale 3 can be calculated by

$$W_{\text{data},3} = (a_{n_1,n_2})_{s_{\text{wedge},3} \times W_{\text{wedge},3}}, \quad (36)$$

where

$$a_{n_1,n_2} = \begin{cases} f'_{\text{hipass}_3}(n_1, n_2), & V_{\text{col}_3}(n_2) > 0, \\ 0, & V_{\text{col}_3}(n_2) \leq 0, \end{cases} \quad (37)$$

$s_{\text{wedge},3}$, $W_{\text{wedge},3}$ is the length and width of the discrete locating window of wedge wave at scale 3, and V_{col_3} is condition vector at scale 3.

Step 5. Repeat Step 3, hence generating the Curvelet coefficients at scale 2, $C_{2,l}$, $l = 1, 2, \dots, 16$.

Note that the discrete locating window of wedge wave at scale 2 can be calculated by

$$W_{\text{data},2} = (a_{n_1,n_2})_{s_{\text{wedge},2} \times W_{\text{wedge},2}}, \quad (38)$$

where

$$a_{n_1,n_2} = \begin{cases} f'_{\text{hipass}_2}(n_1, n_2), & V_{\text{col}_2}(n_2) > 0, \\ 0, & V_{\text{col}_2}(n_2) \leq 0, \end{cases} \quad (39)$$

and V_{col_2} is condition vector at scale 2.

Step 6. Inverse 2DFFT is applied to the low-pass signal at scale 2, $f'_{\text{lowpass}_2}(n_1, n_2)$, generating the Curvelet coefficient at scale 1 $C_{1,1}$.

The detailed structure of the Curvelet coefficients obtained by FDCT_WARPING is shown in Table 1.

2.3.2. Fingerprint Image Noise Filtration Technique. Noise always arises from the acquiring fingerprint images. The noise may result in the vagueness and many discontinuities of ridges (or valleys) in the image and thus affects accurate feature extraction and recognition. So, it is necessary and important to denoise in fingerprint images.

The relationship of the Curvelet coefficients between the different scales is similar to the relationship of the wavelet coefficients; that is, there exists strong correlation between them.

From Table 1, there are 16 and 32 orientations at scale 2 and scale 3, respectively. Each Curvelet coefficient matrix is at scale 2 and each orientation corresponds to two adjacent matrices generated at scale 3. The ridges in a fingerprint image correspond to the Curvelet coefficients with large magnitude at scale 2. Each Curvelet coefficient matrix at scale 2 is decomposed into two Curvelet coefficient matrices at scale 3 and at two adjacent orientations. The corresponding two Curvelet coefficient matrices at scale 3 also have large magnitude, while the magnitude of the Curvelet coefficients corresponding to the noise dies out swiftly from scale 2 to scale 3. So, we use the direct spatial correlation of Curvelet coefficients at scale 2 and scale 3 to accurately distinguish ridges from noise. For scales 4 and 5, we adopt hard threshold method to filter the noise. Finally, we reconstruct all the Curvelet coefficients by the technique [17] and accomplish fingerprint image filtration.

The proposed noise filtration technique has the following steps.

Step 1. Noise filtration of Curvelet coefficient matrices at scale 2 and scale 3, respectively.

This section details the major steps of the proposed noise filtration algorithm of Curvelet coefficient matrices generated at scales 2 and 3.

Assume each matrix to be at scale 2 and orientation l , $C_{2,l}$, corresponds to two adjacent matrices generated at scale 3, $C_{3,2 \times (l-1)+1}$ and $C_{3,2 \times (l-1)+2}$, (l ranges from 1 to $16 \times 2^{\text{ceil}((5-3)/2)}$). Let (r_0, c_0) be the size of $C_{2,l}$. The sizes of $C_{3,2 \times (l-1)+1}$ and $C_{3,2 \times (l-1)+2}$ are $(r_1 \times c_1)$ and $(r_2 \times c_2)$, respectively. The matrices at scales 2 and 3 are filtered as follows.

- (1) Decompose the Curvelet coefficients matrix $C_{3,2 \times (l-1)+1}$ into two matrices A and B with the same size as $C_{2,l}$, $r_0 \times c_0$. The elements of A are extracted from row 1 to r_0 and column 1 to c_0 of $C_{3,2 \times (l-1)+1}$, and the elements of B are extracted from row $r_1 - r_0 + 1$ to r_1 and column $c_1 - c_0 + 1$ to c_1 of $C_{3,2 \times (l-1)+1}$. Consider

$$A = (a_{n_1, n_2})_{r_0 \times c_0}, \quad (40)$$

where $a_{n_1, n_2} = C_{3,2 \times (l-1)+1}(n_1, n_2)$, $n_1 = 1, 2, 3, \dots, r_0$, $n_2 = 1, 2, 3, \dots, c_0$, and

$$B = (a_{n_1, n_2})_{r_0 \times c_0}, \quad (41)$$

where $a_{n_1, n_2} = C_{3,2 \times (l-1)+1}(n_1, n_2)$, $n_1 = r_1 - r_0 + 1, r_1 - r_0 + 2, \dots, r_1$, $n_2 = c_1 - c_0 + 1, c_1 - c_0 + 2, \dots, c_1$.

- (2) Decompose the Curvelet coefficients matrix $C_{3,2 \times (l-1)+2}$ into two matrices D and E with the size of $r_0 \times c_0$:

$$D = (a_{n_1, n_2})_{r_0 \times c_0}, \quad (42)$$

where $a_{n_1, n_2} = C_{3,2 \times (l-1)+2}(n_1, n_2)$, $n_1 = 1, 2, 3, \dots, r_0$, $n_2 = 1, 2, 3, \dots, c_0$, and

$$E = (a_{n_1, n_2})_{r_0 \times c_0}, \quad (43)$$

where $a_{n_1, n_2} = C_{3,2 \times (l-1)+2}(n_1, n_2)$, $n_1 = r_1 - r_0 + 1, r_1 - r_0 + 2, \dots, r_1$, $n_2 = c_1 - c_0 + 1, c_1 - c_0 + 2, \dots, c_1$.

- (3) Calculate the four multiplication coefficient matrices (m_k , $k = 1, 2, 3, 4$) between $C_{2,l}$ and the four matrices A , B , D , and E , respectively. Consider

$$\begin{aligned} m_1(n_1, n_2) &= C_{2,l}(n_1, n_2) \times A(n_1, n_2), \\ n_1 &= 1, 2, \dots, r_0, \quad n_2 = 1, 2, \dots, c_0, \\ m_2(n_1, n_2) &= C_{2,l}(n_1, n_2) \times B(n_1, n_2), \\ n_1 &= 1, 2, \dots, r_0, \quad n_2 = 1, 2, \dots, c_0, \\ m_3(n_1, n_2) &= C_{2,l}(n_1, n_2) \times D(n_1, n_2), \\ n_1 &= 1, 2, \dots, r_0, \quad n_2 = 1, 2, \dots, c_0, \\ m_4(n_1, n_2) &= C_{2,l}(n_1, n_2) \times E(n_1, n_2), \\ n_1 &= 1, 2, \dots, r_0, \quad n_2 = 1, 2, \dots, c_0. \end{aligned} \quad (44)$$

- (4) Filter the Curvelet coefficient matrices $C_{3,2 \times (l-1)+1}$ and $C_{3,2 \times (l-1)+2}$ by

$$\begin{aligned} A'(n_1, n_2) &= \begin{cases} A(n_1, n_2), & ||m_1(n_1, n_2)| - |m_3(n_1, n_2)|| > T_s, \\ 0, & \text{otherwise,} \end{cases} \\ D'(n_1, n_2) &= \begin{cases} D(n_1, n_2), & ||m_1(n_1, n_2)| - |m_3(n_1, n_2)|| > T_s, \\ 0, & \text{otherwise,} \end{cases} \\ B'(n_1, n_2) &= \begin{cases} B(n_1, n_2), & ||m_2(n_1, n_2)| - |m_4(n_1, n_2)|| > T_s, \\ 0, & \text{otherwise,} \end{cases} \\ E'(n_1, n_2) &= \begin{cases} E(n_1, n_2), & ||m_2(n_1, n_2)| - |m_4(n_1, n_2)|| > T_s, \\ 0, & \text{otherwise,} \end{cases} \end{aligned} \quad (45)$$

where A' , D' , B' , and E' are the Curvelet coefficient matrices at scale 3 after filtration, the operation $|\cdot|$ returns the complex modulus (magnitude) of the input, and T_s is the threshold. For example, if $||m_1(n_1, n_2)| - |m_3(n_1, n_2)|| > T_s$, we assume that the Curvelet coefficients correspond to the ridges of the image. Otherwise, the Curvelet coefficients correspond to the noise of the image, which are assigned to 0.

- (5) When filtering the Curvelet coefficient matrix $C_{2,l}$, if any of the filtered Curvelet coefficient matrices (A' , D' , B' , and E') equal to Z , $C_{2,l}$ is considered as noise and assigned to Z . Where Z is a matrix with all elements are zero.
- (6) repeat (1) to (5) with 16 times (the number of orientation of Curvelet coefficients at scale 2).

After (1)–(5), all the Curvelet coefficients at scale 2 and scale 3 are filtered.

Step 2. Noise Filtration of Curvelet coefficient matrices at scale 4 and scale 5, respectively.

The Curvelet coefficient matrices generated at scale 4 are filtered by

$$C'_{j,l}(i, j) = \begin{cases} C_{j,l}(n_1, n_2), & |C_{j,l}(n_1, n_2)| > \text{thresh} \times E_{j,l}, \\ 0, & \text{otherwise,} \end{cases} \quad (46)$$

where $C'_{j,l}$ are the filtered Curvelet coefficient matrices, $|\cdot|$ is the complex modulus operation, and thresh is the threshold; in this paper, thresh = 1.5, and

$$E_{j,l} = \frac{\sum_{i=1}^n \sum_{j=1}^m \sqrt{|C_{j,l}(i,j)|^2}}{n \times m}, \quad (47)$$

where (n, m) is the size of matrix $C_{j,l}$.

The Curvelet coefficient matrices generated at scale 5 are filtered in the same way as the Curvelet coefficient matrices generated at scale 4. Note that at scale 5 thresh = 2.

Step 3. After the coefficients at scale 2, 3, 4, and 5 are filtered, we reconstruct the coefficients using the technique [16] and accomplish image noise filtration.

T_s in (45) can be acquired by the statistics of difference of correlation coefficients in adjacent directions at the same scale. Finally, $T_s = 100$ is selected by many experiments. Figure 1 shows the noise filtration results of five types of fingerprint image by proposed noise filtration algorithm.

From Figure 1 (x):(B) ($x = a, b, c, d, e$), we can see many discontinuities of ridges in the original image can be smoothed after filtering and the direction of ridge is well followed, which founds the good basis for accurate feature extraction and recognition. We demonstrate Curvelet coefficients at different scales of five types of filtered images in Figure 2.

As Figure 2(a) to Figure 2(e) show, there are strong orientations in the Curvelet coefficients images. The white parts in the images represent partial edges of the ridge of fingerprint image in different orientations. Meanwhile, it means the significant Curvelet coefficients of images. The low-frequency (coarse scale) coefficients are stored at the center of the display. The Cartesian concentric coronae show the coefficients at different scales; the outer coronae correspond to higher frequencies. There are four strips associated with each corona, corresponding to the four cardinal points; these are further subdivided in angular panels. Each panel represents coefficients at a specified scale and along the orientation suggested by the position of the panel.

2.4. Fingerprint Feature Extraction. Haralick et al. [18] first proposed gray-level cooccurrence matrix (GLCM) for texture descriptions in the 1970s. It is still popular until today and widely used in various texture classifications [19–23], because of its good statistic performance. The GLCM is a second order statistics method which describes the spatial interrelationships of the grey tones in an image.

GLCM contains elements that are counts of the number of pixel pairs, which are separated by certain distance and at some angular direction. Typically, the GLCM is calculated in a small window, which scans the whole image. The texture feature will be associated with each pixel.

In our studies, GLCM is computed based on two parameters, which are the distance between the pixel pair d and their angular relationship θ . $d = 1$ and θ are quantized in four directions ($0^\circ, 45^\circ, 90^\circ$, and 135°). For image I , defined square

TABLE 2: Direction values.

θ	0°	45°	90°	135°
θ_0	0	1	1	1
θ_1	1	1	0	-1

window $N \times N$, brightness levels i and j , the nonnormalized GLCM p_{ij} are defined by

$$p_{i,j,\theta} = \sum_{x=1}^N \sum_{y=1}^N C \left\{ (I(x, y) = i)^{(I(x \pm d\theta_0, y \mp d\theta_1) = j)} \right\}, \quad (48)$$

where $C\{\cdot\} = 1$ if the argument is true and $C\{\cdot\} = 0$, otherwise. The signs \pm and \mp in (10) mean that each pixel pair is counted twice: once forward and once backward in order to make the GLCM diagonally symmetric. For each direction, θ_0 and θ_1 are shown in Table 2.

The procedures of feature extraction are as follows.

Step 1. Scale the grayscale values in Curvelet transform coefficients into 8 levers and compute the GLCMs of Curvelet coefficients at scale 1 $C_{1,1}$ and calculate 16 texture features based on 4 GLCMs:

- (1) Angular second moment (ASM)

$$f_1 = \sum_{i=0}^{G-1} \sum_{j=0}^{G-1} p(i, j)^2. \quad (49)$$

- (2) Contrast (CON)

$$f_2 = \sum_{n=0}^{G-1} n^2 \left\{ \sum_{i=0}^{G-1} \sum_{j=0}^{G-1} p(i, j)^2 \right\}, \quad (50)$$

where $|i - j| = n$.

- (3) Correlation (COR)

$$f_3 = \frac{\sum_{i=0}^{G-1} \sum_{j=0}^{G-1} (ij) p(i, j) - \mu_1 \mu_2}{\sigma_1^2 \sigma_2^2}, \quad (51)$$

where

$$\mu_1 = \sum_{i=0}^{G-1} i \sum_{j=0}^{G-1} p(i, j), \quad \mu_2 = \sum_{i=0}^{G-1} j \sum_{j=0}^{G-1} p(i, j),$$

$$\sigma_1^2 = \sum_{i=0}^{G-1} (i - \mu_1)^2 \sum_{j=0}^{G-1} p(i, j), \quad (52)$$

$$\sigma_2^2 = \sum_{i=0}^{G-1} (j - \mu_2)^2 \sum_{i=0}^{G-1} p(i, j).$$

- (4) Entropy (ENT)

$$f_4 = - \sum_{i=0}^{G-1} \sum_{j=0}^{G-1} p(i, j) \log p(i, j). \quad (53)$$

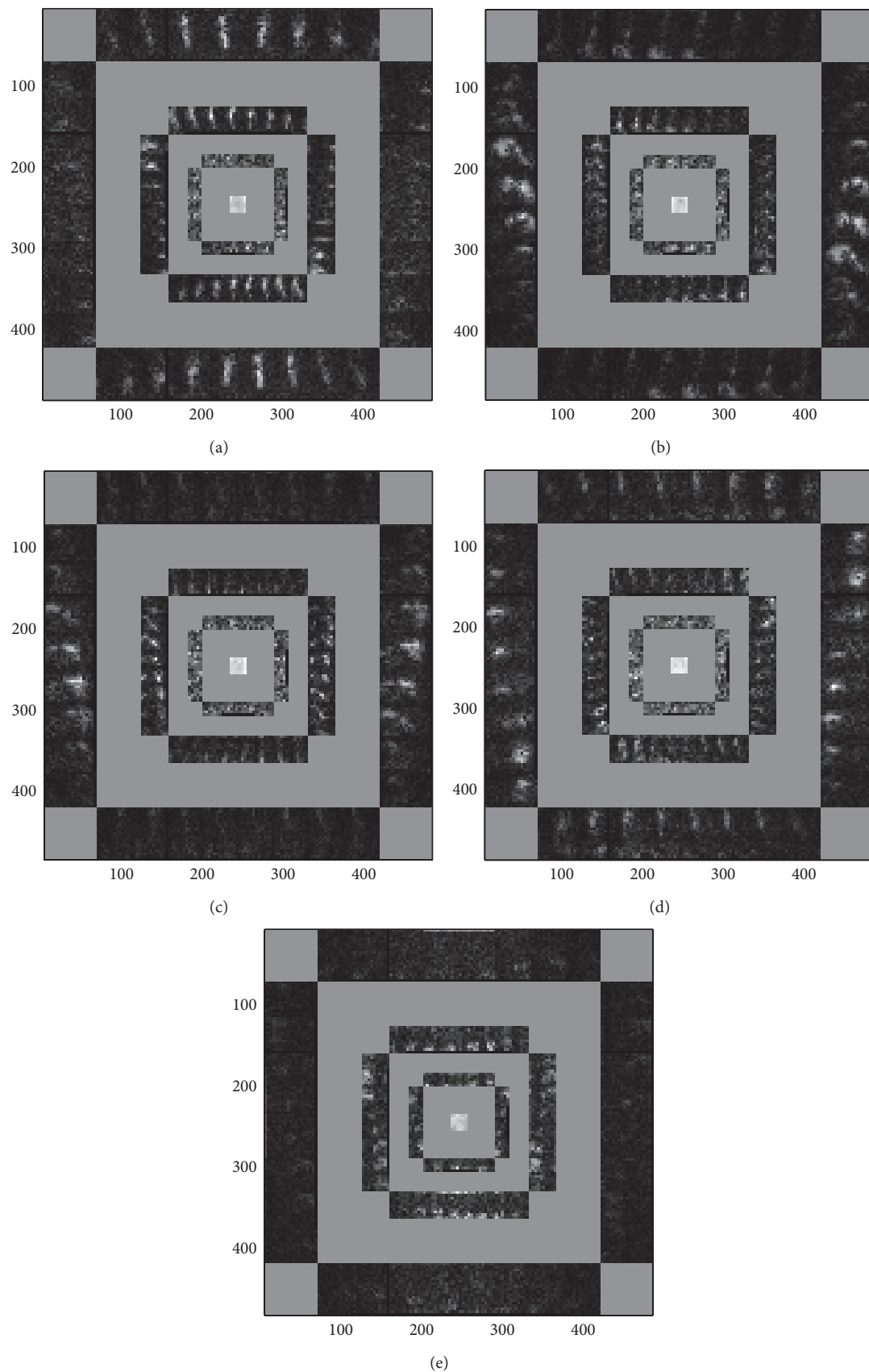


FIGURE 2: Curvelet coefficients of five filtered fingerprint classes. (a) Right loop (R), (b) left loop (L), (c) whorl (W), (d) arch (A), and (e) tented arch (T).

Step 2. Calculate averaged l_1 -norm of Curvelet coefficients in 8 directions at the second scale $C_{2,l}$ and acquire 8 texture features according to (51). Consider

$$E_l = \frac{1}{m_1 \times m_2} \sum_i^{m_1} \sum_j^{m_2} |C_{2,l}(i, j)|, \quad (54)$$

where, (m_1, m_2) is the size of the matrix $C_{2,l}$, and $l = 1, 2, 3, 4, 5, \dots, 16$.

Step 3. Calculate averaged l_1 -norm of Curvelet coefficients in 16 directions at the third scale $C_{3,l}$ and acquire 16 texture features according to (54).

Step 4. Calculate averaged l_1 -norm of Curvelet coefficients in 16 directions at the fourth scale $C_{4,l}$ and acquire 16 texture features according to (54).

Step 5. Calculate averaged l_1 -norm of Curvelet coefficients at the fifth scale $C_{5,1}$ and acquire 1 texture feature.

Note that in Step 2, Step 3, and Step 4, we only calculate the averaged l_1 -norm of Curvelet coefficients in even directions to assure the classification accuracy and reduce the recognition time. So, a feature vector containing 57 components for each image can be extracted.

3. Experiment Results

3.1. Datasets. NIST special fingerprint database 4(NIST-4) is one of the most important benchmarks for fingerprint classification. Most published results on fingerprint classification are based on this database. For comparison with other approaches, we also perform our fingerprint classification algorithm on this database for the five-class fingerprint classification problem. Since fingerprint classes A (arch) and T (tented arch) have a substantial overlap, it is very difficult to separate these two classes. Therefore, we also report our results for the four-class classification problem, where classes A and T have been merged into one class. NIST-4 contains 4000 fingerprints of size 480×512 pixels, taken from 2000 fingers. Each finger has two impressions (f and s). The first fingerprint instances are numbered from f0001 to f2000 and the second fingerprint instances are numbered from s0001 to s2000. All fingerprints in this database are used in our experiment. We form our training set with the first 2,000 fingerprints from 1,000 fingers (f0001 to f1000 and s0001 to s1000) and the test set contains the remaining 2,000 fingerprints (f1001 to f2000 and s1001 to s2000).

To eliminate the large difference between the feature vectors, each feature vector v_k is normalized according to

$$v_k(i) = \frac{v_k(i) - v_{\min}(i)}{v_{\max}(i) - v_{\min}(i)}, \quad (55)$$

where $v_k(i)$ represents the i th element of vector v_k , $v_{\min}(i)$ denotes the minimum of the i th element of all the row vectors, and $v_{\max}(i)$ denotes the maximum of the i th element of all the row vectors.

TABLE 3: Fingerprint classification results on NIST-4.

True class	Hypothesized class				
	A	T	L	R	W
A	432	12	3	1	2
T	28	296	8	4	0
L	4	5	370	0	4
R	3	8	1	386	3
W	3	1	6	5	380

3.2. Experiment Results and Analysis. The performance of a fingerprint classification algorithm is often measured in terms of accuracy. The accuracy is computed as the ratio between the number of correctly classified fingerprint and the total number of fingerprints in the test set. Each image is labeled with one or more of the five classes (W, R, L, A, and T). To simplify the training procedure, we make use of only the first label of a fingerprint to train our system. For testing, however, we make use of all the labels for a fingerprint and consider the output of our classifier to be correct if the output matches any one of the labels. This is in line with the common practice used by other researchers in comparing the classification results on the NIST-4 database.

Classification accuracy does not always increase with increasing K of the K -nearest neighbor classifier; there exists an optimal value of K for finite training sample size classification problems. According to the method in [24], in our experiments, 10 nearest neighbors ($K = 10$) are considered. The classification results of our proposed approach are shown in Table 3. The diagonal entries in Table 3 show the number of test patterns from different classes which are correctly classified.

From Table 3, we can conclude that the proposed algorithm achieves an accuracy of 94.6 percent for the five-class classification task. For the four-class classification task (where classes A and T were collapsed into one class), an accuracy of 96.8 percent is achieved.

Experiment. To evaluate the performance of the proposed algorithm, we have compared the proposed approach to wavelet-based, GLCM-based, and Curvelet-based, respectively. We use wavelet transform to decompose gray images into five scales wavelet coefficients using wavelet bases "Symmlets 4, 5, 6, 8, and 9" and calculate averaged l_1 -norm of wavelet coefficients at each scale. Finally, WT feature vector with dimension of 16 are acquired. The reason using "Symmlets 4, 5, 6, 8, and 9" is that in the work of Tico et al. [10] best results were obtained with these five wavelet bases. In Table 4, we show the comparison results for the five-class classification.

From Table 4, we can conclude that our algorithm achieves higher accuracy of classes W by reducing the misclassification of W as L or R. Our algorithm also achieves higher accuracy of classes R by reducing the misclassification of R as A. Finally, our algorithm achieves higher accuracy of classes A by reducing the misclassification of A as T.

TABLE 4: Comparison of accuracy on NIST-4 for the five-class classification.

Features	Accuracy A	Accuracy T	Accuracy L	Accuracy R	Accuracy W
Wavelet (Symmlet 4)	92%	79.7%	94.2%	93.3%	93.7%
Wavelet (Symmlet 5)	92%	82.7%	94.5%	93.5%	93.1%
Wavelet (Symmlet 6)	92%	83.7%	94.2%	93.0%	93.7%
Wavelet (Symmlet 8)	92%	82.7%	94.2%	93.0%	93.7%
Wavelet (Symmlet 9)	92%	81.2%	94.2%	93.0%	93.7%
GLCM	78.4%	77.7%	79.4%	72.8%	82.7%
Curvelet	93.6%	84.7%	95.0%	94.0%	94.5%
Proposed algorithm	96.0%	88.1%	96.6%	96.3%	96.2%

Also, Curvelet-based is better than wavelet-based and GLCM-based. The reason is CT can better capture the direction of fingerprint ridge than WT and GLCM. Furthermore, the proposed algorithm can provide much more information on the ridge direction by combining the good statistic performance of GLCM and well capturing the direction of CT.

Most of misclassifications in the proposed approach are caused by heavy noise in the poor quality fingerprints, where it is very difficult to correctly extract Curvelet coefficients.

4. Conclusion

In this paper, we present an efficient fingerprint classification algorithm that uses CT and GLCM to model the feature set of fingerprint. There are two main contributions in this paper. Firstly, we construct Curvelet filter that can smooth the discontinuities of ridges and remove the noise in the original image. As a result, the direction of ridge is well followed. Secondly, in combination with the effectiveness of CT and GLCM, we propose to construct a 53-dimensional feature vector as classifier input that can represent curves singularities and the statistics in fingerprint image with compact feature. We have tested our algorithm on the NIST-4 database and a very good performance has been achieved (94.6 percent for the five-class classification problem and 96.8 percent for the four-class classification problem with 1.8 percent rejection). These good performances of the proposed algorithm could be ascribed to the high information contents of Curvelet features and to the combination of GLCM and CT.

Our system takes about 1.47 seconds on a AMD E-350 PC to classify one fingerprint, which needs to be improved. Since image decomposition (filtering) steps account for 82 percent of the total compute time, special purpose hardware for Curvelet transform can significantly decrease the overall time for classification.

Conflict of Interests

The authors declare that there is no conflict of interests regarding the publication of this paper.

Acknowledgments

The authors are grateful for the anonymous reviewers who made constructive comments. This work is supported by the National Natural Science Foundation of China (no. 61203302 and no. 51107088), the Tianjin Research Program of Application Foundation, and Advanced Technology (14JCY-BJC18900).

References

- [1] J.-M. Guo, Y.-F. Liu, J.-Y. Chan, and J.-D. Lee, "Fingerprint classification based on decision tree from singular points and orientation field," *Expert Systems with Applications*, vol. 41, no. 2, pp. 752–764, 2014.
- [2] D. Peralta, I. Triguero, R. Sanchez-Reillo, F. Herrera, and J. M. Benitez, "Fast fingerprint identification for large databases," *Pattern Recognition*, vol. 47, no. 2, pp. 588–602, 2014.
- [3] M. Liu, "Fingerprint classification based on Adaboost learning from singularity features," *Pattern Recognition*, vol. 43, no. 3, pp. 1062–1070, 2010.
- [4] H. Ching-Tang and H. Chia-Shing, "Fingerprint identification based on MOPSO in SVM," *Applied Mechanics and Materials*, vol. 479–480, pp. 810–817, 2014.
- [5] K. Cao, L.-J. Pang, J.-M. Liang, and J. Tian, "Fingerprint classification by a hierarchical classifier," *Pattern Recognition*, vol. 46, no. 12, pp. 3186–3197, 2013.
- [6] M. Liu and P. Yap, "Invariant representation of orientation fields for fingerprint indexing," *Pattern Recognition*, vol. 45, no. 7, pp. 2532–2542, 2012.
- [7] F. Liu, Q.-J. Zhao, and D. Zhang, "A novel hierarchical fingerprint matching approach," *Pattern Recognition*, vol. 44, no. 8, pp. 1604–1613, 2011.
- [8] M. U. Munir, M. Y. Javed, and S. A. Khan, "A hierarchical k-means clustering based fingerprint quality classification," *Neurocomputing*, vol. 85, no. 15, pp. 62–67, 2012.
- [9] A. K. Jain, S. Prabhakar, and L. Hong, "A Multichannel approach to fingerprint classification," *IEEE Transactions on Pattern Analysis and Machine Intelligence*, vol. 21, no. 4, pp. 348–359, 1999.

- [10] M. Tico, P. Kuosmanen, and J. Saarinen, "Wavelet domain features for fingerprint recognition," *Electronics Letters*, vol. 37, no. 1, pp. 21–22, 2001.
- [11] C.-B. Tao and G.-D. Liu, "Fingerprint image enhancement algorithm based on FDCT," *Advanced Materials Research*, vol. 255–260, pp. 2047–2051, 2011.
- [12] M.-H. Liu, "Fingerprint classification based on Adaboost learning from singularity features," *Pattern Recognition*, vol. 43, no. 3, pp. 1062–1070, 2010.
- [13] T. Mandal and Q. M. J. Wu, "A small scale fingerprint matching scheme using digital curvelet transform," in *Proceedings of the IEEE International Conference on Systems, Man and Cybernetics (SMC '08)*, pp. 1534–1538, October 2008.
- [14] J. Liu and W. L. Wang, "A fingerprint matching algorithm based on reference point of central area," *Computer Applications and Software*, vol. 28, no. 2, pp. 30–33, 2011.
- [15] E. J. Candese and D. L. Donoho, "New tight frames of curvelets and optimal representations of objects with piecewise C^2 singularities," *Communications on Pure and Applied Mathematics*, vol. 57, no. 2, pp. 219–266, 2004.
- [16] E. Candès, L. Demanet, D. Donoho, and L. Ying, "Fast discrete curvelet transforms," *Journal of Multiscale Modeling and Simulation*, vol. 5, no. 3, pp. 861–899, 2006.
- [17] <http://www.curvelet.org/download/download.html>.
- [18] R. M. Haralick, K. Shanmugam, and I. Dinstein, "Textural features for image classification," *IEEE Transactions on Systems, Man and Cybernetics*, vol. 3, no. 6, pp. 610–621, 1973.
- [19] S. Hu, C. Xu, W.-Q. Guan, Y. Tang, and L. Yan, "Texture feature extraction based on wavelet transform and gray-level co-occurrence matrices applied to osteosarcoma diagnosis," *Bio-Medical Materials and Engineering*, vol. 24, no. 1, pp. 129–143, 2014.
- [20] V. S. Thakare and N. N. Patil, "Classification of texture using gray level co-occurrence matrix and self-organizing map," in *Proceedings of the International Conference on Electronic Systems, Signal Processing, and Computing Technologies*, pp. 350–355, 2014.
- [21] A. Suresh and K. L. Shunmuganathan, "Feature fusion technique for colour texture classification system based on gray level co-occurrence matrix," *Journal of Computer Science*, vol. 8, no. 12, pp. 2106–2111, 2012.
- [22] R. A. Pramunendar, C. Supriyanto, D. H. Novianto, I. N. Yuwono, G. F. Shidik, and P. N. Andono, "A classification method of coconut wood quality based on Gray Level Co-occurrence matrices," in *Proceedings of the IEEE International Conference on Robotics, Biomimetics, and Intelligent Computational Systems (ROBIONETICS '13)*, pp. 254–257, Yogyakarta, Indonesia, November 2013.
- [23] M.-D. Bi, Z.-G. Sun, and Y.-S. Li, "Textural fabric defect detection using adaptive quantized Gray-level Co-occurrence Matrix and Support Vector description data," *Information Technology Journal*, vol. 11, no. 6, pp. 673–685, 2012.
- [24] L. Wang and M. Dai, "Application of a new type of singular points in fingerprint classification," *Pattern Recognition Letters*, vol. 28, no. 13, pp. 1640–1650, 2007.

Research Article

Research on Construction Optimization of Three-Connected-Arch Hydraulic Underground Cavities Considering Creep Property

Bao-yun Zhao,^{1,2} Nian-chun Xu,² Zi-yun Li,² and Tong-qing Wu^{2,3}

¹ Chongqing Key Laboratory of Geomechanics & Geoenvironmental Protection, Department of Civil Engineering, Logistical Engineering University, Chongqing 401311, China

² Department of Civil Engineering and Architecture, Chongqing University of Science & Technology, Chongqing 401331, China

³ Key Laboratory of Hydraulic & Waterway Engineering of the Ministry of Education, Chongqing Jiaotong University, Chongqing 400074, China

Correspondence should be addressed to Bao-yun Zhao; baoyun666@163.com and Nian-chun Xu; 351601872@qq.com

Received 8 June 2014; Accepted 21 June 2014; Published 6 August 2014

Academic Editor: Kim M. Liew

Copyright © 2014 Bao-yun Zhao et al. This is an open access article distributed under the Creative Commons Attribution License, which permits unrestricted use, distribution, and reproduction in any medium, provided the original work is properly cited.

In order to prevent the creep of surrounding rock in long-term construction, with consideration of different construction methods and other factors during the construction of large-scale underground cavity, three different construction schemes are designed for specific projects and a nonlinear viscoelastic-plastic creep model which can describe rock accelerated creeping is introduced and applied to construction optimization calculation of the large-scale three-connected-arch hydraulic underground cavity through secondary development of FLAC^{3D}. The results show that the adoption of middle cavity construction method, the second construction method, enables the maximum vault displacement of 16.04 mm. This method results in less stress redistribution and plastic zone expansion to the cavity's surrounding rock than the other two schemes, which is the safest construction scheme. The conclusion can provide essential reference and guidance to similar engineering for construction optimization.

1. Introduction

Since the construction period of large-scale underground cavity engineering is long, the creep property of rock mass is relatively obvious, and many large-scale underground cavities collapse and finally break down due to deformation which is continuously developing with time. The selection of reasonable construction scheme is one of the main ways to prevent and control surrounding rock's creep of the underground cavity.

In the past years, numerous scholars at home and abroad acquired lots of achievements in underground cavity construction safety [1, 2] and its optimization [3, 4] and acquired abundant accomplishment in rock mass creep constitutive model [5], creep parametric inversion [6], engineering application [7], and so forth as well. Meanwhile, lots of mathematical softwares or numerical methods were used to solve engineering problems, such as finite element method

[8], meshless or meshfree method [9, 10], discrete element method [11, 12], and Fast Lagrangian Analysis of Continua (FLAC) [13]. FLAC^{3D} is a three-dimensional software that uses full dynamics equation and has a good secondary development interface, which can simulate and help analyze the three-dimensional structure behavior and plastic flow of soil, rock, and other materials. FLAC has become the fastest and the most influential numerical analysis software in geotechnical mechanics and engineering.

This paper takes research on a three-connected-arch front inflow pool of an underground water intake pumping station somewhere in Shenzhen; before construction of the project, the FLAC^{3D} software [13], with secondary development of the nonlinear creep model, is applied by adopting the method of numerical simulation to survey for a construction method appropriate for the long-span hydraulic underground cavity of this region, and the optimal safety construction method has been proposed through comparative study on numerical

simulation response, plastic zone expansion, and so forth of surrounding rock displacement variation of three kinds of construction methods. This research result can provide reference and guidance for the similar projects.

2. Project Profile

The underground pump station is with floor elevation of the front inflow pool at 17.3 m, while ground elevation of current situation at 55.0 m, with net width of the underground pump station at 26.9 m, net length at 23.7 m, and net height at 15.2 m. It consists of 3 cavities, with span of single cavity exceeding 8.1 m; 12.61 m in the second half of the middle cavity is not equipped with wall support, bearing by cross walls at two sides. The horizontal layout of the pool support structure and the cross-section of the second half of the pool are shown in Figures 1 and 2.

The project is proposed to be constructed among the valleys; the valley bottom is at the ground elevation of 53.1~56.2 m, being relatively plain. The formation lithology of the pump room is mainly distributed with residual soil at the elevation of 55.0~49.8 m, moderately weathered limestone at the elevation of 49.8~26.0 m, and moderately weathered quartz sandstone at the elevation under 26.0 m.

3. Nonlinear Viscoelastic-Plastic Creep Constitutive Model

The nonlinear viscoelastic-plastic creep model is a tandem compound of a nonlinear viscoelastic-plastic body (the third part in Figure 3) and a Burgers creep model [14], as shown in Figure 3. And see the FLAC^{3D} secondary development of the model in the document manual [15].

Wherein, when $\sigma \leq \sigma_\infty$ (long-term strength or yield strength), the third part does not work, and the model is transformed into Burgers creep model; the creep equation of the model is as follows:

$$\varepsilon = \frac{\sigma_0}{E_1} + \frac{\sigma_0}{\eta_1} t + \frac{\sigma_0}{E_2} \left(1 - \exp \left(-\frac{E_2}{\eta_2} t \right) \right). \quad (1)$$

When $\sigma > \sigma_\infty$, the creep equation of the creep model is as follows:

$$\varepsilon = \frac{\sigma_0}{E_1} + \frac{\sigma_0}{\eta_1} t + \frac{\sigma_0}{E_2} \left(1 - \exp \left(-\frac{E_2}{\eta_2} t \right) \right) + \frac{\sigma_0 - \sigma_\infty}{\eta_3} t^n. \quad (2)$$

Here, $\eta(n, t) = t^{n-1}/\eta_3$, where η_3 is the initial value of $\eta(n, t)$.

4. Calculation Model and Excavation Scheme

4.1. Numerical Model. A plane strain model is adopted for calculation; the model consists of moderately weathered quartz sandstone, moderately weathered limestone, and residual soil from the bottom up; the PBA model has 16092 units and 24675 nodes in total, and side-middle cavity method has 15884 units and 24372 nodes in total. The horizontal displacement at left and right boundaries of the whole model is restrained, the vertical displacement of the

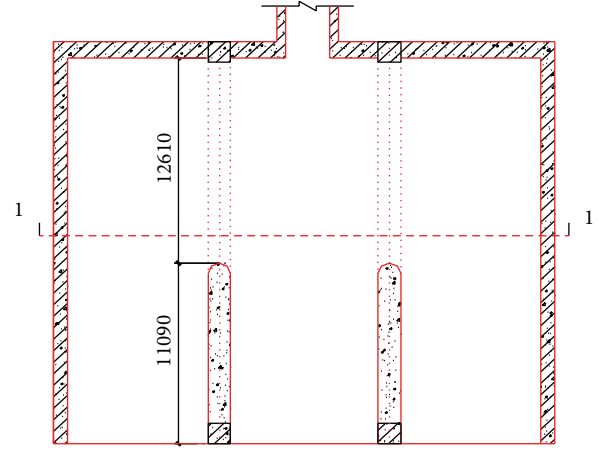


FIGURE 1: Plane figure of the front inflow pool.

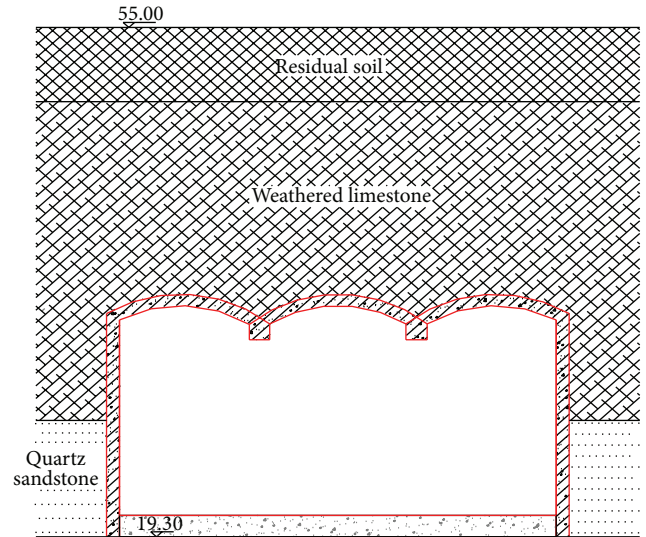


FIGURE 2: Cross-section (1-1) drawn of the front inflow pool.

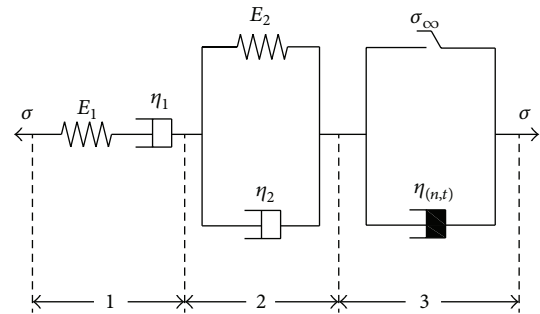


FIGURE 3: Nonlinear viscoelastic-plastic creep model.

lower boundary of the model is restrained, and the upper boundary is the free boundary. See the mesh generation of calculation model in Figure 4.

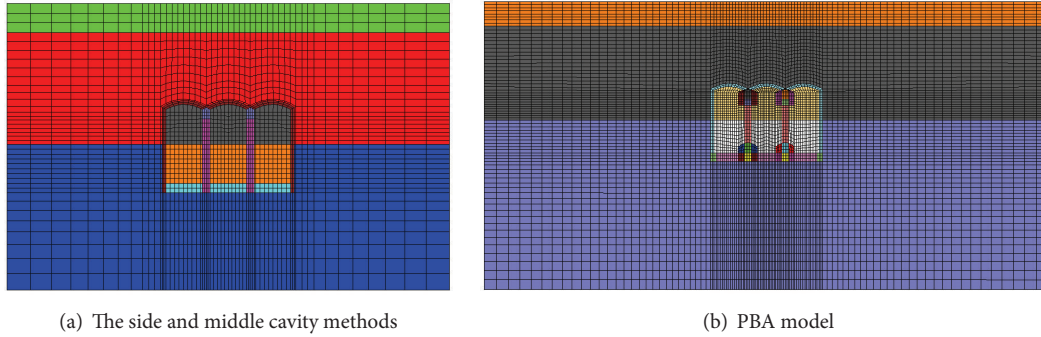


FIGURE 4: The numerical calculation model.

4.2. The Modeling Details

4.2.1. Parameter Selection. During the numerical analog calculation process, the elastic constitutive is adopted for initial support and secondary support. The Mohr-Coulomb constitutive is adopted for calculating the initial ground stress, and, according to the geological exploration report and indoor experiment results, the basic mechanical property and the support structure parameters of the surrounding rock at the location of the pump station can be seen in Table 1. And the mechanical property of initial support anchor rod is shown in Table 2.

4.2.2. The Creep Calculation Details. The second-phase engineering of the three-connected-arch underground pump station mentioned in this paper is going through feasibility analysis and verification of the design stage, and site displacement deformation monitoring data is not available yet; therefore, only the moderately weathered limestone which is affected much by excavation disturbance is conducted with creep calculation (that was used the nonlinear visco-elastic-plastic creep constitutive model, while other rock mass still used Mohr-Coulomb constitutive model), and the creep calculation parameter can be obtained through inversion of the site monitoring displacement data of the first-phase engineering construction; the parameter inversion is realized by adopting quasi-Newton algorithm (BFGS algorithm) Matlab programming as well, as shown in Table 3.

Three-step method was used in each cavity excavation and creep calculation age of every step is 15 days. In the process of calculation, the unbalanced force rate is set as $1e-6$, and the time step is $1e-4$.

4.3. Simulation Scheme of Construction Method. According to the construction experience of long-span underground cavity at home and abroad, and combining with structural features of the underground cavity mentioned in this paper, three excavation construction methods are designed here for numerical simulation optimization calculation. Excavation footage for each construction method is 2 m, and construction among stairs is staggered for 6 m. 30 cm of sprayed concrete and 3 m of anchor rod are adopted for initial support.

4.3.1. Construction Method I. Construction Procedures of Middle Cavity Method (See Figure 5)

Step 1. Excavate the first, second, and third parts of rock mass of middle cavities, hang bar-mat reinforcement at surrounding rock in sequence, blow the anchor rod, and conduct with sprayed concrete.

Step 2. Cast ground beam 4, concrete floor 5, stand wall 6, top beam 7, and second lining 8 of the middle cavity.

Step 3. Excavate the ninth, tenth, and eleventh parts of the rock mass of the left cavity, dismantle the temporary support of corresponding part, and conduct the initial support such as anchor rod, and sprayed concrete.

Step 4. Cast the ground beam 12, floor 13, and left wall 14 and the second lining 15 of the left cavity.

Step 5. Excavate the right cavity with the same method as the left cavity.

4.3.2. Construction Method II. Construction Procedures of Side Cavity Method (See Figure 6)

Step 1. Excavate the left cavities 1, 2, and 3, and perform initial support.

Step 2. Cast the ground beam 4, stand column 5, top beam 6, floor 7, side wall 8, and the second lining 9.

Step 3. Excavate the right cavities 10, 11, and 12 with the same method, and perform the initial support.

Step 4. Cast the ground beam 13, stand wall 14, top beam 15, floor 16, side wall 17, and the second lining 18.

Step 5. Excavate the cavities 19, 20, and 21, dismantle the temporary anchor rod, and complete the lining 22 and the floor 23.

TABLE 1: The rock mass parameters.

Surrounding rock	E/GPa	ν	C/Pa	$\varphi/^\circ$	σ_t/Pa	$\rho/\text{kg}\cdot\text{m}^3$
Residual soil	$1.8e-4$	0.3	$1e4$	20	$1e4$	1900
Weakly weathered limestone	10	0.32	$1e6$	35	$1e6$	2400
Weak weathering quartz sandstone	15	0.27	$1e6$	40	$1e6$	2500
Primary lining	25	0.22				2300
Secondary lining	30	0.2				2500

TABLE 2: Mechanics parameters of cable and grout.

The basic parameters	Unit	Values
Cable elastic modulus	(Gpa)	200
Cohesive force of cement slurry	(kN/m)	800
Friction coefficient of cement slurry	($^\circ$)	38
Stiffness of cement slurry	(N/m ²)	$6.33E9$
Outer perimeter of cement slurry	(m)	0.5024
Cable cross-sectional area	(m ²)	$1.20E-3$
Cable tensile yield strength	(MN)	200

TABLE 3: The nonlinear creep model parameters.

E_1 (GPa)	η_1 (GPa·d)	E_2 (GPa)	η_2 (GPa·d)	η_0 (GPa·d)	n
9.626	103.179	4.96	92.13	2.13	1

4.3.3. Construction Method III. Construction Procedures of PBA (See Figure 7)

Step 1. Excavate pilot tunnels 1, 2, 3, and 4, hang the bar-mat reinforcement, blow the anchor rod, and spray the concrete.

Step 2. Cast the ground beams 3 and 7, dig holes and cast stand columns 5 and 8, cast the top beams 6 and 9, excavate the rock mass 10, and cast the second lining 11.

Step 3. Symmetrically excavate the side cavity rock masses 12, 13, and 14, dismantle the temporary support, and conduct initial support; cast side ground beam 15, floor 16, side wall 17, and the second lining 18 in sequence.

Step 4. Excavate the bottom rock masses 19 and 20 of the middle cavity, dismantle the temporary support structure, and cast the floor 21 of the middle cavity.

5. Results of Construction Optimization Calculation

5.1. Surrounding Rock Creep Property Analysis. Figure 8 shows the excavation-completed surrounding rock displacement contour maps of three excavation methods after performing the second support; it can be seen that the maximum range of surrounding rock displacement deformation under

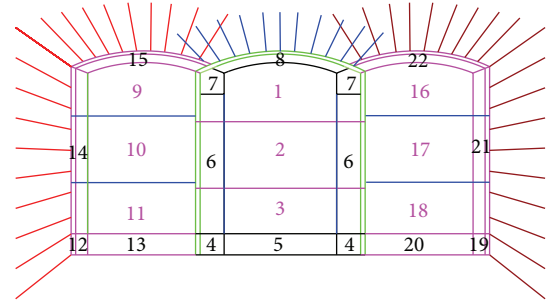


FIGURE 5: Construction steps of middle cavity method.

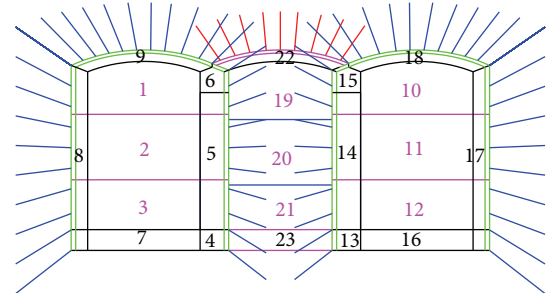


FIGURE 6: Construction steps of side cavity method.

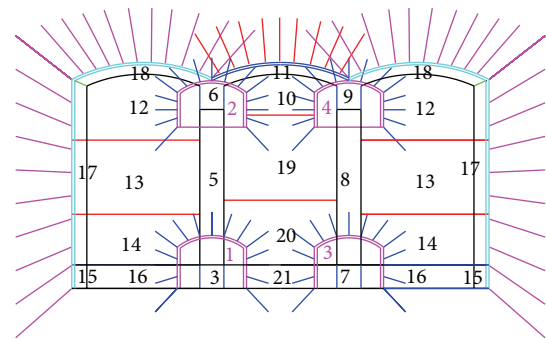


FIGURE 7: Construction method of PBA.

the three excavation methods is focused at the vault part of the three cavities.

Figure 9 shows, respectively, cavity vault part surrounding rock displacement monitoring curves of three construction methods. Each curve in the figure reflects the creep condition of the vault at each construction phase. Table 4 shows percentage statistics of vault maximum accumulative creep value and increment at each construction phase; it can

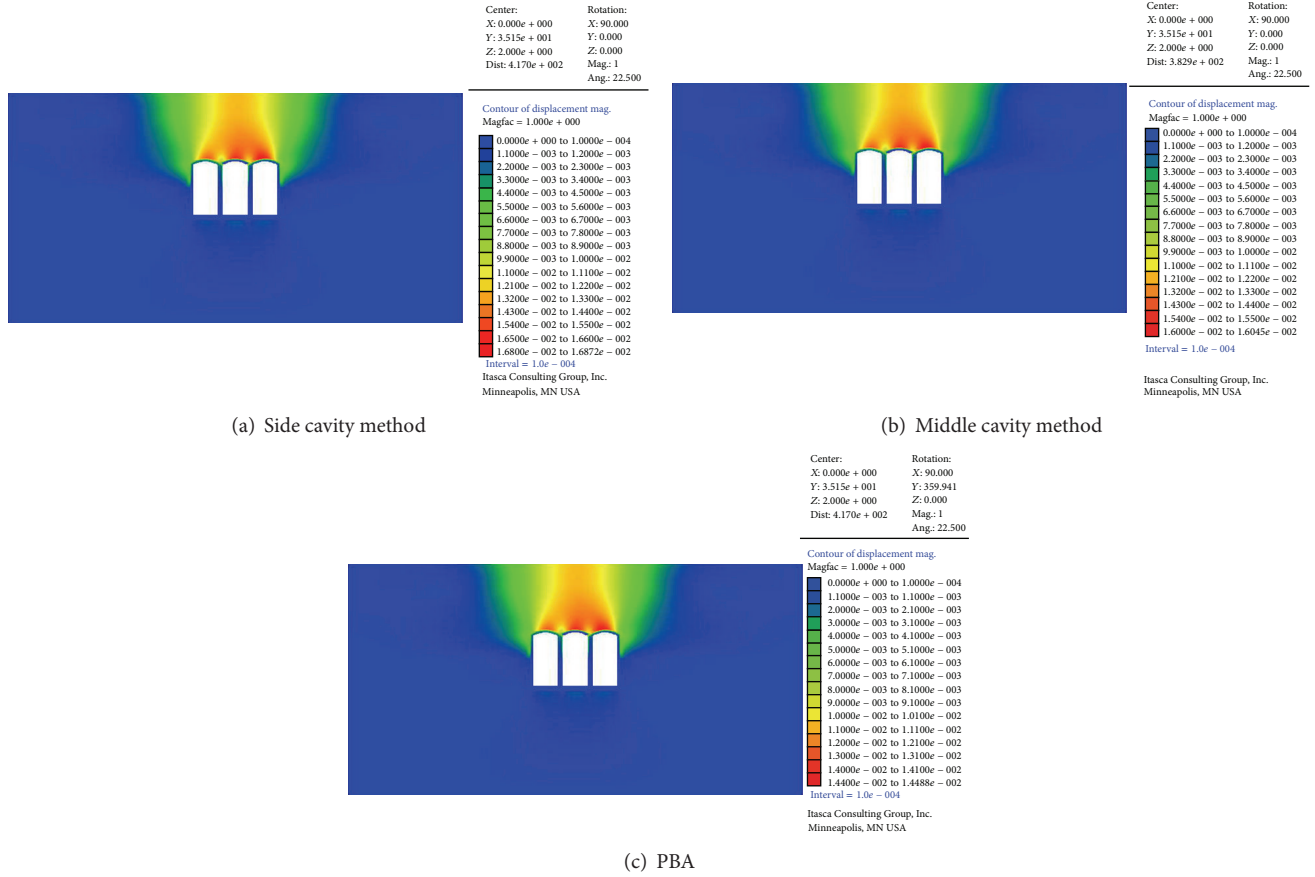


FIGURE 8: Displacement contour map after excavation completed.

TABLE 4: Comparative table for maximum settlement value of phased excavation in different methods.

Construction method	First stage	Excavation complete	
	Vault maximum accumulative creep value (mm)		Increment (%)
Side cavity method	13.49	16.26	3.30
Middle cavity method	14.06	16.04	6.01
PBA method	5.09	14.18	3.35

be seen that the first-phase creep value of the side cavity method is relatively lower, being 13.49 mm, while the creep increment of the right cavity at second phase increases to 16.68%; the vault creep value is 16.04 mm by adopting middle cavity method for excavation, which is 0.22 mm lower than that of side cavity method; for PBA construction, the excavation of pilot tunnel releases part of stress in the surrounding rock, and the beam, stand column, and the middle cavity vault second lining and other permanent supports provide well restraining effect for surrounding rock deformation in the subsequent construction, which makes the cavity maximum vault accumulative deformation being merely 14.18 mm.

By comparing three construction methods, it can be obtained that the PBA construction is the optimal excavation construction scheme in the point of surrounding rock displacement, and the middle cavity method follows.

5.2. Stress Field Distribution Rule of Surrounding Rock. The surrounding rock maximum and minimum principle stresses variation contour map obtained after excavation completed through three excavation construction methods can be seen in Figures 10, 11, and 12. In the FLAC software, it is ruled that tension stress is positive, while pressure stress is negative; therefore, in the figure, SMin actually represents the maximum principle stress, while SMax represents the minimum principle stress. Table 5 is the numerical statistics table of maximum and minimum stresses.

All the three excavation methods enable stresses of the surrounding rock being redistributed and stress concentration appearing at the vault and the bottom part of the three cavities; the middle cavity method and the side cavity method cause the equal maximum pressure stress at 2.04 MPa, while the PBA construction causes the maximum pressure stress

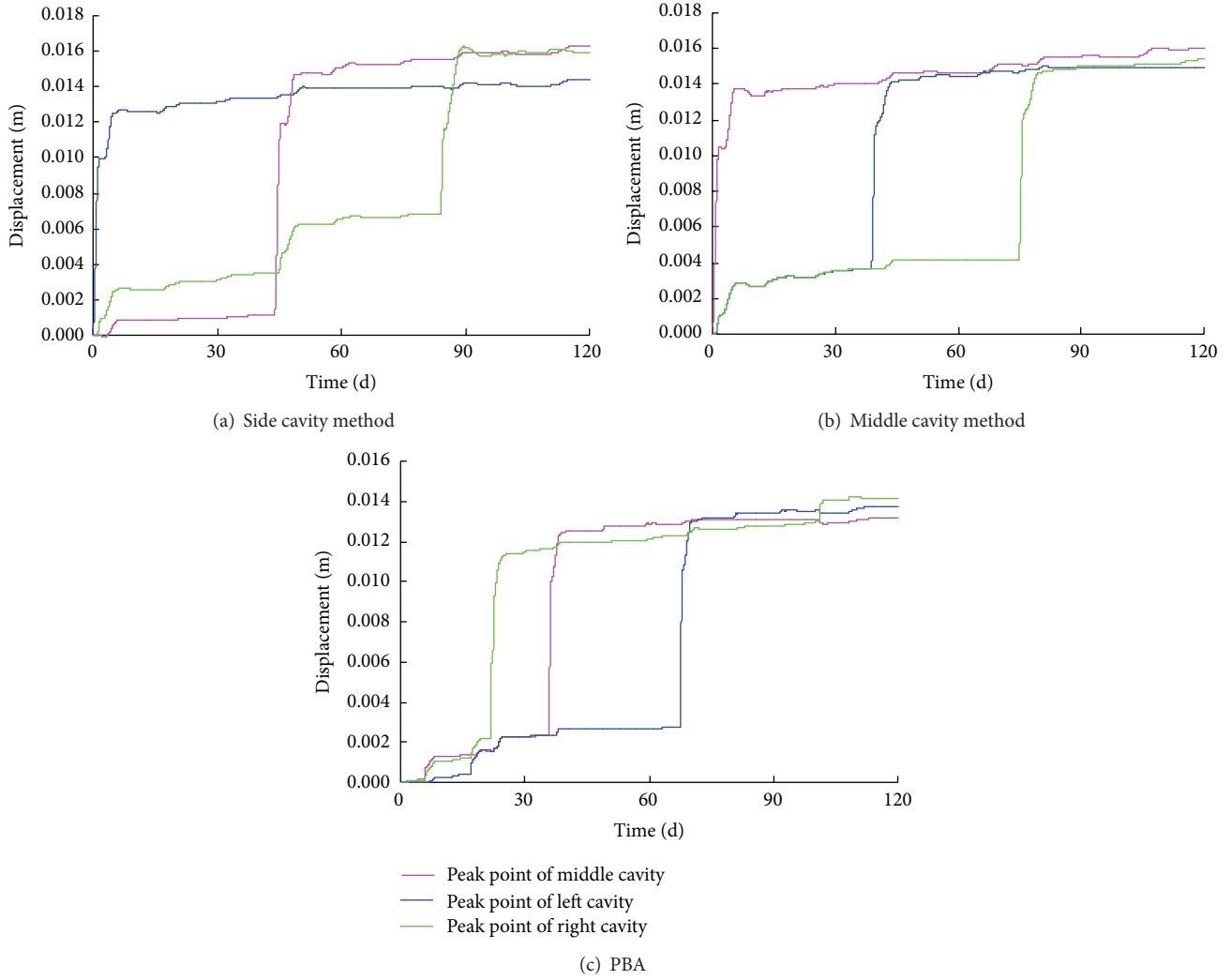


FIGURE 9: Creep curve at vault monitoring point of excavated cavity.

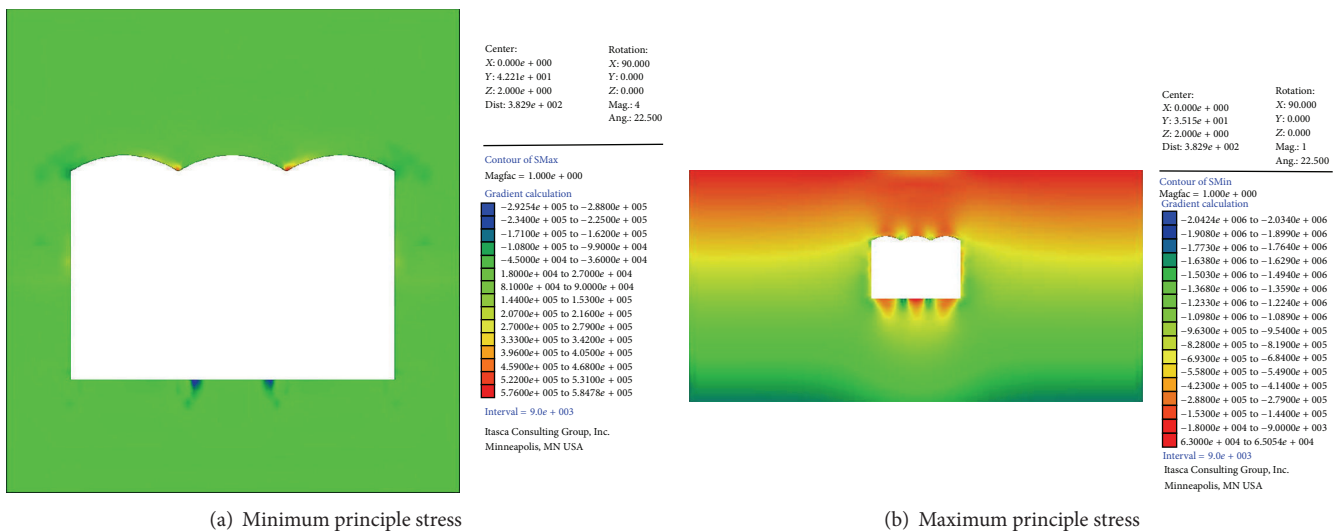


FIGURE 10: Surrounding rock principle stress contour of side cavity method.

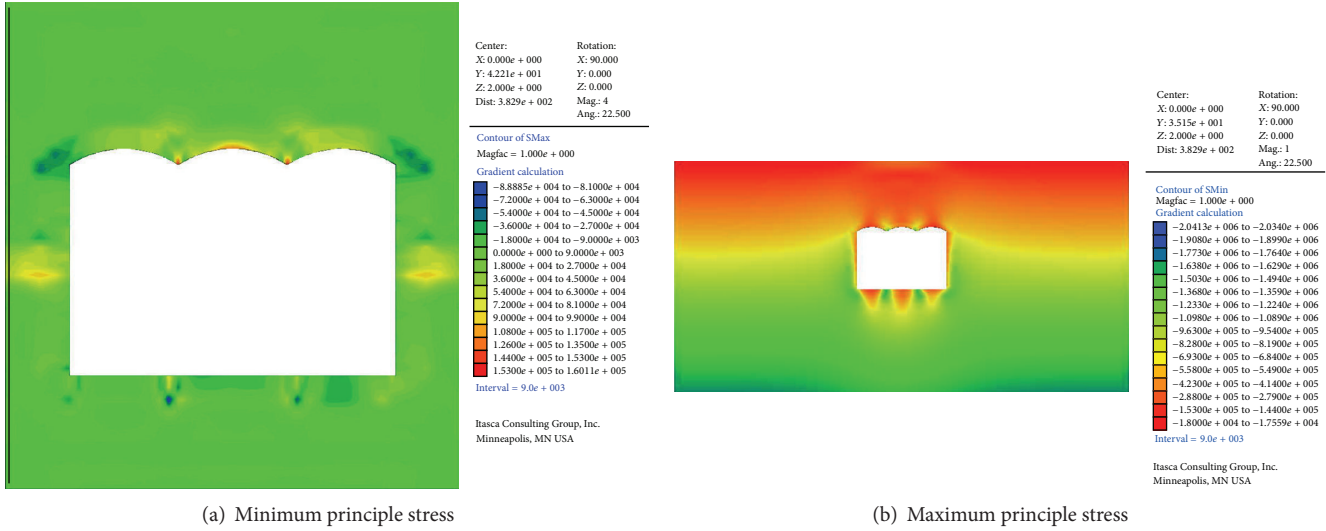


FIGURE 11: Surrounding rock principle stress contour map of middle cavity method.

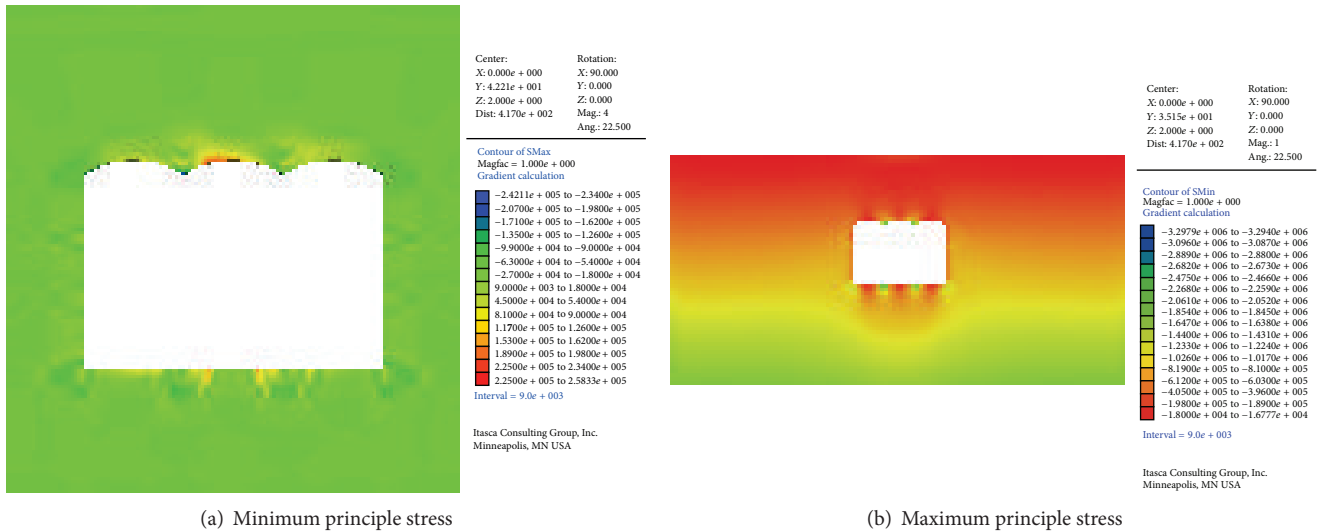


FIGURE 12: Surrounding rock principle stress contour map of PBA.

at 3.30 MPa; they all cause the surrounding rock generating tension stress area and tension stress serious concentration appearing near the vault of the middle cavity; the tension stress of the side cavity method is greatest, 0.58 MPa; then the PBA follows, which is 0.26 MPa; the middle cavity method provides the lowest stress, 0.16 MPa.

5.3. Force Characteristic Analysis of Support Structure

5.3.1. Anchor Rod Support. Figure 13 is the anchor rod axial force diagram of three excavation methods after the excavation is completed; in the diagram, black indicates the tension force of the anchor rod, and red indicates the pressure force of the anchor rod. In the three excavation methods, the position with the maximum force of the anchor rod is the vault, wherein pressure of the anchor appears at both sides

of the vault of every cavity in the side cavity method and the middle cavity method, and the maximum axial force of the construction anchor rods of the two methods is, respectively, 25190 N and 27640 N; and for the PBA construction the anchor rods at the top of the cavity are all pressed, and the maximum tension load of the anchor rod is 26450 N.

Seen from the axial force characteristic of the anchor rod, the anchor rod bears the most sufficient force through middle cavity method for construction, and the side cavity method follows.

5.3.2. The Second Lining. Figures 14, 15, and 16 show, respectively, distribution diagram of minimum and maximum principle stress of secondary support.

TABLE 5: Comparative table of phase-excavation surrounding rock stress in different construction methods.

Construction method	Maximum pressure stress (MPa)	Maximum tension stress (MPa)	Ratio
Side cavity method	2.04	0.58	3.52
Middle cavity method	2.04	0.16	12.75
PBA method	3.30	0.26	12.69

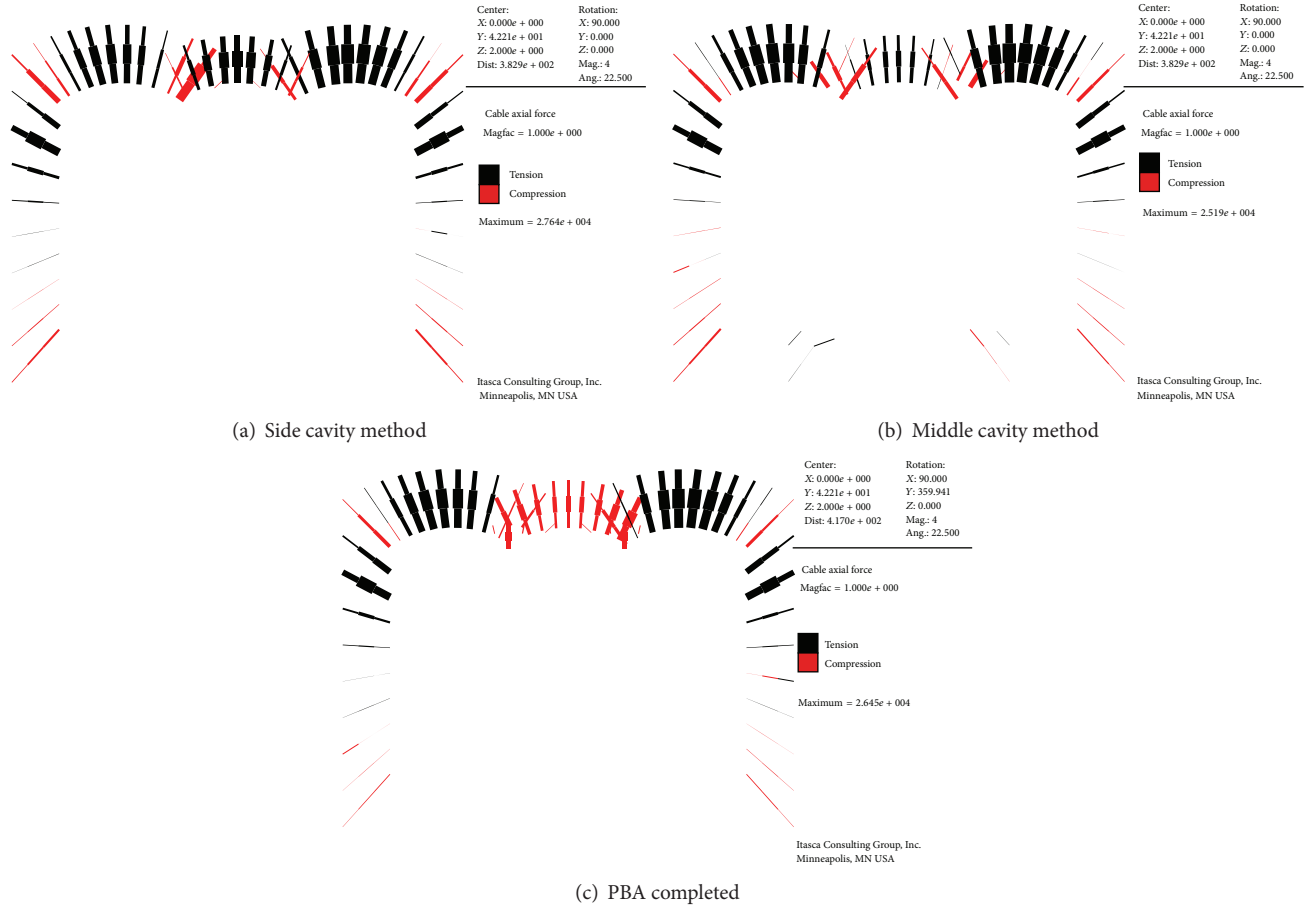


FIGURE 13: Anchor rod axial force after the excavation is completed.

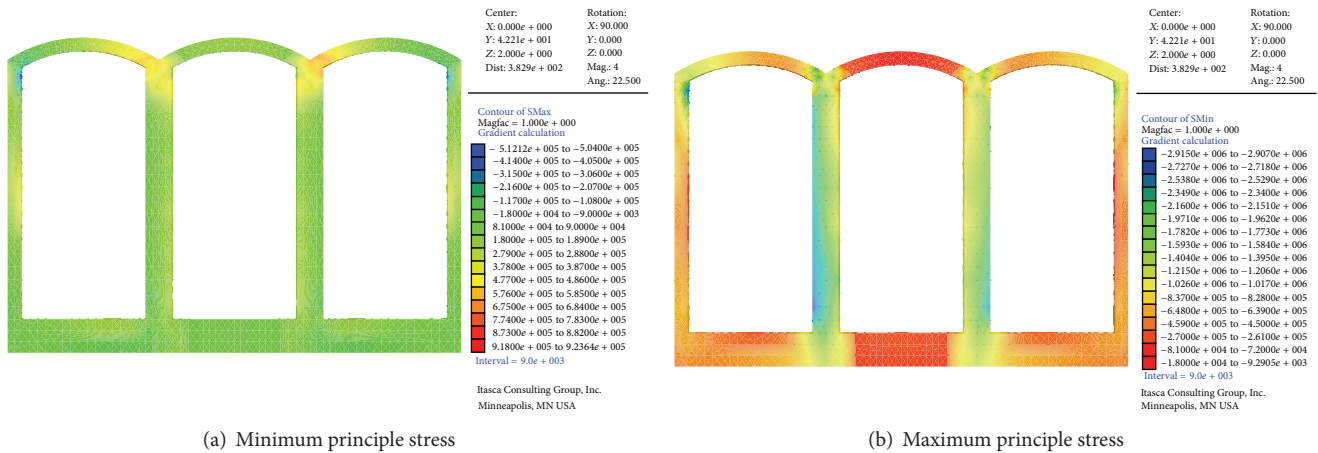


FIGURE 14: Second lining principle stress contour of side cavity method.

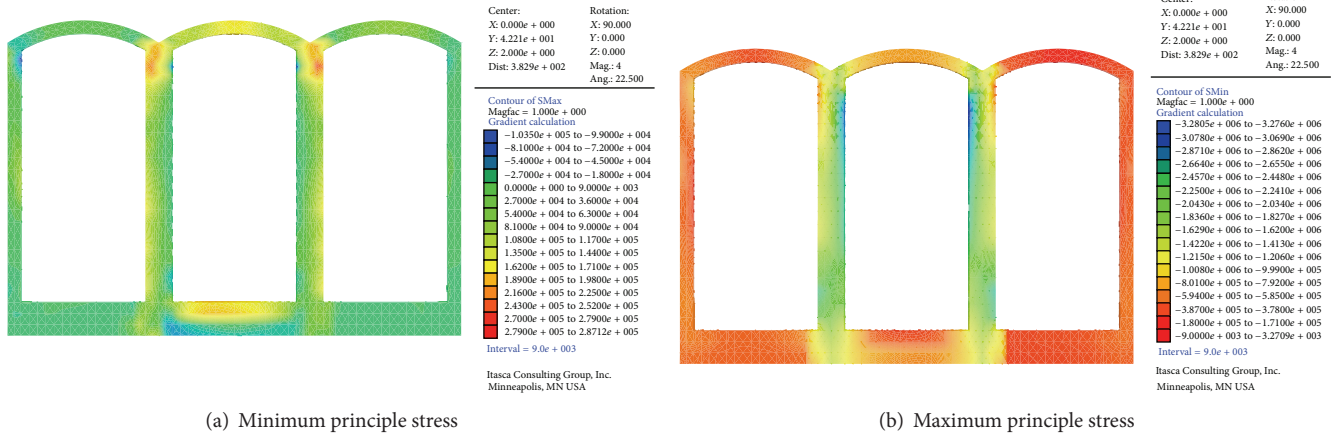


FIGURE 15: Second lining principle stress contour of middle cavity method.

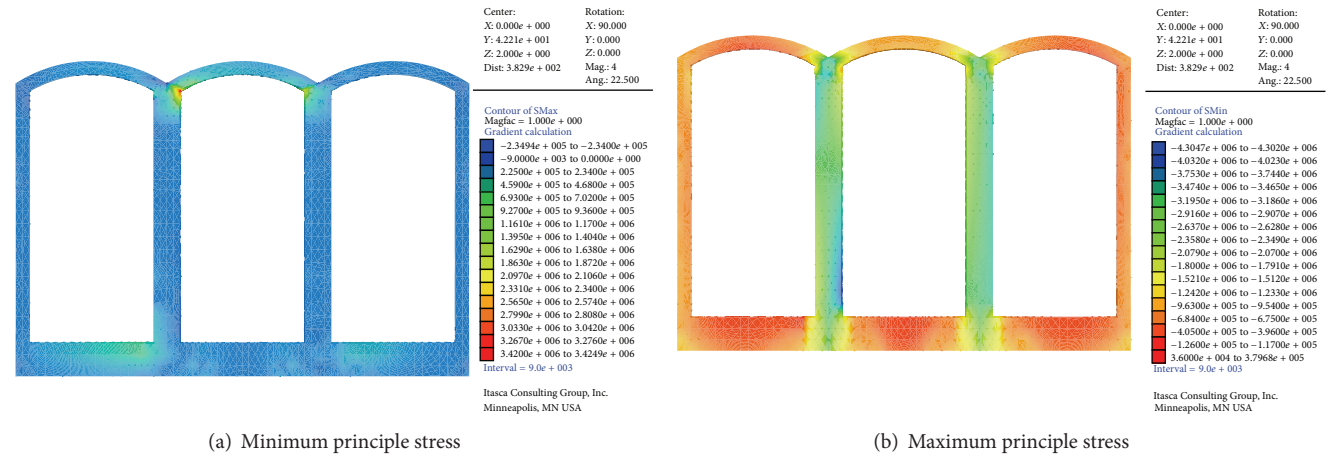


FIGURE 16: The second lining principle stress contour map of PBA.

Seen from the figure, the main distribution rule of the maximum principle stress of the secondary support is basically the same, the maximum value always appears at two sides of the middle cavity and the joint part of two side cavities; the maximum value of the middle cavity method is 0.287 MPa and that of PBA is 0.34 MPa; the minimum principle stress concentration mainly appears at the stand column and support position of the beam; the maximum value of side cavity construction is -2.92 MPa, while that of middle cavity construction is -3.28 MPa and that of PBA construction is -4.30 MPa. Concrete is mainly a pressure part; the appearance of tension stress might lead to tension failure in the secondary support concrete. The construction by middle cavity method provides relatively lighter secondary support force, without heavy tension stress, so as to be the optical support scheme.

5.4. Distribution Feature Analysis of Plastic Zone around the Cavity. Even the creep property of the surrounding rock is

considered in the construction, and the calculated maximum value of displacement and stress is not great; the underground cavities may also come up with surrounding rock falling, collapse, and other unstable phenomenon. Therefore, the surrounding rock plastic zone distribution during the construction of the cavities will be considered as well.

After the construction is completed, the plastic zone distribution can be seen in Figures 17(a), 17(b), and 17(c). It can be seen from the figure that the surrounding rock plastic yielding area of PBA is the largest, and the construction of middle cavity method causes smaller plastic yielding area to the surrounding rock of the cavity.

Therefore, after comprehensive comparison and analysis of surrounding rock creep property, surrounding rock stress field distribution features, support structure force characteristics, and construction caused by surrounding rock plastic zone expansion condition, this paper shows the point that in the three construction schemes, the middle cavity method is the optimum scheme, and the PBA follows.

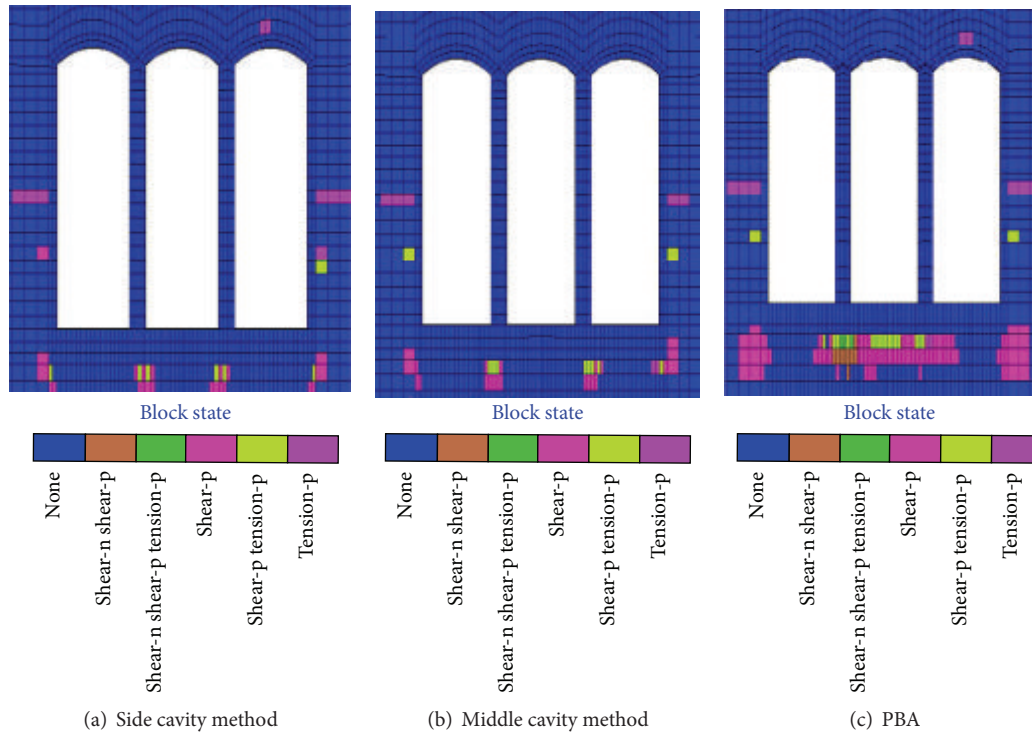


FIGURE 17: Surrounding rock plastic zone expansion.

6. Conclusions

When the nonlinear viscoelastic-plastic creep model is adopted, the construction development scheme for long-span three-connected-arch underground hydraulic cavity somewhere in Shenzhen is optimized, and the following conclusions are obtained.

- (1) The nonlinear viscoelastic-plastic creep model can be well applied to the construction optimization analysis for large-scale underground cavities.
- (2) From the point of surrounding rock's creep displacement, it is obtained that the PBA is the optimal scheme, and the middle cavity method follows.
- (3) Seen from the point of surrounding rock's stress, the force characteristic of support structure, the expansion of surrounding rock's plastic zone, and difficulty level of construction, the middle cavity method is the optimal scheme.
- (4) From the comparison and selection of numerical simulated construction of the three construction schemes, the cavity vault displacement is 16.04 mm by adopting the middle cavity method for construction, this method causes smaller stress redistribution to the cavity surrounding rock, the maximum tension stress in the surrounding rock is only 0.16 MPa, and even the plastic zone expansion is smaller than the other two schemes, so it is the optimal construction scheme.

Conflict of Interests

The authors declare that there is no conflict of interests regarding the publication of this paper.

Acknowledgments

This work was funded by the Natural Science Foundation of China (41302223), Chongqing Research Program of Basic Research and Frontier Technology (cstc2013jcyjA90004), Research Foundation of Chongqing University of Science & Technology (CK2011B28, CK2014Z10, and CK2013B27), and Key Laboratory of Hydraulic & Waterway Engineering of the Ministry of Education (SLK2013B03).

References

- [1] J. H. Yang, W. B. Lu, Z. G. Zhao, P. Yan, and M. Chen, "Safety distance for secondary shotcrete subjected to blasting vibration in Jinping-II deep-buried tunnels," *Tunnelling and Underground Space Technology*, vol. 43, pp. 123–132, 2014.
- [2] G. Y. Fu and G. W. Ma, "Extended key block analysis for support design of blocky rock mass," *Tunnelling and Underground Space Technology*, vol. 41, pp. 1–13, 2014.
- [3] M. Pejić, "Design and optimisation of laser scanning for tunnels geometry inspection," *Tunnelling and Underground Space Technology*, vol. 37, pp. 199–206, 2013.
- [4] H. H. Zhu, F. Huang, and Q. W. Xu, "Model test and numerical simulation for progressive failure of weak and fractured tunnel surrounding rock under different overburden depths," *Chinese*

- Journal of Rock Mechanics and Engineering*, vol. 29, no. 6, pp. 1113–1122, 2010.
- [5] H. Y. Pan, H. W. Zhang, S. G. Li, T. J. Zhang, and H. F. Lin, “Research on creep model and delay instability of coal-rock containing gas,” *Disaster Advances*, vol. 6, no. S1, pp. 273–277, 2013.
 - [6] Z. G. Ma, Z. Huang, G. Peng, L. Zhang, and D. Ma, “Experimental study on creep behavior of saturated disaggregated sandstone,” *International Journal of Rock Mechanics & Mining Sciences*, vol. 66, pp. 76–83, 2014.
 - [7] W. Zhu, Y. Qi, Y. Guo, and W. Yang, “3D damage rheology analysis of deformation and fracture of surrounding rocks in Jinping I hydropower station underground powerhouse,” *Chinese Journal of Rock Mechanics and Engineering*, vol. 31, no. 5, pp. 865–872, 2012.
 - [8] X. J. Dong, Z. K. Peng, W. M. Zhang, H. X. Hua, and G. Meng, “Research on spillover effects for vibration control of piezoelectric smart structures by ANSYS,” *Mathematical Problems in Engineering*, vol. 2014, Article ID 870940, 8 pages, 2014.
 - [9] L. W. Zhang, Z. X. Lei, K. M. Liew, and J. L. Yu, “Static and dynamic of carbon nanotube reinforced functionally graded cylindrical panels,” *Composite Structures*, vol. 111, pp. 205–212, 2014.
 - [10] R. J. Cheng, L. W. Zhang, and K. M. Liew, “Modeling of biological population problems using the element-free kp-Ritz method,” *Applied Mathematics and Computation*, vol. 227, pp. 274–290, 2014.
 - [11] T. Kazerani and J. Zhao, “A microstructure-based model to characterize micromechanical parameters controlling compressive and tensile failure in crystallized rock,” *Rock Mechanics and Rock Engineering*, vol. 47, no. 2, pp. 435–452, 2014.
 - [12] T. Kazerani, “Effect of micromechanical parameters of microstructure on compressive and tensile failure process of rock,” *International Journal of Rock Mechanics and Mining Sciences*, vol. 64, pp. 44–55, 2013.
 - [13] Itasca Consulting Group, *FLAC 3D (Version 3.0) User's Manual*, Itasca Consulting Group, Minneapolis, Minn, USA, 1997.
 - [14] B. Y. Zhao, D. Y. Liu, Z. M. Zheng, and K. K. Xue, “Non-linear visco-elastic plastic creep model of rocks based on the short time triaxial creep test,” *Journal of Mining and Safety Engineering*, vol. 28, no. 3, pp. 446–450, 2011.
 - [15] B. Y. Zhao, D. Y. Liu, Y. R. Zheng, and Q. Dong, “Secondary development and slope application discussion of the non-linear visco-elastic plastic creep model in Flac^{3D} software,” *Disaster Advances*, vol. 5, no. 4, pp. 1231–1236, 2012.

Research Article

Numerical Simulation of Soil Water Movement under Subsurface Irrigation

Xinqiang Qin, Xianbao Duan, Lijun Su, Xiaoqin Shen, and Gang Hu

Department of Applied Mathematics, Xi'an University of Technology, Xi'an 710048, China

Correspondence should be addressed to Xinqiang Qin; xqqin2007@163.com

Received 30 April 2014; Revised 14 July 2014; Accepted 14 July 2014; Published 3 August 2014

Academic Editor: Kim M. Liew

Copyright © 2014 Xinqiang Qin et al. This is an open access article distributed under the Creative Commons Attribution License, which permits unrestricted use, distribution, and reproduction in any medium, provided the original work is properly cited.

By constructing a radial basis function collocation method combined with a difference method, a two-dimensional mathematical model with boundary conditions of soil water movement under irrigation is proposed. The nonlinear term is dealt with a difference method and the equation is solved using an implicit scheme. In addition, the existence and uniqueness of the solution to the soil water movement equation are proven. Numerical results show that the proposed method has high precision and is easier to use than traditional methods. Moreover, the selection of parameter c plays an important role in guaranteeing calculation precision. It lays the foundation for the numerical solutions to high-dimensional soil water movement equations.

1. Introduction

Between 1960 and 2000, numerical techniques such as boundary element and finite element methods have made spectacular advances in the computation of physical phenomena in engineering and sciences. Particularly, the last two decades have witnessed substantial efforts in developing a new class of numerical methods. These methods, using traditional methods that require certain underlying meshes such as the triangulation of a region for computation, were primarily developed for simulating low-dimensional application problems. However, designing relevant meshes is usually quite a difficult task for two-dimensional regions and might become impossible for higher-dimensional problems.

However, the triangulation process is too time consuming, even if a sophisticated mesh-generator is employed. In fact, for a given distribution of points, it is possible to achieve a mesh quickly, but this always requires a considerable number of iterations including manual interaction before reaching a satisfactory mesh.

Meshless methods were first introduced by Lucy, and Gingold and Monaghan in 1977 [1, 2]. Further works, such as Nayroles et al. [3], Belytschko et al. [4], Schaback [5], Sukumar et al. [6], Wu [7], and Wendland [8, 9] (see books [10, 11]), attempted to reduce or even eliminate the need

for discretization of a domain or surface in the context of numerical solutions for boundary and initial value problems. These rapidly developed methods can not only reduce the large costs of labor, but also spare computational time compared to the finite element method, boundary element method, and other mesh-dependent methods.

The initial idea of meshless methods could date back to the smooth particle hydrodynamics (SPH) method for modeling astrophysical phenomena [1, 2]. In 1992, Nayroles et al. proposed the diffuse element method (DEM) [3]. In 1994, Belytschko et al. improved the DEM and introduced the element-free Galerkin method (EFG) [4]. Since then, there has been a great deal of research into meshless methods. Meshless methods, such as the reproducing kernel particle method (RKPM) by Liu et al. [12], Hp-cloud method by Duarte and Oden [13], natural element method (NEM) by Sukumar et al. [6], partition of unity finite element method (PUFEM) by Babuška and Melenk [14], and meshless Galerkin method using radial basis functions (RBF) by Wendland [9], have also been described in literatures. The major differences between these meshless methods, all of which can be classified as Galerkin methods, come only from the techniques used for interpolating the trial functions. Even though no mesh is required in these methods for the interpolation of the trial or test functions and the solution

variables, the use of shadow elements is unavoidable during the integration of the symmetric weak form. Therefore, these methods are not truly meshless.

The finite point method (FPM) introduced by Oñate et al. [15], which is based on the moving least-squares and the collocation method, is a truly meshless method. Other truly meshless methods include the PCM [16], the Hp-meshless clouds [17], the LBIE [18], the LSC [19], and the WLSM [19] among others. In particular, in 1990, Kansa introduced the radial basis function (RBF) collocation method for solving elliptic, hyperbolic, and parabolic partial differential equations (PDEs) [20]. Later, the RBF was further developed by Schaback [5] and Fasshauer [21]. Hon et al. applied the RBF to the numerical computation of the variable normal equations, nonlinear Burgers equation, and shallow water wave equation [22]. In 1999, Ripa carried out work on selecting the correct shape parameter c for the RBFs [23]. Another class of RBF was further developed by Wendland [8, 9], Wu [7], and Buhmann [24]. Zhang et al. have made more research on element-free kp-Ritz method and applied it to solve different problems [25–29]. Therefore, the collocation-based meshless method has been an important meshless method in the current literature [30].

By creating a univariate basis function with an Euclidean norm, meshless methods are often naturally radically symmetric, and the high-dimensional problem can be turned into virtually one-dimensional one. Consequently, the study of the numerical solutions of PDEs through radial basis function interpolation has yielded a number of significant results.

1.1. The Problem and the Approach to Solve the Problem. The FEM has difficulty in remeshing and adaptive analysis. In contrast, meshless methods do not require a mesh to discretize the domain, and the approximate solution is constructed entirely with a set of scattered nodes [31]. However, meshless methods may lead to lower computational efficiency than FEM because more computational effort for the meshless interpolation and numerical integrations are required [32]. Hence, the improvement of the computational efficiency of meshless methods targeted at meshless interpolation and numerical integrations becomes an important issue. Other concerns or weaknesses of the existing meshless methods include difficulty in introducing the essential boundary conditions, a greater cost in evaluating the shape function derivatives, problems in handling discontinuities such as those due to heterogeneous material distributions, and the need for complicated node connectivity to ensure accurate results.

A truly meshless method, based on collocation with radial basis functions and radial basis functions are chosen to represent the solutions of PDEs, is the main focus of this paper. Moreover, the collocation-based meshless method is a truly meshless technique without mesh discretization. This method has the advantage of higher accuracy, convenient for computing, and has been successfully applied to numerical solutions of various PDEs. By using collocation with radial basis functions, the partition of the domain is not needed; hence the method can be applied to complex domains and

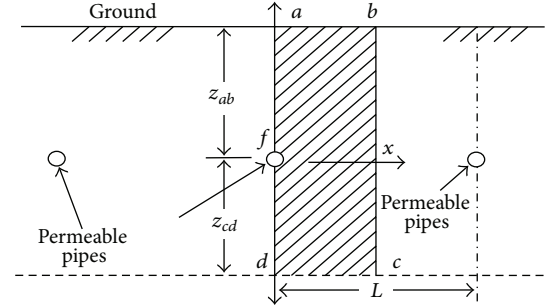


FIGURE 1: Schematic diagram of flow region.

overcomes some drawbacks of the traditional finite element method. It only needs to compute the shape functions and their derivatives, while the finite element method requires a calculation of the relevant integrals that often lowers the efficiency of computation significantly. The boundary conditions are relatively easier to be imposed without special manipulation. Finally, the way of obtaining the solutions to the PDEs is intuitive. From a practical point of view, this approach can achieve higher accuracy with more easily coded computer programs. Therefore, the collocation method with radial basis function interpolation can produce good results.

1.2. Mathematical Model of Soil Water Movement. Assume that permeable pipes in fields are parallel and have the same spacing and depth. Figure 1 shows a soil profile which is perpendicular to the permeable pipeline. Assuming that the water flow in the soil is negligible, then the problem considering irrigation can be solved as a plane problem. Obviously, in the case of Figure 1, it is sufficient to focus on soil water movement in the shaded part $abcd$, namely, the flow region.

In the region of soil water flow, both perpendiculars ad and bc are symmetrical lines, where ad traverses through the center of a permeable pipe and bc is equidistant from two adjacent permeable pipes. The symmetry means that the water flux along the normal direction of two lines equals zero. Line ab , the earth's surface, is the upper boundary of the region of soil water flow. The water flow which crosses line ab is affected by the soil's conveyance capacity, which is in turn related to the surface soil transpiration and strength of rainfall. By ignoring the transpiration and rainfall effects, the water flux across ab is zero. Line dc is the lower boundary of the region of soil water flow but is deep enough so that water movement caused by irrigation cannot reach it.

Assume that, in the region of soil water flow, the soil water flow is continuous in time and space, obeying the law of mass conservation. Then we can develop mathematical models of the soil water movement based on the physical process through the area.

The mathematical model of 2D water movement in unsaturated soil can be established as

$$\frac{\partial \theta}{\partial t} = \frac{\partial}{\partial x} \left(D(\theta) \frac{\partial \theta}{\partial x} \right) + \frac{\partial}{\partial z} \left(D(\theta) \frac{\partial \theta}{\partial z} \right) + \frac{\partial K(\theta)}{\partial z}, \quad (1)$$

where θ is the volumetric soil water content; $D(\theta)$ and $K(\theta)$ both are continuous functions which denote the diffusivity and hydraulic conductivity of the unsaturated soil flow respectively; t is time and z is the distance with the upward direction defined as positive.

The remainder of this paper is organized as follows. In Section 2, we introduce the construction of the meshless method based on the collocation method with radial basis functions, where the explicit schemes for the given equation are proposed and the existence and uniqueness of the solution to the method are proved. In Section 3, we give some applications and apply the method developed in this paper to examine the appropriateness and efficiency of the numerical solutions and to analyze the factors influencing the accuracy. We also compare our method to FEM. Section 4 comprises the conclusions and remarks.

2. Construction of a Meshless Method Based on Collocation with Radial Basis Functions

2.1. Radial Basis Functions. Radial basis functions (RBFs), also known as distance basis functions, are a type of functions with a basic variable d_j ($d_j = \|x - x_j\|$). They are isotropic and simple in form and can be solved easily with numerical calculation. The method, which combines radial basis functions with collocation, has many advantages when solving the partial differential equation [33, 34]. It has no correlation with the space dimensions and does not need any element or mesh for interpolation. Therefore, it is a truly meshless method. Currently, FEM [35] and FDM [36–38] are mostly used to solve soil moisture movement equations. With the development of meshless methods in recent years, many scholars now solve the soil water seepage problem using the finite volume method [39] and the RBF method [40]. The mathematical models of soil water movement are usually convection-diffusion equations, meaning that numerical oscillation occurs frequently when FDM or FEM is used. However, the radial basis function collocation method can solve many of these problems.

2.2. Construction of Radial Basis Function Collocation Method. The 2D soil water movement equation is

$$\begin{aligned} \frac{\partial \theta}{\partial t} &= \frac{\partial}{\partial x} \left(D(\theta) \frac{\partial \theta}{\partial x} \right) + \frac{\partial}{\partial z} \left(D(\theta) \frac{\partial \theta}{\partial z} \right) \\ &\quad + \frac{\partial K(\theta)}{\partial z}, \quad (x, z) \in \Omega, \\ \theta(x, z, 0) &= \theta_0, \quad (x, z) \in \Omega, \\ \theta(x, z, t) &= \theta_1, \quad (x, z) \in \partial\Omega, \end{aligned} \quad (2)$$

where θ is the volumetric soil water content, $D(\theta)$ and $K(\theta)$ are the diffusivity and hydraulic conductivity of the unsaturated soil flow, respectively, t is time, and z is the distance with the upward direction defined as positive. θ_0 is the initial water content, θ_1 is the constant water content of ground under humid conditions, Ω is the seepage region, and $\partial\Omega$ is the boundary of Ω .

Because the quadratic term in (2) is nonlinear, we cannot use the collocation method directly. Thus, we apply centered differences to deal with the nonlinear term in (x_i, z_j) :

$$\begin{aligned} \frac{\partial}{\partial x} \left[D(\theta) \frac{\partial \theta}{\partial x} \right]_{x=x_i} &\approx \frac{1}{2\Delta x} \left\{ \left[D(\theta) \frac{\partial \theta}{\partial x} \right]_{x=x_{i+1}} - \left[D(\theta) \frac{\partial \theta}{\partial x} \right]_{x=x_{i-1}} \right\} \\ &= \frac{1}{2\Delta x} \left[D(\theta_{i+1,j}) \left(\frac{\partial \theta_{i+1,j}}{\partial x} \right)_{x=x_{i+1}} - D(\theta_{i-1,j}) \left(\frac{\partial \theta_{i-1,j}}{\partial x} \right)_{x=x_{i-1}} \right], \\ \frac{\partial}{\partial z} \left[D(\theta) \frac{\partial \theta}{\partial z} \right]_{z=z_j} &\approx \frac{1}{2\Delta z} \left\{ \left[D(\theta) \frac{\partial \theta}{\partial z} \right]_{z=z_{j+1}} - \left[D(\theta) \frac{\partial \theta}{\partial z} \right]_{z=z_{j-1}} \right\} \\ &= \frac{1}{2\Delta z} \left[D(\theta_{i,j+1}) \left(\frac{\partial \theta_{i,j+1}}{\partial z} \right)_{z=z_{j+1}} - D(\theta_{i,j-1}) \left(\frac{\partial \theta_{i,j-1}}{\partial z} \right)_{z=z_{j-1}} \right], \end{aligned} \quad (3)$$

where Δx and Δz are spatial intervals, respectively. (x_i, z_j) are boundary points when $i, j = 1, N$, are inner points when $i, j = 2, 3, \dots, N-1$.

Discretizing the left side of (2) with forward differences gives

$$\left(\frac{\partial \theta}{\partial t} \right)_{(x_i, z_j)}^{t=t^{n+1}} \approx \left(\frac{\theta^{n+1} - \theta^n}{\Delta t} \right)_{(x_i, z_j)} = \frac{\theta_{i,j}^{n+1} - \theta_{i,j}^n}{\Delta t}. \quad (4)$$

Discretizing the third term in the right side of (2) with central differences gives

$$\left(\frac{\partial K(\theta)}{\partial z} \right)_{(x_i, z_j)}^{t=t^{n+1}} \approx \frac{K(\theta_{i,j+1}^{n+1}) - K(\theta_{i,j-1}^{n+1})}{2\Delta z}. \quad (5)$$

Let function $\tilde{\theta}(X, t^n)$ be an approximation of $\theta(X, t^n)$:

$$\tilde{\theta}(X, t^n) = \sum_{i=1}^{N_I} \alpha_i^n \varphi(\|X - I_i\|) + \sum_{i=1}^{N_b} \beta_i^n \varphi(\|X - B_i\|), \quad (6)$$

where $X = (x, z)$, $I_i \in \Omega$, and $B \in \partial\Omega$. N_I is the number of the nodes in the region and N_b is the number of the nodes on the border.

Applying collocation method, (6) should satisfy the differential equation for the region Ω in (7) and boundary conditions on the borders $\partial\Omega$ in (8). That is,

$$\begin{aligned} & \sum_{i=1}^{N_I} \alpha_i^n \left(\varphi(\|I_j - I_i\|) - \frac{d}{dx} \left(D(\theta^n(I_j)) \frac{d\varphi(\|I_j - I_i\|)}{dx} \right) \right. \\ & \quad \left. - \frac{d}{dz} \left(D(\theta^n(I_j)) \frac{d\varphi(\|I_j - I_i\|)}{dz} \right) \right) \\ & + \sum_{i=1}^{N_b} \beta_i^n \left(\varphi(\|I_j - B_i\|) \right. \\ & \quad \left. - \frac{d}{dx} \left(D(\theta^n(I_j)) \frac{d\varphi(\|I_j - B_i\|)}{dx} \right) \right. \\ & \quad \left. - \frac{d}{dz} \left(D(\theta^n(I_j)) \frac{d\varphi(\|I_j - B_i\|)}{dz} \right) \right) \\ & = \theta_{i,j}^n + \frac{\partial K(\theta^n(I_j))}{\partial z}, \quad j = 1, 2, \dots, N_I, \end{aligned} \quad (7)$$

$$\begin{aligned} & \sum_{i=1}^{N_I} \alpha_i^n \varphi(\|B_j - I_i\|) + \sum_{i=1}^{N_b} \beta_i^n \varphi(\|B_j - B_i\|) \\ & = \theta_1^n(B_j), \quad j = 1, 2, \dots, N_b. \end{aligned} \quad (8)$$

Let

$$\begin{aligned} \psi(\|X - I\|) &= \varphi(\|X - I\|) \\ & - \frac{d}{dx} \left(D(\theta(X)) \left(\frac{d\varphi(\|X - I\|)}{dx} \right) \right) \\ & - \frac{d}{dz} \left(D(\theta(X)) \left(\frac{d\varphi(\|X - I\|)}{dz} \right) \right) \\ f^n(I_j) &= \theta^{n-1}(I_j) + \frac{\partial K(\theta^n(I_j))}{\partial z}. \end{aligned} \quad (9)$$

Then (7) and (8) can be expressed with the following matrix equation:

$$\mathbf{H}\mathbf{U} = \mathbf{F}, \quad (10)$$

where

$$\begin{aligned} \mathbf{H} &= \begin{bmatrix} \psi(0) & \cdots & \psi(\|I_1 - I_{N_I}\|) & \psi(\|I_1 - B_1\|) & \cdots & \psi(\|I_1 - B_{N_b}\|) \\ \vdots & \vdots & \vdots & \vdots & \vdots & \vdots \\ \psi(\|I_{N_I} - I_1\|) & \cdots & \psi(0) & \psi(\|I_{N_I} - B_1\|) & \cdots & \psi(\|I_{N_I} - B_{N_b}\|) \\ \varphi(\|B_1 - I_1\|) & \cdots & \varphi(\|B_1 - I_{N_I}\|) & \varphi(0) & \cdots & \varphi(\|B_1 - B_{N_b}\|) \\ \vdots & \vdots & \vdots & \vdots & \vdots & \vdots \\ \varphi(\|B_{N_b} - I_1\|) & \cdots & \varphi(\|B_{N_b} - I_{N_I}\|) & \varphi(\|B_{N_b} - B_1\|) & \cdots & \varphi(0) \end{bmatrix}, \\ \mathbf{U} &= [\alpha_1^n, \alpha_2^n, \dots, \alpha_{N_I}^n, \beta_1^n, \beta_2^n, \dots, \beta_{N_b}^n]^T, \\ \mathbf{F} &= [f_1^n(I_1), f_1^n(I_2), \dots, f_1^n(I_{N_I}), \theta_1^n(B_1), \theta_1^n(B_2), \dots, \theta_1^n(B_{N_b})]^T. \end{aligned} \quad (11)$$

2.3. The Existence and Uniqueness of the Solution. Let

$$\begin{aligned} \mathbf{A}_1 &= \begin{bmatrix} \psi(0) & \cdots & \psi(\|I_1 - I_{N_I}\|) \\ \vdots & \ddots & \vdots \\ \psi(\|I_{N_I} - I_1\|) & \cdots & \psi(0) \end{bmatrix}, \\ \mathbf{A}_2 &= \begin{bmatrix} \psi(\|I_1 - B_1\|) & \cdots & \psi(\|I_1 - B_{N_b}\|) \\ \vdots & \ddots & \vdots \\ \psi(\|I_{N_I} - B_1\|) & \cdots & \psi(\|I_{N_I} - B_{N_b}\|) \end{bmatrix}, \\ \mathbf{A}_3 &= \begin{bmatrix} \varphi(\|B_1 - I_1\|) & \cdots & \varphi(\|B_1 - I_{N_I}\|) \\ \vdots & \ddots & \vdots \\ \varphi(\|B_{N_b} - I_1\|) & \cdots & \varphi(\|B_{N_b} - I_{N_I}\|) \end{bmatrix}, \end{aligned}$$

$$\mathbf{A}_4 = \begin{bmatrix} \varphi(0) & \cdots & \varphi(\|B_1 - B_{N_b}\|) \\ \vdots & \ddots & \vdots \\ \varphi(\|B_{N_b} - B_1\|) & \cdots & \varphi(0) \end{bmatrix}. \quad (12)$$

Then $H = \begin{bmatrix} A_1 & A_2 \\ A_3 & A_4 \end{bmatrix}$. For (10), the following theorem is obtained.

Theorem 1. *If the Fourier transform $F[\phi]$ of $\phi(\omega)$ is almost everywhere larger than 0 and $(\mathbf{A}_3\mathbf{A}_1^{-1}\mathbf{A}_2 - \mathbf{A}_4)^{-1}$ exists, then H is invertible. Consequently, the matrix equation (10) has a unique solution.*

Proof. First, we can show that \mathbf{A}_1^{-1} and \mathbf{A}_4^{-1} exist. According to the characteristics of radial basis function, matrix \mathbf{A}_1 is

symmetric. Then we show that it is positive definiteness. For $\forall \xi (\xi \neq 0) \in R^{N_b}$,

$$\begin{aligned} (\mathbf{A}_1 \xi, \xi) &= \sum_{j=1}^{N_b} \sum_{k=1}^{N_b} \xi_j \xi_k \varphi_j(x'_j) \\ &= \sum_{j=1}^{N_b} \sum_{k=1}^{N_b} \xi_j \xi_k \varphi(\|x_j - x_k\|) \\ &= \left(\frac{1}{2\pi}\right)^{N_b} \int_{-\infty}^{+\infty} F[\varphi] |\xi(\omega)|^2 d\omega > 0, \end{aligned} \quad (13)$$

where $\xi(\omega) = \sum_{j=1}^{N_b} \xi_j e^{i\langle \omega, x_j \rangle}$. So \mathbf{A}_1 is a symmetric positive definite matrix; that is, \mathbf{A}_1^{-1} exists.

Because $\varphi(r)$ is an even function, then $-\varphi(r)$ is an even function too. Moreover, $F[-\varphi] = -(i\omega)^2 F[\varphi] = \omega^2 F[\varphi] > 0$. Similarly, \mathbf{A}_4 is also a symmetric positive definite matrix. Hence, \mathbf{A}_4^{-1} exists. Now, we have

$$\begin{bmatrix} \mathbf{E} & -\mathbf{A}_2 \mathbf{A}_4^{-1} \\ \mathbf{0} & \mathbf{E} \end{bmatrix} \begin{bmatrix} \mathbf{A}_1 & \mathbf{A}_2 \\ \mathbf{A}_3 & \mathbf{A}_4 \end{bmatrix} = \begin{bmatrix} \mathbf{A}_1 - \mathbf{A}_2 \mathbf{A}_4^{-1} \mathbf{A}_3 & \mathbf{0} \\ \mathbf{A}_3 & \mathbf{A}_4 \end{bmatrix}. \quad (14)$$

Computing the determinants of both sides of (14), we have

$$|\mathbf{H}| = \begin{vmatrix} \mathbf{A}_1 & \mathbf{A}_2 \\ \mathbf{A}_3 & \mathbf{A}_4 \end{vmatrix} = |\mathbf{A}_1 - \mathbf{A}_2 \mathbf{A}_4^{-1} \mathbf{A}_3| \cdot |\mathbf{A}_4|. \quad (15)$$

As $(\mathbf{A}_3 \mathbf{A}_1^{-1} \mathbf{A}_2 - \mathbf{A}_4)^{-1}$ exists,

$$\begin{aligned} &(\mathbf{A}_1 - \mathbf{A}_2 \mathbf{A}_4^{-1} \mathbf{A}_3) \\ &\times \left[\mathbf{A}_1^{-1} - \mathbf{A}_1^{-1} \mathbf{A}_2 (\mathbf{A}_3 \mathbf{A}_1^{-1} \mathbf{A}_2 - \mathbf{A}_4)^{-1} \mathbf{A}_3 \mathbf{A}_1^{-1} \right] \\ &= \mathbf{E} - \mathbf{A}_2 (\mathbf{A}_3 \mathbf{A}_1^{-1} \mathbf{A}_2 - \mathbf{A}_4)^{-1} \mathbf{A}_3 \mathbf{A}_1^{-1} \\ &\quad - \mathbf{A}_2 \mathbf{A}_4^{-1} \mathbf{A}_3 \mathbf{A}_1^{-1} + \mathbf{A}_2 \mathbf{A}_4^{-1} \mathbf{A}_3 \mathbf{A}_1^{-1} \mathbf{A}_2 \\ &\quad \times (\mathbf{A}_3 \mathbf{A}_1^{-1} \mathbf{A}_2 - \mathbf{A}_4)^{-1} \mathbf{A}_3 \mathbf{A}_1^{-1}. \end{aligned} \quad (16)$$

In addition,

$$\begin{aligned} &\mathbf{A}_2 \mathbf{A}_4^{-1} \mathbf{A}_3 \mathbf{A}_1^{-1} \mathbf{A}_2 (\mathbf{A}_3 \mathbf{A}_1^{-1} \mathbf{A}_2 - \mathbf{A}_4)^{-1} \mathbf{A}_3 \mathbf{A}_1^{-1} \\ &\quad - \mathbf{A}_2 (\mathbf{A}_3 \mathbf{A}_1^{-1} \mathbf{A}_2 - \mathbf{A}_4)^{-1} \mathbf{A}_3 \mathbf{A}_1^{-1} \\ &= \mathbf{A}_2 \mathbf{A}_4^{-1} (\mathbf{A}_3 \mathbf{A}_1^{-1} \mathbf{A}_2 - \mathbf{A}_4) \\ &\quad \times (\mathbf{A}_3 \mathbf{A}_1^{-1} \mathbf{A}_2 - \mathbf{A}_4)^{-1} \mathbf{A}_3 \mathbf{A}_1^{-1} \\ &= \mathbf{A}_2 \mathbf{A}_4^{-1} \mathbf{A}_3 \mathbf{A}_1^{-1}. \end{aligned} \quad (17)$$

By (16) and (17), we obtain

$$\begin{aligned} &(\mathbf{A}_1 - \mathbf{A}_2 \mathbf{A}_4^{-1} \mathbf{A}_3) \\ &\times \left[\mathbf{A}_1^{-1} - \mathbf{A}_1^{-1} \mathbf{A}_2 (\mathbf{A}_3 \mathbf{A}_1^{-1} \mathbf{A}_2 - \mathbf{A}_4)^{-1} \mathbf{A}_3 \mathbf{A}_1^{-1} \right] = \mathbf{E}. \end{aligned} \quad (18)$$

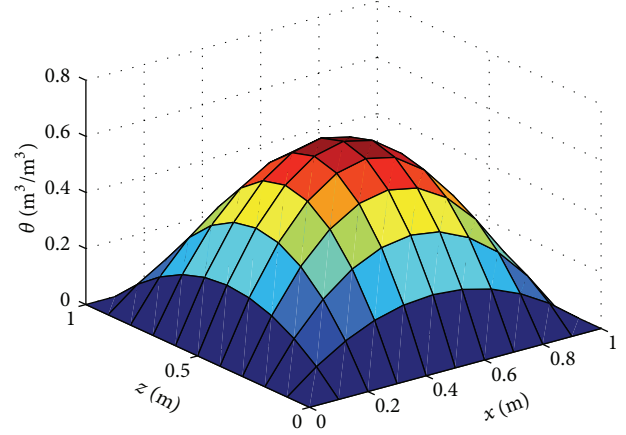


FIGURE 2: The exact solutions of Example 1.

So

$$\begin{aligned} &(\mathbf{A}_1 - \mathbf{A}_2 \mathbf{A}_4^{-1} \mathbf{A}_3)^{-1} \\ &= \mathbf{A}_1^{-1} - \mathbf{A}_1^{-1} \mathbf{A}_2 (\mathbf{A}_3 \mathbf{A}_1^{-1} \mathbf{A}_2 - \mathbf{A}_4)^{-1} \mathbf{A}_3 \mathbf{A}_1^{-1}. \end{aligned} \quad (19)$$

According to (15) and (19), we know that $|\mathbf{H}| \neq 0$. Thus, the matrix equation (10) has a unique solution. Now the numerical solution to problem (1), based on the radial basis function collocation method, can be calculated. \square

3. Numerical Examples

Example 1. Solve the following linear model using the radial basis function collocation method:

$$\begin{aligned} \frac{\partial \theta}{\partial t} &= \frac{\partial}{\partial x} \left(D(\theta) \frac{\partial \theta}{\partial x} \right) + \frac{\partial}{\partial z} \left(D(\theta) \frac{\partial \theta}{\partial z} \right) + f, \\ (x, z) &\in \Omega = [0, 1] \times [0, 1], \end{aligned} \quad (20)$$

$$\theta(x, z, 0) = \theta_0, \quad (x, z) \in \Omega,$$

$$\theta(x, z, t) = \theta_1, \quad (x, z) \in \partial\Omega, \quad t > 0.$$

Let $D(\theta) = 1$; then the analytic solution of (20) is $\theta(z, t) = (x^2 - x)(z^2 - z)t$ and $f = (x^2 - x)(z^2 - z) - 2t(x^2 + z^2 - x - z)$. The values of θ_0 and θ_1 are determined by analytic solution using a spatial step $h = 0.1$ and a time step $\Delta t = 0.01$ from $t = 0$ to $t = 10$. The Gaussian function $\exp(-cr^2)$ is selected as the radial basis function and the error estimate is based on L_2 -norm. The numerical and exact solutions of Example 1 are shown in Figures 2 and 3, respectively.

Table 1 shows a comparison of this method with FEM, where $h = 0.1$ and $t = 10$.

Next, we consider the time step $\Delta t = 0.01$, a different spatial step, and different parameters c in the Gaussian function $\exp(-cr^2)$. The results are shown in Table 2.

For the linear model, Figures 1–4 and Table 1 show that the method presented in this paper is feasible. And comparing it with the traditional method, it showed good accuracy and rapid convergence rate. And Table 2 shows that

TABLE 1: The results of the new method compared with FEM.

Numerical methods	t	Calculation errors	Calculation time(s)	Degree of convergence
New method	0.5	$8.4197e-004$	1.230020	2.7300
	1.0	$9.1056e-004$	2.427944	2.4725
FEM	0.5	$1.0017e-003$	1.021520	2.6720
	1.0	$1.6667e-003$	3.825802	2.2707

TABLE 2: Numerical solutions of Example 1 related to the parameter and spatial step.

Spatial step	Parameters c	Calculation errors	Calculation time(s)
0.1	9.0	$3.4000e-003$	1.372784
	9.5	$9.1056e-004$	2.427944
	9.6	$3.4000e-003$	1.580791
0.25	0.33	$1.1000e-003$	0.672394
	0.35	$5.7098e-004$	0.659509
	0.4	$9.2511e-004$	0.659885

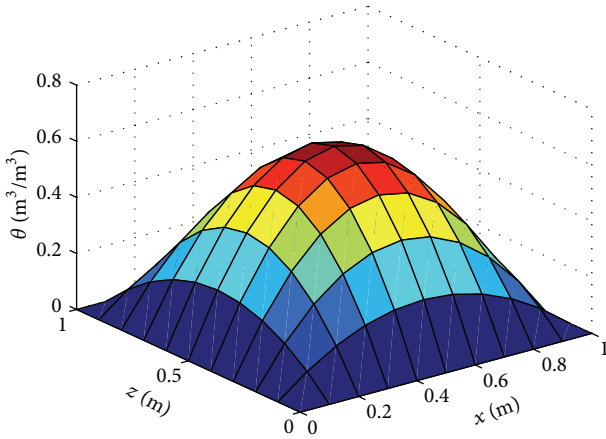


FIGURE 3: Numerical solutions using the radial basis function collocation method.

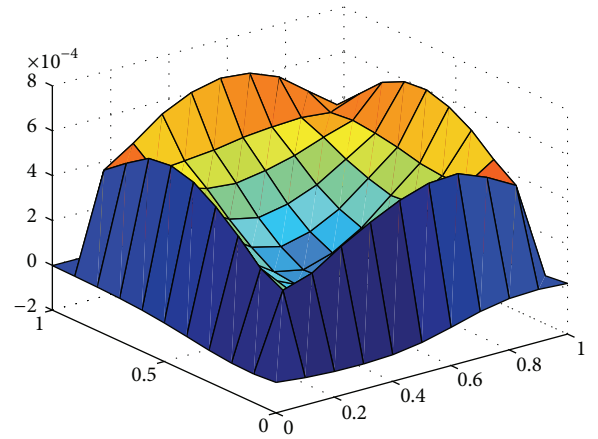


FIGURE 4: The error graph of the new method.

the computational accuracy and computing time are both related to the selections of parameter c in the radial basis functions and the spatial step.

Example 2. We consider the 2D horizontal absorption soil water movement equation:

$$\begin{aligned}
 \frac{\partial \theta}{\partial t} &= \frac{\partial}{\partial x} \left(D(\theta) \frac{\partial \theta}{\partial x} \right) + \frac{\partial}{\partial z} \left(D(\theta) \frac{\partial \theta}{\partial z} \right) + f, \\
 (x, z) &\in \Omega = [0, 1] \times [0, 1], \\
 \theta(x, z, 0) &= \theta_0, \quad (x, z) \in \Omega, \\
 \theta(x, z, t) &= \theta_1, \quad (x, z) \in \partial\Omega, \quad t > 0.
 \end{aligned} \tag{21}$$

Here $D(\theta) = 0.01e^\theta$, $f = -0.02t^2(x - x^2)(z - z^2)(x^2 - x + z^2 - z) - 0.01t^2(z^2(2xz - z - 2x + 1)^2 + x^2(2xz - 2z - x + 1)^2 + (x - x^2)(z^2 - z))$ and the analytic solution is $\theta(x, z, t) = (x^2 - x)(z^2 - z)t$. The values of θ_0 and θ_1 are determined by analytic solution. It is a nonlinear equation with the spatial step

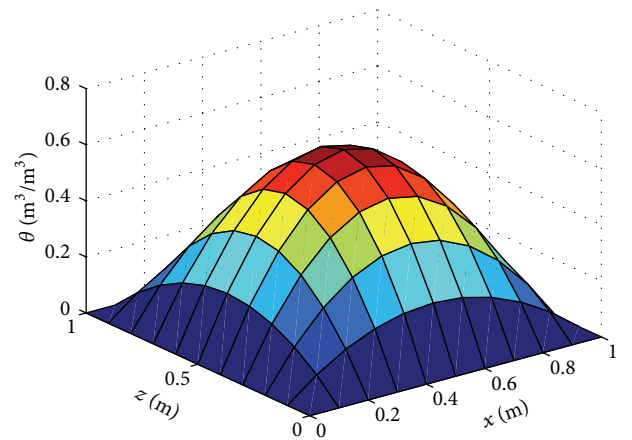


FIGURE 5: The exact solutions of Example 2.

$h = 0.1$ and time step $\Delta t = 0.01$ from $t = 0$ to $t = 10$. The radial basis function is also a Gaussian function $\exp(-cr^2)$ ($c > 0$). The error estimate is based on L_2 -norm.

TABLE 3: The results of the new method compared with FEM for Example 2.

Numerical methods	t	Calculation errors	Calculation time(s)	Degree of convergence
New method	0.5	$4.6462e-005$	2.100832	3.6871
	1.0	$9.6914e-005$	3.782251	3.2203
FEM	0.5	$1.0701e-004$	2.201250	3.4186
	1.0	$1.5367e-004$	3.882052	3.0664

TABLE 4: Numerical solution based on different spatial steps and different parameters in Example 2.

Spatial step	Parameters c	Calculation errors	Calculation time(s)
0.1	10	$3.1488e-004$	2.995965
	11	$9.6914e-005$	3.782251
	12	$1.0218e-004$	4.800045
0.25	0.45	$1.5427e-004$	1.682164
	0.50	$7.7579e-005$	1.645171
	0.55	$9.8661e-005$	1.686100

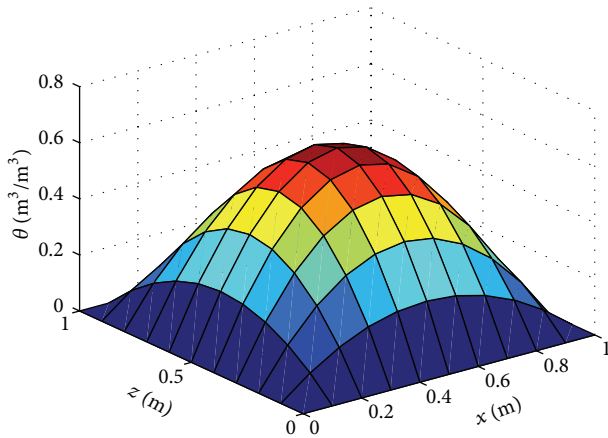


FIGURE 6: Numerical solutions using the radial basis function collocation method.

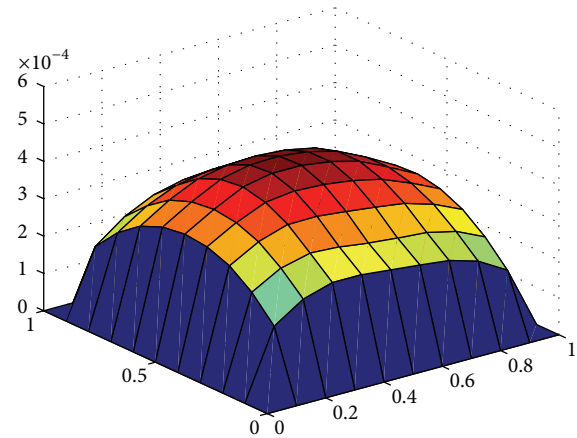


FIGURE 7: The error graph.

The numerical and exact solutions of Example 2, along with the error, are shown in Figures 5, 6, and 7, respectively.

Table 3 shows the comparison of this method with FEM, where $h = 0.1$ and $t = 10$.

For the time step $\Delta t = 0.01$, we give the results of the new method based on different spatial steps and different parameters c . These are shown in Table 4.

For the nonlinear soil water movement equation, we can get the same conclusions as in linear equation.

4. Conclusions

In this paper, a mathematical model with the boundary conditions for soil water movement under irrigation has been developed by constructing a radial basis function collocation method. The existence and uniqueness of the solution were proven. Several numerical examples show that the proposed method yields higher precision and is easier to solve 2D soil

water movement equations than traditional methods. Moreover, the selection of the time, spatial steps, and parameter c has a direct influence on calculation accuracy. Therefore, it is necessary to study the combination of steps, radial basis function, and parameter c to obtain the numerical solutions. In addition, it lays the foundation for the numerical solutions to high-dimensional soil water movement equations, which is very important.

Conflict of Interests

The authors declare that there is no conflict of interests regarding the publication of this paper.

Acknowledgments

This paper is supported by National Natural Science Foundation of China (NSFC 11101330, 51305344) and Scientific Foundation of Shaanxi Province (2014K05-22).

References

- [1] L. B. Lucy, "A numerical approach to the testing of the fission hypothesis," *The Astronomical Journal*, vol. 82, pp. 1013–1024, 1977.
- [2] R. A. Gingold and J. J. Monaghan, "Smoothed particle hydrodynamics: theory and application to non-spherical stars," *Monthly Notices of the Royal Astronomical Society*, vol. 181, pp. 375–389, 1977.
- [3] B. Nayroles, G. Touzot, and P. Villon, "Generalizing the finite element method: diffuse approximation and diffuse elements," *Computational Mechanics*, vol. 10, no. 5, pp. 307–318, 1992.
- [4] T. Belytschko, Y. Y. Lu, and L. Gu, "Element-free Galerkin methods," *International Journal for Numerical Methods in Engineering*, vol. 37, no. 2, pp. 229–256, 1994.
- [5] R. Schaback, "Improved error bounds for scattered data interpolation by radial basis functions," *Mathematics of Computation*, vol. 68, no. 225, pp. 201–216, 1999.
- [6] N. Sukumar, B. Moran, and T. Belytschko, "The natural element method in solid mechanics," *International Journal for Numerical Methods in Engineering*, vol. 43, no. 5, pp. 839–887, 1998.
- [7] Z. Wu, "About the convergence of interpolation with radial basis function," *Annals of Mathematics*, vol. 14A, pp. 480–486, 1993.
- [8] H. Wendland, "Piecewise polynomial, positive definite and compactly supported radial functions of minimal degree," *Advances in Computational Mathematics*, vol. 4, no. 1, pp. 389–396, 1995.
- [9] H. Wendland, "Meshless Galerkin methods using radial basis functions," *Mathematics of Computation*, vol. 68, no. 228, pp. 1521–1531, 1999.
- [10] S. N. Atluri and S. Shen, *The Meshless Local Petrov—Galerkin (MLPG) Method*, Tech Science Press, Encino, Calif, USA, 2002.
- [11] G. R. Liu, *Meshfree Methods: Moving beyond the Finite Element Method*, CRC Press, Boca Raton, Fla, USA, 2002.
- [12] W. K. Liu, Y. Chen, R. A. Uras, and C. T. Chang, "Generalized multiple scale reproducing kernel particle methods," *Computer Methods in Applied Mechanics and Engineering*, vol. 139, no. 1–4, pp. 91–157, 1996.
- [13] C. A. Duarte and J. T. Oden, "An \mathcal{H}^s - \mathcal{H}^s adaptive method using clouds," *Computer Methods in Applied Mechanics and Engineering*, vol. 139, no. 1–4, pp. 237–262, 1996.
- [14] I. Babuška and J. M. Melenk, "The partition of unity method," *International Journal for Numerical Methods in Engineering*, vol. 40, no. 4, pp. 727–758, 1997.
- [15] E. Oñate, S. Idelsohn, O. C. Zienkiewicz, and R. L. Taylor, "A finite point method in computational mechanics: applications to convective transport and fluid flow," *International Journal for Numerical Methods in Engineering*, vol. 39, no. 22, pp. 3839–3866, 1996.
- [16] N. R. Aluru, "A point collocation method based on reproducing kernel approximations," *International Journal for Numerical Methods in Engineering*, vol. 47, no. 6, pp. 1083–1121, 2000.
- [17] T. J. Liszka, C. Duarte, and W. W. Tworzydło, "Hp-meshless cloud method," *Computer Methods in Applied Mechanics and Engineering*, vol. 139, no. 1–4, pp. 263–288, 1996.
- [18] T. Zhu, J. Zhang, and S. N. Atluri, "A local boundary integral equation (LBIE) method in computational mechanics, and a meshless discretization approach," *Computational Mechanics*, vol. 21, no. 3, pp. 223–235, 1998.
- [19] X. Zhang and Y. Liu, *Meshless Methods*, Tsinghua University Press, Beijing, China, 2004.
- [20] E. J. Kansa, "Multiquadrics—a scattered data approximation scheme with applications to computational fluid-dynamics. I. Surface approximations and partial derivative estimates," *Computers & Mathematics with Applications*, vol. 19, no. 8–9, pp. 127–145, 1990.
- [21] G. E. Fasshauer, "Solving differential equations with radial basis functions: multilevel methods and smoothing," *Advances in Computational Mathematics*, vol. 11, no. 2–3, pp. 139–159, 1999.
- [22] Y. C. Hon, K. F. Cheung, X. Z. Mao, and E. J. Kansa, "Multiquadric solution for shallow water equations," *Journal of Hydraulic Engineering*, vol. 125, no. 5, pp. 524–533, 1999.
- [23] S. Rippa, "An algorithm for selecting a good value for the parameter c in radial basis function interpolation," *Advances in Computational Mathematics*, vol. 11, no. 2–3, pp. 193–210, 1999.
- [24] M. D. Buhmann, "A new class of radial basis functions with compact support," *Mathematics of Computation*, vol. 70, no. 233, pp. 307–318, 2001.
- [25] L. W. Zhang, Y. J. Deng, and K. M. Liew, "An improved element-free Galerkin method for numerical modeling of the biological population problems," *Engineering Analysis with Boundary Elements*, vol. 40, pp. 181–188, 2014.
- [26] R. J. Cheng, L. W. Zhang, and K. M. Liew, "Modeling of biological population problems using the element-free kp-Ritz method," *Applied Mathematics and Computation*, vol. 227, pp. 274–290, 2014.
- [27] P. F. Guo, L. W. Zhang, and K. M. Liew, "Numerical analysis of generalized regularized long wave equation using the element-free kp-Ritz method," *Applied Mathematics and Computation*, vol. 240, pp. 91–101, 2014.
- [28] J. W. Yan, L. W. Zhang, K. M. Liew, and L. H. He, "A higher-order gradient theory for modeling of the vibration behavior of single-wall carbon nanotubes," *Applied Mathematical Modelling*, vol. 38, no. 11–12, pp. 2946–2960, 2014.
- [29] Z. X. Lei, L. W. Zhang, K. M. Liew, and J. L. Yu, "analysis of carbon nanotube-reinforced functionally graded cylindrical panels using the element-free kp-Ritz method," *Composite Structure*, vol. 113, pp. 328–338, 2014.
- [30] X. F. Pan, X. Zhang, and M. W. Lu, "Meshless Galerkin least-squares method," *Computational Mechanics*, vol. 35, no. 3, pp. 182–189, 2005.
- [31] Y. Gu and L. Zhang, "Coupling of the meshfree and finite element methods for determination of the crack tip fields," *Engineering Fracture Mechanics*, vol. 75, pp. 986–1004, 2008.
- [32] Y. Duan and Y. Tan, "On condition number of meshless collocation method using radial basis functions," *Applied Mathematics and Computation*, vol. 172, no. 1, pp. 141–147, 2006.
- [33] H. Hu, Z. Li, and A. H. Cheng, "Radial basis collocation methods for elliptic boundary value problems," *Computers and Mathematics with Applications*, vol. 50, no. 1–2, pp. 289–320, 2005.
- [34] L. Su, X. Qin, B. Miao, and Q. Wang, "Radial basis function collocation method with difference for nonlinear convection-dominated diffusion equations," in *Proceedings of the 6th International Conference on Natural Computation (ICNC '10)*, pp. 3203–3207, Yantai, China, August 2010.
- [35] W. Guo, B. Li, Z. Ji, Y. Jiang, and F. Yan, "Two-dimensional numerical simulation of soil water infiltration under bed-irrigating sowing," *Transactions of the Chinese Society of Agricultural Engineering*, vol. 17, no. 2, pp. 24–27, 2001.
- [36] S. P. Neuman, "Saturated-unsaturated seepage by finite elements," *Journal of the Hydraulics Division*, vol. 99, no. 12, pp. 2233–2250, 1973.

- [37] H. Zhang and S. Chen, "Numerical simulation of infiltration in unsaturated soil," *Rock and Soil Mechanics*, vol. 24, no. 5, pp. 715–718, 2003.
- [38] X. Lu and D. H. Wu, "Numerical simulation of infiltration in unsaturated soil," *China Water Transport*, vol. 4, no. 4, pp. 136–137, 2006.
- [39] H. R. Li and Z. D. Luo, "Semi-discrete finite volume element simulation for two-dimensional unsaturated soil water flow problem," *Mathematica Numerica Sinica*, vol. 33, no. 1, pp. 57–68, 2011.
- [40] D. Zhou and H. Wang, "Application of RBF in simulation of groundwater flow," *Journal of Liaoning Normal University*, vol. 31, no. 4, pp. 390–392, 2008.

Research Article

A Meshfree Quasi-Interpolation Method for Solving Burgers' Equation

Mingzhu Li,^{1,2} Lijuan Chen,¹ and Qiang Ma²

¹ School of Science, Qingdao Technological University, Qingdao 266033, China

² Department of Mathematics, Harbin Institute of Technology at Weihai, Weihai 264209, China

Correspondence should be addressed to Qiang Ma; hitmaqiang@hotmail.com

Received 26 April 2014; Revised 29 June 2014; Accepted 1 July 2014; Published 16 July 2014

Academic Editor: Kim M. Liew

Copyright © 2014 Mingzhu Li et al. This is an open access article distributed under the Creative Commons Attribution License, which permits unrestricted use, distribution, and reproduction in any medium, provided the original work is properly cited.

The main aim of this work is to consider a meshfree algorithm for solving Burgers' equation with the quartic B-spline quasi-interpolation. Quasi-interpolation is very useful in the study of approximation theory and its applications, since it can yield solutions directly without the need to solve any linear system of equations and overcome the ill-conditioning problem resulting from using the B-spline as a global interpolant. The numerical scheme is presented, by using the derivative of the quasi-interpolation to approximate the spatial derivative of the dependent variable and a low order forward difference to approximate the time derivative of the dependent variable. Compared to other numerical methods, the main advantages of our scheme are higher accuracy and lower computational complexity. Meanwhile, the algorithm is very simple and easy to implement and the numerical experiments show that it is feasible and valid.

1. Introduction

Burgers' equation plays a significant role in various fields, such as turbulence problems, heat conduction, shock waves, continuous stochastic processes, number theory, gas dynamics, and propagation of elastic waves [1–5]. The one-dimensional Burgers' equation first suggested by Bateman [6] and later treated by Burgers [1] has the form

$$U_t + UU_x - \lambda U_{xx} = 0, \quad (1)$$

where $\lambda > 0$ is the coefficient of kinematic viscosity and the subscripts x and t denote space and time derivatives. Initial and boundary conditions are

$$\begin{aligned} U(x, 0) &= f(x), \quad a \leq x \leq b, \\ U(a, t) &= \beta_1, \quad U(b, t) = \beta_2, \quad t \geq 0, \end{aligned} \quad (2)$$

where β_1 , β_2 , and $f(x)$ will be chosen in a later section.

Burgers' equation is a quasi-linear parabolic partial differential equation, whose analytic solutions can be constructed

from a linear partial differential equation by using Hopf-Cole transformation [1, 2, 7]. But some analytic solutions consist of infinite series, converging very slowly for small viscosity coefficient λ . Thus, many researchers have spent a great deal of effort to compute the solution of Burgers' equation using various numerical methods. Finite difference methods were presented to solve the numerical solution of Burgers' equation in [8–11]. Finite element methods for the solution of Burgers' equation were introduced in [12–15]. Recently, various powerful mathematical methods such as Galerkin finite element method [16, 17], spectral collocation method [18, 19], sinc differential quadrature method [20], factorized diagonal padé approximation [21], B-spline collocation method [22], and reproducing kernel function method [23] have also been used in attempting to solve the equation.

In 1968 Hardy proposed the multiquadric (MQ) which is a kind of radial basis function (RBF). In Franke's review paper, the MQ was rated as one of the best methods among 29 scattered data interpolation and ease of implementation. Since Kansa successfully applied MQ for solving partial differential equation, more and more researchers have been attracted

by this meshfree, scattered data approximation scheme [24]. The meshfree method uses a set of scattered nodes, instead of meshing the domain of the problem. It has been successfully applied to solve many physical and engineering problems with only a minimum of meshing or no meshing at all [25–30]. In recent years, many meshfree methods have been developed, such as the element-free Galerkin method [31], the smooth particle hydrodynamics method [32], the element-free kp-Ritz method [33–36], the meshless local Petrov-Galerkin method [37], and the reproducing kernel particle method [38].

With the use of univariate multiquadric (MQ) quasi-interpolation, solution of Burgers' equations was obtained by Chen and Wu [39]. Moreover, Hon and Mao [40] developed an efficient numerical scheme for Burgers' equation applying the MQ as a spatial approximate scheme and a low order explicit finite difference approximation to the time derivation. Zhu and Wang [41] presented the numerical scheme for solving the Burgers' equation, by using the derivative of the cubic B-spline quasi-interpolation to approximate the time derivative of the dependent variable and a low order forward difference to approximate the time derivative of the dependent variable. In this paper, we provide a numerical scheme to solve Burgers' equation using the quartic B-spline quasi-interpolation. Then we do not require to solve any linear system of equation so that we do not meet the question of the ill-condition of the matrix. Therefore, we can solve the computational time and decrease the numerical error.

This paper is arranged as follows. In Section 2, the definition of quartic B-spline has been described and univariate quartic B-spline quasi-interpolants have been presented. In

Section 3, we mainly propose the numerical techniques using quartic B-spline interpolation to solve Burgers' equation. In Section 4, numerical examples of Burgers' equation are presented and compared with those obtained with some previous results. At last, we conclude the paper in Section 5.

2. Univariate Quartic B-Spline Quasi-Interpolant

For an interval $I = [a, b]$, we introduce a set of equally-spaced knots of partition $\Omega = \{x_0, x_1, \dots, x_n\}$. We assume that $n \geq 5$, $x_i = a + ih$ ($i = 0, 1, \dots, n$), $x_0 = a$, and $x_n = b$. Let $S_4[\pi]$ be the space of continuously-differentiable, piecewise, quartic-degree polynomials on π . A detailed description of B-spline functions generated by subdivision regarding the B-splines basis in $S_4[\pi]$ can be found in [45].

The zero degree B-spline is defined as

$$N_{i,0}(x) = \begin{cases} 1, & x \in [x_i, x_{i+1}], \\ 0, & \text{otherwise,} \end{cases} \quad (3)$$

and, for positive constant p , it is defined in the following recursive form:

$$N_{i,p} = \frac{x - x_i}{x_{i+p} - x_i} N_{i,p-1}(x) + \frac{x_{i+p+1} - x}{x_{i+p+1} - x_{i+1}} N_{i+1,p-1}, \quad (4)$$

$$p \geq 1.$$

We apply this recursion to get the quartic B-spline $N_{i,4}(x)$, which is defined in $S_4(\pi)$ as follows:

$$N_{i,4}(x) = \frac{1}{24h^4} \begin{cases} (x - x_{i-2})^4, & x \in [x_{i-2}, x_{i-1}], \\ (x - x_{i-2})^4 - 5(x - x_{i-1})^4, & x \in [x_{i-1}, x_i], \\ (x - x_{i-2})^4 - 5(x - x_{i-1})^4 + 10(x - x_i)^4, & x \in [x_i, x_{i+1}], \\ (x - x_{i+3})^4 - 5(x - x_{i+2})^4, & x \in [x_{i+1}, x_{i+2}], \\ (x - x_{i+3})^4, & x \in [x_{i+2}, x_{i+3}], \\ 0, & \text{otherwise.} \end{cases} \quad (5)$$

As usual, we add multiple knots at the endpoints: $a = x_{-4} = x_{-3} = \dots = x_0$ and $b = x_n = x_{n+1} = \dots = x_{n+4}$.

In [24], univariate quartic B-spline quasi-interpolants (abbr. QIs) can be defined as operators of the form

$$Q_4(f) = \sum_{j=1}^{n+4} \mu_j N_{j,4}. \quad (6)$$

The coefficients are listed as follows:

$$\begin{aligned} \mu_1(f) &= f_1, \\ \mu_2(f) &= \frac{17}{105}f_1 + \frac{35}{32}f_2 - \frac{35}{96}f_3 + \frac{21}{160}f_4 - \frac{5}{244}f_5, \end{aligned}$$

$$\mu_3(f) = -\frac{19}{45}f_1 + \frac{377}{288}f_2 + \frac{61}{288}f_3 - \frac{59}{480}f_4 + \frac{7}{288}f_5,$$

$$\mu_4(f) = \frac{47}{315}f_1 - \frac{77}{144}f_2 + \frac{251}{144}f_3 - \frac{97}{240}f_4 + \frac{47}{1008}f_5,$$

$$\begin{aligned} \mu_j(f) &= \frac{47}{1152}(f_{j-4} + f_{j+1}) - \frac{107}{288}(f_{j-3} + f_{j-1}) \\ &\quad + \frac{319}{192}f_{j-2}, \quad j = 5, \dots, n, \end{aligned}$$

$$\begin{aligned} \mu_{n+1}(f) &= \frac{47}{315}f_{n+2} - \frac{77}{144}f_{n+1} + \frac{251}{144}f_n - \frac{97}{240}f_{n-1} \\ &\quad + \frac{47}{1008}f_{n-2}, \end{aligned}$$

$$\begin{aligned}
\mu_{n+2}(f) &= -\frac{19}{45}f_{n+2} + \frac{377}{288}f_{n+1} + \frac{61}{288}f_n - \frac{59}{480}f_{n-1} \\
&\quad + \frac{7}{288}f_{n-2}, \\
\mu_{n+3}(f) &= \frac{17}{105}f_{n+2} + \frac{35}{32}f_{n+1} - \frac{35}{96}f_n + \frac{21}{160}f_{n-1} \\
&\quad - \frac{5}{244}f_{n-2}, \\
\mu_{n+4}(f) &= f_{n+2},
\end{aligned} \tag{7}$$

and $f_i = f(t_i)$, $t_i = (1/2)(x_{i-2} + x_{i-1})$, $i = 1, \dots, n+2$. For $f \in C^5(I)$, we have the error estimate

$$\|f - Q_4(f)\|_\infty = O(h^5). \tag{8}$$

We use Π_4 to denote the space of polynomials of the total degree at most 4. In general, we impose that Q_4 is exact on the space Π_4 ; that is, $Q_4(p) = p$ for all $p \in \Pi_4$. As a consequence of this property, the approximation order of Q_4 is $O(h^5)$ on smooth functions. In this paper, the coefficient μ_j is a linear combination of discrete values of f at some points. The main advantage of QIs is that they have a direct construction without solving any system of linear equations. Moreover, they are local in the sense that values of $Q_4 f(x)$ depend only on values of f in a neighborhood of x . Finally, they have a rather small infinity norm and, therefore, are nearly optimal approximant.

Differentiating interpolation polynomials leads to the classic finite difference for the approximate computation of derivatives. Therefore, we can draw a conclusion of approximating derivatives of f by derivatives of $Q_4 f$. The general theory will be developed elsewhere. We can evaluate the value of f at x_i by $(Q_4 f)' = \sum_{j=1}^{n+4} \mu_j(f) N'_{j,4}$ and $(Q_4 f)'' = \sum_{j=1}^{n+4} \mu_j(f) N''_{j,4}$. $N'_{j,4}$ and $N''_{j,4}$ can be computed by the formula of B-spline's derivatives as follows:

$$N_{i,4}^{(k)} = \frac{4!}{(4-k)!} \sum_{j=1}^n \alpha_{k,j} N_{i+j,4-k}, \tag{9}$$

where

$$\begin{aligned}
\alpha_{0,0} &= 1, \\
\alpha_{k,0} &= \frac{\alpha_{k-1,0}}{x_{i+3-k} - x_i}, \\
\alpha_{k,k} &= \frac{-\alpha_{k-1,k-1}}{x_{i+5} - x_{i+k}}, \\
\alpha_{k,j} &= \frac{\alpha_{k-j,j} - \alpha_{k-1,j-1}}{x_{i+j+5-k} - x_{i+j}}.
\end{aligned} \tag{10}$$

By some trivial computations, we can obtain the value of $N_{i,4}^{(k)}$ ($k = 0, 1, 2, 3$) at the knots, which are illustrated in

TABLE 1: The values of $N_{i,4}^{(k)}(x)$ at the knots.

	x_{i-1}	x_i	x_{i+1}	x_{i+2}	Otherwise
$N_{i,4}(x)$	$\frac{1}{24}$	$\frac{11}{24}$	$\frac{11}{24}$	$\frac{1}{24}$	0
$N'_{i,4}(x)$	$\frac{1}{6h}$	$\frac{3}{6h}$	$-\frac{3}{6h}$	$-\frac{1}{6h}$	0
$N''_{i,4}(x)$	$\frac{1}{2h^2}$	$-\frac{1}{2h^2}$	$-\frac{1}{2h^2}$	$-\frac{1}{2h^2}$	0
$N'''_{i,4}(x)$	$\frac{1}{h^3}$	$-\frac{3}{h^3}$	$\frac{3}{h^3}$	$-\frac{1}{h^3}$	0

Table 1. Then, we get the differential formulas for quartic B-spline QIs as

$$f' = \sum_{j=1}^{n+4} \mu_j(f) N'_{j,4}, \tag{11}$$

$$f'' = \sum_{j=1}^{n+4} \mu_j(f) N''_{j,4}.$$

3. Numerical Scheme Using the Meshfree Quasi-Interpolation

In this section, we present the numerical scheme for solving Burgers' equation based on the quartic B-spline quasi-interpolation.

Discretizing the Burgers' equation

$$U_t + UU_x - \lambda U_{xx} = 0, \tag{12}$$

in time with meshlength τ , we get

$$\frac{U_j^{k+1} - U_j^k}{\tau} + U_j^k (U_x)_j^k - \lambda (U_{xx})_j^k = 0. \tag{13}$$

We can get

$$U_j^{k+1} = U_j^k + \tau U_j^k (U_x)_j^k - \tau \lambda (U_{xx})_j^k, \tag{14}$$

where U_j^k is the approximation of the value of $U(x, t)$ at the point (x_j, t_k) . Then, we can use the derivatives of the quartic B-spline quasi-interpolant $Q_4 U(x_j, t_k)$ to approximate $(U_x)_j^k$ and $(U_{xx})_j^k$. To dump the dispersion of the scheme, we define a switch function $g(x, t)$, whose values are 0 and 1 at the discrete points (x_j, t_k) , as follows:

$$g(x_j, t_k) = \max \left\{ 0, 1 + \min \left\{ 0, \text{sign} \left((U_x)_j^k \cdot (U_x)_l^k \right) \right\} \right\}, \tag{15}$$

where $l = j - \text{sign}(U_j^k)$. Thus, the resulting numerical scheme is

$$U_j^{k+1} = U_j^k + \tau U_j^k (U_x)_j^k g(x_j, t_k) - \tau \lambda (U_{xx})_j^k. \tag{16}$$

Starting from the initial condition, we can compute the numerical solution of Burgers' equation step by step using the B-spline quasi-interpolation scheme (16) and formulas (11).

TABLE 2: Comparison of exact and numerical solution at $t = 0.001$.

x	$\lambda = 1$			$\lambda = 0.5$		
	Our method	Asai [42]	Exact	Our method	Asai [42]	Exact
0.1	0.653563	0.653589	0.653544	0.327870	0.327874	0.327870
0.2	1.305519	1.305611	1.305534	0.655028	0.655078	0.655069
0.3	1.949321	1.949485	1.949364	0.978449	0.978427	0.978413
0.4	2.565977	2.566103	2.565925	1.288417	1.288485	1.288463
0.5	3.110769	3.110992	3.110739	1.563014	1.563096	1.563064
0.6	3.492902	3.493222	3.492866	1.756653	1.756691	1.756642
0.7	3.549538	3.550079	3.549595	1.787184	1.787281	1.787206
0.8	3.050089	3.050702	3.050134	1.537658	1.537794	1.537694
0.9	1.816492	1.817077	1.816660	0.916795	0.916941	0.916860

TABLE 3: The computational results at $t = 0.5$ for $\lambda = 0.01$ with $h = 1/36$ and $\tau = 0.01$.

	BSQI [41]	MQQI [39]	QBCM I [17]	QBGM I [43]	Our method
$L_2 \times 10^3$	3.43253	5.77786	0.77033	1.92558	0.85269
$L_\infty \times 10^3$	9.26698	20.8467	3.03817	6.35489	3.79716

4. Numerical Results

To investigate the applicability of the quasi-interpolation method to Burgers' equation, four selected example problems are studied. To show the efficiency of the present method for our problem in comparison with the exact solution, we use the following norms to assess the performance of our scheme:

$$L_\infty = \max_j |U_j^{\text{exact}} - U_j^{\text{num}}|,$$

$$L_2 = \sqrt{h \sum_{j=1}^n (U_j^{\text{exact}} - U_j^{\text{num}})^2}. \quad (17)$$

Example 1. Burgers' equation is solved over the region $[0, 1]$ and the initial and boundary conditions are given in Asaithambi [42]:

$$U(x, 0) = \frac{2\lambda\pi \sin \pi x}{\alpha + \cos \pi x} \quad (\alpha > 1), \quad (18)$$

$$U(0, t) = 0, \quad U(1, t) = 0, \quad t > 0,$$

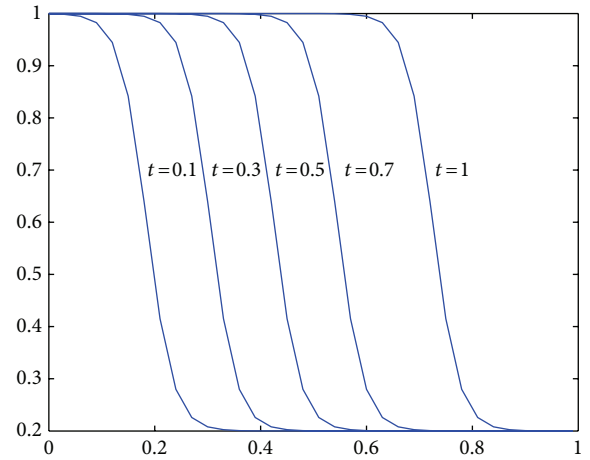
and the exact solution of this problem has the following nice compact closed-form, as given by Wood [46]:

$$U(x, t) = \frac{2\lambda\pi e^{-\pi^2 \lambda t} \sin \pi x}{\alpha + e^{-\pi^2 \lambda t} \cos \pi x} \quad (\alpha > 1). \quad (19)$$

In this computational study, we set $\alpha = 2$, $h = 0.025$, $\Delta\tau = 0.0001$. The comparison of the numerical solutions obtained by the present method, at the different coefficient of kinematic viscosity λ , are presented with the solutions obtained by Asaithambi [42] and the exact solution in Table 2.

Example 2. In this example, we consider the exact solution of Burgers' equation [47]:

$$U(x, t) = \frac{\alpha + \mu + (\mu - \alpha) \exp \eta}{1 + \exp \eta}, \quad 0 \leq x \leq 1, t \geq 0, \quad (20)$$

FIGURE 1: The numerical solutions with $h = 1/36$, $\tau = 0.01$ for $\lambda = 0.01$.

where $\eta = (\alpha(x - \mu t - \gamma))/\lambda$, α , μ , and γ are constants. The boundary conditions are

$$U(0, t) = 1, \quad U(1, t) = 0.2, \quad t \geq 0, \quad (21)$$

and initial condition is used for the exact solution at $t = 0$.

We solve the problem with $\alpha = 0.4$, $\mu = 0.6$, and $\gamma = 0.125$ by our method. In Table 3, L_2 and L_∞ errors at the time level $t = 0.5$ are compared with the error obtained by Chen and Wu [39], Zhu and Wang [41], Dağ et al. [17], and Saka and Dağ [43]. For comparison, the parameters are adopted as time step $\tau = 0.01$, space step $h = 1/36$, and viscosity coefficient $\lambda = 0.01$. From Table 3, we can find that our method provides better accuracy than most methods through the L_2 and L_∞ error norms. The profiles of initial wave and its propagation are depicted at some times in Figure 1.

TABLE 4: Comparison of results at different time for $\lambda = 0.1$ with $h = 0.025$ and $\tau = 0.0001$.

x	t	Hassanien [44]	Kutluay [11]	Ozis [15]	Our method	Exact
0.25	0.4	0.3089	0.3083	0.3143	0.3089	0.3089
	0.6	0.2407	0.2404	0.2437	0.2407	0.2407
	0.8	0.1957	0.1954	0.1976	0.1957	0.1957
	1.0	0.1626	0.1624	0.1639	0.1626	0.1626
	3.0	0.0272	0.0272	0.0274	0.0272	0.0272
0.50	0.4	0.5696	0.5691	0.5764	0.5696	0.5696
	0.6	0.4472	0.4468	0.4517	0.4472	0.4472
	0.8	0.3592	0.3589	0.3625	0.3592	0.3592
	1.0	0.2919	0.2916	0.2944	0.2919	0.2919
	3.0	0.0402	0.0402	0.0406	0.0402	0.0402
0.75	0.4	0.6254	0.6256	0.6259	0.6257	0.6254
	0.6	0.4872	0.4570	0.4903	0.4872	0.4872
	0.8	0.3739	0.3737	0.3771	0.3739	0.3739
	1.0	0.2875	0.2872	0.2902	0.2875	0.2875
	3.0	0.0298	0.0297	0.0133	0.0298	0.0298

Example 3. Consider Burgers' equation with the initial condition

$$U(x, 0) = \sin(\pi x), \quad 0 \leq x \leq 1 \quad (22)$$

and the boundary conditions

$$U(0, t) = U(1, t) = 0. \quad (23)$$

The analytical solution of this problem was given by Cole [2] in the term of an infinite series as

$$U(x, t) = \frac{2\pi\lambda \sum_{k=1}^{\infty} k A_k \sin(k\pi x) \exp(-k^2\pi^2\lambda t)}{A_0 + \sum_{k=1}^{\infty} A_k \cos(k\pi x) \exp(-k^2\pi^2\lambda t)} \quad (24)$$

with the Fourier coefficients

$$A_0 = \int_0^1 \exp\{-(2\pi\lambda)^{-1}(1 - \cos(\pi x))\} dx,$$

$$A_k = 2 \int_0^1 \exp\{-(2\pi\lambda)^{-1}(1 - \cos(\pi x))\} \cos(k\pi x) dx, \quad k \geq 1. \quad (25)$$

In Table 4, we have computed the numerical solutions of this example at differential time levels with parameter values $\lambda = 0.1$, $h = 0.025$, and $\tau = 0.0001$. The comparison of our results with the exact solutions as well as the solutions obtained in [11, 15, 44] is reported in Table 4. From Table 4, we can find that the presented scheme provides better accuracy. Moreover, in Tables 5, 6 and 7, we compare our method with Hon and Mao's scheme, Chen and Wu's MQQI method, and Zhu's BSQI method at $t = 1$ with $\tau = 0.001$, $h = 0.01$ for $\lambda = 0.1, 0.01, 0.0001$, respectively. For the MQQI method, the shape parameter $c = 7.2 \times 10^{-3}, 2.9 \times 10^{-3}, 1.43 \times 10^{-4}$ for Table 5, respectively, as [39]. Solutions found with the present method are in good agreement with the result and better than other methods. These show that the method works well.

Example 4. We consider particular solution of Burgers' equation:

$$U(x, t) = \frac{x/t}{1 + \sqrt{t/t_0} \exp(x^2/4\lambda t)}, \quad t \geq 1, \quad 0 \leq x \leq 1, \quad (26)$$

where $t_0 = \exp(1/8\lambda)$. Initial condition is obtained from when $t = 1$ is used. Boundary conditions are $U(0, t) = U(1, t) = 0$. Analytical solution represents shock-like solution of the one-dimensional Burgers' equation. Parameters $h = 0.02, 0.005$ and $\lambda = 0.005, 0.01$ are selected for comparison over the domain $[0, 1]$. Accuracy of our method is shown by calculating the error norms. These together with some previous results are given in Table 8. Table 8 shows that our method provides better accuracy than MQQI method and BSQI method. Although the accuracy is not higher than that of QBCM method, we know that, at each time step, the complexity of our method is lower than theirs. The numerical solutions are depicted with $h = 0.02$, $\tau = 0.001$, and $\lambda = 0.005$ for $t \leq 4$ in Figure 2.

5. Conclusion

Following the recent development of the quasi-interpolation method for scattered data interpolation and the meshfree method for solving partial differential equations, this paper combines these ideas and proposes a new meshfree quasi-interpolation method for Burgers' equation. The method does not require solving a large size matrix equation and, hence, the ill-conditioning problem from using B-spline functions as global interpolants can be avoided. We have made comparison studies between the present results and the exact solutions. The agreement of our numerical results with those exact solutions is excellent. For the high-dimensional

TABLE 5: Comparison of results at $t = 1$ for $\lambda = 0.1$.

x	Hon and Mao [40]	MQQI [39]	BSQI [41]	Our method	Exact
0.1	0.0664	0.07124	0.06628	0.06630	0.06632
0.2	0.1313	0.13431	0.13115	0.13119	0.13121
0.3	0.1928	0.19339	0.19269	0.19271	0.19279
0.4	0.2481	0.24538	0.24792	0.24797	0.24803
0.5	0.2919	0.28517	0.29175	0.29185	0.29191
0.6	0.3159	0.30473	0.31580	0.31598	0.31607
0.7	0.3079	0.29288	0.30791	0.30800	0.30810
0.8	0.2534	0.23784	0.25337	0.25344	0.25372
0.9	0.1459	0.13542	0.14583	0.14587	0.14606

TABLE 6: Comparison of results at $t = 1$ for $\lambda = 0.01$.

x	Hon and Mao [40]	MQQI [39]	BSQI [41]	Our method	Exact
0.1	0.0755	0.07868	0.07530	0.07538	0.0754
0.2	0.1507	0.15202	0.15049	0.15066	0.1506
0.3	0.2257	0.22554	0.22544	0.22573	0.2257
0.4	0.3003	0.29904	0.30002	0.30028	0.3003
0.5	0.3744	0.37226	0.37407	0.37437	0.3744
0.6	0.4478	0.44484	0.44742	0.44778	0.4478
0.7	0.5202	0.51643	0.51985	0.52038	0.5203
0.8	0.5913	0.58622	0.59106	0.59151	0.5915
0.9	0.6607	0.62956	0.65964	0.66007	0.6600

TABLE 7: Comparison of results at $t = 1$ for $\lambda = 0.0001$.

x	Hon and Mao [40]	MQQI [39]	BSQI [41]	Our method
0.05	0.0422	0.0422	0.0422	0.0422
0.16	0.1263	0.1263	0.1262	0.1262
0.27	0.2103	0.2103	0.2096	0.2103
0.38	0.2939	0.2939	0.2928	0.2939
0.50	0.3769	0.3769	0.3754	0.3769
0.61	0.4592	0.4592	0.4573	0.4592
0.72	0.5404	0.5404	0.5381	0.5404
0.83	0.6203	0.6201	0.6174	0.6203
0.94	0.6983	0.6957	0.6947	0.6983

TABLE 8: Comparison of results at different times for $\tau = 0.01$.

	$L_2 \times 10^3$	$L_\infty \times 10^3$	$L_2 \times 10^3$	$L_\infty \times 10^3$	$L_2 \times 10^3$	$L_\infty \times 10^3$
$h = 0.02, \lambda = 0.005$	$t = 1.8$	$t = 1.8$	$t = 2.4$	$t = 2.4$	$t = 3.2$	$t = 3.2$
BSQI [41]	1.66464	5.12020	2.06695	6.31491	2.36889	6.85425
QBCM I [17]	0.19127	0.54058	0.14246	0.39241	0.93617	5.54899
QBCM II [17]	0.49130	1.16930	0.41864	0.93664	1.28863	7.49147
MQQI [39]	6.88480	25.6767	7.89738	27.2424	8.56856	2.68122
Our method	0.6642	0.91725	0.7573	1.1465	0.8592	1.2103
$h = 0.02, \lambda = 0.01$	$t = 1.8$	$t = 1.8$	$t = 2.4$	$t = 2.4$	$t = 3.2$	$t = 3.2$
BSQI [41]	0.82751	2.59444	0.98595	2.35031	1.58264	5.73827
QBCM I [17]	0.17014	0.40431	0.20476	0.86363	1.29951	6.69425
QBCM II [17]	0.24003	0.48800	0.30849	1.14760	1.57548	8.06798
MQQI [39]	5.89555	14.7550	6.64358	15.9892	6.90385	16.3403
Our method	0.82751	0.50367	0.46281	1.05625	0.88261	4.73827

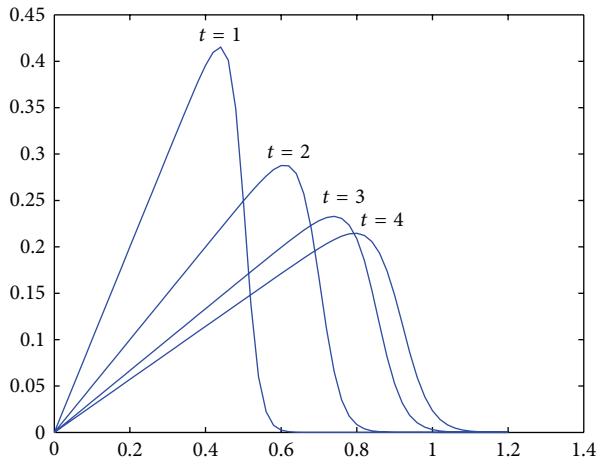


FIGURE 2: The numerical solutions for $t \leq 4$.

Burgers' equations, we believe our scheme can also be applicable. In this case, we would use multivariate spline quasi-interpolation instead of univariate spline quasi-interpolation. We will consider these problems in our future work.

Conflict of Interests

The authors declare that there is no conflict of interests regarding the publication of this paper.

Acknowledgments

This work is supported by the Disciplinary Construction Guide Foundation of Harbin Institute of Technology at Weihai (no. WH20140206) and the Scientific Research Foundation of Harbin Institute of Technology at Weihai (no. HIT(WH)201319).

References

- [1] J. M. Burgers, "A mathematical model illustrating the theory of turbulence," *Advances in Applied Mechanics*, vol. 1, pp. 171–199, 1948.
- [2] J. D. Cole, "On a quasi-linear parabolic equation occurring in aerodynamics," *Quarterly of Applied Mathematics*, vol. 9, no. 3, pp. 225–236, 1951.
- [3] M. J. Lighthill, "Viscosity effects in sound waves of finite amplitude," in *Surveys in Mechanics*, pp. 250–351, 1956.
- [4] L. A. Pospelov, "Propagation of finite amplitude elastic waves (Longitudinal elastic wave of finite amplitude propagation in isotropic solid)," *Soviet Physics-Acoustics*, vol. 11, pp. 302–304, 1966.
- [5] B. van der Pol, "On a non-linear partial differential equation satisfied by the logarithm of the Jacobian theta-functions, with arithmetical applications. I, II," *Indagationes Mathematicae*, vol. 13, pp. 261–284, 1951.
- [6] H. Bateman, "Some recent researches on the motion of fluids," *Monthly Weather Review*, vol. 43, no. 4, pp. 163–170, 1915.
- [7] E. Hopf, "The partial differential equation $U_x + UU_t = U_{xx}$," *Communications on Pure and Applied Mathematics*, vol. 3, no. 3, pp. 201–230, 1950.
- [8] I. A. Hassanien, A. A. Salama, and H. A. Hosham, "Fourth-order finite difference method for solving Burgers' equation," *Applied Mathematics and Computation*, vol. 170, no. 2, pp. 781–800, 2005.
- [9] M. Ciment, S. H. Leventhal, and B. Weinberg, "The operator compact implicit method for parabolic equations," *Journal of Computational Physics*, vol. 28, no. 2, pp. 135–166, 1978.
- [10] R. S. Hirsh, "Higher order accurate difference solutions of fluid mechanics problems by a compact differencing technique," *Journal of Computational Physics*, vol. 19, no. 1, pp. 90–109, 1975.
- [11] S. Kutluay, A. R. Bahadir, and A. Özdeş, "Numerical solution of one-dimensional Burgers equation: explicit and exact-explicit finite difference methods," *Journal of Computational and Applied Mathematics*, vol. 103, no. 2, pp. 251–261, 1999.
- [12] P. Arminjon and C. Beauchamp, "A finite element method for Burgers' equation in hydrodynamics," *International Journal for Numerical Methods in Engineering*, vol. 12, no. 3, pp. 415–428, 1978.
- [13] L. Iskandar and A. Mohsen, "Some numerical experiments on the splitting of Burgers' equation," *Numerical Methods for Partial Differential Equations*, vol. 8, no. 3, pp. 267–276, 1992.
- [14] P. C. Jain and M. Raja, "Splitting-up technique for Burgers' equations," *Indian Journal of Pure and Applied Mathematics*, vol. 10, pp. 1543–1551, 1979.
- [15] T. Öziş, E. N. Aksan, and A. Özdeş, "A finite element approach for solution of Burgers' equation," *Applied Mathematics and Computation*, vol. 139, no. 2-3, pp. 417–428, 2003.
- [16] A. Dogan, "A Galerkin finite element approach to Burgers' equation," *Applied Mathematics and Computation*, vol. 157, no. 2, pp. 331–346, 2004.
- [17] İ. Dağ, B. Saka, and A. Boz, "B-spline Galerkin methods for numerical solutions of the Burgers' equation," *Applied Mathematics and Computation*, vol. 166, no. 3, pp. 506–522, 2005.
- [18] A. H. Khater, R. S. Temsah, and M. M. Hassan, "A Chebyshev spectral collocation method for solving Burgers'-type equations," *Journal of Computational and Applied Mathematics*, vol. 222, no. 2, pp. 333–350, 2008.
- [19] A. K. Khalifa, K. I. Noor, and M. A. Noor, "Some numerical methods for solving Burgers equation," *International Journal of Physical Sciences*, vol. 6, no. 7, pp. 1702–1710, 2011.
- [20] A. Korkmaz and I. Dağ, "Shock wave simulations using sinc differential quadrature method," *Engineering Computations*, vol. 28, no. 6, pp. 654–674, 2011.
- [21] K. Altıparmak and T. Öziş, "Numerical solution of Burgers' equation with factorized diagonal Padé approximation," *International Journal of Numerical Methods for Heat and Fluid Flow*, vol. 21, no. 3-4, pp. 310–319, 2011.
- [22] İ. Dağ, D. Irk, and A. Şahin, "B-spline collocation methods for numerical solutions of the Burgers' equation," *Mathematical Problems in Engineering*, vol. 2005, no. 5, pp. 521–538, 2005.
- [23] S. S. Xie, S. Heo, S. Kim, G. Woo, and S. Yi, "Numerical solution of one-dimensional Burgers' equation using reproducing kernel function," *Journal of Computational and Applied Mathematics*, vol. 214, no. 2, pp. 417–434, 2008.
- [24] P. Sablonniere, "Univariate spline quasi-interpolants and applications to numerical analysis," *Rendiconti del Seminario Matematico*, vol. 63, no. 3, pp. 211–222, 2005.

- [25] Y. Ren and X. Li, "A meshfree method for Signorini problems using boundary integral equations," *Mathematical Problems in Engineering*, vol. 2014, Article ID 490127, 12 pages, 2014.
- [26] R. J. Cheng, L. W. Zhang, and K. M. Liew, "Modeling of biological population problems using the element-free kp-Ritz method," *Applied Mathematics and Computation*, vol. 227, pp. 274–290, 2014.
- [27] L. W. Zhang, Y. J. Deng, and K. M. Liew, "An improved element-free Galerkin method for numerical modeling of the biological population problems," *Engineering Analysis with Boundary Elements*, vol. 40, pp. 181–188, 2014.
- [28] L. W. Zhang, P. Zhu, and K. M. Liew, "Thermal buckling of functionally graded plates using a local Kriging meshless method," *Composite Structures*, vol. 108, pp. 472–492, 2014.
- [29] Z. X. Lei, L. W. Zhang, K. M. Liew, and J. L. Yu, "Dynamic stability analysis of carbon nanotube-reinforced functionally graded cylindrical panels using the element-free Kp-Ritz method," *Composite Structures*, vol. 113, pp. 328–338, 2014.
- [30] K. M. Liew, Z. X. Lei, J. L. Yu, and L. W. Zhang, "Postbuckling of carbon nanotube-reinforced functionally graded cylindrical panels under axial compression using a meshless approach," *Computer Methods in Applied Mechanics and Engineering*, vol. 268, pp. 1–17, 2014.
- [31] T. Belytschko, Y. Y. Lu, and L. Gu, "Element-free Galerkin methods," *International Journal for Numerical Methods in Engineering*, vol. 37, no. 2, pp. 229–256, 1994.
- [32] J. J. Monaghan, "An introduction to SPH," *Computer Physics Communications*, vol. 48, no. 1, pp. 89–96, 1988.
- [33] K. M. Liew, X. Zhao, and T. Y. Ng, "The element-free Kp-Ritz method for vibration of laminated rotating cylindrical panels," *International Journal of Structural Stability and Dynamics*, vol. 2, no. 4, pp. 523–558, 2002.
- [34] K. M. Liew, H. Y. Wu, and T. Y. Ng, "Meshless method for modeling of human proximal femur: treatment of nonconvex boundaries and stress analysis," *Computational Mechanics*, vol. 28, no. 5, pp. 390–400, 2002.
- [35] K. M. Liew, Y. C. Wu, G. P. Zou, and T. Y. Ng, "Elasto-plasticity revisited: Numerical analysis via reproducing kernel particle method and parametric quadratic programming," *International Journal for Numerical Methods in Engineering*, vol. 55, no. 6, pp. 669–683, 2002.
- [36] K. M. Liew, X. L. Chen, and J. N. Reddy, "Mesh-free radial basis function method for buckling analysis of non-uniformly loaded arbitrarily shaped shear deformable plates," *Computer Methods in Applied Mechanics and Engineering*, vol. 193, no. 3–5, pp. 205–224, 2004.
- [37] S. N. Atluri and T. Zhu, "A new Meshless Local Petrov-Galerkin (MLPG) approach in computational mechanics," *Computational Mechanics*, vol. 22, no. 2, pp. 117–127, 1998.
- [38] W. K. Liu, S. Jun, and Y. F. Zhang, "Reproducing kernel particle methods," *International Journal for Numerical Methods in Fluids*, vol. 20, no. 8–9, pp. 1081–1106, 1995.
- [39] R. Chen and Z. Wu, "Applying multiquadratic quasi-interpolation to solve Burgers' equation," *Applied Mathematics and Computation*, vol. 172, no. 1, pp. 472–484, 2006.
- [40] Y. C. Hon and X. Z. Mao, "An efficient numerical scheme for Burgers' equation," *Applied Mathematics and Computation*, vol. 95, no. 1, pp. 37–50, 1998.
- [41] C. Zhu and R. Wang, "Numerical solution of Burgers' equation by cubic B-Spline quasi-interpolation," *Applied Mathematics and Computation*, vol. 208, no. 1, pp. 260–272, 2009.
- [42] A. Asaithambi, "Numerical solution of the Burgers' equation by automatic differentiation," *Applied Mathematics and Computation*, vol. 216, no. 9, pp. 2700–2708, 2010.
- [43] B. Saka and I. Dağ, "Quartic B-spline collocation method to the numerical solutions of the Burgers' equation," *Chaos, Solitons and Fractals*, vol. 32, no. 3, pp. 1125–1137, 2007.
- [44] I. A. Hassanien, A. A. Salama, and H. A. Hosham, "Fourth-order finite difference method for solving Burgers' equation," *Applied Mathematics and Computation*, vol. 170, no. 2, pp. 781–800, 2005.
- [45] C. de Boor, *A Practical Guide to Splines*, Springer, New York, NY, USA, 1978.
- [46] W. L. Wood, "An exact solution for Burgers' equation," *Communications in Numerical Methods in Engineering*, vol. 22, no. 7, pp. 797–798, 2006.
- [47] I. Christie, D. F. Griffiths, and A. R. Mitchell, "Product approximation for nonlinear problems in the finite element method," *IMA Journal of Numerical Analysis*, vol. 1, no. 3, pp. 253–266, 1981.

Research Article

Pressure Pulsations of the Blade Region in S-Shaped Shaft-Extension Tubular Pumping System

Fan Yang and Chao Liu

School of Hydraulic, Energy and Power Engineering, Yangzhou University, Jiangsu, China

Correspondence should be addressed to Fan Yang; sqzyyangfan@126.com

Received 19 April 2014; Revised 4 June 2014; Accepted 12 June 2014; Published 6 July 2014

Academic Editor: L. W. Zhang

Copyright © 2014 F. Yang and C. Liu. This is an open access article distributed under the Creative Commons Attribution License, which permits unrestricted use, distribution, and reproduction in any medium, provided the original work is properly cited.

The three-dimensional unsteady numerical method is applied to investigate the pressure fluctuation of the S-shaft extension pumping system. Some monitor pointers are set at the key positions of blade region to capture the changing rules of the pressure pulsations, from which the data are collected through time-domain and spectrum analysis. The predicted head and efficiency were validated by the comparison with the tested results, and the comparison result shows that the unsteady flow characteristic of pumping system can be simulated by this method. The pulsating amplitude decreases gradually from blade tip to hub, under the condition of large flow rate for both the inlet and outlet of the impeller, in the way different from the smaller flow rate condition. Through adjusting the impeller rotation speed and the number of blades, the dominant frequency can be controlled. For the same monitor point at the impeller, as the flow coefficient is becoming larger, the pulsating amplitude decreases, in which case, it decreases firstly and then increases between the impeller and the guide vane, and the pulsating amplitude is smallest on the high efficiency condition. The rotation speed of impeller has little effect on the dominant frequency at the outlet of guide vane.

1. Introduction

Hydraulic model, composed of impeller and guide vane, plays an important role for high performance of hydraulic machinery system, of which the safety and efficiency depend on the hydrodynamic characteristics. The model pressure pulsation of interior flow is very difficult to be measured by traditional experimental equipment. Today, the pressure is often analyzed by numerical simulation. Wang et al. in [1] studied the unsteady flow feature in axial-flow pump based on the Reynolds-averaged Navier-Stokes method and the large eddy simulation method. Shi et al. in [2] applied the standard turbulent $k-\varepsilon$ model and SIMPLEC algorithm to investigate the pressure fluctuation induced by the rotor-stator interactions of the mixed-flow pump. Wu et al. in [3] used the Reynolds-averaged Navier-Stokes equations coupled with the RNG $k-\varepsilon$ turbulent flow of the whole flow passage of a prototype Kaplan turbine. Shi et al. in [4] studied the dynamic pressure gradient model of axial piston and parameters optimization for stabilizing the pressure gradient in pressure rising and control the pressure of piston chamber.

Liu et al. in [5] studied characteristics of pressure pulsation of pump-turbines with misaligned guide vanes based on CFD commercial software. And some other domestic scholars have focused on the study of the pressure pulsation of interior flow in centrifugal pump by numerical simulation and test in [6–10].

In china, research on pressure pulsation of pumping system with low head has become a hotspot. Wang et al. in [11] analyzed the impeller elevation, unsteady flow, hydraulic thrust, and the zero-head flow of the slanted axial pumping system, using fluent software. Zhu et al. in [12] studied pressure pulsation of tubular pump internal pressure pulsation based on large eddy simulation data. Yang and Liu in [13] studied the characteristics of pressure pulsation of mixed-flow pumping system, for irrigation and drainage, through performance test. Given the fact that pressure pulsation of blade region in shaft-extension tubular pumping system is rarely studied domestically, in this paper, taking the S-shaped shaft-extension as the research object, three-dimensional flow field of pumping system has been simulated by the programming of the commercial code ANSYS-CFX; it was

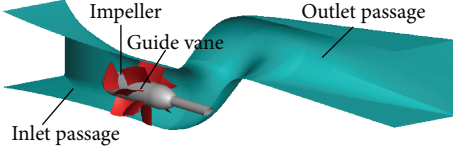


FIGURE 1: Perspective of S-shaped shaft-extension tubular pumping system.

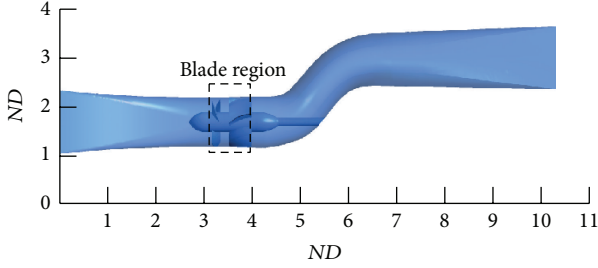


FIGURE 2: Blade region.

analyzed on three different operating conditions, offering a reference for safer and more stable operation of this type of pump.

2. Pumping System Geometry and Numerical Method

Figure 1 shows 3D geometric of S-shaped shaft tubular pumping system model, with specific speed $n_s = 970$ and impeller diameter 300, which is used to simulate and measure its entire flow field. The impeller has 3 blades and the stator has 7 blades. The rotating speed n is 1450 r/min. The average tip clearance of impeller is 0.2 mm at blade angle 0° , which are the same as those of the experimental model. The blade region is defined as Figure 2, N is integer, and D is impeller diameter.

The grid quality in the impeller and guide vane will affect the accuracy of pumping system simulation. Accordingly, H/J/L-type topology structure is applied to the impeller, and H-type topology structure is applied to the guide vane. O-type grid is used at the blade surface region to control boundary layer distribution. Grid refinement is applied to impeller with 18 nodes in the tip clearance. A structured grid system is constructed in the computational domain. Surface grid of every flow component is shown as Figure 3.

Prior to step for analysis of pumping system, in order to determine the optimal number of grids, a preliminary grid dependency test with numbers of nodes ranging from 1000000 to 2200000 is carried out. The computations have shown that grid convergence has been obtained for the performance of the S-shaped shaft-extension tubular pumping system at $K_Q = 0.460$, as shown in Figure 4. With the increase of grid numbers, the head coefficient K_H and efficiency η change greatly at first then change very little gradually. Finally, the appropriate number of grid numbers for the simulation was determined by the preliminary simulation results. In the

present study, grid number 1516416 is selected as the optimum number of grids.

The commercial URANSE-CFD-Solver ANSYS CFX 14.0 was used. ANSYS CFX uses the element based finite volume method and an algebraic multigrid approach. The timestep for the transient calculation (eight impeller revolutions) represented 1 of rotation. So, 2880 timesteps are calculated. Every timestep consisted of 8 to 22 inner coefficient loops. The turbulence effects are modeled by the RNG $k-\varepsilon$ turbulence model. The RNG model provides a way to account for the effects of swirl or rotation by modifying the turbulent viscosity appropriately. A uniform axial velocity based on the mass-flowrate is specific at the inlet for each computation run, and the total pressure at the outlet is set to 1.2 atm. The transient rotor-stator method is used for interface condition between the rotating impeller and stationary diffuser. Scalable wall functions are used to simulate the boundary layers. Adiabatic and hydraulically smooth walls with no slip condition were considered at solid boundaries. Periodic boundaries are set at the blade passage interfaces.

3. Performance Prediction and Results Comparison

3.1. Test Device and Method. Physical model of pumping system is tested in the Hydrodynamic Engineering Laboratory of Jiangsu Province. Physical model is shown in Figure 5. The sketch of the complete test rig is shown in Figure 6. Pumping system head is measured by differential pressure transmitter EJA110A, and measuring sections are chosen in the tanks with the inlet and outlet passages for concluding hydraulic loss of inlet and outlet sections. Torque is measured by ZJ type torque meter, which is transmitted by pump shaft. Flowrate is measured by E-mag type electromagnetic flowmeter.

3.2. Results Comparison. According to test data, the highest efficiency of pumping system is 83.55% at blade angle $\theta = -2^\circ$, with flowrate coefficient K_Q of 0.443 and head coefficient K_H of 0.828. With flowrate coefficient K_Q of 0.478 and head coefficient K_H of 0.887 at blade angle $\theta = 0^\circ$, the efficiency η is 82.57%. Dynamic characteristics prediction method is shown in

$$\begin{aligned} \bar{Q} &= \frac{\sum_{i=1}^M \dot{Q}_i}{M}, & \bar{H} &= \frac{\sum_{i=1}^M \dot{H}_i}{M}, & \bar{P} &= \frac{\sum_{i=1}^M \dot{P}_i}{M}, \\ \bar{\eta} &= \frac{\rho g \bar{Q} \bar{H}}{M}, & K_Q &= \frac{\bar{Q}}{n D^3}, & K_H &= \frac{g \bar{H}}{n^2 D^2}. \end{aligned} \quad (1)$$

The prediction data agree with the experimental head and efficiency, as shown in Table 1. From the predicted results, the maximal deviation of K_H is 3.15%, and the maximal deviation of η is 3.07% in the unsteady simulation. The simulation results agree with test data very well.

To verify the simulation with RNG $k-\varepsilon$ turbulence model and Reynolds time-averaged equation, a comparison between the simulation and experimental results is made, as shown in Figure 7. The position concerning the pressure fluctuations is a measuring point on the outlet section of the inlet passage.

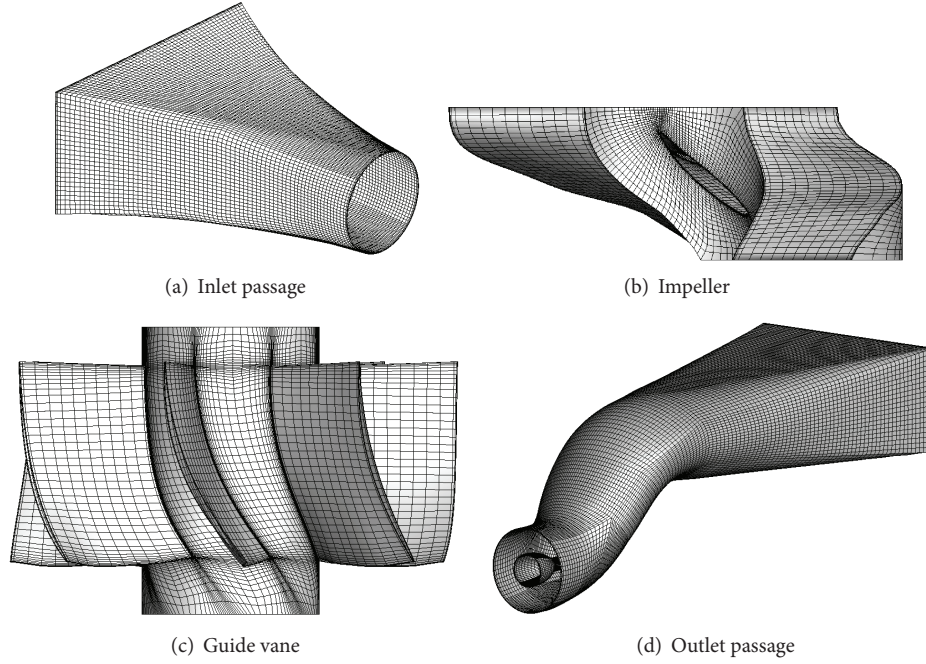


FIGURE 3: Computational grids.

TABLE 1: Experimental and predicted results.

Flow coefficient K_Q	Test results K_H	Unsteady prediction K_H	Deviation/%
0.368	1.249	1.222	2.16
0.402	1.143	1.107	3.15
0.460	0.945	0.964	2.01
0.508	0.761	0.774	1.71
0.552	0.529	0.524	0.95
Flow coefficient K_Q	Test results $\eta/\%$	Unsteady prediction $\eta/\%$	Deviation/%
0.368	69.92	71.10	1.69
0.402	75.72	74.87	1.12
0.460	81.66	81.57	0.11
0.508	81.23	80.47	0.94
0.552	70.02	72.17	3.07

The numerically calculated pressure fluctuation follows the trend very well as compared to the experimental ones. The dominant frequencies and their amplitudes for simulation and experimental results are 72.5 Hz, 0.0530, 72.5 Hz, 0.0491, respectively. This indicated that the simulation with RNG $k-\epsilon$ turbulence model and Reynolds time-averaged equation could be used to predict the pressure fluctuation in the pumping system in the view of engineering.

4. Pressure Pulsation Results and Discussions

To analyze pressure pulsation of blade region, 26 monitoring points are made in the blade region to monitor it and the developing trend thereof. Four groups of measuring points are shown in Figure 8, distributed as 8 measuring points

(P01~P08) in the impeller inlet, 4 measuring points (P09~P16) between the impeller and guide vane, 4 measuring points (P17~P20) inside the guide vane, and 6 measuring points (P21~P26) in the guide vane outlet.

In the analysis of pressure pulsation of blade region, mathematical statistics and spectrum analysis are applied. Hydraulic pressure process is assumed to be a stationary stochastic process for spectrum analysis, and the irregular pressure pulsation is decomposed into many superimposed results of simple harmonic wave, including different amplitudes, frequencies, and phases. Spectrum analysis is adopted by many scholars for pressure pulsation analysis, for it can overcome the shortage of randomness of mathematical statics; in this paper it is used in the blade region, whereby pressure coefficient C_p is defined in [2], and fast Fourier

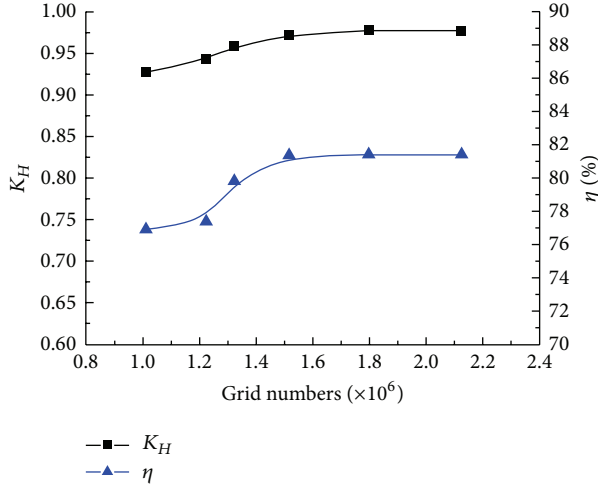


FIGURE 4: Verification of grid independence to prediction of performances.



FIGURE 5: Physical model.

transform (FFT) is applied to show the unsteady pressure features in frequency domain based on the pressure time domain data results of unsteady simulation.

In this calculation model, pressure of pumping system acquired can meet the periodic requirements after 1440 timesteps, whereby the 7th rotating cycle is chosen for the analysis of the unsteady characteristics.

4.1. Pressure Pulsation of Impeller Inlet. The pulsation spectrums of 8 monitoring points in 3 different operating conditions for pumping system in 3 different operating conditions are shown in Figure 9. Pulsation amplitude increases gradually from the hub to the tip in different operating conditions. The pressure coefficient magnitude of monitoring point P01 is 1.381 times that of monitoring point P04, and the pressure coefficient magnitude of monitoring point P08 is 1.379 times that of monitoring point P05 in small flowrate condition $K_Q = 0.368$. The pressure coefficient magnitude of monitoring point P01 is 1.405 times that of monitoring point P04, and the pressure coefficient magnitude of monitoring point P08 is 1.410 times that of monitoring point P05 in high efficiency condition $K_Q = 0.460$. The pressure coefficient magnitude of monitoring point P01 is 1.348 times that of monitoring point P04, and the pressure coefficient magnitude of monitoring point P08 is 1.352 times that of monitoring point P05 in large flowrate condition $K_Q = 0.552$. It is obvious that the trend of pressure amplitude is the same in two sides of impeller inlet. The velocity flow field of impeller

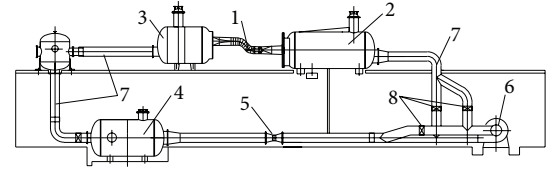


FIGURE 6: Sketch of test rig. (1) Pumping system model, (2) inlet water tank, (3) outlet water tank, (4) surge tank, (5) electromagnetic flowmeter, (6) auxiliary pump, (7) pipeline, and (8) valve.

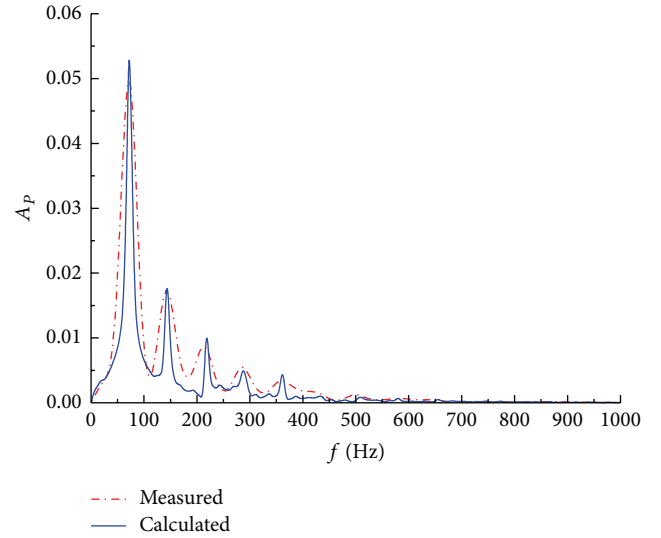


FIGURE 7: Pressure fluctuations for a position in inlet passage.

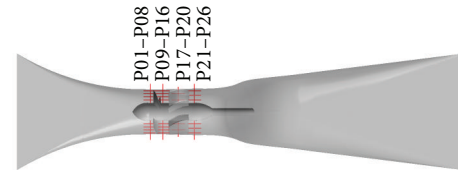


FIGURE 8: Pressure monitoring points.

inlet is symmetric distribution. The rotating of impeller has little effects on the distribution of velocity components at the impeller inlet. For the same monitoring points, pressure pulsation amplitude decreases gradually with the increase of flowrate. The dominant frequency of every monitoring point is 72.5 Hz in impeller inlet, which is equal to the blade passing frequency. Pressure pulsation of impeller inlet is mainly influenced by rotating speed of impeller and blade numbers.

4.2. Pressure Pulsation between Impeller Outlet and Guide Vane Inlet. The pulsation spectrums of P09~P16 are shown in Figure 10. In small flowrate operating condition $K_Q = 0.368$, the relative difference of pressure pulsation is higher for symmetric point, the minimum relative difference is 7.47%, and the maximum relative difference is 19.35%. In high efficiency operating condition $K_Q = 0.460$, the minimum relative difference of symmetric points is 11.76%, and the

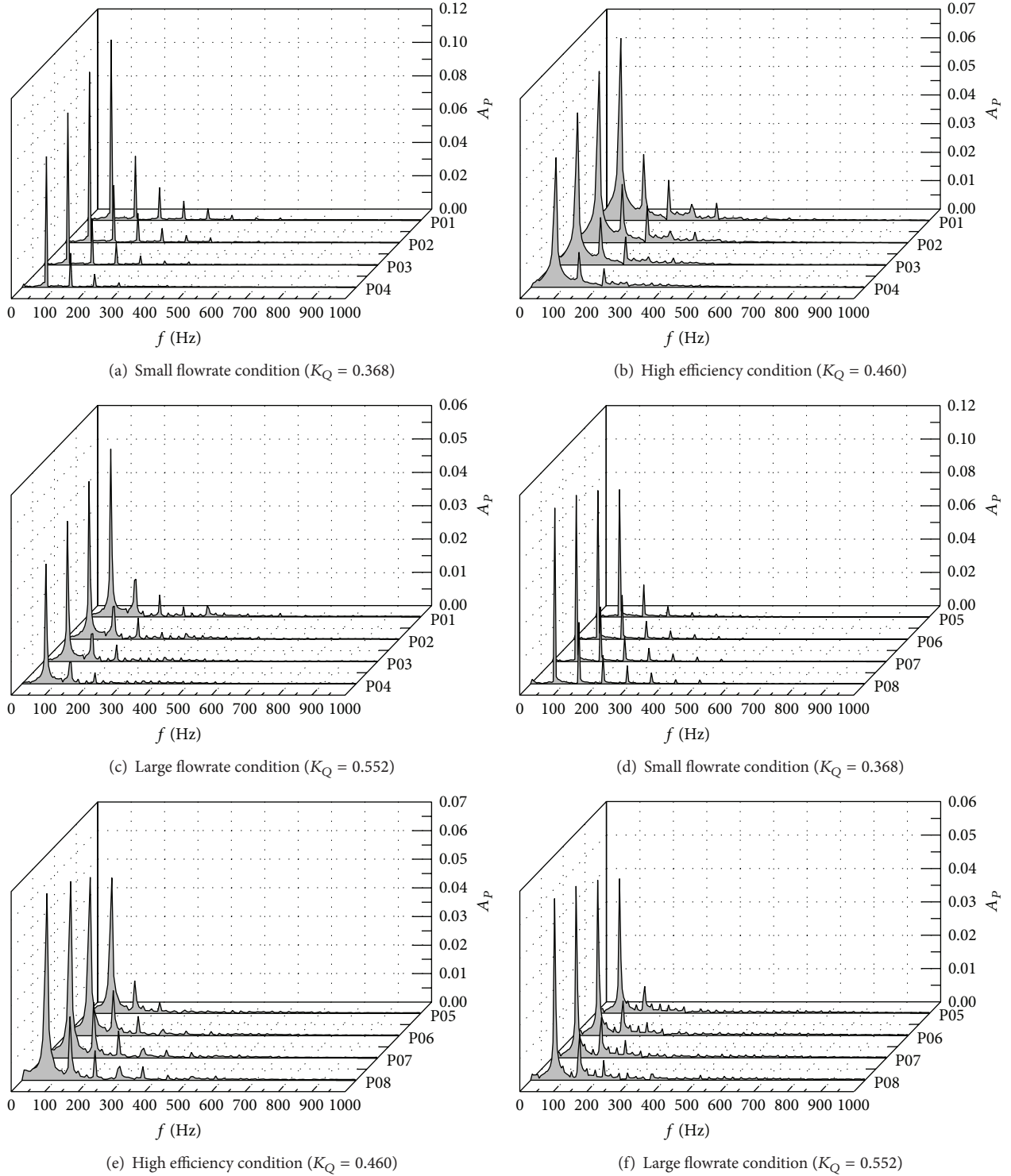


FIGURE 9: The pulsation spectrums of P01~P08 at impeller inlet under different operating conditions.

maximum relative difference is 22.39%. Compared with small flowrate and high efficiency operating conditions, the relative difference of symmetric points is larger in large flowrate operating condition $K_Q = 0.552$; the minimum relative value is 11.81%, and the maximum relative value is 14.56%. The analytic results show that the velocity distribution of impeller

outlet is obviously asymmetric in $K_Q = 0.368$, which is mainly affected by velocity circulation of impeller outlet in this operating condition.

In $K_Q = 0.368$, the pulsation amplitude decreases gradually from P09 to P12, the pulsation amplitude increases firstly then decreases from P16 to P13. The pulsation amplitude

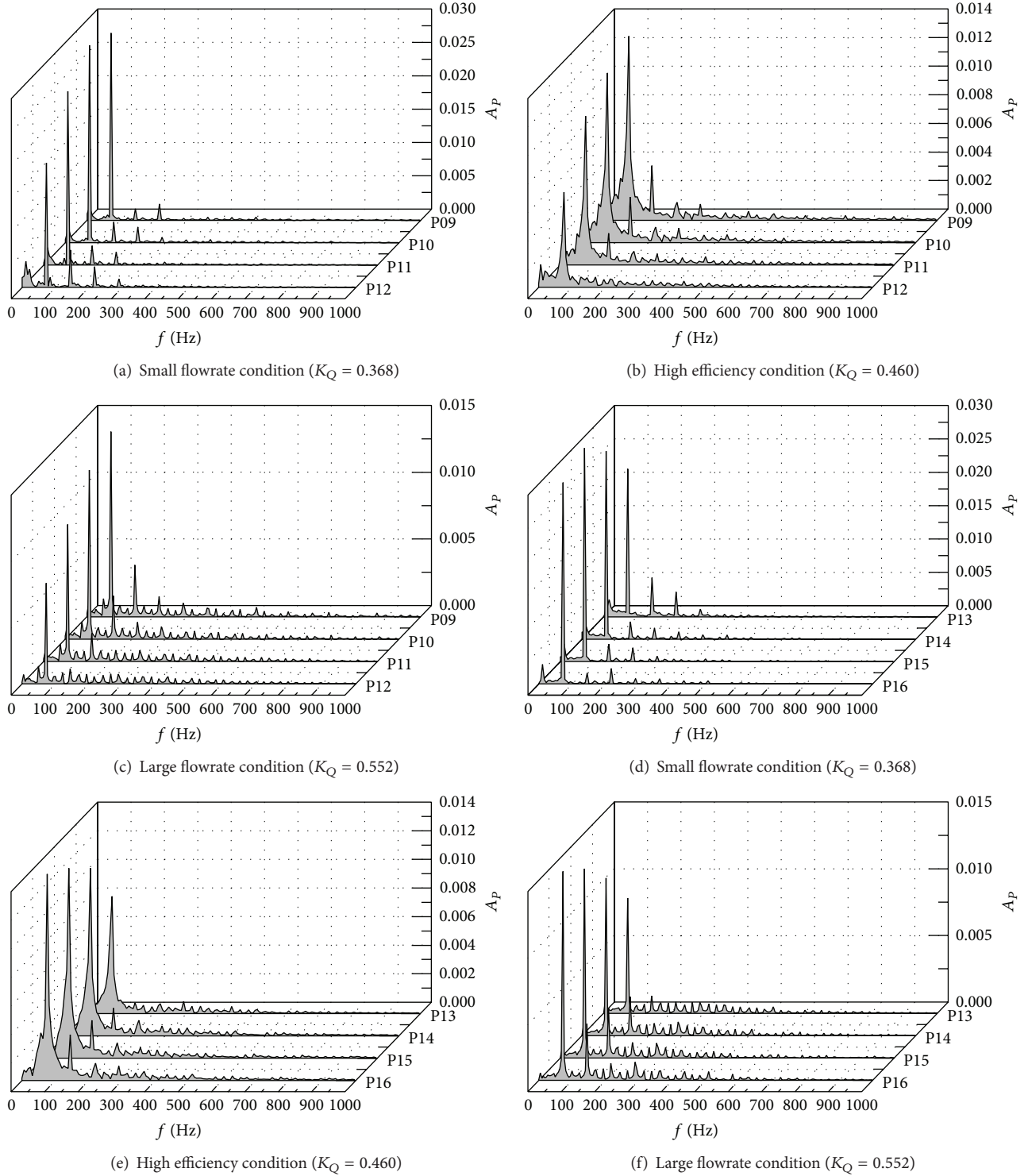


FIGURE 10: The pulsation spectrums of P09~P16 between impeller and guide vane.

decreases gradually from blade tip to hub for monitoring points of the same side in $K_Q = 0.460$ and $K_Q = 0.552$. The internal flow of impeller and guide vane is more complex in small flowrate operating condition, because the characteristic of rotor-stator interaction is very significant. In order to decrease the pressure pulsation between impeller and guide

vane, people should pay attention to select and regulate the pumping system operation conditions. The dominant frequency of P09~P16 is 72.5 Hz, which is affected by both rotation frequency and blade number. The pulsation amplitude of impeller inlet is larger than that between impeller and guide vane in the same operating condition.

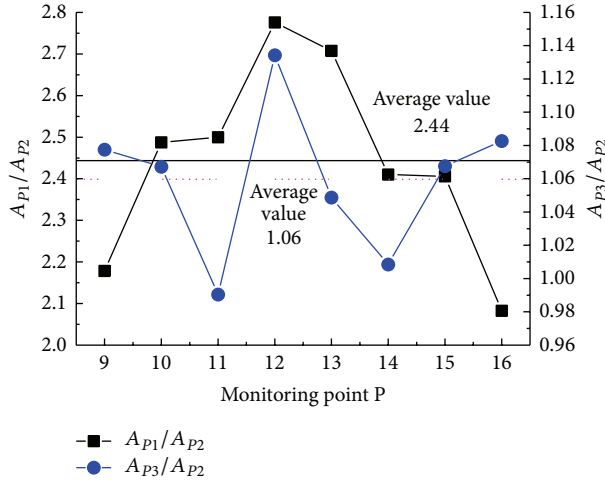


FIGURE 11: The ratio of pressure coefficient amplitude under different conditions.

To further describe change of the pulsation amplitude between impeller and guide vane on three operation conditions, the pressure coefficient amplitude is defined as A_{P1} in $K_Q = 0.368$, the pressure coefficient amplitude is defined as A_{P2} in $K_Q = 0.460$, and the pressure coefficient amplitude is defined as A_{P3} in $K_Q = 0.552$. The pressure coefficient amplitude A_{P2} is used as reference for the same monitoring point in different operating conditions. The calculation results are shown in Figure 11.

In $K_Q = 0.368$, the average value of pressure coefficient amplitude is 2.44 times that in $K_Q = 0.460$ for every monitoring points, and every monitoring point is higher than that in high efficiency operating condition. In $K_Q = 0.552$, the average value of pressure coefficient amplitude is 1.06 times that in $K_Q = 0.460$ for every monitoring point, and every monitoring point is higher than that in high efficiency operating condition except monitoring P09 and P16, while pulsation amplitude of P09 and P16 near blade tip is lower than that in high efficiency operating condition. The pulsation amplitude decreases firstly then increases for monitoring points between impeller and guide vane; in particular, the pulsation amplitude is minimum in high efficiency operating condition.

4.3. Pressure Pulsation of Guide Vane. The pressure pulsation time domain charts and pulsation spectrums of P17~P20 is shown in Figure 12. The results of spectrum analysis for P17~P20 are shown in Table 2, where F1 is dominant frequency and F2 is secondary dominant frequency. The flow of guide vane is far away from impeller outlet, but pressure pulsation of guide vane is affected by impeller rotating. The dominant or secondary frequency of every monitoring point is 72.5 Hz, which is the same as the rotating frequency. Low frequency pulsation is main part of pressure pulsation frequency. The characteristics of pressure pulsation are not obvious, because the internal flow of guide vane is complex. With the flow into guide vane, pressure coefficient amplitude decreases gradually along the flow path, because guide vane

recovers velocity circulation of impeller outlet and makes flow steady. The average pressure pulsation amplitudes in sections of P09~P16 and P17~P20 was taken for example. In $K_Q = 0.368$, the average pressure pulsation amplitude decreases by 16.98% compared with section of P09~P16. The average pressure pulsation amplitude decreases by 65.40% in $K_Q = 0.460$, and the average pressure pulsation amplitude decreases by 70.89% in $K_Q = 0.552$. The velocity circulation of impeller outlet is recovered by guide vane in the high efficiency and large flowrate operating conditions.

4.4. Pressure Pulsation of Guide Vane Outlet. The dominant frequency and pulsation amplitude of P21~P26 are shown in Figure 13 in the three operating conditions of pumping system. In small flowrate coefficient $K_Q = 0.368$, the dominant frequency of P21~P23 is 1.125 times that of rotating frequency, the dominant frequency of P24~P25 is 0.375 times that of rotating frequency, and the dominant frequency of P26 is 0.563 times that of rotating frequency. In high efficiency coefficient $K_Q = 0.460$, the dominant frequency of P21~P23 is 0.563 times that of rotating frequency, the dominant frequency of P24 is 3 times that of rotating frequency, the dominant frequency of P25 is 0.75 times that of rotating frequency, and the dominant frequency of P26 is 0.188 times that of rotating frequency. In large flowrate coefficient $K_Q = 0.552$, the dominant frequency of P21 is 0.882 times that of rotating frequency, the dominant frequency of P22~P25 is 0.176 times that of rotating frequency, and the dominant frequency of P26 is 0.353 times that of rotating frequency. The rotating impeller and blade numbers have little influence on the pressure pulsation of guide vane outlet.

5. Conclusion

The unsteady turbulent flow in the pumping system was simulated based on software ANSYS CFX, and the pressure pulsations of different monitoring points were analyzed. Compared to the test performance results, the unsteady results are in agreement with unsteady prediction results, and the maximal error of unsteady prediction is only 3.15%.

As the flowrate increases, the pressure pulsation amplitude of the same monitoring point decreases gradually in the impeller inlet, and it decreases gradually from blade tip to hub; it is mainly affected by impeller rotating in the impeller inlet, whereby the dominant frequency of this section is 72.5 Hz, 3 times that of rotation frequency.

The pressure pulsation amplitude between impeller and guide vane decreases from blade tip to hub on the high efficiency and large flowrate conditions, while, on the small flowrate condition, the change law from blade tip to hub in the both sides of pump shaft axis is different; it decreases gradually from blade tip to hub in one side and increase earlier then decrease later in another side. The dominant frequency of pressure pulsation between impeller and guide vane is mainly affected by blade numbers and rotation frequency. When $K_Q = (0.368 \sim 0.552)$, the pressure pulsation amplitude decreases at the beginning then increases; it is minimum in the high efficiency area and greatest at the

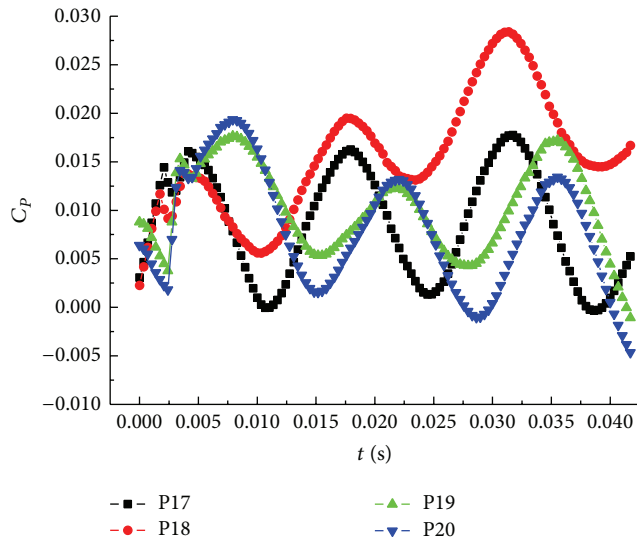
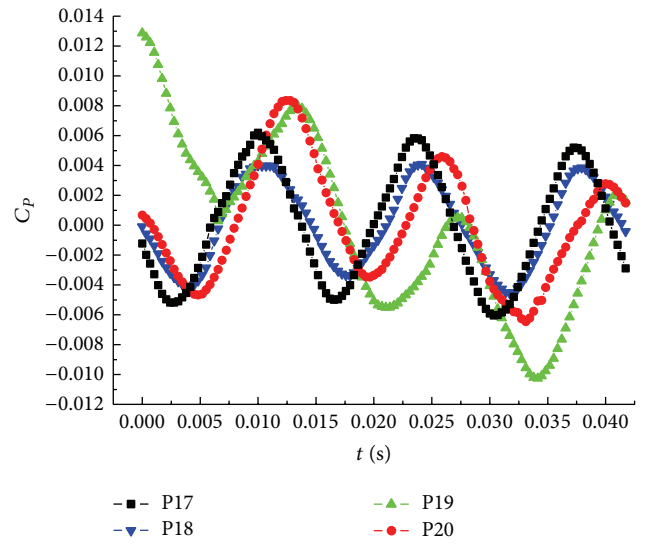
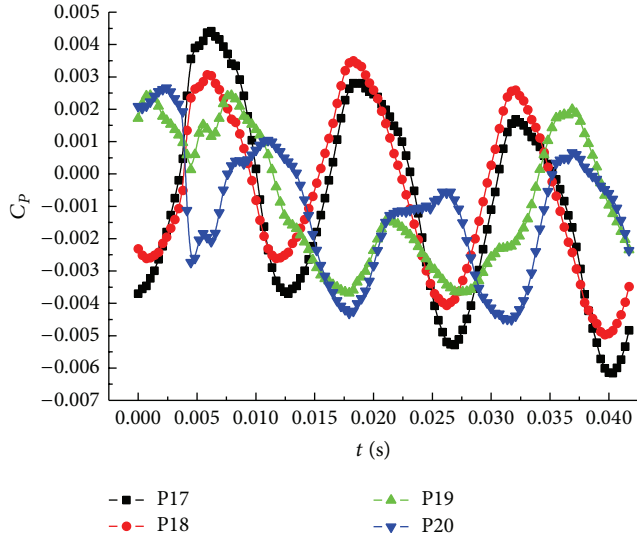
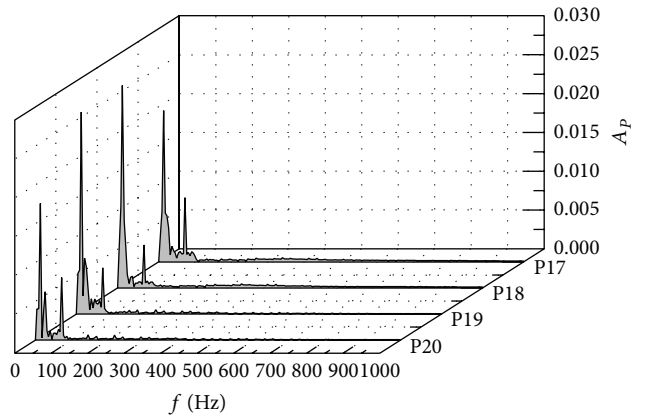
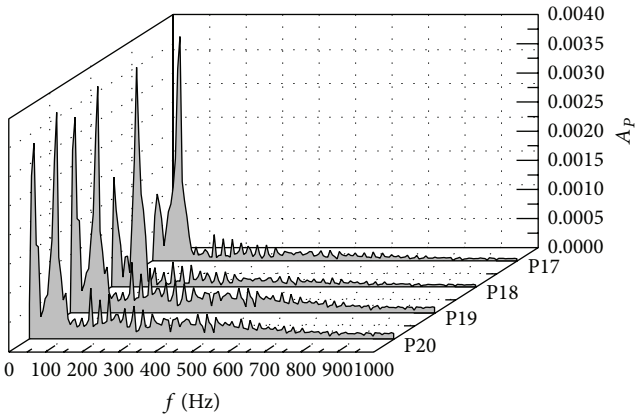
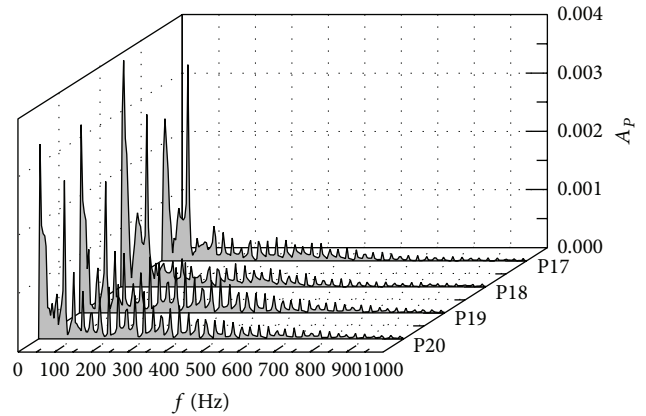
(a) Small flowrate condition ($K_Q = 0.368$)(b) High efficiency condition ($K_Q = 0.460$)(c) Large flowrate condition ($K_Q = 0.552$)(d) Small flowrate condition ($K_Q = 0.368$)(e) High efficiency condition ($K_Q = 0.460$)(f) Large flowrate condition ($K_Q = 0.552$)

FIGURE 12: Time domain and frequency spectra of pressure pulsations of P17~P20.

TABLE 2: Frequency analysis of pressure pulsation of P17~P20.

Flowrate coefficient K_Q	Spectral parameter	P17		P18		P19		P20	
		F1	F2	F1	F2	F1	F2	F1	F2
0.368	f/Hz	13.59	72.50	13.59	72.50	13.59	72.50	13.59	72.50
	A_p	0.0195	0.0083	0.261	0.0055	0.0260	0.0060	0.0176	0.0080
0.460	f/Hz	72.50	66.46	66.46	72.50	72.50	12.08	72.50	12.08
	A_p	0.0039	0.0033	0.0038	0.0026	0.0039	0.0034	0.0039	0.0034
0.552	f/Hz	72.50	8.53	72.50	8.53	4.26	72.50	4.26	72.50
	A_p	0.0034	0.0024	0.0039	0.0030	0.0032	0.0023	0.0033	0.0027

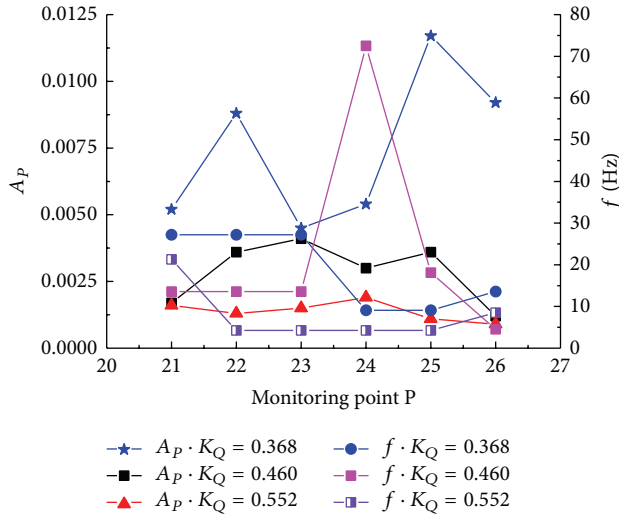


FIGURE 13: Frequency spectra and pressure coefficient amplitude of P21~P26.

impeller inlet, and its average value decreases sharply from the impeller inlet to the guide vane outlet.

The rotation impeller has little influence on the pressure pulsation of guide vane, when the dominant or secondary frequency is 3 times that of rotation frequency. The change of pressure pulsation in the guide vane is not prominent.

Nomenclature

\bar{Q} :	Average flowrate
\dot{Q} :	Static flowrate of every timestep
M :	Total number of timesteps for 1 rotating cycle
\bar{H} :	Average pumping system head
\dot{H} :	Static head of every timestep
\bar{P} :	Average power
\dot{P}_i :	Static power of every timestep
$\bar{\eta}$:	Average efficiency of pumping system
ρ :	Fluid density
g :	Acceleration of gravity
K_Q :	Flowrate coefficient
n :	Rotation speed
D :	Diameter of impeller
K_H :	Head coefficient.

Conflict of Interests

The authors declare that there is no conflict of interests regarding the publication of this paper.

Acknowledgments

This research work was supported by the National Natural Science Foundation of China (Grant nos. 51279173 and 51376155) and the Natural Science Major Program of Jiangsu Provincial Colleges (Grant no. 11KJA570001). Support for construction/assembly of the facility was also provided by the Hydrodynamic Engineering Laboratory of Jiangsu Province.

References

- [1] F.-J. Wang, L. Zhang, Y.-J. Li, and Z.-M. Zhang, "Some key issues of unsteady turbulent numerical simulation in axial-flow pump," *Chinese Journal of Mechanical Engineering*, vol. 117, no. 3, pp. 73–77, 2008.
- [2] W.-D. Shi, P.-P. Zou, D.-S. Zhang, and L. Zhou, "Unsteady flow pressure fluctuation of high-specific-speed mixed-flow pump," *Transactions of the Chinese Society of Agricultural Engineering*, vol. 27, no. 4, pp. 145–152, 2011.
- [3] Y.-L. Wu, S.-H. Liu, H.-S. Dou, S.-F. Wu, and T.-J. Chen, "Numerical prediction and similarity study of pressure fluctuation in a prototype Kaplan turbine and the model turbine," *Computers and Fluids*, vol. 56, pp. 128–142, 2012.
- [4] J. Shi, X. Li, and S.-P. Wang, "Dynamic pressure gradient model of axial piston pump and parameters optimization," *Mathematical Problems in Engineering*, vol. 2014, Article ID 352981, 10 pages, 2014.
- [5] J.-T. Liu, S.-H. Liu, Y.-K. Sun, Y.-L. Wu, and L.-Q. Wang, "Prediction of pressure fluctuation of a pump-turbine at no-load opening," *Journal of Engineering Thermophysics*, vol. 33, no. 3, pp. 411–414, 2012.
- [6] R. Spence and J. Amaral-Teixeira, "Investigation into pressure pulsations in a centrifugal pump using numerical methods supported by industrial tests," *Computers and Fluids*, vol. 37, no. 6, pp. 690–704, 2008.
- [7] G. Pavesi, G. Cavazzini, and G. Ardizzone, "Time-frequency characterization of the unsteady phenomena in a centrifugal pump," *International Journal of Heat and Fluid Flow*, vol. 29, no. 5, pp. 1527–1540, 2008.
- [8] A. E. Khalifa, A. M. Al-Qutub, and R. Ben-Mansour, "Study of pressure fluctuations and induced vibration at blade-passing frequency of a double volute pump," *Arabian Journal for Science and Engineering*, vol. 36, no. 7, pp. 1333–1345, 2011.

- [9] F.-J. Wang, L.-X. Qu, L.-Y. He, and J.-Y. Gao, "Evaluation of flow-induced dynamic stress and vibration of volute casing for a large-scale double-suction centrifugal pump," *Mathematical Problems in Engineering*, vol. 2013, Article ID 764812, 9 pages, 2013.
- [10] R. Barrio, J. Parrondo, and E. Blanco, "Numerical analysis of the unsteady flow in the near-tongue region in a volute-type centrifugal pump for different operating points," *Computers & Fluids*, vol. 39, no. 5, pp. 859–870, 2010.
- [11] Z. Wang, G. Peng, L. Zhou, and D. Hu, "Hydraulic performance of a large slanted axial-flow pump," *Engineering Computations*, vol. 27, no. 2, pp. 243–256, 2010.
- [12] R. Zhu, H. Yan, Q. Fu, and A. Yang, "Numerical calculation of characteristics of tubular pump internal pressure pulsation," *Journal of Hydroelectric Engineering*, vol. 31, no. 1, pp. 220–225, 2012.
- [13] F. Yang and C. Liu, "The flow simulation and experimental study of a large low-head mixed-flow pumping system," *ISRN Mechanical Engineering*, vol. 2013, Article ID 128326, 12 pages, 2013.

Research Article

MINRES Seed Projection Methods for Solving Symmetric Linear Systems with Multiple Right-Hand Sides

Xin Li,¹ Hao Liu,² and Jingfu Zhu³

¹ College of Science, Heilongjiang Bayi Agricultural University, Daqing 163319, China

² College of Science, Nanjing University of Aeronautics and Astronautics, Nanjing 210016, China

³ College of Information Technology, Heilongjiang Bayi Agricultural University, Daqing 163319, China

Correspondence should be addressed to Hao Liu; hliu@nuaa.edu.cn

Received 14 April 2014; Revised 11 May 2014; Accepted 12 May 2014; Published 12 June 2014

Academic Editor: K. M. Liew

Copyright © 2014 Xin Li et al. This is an open access article distributed under the Creative Commons Attribution License, which permits unrestricted use, distribution, and reproduction in any medium, provided the original work is properly cited.

We consider the MINRES seed projection method for solving multiple right-hand side linear systems $AX = B$, where $A \in R^{n \times n}$ is a nonsingular symmetric matrix, $B \in R^{n \times p}$. In general, GMRES seed projection method is one of the effective methods for solving multiple right-hand side linear systems. However, when the coefficient matrix is symmetric, the efficiency of this method would be weak. MINRES seed projection method for solving symmetric systems with multiple right-hand sides is proposed in this paper, and the residual estimation is analyzed. The numerical examples show the efficiency of this method.

1. Introduction

Consider the multiple right-hand side linear systems

$$AX = B, \quad (1)$$

where $A \in R^{n \times n}$ is a nonsingular symmetric matrix, and $B \in R^{n \times p}$.

Equation (1) plays an important role in chemistry, electronics, structures, control, and other problems; see [1, 2] for detail.

In the last few years, the block methods have been developed to solve (1), such as the block conjugate gradient algorithm (BCG) [3], the block generalized minimal residual method [4–6], the block BiCGSTAB method [7], the block QMR method [8], the block least squares method [9], the block Lanczos method [10], and the block IDR(s) method [11] which have been proposed recently. In general, the block methods are faster than solving each one separately.

The meshless methods are extensively used for solving (1); these meshless methods show to be efficient and accurate in terms of their numerical results; see [12–18]. The global methods [19, 20] are also a class of important methods. Following the work [20], many other global methods have been developed, including the global BiCG and global BiCGSTAB

methods [21], the global Hessenberg and global CMRH methods [22], and the polynomial preconditioned global CMRH method [23, 24]. Generally, the global methods are more appropriate for large and sparse systems.

In many practical applications, the right-hand sides are not arbitrary and are very close; then the seed projection methods are often used to solve (1); see [1, 2, 25, 26]. The main idea of this method is selecting one system to be the seed systems firstly, then solving the seed systems by some Krylov subspace method, and creating a Krylov subspace K , then projecting the residual of the other systems, called nonseed systems, onto this Krylov subspace K to get the approximate solutions. The process is repeated with other seed systems until all the systems are solved. The seed projection methods were proposed by Smith et al. [1] for the CG method firstly. When A is unsymmetric, Simoncini and Gallopulos [2] proposed the GMRES seed projection method. Later, a seed method which uses Morgan's Krylov subspace augmented with eigenvectors was presented in [25]. Moreover, the seed method can be used to solve unsymmetric shifted systems with multiple right-hand sides [26]. However, if A is a symmetric matrix, the efficiency of these methods would be weak.

In this paper, we propose the MINRES seed projection method for solving symmetric systems with multiple right-hand sides, and the residual estimation is analyzed.

The paper is organized as follows. In Section 2, we give a quick overview of the GMRES seed projection method. In Section 3, we present the MINRES seed projection method and the residual estimation. In the last section, we show the efficiency of our method by numerical experiments.

2. GMRES Seed Projection Method

In this section, we recall the GMRES seed projection method for solving (1). Details of the algorithm can be found in [2, 25]. We summarize it in the following algorithm.

Algorithm 1 ($X = \text{Gseed}(A, B, X^{(0)}, \varepsilon, m)$). We have the following:

- (1) $X = X^{(0)}$;
- (2) $R = B - AX$;
- (3) for $l = 1, 2, \dots, p$ until all the systems are solved
- (4) $[\sigma, r_\sigma] = \text{SEED}(R)$, $\beta = \|r_\sigma\|_2$;
- (5) for $k = 1, 2, \dots$, until convergence;
- (6) $[V_{m+1}, H] = \text{Arnoldi}(A, r_\sigma)$;
- (7) $\widehat{b}_\sigma = \beta e_1$, where $e_1 = (1, 0, \dots, 0)^T \in R^{m+1}$;
- (8) $\widehat{b}_j = V_{m+1}^T(b_j - Ax_j)$, $j = 1, \dots, p$, $j \neq \sigma$;
- (9) compute y_j by minimizing $\|Hy - \widehat{b}_j\|_2$, $y \in R^m$, $j = 1, \dots, p$;
- (10) $\overline{X} = X + V_m Y$, where $Y = [y_1, \dots, y_p]^T$;
- (11) $\overline{R} = B - A\overline{X}$, $\bar{r}(j) = \|\overline{R}(:, j)\|_2$;
- (12) if $\|\bar{r}(j)\|_2 < \varepsilon$, then delete the j th systems, let w be the number of the j conforming to this condition, and then $p := p - w$;
- (13) if $\|\bar{r}_\sigma\|_2 < \varepsilon$, then delete these seed systems, set $p := p - 1$, and go to 3;
- (14) end(k);
- (15) end(l).

We now make a few descriptions of Algorithm 1. Firstly, we give an initial approximation to the solutions $X^{(0)}$, compute the initial residuals, and select seed systems by a function *SEED*. In this algorithm, *SEED* applied to the R returns σ and r_σ , where σ is the index of column of R having the maximum norm. Secondly, we apply restarted GMRES method for solving the seed systems and function *Arnoldi* applies the Arnoldi procedure to generate an orthogonal basis $V_{m+1} = [v_1, \dots, v_m]$ for the Krylov subspace $K_{m+1}(A, r_\sigma)$. Meanwhile, the nonseed solutions are approximated by projecting the residual $r_j = b_j - Ax_j$ on $K_{m+1}(A, r_\sigma)$ and solving the least square problem $\min_{y_j \in R^m} \|Hy_j - V_{m+1}^T r_j\|_2$. Thirdly, after the seed systems are solved to desired accuracy, new seed systems are selected from the unsolved systems and then the whole procedure is repeated until all the systems are solved. Some

theoretical analysis about the above algorithm can be found in [2, 25].

3. MINRES Seed Projection Method

Based on the MINRES method for solving the symmetric linear systems, in this section, we combine the GMRES seed projection method and the MINRES method and propose the MINRES seed projection method for solving (1). The Arnoldi procedure in GMRES seed projection method is exchanged by Lanczos procedure, and applying the seed projection idea to MINRES method, the MINRES seed projection method is proposed as the following algorithm.

Algorithm 2 ($X = \text{Mseed}(A, B, X^{(0)}, \varepsilon, m)$). We have the following:

- (1) $X = X^{(0)}$;
- (2) $R = B - AX$;
- (3) for $l = 1, 2, \dots, p$ until all the systems are solved;
- (4) $[\sigma, r_\sigma] = \text{SEED}(R)$, $\beta = \|r_\sigma\|_2$;
- (5) for $k = 1, 2, \dots$, until convergence;
- (6) $[Q_{m+1}, \tilde{T}_m] = \text{Lanczos}(A, r_\sigma)$;
- (7) $\widehat{b}_\sigma = \beta e_1$, where $e_1 = (1, 0, \dots, 0)^T \in R^{m+1}$;
- (8) $\widehat{b}_j = V_{m+1}^T(b_j - Ax_j)$, $j = 1, \dots, p$, $j \neq \sigma$;
- (9) compute $d^{(j)}$ by minimizing $\|\tilde{T}_m d - \widehat{b}_j\|_2$, $d \in R^m$, $j = 1, \dots, p$;
- (10) $\tilde{X} = X + Q_m D$, where $D = [d^{(1)}, \dots, d^{(p)}]^T$;
- (11) $\tilde{R} = B - A\tilde{X}$, $\tilde{r}^{(j)} = \|\tilde{R}(:, j)\|_2$;
- (12) if $\|\tilde{r}^{(j)}\|_2 < \varepsilon$, then delete j th system, let w be the number of the j conforming to this condition, and then $p := p - w$;
- (13) if $\|\tilde{r}_\sigma\|_2 < \varepsilon$, then delete this seed systems, set $p := p - 1$, go to 3;
- (14) end(k);
- (15) end(l).

We now make a few descriptions about Algorithm 2. Firstly, we give an initial approximation to the solutions $X^{(0)}$, compute the initial residuals, and select seed systems by a function *SEED*. In this algorithm, *SEED* applied to the R returns σ and r_σ , where σ is the index of column of R having the maximum norm. Secondly, we apply restarted Lanczos method for solving the seed systems and function *Lanczos* applies the Lanczos procedure to generate an orthogonal basis $Q_{m+1} = [q_1, \dots, q_m]$ for the Krylov subspace $K_{m+1}(A, r_\sigma)$. Meanwhile, the nonseed solutions are approximated by projecting the residual $r_j = b_j - Ax_j$ on $K_{m+1}(A, r_\sigma)$ and solving the least square problem $\min_{d^{(j)} \in R^m} \|\tilde{T}_m d^{(j)} - Q_{m+1}^T r_j\|_2$. Thirdly, after the seed systems are solved to desired accuracy, new seed systems are selected from the unsolved systems and then the whole procedure is repeated until all the systems are solved.

According to Algorithm 2, we can get

$$\begin{aligned}\tilde{r}^{(j)} &= b^{(j)} - A\tilde{x}^{(j)} = b^{(j)} - A(x^{(j)} + Q_m d^{(j)}) \\ &= r^{(j)} - AQ_m d^{(j)} = r^{(j)} - Q_{m+1} \tilde{T}_m d^{(j)}\end{aligned}\quad (2)$$

and $Q_{m+1}^T \tilde{r}^{(j)} = Q_{m+1}^T r^{(j)} - \tilde{T}_m d^{(j)}$. In addition, let $P = Q_{m+1} Q_{m+1}^T$ be the orthogonal operator on $K_{m+1}(A, r^{(s)})$. It follows that

$$\begin{aligned}\tilde{r}^{(j)} &= r^{(j)} - AQ_m d^{(j)} = (I - P) r^{(j)} + (P r^{(j)} - AQ_m d^{(j)}) \\ &= (I - P) r^{(j)} + Q_{m+1} (Q_{m+1}^T r^{(j)} - \tilde{T}_m d^{(j)}).\end{aligned}\quad (3)$$

The following property can be attained.

Property 1. The residual $\tilde{r}^{(j)}$ in nonseed systems in Algorithm 2 satisfy

$$\begin{aligned}\|Q_{m+1}^T \tilde{r}^{(j)}\|_2 &= \min_{x \in x^{(j)} + K_m} \|Q_{m+1}^T (b^{(j)} - Ax)\|_2, \\ \|\tilde{r}^{(j)}\|_2^2 &= \|(I - P) r^{(j)}\|_2^2 + \min_{d \in R^m} \|Q_{m+1}^T r^{(j)} - \tilde{T}_m d\|_2^2.\end{aligned}\quad (4)$$

Theorem 3. Set $K_m \equiv K_m(A, r^{(s)})$ as m -dimension Krylov subspace; one has

- (1) for the seed systems: $\tilde{x}^{(s)} \in \{x^{(s)}\} + K_m$, $\tilde{r}^{(s)} \in K_{m+1}$, and $\tilde{r}^{(s)} \perp AK_m \subseteq K_{m+1}$;
- (2) for the nonseed systems: $\tilde{x}^{(j)} \in \{x^{(j)}\} + K_m$, $\tilde{r}^{(j)} \in \{r^{(j)}\} + K_{m+1}$, and $\tilde{r}^{(j)} \perp AK_m$.

Proof. (1) According to the Lanczos method, the conclusion of (1) is right obviously;

(2) since $\tilde{x}^{(j)} = \{x^{(j)}\} + Q_m d^{(j)} \in \{x^{(j)}\} + K_m$, it follows that

$$\tilde{r}^{(j)} = b^{(j)} - A\tilde{x}^{(j)} = r^{(j)} - AQ_m d^{(j)} = r^{(j)} - Q_{m+1} \tilde{T}_m d^{(j)}.\quad (5)$$

Using AQ_m as inner product, we can get

$$\begin{aligned}(AQ_m)^T \tilde{r}^{(j)} &= \tilde{T}_m^T Q_{m+1}^T (r^{(j)} - Q_{m+1} \tilde{T}_m d^{(j)}) \\ &= \tilde{T}_m^T (Q_{m+1}^T r^{(j)} - \tilde{T}_m d^{(j)}).\end{aligned}\quad (6)$$

Since $d^{(j)} = \arg \min_{d \in R^m} \|Q_{m+1}^T r^{(j)} - \tilde{T}_m d\|_2$ is the least squares solution and satisfies the normal equation $\tilde{T}_m^T \tilde{T}_m d^{(j)} = \tilde{T}_m^T Q_{m+1}^T r^{(j)}$, then $(AQ_m)^T \tilde{r}^{(j)} = 0$. \square

4. Numerical Experiments

In order to prove the efficiency of our algorithm, we compare the following methods. (1) MINRES1, it uses MINRES method for solving the multiple right-hand side linear systems one by one and uses the convergent solution of $(j - 1)$ th systems as the iterative initial vector of j th systems when the $(j - 1)$ th systems converge. (2) MINRES2, it uses

MINRES method for solving the multiple right-hand side linear systems one by one, and the initial vector is zero vector. (3) Mseed is MINRES seed projection method.

All numerical experiments are implemented in MATLAB 2009 and run in Intel Pentium Dual T2390 computer. We set $m = 30$; all the tests are stopped as soon as $\|r^{(j)}\|_2 < \varepsilon \equiv 10^{-6}$.

Example 1. A is a 1024×1024 symmetric matrix:

$$A = \begin{bmatrix} 1 & 0.1 & 0.5 & 0.5 & \cdots & 0.5 \\ 0.1 & 2 & 0.1 & & & \\ 0.5 & 0.1 & 3 & 0.1 & & \\ 0.5 & & 0.1 & 4 & \ddots & \\ \vdots & & & & \ddots & 0.1 \\ 0.5 & & & & 0.1 & 1024 \end{bmatrix}.\quad (7)$$

In numerical experiment, the right-hand sides of systems are constructed by two forms as the following, respectively.

Form 1:

$$\begin{aligned}B_1 &= [b^{(1)}, \dots, b^{(p)}], \\ b^{(j)} &\equiv b^{(j)}(t_i) = -\cos\left(5 \cos\left(t_i - \frac{2(j-1)\pi}{128}\right)\right),\end{aligned}\quad (8)$$

where $j = 1, \dots, p$; $t_i = 1 + 0.1(i - 1)$, $i = 1, \dots, n$.

Form 2:

$$\begin{aligned}B_2 &= [b^{(1)}, \dots, b^{(p)}], \quad \text{where } b^{(j)} = Au^{(j)}, \quad u^{(1)} = (1, \dots, 1)^T, \\ u^{(j)} &= j \cdot \cos((2j + i) \times 10^6) \cdot \sin((3(4 - j) + i) \times 10^6), \\ &\quad i = 1, \dots, n, \quad j = 2, \dots, p.\end{aligned}\quad (9)$$

The numerical results are shown in Tables 1 and 2 and the data in bracket is the sum of iterative steps.

In Table 1, the iterative steps of each system are listed and the data in bracket are the sum of iterative steps of all systems. From Table 1, we can know that Mseed can do better than MINRES1 and MINRES2.

Figures 1, 2, and 3 are the convergent curve of three methods, respectively, when the right side is B_1 . And from them, we can see that Mseed can do better than MINRES1 and MINRES2.

Example 2. Next example comes from Matrix Market, and all the matrices are symmetric as shown in Table 3:

$$B_1 = [b^{(1)}, \dots, b^{(p)}], \quad j = 1, \dots, p,\quad (10)$$

where $t_i = 1 + 0.1(i - 1)$, $i = 1, \dots, n$, $B_2 = [b^{(1)}, \dots, b^{(p)}]$, and $b^{(j)} = (1, \dots, 1, \underbrace{0, \dots, 0}_{j-1})^T$.

Let $p = 5$, and the dimensions of projection space $m = 25$ and results of calculation are shown in Table 4.

From Table 4, we can see that Mseed is superior to MINRES method.

TABLE 1: Iterative steps of convergent solution of each system.

Right-hand	Mseed	MINRES1	MINRES2
B_1	(81) 29, 16, 8, 9, 19	(155) 29, 20, 40, 45, 21	(286) 29, 41, 57, 73, 86
B_2	(57) 25, 15, 15, 2, 0	(125) 25, 27, 25, 21, 27	(181) 25, 36, 34, 46, 40

TABLE 2: Convergent time (second) of each method.

Right-hand	Mseed	MINRES1	MINRES2
B_1	17.1720	19.2810	20.8430
B_2	17.0870	18.5620	19.7832

TABLE 3

Matrix name	Order	If diagonal dominance	Conditions number
bcsstm19	817×817	Y	$2.3e + 05$
bcsstk27	1224×1224	N	$7.7e + 04$
bcsstk22	138×138	N	$1.7e + 05$

Example 3. A is a 1000×1000 symmetric matrix:

$$A = \begin{bmatrix} 1 & 0.1 & & & & \\ 0.1 & 2 & 0.1 & & & \\ & 0.1 & 3 & 0.1 & & \\ & & 0.1 & 4 & \ddots & \\ & & & \ddots & \ddots & 0.1 \\ & & & & 0.1 & 1024 \end{bmatrix}. \quad (11)$$

Form 1:

$$B_1 = [b_1, b_2, \dots, b_p], \quad (b_j)_i = -\cos\left(5 \cos\left(i - \frac{2(j-1)\pi}{128}\right)\right), \quad (12)$$

where $j = 1, \dots, p$; $t_i = 1 + 0.1(i-1)$, $i = 1, \dots, n$.

Form 2:

$$B_2 = [b^{(1)}, \dots, b^{(p)}], \quad \text{where } b^{(j)} = Au^{(j)}, \quad u^{(1)} = (1, \dots, 1)^T, \\ u^{(j)} = j \cdot \cos((2j+i) \times 10^3) \cdot \sin((3(4-j)+i) \times 10^3), \\ i = 1, \dots, n, \quad j = 2, \dots, p. \quad (13)$$

The numerical results are shown in Tables 5 and 6 and the data in bracket is the sum of iterative steps.

5. Conclusion

In this paper, we propose the MINRES seed projection method for solving symmetric systems with multiple right-hand sides, and the residual estimation is analyzed. The numerical examples show that our method is effective.

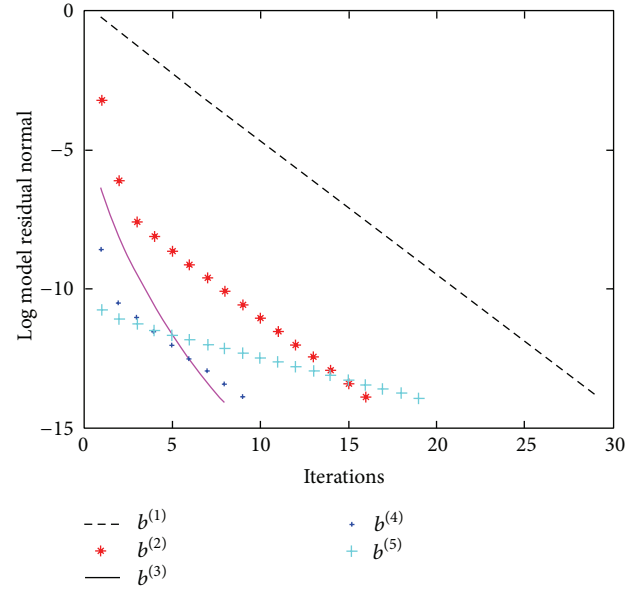


FIGURE 1: MINRES seed projection method.

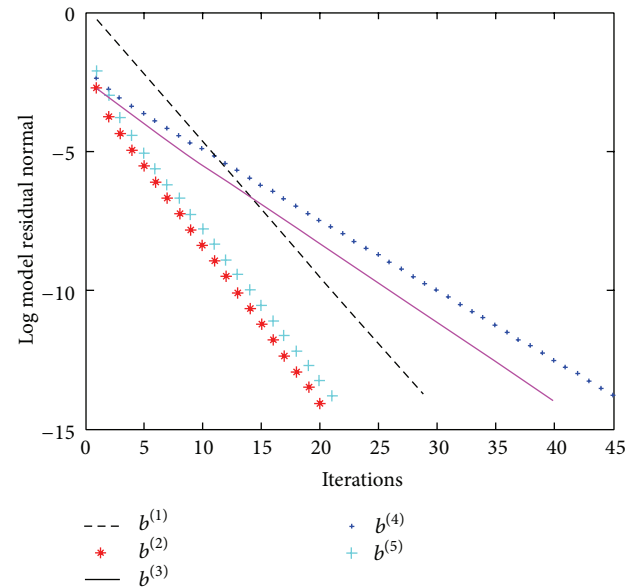


FIGURE 2: MINRES1.

Conflict of Interests

The authors declare that there is no conflict of interests regarding the publication of this paper.

TABLE 4: Convergent iterative steps of each system and CPU time (second).

B	A	Minres seed projection method		Minres2	
		Iterative steps	T1 (s)	Iterative steps	T2 (s)
B_1	bcsstm9	(718) 171, 146, 179, 129, 93	3.13	(980) 171, 201, 241, 191, 176	5.77
	bcsstk27	(781) 211, 187, 154, 124, 105	11.82	(1033) 211, 206, 203, 203, 210	24.98
	bcsstk22	(1833) 984, 574, 142, 119, 14	4.32	(4705) 984, 935, 850, 1014, 922	16.82
B_2	bcsstm9	(475) 175, 124, 62, 68, 46	2.24	(898) 175, 201, 175, 176, 171	5.37
	bcsstk27	(748) 215, 156, 143, 140, 94	11.34	(1079) 215, 216, 216, 216, 216	25.85
	bcsstk22	(2312) 1019, 590, 393, 162, 148	5.33	(5231) 1019, 986, 1079, 1059, 1088	18.85

TABLE 5: Iterative steps of convergent solution of each system.

Right-hand	Mseed	MINRES1	MINRES 2
B_1	(34) 11, 8, 6, 4, 5	(48) 11, 10, 9, 9, 9	(54) 11, 11, 11, 10, 11
B_2	(36) 11, 13, 11, 0, 1	(60) 11, 11, 13, 12, 13	(60) 11, 11, 12, 13, 13

TABLE 6: Convergent time (second) of each method.

Right-hand	Mseed	MINRES1	MINRES2
B_1	4.785072	5.967727	6.053866
B_2	4.934010	5.739067	5.823134

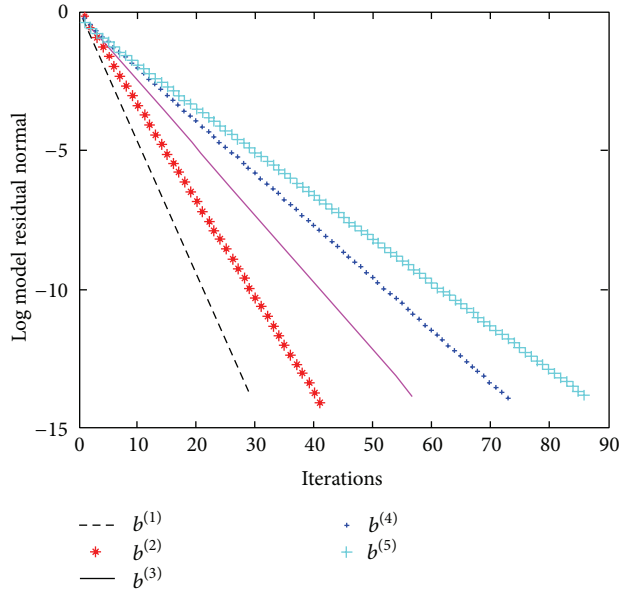


FIGURE 3: MINRES2.

Acknowledgments

The authors would like to express their great thanks to the reviewers, who supplied very good opinions about the paper. The work is supported by the Science and Technology Research Project of Education Department of Heilongjiang Province, no. 12521374.

References

- [1] C. F. Smith, A. F. Peterson, and R. Mittra, "Conjugate gradient algorithm for the treatment of multiple incident electromagnetic fields," *IEEE Transactions on Antennas and Propagation*, vol. 37, no. 11, pp. 1490–1493, 1989.
- [2] V. Simoncini and E. Gallopoulos, "An iterative method for nonsymmetric systems with multiple right-hand sides," *SIAM Journal on Scientific Computing*, vol. 16, no. 4, pp. 917–933, 1995.
- [3] D. P. O'Leary, "The block conjugate gradient algorithm and related methods," *Linear Algebra and Its Applications*, vol. 29, pp. 293–322, 1980.
- [4] B. Vital, *Etude de quelques méthodes résolution de problèmes linéaires de grande taille sur multiprocesseur [Ph.D. thesis]*, Université de Rennes France, Rennes, France, 1990.
- [5] V. Simoncini and E. Gallopoulos, "Convergence properties of block GMRES and matrix polynomials," *Linear Algebra and Its Applications*, vol. 247, pp. 97–119, 1996.
- [6] V. Simoncini and E. Gallopoulos, "Convergence properties of block GMRES and matrix polynomials," *Linear Algebra and Its Applications*, vol. 247, pp. 97–119, 1996.
- [7] A. El Guennouni, K. Jbilou, and H. Sadok, "A block version of BICGSTAB for linear systems with multiple right-hand sides," *Electronic Transactions on Numerical Analysis*, vol. 16, pp. 129–142, 2003.
- [8] R. W. Freund and M. Malhotra, "A block QMR algorithm for non-Hermitian linear systems with multiple right-hand sides," *Linear Algebra and Its Applications*, vol. 254, no. 1–3, pp. 119–157, 1997.
- [9] S. Karimi and F. Toutounian, "The block least squares method for solving nonsymmetric linear systems with multiple right-hand sides," *Applied Mathematics and Computation*, vol. 177, no. 2, pp. 852–862, 2006.
- [10] A. El Guennouni, K. Jbilou, and H. Sadok, "The block Lanczos method for linear systems with multiple right-hand sides," *Applied Numerical Mathematics*, vol. 51, no. 2–3, pp. 243–256, 2004.
- [11] L. Du, T. Sogabe, B. Yu, Y. Yamamoto, and S.-L. Zhang, "A block IDR(s) method for nonsymmetric linear systems

- with multiple right-hand sides,” *Journal of Computational and Applied Mathematics*, vol. 235, no. 14, pp. 4095–4106, 2011.
- [12] L. W. Zhang, P. Zhu, and K. M. Liew, “Thermal buckling of functionally graded plates using a local Kriging meshless method,” *Composite Structures*, vol. 108, pp. 472–492, 2014.
 - [13] K. M. Liew, Z. X. Lei, J. L. Yu, and L. W. Zhang, “Postbuckling of carbon nanotube-reinforced functionally graded cylindrical panels under axial compression using a meshless approach,” *Computer Methods in Applied Mechanics and Engineering*, vol. 268, pp. 1–17, 2014.
 - [14] P. Zhu, L. W. Zhang, and K. M. Liew, “Geometrically nonlinear thermomechanical analysis of moderately thick functionally graded plates using a local Petrov-Galerkin approach with moving Kriging interpolation,” *Composite Structures*, vol. 107, pp. 298–314, 2014.
 - [15] L. W. Zhang, Z. X. Lei, K. M. Liew, and J. L. Yu, “Large deflection geometrically nonlinear analysis of carbon nanotube-reinforced functionally graded cylindrical panels,” *Computer Methods in Applied Mechanics and Engineering*, vol. 273, pp. 1–18, 2014.
 - [16] L. W. Zhang, Z. X. Lei, K. M. Liew, and J. L. Yu, “Static and dynamic of carbon nanotube reinforced functionally graded cylindrical panels,” *Composite Structure*, vol. 111, pp. 205–212, 2014.
 - [17] L. W. Zhang, Y. J. Deng, and K. M. Liew, “An improved element-free Galerkin method for numerical modeling of the biological population problems,” *Engineering Analysis with Boundary Elements*, vol. 40, pp. 181–188, 2014.
 - [18] R. J. Cheng, L. W. Zhang, and K. M. Liew, “Modeling of biological population problems using the element-free kp-Ritz method,” *Applied Mathematics and Computation*, vol. 227, pp. 274–290, 2014.
 - [19] Y. Saad, *Iterative Methods for Sparse Linear Systems*, SIAM, Philadelphia, Pa, USA, 2nd edition, 2003.
 - [20] K. Jbilou, A. Messaoudi, and H. Sadok, “Global FOM and GMRES algorithms for matrix equations,” *Applied Numerical Mathematics*, vol. 31, no. 1, pp. 49–63, 1999.
 - [21] K. Jbilou, H. Sadok, and A. Tinzeft, “Oblique projection methods for linear systems with multiple right-hand sides,” *Electronic Transactions on Numerical Analysis*, vol. 20, pp. 119–138, 2005.
 - [22] M. Heyouni, “The global Hessenberg and CMRH methods for linear systems with multiple right-hand sides,” *Numerical Algorithms*, vol. 26, no. 4, pp. 317–332, 2001.
 - [23] J. Lai, L. Lu, and S. Xu, “A polynomial preconditioner for the CMRH algorithm,” *Mathematical Problems in Engineering*, vol. 2011, Article ID 545470, 12 pages, 2011.
 - [24] K. Zhang and C. Gu, “A polynomial preconditioned global CMRH method for linear systems with multiple right-hand sides,” *Journal of Applied Mathematics*, vol. 2013, Article ID 457089, 7 pages, 2013.
 - [25] G.-D. Gu, “A seed method for solving nonsymmetric linear systems with multiple right-hand sides,” *International Journal of Computer Mathematics*, vol. 79, no. 3, pp. 307–326, 2002.
 - [26] G. D. Gu and W. Y. Zhu, “Seed projection methods for solving unsymmetric shifted systems with multiple right-hand sides,” *Mathematica Numerica Sinica*, vol. 26, no. 2, pp. 211–224, 2004.

Research Article

Numerical Solution of Fractional Integro-Differential Equations by Least Squares Method and Shifted Chebyshev Polynomial

D. Sh. Mohammed

Mathematics Department, Faculty of Science, Zagazig University, Zagazig, Egypt

Correspondence should be addressed to D. Sh. Mohammed; doaashokry203@yahoo.com

Received 10 April 2014; Revised 7 May 2014; Accepted 12 May 2014; Published 12 June 2014

Academic Editor: Kim M. Liew

Copyright © 2014 D. Sh. Mohammed. This is an open access article distributed under the Creative Commons Attribution License, which permits unrestricted use, distribution, and reproduction in any medium, provided the original work is properly cited.

We investigate the numerical solution of linear fractional integro-differential equations by least squares method with aid of shifted Chebyshev polynomial. Some numerical examples are presented to illustrate the theoretical results.

1. Introduction

Many problems can be modeled by fractional Integro-differential equations from various sciences and engineering applications. Furthermore most problems cannot be solved analytically, and hence finding good approximate solutions, using numerical methods, will be very helpful.

Recently, several numerical methods to solve fractional differential equations (FDEs) and fractional Integro-differential equations (FIDEs) have been given. The authors in [1, 2] applied collocation method for solving the following: nonlinear fractional Langevin equation involving two fractional orders in different intervals and fractional Fredholm Integro-differential equations. Chebyshev polynomials method is introduced in [3–5] for solving multiterm fractional orders differential equations and nonlinear Volterra and Fredholm Integro-differential equations of fractional order. The authors in [6] applied variational iteration method for solving fractional Integro-differential equations with the nonlocal boundary conditions. Adomian decomposition method is introduced in [7, 8] for solving fractional diffusion equation and fractional Integro-differential equations. References [9, 10] used homotopy perturbation method for solving nonlinear Fredholm Integro-differential equations of fractional order and system of linear Fredholm fractional Integro-differential equations. Taylor series method is introduced in [11] for solving linear integrofractional differential equations of Volterra type. The authors in [12, 13] give an

application of nonlinear fractional differential equations and their approximations and existence and uniqueness theorem for fractional differential equations with integral boundary conditions.

In this paper least squares method with aid of shifted Chebyshev polynomial is applied to solving fractional Integro-differential equations. Least squares method has been studied in [14–18].

In this paper, we are concerned with the numerical solution of the following linear fractional Integro-differential equation:

$$D^\alpha \varphi(x) = f(x) + \int_0^1 K(x, t) \varphi(t) dt, \quad 0 \leq x, t \leq 1, \quad (1)$$

with the following supplementary conditions:

$$\varphi^{(i)}(0) = \delta_i, \quad n-1 < \alpha \leq n, \quad n \in \mathbb{N}, \quad (2)$$

where $D^\alpha \varphi(x)$ indicates the α th Caputo fractional derivative of $\varphi(x)$; $f(x)$, $K(x, t)$ are given functions, x and t are real variables varying in the interval $[0, 1]$, and $\varphi(x)$ is the unknown function to be determined.

2. Basic Definitions of Fractional Derivatives

In this section some basic definitions and properties of fractional calculus theory which are necessary for the formulation of the problem are given.

Definition 1. A real function $f(x)$, $x > 0$, is said to be in the space C_μ , $\mu \in \mathbf{R}$, if there exists a real number $p > \mu$ such that $f(x) = x^p f_1(x)$, where $f_1(x) \in C[0, 1)$.

Definition 2. A function $f(x)$, $x > 0$, is said to be in the space C_μ^m , $m \in \mathbf{N} \cup \{0\}$, if $f^{(m)} \in C_\mu$.

Definition 3. The left sided Riemann-Liouville fractional integral operator of order $\alpha \geq 0$ of a function $f \in C_\mu$, $\mu \geq -1$, is defined as [19]

$$J^\alpha f(x) = \frac{1}{\Gamma(\alpha)} \int_0^x \frac{f(t)}{(x-t)^{1-\alpha}} dt, \quad \alpha > 0, \quad x > 0, \quad (3)$$

$$J^0 f(x) = f(x). \quad (4)$$

Definition 4. Let $f \in C_{-1}^m$, $m \in \mathbf{N} \cup \{0\}$. Then the Caputo fractional derivative of $f(x)$ is defined as [20–22]

$$D^\alpha f(x) = \begin{cases} J^{m-\alpha} f^{(m)}(x), & m-1 < \alpha \leq m, \quad m \in \mathbf{N}, \\ \frac{D^m f(x)}{Dx^m}, & \alpha = m. \end{cases} \quad (5)$$

Hence, we have the following properties:

- (1) $J^\alpha J^\nu f = J^{\alpha+\nu} f$, $\alpha, \nu > 0$, $f \in C_\mu$, $\mu > 0$,
- (2) $J^\alpha x^\gamma = \frac{\Gamma(\gamma+1)}{\Gamma(\alpha+\gamma+1)} x^{\alpha+\gamma}$, $\alpha > 0$, $\gamma > -1$, $x > 0$,
- (3) $J^\alpha D^\alpha f(x) = f(x) - \sum_{k=0}^{m-1} f^{(k)}(0^+) \frac{x^k}{k!}$,
 $x > 0$, $m-1 < \alpha \leq m$, (6)
- (4) $D^\alpha J^\alpha f(x) = f(x)$, $x > 0$, $m-1 < \alpha \leq m$,
- (5) $D^\alpha C = 0$, C is a constant,
- (6) $D^\alpha x^\beta = \begin{cases} 0, & \beta \in \mathbf{N}_0, \quad \beta < [\alpha], \\ \frac{\Gamma(\beta+1)}{\Gamma(\beta-\alpha+1)} x^{\beta-\alpha}, & \beta \in \mathbf{N}_0, \quad \beta \geq [\alpha], \end{cases}$

where $[\alpha]$ denoted the smallest integer greater than or equal to α and $\mathbf{N}_0 = \{0, 1, 2, \dots\}$.

3. Solution of Linear Fractional Integro-Differential Equation

In this section the least squares method with aid of shifted Chebyshev polynomial is applied to study the numerical solution of the fractional Integro-differential (1).

This method is based on approximating the unknown function $\varphi(x)$ as

$$\varphi_n(x) \cong \sum_{i=0}^n a_i T_i^*(x), \quad 0 \leq x \leq 1, \quad (7)$$

where $T_i^*(x)$ is shifted Chebyshev polynomial of the first kind which is defined in terms of the Chebyshev polynomial $T_n(x)$ by the following relation [23]:

$$T_n^*(x) = T_n(2x-1), \quad (8)$$

and the following recurrence formulae:

$$T_n^*(x) = 2(2x-1)T_{n-1}^*(x) - T_{n-2}^*(x), \quad n = 2, 3, \dots, \quad (9)$$

with initial conditions

$$T_0^*(x) = 1, \quad T_1^*(x) = 2x-1, \quad (10)$$

a_i , $i = 0, 1, 2, \dots$, are constants.

Substituting (7) into (1) we obtain

$$D^\alpha \left(\sum_{i=0}^n a_i T_i^*(x) \right) = f(x) + \int_0^1 K(x, t) \left[\sum_{i=0}^n a_i T_i^*(t) \right] dt. \quad (11)$$

Hence the residual equation is defined as

$$\begin{aligned} R(x, a_0, a_1, \dots, a_n) \\ = \sum_{i=0}^n a_i D^\alpha T_i^*(x) - f(x) - \int_0^1 K(x, t) \left[\sum_{i=0}^n a_i T_i^*(t) \right] dt. \end{aligned} \quad (12)$$

Let

$$S(a_0, a_1, \dots, a_n) = \int_0^1 [R(x, a_0, a_1, \dots, a_n)]^2 w(x) dx, \quad (13)$$

where $w(x)$ is the positive weight function defined on the interval $[0, 1]$. In this work we take $w(x) = 1$ for simplicity. Thus

$$\begin{aligned} S(a_0, a_1, \dots, a_n) \\ = \int_0^1 \left\{ \sum_{i=0}^n a_i D^\alpha T_i^*(x) - f(x) \right. \\ \left. - \int_0^1 K(x, t) \left[\sum_{i=0}^n a_i T_i^*(t) \right] dt \right\}^2 dx. \end{aligned} \quad (14)$$

So, finding the values of a_i , $i = 0, 1, \dots, n$, which minimize S is equivalent to finding the best approximation for the solution of the fractional Integro-differential equation (1).

The minimum value of S is obtained by setting

$$\frac{\partial S}{\partial a_j} = 0, \quad j = 0, 1, \dots, n. \quad (15)$$

Applying (15) to (14) we obtain

$$\begin{aligned} \int_0^1 \left\{ \sum_{i=0}^n a_i D^\alpha T_i^*(x) - f(x) - \int_0^1 K(x, t) \left[\sum_{i=0}^n a_i T_i^*(t) \right] dt \right\} \\ \times \left\{ D^\alpha T_j^*(x) - \int_0^1 K(x, t) T_j^*(t) dt \right\} dx. \end{aligned} \quad (16)$$

By evaluating the above equation for $j = 0, 1, \dots, n$ we can obtain a system of $(n + 1)$ linear equations with $(n + 1)$ unknown coefficients a_i 's. This system can be formed by using matrices form as follows:

$$A = \begin{pmatrix} \int_0^1 R(x, a_0) h_0 dx & \int_0^1 R(x, a_1) h_0 dx & \dots & \int_0^1 R(x, a_n) h_0 dx \\ \int_0^1 R(x, a_0) h_1 dx & \int_0^1 R(x, a_1) h_1 dx & \dots & \int_0^1 R(x, a_n) h_1 dx \\ \vdots & \vdots & \ddots & \vdots \\ \int_0^1 R(x, a_0) h_n dx & \int_0^1 R(x, a_1) h_n dx & \dots & \int_0^1 R(x, a_n) h_n dx \end{pmatrix},$$

$$B = \begin{pmatrix} \int_0^1 f(x) h_0 dx \\ \int_0^1 f(x) h_1 dx \\ \vdots \\ \int_0^1 f(x) h_n dx \end{pmatrix},$$
(17)

where

$$h_j = D^\alpha T_j^*(x) - \int_0^1 K(x, t) T_j^*(t) dt, \quad j = 0, 1, \dots, n,$$

$$R(x, a_i) = \sum_{i=0}^n a_i D^\alpha T_i^*(x) - \int_0^1 K(x, t) \left[\sum_{i=0}^n a_i T_i^*(t) \right] dt,$$

$$i = 0, 1, \dots, n.$$
(18)

By solving the above system we obtain the values of the unknown coefficients and the approximate solution of (1).

4. Numerical Examples

In this section, some numerical examples of linear fractional Integro-differential equations are presented to illustrate the above results. All results are obtained by using Maple 15.

Example 1. Consider the following fractional Integro-differential equation:

$$D^{1/2} \varphi(x) = \frac{(8/3)x^{3/2} - 2x^{1/2}}{\sqrt{\pi}} + \frac{x}{12} + \int_0^1 xt\varphi(t) dt,$$

$$0 \leq x, t \leq 1,$$
(19)

subject to $\varphi(0) = 0$ with the exact solution $\varphi(x) = x^2 - x$.

Applying the least squares method with aid of shifted Chebyshev polynomial of the first kind $T_i^*(x)$, $i = 0, 1, \dots, n$ at $n = 5$, to the fractional Integro-differential

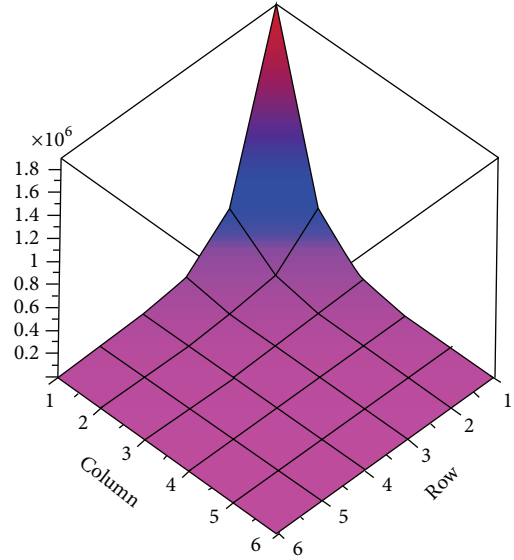


FIGURE 1: The matrix inverse of Example 1.

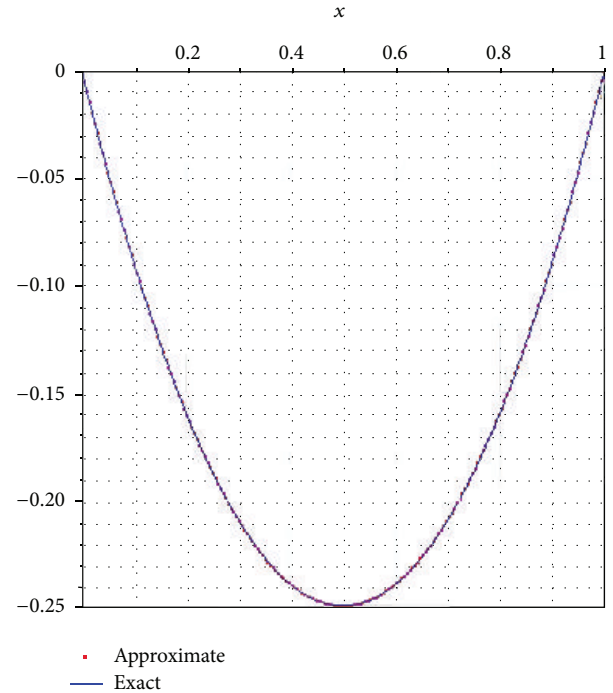


FIGURE 2: Numerical results of Example 1.

equation (19) we obtain a system of (6) linear equations with (6) unknown coefficients a_i , $i = 0, 1, \dots, 5$. This system can be transformed into a matrix equation and by solving this matrix equation we obtain the inverse which is given in Figure 1 and we obtain the values of the coefficients. Substituting the values of the coefficients into (7) we obtain the approximate solution which is the same as the exact solution and the results are shown in Figure 2.

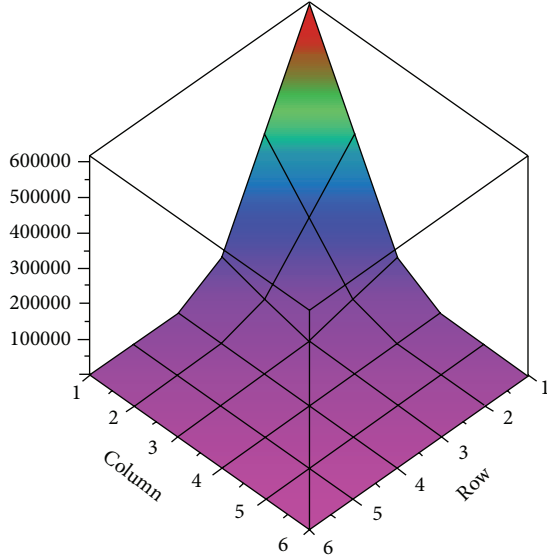


FIGURE 3: The matrix inverse of Example 2.

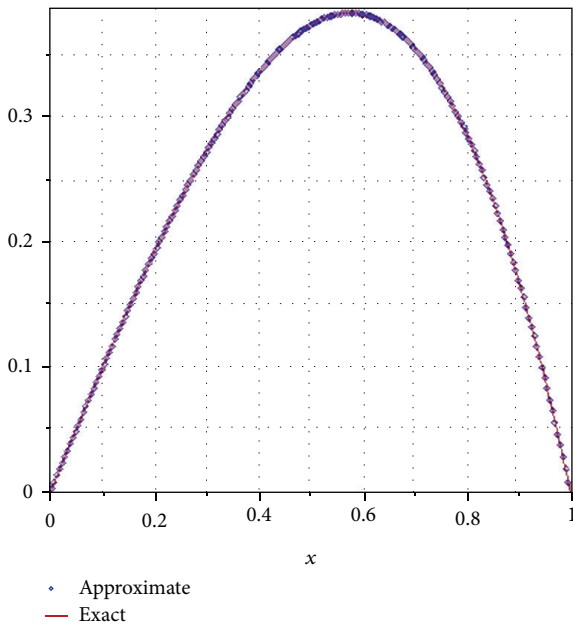


FIGURE 4: Numerical results of Example 2.

Example 2. Consider the following fractional Integro-differential equation:

$$D^{5/6} \varphi(x) = f(x) + \int_0^1 x e^t \varphi(t) dt, \quad 0 \leq x, t \leq 1, \quad (20)$$

subject to $\varphi(0) = 0$, where

$$f(x) = -\frac{3}{91} \frac{x^{1/6} \Gamma(5/6) (-91 + 216x^2)}{\pi} + (5 - 2e)x \quad (21)$$

with the exact solution $\varphi(x) = x - x^3$.

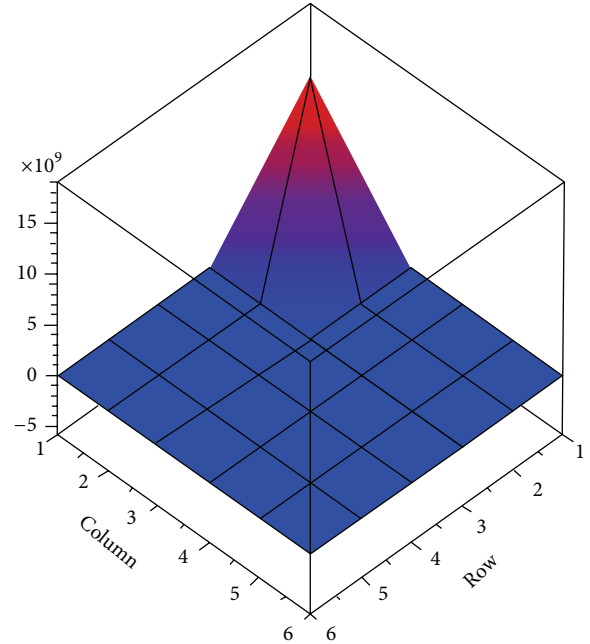


FIGURE 5: The matrix inverse of Example 3.

Similarly as in Example 1 applying the least squares method with aid of shifted Chebyshev polynomial of the first kind $T_i^*(x)$, $i = 0, 1, \dots, n$ at $n = 5$, to the fractional Integro-differential equation (20) the numerical results are shown in Figures 3 and 4 and we obtain the approximate solution which is the same as the exact solution.

Example 3. Consider the following fractional Integro-differential equation:

$$D^{5/3} \varphi(x) = \frac{3\sqrt{3}\Gamma(2/3)x^{1/3}}{\pi} - \frac{1}{5}x^2 - \frac{1}{4}x + \int_0^1 (xt + x^2t^2) \varphi(t) dt, \quad 0 \leq x, t \leq 1, \quad (22)$$

subject to $\varphi(0) = \dot{\varphi}(0) = 0$ with the exact solution $\varphi(x) = x^2$.

Similarly as in Examples 1 and 2 applying the least squares method with aid of shifted Chebyshev polynomial of the first kind $T_i^*(x)$, $i = 0, 1, \dots, n$ at $n = 5$, to the fractional Integro-differential equation (22) the numerical results are shown in Figures 5 and 6 and we obtain the approximate solution which is the same as the exact solution.

5. Conclusion

In this paper we study the numerical solution of three examples by using least squares method with aid of shifted Chebyshev polynomial which derives a good approximation. We show that this method is effective and has high convergency rate.

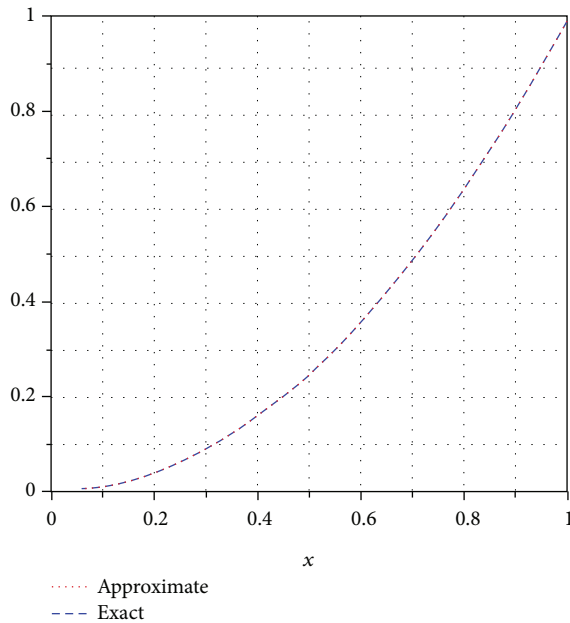


FIGURE 6: Numerical results of Example 3.

Conflict of Interests

The author declares that there is no conflict of interests regarding the publication of this paper.

References

- [1] A. H. Bhrawy and M. A. Alghamdi, "A shifted Jacobi-Gauss-Lobatto collocation method for solving nonlinear fractional Langevin equation involving two fractional orders in different intervals," *Boundary Value Problems*, vol. 2012, article 62, 13 pages, 2012.
- [2] Y. Yang, Y. Chen, and Y. Huang, "Spectral-collocation method for fractional Fredholm integro-differential equations," *Journal of the Korean Mathematical Society*, vol. 51, no. 1, pp. 203–224, 2014.
- [3] A. H. Bhrawy and A. S. Alofi, "The operational matrix of fractional integration for shifted Chebyshev polynomials," *Applied Mathematics Letters*, vol. 26, no. 1, pp. 25–31, 2013.
- [4] E. H. Doha, A. H. Bhrawy, and S. S. Ezz-Eldien, "Efficient Chebyshev spectral methods for solving multi-term fractional orders differential equations," *Applied Mathematical Modelling*, vol. 35, no. 12, pp. 5662–5672, 2011.
- [5] S. Irandoust-pakchin, H. Kheiri, and S. Abdi-mazraeh, "Chebyshev cardinal functions: an effective tool for solving nonlinear Volterra and Fredholm integro-differential equations of fractional order," *Iranian Journal of Science and Technology Transaction A: Science*, vol. 37, no. 1, pp. 53–62, 2013.
- [6] S. Irandoust-pakchin and S. Abdi-Mazraeh, "Exact solutions for some of the fractional integro-differential equations with the nonlocal boundary conditions by using the modification of He's variational iteration method," *International Journal of Advanced Mathematical Sciences*, vol. 1, no. 3, pp. 139–144, 2013.
- [7] S. Saha Ray, "Analytical solution for the space fractional diffusion equation by two-step Adomian decomposition method," *Communications in Nonlinear Science and Numerical Simulation*, vol. 14, no. 4, pp. 1295–1306, 2009.
- [8] R. C. Mittal and R. Nigam, "Solution of fractional integro-differential equations by Adomian decomposition method," *International Journal of Applied Mathematics and Mechanics*, vol. 4, no. 2, pp. 87–94, 2008.
- [9] H. Saeedi and F. Samimi, "He's homotopy perturbation method for nonlinear fredholm integro-differential equations of fractional order," *International Journal of Engineering Research and Applications*, vol. 2, no. 5, pp. 52–56, 2012.
- [10] R. K. Saeed and H. M. Sdeq, "Solving a system of linear fredholm fractional integro-differential equations using homotopy perturbation method," *Australian Journal of Basic and Applied Sciences*, vol. 4, no. 4, pp. 633–638, 2010.
- [11] S. Ahmed and S. A. H. Salh, "Generalized Taylor matrix method for solving linear integro-fractional differential equations of Volterra type," *Applied Mathematical Sciences*, vol. 5, no. 33–36, pp. 1765–1780, 2011.
- [12] J. H. He, "Some applications of nonlinear fractional differential equations and their approximations," *Bulletin of Science, Technology & Society*, vol. 15, no. 2, pp. 86–90, 1999.
- [13] S. A. Murad, H. J. Zekri, and S. Hadid, "Existence and uniqueness theorem of fractional mixed volterra-fredholm integrodifferential equation with integral boundary conditions," *International Journal of Differential Equations*, vol. 2011, Article ID 304570, 15 pages, 2011.
- [14] A. J. Jerri, *Introduction to Integral Equations with Applications*, John Wiley & Sons, London, UK, 1999.
- [15] S. N. Shehab, H. A. Ali, and H. M. Yaseen, "Least squares method for solving integral equations with multiple time lags," *Engineering & Technology Journal*, vol. 28, no. 10, pp. 1893–1899, 2010.
- [16] H. Laeli Dastjerdi and F. M. Maalek Ghaini, "Numerical solution of Volterra-Fredholm integral equations by moving least square method and Chebyshev polynomials," *Applied Mathematical Modelling*, vol. 36, no. 7, pp. 3283–3288, 2012.
- [17] M. G. Armentano and R. G. Durán, "Error estimates for moving least square approximations," *Applied Numerical Mathematics*, vol. 37, no. 3, pp. 397–416, 2001.
- [18] C. Zuppa, "Error estimates for moving least square approximations," *Bulletin of the Brazilian Mathematical Society*, vol. 34, no. 2, pp. 231–249, 2003.
- [19] K. S. Miller and B. Ross, *An Introduction to the Fractional Calculus and Fractional Differential Equations*, A Wiley-Interscience Publication, John Wiley & Sons, New York, NY, USA, 1993.
- [20] A. Arikoglu and I. Ozkol, "Solution of fractional integro-differential equations by using fractional differential transform method," *Chaos, Solitons & Fractals*, vol. 40, no. 2, pp. 521–529, 2009.
- [21] F. Mainardi, "Fractional calculus: some basic problems in continuum and statistical mechanics," in *Fractals and Fractional Calculus in Continuum Mechanics (Udine, 1996)*, vol. 378 of CISM Courses and Lectures, pp. 291–348, Springer, Vienna, Austria, 1997.
- [22] I. Podlubny, *Fractional Differential Equations*, vol. 198 of *Mathematics in Science and Engineering*, Academic Press, San Diego, Calif, USA, 1999, An introduction to fractional derivatives, fractional differential equations, to methods of their solution and some of their applications.
- [23] J. C. Mason and D. C. Handscomb, *Chebyshev Polynomials*, Chapman & Hall/CRC, Boca Raton, Fla, USA, 2003.

Research Article

Structure of Small World Innovation Network and Learning Performance

Shuang Song,^{1,2} Xiangdong Chen,¹ and Gupeng Zhang³

¹ School of Economics and Management, Beihang University, Beijing 100191, China

² Library, Beihang University, Beijing 100191, China

³ College of Technology Management, University of Chinese Academy of Science, Beijing 100049, China

Correspondence should be addressed to Gupeng Zhang; zhanggupeng@163.com

Received 9 April 2014; Accepted 13 May 2014; Published 2 June 2014

Academic Editor: L. W. Zhang

Copyright © 2014 Shuang Song et al. This is an open access article distributed under the Creative Commons Attribution License, which permits unrestricted use, distribution, and reproduction in any medium, provided the original work is properly cited.

This paper examines the differences of learning performance of 5 MNCs (multinational corporations) that filed the largest number of patents in China. We establish the innovation network with the patent coauthorship data by these 5 MNCs and classify the networks by the tail of distribution curve of connections. To make a comparison of the learning performance of these 5 MNCs with differing network structures, we develop an organization learning model by regarding the reality as having m dimensions, which denotes the heterogeneous knowledge about the reality. We further set n innovative individuals that are mutually interactive and own unique knowledge about the reality. A longer (shorter) distance between the knowledge of the individual and the reality denotes a lower (higher) knowledge level of that individual. Individuals interact with and learn from each other within the small-world network. By making 1,000 numerical simulations and averaging the simulated results, we find that the differing structure of the small-world network leads to the differences of learning performance between these 5 MNCs. The network monopolization negatively impacts and network connectivity positively impacts learning performance. Policy implications in the conclusion section suggest that to improve firm learning performance, it is necessary to establish a flat and connective network.

1. Introduction

Many studies have proved that the innovation process has recently become a network process [1]. Innovation network facilitates knowledge sharing, R&D cooperation, and technology complementation between firms, while constraints like distance and culture are playing less important roles. The contacts of firms from different regions and countries are becoming closer, which characterizes the “small world” of innovation network. As the theory of “six-degrees-of-separation” (everyone is six or fewer steps away, by way of introduction, from any other person in the world, so that a chain of “a friend of a friend” statements can be made to connect any two people in a maximum of six steps) proposed by Milgram [2] has been becoming more popular, the closely related theory of “small world” has been receiving much focus [3]. In the small world network, most vertices are far away from each other but could reach each other by passing several other vertices. If we denote the vertices in the small

world network by people, edges between vertices suggest that the two people know each other; then the network where everyone could know each other by a chain of “a friend of a friend” is signified by the phenomenon of “small world.”

The social network is so complex and important that a comprehensive study from the fields of computer science, physics, statistics, sociology, and even economics is carried out [4]. The literature on small worlds has grown rapidly in the social science and management literature [5], like Björneborn [6], Davis et al. [7], Fowler [8], Kogut and Walker [9], Kleinberg [10], Iravani et al. [11], Goyal et al. [12], Baum et al. [13], and Watts [14]. In recent years, many scholars introduced small world theory into innovation network and focused on the “small worldliness” of innovation network, for example, Fleming and Marx [15], Hargadon [16], Chen and Guan [17], Guan and Shi [18], Fleming et al. [19], and Hung and Wang [20]. In a regular innovation network, individuals are constrained by distance and thus can only connect with close neighbors; see Figure 1(a). In small world

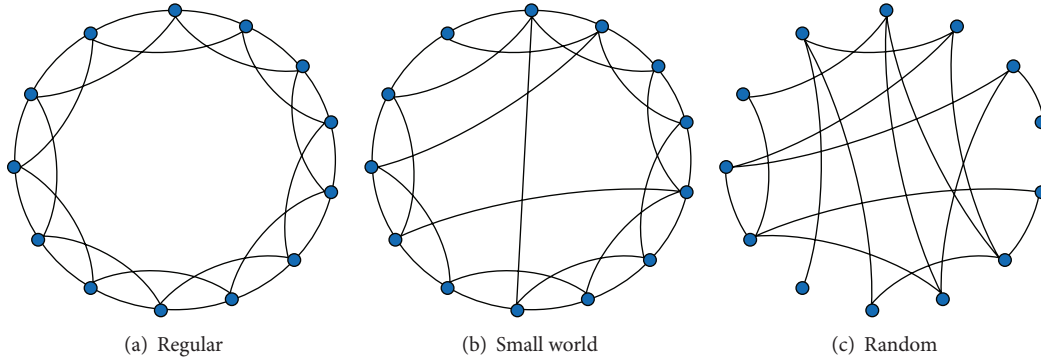


FIGURE 1: Three types of innovation network.

innovation network, minor connections are established by several individuals far from each other; see Figure 1(b). In random innovation network, the connections are totally random and free of distance; see Figure 1(c). Obviously, small world innovation network lies between regular and random innovation networks; that is, most connections are constrained by but some are free of distance. As most real innovation networks lie between regular and random networks, it is common to see small world innovation network, which is playing an important role in the technology progress of firms and even the whole industry [15, 21].

The network system is important to an organization [22, 23]. The structure of small-world networks and of real networks has been probed through the calculation of their diameter as a function of network size [24]. Based on the analysis of the small world network, electric power grid for Southern California, the network of movie-actor collaborations, the neuronal network of the worm *Caenorhabditiselegans* [25], the world-wide web [26], and the network of citations of scientific papers [27, 28], the scale-free network with the distribution of connectivities that decays with a power law tail is proposed. Scale-free networks are also small-world networks, because (i) they have clustering coefficients much larger than random networks [24] and (ii) their path length increases logarithmically with the number of vertices [26]. However, as there are constraints limiting the addition of new links, Amaral et al. [29] suggested that such constraints may be the controlling factor (e.g., aging of vertices and cost of adding new links) for the emergence of scale-free networks; they further presented evidence of the occurrence of three classes of small-world networks according to the constraints: (a) scale-free networks with no constraints, characterized by a vertex connectivity distribution that decays as a power law; (b) broad-scale networks with low constraints, characterized by a connectivity distribution that has a power law regime followed by a sharp cutoff; and (c) single-scale networks with high constraints, characterized by a connectivity distribution with a fast decaying tail (see Figure 2).

It is increasingly acknowledged that network structure plays an important role in explaining the potential of emerging technologies to spread [30–32]. Many studies focused on the patent coauthorship network and the innovation productivity of inventors, for example, Chen and Guan [17],

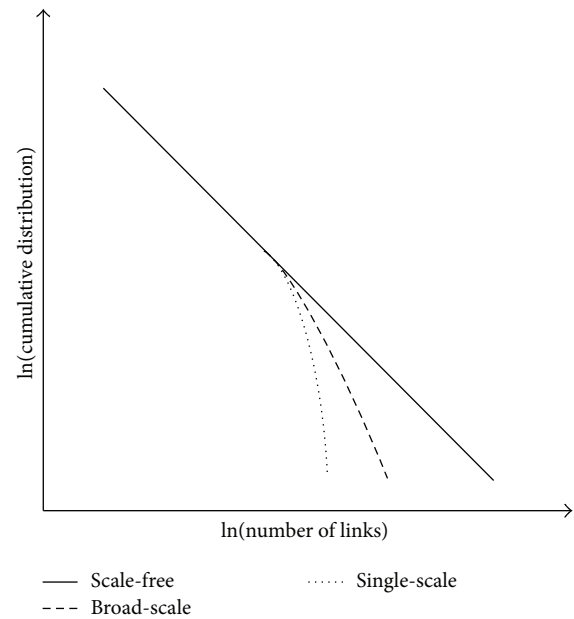


FIGURE 2: Truncation of scale-free connectivity by adding constraints to network.

Fleming et al. [19], and Zhang and Guan [33]. As the patents are mostly coinvented by inventors with complementary knowledge, inventors could gain the necessary knowledge by making a joint research, where the network relationships between inventors are functioning as the intermediaries of knowledge flow. Patent coauthorship network, which reflects the networking relationship between inventors, plays an important role in facilitating the knowledge flow. Inventors are continuously learning from each other through the networks and improve their own knowledge, which in turn improves the organization learning [34].

Networks with different structures would play different roles in improving learning performance [35]. Numerous studies on the network effects between diverse firms have been conducted, focusing on the way in which innovation clusters are continuously achieving competitiveness and improving organization learning performance [36–41]. Finding the effective structure of innovation networks within

the firm may be indicative for firm managers who care about the organization design.

Existing studies may not make an in-depth analysis of the differences of the network structure between firms, leaving an unclear effectiveness of the networks with differing structures. However, measuring and comparing the competitiveness of innovation networks with the real regional firm data may be difficult, since there are other potential multi-impacting factors, for example, R&D input, economic profit, wages, and culture, which make it difficult to identify the effect of innovation networks. With the numerical simulation method, Choi et al. [35] made a comparison of the effectiveness of the innovation networks and found that scale-free network owns the highest learning performance, which is followed by broad-scale and single-scale network. This provided evidence for the significant impact of constraints on network effectiveness, which is proposed by Amaral et al. [29]. However, the structure of real network may differ widely from simulated ones, for example, in real network, most vertices may own relatively low connections, while a small ratio owns relatively high connections. In comparison, most vertices in simulated networks mostly own the same connections. Simulation of the real-world network has been conducted [42–45]. As the structures of real and simulated networks are different, it is necessary to make another empirical study with the real data, so that the learning performance of real networks with different network classification could be studied. This paper contributes to existing literatures by analyzing the real empirical network data with the simulation method. We examine the effectiveness of the real innovation network within the firms with simulation method. This would allow us to exclude other nonnetwork effects and conduct an independent study about the effect of innovation networks. We use the patent coauthorship data in establishing the innovation network and analyze the differences of real network structure and learning performance of 5 selected Chinese companies that filed the largest number of patents in China.

Section 2 classifies the small-world networks. Section 3 presents the computation analysis. Section 4 discusses and Section 5 concludes.

2. Network Modeling

2.1. Small Worldliness. Recent studies mostly utilized two key attributes to measure small world effect: local clustering and global average path length [3]. Clustering coefficient is measured with the number of links with which all neighbors of an inventor are connecting each other, divided by the number of connections among those inventors. For inventor i , the clustering coefficient is

$$CC_i = \frac{\tau_{i,\Delta}}{\tau_{i,3}}, \quad (1)$$

where $\tau_{i,\Delta}$ is the number of triangles that contains inventor i and $\tau_{i,3}$ is the number of connected triples for which the other two inventors are both connected with i . The clustering coefficient (CC) of the network is averaged over all the inventors in the network.

The average path length (PL) is defined to be the average of all the shortest distances between any two inventors. For inventor i , the average path length is

$$PL_i = \frac{1}{n-1} \sum_{j=1, j \neq i}^n (PL_{i,j} + 1), \quad (2)$$

where $PL_{i,j}$ is the number of intermediaries between inventor i and j . If i and j are directly connected, $PL_{i,j} = 0$. The average path length (PL) of the network is averaged over all the inventors in the network.

The small world network is characterized by high local clustering and low distance between inventors, which is distinguished from both random networks that are characterized by low clustering and low average path length and regular networks that are characterized by high clustering and high average path length. However, considering only the real network would be misleading, since the clustering coefficient may be overestimated and the patent length may be underestimated [46]. Following Newman et al. [46] and Humphries and Gurney [47], the CC ratio (CC of the real network/CC of a random network comparison) and PL ratio (PL of the real network/PL of a random network comparison) is introduced so that the estimation could be corrected. The more its CC ratio is greater than 1 and the less its PL ratio, the stronger the small world character is. It is usually measured by the small world quotient (CC ratio/PL ratio) [5, 7, 26]. The larger the quotient is, the greater the network's small world nature is. Humphries et al. [47] and Humphries and Gurney [48] proposed a definition that makes a judgment of the small world network: if PL ratio ≥ 1 and CC ratio $\gg 1$, in other words, CC ratio/PL ratio > 1 , the network is said to be a small world network. Since PL is based on a connected component, both CC and PL are calculated within the largest connected component in this study.

All the indicators, such as CC, PL, and small world quotient, are calculated on the basis of unweighted network. The CC and PL of random network, with both the same number of patents and inventors and equal possibility that two inventors collaborate, are calculated with the method presented by Li et al. [45].

We identify the collaboration of inventors by utilizing the patent coauthorship data; that is, a link is established between two identified inventors as they coinvent a patent. We utilize the patent coauthorship data from SIPO (State Intellectual Property Office of China), which covers a total of over 6 million patents by the year 2011. The number of patents filed during 1992–2010 in SIPO grows at the fastest pace and becomes the second largest database in the world, only less than USPTO (United States Patent and Trademark Office) but greater than JPO (Japanese Patent Office) and EPO (European Patent Office) [18]. The patents in SIPO are classified into 3 categories: invention patent, utility model, and design. Since advanced technologies in China are mostly filed as invention patents [33], we utilize the data of invention patents filed by 5 Chinese companies with the largest number of patent application: two most famous MNCs in IT industry: Huawei and ZTE (Zhongxing Telecommunications Equipment), two largest state-owned MNCs in petroleum industry:

TABLE 1: Summary statistics of patent coauthorship data in the largest connected component.

	Size of largest component ^a	M: number of patents	N: number of inventors	U: average number of patents an inventor filed	V: average number of inventors in a patent
Foxconn	0.5117	6,019	1,839	7.1147	2.1738
Huawei	0.9064	15,690	9,059	4.2328	2.4439
SINOPEC	0.8439	5,210	4,879	5.5433	5.1912
CNPC	0.8061	1,302	3,853	2.4269	7.1820
ZTE	0.9174	11,878	7,050	4.1417	2.4582

^asize of largest component is calculated with the ratio of inventors in the largest connected component to the total inventors.

SINOPEC (China Petroleum & Chemical Corporation) and CNPC (China National Petroleum Corporation), and the large manufacturer Foxconn in China are included.

Since we analyze the innovation network within the company only, we remove the patents coapplied by two or more organizations (mainly composed of companies, universities, and research institutes) from the data, so that the interorganizational network is not taken into account. However, as there are always subsidiaries for large companies, patents coapplied by the parent firm and its subsidiary are included.

People usually own the same name in China, which may mislead the analysis of network structure. It is thus quite necessary but time consuming to distinguish inventors with identical name. However, as we have classified the data by company, it is scarce to see this phenomenon within a company.

The patent data in this study are filed during 2000–2009. Since we study only the largest connected network, we present the summary statistics of only the largest connected component of each company. As is shown in Table 1, the manufacturer Foxconn owns the smallest size numbered at 0.5117, which suggests that the innovation network in Foxconn may not be well connected as there are 48.83% isolated inventors. In comparison, ratio of isolated inventors in the network of IT giants Huawei and ZTE is much lower, which are both lower than 10%. Similarly, the size of largest component of petroleum giants SINOPEC and CNPC is also close.

Although Foxconn owns the fewest inventors, it owns more patents than SINOPEC and CNPC, which suggests that inventors in Foxconn may have done more intensive research and thus filed averagely more patents than the other four companies. In addition, as is shown in the last column, there are on average more inventors cofiling a patent in SINOPEC and CNPC than the others. This may either be because R&D project in petroleum industry requires more cooperative work or because of the bureaucracy of state-owned companies that respect managers by adding their name to the patent, even if they do not contribute to the patent.

In summary, the statistics of largest connected component differs by company. However, they show a similar trend by industry, which suggests that similar industrial invention may lead to common ground of innovation network.

TABLE 2: Small worldliness of innovation network.

	Clustering coefficient	Path length	Small world Q
Foxconn	0.6775	10.4484	1.4443
Huawei	0.6213	5.4428	2.3294
SINOPEC	0.7764	5.3747	2.3893
CNPC	0.8223	6.0095	1.3545
ZTE	0.5544	5.7833	1.8819

As is shown in Table 2, the small world Qs of these 5 MNCs are all greater than 1, which confirms the existence of small world characteristics. CNPC owns a higher clustering coefficient than the other companies, which may facilitate knowledge flow. In comparison, a longer path length between inventors in Foxconn may impede knowledge flow.

2.2. Classification of Network Structure. Differing clustering coefficient, path length, and small world Q suggest different network structures and thus learning performance of 5 companies. We may further investigate this from the perspective of distribution of connections. Since the characteristics of the tail of distribution determine the main effect on learning performance [29, 35], we conduct an in-depth analysis on it. As is shown in Figure 3, the tail of ln-ln cumulative distribution curve of SINOPEC falls on a straight line, indicating an exponential decay of the distribution of connectivities and a broad-scale network according to Amaral et al. [29]. Comparing SINOPEC with an exponential decay, the tails of Huawei and ZTE appear to be falling faster, suggesting a Gaussian decay and broad-scale or single-scale networks. Since both exponential and Gaussian decays indicate that the connectivity distribution is not scale-free [29], we may conclude that there may be inefficiencies in knowledge flow in the real network according to Choi et al. [35].

The cumulative distribution curves of Foxconn and CNPC appear to be complex, with a convex in the tail that dislikes any distribution curve of classified networks mentioned above. Such weird distribution suggests a network with new structure. As is shown in Figure 4, for Foxconn, CNPC, and SINOPEC, there is a flat area in the tail of density curve, which indicates extremely unevenly distributed networks that own minor “super-inventors” who have extremely high connections with other inventors, while for most inventors in the network, the connections are much

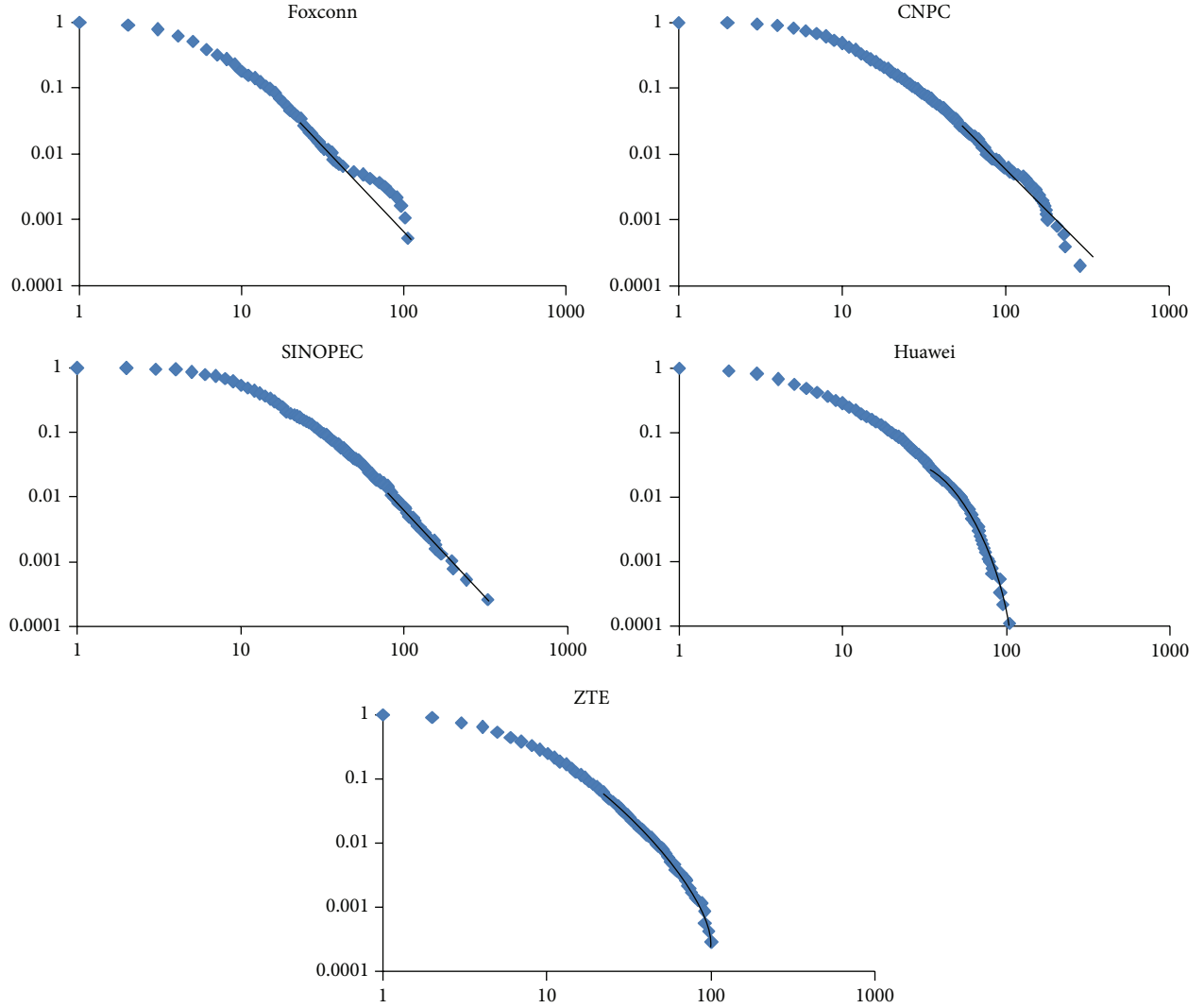


FIGURE 3: In-In cumulative distribution function of connections. x -axis: $\ln(\text{value})$ of inventors' degree as measured by the number of connections to other inventors; y -axis: $\ln(\text{value})$ of cumulative distribution.

fewer. These lead to networks with hierarchical properties. In comparison, this phenomenon is absent from Huawei and ZTE with a smooth density curve, which indicates more evenly distributed networks where there appears to be no “super-inventors.”

As is circled in Figure 4, the scale of the circled flat tails is different. Foxconn owns larger flat tail (0.0049) than CNPC (0.0041), which in turn is larger than SINOPEC (0.0036). A relatively larger flat tail appears to have produced a new structured network, while a relatively smaller flat tail is bound to be scale-free.

Therefore, there is monopolization in terms of technology innovation, which suggests that minor inventors may have controlled most R&D resources and made most inventions by connecting with more other inventors. This monopolization appears to be greater in Foxconn than in CNPC and SINOPEC, while there appears to be no such monopolization in Huawei or ZTE.

2.3. How Important Is Innovation. For firms in different industry, the importance of innovation may be different. As these 5 companies are in different industries, they may make different effort in R&D. Of all these 5 companies, Huawei and ZTE are likely to do more R&D work, since information technology is typically an R&D intensive industry [49]. In petrochemical technology industry in China, SINOPEC and CNPC are also devoted to build up many research institutes and research centers in technology fields of petrochemicals, coal-to-chemicals, commodity polymers, oilfield chemicals, and specialty chemicals (SINOPEC: http://english.sinopec.com/about_sinopec/subsidiaries/research_institutions/20080326/3092.shtml CNPC: <http://www.cnpc.com.cn/en/aboutcnpc/technologyinnovationRandDProgress/>). In comparison, Foxconn, the largest gadget manufacturer in China, is doing more package work for R&D intensive products, for example, iPhone and iPad.

Companies with a greater focus on innovation are more likely to be motivated to improve network efficiency. With

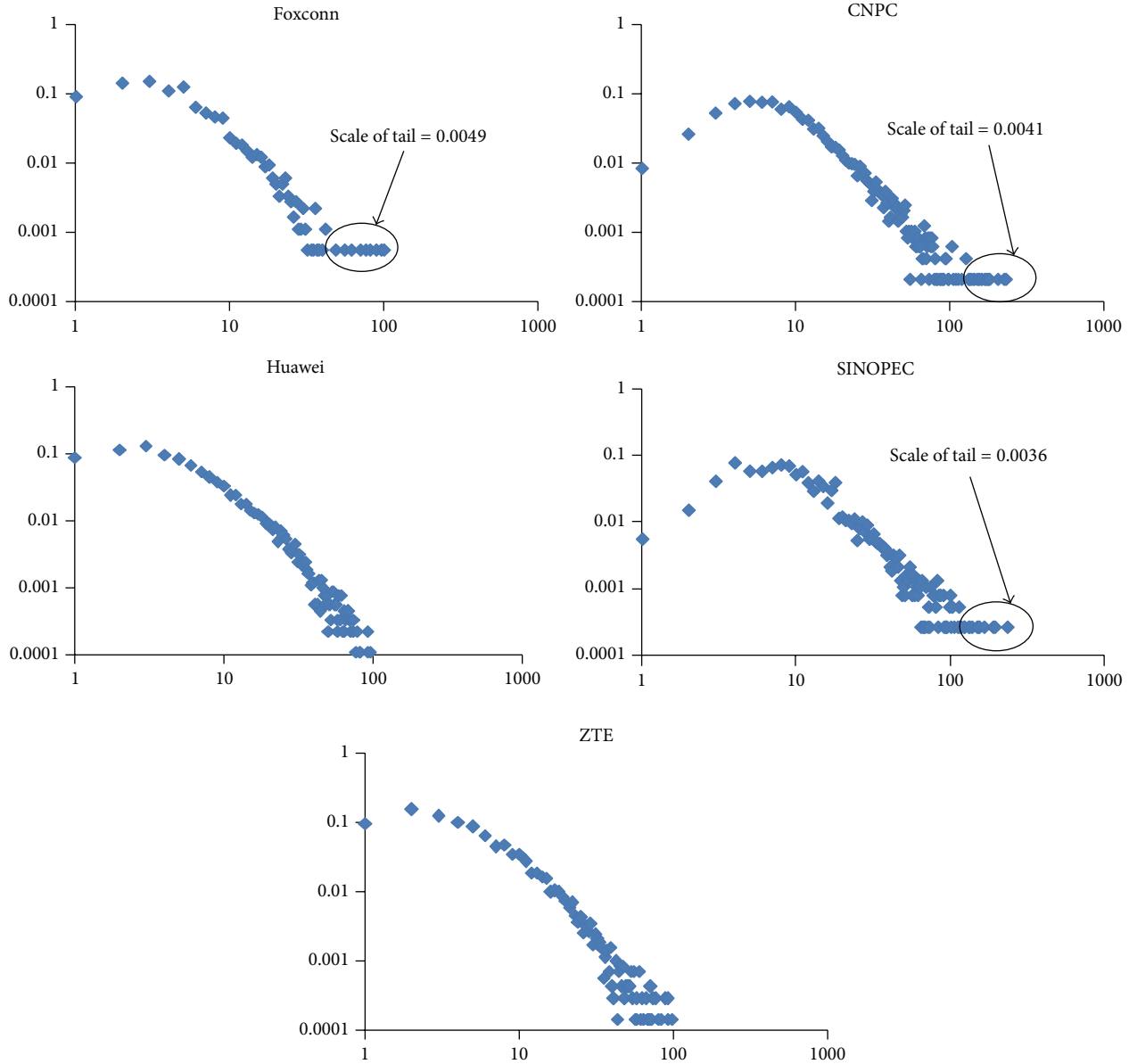


FIGURE 4: In-In density curve of connections (note). Scale of tails is measured with the ratio of circled inventors.

the intention of identifying the importance of innovation by company, we use the data of industrial output and new product output for analysis. Since the value of high tech product is reflected by the market acceptance [50], selected indicators can also reflect the learning performance from the perspective of market value. As is shown in Table 3, although the scale of Foxconn, Huawei, and ZTE is in the same level in terms of industrial output, Foxconn produced much less new product than Huawei and ZTE. In comparison, for the sake of national monopolization, SINOPEC and CNPC own significantly higher industrial output; however, the new product output appears to be in the same level as Huawei and ZTE. In terms of the ratio of new product output, Huawei and ZTE perform better with higher ratio than SINOPEC and CNPC, while Foxconn owns the lowest performance with

lower ratio than the others. As Foxconn do more assembly line production, technology innovation appears to be less important, which makes it less likely to pay much attention to improving the efficiency of innovation network.

Since the ratio of new product output differs by industry and by firms, it is reasonable to conclude that innovation in assembly line manufacturing may thus not be as important as in IT and petroleum industry, which may lead to certain network structures with different effects on learning. Companies that make more effort in R&D work may pay more attention to network design and make more changes that will greatly improve network's performance; thus efficient innovation networks are more likely to be established. On the contrary, manufacturing oriented companies may provide production environment or even set the barriers that impede

TABLE 3: Industrial output and new product output of 5 companies (billion RMB in 2010 price).

	Industrial output	New product output	Ratio of new product output	Year of data included
Foxconn	604.01	3.27	0.0054	2002, 2007, 2009, 2010 ^a
Huawei	466.87	88.64	0.1899	2000, 2002, 2003, 2005–2007, 2009, 2010
SINOPEC	5,147.08	189.01	0.0367	2000, 2002, 2003, 2005–2007, 2009, 2010
CNPC	4,112.46	36.58	0.0089	2000, 2002, 2003, 2005–2007, 2009, 2010
ZTE	164.72	132.13	0.8021	2002, 2003, 2006, 2007, 2009, 2010

Data resources: China Industry Business Performance Data (2001–2011).

^a As the new product output for each company is not recorded all the year, we select the year of data where new product output is recorded.

innovation, so that the rule of standard product manufacturing is followed; thus the structure of innovation network is not likely to be improved.

3. Computation Analysis

With the intention of distinguishing the effectiveness of networks with different structure, we compare firm learning performance by investigating the efficiency of knowledge flow. Let the innovation network be formulated by innovative individuals (denoted by vertex) and their coauthorships (denoted by edge). We use the method of numerical simulation in measuring the effectiveness of knowledge flow based on the real network of 5 companies. In the initial period, we set individuals own heterogeneous knowledge. As the interactions increase, individuals will make a comparison between their own and neighbors' performance. When the individual has lower performance than one of his/her neighbors, he/she is more likely to learn from individuals with higher performance and update his/her own knowledge.

Accordingly, we refer to and extend the organization learning model by March [34]. First, we regard reality as having m dimensions. Since the scale of network to be investigated is relatively large, we extend the sampling interval of each dimension a_s ($s = 1, 2, \dots, m$) by making a_s randomly drawn from the integer set $[-13, -12, -11, -10, -9, -8, -7, -6, -5]$ and $[5, 6, 7, 8, 9, 10, 11, 12, 13]$ with equal probability. Second, we assume there are n innovative individuals that are mutually interactive. The heterogeneous knowledge about the reality is also denoted by a vector with m dimensions, $X_{j,0} = [x_{1,0}, x_{2,0}, \dots, x_{m,0}]$; each dimension will have a value randomly drawn from integer interval $[-13, 13]$ (other intervals do not change our empirical result) with equal probability. The sampling interval of individuals is obviously larger than the reality by adding $[-4, -3, -2, -1, 0, 1, 2, 3, 4]$, which suggests that individual owns no knowledge about the reality in this dimension (March (1991) sets a_s to be randomly drawn from $[-1, 1]$ with equal probability and x_s be randomly drawn from $[-1, 0, 1]$. 0 suggests individual owns no knowledge about the reality in dimension s . Obviously we extend the organization learning model by March (1991) in this study). Since the reality is unknown to any individuals, the knowledge level k_j of individual j is determined by the distance between his/her heterogeneous knowledge and the reality; that is,

$$k_j = \frac{1}{\sum_{s=1}^m (x_{s,j} - a_s)^2}. \quad (3)$$

$(x_{s,j} - a_s)^2$ denotes the distance between j 's heterogeneous knowledge and the reality in dimension s . Obviously, the closer the distance is, the smaller $(x_{s,j} - a_s)^2$ will be and the higher k_j will be. Therefore, a high value of k_j suggests a high level of knowledge.

The knowledge level determines the learning performance to a large extent [34]. However, since the result of innovation activity is highly mobile, it is appropriate to assume that learning performance is a variable and has its own distribution function. March [34] assumed learning performance was normally distributed and argued that higher knowledge level will increase both the expected performance and its variability. March [34] gave an explanation from the perspective of relative competition advantage: if there are $N + 1$ ($N > 1$) innovative individuals, the probability that the $N + 1$ th individual performs better than the other N individuals is usually determined by the area of right hand distribution (which is determined by the variability of performance) of the performance of $N + 1$ th individual. A similar argument can also be found in David [51]. Improving the knowledge level will on the one hand increase the expected performance, but on the other hand will also increase the variability [34]. For example, adoption of a new technology will increase the output theoretically; however, since workers are not familiar with the new technology, the output is more likely to fluctuate in the short run; introducing an individual with heterogeneous knowledge, culture, and attitude into the organization will have a similar effect. As is stated above, it is reasonable to assume that the learning performance y_j of individual j is normally distributed with both expectation and variance being k_j ; that is,

$$y_j \sim N(k_j, k_j^2). \quad (4)$$

In the innovation network, the result of mutually learning process is to a large extent determined by the structural characteristics and network openness [35]. Let individual's openness be denoted by learning rate p , namely, the probability that individual j changes his/her knowledge to i , who owns the highest performance of all j 's partner. We set all the knowledge dimension change independently; then individual j changes his s th dimension knowledge $x_{s,j}$ to i 's $x_{s,i}$ with probability p . A high value of p suggests high openness, which suggests that individual j is more likely to accept knowledge from outside. Choi et al. [35] and March [34] assign the value for p in the interval $[0, 0.9]$. Accordingly, we set p to be 0.1, 0.3, and 0.9 in accordance with the network

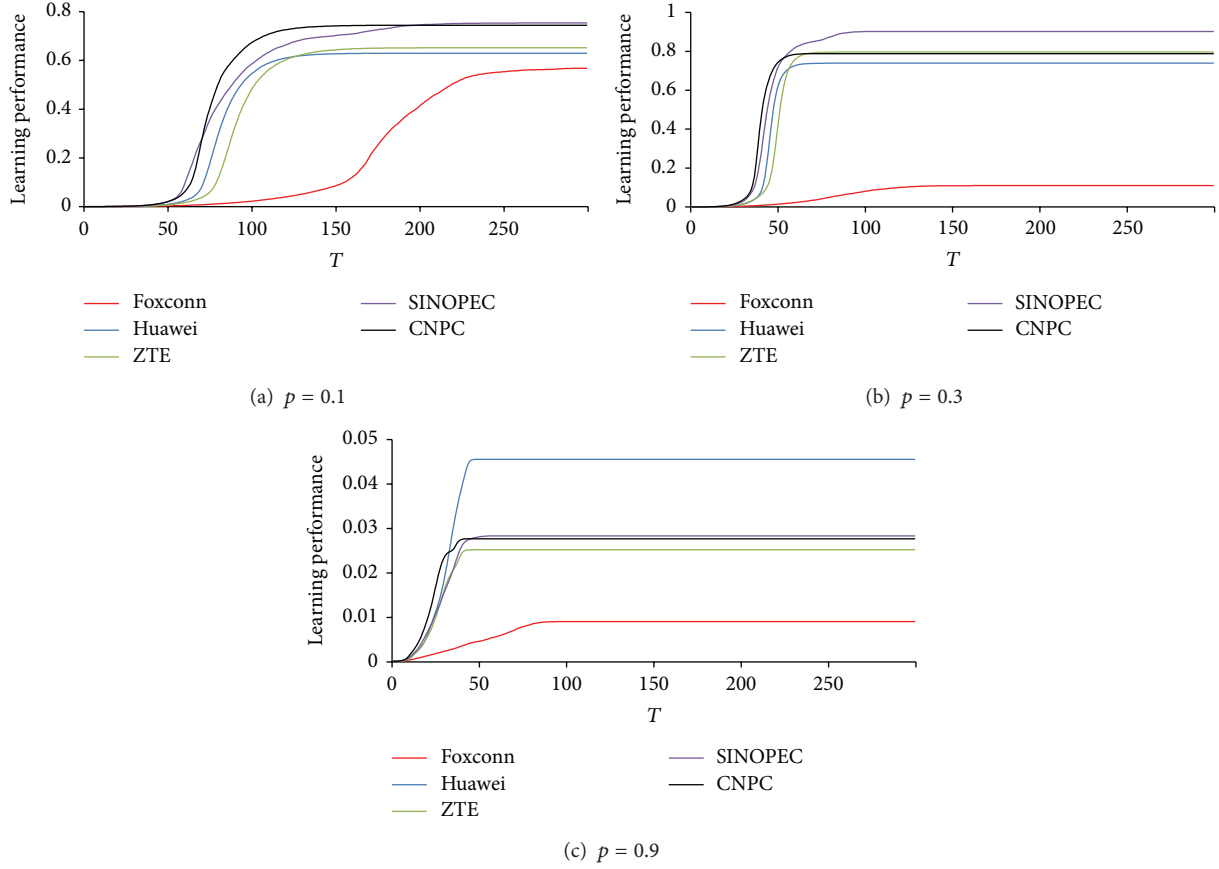


FIGURE 5: Learning performance of network with different openness.

with low, middle, and high openness. We measure the network learning performance \bar{y} by averaging the performance of all individuals in the network; that is, $\bar{y} = \sum_{i=1}^N y_i$. All the empirical results are averaged over 1,000 simulations.

As is shown in Figure 5, the learning performance remains flat in the initial period then rises sharply and converges to a constant value. This trend is similar with Choi et al. [35], whose findings are based on simulated network. Learning performance of networks with lower openness ($p_0 = 0.1$) converges at lower rate but to a higher value; on the contrary, learning performance of networks with higher openness ($p_0 = 0.9$) converges at higher rate but to a much lower value. It appears that network openness contributes positively to convergence rate but negatively to convergence value. This also corresponds with Choi et al. [35], who believe that substantially high openness homogenizes the entire cluster dramatically fast, coming to an equilibrium point before new knowledge is learned that could improve performance, resulting in lower performance throughout the cluster. In comparison, low openness facilitates individuals in achieving higher performance.

Innovation network of Foxconn has the lowest performance with a much lower convergence value than the other 4 networks in all periods. SINOPEC and CNPC own higher learning performance with low network openness, while Huawei owns the highest learning performance with high network openness in later period.

However, the scale of innovation networks of 5 companies is not equal, which may lead to the efficiency differences of knowledge flow between networks. A direct comparison of learning performance should be based on networks with the same scale. Ignoring the network scale may be misleading, for example, learning performance of network with 2 vertices would converge faster at a lower value than network with 10 vertices. However, we may propose that if the real network facilitates knowledge flow much better, it should perform better than other networks with the same scale. Following Davis et al. [7], Newman et al. [46], and Uzzi et al. [5], who estimated the small world quotient of real network by taking into account the random network with the same scale, that is, the same number of edges and vertex, we choose the random network as the reference. We compare the learning performance ratio of real networks, which divides the value of learning performance of real network by the learning performance of random network with the same scale in each period.

As is shown in Figure 6, the converging value of most real networks (except Foxconn) is close to 1 in the later period in Figures 6(a) and 6(b), which suggests that the learning performance of real and random network with low and medium openness is finally almost equal. However, if the openness is high, the converging value of real network is much lower than the random network (see Figure 6(c)). This is because low openness allows individuals to learn from each other for longer periods by delaying the occurrence of

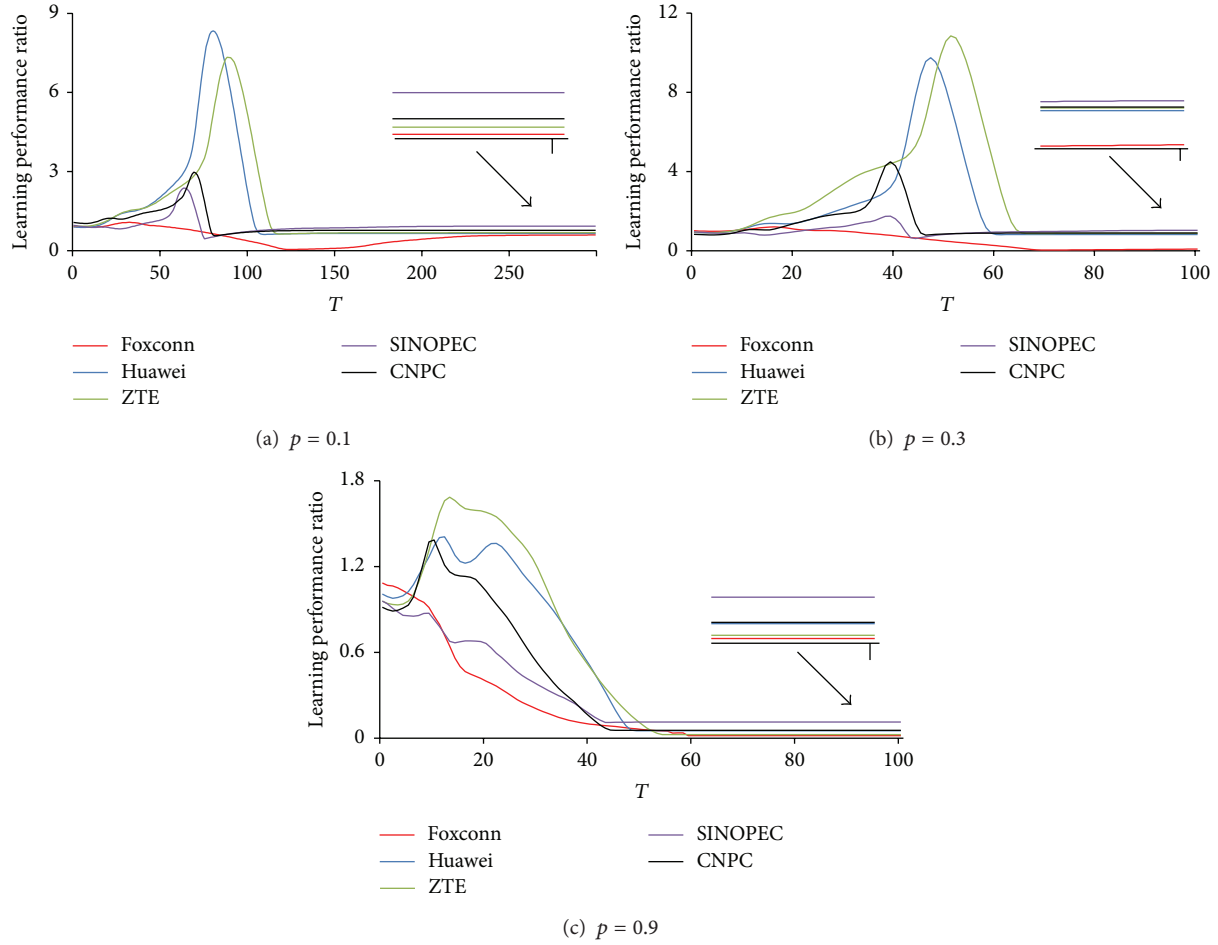


FIGURE 6: Learning performance of network relative to random network.

convergence that terminates knowledge flow. On the contrary, knowledge flow in networks with high openness would stop earlier. In addition, the highest learning performance ratio in preconvergence period in (c) with high openness is also lower than in (a) and (b). As the individuals are closer to each other in random network, knowledge flow would be faster than in real network. Thus earlier convergence would facilitate individuals in random network.

The learning performance ratios of almost all the networks show inverted U shape, which suggests that the learning performance of real network is initially becoming increasingly greater than the random network, but later the differences are becoming smaller.

After being divided by the learning performance of random network, the differences of converging value become smaller. However, the differences are also significant after zooming in the tail of the figure. The network of SINOPEC shows significantly higher convergence value than the other companies in Figures 6(a) and 6(c), while in (b) the differences are smaller. CNPC follows SINOPEC in the innovation convergence period. IT giants Huawei and ZTE are in the middle position. Foxconn owns the lowest converging value in all the network openness.

In initial period, IT giants Huawei and ZTE show much greater learning performance than the other three companies, which suggests that the network structure of Huawei and ZTE benefit knowledge flow better than the other networks in early period. However, they may not converge to higher value compared to the network of SINOPEC and CNPC.

In comparison, learning performance of Foxconn shows the lowest value in all periods, which suggests that the network structure of Foxconn owns the lowest efficiency of knowledge flow compared with the other 4 companies.

4. Discussions

The structure of innovation networks differs widely in reality, which may be the main cause of the differences of learning performance. Huawei and ZTE appear to facilitate learning better than Foxconn, CNPC, and SINOPEC in early period when performance has been increasing (see Figures 5 and 6), while the latter two companies converge to higher learning performance. As the largest manufacturer in China, learning performance in Foxconn appears to be the lowest, which may harm technology innovation according to Shin and Park [52] and Orihata and Watanabe [53]. With a careful analysis,

we may find that the network structure of Foxconn is quite different from the other 4 companies, and also SINOPEC and CNPC are different from Huawei and ZTE, which can be summarized into the following 5 aspects that may be the main cause of learning performance differences.

1st: the innovation network of Foxconn is not well connected, with a smaller size of largest connected component than the other four companies (see Table 1). This would obviously cut the path of knowledge flow and prevent knowledge exchanges between inventors. As inventors are more distant from each other in Foxconn than in the other 4 companies (see Table 2), knowledge flow will have to pass more intermediaries and thus lose efficiency.

2nd: there is network monopolization in Foxconn, CNPC, and SINOPEC, with relatively small ratio of “super-inventors” inventing most technologies (see Figure 4). Since most inventors are connected with these “super-inventors,” innovation networks in the above 3 companies are likely to be hierarchical, where minor inventors account for large ratio of R&D resources by acting as the most important intermediaries of knowledge flow. This network structure may prevent efficient knowledge flow, since inventors with heterogeneous knowledge are not likely to take important positions. People are more likely to learn from “super-inventors” which leads to knowledge homogeneity that harms innovation. This may be another cause of a lower learning performance of Foxconn (see Figures 5 and 6), whose network monopolization is greater than in CNPC and SINOPEC (see Figure 4).

3rd: the network monopolization in SINOPEC leads to a network structure that to some degree harms innovation. As is shown in Figure 6, SINOPEC owns higher performance than Huawei and ZTE in later period, which is mainly due to a scale-free structured network that owns fewer constraints than broad-scale or single-scale networks [29]. However, under the environment of hierarchy characterized by state-run companies, “super-inventor” monopolized networks may harm innovation. This may be the main cause that the learning performance of SINOPEC with scale-free networks falls far behind Huawei and ZTE with broad-scale or single-scale networks in early period, which is different from Choi et al. [35], who found that scale-free network performs better than broad-scale and single-scale networks in all the periods.

4th: the two state-run petroleum giants, SINOPEC and CNPC, have different network structure. The tail of SINOPEC is likely to be scale-free (see Figure 3), while CNPC is not. This may be mainly because CNPC owns higher monopolization level than SINOPEC, which may be the main cause that SINOPEC appears to own more efficient knowledge flow in later period than CNPC (see Figures 5 and 6). However, as a state-run company characterized by bureaucracy, neither SINOPEC nor CNPC could avoid establishing a hierarchical network that suffers efficiency losses.

5th: a relatively flat network structure like Huawei and ZTE (see Figure 4) with R&D resources evenly distributed may facilitate learning. However, as the network appears to be broad-scale or even single-scale, there are still efficiency losses, which make Huawei and ZTE perform worse than SINOPEC and CNPC in later period.

The causes that lead to the differences of network structure may be, on the one hand, the attention paid to the innovation network. As the technology innovation in Foxconn is not so important (see Table 3), it may pay much less attention to improving the network structure and will allow the existence of low efficient innovation network and, on the other hand, the genetic bureaucracy of state-run firms. Although CNPC and SINOPEC pay much attention to innovation, bureaucracy leads to a hierarchical network that is losing efficiency. In addition, since Huawei and ZTE have paid much attention to innovation and are free from bureaucracy, they established relatively efficient innovation networks that facilitate knowledge flow better when learning performance is increasing.

5. Conclusions and Limitations

This paper uses the patent coauthorship data of China in establishing the innovation network of 5 MNCs that filed the largest number of patents in China. The structure of network differs by company and by industry: inventors in the largest Chinese manufacturer Foxconn are more distant from each other, which reduces the network efficiency; the network of petroleum giant SINOPEC is scale-free but connections are hierarchically distributed, while IT giants Huawei and ZTE are broad-scale or single-scale but connections are flatly distributed. We establish the innovation network with the patent coauthorship data by these 5 MNCs and make a classification of these networks according to the distribution curve of connections. We develop an organization learning model by regarding the reality as having m dimensions, which denotes the heterogeneous knowledge about the reality. We set n mutually interactive innovative individuals, who own unique knowledge about the reality. The distance between the knowledge of the individual and the reality denotes the knowledge level of that individual. In the empirical analysis section, we make 1,000 numerical simulations by randomly assigning values to each dimension and get the learning performance of these 5 MNCs. We then make a comparison of the learning performance of these 5 MNCs with differing network structures, where individuals interact with and learn from each other within the small world network. The empirical result shows that different network structures lead to differing learning performance: Huawei and ZTE perform better in early period, which is attributed to a flat distribution of connections that allows inventors with heterogeneous knowledge to take important positions. However, as the networks of Huawei and ZTE are broad-scale or single-scale, efficiency losses are significant in later period. The learning performance of Huawei and ZTE appears to be lower than SINOPEC with scale-free network in later period. In comparison, for Foxconn where technology innovation is less important, the learning performance is the lowest.

Our empirical finding is implicative for company managers from the following aspects. (1st) As carefully and well organized networks (e.g., Huawei, ZTE, CNPC, and SINOPEC with much focus on innovation) would show higher efficiency in knowledge flow and thus perform better

than randomly organized networks, and with not well organized networks (e.g., Foxconn with less focus on innovation), it is quite necessary to make a careful reorganization of the innovation network, even for firms where innovation is less important. (2nd) Since network monopolization may be harmful to innovation, it is beneficial to transfer a hierarchical network to a flat network, where R&D resources are evenly distributed among inventors. (3rd) Since perfectly scale-free networks may never exist in reality, making firm innovation network structure closer to scale-free may be more favorable.

As the learning performances of inventors within the network are simulated, how simulation results correspond with the real learning performance is not analyzed in this study. As the real learning performance is determined by multireal factors, it is necessary to conduct a survey with inventors about these potential impacting factors. Our future attention would possibly be paid to testing the consistency of the simulated learning performance with the survey data of these 5 firms.

Conflict of Interests

The authors declare that there is no conflict of interests regarding the publication of this paper.

Acknowledgments

This work is supported by the National Natural Science Foundation of China (NSFC: 71173009), Beijing Natural Science Foundation (9144036), and Ministry of Education, Humanities and Social Sciences Project (13YJC630219).

References

- [1] M. Dodgson and R. Rothwell, *Handbook of Industrial Innovation*, Edward Elgar, Cheltenham, UK, 1994.
- [2] S. Milgram, "The small world problem," *Psychology Today*, no. 1, pp. 60–67, 1967.
- [3] D. J. Watts and S. H. Strogatz, "Collective dynamics of "small-world" networks," *Nature*, vol. 393, no. 6684, pp. 440–442, 1998.
- [4] T. Hellmann and M. Staudigl, "Evolution of social networks," *European Journal of Operational Research*, vol. 234, no. 3, pp. 583–596, 2014.
- [5] B. Uzzi, L. A. Amaral, and F. Reed-Tsochas, "Small-world networks and management science research: a review," *European Management Review*, no. 4, pp. 77–91, 2007.
- [6] L. Björneborn, "'Mini small worlds' of shortest link paths crossing domain boundaries in an academic Web space," *Scientometrics*, vol. 68, no. 3, pp. 395–414, 2006.
- [7] G. F. Davis, M. Yoo, and W. E. Baker, "The small world of the American corporate elite, 1982–2001," *Strategic Organization*, vol. 1, no. 3, pp. 301–326, 2003.
- [8] J. H. Fowler, "Turnout in a small world," in *Social Logic of Politics*, A. Zuckerman, Ed., Temple University Press, Philadelphia, Pa, USA, 2005.
- [9] B. Kogut and G. Walker, "The small world of Germany and the durability of national networks," *American Sociological Review*, vol. 66, no. 3, pp. 317–335, 2001.
- [10] J. Kleinberg, "Navigation in a small world-It is easier to find short chains between points in some networks than others," *Nature*, vol. 406, p. 845, 2000.
- [11] S. M. Iravani, B. Kolfal, and M. P. Van Oyen, "Call-center labor cross-training: it's a small world after all," *Management Science*, vol. 53, no. 7, pp. 1102–1112, 2007.
- [12] S. Goyal, M. J. van der Leij, and J. L. Moraga-González, "Economics: an emerging small world," *Journal of Political Economy*, vol. 114, no. 2, pp. 403–412, 2006.
- [13] J. A. C. Baum, A. V. Shipilov, and T. J. Rowley, "Where do small worlds come from?" *Industrial and Corporate Change*, vol. 12, no. 4, pp. 697–725, 2003.
- [14] D. J. Watts, *Small Worlds: The Dynamics of Networks between Order and Randomness*, Princeton University Press, Princeton, NJ, USA, 1999.
- [15] L. C. Fleming and M. Marx, "Managing creativity in small worlds," *California Management Review*, vol. 48, no. 4, pp. 6–27, 2006.
- [16] A. Hargadon, *How Breakthroughs Happen: The Surprising Truth About How Companies Innovate*, Bridging Small Worlds, Harvard Business School Press, Boston, Mass, USA, 2003.
- [17] Z. F. Chen and J. C. Guan, "The impact of small world on innovation: an empirical study of 16 countries," *Journal of Informetrics*, vol. 4, no. 1, pp. 97–106, 2010.
- [18] J. C. Guan and Y. Shi, "Transnational citation, technological diversity and small world in global nanotechnology patenting," *Scientometrics*, vol. 93, no. 3, pp. 609–633, 2012.
- [19] L. C. Fleming, C. King III, and A. I. Juda, "Small worlds and regional innovation," *Organization Science*, vol. 18, no. 6, pp. 938–954, 2007.
- [20] S. W. Hung and A. P. Wang, "Examining the small world phenomenon in the patent citation network: a case study of the radio frequency identification (RFID) network," *Scientometrics*, vol. 82, no. 1, pp. 121–134, 2010.
- [21] B. Verspagen and G. Duysters, "The small worlds of strategic technology alliances," *Technovation*, vol. 24, no. 7, pp. 563–571, 2004.
- [22] P. P. Chen and S. W. Gao, "Observer-based feedback stabilization of networked control systems with random packet dropouts," *Mathematical Problems in Engineering*, vol. 2013, Article ID 218682, 7 pages, 2013.
- [23] C. J. Carstens and K. J. Horadam, "Persistent homology of collaboration networks," *Mathematical Problems in Engineering*, vol. 2013, Article ID 815035, 7 pages, 2013.
- [24] D. J. Watts, "Networks, dynamics, and the small-world phenomenon 1," *American Journal of Sociology*, vol. 105, no. 2, pp. 493–527, 1999.
- [25] A. L. Barabási and R. Albert, "Emergence of scaling in random networks," *Science*, vol. 286, no. 5439, pp. 509–512, 1999.
- [26] R. Albert, H. Jeong, and A. L. Barabási, "Diameter of the world-wide web," *Nature*, vol. 401, no. 6749, pp. 130–131, 1999.
- [27] P. O. Seglen, "The skewness of science," *Journal of the American Society for Information Science*, vol. 43, pp. 628–638, 1992.
- [28] S. Redner, "How popular is your paper? An empirical study of the citation distribution," *European Physical Journal B*, vol. 4, no. 2, pp. 131–134, 1998.
- [29] L. A. N. Amaral, A. Scala, M. Barthélemy, and H. E. Stanley, "Classes of small-world networks," *Proceedings of the National Academy of Sciences of the United States of America*, vol. 97, no. 21, pp. 11149–11152, 2000.

- [30] D. J. Spielman, K. Davis, M. Negash, and G. Ayele, "Rural innovation systems and networks: findings from a study of Ethiopian smallholders," *Agriculture and Human Values*, vol. 28, no. 2, pp. 195–212, 2011.
- [31] T. Van der Valk, M. M. H. Chappin, and G. W. Gijssbers, "Evaluating innovation networks in emerging technologies," *Technological Forecasting and Social Change*, vol. 78, no. 1, pp. 25–39, 2011.
- [32] F. Hermans, D. Van Apeldoorn, M. Stuiver, and K. Kok, "Niches and networks: explaining network evolution through niche formation processes," *Research Policy*, vol. 42, no. 3, pp. 613–623, 2013.
- [33] G. P. Zhang and J. C. Guan, "The impact of small world on patent productivity in China," *Scientometrics*, vol. 98, no. 2, pp. 945–960, 2014.
- [34] J. G. March, "Exploration and exploitation in organizational learning," *Organization Science*, no. 21, pp. 71–87, 1991.
- [35] J. Choi, A. Sang-Hyun, and M. Cha, "The effects of network characteristics on performance of innovation clusters," *Expert Systems with Applications*, vol. 40, no. 11, pp. 4511–4518, 2013.
- [36] B. T. Asheim and A. Isaksen, "Regional innovation systems: the integration of local "sticky" and global "ubiquitous" knowledge," *Journal of Technology Transfer*, vol. 27, no. 1, pp. 77–86, 2002.
- [37] R. A. Boschma, "The rise of clusters of innovative industries in Belgium during the industrial epoch," *Research Policy*, vol. 28, no. 8, pp. 853–871, 1999.
- [38] M. P. Feldman, J. Francis, and J. Bercovitz, "Creating a cluster while building a firm: entrepreneurs and the formation of industrial clusters," *Regional Studies*, vol. 39, no. 1, pp. 129–141, 2005.
- [39] E. Giuliani and M. Bell, "The micro-determinants of meso-level learning and innovation: evidence from a Chilean wine cluster," *Research Policy*, vol. 34, no. 1, pp. 47–68, 2005.
- [40] N. Gilbert, P. Ahrweiler, and A. Pyka, "Learning in innovation networks: some simulation experiments," *Physica A: Statistical Mechanics and Its Applications*, vol. 378, no. 1, pp. 100–109, 2007.
- [41] R. Oakey, "Clustering and the R&D management of high-technology small firms: in theory and practice," *R and D Management*, vol. 37, no. 3, pp. 237–248, 2007.
- [42] L. Zhang, W. Zhang, M. Xiao, J. Xie, and Z. Wu, "Unravelling gene networks from steady-state experimental perturbation data," in *Proceedings of the 3rd International Conference on Bioinformatics and Biomedical Engineering (ICBBE '09)*, pp. 1–4, June 2009.
- [43] L. Zhang, X. Ju, Y. Cheng, X. Guo, and T. Wen, "Identifying Tmem59 related gene regulatory network of mouse neural stem cell from a compendium of expression profiles," *BMC Systems Biology*, vol. 5, p. 152, 2011.
- [44] L. Zhang, M. Xiao, Y. Wang, and W. Zhang, "Reverse engineering large-scale genetic networks: synthetic versus real data," *Journal of Genetics*, vol. 89, no. 1, pp. 73–80, 2010.
- [45] Z. W. Li, X. H. Yang, F. L. Jiang, G. Chen, G. Q. Weng, and M. Zhu, "Dynamically weighted clique evolution model in clique networks," *Mathematical Problems in Engineering*, vol. 2013, Article ID 182638, 6 pages, 2013.
- [46] M. Newman, S. H. Strogatz, and D. J. Watts, "Random graphs with arbitrary degree distributions and their applications," *Physical Review E-Statistical, Nonlinear, and Soft Matter Physics*, vol. 64, no. 2, Article ID 026118, pp. 261181–261187, 2001.
- [47] M. D. Humphries and K. Gurney, "Network "small-worldness": a quantitative method for determining canonical network equivalence," *PLoS ONE*, vol. 3, no. 4, Article ID e2051, 2008.
- [48] M. D. Humphries, K. Gurney, and T. J. Prescott, "The brainstem reticular formation is a small-world, not scale-free, network," *Proceedings of Biological Sciences*, vol. 273, no. 1585, pp. 503–511, 2006.
- [49] Office of Technology Assessment United States Congress, *Information Technology R&D: Critical Trends and Issues Summary*, U. S. Congress Office of Technology Assessment, New York, NY, USA, 1985.
- [50] X. H. Liu and T. Buck, "Innovation performance and channels for international technology spillovers: evidence from Chinese high-tech industries," *Research Policy*, vol. 36, no. 3, pp. 355–366, 2007.
- [51] H. A. David, *Order Statistics*, John Wiley, New York, NY, USA, 2nd edition, 1981.
- [52] J. Shin and Y. Park, "Evolutionary optimization of a technological knowledge network," *Technovation*, vol. 30, no. 11-12, pp. 612–626, 2010.
- [53] M. Orihata and C. Watanabe, "Evolutional dynamics of product innovation: the case of consumer electronics," *Technovation*, vol. 20, no. 8, pp. 437–449, 2000.